Utah State University

DigitalCommons@USU

International Symposium on Hydraulic
Structures

Jun 27th, 12:00 AM

Full Proceedings: Hydraulic Structures and Water System Management

International Association for Hydro-Environmental Engineering and Research

United States Society on Dams

Follow this and additional works at: https://digitalcommons.usu.edu/ishs

Part of the Hydraulic Engineering Commons

Utah State University
MERRILL-CAZIER LIBRARY

Hydraulic Structures and Water System Management-ISHS2016 in Perspective

B.M. Crookston[1], and B.P. Tullis[2]
[1]Schnabel Engineering, Inc.
1380 Wilmington Pike, Suite 100, West Chester, Pennsylvania 19382
USA
[2]Utah Water Research Laboratory
Utah State University
8200 Old Main Hill, Logan, Utah 84322-8200
USA
E-mail: bcrookston@gmail.com

ABSTRACT

Hydraulic structures are vital features in our water infrastructure, as they help meet the diverse and challenging demands of society, including conveyance, flood protection, environmental and ecological impacts, and systems management. Indeed, there are a number of challenges facing engineers today. This 6th IAHR International Symposium on Hydraulic Structures (ISHS2016) brought together domestic and international expertise from research, practice, and implementation in a forum for knowledge exchange and networking discussion on critical issues related to hydraulic structure research, performance, operations, maintenance, and community implications. It continued the rich tradition of this series by stimulating interest on advancement in the development and use of hydraulic structure elements and systems. Presentations and discussions were held on advanced tools, applications, and unique approaches needed to develop and implement more effective, environmentally sound, and robust solutions. It is believed that the proceedings of ISHS2016 provide applicable state-of-the-art expertise in hydraulic structure analysis and design to the engineering profession.

Keywords: *Hydraulic Structures, design, hydrodynamics, society demands, engineering challenges, water system management*

1. SYMPOSUM ORGANIZATION

The 6th International Symposium on Hydraulic Structures was held the 27th-30th of June, 2016 on the shores of the Columbia River at the Red Lion Hotel Janzten Beach in Portland, Oregon, USA. A total of about 136 individuals attended ISHS2016 from 18 countries and 5 continents. Organization efforts were handled by two committees: the local organizing committee and the international scientific committee. The Local Organizing Committee consisted of 5 individuals (see following page) who worked closely with IAHR and USSD to organize this event. Special acknowledgement is given to Mr. Larry Stephens who assisted with event planning. The international scientific committee oversaw the technical program and publication of the proceedings. ISHS2016 took place over 4 days. A workshop was held the first day, followed by two days of technical content, and a concluding field tour. Details are discussed in the following sections.

Local Organizing Committee ISHS2016

Martin J. Teal
Chair

Greg S. Paxson
Vice Chair

Brian M. Crookston
Member

Michael Phillips
Member

Eric Halpin
Member

1.1. Workshop on Hydraulics of Stepped Spillways

A full-day workshop on the hydraulics of stepped spillways was organized by Brian Crookston, Hubert, Chanson, and Sherry Hunt (see Fig. 1). The instructors for the workshop were Prof. Dr. Hubert Chanson (University of Queensland) and Dr. Sherry Hunt (USDA-ARS). About 40 individuals attended this specialty workshop, which included hydrodynamics of stepped spillways, applied research, design, operational records, and group discussions. Attendees were provided with a 344-page binder that included instructor slides (in color) and key references (provided in black and white).

Figure 1. Workshop instructors Prof. Dr. Hubert Chanson of UQ (left) and Dr. Sherry Hunt of USDA-ARS (right) (photos courtesy Brian Crookston)

1.2. Technical Presentations

Technical presentations were given Tuesday and Wednesday (see Fig. 2), with three parallel tracks held in the afternoons. Each presentation was 20 minutes in duration, which included a question and answer period at the

conclusion. A total of 136 individuals attended this portion of the technical program. 13 technical sessions were held, each with two moderators. Session moderators included:

Moderators ISHS2016

Steven Barfuss	William Fiedler	Mazurek	Bruce Savage
Daniel Bung	Kevin Griebenow	Joshua Mortensen	Vijay Singh
Hubert Chanson	Brian Hughes	Mario Oertel	Marty Teal
Kathleen Clarkson	Sherry Hunt	Gregory Paxson	Blake Tullis
Brian M. Crookston	Robert Janssen	Michael Pfister	Tony Wahl
Laurie Ebner	Arturo Leon Kerry	Michael Phillips	Brian Wahlin
Sébastien Erpicum			

Four invited keynote lectures were given:

- Prof. Dr. Anton Schleiss, EPFL and ICOLD President – Topic: Interaction of Hydraulic Structures with Air, Water, and Rock – the Challenges of Researchers and Designers.
- Prof. Dr. Vijay Singh, Texas A&M University – Topic: Hydraulic Structures and Entropy-based Modeling
- Mr. Philip Burgi, Retired U.S. Bureau of Reclamation – Topic: Challenges in Design and Use of Hydraulic Structures in Response to New Realities
- Mr. Thomas North, U.S. Army Corps of Engineers – Topic: Hydraulic Structures, the Future of Design

The technical program also included a specialty session on large river basin management and the role of hydraulic structures. Marty Teal served as moderator and provided an introduction to the session. Speakers included:

- Keil Neff, Tennessee Valley Authority – Topic: Tennessee River System
- Daniel Bunk, U.S. Bureau of Reclamation – Topic: Colorado River Basin
- Peter Dickerson, U.S. Army Corps of Engineers – Topic: Columbia River Basin

Figure 2. From left to right: keynote address by Prof. Dr. Anton Schleiss; specialty session by USACE, Reclamation, and TVA; technical presentation by Dr. Michael Pfister; and closing dinner and ceremony (photos courtesy Brian Crookston)

1.3. Field Tour

The final day of the symposium included a technical tour of Multnomah Falls and Bonneville Lock and Dam (see Fig. 3). Approximately 60 individuals attended the tour. The local organizing committee worked closely with key U.S. Army Corps of Engineers personnel; those directly involved in organizing this tour included Michael Phillips,

Brian M. Crookston, Gregory Webb, David Scofield, Peter Dickerson, William Fowler, Jessica Brownlee, Jerry Carroll, Robin Norris, Steven Barton, Brad Bird, Laila Berre, J. R. Inglis, and Greg Paxson. The field tour was restricted to areas open to the public and included the fish hatchery, the lock, a view of the gated spillway, the fish ladder system, and the hydropower house. During lunch, Certificates of Appreciation for David Scofield, Jerry Carroll, Greg Webb, Robin Norris, Laila Berre, and Michael Phillips were presented to those in attendance.

Figure 3. Multnomah Falls and Bonneville Dam Spillway (photos courtesy Brian Crookston)

1.4. Awards

The program also included a welcome reception and a closing ceremony and dinner. At the dinner, awards of appreciation were presented by Mr. Marty Teal and Dr. Blake Tullis to the workshop instructors, the keynote speakers, the specialty session speakers for their efforts and contributions to ISHS2016. The final award was presented to Dr. Brian Crookston for special acknowledgement of his many efforts in organizing ISHS2016.

2. SYMPOSIUM PROCEEDINGS

2.1. Peer Review Process

All papers published in the Proceedings and have been thoroughly peer-reviewed for technical quality and presented at ISHS2016. The Proceedings were published by Utah State University and is available open access at http://digitalcommons.usu.edu/ishs/2016/. Each manuscript includes the ISBN of the Proceedings as well individual direct object identifiers (DOI). Each manuscript is indexed by Scopus and Compendex. Each manuscript is available to users through the USU digital commons portal pursuant to a Creative Commons Attribution-NonCommercial CC BY 4.0 license. The ISHS2016 Scientific Committee was comprised of the following individuals:

International Scientific Committee ISHS2016

Brian M. Crookston
Chair

Blake P. Tullis
Vice Chair

Sébastien Erpicum
Member

Steven L. Barfuss
Member

Michael Pfister
Member

Hubert Chanson
Member

Daniel Bung
Member

Michele Palermo
Member

Rita F. Carvalho
Member

Salvatore A. Todaro
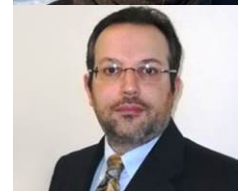Member

Robert Einhellig
Member

Stefano Pagliara
Member

Robert Janssen
Member

Antonio Miglio
Member

Under direction of this committee, a formal and rigorous single-blind peer-review was conducted for each submitted manuscript by the ISHS2016 International Scientific Reviewers. This panel was drawn from IAHR and USSD communities and other international and national experts in fields relevant to the themes of ISHS2016. This Panel was comprised of the following 65 individuals:

International Peer Review Panelists ISHS2016

John Ackers	Rajib Das	Kem Kadavy	Greg Paxson
Mahmud Amin	Subhasish Dash	Korey Kadrmas	Andy Peters
Steven Barfuss	Patrick Dent	Kylan Kegel	Michael Pfister
Kortney Brown	Laurie Ebner	Mohanad Khodier	Michael Phillips
Daniel Bung	Robert Einhellig	Pankaj Kumar	John Renholds
Juan Cabrera	Sébastien Erpicum	Xinquian Leng	Bruce Savage
David Campbell	Stefan Felder	Jorge Matos	Jessica Schmidt
Iacapo Carnacina	William Fiedler	Kerry Mazurek	Roshni T
Rita Carvalho	Travis Ford	Jonny Meyer	Marty Teal
Hubert Chanson	Chris Goodell	Antonio Miglio	Sal Todaro
Guy-Michel Cicereo	Bryan Heiner	Joshua Mortensen	Blake Tullis
Bert Clemmens	Valentine Heller	Dana Moses	Daniel Valero
Gaetano Crispino	Brian Hughes	Mario Oertel	Tony Wahl
Brian Crookston	Sherry Hunt	Giuseppe Oliveto	Brian Wahlin
Loring Crowley	Robert Janssen	Stefano Pagliara	Hang Wang
Jemie Dababneh	Charles Johnson	Michele Palermo	Jeremy Young
			Gangfu Zhang

The Call for Papers was issued in 2015; in response, 112 abstracts were received by the International Scientific Committee by 1 September 2015. All abstracts were reviewed; of those accepted, 91 full draft manuscripts were received. All received manuscripts were reviewed by a minimum of two reviewers, according to the criteria set established by the International Scientific Committee. Special acknowledgements to Dr. Daniel Bung, Dr. Michele Palermo, Dr. Blake Tullis, and Dr. Brian Crookston for their contributions to this effort.

Reviews were uploaded into the USU ISHS2016 repository through digital commons and made available to authors. The authors were sent instructions for access and requested to revise their manuscripts in accordance to the reviewers; comments and recommendations by the Scientific Committee Chair and Vice Chair. The final number of revised papers accepted for oral presentation was 77. However, not all manuscripts were presented in Portland during ISHS 2016 technical sessions; a requirement for publication in the Proceedings. As a result, only 70 manuscripts have been published and included in the Proceedings. In addition, extended abstracts by the four invited keynote lecturers and the three specialty-session speakers have been included with the 70 full manuscripts, to document their participation and important contribution to ISHS 2016. These 7 individuals were:

Prof. Dr. Anton Schleiss – Keynote Speaker   Mr. Peter Dickerson – Specialty Session
Prof. Dr. Vijay Singh, Keynote Speaker   Mr. Keil Neff – Specialty Session

Mr. Phil Burgi, Keynote Speaker   Mr. Daniel Bunk – Specialty Session
Mr. Thomas North, Keynote Speaker

The publication of the proceedings marked a significant contribution of this event, involving about 155 authors from 18 countries and 5 continents. Furthermore, the event website (www.ishs2016.com), to date, has received approximately 30,000 page views in about 13 months from 110 different countries.

2.2. Proceedings Reference

The Proceedings were published by Utah State University and is available open access at http://digitalcommons.usu.edu/ishs/2016/. The full bibliographic reference for the ISHS2016 symposium proceedings is:

Crookston, B.M. and Tullis, B.P. (Eds.) (2016). *Hydraulic Structures and Water System Management.* 6th IAHR International Symposium on Hydraulic Structures, Portland, OR, 27-30 June. ISBN 978-1-884575-75-4.

Each paper of the proceedings includes a cover sheet that includes the correct manuscript reference, such as:

Crookston, B.M. and Tullis B.P. (2016). Hydraulic Structures and Water Systems Management-ISHS2016 in Perspective. In B. Crookston & B. Tullis (Eds.), Hydraulic Structures and Water System Management. 6th IAHR International Symposium on Hydraulic Structures, Portland, OR, 27-30 June (pp. i-viii). doi: 10.15142/T3WW24 (ISBN 978-1-884575-75-4).

3. ACKNOWLEDGEMENTS

ISHS2016 would not have been possible without the generous and active involvement of the members of the local organizing committee, the international scientific committee, key individuals at U.S. Army Corps of Engineers including Mr. Steven Stockton, Mr. Sal Todaro, Mr. Eric Halpin, Mr. Peter Dickerson, Mrs. Robin Norris, and Mr. Michael Phillips. Key support was also provided by USSD President John Wolfhope, Executive Director Mr. Larry Stevens, and USSD Board Members. Sincere appreciation and thanks to the technical reviewers for valuable support during the review process. To keynote speakers, workshop instructors, specialty session presenters, all authors, presenters, and participants: thank you for your participation, support, and enthusiasm. Logistical support for the Proceedings was provided by Becky Thoms, head of digital initiatives at Utah State University – thank you for your patience and many efforts! Also, we wish to express appreciation to Brigitta Field of Utah State University for her assistance during the review process, and to Olivia Young undergraduate student at Cornell University for her efforts.

4. ORGANIZING INSTITUTIONS, SPONSORS, AND SUPPORTING ORGANIZATIONS
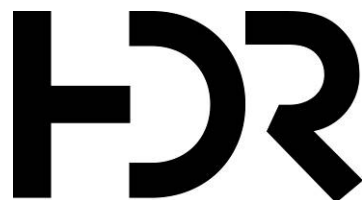
4.1. Organizing Institutions

4.2. Supporting Organizations

The following organizations (listed alphabetically) provided support and assistance for ISHS2016.

American Academy of Water Resources Engineer of ASCE
Association of State Dam Safety Officials
Bechtel Corporation
École Polytechnique Fédéral de Lausanne
FH Aachen University of Applied Sciences
FH Lübeck University of Applied Sciences
Instituto Superior Técnico
International Association of Hydro-environment Engineering and Research
International Congress on Large Dams
Schnabel Engineering
U.S. Army Corps of Engineers
U.S. Bureau of Reclamation
U.S. Federal Energy Commission Université de Liège
United States Society of Dams
University of Queensland
University of Pisa
University of Coimbra
USDA Agricultural Research Service
Utah State University
Utah Water Research Laboratory
West Consultants

4.3. Sponsors

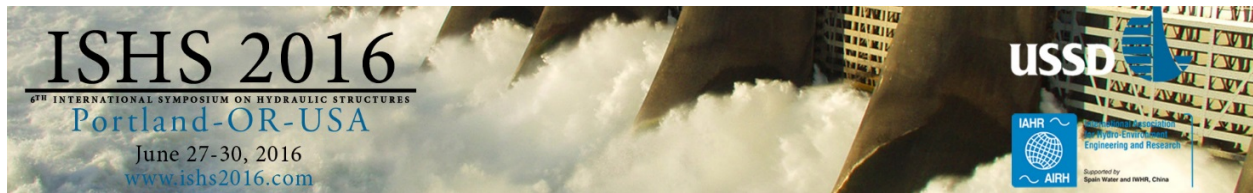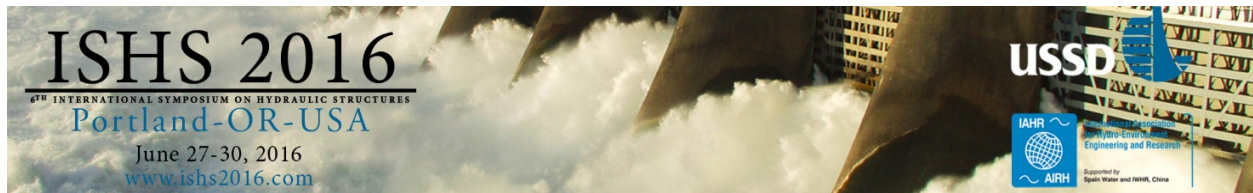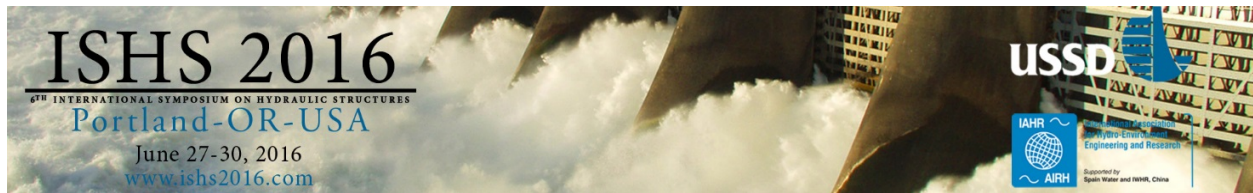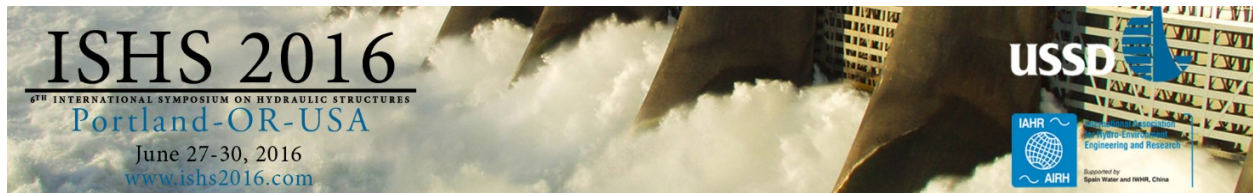Special thanks to our financial sponsors!

Table of Contents

ISHS 2016
6TH INTERNATIONAL SYMPOSIUM ON HYDRAULIC STRUCTURES
Portland-OR-USA
June 27-30, 2016
www.ishs2016.com

USSD

IAHR
Engineering and Research
AIRH
Supported by
Spain Water and IWHR, China

ISHS 2016
6TH INTERNATIONAL SYMPOSIUM ON HYDRAULIC STRUCTURES
Portland-OR-USA
June 27-30, 2016
www.ishs2016.com

USSD

IAHR
AIRH

A Remotely Controlled Siphon System for Dynamic Water Storage Management

Arturo S. Leon and Ali Alnahit
School of Civil & Construction Engineering
Oregon State University
Corvallis, OR 97331
USA
E-mail:arturo.leon@oregonstate.edu

ABSTRACT

Previous research has concluded that upland wetlands could be effective to control small floods, yet for large floods, their value may be greatly reduced as their storage capacity may be exceeded. A potential solution could be to release water from wetlands ahead of (e.g., few days before) a heavy rainfall event that is forecasted to produce flooding. In this case, the wetlands would be partially empty when this rainfall occurs. This work is part of a long-term project that aims at developing a decision support system (DSS) that will determine optimal flooding scenarios with dynamic management of wetlands using siphons. This DSS will incorporate simulation and optimization models with the aim of minimizing flooding losses. The success of this project hinges on the automation of a siphon that can be fully controlled (opened and closed) remotely and that can initiate the flow regardless of the opening time of the valve. To make possible the remote and dynamic release of water from wetlands, we designed and built a siphon system that can be remotely operated by a SCADA-type control. In practice, flood control managers would remotely open and close hundreds or thousands of this type of siphon simultaneously or in arrays. This first paper presents an experimental, numerical (3D), and analytical study of the initiation of siphon flows regulated with a downstream ball valve for rapid and slow valve openings. Three initial water depths in the upstream tank, four different final opening positions for the valve, and three opening times of the valve were investigated. The rate of depletion of the water surface in the upstream tank obtained numerically and analytically agreed well with the experimental results. Furthermore, the proposed siphon system was found to initiate the flow regardless of the opening time of the valve. Overall, the proposed siphon system could be an effective and inexpensive method to dynamically manage the storage of ponds and wetlands for flood control.

Keywords: Experiments, Flood Control, Ponds, Simulation, Siphon, Storage Management, Wetlands

1. INTRODUCTION

In recent decades, the significant and rapid increase of impervious surfaces has increased the risk of flooding. The effects of flooding on the environment are extensive and significant, resulting in an increase of loss of lives and damage to property and crops (NHC, 1997; NWS, 2013). The National Weather Service NWS (2013) reported that direct freshwater flood damages in the U.S. in 2011 and 2012 were $3.9 and $0.5 billion, respectively. There are two common approaches for reducing flood damages: structural and nonstructural measures. The traditional approach (structural measures) can reduce inundation of floodplains in several ways. For instance, reservoirs reduce downstream peak flow rates, levees and flood walls confine the flow of the rivers, and floodways help divert excess flow (ICE, 2002; De Bruijn et al., 2008; Breckpot et al., 2010). Although structural measures can be effective in reducing floods, they have a limited capacity to mitigate floods since only small parts of the watersheds (river and floodplains) are used for flood management.

Since flooding impacts have increased in frequency and severity, there is a new emphasis on evaluating nonstructural and watershed management approaches to determine whether they are effective strategies for flood prediction, prevention, and mitigation (e.g., Breckpot et al., 2010). A report from the Environmental Protection Agency (EPA, 1996) concluded that watershed approaches are the most effective approaches to address water resource challenges. This approach can help to maintain and mimic the natural hydrologic system (Buss, 2005).

Within a watershed, ponds and wetlands can play an important role in flood reduction, increasing water quality, and creating habitats for fauna (Hey and Philippi, 1995; Mitsch and Day, 2006). Ponds and wetlands could also increase flood storage by storing, holding, and percolating water (Costanza et al., 1989; Cole et al., 1997; Godschalk et al., 1999; Erwin,

2009). A study demonstrated that wetlands are able to absorb and hold greater amounts of floodwater than previously thought (Godschalk et al., 1999). A report of the United Nations (UNDP and UNISDR 2006) concluded that upland wetlands could be effective for small floods, but for large floods, their value may be greatly reduced as their storage capacity may be exceeded. In fact, during rainy seasons, mild to heavy rainfall events may occur continuously for days or weeks. In these situations, the benefit of wetlands and ponds for flood mitigation is limited because they may be full of water when a heavy rainfall that is forecasted to produce flooding occurs. One strategy for reducing flooding could be to release part of the water from wetlands and ponds ahead of (e.g., few days before) this heavy rainfall so that some storage is made available for the heavy rainfall.

To make possible the remote and dynamic release of water from ponds and wetlands, we designed and built a siphon system that can be remotely operated (Figure 1). This system (1) requires a simple anchoring of the siphon pipe; (2) can be remotely operated using a SCADA-type control, and can be activated through direct radio, via satellite, wireless radio, or a combination of these communications channels; and (3) does not need significant energy except for keeping the siphon pipe full and for actuating (opening and closing) the downstream valve. For this small requirement of energy, a small solar panel could be used. In practice, hundreds or thousands of these siphons could be operated simultaneously.
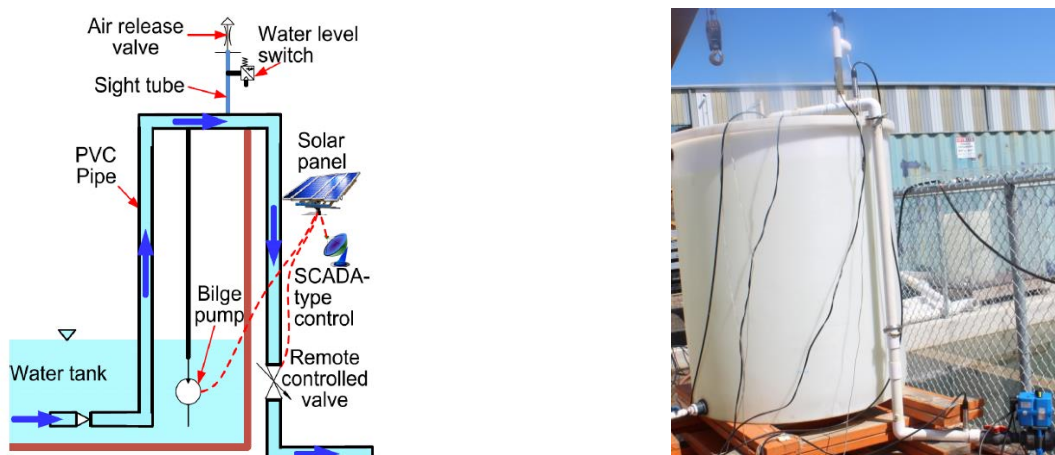
Figure 1. Left (schematic of siphon), Right (Laboratory setup). A video of our automated siphon in action can be seen at https://www.youtube.com/watch?v=LvdyFJlMwZI.

1.1. Siphon Flows

Siphons have been known since early times as simple and inexpensive devices for transferring water using gravitational force (Potter and Barnes, 1971; Garrett, 1991; Hughes, 2010). Siphons work due to the difference in pressure between the atmospheric pressure at the upper reservoir and the top of the siphon (negative gage pressure). This device can effectively remove water from reservoirs and ponds in remote locations. When set up properly, siphons usually require minimal oversight. One important characteristic of siphons is that, once the flow is started, a siphon requires no electricity to keep the liquid flowing up and out of the pond. The siphon will draw liquid out of the pond until the level falls below the intake, allowing air to break the siphon flow, or until the outlet of the siphon equals the level of the pond, whichever comes first. In addition to atmospheric pressure, the density of the liquid, and gravity, the maximum height of the crest in practical siphons is limited by the vapour pressure of the liquid. When the liquid pressure in the siphon drops below the liquid's vapor pressure, tiny vapor bubbles will begin to form at the siphon top, which may stop the flow. Overall, there is a limit for the height of the siphon pipe above the pond water surface elevation. For water at standard atmospheric pressure, the maximum siphon height is approximately 10.3 m, which is the definition of standard pressure. This equals the maximum height of a suction pump, which operates by the same principle. In practice, the maximum height should be smaller than 10.3 m due to head losses and because water will already evaporate as steam before the pressure drops to vacuum pressure (Garrett, 1991).

Considerable research has been conducted on siphons (Potter and Barnes, 1971; Garrett, 1991; Hughes, 2010; Binder and Richert, 2011). Cambiaghi and Schuster (1989) and Govi (1989) introduced a system using siphon principles as an emergency drainage treatment for landslides. Bryant and Jewell (1996) tested the hydraulic performance of a siphon system used to drain a small earthen dam, where comparisons were made between theoretical siphon hydraulic performance and

actual field performance. Leumas (1998) discussed the variables that should be considered in designing siphons and repairs to existing dams. Recently, siphon drainage combined with electropneumatic drainage has been the method for discharging ground water in Europe, especially in France (Mrvik and Bomont, 2011). More recently, Mrvik (2013), Cai et al. (2014), and Boatwright (2014) focused on maintenance and management requirements of siphons. Although there is vast research on siphon flows, the regulation of siphon flows using valves have not been fully explored yet.

This paper aims to investigate the performance of the proposed siphon system when regulated with a valve. In particular, we aim to investigate the reliability of this system to initiate the flow under various conditions. This paper is divided as follows. First, the experimental work is presented. Second, the numerical work is briefly described. Third, the analytical model is briefly introduced. Fourth, the results are presented and discussed. Finally, the key results are summarized in the conclusion.

2. EXPERIMENTAL WORK

The experimental setup consisted of eight components as shown in Figure 2: (1) an upstream tank with a diameter of 1.05 m and a height of 1.6 m; (2) 0.038 m diameter and 4.34 m long PVC pipe; (3) a check valve at the pipe inlet; (4) a submersible pump (200 gallons per hour (GPH)) used to prime the pipe, if necessary; (5) an air valve used to release the air from the system when priming the pipe; (6) an actuator valve used to control the opening/closing of the downstream valve. The actuator and submersible pump are operated using a solar panel (7). The operation of the actuated valve and the air valve and data collection are accomplished using a LabVIEW system (8). Figure 3 shows the dimensions of the tank and siphon pipe. Three pressure transducers (UNIK 5000) with a resolution of ±3.2 mm were installed at three different locations indicated in Figure 4. The sampling rate for the pressure transducers was set to 36 Hz.
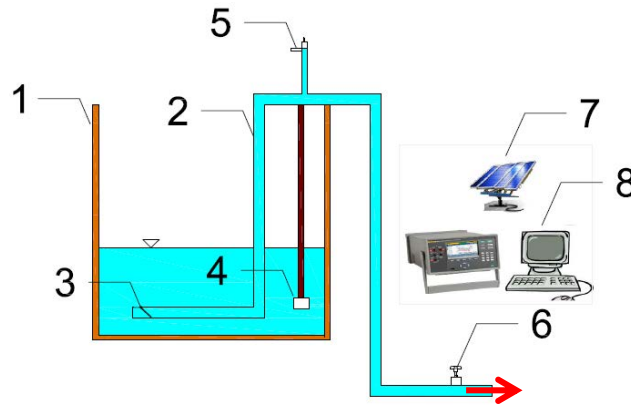
Figure 2. Experimental components: (1) upstream tank; (2) PVC pipe; (3) check valve ; (4) small submersible pump (for priming only); (5) air valve; (6) actuated valve; (7) solar panel (energy); (8) data acquisition system.
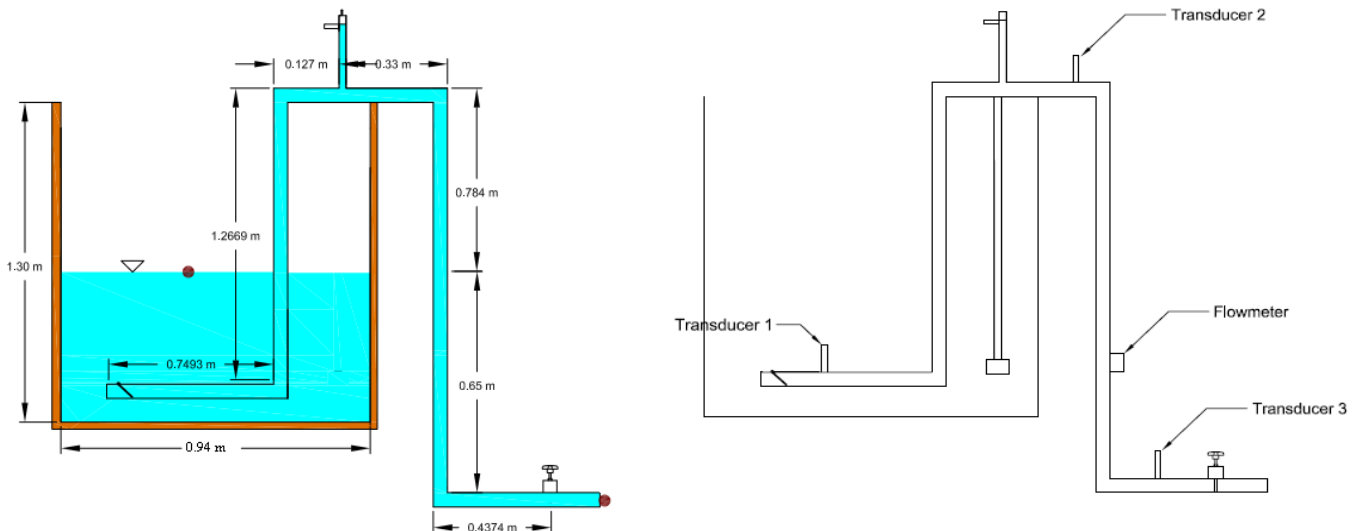
Figure 3. Dimensions of the tank and siphon pipe   Figure 4. Locations of pressure transducers and flowmeter

2.1. Measurement Conditions

The experiments were conducted for three initial water depths in the tank, $H_A=1.14m$, $H_B=0.60m$, and $H_C=0.30m$ (see Figure 5). For each water depth, four different final opening positions for the valve were tested (25%, 50%, 75%, and 100% (fully-open)). The percentages of valve opening refer to the ratio of opening area to the cross-sectional area of the pipe. For instance, a 25% opening means that the area of opening is 25% of the pipe's cross-sectional area. Additionally, three opening times of the valve were tested. The first opening time was 0.1s, which corresponds to a fast opening. The second and third opening times were 30 and 60s, which correspond to a slow opening. Finally, pressure measurements were made for each experiment. Every experiment was repeated at least four times to ensure consistency of results.

2.2. Signal Filtering

Filters of some sort are essential in data acquisition systems to remove selected frequencies from an incoming signal and minimize noise (Holloway, 1958). In this paper, a low pass filter was used to smooth noisy data. The low pass filter removes the corrupting high frequency noises in the data. In order to eliminate unwanted response, the pressure data acquired at 36Hz was filtered using a Chebyshev low-pass filter (MATLAB), which effectively removed frequencies above 4 Hz. An example of the original time series and filtered data is shown in Figure 6. It is pointed out that all experimental figures after Figure 6 display filtered data only.
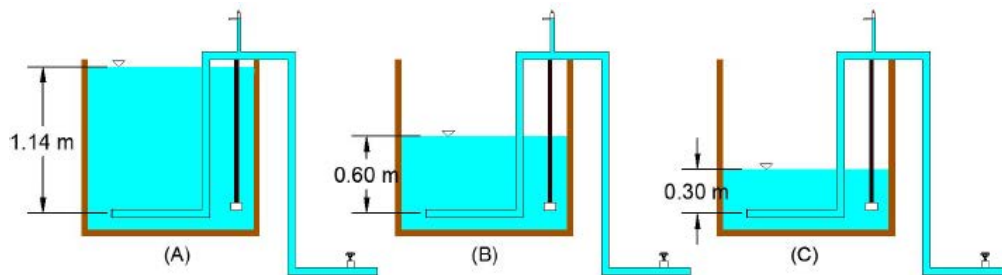
Figure 5. Initial water depths tested: (A) tank near full; (B) tank near half full; (C) tank near 1/3 full
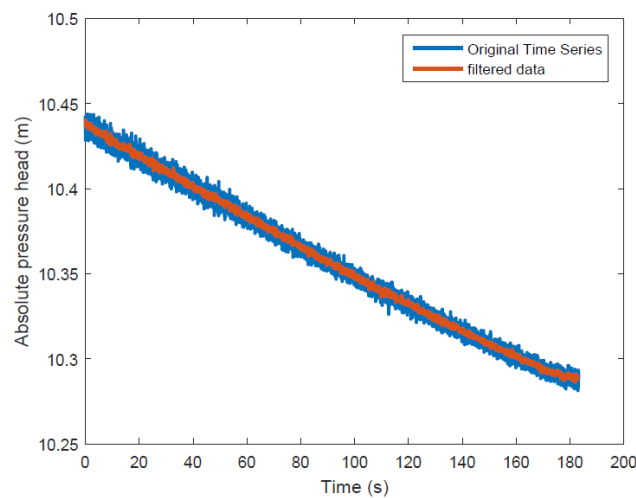
Figure 6. Filtered and unfiltered absolute pressure head versus time for $H = 0.3m$, 25% valve opening and opening time = 0.1s.

3. THREE-DIMENSIONAL NUMERICAL MODELING

The numerical modelling was performed using the 3D Computational Fluid Dynamics (CFD) model Star-CCM+ v7.0. The overall process to simulate the siphon flow consisted of (1) using 3D-CAD model to create a 3D solid geometry; (2) building the mesh; (3) selecting appropriate boundary conditions; (4) selecting the numerical model and parameters of the simulation; (5) ensuring grid convergence; and (6) visualizing the results. A brief discussion of the 3D numerical model is presented next.

To account for the air and water phases, the Volume of Fluid (VOF) method was used. The VOF method solves a single set of momentum equations for both phases. The realizable k-ε model was used to simulate the turbulent flow. As shown in Figure 7, the computational domain of the numerical experiment involved two cylindrical tanks with diameters of 1.06 m (upstream tank) and 0.80 m (downstream tank). The computational domain was extended beyond the outlet of the siphon represented by the second tank. This extension was made to avoid specifying a boundary condition at the outlet of the pipe. To represent the opening of the downstream ball valve in the physical experiment, various valve positions at intermediate times were specified in Star-CCM+. Furthermore, the mesh size was refined around the pipe inlet, outlet, and elbows. A surface wrapper was used to refine the intersecting parts of the system (e.g., the siphon pipe with the downstream valve).
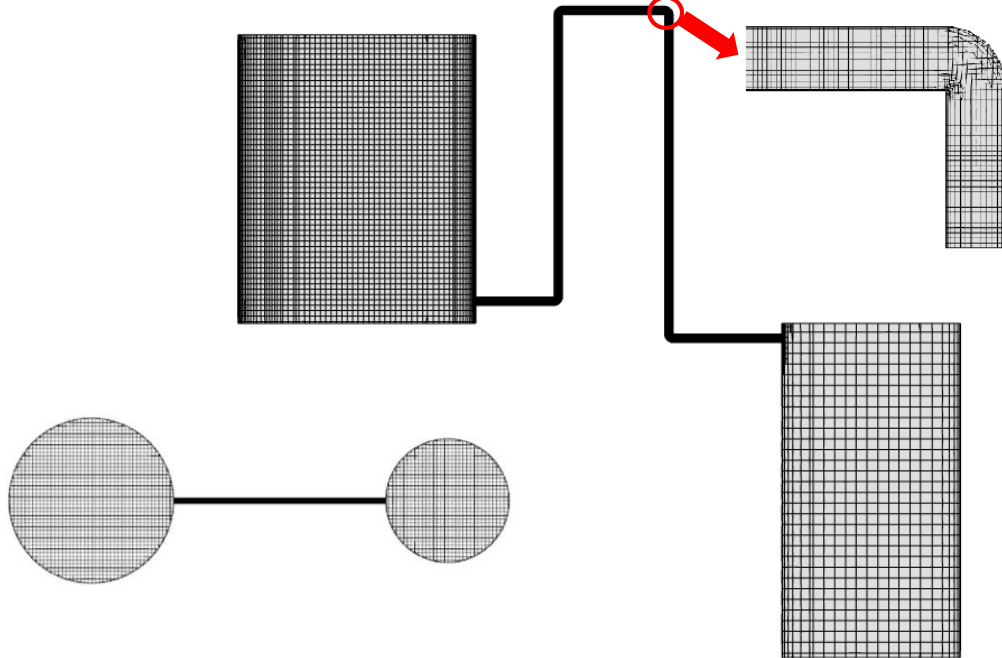
Figure 7. Plan- and side view of computational mesh

For the boundary conditions, the non-slip wall boundary condition was imposed at the pipe wall. Also, the pressure at the top surface of both cylindrical tanks was set to atmospheric pressure. As shown in Figure 8, the pipe was initially primed (e.g., filled with stagnant water), and the initial water surface elevation at the downstream tank was below the elevation of the pipe outlet. The latter was to avoid interfering with the flow at the siphon outlet. The downstream valve was initially closed and started to operate to the desired position (e.g., open) at t (time) = 0.

Due to space limitations, only two snapshots of pressure and velocity for the inlet and outlet regions of the siphon at $t = 500$ s for $H = 0.3$ m, opening time = 0.1 s, and $O = 25\%$ are shown in Figures 9 and 10. As can be observed in Figures 9 and 10, the flow is pretty much one-dimensional except at the bends and around the inlet and outlet regions. This may explain why the one-dimensional analytical model agrees very well with the 3D model and the experiments, as will be shown later.
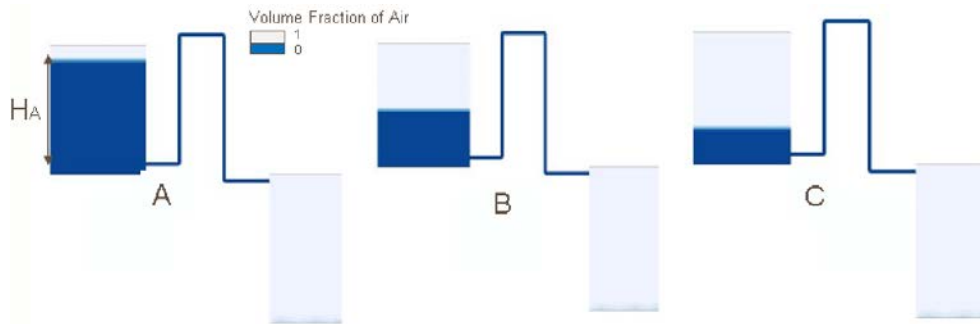
Figure 8. Initial water levels in the tanks used in CFD model
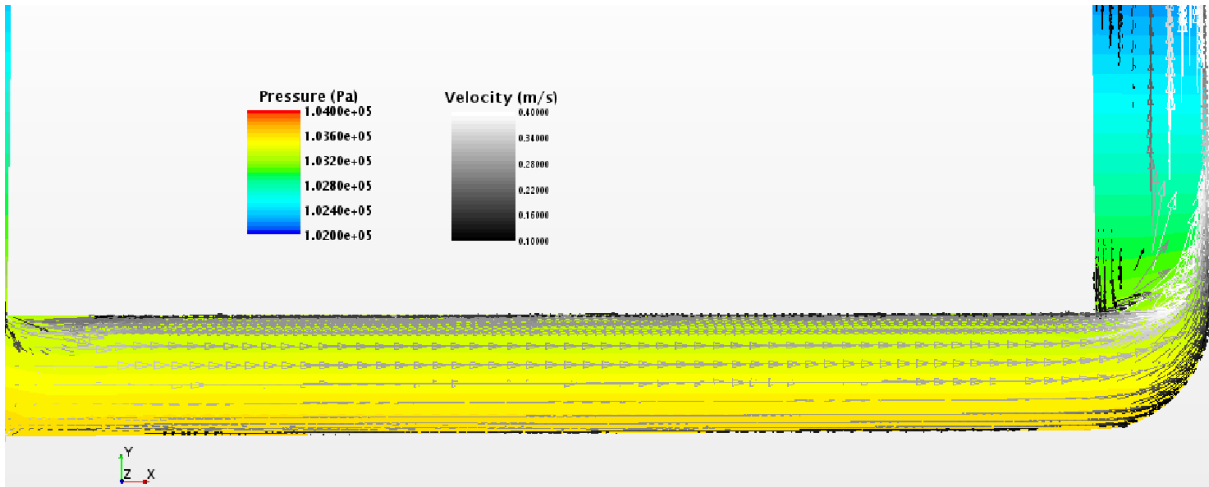
Figure 9. Snapshot of pressure and velocity at the siphon inlet at $t = 500$ s ($H = 0.3$ m, opening time = 0.1 s, and $O = 25\%$)
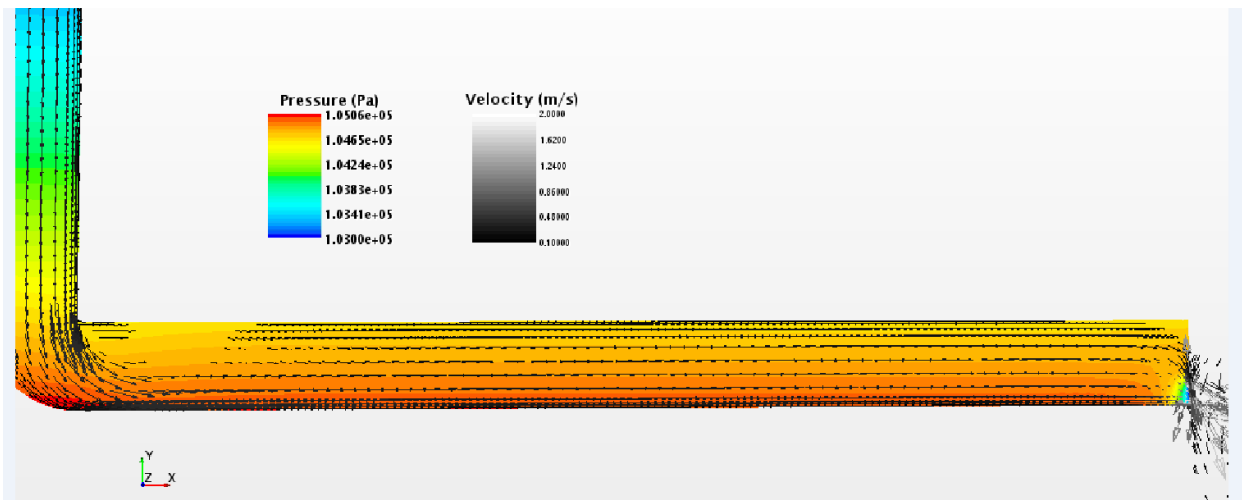
Figure 10. Snapshot of pressure and velocity at the siphon outlet at $t = 500$ s ($H = 0.3$ m, opening time = 0.1 s, and $O = 25\%$)

4. ANALYTICAL SOLUTION

Siphon flows can be analyzed using the energy equation, which is given by the following equation:

$$Z_a + \frac{P_a}{\gamma} + \frac{V_a{}^2}{2g} = Z_b + \frac{P_b}{\gamma} + \frac{V_b{}^2}{2g} + h_f + h_m \qquad (1)$$

where, Z_a is the elevation of the pond water surface (point "a"), Z_b is the elevation of the pipe centerline at the outlet (point "b"), P_a is the pressure at the pond water surface, P_b is the pressure at point "b", V_a is the velocity at the pond water surface, V_b is the velocity at point "b", γ is the specific weight of water, g is the gravitational acceleration, h_f is the total head loss due to pipe friction, and h_m is the sum of local head losses. Because the velocity head at point "a" is relatively small, the velocity at the outlet (point "b") can be written as

$$V_b = \sqrt{2g\left(Z_a - Z_b - h_f - h_m\right)} \qquad (2)$$

To estimate the friction losses, the Darcy-Weisbach formula was used:

$$h_f = \frac{fLV^2}{2gD} \qquad (3)$$

where f is the pipe friction factor, L is the pipe length, V is the pipe cross-sectional averaged flow velocity and D is the diameter of the pipe. The local head losses are estimated as

$$h_m = \sum k_i \frac{V^2}{2g} \qquad (4)$$

where k is the head loss coefficient for the particular pipe fitting (i.e., elbows, check valve, ball valve).

5. RESULTS AND DISCUSSION

5.1. Experimental work

A total of 144 tests were conducted considering three different initial water depths (H), four different final opening positions for the valve (O), and three opening times of the valve. Each experimental condition was repeated at least four times. Fig. 11 shows the measured absolute pressure head versus time at the locations indicated in Figure 4 when the initial water depth in the tank was 0.3m, the final position for the valve opening was 25%, and the opening time was 0.1 s (fast opening). As can be observed in this figure, the pressure at the inlet is higher than that in the outlet at all times. Also note in this figure that the absolute pressure in the siphon top remains below atmospheric pressure (~ 10.3 m of water head) at all times. Thus, the gage pressure at the siphon top is negative at all times. Fig. 12, 13, and 14 show traces of the absolute pressure head at the siphon top, siphon inlet, and siphon outlet for an initial water depth in the tank of 0.3 m, fast valve opening (0.1s) and various final positions for the valve opening. As expected, the greater the final opening area of the valve, the smaller the pressure head at all locations. The latter is because the greater is the hydraulic area, the greater is the flow discharge (and head losses), and hence the smaller is the pressure head at all locations.
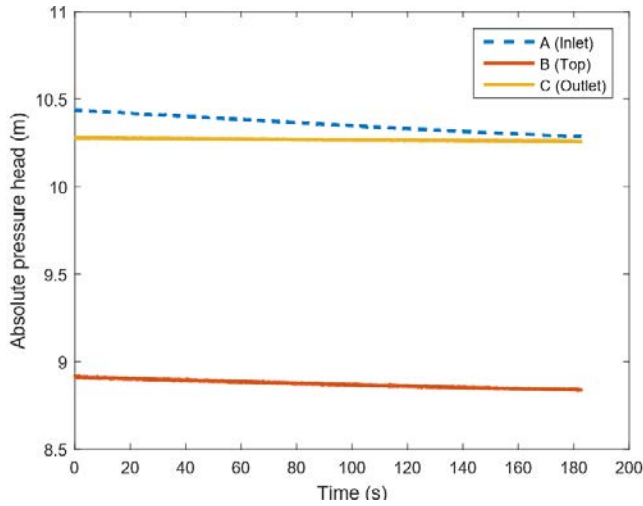
Figure 11. Absolute pressure head versus time for $H = 0.3$ m, $O = 25\%$, opening time = 0.1 s
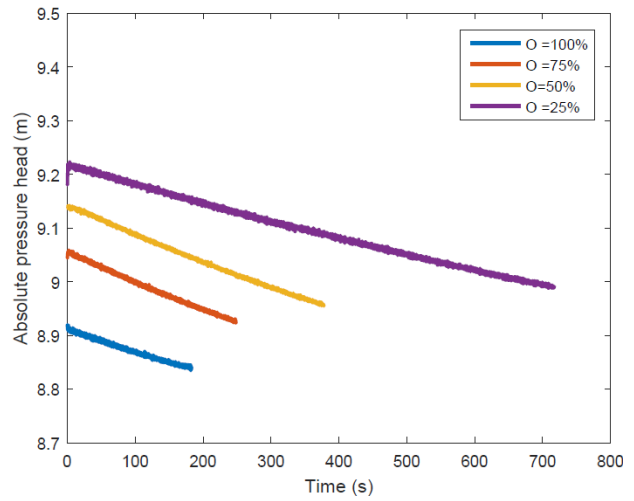
Figure 12. Absolute pressure head versus time at siphon top for $H = 0.3$ m, opening time = 0.1 s and four final positions for the valve opening (O)

Figures 15 and 16 show traces of absolute pressure head at siphon top and siphon outlet for slow openings (30 and 60 s). The initial water depth in the tank was 0.3 m, and the final position for the valve opening was 100% open (fully-open valve). As can be seen in these figures, the pressure decreases with time, indicating that the siphon still initiates the flow for slow openings. We have also tested the siphon for opening times of 5 minutes (not reported here), and the siphon still initiates the flow. Overall, the siphon initiates the flow regardless of the opening time of the valve.

5.2. Comparison between Analytical, Numerical and Experimental Results

Due to space limitations, only the comparison for the absolute pressure head trace at the siphon top for $H = 0.3$m, opening time = 0.1 s, and $O = 75\%$ is shown in Figure 17. As observed in Figure 17, the drainage rate obtained analytically and numerically agrees very well with the experimental results. The results (not shown here) are similar for other conditions. The reader may notice in this figure that the results of the 3D numerical model display a large fluctuation of the pressure right after the siphon flow is started. This relatively large pressure fluctuation, which lasts for few seconds, occurs due to the sudden increase or decrease of the velocity (e.g., Leon et al., 2007, 2008). As shown earlier for the CFD model (Figures 9 and 10), the flow in the siphon is pretty much one-dimensional except at the bends and around the inlet and outlet regions. This may explain why the one-dimensional analytical model agrees very well with the 3D model and the experiments. Thus, a one-dimensional analytical model can be used for predicting the draining rate of ponds with very good accuracy.
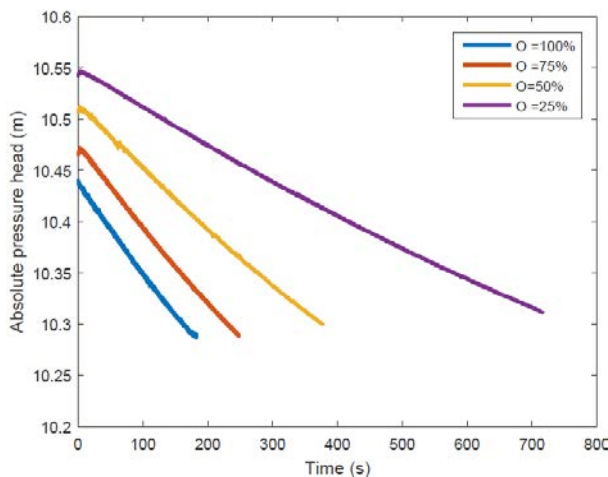
Figure 13. Absolute pressure head versus time at siphon inlet for $H = 0.3$ m, opening time = 0.1 s and four final positions for the valve opening (O)
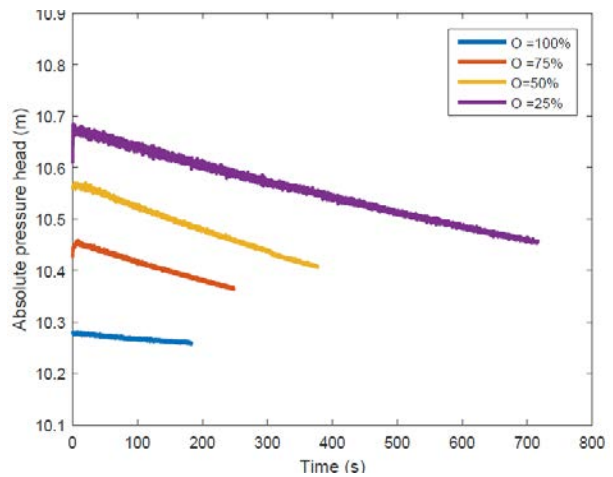
Figure 14. Absolute pressure head versus time at siphon outlet for $H = 0.3$ m, opening time = 0.1 s and four final positions for the valve opening (O)
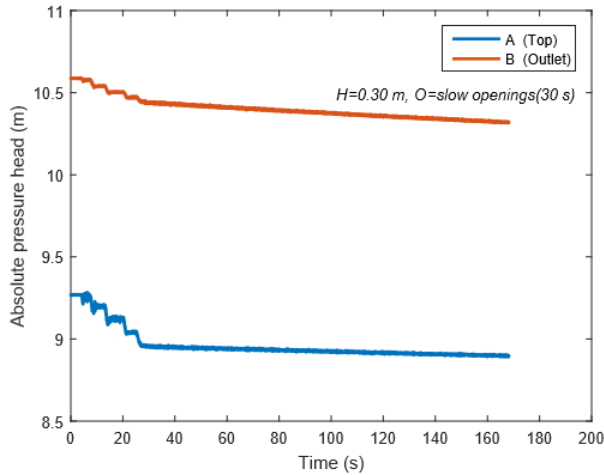
Figure 15. Absolute pressure head traces at siphon top and outlet when the valve is fully opened in 30 s ($H = 0.3$ m).
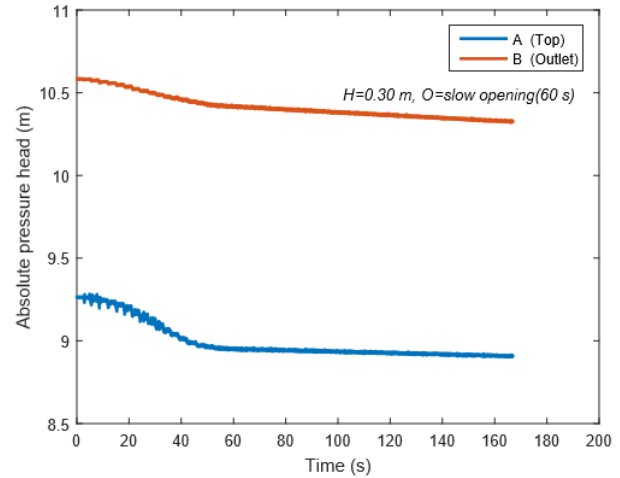
Figure 16. Absolute pressure head traces at siphon top and outlet when the valve is fully opened in 60 s ($H = 0.3$ m).
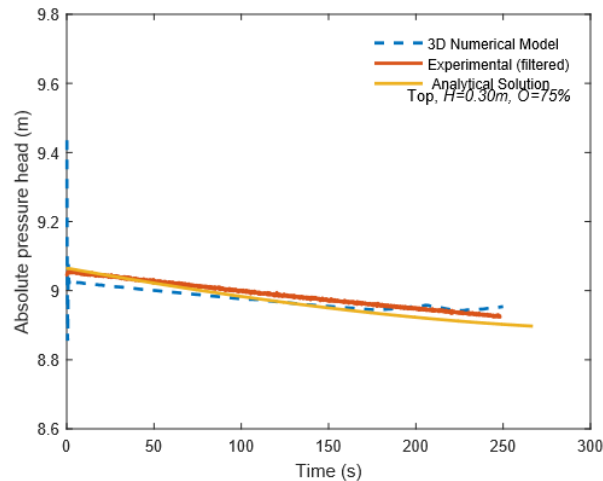
Figure 17. Comparison between numerical, experimental and analytical results of absolute pressure head traces at the siphon top ($H = 0.3$m, opening time = 0.1 s, and $O = 75\%$)

6. CONCLUSION

The initiation of siphon flows regulated with a downstream ball valve for rapid and slow valve openings were investigated analytically, numerically, and experimentally. Three initial water depths in the upstream tank, four different final opening positions for the valve, and three opening times of the valve were investigated. The key results are as follows:

- The rate of depletion of the water surface in the upstream tank obtained numerically and analytically agreed well with the experimental results.
- The flow in the siphon is pretty much one-dimensional except at the bends and around the inlet and outlet regions. This may explain why the one-dimensional analytical model does a very good job predicting the drainage rate.
- The remotely-controlled siphon system was found to initiate the flow regardless of the opening time of the valve. However, small leaks in the pipe may depressurize the siphon pipe and stop the flow.

Overall, the proposed siphon system could be an effective and inexpensive method to dynamically manage the storage of ponds and wetlands for flood control. However, each project site may have specific challenges that need to be considered. For example, the inlet of a siphon must be designed to prevent sediments from entering the pipe.

7. REFERENCES

Binder, P-M. and Richert, A. (2011). The explicit siphon. Physics Education, 46(6):710-711.

Boatwright, J. D. (2014). Air-regulated siphon spillways: Performance, modeling, design, and construction., M.S. Thesis Clemson University, 74 pages.

Breckpot, M., Blanco, T. B., and De Moor, B. (2010). Flood control of rivers with nonlinear model predictive control and moving horizon estimation. *In Proceedings of 49th IEEE Conference on Decision and Control, Atlanta, GA,* pages 6107-6112.

Bryant, S. (1996) and Jewell C.D. Analysis of siphon lake drain performance for a small earthen dam. *In Proceedings of Dam Safety, Seattle, Washington*, Page 12.

Buss, L. S. (2005). Nonstructural flood damage reduction within the US Army Corps of Engineers. Journal of Contemporary Water Research & Education, 130:26-30.

Cai, Y.-L., Sun, H.-Y., Shang, Y.-Q., and Xiong, X.-L. (2014). An investigation of flow characteristics in slope siphon drains. Journal of Zhejiang University SCIENCE A, 15(1):22-30.

Cambiaghi, A. and Schuster, R. (1989). Landslide damming and environmental protection - a case study from northern Italy. *In Proceedings of 2nd International Symposium on Environmental Geotechnology*, *Shanghai, China,* volume 1, pages 381-385.

Cole, C. A., Brooks, R. P., and Wardrop, D. H. (1997). Wetland hydrology as a function of hydrogeomorphic (HGM) subclass. Wetlands, 17(4):456-467.

Costanza, R., Farber, S. C., and Maxwell, J. (1989). Valuation and management of wetland ecosystems. Ecological economics, 1(4):335-361.

De Bruijn, K., Klijn, F., McGahey, C., Mens, M., and Wolfert, H. (2008). Long-term strategies for flood risk management: scenario definition and strategic alternative design. *FLOODsite Consortium*, T14 08 01.

EPA (1996). Why watersheds? Technical report, Environmental Protection Agency. EPA800-F-96-001, February 1996.

Erwin, K. L. (2009). Wetlands and global climate change: the role of wetland restoration in a changing world. Wetlands Ecology and management, 17(1):71-84.

Garrett, R. E. (1991). Principles of siphons. Journal of the World Aquaculture Society, 22(1):1-9.

Godschalk, D., T. Beatley, P. Berke, D. Brower, and E. Kaiser (1999). Natural hazard mitigation: Recasting disaster policy and planning. Island Press, s, Washington, DC.

Govi, M. (1989). The 1987 landslide on Mount Zandila in the Val-tellina, Northern Italy. *Landslide News*, 3:1-3.

Hey, D. L. and Philippi, N. S. (1995). Flood reduction through wetland restoration: The upper Mississippi river basin as a case history. Restoration Ecology, 3(1):4-17.

Holloway, J. L. (1958). Smoothing and filtering of time series and space fields. Advances in geophysics, 4:351-389.

Hughes, S. W. (2010). A practical example of a siphon at work. Physics Education, 45(2):162-166.

ICE (2002). Learning to live with rivers. Report, Institution of Civil Engineers (ICE), London, UK.

Leon, A. S., Ghidaoui, M. S., Schmidt, A. R., and García, M. H. (2007). "An efficient finite-volume scheme for modeling water hammer flows." *Contemporary Modeling of Urban Water Systems*, Monograph 15, W. James (Editor in Chief).

Leon, A. S., Ghidaoui, M. S., Schmidt, A. R. and Garcia, M. H. (2008) "An efficient second-order accurate shock-capturing scheme for modeling one and two-phase water hammer flows." *Journal of Hydraulic Engineering*, 134(7), 970-983.

Leumas, J. (1998). To siphon or not to siphon: That is the question (among others) - A repair history of the Crossgate Dam, ASDSO Annual Conference, Las Vegas, 1998.

Mrvik (2013). Experience with drainage and ground stabilisation by siphon drains in Slovakia. In Proceedings of the 5th International Young Geotechnical Engineers' Conference, volume 2, pages 36-39.

Mrvik, O. and Bomont, S. (2011). Experience with treatment of road structure landslides by innovative methods of deep drainage. *Landslides*, pages 79-90.

Mitsch, W. J. and Day, J. W. (2006). Restoration of wetlands in the Mississippi-Ohio-Missouri (MOM) river basin: Experience and needed research. Ecological Engineering, 26(1):55-69.

NHC (1997). Assessing losses and costs over the last 20 years. Report, National Hurricane Center (NHC).

NWS (2013). May 201, Oklahoma tornadoes and flash flooding. Report, National Weather Service (NWS), Silver Spring, Maryland.

Potter, A. and Barnes, F. H. (1971). The siphon. Physics Education, 6(5), pages 362-366.

UNDP and UNISDR (2006). Integrating disaster risk reduction and climate change adaptation into ecosystem management of coastal and marine areas in south Asia. Technical report, UNDP.

Turbulence and Energy Dissipation in the Developing Non-Aerated and the Fully-Developed Aerated Flows on a Stepped Spillway

G. Zhang[1] and H. Chanson[1]
[1]Dept. of Civil Engineering
The University of Queensland
QLD 4072
Australia
E-mail: h.chanson@uq.edu.au

ABSTRACT

Stepped spillways are characterised by highly turbulent air-water flows and a large rate of energy dissipation compared to smooth chutes. Herein, detailed measurements were performed in both the developing non-aerated and fully-developed air-water flow regions on a large 1V:1H stepped spillway model. In the developing flow region, large total pressure fluctuations and turbulence intensities were recorded next to the pseudo-bottom. Downstream of the inception point, large total pressure fluctuations were recorded, which were mainly induced by density fluctuations. The water turbulence intensities in the air-water flow region did not differ significantly from those in the developing flow region. The steps generated significant form loss, amounting to about 50% of the upstream total energy regardless of discharge. Similar rates of energy dissipation and friction factors were found between the developing non-aerated and fully-developed air-water flow regions. The energy dissipation on stepped chutes was found to be sensitive to the chute slope and relatively little affected by the air-bubble diffusion.

Keywords: Stepped spillways, energy dissipation, turbulence intensity, total pressure, macro-roughness, physical modelling.

1. INTRODUCTION

Stepped spillways have been used as flood release structures for several centuries (Chanson 2001). The steps act as macro-roughness elements and greatly enhance the rate of energy dissipation. In practice, the design unit discharges on stepped chutes are typically large and correspond to the skimming flow regime (Matos 2000). In skimming flows, the water skims over the pseudo-bottom formed by the step edges and usually incorporates strong air-entrainment and turbulent mixing. The interplay between entrained air bubbles and coherent structures remains a challenging research topic (Chanson and Toombes 2002, Bung 2009).

It is the aim of this work to investigate the turbulence properties and energy dissipation performances of skimming flows and understand how they are affected by the air-bubble diffusion. New experiments were conducted in a large-size stepped spillway model (1V:1H) at the University of Queensland with a focus on skimming flows. The total pressure and two-phase flow properties at step edges were measured at the channel centreline via simultaneous sampling of a MEMS-based total pressure transducer and a phase-detection probe. The water-phase turbulence intensities are presented. The results suggest that the chute performances are little affected by air-bubble diffusion but may be sensitive to the geometry of the steps.

2. EXPERIMENTAL FACILITY AND INSTRUMENTATION

New experiments were performed in a large-size stepped spillway model at the University of Queensland. The experimental setup is sketched in Figure 1. The facility consisted of 12 flat steps made with smooth marine ply, each with dimensions 0.1 m length × 0.1 m height × 0.985 m width. The facility was previously used by Zhang and Chanson (2015). Total pressure measurements were taken in both the developing clear-water and fully-developed aerated flow regions at step edges along the chute centreline using a MEMS-based total pressure transducer with a

silicon diaphragm. The pressure transducer had an inner diameter of 1 mm and a precision of 0.5% (full scale). In the aerated flow region, the total pressure transducer was mounted beside a dual-tip phase-detection probe (0.25 mm inner diameter) that recorded the two-phase flow properties. The transverse separation between the two probes was 6.5 mm. The sampling rate and duration were 5 kHz per sensor and 60 s in the developing flow, and 5 kHz per sensor and 180 s in aerated flow region, following Wang et al. (2014). The vertical probe adjustment was controlled by a Mitutoyo™ digital scale with an accuracy of ±0.01 mm. The facility was operated at high Reynolds numbers ($Re = 4q/v$), up to 8.8×10^5. The experimental flow conditions are summarised in Table 1, where Q is the discharge, d_c is the critical flow depth, h is the vertical step height, and Re is the Reynolds number.

Table 1. Summary of experimental flow conditions

Study type	Q (m³/s)	d_c/h	Location	Re
Developing flow	0.083 – 0.216	0.9, 1.1, 1.3,	Step edges 3 – 9	$3.9 \times 10^5 - 8.8 \times 10^5$
Aerated flow		1.5, 1.7	Step edges 5 – 12	
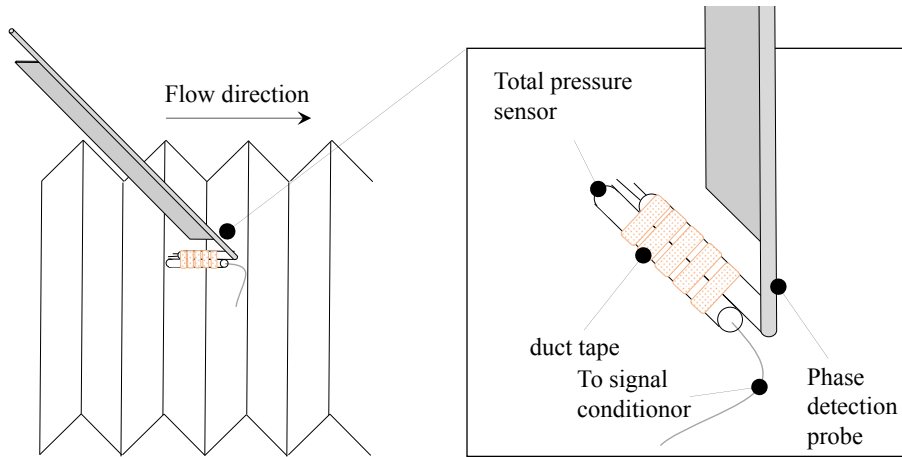
Figure 1. Sketch of experimental setup on the stepped chute at the University of Queensland

3. DEVELOPING FLOW REGION

Total pressure measurements were conducted with the MEMS total pressure transducer in the developing flow region at several step edges upstream of the inception point of free-surface aeration (Table 1). The probe was aligned in the direction of the main flow and recorded the instantaneous total pressure, expressed as

$$\tilde{P}_t = \frac{1}{2}\tilde{\rho}\tilde{U}^2 + \tilde{P}_s \tag{1}$$

where P_t is the total pressure, P_s is the static pressure, ρ is the fluid density, and U is the streamwise fluid velocity. Here and onwards, the overhead tilde (~), capital letters, and lower case letters are used to denote instantaneous, time-averaged, and fluctuating properties, respectively. At each measurement location, the time-averaged total head may be expressed as

$$H_t = \frac{P_t}{\rho_w g} + (1-C)z \tag{2}$$

where ρ_w is the water density, g is the gravity constant, C is the time-averaged void fraction, and z is the vertical elevation above the spillway toe. The dimensionless total head distributions are shown for two step edges in Figure 2, where y is the normal distance from the pseudo-bottom, δ is the boundary layer thickness (obtained from Zhang

and Chanson 2015), and $H_{t,crest}$ is the upstream total head measured with respect to the spillway toe. The data showed two distinct regions: a turbulent boundary layer in which significant viscous dissipation takes place ($y/\delta \le 1$) and a potential flow region above governed by Euler equations ($y/\delta > 1$). The boundary between these two regions is shown with a horizontal dotted and dashed line in Figure 2.

(A) Step edge 3   (B) Step edge 4
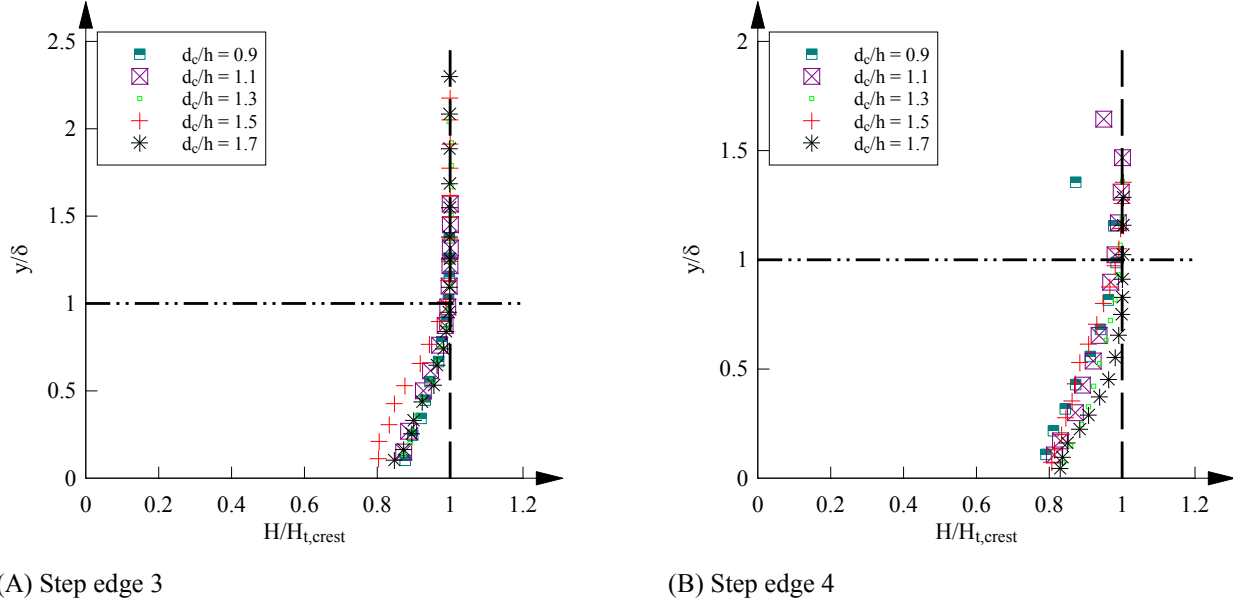
Figure 2. Total head distributions in the developing flow region – Flow conditions: d_c/h = 0.9, 1.1, 1.3, 1.5, 1.7; θ = 45°, h = 0.1 m

The boundary layer region ($y/\delta \le 1$) is characterised by strong boundary-induced turbulent fluctuations and significant viscous dissipation. The lowest order descriptor of the turbulence properties is the turbulence intensity, defined in terms of the local water velocity U_w:

$$Tu = \frac{<u_w^2>^{0.5}}{U_w}$$

(3)

where $<>$ is the averaging operator. When the static pressure fluctuation (p_s) is small and the turbulent water velocity data (u_w) follow a normal distribution, the turbulence intensity may be derived from Equation (1) by subtracting its mean from the original Equation (1), squaring both sides and taking the mean, dividing by $\rho_w U_w^2$ and square-rooting the result. The development yields a relationship between the turbulence intensity and the total pressure fluctuations:

$$Tu = \frac{<p_t^2>^{0.5}}{\rho_w U_w^2}$$

(4)

Arndt and Ippen (1970) derived the same equation and suggested a maximum error of about 5% for a turbulence intensity of 10%. Figure 3 presents typical turbulence intensity distributions in skimming flows at step edges 3 and 4. The streamwise velocity (U_w) and boundary layer thickness (δ) data were measured by Zhang and Chanson (2015) for the same flow conditions in the same facility. For all present data, the largest turbulence intensities were observed next to the pseudo-bottom formed by the step edges. Maximum turbulence intensity values Tu_{max} ranged between 0.3 and 0.45 and decreased with increasing distance from the pseudo-bottom. Next to the boundary layer outer edge ($y/\delta \approx 1$), Tu was about 0.05. Interestingly, non-trivial values of Tu were observed up to $y/\delta = 1.2 - 1.4$, which might arise from irrotational velocity fluctuations in the external flow induced by boundary layer turbulence (Zhang and Chanson 2015). The present data were close to those obtained using PIV (Amador et al. 2006) on a

51.3° steppe chute and those in flows over transverse rib-roughness (Okamoto et al. 1993, Cui et al. 2003). This demonstrates that the probe had an adequate frequency response for turbulence measurements.
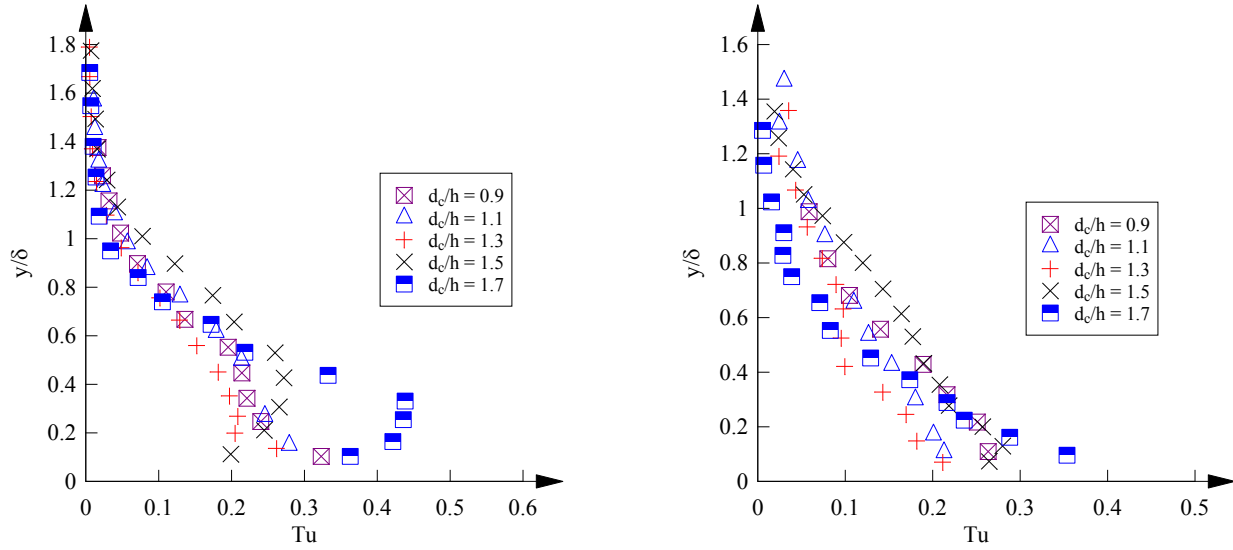
(A) Step edge 3   (B) Step edge 4

Figure 3 – Turbulence intensity distributions in the developing flow region

4. FULLY-DEVELOPED AIR-WATER FLOW REGION

Downstream of the inception point of free-surface aeration, the stepped spillway flow was characterised by strong air-entrainment and turbulent mixing. Typical distributions of time-averaged void fraction (C) and bubble count rate (F) are shown in Figure 4, where F_{max} is the maximum bubble count rate at one cross-section. The void fraction distribution followed an S-shaped distribution typical of skimming flows (Chanson and Toombes 2002, Gonzalez and Chanson 2008, Bung 2009, Felder and Chanson 2011). The data may be described by a solution of the advection-diffusion equation (Chanson and Toombes 2002):

$$C = 1 - \tanh^2\left(K - \frac{y/Y_{90}}{2D_0} + \frac{\left(y/Y_{90} - 1/3\right)^2}{3D_0} \right) \tag{5}$$

where Y_{90} is the depth where $C = 0.9$, K is an integration constant and D_0 is a function of the depth-averaged void fraction. Equation (5) is compared to experimental data in Figure 4. A good agreement is observed, despite of some underestimation for $y/d_c < 0.3$. This might be a result of bubbles trapped in vortices shed from the upstream step edge.

Defined as the number of air-to-water interfaces detected by the probe sensor per second, the bubble count rate is proportional to the specific interfacial area (Chanson 2002). In Figure 4, typical data are presented, showing a characteristic shape with a maximum value at about $y/d_c = 0.4$ ($C = 0.4 - 0.5$). The observation is consistent with past studies on stepped chute flows (e.g. Chanson and Toombes 2002). It was demonstrated (Toombes and Chanson 2008) that the bubble count rate is positively correlated with the void fraction variance (deduced from a binary signal) equalling $C(1-C)$ (Chanson and Carosi 2007), which is maximum at $C = 0.5$.

The aerated flow region exhibited strong total-pressure fluctuations although its characteristic magnitude (i.e. $<p_t^2>^{1/2}$) may not be a good descriptor of the water-phase turbulence because these fluctuations are mostly induced by the density fluctuations (i.e. change in density between air and water as bubbles are detected by the MEMS sensor) when a large number of air-water interfaces is present. In Figure 5, the characteristic total pressure

fluctuation is plotted against the bubble count rate for one discharge ($d_c/h = 0.9$), where $<p_t^2>_{max}^{1/2}$ is the maximum characteristic total pressure fluctuation at each cross-section. The data indicated a strong positive correlation between total pressure fluctuations and bubble count rate. Some hysteresis around $F/F_{max} = 1$ was observed, likely caused by wall effects that were mainly concentrated in the lower air-water flow column. Note that $<p_t^2>^{1/2}/<p_t^2>_{max}^{1/2} \approx 0.2 - 0.3$ next to the free-surface for $F/F_{max} \approx 0$ (refer to Figure 4), which was likely because of system noise and capillary effects.
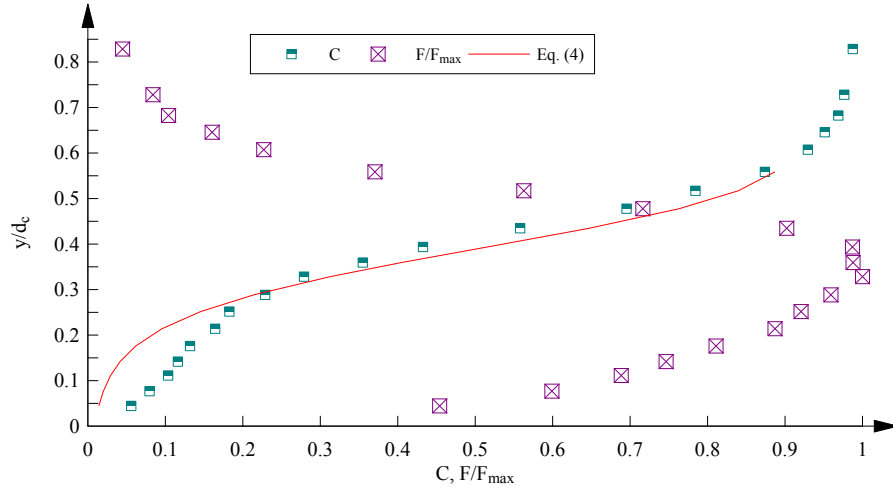
Figure 4. Typical void fraction and bubble count rate distributions in skimming flows – Flow conditions: $d_c/h = 1.1$, step edge 12; $\theta = 45°$, $h = 0.1$ m
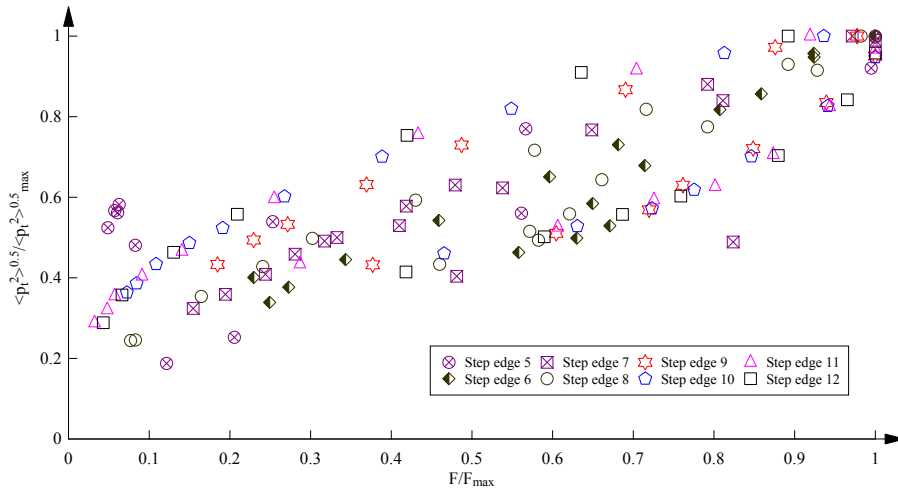
Figure 5. Relationship between dimensionless bubble count rate and total pressure fluctuations – Flow conditions: $d_c/h = 0.9$, $\theta = 45°$, $h = 0.1$ m

For an aerated flow, the water-phase turbulence intensity Tu (Equation (3)) may be derived from Equation (1) using a similar technique as discussed in Section 3. The result yields a relationship between the water-phase turbulence intensity, total pressure standard deviation, time-averaged velocity, and time-averaged void fraction (Zhang and Chanson 2016b):

$$Tu = \sqrt{\dfrac{\dfrac{< p_t^2 >}{\rho_w^2 U_w^4} - \dfrac{C(1-C)}{4}}{\left(1 + \dfrac{1}{2}C\right)(1-C)}} \qquad\qquad (6)$$

The derivation of Equation (6) assumes (a) no-slip between phases: i.e., $U = U_w = U_a$; (b) the density of air is zero; (c) the static pressure fluctuation and capillary effects are negligible; and (d) both the transitions between air and water phases and the probe sensor response are instantaneous. Note that Equation (6) becomes inaccurate for $Tu > 0.4 – 0.5$ because higher order terms were neglected in its derivation. Figure 6 shows typical water-phase turbulence intensity distributions at each step edge downstream of the inception point for four skimming flow conditions, where the void fraction and velocity data were obtained from phase-detection probe signals (Section 2). All data showed turbulence intensity of the water phase between 0.1 and 0.5, irrespective of the flow rate. Local maxima were found next to the pseudo-bottom, ranging between 0.2 – 0.4. The turbulence intensity decreased with increasing distance from the pseudo-bottom with minimum values of about 0.1 – 0.15 next to $y/d_c = 0.3$ ($C = 0.4 – 0.5$). For $y/d_c > 0.3$, the data generally increased with increasing distance from the pseudo-bottom despite showing large scatter. Note that Tu presented minimum values next to locations of maximum bubble count rates ($y/d_c \approx 0.3$). This suggested that a large number of bubbles might introduce an effective spring constant that reduced the rate-of-strain of the water particles. Overall, the aerated flow region exhibited turbulence intensities of the same order of magnitude of, albeit with a much more uniform distribution than, those in the developing clear-water flow region.

5. ENERGY DISSIPATION IN SKIMMING FLOWS

On a stepped chute, a significant fraction of the kinetic energy is dissipated by turbulence generated by the stepped invert. For the clear-water developing and aerated fully-developed flow regions, the depth-averaged total head is defined as

$$H_d = \frac{1}{d}\int_0^d H_t\,dy \qquad\qquad \text{for the developing flow region (7)}$$

$$H_d = \frac{1}{d_e}\int_0^{Y_{90}} H_t\,dy \qquad\qquad \text{for the aerated flow region (8)}$$

where $d_e = \int_0^{Y_{90}}(1-C)\,dy$ is the equivalent clear water depth in the aerated flow region and Y_{90} is the normal distance to the pseudo-bottom from where $C = 0.9$. Figure 7A shows the distributions of H_d along the chute centreline for two skimming discharges, normalised by $H_{t,crest}$. For all discharges, the total head decreased monotonically along the stepped chute. The overall energy dissipation was about 50% of the upstream total head, a result comparable to previous investigations (e.g. Felder and Chanson 2009, 2011, 2014). A closer examination showed some see-saw pattern with a wave length of about 1-2 cavity lengths, which was most evident for the largest discharge ($d_c/h = 1.7$). Such a see-saw pattern in the longitudinal distributions of characteristic air-water flow parameters (e.g. Y_{90}/d_c, V_{90}/V_c) was observed previously (e.g. Matos 2000, Felder and Chanson 2009), supporting the argument by several authors (Chanson et al. 2002, Chanson 2006, Felder and Chanson 2009) that uniform equilibrium conditions might not exist on stepped chutes.

Figure 7B presents the residual head H_{res} (i.e. H_d at the last step edge) normalised by the critical depth d_c. The present data were compared to those in 26.6° chutes with flat steps (Felder and Chanson 2011, 2014) and the reanalysis of the data of Zhang and Chanson (2014) in a 26.6° gabion stepped chute (solid symbols: flat steps; hollow symbols: gabion steps). For all configurations, the residual head generally decreased with increasing discharge. For a given discharge, the residual head was the largest in the 26.6° gabion chute, followed by the present setup. On the gabion chute, form drag was significantly reduced because of ventilation of the step cavities and the interactions between seepage and cavity flows (Zhang and Chanson 2016a). The larger residual head on the present

facility ($\theta = 45°$) compared to the 26.6° chutes with flat steps suggested that the energy dissipation performance was a function of the cavity geometry. A larger cavity aspect ratio (step length/height) might improve the efficiency of energy dissipation by reducing the shedding effects of each roughness element (i.e. step) on the subsequent one.

The significant rate of energy dissipation in stepped chutes was attributed mostly to form loss induced by the steps (Rajaratnam 1990, Chanson 2001, Chanson et al. 2002). The flow is commonly assumed to be quasi-smooth, and the flow resistance is typically expressed using the Darcy-Weisbach friction factor (Rajaratnam 1990, Chanson 2001):

(A) $d_c/h = 0.9$

(B) $d_c/h = 1.1$

(C) $d_c/h = 1.3$

(D) $d_c/h = 1.5$
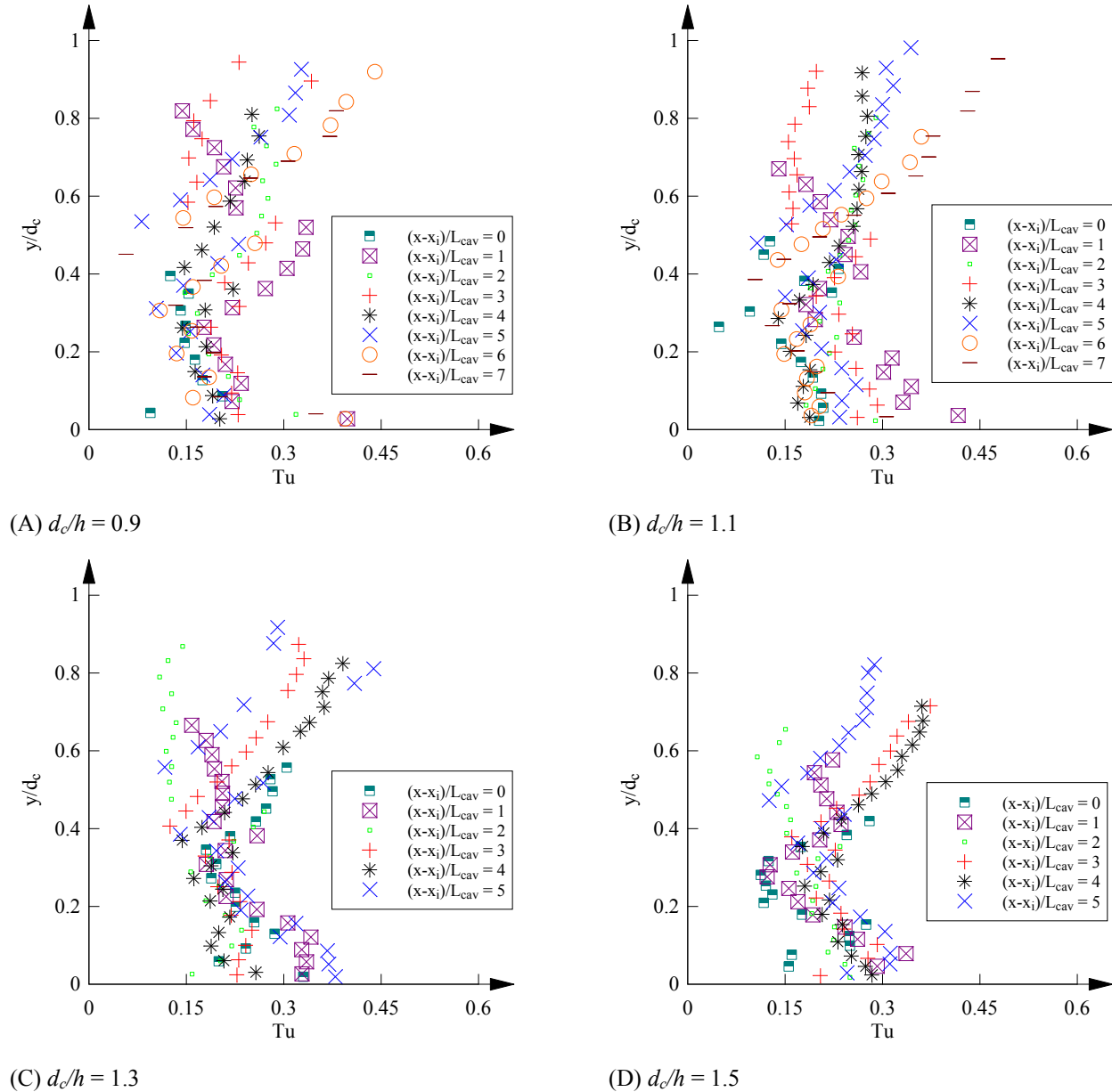
Figure 6. Water phase turbulence intensity at step edges – Flow conditions: $d_c/h = 0.9, 1.1, 1.3, 1.5$; $\theta = 45°$, $h = 0.1$ m
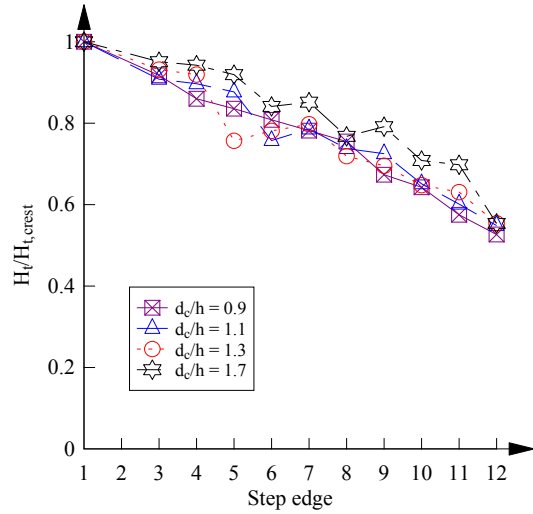
(A) Depth averaged total head along stepped chute
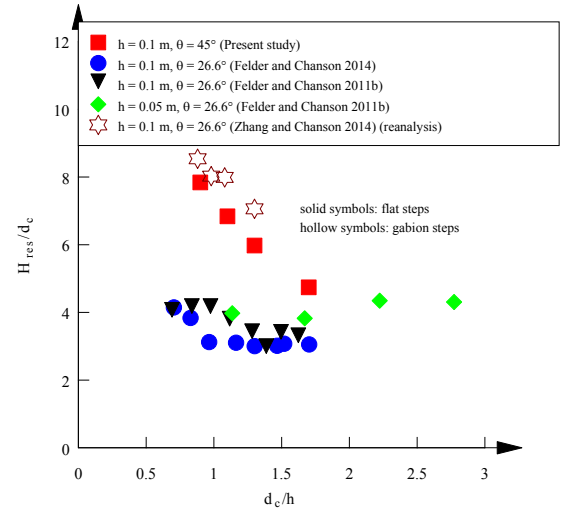
(B) Residual head above the last step edge

Figure 7. Energy dissipation along stepped chutes

$$f_e = 8 S_f \left(\frac{d}{d_c} \right)^3 \qquad \text{for clear water flow (9)}$$

$$f_e = 8 S_f \left(\frac{d_e}{d_c} \right)^3 \qquad \text{for air-water flow (10)}$$

where S_f is the friction slope: i.e., the slope of the total head line. Note that Equations (9) and (10) are only valid for fully developed skimming flows in a wide rectangular channel and may be inappropriate to quantify form losses (Chanson 2001). Present data are plotted in Figure 8, where D_H is the hydraulic diameter. For each discharge, the friction factor was calculated for (a) the clear-water developing flow region upstream of the visually-defined inception point; (b) the air-water flow region downstream of the inception point; and (c) the entire stepped chute (step edge 1 – 12). In the clear-water developing flow, the friction factor was on average $f_e \approx 0.19$, close to the findings of Zhang and Chanson (2015) obtained with a Prandtl-Pitot tube in the same chute. In the aerated flow region, the friction factors are slightly higher, with an average of $f_e \approx 0.27$. The present data are compared to those in stepped chutes with a 26.6° slope (Felder and Chanson 2011, Felder and Chanson 2014). For a given discharge, the present data are generally smaller than those in the 26.6° chutes with the same step height ($h = 0.10$ m). The data obtained with h = 0.05 m showed a different trend that could be linked to scale effects (Felder and Chanson 2011, 2014, 2015). A negative correlation between friction factors and dimensionless roughness height is observed for all data, which is characteristic of form losses.

6. CONCLUSION

New experiments were performed in a large-size stepped spillway model with a 45° slope (1V:1H) and uniform step heights of 0.1 m, with a focus on skimming flows. The total pressure distribution and two-phase flow properties were recorded via simultaneous sampling of a MEMS-based total pressure sensor and a dual-tip phase-detection probe. The water-phase turbulence intensity and energy dissipation performances were reported for both the developing clear-water and fully-developed air-water flow regions.
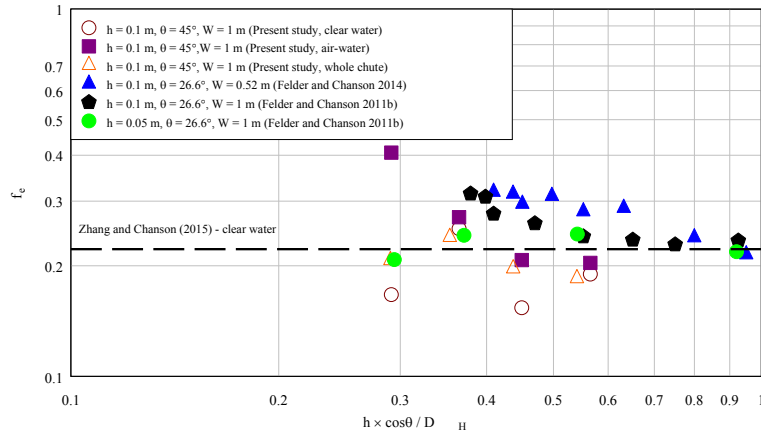
Figure 8. Darcy-Weisbach friction factors in skimming flows above stepped chutes – Flow conditions: $d_c/h = 0.9$, 1.1, 1.3, 1.5, $\theta = 45°$, $h = 0.1$ m (Present study) - Solid symbols indicate air-water data.

The developing flow region consisted of a boundary layer and an irrotational flow region above. In the boundary layer, large total pressure fluctuations and turbulence intensities were recorded, while the potential flow region was governed by the Euler equations. The aerated flow region was characterised by strong air-entrainment and turbulent mixing. Large total pressure fluctuations were recorded, mainly induced by density fluctuations. The water phase turbulence intensities were similar to those in the developing flow region. The overall energy dissipation was about 50% of the upstream total head regardless of discharge. The rate of energy dissipation and friction factors were found to be similar in both the developing clear-water and fully-developed air-water flow regions. The present findings showed that energy dissipation performance of stepped chutes might not be much affected by air-bubble diffusion and might be sensitive to the step cavity geometry.

7. ACKNOWLEDGEMENTS

8. REFERENCES

Amador, A., Sánchez-Juny, M. and Dolz, J. (2006). "Characterization of the nonaerated flow region in a stepped spillway by PIV." *Journal of Fluids Engineering*, Transactions of the ASME, Vol. 128, No. 6, pp. 1266-1273 (DOI: 10.1115/1.2354529).

Arndt, R.E.A. and Ippen, A.T. (1970). "Turbulence measurements in liquids using an improved total pressure probe." *Journal of Hydraulic Research*, Vol. 8, No. 2, pp. 131-158 (DOI: 10.1080/00221687009500300).

Bung, D.B. (2009). "Zur selbstbelüfteten Gerinnenströmung auf Kaskaden mit gemässigter Neigung." ("Self-aerated skimming flows on embankment stepped spillways.") *Ph.D. thesis*, University of Wuppertal, LuFG Wasserwirtschaft and Wasserbau, Germany, 292 pages (in German).

Chanson, H. (2001). "The hydraulics of stepped chutes and spillways." Balkema, Lisse, The Netherlands, 418 pages.

Chanson, H. (2002). "Air-water flow measurements with intrusive phase-detection probes. Can we improve their interpretation?" *Journal of Hydraulic Engineering*, ASCE, Vol. 128, No. 3, pp. 252-255 (DOI: 10.1061/(ASCE)0733-9429(2002)128:3(252)).

Chanson, H. (2006). "Hydraulics of skimming flows on stepped chutes: the effects of inflow conditions?" *Journal of Hydraulic Research*, IAHR, Vol. 44, No. 1, pp. 51-60 (DOI: 10.1080/00221686.2006.9521660).

Chanson, H., and Carosi, G. (2007). "Advanced post-processing and correlation analyses in high-velocity air-water flows." *Environmental Fluid Mechanics*, Vol. 7, No. 6, pp. 495-508 (DOI: 10.1007/s10652-007-9038-3).

Chanson, H., and Toombes, L. (2002). "Air-Water flows down stepped chutes. Turbulence and flow structure observations." *International Journal of Multiphase Flow*, Vol. 28, No. 11, pp. 1737-1761 (DOI: 10.1016/s0301-9322(02)00089-7).

Chanson, H., Yasuda, Y., and Ohtsu, I. (2002). "Flow resistance in skimming flows and its modelling." *Canadian Journal of Civil Engineering*, Vol. 29, No. 6, pp. 809-819 (DOI: 10.1139/l02-083).

Cui, J., Patel, V.C. and Lin, C. (2003). "Large-eddy simulation of turbulent flow in a channel with rib roughness." *International Journal of Heat and Fluid Flow*, Vol. 24, No. 3, pp. 372-388 (DOI: 10.1016/s0142-727x(03)00002-x).

Felder, S., and Chanson, H. (2009). "Energy dissipation, flow resistance and gas-liquid interfacial area in skimming flows on moderate-slope stepped spillways." *Environmental Fluid Mechanics*, Vol. 9, No. 4, pp. 427-441 (DOI: 10.1007/s10652-009-9130-y).

Felder, S., and Chanson, H. (2011). "Air-water flow properties in step cavity down a stepped chute." *International Journal of Multiphase Flow*, Vol. 37, No. 7, pp. 732–745 (DOI: 10.1016/j.ijmultiphaseflow.2011.02.009).

Felder, S., and Chanson, H. (2014). "Effects of step pool porosity upon flow aeration and energy dissipation on pooled stepped spillways." *Journal of Hydraulic Engineering*, ASCE, Vol. 140, No. 4, Paper 04014002, 11 pages (DOI: 10.1061/(ASCE)HY.1943-7900.0000858).

Felder, S., and Chanson, H. (2015). "Scale effects in high-velocity air-water flows on a stepped spillway." *Proc. 36th IAHR World Congress*, The Hague, The Netherlands, 27 June-3 July, Paper 81132, 9 pages.

Gonzalez, C.A., and Chanson, H. (2008). "Turbulence manipulation in embankment stepped chute flows: an experimental study." *European Journal of Mechanics B/Fluids*, Vol. 27, No. 4, pp. 388-408 (DOI: 10.1016/j.euromechflu.2007.09.003).

Matos, J. (2000). "Hydraulic design of stepped spillways over RCC dams." *Proc. The International Workshop on Hydraulics of Stepped Spillways*, Zürich, March 22-24, 2000, pp. 187-194.

Okamoto, S., Seo, S., Nakaso, K. and Kawai, I. (1993). "Turbulent shear flow and heat transfer over the repeated two-dimensional square ribs on ground plane." *Journal of Fluids Engineering*, Transactions of the ASME, Vol. 115, No. 4, pp. 631-637 (DOI: 10.1115/1.2910191).

Rajaratnam, N. (1990). "Skimming flow in stepped spillways." *Journal of Hydraulic Engineering*, ASCE, Vol. 116, No. 4, pp. 587-591 (DOI: 10.1061/(asce)0733-9429(1990)116:4(587)).

Toombes, L., and Chanson, H. (2008). "Interfacial aeration and bubble count rate distributions in a supercritical flow past a backward-facing step." *International Journal of Multiphase Flow*, Vol. 34, No. 5, pp. 427-436 (DOI: 10.1016/j.ijmultiphaseflow.2005.01.005).

Wang, H., Murzyn, F., and Chanson, H. (2014). "Total pressure fluctuations and two-phase flow turbulence in hydraulic jumps." *Experiments in Fluids*, Vol. 55, No. 11, Paper 1847, 16 pages (DOI: 10.1007/s00348-014-1847-9).

Zhang, G., and Chanson, H. (2014). "Step cavity and gabion aeration on a gabion stepped spillway." *Proc. 5th IAHR International Symposium on Hydraulic Structures*, 25-27 June 2014, Brisbane, Australia, H. Chanson and L. Toombes Editors, 8 pages (DOI: 10.14264/uql.2014.37).

Zhang, G., and Chanson, H. (2015). "Hydraulics of the developing flow region of stepped cascades: an experimental investigation." *Hydraulic Model Report No. CH97/15*, School of Civil Engineering, The University of Queensland, Brisbane, Australia, 76 pages.

Zhang, G., and Chanson, H. (2016a). "Gabion stepped spillway: interactions between free-surface, cavity and seepage flows." *Journal of Hydraulic Engineering,* ASCE (DOI: 10.1061/(ASCE) 11 HY.1943-7900.0001120).

Zhang, G., and Chanson, H. (2016b). "Interaction between free-surface aeration and total pressure on a stepped chute." *Experimental Thermal and Fluid Science*, Vol. 74, pp. 368-381 (DOI: 10.1016/j.expthermflusci.2015.12.011).

Experimental Study of Head Loss over Laser Scanned Rock Tunnel

L.R. Andersson[1], I.A.S. Larsson[1], J.G.I. Hellström[1], P. Andreasson[1,2] and A.G. Andersson[1]
[1]Div. of Fluid & Experimental Mechanics
Luleå University of Technology
Luleå
Sweden
[2]Vattenfall Research and Development
Vattenfall AB
Älvkarleby
Sweden
E-mail: robin.andersson@ltu.se

ABSTRACT

Flow in hydropower tunnels is characterized by a high Reynolds number and often very rough rock walls. Due to the roughness of the walls, the flow in the tunnel is highly disturbed, resulting in large fluctuations of velocity and pressure in both time and space. Erosion problems and even partial collapse of tunnel walls are in some cases believed to be caused by hydraulic jacking from large flow induced pressure fluctuations. The objective of this work is to investigate the effects of the rough walls on the pressure variations in time and space over the rock surfaces. Pressure measurement experiments were performed in a 10 m long Plexiglas tunnel where one of the smooth walls was replaced with a rough surface. The rough surface was created from a down-scaled (1:10) laser scanned wall of a hydraulic tunnel. The differential pressure was measured at the smooth surface between points placed at the start and end of the first four 2 m sections of the channel. 10 gauge pressure sensors where flush mounted on the rough surface; these sensors measure the magnitude and the fluctuations of the pressure on the rough surface. The measurements showed significant spatial variation of the pressure on the surface. For example, sensors placed on protruding roughness elements showed low gauge pressure but high fluctuations. The differential pressure indicated a head loss through the tunnel that was almost four times higher than a theoretical smooth channel.

Keywords: Pressure measurements, rough surface, hydropower-tunnel, laser scan, friction factor.

1. INTRODUCTION

Tunnels are often used when transporting water to or from hydropower turbines. In many cases, these tunnels have to be excavated through solid rock, a process which often leads to the occurrence of very large protruding roughness elements on the walls of the tunnels. These roughness elements considerably modify the local cross-sectional area of the tunnel in a more or less stochastic manner. The dynamic action of flow in such tunnels creates disturbances in the flow (Krogstad & Antonia, 1999), (Nakagawa, et al., 2003), (Kruse, et al., 2006) manifesting in, for instance, large pressure variations along the walls of the tunnel; i.e. the rock surfaces are exerted to local net destabilization forces. These forces are likely to contribute to events such as erosion or even partial collapse of the tunnel. These events may, in most applications, be difficult to predict and also hard to detect once they happen. The only indicator of a collapsed tunnel in a hydropower plant may be a substantial drop in turbine efficiency. One method applied with the aim to reduce the destabilizing forces is to "smoothen" the surface and, thus, make it more durable (Barton, et al., 1974); this can be done by spraying concrete on the wall, i.e. shotcreting (Austin & Robins, 1995). The roughness elements of rock tunnels could be considered to be self-similar and random (Perfect, 1997); however, the nature of the roughness elements differ depending on the method used when excavating the tunnel. Rock blasting a tunnel is a rapid method compared to utilizing tunnel boring machines but gives rise to periodic features of the tunnel where large roughness elements of similar size might occur at recurring intervals in the tunnel. These features inhibit the flow, increase the head loss due to friction, and increase the strain on the walls (Andersson, et al., 2012). There might also be new requirements on the tunnels and the operating conditions with the introduction of intermittent energy sources on the market with the demand on the hydropower industry to handle more transient

flow conditions. The purpose of this experiment is to evaluate the pressure fluctuations of a hydro-power tunnel and to determine the effects of wall roughness on the pressure distribution with respect to parameters of wall roughness.

2. EXPERIMENTAL SETUP

The experimental setup consists of a closed-loop water system with a 10 m rectangular Plexiglas channel having one rough surface, a pump, two tanks placed on different levels, and pressure sensors. The high level upstream tank provides a stable driving flow through the tunnel and is connected through a 90° bend with a honeycomb placed at the entrance of the channel to straighten the flow. The honeycomb is 50 mm thick and has a cell diameter of 10 mm. In addition, three guide vanes are mounted inside of the bend to reduce secondary flow effects. The channel is 10 m long to allow the flow to be developed when it reaches the measuring section placed 6 m downstream of the honeycomb. Additionally, the channel is divided into five sections with a height of 200 mm, length of 2000 mm, and a width of 250 mm. The rough surface has an average height of 60 mm and is placed on the left wall in the flow direction of the channel, making the average cross sectional area of each section 250x140 mm^2. The water is collected in the second, downstream tank placed in level with the channel before it is pumped back up to the high-level tank. The flow is controlled with a PID regulator and manual valves and monitored with a flow meter. A schematic of the flow can be seen in Figure 1 where the channel has been mirrored for visual purposes; in the setup, the rough surface is placed on the left wall in the flow direction.
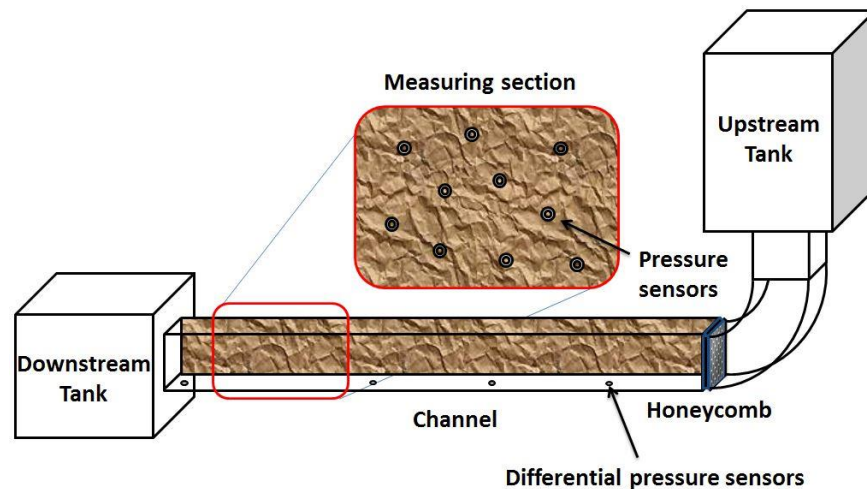
Figure 1. Schematic of the experimental setup used in the campaign, the measuring section started 6 m downstream of the honeycomb, the flow in the figure is from right to left

As mentioned, one sidewall of the tunnel was replaced with a rough surface model (Figure 2). The rough surface is based on a real surface that was captured by a high resolution laser scanning of a rock tunnel, a method that has been proven to be efficient for determining surface roughness (Bråtveit, et al., 2012). The laser scanning was conducted at a resolution of approximately 200 points/m^2. A side wall of the tunnel was extracted and scaled to 1:10 in size; the resulting model is a surface of 250x2000 mm^2 that has an RMS roughness factor of 9.4 mm. The difference between the highest and lowest point on the surface is 56 mm. A right-handed coordinate system is implied throughout this study. The x-axis is directed along the main flow direction with zero at the honeycomb, the y-axis is directed perpendicular to the lower wall pointing upwards, and the z-axis is perpendicular to the rough surface.

Pressure sensors were flush mounted in both the measuring section of the rough surface and every 2 m of the lower channel wall. In the rough surface, the pressure sensors are positioned to represent peaks and valleys of the rough surface (Figure 4). The coordinates for the pressure sensors can be found in
Table 2. The differential pressure sensors were placed on the lower smooth surface on the tunnel. From the differential pressure sensors, it was possible to capture the total head loss over the channel as well as the head loss over specific sections of the channel.

A total of 14 pressure sensors were used in the experiments, 10 pressure sensors in the measuring section and 4 differential pressure sensors. Each differential pressure sensor measures the difference in pressure between two points located at the wall in the inlet and outlet of each of the first four 2 m sections. The pressure sensors used were MTM/N10 104490 from STS, which have a measuring range of 0-10 mwc (meter water column) with an accuracy of ±0.5%. During the experiments, a sampling frequency of 200 Hz was used; all measurements ran between 40-50 minutes and were repeated five times. The magnetic flow meter used was an IFS4000 from Krohne connected to an IFC 110 signal converter. The data acquisition module used in the experiments was a cDAQ-9174 chassis with a Ni9025 module from National Instruments.

Figure 2. The rough surface channel; the pressure gauges can be seen just upstream of the downstream tank

The flow through the channel is pressure driven; the head is adjusted by regulating the water level in the upstream tank placed before the channel inlet (Figure 3), and the water level is regulated by a valve placed under the upstream water tank. The flow rate was regulated by adjusting the pump connected to the loop; the pump was controlled by a PID-regulator (Figure 3), which was connected to a magnetic flow meter. The flow was approximately 63 liters per second ($Re \approx 200\,000$) and differed about ±4% throughout the measured sets.

Figure 3. The upstream water tank and PID-regulator

The upstream water tank was also used when calibrating the pressure sensors. During the calibration, the outlet of the channel was closed and the water level inside of the tank was kept steady at a few different values allowing the pressure sensors to be calibrated. The date and time for each measurement is shown in Table 1, the measurements will follow this denotation throughout the paper.

Table 1. The dates and denotation for each measured set

Date	Denotation
20150602-095023	Set 1
20150602-130400	Set 2
20150602-155523	Set 3
20150603-092302	Set 4
20150603-124918	Set 5

3. RESULTS AND DISCUSSION

The measuring campaign was conducted over two days. All units of pressure are in meter water column [mwc], which will furthermore be denoted as [m]. The head provided by the water tank was kept constant at approximately 3 m. A summary of the measurements can be found in Table 2. The rough surface is placed on one of the side walls of the channel, and, thereby, the height of the pressure sensors differ; this means that the sensors are submitted to different magnitudes of static pressure. These heights can be seen in the sixth column of
Table 2. This effect has been adjusted for by subtracting the height of the sensors from the gauge pressure.

Table 2. Summary of the pressure measurements; the third column(σ) is the standard deviation at each point, z denotes the height above or below the mean height of the roughness elements, the chevrons denote the temporal mean

Sensor	Mean Pressure [m]	σ [m]	$<p_{max}-p_{min}>$ [m]	z [m]	y [m]	x [m]
1	0.3098	0.0295	0.3083	0.0081	0.1210	6.285
2	0.4435	0.0248	0.2410	-0.0049	0.1047	6.490
3	0.2520	0.0272	0.2673	0.0103	0.1828	6.629
4	0.2812	0.0250	0.2399	0.0120	0.0992	6.635

5	0.3352	0.0235	0.2324	-0.0167	0.1598	6.894
6	0.1215	0.0357	0.3676	-0.0005	0.1741	7.060
7	0.4700	0.0225	0.2194	-0.0049	0.0656	7.139
8	0.3262	0.0221	0.2163	-0.0119	0.1551	7.304
9	0.2715	0.0294	0.3028	0.0021	0.1255	7.459
10	0.3121	0.0205	0.1985	-0.0037	0.1427	7.664

3.1. Mean Pressure

In Figure 4, the placement of the pressure sensors on the rough surface are visualized along with one pressure time series. The highest mean pressure can be found in sensors 2, 5, and 7, which are located in valleys on the surface. The high pressure in these zones indicates that there is a loss of velocity in that area due to the sudden decrease of surface elevation, which is to be expected.
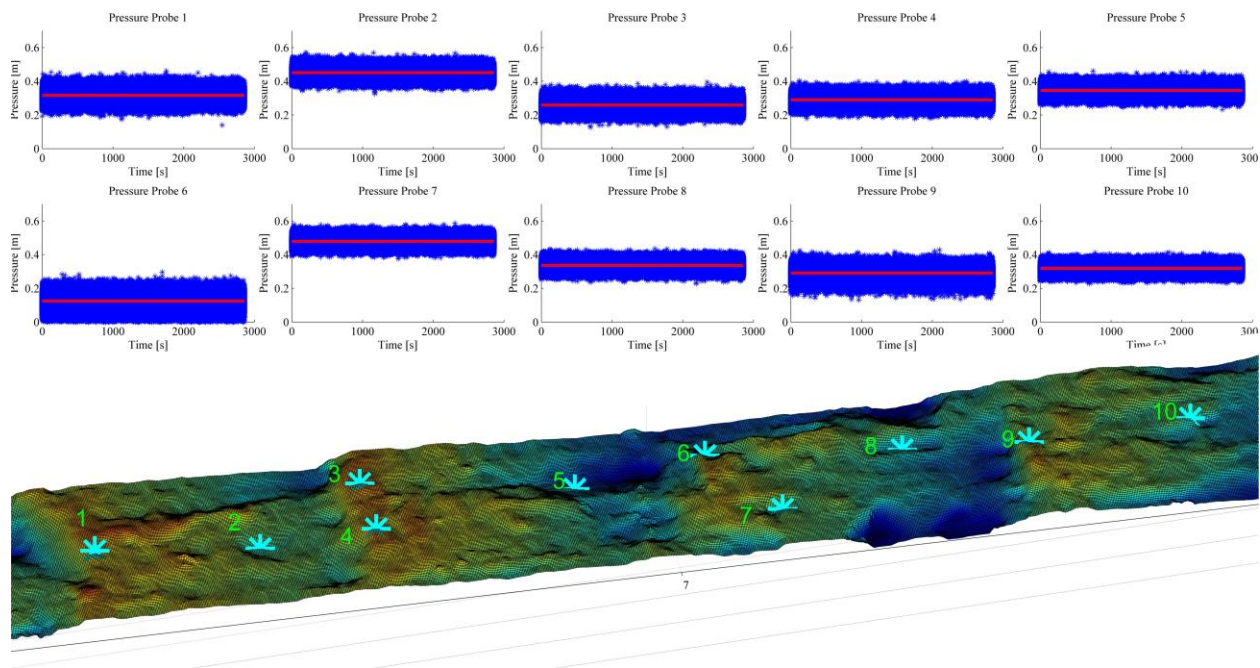
Figure 4. Pressure sensors and the corresponding measured pressure over time, the red lines denotes the average

The results from all five measurements are averaged for each pressure sensor (Figure 5). The figure shows both the amplitudes of the fluctuations and the spread of the averages for each measurement at each point. The difference between each measurement is at most ≈ 10%, which occurs for sensor 9, while the difference for sensor 6 is only ≈ 3%. This shows that the setup in general is insensitive in the sense of reproducing the same conditions during several measurements.
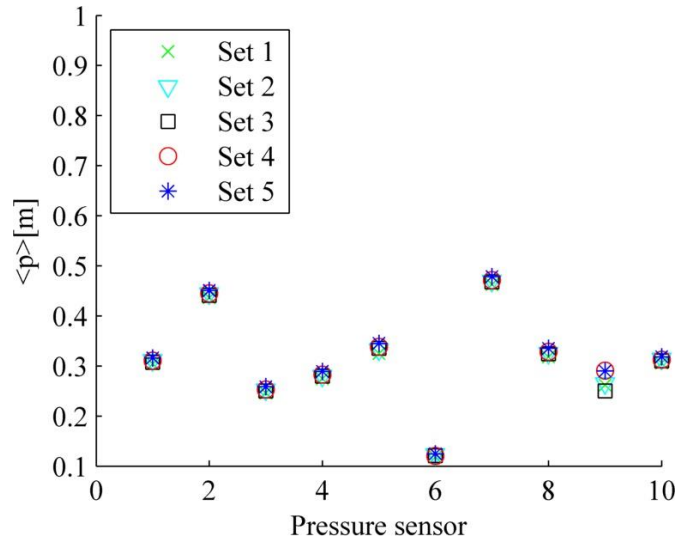
Figure 5. The average pressure in the pressure sensors for all five measurements

The apparent spatial variation in pressure indicates that net forces act on the surface that is not necessarily perpendicular to the main direction of the wall. The largest pressure fluctuations along with the lowest pressure magnitude can be found in position number 6.
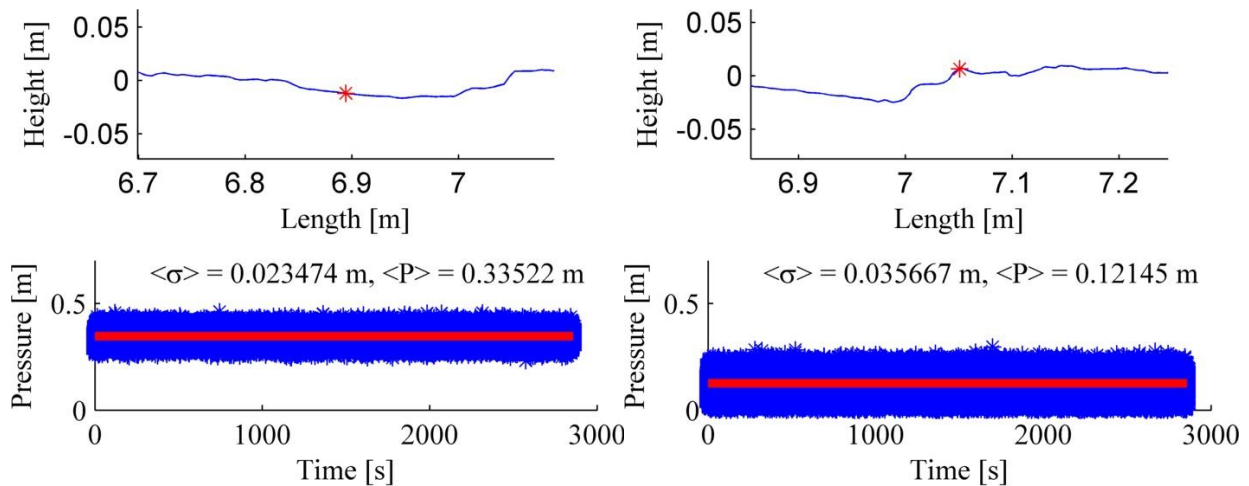
Figure 6. Comparison between pressure point 5 (left) and 6 (right) with the surface profile (top), a measured set (bottom), the standard deviation and the pressure magnitude. The flow goes from left to right.

From Figure 6, it is clear that the gauge pressure is higher in position 5 as compared to position 6. The measurement in sensor 6 shows a higher standard deviation of the pressure than in sensor 5. This can be interpreted as a higher production of turbulence in that position and that there might be some flow separation occurring. Additionally, the distance between these points is merely 166 mm. However, there is evidently a considerable difference in average static pressure and fluctuating pressure. It is not surprising that point 6, which is located on a roughness peak, displays larger fluctuations due to the vorticity generated at the roughness peak; however, the reason for displaying lower average pressure remains to be investigated.

3.2. Differential Pressure

The differential pressure was sampled at the same frequency as the gauge pressure. The differential pressure sensors were placed so that the differential pressure was measured as the difference between the inlet and outlet of each 2 m

section. The total average head loss over the channel is 0.24 m. The measurements from each set of data on each pressure sensor can be found in Figure 7.
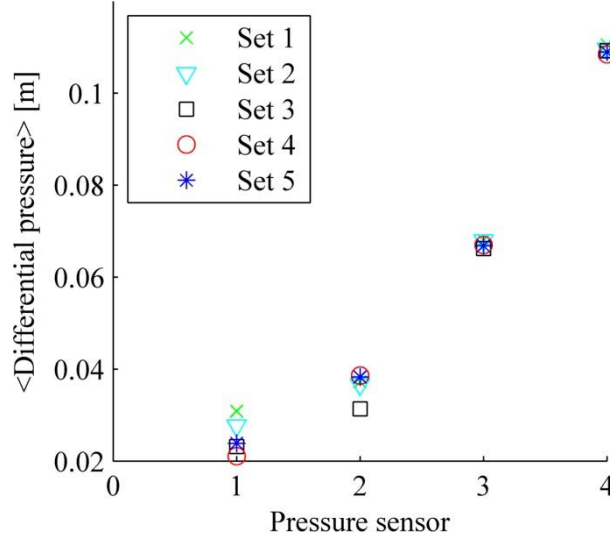
Figure 7. The head loss over the 4 first sections from the entrance of the channel

In the first two sections of the channel, there is some deviation between the differential pressures recorded between the sets; this effect may be due to the valve located under the water tank upstream of the channel. The valve had to be slightly adjusted between the sets and definitely had an impact on the flow at the inlet. However, those discrepancies diminish further downstream in the channel, which points to the conclusion that the perturbations from the valve are small, and the flow is developed in the 4-6 m section and, hence, in the measurement section (6-8 m). One would expect the differential pressure to diminish and approach a constant value through the channel, but instead, the differential pressure seems to increase throughout the channel. The reason for this is unclear, and it needs to be further investigated.

The head loss inside the channel can, to an order of magnitude, be estimated and compared to a theoretical smooth channel by using the Darcy-Weissbach equation (Cengel & Cimbala, 2014):

$$\Delta p = f_d \frac{L \rho}{2} \frac{V^2}{D}, \tag{1}$$

where L is the length of the channel, V is the mean flow velocity, D is the hydraulic diameter of the tunnel, and f_d is the friction factor. We replace D with 4 times the hydraulic radius. The friction factor f_d can be evaluated by using the Colebrook-White equation:

$$\frac{1}{\sqrt{f_d}} = -2 \log \left(2.51 \frac{1}{Re\sqrt{f_D}} + \frac{1}{3.7} \frac{k_s}{D} \right), \tag{2}$$

assuming the sand grain roughness factor k_s to be the RMS roughness height of the surface. This is, however, a rough estimate since some of the roughness elements are significantly larger than the RMS value; hence, the flow around the largest roughness elements rather resembles flow around objects than flow over a uniformly rough surface. The results from the estimation can be found in Table 3.

Table 3. The head loss and friction factor for the experiment

	Smooth surface	Measuring section	Darcy-Weissbach
Δp[m]	0.028	0.109	0.139
f[-]	0.015	0.0582	0.0733

The Darcy-Weissbach equation estimates the head loss and the friction factor about 20% higher than the actual measured pressure.

3.3. Conclusions

Pressure measurements of the flow over a rough surface were performed in a downscaled model of a laser-scanned hydraulic tunnel at a Reynolds number of about 200 000. The pressure fluctuations and the wall friction play a crucial role in a number of flow induced effects, such as erosion and hydraulic jacking. These effects are hard to predict, and, therefore, accurate measurements are valuable. The study revealed a range of mean pressures and pressure fluctuations depending on location of the sensor. The largest magnitude of the average pressure was found in the valleys of the rough surface. The largest pressure fluctuations were found in sensors located at peaks of the surface; this can be an effect of vorticity generated at the roughness elements. From the data, it is clear that the pressures in the channel have a very high spatial variance; pressure sensors positioned relatively close to each other displayed different magnitudes and fluctuations of pressure. This indicates that the net forces acting on the rough surface are not uniform and may have a destabilizing effect on sections of the tunnel walls. Decreasing the size of the protruding elements is therefore of interest when excavating rock tunnels. Differential pressure sensors were mounted along the entire length of the channel, enabling measurement of the head loss over the channel. The differential pressure sensors showed a significant increase of the head loss comparing the first and last measured section of the channel. Assuming the RMS roughness height of the surface to be the sand grain roughness factor, the head loss could (to an order of magnitude) be estimated using the Darcy-Weissbach equation. The head loss and the friction factor in the channel is about four times higher than in a theoretical smooth channel with similar dimensions, which indicates that the rough surface has a substantial effect on the flow.

4. ACKNOWLEDGEMENTS

5. REFERENCES

Andersson, A. G., Andreasson, P., Hellström, J. G. I. & Lundström, S. T., 2012. *Modelling and validation of flow over a wall with large surface roughness.* Rome, u.n.

Austin, S. A. & Robins, P. J., 1995. *Sprayed Concrete: Properties, Design and Application.* u.o.:Whittles Publishing.

Barton, N., Lien, R. & Lunde, J., 1974. Engineering Classification of Rock Masses for the Design of Tunnel Support. *Rock Mechanics,* Volym 6, pp. 189-236.

Bråtveit, K., Lia, L. & Bøe Olsen, N. R., 2012. An Efficient Method to Describe the Geometry and the Roughness of an Existing Unlined Hydro Power Tunnel. *Energy Procedia,* pp. 200-206.

Cengel, Y. A. & Cimbala, J. M., 2014. *Fluid Mechanics: Fundemantals and Applications.* 3rd red. u.o.:McGraw-Hill Education.

Krogstad, P. & Antonia, R., 1999. Surface roughness effects in turbulent boundary layers. *Experiments in fluids,* Volym 27, pp. 450-460.

Kruse, N., Kuhn, S. & Von Rohr, P. R., 2006. Wavy wall effects on turbulence production and large scale modes. *Journal of Turbulence,* Volym 7.

Nakagawa, S., Na, Y. & Hanratty, T., 2003. Influence of a wavy boundary on turbulence. I. Highly rough surface. *Experiments in fluids,* Volym 35, pp. 422-436.

Perfect, E., 1997. Fractal Models for the Fragmentation of Rocks and Soilds: A Review. *Engineering geology,* Volym 48, pp. 185-198.

Free-Surface Aeration in a Steep Stepped Spillway

G. Zhang[1] and H. Chanson[1]
[1]Dept. of Civil Engineering
The University of Queensland
St Lucia, QLD 4072
Australia
E-mail: h.chanson@uq.edu.au

ABSTRACT

Self-aeration has important civil and environmental applications in stepped chutes, ranging from cavitation protection to enhanced air-water mass transfer. Air bubble entrainment occurs when the turbulent stresses in the boundary layer exceed the combined effects of surface tension and buoyancy. The governing equations for air diffusion in the rapidly-varied region next to and in the gradually-varied region away from the inception point of aeration are introduced. New and existing solutions to these equations are discussed and compared with new experimental data. An analytical model for flow bulking is introduced. The concept of negative diffusivity is discussed.

Keywords: *Free-surface aeration, stepped spillways, inception point, rapidly varied flow, physical modelling, turbulent mixing.*

1. INTRODUCTION

Self-aeration on stepped chutes occurs once the turbulent stresses in the turbulent boundary layer exceed the combined effects of surface tension and buoyancy (Rao and Rajaratnam 1961, Ervine and Falvey 1987, Chanson 1993, 2008). This location is known as the inception point of free-surface aeration (Wood et al. 1983, Chanson 1994), where the depth averaged void fraction is about 0.2 (Matos 2000). The flow undergoes some rapid bulking immediately downstream of the inception point, after which some de-aeration might occur (Matos 1999). On a relatively long chute, the flow eventually becomes gradually-varied and tends to a pseudo-equilibrium.

This paper presents a comprehensive analysis of the air diffusion process downstream of the inception point. A new model is proposed to describe flow bulking in the rapidly varied flow region and is compared with experimental results. The concept of negative diffusivity is introduced and is shown to be linked with flow de-aeration.

2. EXPERIMENTAL FACILITY AND INSTRUMENTATION

New experiments were conducted in a large-size stepped spillway model (1V:1H) at the University of Queensland (UQ). The chute consisted of 12 steps made of smooth painted marine ply, each step being 0.1 m long, 0.1 m high, and 0.985 m wide. The chute inflow was controlled by a 1.2 m high broad crested weir with a crest size of 0.6 m × 0.985 m (length × width). The weir crest was rounded at both upstream (0.058 m radius) and downstream (0.012 m radius) edges to ensure a smooth inflow. The experimental facility is sketched in Figure 1. Air-water measurements were conducted with a dual-tip phase detection probe at and between step edges downstream of the inception point. Each tip consisted of an inner and an outer electrode respectively made of silver (0.25 mm diameter) and stainless steel (0.8 mm diameter). Data were sampled at 20 kHz per sensor for 45 s. The probe was mounted along the channel centerline with vertical adjustment controlled by a Mitutoyo™ digital scale with an accuracy of ±0.01 mm.

Detailed air-water flow measurements were performed in the mainstream flow above the pseudo-bottom at every step edge downstream of the inception point. Additional measurements were performed between step edges in the mainstream flow and inside the step cavities. The mainstream and cavity air-water flow measurements were respectively performed with the probe sensor aligned parallel to the pseudo-bottom and to the horizontal step face,

as sketched in Figure 2. All measurements were conducted on the channel centerline. The experimental flow conditions focused on skimming flows corresponding to Reynolds numbers between $3.4 \times 10^5 – 8.8 \times 10^5$ and are summarized in Table 1.

Table 1. Summary of experimental flow conditions

d_c/h	Q (m³/s)	Location	Inception Point	Re
0.9	0.083	step edges 5-12	step edge 5	3.3×10^5
		step cavities: 7-8, 8-9		
1.1	0.112	step edges: 5-12	step edge 5	4.6×10^5
		step cavities: 7-8, 8-9		
1.3	0.145	step edges: 7-12	step edge 7	5.9×10^5
		step cavities: 7-8, 8-9		
1.5	0.179	step edges: 7-12	step edge 7	7.3×10^5
		step cavities: 10-11, 11-12		
1.7	0.216	step edges: 9-12	step edge 9	8.8×10^5
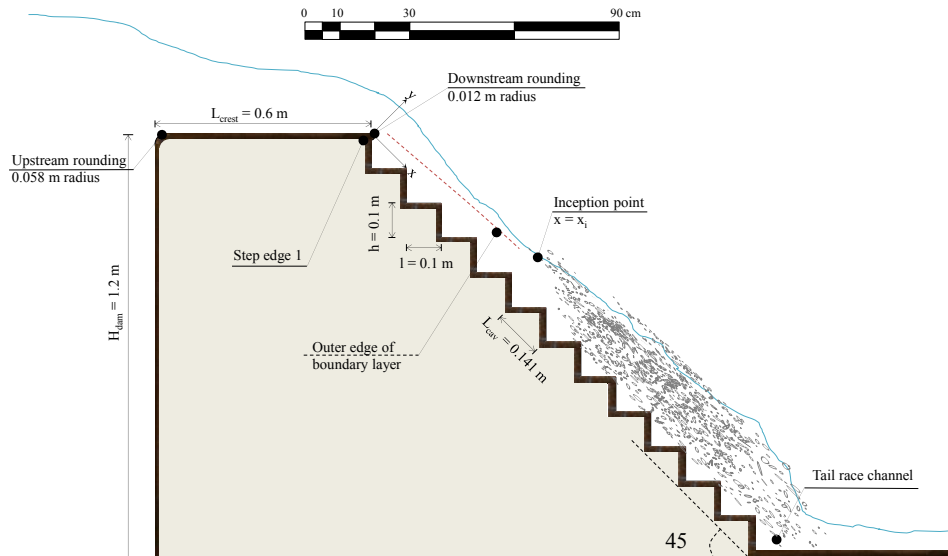
Figure 1. Sketch of the experimental facility.
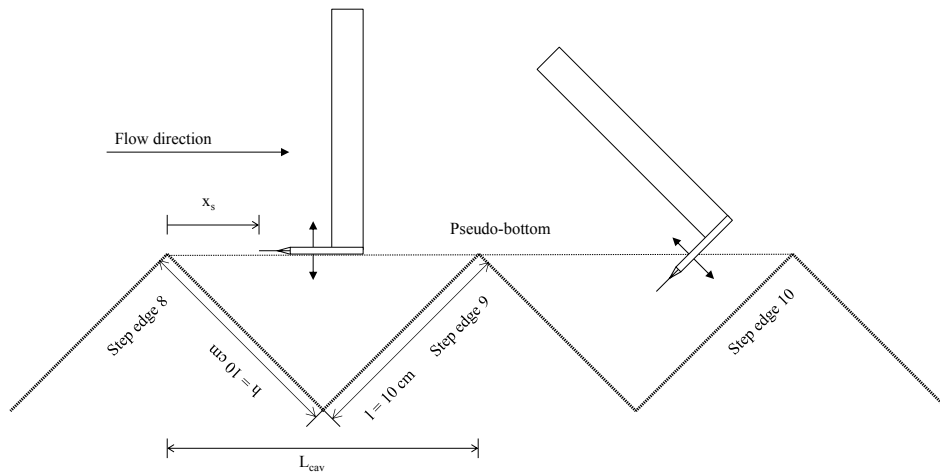
Figure 2. Probe alignment during air-water flow measurements

3. VOID FRACTION DISTRIBUTIONS

On a stepped chute, air is entrained because of interactions between the boundary layer outer edge and the free-surface (Rao and Rajaratnam 1961, Ervine and Falvey 1987, Chanson 1993, 2008). Figure 3 shows typical void fraction distributions at step edges for four dimensionless discharges (d_c/h = 0.9, 1.1, 1.3, 1.5), where y is the normal distance from the pseudo-bottom (y = 0), d_c is the critical depth, C is the time-averaged void fraction, x is the streamwise coordinate measured from the first step edge (Figure 1), x_i is the streamwise coordinate of the inception point, and L_{cav} is the step cavity length. All data followed an inverted S-shape distribution typically observed in skimming flows on stepped chutes with a variety of configurations (Chanson and Toombes 2002, Gonzalez and Chanson 2008, Bung 2009, Felder and Chanson 2011). The void fraction gradient ($\partial C/\partial y$) was maximum at about $C \approx 0.5$, indicating the largest level of air flux at that location (assuming that the gradient-diffusion hypothesis is valid). The void fraction profiles exhibited rapid longitudinal variations over the first 2-3 step edges downstream of the inception point as a result of flow bulking. Considering a control volume (CV) travelling downstream at a uniform velocity and neglecting any wall and buoyancy effects, its void fraction distribution is described by the 1-D diffusion equation:

$$\frac{\partial C}{\partial t} = D_t \frac{\partial^2 C}{\partial y^2}$$

(1)

where C is the void fraction, y is the normal distance from the pseudo-bottom (y = 0), and D_t is a turbulent diffusivity assumed to be independent of y. Assuming $D_t = D_t(t)$ so that the diffusivity is dependent of time, Equation (1) may be solved using the Laplace transform method with the following boundary condition:

$$C_{(y=Y_{50}, t>0)} = 0.5$$

(2)

where Y_{50} is the depth where $C = 0.5$. The solution is

$$C = \frac{1}{2} erfc \left(\frac{Y_{50} - y}{2\sqrt{\dfrac{D_a (x - x_i)}{V_a}}} \right)$$

(3)

where erfc is the complementary error function, V_a is the average streamwise velocity of the CV between x and x_i, and $D_a = \frac{1}{T} \int_0^{t=T} D_t dt$ (with $T = \frac{x - x_i}{V_a}$) is a time-averaged diffusivity. Note that for a steady and uniform flow with homogeneous turbulence, $D_a = D_t$. This solution is similar in form to that of a water jet discharging into the atmosphere (Chanson 1997, Brattberg et al. 1998). In Figure 3, Equation (3) is compared to the experimental data immediately downstream of the inception point (red curve). A good agreement was observed. It is noted that Equation (3) is unsuitable in regions where buoyancy or wall effects are important, particularly far downstream of the inception point of free-surface aeration.

Far downstream of the inception point, the flow became gradually varied, the void fraction profiles showed some self-similarity, and the effects of buoyancy must be accounted for. In this region, the conservation equation of air may be simplified into (Chanson 1995, 1997):

$$0 = \frac{\partial}{\partial y} \left(D_t \frac{\partial C}{\partial y} - u_{r,hyd} C\sqrt{1 - C} \cos \theta \right)$$

(4)

where $u_{r,hyd}$ is the bubble rise velocity in clear water with a hydrostatic pressure gradient and θ is the chute slope. Present data measured at the last step edge (step edge 12) were compared to a solution of Equation (4) obtained by Chanson and Toombes (2002):

$$C = 1 - \tanh^2\left(K - \frac{y/Y_{90}}{2D_0} + \frac{\left(y/Y_{90} - 1/3\right)^2}{3D_0}\right) \qquad (5)$$

where Y_{90} is the depth where $C = 0.9$, K is an integration constant, and D_0 is a function of the depth-averaged void fraction $C_{mean} = \frac{1}{Y_{90}}\int_0^{Y_{90}} Cdy$. Equation (5) generally compares well with the present data, despite some under-estimation for $y/d_c < 0.2 - 0.3$. This might be a result of vortical structures trapping bubbles in their centers and, hence, producing a local concentration of air-bubbles.
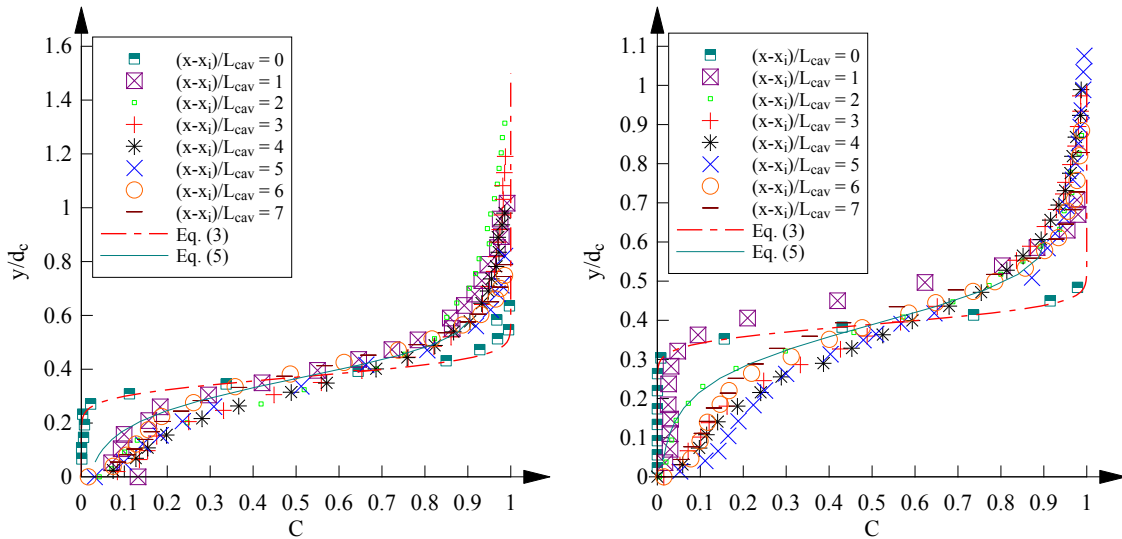
(A) $d_c/h = 0.9$

(B) $d_c/h = 1.1$
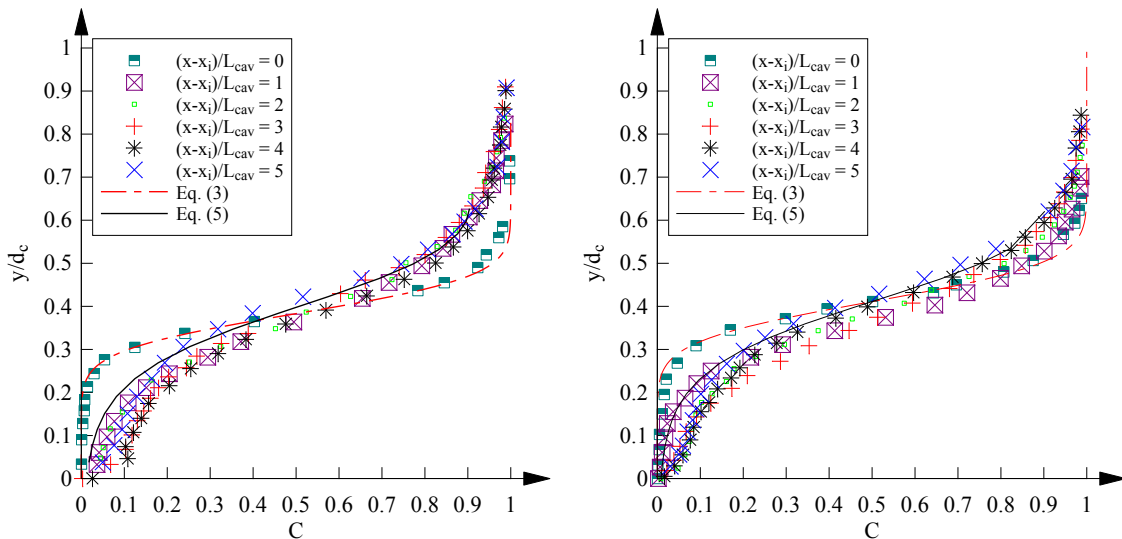
(C) $d_c/h = 1.3$

(D) $d_c/h = 1.5$

Figure 3. Void fraction distributions above step edges – Flow conditions: $\theta = 45°$, $h = 0.10$ m

Figure 4 shows the void fraction contours between step edges 7 and 9 for two skimming flow conditions ($d_c/h = 0.9$, 1.3), where x_s is the streamwise offset from step edge 8, and black symbols indicate measurement locations. For both discharges, the void fraction increased along the step cavity up to about 70% cavity length, then decreased towards the next step edge. This pattern might be a result of advective transport due to flow expansion and contraction over a step cavity. The recirculating cavity fluid trapped bubbles at its centre due to difference in air and water densities and is seen from the void fraction maxima found next to the cavity centres (Figure 4). This is especially evident for the larger discharge (Figure 4B).
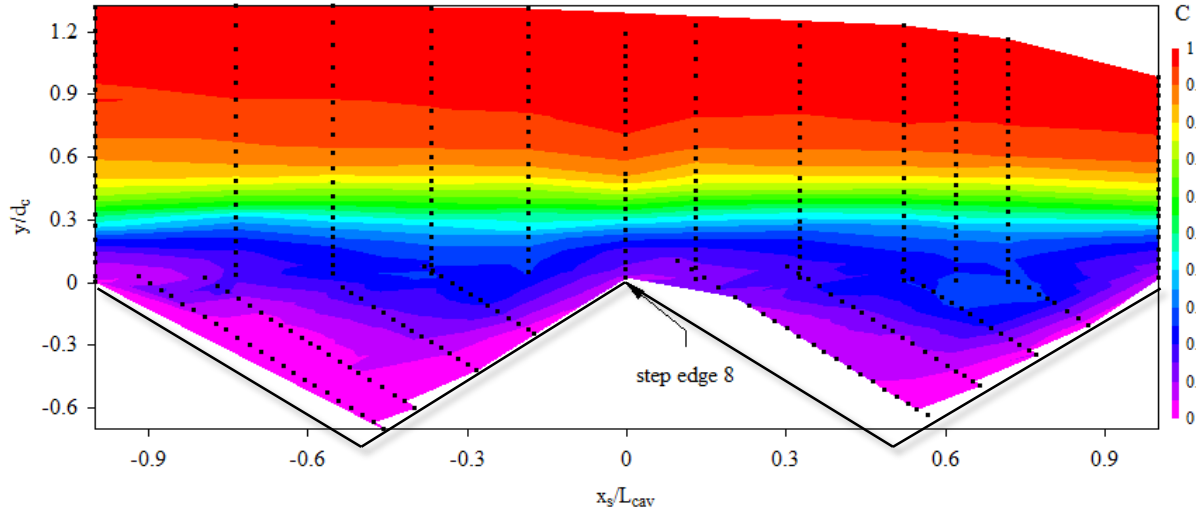
(A)
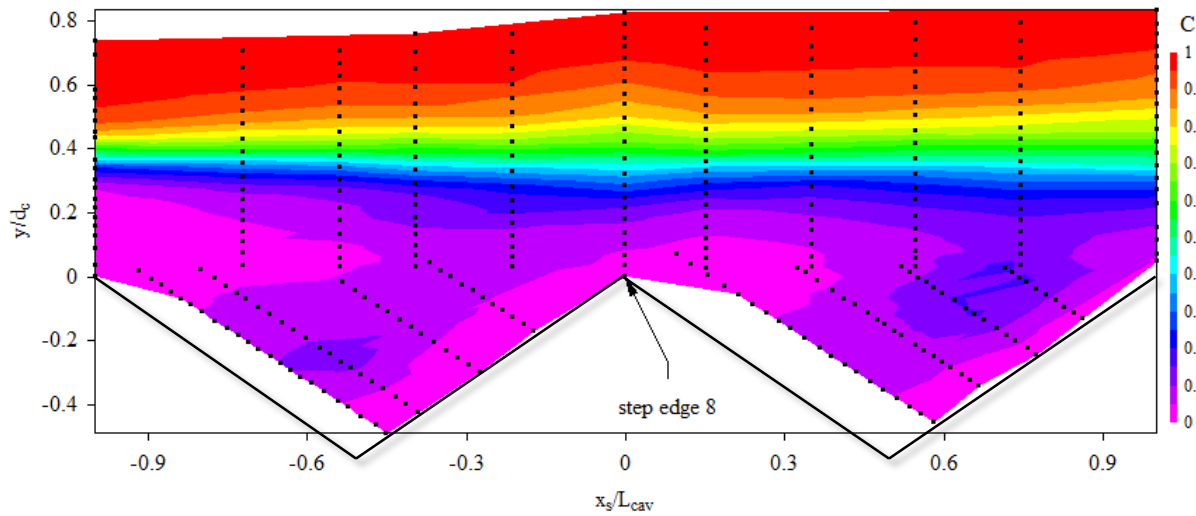
(B)

Figure 4. Void fraction contours between step edges 7 – 9 – Flow conditions: (A) $d_c/h = 0.9$, $Re = 3.4 \times 10^5$; (B) $d_c/h = 1.3$, $Re = 5.9 \times 10^5$; $\theta = 45°$, $h = 0.10$ m – Step faces: solid black lines

4. BUBBLE COUNT RATE DISTRIBUTIONS

In stepped chute flows, the bubble count rate F is defined as half the number of air-water interfaces detected by the probe sensor per second and is proportional to the specific interfacial area (Chanson 2002). The dimensionless bubble count rate distributions at each step edge downstream of the inception point are plotted in Figure 5, where F is the bubble count rate and V_c is the critical velocity. All data approximately followed a bell-shape, with the largest bubble count rate observed at about $y/d_c = 0.3 - 0.4$ corresponding to a void fraction of about 0.5. This observation was consistent with several past studies (Chanson and Toombes 2002, Yasuda and Chanson 2003, Gonzalez and Chanson 2008). It may be reasoned that the bubble count rate should be proportional to the variance of the corresponding binary void fraction signal, which equals $C(1-C)$ and has a maximum at $C = 0.5$ (Chanson and Carosi 2007). Toombes (2002) demonstrated that the relationship between void fraction and bubble count rate may be approximated by:

$$\frac{F}{F_{max}} = 4C(1-C) \qquad (6)$$

where F_{max} is the maximum bubble count rate at a cross-section. Equation (6) is compared to the present data in Figure 6, where the experimental data for $y < Y_{50}$ and $y \geq Y_{50}$ are shown in separate colors. Equation (6) was found to agree reasonably well with the present data for $y \geq Y_{50}$, but it differed significantly from those for $y < Y_{50}$. The non-linearly observed for $y < Y_{50}$ were likely induced by coherent fluctuations generated by the step edge, which implied that successive detections of air-water elements could not be assumed a random process. Away from the pseudo-bottom (i.e. $y \geq Y_{50}$), the effects of coherent structures became negligible and the assumptions for Equation (6) (see Toombes 2002) were more plausible. It is noted that these effects may be taken into account by a more advanced model proposed by Toombes and Chanson (2008).
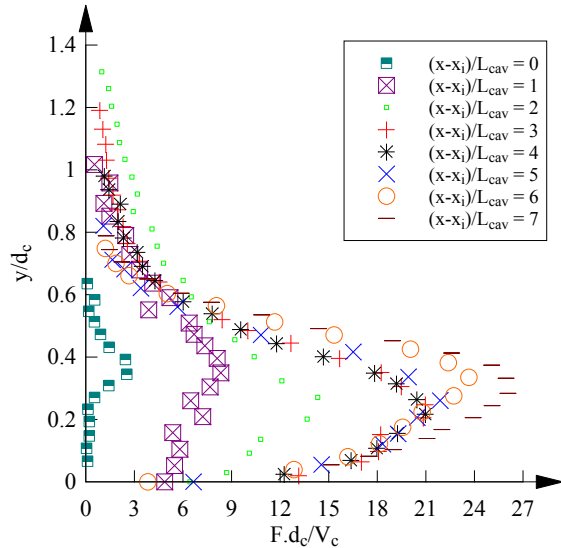
(A) $d_c/h = 0.9$
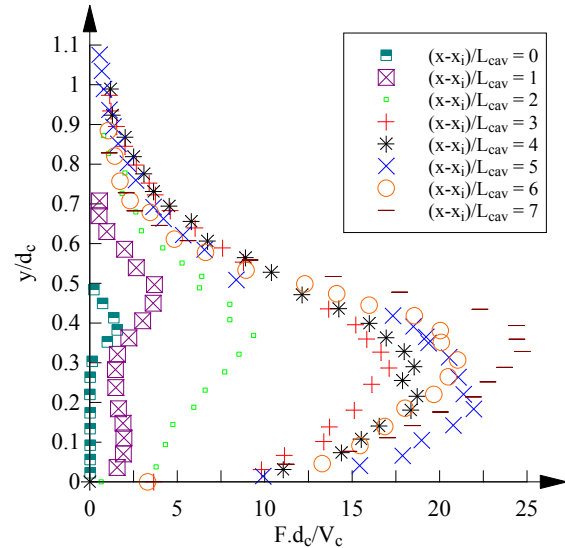
(B) $d_c/h = 1.1$
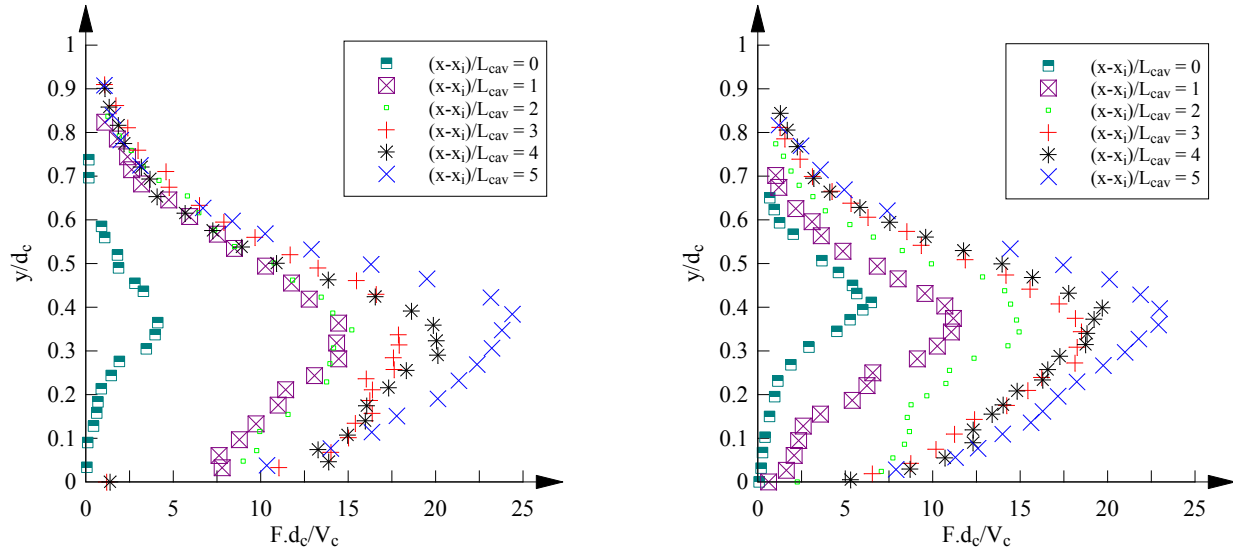
(C) $d_c/h = 1.3$ (D) $d_c/h = 1.5$

Figure 5. Bubble count rate distributions above step edges – Flow conditions: $\theta = 45°$, $h = 0.10$ m
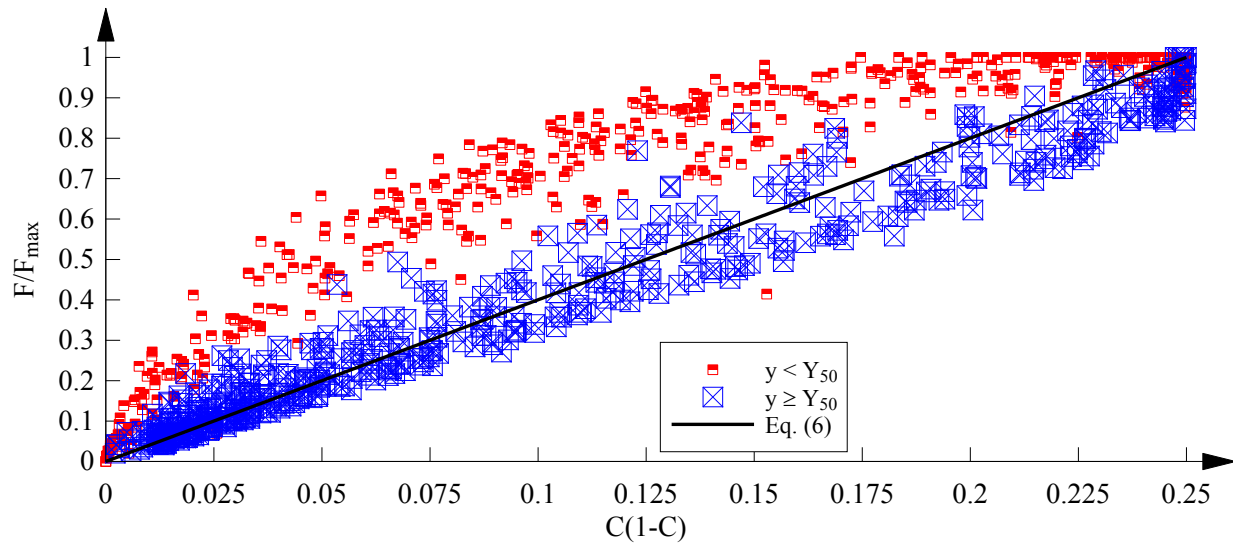
Figure 6. Relationship between void fraction and bubble count rate in skimming flows – Flow conditions: $d_c/h = 0.9, 1.1, 1.3, 1.5, 1.7$, $\theta = 45°$, $h = 0.10$ m

5. SELF-AERATION IN THE RAPIDLY-VARIED FLOW REGION

Immediately downstream of the inception point of aeration, turbulent transport is dominant over advective transport by the mean-flow and buoyancy. The new solution (Equation (3)) provides a satisfactory description of the diffusion process in this region. The flow depth variation in this region is a function of the depth averaged void fraction C_{mean}, which may be derived by integrating Equation (3) from 0 to Y_{90}. The lower limit of the integral may be replaced by $-Y_{90}$ using the method of images to account for any wall effects. The integration result yields:

$$C_{mean} = \frac{1.82\sqrt{\dfrac{D_a(x-x_i)}{V_a}}}{Y_{50} + 1.82\sqrt{\dfrac{D_a(x-x_i)}{V_a}}} \tag{7}$$

Figure 7 compares Equation (7) to the streamwise distributions of C_{mean}, where D_a and Y_{50} were derived from measured void fraction data. The agreement between Equation (7) and present data was generally good, including far downstream of the inception point (i.e. in the gradually-varied flow region). For the present data, the empirically determined apparent diffusivity D_a was best correlated with

$$\frac{D_a}{\sqrt{gd_c^3}} = 0.027e^{-0.276\frac{x-x_i}{L_{cav}}} \qquad (R = 0.876) \tag{8}$$

where R is the normalised correlation coefficient. The dimensionless form of Equation (8) (valid at step edges) suggested that it might be used in conjunction with Equation (7) in prototype applications when diffusivity data is not readily available. A further simplification may be made by letting $Y_{50} = d_i$ where d_i is the flow depth at the inception point (i.e. assuming the streamwise acceleration due to gravity is small). The simplification provides a practical means of estimating the flow bulking height in prototype structures.

A detailed examination of Figure 7 shows that C_{mean} typically increased rapidly immediately downstream of the inception point and reached a local maximum at about 2-4 cavity lengths downstream of the inception point of free-surface aeration, followed by a more gradual decrease. This de-aeration process was also observed by other authors (e.g. Matos 2000). It might occur when too much air was entrained initially. The turbulent diffusivity D_t may be derived by differentiating Equation (8):

$$\frac{D_t}{\sqrt{gd_c^3}} = 0.027\left(1 - 0.276\frac{x-x_i}{L_{cav}}\right)e^{-0.276\frac{x-x_i}{L_{cav}}} \tag{9}$$

Equation (9) is plotted in Figure 8. It is seen that, for the present data, the turbulent diffusivity increased to approximately 3.5 step lengths downstream of the inception point before becoming negative further downstream. Such a negative diffusivity implies a process of de-aeration, and its relation to C_{mean} becomes clear when Equation (1) is integrated from $-Y_{90}$ to Y_{90} (with the use of the method of images):

$$\frac{d}{dt}C_{mean} = \frac{D_t}{Y_{90}}\left(\left.\frac{\partial C}{\partial y}\right|_{y=Y_{90}} - \left.\frac{\partial C}{\partial y}\right|_{y=-Y_{90}}\right) \tag{10}$$

In skimming flows, the bracketed term can be shown to be positive by differentiating Equation (3) with respect to y (as long as the void fraction distribution is adequately described by Equation (3)). Thus, the total rate of change of the depth-averaged void fraction (dC_{mean}/dt) has the same sign as the diffusivity. Note that the present discussion is limited to a 1-D model neglecting any buoyancy effect. For completeness, some fragmented flow may experience a negative bracketed term: e.g., immediately downstream of a drop (Toombes and Chanson 2008).
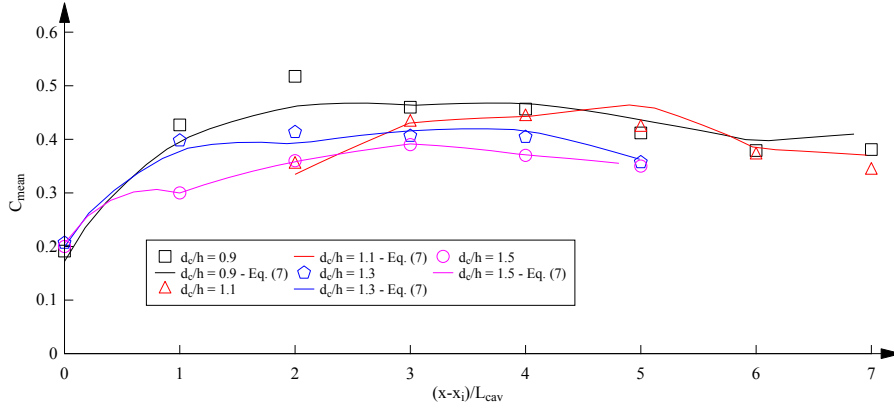
Figure 7. Steamwise distribution of depth averaged void fraction – comparison with Equation (7) – Flow conditions: $\theta = 45°$, $h = 0.10$ m
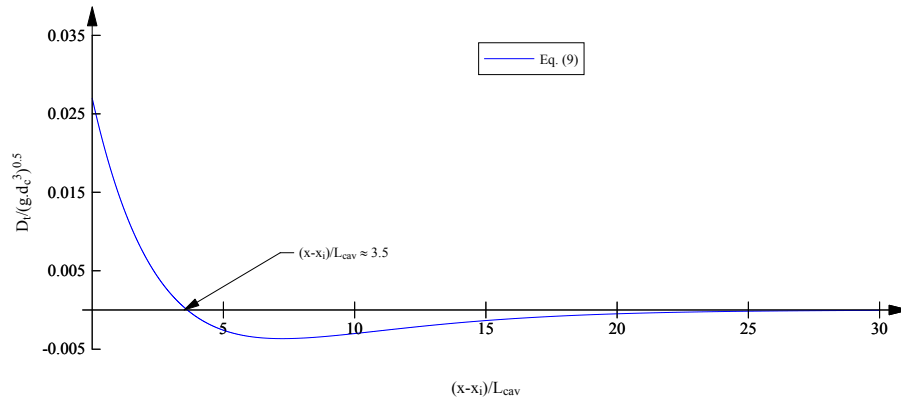
Figure 8. Streamwise distribution of turbulent diffusivity – Flow conditions: $\theta = 45°$, $h = 0.10$ m

6. CONCLUSION

On a stepped chute, self-aeration occurs when the turbulent boundary layer outer edge interacts with the free surface. A rapidly-varied flow region follows immediately downstream of the inception point of aeration. New void fraction distributions in this region were compared successfully to a newly proposed solution to the 1-D diffusion equation. Further downstream, the flow becomes gradually varied, and the experimental data were approximated closely by an existing solution of the steady state 1-D advection diffusion equation. Between step edges, the void fraction distributions showed variations consistent with flow expansion and contraction. The bubble count rate scaled with the void fraction signal variance, although their relationship was biased close to the wall under the influence of coherent motions. A simple model was proposed to describe the flow bulking in the rapidly-varied flow region and showed good agreement with the experimental data. It was found that flow bulking stopped at approximately 3.5 cavity lengths downstream of the inception point. The concept of negative diffusivity was introduced and was shown to be associated with flow de-aeration.

7. ACKNOWLEDGEMENTS

8. REFERENCES

Brattberg, T., Chanson, H., and Toombes, L. (1998). Experimental investigations of free-surface aeration in the developing flow of two-dimensional water jets. *Journal of Fluids Engineering*, Transactions ASME, Vol. 120, No. 4, pp. 738-744 (DOI: 10.1115/1.2820731).

Bung, D.B. (2009). Zur selbstbelüfteten gerinnenströmung auf kaskaden mit gemässigter neigung. ('Self-aerated skimming flows on embankment stepped spillways.') *Ph.D. thesis*, University of Wuppertal, LuFG Wasserwirtschaft and Wasserbau, Germany, 292 pages (in German).

Chanson, H. (1993). Stepped spillway flows and air entrainment. *Canadian Journal of Civil Engineering*, Vol. 20, No. 3, June, pp. 422-435 (DOI: 10.1139/l93-057).

Chanson, H. (1994). Hydraulics of skimming flows over stepped channels and spillways. *Journal of Hydraulic Research*, Vol. 32, No. 3, pp. 445-460 (DOI: 10.1080/00221689409498745).

Chanson, H. (1995). Air bubble diffusion in supercritical open channel flow. *Proc. 12th Australasian Fluid Mechanics Conference,* AFMC, Sydney, Australia, R.W. Bilger Editor, Vol. 2, pp. 707-710.

Chanson, H. (1997). Air bubble entrainment in free-surface turbulent shear flows. Academic Press, London, UK, 401 pages (ISBN 0-12-168110-6).

Chanson, H. (2002). Air-water flow measurements with intrusive phase-detection probes. Can we improve their interpretation? *Journal of Hydraulic Engineering*, ASCE, Vol. 128, No. 3, pp. 252-255 (DOI: 10.1061/(ASCE)0733-9429(2002)128:3(252)).

Chanson, H. (2008). Advective diffusion of air bubbles in turbulent water flows. in Fluid Mechanics of Environmental Interfaces, Taylor & Francis, Leiden, The Netherlands, C. Gualtieri and D.T. Mihailovic Editors, Chapter 7, pp. 163-196.

Chanson, H., and Carosi, G. (2007). "Advanced post-processing and correlation analyses in high-velocity air-water flows." *Environmental Fluid Mechanics*, Vol. 7, No. 6, pp. 495-508 (DOI: 10.1007/s10652-007-9038-3).

Chanson, H., and Toombes, L. (2002). Air-Water flows down stepped chutes. Turbulence and flow structure observations. *International Journal of Multiphase Flow*, Vol. 28, No. 11, pp. 1737-1761 (DOI: 10.1016/s0301-9322(02)00089-7).

Ervine, D.A., and Falvey, H.T. (1987). Behaviour of turbulent water jets in the atmosphere and in plunge pools. *Proc. Institution of Civil Engineers*, Part 2, Mar., 83, pp. 295-314.

Felder, S., and Chanson, H. (2011). Air-water flow properties in step cavity down a stepped chute. *International Journal of Multiphase Flow*, Vol. 37, No. 7, pp. 732–745 (DOI: 10.1016/j.ijmultiphaseflow.2011.02.009).

Gonzalez, C.A., and Chanson, H. (2008). Turbulence manipulation in embankment stepped chute flows: an experimental study. *European Journal of Mechanics B/Fluids*, Vol. 27, No. 4, pp. 388-408 (DOI: 10.1016/j.euromechflu.2007.09.003).

Matos, J. (1999). Air entrainment and energy dissipation on stepped spillways. *Ph.D. thesis*, Technical University of Lisbon, Portugal.

Matos, J. (2000). Hydraulic design of stepped spillways over RCC dams. *Proc. The International Workshop on Hydraulics of Stepped Spillways*, Zürich, March 22-24, 2000, pp. 187-194.

Rao, N.S.G., and Rajaratnam, N. (1961). On the inception of air entrainment in open channel flows. *Proc. 9th IAHR Biennial Congress*, Dubrovnick, Yugoslavia, pp. 9-12.

Toombes, L. (2002). Experimental study of air-water flow properties on low-gradient stepped cascades. *Ph.D. Thesis*, Dept. of Civil Engineering, University of Queensland, Australia.

Toombes, L., and Chanson, H. (2008). Interfacial aeration and bubble count rate distributions in a supercritical flow past a backward-facing step. *International Journal of Multiphase Flow*, Vol. 34, No. 5, pp. 427-436 (DOI: 10.1016/j.ijmultiphaseflow.2005.01.005).

Wood, I.R., Ackers, P., Loveless, J. (1983). General method for critical point on spillways. *Journal of Hydraulic Engineering*, ASCE, 109, 308–312 (DOI: 10.1061/(asce)0733-9429(1983)109:2(308)).

Yasuda, Y., and Chanson, H. (2003). Micro- and macro-scopic study of two-phase flow on a stepped chute. *Proc. 30th IAHR Biennial Congress*, Thessaloniki, Greece, J. Ganoulis and P. Prinos Editors, Vol. D, pp. 695-702.

Towards a New Design Equation for Piano Key Weirs Discharge Capacity

H. Bashiri[1], B. Dewals[1], M. Pirotton[1], P. Archambeau[1] and S. Erpicum[1]
[1]Hydraulics in Environmental and Civil Engineering (HECE)
University of Liege
Belgium
E-mail:

ABSTRACT

Piano Key weirs are Labyrinth-like weirs that can be placed on the top of gravity dams. They represent a powerful solution to increase the discharge capacity of existing dam spillways. For proper design, it is necessary to accurately predict this discharge capacity. In this research, artificial neural network and multiple linear and nonlinear regressions are used to set up a new design equation for the discharge capacity of Piano Key weirs. The effect of each parameter on the discharge capacity of Piano Key weirs is tested in these models. Several non-dimensional parameters are used to define a functional relationship between the inputs and output. These parameters are built from the geometric dimensions of the structure such as weir height, inlet and outlet keys width, overhangs length, water head, and side crest length. Previous experimental data, which were collected at the experimental laboratory of the research group Hydraulics in Environmental and Civil Engineering (HECE), University of Liege, are used for training and testing patterns of the models. Root mean square errors (RMSE) and coefficient of determination (R^2) are used as comparing criteria for the evaluation of the models. The model results compare well with experimental results and other existing equations. They also highlight key geometric parameters governing piano key weirs discharge capacity.

Keywords: Discharge capacity, hydraulic structure, Piano Key weir, artificial neural network, multiple linear regression.

1. INTRODUCTION

The Piano Key weir (PKW) is a modified type of labyrinth weir, which can be placed on the top of gravity dams (Ouamane and Lemperiere 2006). Application of the PKW in reservoirs and rivers has increased in recent years, with projects in France, Vietnam, Sri Lanka, United Kingdom, South Africa, and Australia. The PKW has a complex geometry, and each geometric parameter plays a role on the discharge capacity. The main parameters of PKW geometry are the weir height, the weir unit width, the number of weir units, the side crest length, the inlet and outlet keys widths, the upstream and downstream overhang lengths, and the wall thickness. Figure 1 shows a schematic diagram of a PKW. Various investigations have been done recently on different types of PKWs (Ouamane and Lemperiere 2006; Crookston and Tullis 2010; Machiels et al. 2011; Anderson and Tullis 2012; Leite Ribeiro et al. 2012a; Anderson and Tullis 2013; Machiels et al. 2013; Erpicum et al. 2014).

There are four types of PKWs based on the upstream and downstream overhangs (type A, B, C, and D). According to Figure 2, different types of PKW are described as A) with upstream and downstream overhangs, B) with upstream overhang, C) with downstream overhang, and D) without overhang. Some researchers proposed analytical and numerical equations for calculation of PKW discharge (Leite Ribeiro et al. 2011, 2012b; Kabiri-Samani and Javaheri 2012; Machiels et al. 2014). Leite Ribeiro et al. (2011) applied a non-linear global stepwise regression approach to fit the some dimensionless parameters to propose a mathematical formulation for the PKW. Leite Ribeiro et al. (2012b) investigated the head-discharge relation of A-type PKW experimentally. They showed that relative developed crest length (L/W) and the relative head (P_i/H) had a significant effect on the discharge capacity. Kabiri-Samani and Javaheri (2012) conducted some experiments to investigate the effect of the PKW geometry on the discharge coefficient for free and submerged flow conditions. They used the classical discharge equation for sharp-crested weirs and proposed an empirical equation for the discharge coefficient for all types of PKWs. Machiels et al. (2014) performed an experimental study to evaluate the influence of the main geometric parameters on the discharge capacity of PKWs. They developed an analytical formula to predict the discharge capacity of the weir. Their

equation is the sum of three components: the discharge per unit length of the upstream crest of the outlet, the discharge per unit length of the downstream crest of the inlet, and the discharge per unit length of the unit length of the lateral crest.
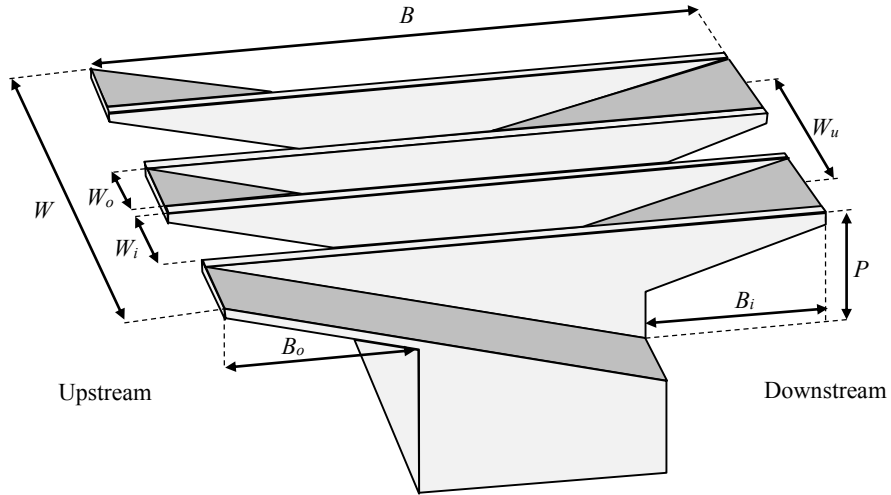
Figure 1. Schematic diagram of a PKW.

The main objectives of the research presented in this paper are to investigate the influence of several geometrical parameters on discharge capacity and to compare the efficiency of some parametrical models to predict the discharge capacity based on basic PKW non-dimensional parameters. Considering the data set of a former study (Machiels et al. 2014), which was collected at the experimental laboratory of the research group Hydraulics in Environmental and Civil Engineering (HECE), University of Liege, different models were tested. In this study, multiple linear regression (MLR), multiple nonlinear regression (MNLR), and artificial neural network (ANN) are applied to develop models for prediction of PKW discharge capacity, and their performance is compared using root mean square error and coefficient of determination. To evaluate the proposed model, we also compared the results with the analytical equation proposed by Leite Ribeiro et al. (2011), Leite Ribeiro et al. (2012b), and Machiels et al. (2014).

(a)

(b)

(c)

(d)
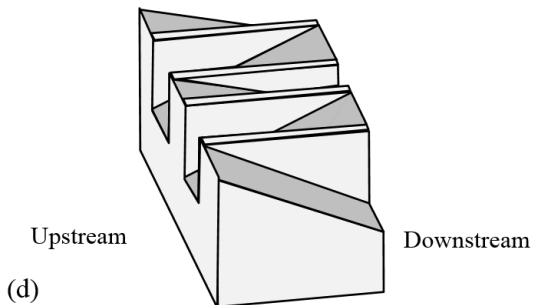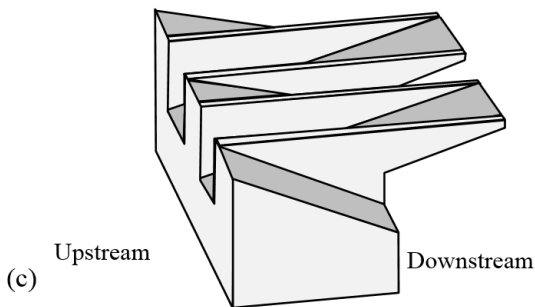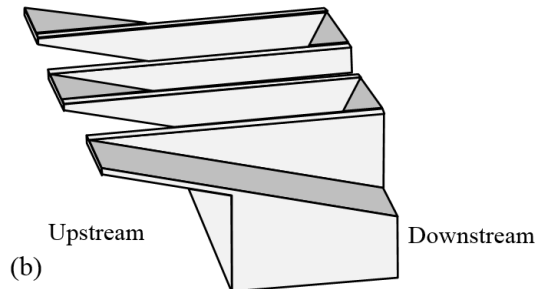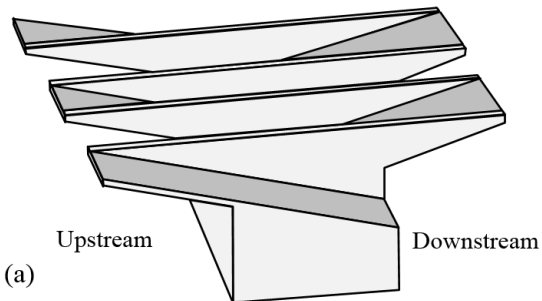
Figure 2. Various types of PKWs: (a) Type A, (b) Type B, (c) Type C, and (d) Type D.

2. METHODS

2.1. Data Set Analysis

The classical discharge equation for a linear free surface weir writes as

$$Q = C_d W \sqrt{2g} H^{3/2} \tag{1}$$

where Q is discharge, g is the acceleration of gravity, H is the total upstream hydraulic head, and W is the weir width. In this study, the non-dimensional discharge coefficient C_d has been investigated based on the discharge per PKW-unit width ($q = Q_u/W_u$). In particular, since this study aims at focusing on the effect of the geometrical parameters of the PKW, different methods have been applied to set up the best function f defined as by the equation below:

$$C_d = f(P/W_u, W_i/W_o, H/P, B/P, B_i/P, B_o/P) \tag{2}$$

where f is the function symbol, P is PKW height, W_i is the inlet key width, W_o is the outlet key width, B_i is downstream overhang length, B_o is upstream overhang length, and B is the side crest length.

Experimental measurements of Machiels et al. (2014) are used as training and testing sets of the MLR, MNLR, and ANN models (1360 tests). The main parameters of their study are listed in Table 1 with their range.

Table 1. Parameter range of PKW in the experiments of Machiels et al. (2014).

Variables	L/W	P/W_u	W_i/W_o	B_o/B_i	H/P	B/P	B_i/P and B_o/P	P_i/P_o
range	5.0	0.33-2	0.46-2.18	0-∞	0.06-3.2	1-6	0-2.67	1

2.2. Multiple Linear Regression

Multiple linear regression (MLR) is a multivariate linear regression method, and its objective is studying the relationship between several independent variables and a dependent variable (Adamowski et al. 2012). The relationship between dependent and independent variables is as follows:

$$y = \alpha_1 x_1 + \alpha_2 x_2 + \cdots + \alpha_n x_n + c \tag{3}$$

where α_i are the slopes or coefficients, c is the intercept, n is the number of observations, y is the dependent variable (predicted), and x is the independent variable (observed data set).

2.3. Multiple Nonlinear Regression

Multiple nonlinear regression (MNLR) models show nonlinear relationships between input and output data. There are a lot of mathematical functions for MNLR. The following represents a MNLR equation, which is used in this study.

$$y = \alpha_1 x_1^{\beta_1} + \alpha_2 x_2^{\beta_2} + \cdots + \alpha_n x_n^{\beta_n} + c \tag{4}$$

where β_i are additional regression coefficients.

2.4. Artificial Neural Network

The artificial neural network (ANN) is an effective model to predict the output based on input data. The ANN learns any complicated nonlinear function through a training procedure. Many papers show the application and performance of ANN in water resources and hydraulic engineering (Adamowski et al. 2012; Emiroglu and Kisi 2013; Jain 2001). The most applied neural network is the multi-layer perceptron (MLP), which includes layers of parallel perceptrons and is known as a feedforward network. The ANN approach provides an effective way to model data-dependent problems and gives a relationship between input and output data (Araghinejad 2014). Figure 3 shows a typical three-layer feedforward network, known as an MLP. One way to get a good result with an ANN model is to follow up some changes in the number of hidden layer, the number of hidden neurons and transfer function. In this study, we used three-layer perceptrons with a sigmoid activation function (Araghinejad 2014).
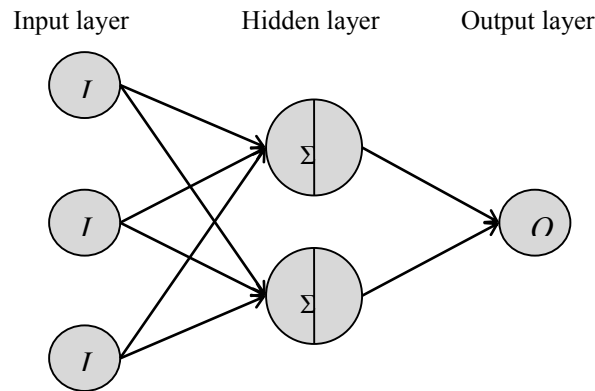
Figure 3. Architecture of a three-layer feedforward network (MLP).

The mathematical equation of MLP approach for calculation of output is (Adamowski et al. 2012)

$$O_k = g_2 \left[\sum_j V_j w_{kj} g_1 \left(\sum_i w_{ji} I_i + w_{j0} \right) + w_{ko} \right] \tag{5}$$

where I_i is input value of node i in the input layer, V_j is the hidden value of node j in the hidden layer, w_{ji} is the weight from input unit i to the hidden unit j, g is the transition function, w_{j0} is the bias for neuron j, w_{kj} is the weight connecting the hidden node j to the output k, w_{j0} is the bias for neuron k, and O_k is the output at node k in the output layer.

2.5. Existing Equations

The results achieved from the best model for each kind of predicting method and their variables are presented in section 3. The predicted results from this study are compared with analytical equations proposed by Leite Ribeiro et al. (2011), Leite Ribeiro et al. (2012b), and Machiels et al. (2014). Leite Ribeiro et al. (2011) applied a non-linear global stepwise regression approach to propose a mathematical formulation for the PKW, as follows:

$$r = \frac{Q_{PKW}}{Q_W} = \frac{C_d L_{eff} \sqrt{2g} H^{\frac{3}{2}}}{C_d W \sqrt{2g} H^{\frac{3}{2}}} \tag{6}$$

where r is the discharge enhancement ratio between the PKW discharge (Q_{PKW}) and the corresponding rectangular sharp-crested weir discharge (Q_W) and C_d is the discharge coefficient ($C_d = 0.42$). L_{eff} is the effective crest length of the PKW that contributes to the overflow. It is defined as $L_{eff} = N(W_i+W_o+2T_s+2B)$ with T_s the side wall width.

$$r = e^{\left[\begin{array}{c} -0.25945\left(\dfrac{P}{W_i}\right)^{1.4}\left(\dfrac{H}{P}\right)^{0.15} + 1.0056\left(\dfrac{L}{W_i}\right)^{0.1}\left(\dfrac{P}{W_i}\right)^{0.5}\left(\dfrac{H}{P}\right)^{0.7} \\ +0.067404\left(\dfrac{L}{W_i}\right)^{0.3}\left(\dfrac{P}{W_i}\right)^{0.1}\left(\dfrac{W_i}{W_o}\right)^{0.25}\left(\dfrac{H}{P}\right)^{0.2} + 13.9156\left(\dfrac{L}{W_i}\right)^{0.35}\left(\dfrac{H}{P}\right)^{0.15} \\ -14.0239\left(\dfrac{L}{W}\right)^{0.35}\left(\dfrac{H}{P}\right)^{0.2} + 0.094 \end{array} \right]} - 1 \qquad (7)$$

Leite Ribeiro et al. (2012b) used a physical based approach to calculate the Q_{PKW} (Eq. (6)). They evaluated the effect of various parameters on Q_{PKW} and divided them into two main groups (primary and secondary parameters). They suggested the equations below for evaluation of the primary effects.

$$\delta = \left(\frac{(L-W)P_i}{WH}\right)^{0.9}; \qquad r = 1+0.24\delta \qquad (8)$$

The effects of the secondary parameters, W_i/W_o, P_o/P_i, $(B_i+B_o)/B$ and R_o/P_o, were considered in the correction factors, as follows:

$$w = \left(\frac{W_i}{W_o}\right)^{0.05}; \quad p = \left(\frac{P_o}{P_i}\right)^{0.25}; \quad b=\left(0.3+\frac{B_o+B_i}{B}\right)^{-0.5}; \quad a=1+\left(\frac{R_o}{P_o}\right)^2 \qquad (9)$$

$$r = 1+0.24\delta(wpba) \qquad (10)$$

Later, Machiels et al. (2014) suggested that the discharge per PKW-unit width ($q = Q_u/W_u$) can be estimated by following equation:

$$q = q_u\frac{W_o}{W_u} + q_d\frac{W_i}{W_u} + q_s\frac{2B}{W_u} \qquad (11)$$

$$q_u = 0.374\left(1+\frac{1}{1000H+1.6}\right)\times\left[1+0.5\left(\frac{H}{H+P_T}\right)^2\right]\sqrt{2gH^3}; \quad q_d = 0.445\left(1+\frac{1}{1000H+1.6}\right)\times\left[1+0.5\left(\frac{H}{H+P}\right)^2\right]\sqrt{2gH^3}$$

$$q_s = 0.41\left(1+\frac{1}{833H+1.6}\right)\left[1+0.5\left(\frac{0.833H}{0.833H+P_e}\right)^2\right]\times\left[\frac{P_e^\alpha+\beta}{(0.833H+P_e)^\alpha+\beta}\right]K_{W_i}K_{W_o}\sqrt{2gH^3}$$

$$P_e = \frac{B_o}{B}P_T + \left(1-\frac{B_o}{B}\right)\frac{P}{2}; \qquad \alpha=\frac{0.7}{S_i^2}-\frac{3.58}{S_i}+7.55; \quad \beta=0.029e^{-1.446/S_i}; \quad K_{W_i}=1-\frac{\gamma}{\gamma+W_i^2}; \quad \gamma=0.0037\left(1-\frac{W_i}{W_o}\right)$$

$$K_{W_o}=1 \text{ for } \frac{H}{W_o}\leq\delta_1; \quad K_{W_o}=\frac{2}{(\delta_2-\delta_1)^3}\left(\frac{H}{W_o}\right)^3 - \frac{3(\delta_2-\delta_1)}{(\delta_2-\delta_1)^3}\left(\frac{H}{W_o}\right)^2 + \frac{6\delta_2\delta_1}{(\delta_2-\delta_1)^3}\left(\frac{H}{W_o}\right) + \frac{\delta_2^2(\delta_2-3\delta_1)}{(\delta_2-\delta_1)^3} \text{ for } \delta_1\leq\frac{H}{W_o}\leq\delta_2$$

$$K_{W_o}=0 \text{ for } \delta_2\leq\frac{H}{W_o}; \qquad \delta_1 = -0.788S_0^{-1.88}+5; \qquad \delta_2 = 0.236S_0^{-1.94}+5$$

$$(12)$$

where q_u is the discharge per unit length of the upstream crest of the outlet key, q_d is the discharge per unit length of the downstream crest of the inlet key, q_s is the discharge per unit length of the lateral crest, α and β are the parameters related to the weir geometry, P_e is the mean side wall height, K_{W_i} and K_{W_o} are factors related to the keys width ratio, γ is parameter fitted on the experimental results, and δ_1 and δ_2 are thresholds.

3. RESULTS AND DISCUSSION

3.1. MLR Model

The MLR models for prediction of discharge capacity of PKWs were developed using a spreadsheet software. The MLR models were trained and tested using various combinations of input data. Initially, all the data were selected as input, and the output was predicted. To examine the effect of each parameter on the discharge capacity, we neglect one parameter in each model. For each variable, we used the 1360 data sets. We used two performance indicators, root mean square error (RMSE) and coefficient of determination (R^2), to analyze the different models. In this model, α_1 through α_6 are coefficients of P/W_u, W_i/W_o, H/P, B/P, B_i/P and B_o/P, respectively (Eq. (3)).
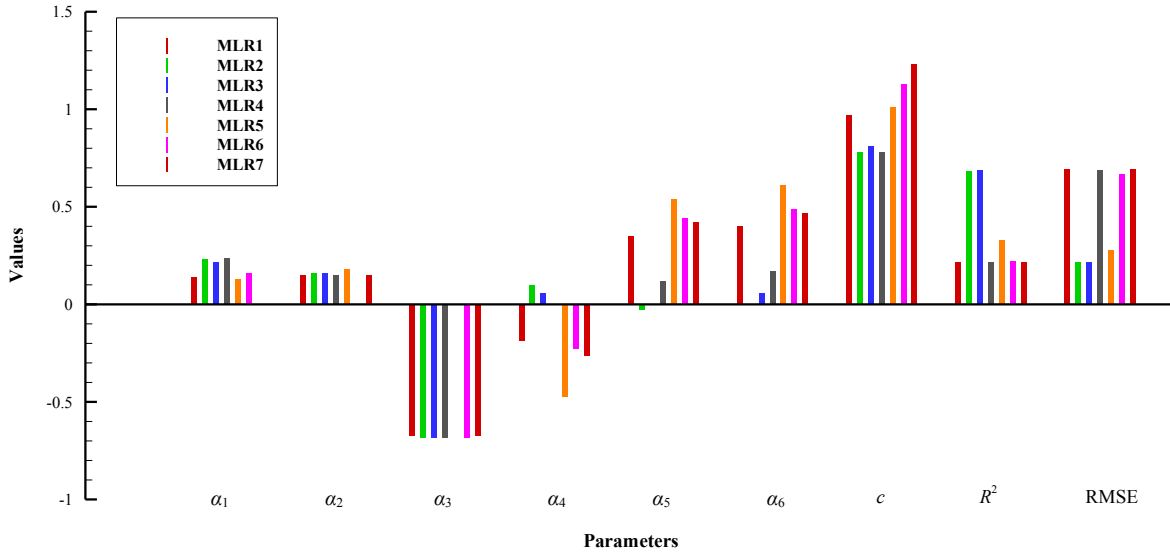
Figure 4. Variables of the MLR models and their performance.

$$R^2 = 1 - \frac{\sum_{i=1}^{N}(O_i - C_i)^2}{\sum_{i=1}^{N}(O_i - \overline{O_i})^2} \tag{13}$$

$$RMSE = \sqrt{\frac{1}{N}\sum_{i=1}^{N}(O_i - C_i)^2} \tag{14}$$

where N is the number of data set, O_i is the observed data, $\overline{O_i}$ is the average value of observed data, and C_i is the calculated data. Figure 4 shows the different MLR models, their coefficients, and their RMSE and R^2 values. All the models were developed in the same way. Comparison of performance indicators shows that the effect of H/P, B_i/P, and B_o/P on the discharge capacity is more than the other parameters.

3.2. MNLR Model

The MNLR models for prediction of discharge capacity of PKW were developed using a solver function in the spreadsheet software. In this study, we tried to minimize the RMSE for prediction of PKW discharge capacity using Eq. (4). The MNLR model coefficients and their performance is shown in Table 2. The comparison between performance indicators shows that the effect of H/P, P/W_u, W_i/W_o, and B/P on the discharge capacity is more than the other parameters. As it is shown in Table 2, neglecting these parameters has a significant effect on the performance indicators.

3.3. ANN Model

The ANN models were trained and tested based on different combinations of input parameters. The Levenberg-Marquardt backpropagation algorithm was used for neural network training. Among the total data, 70% were randomly selected for training, and the remaining 30% were used for validation and testing. Table 3 shows the values of performance indicators and different combinations of input variables in ANN models. In this study, the hidden layer contains 10 neurons and a tangent sigmoid function was employed as the transfer function. The discharge results for experimental and numerical models using the ANN1 model are compared in Figure 5. The results showed that among the parameters, H/P and W_i/W_o have important effects on the discharge capacity.

Table 2. Variables of the MNLR models and their performance.

Model	Equation	RMSE	R^2
MNLR1	$C_d = 0.22(B_o/P)^{0.51} + 0.08(B_i/P)^{0.88} - 1.89(B/P)^{-0.82} - 4(H/P)^{0.11}$ $+ 4(W_i/W_o)^{0.03} + 2.44(P/W_u)^{0.36} - 0.26$	0.1198	0.9050
MNLR2	$C_d = -0.7(B_i/P)^{0.01} - 3.63(B/P)^{-0.45} - 4(H/P)^{0.11}$ $+ 4(W_i/W_o)^{0.03} + 4(P/W_u)^{0.26} - 0.22$	0.1193	0.9058
MNLR3	$C_d = 0.09(B_o/P)^{0.53} - 2.54(B/P)^{-0.64} - 3.41(H/P)^{0.13}$ $+ 3.16(W_i/W_o)^{0.04} + 2.5(P/W_u)^{0.38} - 0.23$	0.1199	0.9049
MNLR4	$C_d = 1.16(B_o/P)^{0.27} + 1.26(B_i/P)^{0.12} - 3.79(H/P)^{0.12}$ $+ 2.21(W_i/W_o)^{0.06} + 4(P/W_u)^{0.07} - 0.37$	0.1349	0.8796
MNLR5	$C_d = -0.69(B_o/P)^{0.05} - 1.02(B_i/P)^{0.05} - 2.83(B/P)^{-0.66}$ $+ 0.67(W_i/W_o)^{0.25} + 3.56(P/W_u)^{0.42} + 0.57$	0.3212	0.3181
MNLR6	$C_d = 0.32(B_o/P)^{0.64} + 0.15(B_i/P)^{1.04} - 1.38(B/P)^{-1.09}$ $- 2.85(H/P)^{0.17} + 4(P/W_u)^{0.21} - 0.27$	0.1320	0.8848
MNLR7	$C_d = 1.61(B_o/P)^{0.001} + 1.15(B_i/P)^{-0.004} - 0.4(B/P)^{-2.97}$ $- 4(H/P)^{0.11} + 1.94(W_i/W_o)^{0.08} - 0.25$	0.1366	0.8766
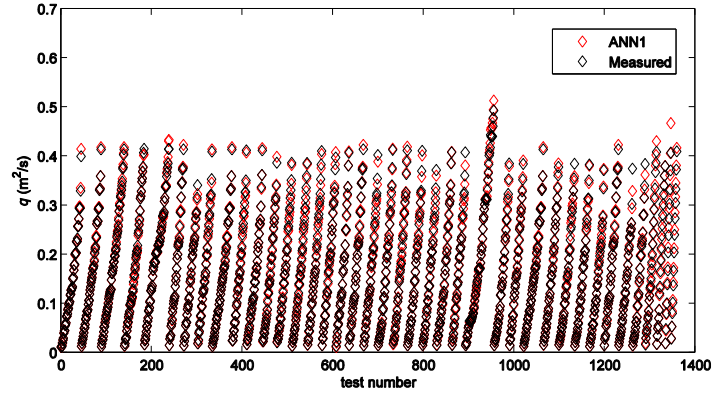
Figure 5. Comparison of predicted versus measured water discharge using the ANN1 model.

3.4. Comparison to Existing Equations

The discharge capacity results using ANN, MNLR, Leite Ribeiro et al. (2011), Leite Ribeiro et al. (2012b), and Machiels et al. (2014) are compared with the experimental data (Figure 6). Figure 6 demonstrates that the ANN model with $R^2 = 0.9982$ and RMSE = 0.0046 was found to provide more accurate results than the others.

Table 3. Performance of ANN models.

Model	Input variables	RMSE	R^2
ANN1	$P/W_u, W_i/W_o, H/P, B/P, B_i/P$ and B_o/P	0.0300	0.9940
ANN2	$P/W_u, W_i/W_o, H/P, B/P$ and B_i/P	0.0364	0.9912
ANN3	$P/W_u, W_i/W_o, H/P, B/P$ and B_o/P	0.0380	0.9904
ANN4	$P/W_u, W_i/W_o, H/P, B_i/P$ and B_o/P	0.0353	0.9917
ANN5	$P/W_u, W_i/W_o, B/P, B_i/P$ and B_o/P	0.3182	0.3308
ANN6	$P/W_u, H/P, B/P, B_i/P$ and B_o/P	0.0712	0.9664
ANN7	$W_i/W_o, H/P, B/P, B_i/P$ and B_o/P	0.0377	0.9906
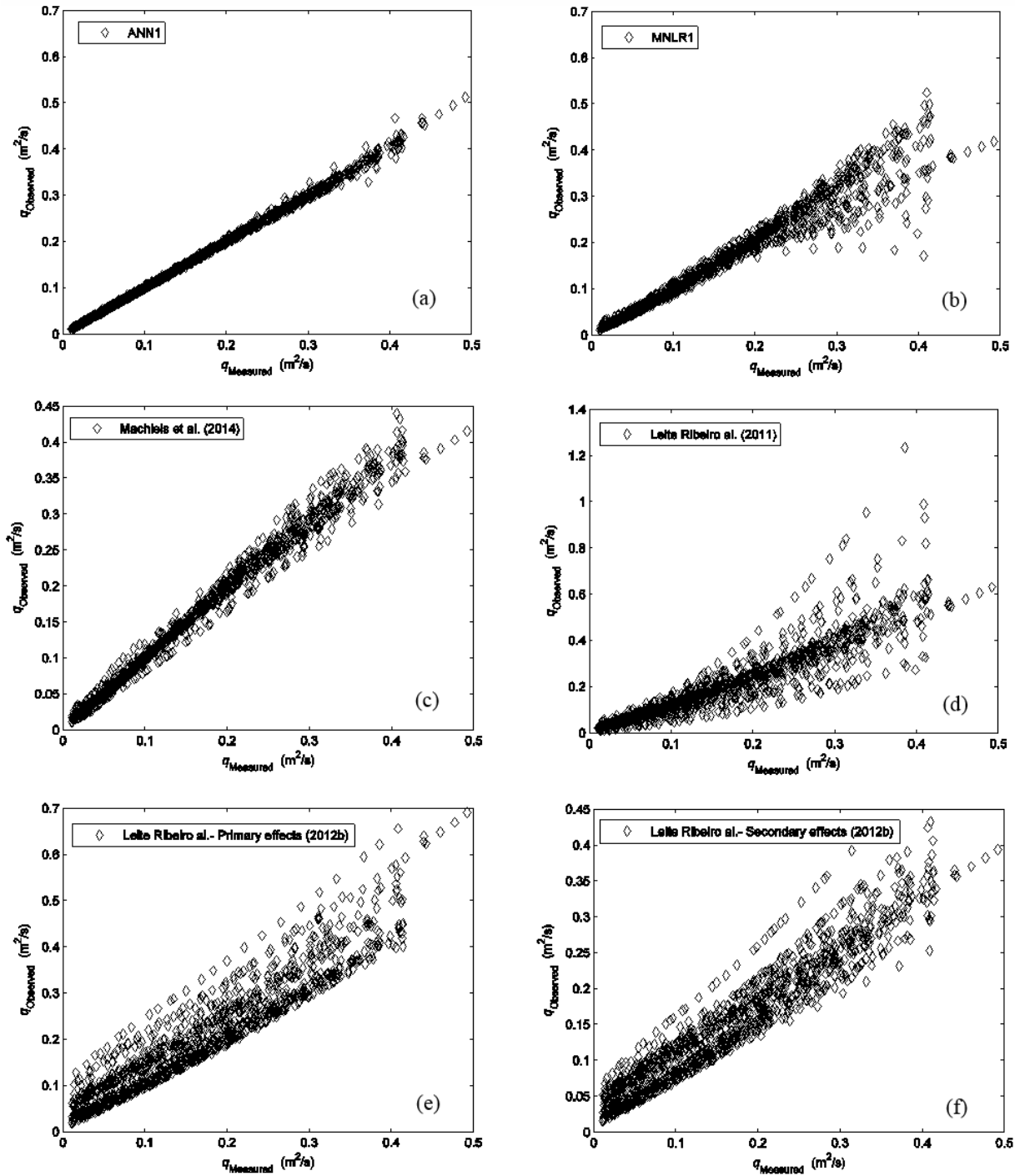
Figure 6. Comparison between measured and computed discharge using (a) ANN, (b) MNLR, (c) Machiels et al. (2014), (d) Leite et al. (2011), (e) Leite et al. (2012b)-Primary effects, and (f) Leite et al. (2012b)-Secondary effects.

4. CONCLUSIONS

Various methods have been applied to set up a predictive equation for PKW discharge capacity considering several non-dimensional geometrical parameters. The measured data for training and comparison were collected at the University of Liege. Existing design equations of Leite Ribeiro et al. (2011), Leite Ribeiro et al. (2012b), and

Machiels et al. (2014) were also considered for comparison. A previous study by Erpicum et al. (2014) highlighted the importance of P/W_u, W_i/W_o, and B_i/B_o. It was determined that H/P, B_i/P and B_o/P are more effective than other parameters in MLR model. Also, H/P, P/W_u, W_i/W_o, and B/P showed significant influence on the discharge capacity in MNLR model. For ANN, it is H/P and W_i/W_o.

Possible future research on prediction of PKWs can include application of other soft computing methods for PKW discharge predicting; evaluation of various analytical equations for the PKW's discharge; and proposing a general and simple equation for all kinds of PKWs using existing data.

5. REFERENCES

Adamowski, J., Chan, H.F., Prasher, S.O., Ozga-Zielinski, B., and Sliusarieva, A. (2012). "Comparison of multiple linear and nonlinear regression, autoregressive integrated moving average, artificial neural network, and wavelet artificial neural network methods for urban water demand forecasting in Montreal, Canada." *Water Resour. Res.,* 48, W01528, doi:10.1029/2010WR009945.

Anderson, R.M., and Tullis, B.P. (2012). "Piano Key Weir: reservoir versus channel application." *J. Irrig. Drain. Eng.,* 138(8), 773-776.

Anderson, R.M., and Tullis, B.P. (2013). "Piano Key Weir hydraulics and labyrinth weir comparison." *J. Irrig. Drain. Eng.,* 139(3), 246-253.

Araghinejad, S. (2014). Data-driven modeling: using MATLAB in water resources and environmental engineering, Springer, Netherlands.

Crookston, B., and Tullis, B.P. (2010). "Hydraulic performance of labyrinth weirs." *Proc.*, *3rd International Junior Research and Engineer Workshop on Hydraulic Structures*, Brisbane, Australia, 39-46.

Emiroglu, M.E., and Kisi, O. (2013). "Prediction of discharge coefficient for trapezoidal labyrinth side weir using a neuro-Fuzzy approach." *Water Resour. Manage.,* 27, 1473-1488.

Erpicum, S., Archambeau, P., Pirotton, M., and Dewals, B.J. (2014). "Geometric parameters influence on Piano Key Weir hydraulic performances." *Proc*., 5th Int. Symp. On Hydraulic Structures, Brisbane, Australia.

Jain, S.K., (2001). "Development of integrated sediment rating curves using ANNs." *J. Hydraul. Eng.,* 127(1), 30-37.

Kabiri-Samani, A., and Javaheri, A. (2012). "Discharge coefficients for free and submerged flow over Piano Key Weirs." *J. Hydraul. Res.,* 50(1), 114-120.

Leite Ribeiro, M., Bieri, M., Boillat, J-L., Schleiss, A.J., Singhal, G., and Sharma, N. (2012a). "Discharge capacity of Piano Key Weirs." *J. Hydraul. Eng.,* 138(2), 199-203.

Leite Ribeiro, Boillat, J-L., Schleiss, A.J., Doucen, O.L., and Laugier, F. (2011). "Experimental parametric study for hydraulic design of PKWs." *Proc*., International Conference on Labyrinth and Piano Key Weirs, Liege, Belgium, 183-190.

Leite Ribeiro, M., Pfister, M., Schleiss, A., and Boillat, J-L. (2012b). "Hydraulic design of A-type Piano Key Weirs." *J. Hydraul. Res.,* 50(4), 400-408.

Machiels, O., Erpicum, S., Dewals, B., Archambeau, P., and Pirotton, M. (2011). "Experimental observation of flow characteristics over a Piano Key Weir." *J. Hydraul. Res.,* 49(3), 359-366.

Machiels, O., Erpicum, S., Archambeau, P., Dewals, B.J., and Pirotton, M. (2013). "Parapet wall effect on Piano Key Weirs efficiency." *J. Irrig. Drain. Eng.,* 139(6), 506-511.

Machiels, O., Pirotton, M., Archambeau, P., Dewals, B., and Erpicum, S. (2014). "Experimental parametric study and design of Piano Key Weirs." *J. Hydraul. Res.,* 52(3), 326-335.

Ouamane, A., and Lemperiere, F. (2006). "Design of a new economic shape of weir." *Proc*., Int. Symp. Dams in the Societies of the 21st Century, Barcelona, CIGB-ICOLD, Paris, 463-470.

Effect of a Large Bed Roughness on Positive Surge Propagation in Canals

S.C. Yeow[1], H. Wang[1] and H. Chanson[1]
[1]School of Civil Engineering
The University of Queensland
Brisbane QLD 4072
Australia
E-mail: h.chanson@uq.edu.au

ABSTRACT

In open channels and water supply canals, the brusque operation of control valves and gates may induce large unsteady flow motions called surges. To date, the literature has focused on the propagation of surges in smooth canals, ignoring the effects of large roughness and debris. Herein, a physical study was conducted under controlled flow conditions to study the turbulent mixing in the close vicinity of a large circular bed roughness element during the upstream propagation of positive surges. Detailed free-surface and instantaneous velocity measurements were conducted with and without the large and flat cylindrical element. For a number of tests, the experiments were repeated 25 times, and the results were ensemble-averaged. The data suggested that the positive surge propagation was associated with large instantaneous free-surface fluctuations for all investigated flow conditions. The velocity measurements showed large variations in longitudinal velocity during the surge generation, as well as large fluctuations of all velocity components. The presence of the large bed element modified the velocity fluctuations and unsteady Reynolds stresses in the vicinity of the element. The present results implied the potential for bed scour around the element during surge propagation.

Keywords: Positive surges, Large cylindrical roughness element, Turbulence, Mixing, Physical modelling, Scour.

1. INTRODUCTION

In open channels, canals, and rivers, a rapid increase in flow depth will induce a positive surge, also called a bore or compression wave (Henderson 1966, Liggett 1994). The positive surge is a translating hydraulic jump. The shape of the bore front is characterized by its Froude number Fr_1, whose expression may be derived based upon momentum considerations for an irregular channel cross-section:

$$Fr_1 = \frac{V_1 + U}{\sqrt{g \times A_1 / B_1}} \tag{1}$$

where V_1 is the initial flow velocity positive downstream, U is the bore celerity positive upstream, g is the gravity acceleration, A_1 is the initial flow cross-section area, and B_1 is the initial free-surface width (Chanson 2012). A well-known geophysical application is the tidal bore, which is a positive surge propagating upstream in an estuarine zone when the tidal flow turns to rising, rushing into a funnel shaped river mouth with shallow waters (Tricker 1965, Chanson 2011a). Figure 1 presents photographs of tidal bores propagating upstream. Tidal bores can be dangerous, adversely impacting man-made structures and endangering lives. In recent years, the Hoogly River bore (Figure 1B) gained in strength due to the completion of upstream dams, and the tidal bore destroyed several bridge structures. The impact of a tidal bore on bridges and bridge piers is rarely documented, although some studies were conducted on the impact of the G15 Shenhai Expressway and G15W Changtai Expressway bridges over the Hangzhou Bay and Qiantang River mouth (China) (Lu et al. 2009). Another example is the 15th century Pont Aubaud bridge on the Sélune River (France) (Chanson 2011b).

To date, there is little information on the impact of man-made structures on positive surges and bores. The literature does not cover the effects of debris and large roughness. The present contribution examines in detail the propagation of positive surges over a large cylindrical roughness element, representative of a damaged bridge pier foundation.

The turbulence and turbulent mixing generated by the passage of the positive surge were carefully documented under controlled flow conditions. The experimental results showed the impact of the large element on the steady and unsteady turbulent shear stresses in the close vicinity of the element.

(A) Undular bore of the Dordogne River (France) on 29 October 2015 (Photograph Hubert Chanson)

(B) Hoogly River bore (India) in March 2015 (Courtesy of Antony Colas)

Figure 1. Photographs of positive surges in natural estuaries

2. EXPERIMENTAL SETUP, INSTRUMENTATION, AND FLOW CONDITIONS

2.1. Experimental Facility and Instrumentation

New experiments were conducted in a new 15 m long 0.5 m wide tilting flume. The bed slope was horizontal for all experiments herein. The flume was made of smooth PVC bed and glass walls. The initially steady flow was supplied by an upstream water tank, 2.0 m long and 1.25 m wide, equipped with baffles and two rows of flow straighteners, leading the water to the flume through a smooth three-dimensional convergent intake. The initial flow conditions could be controlled by a radial gate located next to the channel's downstream end (x = 14.75 m). The positive surge was generated by the rapid closure of a Tainter gate that was located at x = 14.10 m, just upstream of the radial gate (Fig. 2A). The Tainter gate closure time was less than 0.15 s to 0.2 s, and the gate closure time had no impact on surge propagation.

The water discharge was measured with a Venturi meter with an accuracy of 2%. In steady flows, the water depth was measured using rail mounted pointer gauges with an error of ±0.5 mm. The unsteady flow depths were measured with a series of acoustic displacement meters Microsonic™ Mic+25/IU/TC located at several longitudinal distances above the channel centerline: x = 6.1 m, 7.1 m, 8.1 m, 9.1 m, and 14.15 m, with an accuracy of 0.18 mm (Microsonic 2004). The instantaneous velocity measurements were performed using an acoustic Doppler velocimeter (ADV) Nortek™ Vectrino+ (Serial No. VNO 0802) equipped with a three-dimensional side-looking head. The ADV head is seen in Figures 2B and 2C. The error on the velocity data was 1% of the velocity range, herein ± 1 m/s: that is ±0.01 m/s (Nortek 2009). The acoustic displacement meters and ADV were synchronized within 1 ms and sampled simultaneously at 200 Hz. The vertical translation of ADV system was controlled by a fine adjustment traverse connected to a Mitutoyo™ digimatic unit. The error on the vertical position was less than 0.025 mm.
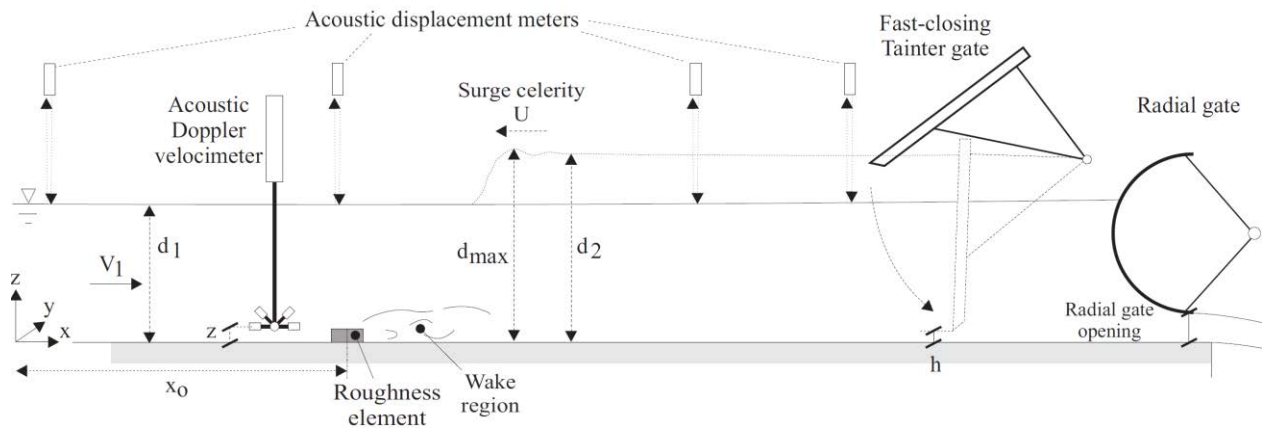
(A) Definition sketch
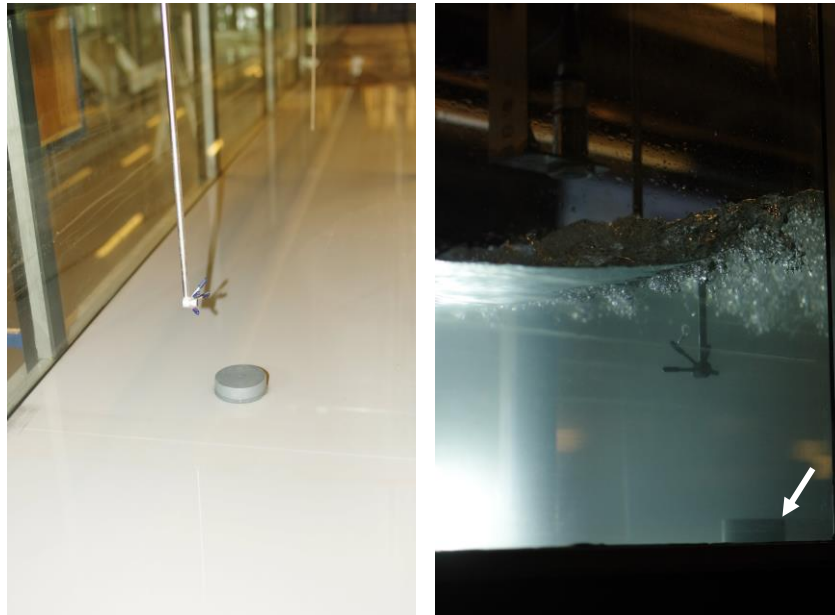
(B, Left) Roughness element in the dry channel looking downstream - (C, Right) Roughness element (white arrow) beneath an advancing bore - Flow conditions: Q = 0.061 m³/s, d_1 = 155 mm at x = 5.9 m, Fr_1 = 1.39

Figure 2. Positive surge propagation in the experimental channel

2.2.   Experimental Configurations

Two bed configurations were investigated. Configuration A consisted of the original smooth PVC bed. In Configuration B, a large cylindrical element was fixed to the PVC bed (Figures 2B and 2C). Its center was located on the channel centerline ($y = 0$) at $x_o = 7.1$ m. The element was made out of PVC, and its dimensions were a diameter: $D = 0.060$ m and a height: $H = 0.020$ m. Three water discharges ($Q = 0.039$, 0.051 and 0.061 m^3/s) were tested (Table 1). For each experiment, the positive surge was generated by the rapid closure of the Tainter gate and the surge propagated upstream as sketched in Figure 2A. The radial gate was fully opened for the breaking bore experiments; it was initially partially closed (Table 1) to raise the initial water depth d_1 during the undular surge experiment.

Several series of experiments were conducted. Series 1 included steady flow velocity measurements upstream and downstream of the large roughness element to document the effects of the element on the initially steady flow and the extent of the wake region downstream of the cylindrical element (see below). At each location, the velocity was sampled at 200 Hz for 180 s. Series 2 consisted of free-surface measurements during the propagation of positive surge. Series 3 encompassed a series of instantaneous velocity measurements during the propagation of positive surge. Both instantaneous and ensemble-average experiments were performed. For each run, the instruments were started 60 s prior to gate closure; the sampling stopped when the surge reached the upstream intake structure. For each set of ensemble-average experiments, a total of 25 runs were repeated in Series 2 and 3. The median free-surface elevations and velocity components were calculated from the total ensemble as well as the fluctuating properties. Table 1 summarizes the experimental flow conditions.

Table 1. Experimental flow conditions for unsteady velocity measurements.

Bed configuration	Q (m^3/s)	d_1 (m)	Radial gate opening (m)	Tainter gate opening h (m)	Fr_1	Surge type
A - Smooth bed	0.061	0.155	N/A	0.025	1.39	Breaking
B - Cylindrical element	0.039	0.200	0.060	0.010	1.11	Undular
		0.130	N/A	0.010	1.35	Breaking
	0.051	0.140	N/A	0.025	1.40	Breaking
	0.061	0.155	N/A	0.025	1.39	Breaking

Notes: d_1: flow depth measured at $x = 6.1$ m; Fr_1: surge Froude number; N/A: radial gate fully opened.

2.3.   Experimental Flow Conditions

This study focused on fully-developed positive surges for which the mean properties became independent of time and space, thus independent of the generation process. Detailed velocity measurements were performed at several locations upstream of, above, and downstream of the cylindrical element on the channel centerline. Additional measurements were recorded at several transverse locations y. The initially steady flow data indicated that the flow was partially developed at $x = 6.1$ m upstream of the element, and the dimensionless boundary layer thickness δ/d_1 ranged between 0.5 and 0.6 depending upon the initial flow conditions.

The presence of the large cylindrical roughness element on the channel bed had an influence on the steady flow conditions. The effect was investigated in terms of the vertical distributions of time-averaged longitudinal velocity and standard deviations of the three velocity components to establish the region of influence of the roughness element. The measurements were performed upstream of, directly at, or above the element and downstream of the roughness element. Overall, the results showed that the large roughness element had little impact on the flow upstream of and at the element, except in its immediate vicinity. Downstream of the element, a wake region was observed. Typical results are shown in Figure 3, where V_x is the longitudinal velocity component, x_o is the longitudinal coordinate of the large element center, and D is its diameter. In Figure 3, the downstream half of the large element is shown with a thick, solid black line. The wake region was detected up to a distance $(x-x_o)/D < 20$, D

being the diameter of the element, with a vertical extent $z/H < 4$ where H is the height of the element, and a transverse extent $-4 < y/D < 4$.
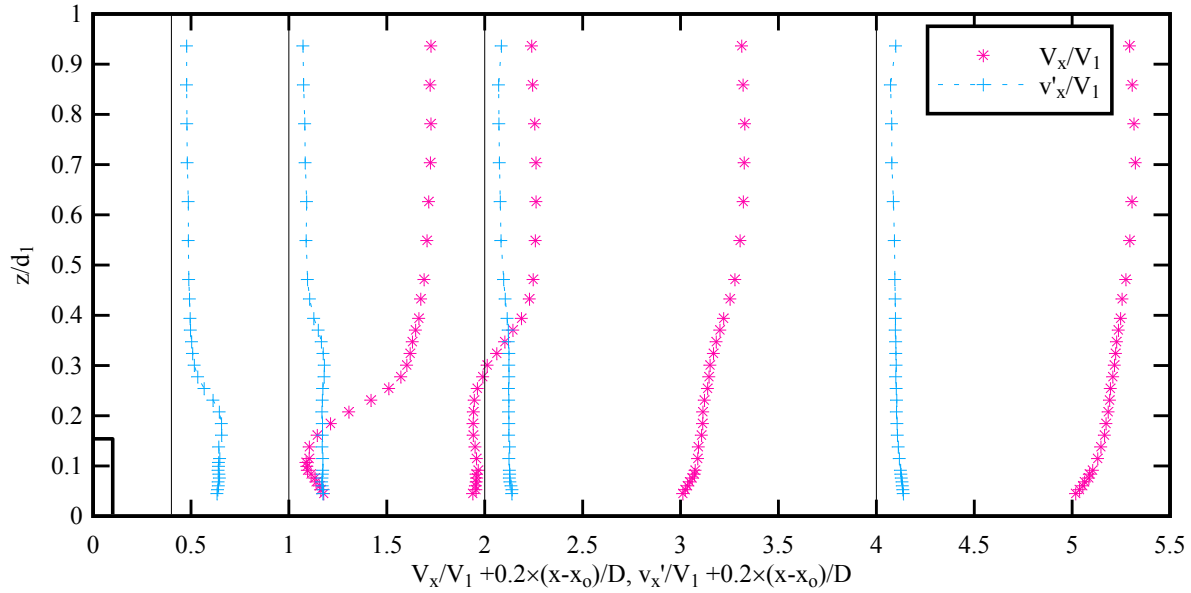
Figure 3. Dimensionless vertical distributions of time-averaged longitudinal velocity and standard deviation of longitudinal velocity downstream of the large element in steady flow - Flow conditions: $Q = 0.038$ m^3/s, $d_1 = 0.130$ m at $x = 5.9$ m, Flow direction from left to right
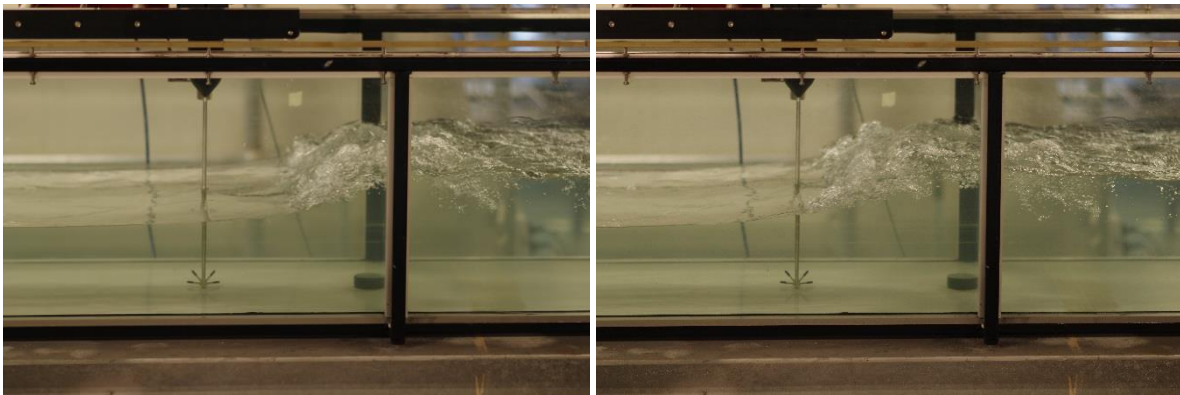
Figure 4. Positive surge propagation above the large roughness element - Flow conditions: $Q = 0.061$ m^3/s, $d_1 = 0.155$ m at $x = 5.9$ m, $Fr_1 = 1.39$, Tainter gate opening after closure: $h = 25$ mm - From left to right: 0.121 s between successive photographs (shutter speed: 1/400 s)

3. BASIC OBSERVATIONS

Free-surface measurements under unsteady flow conditions were conducted for three breaking and one undular bore flow condition (Table 1). The rapid gate closure generated a bore propagating upstream against the initially steady flow. Figure 4 shows a typical sequence of photographs taken during the propagation of the bore. The bore passage was characterised by a rapid rise in free-surface elevation. For $Fr_1 < 1.3$, the bore free-surface was undular: i.e., smooth with the first wave crest followed by a train of secondary undulations. For larger Froude numbers, a marked roller was observed, associated with large scale turbulence and air bubble entrainment (Fig. 4).

The free-surface properties were analyzed based upon the ensemble-average free-surface data. Quantitative results are presented in Figures 5 and 6, in terms of the ratio of conjugate depths and maximum free-surface elevation. In Figure 5, the present data compare well with the Bélanger equation as well as past experimental data in horizontal rectangular channels with smooth and rough inverts. Figure 6 presents the maximum free-surface elevation; both present data and past results are in agreement, showing an upper limit corresponding well to the criterion for solitary wave breaking (Peregrine 1966). The instantaneous free-surface fluctuations were characterized in terms of the difference between the third and first quartiles of the ensemble (d_{75}-d_{25}). The data (not shown) indicated maximum free-surface fluctuations shortly after the bore leading edge, as reported by Leng and Chanson (2016).

Both visual observations and acoustic displacement meter data showed that the presence of the large roughness element had a negligible impact on the free-surface profile and basic free-surface characteristics. As an illustration, the breaking bore data reported in Figures 5 and 6 show no distinctive difference between the two bed configurations.
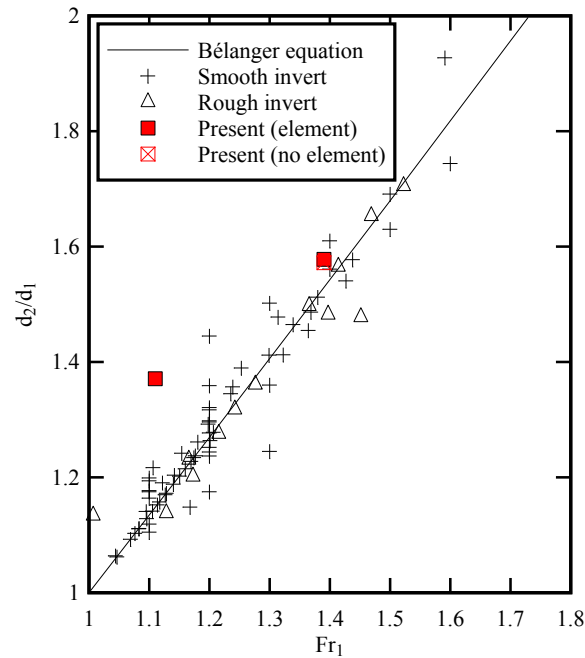
Figure 5. Ratio of conjugate depths d_2/d_1 in positive surges propagating in horizontal rectangular channels - Comparison between present ensemble-averaged data at x = 7.1 m with and without large element and laboratory data on smooth invert (Favre 1935, Treske 1994, Chanson 2010a, Docherty and Chanson 2012, Leng and Chanson 2016) and rough invert (Chanson 2010a, Docherty and Chanson 2012)
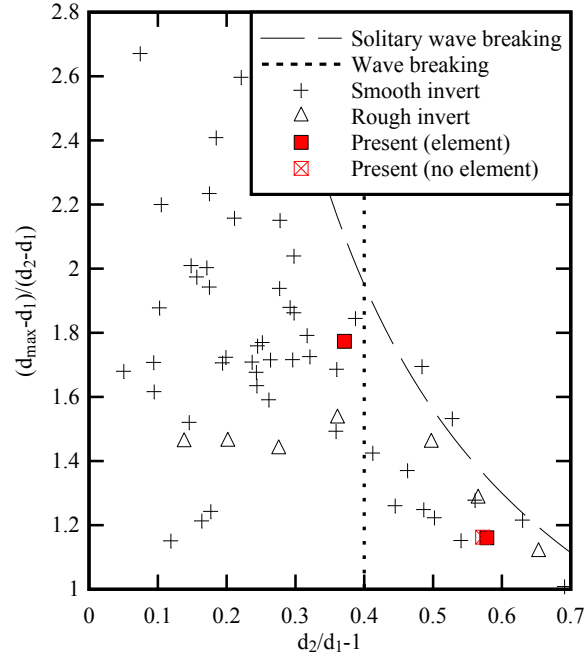
Figure 6. Dimensionless maximum water elevation $(d_{max}-d_1)/(d_2-d_1)$ in positive surges propagating in horizontal rectangular channels - Comparison between present ensemble-averaged data at $x = 7.1$ m with and without large element, smooth invert data (Peregrine 1966, Koch and Chanson 2008, Chanson 2010a,2010b, Leng and Chanson 2016) and rough invert data (Chanson 2010a) and solitary wave breaking onset - Dashed line indicates the onset of breaking at the first wave crest

4. VELOCITY MEASUREMENTS

All the instantaneous velocity measurements showed a sudden deceleration associated with the passage of the positive surge. The rapid deceleration phase was followed by some transient recirculation, previously reported by Docherty and Chanson (2012), Khezri and Chanson (2012), and Leng and Chanson (2016). The passage of the bore was associated with large fluctuations of all three velocity components (data not shown). In absence of large element, the results were close to those of Leng and Chanson (2016) obtained with the same discharge per unit width and comparable Froude numbers. Herein, we focus on the impact of the large roughness element on the velocity field.

The effect of the large element was tested systematically in terms of the instantaneous and ensemble-averaged velocity data for a breaking bore at several transverse locations $y/D = 0$, 0.5, 0.75, and 1. A typical example is presented in Figure 7, showing the time-variations of ensemble-averaged longitudinal velocity $(V_x-V_2)/(V_1-V_2)$ on the channel centerline, where V_2 is the conjugate flow velocity and all velocities are positive downstream, and t is the time from the start of data acquisition (i.e., 60 s prior to Tainter gate closure). The impact of the large element was most significant on the channel centerline for $-5 < (x-x_o)/D < +5$. First, a longer transient recirculation was observed both upstream and downstream of the element. This is illustrated in Figure 7 where d is the instantaneous water depth and the blue arrow highlights the transient circulation duration, nearly twice as long in presence of the large element. Second, the transient recirculation was characterized by stronger velocity recirculation magnitudes: that is, almost 60% larger in presence of the roughness element.
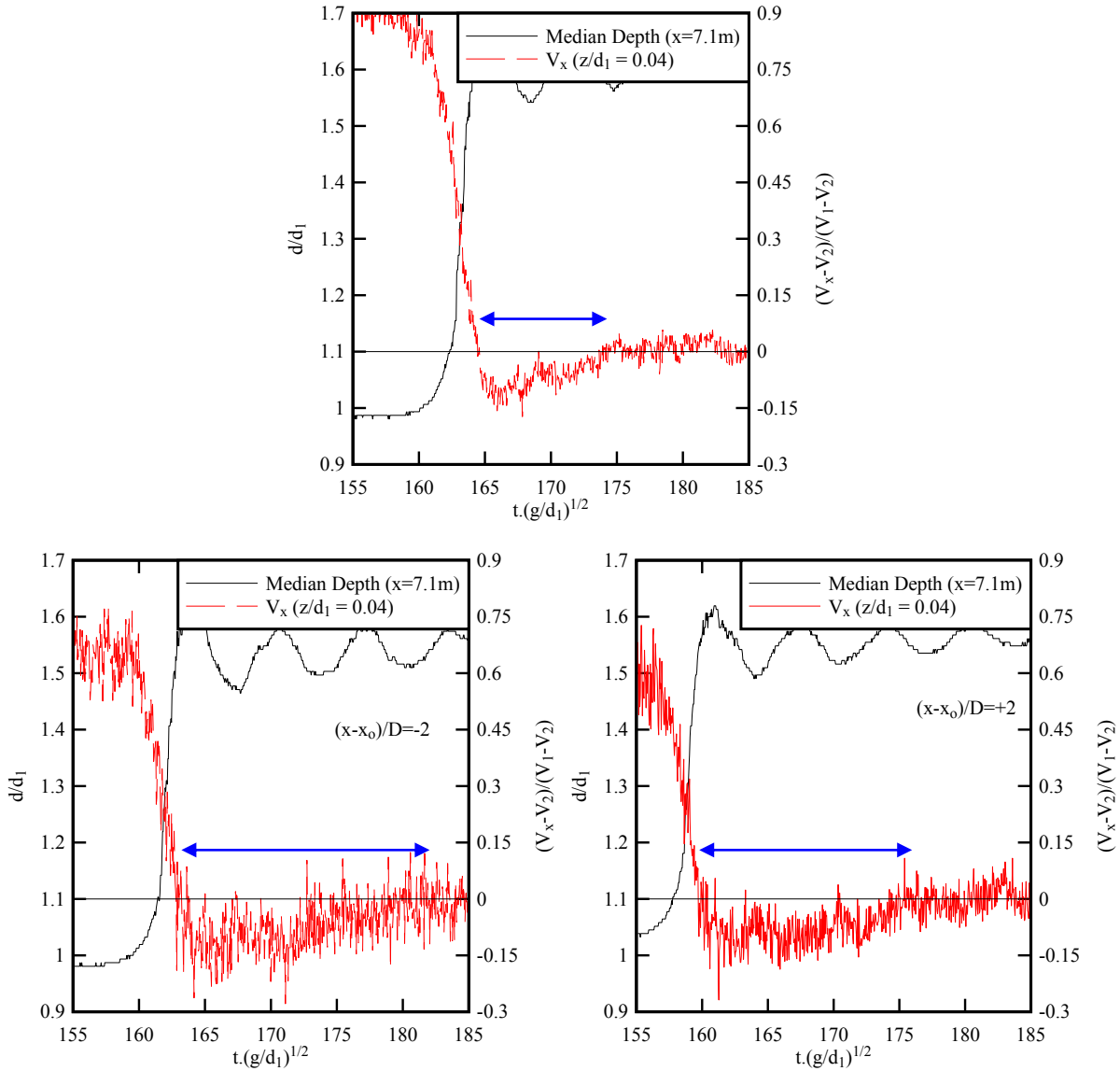
Figure 7. Time variations of ensemble-averaged longitudinal velocity: comparison between bed configuration A (no element) [Top] and bed configuration B: Bottom Left: $(x-x_o)/D=-2$ and Bottom right: $(x-x_o)/D=+2$ - Flow conditions: $Q = 0.061$ m^3/s, $d_1 = 0.155$ m at x = 5.9 m, $Fr_1 = 1.39$, $z/d_1 = 0.04$, $y = 0$ (centerline), Tainter gate opening after closure: $h = 25$ mm

Physically, the advancing positive surge first encountered the wake region downstream of the element (sketched in Figure 2A). The interactions between the wake motion and the surge turbulence induced large velocity fluctuations next to the invert, in the initially steady flow wake region. Once the surge passed the cylindrical element, a 'transient wake' developed upstream of the element. This transient wake was caused by some blockage effect induced by the large roughness element.

5. TURBULENT SHEAR STRESSES

The unsteady flow in positive surges was characterized by large velocity fluctuations that must be associated with large turbulent stresses. The turbulent Reynolds stress equals the fluid density multiplied by the cross-product of the

turbulent velocity fluctuations, $\tau_{ij} = \rho \times v_i \times v_j$ where ρ is the density of the fluid, v is the velocity fluctuation, and $i, j = x, y,$ or z. The Reynolds stress τ_{ij} is representative of the shear stress on the area $dx_i \times dx_j$ of an elementary control volume (dx, dy, dz) (Bradshaw 1971). Herein, the Reynolds stresses were calculated based on the ensemble-average velocity data following Docherty and Chanson (2012) and Leng and Chanson (2016). Measurements were performed with and without the presence of the large cylindrical roughness element. Typical results are presented in Figure 8 in terms of the median shear stresses $\rho \times v_x \times v_x$ and $\rho \times v_x \times v_y$.

The experimental results indicated that the propagation of the surge was associated with a sharp increase in Reynolds stress magnitude during the front passage (Fig. 8), together with large and rapid fluctuations in shear stresses. The maximum Reynolds stresses were typically observed after the bore arrival. The corresponding time lag was comparable with and without the roughness element and close to the findings of Leng and Chanson (2016). Overall, these patterns were observed for all Reynolds stress tensor components.

The presence of the large roughness element was mostly felt upstream of the element and around the element. Lesser effects were observed downstream of the element. Upstream of the element, the surge passage resulted in an increase in the mean normal and tangential stresses immediately upstream of the element at $(x-x_o)/D = -1$. Further upstream, only a slight increase in shear stresses was observed at $(x-x_o)/D < -2$. Around the element (i.e., $(x-x_o)=0$), its presence impacted onto the shear stress data close to the bed at $y/D = 0.75$, and 1, with larger turbulent stress magnitudes.

In open channels and water supply canals, the brusque operation of control gates may induce large unsteady flow motion called surges. Although the effects of such a rapid gate operation must often be restricted, this type of operation may be used to scour silted channels and sewers (Riochet 2008, Sun et al. 2016). The present results showed that a large roughness element may impact both steady and unsteady flow motions. During surge propagation, large shear stress levels were observed around the element that might lead to enhanced scour and bed erosion. The repetition of positive surge events could yield the development of a large scour hole surrounding the cylindrical element.

6. CONCLUSION

In open channels and canals, a sudden rise in water elevation is associated with the propagation of a positive surge. A related flow motion is a tidal bore in a small number of estuaries. To date, the literature focused on the propagation of surges in flat bed channels, and the effects of large roughness elements were un-accounted for. Herein, a physical study was performed to assess the impact of a large and flat cylindrical roughness element on the upstream propagation of positive surges.

The results showed that the large element had negligible impact on the steady and unsteady free-surface properties. The instantaneous velocity measurements showed stronger and longer transient recirculation during the bore passage immediately upstream and downstream of the element. Larger velocity fluctuations were further recorded, and the findings were associated with larger turbulent shear stresses around the roughness element. The results suggested some enhanced scour and bed erosion around the large element and the potential development of a large scour hole in mobile bed channels.

Further investigations should be conducted using mobile bed channels and could encompass both cylindrical element and cylindrical column. The latter would be representative of a bridge pier, and an important application could be the prediction of scour hole development around a pier, for example in a tidal bore affected estuary.
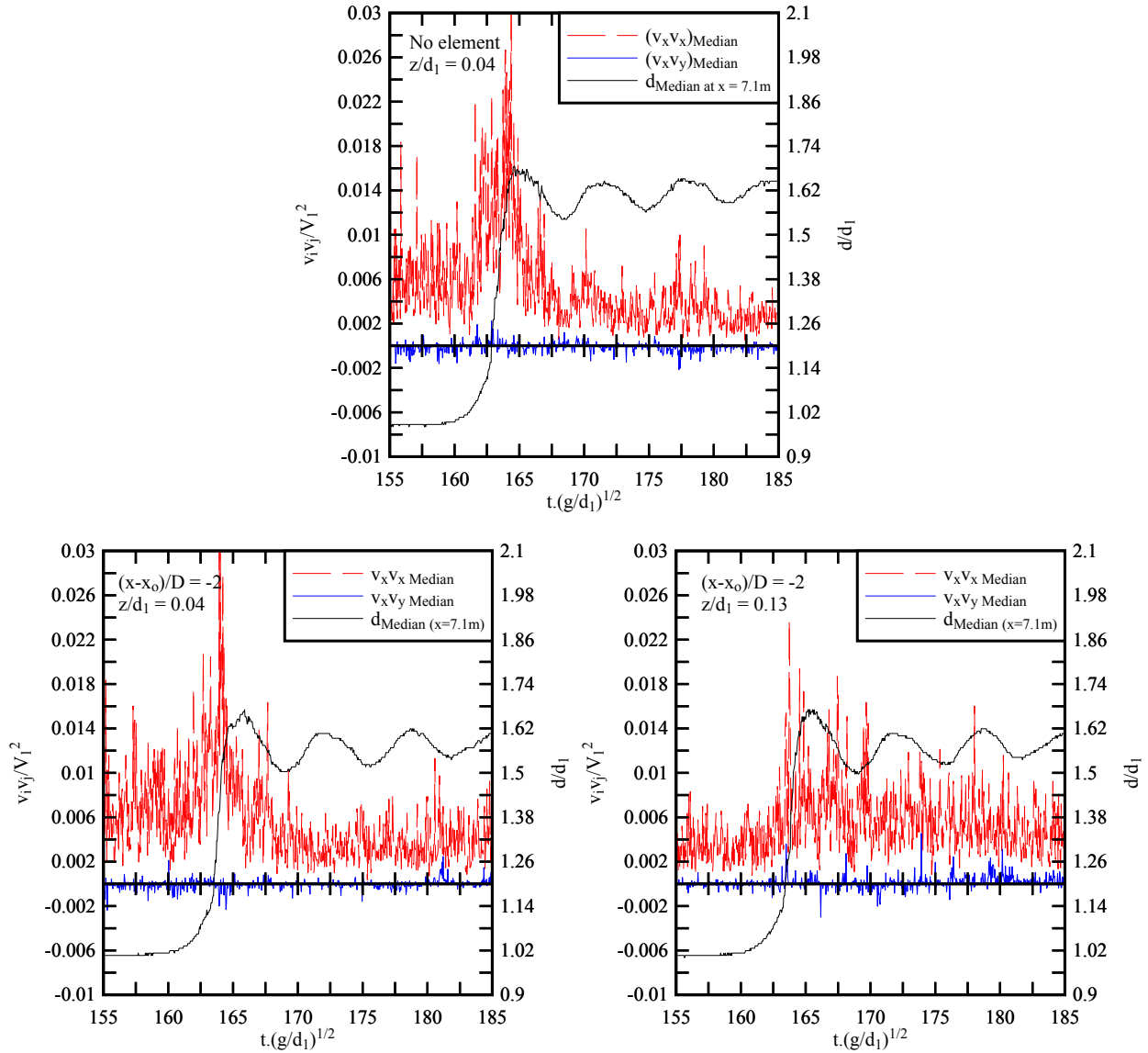
Figure 8. Time variations of ensemble-averaged Reynolds stresses $v_x v_x$ and $v_x v_y$: comparison between bed configuration A (no element) [Top] and bed configuration B [Bottom] at $(x-x_o)/D = -2$ - Flow conditions: $Q = 0.061$ m^3/s, $d_1 = 0.155$ m at $x = 5.9$ m, $Fr_1 = 1.39$, $y = 0$ (centreline), Tainter gate opening after closure: $h = 25$ mm

7. ACKNOWLEDGMENTS

8. REFERENCES

Bradshaw, P. (1971). An Introduction to Turbulence and its Measurement. Pergamon Press, Oxford, UK, The Commonwealth and International Library of Science and technology Engineering and Liberal Studies, Thermodynamics and Fluid Mechanics Division, 218 pages.

Chanson, H. (2010a). Unsteady Turbulence in Tidal Bores: Effects of Bed Roughness. Journal of Waterway, Port, Coastal, and Ocean Engineering, ASCE, Vol. 136, No. 5, pp. 247-256 (DOI: 10.1061/(ASCE)WW.1943-5460.0000048).

Chanson, H. (2010b). Undular Tidal Bores: Basic Theory and Free-surface Characteristics. Journal of Hydraulic Engineering, ASCE, Vol. 136, No. 11, pp. 940-944 (DOI: 10.1061/(ASCE)HY.1943-7900.0000264).

Chanson, H. (2011a). Tidal Bores, Aegir, Eagre, Mascaret, Pororoca: Theory and Observations. World Scientific, Singapore, 220 pages.

Chanson, H. (2011b). Undular Tidal Bores: Effect of Channel Constriction and Bridge Piers. Environmental Fluid Mechanics, Vol. 11, No. 4, pp. 385-404 & 4 videos (DOI: 10.1007/s10652-010-9189-5).

Chanson, H. (2012). Momentum Considerations in Hydraulic Jumps and Bores. Journal of Irrigation and Drainage Engineering, ASCE, Vol. 138, No. 4, pp. 382-385 (DOI: 10.1061/(ASCE)IR.1943-4774.0000409).

Docherty, N.J., and Chanson, H. (2012). Physical Modelling of Unsteady Turbulence in Breaking Tidal Bores. Journal of Hydraulic Engineering, ASCE, Vol. 138, No. 5, pp. 412-419 (DOI: 10.1061/(ASCE)HY.1943-7900.0000542).

Favre, H. (1935). Etude Théorique et Expérimentale des Ondes de Translation dans les Canaux Découverts. Dunod, Paris, France (in French).

Henderson, F.M. (1966). Open Channel Flow. MacMillan Company, New York, USA.

Khezri, N., and Chanson, H. (2012). Undular and Breaking Tidal Bores on Fixed and Movable Gravel Beds. Journal of Hydraulic Research, IAHR, Vol. 50, No. 4, pp. 353-363 (DOI: 10.1080/00221686.2012.686200).

Koch, C., and Chanson, H. (2008). Turbulent Mixing beneath an Undular Bore Front. Journal of Coastal Research, Vol. 24, No. 4, pp. 999-1007 (DOI: 10.2112/06-0688.1).

Leng, X., and Chanson, H. (2016). Coupling between Free-surface Fluctuations, Velocity Fluctuations and Turbulent Reynolds Stresses during the Upstream Propagation of Positive Surges, Bores and Compression Waves. Environmental Fluid Mechanics, Vol. 16, 25 pages (DOI: 10.1007/s10652-015-9438-8).

Liggett, J.A. (1994). Fluid Mechanics. McGraw-Hill, New York, USA.

Lu H.Y., Pan, C.H., and Zeng, J. (2009). Numerical simulation and analysis for combinational effects of two bridges on the tidal bore in the Qiantang River. Proceedings of 5th International Conference on Asian and Pacific Coasts, Singapore, Vol. 3, pp. 325-333.

Microsonic (2004). Instruction manual mic+ Ultrasonic Sensors with one analogue output. Microsonic GmbH, Germany, 3 pages.

Nortek (2009). Vectrino Velocimeter User Guide. Nortek AS, Norway, 42 pages.

Peregrine, D.H. (1966). Calculations of the Development of an Undular Bore. Journal of Fluid Mechanics, Vol. 25, pp. 321-330.

Riochet B (2008). La Sédimentation dans les Réseaux Unitaires Visitables: le Point de Vue d'un Exploitant. Proceedings international meeting on measurements and hydraulics of sewers IMMHS'08, Summer School GEMCEA/LCPC, Bouguenais, 19-21 August 2008, Larrarte F. and Chanson H. (eds), Hydraulic Model Report No. CH70/08, University of Queensland, Brisbane, pp. 11-19 (in French).

Sun, S., Leng, X., and Chanson, H. (2016). Rapid Operation of a Tainter Gate: Generation Process and Initial Upstream Surge Motion. Environmental Fluid Mechanics, Vol. 16, No. 1, pp. 87-100 (DOI: 10.1007/s10652-015-9414-3).

Treske, A. (1994). Undular Bores (Favre-Waves) in Open Channels - Experimental Studies. Journal of Hydraulic Research, IAHR, Vol. 32, No. 3, pp. 355-370.

Tricker, R.A.R. (1965). Bores, Breakers, Waves and Wakes. American Elsevier Publ. Co., New York, USA.

Numerical Investigation of the Flow Field inside a Manhole-Pipe Drainage System

Md Nazmul Azim Beg[1,2], Rita F. Carvalho[1,2], Pedro Lopes[1,2], Jorge Leandro[1,2] and Nuno Melo[1]

[1] Dep. of Civil Engineering, Faculty of Science and Technology,
University of Coimbra
Portugal

[2] MARE - Marine and Environmental Sciences Centre & IMAR - Institute of Marine Research,
University of Coimbra
Portugal
E-mail: mnabeg@uc.pt

ABSTRACT

Urban drainage networks contain a large number of structures. The manhole is the most common and the most important as it connects pieces of sewer pipes to form sewer networks. Understanding the hydraulics of a manhole-pipe drainage system is important as this may sometimes become the bottlenecks of the sewer systems. In this study, the flow structure and flow hydraulics of a specific manhole-pipe sewer system was analysed numerically in view of further research to investigate sediment and suspended solid transport in the system. The numerical model was compared with discharge and water pressure/depth data from an experimental model. Different discharges and water levels at the inlet pipe were applied, and corresponding change of flow hydraulics were analysed. Two scenarios were tested: (1) free surface flow and (2) pressurized flow condition in the pipe. In the numerical analysis, the k-ε turbulent model was used within open source CFD tool OpenFOAM®. The numerical results showed similar flows and water pressure levels to that of the experimental work. Different flow patterns were observed in the manhole at different discharges. This flow pattern will give further insight in assessing pollutant flow inside the system.

Keywords: Urban drainage systems, Manhole-pipe system, OpenFOAM®, velocity profiles, sewer junction

1. INTRODUCTION

Urban drainage is composed of several linking elements. The serviceability of drainage systems depends on their efficiency. One of the most common element of a drainage system is a manhole. It collects storm drainage from gullies (or gutters) and intake pipes and conveys its discharge to its outlet pipe. After the rainfall, the surface runoff passes through the paved and unpaved urban surfaces and collects sediment as one of the pollutants (Deletic 1998). During flood events, manholes sometimes may become pressurised. The turbulence may affect the head loss, hydraulic efficiency, and discharge coefficient of the flow (Granata et al. 2011). Understanding of the flow pattern is important for conducting storm water quality investigations.

To interpret the flow behaviour in practical scenarios, use of experimental and numerical models is a well-recognized procedure. Stovin et al. (2008) have shown a number of possible methods to validate CFD model, while Rubinato (2015) has shown uses of scaled models to quantify hydraulic losses in a manhole. This study has been conducted to investigate the flow pattern of a manhole-pipe drainage system using three dimensional CFD tools OpenFOAM®. The numerical work has been validated with discharge and water pressure/depth data from a previously performed experimental work. Both free surface flow and pressurised flow were simulated. The scope of the present paper is to evaluate the performance of the CFD model to capture the overall hydraulic features of the flow. These results may be used to aid the simulation of a pollutant transport model in the drainage system.

The paper starts by presenting the experimental installation and numerical model used in the section titled "Methodology," followed by the validation of the numerical model in the section "Results and Discussion." Later in the same section, different findings from the numerical model are presented.

2. METHODOLOGY

2.1. Experimental Model

Experimental work was performed in the model setup established at the hydraulic lab of University of Coimbra (Figure 1). The experimental setup has been described in detail by Santos et al. (2008), Leandro et al. (2009), Carvalho et al. (2013), and Leandro et al. (2014). This is a Multi-Link-Element (MLE) setup with a flume and two gullies connected with two manholes. Only the two manholes and the connecting pipe were used for this experiment. The first manhole (made of acrylic) does not have a guided flow channel, while the second manhole has a more complex interior geometric shape with a guided flow channel, following a pre-built commercial design. Both types can be found in Portuguese drainage systems. The connecting pipe has a length of 8.5 m, with a diameter of 0.3 m. The system is equipped with a closed circuit connecting two reservoirs of 36 m³ (main reservoir) and 32 m³ (secondary reservoir). This is supplied by a system of four circulation pumps and controlled by several valves, and electrical control systems. A combination of valves can control the water depth/pressure in the manhole-pipe system. The complete system is equipped with an SCADA system (Supervision, Control, and Data Acquisition) that allows for the operation and monitoring of flow rates and pressures. The system also controls the pumps as necessary.

Figure 1: Multi-Link-Element experimental model setup at the hydraulic lab of the University of Coimbra

A schematic diagram of the experimental setup in the work can be viewed in Figure 2. For the data collection of the experimental model, different pressure sensors were installed at the bottom of both manholes (P11, P23) and through the length of the pipe (P12, P18 and P22) (Figure 2). The sensors measured piezometric pressures for both free surface and pressure flow conditions, which were converted to piezometric head considering the bottom of Manhole 1 as the zero datum. Pressure head differences along the pipe were used to determine conduit head losses.

A number of experimental runs were performed keeping the outlet valve opened at 30% (low flow), 40% (medium flow), and 60% (high flow) to observe different flow velocities inside the pipe and the manhole for a particular surcharge water depth. All discharges and corresponding water pressures throughout the system were recorded after reaching a steady flow condition. 18 of these experimental run results were used for numerical investigation in this study.
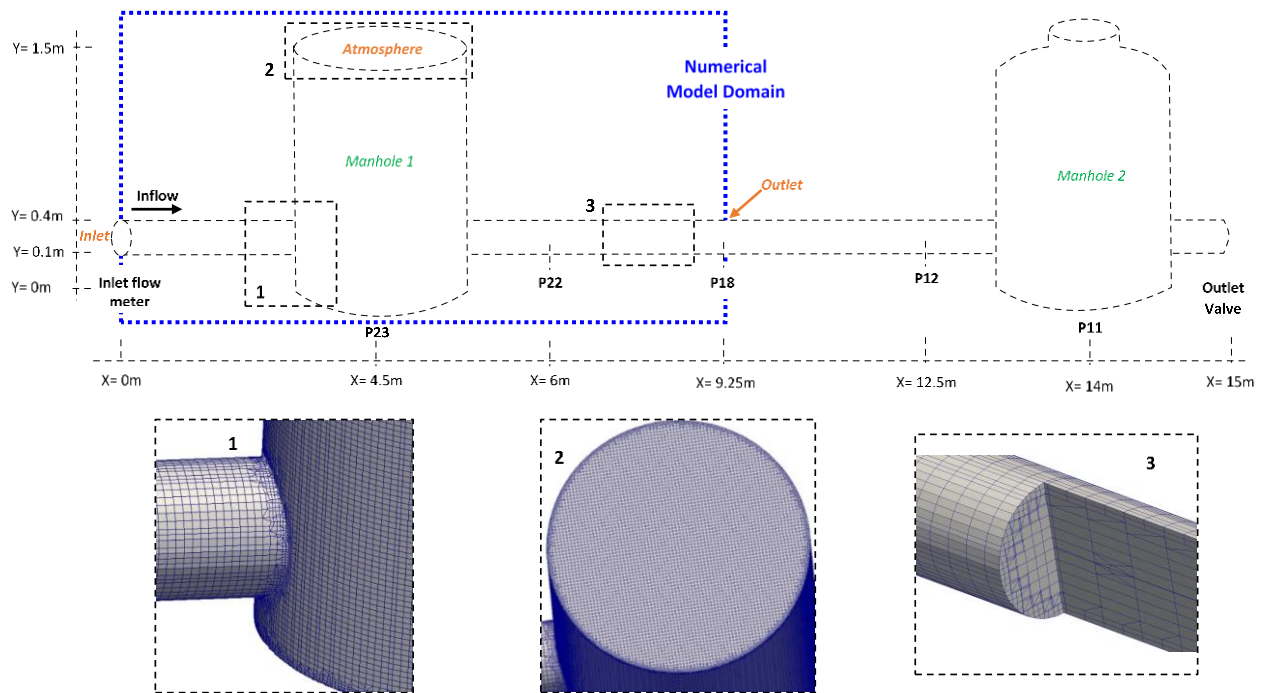
Figure 2: Schematic diagram of the experimental and numerical setup with different locations of the pressure sensors and boundary locations of the numerical model (in orange font) (upper panel) and Computational meshes at some selected locations of the numerical model (lower panel)

2.2. Numerical Model

The numerical model intends to reproduce scenarios similar to the experimental model. The main purpose of numerical modelling is the analysis of the flow characteristics and change of flow patterns when the water enters to the manhole from pipe and vice versa. Another purpose is to check the flow pattern at different pressure and flow velocity combinations. In this study, only manhole 1 with inlet and outlet pipes was evaluated numerical; this manhole type is more common in Portuguese drainage systems. The numerical modelling domain is chosen from x=0 m to x=9.25 m, where the inlet and pressure transducer P18 was located, respectively (Figure 2). The selected manhole for the numerical study did not have a guided flow channel. Numerical study of the other manhole will be done at a later stage.

OpenFOAM® toolbox version 2.3.0 is used in this study. The model simulation has to deal with both liquid and gas phases in order to capture the water surface properly. For this case, the solver *interFoam* is chosen as it can be a powerful tool to predict the free surface flow for sharp interfaces and velocity patterns (Lopes et al. 2015), assuming that the air effect on the flow can be neglected. This solver uses a single set of Navier-Stokes equations, where the velocity is shared by both phases and a Volume of Fluid (VOF) method (Hirt and Nichols 1981) capture the free-surface position. PISO algorithm was chosen for pressure-velocity coupling as it is known for less computational effort in comparison to SIMPLER and SIMPLEC algorithm (Versteeg and Malalasekera 1995). One of the most used and reliable turbulence modelling approaches in OpenFOAM® is Reynolds Average Navier-Stokes (RANS), which was used to model the turbulence of the flow because it has less computational cost than Large Eddy Simulation (LES) (Versteeg and Malalasekera 1995). This turbulence calculation approach uses two closure equations for k (Turbulent Kinetic Energy) and ε (Energy dissipation). The unsteadiness in flow is averaged out in this model and regarded as part of the turbulence (Furbo et al. 2009).

All the numerical results have been acquired at steady state conditions. 18 different scenarios have been simulated, covering both high and low flow conditions as well as high-pressure and low-pressure conditions. Some of the simulations have free surface flow, and some have pressurized flow in the pipe. The work flow for setting up the numerical model is described in the following paragraphs.

2.2.1. Mesh Generation

The computational mesh was constructed using the OpenFOAM® built in mesh generating tool *blockMesh* and *snappyHexMesh* utilities. The *blockMesh* utility divides the model domain into several three-dimensional, hexahedral blocks, while *snappyHexMesh* creates hexahedra and split hexahedra triangulated surface geometries. This utility carves out the smooth outline from a previously created structured mesh with a surface given in Stereolithography (STL) or Wavefront Object (OBJ) format. The STL surface was produced using an open source integration platform for numerical simulations and mesh generator SALOME v.7.5.1. The *blockMesh* plus *snappyHexMesh* create a quasi-regular mesh but variable grid spacing in singularities. For the manhole, all the grid elements featured cubes that measured 0.025m on all sides. For the inlet and outlet pipes, the longitudinal mesh size varied from 0.025m to 0.1m, keeping minimum grid spacing near the manhole-pipe junction and maximum spacing near the distal ends of the inlet and outlet pipes. The transverse mesh sizes were 0.025 m. Boundary meshes were further refined by a factor of two in all three directions (*x*, *y* and *z*) using *castellatedMesh* and a boundary layer is added using *addLayers*. Furthermore, each boundary mesh was implicitly wrapped and smoothed by merging the faces using *snap*.

Thus, the whole computational domain is composed of around 210,000 computational meshes. Some quality parameters of the prepared mesh are given in Table 1. Figure 2 shows some parts of the computational mesh.

Table 1: Mesh quality parameters

Parameter name	Maximum Aspect ratio	Max skewness	Max non-orthogonality	Min face area (m²)	Max face area (m²)	Min volume (m³)	Max volume (m³)
Parameter value	21.87	1.959	65	3.18×10^{-6}	3.37×10^{-3}	8.92×10^{-9}	9.22×10^{-5}

2.2.2. Boundary Conditions

Three open boundaries were used for the computational domain. They were Inlet, Atmosphere ,and Outlet (Figure 2). The inlet boundary only allows incoming flow, while the outlet allows only outward flow. The data for the boundaries have been measured from the experimental model. The upstream boundary values were chosen from the measured discharge at the inlet, while the downstream pressure values were obtained from collected data at P18 pressure transducer.

For a RANS model setup, each of the open boundaries require six different Boundary Conditions (BC). They are *alpha.water* (water fraction in each cell volume), *U* (velocity vector in Cartesian domain), *p_rgh* (relative bottom pressure corresponding to datum), *k* (turbulent kinetic energy), *ε* (energy dissipation), and *nut* (turbulent viscosity). OpenFOAM® allows many ways to apply each boundary type. It has been challenging to find the best combination of the boundary properties for this study as it has two phases at the boundary. Fixed velocity / discharge boundary conditions *U* (Neumann BC) was prescribed at the inlet, while the outlet BC was prescribed as fixed *p_rgh* pressure (Dirichlet BC). The atmosphere BCs were prescribed as *zeroGradient* velocity so that air can be exchanged. The relative pressure condition at the atmosphere was kept as zero. The wall BCs at the manhole and pipe walls were kept as no-slip condition (i.e., velocity = 0). The turbulent modelling parameters (*k*, *ε* and *nut*) were calculated for each case and prescribed at the inlet boundary using the equations as described in FLUENT manual (ANSYS Ins 2009). The Turbulence Intensity (*I*) and the empirical constant (*Cμ*) were chosen as 0.05 and 0.09, respectively. Pre-analysis of the model showed that to capture the boundary layer flow velocity, the mesh size would have to be in the range of 10^{-4} m at the boundary wall. For efficiency with computational time, the mesh size could not be kept that small. Hence, all the internal wall boundary conditions for turbulence closure (*k*, *ε* and *nut* values) were chosen as *wallFunction*. Use of *wallFunction* eliminates the necessity of possible mesh grading as flow in the near boundary wall cell is not resolved but modelled (Greenshields 2015).

2.2.3. Simulation of the Models

After preparing all the mesh and the boundary setups, the model was ready to run. The simulation was done using adjustable run time so that the model could adjust the time step itself. The maximum courant number was set to 0.5.

Each simulation was run for 40 s to reach a steady state condition. For better computational time efficiency, the model was decomposed into 4 parts to run in MPI mode with 4 processors. A multi core Core i7 computer was used, which required approximately 24 hours to complete each simulation.

3. RESULTS AND DISCUSSION

3.1. Validation of the Numerical Model

During the experimental model run, pressure levels were recorded at different locations in the pipe as well as the bottom centre of the manhole. The numerical model was validated with experimental data of flow depth / pressure head and discharge inside the structure so that flow characteristics observed from the numerical results represent similar scenarios created in the experimental model. The comparison was checked with the pressure data at transducer P23, P22, and P18 (see Figure 2). Figure 3 shows the comparison between experimental and numerical simulations in a pressure head vs discharge plot. The dot markers of different colours show data from the experimental model while the triangles show data from the numerical model.

When the depth at P23 / Manhole 1 stays below 0.3 m, the flow remains as free surface flow. As the depth of flow starts increasing, the upstream end will pressurize before the downstream end, which continues to exhibit free surface flow; this situation is termed as transition flow. When the flow depth at P23 exceeds 0.4 m, the flow throughout the length of the structure becomes pressurised.
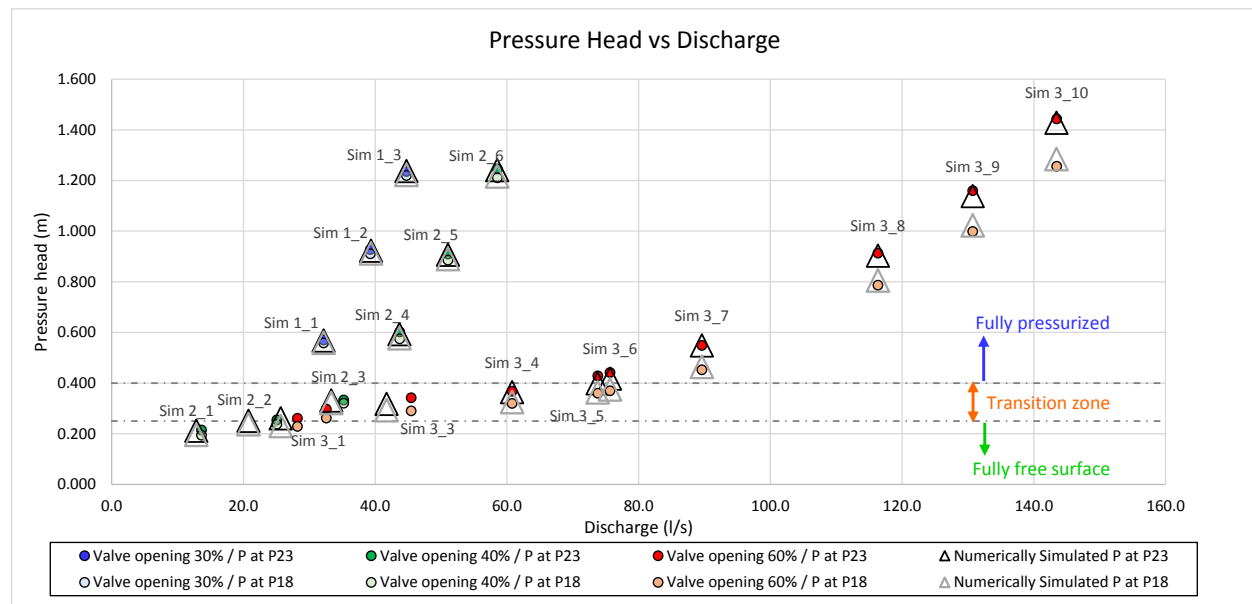
Figure 3: Pressure level vs Discharge in the two manholes from experimental and numerical simulation

It can be seen from Figure 3 that the model has loss of pressure head from P23 to P18. The head loss increases with the increase of upstream discharge. It can be seen that the head loss also increases with increase of pressure in the flow. The head loss is higher in the pressurised flow than that of the free surface flow.

A percentage of error from the pressure head data comparison has been generated (Figure 4). The positive error means the predicted pressure in the numerical model is higher than that of experimental model and vice versa.
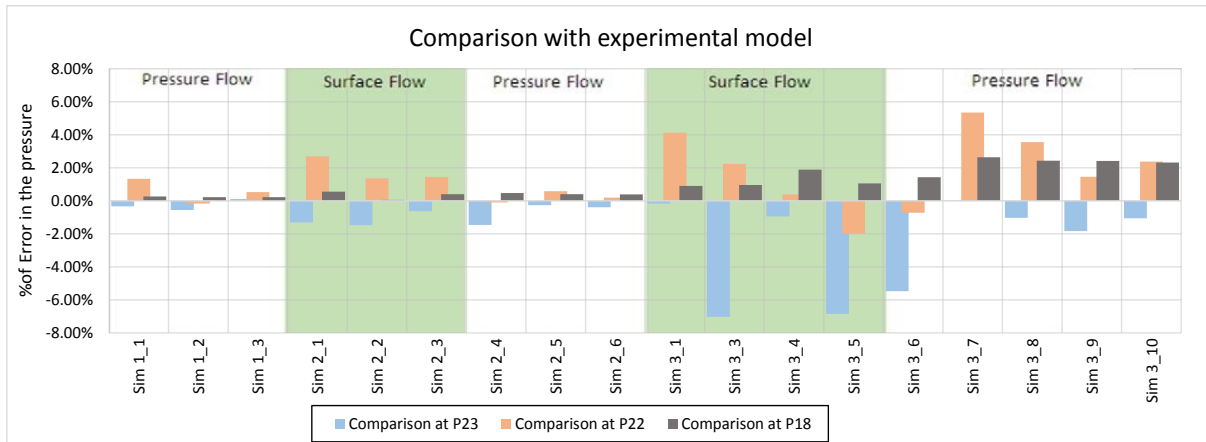
Figure 4: Calibration comparison between numerical and experimental model

It can be seen from Figure 4 that the percentage of absolute error was always less than 7%, which indicates a good agreement with the experimental data.

3.2. Velocity Profile

An analysis of the three dimensional flow profile inside the manhole was examined. In Figure 5, three dimensional velocity profiles can be seen from Sim 3_9. The figure at the left shows the velocities in xz and yz planes, whereas the figures at the right show horizontal velocity fields at different vertical plane.
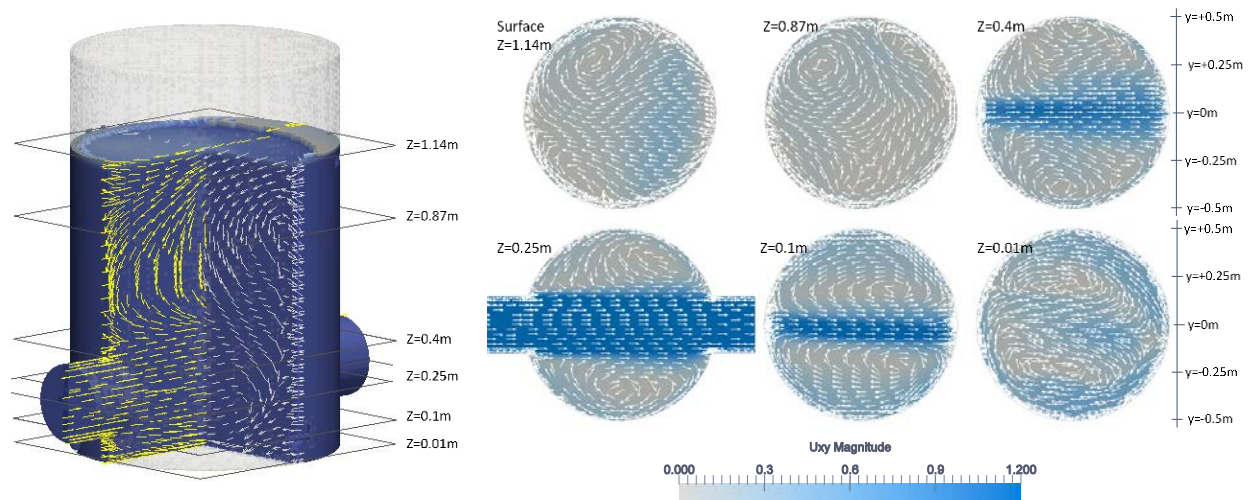
Figure 5: Three dimensional velocity profile from Sim 3_9 xz and yz plane velocity at left panel and xy plane velocity at different horizontal level at right panel

Figure 5 right panel shows that the manhole has different horizontal velocity structures at different water depths. The horizontal flow velocity is the highest between Z=0.1 m and 0.4 m, due to strong flow influence from the inlet pipe. At this depth range, a strong flow flowing toward the right can be observed at the central zone (near y=0 line). The flow turns to the opposite direction near the perimeter, creating a horizontal vortex between the perimeter and the central zone. The location of the centres of the vortex varies with the depth of flow. It can also be seen that at the surface (at Z=1.14 m), the dominant flow is no longer in the positive x-direction (downstream), but in the upstream direction. Some vertical vortex can be observed at the left panel at depth Z=0.8 m to Z= 0.9 m.

3.3. Flow Comparison for Different Inflow

The various simulations were used to check and compared the flow behaviour inside the manhole due to different inflow. Sim 1_3, Sim 2_6, and Sim 3_9 were chosen for these comparisons as these three scenarios have a similar pressure level but different inflow. The inflows in these simulations are 44.73 l/s, 58.53 l/s, and 130.72 l/s, respectively; while the corresponding flow depths at the manhole are 1.24 m, 1.24 m, and 1.14 m.

To compare the vortex eye location between the above mentioned three simulation results, the velocity contours at the long section of the structure are shown in Figure 6. The blue-to-red contour pallet represents the magnitude of the velocity, light green arrows show the velocity direction, and the red dot shows the location of the vortex eye.
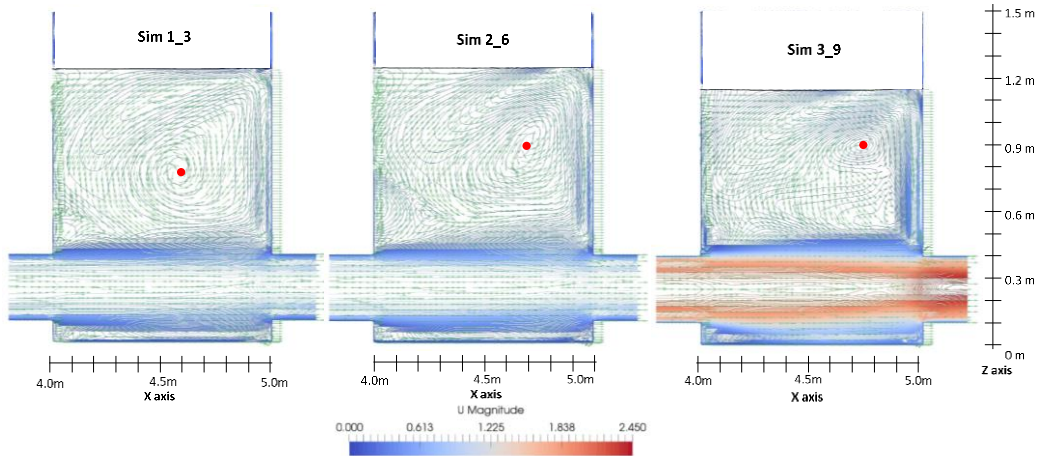
Figure 6: Velocity contour and eye of the vortex from Sim 1_3 (left panel), Sim 2_6 (middle panel) and Sim 3_9 (right panel)

Figure 6 shows that the location of the vortex eye is different in each case. The vortex eye was located at z=0.78 m, 0.9 m, and 0.87 m, which are 37%, 27.4%, and 24% of the flow depth for the water surfaces, respectively. It can also be seen that the vortex eyes move marginally to the right direction (away from the inlet) with the increase of flow.

The stream line path can give good insight into the possible flow path of particulate suspended sediment transport inside the manhole-pipe system. The stream lines presented in Figure 7 show the possible path lines from Sim 1_3, Sim 2_6, and Sim 3_9. The figure at the left shows streamlines seeding from the bottom of the manhole, and the right panel shows streamlines seeding from the centre of the inlet pipe.
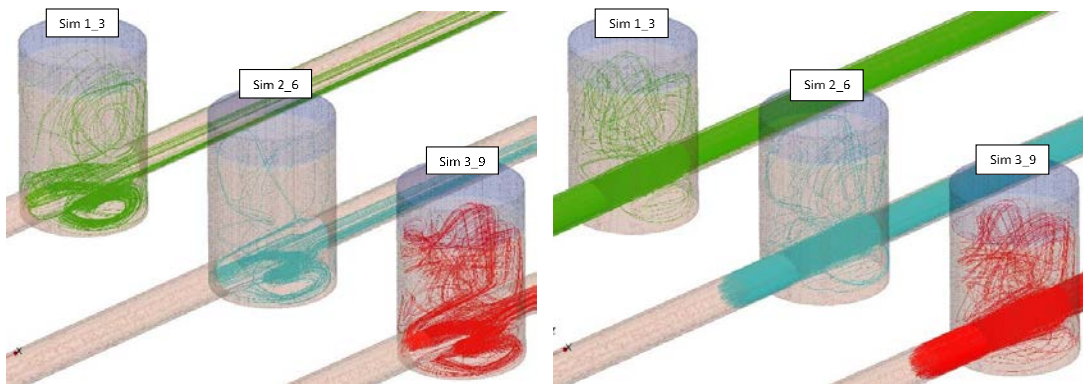
Figure 7: Flow path inside the manhole in Sim 1_3, Sim 2_6 and Sim 3_9 showing seeding from the bottom of the manhole (left panel) and from the pipe (right panel)

Figure 7 indicates that two types of streamlines have different pathways. By analysing the streamlines starting at the bottom centre of the manhole (left panel), it can be said that with the Sim 3_9 scenario with higher flow, it is likely that an at-rest particle at the manhole bottom has a higher probability of approaching the free surface in the manhole than go out through the outlet pipe directly. On the other hand, in the right panel, it can be seen that most of the particles coming through the inlet pipe do not stay inside the manhole. Most of them go out directly through the outlet. However, the Sim 3_9 scenario shows slightly more chance of mixing inside the manhole.

3.4. Flow Analysis under Different Surcharge Pressure

Three numerical simulation results are compared to analyse the change of flow pattern for different surcharge pressure inside the manhole: Sim 1_3, Sim 2_4, and Sim 3_3. These three simulations have similar range of inflow: 44.73 l/s, 43.69 l/s, and 41.72 l/s, respectively. The pressure levels in these three scenarios were 1.24 m, 0.59 m, and 0.32 m, respectively. Sim 1_3 and Sim 2_4 have pressure pipe flow, while Sim 3_3 has free surface flow. Figure 8 shows the velocity contour from the three numerical simulations.
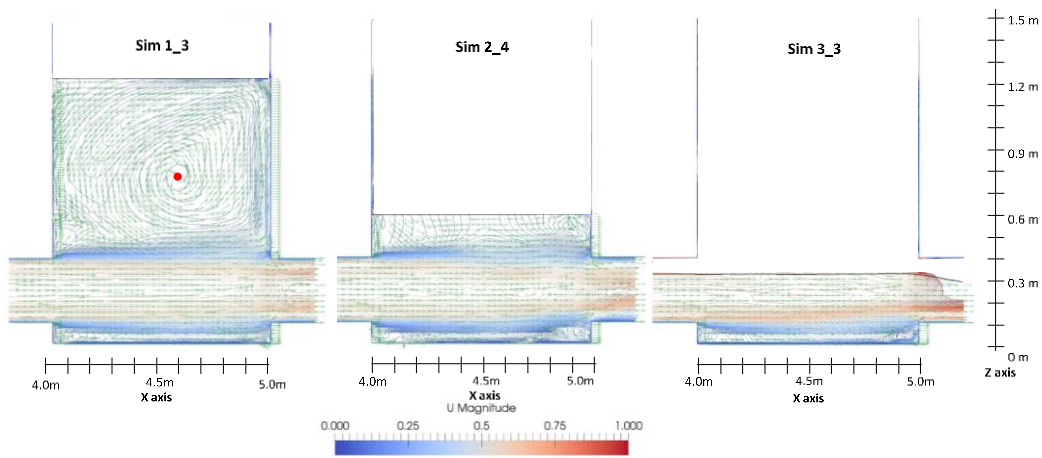
Figure 8: Velocity contour and eye of the vortex from Sim 1_3 (left panel), Sim 2_4 (middle panel) and Sim 3_3 (right panel)

Figure 8 shows that with lower depth of water in Sim 2_4 and Sim 3_3, the simulation does not produce any vortex. The flow vectors in Sim 2_4 and Sim 3_3 are mostly parallel to the dominant flow towards x direction. It is likely that the vortex forms if the water depth increases above a certain level.

The streamline path under the above mentioned three scenarios was analysed in Figure 9.
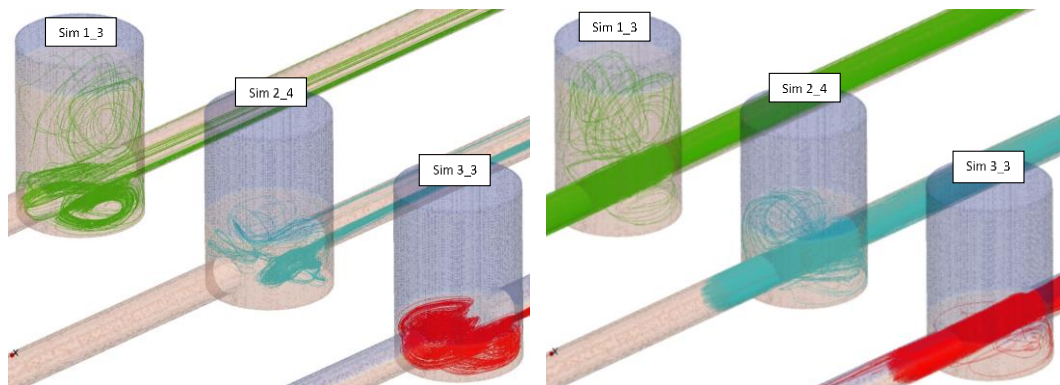
Figure 9: Flow path inside the manhole in Sim 1_3, Sim 2_4, and Sim 3_3 showing seeding from the bottom of the manhole (left panel) and from the pipe (right panel)

It can be seen from Figure 9 that like Figure 7, the streamline path starting from the bottom of the manhole is different from the path starting at the inlet pipe. Analysis of the streamline starting from the bottom of the manhole (left panel) shows that the three scenarios have different path lines. Most of the streamlines in Sim 3_3 circulate inside the pipe rather than going out through the outlet. While in the other two simulations, comparably more streamlines pass through the outlet. Streamlines coming through the inlet pipe (right panel) show that in Sim 2_4 and Sim 3_3, with lower depth of flow; most of the streamlines pass directly through the outlet. While in Sim 1_3, some streamlines coming from the pipe have comparably higher chance to reach at the free surface of the manhole as well as mixing inside the manhole.

3.5. Comparison of Pressure Level at the Manhole Bottom

As the flow enters the manhole and passes through the outlet, the velocity creates a pressure gradient on the manhole floor, which may create an uplift force on any pollutant lying on the floor. A comparison of the pressure variation on the manhole floor was analysed. Five case scenarios are in Figure 10, namely Sim 1_3, Sim 2_6, Sim 3_9, Sim 2_4, and Sim 3_3. As mentioned earlier, Sim 1_3, Sim 2_6, and Sim 3_9 have a similar pressure range with different inflow, while Sim 1_3, Sim 2_4, and Sim 3_3 have a similar ranges of discharge with different pressure levels at the manhole.
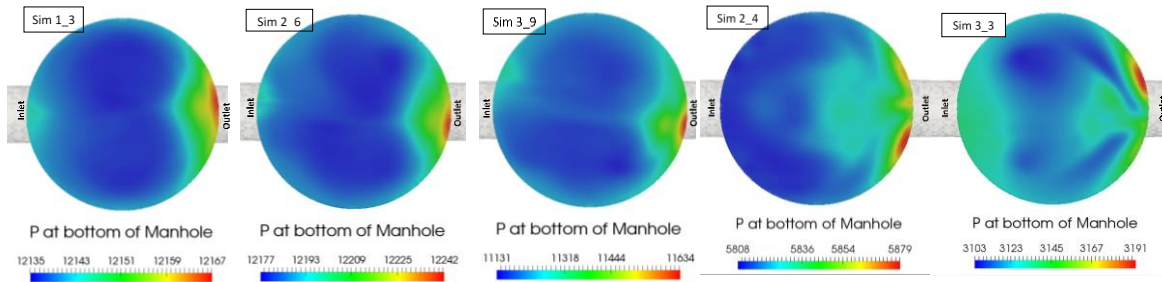
Figure 10: Pressure variation at the manhole bottom from left: Sim 1_3, Sim 2_6, and Sim 3_7, Sim 2_4 and Sim 3_3

Figure 10 demonstrates that the first three simulations, having a similar range of pressure, showed a similar pressure gradient map at the manhole bottom, keeping marginally higher pressure near the inlet and highest pressure near the outlet compared to the central zone. However, each of them has a different range of pressure variation at the bottom. In Sim 1_3, the difference between the highest and the lowest pressure is found in the range of 30 Pa; while this difference rises to the range of 60 Pa and 500 Pa in Sim 2_6 and Sim 3_9, respectively. It is likely that the difference between the highest and the lowest pressure increases with the increase in flow velocity in the inlet.

On the other hand, comparing Sim 1_3, Sim 2_4, and Sim 3_3, where the discharge has similar range, pressure maps at the bottom are not similar. Although these three simulations have a similar range of discharges, having different pressures/flow depths creates different average flow velocities inside the manhole. The average flow velocity is the highest in Sim 3_3 and the lowest in Sim 1_3. The range of pressure variation in Sim 2_4 and Sim 3_3 are in the range of 70 and 90 Pa, respectively, which shows that the pressure variation at the manhole floor increase with higher flow velocity.

4. CONCLUSION

This study provides the first step in the numerical assessment of flow behaviour of a manhole in an urban drainage system. The study presents replication of experimental data using a three dimensional CFD tool, OpenFOAM®. A standard k-ε turbulence modelling approach was used to capture the turbulence phenomena. The flow behaviour was analysed from the numerical model results.

The numerical results showed good agreement with experimental pressure data (less than 7% error). Both free surface flow and pressure flow were analysed. It has been observed that the pressure flow inside the manhole has different horizontal velocity profiles at different water depths. Surcharge flow inside the manhole creates different vortexes at different water depths, which was simulated in the numerical model. The location of the vortex centre changes with the inflow. With higher inflow, the centre rises closer to the surface and moves further from the inlet. It has also been seen that different pressure levels and flow velocities create different pressure gradients in the manhole floor, which might be responsible for different uplift forces to any particular pollutant resting at the manhole floor. Moreover, different flow at the inlet pipe also created different streamline paths inside the manhole. It has also been observed that the stream flow starting from the manhole bottom and coming through the inlet pipe follows different path lines depending on their inflow intensities.

The work will be further continued to develop a numerical approach to better understand the phenomena of particulate transport inside the manhole-pipe drainage system using a transport equation. Datasets obtained in this study will be used to calibrate/validate a numerical model created with the open-source toolbox OpenFOAM®.

5. ACKNOWLEDGEMENTS

6. REFERENCES

ANSYS Ins. (2009). *ANSYS Fluent 12.0 User's Guide*. *October*.

Carvalho, R., Páscoa, P., Leandro, J., Abreu, J., Lopes, P., Quinteiro, R., and Lima, L. M. P. L. (2013). "Experimental investigation of the linking element gully - drop manhole." *Proceedings of 35th IAHR World Congress 2013*, 35th IAHR World Congress 2013.

Deletic, A. (1998). "The first flush load of urban surface runoff." *Water Research*, 32(8), 2462–2470.

Furbo, E., Harju, J., and Nilsson, H. (2009). *Evaluation of turbulence models for prediction of flow separation at a smooth surface*. *Project Report - Uppsala Universitet*, Uppsala.

Granata, F., Marinis, G. de, Gargano, R., and Hager, W. H. (2011). "Hydraulics of Circular Drop Manholes." *Journal of Irrigation and Drainage Engineering*, 137-2(February), 537–552.

Greenshields, C. J. (2015). *OpenFOAM User Guide*.

Hirt, C. W., and Nichols, B. D. (1981). "Volume of fluid (VOF) method for the dynamics of free boundaries." *Journal of Computational Physics*, 39(1), 201–225.

Leandro, J., Abreu, J., and de Lima, J. L. M. P. (2009). "Laboratory set-up to validate a dual drainage concept numerical model." *8th International Conference on Urban Drainage Modelling*, Tokyo, Japan, 1–7.

Leandro, J., Lopes, P., Carvalho, R., Páscoa, P., Martins, R., and Romagnoli, M. (2014). "Numerical and experimental characterization of the 2D vertical average-velocity plane at the center-profile and qualitative air entrainment inside a gully for drainage and reverse flow." *Computers & Fluids*, 102(June), 52–61.

Lopes, P., Leandro, J., Carvalho, R. F., Páscoa, P., and Martins, R. (2015). "Numerical and experimental investigation of a gully under surcharge conditions." *Urban Water Journal*, 12(6), 468–476.

Rubinato, M. (2015). "Physical scale modelling of urban flood systems." University of Sheffield.

Santos, F., Carvalho, R., and Sancho, F. (2008). "Performance of a Multipurpose Hydraulic Channel." *2nd International Junior Researcher And Engineer Workshop On Hydraulic Structures*, 2nd International Junior Researcher And Engineer Workshop On Hydraulic Structures, Pisa, 1–7.

Stovin, V. R., Guymer, I., and Lau, S. D. (2008). "Approaches to validating a 3D CFD manhole model." *11th International Conference on Urban Drainage (11ICUD)*, 1–10.

Versteeg, H. K., and Malalasekera, W. (1995). *An Introduction to Computational Fluid Dynamics - The Finite Volume Method. Fluid flow handbook. McGraw-Hill …*, Longman Scientific and Technical, Essex, Eng.

Predicting Velocity at Limit of Deposition in Storm Channels using two Data Mining Techniques

H. Bonakdari[1], I. Ebtehaj[1]
[1]Dept. of Civil Engineering
Razi University
Kermanshah
Iran
E-mail: bonakdari@yahoo.com

ABSTRACT

In storm channel system design, the system should have the ability to transfer the entire input flow to the system as well as prevent sediment settling. Existing methods of determining the velocity at limit of deposition are minimum velocity or regression-based equations. Because minimum velocity methods fail to consider the effective flow and sediment transfer parameters and regression-based equations are not flexible in terms of various hydraulic conditions, they do not perform well. Thus, using such equations leads to a lack of designs with optimum, confident coefficients. In this study, Extreme Learning Machines (ELM) are employed to predict velocity at limit of deposition. ELM is a new algorithm for single-hidden layer feed-forward neural network (SLFN) training, which overcomes problems caused by gradient algorithms such as low velocity in network training. In this study, dimensional analysis is applied to identify the effective parameters on estimating the velocity at limit of deposition followed by ELM to predict the parameter values. ELM performance is compared with artificial neural networks (ANN) and regression-based equations. According to the results, using ELM increases the convergence speed to obtain optimum velocity results and is accordingly more accurate. The results represent the superior performance of ELM compared to existing regression-based equations.

Keywords: Artificial Neural Network (ANN), Extreme Learning Machines (ELM), sediment transport, storm sewer, velocity at limit of deposition.

1. INTRODUCTION

One of the most important concerns in storm water channel design is sediment transfer. Depending on flow velocity, solids in the flow path are washed and transferred by the flow and then enter the storm channel. If the flow entering the channel at a fixed slope does not have sufficient velocity to transfer the input sediment to the channel, sedimentation will occur on the bed. The presence of sediment on the channel bed causes an increase in bed roughness and a decrease in flow cross section, which is associated with flow capacity transfer reduction. Moreover, the velocity distribution and shear stress in the channel are altered. Therefore, a method is required to determine the minimum velocity required to prevent sediment deposition (i.e. minimum velocity at limit of deposition). One of the easiest methods entails using constant velocity in the range of 0.3-1 m/s according to different research works (Ebtehaj et al. 2014). As minimum velocity does not consider the effective parameters on sediment transport in channels, it often leads to velocity overestimation and underestimation with high relative errors (Nalluri and Ab Ghani 1996). Therefore, several researchers have employed different experimental data concerning the effective parameters on sediment transport, such as pipe diameter, flow resistance, hydraulic radius, particle diameter, etc., and presented different relationships using nonlinear regression. May et al. (1996) utilized 7 different datasets including a wide range of different variables and presented a semi-empirical relationship to calculate the limiting velocity as follows:

$$C_V = 3.03 \times 10^{-2} \left(\frac{D^2}{A} \right) \left(\frac{d}{D} \right)^{0.6} \left(\frac{V^2}{g(s-1)D} \right)^{1.5} \left(1 - \frac{V_t}{V} \right)^4 \tag{1}$$

$$V_t = 0.125 \sqrt{g(s-1)d} \left(\frac{y}{d} \right)^{0.47} \tag{2}$$

where C_V is the volumetric sediment concentration, D is the pipe diameter, A is the cross-sectional flow area, s is the specific gravity of sediment ($=\rho_s/\rho$), y is the flow depth, d is the median diameter of particles, V is the flow velocity, g is the gravitational acceleration, and V_t is the velocity required for incipient sediment motion (Equation 2).

Azamathulla et al. (2012) applied dimensional analysis and considered the sediment transport dimensionless parameters, viz. dimensionless particle number ($D_{gr}=(d(s-1)/v^2)^{1/3}$), volumetric sediment concentration (C_V), relative median diameter of particles to hydraulic radius (d/R), and overall sediment friction factor (λ_s). They presented the following relationships.

$$Fr = \frac{V}{\sqrt{g(s-1)d}} = 0.22C_V^{0.16}D_{gr}^{-0.14}\left(\frac{d}{R}\right)^{-0.29}\lambda_s^{-0.51} \tag{3}$$

$$\lambda_s = 0.851\lambda_c^{0.86}C_V^{0.04}D_{gr}^{0.03} \tag{4}$$

where λ_c is the clear water friction factor of the channel and Fr is the densimetric Froude number. Ebtehaj et al. (2014) used a wide range of data and modified Vongvisessomjai et al.'s (2010) equation as follows:

$$Fr = \frac{V}{\sqrt{g(s-1)d}} = 4.49C_V^{0.21}\left(\frac{d}{R}\right)^{-0.54} \tag{5}$$

The main problem with regression methods is the lack of accuracy in different hydraulic conditions. This relationship's results for different hydraulic conditions are different from the conditions used to determine the relationship, and it does not produce good results (Ebtehaj et al. 2014). Thus, some methods that have the ability to identify the complex relationship of nonlinear systems are still required.

In recent years, artificial intelligence (AI) has been used in hydraulic and water engineering (Ebtehaj and Bonakdari 2013; Khoshbin et al. 2015; Gholami et al. 2015; Karimi et al. 2015) and good estimations of different hydraulic parameters have been obtained. Thus, AI can be used as an alternative method to regression-based methods. Several AI methods, such as group method of data handling, gene expression programming, adaptive neuro fuzzy inference system, and a hybrid of ANN and an evolutionary algorithm (Azamathulla et al. 2012; Bonakdari and Ebtehaj 2015; Ebtehaj and Bonakdari 2014, 2015a) have been used to determine sediment transportation in stormwater sewer channels. One of the methods that is frequently used in sediment transport prediction is the Artificial Neural Network (ANN) (Ebtehaj and Bonakdari 2013, 2014). Extreme Learning Machines (ELM) is a new and simple method as a single-layer feed-forward neural network (SLFNN) whose velocity prediction is much higher than ANN. This method has demonstrated good performance in various applications, but based on the authors' knowledge, this method has not been used to predict sediment transport until now.

The main aim of this study is to predict the velocity at limit of deposition using Extreme Learning Machines (ELM). First, dimensional analysis is used to determine the effective parameters on limiting velocity estimation. Then ELM is used to predict the limiting velocity. Subsequently, the method results presented in this study are compared with ANN results and regression-based equations. Additionally, the effect of each input parameter on the proposed model is evaluated using sensitivity analysis.

2. MATERIALS AND METHODS

2.1. Artificial Neural Network (ANN)

The Artificial Neural Network (ANN), which is designed based on the human brain neuron system, is applied in diverse fields such as prediction, classification, and pattern recognition (Haykin 1999). ANN is a parallel data processing system that obtains the mapping between datasets in input-output form. A feed-forward MLP neural network generally consists of three different layers (an input layer, an output layer, and one or more hidden layers). Each layer of neurons is in contact with the next layer, and there is no connection between neurons in one layer. The neurons' output is calculated with the following equation:

$$y_m = F(r_m) \tag{6}$$

$$r_m = \sum_{i=1}^{n} (w_{mi} x_i + b_m) \tag{7}$$

where y_m is the output signal of a neuron, F is the activation function, r_m is the linear combiner output, x_i is the input signal, w_i is the synaptic weight, and b_m is the bias. Owing to the good performance of the sigmoid activation function in previous studies (Ebtehaj and Bonakdari 2013, 2015b), this activation function is used in the present study. It is defined as follows:

$$f(x) = \frac{1}{1 + exp(-x)} \tag{8}$$

To train the ANN, the Levenberg-Marquardt (LM) algorithm is applied, which is recognized as the best algorithm among gradient-based algorithms for predicting sediment transport (Ebtehaj and Bonakdari 2015b). The algorithm uses experimental observed inputs to estimate the weights and bias. The number of layers, number of neurons in hidden layers, number of iterations, and learning rate was 3, 19, 1000, and 0.5, respectively.

2.2. Extreme Learning Machines (ELM)

To overcome the problems of ANN, such as local minima, over-fitting, and long computational time, Huang et al. (2006) proposed a single-layer feedforward neural network (SLFNN) known as Extreme Learning Machines (ELM). The main difference between ELM and traditional ANN in terms of parameter determination lies in the feedforward network's input weights and bias. Unlike ANN, in the ELM method, it is not necessary to determine these as they are obtained randomly. However, the output weight values are calculated using the Moore-Penrose generalized inverse. Thus, according to the random selection of weights and biases, SLFNN can be considered a linear system. This characteristic leads to considerably faster calculations by ELM than ANN. Considering a data series with N different samples as (x_i, t_i), the ELM algorithm with $\tilde{N}$ hidden neurons is expressed as follows:

$$\sum_{i=1}^{\tilde{N}} \beta_i G(x_j; w_i, b_i) = o_j \qquad j = 1, 2, 3, ..., N \tag{9}$$

where $\beta_i = [\beta_{i1}, \beta_{i2}, \beta_{i3}, ..\beta_{im}]^T$ is the connecting weight vector between the ith hidden neuron and the output neurons, $G(x_j; w_i, b_i)$ is the ith hidden node related to x_j as the input and b_i, and $w_i = [w_1, w_2, w_3, ..., w_{\tilde{N}}]$ are the hidden node learning parameters. Regarding the $x = [x_1, x_2, x_3, ..., x_N]$, $w = [w_1, w_2, w_3, ... w_N]$, $b = [b_1, b_2, b_3, ..., b_N]$ parameters, an ELM algorithm with $\tilde{N}$ hidden neurons can approximate the $g(x)$ function with N samples as follows:

$$\sum_{j=1}^{N} \left\| o_j - t_j \right\| = 0 \tag{10}$$

In fact, a combination of β_i, w_i and b_i exists as

$$H(x; w, b)\beta = T \tag{11}$$

in which

$$H(x_1, ... x_{\tilde{N}}, w_1, ..., w_{\tilde{N}}, b_1, ... b_{\tilde{N}}) = \begin{bmatrix} G(x_1, w_1, b_1) & ... & G(x_1, w_{\tilde{N}}, b_{\tilde{N}}) \\ . & ... & . \\ . & ... & . \\ . & ... & . \\ G(x_N, w_1, b_1) & ... & G(x_N, w_{\tilde{N}}, b_{\tilde{N}}) \end{bmatrix}_{N \times \tilde{N}}, \quad \beta = \begin{bmatrix} \beta_1^T \\ . \\ . \\ . \\ \beta_{\tilde{N}}^T \end{bmatrix}_{\tilde{N} \times m}, \quad T = \begin{bmatrix} t_1^T \\ . \\ . \\ . \\ t_N^T \end{bmatrix}_{N \times m}$$

Fixed weights w_i and hidden layer bias b_i in ELM training are comparable to the least squares solution (β) of the linear system ($H = \beta T$) as follows:

$$\left\|H\left(w_1,\ldots,w_{\tilde{N}},b_1,..b_{\tilde{N}}\right)\beta - T\right\| = \min_{\beta}\left\|H\left(w_1,\ldots,w_{\tilde{N}},b_1,..b_{\tilde{N}}\right)\beta - T\right\| \quad \backslash \tag{12}$$

The above linear equation can be rewritten as

$$\widehat{\beta} = H^+ T \tag{13}$$

For RBF hidden nodes with Gaussian function $g(.)$, the following equation is used:

$$G\left(x_j;w_i,b_i\right) = g\left(b_i\left\|x_j - w_i\right\|\right) \tag{14}$$

where b_i and w_i are the impact factor and centre of the ith RBF node, respectively. In this study, to develop ELM for predicting velocity at limit of deposition, the neuron number in the hidden layer and the number of iterations was equal to 17 and 3000, respectively.

2.3. Goodness of Fit

To evaluate the accuracy of models GEP (1) to GIP (4), the statistical indices mean average percentage error (*MARE*), root mean square error (*RMSE*), correlation coefficient (*R*), scatter index (*SI*), and *BIAS* are used as follows:

$$MAPE = \frac{100}{n}\sum_{i=1}^{n}\left(\frac{\left|(Fr)_{(Predicted)_i} - (Fr)_{(Observed)_i}\right|}{(Fr)_{(Observed)_i}}\right) \tag{15}$$

$$RMSE = \sqrt{\frac{1}{n}\sum_{i=1}^{n}\left((Fr)_{(Predicted)_i} - (Fr)_{(Observed)_i}\right)^2} \tag{16}$$

$$R = \frac{\sum_{i=1}^{n}\left((Fr)_{(Observed)i} - \overline{(Fr)}_{(Observed)}\right)\left((Fr)_{(Predicted)i} - \overline{(Fr)}_{(Predicted)}\right)}{\sqrt{\sum_{i=1}^{n}\left((Fr)_{(Observed)i} - \overline{(Fr)}_{(Observed)}\right)^2\sum_{i=1}^{n}\left((Fr)_{(Predicted)i} - \overline{(Fr)}_{(Predicted)}\right)^2}} \tag{17}$$

$$SI = \frac{RMSE}{(Fr)_{(Observed)}} \tag{18}$$

$$BIAS = \frac{1}{n}\sum_{i=1}^{n}\left((Fr)_{(Predicted)_i} - (Fr)_{(Observed)_i}\right) \tag{19}$$

3. METHODOLOGY

Laboratory and analytical studies conducted on sediment transport in stormwater channels show that the minimum velocity required to prevent sediment deposition on the channel bed (limiting velocity) depends on the hydraulic conditions, channel geometry, and input sediment characteristics (Ab Ghani 1993; May et al. 1996; Vongvisessomjai et al. 2010; Azamathulla et al. 2012; Ebtehaj et al. 2013; 2014; 2015a). Thus, the functional equation between the limiting velocity and the effective parameters can be expressed as follows:

$$V = f(R,d,C_V,g,s,D_{gr}) \tag{20}$$

where V is the limiting velocity, R is the hydraulic radius, d is the median diameter of particles, C_V is the volumetric sediment, g is the gravitational acceleration, s is the specific gravity of sediment, and D_{gr} is the dimensionless particle number. As the dimensionless parameters can lead to more accurate prediction of sediment transport in stormwater

channels compared with using dimensional parameters, dimensional analysis and a dimensionless functional equation are used to estimate the limiting velocity using ELM presented as follows:

$$Fr = \frac{V}{\sqrt{g(s-1)d}} = f(C_V, D_{gr}, d/R, \lambda_s)$$ (21)

The relationship above is used to develop the ELM method to predict the limiting velocity. In this study, 218 data were collected from three different datasets (Ab Ghani 1993; Ota and Nalluri 1999; Vongvisessomjai et al. 2010) to model the Fr using ELM. Via random selection, 30% of data (65 data) were chosen for model testing and the remaining 70% (153 data points) were used for model training. Additional explanations about the experimental data are provided in previous studies (Ebtehaj and Bonakdari 2013; Ebtehaj et al. 2014). The data ranges employed are as follows: $1<C_V$ (ppm)<1280; $0.006<d/R<0.246$; $0.84<y/D<0.133$; $5.06<D_{gr}<142$; $0.013<\lambda_s<0.053$.

4. RESULTS AND DISCUSSION

Figure 1 compares the performance of two feedforward neural networks (FNN), including ELM and ANN. This figure shows that ELM has good precision in Fr estimation. All values determined by this method were estimated with less than 10% relative error, with the highest relative error in Fr estimation by ELM being around 9%. The average relative error presented by the model was about 2.5%, which indicates the high accuracy of this model in limiting velocity estimation. ANN also performed well and estimated about 60% of the total determined data with less than 10% relative error. The statistical index values indicate that between the values of both indices shown in Figure 1, they were higher for ANN ($RMSE = 0.15$ & $MAPE = 2.54$) than for ELM ($RMSE = 0.15$ & $MAPE = 2.54$). In addition, the error distribution of Fr estimation indicates ELM's superiority over ANN in estimating this parameter. Therefore, besides the fact that ELM modelling is much more rapid than ANN, model accuracy is significantly higher than ANN as well.
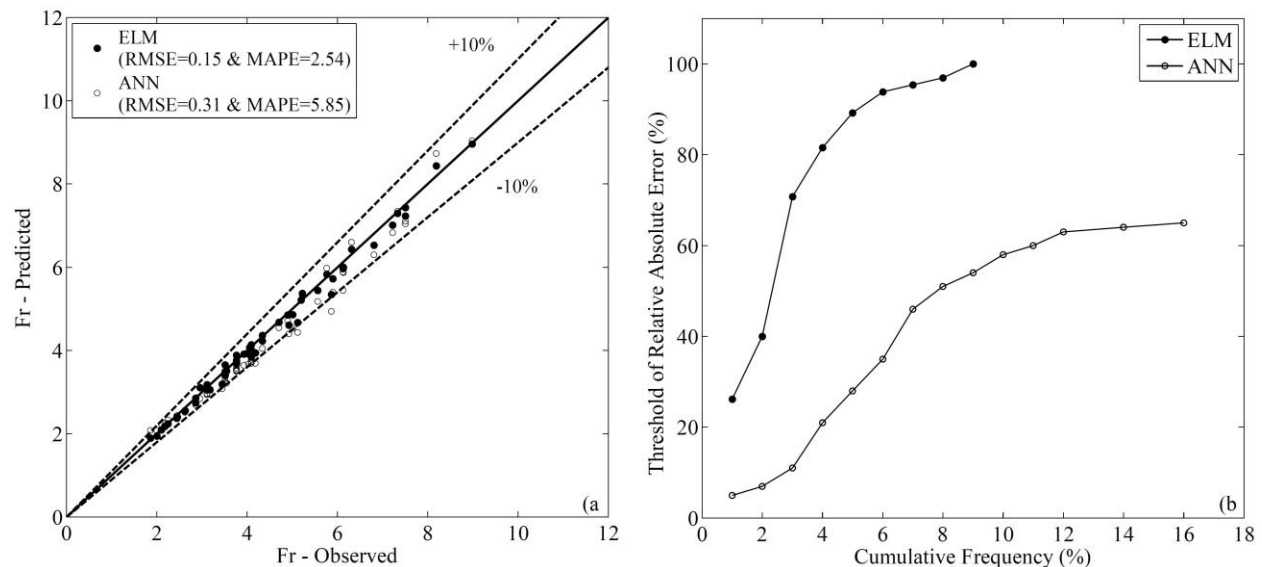
Figure 1 (a) Scatter plot for ELM and ANN, and (b) error distribution for ELM and ANN

ELM with relative error below 3% ($MAPE = 2.54$) estimated the Fr parameter with high accuracy. All estimations made by this method have less than 10% relative error. Also, according to the presented error distribution, about 90% of estimations have less than 5% relative error. The BIAS of -0.07 indicates that the values estimated by ELM are on average 0.07 lower than the observed laboratory values. In fact, the model performs with underestimation due to the lack of statistical indices, but this ELM underestimation performance does not lead to significant problems with sediment deposition. Ebtehaj et al.'s (2014) relation uses only two parameters, C_V and d/R, in Fr estimation and other parameters considered by ELM (D_{gr} and λ_S) are not as effective. This equation shows relatively good performance, but with increasing the Fr value, the model performs with underestimation. Because the relative error values of Ebtehaj

et al.'s (2014) equation are over 10%, using this relationship may lead to sediment deposition on the channel bed although the statistical index values in Table 1 show that this model generally performs well ($R^2 = 0.99$; $MAPE = 7.51$, $RMSE = 0.54$, $SI = 0.13$, $BIAS = -0.38$).

A comparison of Ebtehaj et al.'s (2014) relationship with the ELM results indicates that the average relative error is about 3 times higher than the index for ELM. Azamathulla et al.'s (2012) relationship, which has similar inputs to the ELM inputs (C_V, d/R, D_{gr} and λ_S) does not exhibit high accuracy but rather underestimation performance *(BIAS = -1.1)* and the estimated values compared to the observed values are greatly different. By increasing the *Fr* value, the estimation error increases with this relationship. Using this relationship leads to significant sediment deposition on the channel bed and reduced transmission capacity. Among the models presented in Table 2, this relationship has the weakest performance. The relative error is about 21% (*MAPE = 21.52*), which is almost 10 times higher than this index value for ELM. May et al.'s (1996) relationship is a semi-empirical equation and performs with underestimation (*BIAS = -0.04*). The index value for May et al.'s (1996) model compared to other models has the lowest absolute value because this relationship approximates the estimated values as both less and more than the experimental values with large errors, and the sum of the negative and positive values results in decreased *BIAS*. The *MAPE* index shows that the average *Fr* estimation accuracy of this model is about 9% (*MAPE = 9.21*) compared with the two ELM models, and Ebtehaj et al.'s (2014) equation shows weaker performance. The error distribution diagram shows that May et al.'s (1996) relationship estimates 20% of data with more than 20% relative error and a maximum of 35% relative error. Therefore, using May et al.'s (1996) relationship in stormwater channel design with large error in both underestimation and overestimation leads to significant sediment deposition on the channel bed and uneconomic plans, respectively.
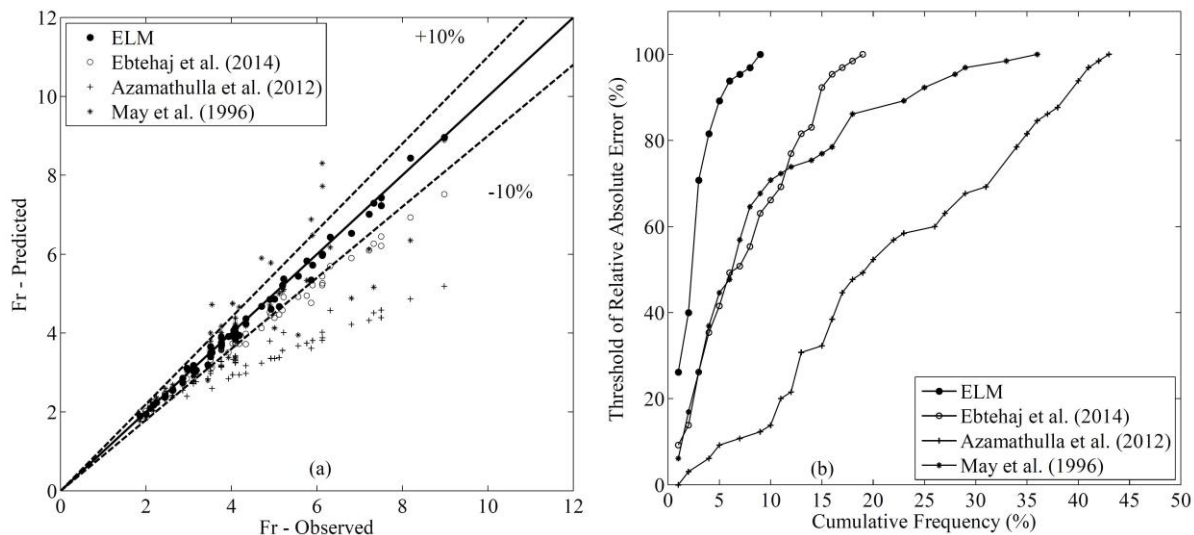
Figure 2. (a) Comparison of ELM and regression-based equations and (b) Scatter plot error distribution

Table 1. Comparison of ELM and regression-based equations using statistical indices

Method	R^2	MAPE	RMSE	SI	BIAS
ELM	0.997	2.54	0.15	0.04	-0.07
Ebtehaj et al. (2014)	0.995	7.51	0.54	0.13	-0.38
Azamathulla et al. (2012)	0.968	21.52	1.44	0.33	-1.10
May et al. (1996)	0.904	9.21	0.70	0.16	-0.04

Table 2 evaluates the effect of each parameter considered in this study as an effective parameter in $Fr = f(C_V, D_{gr}, d/R, \lambda_s)$ estimation. Models ELM (2) to ELM (5) that do not include one of the parameters in Fr estimation are less accurate than ELM (1). In fact, it is necessary to use the parameters provided in relationship 21 to

predict Fr. Among the $C_V, D_{gr}, d/R, \lambda_s$ parameters; not using the volumetric sediment concentration (C_V) parameter caused the greatest reduction in modelling accuracy. The relative error was about 10 times higher than ELM (1) (MAPE = 21.89). This status is also evident for the RMSE, SI, and R^2 indices. In all models, the *Fr* prediction process was constant and ELM performed with underestimation. Not using the overall sediment friction factor (λ_S) and relative median diameter of particles to hydraulic radius (*d/R*) parameters demonstrated approximately the same results and led to the lowest decrease in modelling accuracy. However, the lack of these two parameters increased the relative error value in *Fr* estimation by about 10% in using ELM.

Table 2. ELM model sensitivity analysis results

Model	Input combination	R^2	MAPE	RMSE	SI	BIAS
ELM (1)	$Fr = f(C_V, D_{gr}, d/R, \lambda_s)$	0.997	2.54	0.15	0.04	-0.07
ELM (2)	$Fr = f(C_V, D_{gr}, d/R)$	0.914	12.49	0.74	0.17	-0.34
ELM (3)	$Fr = f(C_V, D_{gr}, \lambda_s)$	0.931	12.86	0.68	0.16	-0.27
ELM (4)	$Fr = f(C_V, d/R, \lambda_s)$	0.859	15.89	0.90	0.21	-0.27
ELM (5)	$Fr = f(D_{gr}, d/R, \lambda_s)$	0.563	21.89	1.34	0.31	-0.17

5. CONCLUSIONS

Regarding the importance of determining the limiting velocity to prevent sediment deposits entering stormwater channels, Extreme Learning Machines (ELM) were employed in this study to predict the limiting velocity. First, dimensional analysis of the important parameters in limiting velocity estimation was done. The parameters are dimensionless particle number (D_{gr}), volumetric sediment concentration (C_V), relative median diameter of particles to hydraulic radius (*d/R*), and overall sediment friction factor (λ_S). ELM was used to predict the *Fr* parameter. According to the modeling results, ELM showed good accuracy in *Fr* estimation (R^2 = 0.997, *MAPE* = 2.54, *RMSE* = 0.15, *SI* = 0.04, *BIAS* = -0.07) as all estimated values had less than 10% relative error. To examine the proposed method's accuracy, the ELM results were compared with the ANN artificial intelligence method and regression methods. The results signified that ELM produced better results than ANN and the regression methods. Although ANN demonstrated good results, this method sometimes had relatively high error estimates that are associated with uncertainty. Among the regression methods, Ebtehaj et al. (2014) and Azamathulla et al.'s (2012) showed the strongest and weakest performance, respectively. Also, through sensitivity analysis on ELM, it was observed that not using each of the four input parameters significantly impacts ELM modeling results; the greatest error increase was related to ELM (5), in which the C_V parameter was not considered as an input parameter, and, consequently, the relative error increased up to about 24%.

6. REFERENCES

Ab Ghani, A. (1993). Sediment Transport in Sewers, Ph.D. Thesis, University of Newcastle Upon Tyne, UK.

Azamathulla, H.Md., Ab Ghani, A., and Fei, S.Y. (2012). "ANFIS – based approach for predicting sediment transport in clean sewer." *Appl. Soft Comput.*, 12(3), 1227-1230.

Bonakdari, H., and Ebtehaj, I. (2014). "Verification of equation for non-deposition sediment transport in flood water canals." *Proc., 7th International Conference on Fluvial Hydraulics, RIVER FLOW 2014*; Lausanne; Switzerland; 1527-1533.

Bonakdari, H., and Ebtehaj, I. (2015). "Comparison of two data-driven approaches in estimation of sediment transport in sewer pipe." *E-proceedings of the 36th IAHR World Congress*, The Hague, the Netherlands.

Chacko, B.P., Krishnan, V.V., Raju, G., and Anto, P.B. (2012). "Handwritten character recognition using wavelet energy and extreme learning machine." *Int. J. Machine Learn. Cyb.*, 3(2), 149-161.

Deo, R.C., Sahin, M. (2015). "Application of the extreme learning machine algorithm for the prediction of monthly Effective Drought Index in eastern Australia." *Atmos. Res.*, 153, 512-525.

Ebtehaj, I., and Bonakdari, H. (2013). "Evaluation of Sediment Transport in Sewer using Artificial Neural Network." *Eng. Appl. Comput. Fluid Mech.*, 7(3), 382–392.

Ebtehaj, I., and Bonakdari, H. (2014). "Performance Evaluation of Adaptive Neural Fuzzy Inference System for Sediment Transport in Sewers." *Water Resour. Manag.*, 28(13), 4765–4779.

Ebtehaj, I., and Bonakdari, H. (2015a). "Assessment of evolutionary algorithms in predicting non-deposition sediment transport." *Urban Water J.*, doi:10.1080/1573062X.2014.994003.

Ebtehaj, I., and Bonakdari, H. (2015b). "Bed load sediment transport estimation in a clean pipe using multilayer perceptron with different training algorithms." *KSCE J. Civil Eng.*, 1-9. doi:10.1007/s12205-015-0630-7.

Ebtehaj I., Bonakdari H. and Sharifi A. 2014 Design criteria for sediment transport in sewers based on self-cleansing concept. *J Zhejiang Univ. Sci-A*, 15(11):914-924.

Gholami, A., Bonakdari, H., Zaji, A.H., Akhtari, A.A., and Khodashenas, S.R. (2015). "Predicting the velocity field in a 90° Open channel bend using a gene expression programming model." *Flow Meas. Instrum.* 46, 189-192.

Haykin, S.S. (1999). Neural networks: a comprehensive foundation, USA: Prentice Hall International.

Huang, G.B., Qin-Yu, Z., and Chee-Kheong, S. (2006). "Extreme learning machine: theory and applications." *Neurocomputing*, 70(1–3), 489–501.

Karimi, S., Bonakdari, H., and Gholami, A. (2015). "Determination Discharge Capacity of Triangular Labyrinth Side Weir using Multi-Layer Neural Network (ANN-MLP)." *Curr., World Environ.*, 10, 111-119.

Khoshbin, F., Bonakdari, H., Ashraf Talesh, S.H., and Ebtehaj, I., Zaji, A.H., and Azimi, H., (2015). "Adaptive neuro-fuzzy inference system multi-objective optimization using the genetic algorithm/singular value decomposition method for modelling the discharge coefficient in rectangular sharp-crested side weirs." Engineering Optimization. doi:10.1080/0305215X.2015.1071807.

Malathi, V., Marimuthu, N.S., Baskar, S., and Ramar, K. (2011). "Application of extreme learning machine for series compensated transmission line protection." *Eng. Appl. Artif. Intell.*, 24(5), 880-887.

May, R.W.P., Ackers, J.C., Butler, D., and John, S. (1996). "Development of design methodology for self-cleansing sewers." *Water Sci. Technol.*, 33(9), 195-205.

Nalluri, C., and Ab Ghani, A. (1996). "Design options for self-cleansing storm sewers." *Water Sci. Technol.*, 33(9), 215-220.

Ota, J.J., and Nalluri, C. (1999). "Graded sediment transport at limit deposition in clean pipe channel." *28th* International Association for Hydro-Environment Engineering and Research, Graz, Austria.

Vongvisessomjai, N., Tingsanchali, T., and Babel, M.S. (2010). "Non-deposition design criteria for sewers with part-full flow." *Urban Water J.*, 7(1), 61-77.

Wu, S., Wang, Y., and Cheng, S. (2013). "Extreme learning machine based wind speed estimation and sensorless control for wind turbine power generation system." *Neurocomputing*, 102, 163-175.

Study on the Proceeding of Hydraulic Problem of Simulating Natural Fish Passage

Zhijuan Wang[*], Qingyuan Yang, Bole Jiang, Minghai Huang ,Yong He
Yangtze River Scientific Research Institute
Wuhan, Hubei, China, 430010
Email:10587394@qq.com

ABSTRACT

Conference Topics: *Environmental and Ecological Impacts-Fish passage*

Fish passages in water conservancy projects are important means of improving river connectivity and reducing the impacts on the ecological environment. Simulating natural fish passage, which repairs the fish ecological corridor by changing the structure and section type of the traditional artificial fish passage similar to a natural fish way, has been promoted and applied in recent years. Furthermore, the hydraulic research on the simulating of natural fish passage has made great progress. In this paper, the structural characteristics and requirements of the key factors that affect the fish's passing through these structures are analyzed by several cases of typical fish passage in China and other countries. The hydraulic problems involved, the determination method, and the interaction rules of the hydraulic essential factor of the simulating natural fish passage are presented in this paper.

Keywords: *Simulating natural passage, hydraulic essential factor, structure character, ecological corridor.*

1. RESEARCH BACKGROUND

In order to make full use of hydropower resources, dams, water gates, and other water retaining structures are built on rivers and lakes for flood control, power generation, irrigation, etc. At present, China has built more than 40 hydropower stations, covering nearly every major river. After the construction of dams and other hydraulic structures in the river, fish habitat environment is changed and fish activity is influenced. With the gradual enhancement of people's awareness of environmental protection, how to ensure the survival and reproduction of fish effectively, and how to balance the dam construction and ecological environment, there is an urgent need for water conservancy projects to consider an ecological study. The fish passage is the facilities constructed for fish, which can help the fish migrate through the dams and restore certain ecosystem function.

Traditional fishway mainly include the weir pool type, hole pool type, and Daniel type. As the engineering measures for the protection of fish resources within rivers, such fishway facilities have a large number of applications. Traditional fishways are designed to fulfill the requirements of the hydraulics, such as certain velocity, depth, and other indicators and use masonry or concrete for construction. Although the flow structure meets the needs of fish, the environment is far different from the natural environment, which led to ecological integrity declining. Therefore, the efficiency for fish passing was poor, which led to some of the fishway being abandoned.

Simulating natural fishway comes from the viewpoint of ecology. They are designed based on the fish habits, hydraulic characteristics, ecological protection, and natural river flow characteristics. In order to make fishes passing inside the fishway as similar as possible to the natural river and the migratory habits of fish, it is often used in low head dams.

The principle of simulating natural fishway is setting river tributaries that are similar to the natural river for fish migration through in position near the hydro-junction or other suitable location. Generally, at the bottom of the fishway, sand, gravel, and pebbles are used ups and downs to form the rough bottom slope. Soil, wood, vegetation, and rocks are used to form a curved slope surface of the fishway. Ecological gabion with natural materials, stone, or rock ridge are used to form a contraction section to control the flow, and a deep pool and shoal shape are used to

simulate the natural rivers or streams with abundant variety of slope as far as possible. Therefore, the channel has the character of "twists and turns, pool and shoal, fast and slow, deep and shallow."

Simulating natural fish passage in a fishway is a part of its ecological restoration function, and it compensates for the part of the water environment lost due to the water storage by the water reservation. After the natural materials at the bottom of the channel and the slope of the passage were eroded and nutrients transported by the water, stone clearance was filled with sand and aquatic organisms, which began to generate new benthic and planktonic communities to form places available for fish habitat, migration, and breeding. Therefore, imitation of natural fishway can not only realize need for fish migration as a traditional fishway, it can also effectively protect the ecological continuity and integrity. It has a strong ecological effect and has gradually become the new trend of fishway construction.

2. RESEARCH STATUS AND DEVELOPMENT TRENDS

In Europe, history of fishway building comes from 300 years ago. In 1662, Bearn province, which lies in southwest France, had enacted provisions to build passage for fish to up and down through the weir dam, and some simple fishway were built. From the end of 19th century to the beginning of the 20th century, Belgian Denil did long-time research on the rough chute and invented the Denil fishway, which is still in use today. In 1938, the first large-scale modern fish passage with a fish collection system in the world, the Bonneville dam on Columbia River in the United States, was built. After that, many more fishway were built: the fish lift, fish gate, fish collection boat, etc. According to incomplete statistics, by the early 1960s, there were more than 200 fish facilities in the United States and Canada, more than 100 in Western European countries, 18 seats in the former Soviet Union, and 67 seats in Japan in 1933. In the late 19th century, the number of fishway increased sharply; North America had nearly 400 seats; In Japan, it was more than 1400 seats. The highest is the North Branch Dam fishway (water head 60 meters), and the longest fishway is Brazil's Itaipu fishway (full-length 10K m). With the increasing awareness of environmental protection, more and more fishway projects were built at present [1].

Figure 1. Natural Bypass Channel for   Figure 2. The Natural Bypass Channel for Shad the Adour River
Salmon in Loue River
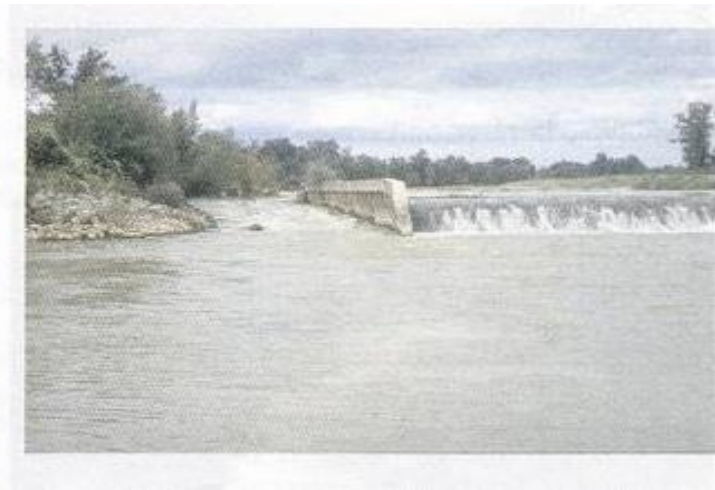
In China, the first fish way is built in the Qililong Station in Fuchunjiang Rive in Zhejiang province in 1958. In 1960s, more than 30 fishway were built in Heilongjiang and Jiangsu province, such as the Liyu Port, the Doulong Bay, the Taiping gate, and so on. Up to year of 2000, water conservancy with all kinds of fishway is more than 40 in China. After the 1880s，a lot of research work was done for the protection of Chinese sturgeon before the construction of Gezhouba Water conservancy in the Changjiang River, but eventually, the artificial breeding and stocking method was chosen to solve the migration problem of rare fish such as sturgeon. After that, facilities for fish

were no longer considered when building the dam in all the rivers of China, which almost led to stagnation of fishway research work in the next 20 years [2].

A lot of research work has been done on the fishway by several major research institutes and universities in our country. Xingyong Wang and Jun Guo summarized the fishway research and construction of the domestic and foreign country. Zhiyong Dong studied the hydraulic characteristics of ipsilateral vertical slot fishway by a large-scale fishway model, investigated the response of fish to different flow, and proposed the ipsilateral vertical slot fishway the improvement measures. Qinglei Cao did a lot of study on the hydraulic properties of fishway by the style of vertical slot in opposite side, including the fishway flow, velocity, turbulence, kinetic energy, shear stress, etc.; almost all the hydraulic characteristic value impact on fish were comprehensively studied. Li Bao did research on the layout and structure of the corner of vertical slot fishway, and the results show when a "L" shaped baffle structure is settled in the curve of rectangular channel, it will form a better flow field for fish migration needs

Environmental protection in hydropower projects is a process of continuous development. In recent years, research on the imitation natural fishway is increasing. Imitation natural fishway is typical technology in line with the principle of harmony between man and nature. Germany, Switzerland, Finland, Australia, Japan, and other countries have carried out more practice since its inception. For example, the simulating natural fishway in Itaipu Hydropower Station meets fish migratory and spawning demands very well and improves fish spawning environmental condition downstream of the dam. The Antonio Santo project, Brazil, in the construction, also includes the imitation natural fish passage to reduce the damage to the environmental condition for fish. The natural bypass channel of the salmon in the Loue River in Germany, and on the natural bypass for the West herring in Adour River in the southwest of France, all have good effect on the ecological continuity [2].

In China, Shuangke Sun did some research work on an environment-friendly natural fishway. It was found that compared with traditional engineering fishway, the imitation natural fishway has higher efficiency of fish passing due to the environmental condition familiar to fish. He did a comprehensive study on the design concept, type, structure, design principles, and hydrodynamic calculation method of imitating a natural-type fishway. Guang Nian Yu and Yian Wang, by the means of the 1:20 model test, did the research on imitation natural fishway of low head hydropower station. By series of optimization experiments on the structure of the pool, they got the plane layout of the imitation natural fishway suitable for low head hydropower station in China. Yu Yang did research work on the ecological landscape function of fishway, introducing the idea of enhancing connectivity in ecology in the river by taking hydraulics and ecological hydraulics into account in the process of fishway design, which builds the fishway not only meet the requirements of the fish migration, but also to increase the requirement of connectivity of the ecological landscape [3][4].

3. CLASSIFICATION AND STRUCTURE CHARACTERISTICS OF THE IMITATION NATURAL FISHWAY

In this paper, according to the width and depth of the section and the internal structure, fish passage is divided into two kinds: wide–shallow shape and narrow-deep shape. Under normal conditions, when the space is adequate and the water head is low, it is more suitable to choose shallow-wide shape because it can meet the needs of the structural characteristics of imitation of natural fishway itself and flow condition needs the of fish. However, with the improvement of the consciousness of environmental protection, before the construction of hydropower station in some river with rich fish resources but the channel is relatively narrow, also called for the construction of the imitation of natural fishway, so the width of fishway is restrict by overall arrangement and quantity, thereby formed a deep-narrow shape cross section.

Shallow-wide shape imitation natural fishway are generally divided into pool-shoal type and roughness ramp type. Pool-shoal type fishway with step structure to form the pools and shoals, in steep short channels or shallow shoals formed by low weir, velocity is higher, and the pool is on the contrary, the higher the water level between the two adjacent pool, the bigger the velocity of the shoal between the pools. The velocity of shoal must be less than the rush speed of small fish, and the velocity in the pool should be in continued speed range of fish (showed in Figure 3). The roughness ramp type is constituted by a long chute, as shown in Figure 4. It can be divided according to the boulder

stacking rules regular piled and loose piled the block stone architecture, loosely stacked rubble structure and boulders staggered structure.
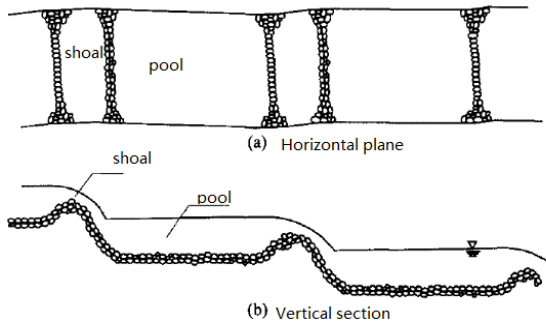
Figure 3. Pool-Shoal Type
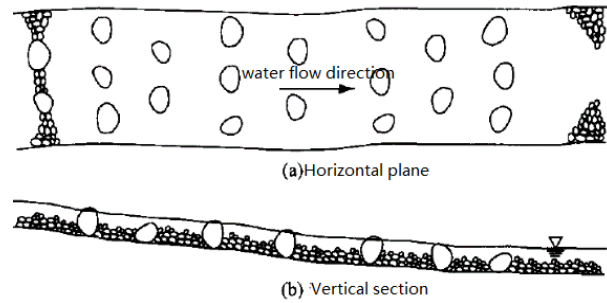
Figure 4. Roughness Ramp Type

Due to the water depth, the hydraulic characteristics of the flow are influenced by the change of the side wall, which leads to the change of the longitudinal and transverse distribution of the velocity. If the target fish is a single population, the swimming ability difference is small, so creating suitable condition is a little easier, but for the construction of the imitation natural fishway in the rivers with rich target fish population for migratory, it is more difficult to build an imitation natural fishway and meet the need of winding characteristics and a variety of fish migration flow requirements.

In order to solve this problem, a full investigation to the characteristics of the target species is required in order to know the parameters of fish populations, such as migration period, individual size, population size, behavior rules, and ecological requirements. Then by screening, classification and analysis, to determine the object of study and its requirements on flow, and then begin to study on the narrow deep fishway hydraulic. By fully understanding and grasping the flow structure, to find out the key factors that influence the structure of flow, and summarized the rules, then to optimize the size to make a channel to meet the target population migration needs.
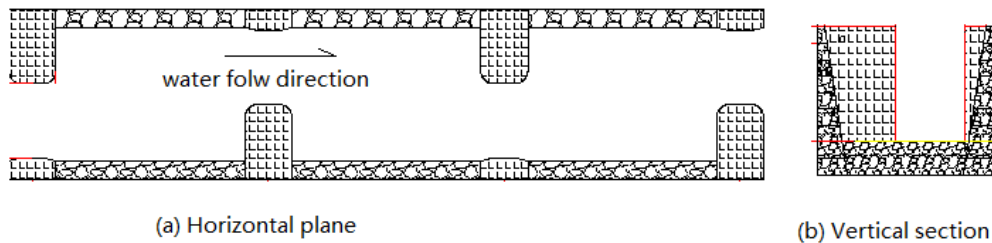
Figure 5. Deep-Narrow Type Simulating Natural Fishway

Preliminary results of the study show that the hydraulics characteristics structure of deep-narrow type fishway is generally affected by several parts, as shown in Figure 5. First of all, it is the shape and area of the contraction section. A bayonet is provided at a certain distance in the pool to forming flow contraction, to increase the internal resistance of the fishway, and to improve pool flow conditions. Bayonet in imitation natural fishway is a key factor that controls the flow and fall of the fishway, and the velocity of the contraction section is one of the most important hydraulic indexes of the fishway and should be controlled below the critical velocity of a fish. The area of the contraction section should not be too big or too small; on the one hand, if it is very small, velocity is relatively large, and if it is too big, the decrease of the fishway resistance will be declined and the flow, velocity, water drop, the volume dissipation rate index, will increase then it is unable to form a suitable flow environment. Therefore, the area of contraction section is one of the most important indexes of fishway hydraulic conditions.

Secondly, the length of the pool room. As water flows, passing through the contraction section and going into the pool room, the flow section becomes wider, so water flow will diffuse laterally due to the narrow section. During the diffusion process, the mainstream encountered two side walls to reciprocate so as to achieve water environment as

"twists and turns, pool and shoal." The length of the pool is the main factor to determine whether the flow can make full diffusion. If the pool room is too short, number of the bayonet will be increased, it will not only cause the loss of the project cost, but also can cause the flow diffusion insufficiency, which the effective water flow environment will not form. On the other hand, if too long, water drop between two pool rooms is too large, which will result in the flow velocity in bayonet too high, so the length of the pool room is an important indicator decided the flow conditions in the fishway.

Finally, it is the energy dissipation facilities in the pool and the bottom roughness. Narrow-deep imitation natural fishway, tend to cause concentrated velocity, auxiliary facilities for energy dissipation can be settled in the pool, which size and the position will decide the effect of energy dissipation, and the bottom roughness type will play a role in changing the flow field character.

For this kind of narrow and deep type imitation-natural fish passage, the water flow structure variety abundant and easy be affected by the figure of the side wall, the flow field is very complicated, and the related research is still in the initial stage, so it lacks reference experience for the layout of the internal structure at home and abroad.

4. EVERIMENTAL AND NUMERICAL STUDY ON DEEP -NARROW TYPE SIMULATING NATURAL FISHWAY

In this study, a deep-narrow type simulating natural fishway in Changjiang River is investigated by a 1:5 physical model. The fishway is designed to fulfil the needs of plenty of fish. The bottom velocity should be below 0.5m/s, and middle and surface velocity should not above 1.5m/s. The demand condition is critical, and former experiments have shown the velocity in contract section and bottom can't meet the demand.

After a series of modifications, an optimization plan is proposed by setting different configure of section along vertical direction to make the flow structure changing along the direction. Furthermore, the flows at different altitudes can impact and mediate each other, and so the small fish can get a friendly bottom passage to pass the fishway, and larger fishes can get though from the middle and surface of the fishway. Velocity distributions measured during experiments and numerical simulations are presented below.
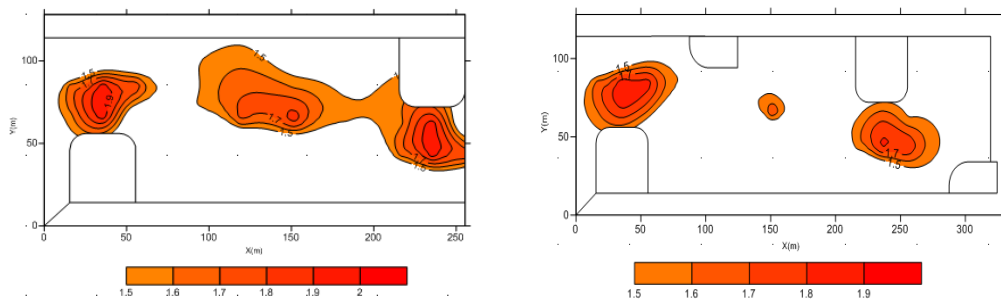
Figure 6. surface regions where velocity above 1.5m/s   Figure 7. middle regions where velocity above 1.5m/s
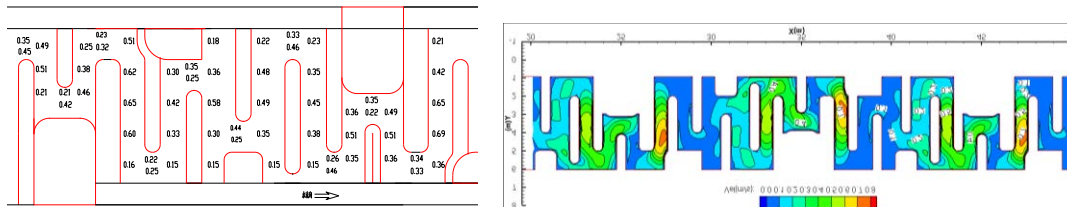
Figure 8. measured bottom velocity   Figure 9. bottom velocity contour got by numerical simulation

5. EXISTING PROBLEMS AND PROSPECTS

Although there have been some achievements of imitation natural fishway research that can be applied in engineering, there are still some problems in need of further study:

Compared with the traditional fishway, the structure of the imitation-natural fishway contact with ecology more closely, so the investigator not only needs to understand the relevant knowledge of hydraulics, but also needs to master biology-related knowledge and the ecological corridor related to environmental art, which belongs to the diversity and complexity.

Generally, the traditional imitation-natural fishway is wide shallow type, but this kind of fishway calls for more area and higher requirements for the layout of the hydraulic structures. The deep-narrow type has good adaptability, but the fishway flow field is more complex and easily affected by the side wall and the internal structure. Researching how to layout the internal structure reasonably and forming a theory system that can be recognized in the industry and engineering application is the main goal for narrow-deep imitation natural fishway research work.

Like the traditional fishway, imitation-natural fishway is still faced with problems of sediment deposition. Sediment deposition is the main cause of abandoned fishway both at home and abroad. Therefore, while studying on simulating natural fishway, research on reducing the sediment deposition siltation should be in advanced by means other than the old way of repairmen after construction.

6. ACKNOWLEDGMENTS

7. REFERENCES

[1] LI Shengqing, DING Xiaowen, LIU Daoning, Overview of Nature-Simulating Fishway [J], Yangtze River, 2014.11:70-75

[2] ZULHASH U M，MAEKAWAK, OHKUBOH. Tumbling flow in steeped weir channel fishway[J]．Resources and Environment in the Yangtze Basin, 2001, l0(1)：60-67．(in Chinese)

[3]SUN Shuang-ke, ZHANG Guo-qiang, Environment-friendly flshway in close-to-nature types[J], Journal of China Institute of water resources and Hydropower Research,Vol.10 no.1 March. 2012:41-47

[4] WANG Xing-yong，GUO Jun. Brief Review on Research and Construction of Fishways at Home and Abroad [J], Journal of China Institute of water resources and Hydropower Research,Vol.3 no.3 Sept. 2005:222-228.

Folsom Dam Auxiliary Spillway – Design Innovations and Construction Lessons Learned

C.Y. Wan[1], and C.M. Nolan[1]

[1]US Army Corps of Engineers, Sacramento District
1325 J Street
Sacramento, CA 95814
USA
E-mail: cheuk.y.wan@usace.army.mil

ABSTRACT

The new Folsom Dam Auxiliary Spillway gated Control Structure, part of the overarching Joint Federal Project, was recently completed. To make operation and maintenance activities for this activity more user-friendly, this project implemented innovative designs, and a select few related to the tainter gate (seals, dogging system, and anchor inspection access) are presented in this paper. This project also provided additional monitoring capacity to the trunnion anchors, both during and post-construction, both physical and data, with great results. Furthermore, this paper discusses some lessons learned on tainter gate specifications during gate construction and installation. Building and bridge construction specifications were generally used in project specifications; however, there are components on the tainter gate that require special attention, such as ASME tolerances and high strength bolting in connections with multiple thick plies. Additionally, this paper suggests specification language and practices to better meet the design intent in terms of fabrication and construction tolerances.

Keywords: *Tainter Gate, Specification, Slip Critical, Fracture Critical, Dogging, Seal*

1. INTRODUCTION

The new Folsom Dam Auxiliary Spillway Control Structure, located 37km (23miles) north east of Sacramento, California, is part of the Joint Federal Project (JFP), which the U.S. Bureau of Reclamation and the U.S. Army Corps of Engineers executed jointly by distributing cost sharing. The non-Federal sponsors for the JFP are the Central Valley Flood Protection Board (CVFPB) and the Sacramento Area Flood Control Agency (SAFCA). The auxiliary spillway is located southeast of the existing main Folsom Dam. Other principal features of the auxiliary spillway include an approximately 335m (1100ft) long approach channel, a 640m (2100ft) long concrete-lined spillway chute, a 208m (682ft) feet stepped concrete chute, and a concrete-lined stilling basin with baffle blocks. See Figure 1. The control structure was completed in the summer of 2015. The entire auxiliary spillway is expected to be finished in 2017.

The Control Structure is a reinforced concrete gravity structure comprised of two 27.4m (89.75ft) wide independent flow-through monoliths flanked by non-flow-through monoliths on each side. Both flow-through monoliths house three submerged tainter gates, each 7m (23ft) feet wide by 10.4m (34ft) high, measured from the soffit of the conduit to the gate sill. See Figure 2. Each of the six tainter gates has its own dedicated upstream bulkhead gate for operation and maintenance (O&M) and security purposes (Figure 3). Each tainter gate is supported by a dedicated built-up box trunnion girder and sixteen 7.62cm (3in) diameter 1034MPa (150 ksi) post-tensioned anchors. Each tainter gate is operated by a pair of hydraulic cylinders.

In this project, the structural and mechanical design team implemented a novel design approach on a number of tainter gate appurtenances. The following section describes these designs, which were intended to provide improvement upon typical tainter gate features. At the end of the paper, lessons learned during gate fabrication and installation on specifications are also presented.
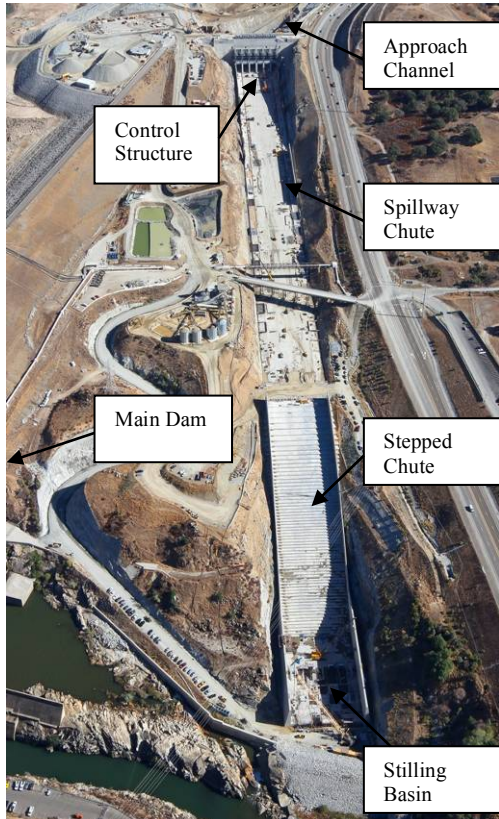
Figure 1. Folsom Dam Auxiliary Spillway, Aerial View

Labels on Figure 1: Approach Channel, Control Structure, Spillway Chute, Main Dam, Stepped Chute, Stilling Basin

Figure 2. Auxiliary Spillway tainter gate

Labels on Figure 3: PIERS, TRUNNION GIRDER, TAINTER GATE, BULKHEAD GATE, TRUNNION ANCHORAGE, FLOW

SECTION

DOWNSTREAM ELEVATION OF ONE MONOLITH
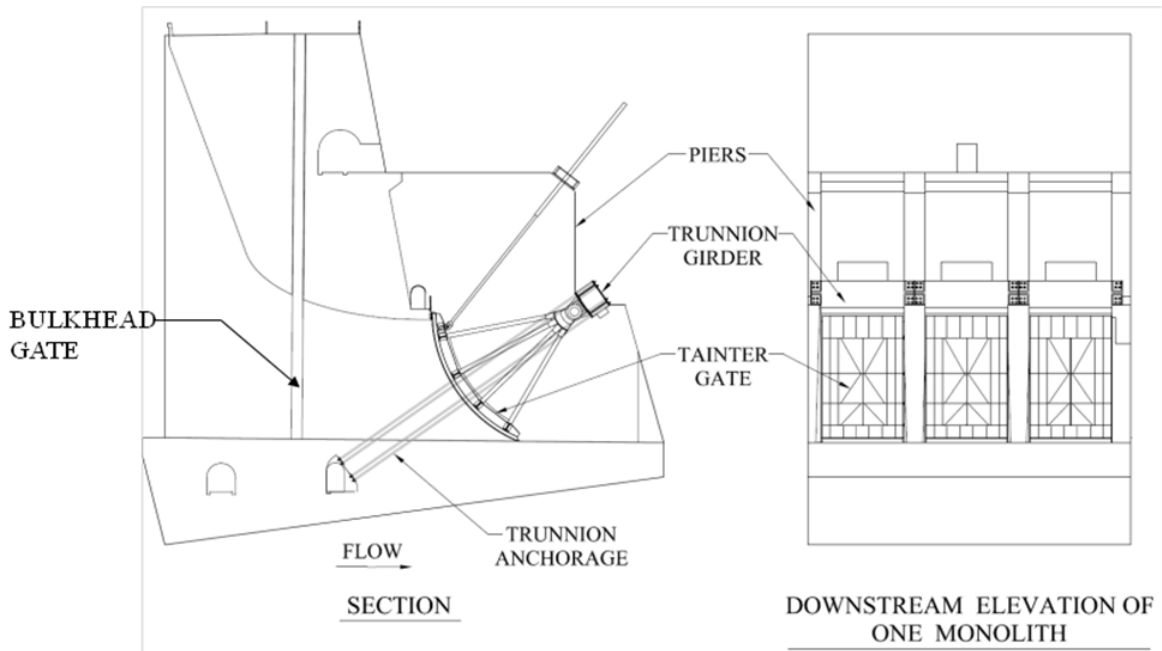
Figure 3. Auxiliary Spillway Flow-through Monoliths

2. INNOVATIVE DESIGN FEATURES

2.1.Gate Top Seal System

For submerged tainter gates, or tainter valves, a seal is attached to the top of gate and seals against some sort of headwall, or the seal is attached to the headwall and seals against the gate. At JFP, a redundant system was employed, with a seal on the headwall (swipe seal) and a seal on the gate (top seal). The top seal is a rubber J bulb seal with a 1.27cm (0.5in) preset that mates with stainless steel plate embedded in the concrete headwall. The swipe seal is a "top hat" shape with a 0.635cm (0.25in) preset. Adjustability for presets was provided by overslotted bolt holes (top seal) and adjustable anchor bolts and shims (swipe seal). Typically for submerged tainter gates, access to the headwall directly upstream of the skin plate is limited or not available when the gate is opened. However, at JFP, a walkway was provided for safe access in the headwall area during gate operations, enabling O&M staff and engineers to monitor the performance of the seals and the gate itself, with close-up visual monitoring and by directly contacting the skin plate to check for excess gate vibration, etc. Note that the actual sealing performance of the seals will be tested during wet commissioning in 2017.

The top seal is most effective when the gate is fully closed, and it only remains effective until the seal completely disengages, which occurs after the seal travels upward about 30cm (1ft) during gate opening. Note that top seal friction was included in the tainter gate design, and it mainly increased the trunnion friction moment and hydraulic cylinder force for small gate openings.

Much of the JFP was modeled after Oroville Dam, which included an inflatable seal installed near the top seal region on the headwall. Since this system had minimal success in sealing, the JFP design team selected a rubber swipe seal design (see Figure 4), which will be in contact with the gate skin plate (to some degree) at any opening. The preset is established by compression from the gate skin plate, and, thus, the preset changes with skin plate deflection. To compensate for the skin plate deflection in the downstream direction due to hydrostatic pressure, a series of 10cm (4in) wide "charging gaps" was included in the design to allow water to enter from behind the swipe seal to deflect the seal in the downstream direction (Figure 5). Based on the swipe seal stiffness, it was estimated that pressure provided by the charging gap could deflect the seal in the downstream direction by 0.6cm (0.24in) at maximum pool. Combined with the preset, the swipe seal will remain in contact with the skin plate except for some of the extreme load cases, where some leakage is acceptable. Note that swipe seal compression and its associated seal friction were included in the tainter gate design, and it mainly increased the trunnion friction moment and hydraulic cylinder force.
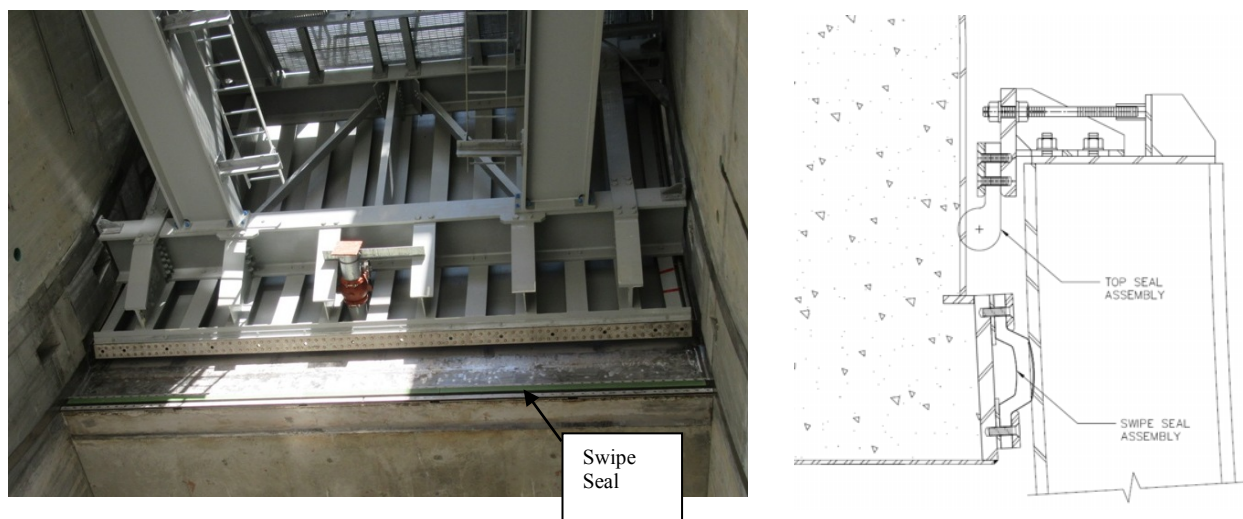
Figure 4. (Left) Gate in Fully Opened Position, Exposing Swipe Seal. (Right) Top Seal and Swipe Seal, with Tainter Gate in Closed Position
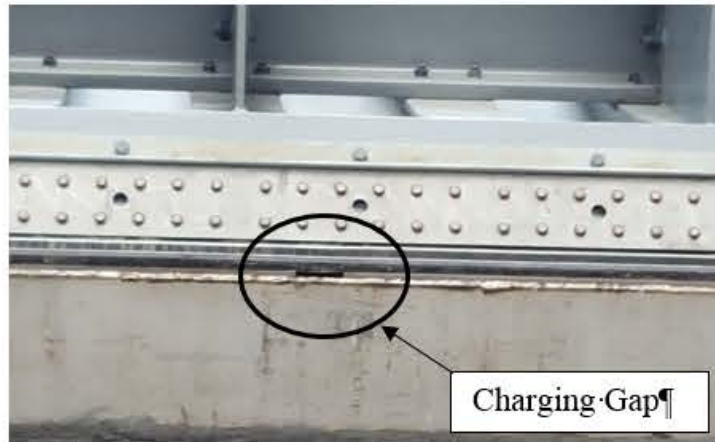
Figure 5. Swipe Seal Charging Gap

In order to maximize skin to seal contact, tight tolerances were set to establish a smooth, consistent gate radius. First, flatness of the 7m (23ft) by 13.7m (45ft, arc length) skin plate was required to be within 2.54mm (0.10in). In other words, the depth of any dimples on the skin plate needed to be less than 2.54mm deep. In order for the contractor to demonstrate that no tolerance was exceeded, a laser tracking 3D measurement system by FARO was employed, which has accuracy to 0.0254mm (0.001in). The gate radius measured from the center of the trunnion to the upstream face of the skin plate is 12m (39.5ft), with an allowable deviation of only 1.6mm (0.0625in). It was recognized during design that this is a very tight tolerance for such a large surface, causing the fabricator to request a relaxation of the requirement, but the request was denied, and the fabricator, with advanced technologies and excellent planning and workmanship, was able to meet the tolerances with a few tolerable exceptions.

It was observed during tainter gate dry commissioning that the swipe seal induced additional wear and tear on the skin plate paint system during initial operations, but it was limited to a fraction of the top coat, and no further damage was observed after the first operation. It was most likely caused by unevenness of the underlying metalizing. A thicker top coat could have been applied to counteract the initial break in, but the top coat would be more brittle and possibly delaminate. In many ways, a stainless steel overlay would be the best solution since the skin plate would be virtually free of corrosion, eliminating future operational maintenance repainting efforts. The stainless steel surface would also be machined to a very smooth surface compared to a metallized and painted surface, reducing the wear and tear and thereby increasing the life of the swipe seal. However, such a large stainless surface would be very expensive, possibly increasing gate weight. It is suggested, therefore, that future designs consider the two options to determine whether the O&M savings of a stainless steel overlay outweighs the potential added initial costs. A critical factor in such an economic exercise would be whether a smoother skin plate surface would realistically prolong the life of the swipe seal.

2.2. Side Seal Cavity

In typical tainter gates and tainter valves, the embedded stainless steel plates in the piers run the full length of gate travel, such that the side seals are engaged and preset for the full range of motion. While this is simpler for pier construction, this unnecessarily increases the wear and tear on the side seal. Moreover, side seal installation and the eventual replacement are difficult due to limited access with the gate and skin plate in place. Thus, for seal O&M efforts, skin plate modification is not uncommon as means for accessing the side seal. The JFP team determined that a side seal cavity can eliminate these problems and selected it for the design (Figure 6).

For this project, the embedded stainless steel side seal plates extend from the sill to their termination point slightly higher than the soffit of the headwall. Above the termination, a 12.7cm (5in) deep side seal cavity was provided in each pier (see Figure 4). The transition from the open cavity to the side seal plate includes an embedded plate that

angled into the pier, which enables the side seal preset to smoothly reestablish when closing the gate and the preset to slowly disengage when opening the gate.
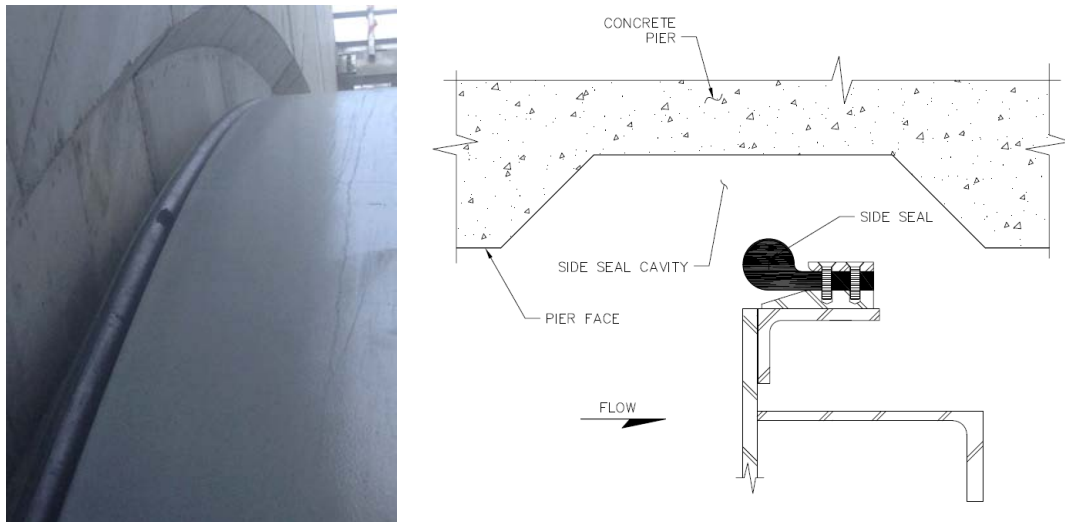
Figure 6. Side Seal Cavity (Left: viewed from upstream. Right: viewed from top)

Though it required more customization on the pier reinforcement, the side seal cavity already paid dividends during gate seal installation. The contractor attached the field-spliced perimeter seal (top J bulb seal, each of the side seals, and the bottom seal) to a segmented steel frame and was able to easily bolt the seal to the skin plate with the gate in the opened position (Figure 7). It is anticipated that future seal removal and replacement will be relatively problem free.
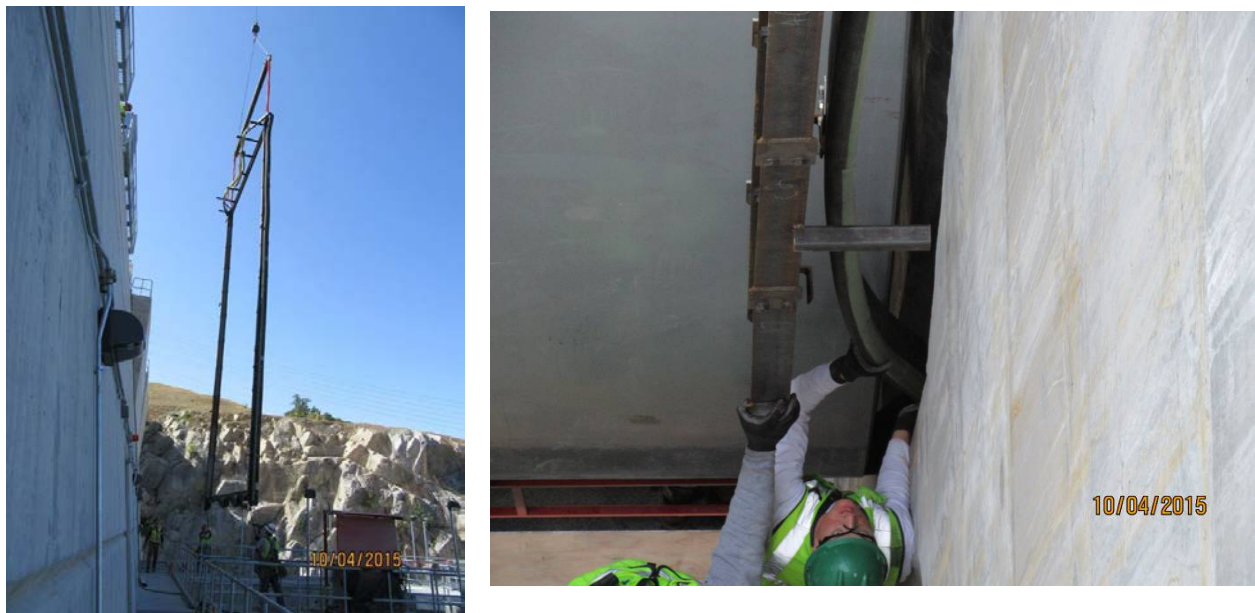
Figure 7. Perimeter Seal Mounted on Steel Frame, and During Installation

2.3. Multi-Elevation Dogging System

During design, the O&M staff at Folsom expressed desire to have a redundant gate support system when the tainter gates were opened during maintenance activities; one example is the aforementioned seal replacement, which can be deployed quickly and readily. There are also maintenance activities for which holding the tainter gate partially opened is advantageous, including gate bottom seal repair, partial gate skin plate repaint, conduit inspection, etc. A typical system to temporarily hold the gate open is called a dogging system, a term originated from historic nautical term "dog," which meant to secure a movable feature. A cursory search on tainter gate dogging systems did not yield any significant guidance on the design and operation of the dogging system that suited the JFP's needs or worked for the unique JFP geometry.

Figure 8. Dogging Devices (Circled) - Engaged and Disengaged
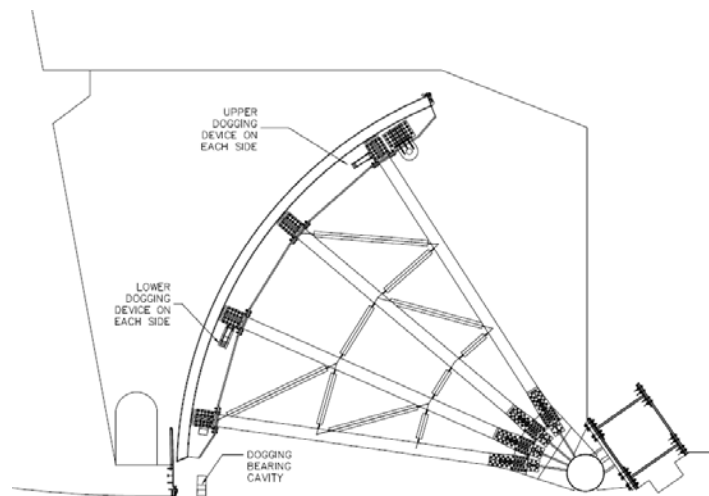
Figure 9. Upper and Lower Dogging Devices

Typical dogging systems involve chains that lock the gate in a single position. A variety of concepts were brainstormed and considered for the dogging system. Ultimately, a sleek, simple, multi-elevation system was employed. It features two pairs of dogging devices per gate – upper dogs on Girder 1 and lower dogs on Girder 3 – and three pockets in each pier face, which contain bearing plates. The dogging device includes a steel tube (HSS)

whose load is transmitted through the W27 girder cross section by a series of stiffener plates. The dogging device rotates about a pin, such that it is oriented vertically when disengaged and is angled normal to the embedded bearing plate when engaged. The dogging device rotates manually (eliminating risks of potential equipment breakdown) with a lever that is accessible from platforms on the gate. See Figures 8 and 9 for device. The dogging device was designed to bear in compression, transmitting the weight of the gate and the potential pushing force from the hydraulic cylinder. An ultra-high molecular weight, plastic bearing pad was attached to the ends of the dogging device to protect the surfaces and improve grip on the engaged dogging device.

With this simple system, the gate can safely maintain 6 different positions, from approximately 1.2m (4ft) to fully open. The added benefit of a multi-elevation dogging system was realized during erection of the tainter gate and subsequent construction activities. By having a redundant support system, safe access and working conditions were provided under the tainter gate, eliminating the need for scaffolding or other means of temporary supports. The ability to lock the gate in multiple elevations also helped the contractor save time from locking the gate completely opened or partially opened whenever long-term access through the conduit was needed.

2.4. Trunnion Anchorage

Each tainter gate is anchored to the concrete control structure by sixteen 7.62cm (3in) diameter 1034MPa (150 ksi) post-tensioned trunnion anchors. For any tainter gate, trunnion anchors are vulnerable to failure due to corrosion. Especially when constantly loaded from the post-tensioning, its failure can happen very quickly and often without warning signs. Thus, double corrosion protection was included in the JFP anchors, provided by HDPE ducts (which extend full length through the piers) and grout. Visual inspection of the full length of embedded anchors is not possible. Typically, anchors are only accessible on the live end, and the ends are covered by a protective steel box, which can be removed to facilitate inspection. Innovations on the JFP design include extending the anchors deep into the structure, adding an inspection gallery (See Figure 10), and installing Plexiglass protection boxes on both the dead ends and the live ends. The ability to visually inspect the anchor ends increases the chances of seeing any potential signs of anchor failure, such as rust, water coming out from the anchor ducts, signs of movement, etc. Note that Plexiglass was used instead of steel as an anchor end enclosure to provide improved inspectability, taken as a lesson learned from Oroville Dam, where plexiglass enclosure provided excellent visibility to the anchor live end.
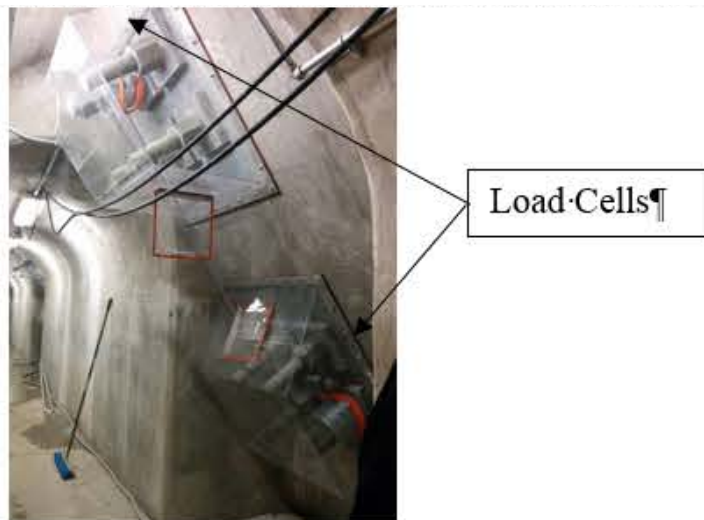
Figure 10. Inspection Gallery

3. CONSTRUCTION ACTIVITIES

3.1. Overview

Besides the aforementioned features that are primarily for permanent O&M purposes, this project includes noteworthy features and specification requirements that affected construction and performance. Associated lessons learned are presented in this section.

3.2. Trunnion Anchor Monitoring

Vibrating wire load cells were installed on 25% of the anchors at the dead end to provide a means to monitor residual prestress in the anchor during construction and for future operations. (See Figure 10.) The load cells were useful during construction in providing quality assurance of the prestress level during the sequenced stressing operation over a period of months and in providing real-time post-tensioning losses once stressing and grouting were completed. These large diameter anchors are cold-rolled, which translates to atypical and somewhat uncertain relaxation characteristics. Ultimately, the AASHO-calculated relaxation losses proved conservative.

The load cells will continue to help monitor the long-term integrity of the anchor and preempt sudden failures, though in a more limited capacity. Since the anchors are fully threaded, the grout re-characterizes the length of anchors between the ends from "free stressing" to "grouted," preventing free movement of the anchors. Thus, the presence of grout hinders the ability of the load cells to detect losses some distance away from the load cell location. As a result, in order to provide the O&M staff a complete picture to assess the condition of the trunnion anchors, a second method was used. The dispersive wave method, patented by the company FDH Velocitel, records the frequency response of an anchor when it is subjected to different kinds of light tapping at both ends of the anchor. Since the anchor's frequency response is a function of anchor tension, by comparing the frequency response to the response when the anchor was first tensioned, a quantitative sense of the remaining anchor prestress can be determined (See Figure 11). The dispersive wave technology has advanced since it was utilized at JFP, and, currently, the Corps has an ID/IQ contract for the acquisition of dispersive wave testing to determine the amount of post-tension force in existing tainter gate trunnion anchors (USACE, 2015).

Based on the positive experiences of inspecting and testing both anchor ends, and of gathering tension data on anchor during and after construction, it is recommended that future designers also consider incorporating accessibility to both ends of the anchors, consider installing load cells, and definitely utilize state of the art monitoring technology such as the dispersive wave method to monitor the trunnion anchors.
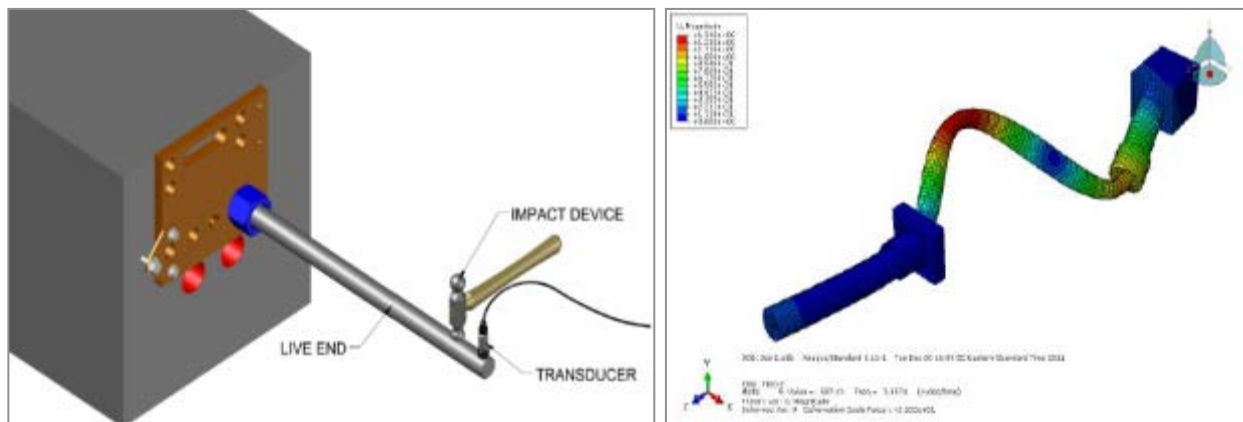
Figure 11. Dispersive Wave Example (FDH Velocitel, Trunnion Anchorage Road Analysis at Folsom Dam, Final Report, 2015)

3.3. Fracture Critical Designation

A tainter gate is a unique structure, so even though Corps guide specifications are available, the project specification has to be tailored for the specific project, and caution must be taken when importing requirements from multiple sources (specifications and codes), which can be contradictory. In addition, specifications and codes might not be up to date with current technology or may have other limitations. One such conflict is the concept of fracture critical members, which was borrowed from the bridge industry to address fatigue failure due to repetitive bridge loading. For a tainter gate, even though hydrodynamic loading differs with earthquake loading in terms of the length of sustained loading, the determinacy of the number of cycles, and the load magnitude, applying analyses and detailing employed for earthquake loading on tainter gate design would still yield a design that is resilient to repeated vibration cycles from hydrodynamic forces.

Designers would generally specify the fracture critical requirement for welds and steel material and then rely on requirements in established specifications and codes such as AASHTO-LRFD and AWS D1.5. Designers would also generally aim to design connections with fatigue stress category C or better because of the fatigue design parameters in the AISC Steel Construction Manual. Since those specifications and codes are inherently created for buildings and bridges, they do not always cover concerns that a tainter gate designer would face. For example, in this project, the tainter gate strut arms were identified as fracture critical members. The designer determined that even though the strut arms were compression members, the fracture critical designation was prudent because of the potential range of stresses in loading cycles and because failure of these critical members could lead to loss of life. This application of the fracture critical member call-out differs from AASHTO, which defined it as a component in tension whose failure is expected to result in the collapse of the bridge or the inability of the bridge to perform its function (AASHTO, 2014). The fracture critical call-out is a good short-handed way for designers to require increased material hardness, additional material testing, material traceability, rigorous weld testing requirement, etc. that would ensure better material quality and workmanship. For this project, which included a fabricator who knew the code well enough to attempt to re-interpret the contract requirements regarding the struts, this issue was resolved with constant dialogue with the fabricator, as well as in person pre-construction conference and periodic quality-assurance visits. However, a better solution to avoid contractual confusion is for the designer to redefine fracture critical members as those identified on drawings, not allowing deference to the definition from codes.

3.4. Slip Critical Bolting

Another code issue experienced for the JFP was related to high-strength bolting. For the structural bolting on the tainter gate, all bolts were specified to be tightened to the prescribed slip critical pre-tension in RCSC (and to have a slip coefficient of 0.35 on the faying surfaces) to improve their fatigue behavior. According to RCSC, all bolts were required to be tightened to snug tight before continue tightening to the target pretension. However, the definition of snug tight was vague and evolved over time. In the 2004 RCSC Specification, "The snug-tightened condition is the tightness that is attained with a few impacts of an impact wrench or the full effort of an ironworker using an ordinary spud wrench to bring the connected plies into firm contact," while in the 2009 Specification, "Snug tight is the condition that exists when all of the plies in a connection have been pulled into firm contact by the bolts in the joint and all of the bolts in the joint have been tightened sufficiently to prevent the removal of the nuts without the use of a wrench." While the 2009 Specification added language to further define the snug tight condition, it remains vague on the definition of "firm contact." In this project, most connections either had typical plate thickness and/or number of plies, and few challenges arose during bolting. However, at the tainter gate strut arm to trunnion hub connection, due to difference in web plate thickness of these two features, the web bolted splice was approximately 7.62cm (3in) thick with a total of 5 plies, including shims. During routine QA inspection, it was discovered that bolts that were previously snug tightened had become loose, despite following RCSC's requirement. Through trial and error, and after examination per the arbitration clause in RCSC, it was discovered that due to the unusual plate thicknesses, the number of plies, the typical plate unevenness, and the size and spacing of the bolts, the typical snug tight procedure prescribed by RCSC was not enough to truly bring bolts into snug tight. The consequence of bolts not being snug-tight before tensioning is that bolts do not achieve their required pre-tension force, and then the connection is subject to slippage or improper transmission of loads. Ultimately, in the aforementioned web connection, the contractor used an impact wrench to snug-tighten the bolts and proactively performed 100% pretension QC on all slip critical bolts on the tainter gate.

For future projects, particularly for unusually thick connections, it is recommended that mockup (to prove the bolting procedure) and bolt tension QC/QA (at least initially) be required in the specifications to supplement the RCSC specification. A multiple stepped snug tightening sequencing, written by the contractor and approved by the Engineer, requiring workers to check the snug-tightness of all bolts in a connection immediately after snug-tightening the last bolt may also be justified for unusually thick connections.

3.5.   Steel Erection

In typical building design, steel erection has the benefit of compression members in bearing due to gravity. Conversely, for erection of tainter gates, whose geometry and orientation are variable, such benefit does not exist, and special attention is often needed. An applicable example for the JFP gates is the bolted connection where the strut arm connects to the trunnion hub assembly. The orientation of this connection is such that gravity tends to increase a gap between the two plies. If a specific bearing tolerance is not specified (e.g. mill to bear according to AWS), the fabricator would be permitted per code to leave a gap between the two members, putting the bolts in unintended shear and possibly creating a compromised connection unknowingly. It is recommended that the work plan require an explicit description of the fit up process to assure that it is well-planned and successful. A specific means of checking the fit up (e.g., an X inch thick feeler gauge shall not fill Y% of the contact area) should also be provided by the designer, determined with consideration of limitations of such requirements due to inaccessibility of the contact area (behind splice plates).

4.   CONCLUSION

Brand new dams and gates are fairly rare nowadays, so the engineering community can all benefit from sharing fresh ideas and lessons learned. The design, fabrication, and construction of the Folsom JFP tainter gates included a few novel design features that were intended to provide safe access to O&M staffs, convenient means for seal installation and removal, and reliable means (both visual and non-destructive technology) to monitor the health of the trunnion anchor post-tensioning system. With this paper, it is hoped that engineers designing or studying similar systems may be inspired to find creative solutions or improve the quality and ease of the construction processes.

5.   ACKNOWLEDGMENTS

6.   REFERENCES

AASHTO (American Association of State Highway and Transportation Officials). (2007). *LRFD Bridge Design Specifications*, 4th Ed, Washington, D.C.

AISC (American Institute of Steel Construction). (2008). *Steel Construction Manual*, 13th Ed, Chicago, IL.

AWS (American Welding Society). (2015). "Bridge Welding Code", *AWS D1.5*, Miami, FL.

FDH Velocitel. (2015). "Trunnion Anchorage Road Analysis at Folsom Dam, Final Report," Northbrook, IL.

RCSC (Research Council on Structural Connections). (2004, 2009). *Specification for Structural Joints Using High-Strength Bolts*, Chicago, IL.

USACE (U.S. Army Corps of Engineers). (2015). "National ID/IQ Contract for Testing of Trunnion Girder Anchor Rods." *Engineering and Construction Bulletin No. 2015-20*, Washington, DC.

Water System Operator Training for the Central Arizona Project

Brian Wahlin[1] and Bert Clemmens[1]
[1]WEST Consultants, Inc.
Tempe, AZ 85284
USA
E-mail: bwahlin@westconsultants.com

ABSTRACT

The Central Arizona Project (CAP) is designed to bring about 1.85 billion cubic meters (1.5 million acre-feet) of Colorado River water per year to Maricopa, Pima, and Pinal counties in Arizona. The CAP canal system is a 540-km (336-mile) long system of conveyance aqueducts, tunnels, pumping plants, and pipelines that is monitored and remotely controlled using Supervisory Control and Data Acquisition (SCADA) software from CAP headquarters in Phoenix, AZ. Because the CAP is crucial to the renewable water supply in Arizona, operating the canal effectively is of utmost importance. Typical day-to-day operations for Water System Operators on the CAP involve efficiently conveying water through the system while meeting water orders from the various customers along the canal. The Water System Operators are also expected to respond to emergency conditions while protecting the infrastructure in the canal and minimizing interruptions to the water orders. Since day-to-day operations do not adequately prepare Water System Operators for emergency conditions, CAP has utilized a unique training tool that replaces the real canal with a hydraulic simulation model without requiring any modifications to the existing SCADA setup. Using this training tool, the new Water System Operators can now be trained to operate the CAP canal system under a much wider range of flow conditions and emergency situations without endangering the actual canal system, wasting water, or interrupting water orders. The training tool gives the Water System Operators a larger knowledge base with which to handle emergency situations and conveys experience and institutional knowledge to new Water System Operators.

Keywords: *Irrigation systems, canal and diversion structures, canal management, operator training*

1. INTRODUCTION

1.1. The Central Arizona Project

The Central Arizona Project (CAP) is Arizona's largest renewable water supply and was constructed to help the state conserve its groundwater by importing surface water from the Colorado River. CAP was designed to deliver an average of 1.85 billion cubic meters (1.5 million acre-feet) of water per year to residents of Maricopa, Pima, and Pinal counties (see Figure 1), making it a critical economic lynchpin for the region. CAP delivers untreated water to three major types of customers: municipal and industrial, agricultural, and Native American users. The customers are then responsible for their own water treatment. The CAP canal travels 540 km (336 miles) across the state of Arizona. The canal begins at Lake Havasu, continues through the Phoenix metropolitan area, and ends in Tucson. CAP consists of 14 pumping plants, 1 pump/generating plant, 10 siphons, 3 tunnels, and more than 45 turnouts for customer deliveries. During its travels across the state of Arizona, water is pumped more than 850 vertical meters (2,800 vertical feet) and flows through the canal via gravity following the natural contours of the land. Construction of the system began in 1973 and was substantially complete in 1993.
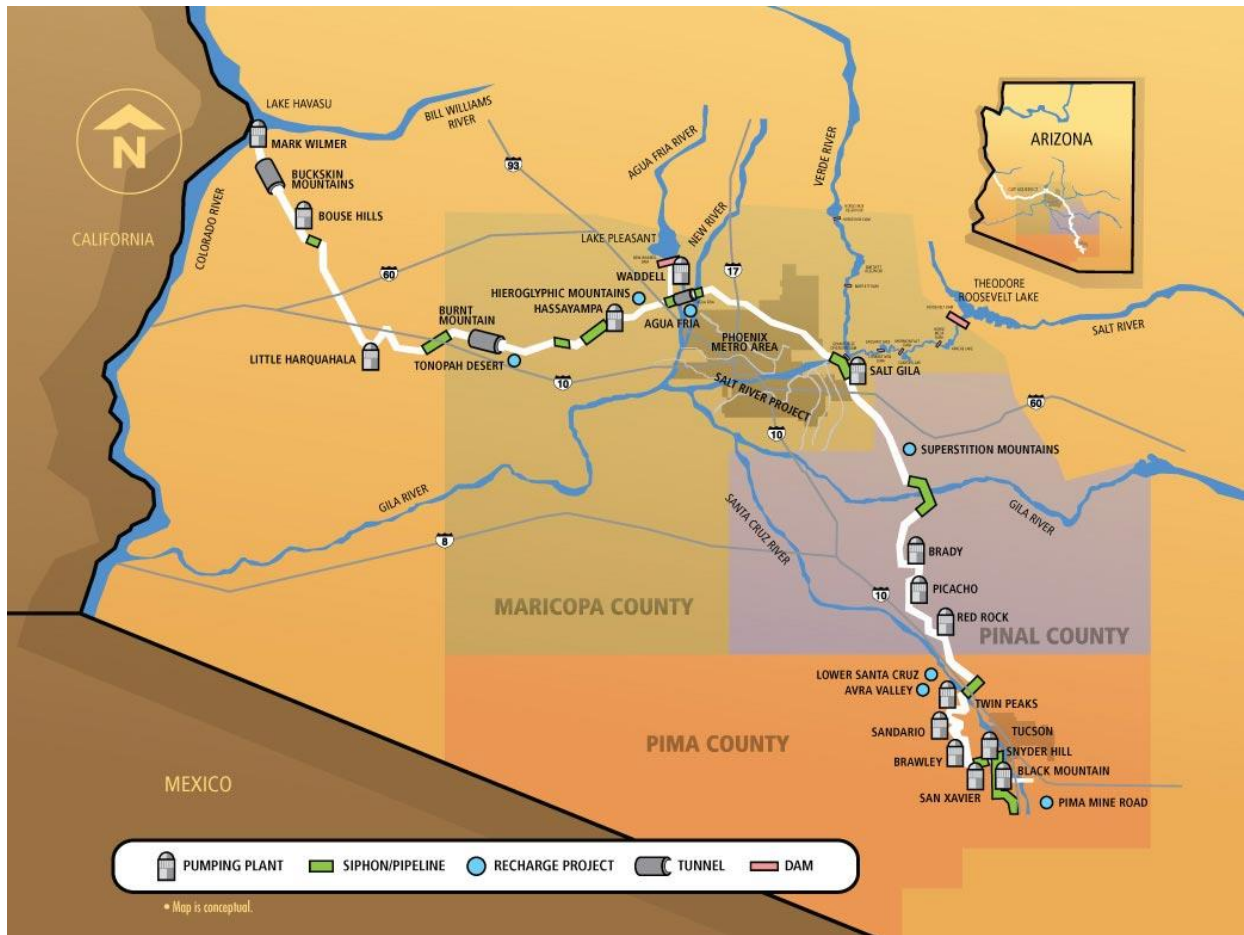
Figure 1. Schematic diagram of the CAP canal system

1.2. Central Arizona Project's Control Center

The entire CAP canal system is remotely monitored and controlled via a Supervisory Control and Data Acquisition (SCADA) system from CAP's Control Center, located at CAP headquarters in Phoenix, AZ. Real-time data from the CAP canal system is transmitted to the CAP's headquarters and displayed on various computer screens (a typical SCADA screen is shown in Figure 2). Information displayed includes water levels in the various pools, gate positions, flow rate estimates through structures, turnout deliveries, and pump status (e.g., on, off, or failed). There are more than 1,000 real time SCADA displays that the operators can use to assist in the operation of the system. At any given time, 30 million cubic meters (8 billion gallons) of water are managed from the Control Center, which is staffed by at least 2 Water System Operators 24 hours a day, 7 days a week.

The main goal of the CAP Water System Operators is to effectively route flow changes through the canal system in order to meet customer demands without causing fluctuations in water levels that could disrupt service to other customers or potentially overtop and damage the canal. The Water System Operators have various tools at their disposal with which to operate the canal system. The Water System Operators can

- Turn pumps on or off;
- Move gates up or down; and
- Change customer deliveries
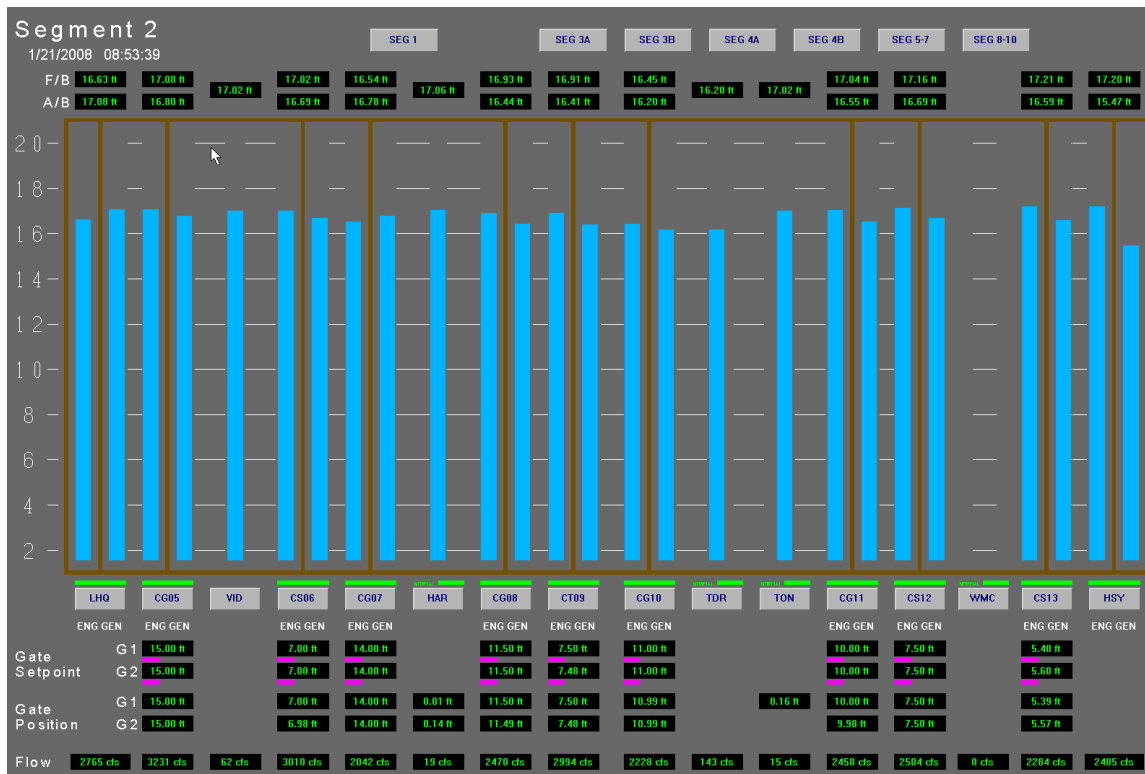
Figure 2. Typical SCADA screen for CAP (bars indicate water depths)

2. COMPLEXITIES IN OPERATING OPEN-CHANNEL SYSTEMS

Initially, operating an open-channel system like the CAP canal system may appear to be fairly straightforward because, for any pool in the system, the inflow into the pool equals the outflow from the pool plus the change in storage volume over time. However, there are many aspects of open-channel flow that make the operation of the system more difficult than it first seems:

- Operators must handle unscheduled changes in demand, which can arise from check structure failures, pump failures, vandalism, or other emergency situations.
- Operators must deal with safety concerns. Obviously, overtopping the canal can cause serious damage to the canal system. In addition, lowering the water surface too quickly can cause structural damage to the canal lining.
- Operators must deal with the uncertainties inherent in the canal system. Regardless of the measurement method used, there will always be uncertainty associated with various properties of the system, such as flow rate, stage, and roughness. In addition, some of these properties, such as canal roughness, can change with time (e.g., weeds or algae can grow in the summer, changing the roughness of the canal). If left unaccounted for, these uncertainties cause the water deliveries to be different than desired.
- Operators must deal with transient effects that characterize unsteady flow, such as delay times, dispersion effects, changes in storage volume, and hydraulic interactions between the pools.
- Operators must rely on experience to effectively operate an open-channel system. Even after learning how to manage the canal on a day-to-day basis, operators may not be able to handle emergency situations effectively because these scenarios were never addressed in their training.

Because of the importance, difficulty, and complexity of operating an open-channel canal system like CAP, Water System Operators require a significant amount of training before they can effectively manage the system.

2.1. SCADA Systems and Open-Channel Systems

SCADA systems are very popular in manufacturing plants and municipal water delivery systems. In recent years, SCADA systems have become more popular with irrigation districts. Currently, there are several irrigation districts that use a SCADA system to monitor and control their open-channel systems. A few of the irrigation districts with SCADA systems include the Central Arizona Project, the Salt River Project, the Imperial Irrigation District, the Maricopa-Stanfield Irrigation and Drainage District, and the Central Arizona Irrigation and Drainage District.

2.2. SCADA Training at the Central Arizona Project

Typically, new Water System Operators at CAP are required to complete up to 18 months of training and supervision before they are allowed to operate the canal system independently. Even after this training period is complete, the Water System Operators' training will have been limited to day-to-day operations. The newly trained Water System Operators will have little experience operating the canal under a wide range of flow conditions. The new operators will also have little training on how to operate the canal under emergency conditions, since setting up a real-world emergency training scenario would put the canal system at risk or interrupt water deliveries.

2.3. Additional Difficulties with SCADA Training

Strand et al. (2005) lists several problems associated with the SCADA training at typical irrigation districts. Some of these issues do not apply to the CAP Canal but are common in smaller irrigation districts. These problems are summarized in the following paragraphs.

First, the Water System Operators employed by many irrigation districts can come from a wide variety of backgrounds and have varying levels of canal experience. For example, at the Salt River Project (SRP), a very large organization, operators generally work their way through the hierarchy of the canal operations system. Most start as a zanjero (i.e., someone who patrols irrigation ditches and opens canal gates to deliver water) and eventually work their way to the control room. Through this experience, they gain working knowledge of system topology, pool transmission delays, problem check structures, etc. This knowledge is invaluable once they are in the control room. While smaller organizations do promote some field operators, or zanjeros, to SCADA operator positions, these smaller districts are sometimes forced to hire SCADA operators with little or no canal operation experience.

Second, regardless of the level of applicable canal experience, the learning curve for a SCADA system can be quite steep, especially for an operator with limited computer experience. Many operators require some training to gain familiarity with a networked computer environment as well as managing other duties in conjunction with operating the canal.

Finally, SCADA operators are also trained in a "live" environment while operating a real canal. At CAP and SRP, the environment is generally focused on running the canal system on a day-to-day basis. There are separate departments that handle ordering, billing, and payment receipts. At smaller irrigation districts, like the Central Arizona Irrigation and Drainage District (CAIDD), the canal operators handle all of those financial/clerical tasks in addition to operating the canal. For those with little or no canal experience, the distraction of dealing with the business functions can be overwhelming and can hinder progress in understanding the canal system from an operational perspective.

3. SCADA TRAINING TOOL FOR CAP

Effective operation of the canal system is imperative at CAP from both a safety aspect and a customer satisfaction aspect. Water System Operators must learn how to efficiently utilize the tools at their disposal in order to effectively route water to their customers. In an effort to have more robust training of their Water System Operators, CAP commissioned the development of a training tool that allows their Water System Operators to be trained on a hydraulic model of the canal instead of the real canal. In essence, the simulation tool would act like a flight

simulator does in training pilots. Using this training system, Water System Operators can be trained to operate a canal system under a wide range of flow conditions, including emergency situations, without endangering the actual canal system, interrupting customer deliveries, or wasting water. This training tool was developed for Segment 2 of the CAP canal system, which stretches 100 km (62 miles) from the Little Harquahala pumping plant to the Hassayampa pumping plant (see Figure 1).

3.1. SCADA Training with Hydraulic Simulation

In the past, researchers at the U.S. Arid Land Agricultural Research Center (ALARC) created a training tool that replaces the real canal with a hydraulic simulation model (SOBEK) without requiring any modifications to the existing SCADA set up. Employees at WEST Consultants, Inc. modified this training tool so that it works with HEC-RAS as the hydraulic simulation model. The training tool is composed of five main components:

- a SCADA system;
- a hydraulic model of the canal system and the HEC-RAS computer program;
- an intermediate software package (SimSuite) that emulates field hardware and maintains physical information such as gate positions, water levels, and turnout flows;
- an External Data Interface (WEST-EDI) software package that communicates between the hydraulic and intermediate software package; and
- a proctor software program (SimProctor) used to assist in the training of the Water System Operators.

In a typical set up for Water System Operator training, the SCADA system would be installed on one computer (i.e., the Trainee Computer) while the hydraulic model, SimSuite, SimProctor, and WEST-EDI would be installed on a second computer (i.e., the Proctor Computer) as shown in Figure 3. The two computers are then connected using a serial cable. Setting the training tool up in this manner isolates the SCADA system from the rest of the training tool. In addition, setting the training tool up in this manner does not allow the training tool to make changes to the actual canal system (i.e., the training tool is "offline").

Water System Operator trainees can be given tasks to route flows through the system or respond to emergencies using the SCADA system on the Trainee Computer. Using the Proctor Computer, the proctor can observe the effectiveness with which the trainees perform the tasks. In addition, the SimProctor program can be used to make unexpected or emergency changes to the system that the trainees must respond to in an effective manner (e.g., change offtake flows, freeze gates, fail pumps, etc.). If the trainees do not perform satisfactorily on a given test, the entire system can be reset, and the scenario can be repeated until the trainee's performance improves. All of this is accomplished without endangering the real canal system, interrupting customer deliveries, or wasting water.
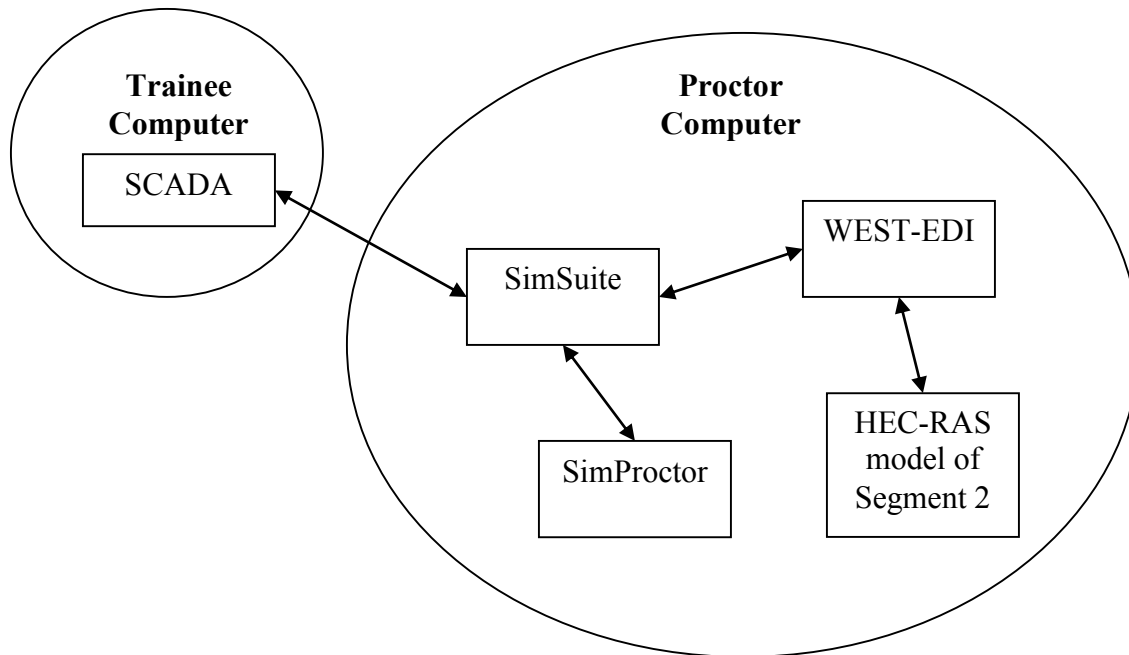
Figure 3. Training tool configuration

3.2. CAP SCADA System

In this application for CAP, the decision was made to re-create the SCADA screens on a completely separate computer system that was not connected to CAP's local area network or the internet. Since only Segment 2 was being analyzed, the re-development of the SCADA screens was not difficult or time consuming. The newly developed SCADA screens for Segment 2 of the CAP canal system were almost identical to the screens being used by the CAP operators at the time. Separate SCADA screens were developed for

- Check structures 5 through 13;
- Havasu pumping station;
- Little Harquahala pumping station;
- Hassayampa pumping station;
- Vidler turnout;
- Harquahala turnout;
- Tonopah turnout;
- Tonopah Desert Recharge (TDR) turnout; and
- Western Maricopa Combine (WMC) turnout.

Figure 4 shows a Google Earth image of Segment 2 with the pumping plants and check structures labelled. The turnouts mentioned in the list above are typically just upstream of a check structure. In Segment 2, all check structures consist of two radial gates (a typical check structure can be seen in Figure 6). Trainees have the ability to change the gate positions for each gate individually at each check structure as well as the flow deliveries at each turnout. In addition, trainees can turn each individual pump on and off at each pumping plant (the Hassayampa Pumping Plant is shown in Figure 5). For definition, pump control refers to whether a pump is on or off (as set by the trainees). Pump status refers to whether a pump is nominal (can be turned on or off) or failed. While the pump control is set by trainees from the SCADA screens, the pump status is set by the proctor through the SimProctor program.

Figure 4. Google Earth image of Segment 2 of the CAP Canal

Figure 5. Hassayampa Pumping Plant

Figure 6. Typical radial gate at a check structure on the CAP Canal

3.3. Hydraulic Simulator and Model

The hydraulic simulator for the SCADA training tool is HEC-RAS v. 4.1, which is an unsteady hydraulic simulator developed by the Hydrologic Engineering Center of the U.S. Army Corps of Engineers. HEC-RAS is designed to perform one-dimensional hydraulic calculations for a full network of natural and constructed channels (note that the recently released HEC-RAS v. 5.0 can also perform two-dimensional hydraulic simulations). An unsteady HEC-RAS model was created for Segment 2 of the CAP canal. This unsteady hydraulic model was the most important component of the training tool. If the hydraulic model does not accurately predict water levels for various changes in gate position, turnout flow, or pumping, then the training tool will not be effective because the hydraulic responses that the trainees learn from the training tool will not be the same as those found in the real world. To assure that the hydraulic model was correct, the CAP's custom calibrations for the radial gates were coded into HEC-RAS using the Rules internal boundary conditions. The roughness coefficient for the canal was chosen based on recommendations from CAP personnel. The final hydraulic model for Segment 2 was approximately 100 km (62 miles), and it consisted of 3 pumping stations, 9 radial gate check structures, 5 turnouts, 3 siphons, and one tunnel.

3.4. SimSuite

The SCADA training tool also requires an intermediate software package that emulates the Remote Terminal Unit (RTU) or Programmable Logic Controller (PLC), its associated sensors and relays, and the gate motor. In the real system, RTUs pass canal information (e.g., gate positions, water levels, etc.) to the SCADA system via some sort of radio system. The RTUs also take commands from the SCADA system (e.g., changes in gate position) and implement those commands in the field. In the training tool, the SimSuite program acts as a virtual RTU that gathers information from the HEC-RAS model (e.g., gate positions, water levels, etc.) and passes it to the SCADA system. Likewise, commands from the SCADA system (e.g., changes in gate position) are sent to the virtual RTU in SimSuite, and these commands are then passed on to the HEC-RAS model. Perturbations such as noise, a stuck gate, or a failed pump can be introduced into SimSuite through SimProctor and transmitted to the SCADA system. This software was written by ALARC employees for their applications and was used unchanged here.

3.5. SimProctor

The SimProctor program is used to observe the canal model status from the Proctor Computer. Using this program, the proctor or supervisor can observe the following:

- water levels of the various pools in the canal system;
- gate positions at the various check structures;
- control of each individual pump;
- status of each individual pump; and
- flow rate through each check structure, turnout, and pump station.

The proctor also has the ability to

- change the gate positions for each gate;
- fail any gate;
- change the flow rate at each turnout;
- change the control for each pump (i.e., turn the pumps on or off); and
- change the status of each pump (i.e., change the status from nominal to fail).

Note that there is no indication on the SCADA screens that the gate has failed; the gate simply does not move to the requested position. When a pump fails, it is displayed as orange on the SCADA system.

3.6. WEST-EDI

In the application described by Strand et al. (2005), MATLAB was used as the interface from SimSuite to the unsteady flow simulation software. Since a connection between MATLAB and HEC-RAS does not exist, the WEST-External Data Interface (EDI) program was developed to connect HEC-RAS to SimSuite. The function of the WEST-EDI program is to pull information (e.g., water levels, gate positions, etc.) from the HEC-RAS program and then pass it to the SimSuite program. Also, commands from the SCADA system are passed to the WEST-EDI program via SimSuite. These commands are then passed to HEC-RAS. A screen shot of the WEST-EDI program is shown in Figure 7.

4. SCENARIO DEVELOPMENT

Initially, three basic flow scenarios were developed along with the training tool for CAP: a high flow condition, a medium flow condition, and a low flow condition. All three of these scenarios start out with the water levels near typical operating levels. Once the training tool has started, trainees must operate the SCADA system to effectively route flow changes through the hydraulic model of Segment 2 while also responding to uncertainties and

emergencies that cause the water levels to deviate. In using these basic scenarios, personnel at CAP have indicated that the hydraulic model responds to flow changes in a similar manner to the real system. Obviously, these three basic flow scenarios were not sufficient to effectively train their Water System Operators over a wide range of flow conditions. Thus, CAP developed a test bank of ten scenarios that their Water System Operator trainees must pass before they are allowed to operate the canal system independently. This test bank of flow scenarios covered a wide range of flow conditions, including emergency scenarios.
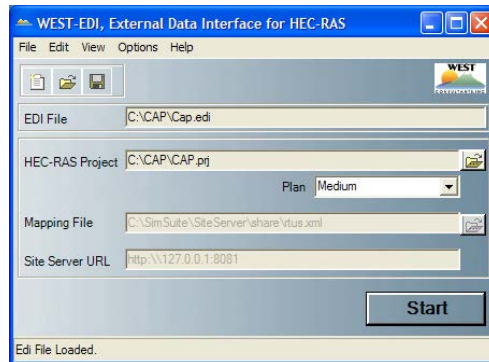
Figure 7. Screen shot of the WEST-EDI program interface

5. SUMMARY

A training tool, designed to train new Water System Operators on how to operate the canal system more effectively, was developed for the Central Arizona Project. The main idea behind the training tool concept is that the communication between the SCADA system and the radios in the field is "cut" and replaced with a connection between the SCADA system and a hydraulic model of the canal system. In this way, the Water System Operators can be trained on the hydraulic model of the canal system instead of the real canal. The training tool operates in a manner similar to how a flight simulator is used to train pilots.

The training tool is composed of five components installed on two different computers: 1) the SCADA system, 2) the SimSuite program, 3) the SimProctor program, 4) the WEST-EDI program, and 5) the HEC-RAS unsteady hydraulic model and computer program. The Trainee Computer has the SCADA system installed on it. The Proctor Computer has SimSuite, SimProctor, WEST-EDI, HEC-RAS, and the corresponding hydraulic model of the canal system installed on it.

The key component to the training tool is an accurate hydraulic model. A hydraulic model that does not accurately predict water surface changes due to gate movements, turnout flow changes, or pump changes will not effectively train the Water System Operators on the real system. Care was taken in the development of the hydraulic model to assure that the hydraulic modeling accurately predicts the real world. CAP personnel have stated that training tool does respond like the real canal system, indicating that the hydraulic model is adequate.

CAP developed a test bank of scenarios that Water System Operator trainees must pass before they are allowed to operate the canal system independently. This test bank of flow scenarios covered a wide range of flow conditions, including emergency scenarios. Because of this training tool, Water System Operators at CAP now have a much broader experience base from which to draw upon while operating the canal system.

6. REFERENCES

Strand, R.J., Clemmens, A.J., and Denny, N.T. (2005). "Training SCADA Operators with Real-Time Simulation." *Proc., 2005 Water Management Conference: SCADA and Related Technologies for Irrigation District Modernization*, USCID, Vancouver, WA, October 26-29, 2005, p. 319-328.

Visual and Photogrammetric Observations of an Internal Erosion Failure

T.L. Wahl, R.V. Rinehart, M.J. Klein, J. Rittgers[1]
[1]Bureau of Reclamation
P.O. Box 25007
Denver, CO 80225
USA
E-mail: twahl@usbr.gov

ABSTRACT

A 0.91-m (3-ft) high, homogeneous, silty clay embankment was tested to investigate erosion processes occurring during failure by internal erosion. The embankment was constructed in a 3.79-m (12.44-ft) wide test flume equipped with a clear acrylic viewing window at the abutment where failure was initiated. Failure was initiated at mid-height when an embedded 12-mm (½-inch) diameter rebar was removed from the embankment. The test lasted approximately 48 minutes, and during that time, the erosion pipe enlarged dramatically. The test was stopped just before the collapse of the soil bridge over the enlarged pipe.

Erosion was visually monitored during the test with video cameras and arrays of still cameras imaging the top of the embankment and the visible abutment. Still photos provided time-lapse imagery and were also used to develop a time-lapse 3D photogrammetric model of the developing erosion channel with estimated areal extents of erosion. Water levels and flow rates were also measured during the test, and data were recorded from an array of geophysical sensors installed on the embankment crest and downstream surface. The embankment materials were characterized before and during construction with in situ measurements of water content, dry density, and erodibility. This paper primarily summarizes the visual observations and discusses significant flow features that appear to be important in the erosion process.

Keywords: Internal erosion, dam breach, physical modeling, numerical modeling, photogrammetry

1. INTRODUCTION

The ability to model erosion and breaching processes of embankment dams is crucial both for making accurate predictions of potential flooding and for planning the emergency response to a potential dam failure. Models for simulating dam failure have become more physically based in recent years, especially for failures initiated by overtopping flow. Some physically-based models (e.g., EMBREA and WinDAM C) now also have the capability to simulate failures resulting from internal erosion. During the past two decades, there have been several large-scale laboratory tests of overtopping-initiated failures of homogeneous embankments that have helped increase understanding of the important erosion mechanisms in that failure mode; these tests have helped to inform the development of mathematical models of the dominant processes for breach development due to overtopping flow. Testing of internal erosion failures has been more limited thus far, as has testing of zoned embankment configurations.

1.1. Purpose

The Bureau of Reclamation has worked for many years to improve capabilities for modeling embankment failure, with initial emphasis on dams impounding water storage reservoirs and, more recently, also considering canal embankments (Wahl and Lentz 2011). Because internal erosion is an important failure mode in both environments, Reclamation has also been interested recently in new instrumentation and monitoring techniques that can provide early detection of seepage or internal flow that could eventually develop into an embankment breach. To address both of these objectives, Reclamation's Dam Safety Technology Development Program is funding laboratory tests aimed at improving the understanding of embankment erosion processes while also providing an environment in

which new geophysically-based internal flow detection methods can be tested. This program is intended to eventually include tests of zoned embankments, but the first test conducted in the program was an internal erosion failure of a homogeneous silty clay embankment. The Nuclear Regulatory Commission is also a partner in this research, with a specific interest in zoned and rockfill dams.

2. TEST FACILITY

A new test facility was constructed in Reclamation's indoor hydraulic laboratory in Denver, Colorado, in late 2014. The facility provides a 3.79-m (12.44-ft) wide embankment test section in a headbox that is elevated above a large tailbox intended to capture the flow released during a breach test (Figure 1). Capturing the entire flow volume allows sediment to be retained and settled out before water is returned to the lab sump, minimizing the impact on other lab operations. The finite volume of the tailbox limits the total testing time to a few minutes once a breach has enlarged significantly. For tests involving relatively clean embankment soils, flow can be released out the tailwater box back to the lab sump through a spillway section, allowing tests to be run for a longer time period.

Sidewalls of the embankment test section are constructed with a 1H:10V slope to allow for effective compaction of embankment materials against the abutments. The left side abutment is constructed from 19-mm (3/4-in.) thick acrylic to allow viewing of erosion processes during a test.

Figure 1. Embankment breach test facility viewed from the upstream end of the headbox, overlooking the completed test embankment.

3. EMBANKMENT CONSTRUCTION

The embankment was constructed beginning about June 17, one week before the test date of June 25, 2015. Soils were stockpiled in the laboratory and moisturized before being placed into embankment lifts that averaged about 10-15 cm (4-6 in.) compacted thickness. Compaction was accomplished using a pneumatic hammer with a circular foot approximately 15 cm in diameter, with the soil surface covered during compaction by a conveyor belt blanket to

help distribute compaction energy. When the embankment was constructed to about 50% of the desired final height, an in situ submerged jet erosion test (ASTM D5852) was run to measure soil erodibility properties, and a sand cone density test (ASTM D1556) was performed to evaluate density and water content (Figure 2). The rebar that would be withdrawn to initiate flow and erosion was also placed at the left abutment. A second sand cone test was run at an elevation of 0.76 m (2.5 ft) just before reaching the final height of 0.91 m (3 ft). Water contents were measured periodically from the moisturized soil stockpile throughout construction. The final crest thickness of the embankment was 0.30 m (1 ft), and upstream and downstream slopes were 2H:1V. The crest length of the finished embankment was 3.97 m (13.04 ft).

Figure 2. Sand cone (foreground) and submerged jet erosion tests (back, left)
underway during a pause in embankment construction.

3.1. Soil Properties

The soil used to construct the embankment was obtained from a former borrow area for Reclamation's Bonny Dam, about 21 miles north of Burlington, CO. Prior to the start of embankment construction, soil samples were sent to an outside lab for index properties testing. The soil was classified as silty clay (CL-ML) with the following properties:

- 89% fines,
- 11% sand,
- 8% clay (finer than 0.002 mm),
- liquid limit, LL=27,
- plasticity limit, PL=21,
- plasticity index, PI=6,
- optimum water content = 17% (standard Proctor), and
- $\gamma_{d,max}$ = 1.685 g/cm^3 (105.2 lb/ft^3).

Submerged jet erosion tests (ASTM D5852; Hanson and Cook 2004) were performed on the soil specimens created during the standard Proctor compaction test. This test measures soil erodibility by directing a submerged 6-mm (¼-in.) diameter jet at the soil surface to create a scour hole. The observed scour depth versus time data are used to determine the basic parameters (k_d, τ_c) of the linear excess stress equation used to model soil erosion rate:

$$\varepsilon_r = 10^{-4} k_d (\tau - \tau_c) \qquad (1)$$

where ε_r is the soil erosion rate (cm/s), k_d is the detachment rate coefficient [cm^3/(N-s)], τ is the applied hydraulic shear stress, and τ_c is the critical shear stress (Pa) needed to initiate erosion.

The sand cone test performed at mid-height of the embankment showed that the water content was close to optimum (17.3%) and compaction was very effective with a density that was 98% of the standard Proctor maximum value. The second sand cone test performed near the top of the embankment showed somewhat drier compaction conditions (water content = 15.6%) and a lower density, about 93.5% of maximum. Jet test results from the compaction test specimens and the in situ test at mid-height of the embankment are shown in Figure 3. The k_d value [10 cm^3/(N-s)] obtained in the in situ test at mid-height indicates a soil that is very erodible (Hanson and Simon 2001) despite the good compaction achieved at that level.
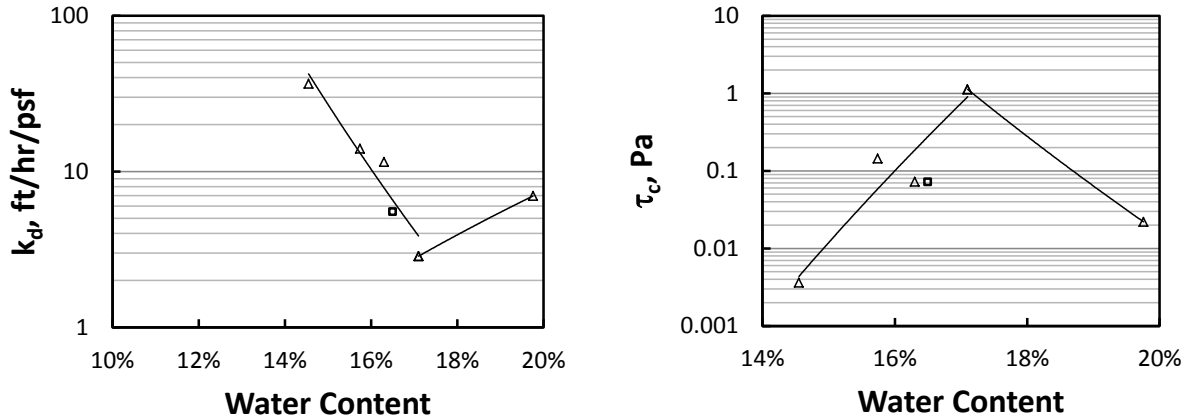
Figure 3. Detachment rate coefficients (k_d) and critical shear stresses (τ_c) determined from submerged jet erosion tests ($\square$ = in situ, Δ = compaction-test specimens), with trend lines shown for dry- and wet-of-optimum water contents.

4. INSTRUMENTATION

4.1. Hydraulic Measurements

Flow into the headbox is measured by the laboratory's fixed set of venturi flow meters. The facility was designed with the intention for tests to be run with a constant inflow rate matching the expected maximum breach discharge; excess inflow in the early stages of a test is spilled out of the headbox through a spillway section with a crest elevation that can be increased during a test by dropping stoplogs into place. This allows a relatively constant upstream head to be maintained during the early stages of breach initiation. Flows through the spillway section are measured by a long-throated flume so that net breach outflow discharges can be calculated.

During the earliest phases of breach initiation, when flow through a developing internal erosion channel might be very small, there is insufficient accuracy in the venturi meter and flume measurements of inflow and spillway flow to allow good estimation of flows through the embankment. During this phase, flows through the embankment are directed to a small supercritical flow flume.

4.2. Imaging

Two arrays of still photo cameras were used to record images of the internal erosion taking place at the left abutment of the embankment test section and any headcut erosion taking place on the downstream slope of the embankment. Eight cameras were set up to take photos through the acrylic abutment wall, and 6 cameras were positioned

overhead to obtain photos of the surface of the left end of the embankment. Each camera's field of view included photogrammetry targets to enable subsequent image analysis. The 14 cameras were synchronized together to collect simultaneous images at 10 second intervals during the test. Following the completion of test, these images were processed to create time-lapse three-dimensional photogrammetry models of the observed erosion channels (i.e., 4D photogrammetry).

Additional still cameras were set up at two different downstream viewing positions during the construction of the test facility and during the first test to record time-lapse progress of construction activities and the breach test. Video cameras also recorded the test from 2 locations, one viewing the downstream embankment slope and the other viewing the left abutment through the acrylic window.

4.3. Geophysical Sensors

A large array of geophysical sensors was installed on the day before the test (Figure 4). The sensors included passive seismic and soil self-potential sensors.
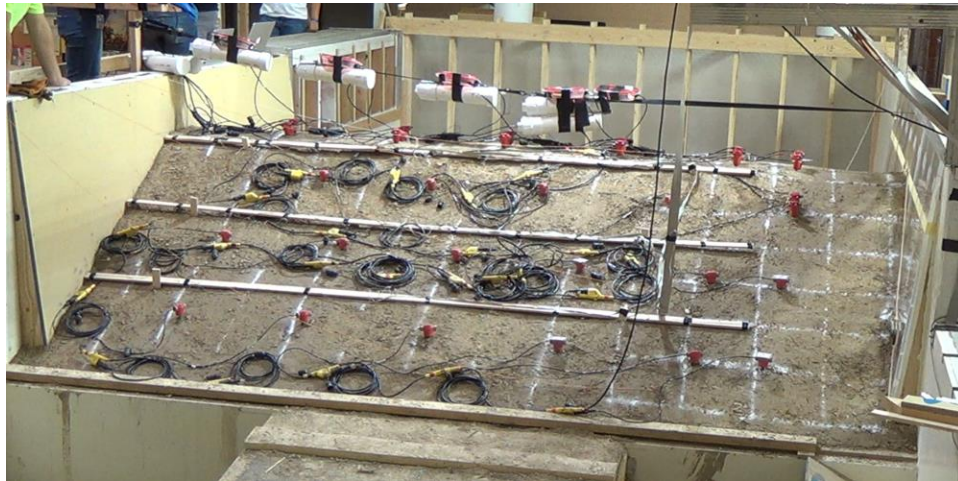
Figure 4. Geophysical sensors installed on the crest and downstream slope of the embankment.

5. TEST OBSERVATIONS

The test was started with an inflow of 0.45 m³/s (16 ft³/s) established into the model headbox. Stoplogs on the headbox spillway were adjusted to bring the water surface up to about 75 mm (3 in.) from the crest of the embankment or about 8% freeboard. The rebar was withdrawn from the embankment using a manual winch. Water levels in the headbox, tailbox, and at the spillway flume were recorded during the test by an automated data acquisition system. Flow measurements at the supercritical flow flume were made manually for the first few minutes of the test. Unfortunately, a cleat temporarily installed during embankment construction was found left in place, and within a few minutes, it began to prevent the flow from cleanly entering the supercritical flume. This fact, along with some calibration problems related to water levels sensors and the long throated flume in the spillway channel, prevented accurate breach channel flow rate data from being obtained during the test. Fortunately, photo, video, and geophysical data was collected quite successfully during the test. The photo and video records provided interesting insights about flow mechanisms and erosion processes. The geophysical data are not presented in this paper.

Erosion of the internal channel (pipe) created by removal of the rebar started immediately, indicated by muddy water exiting onto the downstream slope of the embankment. However, the erosion channel was not visible against the clear acrylic abutment wall until about 3-4 minutes after removal of the rebar. For about 15 minutes, the erosion channel appeared to enlarge uniformly along its length. As the height of the eroded channel approach one half of the

upstream head above the invert of the channel, accelerated scour of the floor of the channel began just downstream from the entrance (Figure 5). The mechanism driving this appeared to be a strong counter-rotating eddy in the channel entrance created by streamlined flow entering the floor of the channel and a strong contraction from the roof of the entrance, where water from the upper part of the reservoir needed to turn a greater than 90º corner to enter the channel (Figure 6). The flow structure was very similar to that of a submerged hydraulic jump that might be observed downstream of a partially open sluice gate. Coincident with formation of this scour in the floor of the entrance, accelerated scour of the roof of the channel began about 4-5 diameters further downstream, seemingly due to a deflection of flow out of the scour hole and up toward the roof. For several minutes, a system of stationary, alternating vortices persisted in the enlarging eroded channel. As the channel enlarged further, this flow structure broke down and seemed less dominant.

The test was stopped after a total of about 48 minutes due to the tailbox filling to its capacity. After flow was shut off and the reservoir had drained, it became evident that horizontal enlargement of the channel had also been very significant, especially around the entrance to the channel (Figure 7). The width of the eroded channel was much greater just inside the entrance than it was at the opening visible from the upstream side of the embankment (Figure 8). Distinct lift lines were visible in the eroded channel walls, and erosion had either accelerated along weak layers or was just generally more rapid in a horizontal direction, perhaps due to the non-isotropic compaction structure of the soil. The three-dimensional nature of the flow approaching the channel entrance may have also contributed to a difference in horizontal and vertical erosion rates. There was a large overhang at the entrance to the eroded channel with the widest eroded section being near the invert of the channel. It appeared that lateral flow along the embankment face had created a vortex in the entrance of the channel that accelerated lateral erosion of the channel (Figure 9). This flow structure seems similar to that observed by other investigators during the later stages of breach widening (e.g., in fuse plug embankment erosion tests by Pugh [1985]). Here, there seems to be evidence that such a structure may be important even before the breach has fully formed and moved into the dominantly widening phase.

t=6 min	t=12	t=18
t=24	t=30	t=36
t=42	t=48	post-test
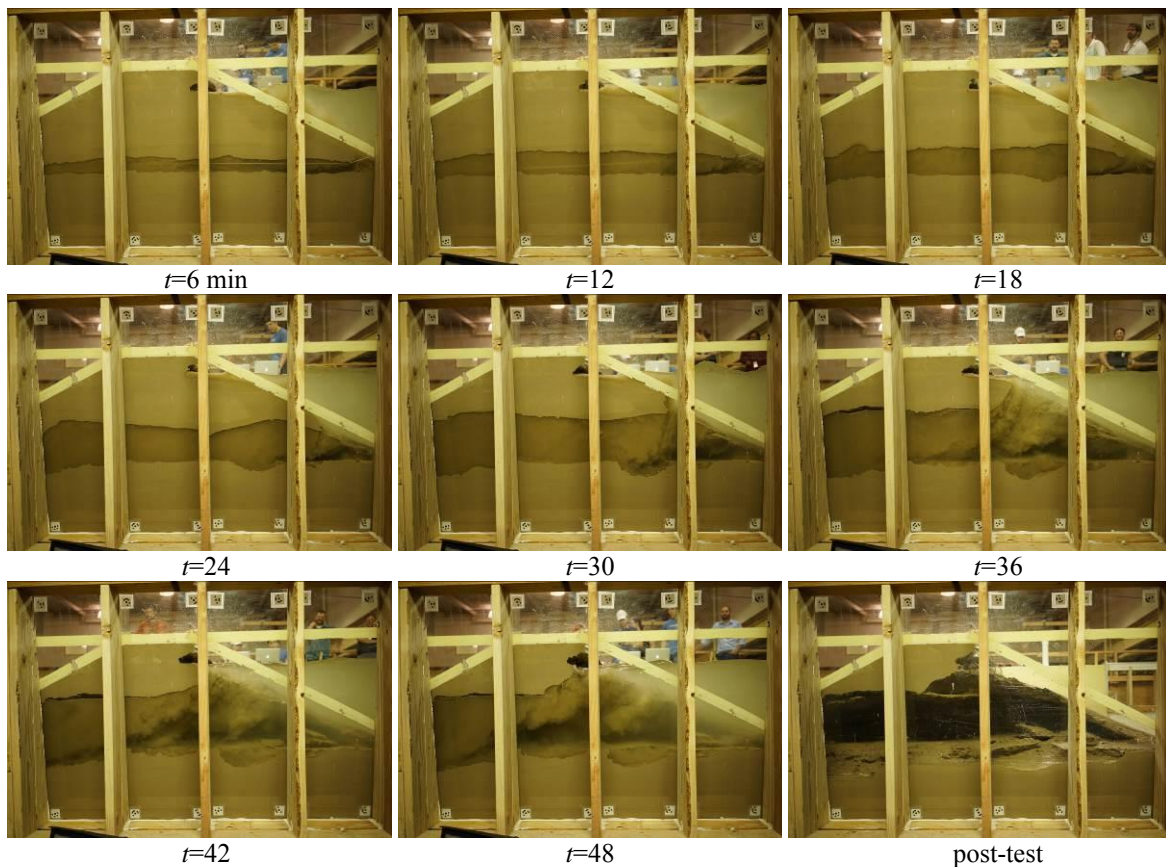
Figure 5. Time lapse photos at 6 minute intervals. The photos show progressive development of the internally eroded flow passage. Note the structure of the flow that leads to development of an enlarged chamber at the upstream end of the conduit. The final photo was taken after the headbox had drained.
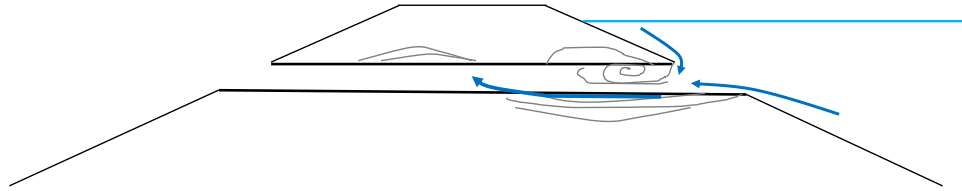
Figure 6. Sketch showing flow structure and related erosion patterns observed during internal erosion test.

Figure 7. Post-test photo illustrating significant widening of the erosion channel, especially near its base.

Figure 8. Post-test overhead view of the entrance to the internal erosion flow channel.

One flow feature that was unexpectedly absent from the test was significant headcut erosion where the flow exited the internal erosion channel onto the downstream slope of the embankment. This has been a feature of some

previous erosion tests involving piping of relatively weak soils (Hanson et al. 2010). However, in this test, there was very little downward erosion of the downstream slope. This is believed to be due, at least in part, to the fact that the lower half of the embankment seemed to be better compacted than the upper half, based on the sand cone density test results. This may have been due to a combination of lower water content and the natural difficulty of compacting the lifts as the embankment grew taller and narrower. Erosion of the internal channel also seemed to take place mostly in the upward direction. One other possible factor in this is the contribution of gravity forces to destabilizing the roof of the channel. Since this soil was relatively weak (even where well compacted), as shown by the erodibility tests, the gravitational contribution could have been relatively significant, leading to more rapid upward growth of the erosion channel.
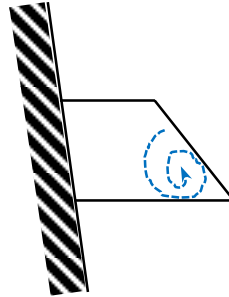
Figure 9. Sketch showing an idealized view looking downstream during enlargement of the internal erosion flow channel. This type of vortex formation may lead to accelerated widening of the base of the channel.

5.1. Photogrammetry

Following completion of the test, approximately 120 GB of fixed camera imagery was processed to create 4D photogrammetry models of the erosion visible through the clear abutment wall and on the downstream slope (4D=3 spatial dimensions plus time). Two images from the abutment model are shown in Figure 10. At each time step, flow cross-sectional areas of the eroded channel were calculated. These data will be valuable for making later comparisons to numerical model simulations of the test.

Figure 10. Two images from the 4D photogrammetry model of the internal erosion flow channel. In gray areas the model was not able to resolve the far side of the channel due to turbidity or other image quality problems.

6. CONCLUSIONS

The first test conducted in Reclamation's new embankment breach research facility demonstrated the value of advanced imagery data collection techniques, including time lapse photos, high definition video, and photogrammetric image analysis. The structure of the flow in the developing internal erosion channel was quite complex and exhibited structures and details that are typically not considered in idealized mathematical models used

to predict erosion rates and breach development. Whether these details can or should be incorporated into future modeling efforts remains to be determined during future research.

7. ACKNOWLEDGMENTS

8. REFERENCES

ASTM Standard D1556 (2015). Standard test method for density and unit weight of soil in place by sand-cone method. American Society for Testing and Materials, West Conshohocken, PA.

ASTM Standard D5852 (2007). Standard test method for erodibility determination of soil in the field or in the laboratory by the jet index method. American Society for Testing and Materials, West Conshohocken, PA.

Hanson, G.J. and Simon, A. (2001). "Erodibility of cohesive streambeds in the loess area of the midwestern USA." *Hydrological Processes*, Vol. 15, pp. 23-38.

Hanson, G.J. and Cook, K.R. (2004). "Apparatus, test procedures, and analytical methods to measure soil erodibility in situ." *Applied Engineering in Agriculture*, 20(4):455-462.

Hanson, G.J., Tejral, R.D., Hunt, S.L. and Temple, D.M. (2010). "Internal erosion and impact of erosion resistance," *Proceedings of the 30th Annual USSD Conference*, United States Society on Dams, Denver, CO.

Pugh, C.A., (1985). *Hydraulic Model Studies of Fuse Plug Embankments*. Report No. REC-ERC-85-7, Bureau of Reclamation, Denver, CO.

Wahl, T.L. and Lentz, D.J. (2011). Physical hydraulic modeling of canal breaches. Hydraulic Laboratory Report HL-2011-09, U.S. Dept. of the Interior, Bureau of Reclamation, Denver, Colorado, 56 pp.

Designing a Steel Gate Dam Across an Ephemeral River – Tempe Town Lake Dam Design

Stewart S. Vaghti, P.E., CFM[1], Dean B. Durkee, Ph.D., P.E.[1], and Andrew J. Lynch, P.E.[1]
[1]Gannett Fleming, Inc.
Phoenix, AZ 85016
USA
E-mail: svaghti@gfnet.com

ABSTRACT

After the existing Tempe Town Lake downstream dam failed unexpectedly in 2010, the City of Tempe, AZ, USA was tasked with designing and constructing a replacement dam to maintain their lake, pass flows in the ephemeral Salt River, and deliberately lower water levels to avert flooding. Through an alternatives evaluation process, a hydraulically operated steel gate system was selected from a field of twenty studied alternative configurations to replace the existing rubber bladder system.

The gate design produced eight 32.3 meter (106 foot) long, 6.4 meter (21 foot) tall, and 118,000 kilogram (260,000 pound) steel gates operated by single-acting hydraulic cylinders and powered by a power unit featuring two 1,893 cm^3/s (30 gpm) axial piston pumps, each powered by a 37 kW (50 hp) motor. With local and remote monitoring and control capability, the system is designed to control the gates under automatic or manual control mode.

The design also includes a foundation seepage control and collection system using a cement-bentonite cutoff wall and drainage blanket; a scour wall; a stilling basin designed to accommodate variable crest elevations; instrumentation and controls designed to maintain the recreational lake while preventing unintended flooding; and an operations, maintenance, and dam monitoring plan all designed to maintain dam safety, avert flooding, and preserve the City of Tempe's valuable resource, Tempe Town Lake.

This paper presents the selection, approach, challenges, and results of designing the hydraulically operated steel crest gate system designed to maintain Tempe Town Lake and deliberately lower it to avert flooding.

Keywords: *Hydraulically operated, Steel, Crest Gates*

1. INTRODUCTION

The Salt River was historically a perennial river providing water to the Phoenix valley for agriculture, the Hayden Flour Mill and Hayden Ferry, refuge during the hot summer months, and an unpredictable flooding hazard. Beginning in the early 1900s, construction of Roosevelt Dam on the upper Salt River reduced flows in the river through the valley (City of Tempe, 2015) and started a shift in the river dynamics, which eventually resulted in the current ephemeral river. With five (5) dams eventually constructed upstream of the City of Tempe, the Salt River became a dry river bed attracting landfills, quarry mining, and industrial businesses (City of Tempe, 2015).

In 1966, a design competition at Arizona State University's College of Architecture envisioned an inland seaport concept along the Salt River (City of Tempe, 2015) that began a series of studies, an advisory commission, funding support, master planning, and eventually the design and construction of the 0.89 km^2 (220-acre) Tempe Town Lake. The lake was opened in 1999, anchored by a downstream dam consisting of four rubber bladders (Figure 1).

Figure 1. Tempe Town Lake

The investment paid off as the urban lake spurred development, recreation, and outdoor activities such as boating, jogging, biking, the Ironman Arizona triathlon, festivals, concerts, and fishing.

In 2010, one of the bladders failed unexpectedly resulting in the loss of the lake and its nearly 3,750 m^3 (one billion gallons) of water. The original bladders had an expected design life of 20 years, but early signs of distress were observed, which initiated their replacement after 10 years. Because the City was already in the process of replacing the bladders when the failure occurred, restoring the valuable asset only took three months after the failure. An independent analysis attributed failure to intra-carcass pressurization of the bladder, which was accelerated by climatic conditions of the desert southwest. The bladder manufacturer provided the replacement bladders under a five-year lease agreement, after which they must be removed. The City was tasked with finding a replacement option and removing the existing rubber bladders by the end of the bladder lease period. Through an alternative evaluation process, design, and construction, the City is near completion of a replacement dam to preserve Tempe Town Lake and the value it brings to the community.

2. ALTERNATIVE EVALUATION

The alternative evaluation process identified "must have" and "should have" evaluation criteria and potential dam replacement technologies. "Must have" criteria are considered essential to the acceptable performance of the project while "should have" criteria represents important desired characteristics (Gannett Fleming, 2012). The criteria are summarized in Table 1.

Table 1. Summary of Final Project Criteria

Must Have Project Criteria
Safety
Maintain or improve current level of flood protection
Minimize the reduction in flood passage capacity
Minimize the increase in flood impacts to surrounding areas
Ability to capture the tail end of a flood event to maintain the full lake condition during higher frequency events
Maintain structural integrity of the dam under maximum design discharge
Reliably lowered when needed
Design must be compatible with pedestrian bridge and immediate surrounding area
Meet the December 28, 2015 bladder lease end date
High degree of reliability
Meets regulatory requirements
Maximize value (cost/benefit)
Demonstrated performance in this climatic environment
Should Have Project Criteria
Ability to capture the tail end of a flood event to maintain the full lake condition following design flood
Minimize operations and maintenance costs
Simplicity of operation
Proven technology
Design that allows the lake to be maintained during construction
Maintain current lake bottom grade
Minimize downstream scour
Vandalism prevention
Maintain original design lake level
Minimize environmental impacts
Aesthetically compatible
Maintain the existing pier configuration and minimize structural modifications as much as possible

An initial list of twenty alternative configurations were evaluated and eventually reduced down to four viable alternatives, as the other sixteen did not meet the "must have" criteria or had other fatal flaws.   The alternatives and their respective fatal flaw(s) are in Table 2.

Of the twenty configurations, the pneumatically operated hinge crest gates (Obermeyer); hydraulically/cable operated steel gate; dyrhoff rubber dams (Sumitomo); and fusegates (Hydroplus) were carried forward for additional analysis.   The fusegate was soon after eliminated due to operational limitations.   The team more thoroughly evaluated the remaining three alternatives, including performing a Failure Modes and Effects Analysis (FMEA) to identify potential failure modes associated with the foundation and the structure (gate). Through the FMEA process, four credible failure modes were identified that impacted the designs. Comparative capital construction and life cycle costs were then performed to assist with the alternative selection. Both the downstream Obermeyer and downstream hydraulically operated steel gates were recommended as feasible alternatives to replace the existing rubber bladders. The hydraulically operated steel gates system was eventually selected primarily due to durability concerns of the rubber air bladders used for both the rubber bladder dam and Obermeyer's gates.

Table 2. Summary of Project Alternatives

Alternative	Initial Evaluation Status
Inflatable dams (water-filled)	Fatal flaw (safety and operational constraints)
Ogee crest weirs	Fatal flaw (hydraulic and sediment constraints)
Labyrinth weirs	Fatal flaw (hydraulic and sediment constraints)
Bridgestone dual body rubber dams	Fatal flaw (no longer available)
Radial gates (tainter gates)	Fatal flaw (flood control criteria)
Vertical lift gates	Fatal flaw (cost)
Swing gates	Fatal flaw (ineffective at capturing tailwater)
Bottom hinge crest gates (Balscule gate)	Fatal flaw (flood control criteria)
Collapsible Fusegates (Hydroplus Folding Fusegate)	Fatal flaw (ineffective at capturing tailwater)
Earth Embankment/Fuse Plug	Fatal flaw (poor performance and reliability)
Combined concrete outer dams with inner gates	Fatal flaw (flood control criteria)
Combined half-height concrete dam with crest gates	Fatal flaw (flood control criteria)
Combined labyrinth weir outer dam with inner gates	Fatal flaw (flood control criteria)
Fuse plugs of various configurations (Hydroplus)	
Pneumatically operated hinge crest gates (Obermeyer) 30 meters (100 feet) downstream of existing dam	
Obermeyer hinge crest gates between existing piers	
Hydraulically operated hinged crest gates 30 meters (100 feet) downstream of existing dam	
Hydraulically operated hinged crest gates between existing piers with 1 addition pier per span	
Hydraulically operated hinged crest gates between existing piers with 2 addition pier per span	
Dyrhoff rubber dams (Sumitomo)	

3. DESIGN

After selecting the hydraulically operated steel gate system as the replacement alternative, the design process began by siting the dam across the Salt River and modeling its impacts to the floodway. Detailed design could not commence until the siting satisfied the following three "must have" criteria related to flood protection: maintain or improve current level of flood protection; minimize the reduction in flood passage capacity; and minimize the increase in flood impacts to surrounding areas.

During the 60 percent design phase, the contractor was procured for constructability reviews, cost estimations, and early involvement as the design progressed. The design of the steel gates was accomplished through the preparation of a performance specification used to procure the gate vendor after the 60 percent design phase of the dam. Once the gate vendor was on board, the steel gate design was completed concurrent with the final design of the foundation, superstructure, and supporting facilities. See Figure 2 for a rendering of the replacement dam.
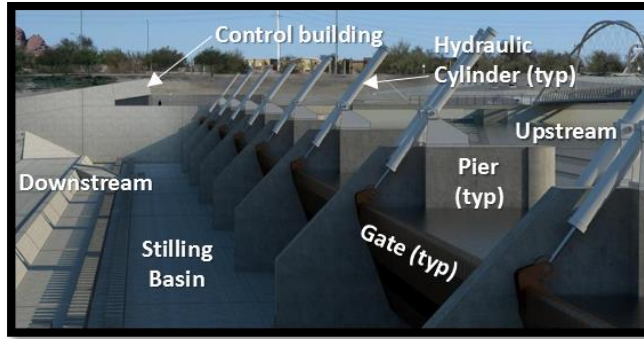
Figure 2. Replacement Dam Rendering

3.1. Design Flood Analysis

Maintaining or improving the current level of flood protection and minimizing the increase in flood impacts to surrounding areas are "must have" design criteria. For this section of the Salt River, the City of Tempe and the Flood Control District of Maricopa County (FCDMC) manage the river and its levees for a reach capacity of 5,947 m^3/s (210,000 ft^3/s) and a 100-year flow of 4,786 m^3/s (169,000 ft^3/s). The addition of the new dam must minimize increases in upstream water surface elevations during the design events over what would occur under the existing condition. Hydraulic modelling was performed using the U.S. Army Corps of Engineers' (USACE) computer program, HEC-RAS (version 4.1) to estimate the design flow inundation limits and corresponding levee freeboard heights. An iterative approach was used for establishing the elevation of the concrete superstructure and the spacing and width of the concrete piers (Gannett Fleming, 2014). The team evaluated factors such as river hydraulics, operational considerations, structural limitations, gate size limitations, and costs. The results produced a superstructure elevation of 344.7 meters (1131 feet) above mean sea level supporting seven new piers spaced to receive eight identical gates, each 32.3 meters (106 feet) long and 6.4 meters (21 feet) tall. For the design events, the proposed structure increases the water surface elevation approximately 0.3 meters (1.0 foot) at the new dam. The change in water surface elevation decreases upstream of the new dam to zero net increase approximately 4.8 kilometers (3 miles) upstream from the new dam. The HEC-RAS modeling indicates the increase in water surface elevations are still contained within the existing levees and still meet the Federal Emergency Management Agency's (FEMA's) 100-year freeboard requirements. FEMA requires that the 100-year peak flow condition maintain a minimum of 0.9 meters (3 feet) of freeboard where there are no structures and a minimum of 1.2 meters (4 feet) of freeboard at bridges and/or culvert structures (FEMA, 2012). Figure 3 illustrates the estimated increase in water surface elevation due to the construction of the new dam.
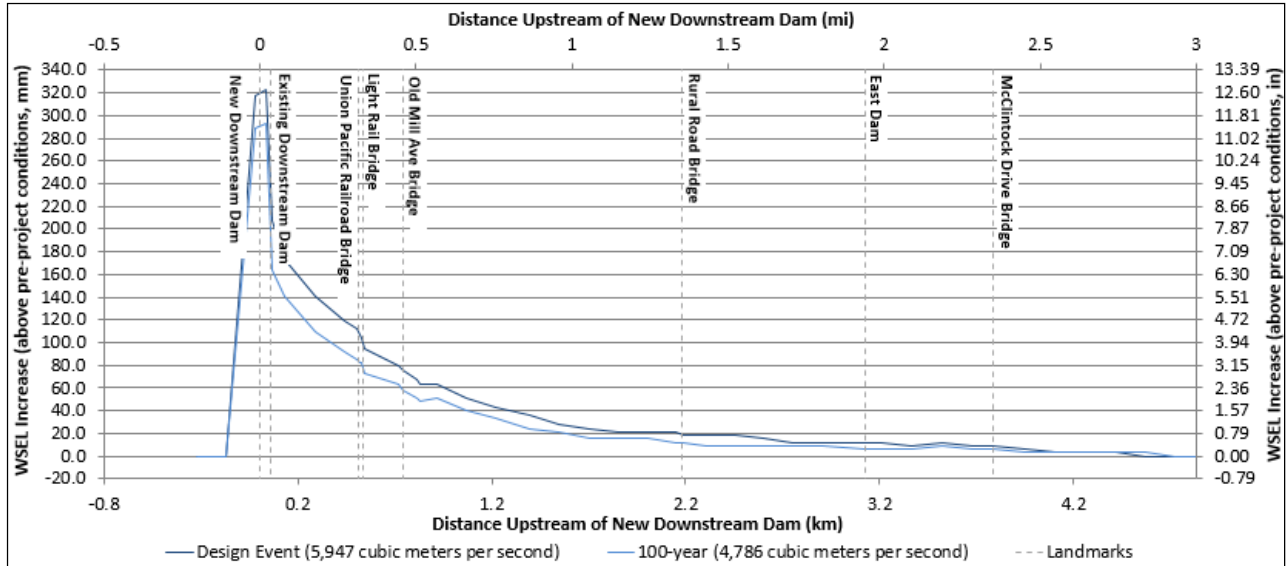
Figure 3. Water Surface Elevation Increase Due to the New Downstream Dam

3.2. Foundation and Superstructure

The steel gates are supported by a 15.2 meter (50 foot) wide by 6.1 meter (20 foot) deep structure consisting of a roller-compacted concrete foundation founded on "basin fill" material and a reinforced concrete superstructure. Seepage through the foundation is controlled with a cement-bentonite cutoff wall that extends to bedrock; an extension of the lake's existing shoreline cutoff walls; a conventional concrete facing system integral with the roller-compacted concrete foundation; and a seepage collection system. The seepage collection system under the dam and stilling basin consists of a drainage blanket and perforated drain pipes. See Figure 4 for the typical section.
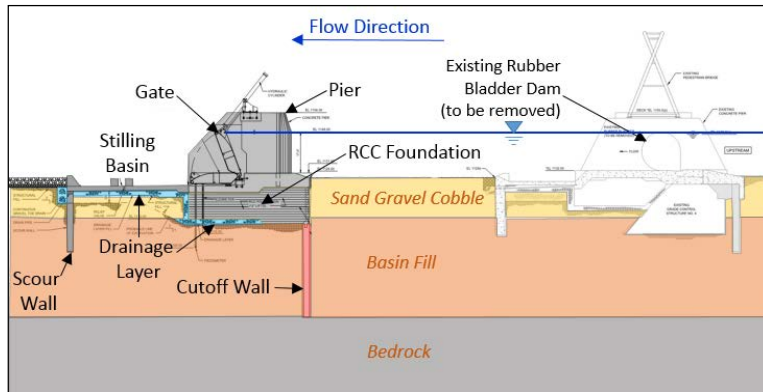
Figure 4. Typical Section

Loading conditions and target factors of safety for dam foundation sliding and stability were developed based on guidance from the U.S. Army Corps of Engineers (USACE) Gravity Dam Design (EM 1110-2-2200); the USACE Design of Hydraulic Steel Structures (ETL 1110-2-584); and the Federal Energy Regulatory Commission (FERC) (Gannett Fleming, 2014). Table 3 is a summary of the loading conditions and their respective factor of safety.

Table 3. Summary of Sliding and Stability Factors of Safety

	Gate Position	Upstream WSE* m (ft)	Load Condition	Factor of Safety
Normal Pool	Closed	349.9 (1148.0)	Usual	2.0
Flood Discharge	Closed	350.5 (1150.0)	Unusual	1.7
Normal Pool plus 1 coffer dam	Closed	349.9 (1148.0)	Unusual	1.7
Normal Pool with Seismic	Closed	349.9 (1148.0)	Unusual	1.7
Normal Pool with 2 coffer dams	Closed	349.9 (1148.0)	Extreme	1.3
Flood Discharge with 2 coffer dams	Closed	350.5 (1150.0)	Extreme	1.3
Normal Pool with Seismic and 1 Cofferdam	Closed	349.9 (1148.0)	Extreme	1.3
Flood Discharge with Seismic	Closed	350.5 (1150.0)	Extreme	1.3
Flood Discharge with 1 Cofferdam and Seismic	Closed	350.5 (1150.0)	Ultra-Extreme	1.1
Flood Discharge with Full Downstream Scour	Closed	350.5 (1150.0)	Ultra-Extreme	1.1

* Water Surface Elevation (WSE) above mean sea level, SI Units (English Units)

Additional loading conditions were evaluated to establish the maximum cylinder loads used for the structural design of the concrete piers and concrete superstructure. For all conditions evaluated, a conservative "no tailwater condition" downstream of the gates was assumed. An upstream water surface elevation of 350.5 m (1150 ft) was also conservatively assumed as it also generates loads greater than the maximum water surface elevation of 349.9 m (1148 ft) the gate's control programming and standard operating procedures are designed to maintain. Table 4 summarizes the various loading conditions and their respective maximum cylinder forces.

Table 4. Summary of Cylinder Design Loading Conditions

Gate Position and Loading Condition	Upstream WSE* m (ft)	Drawdown WSE* at Crest m (ft)	Cylinder Force kN (kip)
Closed with no overtopping (normal pool)	349.9 (1148.0)	349.9 (1148.0)	1,139 (256)
Closed with 0.6 m (2 ft) of overtopping & drawdown	350.5 (1150.0)	350.3 (1149.4)	1,379 (310)
Closed with 0.3 m (1 ft) of overtopping & debris loading	350.2 (1149.0)	350.2 (1149.0)	1,437 (323)
25% open with WSE at 350.5 (1150.0) & drawdown	350.5 (1150.0)	350.1 (1148.5)	1,459 (328)
50% open with WSE at 350.5 (1150.0) & drawdown	350.5 (1150.0)	349.1 (1145.3)	1,441 (324)
50% open with WSE at 350.5 (1150.0) & no drawdown	350.5 (1150.0)	350.5 (1150.0)	1,753 (394)
75% open with WSE at 350.5 (1150.0) & drawdown	350.5 (1150.0)	347.7 (1140.8)	1,681 (378)
100% open with WSE at 350.5 (1150.0) & drawdown	350.5 (1150.0)	346.6 (1137.3)	1,459 (328)

* Water Surface Elevation (WSE) above mean sea level, SI Units (English Units)

The structural design of the concrete piers and concrete superstructure is based on the maximum calculated cylinder force of 1,753 kN (394 kip) and further checked against a cylinder force of 2,224 kN (500 kip). The hydraulic cylinders are designed for a bearing capacity of 2,002 kN (450 kip) at a safety factor of two. The reinforced concrete design was performed in accordance with the American Concrete Institute Manual of Standard Practice for Detailing Reinforced Concrete Structures (ACI Committee 315).

3.3. Stilling Basin

Similar to the design loads, the stilling basin design had to consider variable gate positions and variable water surface elevations produced by the normal operation of the gates. Gate operational flexibility affords the City several benefits such as
- reducing scour potential at the abutments by releasing flow over the center gates first;
- maximizing the efficiency of the stilling basin and downstream scour protection by releasing flow uniformly over all eight gates;

- managing the depth over the gate(s) while maintaining the normal pool elevation by releasing flows over a single gate or any combination of multiple gates; and
- accommodating certain gates that are out of service or downstream areas that are under repair by releasing flows over select gates.

The stilling basin for the new dam is designed based on guidance from USACE Hydraulic Design of Navigation Dams (EM 1110-2-1605). Due to the operational and geometric variability, the stilling basin was first designed assuming all eight gates are lowered uniformly. The nappe profiles generated by the uniform operation of all eight gates at variable crest elevations are shown in Figure 5.
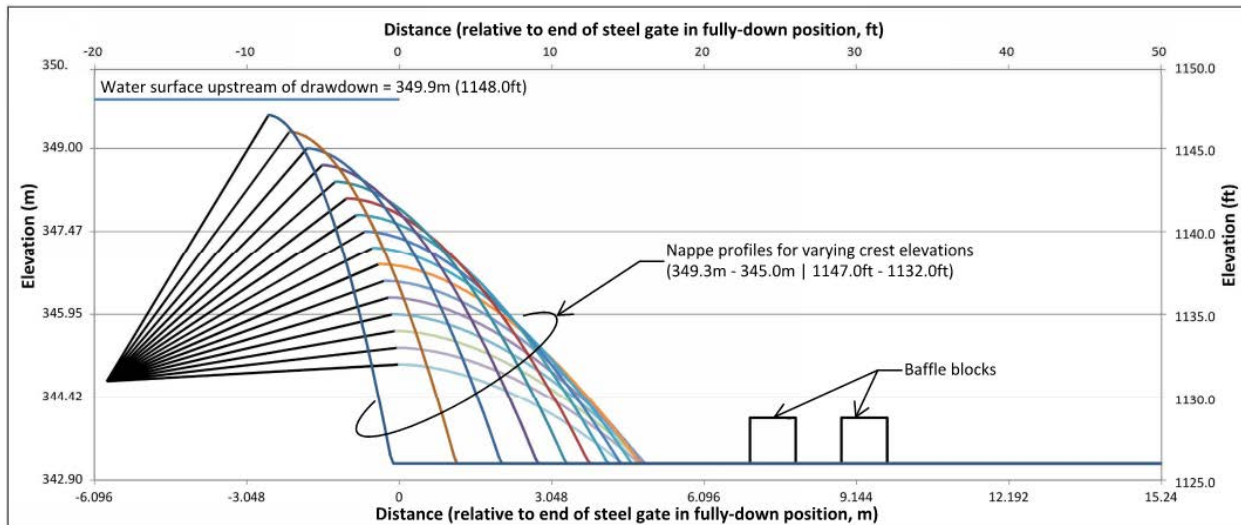
Figure 5. Evaluation of Under-Nappe Profiles for Varying Crest Elevations

After the stilling basin design was complete, alternative operational scenarios were evaluated to understand how the basin would perform under variable gate operations. The evaluations indicate adequate performance with up to approximately 0.6 meters (2 feet) over any gate or subset of gates (i.e. any combination of up to seven of the gates). In the event that additional discharge capacity is required that exceeds 0.6 meters (2 feet) of overtopping, all eight gates are lowered uniformly until the required discharge capacity is met. The operational programming is designed to manage the overtopping depth, and the Operations and Maintenance Manual provides further guidelines for optimizing the effectiveness of the stilling basin.

3.4. Gate Control Instrumentation and Alarms

Maintaining the desired pool elevation is important for users that depend on the numerous lake marinas and the City of Tempe. Of greater importance is the pool level monitoring for safe and effective operation of the gates. Incorrect readings or delayed gate operation could lead to undesirable dam loading conditions, overtopping of the levees, and possibly the flooding of Tempe.

The electrical control system uses a programmable logic controller (PLC) system to monitor and control digital and analog Input/Output (I/O) signals (Gannett Fleming, 2015). Instrumentation system components are interconnected with a fiber optic communication network for protection against electrical transients, which mitigates the need for surge protection devices at both ends of the outdoor wired signal runs (Gannett Fleming, 2015). Four ultrasonic level transmitters are provided to measure and report the pool level. Transmitters are provided at both the north and south sides of the lake to account for differential levels that may exist because of wind effects and for redundancy. Each location includes two transmitters for added redundancy. The level signal is a primary control signal, so its integrity is important for correct dam operation. The safety controller compares the paired level signals at either side of the lake to verify their reliability, allowing the controller to detect a false condition while not interrupting the control readings. To help prevent unwanted loading conditions, flow depths over the gates are monitored and an

alarm is generated when the depth exceeds 0.6 meters (2 feet), and an additional alarm is generated when the depth reaches 1.7 meters (5.6 feet). When flow depths over the gates exceeds 1.7 meters (5.6 feet), a countdown ensues before the control system lowers the gates automatically. Also, timers in the programming proof signals before automatic control adjustments are made. The transmitters are located 61 meters (200 feet) upstream of the gates so that readings are taken outside the water surface drawdown profile. For additional protection and to help prevent overtopping of the levees, separate high level alarm floats are located at the north and south abutments to detect an emergency high-level condition should the pool level reach elevation 350.5 meters (1150.0 feet), 0.6 meters (2 feet) above the normal pool elevation of 349.9 meters (1148 feet). The high alarm level floats are also in pairs for redundancy, which also increases the reliability and accuracy of a high level detection. Manual backup to the pool level instruments is provided by a staff gauge at the northernmost pier (no. 7) and by a staff gauge on the north abutment wall. The gauges can be read directly by an operator from the control building, upstream pedestrian bridge, or north abutment area.

To monitor the hydraulic cylinders' status, they are equipped with temperature sensors, proximity switches, and oil leak detectors. Alarms are generated when the cylinder oil temperatures reach a predetermined warning temperature set point and eventually lock out operation of the corresponding gate when temperatures exceed a set temperature. Two hydraulic oil leak pressure transmitters monitor for a cylinder tube seal leak at the interstitial space between the primary rod end seal and the secondary outboard end seal. The proximity switch alarms are designed to monitor when the gates have reached the fully closed position or the fully open position to prevent the hydraulic power unit (HPU) pumps and valves from staying energized longer than necessary.

Each gate position is monitored by a Rittmeyer RIVERT angle transmitter providing a continuous feedback signal of the gates angle and corresponding crest elevation. When the continuous feedback signal does not match a corresponding command for a pre-determined amount of time, alarms are generated and the corresponding gate(s) are locked out of operation for any automatic mode operation. The corresponding gate(s) may still be operated in manual mode if it is determined that the alarm is a result of a sensor failure. These alarms and safety features are designed to prevent racking of the gates and extreme loads for scenarios such as binding at the hinges, debris blockage, or other adverse conditions.

The HPU is equipped with over twenty automatic monitoring capabilities designed for operational and alarm functions. From simple pump/motor running status readings to the hydraulic oil cleanliness and water content readings, the HPU's status is well monitored to help maintain proper function.

3.5. Hydraulic Power Unit and Cylinders

The gates are held by 6.9 meter (274 inch) stroke and 40.6 centimeter (16 inch) bore single-acting cylinders that are powered by a 152 bar (2,200 psi) hydraulic power unit (HPU) featuring two 1,893 cm^3/s (30 gpm) axial piston pumps, each powered by a 37 kW (50 hp) motor. The dual-pump system provides redundancy to the operation of the gates in the event that a pump or motor is out of commission. Supported by a separate 19,700 liter (5,200 gal) hydraulic fluid reservoir, the system is designed to lower all eight gates through full stroke within 30 minutes and raise all eight gates through full stroke within 120 minutes. The HPU delivers Mobil EAL^{TM} hydraulic oil to the cylinders by schedule 40 Type 304 stainless steel hydraulic lines. Accessibility to the 1,980 meters (6,500 feet) of hydraulic piping is important to facilitate scheduled inspections for leaks, damage, or other conditions that could impact the operation of the gates. To help facility inspections and maintenance, 90 percent of hydraulic piping is accessible within a concrete trench protected by either a fiber reinforced polymer (FRP) cover or a reinforced concrete cover. The remaining 10 percent of piping is sleeved within the piers where they can be removed and replaced if necessary.

The single-acting cylinders allow passive lowering of the gates, which is an important design approach in the riverine condition where debris can accumulate around the gates. The Salt River can produce heavy sediment and debris conditions during prolonged flow events. The passive lowering of the gates prevents inducing compressive forces in the cylinders in the event of debris blockage.

3.6. Structure Instrumentation and Monitoring

In addition to the instrumentation and monitoring for the gate operation, the dam structure and hydrostatic conditions are monitored with structural monitoring points and piezometers. A total of six piezometers are located downstream of the gates: two near the left abutment at Gate #1; two near the center of the dam; and two near the right abutment at Gate #8. Each set of two piezometers includes one that extends into the drainage layer and one that extends below the RCC foundation to elevation 335.3 (1100.0). The piezometers are vibrating wire-type piezometers and feed into the supervisory control and data acquisition (SCADA) system where the data is stored and accessible through the controls readout screen. Survey prisms are located on each pier for measuring horizontal movements of the dam over time. In addition, brass surface monuments are located immediately downstream of the piers in the stilling basin area to allow level measurements to track vertical movements of the dam and foundation.

4. DESIGN CHALLENGES

4.1. Schedule and Permitting

By the time the dam replacement alternative was selected, the City had three and one-half years left in their schedule to design and construct the hydraulically operated steel gate dam. To help expedite construction, phased design packages were created and permitted to allow early construction for site preparation work and foundation work. This allowed more time for final design of the gates, superstructure, and supporting facilities.

4.2. Gate Buoyancy

Crest gates typically sit atop a dam or spillway where tailwater rarely creates a submerged condition. Because the gates are in a riverine condition, they are subject to buoyancy forces during flow events that submerge the gates. Floatation of the gates obstructs the flow, thus increasing the water surface elevation and the inundation limits during large flood events. The conservation of momentum Eq. (1) was used to estimate the floatation of the gates for the 100-year and Reach Capacity design events where m_1 is an initial mass, v_1 is the initial velocity, m_2 is the final mass, and v_2 is the final velocity.

$$m_1 * \Delta v_1 = -m_2 * \Delta v_2 \tag{1}$$

The project did not have the benefit of a hydraulics laboratory scale model to help validate the results; therefore, performance data from similar gates along the North Canadian River in Oklahoma City were reviewed and compared with the calculations. The Oklahoma City gates are manufactured by the same gate vendor as Tempe's gates and are similar in design, scale, and function. The results indicate buoyancy forces will cause the gates to float between 7.4 degrees and 9.7 degrees during the design events, and the reviewed performance data from the Oklahoma City gates is consistent with the findings. Ballasting of the gates is being implemented to help counteract the buoyancy by placing a cement grout within selected gate chambers. The grout is placed within the upper end chambers of the gates (see Figure 6) allowing the added weight to transfer to the cylinder connection points without creating unwanted stresses within the rest of the gate.

Figure 6. Gate Ballasting

4.3. Cylinder and Gate Maintenance

The ability to maintain the lake while performing scheduled and unscheduled cylinder and gate maintenance is a priority for the City. To achieve this, an upstream dogging system was designed to hold the gates in their full up (closed) position (see Figure 7). Structurally, the dogging rods mimic the cylinder loading condition, which provides continuity in the structural design. Each dogging rod position is monitored with a switch to lock out operation of the respective gate cylinders when the dogging rods are engaged. Additionally, each gate bay can receive a coffer dam for accessing the upstream side of the gate without draining the lake (see Figure 8).
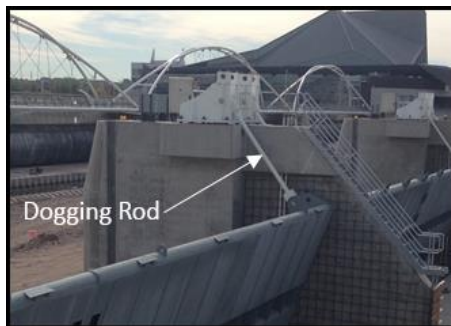
Figure 7. Gate supported by the dogging rods

Figure 8. Coffer Dam

5. CONCLUDING REMARKS

This paper presents a review of the selection, approach, challenges, and results of designing the hydraulically operated steel gate system across the ephemeral Salt River necessary to maintain Tempe Town Lake. The selection of the dam technology considered safety, impacts to the river's discharge capacity, operational flexibility, cost, maintenance, and the harsh weather of the Sonoran Desert. Selection and design of the instrumentation balanced the need to monitor the structure's health, prevent irreversible damage, and maintain the lake's normal pool while also preventing flooding during flow events. The resulting gate system is designed to meet the needs of the City of Tempe and maintain the value Tempe Town Lake brings to the community.

6. ACKNOWLEDGMENTS

7. REFERENCES

ACI Committee 315. (n.d.). ACI 315. *American Concrete Institute Manual of Standard Practice for Detailing Reinforced Concrete Structures.*

City of Tempe. (2015). *Historic Timeline.* Retrieved December 18, 2015, from City of Tempe Arizona: http://www.tempe.gov/city-hall/community-development/tempe-town-lake/fast-facts-coloring-book-slideshows-and-videos/historic-timeline

FEMA. (2012, October 24). National Flood Insurance Program Code of Federal Regulations: 65.10(b)(1)(i). *Mapping of areas protected by levee systems.*

Gannett Fleming. (2012, March 27). *Tempe Town Lake Downstream Dam Replacement - Alternatives Evaluation Report. Phoenix*: Gannett Fleming.

Gannett Fleming. (2014). *Final Hydraulic Analysis Report.* Phoenix: Gannett Fleming.

Gannett Fleming. (2014). *Tempe Town Lake Downstream Dam Replacement, Structural Calculations - Volume 1 (Foundation)*. Phoenix: Gannett Fleming.

Gannett Fleming. (2015). *Tempe Town Lake Downstream Dam Replacement Engineering Design Report.* Phoenix: Gannett Fleming.

United States Army Corps of Engineers. (1995, June 30). *Gravity Dam Design, EM 1110-2-2200.* Washington, DC: Department of the Army.

United States Army Corps of Engineers. (2014, June 30). *Design of Hydraulic Steel Structures, ETL 1110-2-584.* Washington, DC: Department of the Army.

Shear Stress Distribution Prediction in Circular Channels using Tsallis Entropy

H. Bonakdari[1] and Z. Sheikh Khozani[2]
[1]Professor, Department of Civil Engineering (bonakdari@yahoo.com)
Razi University
Kermanshah
Iran
[1]Ph.D. Candidate, Department of Civil Engineering (y.sheikh2131@gmail.com)
Razi University
Kermanshah
Iran

E-mail: bonakdari@yahoo.com

ABSTRACT

Detailed knowledge of flow and shear stress distribution in channels is essential in accurately calculating the rates of sediment transport and deposition for geomorphic adjustment. Circular cross sections are usual in sewer channels, and the sedimentation of suspended material is a significant matter in such sections. In this study, an analytical model is extended to predict the shear stress distribution in circular channels based Tsallis entropy concept. A new formula for estimating shear stress distribution in circular channels is derived by maximizing the Tsallis entropy subject to mass conservation. The distribution derived from the Tsallis entropy is examined using experimental data. The Tsallis entropy-based shear stress distribution appears to be in reasonable agreement with the measurements. According to the results, with increasing flow depth the proposed model showed good fit with the laboratorial outcomes and with mean Root Mean Square Error (RMSE) of 0.0516 it presented high performance in predicting shear stress distribution in circular channels. The results of equation derived of Tsallis entropy were compared with the results of another equation based Shannon entropy that proposed by other researchers. Based the results, the proposed model with PE of 0.0083 performed better than equation based Shannon entropy with PE of 0.0091. In highest flow depth, both models performance was the same, but for other flow depths, the proposed model performs better than Shannon entropy. The principal differences between the measured and calculated data are the results of secondary circulation, which are not included in the calculation. The main advantage of these new equations is that they are simpler than previous equations extracted with the entropy concept; besides, their parameters can be easily acquired based on a quadratic equation, and it is not necessary to solve complicated equations to obtain the entropy parameters. Since the obtained equations are simpler than those based on the entropy concept and their results are more accurate, they can be applied confidently for circular channels.

Keywords: *Circular channel, Lagrange multipliers, Shear stress distribution, Tsallis entropy.*

1. INTRODUCTION

Shear stress distribution plays an essential role in increasing the precision of erosion and sedimentation rates in channels and in designing stable channels. Estimating shear stress distribution experimentally in different channel cross-sections was seen in numerous studies (e.g. Rajaratnam and Ahmadi 1981; Knight 1981; Tominaga et al. 1989; Rhodes and Knight 1994; Torfs 1995; Knight and Sterling 2000; Atabay et al. 2004; Seckin et al. 2006; Pechlivanidis et al. 2014). Numerical and analytical methods were extended to predict shear stress distribution; since these methods were not consist, experimental methods such as Khodashenas and Paquier (1999), Guo and Julien (2005), Sterling and Knight (2002), Kabiri Samani et al. (2013), Bonakdari et al. (2015a), and Chen et al. (2015) were employed. Circular cross section is common frequently used in sewers ducts that accurate awareness of shear stress values in this section has high influence in sedimentation of suspended material. Many studies were done to predict shear stress values in this section. Berlamont et al. (2003) had calculated shear stress in circular pipes with a diameter of 1m using

computational fluid dynamic (CFD). Their simulations were done for different roughness heights, filling ratios, and mean flow velocities by using an isotropic turbulence model. Sterling and Knight (2002) employed Shannon entropy concept to estimate shear stress distribution in circular, circular with a flat bed, and trapezoidal channels. Sheikh and Bonakdari (2015) applied a Shannon entropy based power law to estimate shear stress distribution in circular and trapezoidal channels; they validated their results with experimental data and deducted their method is more accurate. Another entropy approach is Tsallis entropy, which Bonakdari et al. (2015b) used to predict shear stress distribution in channels with different cross sections. They used a set of implicit equations to compute entropy parameters. Because of the importance of shear stress distribution in circular channels, this study presents new equations to estimate shear stress distribution using Tsallis entropy. The aim of this study is decreasing computation of the equation proposed by Bonakdari et al. (2015b). For this aim, a new parameter G is introduced that, using this parameter, calculates the Lagrange multipliers that is not required in Tsallis entropy equations by other researchers.

2. MATERIAL AND METHODS

2.1. Tsallis Entropy

Tsallis (1988) presented a generalized form of Shannon entropy or Boltzmann-Gibbs entropy that for shear stress distribution can be written as

$$H(\tau) = \frac{1}{m-1}\left[1 - \int_0^{\tau_{max}} [f(\tau)]^m d\tau\right] = \frac{1}{m-1}\int_0^{\tau_{max}} f(\tau)\left(1 - [f(\tau)]^{m-1}\right)d\tau \tag{1}$$

where τ is the shear stress value at a specific point, $f(\tau)$ is the probability density function, and m is a real number. The entropy maximization principle may be employed to determine the probability density function, $f(\tau)$. To obtain $f(\tau)$, maximizing entropy function $H(\tau)$ subject to the specified constraints or principal of maximum entropy (POME) (Jaynes 1957a,b) were applied. These constraints are total probability and conservation of mass, which can be specified as the following two equations, respectively.

$$C_1 = \int_0^{\tau_{max}} f(\tau)d\tau = 1 \tag{2}$$

$$C_2 = \int_0^{\tau_{max}} \tau f(\tau)d\tau = \tau_{mean} \tag{3}$$

Jaynes (1957a,b) formulated the POME, based on which, the probability density function can be obtained by maximizing the uncertainty expressed by entropy, subject to given constraints in Eqs. (2) and (3). The probability so derived will be least biased toward the information not given about shear stress distribution. To maximize the entropy function given by Eq. (1), subject to the specified constraints Eqs. (2) and (3), the Lagrange multiplier method is applied as follows:

$$\frac{\partial}{\partial f(\tau)}\left[\frac{1}{m-1}f(\tau)\left(1 - (f(\tau))^{m-1}\right)\right] + \lambda_1 \frac{\partial[f(\tau)]}{\partial f(\tau)} + \lambda \frac{\partial[\tau f(\tau)]}{\partial f(\tau)} = 0 \tag{4}$$

where λ_1 and λ are the Lagrange multipliers. Therefore $f(\tau)$ expressed as

$$(f(\tau))^{m-1} = \frac{m-1}{m}\left(\frac{1}{m-1} + \lambda_1 + \lambda\tau\right) \tag{5}$$

To simplified form of Eq. (5) is

$$f(\tau) = \left(\frac{m-1}{m}\left[\lambda' + \lambda\tau\right]\right)^{\frac{1}{m-1}} \tag{6}$$

where $\lambda' = \frac{1}{m-1} + \lambda_1$

Equation (6) computes the probability density function. As seen in this equation, to obtain $f(\tau)$, the Lagrange multipliers should calculate at first that these multipliers were obtained by Eqs. (2) and (3) as

$$\left[\lambda' + \lambda\tau_{\max}\right]^{\frac{m}{m-1}} - \left[\lambda'\right]^{\frac{m}{m-1}} = \lambda\left(\frac{m}{m-1}\right)^{\frac{m}{m-1}} \tag{7}$$

$$\frac{\tau_{\max}}{\lambda}\left[\lambda' + \lambda\tau_{\max}\right]^{\frac{m}{m-1}} - \frac{1}{\lambda^2}\left(\frac{m-1}{2m-1}\right)\left[\lambda' + \lambda\tau_{\max}\right]^{\left(\frac{m}{m-1}\right)+1} + \frac{1}{\lambda^2}\left(\frac{m-1}{2m-1}\right)\left[\lambda'\right]^{\left(\frac{m}{m-1}\right)+1} = \left(\frac{m}{m-1}\right)^{\left(\frac{m}{m-1}\right)}\tau_{mean} \tag{8}$$

Bonakdari et al. (2015b) used these equations and solved them simultaneously to compute Lagrange multipliers. Also, for obtaining mean and maximum shear stress, they utilized equations presented by Knight et al. (1994). These equations were introduced as the following:

$$\frac{\tau_{mean(w)}}{\rho g R S} = 0.01\% SF_w\left(1 + P_b/P_w\right) \tag{9}$$

$$\frac{\tau_{mean(b)}}{\rho g R S} = \left(1 - 0.01\% SF_w\right)\left(1 + P_b/P_w\right) \tag{10}$$

$$\frac{\tau_{\max(w)}}{\rho g R S} = 0.01\% SF_w\left[2.0372\left(P_b/P_w\right)^{0.7108}\right] \tag{11}$$

$$\frac{\tau_{\max(b)}}{\rho g R S} = \left(1 - 0.01\% SF_w\right)\left[2.1697\left(P_b/P_w\right)^{-0.3287}\right] \tag{12}$$

where $\tau_{\max(w)}$ and $\tau_{\max(b)}$ are the maximum and $\tau_{mean(w)}$ and $\tau_{mean(b)}$ the mean shear stresses at the wall and bed, respectively, ρ is the fluid density, g the gravitational acceleration, R the hydraulic radius, S the bed slope, P_b and P_w the wetted perimeter corresponding to the bed and wall of the channel, respectively, and $\%SF_w$ is the percentage of shear force carried by walls that can be computed as follows:

$$\%SF_w = C_{sf}\exp\left(-3.23\log\left(P_b/C_2 P_w + 1\right) + 4.6052\right) \tag{13}$$

in which $C_{sf} = 1.0$ for $\frac{P_b}{P_w} \leq 4.374$, otherwise $C_{sf} = 0.5857\left(P_b/P_w\right)^{0.28471}$ and in subcritical flow $C_2 = 1.5$.

2.2. Shear Stress Distribution

Bonakdari et al. (2015b) supposed that the probability of shear stress is equal to or less than τ is y/L; on the other hand, the shear stress cumulative density function is defined as the ratio of y to L as

$$F(\tau) = \int_0^\tau f(\tau)d\tau = \frac{y}{L} \tag{14}$$

where τ is the shear stress, y is the distance from the boundary, and L is defined as the channel length when shear stress is maximum. Bonakdari et al. (2015b) employed the Tsallis entropy method to predict shear stress distribution in circular and rectangular channels using the equation as follows:

$$\tau = -\frac{\lambda'}{\lambda} + \frac{1}{\lambda}\left(\frac{m}{m-1}\right)\left[\lambda\left(\frac{y}{L}\right) + \left(\left(\frac{m-1}{m}\right)\lambda'\right)^{\left(\frac{m}{m-1}\right)}\right]^{\left(\frac{m-1}{m}\right)} \tag{15}$$

To calculate the shear stress value from Eq. (15), the Lagrange multipliers values are required, which can be calculated from Eqs. (7) and (8). To get ride the complex calculation, the new dimensionless parameter G is introduced. We considered the G parameter has a relation between $f(0)$ and $f(\tau_{\max})$, therefore,

$$\frac{f(0)}{f(\tau_{\max})} = \frac{\left(\frac{m-1}{m}\lambda'\right)^{\frac{1}{m-1}}}{\left(\frac{m-1}{m}\left(\lambda' + \lambda\tau_{\max}\right)\right)^{\frac{1}{m-1}}} = \left(1 - \frac{\lambda\tau_{\max}}{\lambda' + \lambda\tau_{\max}}\right)^{\frac{1}{m-1}} \tag{16}$$

Therefore, we have

$$\frac{f(0)}{f(\tau_{\max})} = (1 - G)^{1/m-1} \tag{17}$$

where G in defined as

$$G = \frac{\lambda\tau_{\max}}{\lambda\tau_{\max} + \lambda'} \tag{18}$$

When $G=0$, then $f(0) = f(\tau_{\max})$ and the probability density function (PDF) of shear stress tends to be uniform. If $y=L$ when $\tau = \tau_{\max}$, then Eq. (15) yields the following:

$$\tau_{\max} = -\frac{\lambda'}{\lambda} + \frac{1}{\lambda}\left(\frac{m}{m-1}\right)\left[\lambda + \left(\left(\frac{m-1}{m}\right)\lambda'\right)^{\left(\frac{m}{m-1}\right)}\right]^{\left(\frac{m-1}{m}\right)} \tag{19}$$

By dividing Eq. (10) by Eq. (15) and replacing G, we have

$$\frac{\tau}{\tau_{\max}} = 1 - \frac{1}{G}\left(1 - \left\{\left(\frac{m}{m-1}\right)^{\frac{m}{m-1}}\frac{G}{\tau_{\max}}\left[\left(\frac{y}{L}\right) - 1\right] + 1\right\}^{m-1/m}\right) \tag{20}$$

At $y=0$ the shear stress is, $\tau_0 = 0$; therefore, Eq. (20) becomes

$$0 = 1 - \frac{1}{G}\left(1 - \left[1 - \left(\frac{m}{m-1}\right)^{\frac{m}{m-1}}\frac{G}{\tau_{\max}}\right]^{m-1/m}\right) \Rightarrow \left(\frac{m}{m-1}\right)^{\frac{m}{m-1}}\frac{G}{\tau_{\max}} = 1 - (1-G)^{m/m-1} \tag{21}$$

By replacing Eq. (21) in Eq. (20), the simpler form obtains as

$$\frac{\tau}{\tau_{\max}} = 1 - \frac{1}{G}\left(1 - \left\{(1-G)^n + \left[1 - (1-G)^n\right]\left(\frac{y}{L}\right)\right\}^{1/n}\right) \tag{22}$$

where $n = \frac{m}{m-1}$ and G is a dimensionless parameter that calculated by Eq. (17). Computing values of the parameter G using Eq. (12) requires to values of Lagrange multipliers; therefore, the relation of the G parameter with the mean and maximum shear stress data is presented in Figure 1.
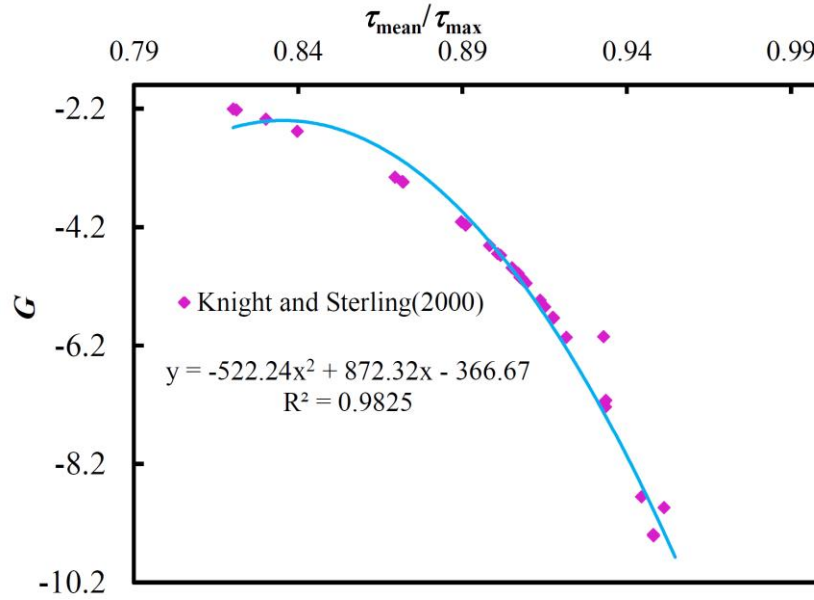
Figure 1. Relationship between G and $\dfrac{\tau_{mean}}{\tau_{max}}$.

As seen in Figure 1, the trend line can be presented with a second order polynomial function that has a coefficient of determination up to 0.9901. Equation (2) shows the relation between G parameter and ratio of mean and maximum shear stress and a quadratic equation that is obtained by computing the observed mean and maximum shear stress value. This equation was defined as

$$G = -522.24\left(\frac{\tau_{mean}}{\tau_{max}}\right)^2 + 872.32\left(\frac{\tau_{mean}}{\tau_{max}}\right) - 366.67 \tag{23}$$

With use of Eq. (22), we can avoid the complicated computation of Lagrange multipliers. Also, a simpler equation was obtained than equations proposed by Bonakdari et al. (2015b).

2.3. Shannon Entropy

Sterling and Knight (2002) used Shannon entropy to calculate shear stress distribution in circular, circular channel with a flat bed, and trapezoidal channels. The derived equation by Sterling and Knight (2002) for circular channels is as follows:

$$\tau = \frac{1}{\lambda}\ln\left[1 + \left(e^{\lambda\tau_{max}} - 1\right)\frac{y}{L}\right] \tag{24}$$

where λ is Lagrange multipliers that with knowledge of maximum shear stress it can be estimated as

$$\lambda = \left[\frac{\tau_{max}e^{\lambda\tau_{max}}}{e^{\lambda\tau_{max}} - 1} - \rho gRS\right]^{-1} \tag{25}$$

In this paper, the results of the proposed method by Sterling and Knight (2002) will be compared with the proposed model.

2.4. Experimental Data

The data used in this study were collected from Knight and Sterling (2000). They measured shear stress distribution in circular and circular channels with flat bed for several flow depths. The experiments of Knight and Sterling (2000)

were conducted in a flume with 610 mm width, 365 mm depth, and 21.26 m length. Their experimental conduit was constructed from several plastic PVC pipe sections and one 2m-long acrylic clear section that each pipe section had an internal diameter D of 244 mm with wall thickness of 3 mm. Figure 2 shows the cross section of the circular channel. In this figure, D is channel diameter and y is transverse coordinate (origin at the water/air interface). A summary of the hydraulic parameters in a set of experimental data is tabulated in Table 1, where h is the flow depth, S_0 is the channel length slope, Q is the discharge in the channel, U is the average velocity, Fr is the Froude number, and Re is the Reynolds number.
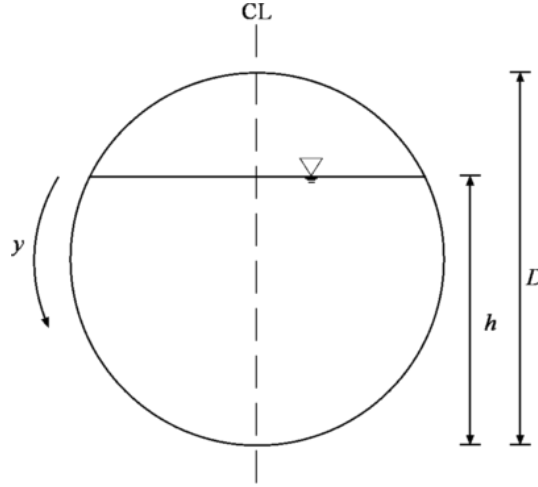
Figure 2. Circular channel cross section and notation.

Table 1. Summary of the main hydraulic parameters in a circular channel.

t/D	h(mm)	h/D	S_0	Q (Ls^{-1})	U (m/s)	Fr	Re ($\times 10^4$)
	81.3	0.333	0.001	5.36	0.394	0.516	6.49
0	123.5	0.506	0.001	11.7	0.493	0.505	11.0
	162.6	0.666	0.001	17.3	0.524	0.441	13.5
	201.5	0.826	0.001	22.9	0.554	0.375	15.0

2.5. Goodness of Fit of Model Performance

Five statistical evaluation criteria were used to assess the models' performances in predicting shear stress distribution. These criteria are the Root Mean Squared Error (*RMSE*), Percentage of Error (*RE*), the Coefficient of Residual Mass (*CRM*), and the average absolute deviation (*δ%*), which were defined as:

$$RMSE = \sqrt{\frac{\sum_{i=1}^{n}(T_{ip} - T_{im})^2}{n}} \tag{26}$$

$$RE = \sum_{i=1}^{n}\left|\frac{T_{ip} - T_{im}}{T_{im}}\right| \times 100 \tag{27}$$

$$CRM = \frac{\left(\sum_{i=1}^{n}T_{im} - \sum_{i=1}^{n}T_{ip}\right)}{\sum_{i=1}^{n}T_{im}} \tag{28}$$

$$\delta = \frac{\sum\limits_{i=1}^{n}\left|T_{ip} - T_{im}\right|}{\sum\limits_{i=1}^{n}T_{ip}} \times 100 \qquad\qquad (29)$$

where T_{ip} is the predicted shear stress by model, T_{im} is the shear stress measured in the laboratory, and n is the number of cases. Positive values of *CRM* indicate that the model underestimates the observed values and negative values indicate the overestimation trend of the applied model.

3. RESULTS AND DISCUSSION

The results of the proposed model compared with Shannon entropy in estimating shear stress distribution in circular channels were tabulated in Table 2. With increasing flow depth, the model predictions are closer to experimental data. In h/D=0.333, the prediction of model is overestimated with a *CRM* of -0.0063, and for other flow depths, it is underestimated. For h/D=0.826, although the flow depth increases but the results of statistical parameters proposed model and Shannon entropy are not good than other flow depth. For this flow depth, the results of both models are the same. It can be deducted in higher flow because of existing intensive secondary flows with filling channel section the proposed model performance increases. It is noteworthy that even in higher flow depth the results of model are in acceptable range. The proposed model by Sterling and Knight (2002) with increasing flow depth decreases. For all flow depths, the proposed model with mean *RMSE* of 0.0516 showed the good performance in estimating shear stress distribution in circular channels than Shannon entropy with mean *RMSE* of 0.0582.

Table 2. Statistical parameter results for shear stress distribution in circular channel.

h/D	Tsallis Entropy				Shannon Entropy			
	RMSE	*PE*	*CRM*	$\delta\%$	*RMSE*	*PE*	*CRM*	$\delta\%$
0.333	0.0485	0.0059	-0.0063	3.3008	0.0585	0.0087	0.0043	5.4318
0.506	0.0430	0.0062	0.0026	2.8296	0.0444	0.0060	0.0224	2.8742
0.666	0.0435	0.0069	0.0071	2.6681	0.0585	0.0073	0.0257	2.7690
0.826	0.0714	0.0142	0.0138	4.9397	0.0714	0.0142	0.0138	4.9397

Also, the results of Tsallis entropy and Shannon entropy models in estimating shear stress distribution in circular channels are shown in Figure 3. In this figure, P is all wetted perimeter of channel and y is transverse coordinate. With increasing flow depth, the shear stress values in conjugated of water and air increase so that the models could simulate this state. It is obviously seen that the performance of proposed model in predicting shear stress distribution in range of $0.2<y/P<0.8$ is higher than other ranges so that the predicted values of shear stress is coincided on measured values. As seen in Figure 3, with increasing flow depth, the predicted values by model are very close to experimental data. In h/D=0.333, the model predictions for range of $y/P<0.2$ and $y/P>0.8$ are underestimated since the flow depth is very low, and with increasing flow depth, the ability of model in estimating shear stress in these ranges increases. For h/D=0.826, the measured values of shear stress are as a straight line because of the channel section is full and secondary flow effect on shear stress values. Since the effect of secondary flows not be considered in the proposed model, the model performance decreases in h/D=0.826 than other flow depths but results are in safety margin. As seen in Figure 3a and b, the predictions of proposed model by Sterling and Knight (2002) for $0.2<y/P<0.8$ are underestimated, but other ranges of y/P coincide with the proposed model. According to the results of Figure 3 of a comparison between Shannon and Tsallis entropy, the proposed model based Tsallis entropy demonstrates better performance than Shannon entropy, which is presented by Sterling and Knight (2002).
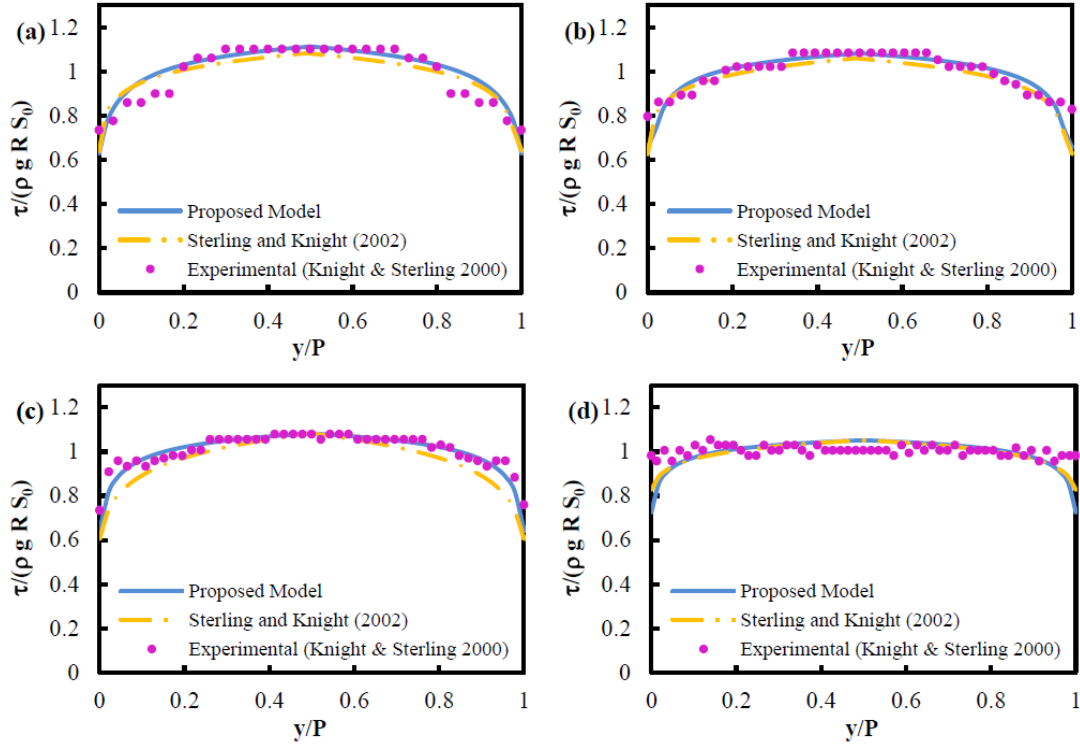
Figure 3. Shear stress distribution in circular channel for (a) *h/D*=0.333, (b) *h/D*=0.506, (c) *h/D*=0.666, (d) *h/D*=0.826.

4. CONCLUSION

Shear stress distribution affects sedimentation and erosion rates. Since circular cross sections are usual in sewer channels and the sedimentation of suspended material is a significant matter in such sections, in this paper, an analytical model was extended to estimate the shear stress distribution in circular channels. The model based Tsallis entropy concept was extended, and an equation for predicting shear stress distribution was presented. To overcome difficulty of computation of Lagrange multipliers, a new parameter G was introduced. Using the dimensionless parameter G to estimate shear stress only need to solve a quadratic equation that related to maximum and mean shear stress values. With this method, the shear stress distribution along a wetted perimeter in four flow depths of circular channels were computed. The results demonstrated the model performance in predict shear stress distribution increased with increasing flow depth. The model could predict shear stress distribution with mean *RMSE* of 0.0516. Although in analytical model presented in this paper the effect of secondary flows was ignored, but the model predicts shear stress distribution with high precision. Also, the proposed model performance compared with the results of presented equation by Sterling and Knight (2002) based Shannon entropy. The results showed the proposed model with *PE* of 0.0083 performed better than equation based Shannon entropy with *PE* of 0.0091.

5. REFERENCES

Atabay, S., Knight, D.W., and Seckin, G. (2004). "Influence of a mobile bed on the boundary shear in a compound channel." *Proc., Int. Conf. River Flow* 2004, Napoli, Italy, Taylor & Francis Group, London, 1, 337-345.

Berlamont, J.E., Trouw, K., and Luyckx, G. (2003). "Shear stress distribution in partially filled pipes." *J. Hydraul. Eng.,* 129(9), 697-705.

Bonakdari, H., Tooshmalani, M., and Sheikh, Z. (2015a). "Predicting shear stress distribution in rectangular channels using entropy concept." *Int. J. Eng.,* 28(3), 357-364.

Bonakdari, H., Sheikh, Z., and Tooshmalani, M. (2015b). "Comparison between Shannon and Tsallis entropies for prediction of shear stress distribution in open channels." *Stoch. Environ. Res. Risk Assess.,* 29(1), 1-11.

Chen, G., Gu, Sh., Huai, W., and Zhang, Y. (2015)." Boundary shear stress in rectangular ice-covered channels." *J. Hydraul. Eng.,* DOI: 10.1061/(ASCE)HY.1943-7900.0001004.

Guo, J., and Julien, P.Y. (2005). "Shear stress in smooth rectangular open-channel flow." *J. Hydraul. Eng.,* 131(1), 30-37.

Jaynes, E.T. (1957a). "Information theory and statistical mechanics I." *Phys. Rev.,* 106(4), 620-630.

Jaynes, E.T. (1957b). "Information theory and statistical mechanics II." *Phys. Rev.,* 108(2), 171-190.

Kabiri-Samani, A., Farshi, F., and Chamani, M.R. (2013). "Boundary shear stress in smooth trapezoidal open channel flows." *J. Hydraul. Eng.,* 139(2), 205-212.

Khodashenas, S.R., and Paquier, A. (1999). "A geometrical method for computing the distribution of boundary shear stress across irregular straight open channels." *J. Hydraul. Res*., 37, 381-388.

Knight, D.W. (1981). "Boundary shear in smooth and rough channels." *J. Hydraul. Div.* 107(7), 839-851.

Knight, D.W., and Sterling, M. (2000). "Boundary shear in circular pipes running partially full." *J. Hydraul. Eng.,* 126(4), 263-275.

Pechlivanidis, G.I., Keramaris, E., Pechlivanidis, I.G., and Samaras, G.A. (2014). "Shear stress estimation in the linear zone over impermeable and permeable beds in open channels." *Desalin. Water Treat*., DOI: 10.1080/19443994.2014.933622.

Rajaratnam, N., and Ahmadi, R. (1981). "Hydraulics of channels with flood-plains." *J. Hydraul. Res.,* 19(1), 43-60.

Rhodes, D.G., and Knight, D.W. (1994). "Distribution of shear force on boundary of smooth rectangular duct." *J. Hydraul. Eng.,*120(7), 787-807.

Seckin, G., Seckin, N., and Yurtal, R. (2006). "Boundary shear stress analysis in smooth rectangular channels." *Can. J. Civil Eng*., 33, 336-342.

Sheikh, Z., and Bonakdari, H. (2015). "Prediction of boundary shear stress in circular and trapezoidal channels with entropy concept." *Urban Water*, DOI: 10.1080/1573062X.2015.1011672.

Sheikh Khozani, Z., and Bonakdari, H. (2015). "Comparison of five different models in predicting the shear stress distribution in straight compound channels." *J. SCI. IRAN*., in press.

Sheikh Khozani, Z., Bonakdari, H., and Zaji A.M. (2015). "Application of soft computing technique in prediction percentage of shear force carried by walls in rectangular channel with Non-homogenous roughness." *Water Sci. Technol*., DOI: 10.2166/wst.2015.470.

Sterling, M., and Knight, D.W. (2002). "An attempt at using the entropy approach to predict the transverse distribution of boundary shear stress in open channel flow." *Stoch. Environ. Res. Risk Assess.*, 16(2), 127-142.

Tominaga, A., Nezu, I., Ezaki, K., and Nakagawa, H. (1989). "Three-dimensional turbulent structure in straight open channel flows." *J. Hydraul. Res.,* 27, 149-173.

Torfs, H. (1995). ''Erosion of mud/sand mixtures.'' PhD dissertation, KULeuven, Belgium.

Tsallis, C. (1988). "Possible generalization of Boltzmann–Gibbs statistics." *J. Stat. Phys.,* 52, 479-487.

Repair of Failing Spirit Lake Outlet Tunnel at Mount St. Helens

J.P. Britton, PE, PhD[1], S.K. Askelson, PE[1], C.M. Budai, RPG, CEG, PMP[1], and D.H. Scofield, PE, RPG, CEG[1]

[1]U.S. Army Corps of Engineers
Portland District
Portland, OR 97204
USA
E-mail: Jeremy.p.britton@usace.army.mil

ABSTRACT

The 18 May 1980 eruption of Mount St. Helens resulted in one of the largest debris avalanches recorded in history. The debris avalanche blocked the natural outlet of Spirit Lake. To prevent an uncontrolled and catastrophic lake break-out, the U.S. Army Corps of Engineers (USACE) constructed the Spirit Lake Outlet Tunnel from 1984 to 1985. Because Spirit Lake is located in the Mount St. Helens National Volcanic Monument, the project was transferred to the U.S. Forest Service (USFS) for ownership and management. During original tunnel construction, the most difficulty occurred within the 90-m-wide Julie and Kathy L. shear zone complex. In 1996, tunnel walls within this complex experienced significant convergence, which required major repair along a 30 m segment. During inspections in 2014 and 2015, a 10 m segment at the upstream end of the complex, which had experienced slow heave in the past, was observed to have experienced an increase in heave of approximately 0.6 m, which decreased the hydraulic capacity of the tunnel below acceptable limits. The USACE, in accordance with and with funding from the USFS, designed a repair based on the rib set-shotcrete support system that was used for the 1996 repair. In addition to removing and arresting the heave, the 2015 repair was sized to be compatible with a future potential rehabilitation involving stabilizing and re-grading the invert profile of the Julie and Kathy L. shear zone complex. The 2015 repair construction contract was awarded in September 2015 for $3 million.

Keywords: Tunnel, heave, steel ribs, shotcrete, Mount St. Helens, Spirit Lake.

1. BACKGROUND

Mount St. Helens is located in southwest Washington, about 72 km northeast of the Portland-Vancouver metropolitan area (Figure 1) and is part of the Cascade Range that runs from British Columbia through Washington, Oregon, and into northern California. The range is made up of active volcanoes comprising a part of the Pacific "Ring of Fire". Mount St. Helens erupted on May 18, 1980, resulting in a catastrophic landslide that released millions of tons of sediment into the upper North Toutle River drainage basin. A massive debris avalanche completely filled Spirit Lake, located about 6 km north of the mountain, blocking the lake's outlet to the North Fork Toutle River and raising the lake level some 60 m (200 ft).

After the eruption, the U.S. Army Corps of Engineers (USACE) conducted investigations to determine the stability of the debris dam that blocked Spirit Lake. The debris dam consists mainly of debris avalanche deposit material, ranging from silt to boulder in size, overlain by rock fragments from the blast deposit. The uppermost material consists of a fine-grained ash and pumice deposit that is easily erodible.

In 1982, a governmental task force was formed to evaluate the hazard posed by the blockage of Spirit Lake. The group determined that the debris blockage could not safely pond water above elevation 1,059 m (3,475 ft) due to the character of the material and that Spirit Lake would reach elevation 1,059 m by March 1983. The lake could not be allowed to reach that elevation due to the potential for failure of the debris blockage from piping through the uppermost ash material and the resulting catastrophic flooding, widespread damage to downstream communities, and interruption of Columbia River navigation. Swift and Kresch (1983) provided inundation maps based on a hypothetical failure of the debris blockage.

An emergency pumping station was constructed to pump water from Spirit Lake over the debris blockage and into the North Fork Toutle River as an interim measure to maintain a safe lake level while a long-term solution was studied and determined. The pumping facility consisted of 20 pumps mounted on a barge near the shore of Spirit Lake. Water was pumped from the lake through 1,050 m (3,450 ft) of 1.5-m (5-ft) diameter steel pipe across the debris blockage to a stilling basin and, from there, to the North Fork Toutle River.

Once the lake level was stabilized through the interim pumping facility, a permanent safe lake level was determined (1,055 m or 3,460 ft), and alternatives for a permanent lake outlet were evaluated. Alternatives included 1) a buried conduit, 2) an open channel, 3) a tunnel, and 4) a permanent pumping facility. Various alignments for each alternative were evaluated, along with criteria related to location within the National Volcanic Monument, constructability, and cost. Because some of the alignments crossed the potentially unstable debris blockage, long-term stability, downstream impacts from erosion and sediment transport, water quality impacts, and effect on stability of the Spirit Lake and Coldwater Lake debris blockages were other important considerations. Each alternative was also evaluated for the ability to withstand impacts from future volcanic or seismic events due to the proximity of the mountain. Based on these considerations, a straight tunnel extending about 2,590 m (8,500 ft) from the west side of Spirit Lake through Harry's Ridge to South Coldwater Creek was selected as the preferred alternative. The Spirit Lake Outlet Tunnel was constructed by the USACE and turned over to the U.S. Forest Service as owners in 1985. Sager and Chambers (1986) and Sager and Budai (1989) describe original tunnel construction.
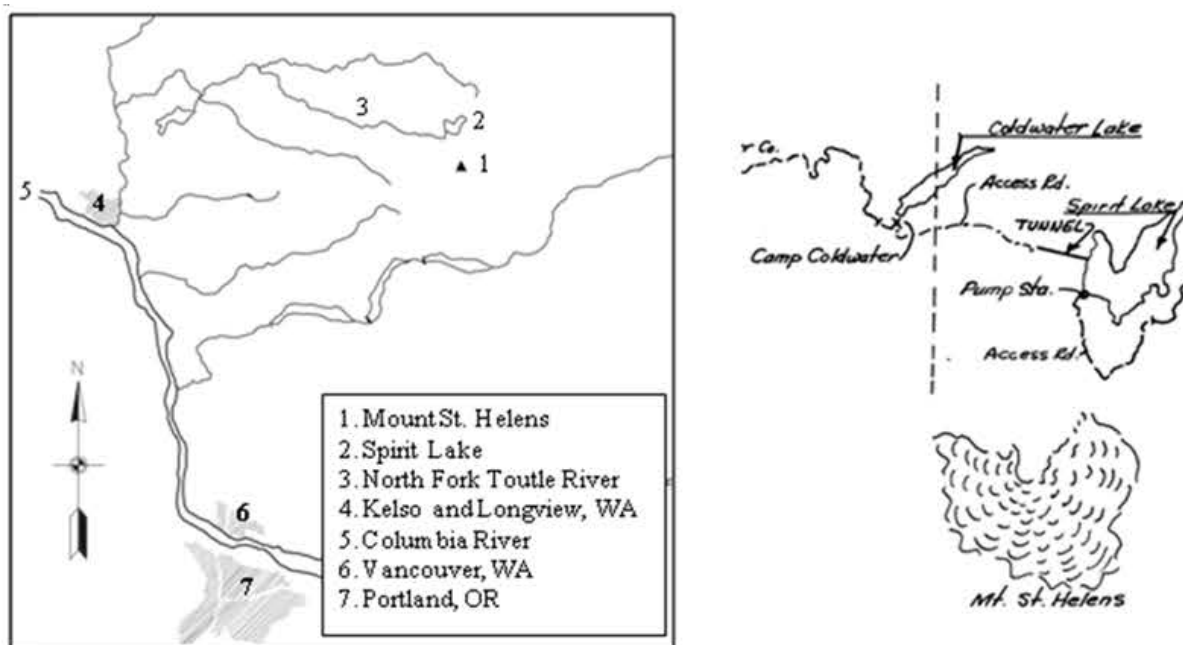
Figure 1. Map of region, left, and Spirit Lake vicinity, right. Spirit Lake map clipped from figure in USACE (1987)

2. TUNNEL DESIGN AND CONSTRUCTION

2.1. Hydrology and Hydraulic Design

The Design Memorandum for the project (USACE 1984) provides a full description of the hydrology and hydraulic design. Select relevant information is provided below.

Spirit Lake is the largest alpine lake affected by the May 1980 eruption of Mount St. Helens. Originally, the lake was approximately 56 m (185 ft) deep with a surface area of 5 km² (1,260 acres). The pre-eruption lake surface

fluctuated around elevation 975 m (3,200 ft) NGVD. During the eruption, Spirit Lake was displaced by debris from Mount St. Helens. The displaced lake came to rest at a pool elevation of 1,038 m (3,404 ft) NGVD, approximately 62 m (204 ft) higher than the original water surface. The minimum crest elevation of the debris dam forming Spirit Lake is approximately 1,079 m (3,540 ft) NGVD.

Spirit Lake was not only relocated, but the hydrologic characteristics of the watershed were altered. The pre-eruption 38.6 km² (14.9 mi²) commercial/recreational forest land watershed was changed to a 46.6 km² (18 mi²) basin denuded of vegetation. The increase in drainage is from the north slope of Mount St. Helens. Surface water from the southwest now flows from the rampart of the Mount St. Helens crater through a deeply carved chasm onto a flat area of avalanche debris. The areas to the east, north, and west of the lake are extremely steep and produce rapid runoff that flows directly into the lake.

The climate of the area is predominately a mid-latitude west coast marine type. Summers are comparatively dry and cool, and winters are cloudy, mild, and wet. During the wet season, rainfall is usually of light to moderate intensity and continuous over a period of time, rather than of the heavy short-duration type storms. However, rainfall of heavy intensity can be expected as more intense weather systems move inland. Mean annual rainfall precipitation over the Spirit Lake Basin ranges from 229 cm (90 in.) to over 305 cm (120 in.); the basin average is about 254 cm (100 in.). About half of the annual precipitation occurs between November and February.

Precipitation in the form of snow is a significant hydrologic factor in the Spirit Lake vicinity. The mean annual snowfall amount ranges from 236 cm (93 in.) to 1,250 cm (493 in.) with a basin mean of 719 cm (283 in.). Maximum observed snow depths at the pre-eruption Spirit Lake snow station ranged from 25 cm (10 in.) in early November to 416 cm (164 in.) in mid-to-late March. The snowpack can reach water content densities of 30 to 40 percent prior to the spring melt.

Flood frequency peak discharge data were determined for the Spirit Lake basin using a rainfall/runoff model of the basin based on the HEC-1 computer program. Precipitation-frequency data were determined per Miller et al. (1973). Losses used were minimal rates due to basin topography and lack of ground cover and soil mantle.

A Probable Maximum Flood (PMF) analysis assumed maximum flood-producing elements and conditions arranged in a sequence that will produce the most critical flood runoff. These meteorological and hydrological elements are probable maximum precipitation for the critical storm period, maximum basin snow cover, maximum temperatures during the design storm, minimum surface losses, and a unit hydrograph that will reflect the runoff for a storm the magnitude of the PMF. The peak discharge of the PMF derived for Spirit Lake is 1,220 m³/s (43,000 cfs). The total volume of the PMF, including base flow, is 60 million m³ (49,000 acre-feet).

To size the required outlet structure and tunnel capacity, the PMF was routed through Spirit Lake beginning at an elevation of 1,049 m (3,441 ft) NGVD and was preceded by a large antecedent flood (100-year event). The total volume of the two floods is 69 million m³ (56,000 acre-feet). Peak regulated outflow was 15.6 m³/s (550 cfs), and the maximum lake elevation during the flood event was 1,054 m (3,459 ft) NGVD.

Long-term operating criteria were adopted for hydraulic design guidance as follows: flow depth within the tunnel no greater than three-quarters of the tunnel height, Spirit Lake to be considered normal at pool elevation 1,049 m (3,440 ft) NGVD, the intake gate to remain fully open after initial drawdown, and pool fluctuations should be within 1.5 m (5 ft) above normal during most flood events. The maximum temporary safe lake elevation was determined to be 1,055 m (3,460 ft) NGVD. The project was designed to limit all possible hydrologic raises in the lake level to this elevation.

Hydraulic sizing of the tunnel was dictated by the selection of hydraulic parameters that allow flow within the tunnel to be at atmospheric (open channel) conditions. Concern was raised that pressurization of the tunnel without periodic air relief for negative pressures could result in collapse of the tunnel walls. A maximum flow capacity of 15.6 m³/s (550 cfs) was required for the tunnel and intake to pass flows without raising the lake level more than 1.5 m (5 ft) under normal conditions, or above elevation 1,055 m (3,460 ft) NGVD under PMF conditions. Design computations indicated that a tunnel diameter of 3.3 m (10.8 ft) would provide the required flow capacity while allowing for minor offsets during construction and variations in finished tunnel roughness.

2.2. Geology

The Spirit Lake tunnel is located in the western flank of the Cascade Range, a major north-south trending mountain range of volcanic origin. The tunnel penetrates through older volcanic sequences comprising Harry's Ridge. The geology of the tunnel was mapped in detail at a scale of 1:120 at the time of construction. A generalized geologic profile of the tunnel is shown in Figure 2. This description is taken from USACE (1987). General stratigraphy is Tertiary-age, predominantly volcanic tuffs overlain by predominantly basalt and andesite lava flows. Both units have been intruded by basaltic dikes. The rock sequence has been regionally deformed, sheared, and faulted, and it now dips about 30-40 degrees to the east. Strike of the flows and tuffs is nearly normal to the tunnel centerline.
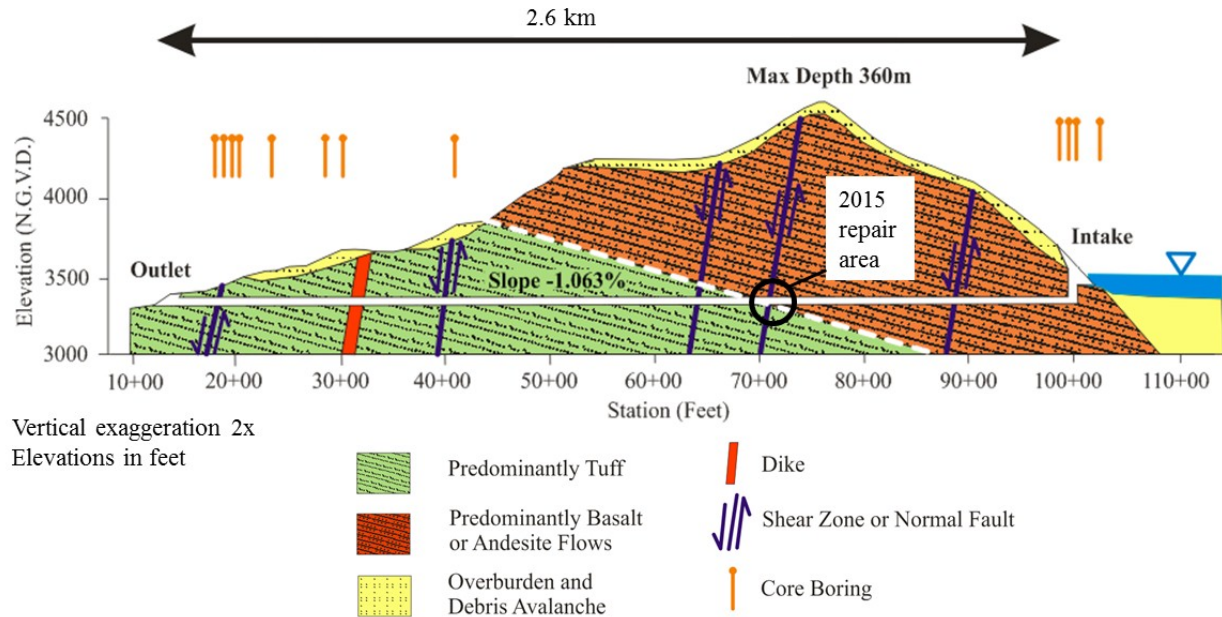
Figure 2. Geologic profile along tunnel (left is west, right is east)

The western two-thirds of the tunnel penetrates a sequence of tuffaceous rock types including fine-grained, lapilli, tuff breccias, localized layers of welded tuff, and minor lava flow sequences (USACE 1987). The tuffs are primarily a light-green, dense, fresh rock with angular, multi-colored fragments in the lapilli beds, with strengths of 34 MPa to 100 MPa (710 – 2,100 ksf). Interbedded lava flows range from less than 30 m (100 ft) to greater than 100 m (330 ft) thick, with strengths between 100 MPa and 250 MPa (2,100 – 5,200 ksf). Flow rock is generally comprised of multiple flows separated with flow breccia. The eastern one-third of the tunnel penetrates a sequence of predominantly basaltic and andesitic lava flows with minor amounts of interbedded volcanic tuffs. The geologic contact between the two units is composed of soft, decomposed tuffs.

Twelve shear zones and faults were encountered along the tunnel. The affected areas varied from 1 m (3 ft) to upwards of 20 m (66 ft). The primary condition of the shear zones is fractured rock in various stages of decomposition and some plastic to low plasticity fines. Within the shear zones are thin seams of clay gouge. Most of these shears are steeply dipping and cross the tunnel nearly normal to the centerline. The most serious shear zones were the Julie and Kathy L. shear zones, where two zones of about 15 and 20 m (49 and 66 ft) were encountered near the geologic contact and maximum ground cover. The shears were in ashy volcanic tuffs decomposed to weak rock and swelling clays. Spalling and squeezing ground occurred, and the grippers on the tunnel boring machine could not grip the rock. In addition, the soft clay caused significant deviation of the vertical alignment. Hand mining was required in some areas so that steel sets could be placed.

No large, sustained groundwater inflows were encountered along the length of the tunnel. Small inflows (19 l/min / 5 gpm or less) were occasionally encountered from rock fractures (USACE 1987).

2.3. Tunnel Construction and Support

Except for the downstream 70 m (225 ft) of the tunnel, which was excavated using drill-and-blast methods, the majority of the tunnel (2,500 m or 8,200 ft) was excavated using a tunnel boring machine (TBM). The TBM excavated the tunnel to a diameter of 3.4 m (11 ft). Three types of support systems were used depending on the rock conditions. The entire tunnel invert was lined with pre-cast or cast-in-place concrete. In "good rock" (55% of tunnel), no treatment was used on the walls and crown. In "fractured rock" (35% of tunnel), the walls and crown were covered with a minimum of 50 mm (2 in.) of steel fiber-reinforced shotcrete. In "sheared rock" (10% of tunnel), a rib set-shotcrete support system was used for the walls and crown (285 degrees of the tunnel circumference).

Rock loads for design were evaluated using the modified Terzaghi system. For the worst rock conditions, characterized by sheared rock and squeezing ground, a rock load of 410 kPa (8,570 psf) was used (USACE 1984). No groundwater pressure was assumed. Where needed, drains were installed 1.5 m (5 ft) into the crown during construction. The original design of the rib set-shotcrete system called for W150 mm x 37 kg/m (W6 in. x 25 lb/ft) rib sets with a steel yield strength of 248 MPa (36 ksi). A contractor proposal was accepted by the USACE to use W100x19 (W4x13) rib sets instead. The standard rib set spacing was to be 1.2 m (4 ft). The spacing could be reduced to as little as 0.3 m (1 ft) if squeezing ground conditions were encountered (USACE 1984).

In general, tunneling progress during construction was good. The problem area, where construction was difficult and slow, was the 90-m-wide (300-ft-wide) Julie and Kathy L. shear zone complex (station 72+50 to 75+50). Before encountering this complex, the tunnel advancement rate had been 1,178 m (5,834 ft) in 11 weeks. The TBM got stuck for two days near the beginning of the complex. It took about 4 weeks to advance the next 72 m (235 ft) (USACE 1987). Rib sets were placed as close as 0.6 m (2 ft) apart in two areas of the complex, including 20 m (66 ft) of sheared ashy tuff adjacent to (downstream of) the geologic contact with basalt. No rib sets were placed upstream of the geologic contact. Some pre-cast concrete invert sections were damaged and removed in the Julie and Kathy L. shear zone complex. Steel struts were installed instead, and the invert was covered with cast-in-place concrete. A significant flow of groundwater occurred into the tunnel when the permeable geologic contact was first encountered. Within one week, the trapped water had drained and only seeps remained.

The Spirit Lake Outlet Tunnel Foundation Report (USACE 1987) included a section describing conditions that could produce future problems. For the tunnel, "Slight possibility of ground adjustments in shear zones, especially the Julie – Kathy L. complex." The conditions in the Julie and Kathy L. shear zone complex have indeed produced problems requiring repairs.

3. 1996 TUNNEL REPAIR

Routine inspections of the tunnel were conducted annually from the time the tunnel went into operation in 1985. These inspections sometimes resulted in minor patchwork repair contracts, with many of these repairs occurring repeatedly between stations 73+50 and 74+50. In October 1992, the inspection team found significant problems in this area of the tunnel, including large sections of shotcrete that had pulled away from the tunnel walls, uplifted and cracked precast invert segments, and sheared and buckled rib sets. The exposed areas were sealed with concrete to allow for continued operation of the tunnel while funding was secured and contract specifications were prepared to repair the tunnel.

A rib set-shotcrete support system was used for the repair. The repair support system was more robust than the original rib set-shotcrete support system. The loading conditions included the same rock load of 410 kPa (8,570 psf) that was used for the worst rock conditions in the original design, plus an assumed hydrostatic load of 203 kPa (4,243 psf), for a total design load of 613 kPa (12,813 psf). The design beam shape and yield strength were increased to W200x42 (W8x28) and 345 MPa (50 ksi), from the W100x19 (W4x13) and 248 MPa (36 ksi) used for the original rib sets. Thirty-four new rib sets were installed within the 30 m (100 ft) repair area. These were full-circle rib sets, not the 285-degree rib sets and invert struts used for original construction. The original rib sets were spaced at 0.6 m (2 ft) in one part of the area and 1.2 m (4 ft) in the other part. The repair involved excavating midway between the original rib sets to install the new rib sets, then covering them with steel fiber-reinforced silica

fume shotcrete above the springline and cast-in-place concrete below the springline. The original rib sets were left in place. The 1996 repair has performed well, with no signs of movement.

4. 2003 TUNNEL SURVEY AND HYDRAULIC ANALYSIS

Changes in invert slope in the vicinity of the Julie and Kathy L. shear zone complex have been a known issue since tunnel construction. In 2003, a survey was completed to establish a baseline for future monitoring and provide a basis for hydraulic modeling of the existing tunnel conditions. See Figure 3.

Survey data was used to develop HEC-RAS cross sections for hydraulic modeling. The hydraulic model consisted of steady state flow analysis allowing a mixed flow regime (supercritical and subcritical flow regimes possible), with simulated flow rates of 0.71 m^3/s (25 cfs) to 18.4 m^3/s (650 cfs). Sensitivity analyses performed on model boundary conditions and roughness coefficients showed that results in the area of interest were not significantly affected by changes in these parameters.

Analyzing model results indicated that the abrupt changes in the invert slope at stations 74+45 and 75+65 (see Figure 3) result in a hydraulic jump forming near station 77+25. The tunnel would not be able to pass the design flow of 15.6 m^3/s (550 cfs) without violating the flow depth design criterion. Furthermore, USACE (1980) describes how slug flow can develop when the water surface exceeds 80-85% of the conduit height due to unaccounted-for air bulking, particularly with hydraulic jumps.

A HEC-RESSIM model was used to assess the increase in flood risk associated with restricting the Spirit Lake outflow. Flood risk is the risk of the lake elevation exceeding the maximum safe level during a flood event, which could result in debris blockage failure and lake break-out. The minimal increase in flood risk associated with a safe, lower outflow was deemed acceptable compared to the risk associated with pressurization and/or slug flow within the tunnel. A recommendation was made to restrict flow in the tunnel to 9.9 m^3/s (350 cfs) by partially closing the intake gate to three-quarters open. Figure 3 shows the water surface profile for this flow.

5. RECENT TUNNEL DISTRESS

Significant tunnel invert heave was discovered during a routine inspection in October 2014 (See Figure 4). The heave is located at the upstream end of the Julie and Kathy L. shear zone complex, in the vicinity of the geologic contact between volcanic tuffs and lava flows and the high-angle Kathy L. shear zone, which required extensive steel supports during original construction. The heave location is about 30 m (100 ft) upstream of the 1996 repair area. The location is identified in Figure 2 as the 2015 repair area.

Figure 5 shows the geologic mapping from original construction and the approximate extent of heave. The heave began a long time ago due to high ground pressures, the weakness of the sheared tuff dipping beneath the tunnel, the adverse orientation of fractures in the basalt, and the absence of steel rib sets. For several years, the amount of heave remained steady at approximately 61 cm (24 in.). The distress was limited to the tunnel invert; the shotcrete lining on the walls and crown showed no cracking or distress. During the October 2014 inspection, 46 cm (18 in.) of additional heave was measured. Existing cracks in the cast-in-place concrete invert showed severe dilation. Again, the walls and crown showed no distress. A follow-up inspection in April 2015 revealed another 10 cm (4 in.) of heave. The tunnel diameter had now been reduced to approximately 2.1 m (6.8 ft). This segment of the tunnel was in an active state of heave failure.

The geometry in the 2003 HEC-RAS hydraulic model was updated with the 2015 physical measurements of the heave. Invert elevations were adjusted in the reach near tunnel station 75+75 to represent the measured reduction of tunnel cross sectional area. The results of the hydraulic modelling indicated that the tunnel would no longer pass 9.9 m^3/s (350 cfs) without violating the flow depth design criterion. Flow within the tunnel would require further restriction to 7.1 m^3/s (250 cfs) to operate within design criteria. This further reduction in project outflow would significantly increase the risk of unsafe lake levels, which was deemed unacceptable. A repair was needed.
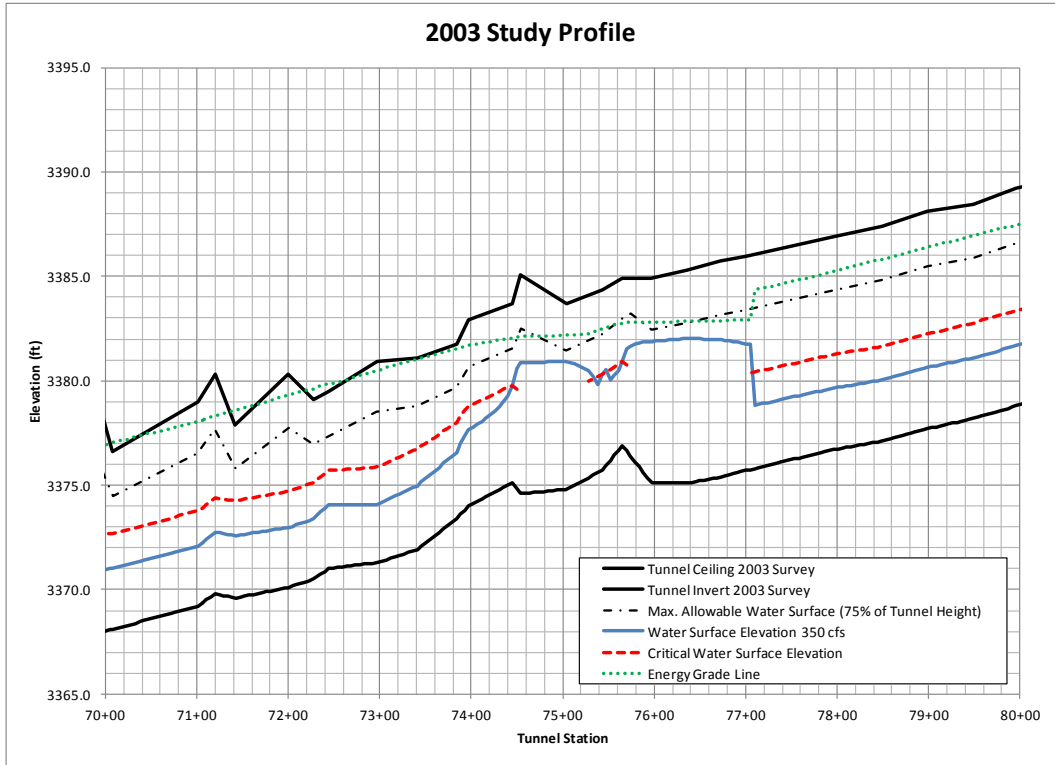
Figure 3. Water surface profile for flow of 9.9 m^3/s (350 cfs) and 2003 geometry conditions

Figure 4. Photo of heave in tunnel
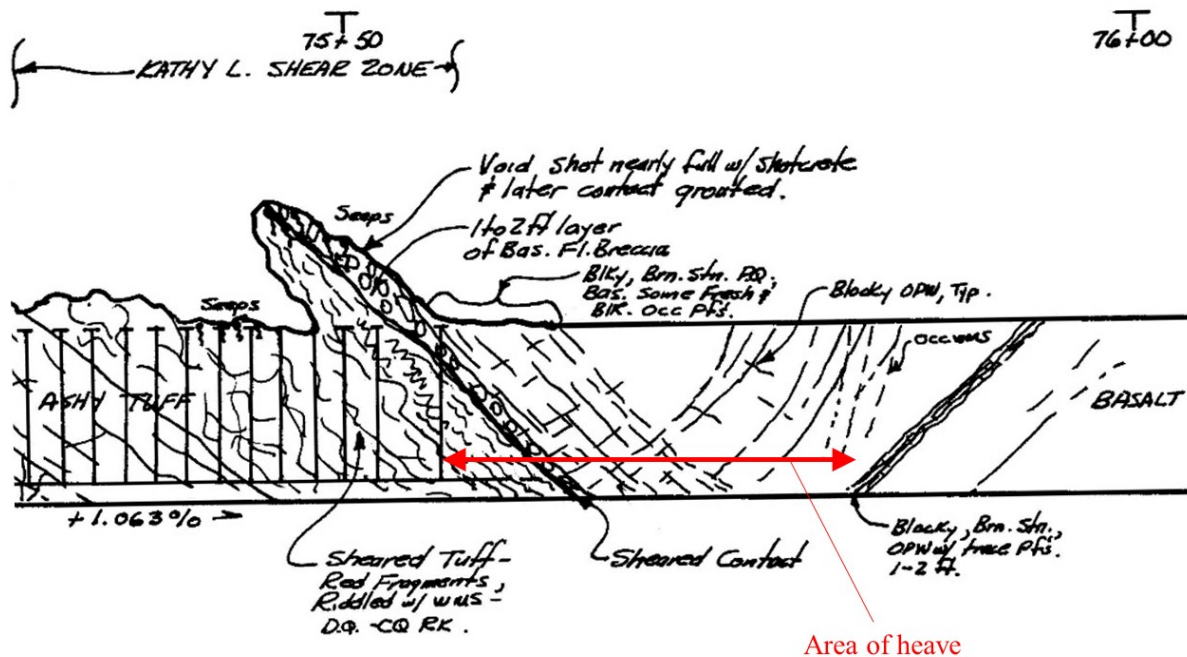
Figure 5. Geology in area of heave (from USACE 1987)

6. 2015 REPAIR DESIGN

The time period from the beginning of repair design to award of the construction contract, including development of plans and specifications and several reviews, was five months, from near the end of April to near the end of September, 2015. Given the continuing heave observed in April, it was considered critical to repair the tunnel before another full winter season of high flows. The design team spent a short amount of time considering various repair options and quickly settled on the rib set-shotcrete support system approach that had been successful for the 1996 repair.

The loading conditions in the area of the 1996 repair were more severe than the loading conditions in the area of the 2015 repair. In the 1996 repair area, the full tunnel circumference was subjected to squeezing ground conditions. In the 2015 repair area, only the invert was subjected to squeezing ground conditions from the sheared tuff dipping below the fractured basalt. The tunnel walls and crown showed no signs of distress. The 2015 repair design called for the installation of full-circle W200x42 (W8x28) rib sets (with 345 MPa/50 ksi steel) on 0.6 m (2 ft) centers. This was the same rib set design as used in 1996, except no rib sets were spaced at 1.2 m (4 ft). The 2015 repair design then called for the rib sets to be covered with a minimum of 50 mm of steel fiber-reinforced shotcrete.

Figure 6 shows both a profile and section of the 2015 repair design. The heave invert profile was measured in April 2015. The heaved material was assumed to consist of about 0.3 m (1 ft) of cracked concrete overlying blocky basalt and sheared tuff. During inspections, it was difficult to observe the invert conditions near the upstream end of the area due to the pool of water behind the crest of the heave profile. The plan was to assess the need to extend the repair into the "optional segment" shown in Figure 6 after the contractor established a cofferdam upstream of the area. At the downstream end of the repair, the exposed and deformed original rib set at station 75+53 was to be removed.
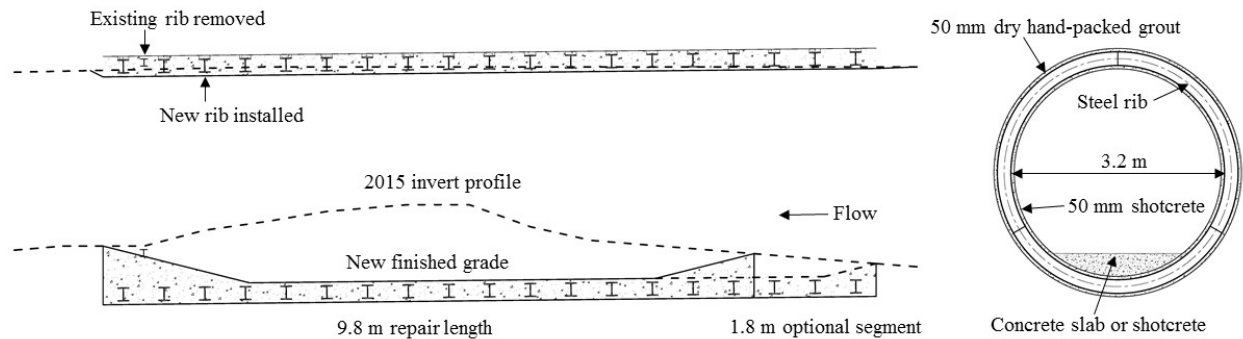
Figure 6. 2015 Repair design profile and section

For safety purposes, the contract required the excavation and support system installation to occur in 1.2 m (4 ft) increments, which covered two rib sets. The grout and shotcrete were required to attain 70% of the design compressive strength (27,600 kPa/4,000 psi at 28 days) before the next 1.2 m excavation increment could be made. The contract allowed for 1.5 m (5 ft) drains to be installed as needed in the walls and crown. The permeable geologic contact at the downstream end of the repair area was exposed to the open tunnel in small areas, and no flow was observed coming from the contact during inspections leading up to the repair.

The 2003 HEC-RAS hydraulic model was updated with the proposed repair geometry. Invert elevations were adjusted to represent the repair cross sectional area with a diameter of 3.1 m (10.2 ft). The results of the hydraulic modelling indicated that the tunnel would pass 11.3 m^3/s (400 cfs) without violating the flow depth design criterion (see Figure 7). This flow capacity is greater than the 2003 restricted capacity of 9.9 m^3/s (350 cfs). The additional flow capacity will allow for larger gate openings, which will result in lower Spirit Lake elevations. This will decrease the likelihood of exceeding the safe lake elevation. Furthermore, the lower lake elevations will result in less head on the gate, which will reduce the potential of higher flows within the tunnel. This will further decrease the risk of pressurization and/or slug flow within the tunnel.

The 3.2-m inside diameter of the new rib sets (tunnel inside diameter of 3.1 m after application of shotcrete) was chosen in order to achieve an invert profile compatible with a future potential rehabilitation involving stabilizing and re-grading the invert profile of the Julie and Kathy L. shear zone complex. The potential rehabilitation would create a constant tunnel cross-section and slope from station 73+41 to 76+36. The results of hydraulic modeling indicate that the rehabilitated tunnel would pass in excess of 15.6 m^3/s (550 cfs) without violating the flow depth design criterion, restoring the capacity of the Spirit Lake tunnel system to its original design capacity. Note that this inside tunnel diameter of 3.1 m (10.2 ft) is slightly less than, but close to, the 3.3 m (10.8 ft) diameter from original design, which allowed for minor offsets during construction and variations in finished tunnel roughness.

7. 2015 REPAIR CONSTRUCTION

A contract was awarded to the prime contractor Catworks Construction and their tunnel subcontractor LRL Construction on 24 September 2015 for $3 million. While the original intent was to perform construction during the fall of 2015, various delays pushed the beginning of construction inside the tunnel to January 2016. At the time this paper was submitted, in late December 2015, the steel rib sets had been fabricated, construction access to the tunnel outlet (downstream end) had been established, and the majority of construction submittals had been submitted and approved. The authors intend to describe the repair construction during the Symposium in June 2016.

The contractor did submit a variation to the original design. Instead of fully blocking the rib sets with hand-packed grout and using shotcrete as lagging, the contractor proposed a steel lagging and grouting design. Steel channel lagging would be placed between the rib sets and the volume between the excavated ground and the steel ribs/lagging would be filled with non-shrink grout. The ribs and lagging would then be covered with shotcrete (with synthetic as opposed to steel fibers). This contractor proposal was accepted.

145
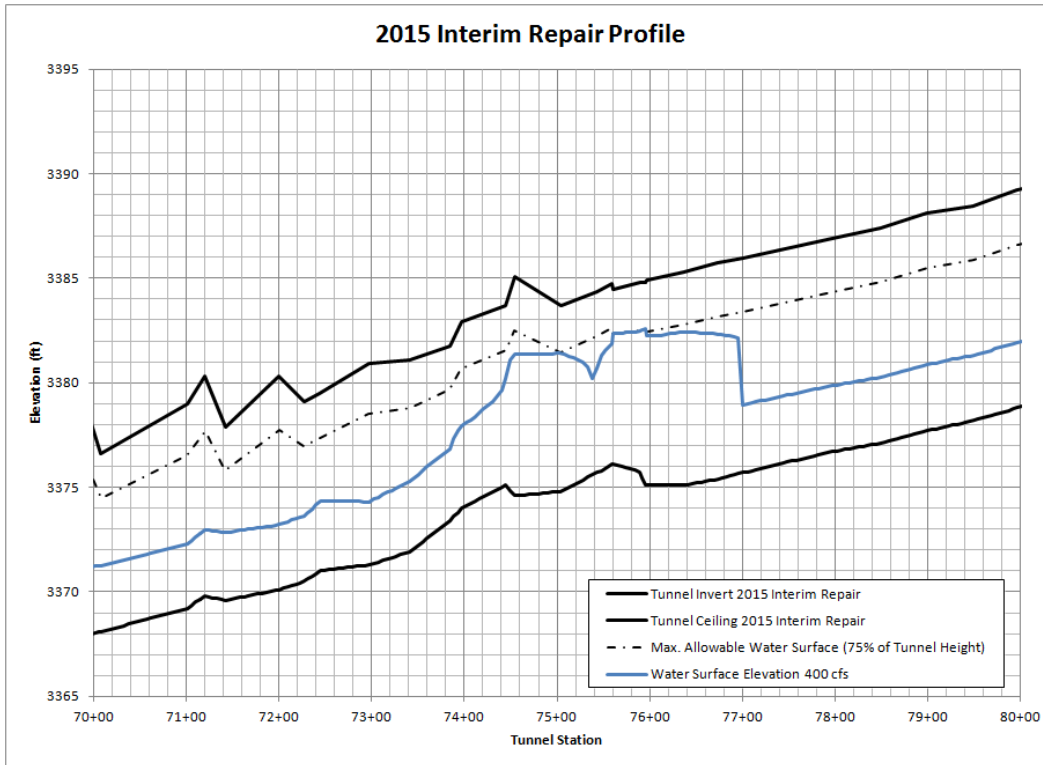
Figure 7. Water surface profile for flow of 11.3 m³/s (400 cfs) and 2015 repair geometry conditions

8. CONCLUSIONS

A rib set-shotcrete support system has been successfully used for support in the tunnel in areas of weak ground (shear zones and the tuff/basalt geologic contact). Within the Julie and Kathy L. shear zone complex, which includes soft and squeezing ground conditions, repair designs in 1996 and 2015 used full-circle W200x42 (W8x28) rib sets, with 345 MPa (50 ksi) steel, on 0.6 m (2 ft) centers. The 2015 contractor-proposed design used steel lagging and grout instead of shotcrete for lagging. Given the positive long-term stability performance of the 1996 repair and the successful implementation of the 2015 repair, this rib set design should be one alternative to consider for the future potential rehabilitation of the entire Julie and Kathy L. shear zone complex.

9. REFERENCES

Miller, J.F., Frederick, R.H., and Tracey, R.J. (1973). "NOAA Atlas 2, Precipitation-Frequency Atlas of Western United States, Volume IX – Washington." National Oceanic and Atmospheric Administration.

Sager, J.W. and Chambers, D.R. (1986). "Design and construction of the Spirit Lake outlet tunnel, Mount St. Helens, Washington." *Landslide Dams: Processes, Risk, and Mitigation,* R.L. Schuster (editor), American Society of Civil Engineers, Geotechnical Special Publication 3, pp. 42-58.

Sager, J.W. and Budai, C.M. (1989). "Geology and construction of the Spirit Lake outlet tunnel, Mount St. Helens, Washington." *Engineering Geology in Washington, Washington Division of Geology and Earth Resources*, R.W. Galster (editor), Bulletin 78, vol. 2, pp. 1229-1234.

Swift III, C.H. and Kresch, D.L. (1983). "Mudflow hazards along the Toutle and Cowlitz Rivers from a hypothetical failure of Spirit Lake blockage, U.S. Geological Survey Water-Resources Investigations Report 82-4125."

USACE (1980). "EM-1110-2-1602, Hydraulic Design of Reservoir Outlet Works." U.S. Army Corps of Engineers, Washington, D.C., Appendix D.

USACE (1984). "Spirit Lake Outlet Tunnel, Washington: Design Memorandum No. 1." U.S. Army Corps of Engineers, Portland District, Portland, Oregon.

USACE (1987). "Foundation Report: Spirit Lake Outlet Tunnel, Spirit Lake, Washington." U.S. Army Corps of Engineers, Portland District, Portland, Oregon.

The Hydraulic Design of an Arced Labyrinth Weir at Isabella Dam

E.A. Thompson[1], N.C. Cox[2], L.L. Ebner[3], and B.P. Tullis[4]
[1]Sacramento District Corps of Engineers
US Amy Corps of Engineers
1325 J Street
Sacramento, CA 95814
USA
[2]McMillen Jacobs Associates
1401 Shoreline Drive, Suite 100
Boise, ID 83702
USA
[3]Portland District Corps of Engineers
US Amy Corps of Engineers
333 SW First Avenue
Portland, Oregon 97208
USA
[4]Utah Water Research Laboratory
Utah State University
8200 Old Main Hill
Logan, Utah 84322-8200
USA
E-mail: Ethan.A.Thompson@usace.army.mil

ABSTRACT

The Sacramento District Corps of Engineers is designing modifications to the Isabella Dam located on the Kern River in the Tulare Lake Basin in the southern portion of the San Joaquin Basin, in Kern County, California. These modifications include raising the elevation of two high head dams (185 ft and 100 ft respectively) by 16 ft, modifying a service spillway to better suit the needs of flood capacity, and creating a new arced labyrinth weir emergency spillway in order to safely pass the probable maximum flood (PMF).

The rating curve for the arced labyrinth weir emergency spillway was based on information published in a PhD dissertation (Crookston, 2010) and a Master's Thesis (Christensen, 2012) from Utah State University. The proposed prototype weir geometry was a 10-cycle arced labyrinth with a 16° sidewall angle. As the published hydraulic performance data were limited to arced labyrinth weirs with 6°, 12°, and 20° sidewall angles, a spreadsheet program was developed to predict the rating curve for the prototype 16° weir using a double quadratic spline interpolation of the 12° and 20° discharge coefficient data. The spreadsheet was used to tailor the design of the arced labyrinth weir to the specific project needs. The spreadsheet was also used to evaluate the hydraulic and economic implications of over six-thousand different arced labyrinth weir/apron designs.

The prototype design verification program used a composite spillways modelling approach, which included a 1:45 scale physical model study at the Utah Water Research Laboratory (Utah State University) and CFD modelling conducted by the USACE Portland District (Hydraulic Design Section). The goal of the composite modelling was to validate the theoretical rating curve for the arced labyrinth weir given a non-ideal approach condition with the potential for submergence effects decreasing the discharge over the weir. The selected arced labyrinth weir theoretical rating curve was compared to the physical model and the CFD model results of the labyrinth weir. The physical model and CFD model results confirmed that the rating curves developed using traditional methods (discharge coefficients, velocity head, etc.) are valid and that the designed configuration of the service spillway and labyrinth weir will safely pass the PMF within the target pool elevation.

Keywords: Labyrinth Weir, Cost Optimization, Rating Curve, Physical Model, CFD.

1. INTRODUCTION

Isabella Lake Reservoir is located on the Kern River in Kern County, California (See Figure 1). The project is approximately 42 miles northeast of the city of Bakersfield and one mile upstream of the town of Lake Isabella. Isabella Dam consists of two earthen embankment dams: a main dam blocking the Kern River and an auxiliary dam located in the hot springs valley (there are no historic evidences of an old riverbed in this valley). The two dams are separated by a natural topographic feature where the Kern County Fault is located.
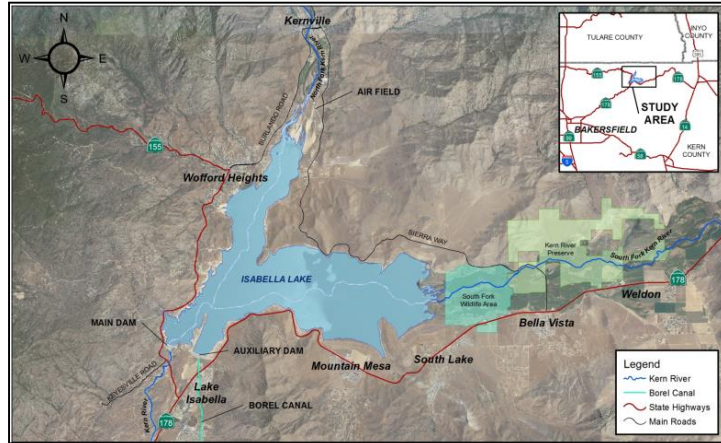
Figure 1. Location of Lake Isabella

The main dam has a maximum height of 185 feet, a crest length of 1,695 feet, and a top width of 20 feet. The crest elevation is 2,637.26 feet, which provides 6.5 feet of freeboard above the original Spillway Design Flood elevation of 2,630.76 feet. The existing outlet works and spillway are located within the main dam and left abutment, respectively (See Figure 2).

The auxiliary dam has a maximum height of 100 feet, a crest length of 3,257 feet, and a top width of 20 feet. The crest elevation is 2,637.26 feet. There is 6.5 feet of freeboard above the Spillway Design Flood peak elevation of 2,630.76 feet. The Borel Canal conduit is located within the auxiliary dam embankment.
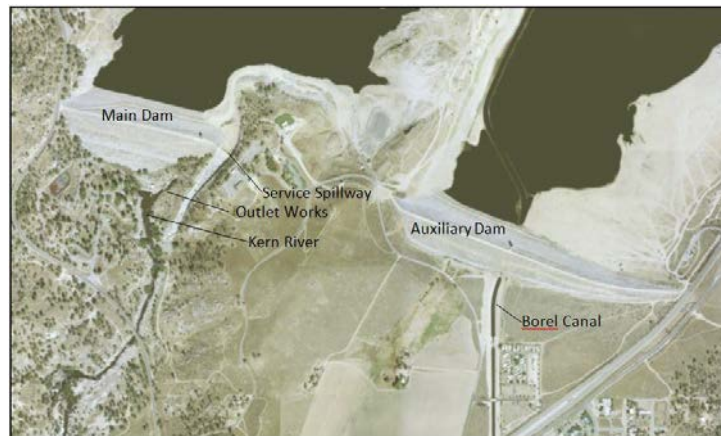
Figure 2. Existing Isabella Dam Project

Proposed spillway modifications include modifying the existing service spillway, constructing a new emergency arced labyrinth spillway, and creating a new spillway at Highway 155. In addition to the new and modified spillways, both the main dam and the auxiliary dam will be raised 16 feet as part of the overall project. The new

dam crest elevation will be 2653.26 (all elevations are referenced to North American Vertical Datum 1988 or NAVD88).

The general design procedure for the proposed arced labyrinth weir emergency spillway was based on information published in a PhD dissertation (Crookston (2010)) completed at Utah State University. Discharge coefficient data from Crookston (2010) and Christensen (2012) was used in developing the rating curve for the proposed labyrinth weir. In addition, a composite modelling approach was used that included CFD and physical modelling to develop the appropriate site specific approach conditions to the weir, verify the theoretical derived rating curve for the emergency labyrinth weir, and design the spillway chute to prevent submergence of the weir.

2. EMERGENCY SPILLWAY ALTERNATIVE SELECTION

An emergency spillway will be constructed at Isabella Dam between the main and auxiliary dams and next to the existing service spillway. The purpose of the new emergency spillway is to provide additional discharge capacity to pass the current estimated probable maximum flood (PMF). The new emergency spillway is designed as an arced labyrinth weir to reduce the footprint and minimize excavation requirements. The emergency spillway will discharge a short distance downstream of the existing service spillway into the Kern River.

During the Dam Safety Modification Report (DSMR) phase of the study, a large array of emergency spillway alternatives and dam raise alternatives were evaluated to increase Isabella Dam's capacity to pass and attenuate the PMF. Among the spillway alternatives considered, the following were included: a gated spillway, an un-gated ogee spillway, a broad-crested weir spillway, a side-channel spillway, a fuse gate spillway, and a labyrinth spillway. The effects of each alternative on downstream discharge capacity, flood protection levels, maximum reservoir pool elevations, and existing spillway adequacy were investigated.

Various alternatives were evaluated either as a widening of the existing spillway or as a new emergency spillway separate from the existing spillway. The majority of the alternatives evaluated varied either the crest elevation of the spillway, the spillway approach elevation, or the maximum allowable reservoir pool elevation (determining the dam raise needed). Several of these spillway alternatives were ultimately eliminated due to excessive maintenance, response to earthquake loadings, low efficiency, and depths of excavation that could cause dam safety problems. Various configurations of a labyrinth or fuse gate spillway were studied in greater detail due to their efficiency of passing the PMF within a smaller footprint. A linear labyrinth weir was the preferred alternative proposed with the DSMR. At the start of the Planning, Engineering, and Design (PED) phase, an arced labyrinth weir layout was considered and ultimately selected since it provided even greater efficiency. The final refinements to the arced labyrinth weir included a cost comparison between several weirs, also ensuring that the weir abutments were tied into high ground and that the weir performance was optimized.

The crest and apron of the emergency spillway is at elevation 2637.26 and 2609.26, respectively. The emergency spillway is an arced labyrinth weir to increase the unit discharge and reduce the excavation. This configuration was chosen to prevent the excavation from encroaching into the weaker fault shear zone while still providing the hydraulic capacity to pass the updated PMF.

3. ARCED LABYRINTH WEIR DESIGN

3.1. Geometric Layout

The general design procedure and parameters for an arced labyrinth weir are described in Crookston (2010). The parameters are shown in Figure 3. There are several variables, making for a large number of potential design configurations compared to a linear labyrinth weir. An excel spreadsheet was setup with the support of a macro to generate the cost associated with over 6,000 different designs. Each design had a total discharge capacity of 402,000 cfs, which is sufficient to pass the PMF when combined with the service spillway. The weir height, P was set to 28 ft for all the designs. In addition, based on site specific constraints, the width or chord length of the arced

labyrinth weir, W_{chord} was set to $W_{chord} \leq 800$. Similarly, the central weir arc angle Θ was constrained to $\Theta \leq 120°$. A few key parameters were adjusted incrementally to generate the various designs and associated costs for the weir. Adjusted parameters included the sidewall angle, α, the cycle arc angle, θ, and the number of cycles, N. The parameters were varied within the following ranges:

Sidewall Angle: $6° \leq \alpha \leq 20°$
Cycle Arc Angle: $1° \leq \theta \leq 30°$
Number of Cycles: $4 \leq N \leq 30$
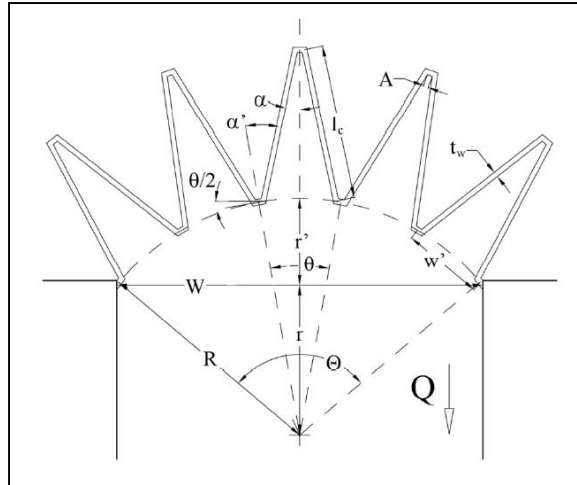
Figure 3. Arced Labyrinth Weir Geometric Layout (Crookston 2010).

The cost of the arced labyrinth weir was estimated assuming a unit cost for the labyrinth weir walls, abutment walls, and the concrete apron using unit costs of $1000/cubic yard, $500/cubic yard, and $300/cubic yard, respectively. The result of the estimated cost of each labyrinth design and weir length for each arced labyrinth weir evaluated is shown in Figure 4.
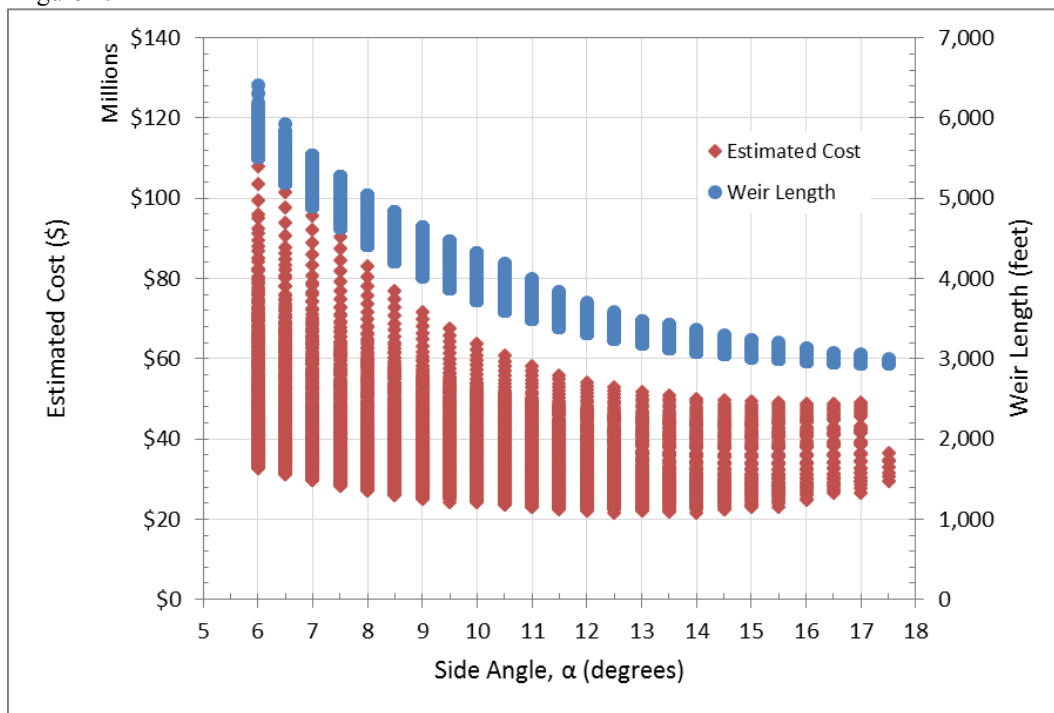
Figure 4. Estimated Cost of Labyrinth Weir vs. Side Angle and Weir Length.

The range of design parameters considered was limited to a range where existing experimental data were available. Based on the results of the spreadsheet analysis, the designs were narrowed down to three similar alternatives shown in Figure 5. The three weirs included a 20-cycle weir, a 12-cycle weir, and a 7-cycle weir. Additional information for each weir is shown in Table 1. The 12-cycle weir was ultimately selected by balancing needs for hydraulic efficiency and cost. The 12-cycle weir also closely represented weirs studied in the experimental data; hence, there was more confidence in its design. See the layout of the 12-cycle weir in Figure 6.

Figure 5. Final Arced Labyrinth Designs

Table 1. Labyrinth Weir Final Designs Comparison

	Angle of Side Legs α	Number of Cycles N	Cycle Arc Angle θ	W_{chord} (feet)	Depth of Labyrinth B (feet)	Total Weir Length L_c (feet)	Total Arc Angle Θ
20-Cycle Weir	14^0	20	6^0	800.91	78.76	3,367	120^0
12-Cycle Weir	16^0	12	10^0	790.83	123.32	3,149	120^0
7-Cycle Weir	15^0	7	17^0	699.90	207.25	3,045	119^0
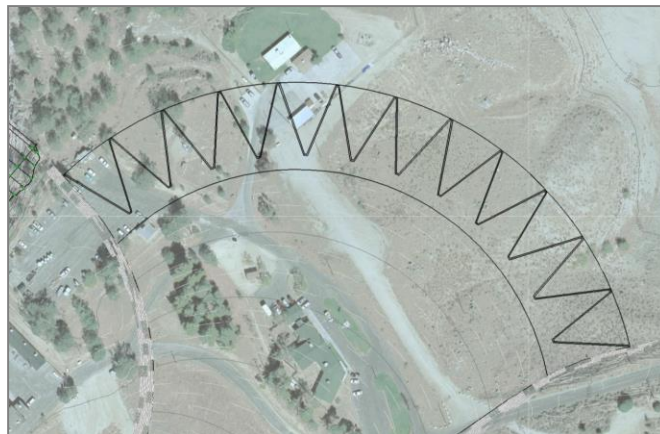
Figure 6. 12-Cycle Weir Layout

3.2. Rating Curve

The discharge for the arced emergency spillway was determined using the method described in Crookston (2010). Additional information for determining the discharge coefficient for arced labyrinth weirs was obtained from Christensen (2012). Equation 1 was used to calculate the discharge.

$$Q = \frac{2}{3} C_d L_c \sqrt{2g}\, H_T^{3/2} \tag{1}$$

Where: Q = Rate of Discharge (ft³/sec)
C_d = Discharge Coefficient f(H_T/P, α, θ, Crest Shape)
L_c = Total Centerline Length of Weir (ft)
g = Acceleration Constant of Gravity (ft/sec²)
H_T = Total Upstream Head above Crest (ft)

Discharge coefficients used were taken from experimental results in Crookston (2010) and Christensen (2012). Experimental results were limited to a sidewall angle of 6º, 12º, and 20º. A spreadsheet program was developed to predict the rating curve for the prototype 16º weir using a double quadratic spline interpolation of the available experimental discharge coefficient data. Figure 7 shows the discharge coefficient for sidewall angle of 16º (with θ=10º) derived from interpolation compared to the experimental results for sidewall angles of $\alpha = 6º$, 12º, and 20º, with varying cycle arc angles of $\theta = 0º$, 10º, 20º, and 30º. See Figure 11 for the resulting rating curve for the chosen design.
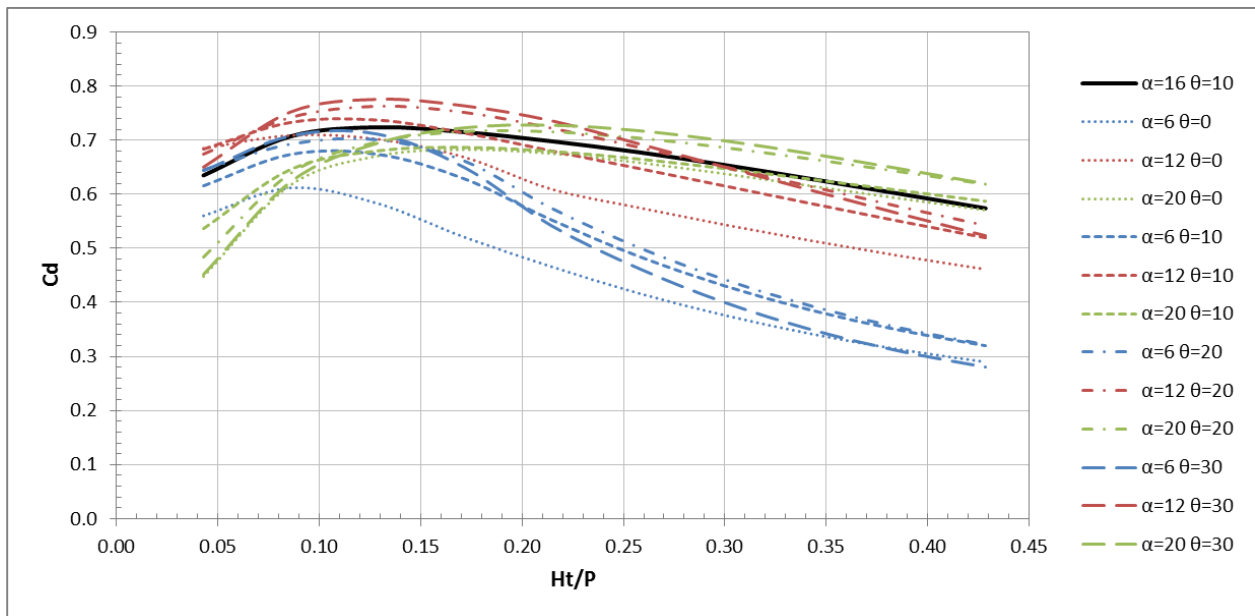
Figure 7. C_d vs H_T/P

4. MODEL VALIDATION

4.1. Physical Model

A physical model was created at the Utah Water Research Laboratory (UWRL) at Utah State University, located in Logan, Utah, to support design efforts of both the service and emergency spillways. The physical model was a 1:45 Froude scale model. The model included a portion of the reservoir, the ogee and labyrinth spillways, and discharge channels. Three separate configurations of the emergency spillway were evaluated with the physical model (See

Figure 8). In each case the design and location of the labyrinth weir remained the same while the design of the downstream spillway chute changed. The initial (baseline) configuration resulted in submergence of the weir at the PMF discharge due to the orientation of the weir to the chute and the relative mild slope downstream of the weir. The submergence was most pronounced along the left side and middle of the weir looking downstream and, to a lesser extent, on the right side. This resulted in a reservoir pool above the target design reservoir pool elevation by about 2 ft. Figure 9 shows the submergence of the weir at the PMF discharge.
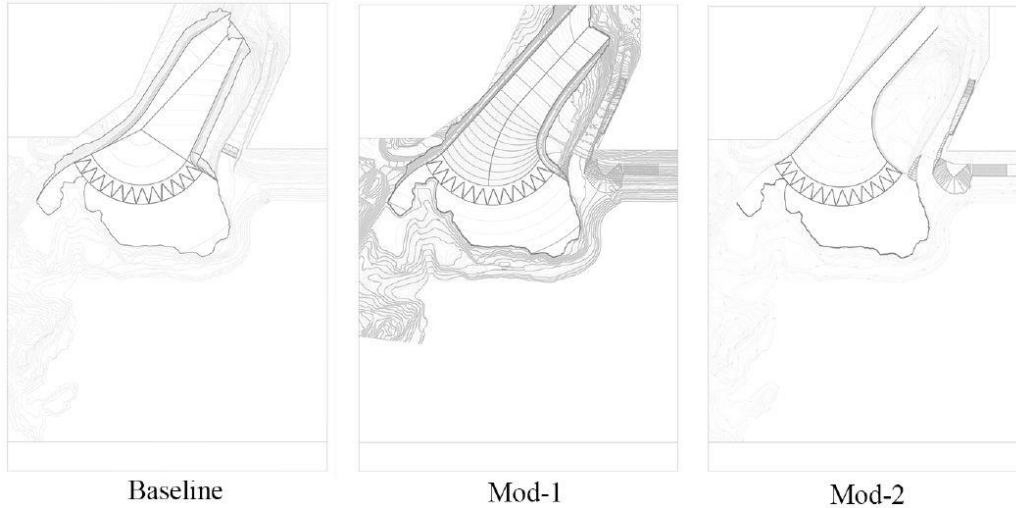
Figure 8. Labyrinth Weir Configurations Tested in the Physical Model Study

Figure 9. Submerged Weir (Baseline Design Configuration)

A subsequent design of the spillway chute (Mod-1 in Figure 8) eliminated the submergence issue by creating a steeper invert slope.

The chute was further optimized with the use of the physical model by narrowing the chute to eliminate an area along the right side of the chute that was not actively conveying flow. The revised design resulted in a significant reduction in channel excavation and cost to the project. This revised design is Mod-2 shown in Figure 8, and the results of the physical model test at the PMF discharge are shown in Figure 10. Note in Figure 10 the lack of submergence on the weir.

Figure 10. Physical Model @ *Q*=506kcfs (PMF Discharge) Final Emergency Spillway Configuration

Additional rating curve data for the labyrinth weir was developed from the physical model. This was done by blocking off the service spillway and only allowing flow over the labyrinth weir. The data points are compared to the theoretical rating curve in Figure 11. There is a good fit between the two data sets; the largest discrepancy is at the lower end of the curve, which is likely due to scale effects from low head on the labyrinth weir crest.
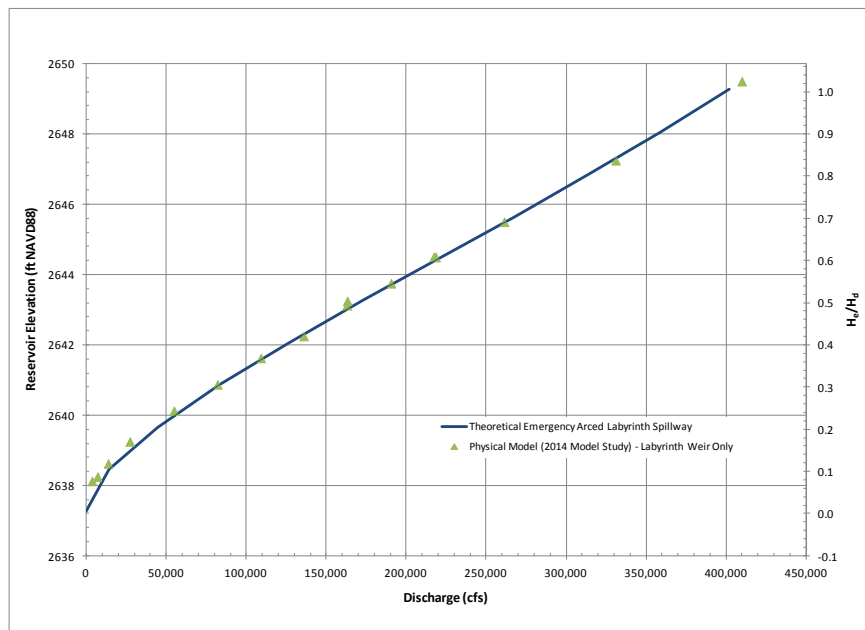
Figure 11. Emergency Arced Labyrinth Spillway Rating Curve

4.2. CFD Model

A series of three-dimensional (3D) computational fluid dynamics (CFD) models of the Isabella Reservoir and spillways was conducted to support the design calculations and physical model. CFD modeling was completed using Star-CCM+, a commercially available software package for 3D modeling applications. The numerical modeling effort focused mainly on the following:

- Verifying the spillway rating curves developed using design equations, which were validated with the physical model.

- Addressing concerns about physical model scale effects and truncation of the forebay in the physical model.
- Providing more hydraulic condition resolution than possible using either the physical model or the 2D numerical model (i.e. flow conditions over Engineer Point, flows down the spillway chutes, etc).

To assure appropriate representation of the labyrinth weir within the various CFD models, a sectional CFD model of a labyrinth spillway was first created to validate against existing physical model studies. The model grid was developed to ensure sufficient resolution in the CFD model; the primary goal was to provide adequate resolution near the weir to accurately resolve the free surface flowing over the weir, resulting in favorable comparisons to physical model measurements. For validation against existing physical model studies, Brian Crookston's work (Crookston 2010) was used as a baseline for the comparison. The CFD model was developed to match the Utah Water Research Laboratory (UWRL) Flume and labyrinth weir geometry so that an appropriate comparison could be made. A comparison of the CFD model results is done through calculation of a discharge coefficient (C_d) from the model output, which is then compared to the physical model results. This comparison is shown in Figure 12. Results generally showed close agreement between the CFD modeling and the laboratory experiments, though there is lesser agreement at lower values of H_T/P.
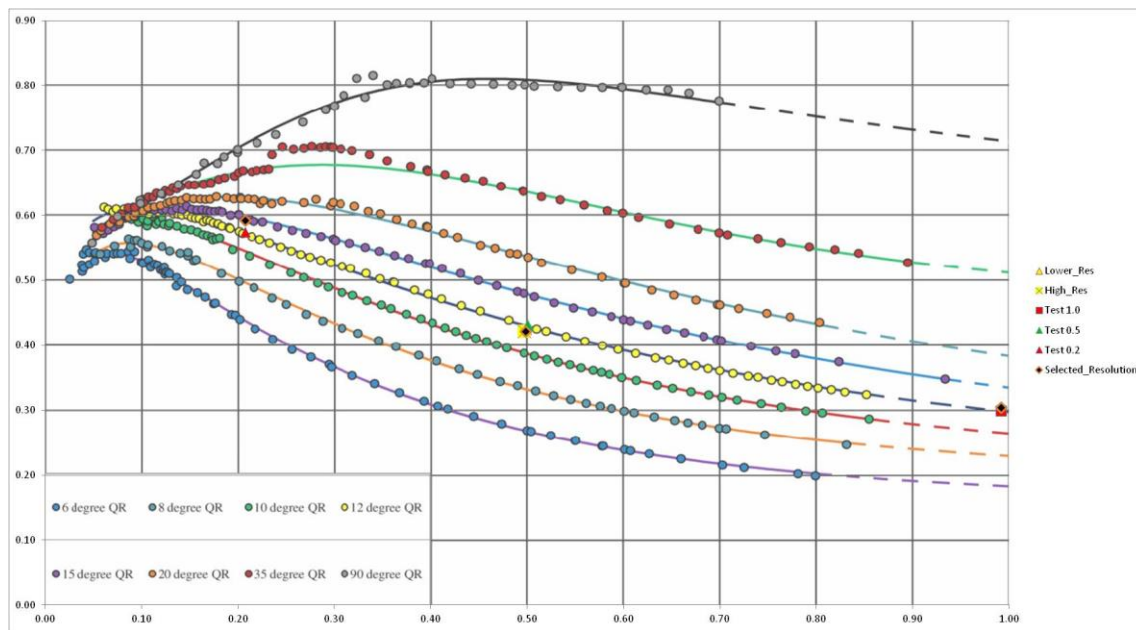
Figure 12. Comparison of CFD Simulations to Physical Model Results (Crookston 2010)

Discharge data for the design labyrinth weir was collected for the emergency spillway and compared to the design data. The comparison is shown in Table The results show very close agreement between the emergency spillway design data and CFD model results.

Table 2. Comparison of Flows for the Emergency Spillway Only

Reservoir Elevation (feet, NAVD88)	Design Data (cfs)	CFD (cfs)	
2637.26	0	0	0
2641.76	115,514	117,054	-1%
2645.26	252,467	246,585	2%
2649.26	402,000	399,845	1%

5. CONCLUSIONS

The new emergency spillway weir for Isabella dam was designed as an arced labyrinth weir. The use of the design procedure and data from Crookston (2010) and Christensen (2012) proved successful in developing the design for a large arced labyrinth weir. The theoretical design based on published information was validated with both physical and CFD numerical modelling.   The spillway chute, in particular, is an important feature because of the potential for submergence due to concentrated flows from the weir in the downstream chute.   For an arced labyrinth weir, the chute must be properly oriented and the invert must be placed at a steep enough slope so that submergence of the weir does not occur for the critical design flows.

6. REFERENCES

Christensen, Nathan A., (2012). "Flow Characteristics of Arced Labyrinth Weirs". Master of Science Thesis, Utah State University, Logan, Utah.

Crookston, Brian M., (2010). "Labyrinth Weirs". All Graduate Theses and Dissertations. Paper 802. Utah State University, Logan, Utah. http://digitalcommons.usu.edu/etd/802.

Continuing Sediment Management at Mount St. Helens: Raising the Spillway of the Sediment Retention Structure

J.P. Britton, P.E., Ph.D.[1], C.J. Nygaard, P.E.[1], and S.J. Schlenker, P.E., Ph.D.[1]
[1]U.S. Army Corps of Engineers
Portland District
Portland, OR 97204
USA
E-mail: Jeremy.p.britton@usace.army.mil

ABSTRACT

The Sediment Retention Structure (SRS) was constructed by the U.S. Army Corps of Engineers (USACE) from 1987 to 1989 to trap sediment eroding from the Mount St. Helens debris avalanche, for the purpose of maintaining flood risk levels downstream in the Cowlitz River. In 1998, the operation of the SRS changed, and the sediment trapping efficiency decreased. The USACE began studies and an alternatives analysis to identify a long-term plan given the current conditions. The studies and alternatives analysis led to a preferred adaptive-management plan including up to three incremental SRS spillway raises to trap more sediment. The first spillway raise was constructed in 2012. The 2.1-m-high structure was constructed using 8,700 cubic meters of Roller Compacted Concrete (RCC). The RCC structure was set back from the original spillway crest to allow room for the subsequent two raises. The primary hydraulic design goals were downstream fish passage and the promotion of a separated and vegetated floodplain terrace in the flat sediment plain above the spillway. The main features of the spillway raise included the RCC structure, a plunge pool, and a channel excavated in rock connecting to the original spillway crest. The RCC structure was designed with a three-tiered crest, and angled RCC sills were constructed on the downstream face to collect and concentrate low flows and to dissipate energy at high flows. The spillway raise has increased the trapping efficiency of the SRS and maintained flood risk levels in the Cowlitz River downstream.

Keywords: Mount St. Helens, Sediment Retention Structure, spillway raise, Roller Compacted Concrete, fish passage.

1. BACKGROUND AND PURPOSE

The 18 May 1980 eruption of Mount St. Helens in Washington State resulted in a debris avalanche of approximately 2.3 billion cubic meters (3 billion cubic yards). Sediments eroding from the avalanche and depositing downstream in the lower Cowlitz River decrease the capacity of the river and increase flood risk for communities with a population of 50,000. In 1985, the U.S. Army Corps of Engineers (USACE), Portland District developed a 50-year plan to manage the sediment and maintain authorized flood risk levels along the Cowlitz River. The main feature of the plan was the Sediment Retention Structure (SRS) on the North Fork Toutle River. The SRS was constructed from 1987 to 1989 for the single purpose of trapping sediment eroding from the Mount St. Helens debris avalanche.

The SRS consists of an earth- and rock-fill embankment dam, an outlet works, and an un-gated spillway excavated in rock. The outlet works is a concrete structure containing six rows of pipes. When all flow passed through the outlet works, the sediment trapping efficiency was about 80 – 90%. The rows of pipes were closed from the bottom up as sediment filled behind the SRS. In 1998, the outlet works pipes were all closed, and all flow passed over the spillway. In this condition, the sediment trapping efficiency dropped to about 30 – 40% and more sediment began to deposit in the Cowlitz River.

The 1985 plan identified dredging in the Cowlitz River as the means to maintain flood risk levels once the SRS became run-of-river (all flow over spillway). Dredging is not as easy today due to development along the river and Endangered Species Act listings. In the late 2000s, the Portland District began studies and an alternatives analysis to identify a new long-term plan.
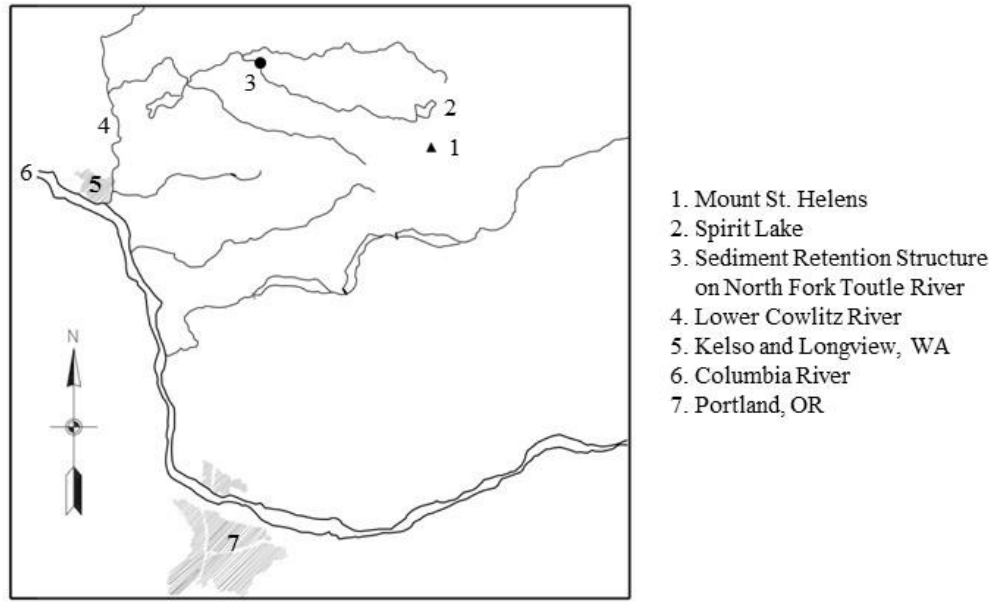
Figure 1. Map of Region (Washington and Oregon, USA)

The purpose of this paper is to describe the design, construction, and performance of the 2012 SRS spillway raise, which was the first implemented action of the new long-term plan for maintaining the authorized flood risk levels in the Cowlitz River. The main purpose of the spillway raise was to trap sediment and reduce sedimentation in the Cowlitz River. Hydraulic design goals for the structure included downstream fish passage and promotion of a separated and vegetated floodplain terrace in the flat sediment plain upstream.

2. A NEW LONG-TERM PLAN

2.1. STUDIES

Five studies played major roles in the alternatives analysis: sediment budget study, debris avalanche erosion rate study, Future Expected Deposition Scenario (FEDS) analysis, mudflows study, and probable maximum flood study.

In the onset of the current planning study for the new long-term plan, The Biedenharn Group, LLC was retained under contract with the Portland District to develop a comprehensive sediment budget for the Toutle River basin. The purpose of the Biedenharn study (Biedenharn Group, LLC 2010) was to present a sediment budget for the basin that identifies the existing watershed sediment sources, pathways of sediment transport, and sinks of temporary sediment storage based on all available data at the time as well as existing basin conditions. The results from this study were used to forecast sediment loads out to 2035.

The sediment budget relies heavily on U.S. Geological Survey (USGS) gages in the Cowlitz River and Toutle River basins, which provide a long-term estimate of the suspended sediment loads. An unbroken data record extends from the present to, in some cases, the early years immediately after the eruption. More recently, hydrosurvey in the lower 32 km (20 mi) of the Cowlitz River has provided a record of sediment deposition since 2009. Light Detection and Ranging (LiDAR) data has added to this information by providing sediment plain deposition and essential information to characterize the persistent sediment loads coming from the debris avalanche.

A relatively high degree of uncertainty still exists regarding future sediment yield from the debris avalanche, both in terms of total yield and variability of yield. The best available scientific analyses of future yield have widely varying conclusions: a near future of persistent high load (Major 2004 and Meadows 2014) or one of continued

decay (USDA 2012). Data collection into the future will be the best (any maybe the only) way to know with certainty how sediment yields from large volcanic debris avalanches mature.

To apply a measure of conservatism in the estimate of future sediment loading, the no-decay assumption was applied to the forecast of future sediment loads from the debris avalanche. However, to respond to the inherent uncertainty in the primary driver of sedimentation in the Cowlitz River (sediment yield from the debris avalanche), an adaptive approach is desirable. Any feasible management strategy should be able to accommodate the conservative sediment input of the adopted approach but would be scalable if significant decay does occur.

The FEDS analysis and report (USACE 2011b) introduced the hydraulic and sediment transport tools used to evaluate performance of alternatives for development of the new long-term sediment management plan. The FEDS approach and models rely on sediment budget inputs to forecast performance into the future. With the suite of models described in the FEDS analysis, it is possible to produce a probabilistic Cowlitz River flood risk performance metric for future conditions with and without alternatives. This probabilistic future performance metric was used to determine if a proposed measure or suite of measures (alternative) is viable in protecting the communities.

Two of the potential measures involved modifying the SRS are raising the entire structure or raising the spillway only. A mudflows study and probable maximum flood (PMF) study were done in order to evaluate these measures.

For design of the SRS in the 1980s, the requirement to pass the Operating Basis Mudflow (OBM) without overtopping the dam was the critical criterion for sizing the spillway and resulted in a height difference between the spillway crest and the dam crest of 18 m (60 ft). The OBM was based on an "intra-episode" eruptive event roughly the size of the June 1980 eruption (a smaller eruption following the main eruption on May 18) occurring at a time of maximum snowpack, as this event represented the largest mudflow event that was considered realistic during the project lifetime. The volume of the OBM was assumed to be 57 million cubic meters (75 million cubic yards). The Portland District now believes that the most appropriate OBM would be a smaller-volume event (USACE 2013). The USGS Cascades Volcano Observatory modeled two new mudflow scenarios: a mudflow caused by failure of the debris avalanche blockage forming Castle Lake (56 million cubic meters) and a mudflow originating in the crater of Mount St. Helens (25 million cubic meters). For both scenarios, the mudflows never reach the SRS (Denlinger 2012). As the mudflows progress downslope, the flows spread out over the sediment plain and into embayments. With this result, the OBM was no longer the controlling criterion for determining the height of the dam above the spillway crest. The controlling criterion was now the PMF.

The recalculation of the PMF is documented in USACE (2011a). The primary reason for reinvestigation was to update the PMF to reflect the most recent hydrometeorological report, HMR No. 57 (Hansen et al. 1994). The HMR is used to calculate the probable maximum precipitation (PMP), which forms the basis of the PMF. During the course of the reinvestigation, all aspects of the PMF calculation were revisited and updated, including the PMP, unit hydrograph, and bulking assumption. The 2011, PMF recalculation effectively reduced the design PMF from 6,030 cubic meters per second (cms) (213,000 cubic feet per second, cfs) to 3,400 cms (120,200 cfs), a 44% reduction in peak flow.

2.2. ALTERNATIVES

The Portland District evaluated several measures for managing sediment. Three alternatives proved capable of maintaining the authorized flood risk levels along the Cowlitz River (USACE 2011b): 1) a single large raise of the SRS, 2) a dredging program in the Cowlitz River, and 3) a phased approach involving three incremental SRS spillway raises followed by the construction of dikes in the sediment plain above the SRS, with dredging in the Cowlitz River on an as-needed basis only. The phased approach was selected as the least costly, most adaptable alternative. The reductions in the OBM and PMF allowed for the SRS spillway to be raised up to 9.1 m (30 ft) without needing to raise the dam crest. Three incremental 3-m (10-ft) spillway raises, built as needed, are desirable to 1) limit the pool above the SRS to optimize sediment trapping efficiency (large pools unnecessarily trap fine sediment that would not deposit in the Cowlitz River) and 2) respond to the remaining uncertainty in future sediment erosion and deposition rates.

The remainder of this paper describes the design, construction, and performance of the first SRS spillway raise.

3. 2012 SEDIMENT RETENTION STRUCTURE SPILLWAY RAISE

The first spillway raise was planned for 2012. A limitation in funding meant that the first spillway raise height could only be 2.1 m (7 ft) instead of the originally planned 3 m (10 ft).

Roller-Compacted Concrete (RCC) was selected for the spillway raises due to its proven performance in the environment and the need for rapid construction. The first flows over the spillway, in the winter of 1995 to 1996, eroded weak/highly fractured rock in the spillway. RCC was used to fill and repair the eroded areas. The RCC has performed well. It has not eroded significantly under the continuous sediment-laden flow over the spillway since 1998. In addition, an advantage of RCC is that it can be placed rapidly. The in-water work window for the North Fork Toutle River was limited to July 1 through October 7.

Figure 2 shows the planned outlines of the three spillway raise increments. The intent is for the slope of the final raise to match the slope of the original spillway (7%). The first two raises have overall downstream slopes of 10% and are positioned such that all three raises share a common upstream face.
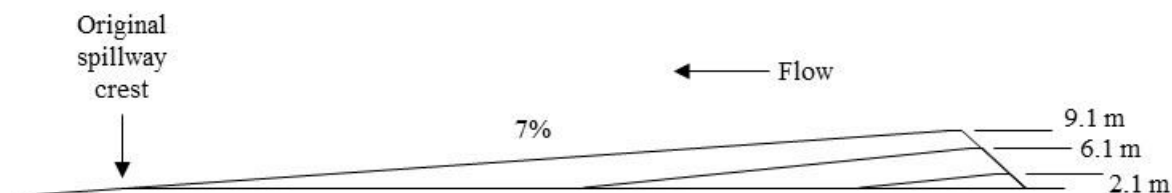
Figure 2. Outlines of three spillway raise increments

3.1. HYDRAULIC GOALS, CRITERIA, AND DESIGN

An advantage of using small, incremental spillway raises is the ability to optimize the sediment trapping efficiency. In terms of downstream sedimentation, equilibrium can be achieved with SRS trapping efficiencies in the 45 to 60% range at current sediment inflow rates. The SRS spillway raise approach increases the spillway elevation approximately 3 m at a time in successive raises. The maximum pool depth is limited by these spillway raises and results in a trapping efficiency close to the desired equilibrium condition. Immediately after construction of the first raise, the observed trapping efficiency was between 60 and 70%. As the small pool fills and the upstream valley slope begins to steepen, the trapping efficiency will to drop toward the pre-raise conditions (approximately 35%). Monitoring of debris avalanche sediment loading and downstream sedimentation trends will inform if an additional spillway raise is needed to maintain flood risk levels.

The progressive drop in overall SRS trapping efficiency expected with incremental spillway raises may take as many as 10 years depending on hydrology and incoming sediment load. Furthermore, if significant decay in avalanche erosion occurs in the intervening period, the trapping efficiency of the SRS required for downstream equilibrium may decrease as well. Monitoring of the hydrology, hydraulics, and sediment trends in the system is critical in making decisions that optimize the performance of the phased construction approach.

One of the design goals of the spillway raise and downstream channel was to provide safe passage of downstream migrating juvenile fish (primarily steelhead and Coho salmon). The chief intent of the juvenile fisheries criteria was to prevent the occurrence of harmful sheet flow and stranding of fish within a 90% duration of the historic discharges during the juvenile fish passage season (primarily April through May). Hydrologic analyses were conducted over a 25-year record (1986-2011). For the two month migration period, a daily flow rate of 15.4 cms (545 cfs) was estimated to be exceeded 95% of the time and defined the low design discharge. The high design

discharge was defined as the 5% exceedance discharge for a full twelve-month period and was determined to be 47.3 cms (1,670 cfs).

Design criteria for the low design discharge required a minimum flow depth of 0.3 m (1 ft) at the thalweg. The low flow channel on the spillway raise was delineated by notch openings between the lowest sills on the crest and between the sills on the 10%-sloped section down to original grade.

Design criteria for the high design discharge required the containment of flow within a channel excavated through the original flat grade that would connect the notched channel from the raised spillway section on the upstream side to the brink of the original 7% spillway grade on the downstream side (Figure 3). This is to prevent overland sheet flow and stranding of fish over the flat grade between the spillway raise section and the 7% grade break at high design discharge.
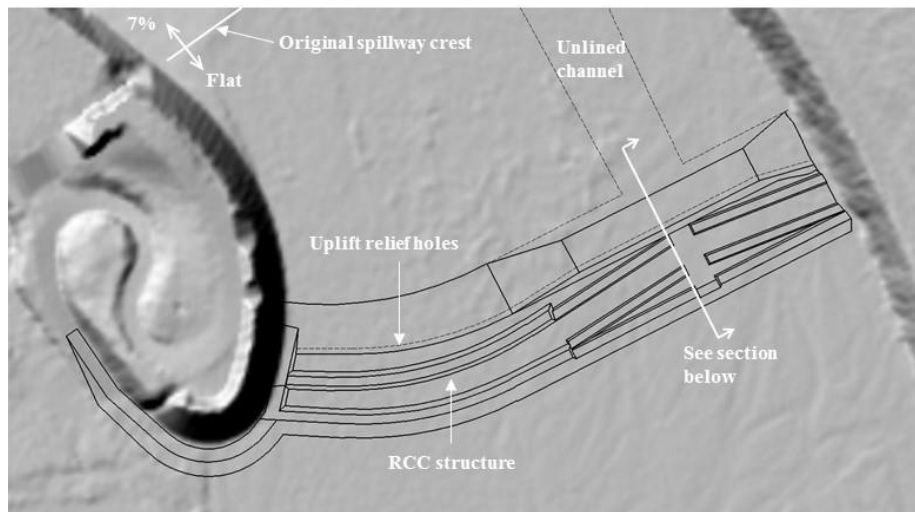
Figure 3. Spillway raise plan
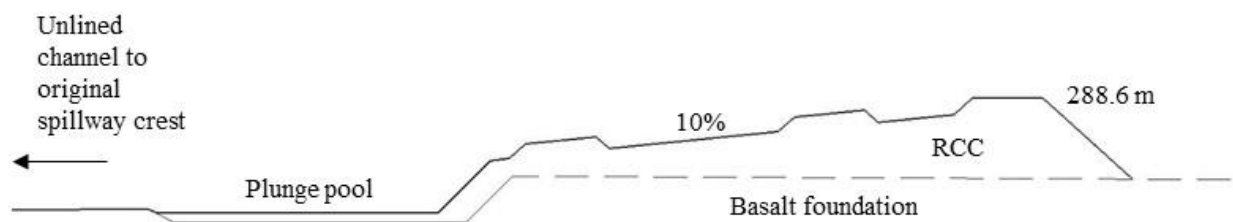
Figure 4. Spillway raise section

The shape of the spillway raise influences the geomorphic response of the sediment plain immediately upstream of the structure. The historic spillway was a flat weir crest approximately 122 m (400 ft) wide. Construction tolerances and surface erosion resulted in flow concentration during low flows, but the overall effect was a very flat flow-stage rating curve between low flow and the 50% annual exceedance probability channel forming flows. This near sheet flow resulted in an upstream morphology with no concentrated flow or deep channel and little opportunity for fluvial deposition that could create distinct floodplain terraces. The resulting landscape in the 500 m upstream of the spillway was an unvegetated, rapidly shifting, and dense network of small braided channels.

The 2012 design increases the relative stage between low and channel forming flow from 1.3 m in the historic condition to 1.9 m in the with-project condition. This was done in an attempt to differentiate between the summer low flow and flood event sediment regimes and promote the development of a separated and vegetated floodplain

terrace. Field evidence from the summer of 2013 (Figure 5) shows the development of proto floodplain and emergence of grasses. While encouraging for long-term revegetation and associated floodplain roughness in the sediment plain, grasses did not emerge in the summer of 2014 for unknown reasons. The USACE will continue to monitor the system for the primary performance metric but will also look for opportunities to improve basic designs like the weir crest shape.

Figure 5. Conditions upstream of SRS spillway raise in summer 2013

The convergence of design concerns regarding upstream geomorphology and downstream juvenile fish passage led to a three-tiered crest. The lower two levels are intended to pass fish within the design juvenile range of low and high flow rates. The crest was shaped to contain the high design juvenile discharge and to assure the flow depth will be at least 0.3 m at low design juvenile discharge. The invert of the 6.1 m (20 ft) wide opening of the low flow channel represents the bottom tier on the crest, which is 1.7 m (5.5 ft) higher than the original crest. The second level is 2.1 m (7 ft) higher than original crest and represents nominal height of the spillway crest raise. The combined opening width of the first and second levels is 76 m (250 ft), which defines the maximum extent of the low flow channel through the crest. The third level is 2.7 m (9 ft) higher than original grade and is set strictly on the left side of the crest to reduce the concentration of unit discharge adjacent to the dam abutment. The low flow channel is on the right side of the crest to draw the concentrated flow away from the abutment. The full width of the raised spillway crest is about 165 m (540 ft). Because the raised spillway was placed upstream of the original crest, the new spillway crest is 35% wider than the original crest, which increases flow capacity. A schematic of an upstream view of the crest is shown in Figure 6 along with computed pool levels for various flow rates.

Comparative rating curves for the raised and original spillway crests are shown in Figure 7. Due to the three-tiered configuration of the raised spillway, the new rating curve is steeper than the original at lower (normal) flow rates, whereas the larger opening width leads to a flatter rating curve at the flood discharges. The rating curve for the ultimate 9.1 m (30 ft) spillway raise is also shown and illustrates that the PMF will not encroach upon freeboard in spite of the ultimate spillway raise. This is because the PMF has been revised downward, as is described above.
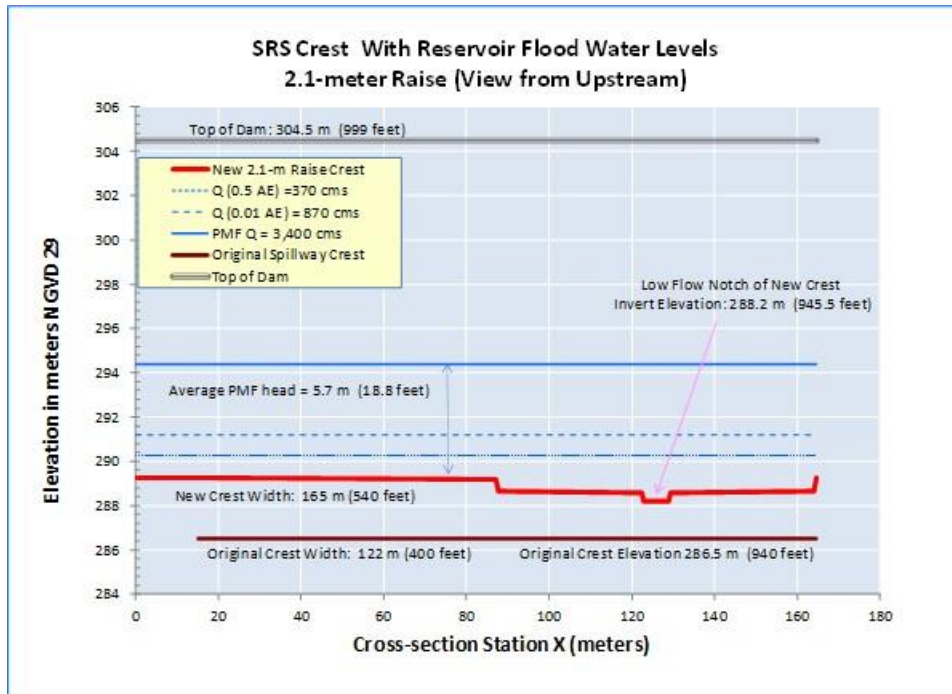
Figure 6. SRS 2.1 m spillway crest shape (exaggerated vertical scale)
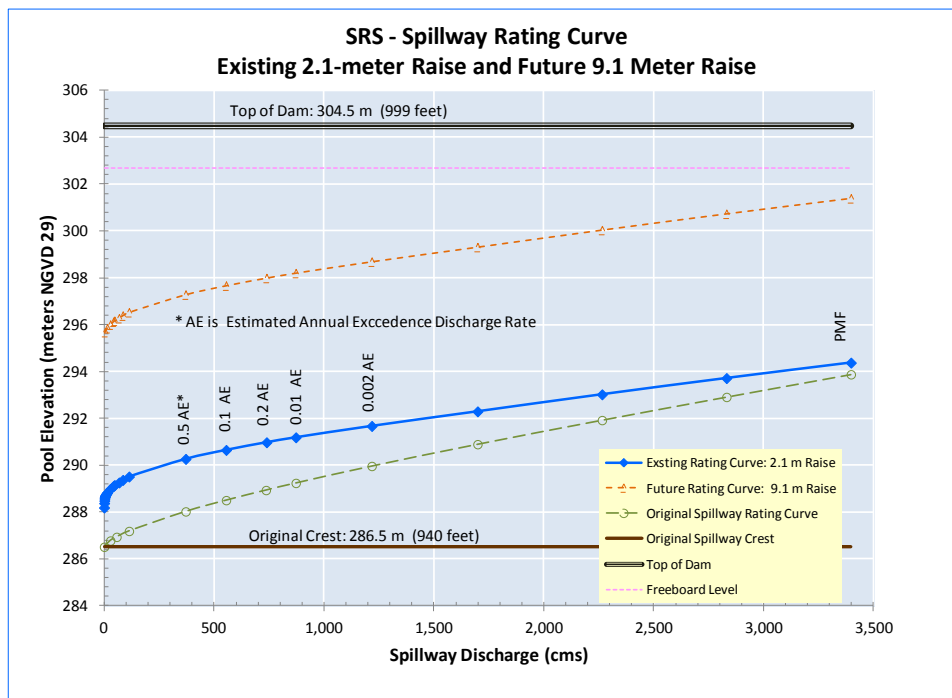
Figure 7. SRS spillway rating curves

The spillway channel downstream of the crest is comprised of three features: RCC sloped section with RCC sills, plunge pool for collecting juvenile fish, and excavated channel to the edge of the original 7% grade (Figure 4).

Downstream of the crest, the RCC slopes 10% from the crest invert elevation of the low flow channel down to the existing grade. The approximate stream length of the sloping RCC section is 26 m (85 ft.) To slow the flow during low discharges and to dissipate energy at high discharges, two rows of sills were added to the 10%-sloped surface downstream of the crest. The opening widths match the widths on the crest. The sills are angled slightly down the slope (10:1 lateral to slope distance) so that when flow subsides, any residual fish and sediment will drain along the toe of the sills towards the low flow channel. When discharge ramps up, the flow will expand from inside-out from the low flow channel. Most juvenile fish and larger sediments will remain entrained in the more concentrated flow in the center.

At the downstream end of the sloped RCC section, flow contained by the low flow channel is collected by a 91 m (300 ft) wide plunge pool. Excess discharge above high juvenile design flow will bypass the plunge pool and flow overland over unchanged horizontal original grade. The plunge pool is needed as a collector of flow below high juvenile design and as a transition to the excavated channel.

The excavated channel connects the plunge pool to the brink of the original 7% spillway grade. The purpose of the excavated channel is to safely and swiftly convey fish without stranding. The channel has a trapezoidal shape with bottom width of 12 m (40 ft) and 2:1 horizontal to vertical side slopes. The minimum excavation depth is 1.7 m (5.5 ft) at the upstream end, and the maximum excavation depth is about 3 m (10 ft), as the channel thalweg is sloped at 1% grade. The channel contains the high design juvenile discharge, and the flow depth exceeds the minimum required depth at the low design discharge. Channel velocities will range between 1.2 m/s (4.0 ft/s) at low design discharge to 2.2 m/s (7.2 ft/s) at high design discharge. Where the flow reaches the edge of the original spillway crest, the channel connects to an existing natural channel that had previously been eroded into the rock during past spillway usage.

3.2. CONSTRUCTION

The spillway raise contract was awarded to LKE Corporation for $4.5 million in July 2012. River diversion was accomplished in two phases. In phase one, the river was diverted to the left side of the existing spillway—through 10 culverts beneath a temporary access road—while the right side of the RCC structure was constructed behind a cofferdam. In phase two (Figure 8), the river was diverted through the low flow channel of the RCC structure while the left side of the RCC structure was constructed behind a cofferdam. The work was performed during late summer when flows in the river are at their lowest.

The contractor placed a total of 8,700 cubic meters (11,400 cubic yards) of RCC on twelve days within a nineteen day period. The RCC 90-day strength was specified to be 31 MPa (4,500 psi) for durability against the erosive sediment-laden flows. Figure 9 shows the completed structure.

Figure 8. SRS spillway raise during construction

Figure 9. Completed spillway raise, 17 October 2012

3.3. PERFORMANCE

The 2012, the SRS spillway crest raise has proved highly effective in increasing the trapping efficiency of the SRS and preventing problematic deposition in the lower Cowlitz. The USACE has collected LiDAR data of the sediment plain as well as bathymetry in the lower Cowlitz for 2013 and 2014 following the crest raise. The USACE has further funded the USGS to collect suspended sediment samples in the Toutle River downstream of the SRS. Analysis of this data, along with field observation of the sediment plain, demonstrates performance of the project. The small, still-water pool created upstream of the spillway by the crest raise was filled with sediment during the first winter following construction. Despite the obvious loss of the pool due to filling with sediment, the crest raise effectively decreases the valley slope upstream of the spillway, decreasing sediment transport capacity in the reach. This decrease in transport capacity is the fundamental long-term action. Data shows that the trapping efficiency of the SRS has been increased to the mid 60% range following construction: 67% in water year 2013 and 63% in 2014. These are the highest two values observed in the system since post-outlet-works-shutdown data collection began in 2002 (Figure 10).

Hydrosurvey further shows that net erosion occurred in the lower 32 km (20 mi) of the Cowlitz River in both water years 2013 and 2014. These successive years of net erosion are the first years of credible data that indicate a change in the depositional trend since 2003. With deposition in the lower Cowlitz and its associated effects on flood protection as the primary driver for USACE involvement, the transition of the lower Cowlitz from depositional to erosional due to the SRS spillway crest raise is a great success for the project and USACE.

4. CONCLUSIONS

The new long-term plan for maintaining flood risk levels in the Cowlitz River is a phased approach beginning with three incremental SRS spillway raises. The purpose of the spillway raises is to trap sediment and reduce sedimentation in the Cowlitz River. The first spillway raise, constructed in 2012, was effective in increasing the trapping efficiency of the SRS and maintaining the authorized flood risk levels. RCC proved to be a viable material and should be used for the next two spillway raises. The 2012, spillway raise met the downstream fish passage design goals. More time is needed to monitor the development of a separated and vegetated floodplain terrace in the sediment plain above the spillway raise.
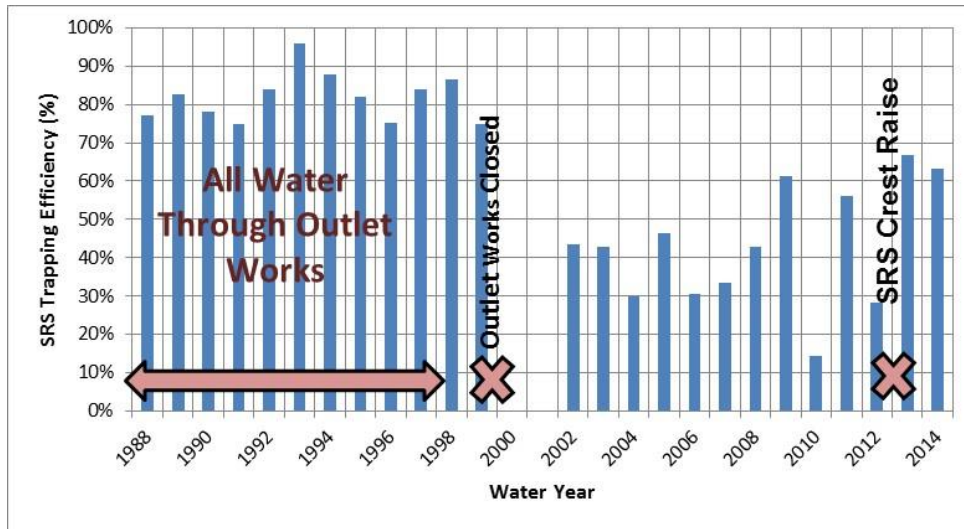
Figure 10. SRS trapping efficiency over time

5. REFERENCES

Biedenharn Group, LLC (2010). "Toutle/Cowlitz River Sediment Budget." Report for the U.S. Army Corps of Engineers, Portland District.

Denlinger, R.P. (2012). "Effects of Catastrophic Floods and Debris Flows on the Sediment Retention Structure, North Fork Toutle River, Washington." U.S. Geological Survey Open-File Report 2011–1317.

Hansen, E.M., Fenn, D.D., Corrigan, P., Vogel, J.L., Schreiner, L.C., and Stodt, R.W. (1994). "Hydrometeorological Report No. 57." National Weather Service, Silver Spring, MD.

Major, J.J. (2004). "Post-eruption suspended sediment transport at Mount St. Helens: Decadal-scale relationships with landscape adjustments and river discharges." Journal of Geophysical Research, 109, 1-22.

Meadows, T. (2014). "Forecasting Long-Term Sediment Yield from the Upper North Fork Toutle River, Mount St. Helens, USA." University of Nottingham Doctor of Philosophy Thesis.

USACE (2011a). "Development of the PMF for the SRS." Portland District, Portland, OR.

USACE (2011b). "Mount St. Helens Future Expected Deposition Scenario (FEDS)." Portland District, Portland, OR.

USACE (2013). "Mount St. Helens, Washington, Design Documentation Report No. 16, Sediment Retention Structure 7-foot Spillway Raise." Portland District, Portland, OR.

USDA (2012). "Analysis of Long-Term Sediment Loadings from the Upper North Fork Toutle River System, Mount St. Helens, Washington." National Sedimentation Laboratory Technical Paper No. 77.

Effect of a Deflector Aerator on Stepped Spillway Flow

S. Terrier[1], M. Pfister[1] and A.J. Schleiss[1]
[1]Laboratory of Hydraulic Constructions (LCH)
École polytechnique fédérale de Lausanne (EPFL)
Station 18, CH-1015 Lausanne
Switzerland
E-mail: stephane.terrier@epfl.ch

ABSTRACT

Systematic physical model tests are performed on a stepped spillway equipped with a bottom aerator at the beginning of the stepped part. A deflector is used to issue a jet in order to initiate air entrainment into the flow. A horizontal slot located in the vertical face of the first step allows for air supply underneath the flow. The cavity subpressure was measured to ensure optimal aerator performance, namely atmospheric pressure conditions. The air discharge entrained below the jet is measured to derive the aerator air entrainment coefficient. The local air concentrations are spatially measured downstream of the aerator at regularly spaced profiles, allowing the investigation of air transport and detrainment as well as the average and bottom air concentrations. The present paper focuses on the resulting spatial distribution of air concentration for five deflector geometries. The chute angle, step height, approach flow Froude number, and approach flow depth were kept constant so that the differences occur mostly on the jet length and air entrainment coefficient. The flow depth and the air concentration rapidly converge towards quasi-uniform flow values downstream of the aerator.

Keywords: aerator, air concentration, air entrainment, cavitation, deflector, stepped spillway

1. INTRODUCTION

Chute aerators are installed to prevent cavitation damages, and they were studied in detail on *smooth* bottom spillways in terms of global air entrainment coefficient (Koschitzky 1987; Chanson 1988; Rutschmann 1988; Skripalle 1994; Kökpinar and Göğüş 2002) as well as streamwise air transport (Kramer 2004; Pfister 2008).

In parallel, *stepped* spillways have become widespread in the past decades. Research has shown that stepped spillways may be endangered by cavitation even more than smooth spillways, particularly for high, specific discharges. The most critical location is just upstream of the self-aeration at the inception point, with already high velocities. Pressure investigations on the upper part of the vertical face of steps showed that a flow velocity higher than 15 m/s could cause cavitation, which would limit the specific discharge to $q = 14$ m^2/s for a chute angle $\varphi = 51.3$ ° and a step height $s = 1.2$ m (Amador et al. 2009). Using acoustic measurements in a reduced ambient pressure facility, a critical cavitation index $\sigma_c = 0.3$–0.4 was obtained for a chute angle $\varphi = 21.8$ ° and $\sigma_c = 0.60$–0.65 for $\varphi = 68.2$ ° (Frizell et al. 2013). This is significantly higher than the critical value of $\sigma_c = 0.2$ for smooth chutes (Falvey 1990) and leads to specific discharges around $q = 15$ m/s at the inception point (Pfister and Boes 2014). As a consequence, besides issues of energy dissipation, the specific discharge of stepped spillways is usually limited to lower values than on smooth spillways. In order to overcome that limitation, flow aeration – mainly at the beginning of the chute – is necessary. However, Chanson (2015) questions the increased cavitation risk on stepped chutes.

Until now, only preliminary studies exist for the design of such aerators. Stepped chute aerators were first studied by Pfister et al. (2006a; b) and Schiess Zamora et al. (2008) for fixed aerator geometries, and only the discharge was varied. A comparison of smooth and stepped chute aerators was presented by Terrier et al. (2015).

2. PHYSICAL MODEL TESTS

Tests were performed on a physical model at the Laboratory of Hydraulic Constructions of EPFL. The channel has a streamwise length of 8.0 m, a width of 0.5 m, and an adjustable bottom angle φ (Figure 1). A jetbox generates the transition between the pressurized flow of the water supply system to a free surface flow in the channel. Unlike a standard ogee, it allows the independent variation of the approach flow depth h_o and Froude number $F_o = u_o/(gh_o)^{0.5}$, with u_o = approach flow velocity and g = gravity acceleration. Unit discharges up to $q = 0.486$ m²/s are supplied. At the exit of the jetbox, the channel bottom is smooth for 0.47 m. Thereafter, sixty steps with a height of $s = 0.06$ m follow. The step height can be halved by adding inserts. The transition point between the two bottom surfaces is the origin of the coordinates x and z.

The aerator is located at the transition between the smooth and the stepped bottom. It consists of a deflector and an air supply system providing air into the first step. There is no offset between the upper smooth chute bottom and the pseudo-bottom of the stepped chute. The deflector is characterized by its angle α and its height t. The deflector lip is located at the coordinate $x = 0$. Air is supplied to the nappe below the jet through a 0.02 m high transversal slot in the vertical face of the first step. An airtight chamber with wide dimensions to avoid head losses – which would influence the jet length – is feeding the nappe. Air enters the chamber through a circular duct.
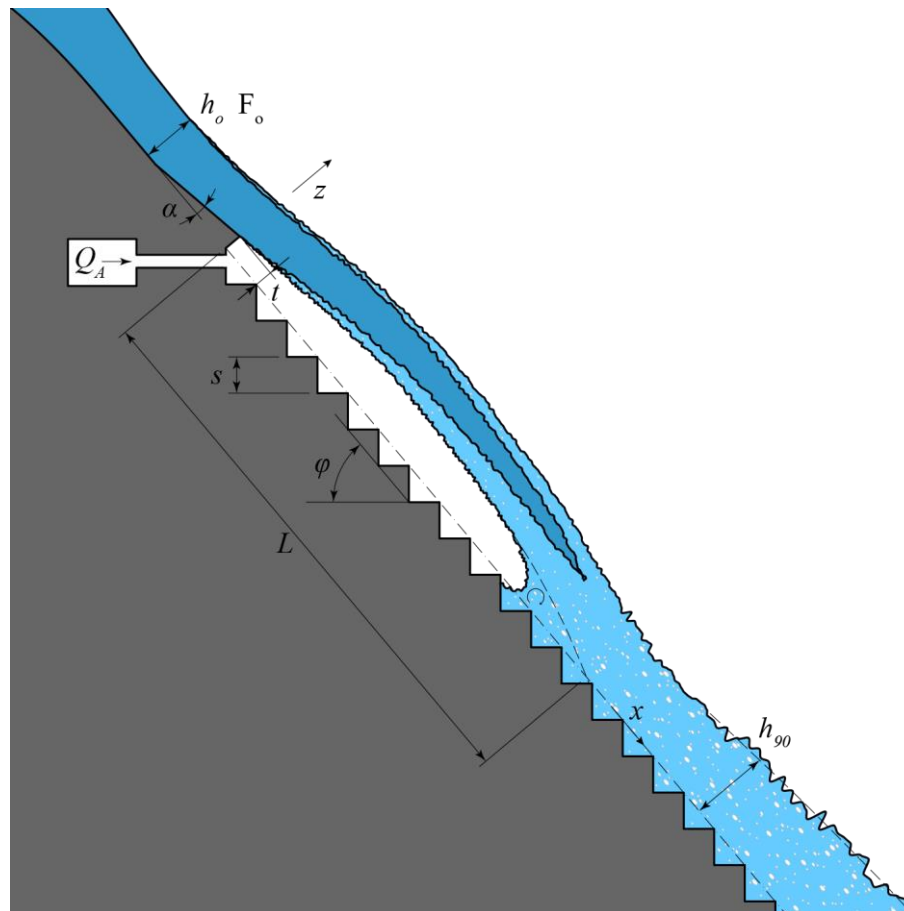
Figure 1. Definition sketch: approach flow depth h_o, approach flow Froude number F_o, deflector angle α, deflector height t, chute angle φ , step height s, jet length L and flow depth h_{90}

The air velocity is measured in the center of the air duct with a thermoelectric anemometer (Schiltknecht, Switzerland). The air discharge q_A is calculated by integrating the logarithmic velocity profile after verifying that the flow is turbulent in the air duct. A dual-tip fiber optical probe (RBI Instrumentation, France) is used to measure local

air concentrations in the flow. It is based on the different refraction index between air and water phases and uses a sampling rate of 1 MHz. The probe is fixed on an automatic positioning system that allows movement along the streamwise axis x and the depth axis z. Profiles are measured along the channel at regularly spaced intervals. A profile consists of 25 points, each measured during 20 s. All profiles start at a step edge with the closest point at $z \approx$ 0.003 m. A U-shaped glass manometer is used to measure the air cavity subpressure Δp and verify that it does not affect the jet or the air entrainment. The effect of subpressure remains small if $\Delta p/h_o < 0.10$ (Tan 1984; Chanson 1988; Rutschmann 1988; Pfister 2011), and this criteria was satisfied with a maximum subpressure $\Delta p/h_o = 0.03$.

To systematically investigate stepped spillways aerators, six parameters are varied: the chute parameters φ and s, the flow parameters F_o and h_o, and the deflector parameter α and t (Figure 1). References tests without an aerator are performed to assess the relative effect of the aerator compared to the situation without an aerator. The results of the reference tests are similar to the stepped spillways literature. Herein, only the variation of the deflector parameters is presented (Table 1). The other parameters were kept constant with $\varphi = 30\,°$, $s = 0.06$ m, $F_o = 5.5$, and $h_o = 0.075$ m.

Two-phase flows are sensitive to scale effects. Under the Froude similitude, the viscous force represented by the Reynolds number $R_o = u_o h_o/\nu$ is underestimated, and the surface tension force represented by the Weber number $W_o^{0.5} = u_o/(\sigma_w/\rho h_o)^{0.5}$ is overestimated, with ν = kinematic viscosity, σ_w = surface tension, and ρ = density. The tests presented herein all have the same approach flow condition with $R_o = 3.5 \cdot 10^5$ and $W_o = 153$, which respects the recommendations to limit scale effects related to the air concentration (Pfister and Chanson 2014).

Table 1 – Deflector geometry of the tests presented given, the deflector angle α, deflector height t, as well as he measured jet length L, air entrainment coefficient $\beta = q_A/q$ and cavity subpressure $\Delta p/h_o$

Test	α [°]	t [m]	L [m]	β [-]	$\Delta p/h_o$
R	-	-	-	-	-
A15	9.46	0.015	0.86	0.080	0.01
A30	9.46	0.030	1.22	0.124	0.01
B15	14.04	0.015	1.23	0.127	0.01
B30	14.04	0.030	1.63	0.160	0.01
B45	14.04	0.045	1.85	0.193	0.03

3. RESULTS

3.1. General Observations and Water Depth

Figure 2 shows photos of the upper channel half. The smooth bottom reach and the deflector can be seen on the left; the jetbox is outside of the picture. The reference test shows a progressive roughening of the surface without air entrainment in the first part. The surface inception point occurs shortly after the start of the stepped part near the 8th step. The streamwise position of the inception point oscillates with time. Downstream of the latter, the flow becomes white and aerated. The surface is irregular, and some spray is visible.

Aerated tests reveal that both jet surfaces become white and, thus, aerated. The jet has a regular and stable trajectory. Downstream of the impact, some spray with irregular splashing is visible. The splashing can reach the height of the jet.

The spatial air concentration field reveals the amount of air entrained (Figure 3). Apparent "steps" in the jet results from the interpolation code and are not physically based. This applies also for the sudden increase and decrease of concentration in the jet core at $x = 1.35$ for tests B30 and B45. The reference test indicates a surface inception at $x \approx$ 1.0 m, with a high increase of air entrainment close to the surface but much slower at the bottom.

For aerated tests, the thickness of the jet blackwater core progressively decreases with the length, and an air concentration of $C > 0.10$ is rapidly attained. A rapid evolution of air concentration occurs at the jet impact. The bottom air concentration decreases as a result of the impact pressure. Tests A30, B15, and B30 show a kind of bottom roller before the jet impact. Downstream of the impact, there is a gradual variation of the air concentration tending to equilibrium. The spray previously observed is not detected.

The flow depth z_{90} is defined by the depth where $C = 0.90$. For the reference test, z_{90} gradually increases as the flow becomes progressively aerated (Figure 4). Surface inception – at $x \approx 1$ m – causes a higher increase in the flow depth before it stabilizes at a value of $z_{90} = 0.111$ m. The jet lifts the water surface of the aerated tests in the first part of the channel. The depth at the impact is highly similar to the depth of the reference test at the same location. Downstream of the impact, the water level is stable at a level similar to the reference test. There is a slight oscillation of the surface, which is particularly apparent for tests B30 and B45 with the longer jets. The flow depth at the end of the channel is consistent with the value of 0.114 m according to Boes and Hager (2003).
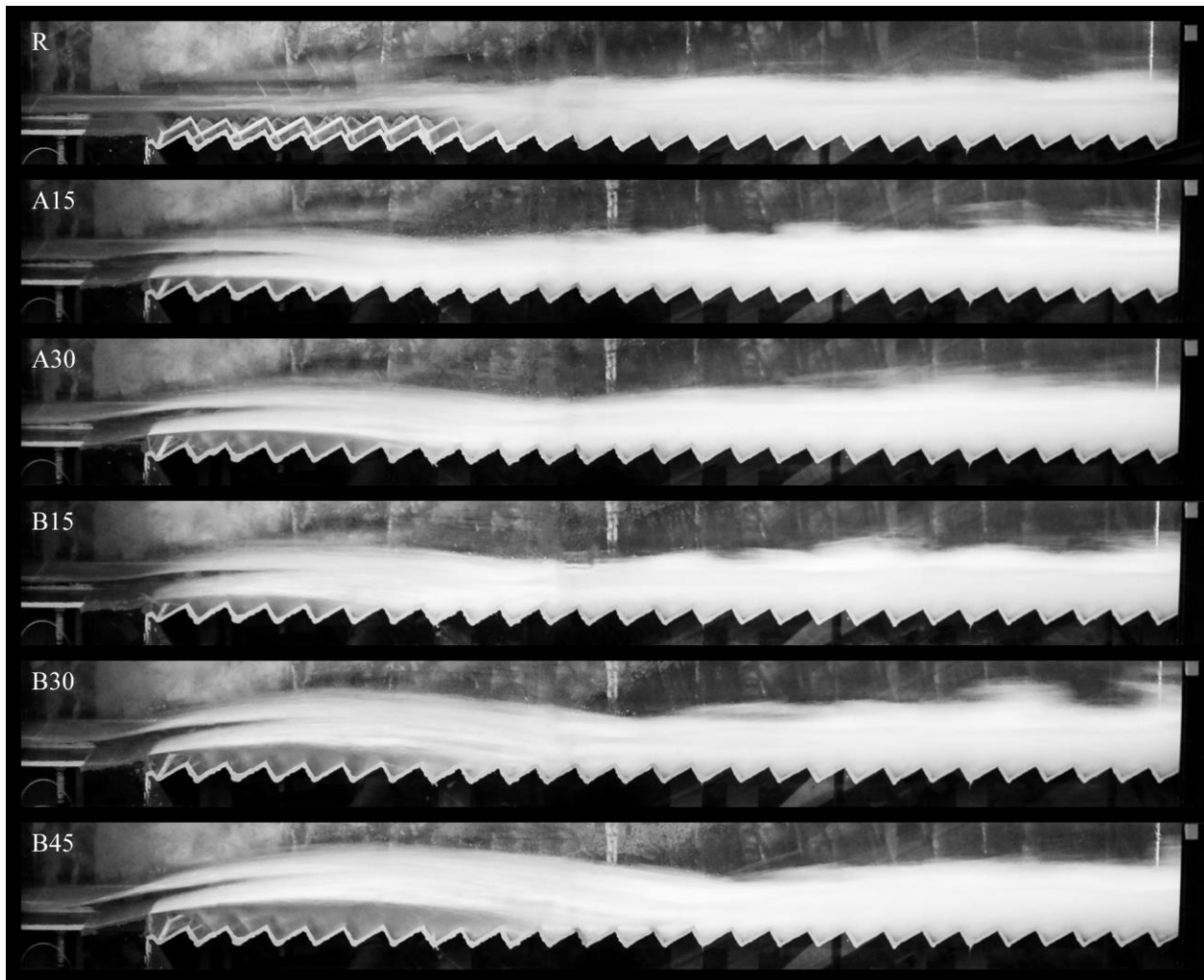
Figure 2. Photos of the upper channel flow for reference test R without aerator, and tests A15, A30, B15, B30, and B45 with aerator (cf. Table 1)
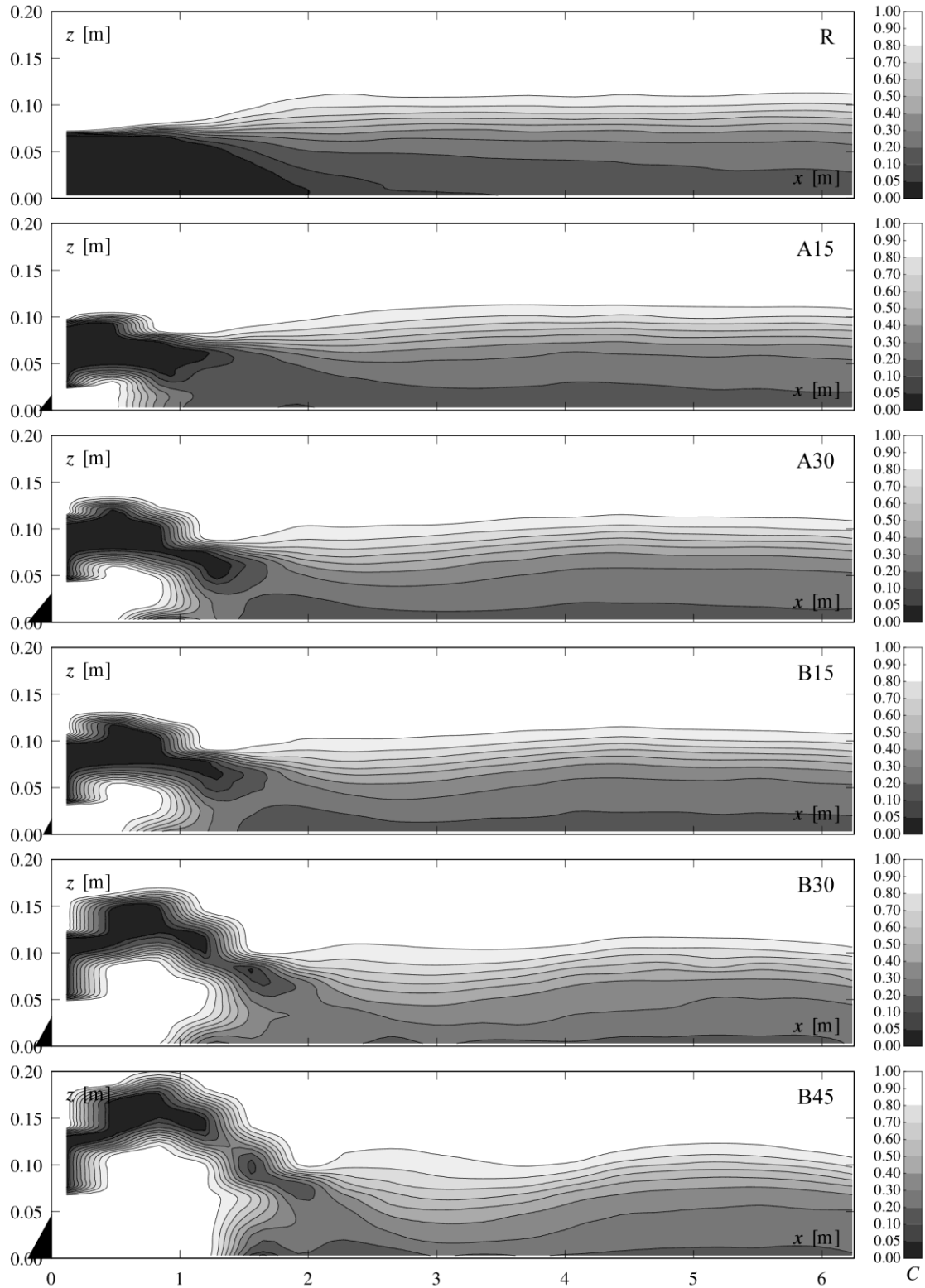
Figure 3. Contour plots of the air concentration $C(x, z)$ for reference test R without aerator, and tests A15, A30, B15, B30, and B45 with aerator (cf. Table 1)
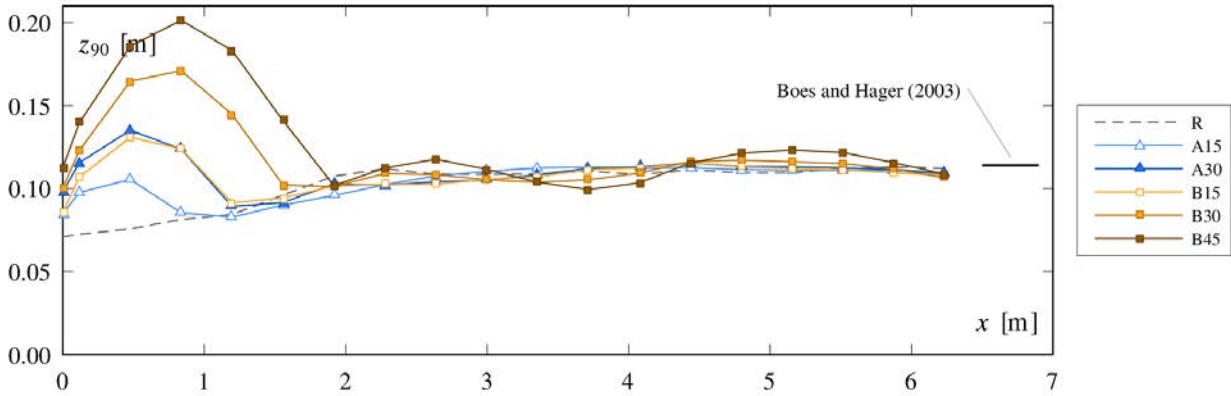
Figure 4. Water surface elevation z_{90} for the performed tests compared with uniform flow value from Boes and Hager (2003) (cf. Table 1 for test characteristics)

3.2. Air Entrainment Coefficient

The air entrainment coefficient $\beta = q_A/q$ increases with the deflector angle α and the deflector height t. This effect is directly linked to the increase of the jet length L (Figure 5). The relation $\beta = 0.0076L/h_o$ ($r^2 = 0.983$) is only valid for the specific φ, F_o and h_o tested herein and with negligible cavity subpressure. Deflector A30 and B15 coincidentally have about the same jet length and, therefore, a similar air entrainment coefficient.
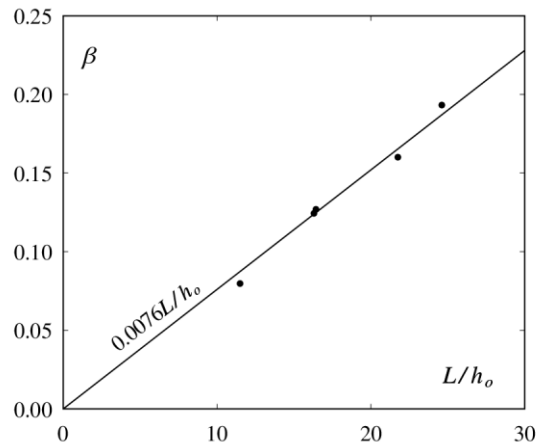
Figure 5. Air entrainment coefficient β as a function of the relative jet length L/h_o

3.3. Average Air Concentration

The average air concentration C_a is obtained by integrating the local air concentration from the bottom to z_{90} (lower surface z_{90} instead of the bottom for the jet) according to the definition of Straub and Anderson (1958). The streamwise development of C_a is shown in Figure 6. The value $C_a > 0$ at $x = 0$ m is due to the pronounced concentration gradient at the surface and the measurement technique. The average air concentration is obtained by integrating the air concentration profile with a linear interpolation between the measured points. This artificially adds air close to the surface. For aerated tests, there are two surfaces, and, therefore, the initial C_a is twice the value of the reference test R.

The development of the average air concentration in the jet is nearly identical for all aerated tests. The value decreases to a minimum at around $x = L$. The decrease is negligible for test A15, but the profile spacing might not be

able to accurately detect the maximum attained in the jet or the minimum at the jet impact. Then, the average air concentration increases again and reaches a maximum. This maximum is linked to the reflection of the jet on the steps. Series A and B both show an increase of the maximum with the increase of the deflector height t. The maximum also increases with the deflector angle α. Finally, the average air concentration stabilizes for all tests and converges to $C_a \approx 0.40$.

The uniform flow average air concentration for stepped chutes is the same as for smooth chutes (Boes 2000; Matos 2000). The values attained at the end of the channel compare well to Hager (1991), Chanson (1993), and Wilhelms and Gulliver (2005). A good agreement is also found for the indirect relation of Boes and Hager (2003) for stepped chutes, as suggested by Matos (2005).
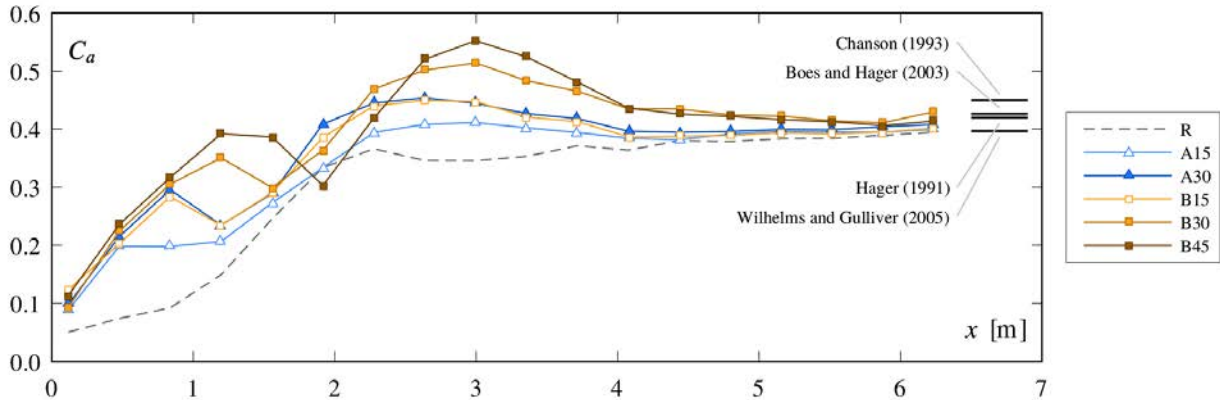
Figure 6. Average streamwise air concentration C_a development for the performed tests compared with uniform flow values according to different authors (cf. Table 1 for test characteristics)

3.4. Bottom Air Concentration

To protect the chute against cavitation, a bottom concentration above some percent is required where cavitation potentially occurs (Peterka 1953; Rasmussen 1956; Russell and Sheehan 1974). For the reference test R, the bottom inception point defined by $C_b = 0.01$ occurs at $x = 1.52$ m (Figure 7). The bottom air concentration then increases and reaches a value around $C_b = 0.15$ at the end of the channel.
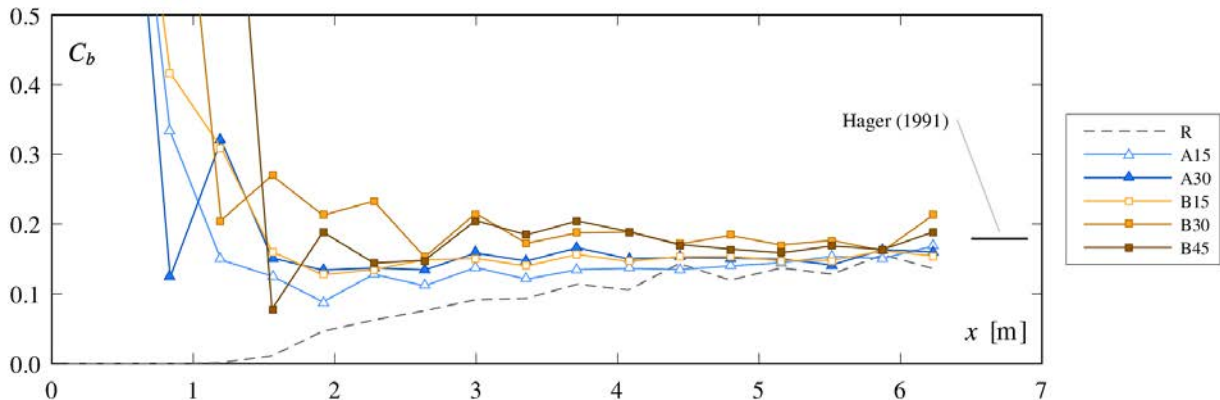
Figure 7. Streamwise bottom air concentration C_b development for the performed tests compared with uniform flow value for smooth chute (Hager 1991) (cf. Table 1 for test characteristics)

Tests with an aerator all follow the same trend, with a streamwise offset due to different jet lengths. At the beginning, while the flow is lifted off the bottom, the bottom air concentration is by definition $C_b = 1$ (air). The bottom air concentration rapidly decreases at the jet impact as water is encountered. Immediately before the impact, a minimum occurs – especially for tests A30 and B45 – as the roller is encountered. The roller velocity is low comparted to the jet velocity, and air is rapidly detrained as a consequence of the low turbulence. No cavitation can occur here due to the low velocity. For tests A15 and B15, there is no distinctive roller drop, which can be explained by a smaller roller or the absence of a profile in the roller. After the jet impact, the bottom air concentration rapidly attains an almost constant value. This value appears to be proportional to the jet length, as longer jets have a higher average air concentration. All tests then converge to a value around $C_b = 0.16$ at the end of the channel. It is interesting to note that C_b is close from the uniform flow value of $C_b = 0.18$ predicted by Hager (1991) for smooth chutes.

The good agreement of z_{90}, C_a and C_b with respective uniform flow values indicates that quasi-uniform flow state was reached at the end of the channel.

3.5. Air Concentration Profiles

Air concentration profiles in the middle ($x = 3$ m) and at the end ($x = 6.24$ m) of the channel are compared in Figure 8. In the middle of the channel, there is more air entrained for longer jets as previously observed for the air entrainment coefficient. At the end of the channel, all the profiles are nearly identical, with some differences close to the bottom.

The profile of test A15 changes very little between $x = 3.00$ m and $x = 6.24$ m, with some slight air detrainment on the upper half. This indicates that the reference test entrains more air towards the bottom on the second half of the channel, while tests A30, B15, B30, and B45 are subject to detrainment on the whole depth of the profile. Above the surface ($Z > 1$) for $x = 3.00$ m, tests B30 and B45 have a lower concentration, revealing that at this location there is more spray.
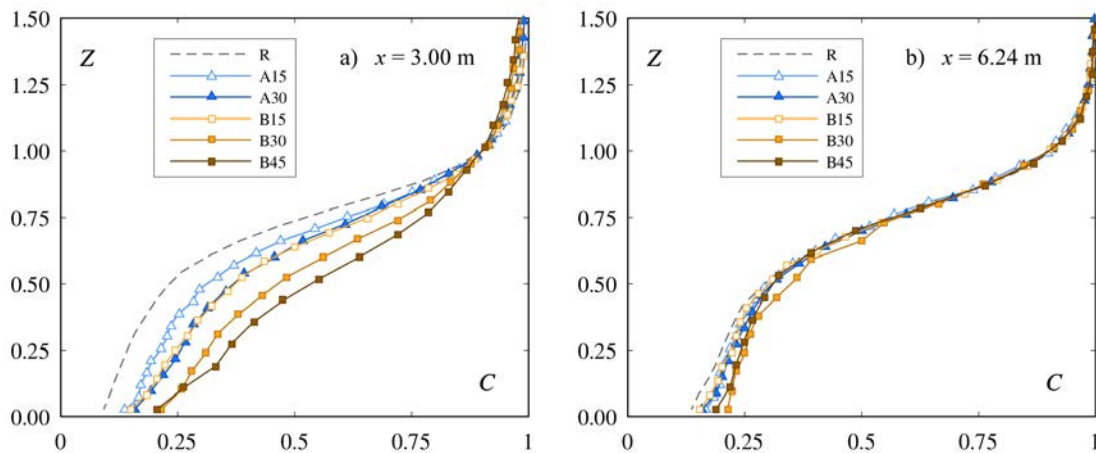
Figure 8. Air concentration profiles with $Z = z/z_{90}$ (cf. Table 1 for test characteristics)

4. CONCLUSIONS

An aerator consisting of a deflector and an air duct was placed at the transition between a smooth bottom chute and a stepped chute (end of ogee crest on a dam). Different deflector geometries as well as a reference set-up without aerator were tested for identical flow and chute conditions. Besides the jet, the surface perturbations downstream are small, and the jet impact generates spray. Quasi-uniform flow conditions are attained after $x \approx 3–5L$.

The major difference between the deflectors tested is the jet length, which has a direct and linear influence on the air entrainment coefficient β. After the jet impact, the bottom air concentration is close to or above the uniform flow value. Note that the minimum deflector angle tested was $\alpha = 9.46\,°$, and a flatter deflector might lead to smaller bottom air concentration. The bottom air concentration is above a few percent as recommended to protect against cavitation damages.

The smallest deflector, A15 with $\alpha = 9.46\,°$ and $t/h_o = 0.2$, shows an adequate air entrainment rapidly tending to uniform flow with minimal surface perturbation. Steeper or higher deflectors entrain more air that is rapidly detrained after the jet impact. Deflector A15 is an optimal deflector for the specific conditions tested (chute angle $\varphi = 50\,°$, step height of $s/h_o = 0.8$, and approach flow Froude number $F_o = 5.5$). Other chute or flow parameters were not presented in this paper and change the effect of the deflector geometry.

5. ACKNOWLEDGMENTS

6. REFERENCES

Amador, A., Sánchez-Juny, M., and Dolz, J. (2009). "Developing flow region and pressure fluctuations on steeply sloping stepped spillways." *Journal of Hydraulic Engineering*, 135(12), 1092–1100.

Boes, R. M. (2000). *Zweiphasenströmung und Energieumsetzung an Grosskaskaden*. VAW Mitteilungen 166, ETH Zürich.

Boes, R. M., and Hager, W. H. (2003). "Hydraulic design of stepped spillways." *Journal of Hydraulic Engineering*, 129(9), 671–679.

Chanson, H. (1988). "Study of air entrainment and aeration devices on a spillway model." University of Canterbury, New Zealand.

Chanson, H. (1993). "Self-aerated flows on chutes and spillways." *Journal of Hydraulic Engineering*, 119(2), 220–243.

Chanson, H. (2015). "Discussion of 'Cavitation potential of flow on stepped spillways' by K. Warren Frizell, F. M. Renna, and J. Matos." *Journal of Hydraulic Engineering*, 141(5), 07014025.

Falvey, H. T. (1990). *Cavitation in chutes and spillways*. Engineering monographs 42, U.S. Dept. of the Interior, Bureau of Reclamation, Denver, Colorado.

Frizell, K. W., Renna, F. M., and Matos, J. (2013). "Cavitation potential of flow on stepped spillways." *Journal of Hydraulic Engineering*, 139(6), 630–636.

Hager, W. H. (1991). "Uniform aerated chute flow." *Journal of Hydraulic Engineering*, 117(4), 528–533.

Kökpinar, M. A., and Göğüş, M. (2002). "High-speed jet flows over spillway aerators." *Canadian Journal of Civil Engineering*, 29(6), 885–898.

Koschitzky, H.-P. (1987). *Dimensionierungskonzept für Sohlbelüfter in Schussrinnen zur Vermeidung von Kavitationsschäden*. Mitteilung 65, Institut für Wasserbau, TU Stuttgart.

Kramer, K. (2004). *Development of aerated chute flow*. VAW Mitteilungen 183, ETH Zürich.

Matos, J. (2000). "Discussion of 'Characteristics of skimming flow over stepped spillways' by M. R. Chamani and N. Rajaratnam." *Journal of Hydraulic Engineering*, 126(11), 865–869.

Matos, J. (2005). "Discussion of 'Hydraulic design of stepped spillways' by R. M. Boes and W. H. Hager." *Journal of Hydraulic Engineering*, 131(6), 525–527.

Peterka, A. J. (1953). "The effect of entrained air on cavitation pitting." *Proc.*, *Minnesota International Hydraulic Convention*, ASCE, New York, Minneapolis, 507–518.

Pfister, M. (2008). *Schussrinnenbelüfter Lufttransport ausgelöst durch interne Abflussstruktur*. VAW Mitteilungen 203, ETH Zürich.

Pfister, M. (2011). "Chute aerators: steep deflectors and cavity subpressure." *Journal of Hydraulic Engineering*, 137(10), 1208–1215.

Pfister, M., and Boes, R. (2014). "Discussion of 'Skimming, nonaerated flow on stepped spillways over roller compacted concrete dams' by I. Meireles, F. Renna, J. Matos, and F. Bombardelli." *Journal of Hydraulic Engineering*, 140(10), 07014012.

Pfister, M., and Chanson, H. (2014). "Two-phase air-water flows: Scale effects in physical modeling." *Journal of Hydrodynamics, Ser. B*, 26(2), 291–298.

Pfister, M., Hager, W. H., and Minor, H.-E. (2006a). "Bottom aeration of stepped spillways." *Journal of Hydraulic Engineering*, 132(8), 850–853.

Pfister, M., Hager, W. H., and Minor, H.-E. (2006b). "Stepped chutes: Pre-aeration and spray reduction." *International Journal of Multiphase Flow*, 32(2), 269–284.

Rasmussen, R. E. H. (1956). "Some experiments on cavitation erosion in water mixed with air." *Proc.*, *International Symposium on Cavitation in Hydrodynamics*, National Physical Laboratory, London, 1–25.

Russell, S. O., and Sheehan, G. J. (1974). "Effect of entrained air on cavitation damage." *Canadian Journal of Civil Engineering*, 1(1), 97–107.

Rutschmann, P. (1988). *Belüftungseinbauten in Schussrinnen*. VAW Mitteilungen 97, ETH Zürich.

Schiess Zamora, A., Pfister, M., Hager, W. H., and Minor, H.-E. (2008). "Hydraulic performance of step aerator." *Journal of Hydraulic Engineering*, 134(2), 127–134.

Skripalle, J. (1994). *Zwangsbelüftung von Hochgeschwindigkeitsströmungen an zurückspringenden Stufen im Wasserbau*. Mitteilung 124, Technische Universität, Berlin, Germany.

Straub, L. G., and Anderson, A. G. (1958). "Self-aerated flow in open channels." *Journal of the Hydraulics Division*, 84(7), 456–486.

Tan, T. P. (1984). *Model Studies of Aerators on Spillways*. Research report 84-6, University of Canterbury, Christchurch, New Zealand.

Terrier, S., Pfister, M., and Schleiss, A. J. (2015). "Comparison of chute aerator effect on stepped and smooth spillways." *Proc.*, *36th IAHR Congress*, The Hague, The Netherlands.

Wilhelms, S. C., and Gulliver, J. S. (2005). "Bubbles and waves description of self-aerated spillway flow." *Journal of Hydraulic Research*, 43(5), 522–531.

Training of River Mouths of the Kerala Coast in India

V. Sundar[1] and S.A. Sannasiraj[1]
Dept. of Ocean Engineering
Indian Institute of Technology Madras
Chennai
India
E-mail: vsundar@iitm.ac.in, sasraj@iitm.ac.in

ABSTRACT

The coastal regions of Kerala are mostly dynamic in nature and is accentuated as the result of various developmental activities taking place along the coastline. Choking of river mouths and sandbar formation is a persistent perennial problem occurring in the tropical states of the Indian sub-continent during non-monsoon seasons. Predominant sediment transport is attributed as a major reason for this occurrence. Critical locations along the Kerala coast were identified to be Cheruvathur, Korapuzha, and Chettuvai. Training of river mouths was identified as the long-term solution for the aforementioned problem, and, hence, the same were proposed for construction after carrying out a detailed study by adopting numerical modeling techniques. The magnitude and direction of the net sediment drift was evaluated. The patterns of shoreline changes corresponding to the proposed training walls were assessed. Wave transformation studies for typical monthly wave climate were performed to analyze the phase and amplitude variation in the presence of proposed structures. The detailed analysis of the results from the numerical model that were analyzed are presented and discussed in this paper. Post implementation of the proposed training walls, desirable effects were yielded.

Keywords: Training wall, Sandbar formation, Long shore sediment transport, Numerical modeling.

1.   INTRODUCTION

Sandbar formation and chocking of river mouths is one of the most commonly occurring phenomena along the south west coast of India, particularly along the Kerala coast. Herein, the shoreline changes are dynamic in nature, which has resulted due to several developmental activities taking place along the coast. Also, the population distribution is comparatively denser in close proximity to the sea shore because the local population is mostly reliant on fishing related activities. The river mouths along Cheruvathur, Korapuzha, and Chettuvai were identified to undergo severe choking and predominant sandbar formation, preventing the ease of flow of river stream water into the ocean. The main objective of this paper is to discuss the proposed training of river mouths at Cheruvathur and to highlight a similar study at Korapuzha and Chettuvai along the coast of Kerala.

2.   DESCRIPTION ABOUT THE STUDY AREA

Cheruvathur is a coastal town is located at 13˚13'N and 75˚7'60'' E along the south west coast of India. The Chandragiri river flows through this town and eventually drains into the Arabian Sea. The site experiences a predominant net southerly drift of sediment transport, resulting in sandbar formation at the confluence of the river and Arabian Sea. This necessitated a detailed study on suitable remedial to prevent the sandbar formation and to establish a smooth flow of water from the river into the Ocean. The proposed measure should also beneficially satisfy the needs of the fishermen community, where it could also alleviate maneuvering problems of fishing boats.

3. LITTORAL DRIFT ESTIMATE

From visual observation and the by the experience of the local departments, the site was identified to undergo a net southerly drift of sediment transport. However, to devise an efficient plan and design, both magnitude and the direction of the net drift had to be estimated. Therefore, the distribution of longshore currents across the surf zone and the monthly sediment transport estimate based on energy flux method has been predicted using Komar (1969), CERC (1984), and by integrating the distribution across the surf zone (Komar, 1976).

4. NUMERICAL MODEL FOR WAVE TRANSFORMATION

The combined refraction-diffraction equation that describes the propagation of periodic, small amplitude surface gravity waves over an arbitrarily varying mild sloped sea bed according to (Berkhoff, 1972), and also discussed by Li (1994), is

$$\nabla . CCg \nabla \varphi + \frac{Cg}{C} \sigma^2 \varphi = 0 \tag{1}$$

where φ - Complex velocity potential
       σ - Angular wave frequency
       C - Phase celerity and
       Cg - Group celerity.

The above equation is transformed into a Helmholtz equation of the form,

$$\nabla^2 \phi + K^2(x, y)\phi = 0 \tag{2}$$

using the following relations

$$\phi = \varphi(CCg)^{0.5} \ and \ K^2 = k^2 - \frac{\nabla^2(CCg)^{0.5}}{(CCg)^{0.5}} \tag{3}$$

where k = wave number
       K and ϕ are modified wave number and Wave potential function

A finite difference scheme is employed for the numerical discretization of Helmholtz equation. The derivatives are approximated using centered difference scheme. Writing the discretized form of the Eq. for each grid in the domain and applying suitable boundary conditions, the system of resulting algebraic equations can be written in matrix form as

$$A\phi = f \tag{4}$$

Where 'A' is the coefficient matrix, ϕ is the nodal values of velocity potential, and f is a vector obtained from the boundary conditions. The numerical solution of the above system of equations is arrived using generalized conjugate gradient method. The method successively estimates new approximations to the solution, considering the direction of residual error vector, till the prescribed accuracy is achieved. The offshore boundary is modelled as an open boundary in which case-only incident waves and reflected waves are allowed to propagate. The lateral boundary as well as the shore is considered to absorb the wave energy. The groins or any other obstruction is treated as partially reflecting boundaries by prescribing the reflecting coefficients. The model requires the wave characteristics (viz. wave height, wave period, and direction) and the water depths at all the grid points. It also requires the location of the groins. The model gives the wave characteristics inside the domain. The Department of Ocean Engineering, IIT Madras has developed numerical models on the diffraction-refraction of waves due to the presence of near-shore structures. The model is developed using the mild slope equation because of its generality in dealing with complex wave fields. The mild slope equation is solved by generalized conjugate gradient method as it has a fast convergence rate.

5. SHORELINE EVOLUTION MODEL

5.1. Prediction of Offshore Boundary Data

Snell's law (also known as Snell-Descrates law and the law of refraction) that governs the wave refraction is given by

$$\frac{\sin \theta_0}{\sin \theta} = \frac{C_0}{C}$$ (5)

where, C_0 is the deep water wave celerity (deep water wave length $Lo = 1.56\ T2$) and C is the wave celerity. The angle conventions for the seabed contours, as well as for the wave direction used for the numerical model are shown in Figure.1.
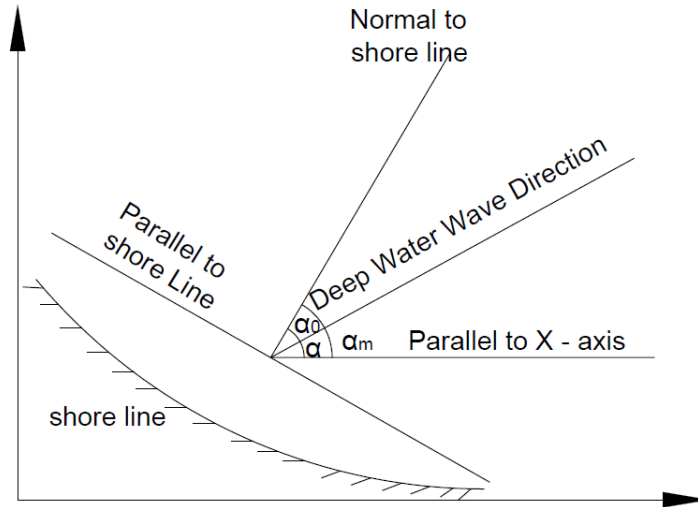
Figure 1. Angle conventions used in the numerical model.

The deep-water wave angles were converted to that corresponding to shallow waters through the Snell's law, taking into consideration of the inclination of shoreline with respect to geographic North. These shallow water wave angles were then expressed with reference to shore normal according to the angles conventions employed in the present numerical model. The conservation of energy while the wave propagates from deep to shallow waters is adopted to obtain the wave height at shallow water depth, i.e., the offshore boundary for the wave transformation model.

There are several configurations of coastal protection structures with respect to the shoreline, among which structures normal to the shore are most common. The construction of a shore-connected structure often leads to changes in the shoreline. This warrants a study on the shoreline due to presence of the shore-connected structures. Such a study is very much essential in planning stage, so as to assess the impact of shore connected structures on the adjacent shoreline. Numerical models offer the capability to study the effect of the wave characteristics, structure dimensions and other associated parameters in providing reasonable estimates of the shoreline response. When a structure is constructed normal to the shoreline, it will intercept the free passage of longshore sediment transport, resulting in an imbalance in the quantity of sediment in the near shore, especially near the structure. This leads to accretion on the up drift side and erosion on the down drift side of the structure. The Department of Ocean Engineering, IIT Madras has developed numerical models on the prediction of shoreline changes due to the presence of near-shore structures.

5.2. Mathematical Formulation

KRAUS and HARIKAI (1983) proposed a numerical scheme to solve the one-line model using Crank Nicholson implicit finite difference method. The non-dimensional equation of shoreline is written as

$$y^*_{n,t^*+1} = B\left\{Q^*_{n,t^*+1} - Q^*_{n+1,t^*+1}\right\} + C_n \tag{6}$$

where,

$$B = \frac{\delta t^*}{2 \times \delta x^*} \ and \ C_n = B\left\{Q^*_{n,t^*} - Q^*_{n+1,t^*} + 2\delta x^* q^*_{n,t^*}\right\} + y^*_{n,t^*}$$

The non-dimensional shoreline is divided into 'n' grid points at equal non-dimensional interval, δx^*. Then shoreline changes over a non-dimensional time, δt^* is calculated using Crank-Nicholson finite difference scheme.

In this method, Q^* at the time interval ($t^* +1$) is expressed in terms of the shoreline co-ordinate of y^*, first isolating the term involving α_{sp} (angle of shoreline normal to x-axis) using trigonometric identities. One of the term involving α_{sp} is then expressed as first order quantities in y^* at time step (t^*+1).

$$Q^* = K_D^2 \cos(\alpha_o) \sin(\alpha_b) \tag{7}$$

where, $\alpha_o = \alpha - \alpha_{sp}$ and α is wave direction with respect to x-axis. The elliptical form of mild slope equation, which deals with combined refraction diffraction is defined as

$$Q^* = K_D^2 \cos(\alpha - \alpha_{sp}) \sin(\alpha_b)$$

$$Q^* = K_D^2 \sin(\alpha_b) \left\{\cos(\alpha)\sin(\alpha_{sp}) \cot(\alpha_{sp}) + \sin(\alpha) \sin(\alpha_{sp})\right\} \tag{8}$$

$$Q^* = E_n \left\{y_{n-1,t^*+1} - y^*_{n,t^*+1}\right\} + F_n$$

where,

$$E_n = K_D^2 \left\{\cos(\alpha)\sin(\alpha_{sp,t^*})\sin(\alpha_{b,t^*})\right\}/\delta x^* \ and \ F_n = K_D^2 \left\{\sin(\alpha_{sp,t^*})\sin(\alpha_{b,t^*})\right\}$$

Substituting the above equations gives the final equation, as given below:

$$BE_n Q^*_{n-1,t^*+1} - (1 + 2BE_n)Q^*_{n,t^*+1} + BE_n Q^*_{n+1,t^*+1} = E_n[C_n - C_{n-1}] - F_n \tag{9}$$

The above equations represent a set of (N-1) linear equation for (N-1) unknowns. The end values are specified as boundary conditions, that is, $Q^*_1 = 0$ and $Q^*_{N+1} = Q^*_N$. The above equation results into a tridiagonal form, which is solved for Q^*. This process is repeated for the entire duration, and any non-dimensional quantity is converted into real quantities using the corresponding scale factors. The program has been validated with published results. The coastal line is discretized into number of grids with an equal spacing of 10m. The co-ordinates of the existing shoreline were provided. The length of the structure and grain size of the sediments required for the calculation of active depth of the sediment transport and water depth at the tip of the structure are the inputs given to the model. In addition to these, the monthly wave characteristics and the number of years over which the shoreline change is desired to be mentioned. The output shows the predicted shoreline changes after a period of 1, 5, 10, 15, 20, and 25 years. The upstream of the structures shows advancement of the shoreline position, while, the downstream end shows the erosion.

6. RESULTS AND DISCUSSIONS

6.1. Cheruvathur

The site understudy has an existing pair of jetties in the north and south of the Mandakara creek, and after a detailed study and analysis, a pair of training walls were proposed to be constructed such that the creek remains open and the tidal inlets enters the basin thereby promoting ease of flow from the stream into the sea and also avoiding sandbar formation. Figure 2 shows the layout- of proposed training walls. Figure 3 shows the location map of the site before and after the construction of training walls.
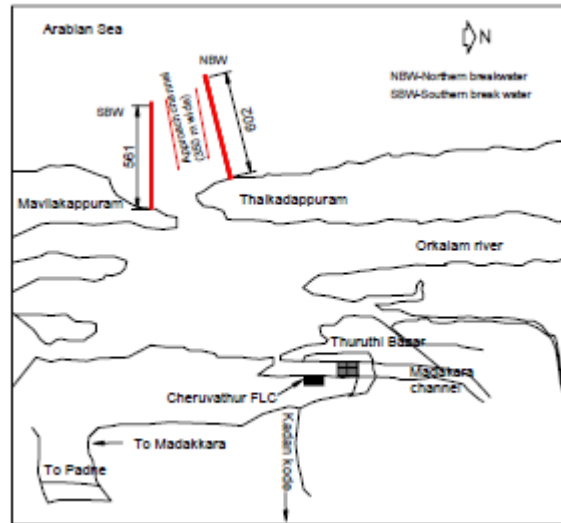
Figure 2. Layout of the proposed training wall

Figure 3. Google earth imagery of Cheruvathur

6.2. Littoral Drift and Shoreline Evolution

The wave data from NIO wave atlas (Chandramohan *et al.,* 1990) has been analyzed to obtain the average wave height, wave period and wave direction, from which the average breaking wave characteristics were derived. Table 1 show the monthly predominant deep water wave direction and Table 2 provides the wave characteristics used for

tranquility studies. The results indicate that the mean breaker height varies from about 0.9 to 1.9m. The breaker height is observed to be a maximum of the order of 1.76m and 1.94m during the months of June and July respectively. The wave direction is towards north only during the months of May and June, whereas, for all other months it is towards the south. The net sediment transport from the above three methods was computed to be in the order of 0.6×10^6 cu.m/yr. Figure 4 shows the monthly sediment transport rate at Cheruvathur.

<table>
<tr><td colspan="2">Table 1. Monthly predominant wave climate</td><td colspan="4">Table 2. Wave characteristics for tranquility studies</td></tr>
<tr><td>Month</td><td>θ_o (deg)</td><td>Month</td><td>H_{avg} (m)</td><td>T (s)</td><td>θ (deg)</td></tr>
<tr><td>January</td><td>300 –360</td><td>January</td><td>1.25</td><td>6.5</td><td>-36</td></tr>
<tr><td>February</td><td>300-360</td><td>February</td><td>1.25</td><td>6.5</td><td>-36</td></tr>
<tr><td>March</td><td>300-360</td><td>March</td><td>1.25</td><td>6.5</td><td>-36</td></tr>
<tr><td>April</td><td>270-360</td><td>April</td><td>1.25</td><td>6.5</td><td>-20</td></tr>
<tr><td>May</td><td>230-320</td><td>May</td><td>2.5</td><td>7.5</td><td>6</td></tr>
<tr><td>June</td><td>230-300</td><td>June</td><td>2.5</td><td>7.5</td><td>6</td></tr>
<tr><td>July</td><td>250-290</td><td>July</td><td>2.75</td><td>7.5</td><td>-6</td></tr>
<tr><td>August</td><td>250-290</td><td>August</td><td>2</td><td>7.5</td><td>-6</td></tr>
<tr><td>September</td><td>280-300</td><td>September</td><td>1.75</td><td>6.5</td><td>-26</td></tr>
<tr><td>October</td><td>260-310</td><td>October</td><td>1.25</td><td>6.5</td><td>-13.5</td></tr>
<tr><td>November</td><td>340-360</td><td>November</td><td>1.25</td><td>6.5</td><td>-42</td></tr>
<tr><td>December</td><td>340-360</td><td>December</td><td>1.25</td><td>6.5</td><td>-42</td></tr>
</table>

Where H_{avg} - Average wave height; T - Wave period; θ - Wave angle with respect to shore normal
θ_o – Deep water wave direction with respect to geographic North
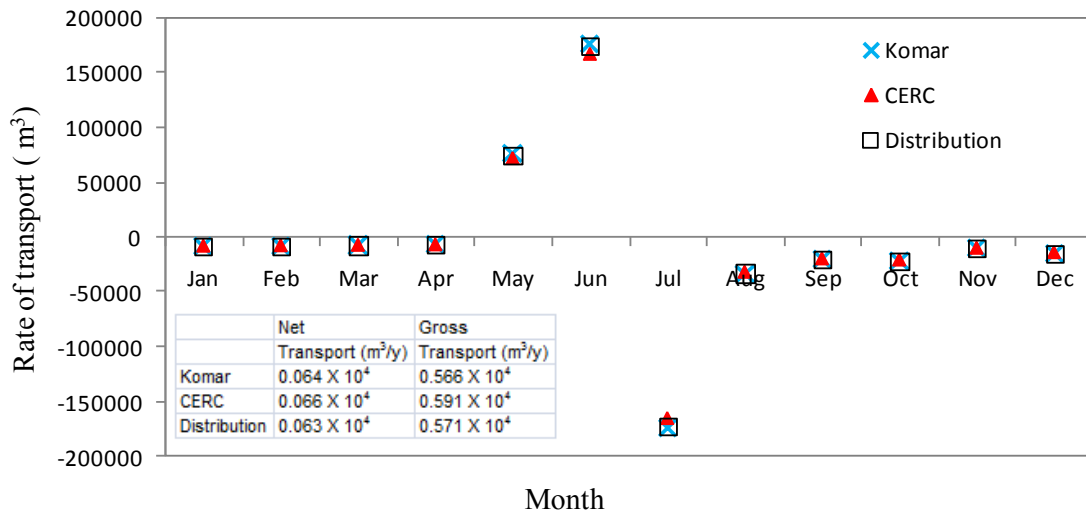
Figure 4. Monthly sediment transport rate at Cheruvathur

The numerical model to predict the shoreline evolution due to the shore-connected structures has been used to predict the shoreline changes due to the proposed training walls. The numerical model has run for finally

recommended layout, discussed under section 6.5. The grain size (*D50*) is 0.25mm. The wave characteristics given as the input to the numerical model are as per Table 2. The length of the training wall, water depth at the end of the breakwater, and the present status of the shore are given as the input to the numerical model. The numerical model has run for the mean wave heights for different months, and the corresponding shoreline changes are shown in Figure 5.
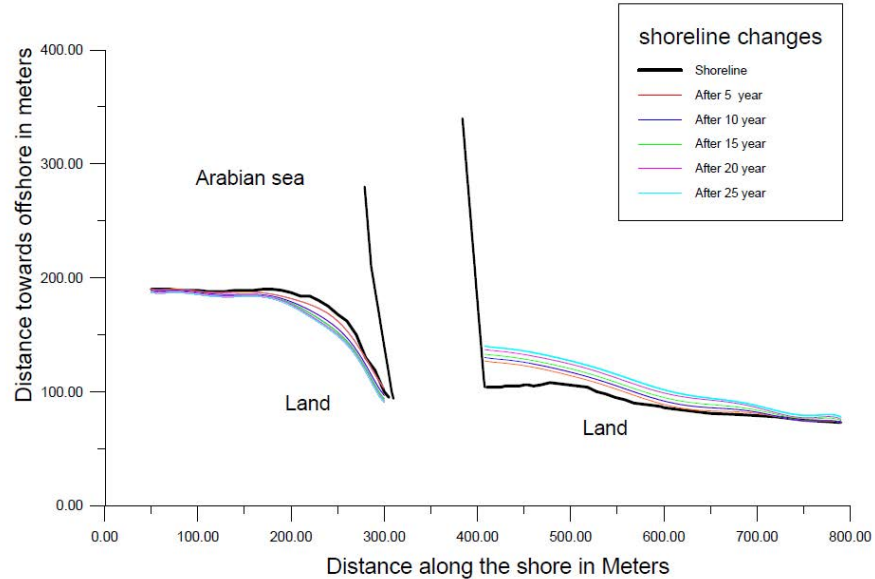
Figure 5. Variation of shoreline over the years

The cumulative effect of the wave characteristics and the presence of the breakwaters on the adjoining shorelines have been studied. The results indicate the shoreline advancement towards the ocean on the north of NBW is effectively over a distance of about 150m. This is the effect over a period of 25 years. The shoreline near the breakwater is expected to advance to a distance of about 50m towards the ocean. However, the discharge from the river Cheruvathur will wash away the sediments into deeper ocean, particularly during the months June to August. In order to ascertain the washing away of the sediments that are likely to be deposited near the mouth, the fall velocity W was calculated for the mean grain size, *D* of 0.25mm and with the empirical relationship $W = 6.5 \, X \, D^{\frac{1}{2}}$, where *D* and *W* are in m and m/s, respectively. In this way, the fall velocity works out to be 0.1m/s. This is extremely small compared to the velocity in the river Cheruvathur. On the southern side, the erosion is seen to take place over a period of 20 years, which is, however, much less.

6.3. Wave Tranquility Studies

The total stretch considered for the numerical modeling is 2.42 km along the shoreline and up to 5m bottom contours in the offshore-onshore direction. The numerical model has been executed for the proposed layout with the wave characteristics as reported in the above table.

Typical results on the distribution of wave height and wave phase contours for the month of January, February, and March with shore normal angle of -36° is evaluated Figure 6. Due to the irregularity in the bathymetry, the waves are found to be steep at certain locations in the area towards the sea away from the breakwater. The phase contours clearly demonstrates the phenomenon of wave diffraction. The bending of the wave fronts and penetration into the harbour basin are clearly seen. Figure 6 shows the wave height and phase contours for the wave characteristics for the months January to March.
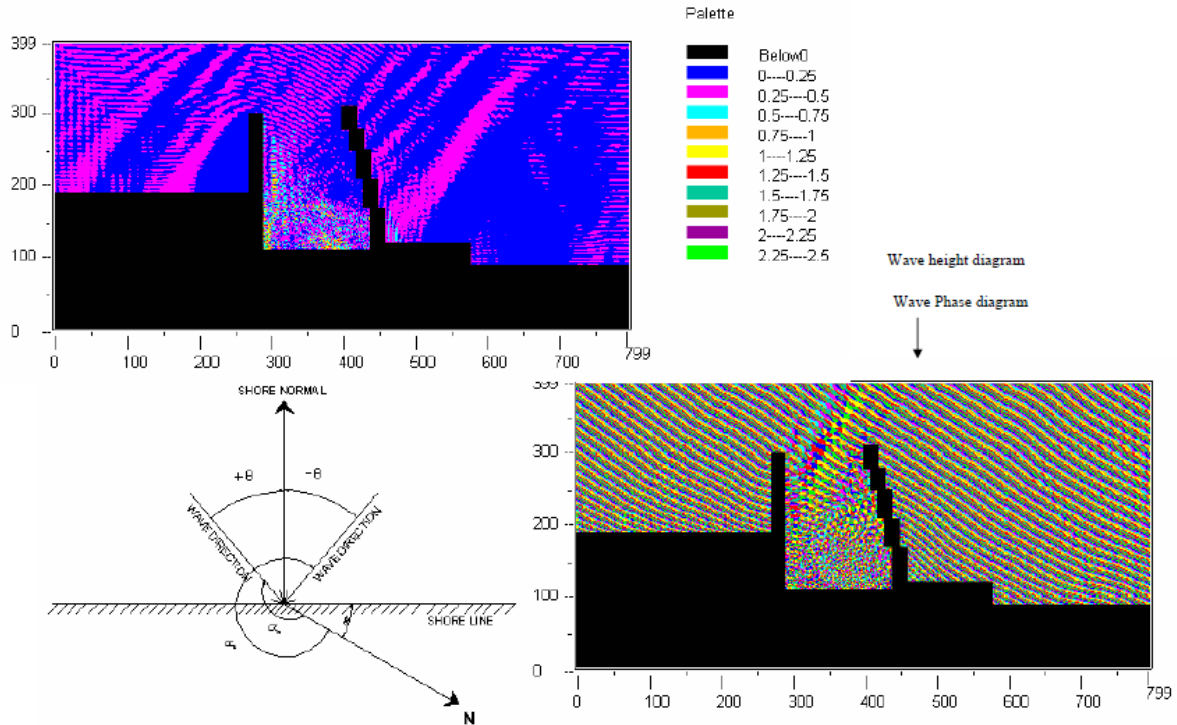
Figure 6. Wave height and phase contours for H_{avg}=1.25m, T=6.5s, θ=-36°

7. SIMILAR PROJECTS

Similar problems of river mouth choking and sandbar formation was also observed at these sites. Training of river mouths was evaluated as a viable solution. The imageries on the results from the other sites, namely Korapuzha (11° 9'41.44"N and 75°48'11.40"E), Chettuvai (10°30'32.26"N and 76° 2'20.14"E), Perumanathura (8°37'59.41"N and 76°47'11.98"E), and Beypore (11° 9'41.10"N and 75°48'11.70"E) are projected in Figs 7, 8, 9, and 10, respectively.

Figure 7. Google earth imagery of Korapuzha

Figure 8. Google earth imagery of Chettuvai
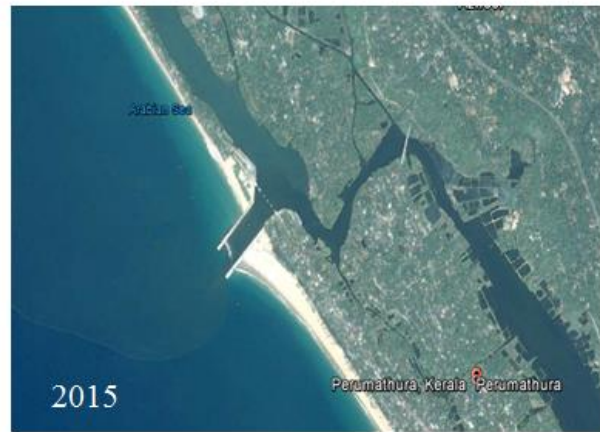
Figure 9. Google earth imagery of Perumanathura
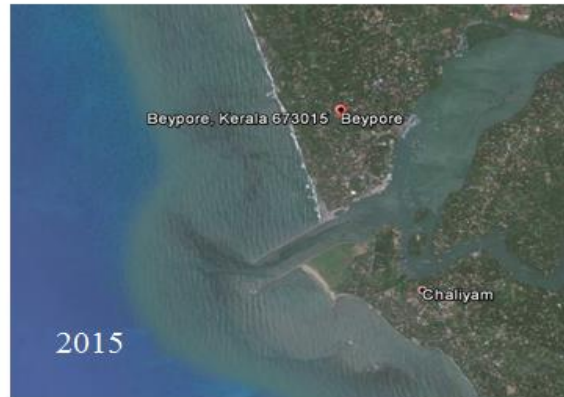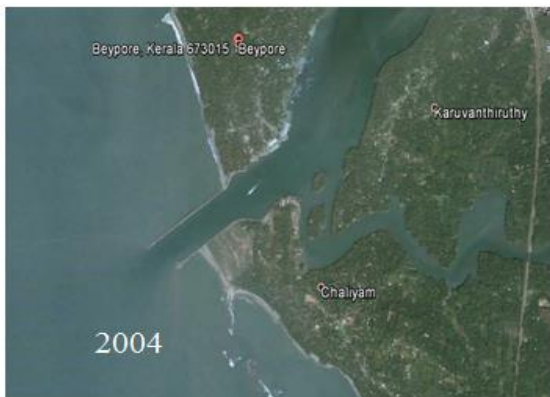
Figure 10. Google earth imagery of Beypore

8. CONCLUSION

We discussed in detail the process of training of river mouths in Kerala coast at Cheruvathur, Chettuvai, and Korapuzha. Every detail is designed with consideration of wave action of storm surge. Littoral drift estimates quantify the magnitude, and direction of sediment transport and the shoreline behavior post construction of the proposed measure is evaluated through numerical modeling, and it clearly demonstrates the effectiveness of the training walls.

9. REFERENCES

Berkhoff, J. C. W. (1972), "Computation of combined refraction–diffraction", *Proceedings 13th International Conference on Coastal Engineering*, Vancouver, pp. 471–490

Chandramohan, P.; Sanil Kumar, V., and Anand, M., (1990). "*Wave* Atlas for the Indian Coast", Goa, India:National Institute of Oceanography, Ocean Engineering Division, 312 p.

Kraus, N.C., and Harikai, S. 1983. Numerical Model of the Shoreline Change at Oarai Beach. Coastal Engineering, 7(1), 1-28.

Komar, P.D. (1976a), "Beach process and sedimentation", *Prentice –Hall Englewood Cliffs, N.J.,* 429p.

Komar, P.D. (1976b), Longshore currents and sand transport on ocean Eng. III, *ASCE* ,pp 333-354.

Li, B. (1994). "Generalized Conjugate Gradient Model for the Mild Slope Equation.", *Coastal engineering journal,* Vol. 23, pp-215-225.

Impacts of Tailwater on the Design of Several Stilling Basins in the USA

L.E. Shearin-Feimster[1]
[1] Schnabel Engineering
11A Oak Branch Drive
Greensboro, NC 27407
USA

E-mail: lshearin@schnabel-eng.com

ABSTRACT

The dissipation of excess energy from flows exiting a spillway is often needed to prevent or reduce to acceptable levels conceivable negative impacts to the downstream channel, spillway, and dam (e.g., erosion, undermining). The optimization of a hydraulic jump type stilling basin using general-purpose, published design methodologies (i.e., USBR, SAF, etc.) for a project can be challenging, as these methodologies may not account for all site specific conditions and structure formulations by designers. Also, it is not often clear to a designer as to which flow rates (and corresponding flood events) will have the greatest influence on the basin geometry and features (i.e., jump formation location and stability). This can be further obscured for projects where a high tailwater condition is predicted during flood events.

This paper presents several recent dam rehabilitation projects where a high tailwater impacted the designs of the stilling basins. Each project features a different spillway, chute, and basin configuration. An overview of each site and summary of key challenges encountered during the design of the spillways and stilling basins is included. In addition, a discussion of which design methods were selected, why they were selected, and additional measures that were taken to address the uncertainties at the site is included. This documentation of unique site conditions and design methodologies for stilling basins is intended to show the importance of collaboration between the designer and the owner in selecting a design approach for a specific situation.

Keywords: *spillways, energy dissipation, tailwater, hydraulic jump, stilling basin*

1. INTRODUCTION

Each dam site and spillway system has unique characteristics. This includes factors such as layout, required spillway capacity and downstream tailwater conditions. In addition, the dam spillway systems are also frequently constrained by time and budget limitations. These constraints often lead to the designer using published predictive methods in less than ideal scenarios. The ideal solution to design the spillways and stilling basins would often be to use a physical model, Computational Fluid Dynamics (CFD) model, or combination of the two. The focus for the designs discussed in this paper is the calculation of the energy dissipation that is ultimately used to design a stilling basin. The size of the stilling basin is a critical consideration in the design process. It should be large enough to transition the flow to the downstream channel without endangering the integrity of the dam. However, to be cost-effective, the stilling basin should not be larger than necessary to adequately dissipate energy.

Many times, due to the unique site characteristics, calculating the energy dissipation system requires using predictive methods as approximations of the site. This often requires a piecemeal approach of mixing different methods since many sites do not fit one particular method. For example, one method would be used to calculate the flow over the spillway crest, a different method to account for losses at the bottom of the weir onto the concrete pad, and a third method would be used to account for the losses down a stepped section of the chute. Another condition that is difficult to account for is designing a stilling basin for tailwater depths that vary significantly from the conjugate depth. At some sites, the stilling basin can be raised or lowered to improve this relationship; however, there are limits to how much this can be done. This can lead to over design of stilling basins at locations with high tailwater.

The following sections discuss four projects where the energy dissipation was analyzed and the methods used to design the stilling basins.

2. TERMINOLOGY

The spillways and stilling basins discussed in the following sections were designed using a specific design storm determined by the appropriate regulatory agency. The design storms are related to the Probable Maximum Precipitation (PMP) or the Probable Maximum Flood (PMF). The PMP is theoretically the largest storm event that can occur at a particular location for a particular duration. The PMF is the flood resulting from the PMP. Frequency storms were also taken into consideration.

Designing a stilling basin involves calculating the appropriate length and elevation of the basin as well as the type of basin. Factors taken into account to design the basin are the depth of tailwater, the depth of flow downstream of the hydraulic jump, the depth of flow upstream of the hydraulic jump, and the energy head. For the purposes of this paper, the following terms will be used. The tailwater is the depth of flow downstream of the dam for a specific flow rate or storm based on a hydraulic model of the downstream channel. The conjugate depth is the depth of flow downstream of the hydraulic jump. The entrance depth is the depth of flow upstream of the hydraulic jump. The energy head measured as a depth is the metric used to calculate the energy in the system at a given location. The residual energy head is the energy head at the entrance of the stilling basin.

Three design approaches are discussed in conjunction with the case studies; physical models, CFD models, and predictive methods. A physical model study is a scale model of the proposed design usually built by a hydraulic research lab. Various specified flow rates are passed through the proposed structure to evaluate the impacts. A CFD model is a two- or three-dimensional computer representation of the proposed design. Like the physical model, the CFD model evaluates various flow rates as they are passed through the proposed structure. If both a physical and CFD model are used for the same proposed structure, the physical model can be used to calibrate the CFD model parameters. The term predictive model, for the purpose of this paper, refers to equations and methods published in journals and manuals. These are most commonly used at the conceptual design phase, for more simple designs, and in cases when the design budget or time frame does not allow for a physical or CFD model.

3. CASE STUDY #1: LAKE TOWNSEND DAM

3.1. Site Description

Lake Townsend Dam is the primary water supply dam for the City of Greensboro, North Carolina. The dam has a 7-cycles labyrinth spillway and an earthen embankment. The earthen embankment is designed to overtop by up to 1.5m (5-ft) to pass the required design storm of the ¾ PMP in accordance with North Carolina Dam Safety regulations. The labyrinth contains two cycles with a crest elevation 0.3m (1 ft) lower than the other five cycles. Downstream of the lowered labyrinth section are three steps that are from upstream to downstream 1.2m (4-ft), 2.4m (8-ft), and 1.2m (4-ft) high. Downstream of the higher labyrinth cycles are two steps, one 1.2m (4-ft) and one 1.8m (6-ft). The steps were configured to match the valley's shape so that the amount of excavation required to install them was reduced. The configuration also allowed the flow to be in line with the downstream stream channel under typical flow conditions.

The tailwater at the site is significant for even relatively small storms. Under normal conditions, the tailwater is located at the bottom of the second step downstream of the lower cycles, or 1.2 m (4-ft) above the stream bed. During the 50-year storm, the tailwater is located at the base of the labyrinth walls, or 4.9 m (16-ft) above the stream bed. During a storm equal to the spillway capacity (approximately 60% of the Probable Maximum Precipitation), the tailwater is located at the normal pool elevation (crest of lower cycles). When the dam reaches full capacity, including the overtopping of the embankment, the tailwater is located just below the top of the embankment. One important factor causing the high tailwater at this site is a run of the river dam located 2,400 m (2 miles) downstream that has a crest elevation only 0.5 m (1.5 ft) lower than the low section of the stilling basin at Lake Townsend.

Figure 1. Overview of Lake Townsend Dam

3.2. Discussion of Design Approach

The owner of Lake Townsend Dam prioritized doing the work upfront to design an efficient dam and reduce costs during and after construction. This resulted in an investigation and design budget and schedule that allowed for a physical and three-dimensional CFD model study. The owner was very interested in performing the model studies to improve overall design and reduce the construction budget.

During the design of Lake Townsend, the energy dissipation was designed using a combination of a 1:21 scale physical model study and CFD modeling due to the sites uniqueness and the extreme amount of tailwater at the site. The physical model was used to evaluate the effects of tailwater on the labyrinth weir and provide calibration values for the CFD model. The both the physical and CFD models were used to evaluate various alternatives for the energy dissipation.

A stepped chute or series of drops was proposed downstream of the labyrinth weir. This configuration is believed to be more cost effective to construct than a sloping chute and traditional energy dissipation structure. The steps provide energy dissipation, particularly for lower flows. For higher flows, the tailwater tends to submerge the flow downstream of the weir, reducing the magnitude of energy dissipation. Several configurations were evaluated using the CFD and physical model such as 1.2 m (4-ft high) steps, 0.6 m (2-ft) high steps, and a sloping apron. The selected configuration consists of a four-foot drop to a sixteen-foot flat section to an eight-foot drop. A third four-foot drop will be provided at the north end of the spillway where low stage flows are directed into the downstream channel. The CFD model results indicated that for flows greater than approximately 50-year storm, the high energy flow did not reach the channel bottom. The selected configuration was found to be more effective at dissipating energy than the other options tested. Without the physical and CFD models, the stilling basin would likely have been overly conservative by being sized to pass a much larger storm event.

4.   CASE STUDY #2: FOX CREEK MPS #4

4.1. Site Description

Fox Creek MPS #4 is located near Flemingsburg, Kentucky. The dam is used for flood control and recreation. The primary spillway is a pipe and riser that discharges into the concrete stilling basin. The dam consists of an earthen embankment and a 90 m (295 ft) wide Roller Compacted Concrete (RCC) ogee shaped auxiliary spillway over the embankment. The auxiliary spillway discharges into a chute that converges by 15 degrees down the stepped section to the stilling basin. The stilling basin is a United States Bureau of Reclamation (USBR) Type II stilling basin with two stages. A Type II stilling basin is a concrete apron with an end sill. The two stages were designed so that the primary spillway outlet would discharge in line with the downstream channel. Under normal conditions, the tailwater is located 0.3 m (1-ft) above the low stage of the stilling basin

and 0.9 m (3 ft) below the second stage of the stilling basin. During the ¼ PMP storm, the tailwater is located 0.2 m (0.7 ft) above from the second stage of the stilling basin. During the design storm (PMP), the tailwater is located 0.12 m (0.4 ft) above the first step, located immediately downstream of the ogee spillway slab, so, essentially, the entire stepped section of the spillway chute is submerged.

Figure 2. Overview of Fox Creek MPS #4

4.2. Discussion of Design Approach

The owner of Fox Creek MPS #4 was primarily concerned with finishing the project by a specific deadline. The project was funded by the American Reinvestment and Recovery Act of 2009. This funding was designated for shovel-ready projects. For Fox Creek MPS #4 rehabilitation to be considered shovel ready, the design had to be submitted for review 4 months after the geotechnical investigation was completed. If this deadline was not met, the funding would be reallocated to another project. Therefore, a physical or CFD model study, which would have been the preferred design method, was not completed. Instead, predictive models were used as the primary design tool.

The second main concern at the project site was the property boundaries. The dam owner's property boundary did not extend far beyond the toe of the dam or to the sides of the dam. To address the limited boundary and the short schedule, the dam layout was completed initially to fit it in the site, and then analyzed to make sure it would safely convey the design storm. If the design did not meet the requirements, the property acquisition process may have caused the deadline to be missed. To keep the structure within the property limits, steps were added to the downstream spillway slope to provide some energy dissipation and decrease the stilling basin length.

The primary method used to calculate step dissipation for Fox Creek MPS #4 was Dr. Sherry Hunt's paper "Energy Dissipation for Flat-sloped Stepped Spillways Using New Inception Point Relationship" from the 2009 Proceedings of the ASDSO Annual Conference. Hunt's physical model in this study has a 4H:1V slope, and the results are considered applicable to slopes ranging from 4H:1V to 2.5H:1V. The spillway slope at Fox Creek MPS #4 was 2.5H:1V, so this method was considered applicable. Hunt's procedure in this paper did not take into account the converging walls. This was one factor in the decision to design the walls for the PMF and the stilling basin for the 2/3 PMF. Using Hunt's procedure to evaluate the energy dissipation the steps provided, the stilling basin that was contained within the site was considered adequate.

Because this method did not account for the converging walls, an additional predictive method and a similar model study were also considered. The predictive method used was presented by Hubert Chanson in Appendix 7 of his book titled "Hydraulics of Stepped Chutes and Spillways." This method is considered to be appropriate for steep slopes. The stepped section of the proposed auxiliary spillway for Fox Creek MPS #4 has a slope of 2.5H:1V. This slope often is or is near the dividing line for what is considered to be a steep slope versus a flat slope in the methods developed to analyze stepped spillways (Chanson 2002). In addition, Chanson specifies that this method is to be used for a preliminary design. The results of this method were very similar to the results using Hunt's method and agreed that the design that fit the site was sufficient.

One of the stepped chute alternatives evaluated in the Lake Townsend CFD model was very similar to the proposed design of Fox Creek MPS #4. The Townsend alternative used 1.2 m (4-ft) high steps on a 2.5H:1V

slope with a very similar unit discharge and tailwater location as Fox Creek. Because of the high tailwater during the design storm, we anticipated that the energy would dissipate prior to reaching the downstream end of the stilling basin. The Townsend CFD model alternative similar to the Fox Creek MPS #4 site indicated that this was the case. The results of the Townsend CFD model were used as a qualitative check that the proposed design in conjunction with the other calculations appeared to safely pass the required design storm.

Because the site has characteristics that did not fit a specific predictive model procedure, two predictive models and a similar CFD model were used to ensure that the design that fit within the property boundaries of the site was appropriate. Using a CFD and physical model may have allowed a more effective design to be used; however, the owner's main concern was ensuring that the funding would be available. If the deadline had not been met, funding would likely have been suspended, potentially leaving a dam with inadequate spillway capacity in place.

5. CASE STUDY #3: BULLOCK PEN DAM

5.1. Site Description

Bullock Pen Lake Dam is located in Crittenden, Kentucky. The dam retains Bullock Pen Lake, which is used for recreation and water supply for the town of Crittenden. Bullock Pen Lake Dam was constructed in 1953. Within a few years after construction and shortly after initial filling of the reservoir, erosion of the shale in the excavated rock spillway channel was observed.

The proposed structure will consist of a reinforced concrete labyrinth spillway over the current dam embankment. The labyrinth spillway will consist of 12.5 cycles and a total width of 79 m (260 ft). The labyrinth has two stages. The first stage will consist of 4 cycles at normal pool elevation, and the second stage will consist of 8.5 cycles with a crest 0.3-m (1-ft) higher than the normal pool elevation of the lake. The labyrinth spillway will discharge into a stepped chute and then into a USBR Type 1 stilling basin located at the toe of the embankment. Flows from the stilling basin will discharge into a riprap-lined outlet channel. Under normal conditions, the tailwater will be located 0.3-m (1-ft) above the low stage of the stilling basin and 0.9-m (3-ft) below the second stage of the stilling basin. During the 10-year storm, the tailwater will be located at the elevation of the lowest step of the chute. During the PMP, the tailwater will be located 0.27-m (0.9-ft) above the labyrinth spillway slab, submerging the stepped section of the spillway chute.
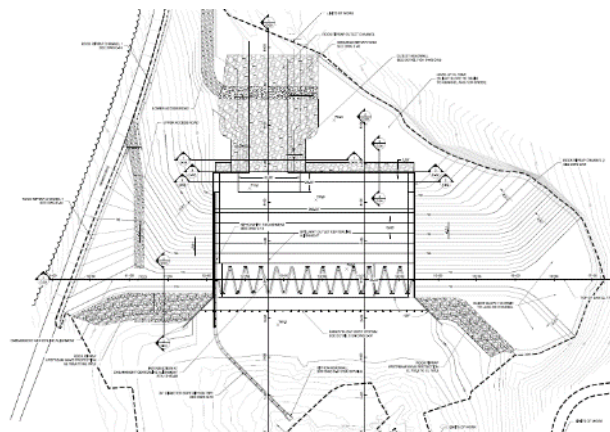
Figure 3. Proposed Layout of Bullock Pen Dam

5.2. Discussion of Design Approach

Due to the site complications, both a CFD model and predictive methods were used to analyze the energy dissipation at this site. The owner's schedule allowed time for the CFD modeling; however, there was not time or funding available to do a physical model. The design approach was to design the stilling basin using the predictive methods and use the CFD model to check the results of the predictive methods for reasonableness.

A piecemeal approach was used to design the stilling basin. The energy head loss resulting from the fall from the crest of the labyrinth to the base of the labyrinth wall was estimated using a method developed by Lopes (2009). The energy head loss down the stepped chute was estimated using Hunt's 2014 work. The selected stilling basin was a USBR type 1 basin, which is a concrete apron.

The CFD model showed that the hydraulic jump occurred over the stepped chute due to the high tailwater. The energy dissipation was calculated to be less than the predictive models; however, the velocity of flow at the exit of the stilling basin was lower than predicted. This is most likely do to the high tailwater at the site that the predictive models do not take into account. The results of the CFD model confirmed that the spillway layout designed using the predictive methods is appropriate for the site conditions.

6. CASE STUDY #4: SALEM LAKE DAM

6.1. Site Description

Salem Lake Dam retains Salem Lake, which is the second largest source of drinking water for the City of Winston Salem, NC. The lake is also used for recreational purposes. Salem Lake Dam consists of a concrete gravity dam. The dam consists of an overflow section and a non-overflow section. The overflow section consists of a conventional concrete ogee spillway that has two stages, the first one at normal pool and a second one (the high-stage) located on either side of the low-stage weir with the crest at 0.5 m (1.7 ft) above normal pool. The downstream face of the overflow section consists of steps. The dam's non-overflow sections are located on either side of the overflow section. Zoned earthen embankments tie into the non-overflow sections out to the abutments. The non-overflow section and the earthen portions have a crest 3.8 m (12.5 ft) above the normal pool. The overflow section of the dam has an ogee shaped crest. During the ½ PMP storm, the tailwater submerges the spillway by 0.12 m (0.4 ft).

Figure 4. Overview of Salem Lake Dam

6.2. Discussion of Design Approach

Salem Lake was analyzed using predictive methods primarily due to the relatively simple design and the results of the rock scour analysis. Energy Dissipation was analyzed to avoid scouring of the downstream area. This scour can threaten the integrity of the dam if it becomes extensive. During the geotechnical investigation, the stream bed was found to have good quality gneiss. This discovery prompted an analysis performed by Dr. George Annandale using his method (Annandale 2006). This procedure entailed comparing the erosive capacity of the water that will flow over the dam spillway and the erosion resistance of the rock at the dam abutments and foundation. The analysis concluded that the rock is unlikely to scour during the design storm flows. The calculations took the downstream tailwater into account.

After discussing the results with the owner, the decision was made to have a rock-lined stilling basin for a storm smaller than the design storm. This decision was made because if the stilling basin's capacity was exceeded, it would not pose a dam safety hazard. After comparing the difference between the upstream reservoir elevation and the downstream tailwater elevation for various storm events, the 500-year storm was selected.

7. CONCLUSIONS

The design methods for a project can be limited by external factors such as time, funding, property boundaries, or a combination of factors. In these cases, consideration should be given to the complexities of the site and structures that may not be taken into account with the method or methods selected. Conveying the unknown effects of these factors should be discussed with the owners so that they understand the risk they are taking on with the selected design. In addition, the owner should be made aware of measures that could be taken in advance of, during, or after a major flooding event when the design limits are tested.

8. ACKNOWLEDGMENTS

These projects were originally analyzed for the following organizations by Schnabel Engineering:
- City of Greensboro, NC
- USDA-NRCS Kentucky
- Commonwealth of Kentucky
- City of Winston-Salem, NC

9. REFERENCES

Annandale, G.W. Scour Technology, McGraw-Hill, New York. 2006

Chanson, H. The Hydraulics of Stepped Chutes and Spillways.2002

Hunt, S.L., and K.C. Kadavy. (2009). "Energy Dissipation for Flat-sloped Stepped Spillways using New Inception Point Relationship." In the Proceeding of the Association of State Dam Safety Officials Annual Conference, Ft. Lauderdale, Florida. (CD-ROM)

Hunt, S. et al, "Simplistic Design Methods for Moderate-Sloped Stepped Chutes." Journal of Hydraulic Engineering, 2014

Lopes, R., Matos, J., and Melo, J. (2006). "Discharge capacity and residual energy of labyrinth weirs." Proc. of the Int. Junior Researcher and Engineer Workshop on Hydraulic Structures (IJREWHS '06), Montemor-o-Novo, Hydraulic Model Report No. CH61/06, Div. of Civil Engineering, the University of Queensland, Brisbane, Australia, 47-55.

NRCS National Engineering Handbook Section 5 – Hydraulics 1956

NRCS National Engineering Handbook Part 630 – Hydrology 1997

U.S. Department of Interior, Bureau of Reclamation. Engineering Monograph No. 25 "Hydraulic Design of Stilling Basins and Energy Dissipators". 1984

Experimental study of large scale plunging jets

G. GUYOT[1,5], M. RODRIGUEZ[2], M. PFISTER [3], J.P. MATAS[4] and A. CARTELLIER [5]

[1]EDF Hydraulic Engineering Center
Savoie Technolac, 73370 Le Bourget du lac, France
[2]CERG Lab
7, rue Lavoisier, 38800 Le Pont de Claix, France
[3] Laboratory of Hydraulic Constructions (LCH)
EPFL
Station 8, 1015, Lausanne, Suisse
[4]LMFA - Université Claude Bernard Lyon I
43, boulevard du 11 novembre 69 622 Villeurbanne Cedex, France
[5] Université Grenoble Alpes, CNRS, LEGI, F-38000 Grenoble, France
E-mail: gregory.guyot@edf.fr

ABSTRACT

The lack of knowledge regarding air entrainment caused by large jets in hydraulic structures, such as downstream Pelton turbines, has led EDF (Electricité de France) to carry out a test series to optimize the La Coche Power plant. The data extracted from this work have been used in the frame of a research project.

A first experiment, performed on a large jet impacting the free surface of an open channel, has confirmed that physical phenomena concerning the behavior of large scale plunging jets are still not well understood. The main parameters that have been measured are the penetration depth, the entrained air flow rate, the average bubble size below the free surface, and the rising slope of the bottom boundary of the bubble plume. Globally, when comparing the data collected downstream of the jet impact zone with the predictions proposed in the literature, the different relations are not scalable with the jet dimension. Moreover, it appeared that these parameters are intimately linked to the jet state upstream the impact point. Consequently, a second experimental set-up was designed to measure the dynamic pressure and the void fraction inside the jet. These results have shown that even an elementary parameter such as the breaking length is not well predicted by existing formula. Indeed, high-frequency videos have proved that in certain cases, the jet is still continuous while literature predicts a broken jet. In addition, the experimentations show that the jets are flapping during the fall and thereby impacting the free surface over an enlarged region.

Keywords: Plunging jet, air entrainment, experimental jet statement, large jets.

1. INTRODUCTION

Air entrainment caused by a transition between free-surface flows and confined flows often occurs in hydro-power projects. In literature regarding the air entrainment due to a plunging jet, only five references are close to the hydro-power structures scales concerning the jet diameter range, which is typically more than 10 centimeters. These are Donk (1981), Falvey et al.(1987), Evans et al.(1992), Ervine and al.(1997), and Duarte, (2014). When considering the same range of falling height, only the four following references are close to the targeted conditions: Elsawy et al. (1980), McKeogh et al. (1981), Falvey H. et al.(1987), and Ervine et al.(1997). If both the jet diameter and the fall height are considered, only the studies of Falvey et al. (1987) and of Ervine et al.(1997) happen to be close to the present configuration. An improved knowledge of the air-disturbed flows would obviously enable researchers to increase the efficiency of design studies when assessing the feasibility or evaluating the cost of hydro-power projects. The main application fields are the jet impact in a downstream basin of a Pelton turbine or the jet impact on a concrete structure. Hence, an experiment dedicated to the "La Coche Pelton" hydraulic power-plant enhancement (EDF France) is valuable to define the air flow rate entrained by the vertical jet, the bubbles size, and the penetration depth in the downstream flow. Two jet diameters have been used with three different discharges and with two large-scale apparatus. Around 800 points have been garnered for the downstream flow, and around 220 points have been measured in the plunging jet. The purpose is to investigate the mechanisms that cause air

entrainment downstream of the impact and the behavior of the bubble cloud in the downstream flow. This article tackles the preliminary step of the planned experimental study. First, the experimental apparatus and the jet configurations will be detailed. Then, the key variables in the bubble plume will be discussed. Finally, void fraction and pressure measurements within the jet will be presented in the last section. In addition, the reliability of the break-up length predictions will be discussed.

2. EXPERIMENTAL APPARATUS

Two experimental apparatuses were used to evaluate the jet impact and the behavior of the air entrained under the free surface. The first one was erected on the Pont de Claix channel (EDF France). This first experimental set-up (Figure 1, Figure 2) aimed at analyzing the behavior of the air entrained by the jet under the free surface in the downstream channel. The second one (Figure 5) was erected at the CERG (Centre d'Etude et de Recherche de Grenoble) in Grenoble (France) to provide data regarding the jet structure before its impact.

2.1. General Jet Configurations

Table 1: The five jets configuration studied on the two apparatus

Nozzle diameter (D_0)(mm)	135	135	164	164	164
Jet Flow rate (Q)(L/s)	80	110	50	80	110
Nozzle outlet velocity (V_0) (m/s)	5.59	7.68	2.37	3.79	4.73
Nozzle outlet Reynolds number (Re)	754512	1037454	388183	621092	776366
Nozzle outlet Froude number (Fr)	4.86	6.68	1.87	2.99	3.73
Nozzle outlet Weber number (We)	57766	109215	12587	32221	50346

$$Re = \rho_l V_0 D_0 / \mu \qquad \text{Reynolds Number} \qquad (1)$$

$$Fr = V_0 / \sqrt{g D_0} \qquad \text{Froude Number} \qquad (2)$$

$$We = \rho_l V_0^2 D_0 / \sigma \qquad \text{Weber Number} \qquad (3)$$

In the equations (1,2,3), g is gravity acceleration, V_0 is the average velocity at the nozzle outlet, D_0 is the nozzle diameter, m is the liquid dynamic viscosity, r_l is the volumetric mass density of the liquid, and s is surface tension. The Reynolds numbers indicate that the flow is fully turbulent at the nozzle outlet, whereas the Weber numbers show that inertia largely dominates capillarity.

2.2. Channel Experimental Apparatus

(a)   (b)   (c)

Figure 1: View of the channel upstream (a), of the experimental platform (b), of the channel downstream (c).

(a)   (b)
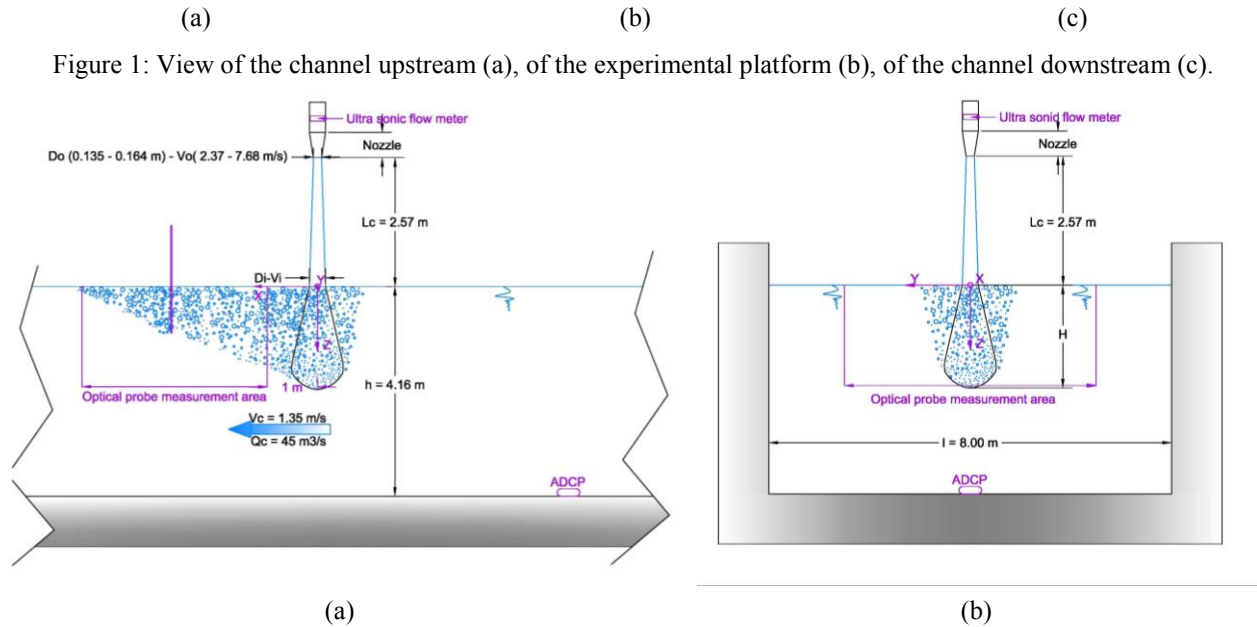
Figure 2: Streamwise section sketch (a) and transverse section sketch (b) of the channel experimental apparatus

The experimental apparatus was located 300 m downstream of the inlet weir of the straight channel and 500 m upstream of the channel end. The channel is 8 meters wide (l) and 5 meters deep. The water level in the channel was controlled by an inlet weir. The channel flow rate (Q_c) was imposed by a hydro power plant downstream. The available range of channel flow rates was 35-80 m^3s^{-1}. For practical reasons, the channel flow rate (Q_c) was set to 45 m^3s^{-1}. Thus, the average channel velocity (V_c) under the jet was 1.35 ms^{-1} (Figure 1). The stability of the Channel velocity and flow rate was checked by a SonTek Acoustic Doppler current profiler (ADCP) upstream the apparatus. The flow depth (h) of the channel was set to ensure a 2.57 m falling height (L_c) between the jet nozzle and the free water surface (Figure 2).

The jet flow rate (Q) was pumped out of the channel by two pumps, which fed the PVC 164.3 mm internal diameter circular pipe network. The outlet of this network was the injector itself (Figure 3), which comprised a divergent (I.D. 164 mm to 320 mm) linked to a 600 mm of 320 mm I.D. pipe. A 90° Elbow links the inlet network to the injector. Two calming flow straighteners were located in the straight part to decrease the turbulence level before the nozzle inlet. The two nozzles, presented in Figure 3, are conical with the same convergent 0.32 (H/V) slope (Figure 3). The nozzle outlet internal diameters (D_0) are 164 mm and 135 mm with a respective length of 500mm and 592mm. Consequently, the jet falls down in an atmospheric surrounding. A Krohne Optisonic ultrasonic flow meter located upstream the injector enabled measurement of the flow rate.

All the results regarding air entrainment were obtained with an RBI optical probe. This probe was attached to a mast that was able to move in the three directions: *X*, upstream-downstream (from 1 m downstream the jet to the end of the bubble cloud); *Y*, left bank- right bank (between -2.5 m to 2.5m centered on the jet); and *Z*, flow depth (up 2 m penetration depth H), as shown in Figure 2 and Figure 3. For each jet configuration, that probe was used to provide the void fraction, the penetration depth, and the bubble plume shape along three channel sections downstream the jet. The first measurement section was located 1 m downstream the jet, the second one took place at the middle of the white water induced by the jet, and the last was located around 0.30 m before the disappearance of the surface white water.
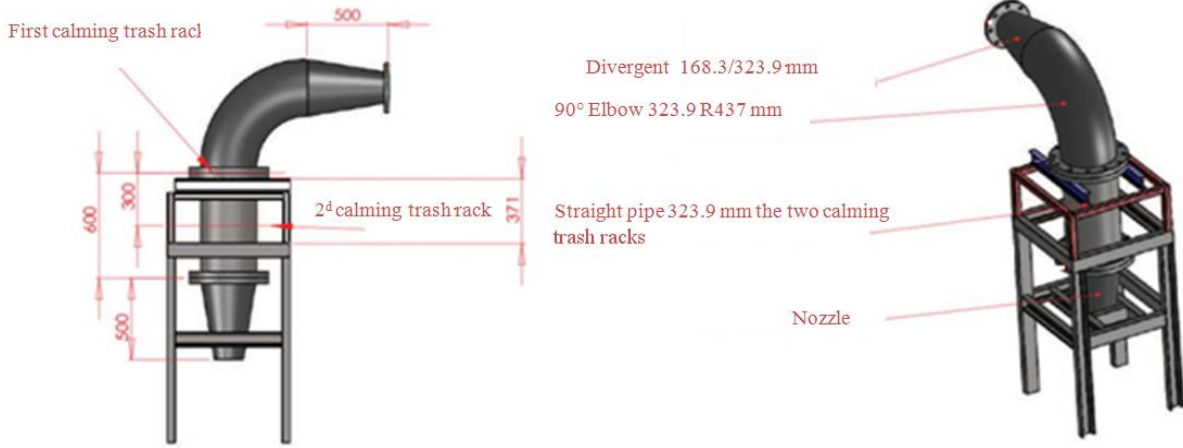
Figure 3: Injector details of the two apparatus

If the void fraction measured by the optical probe was below 0.02, it was assumed that the probe was outside the bubble plume. Hence, this criterion enables the determination of both the penetration depth $Z\,max$ and the lateral extent $X\,max$ of the bubble plume. A total of 800 measurement points were recorded during the channel experimental runs.
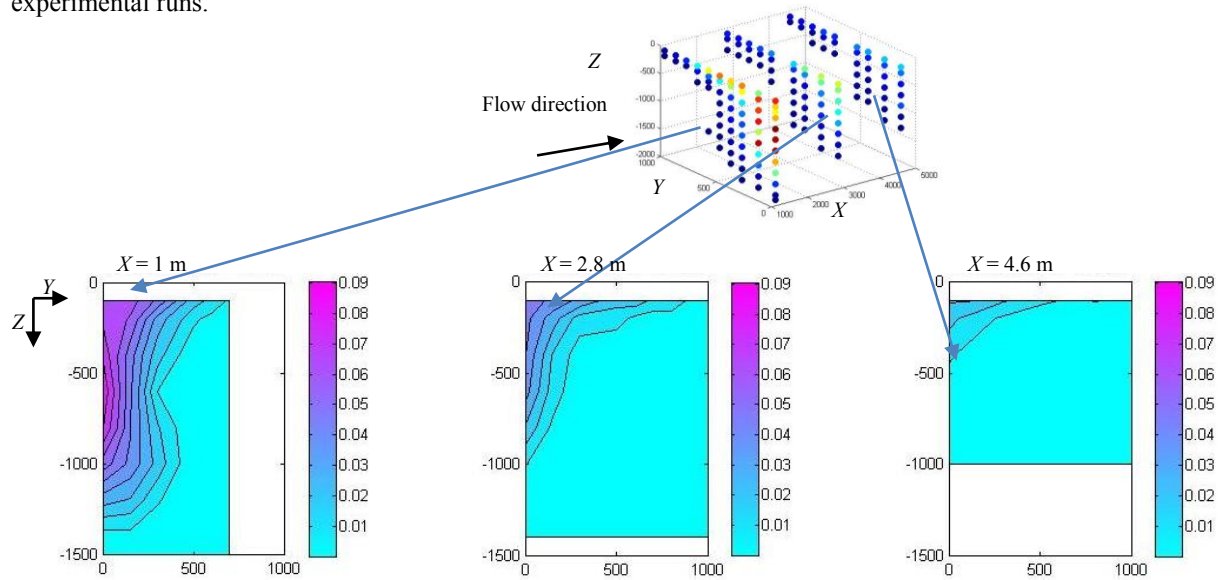
Figure 4: Iso-contours of the void fraction (color scale) over the three half vertical cross-sections located 1, 2.8 and 4.6 m downstream the jet impact location (D_0 =135 mm, Q=0.11 m^{3}s^{-1}).

$$\alpha = \frac{\sum Tg}{Tt}$$ *Void fraction definition*   (4)

Basically, the optical probe signal provides the indicator function of the phases detected by the probe tip. Hence, the void fraction (**a**) is simply the total time spent in the gas phase (Tg) divided by the acquisition time (T$_t$). Void fraction maps over all three sections can then be drawn as shown figure 4.

2.3. Lab Experimental Apparatus

The same hydraulic network was erected at the CERG, but in this second set-up, the jet fell into a dry channel. The void fraction and the dynamic pressure were measured over 3 jet cross-sections located 0.27 m, 0.94 m, and 2.57 m

downstream the nozzle outlet (Figure 5). A minimum of 11 measurement points were collected along a jet diameter, the latter was determined by visualization. Around 220 points were collected during these runs.

The dynamic pressure sensor is a FGP sensor XPM5-S126 with a 10 kHz sampling rate. A minimum of 50,000 pressure values have been recorded for each pressure, representing about a 5 second run. High-speed cameras gave the opportunity to collect movies of the different jets during laboratory runs. All high-speed movies were recorded after the completion of dynamic pressure and void fraction measurements. Video tools were 2 Phantom Miro M310 cameras (5,040 frames per second for a 896*720 pixels resolution), used with three objectives Nikkon, 60 micro Nikkor, Nikkon 105 micro Nikkor 180 mm APO macro Sigma. The lighting system comprised two alpha 4K 4kW electronic ballast and a Chimera Lighting box.

| (a) | (b) | (c) |
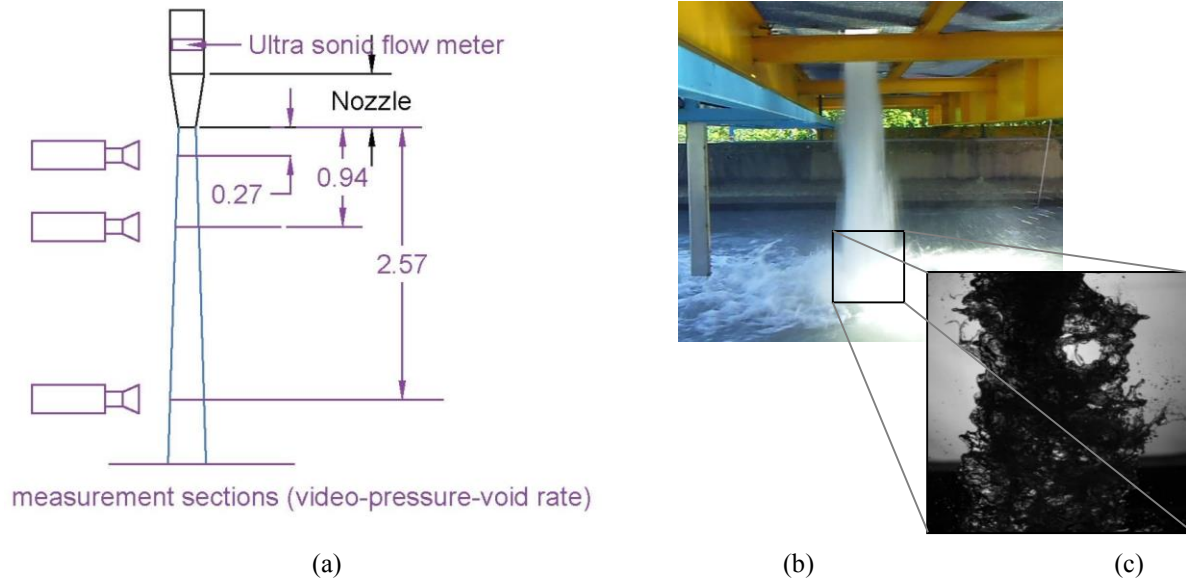
Figure 5: Sketch of the CERG lab experimental apparatus (a), view of the jet between Z= 1 m to 2.57 m (exposure time 1/24 s) (b) and image at Z= 2.57 m falling depth (exposure time 1/5000 s) (c) for the nozzle D_0=135 mm, Q =0.11 m3s-1.

3. PLUNGING JET AIR ENTRAINMENT

3.1. Bubble Size under the Free Surface

We assume that the typical time after which a bubble is entrained at the velocity of the liquid can be estimated as about 1/3 of the diffusion time (t):

$$\tau = \frac{d^2}{\nu} \qquad \textit{Diffusion time} \qquad (5)$$

where d is the bubble diameter (m) and ν the kinematic viscosity (m²s⁻¹) of the surrounding fluid. For millimeter size bubbles in water, the order of magnitude of 1/3*t is 0.3 s. Thus, the bubble velocity in the first section located 1 meter downstream the jet impact is already equal to the water velocity (1.35 m s⁻¹). Consequently, the measured bubble diameter (d) can be obtained by multiplying the average gas residence time (T_g) detected by the probe by the average channel velocity (V_c) along the horizontal, namely:

$$d = T_g * V_c \qquad \textit{Measured bubble diameter} \qquad (6)$$

The average measured bubble diameter for all experimental conditions happens to be comprised between 2.2 and 2.8mm. Only one reference addressing the question of bubble diameter has been found (Simonin, 1959). The first attempt to predict the bubble diameter was based on equation (7) coupled with equation (14) that forecast the air

entrained flow rate (Figure 6). The second way of predicting bubble size was to calculate the average bubble size using the measured entrained air flow rate in equation (7). Whatever way was used, the calculation provides a bubble size slightly above 3mm, and thus overestimates the experimental value. This shows that the bubble size created by jets similar to the one currently studied is not well predicted, even though the order of magnitude is correct.
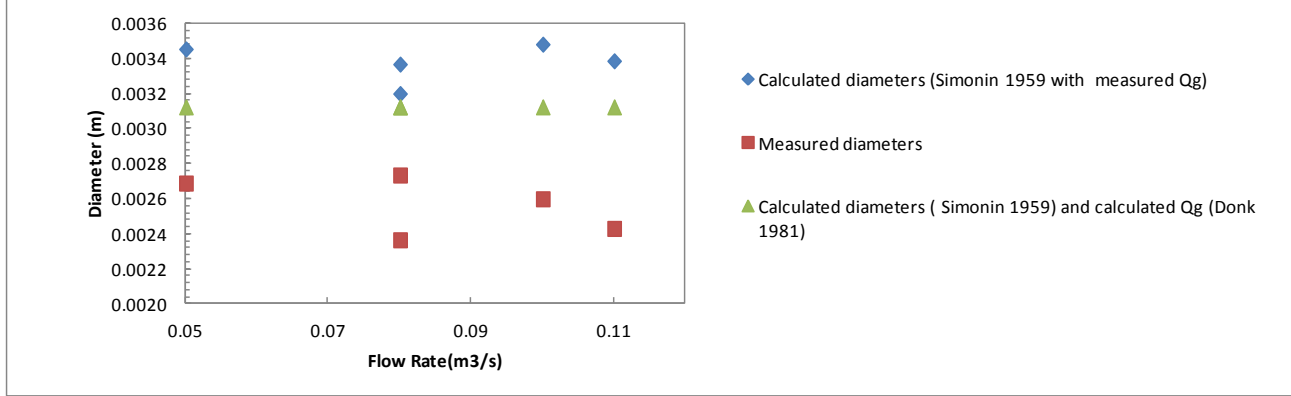
Figure 6: Evaluation of the bubble average diameter

$$d = 4.3 * 10^{-3} \left(\frac{Q_g}{Q} \right)^{1/3} \qquad \textit{Average bubble diameter (m) (Simonin)} \qquad (7)$$

In equation (7), Q_g is the entrained air flow rate and Q is the jet flow rate (m³s⁻¹).

3.2. Penetration Depth

A simple way to evaluate the uncertainty on the penetration depth due to the location of the first measurement section is to analyze the bubble movement. With the same assumption as in the previous section, the bubble horizontal velocity is equal to V_c. The bubble ascent velocity range given in Clift et al. (1978) is between 0.15 ms⁻¹ (contaminated water) and 0.3 ms⁻¹ (distilled water) for a Morton number equal to 2.57 10⁻¹¹. Hence, the ascent slope (ascent velocity/bubble horizontal velocity) range is 0.11 to 0.22 depending on the water quality. It indicates that the uncertainty on the penetration depth due to the location of the first measurement section on the first apparatus is at most 0.22 m. Thus, the measured penetration depth has been directly compared to the calculated ones.

$$M = \frac{g\mu^4 \left(\rho_l - \rho_g \right)}{\rho_l^2 * \sigma^3} \qquad \textit{Morton number} \qquad (8)$$

In equation (8), g is gravity acceleration, μ is the liquid dynamic viscosity, ρ_l and ρ_g are the volumetric mass density of the liquid and of the gas, and σ is surface tension.

Two procedures have been proposed to predict the penetration depth (H). Some authors have used the continuity or momentum equations [Clanet et al. (1997) and Albertson et al. (1950), followed by Falvey et al. (1987)] to determine semi empirical equations that provide the penetration depth. Others, such as McKeogh et al. (1981) and Nakasone (1987), have proposed empirical formulae (see Table 2). The predictions for our flow conditions range from 1 to 10 m. The experimental measurements happen to be close to the Nakasone results (Figure 7).

Table 2: Penetration depth relations

$H = 2.6 * (V_i D)^{0.7}$	$\frac{V_i}{U_T} = 3.12 * \left[\frac{D}{H} + 4 * \tan(\alpha) \left(4 \frac{H}{D} \right) * \tan^2(\alpha) \right]$	$H = \frac{2}{3} * H_C$	$\frac{H}{D} = \frac{1}{2\tan(\alpha)} \frac{V_i}{U_T}$
(9) McKeogh et al. (1981)	*(10) Falvey et al.(1987)*	*(11) Nakasone, (1987)*	*(12) Clanet et al.(1997)*

In the previous equations (9,10,11,12), V_i is the jet velocity at impact, U_t is the bubble terminal velocity, D the jet diameter at impact, H the penetration depth, and α the jet open angle under the free surface.

The comparison points out the fact that only the Nakasone proposal is close to the current experimental data.
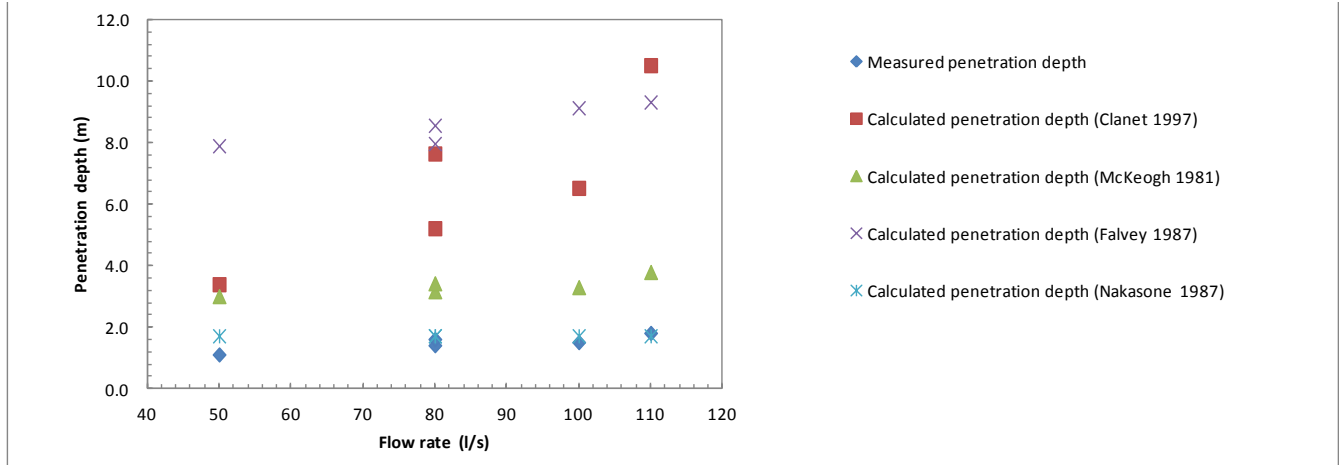
Figure 7: Penetration depth measurements (X=1m) compared with literature predictions.

3.3. Ascent Slope of the Bubble Plume Bottom
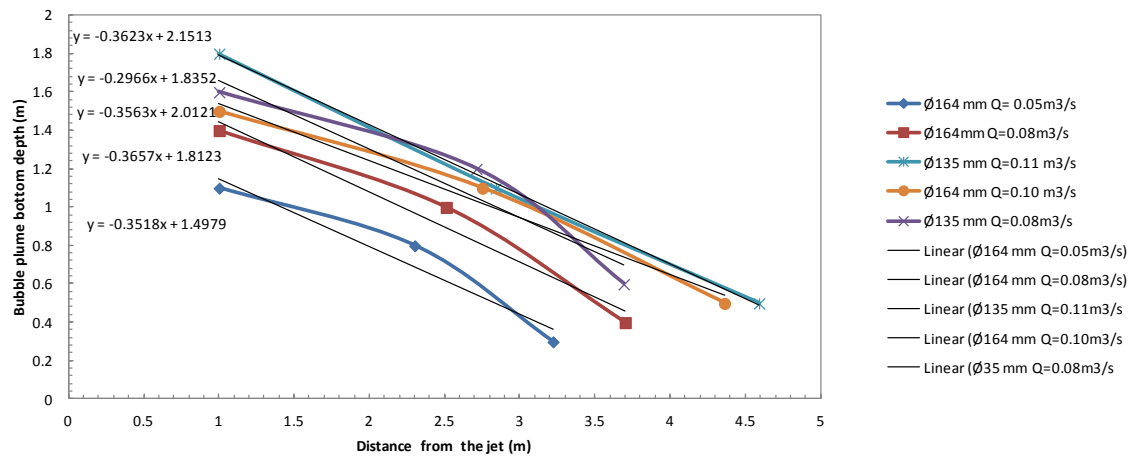
Figure 8: Ascent slope of the bubble plume bottom for all the jet cases

It is possible to measure the bubble penetration depth in all sections. Hence, it is possible to determine the measured ascent slope of the bottom of the bubble plume. The average slope for the 5 cases is equal to 0.35 as shown in Figure 8. With the assumption that the average channel velocity is also the bubble horizontal velocity, the average ascent velocity of bubbles is equal to 0.48 ms^{-1}. This means that the average bubble diameter would be over 10 mm. These results show without doubt a gap between the predictions of bubble size, of the jet depth penetration, and of the physical behavior of the bubble plume. To conclude, the dynamic ascent of the bubble plume was measured and happens to be quite different from the dynamics of isolated bubbles.

3.4. Entrained Air Flow Rate (Q_g)

$$Q_g = 1.3*10^{-4}\left(\frac{1}{2}\rho_l*Q*V_i^2\right)^{0.61}$$

Air flow rate entrained by Elsawy and al.(1980) (13)

$$Q_g = 0.09*Q*\left(\frac{L_c}{D_0}\right)^{0.65}$$ *Air flow rate entrained by Donk, (1981)* (14)

In equations (13, 14), L_c (m) is the fall height between the nozzle and the free surface.
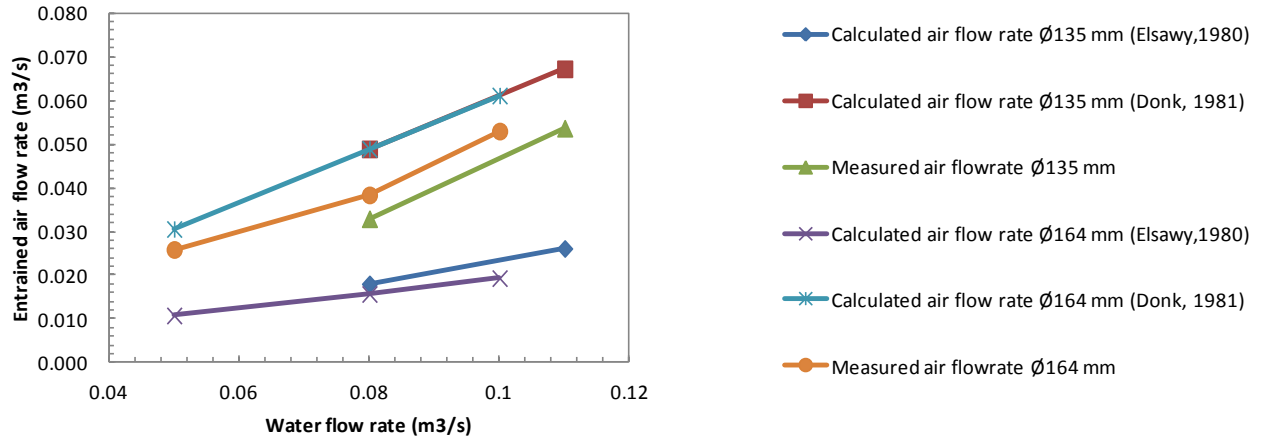
Figure 9: Comparison between measured entrained air flow rate and calculated one.

The above two predictions for the entrained air flow rate have been compared and analyzed in Bin's review paper (1993) on air entrainment. The experimental set-ups considered by Bin correspond to jet powers $N_j = 0.5*\rho_l*Q*V_i^2$ up to 100 W. For the present conditions, the jet power is around 10 kW, which is two orders of magnitude larger.

$$F_l = \alpha*V_c \longrightarrow Q_g = \sum_i F_l*S_i \quad \text{Calculated entrained air flow rate}$$ (15)

In equation (15), S_i (m^2) is the influence area of the local flux.
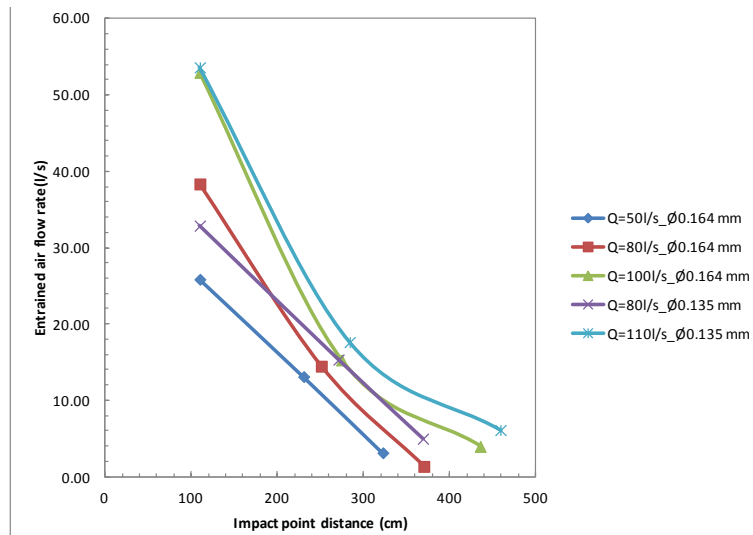
Figure 10: Experimental results for the entrained air flow rate downstream the jet impact point.

A local gas flux (Fl, ms^{-1}) can be calculated as the measured void rate multiplied by the bubble velocity taken equal to the channel velocity. The entrained air flow rate (Q_g) (m^{3}s^{-1}) is then derived by integrating the local flux over the channel cross-section. Measured air entrained flow rates lie between the two predictions, but the interval between the two predictions (Figure 9) varies by a factor of three. In Figure 10, the measured air flow rate evolution downstream the jet impact has been drawn. In the current cases, the ratio (Q_g/Q) is between 40% and 54% at 1 m downstream the impact point. This ratio rapidly decreases down to 10% at 5 m downstream the jet impact location. Evaluating the error precisely linked with the measured air flow rate is challenging. Consequently, the comparison results point out the lack of accuracy on the air entrainment prediction for this kind of jet.

4. JET STATE

The jet state during the fall is investigated to compare the experimental results with the available literature. In particular, the calculation of the turbulent intensity (Tu) jets is needed to compare with Ervine's studies.

4.1. Jet Dynamic Pressure

A simplified calculation of the mean dynamic pressure can be achieved assuming a free-fall velocity converted into a dynamic pressure (Table 3), and the measured dynamic pressure are shown in Figure 11.
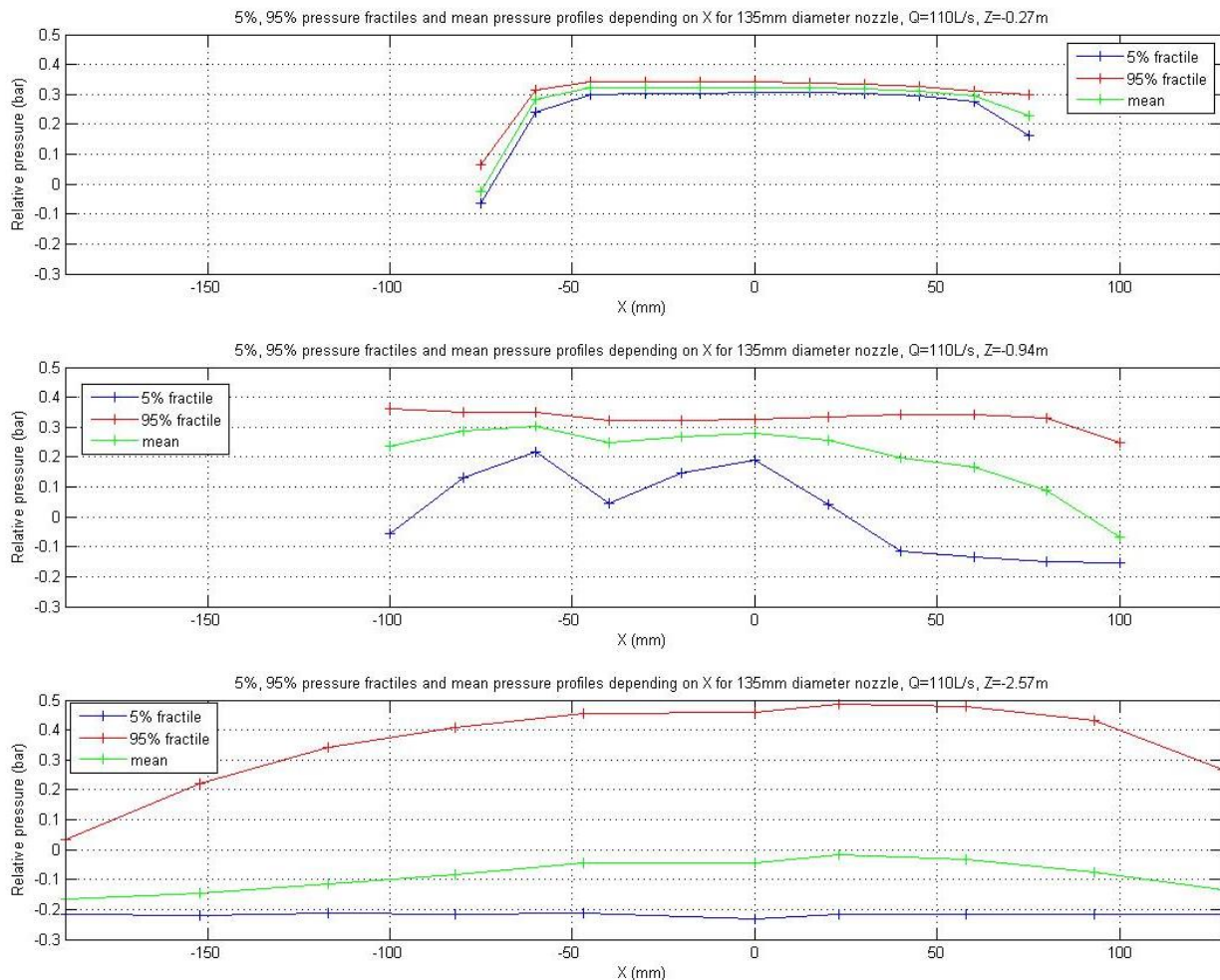
Figure 11: Dynamic pressure across the jet on the three measurement sections below the 135 mm nozzle Q =110 l/s.

Table 3: Simplified calculated dynamic pressure for all the measured sections and cases.

Fall height under the Nozzle (L_c) (m)	Calculated dynamic pressure Ø 135mm Q 80L/s (bar)	Calculated dynamic pressure Ø 135mm Q 110L/s (bar)	Calculated dynamic pressure Ø 164mm Q 50L/s (bar)	Calculated dynamic pressure Ø 164mm Q 80L/s (bar)	Calculated dynamic pressure Ø 164mm Q 100L/s (bar)
0	0.153	0.290	0.028	0.071	0.111
0.27	0.179	0.316	0.053	0.098	0.138
0.94	0.245	0.382	0.119	0.163	0.204
2.57	0.405	0.542	0.279	0.323	0.364

The calculated values (Table 3) are close to the values measured (Figure 11) in the jet center for the first two or three sections depending on the case, but the last section's values differ from the calculated values.

The measured pressures are generally lower than the calculated ones. We believe that the perturbations induced by the surrounding air are directly causing the observed deceleration.

In addition, the spectral densities of the pressure fluctuations were computed. The spectral density is the Fourier transform applied to discrete fluctuation pressure data. The goal was to understand the jet fluctuations thanks to the dynamic pressure measurement. For all cases, no clear density peak appears on the spectra. The explanation of this unexpected observation may be that the pressure sensor is fixed in space whereas the jet is flapping as illustrated on figure 5c (taken with a high shutter speed). Consequently, this way of measuring cannot provide precise jet pressure fluctuations. However, it is observed that the energy (>10^{-5} Bar^2/Hz) is mainly concentrated in the low frequencies (<10^2Hz).
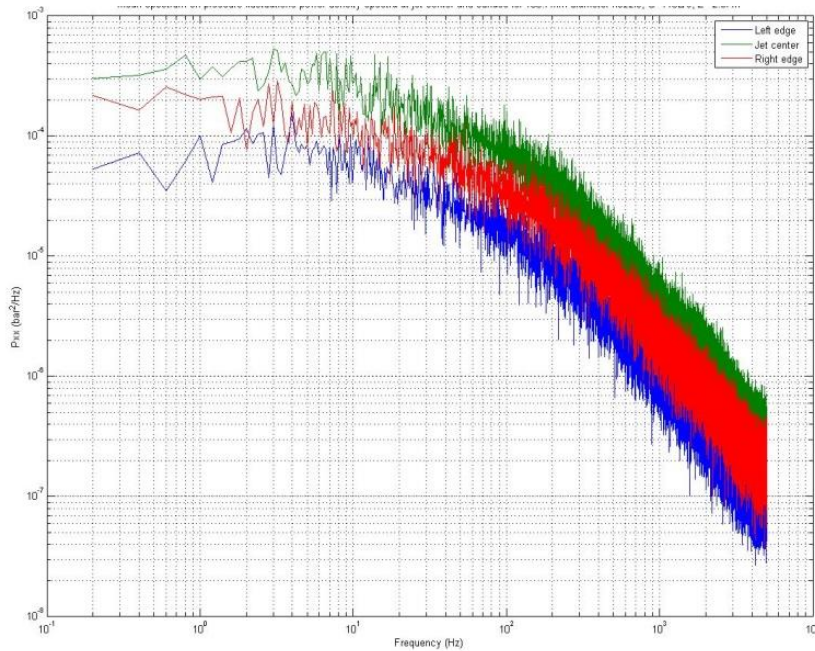
Figure 12: Power spectral density of dynamic pressure fluctuations D_0 135 mm Q= 110 l/s ,Z= 2.57 m

4.2. Turbulence Intensity (Tu)

Table 4: *Tu* estimated value for the different cases.

D_0 (m)	0.135	0.135	0.164	0.164	0.164
Q (m³s⁻¹)	0.08	0.11	0.05	0.08	0.10
Tu (%)	5	3	20	8	7

$$Tu = \frac{\sqrt{1/n \sum_1^n P_{iT}}}{\sqrt{P_M}} \qquad Tu \; calculation \tag{16}$$

Equation 16 defines the Turbulence intensity (*Tu*) where n is the number of pressure values recorded in one run, P_{iT} is the instantaneous total pressure, and *Pm* is the average pressure (*Pa*).

The *Tu* have been estimated with the analysis of the dynamic pressure in the jet cross-section located at *Z*=0.27m. A local Tu has been calculated as described in the previous equation (16) for each measurement point located in the jet (*a* >0.8). The final *Tu* is an average of all the local *Tu* inside the jet. The uncertainty regarding this *Tu* value is large because of the difficulties in estimating the jet diameter at the section *Z*=0.27m. The 20% uncertainty value given for the 164 mm diameter and 0.05 m³s⁻¹ flow rate is due to this reason. In this case, the jet fluctuations began before the 0.27 m section. The experimental set up was not well adapted to this parameter because the pressure sensor is static, whereas the jet is moving radially (see section 2.3).

4.3. Void Rate
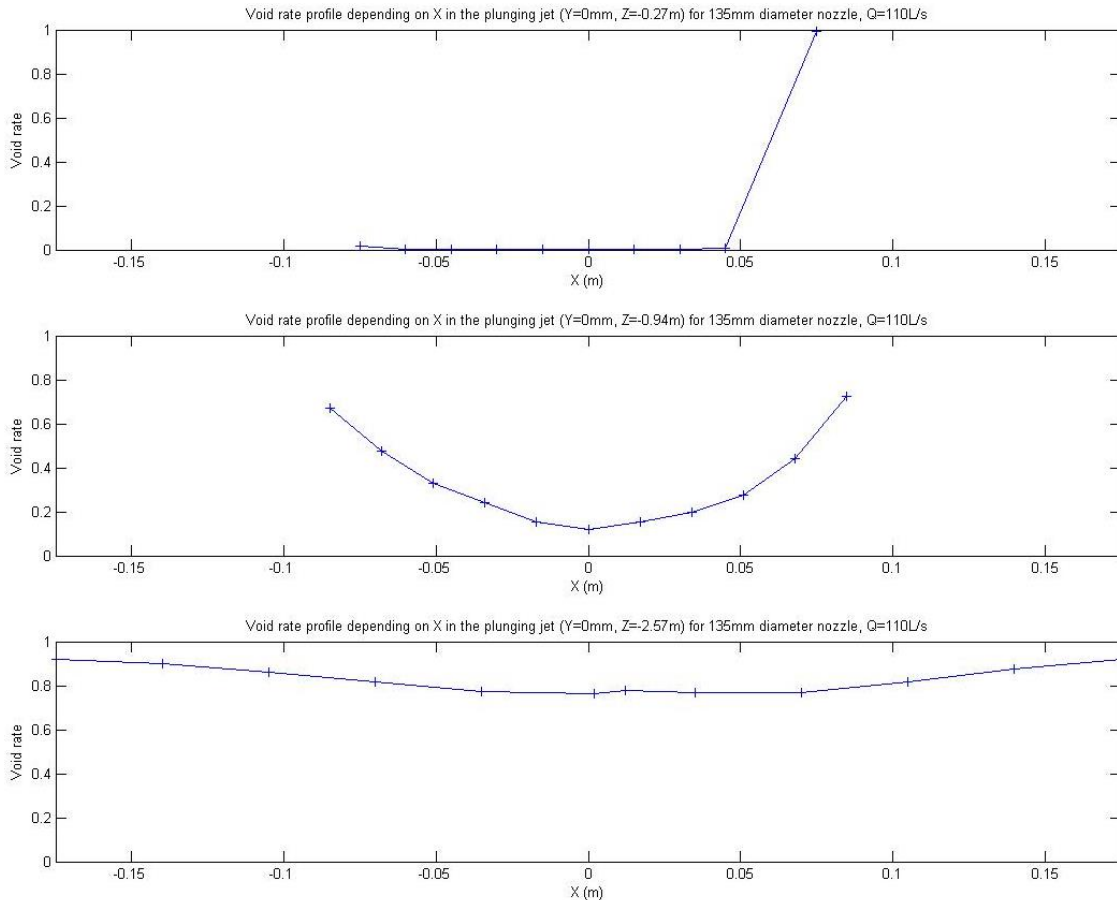
Figure 13: Void fraction profiles across the jet at different distances from the nozzle (*D₀* 135mm, *Q* =110 l/s)

For all cases, the void fraction in the first measurement section is equal to zero, indicating that the ambient air has not yet disturbed the jet. The point where the void fraction is equal to 100% shows that the probe was located at the border of the jet (Figure 13).

For the other sections, the air penetration is well defined by the measurements. Especially at the 2.57 m section, the over 80% void fraction value may indicate that the jet is atomized (Figure 13). Again, the problem is that the probe was static in a fluctuant jet; this induces the same consequences as pressure measurement. The void fraction is close to 100% all over the last section (2.57 m). Accordingly, it may easily be extrapolated that the jet is highly aerated.

4.4. Breakup Length

The length after which the jet becomes a discontinuous structure is usually called the breakup length. Different formulae to predict the break-up length have been proposed (Bin, 1993):

Table 5: Breakup length relations proposed in the literature

$\dfrac{L_b}{D_0} = \dfrac{1.05}{1.14 * Tu}$	$L_b = 6 * Q^{0.32}$	$L_b = C * Q^s$
(17) Ervine and al., 1997	*(18) Horeni (1956) quoted in Le Castillo, (2007)*	*(19) Elsawy and al., (1980)*

In the previous equations (17, 18, 19), *Tu* is the turbulent intensity, L_b the breakup length, and *C* and *S* are empirical coefficients related to the turbulence intensity.
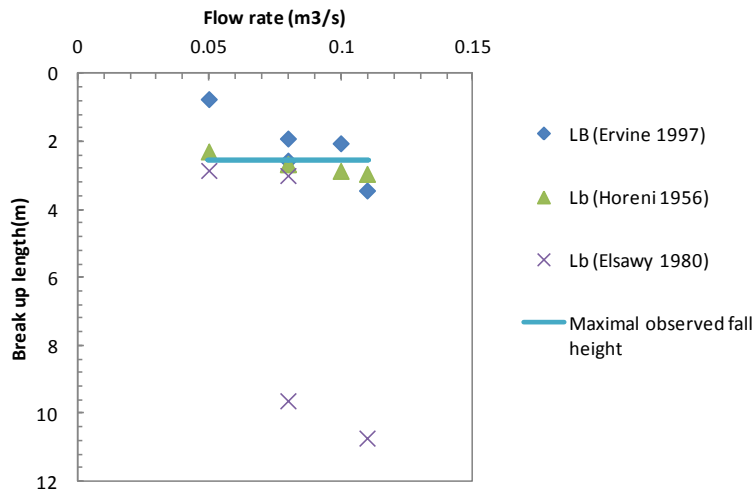
Figure 14: Comparison between different literature breakup lengths

To exploit the proposal of Ervine et al., we considered two reasonable values for *Tu*, close to what is expected in a fully developed pipe flow, namely *Tu*=3% for Ø135 mm and *Tu*= 8% for Ø164mm. This comparison coupled with the jet void rate and dynamic pressure before the impact suggests that for 3 cases out of 5, the jet is atomized or nearly atomized (Figure 14).

The high-speed videos have proved that none of the jets has broken. Instead, lateral jet undulations are significant. Thus, imaging with a low-speed camera leads to a misunderstanding of the jet structure during the fall. In a nutshell, the jet flapping is the explanation of the large void fraction and of the pressure fluctuations observed.

In conclusion, the classical relations seem to be inapplicable to the jets considered in these experiments. The videos show that while other results suggested an atomized jet, the jet is actually not atomized but destabilized during its fall (Figure 5).

5. CONCLUSION

For five large jets, the flow rate and a 2.57m fall height were tested. From a survey of the bibliography, the air entrainment consequences of large plunging jets happen to have been scarcely investigated. The main unknown variables such as the bubble diameter, the penetration depth, the bubble plume bottom ascent velocity and the entrained air flow rate have been measured and compared to the main relationships available in the literature. It has incontestably been pinpointed that the case of large-scale jets is still not well understood and that air entrainment in such conditions still escapes prediction. The jet structure before impact is probably the key point to forecast the jet consequences in terms of bubble generation. That is the reason why a second investigation has been focused on the jet structure. It has been underlined that conventional imaging methods coupled with human vision lead to a misunderstanding mainly because of the jet flapping motion. Therefore, only high-frequency imaging enables correct analysis of the motion and the real behavior of the jet during its fall. The conclusion is that it is still necessary to find the correct parameters that govern the evolution of a large jet from the nozzle to the plunge pool. To reach this purpose, a large scale experiment should be carried out to connect bibliographic results concerning small and medium scales with large-scale jets.

6. ACKNOWLEDGMENTS

7. REFERENCES

Albertson, M.L., Dai, Y.B., Jensen, R.A., Rouse, H., (1950), Diffusion of Submerged Jets. American Society of Civil Engineers, Vol. 115, No. 1, January 1950, pp. 639-664

Biń, A.K., (1993). Gas entrainment by plunging liquid jets. Chemical Engineering Science 48, 3585–3630.

Castillo, L.G., (2007). Pressures Characterization of Undeveloped and Developed Jets in Shallow and Deep Pool, IAHR World congress, Venise.

Clanet, C., Lasheras, J.C., (1997). Depth of penetration of bubbles entrained by a plunging water jet. Physics of Fluids 9, 1864.

Clift, R., Grace, J.R., and Weber, M.E. (1978), Bubbles, Drops, and Particles, Academic Press, New York.

Donk, J. van de, (1981). Water aeration with plunging jets. Dutch Efficiency Bureau, Pijnacker.

Duarte, R.X., (2014). Influence of Air Entrainment on Rock Scour Development and Block Stability in Plunge Pools. EPFL, Lausanne.

Elsawy, E., Mckeogh, E., Ervine, D., (1980). Effect of turbulence intensity on the rate of air entrainment by plunging water jets. ICE Proceedings 69, 425–445

Ervine, D.A., Falvey, H.T., Withers, W., (1997). Pressure fluctuations on plunge pool floors. Journal of Hydraulic Research 35, 257–279.

Evans, G.M., Jameson, G.J., Atkinson, B.W., (1992). Prediction of the bubble size generated by a plunging liquid jet bubble column. Chemical Engineering Science 47, 3265–3272.

Falvey, H., Ervine, D., (1987). Behavior of turbulent water jets in the atmosphere and in plunge pools, ICE Proceedings 83, 295–314.

McKeogh, E.J., Ervine, D.A., (1981). Air entrainment rate and diffusion pattern of plunging liquid jets. Chemical Engineering Science 36, 1161–1172.

Nakasone, H., (1987). Study of Aeration at Weirs and Cascades. Journal of Environmental Engineering 113, 64–81.

Simonin RF, (1959). Recherches théorétiques et expérimentales sur l'entrainement d'air par une veine d'eau cylindrique percutant dans une masse d'eau. Presented at the 8th Congress of IAHR, AIRH, Montreal.

Evaluation of Spillway Stilling Basin Performance and Reservoir Sediment Flushing in a Physical Model
Case Study: Due Hydroelectric Project in Ecuador

Ali Habibzadeh[1], Brian Hughes[2] and Hernan Barahona[3]

[1] Project Engineer, Northwest Hydraulic Consultants Ltd.
9819 – 12 Avenue SW, Edmonton, AB, Canada T6X 0E3

[2] Principal, Northwest Hydraulic Consultants Ltd.
30 Gostick Place, North Vancouver, BC, Canada V7M 3G3

[3] General Manager, Hidroalto S.A., Calle del Establo Lote 50
Edificio Site Center Torre 3 Of. 305, Quito, Ecuador

AHabibzadeh@nhcweb.com

ABSTRACT

The Due Hydroelectric Project is a proposed 50 MW run-of-river hydroelectric project being developed by Hidroalto SA. The project will be located on the Rio Due in Ecuador. The civil works of the intake facility will be comprised of a 133.45 m wide diversion weir with two overflow spillways and six gated sluice channels, a four bay intake structure with sediment excluder, and a fish bypass facility. Northwest Hydraulic Consultants (NHC) evaluated the initial design of the Due intake and spillway facilities using a 1:35 Froude-scaled physical model for river discharges ranging from the intake design discharge of 57.2 m³/s to the 1000-year flood of 2,339 m³/s.

The testing in the physical model revealed some deficiencies in the performance of the initial design of the spillway stilling basins and some opportunities to reduce construction costs. Modifications to the initial design were proposed and evaluated in the model during the design optimization testing phase. The final recommended modifications included adding a new stilling basin wall separating one of the overflow spillways from adjacent sluice channels, reducing the length of the stilling basin, decreasing the height and thickness of the stilling basin walls, and modifying pier noses to reduce flow disturbances. Furthermore, a sluice gate operation guideline was developed in order to maintain sufficient energy dissipation within the stilling basins for the range of river discharges covered in the study.

The physical model was also utilized to evaluate the reservoir sediment flushing procedure and the performance of the intake sediment excluder. Fine sand was used in the model to simulate the reservoir deposits such that qualitative observations of the sediment flushing could be made. Accordingly, a sluice gate operating guideline was developed to maximize the sediment flushing from the reservoir. Finally, the physical model used light-weight sediments to evaluate the efficacy of the intake sediment excluder in trapping sediment to qualitatively observe the sediment load into the intake and the particle trapping process. Modifications to the intake sediment excluder were recommended to improve sediment trapping efficiency and reduce construction costs.

Keywords: Physical model, spillway, stilling basin,sSediment flushing, energy dissipation, sluice gate.

1. INTRODUCTION

1.1.   General

The Due Hydroelectric Project is a proposed 50 MW run-of-river hydroelectric project being developed by Hidroalto SA. The project will be located on the Due River in Ecuador. The intake facility will withdraw water from

the Due River at a design flow of 57.2 m³/s, with 6.2 m³/s diverted through a sediment bypass pipe and the remaining 51 m³/s entering a 4.8 m diameter penstock.

As shown in Figures 1, 2, and 3, the civil works of the project will be comprised of a 133.45 m wide diversion weir, with two overflow spillways (crest elevations at El. 619.0 m) and six 6.0 m wide gated sluice channels; a four bay intake structure with sediment excluder; a 4.8 m diameter power tunnel/penstock; and a fish bypass facility. All six sluice gates are 6.0 m wide and 7.0 m high with invert elevations set at El. 610.0 m (for sluice gates #1 to #4) and El. 609.0 m (for sluice gates #5 and #6).
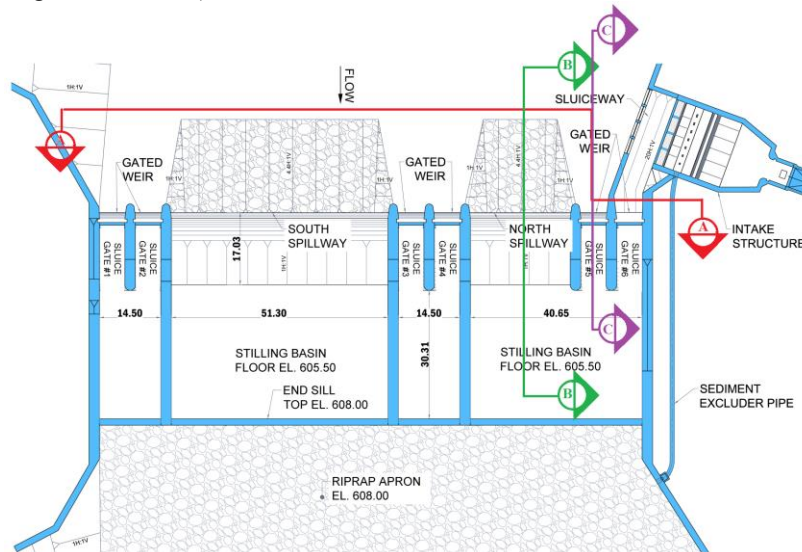
Figure 1. General arrangement of the initial design of the Due Hydroelectric facility.
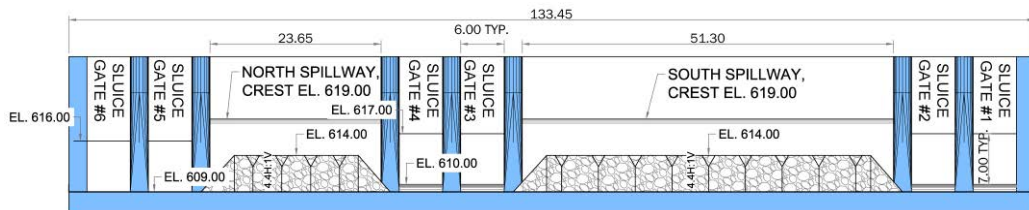
Figure 2. Section view looking downstream (Section A-A in Figure 1) at the initial design of the facility.
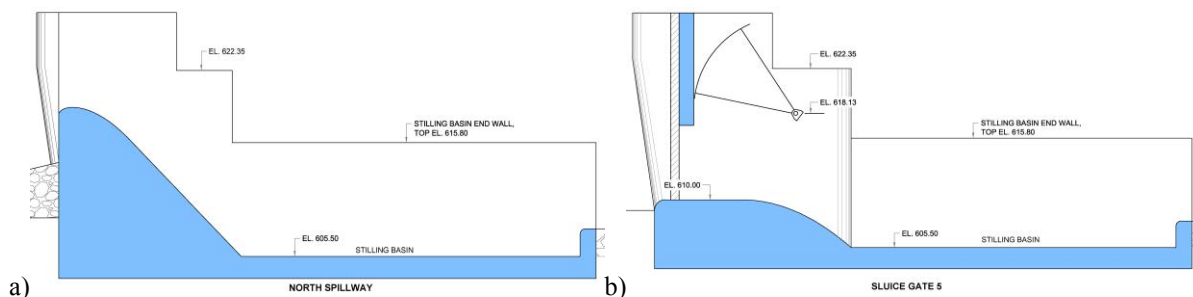
Figure 3. Section views of the initial design of the a) North Spillway (Section B-B in Figure 1), and b) Sluice Gate 5 (Section C-C in Figure 1).

The normal and maximum head pond operating levels are El. 619.0 m and El. 622.5 m, respectively. The riverbed material at the proposed site consists of coarse sand with a median diameter of $D_{50} \approx 2$ mm. Also, riprap protection with a minimum diameter of 1.0 m is suggested to armour the bed downstream of the stilling basins. Table 1

summarizes the hydrology for the project site. The performance of the facility was evaluated at river discharges of 59 m^3/s, 300 m^3/s, 400 m^3/s, 1100 m^3/s, and 2339 m^3/s.

Table 1. Project Hydrology.

Discharge Event	Discharge (m^3/s)
Intake design discharge (including sediment excluder and fish bypass flows)	59
10-year flood	1,517
20-year flood	1,666
50-year flood	1,833
100-year flood	1,945
1000-year flood	2,339

1.2.   Study Objectives

Northwest Hydraulic Consultants (NHC) was retained by Hidroalto to construct and test a physical hydraulic model of the proposed spillway and intake facilities. The overall objective of the model study was to confirm the hydraulic conditions through the spillway and intake structures and to assess the sediment transport conditions in the vicinity of the intake and diversion weir. Specifically, the study was focused on the following objectives:

- Simulate the passage of the flood hydrograph over the overflow (ungated) spillways and sluice gates (bottom outlets) to determine rating curves, hydraulic grade line data and mid-depth velocities;
- Simulate the behavior of stilling basins for both the spillway and sluice gates to ensure acceptable energy dissipation;
- Analyze scour and protection requirements downstream of stilling basins;
- Simulate flushing of sediments from in front of the intake and spillways for predicted future sedimentation patterns in the reservoir; and,
- Simulate the behavior of the intake and sediment exclusion works to minimize the amount of sediment entering the intake and penstock/tunnel, minimize vortex activity at the entrance to the penstock/tunnel, and reduce intake head losses.

Figure 4. Plan view of the physical model.

2. MODEL DESCRIPTION

A 1:35 scale model following the Froude scaling criteria was fabricated to study the performance of the spillways and the intake. The model reproduced a 600 m long reach of the river, extending approximately 450 m upstream and 150 m downstream of the proposed spillway. The model reproduced details of the spillway, sediment sluicing and sediment excluder facilities, the intake structure, the penstock entrance, and approximately ten diameters of the penstock. Figure 4 shows a plan view of the physical model layout. At a 1:35 scale, the model was approximately 17 m long and was able to reproduce a prototype discharge up to the 1000-year flood event of 2,339 m³/s (equivalent to 323 l/s in the model).

2.1. Model Scaling and Similitude

Scale hydraulic models require that the force relationships in the model and prototype are dynamically similar. To achieve this similarity, inertial to gravity, pressure, viscous, and surface tension forces must be the same between model and prototype; only a 1:1 scale model can fully satisfy these criteria. Modeling at a reduced scale involves identifying the primary force relationship to accurately simulate prototype conditions, then selecting a model scale to minimize any scale effects.

For free-surface flow conditions, such as those being simulated for the Due Hydroelectric Project Intake Facility, inertial and gravitational forces are the dominant forces that define the hydrodynamic flow conditions (ASCE 2000). As a result, the Froude number is the key force ratio that must be equal in both the model and prototype. That is,

$$\frac{F_M}{F_P} = 1 \tag{1}$$

in which subindices M and P represent model and prototype, respectively, and F refers to the Froude number, which is equal to the ratio of the inertial to gravitational forces defined as:

$$F = \frac{U}{\sqrt{gy}} \tag{2}$$

Here, U is the mean velocity, g is acceleration due to gravity, and y is the flow depth.

In addition to Froude number equality, the model scale should be large enough to allow flow visualization, accurate measurements of water levels and velocities, and to provide sufficient dimensional control to ensure the model study objectives can be met. Based on satisfying these objectives and the above similitude requirements, NHC constructed and tested the Due Intake model at an undistorted scale of 1:35. At this scale, adherence to Froude criterion for similitude results in the scale relationships as outlined in the table below in which, L_r represents the scale factor (i.e., 1:35).

Table 2. Model Scale Relationships.

Parameter	Relationship	Value
Length	L_r	1:35
Time, Velocity	$L_r^{1/2}$	1:5.92
Discharge	$L_r^{5/2}$	1:7,247

Using a Froude-scaled physical model results in underestimation of the vortex activity due to scale effects resulting from inequality of Reynolds numbers (i.e., viscosity effects) in the model and prototype. As discussed later, increasing discharge rates in the model can provide a better representation of the vortex activity in the prototype. Also, Froude-scaled models can only fulfill the sediment transport similarity criteria in distorted models or by reducing the model particle density (Heller 2011) as described below.

2.2. Sediment Transport Scaling

Fine sand was supplied to the model, allowing the bed levels to build up to an elevation of approximately El. 612.0 m upstream of the spillway and intake structures. The fine sand used in the model had a mean size of 0.2 mm, which is representative of 7.0 mm gravel in the prototype, and a specific gravity of 1.04. In addition, a light-weight model sediment (gilsonite) was used as a tracer material to evaluate the transport and deposition of finer sediments in the vicinity of the intake structure. The particle size distribution curves of the model and prototype material are shown in Figure 5. As shown in Figure 5, the material used in the model roughly covers the range between D_{40} to D_{60} of the prototype sediments.

For simulation of the finer prototype sediments, the dimensionless parameters representing a loose-boundary model include the particle Reynolds number and the densimetric Froude number (i.e., Shields Parameter). The geometric scaling of the particle sizes is limited by the fact that cohesion will begin to influence sediment behavior in the model if the down-scaled particles are within the silt and clay size range. Since water is most often used in the model, the particle density is usually the parameter that can be varied within the model when trying to represent finer sediments.
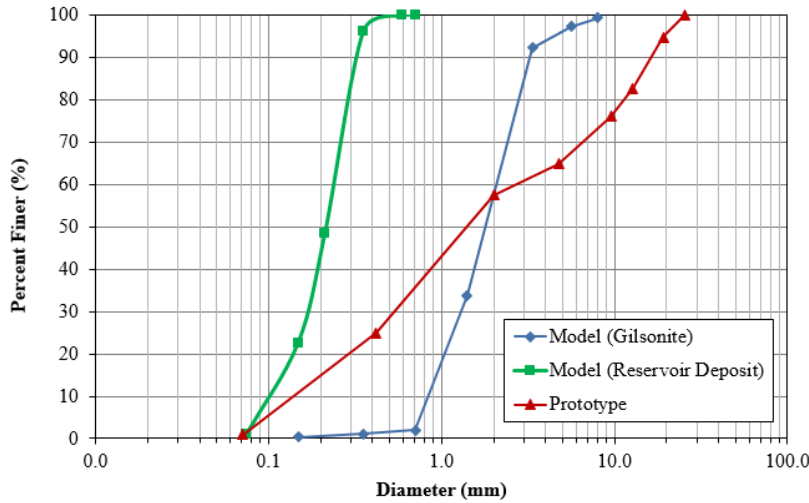
Figure 5. Particle size distribution of the model and prototype material.

For the Due model study, sediment similitude was based on scaling the corresponding sediment movement threshold (i.e., densimetric Froude number F_D presented in Eq. 3, Raudkivi 1976) rather than the Reynolds number. That is, the sediment size was scaled in the model such that it reproduced the corresponding critical shear stress θ (Eq. 2, Raudkivi 1976) required to initiate motion for the sediment size in the prototype.

$$F_D = \frac{U}{\sqrt{(s-1)gD}} \qquad (3)$$

Here, F_D is the densimetric Froude number, U is the mean velocity, s is the ratio of sediment and fluid densities, g is acceleration due to gravity, and D is the sediment particle diameter.

$$\theta = \frac{\tau}{(\rho_s - \rho)gD} \qquad (4)$$

in which θ is the Shields number or the dimensionless shear stress, τ is the shear stress, and ρ_s and ρ are the density of sediment and fluid, respectively.

Following this approach, the shear stress driving the entrainment (initiation of motion) of the sediment particles, with the given size and density in the model, should provide a reasonable representation of the prototype material.

However, with all these precautions, the sediment test results should be considered as qualitative and are useful to compare the performance of one configuration to another, but cannot be used to accurately predict sediment loads or concentrations that may occur in the prototype.

The model gilsonite sediment was injected at approximately approximately 50 m (1.5 m model) upstream of the intake structure. Sediment injection was conducted by gradually releasing a measured volume of (pre-wetted) gilsonite from a 18 cm × 66 cm (model) perforated plate, resulting in a relatively uniform release of sediment particles into the flow approaching the intake structure. This process is shown in Figure 6.

Figure 6. Photo showing injection of sediment upstream of the intake.

3. RESULTS AND DISCUSSION

3.1. Spillway and Stilling Basin Performance

At river discharges of 2,339 m³/s and 1,100 m³/s, with all sluice gates fully open, the stilling basins downstream of the sluice gates performed poorly. The hydraulic jump was swept out of the stilling basins and high-velocity flow plunged into the downstream river channel, causing significant damage to the riprap protection (see Figure 9a).

Similarly, when all sluice gates were closed and all flow passed over the spillways, the stilling basins downstream of the spillways were not effective at dissipating energy. The hydraulic jump was swept out of the spillway stilling basins and formed downstream of the end sill, resulting in significant riprap scour.

Evaluation of the initial design of the stilling basins in the physical model showed that modifications to the design could be made to improve the performance. Based on the results of the model study, the following modifications in the initial design of the spillway facility were recommended:
- The lengths of the stilling basins were reduced by 5 m, provided the recommended gate operation guidelines are incorporated;
- A set of four baffle blocks were added within each sluice gate stilling basin approximately 16 m downstream of the toe of the sluiceway chute;
- A full-length wall was installed in the stilling basin between the north overflow spillway and sluice gate 5;
- The width of all stilling basin walls was reduced from 2.5 m to 1.25 m by incorporating a 12.5 m long 1:10 tapered transition that starts at the toe of the sluiceway chute and is straight on the spillway side;
- The height of all stilling basin walls was reduced by 2 m (i.e., the top elevation of the stilling basin walls was lowered to El. 613.80 m); and,
- The pier noses between sluice gates were replaced with 6.25 m long 1:10 tapered transition terminating in a 1.25 m diameter rounded nose. The pier noses can have the same top elevation as the stilling basin walls (El. 613.8 m).

A section view of the final design of facility is shown in Figure 7. Further evaluation of the spillways and stilling basins demonstrated that proper operation of the spillways and sluice gates is critical in order to maintain a satisfactory performance of the facility as described below.
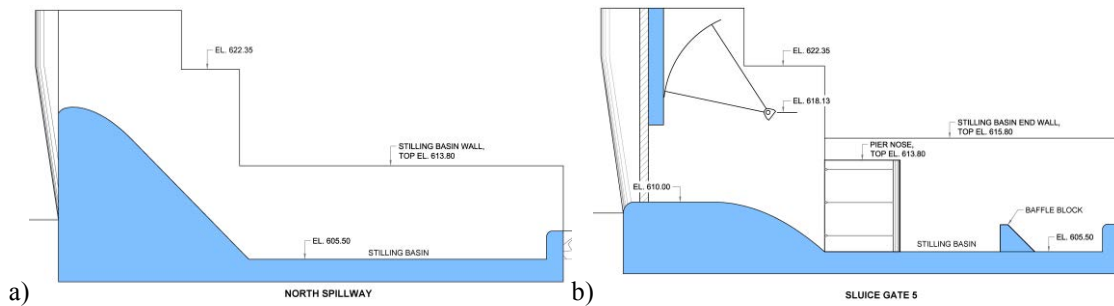
Figure 7. Section views of the final design of the a) North Spillway (Section B-B in Figure 1), and b) Sluice Gate 5 (Section C-C in Figure 1).

3.2. Spillway and Sluice Gate Operation

In order to assess what the maximum spillway discharge could be to avoid scour damage to the riprap downstream of the stilling basin, the model discharge was progressively increased with all flow passing over the north and south overflow spillways, and the stilling basin performance was evaluated continuously. It was observed that for spillway discharges up to approximately 800 m³/s, which corresponds to a reservoir water level of approximately El. 622.0 m, the performance of the spillway stilling basins was satisfactory with no riprap scour. For spillway discharges above 1,300 m³/s, corresponding to reservoir water levels above El. 623.0 m, the stilling basins were found to be ineffective at dissipating energy, and the high-velocity flow leaving the stilling basin caused considerable damage to the downstream riprap protection. For spillway discharges between 800 m³/s and 1,300 m³/s (reservoir water level between El. 622.0 m and El. 623.0 m), the stilling basins were partially effective at energy dissipation, and some minor riprap scour was observed.

Following these tests, the model was used to develop operating rules for the sluice gates in order to limit the reservoir levels to less than El. 623.0 m, corresponding to spillway discharges less than 1,300 m³/s, during larger flood events. The operating rules were developed by progressively increasing the model discharge and determining the sluice gate operations to ensure the hydraulic jumps formed near the upstream ends of the stilling basins, the scour of the downstream riprap was minimized, and the distribution of flow velocities across the downstream channel was uniform.
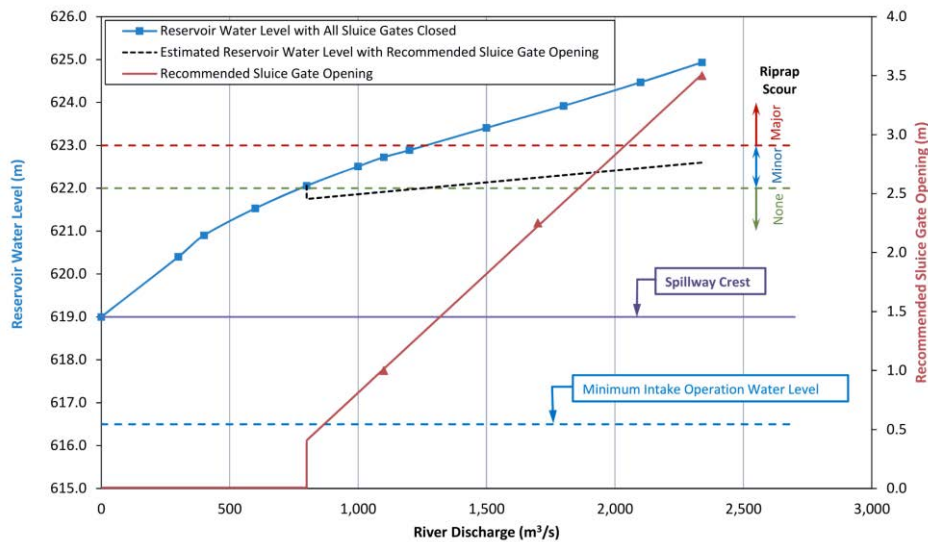
Figure 8. Reservoir water level and recommended sluice gate operation.

Based on these tests, a recommended operation chart for the facility was developed, as shown in Figure 8. This chart presents a relationship between reservoir water level and riprap scour and outlines the recommended gate operations. To maintain satisfactory stilling basin performance, it is recommended that sluice gates 1 to 5 be operated for river flows exceeding approximately 800 m^3/s. At a river discharge of 800 m^3/s, it is recommended that sluice gates 1 to 5 should be opened by 0.5 m; as the river flow increases to 1,100 m^3/s, the sluice gate openings should be increased to 1.0 m; and if the river discharge continues to increase, the gate openings should be increased linearly to achieve a gate opening of 3.5 m at a river discharge of 2,339 m^3/s (see Figure 9). Following the recommended sluice gate operation resulted in satisfactory performance of the stilling basins (see Figure 9b).

a)   b)
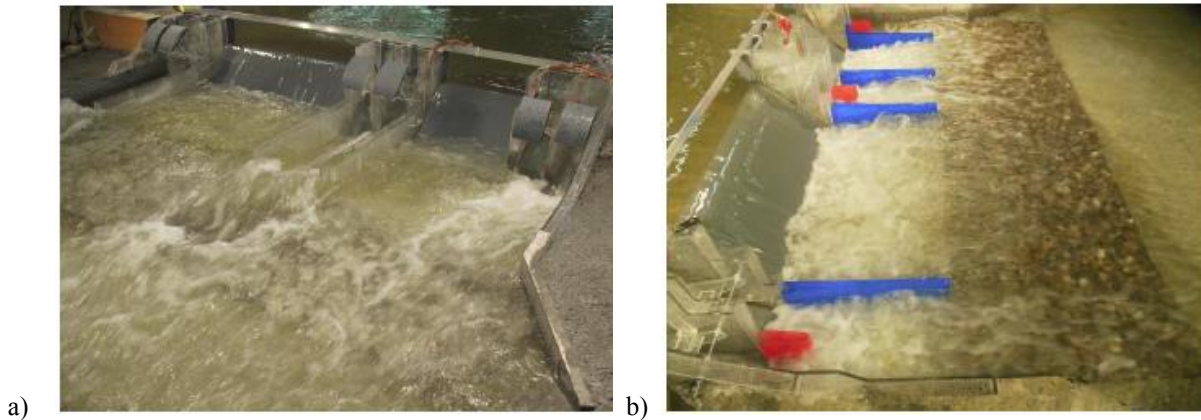
Figure 9. Performance of the stilling basins at a river discharge of 2,339 m^3/s.

a) Initial design with the sluice gates fully open, and b) Modified design with recommended sluice gate operation.

3.3.   Intake Performance

3.3.1.   Vortex Activity

The flow patterns at river discharges of 400 m^3/s and 300 m^3/s were uniform towards the intake. However, the flow entering the intake was slightly non-uniform, which resulted in an intermittent surface vortex (Type 2 dye core) forming just upstream of the penstock entrance adjacent to the left (west) side of the intake. A description of vortex types can be found in Knauss (1987). It is estimated that this surface vortex was present for less than 5 percent of the time; however, due to scale effects in the model, it is expected that the strength and frequency of the vortex activity will be greater in the prototype than observed in the model.

With the intake operating at 57.2 m^3/s over a range of river discharges from 59 m^3/s to 400 m^3/s, intermittent Type 2 surface vortices (dye core) existed within the intake just upstream of the penstock entrance with a frequency of less than 10 percent of the time. However, as noted previously, the surface vortex activity observed in the model is under-estimated due to scale effects. To compensate for this, surface vortex activity within the intake was evaluated at a discharge equal to 1.5 times the Froude-scaled discharge. At the increased intake withdrawal, intermittent Type 2 (dye core) vortices were observed but the frequency of the vortices increased to approximately 50 percent of the time, which is likely more representative of what will be observed in the prototype facility. This is based on the recommendations by HI (2012) to repeat selected tests at 1.5 times the Froude scaled flows to compensate for any possible scale effects on free surface vortices.

Based on the increased frequency of the surface vortex activity observed at the higher withdrawal discharge and at the lower water level, it was recommended that vortex suppression devices be installed in the intake. The proposed design consisted of a set of six horizontal pipes, referred to as "vortex breaker pipes" that were installed at a centerline elevation of El. 615.5 m immediately upstream of the penstock entrance. The pipes have a diameter of 0.2 m and were installed at a center-to-center spacing of 0.6 m (clearance of 0.4 m between pipes). Testing conducted

with these pipes installed in the model indicated that they were effective at dissipating the Type 2 surface vortices before they were able to enter the penstock.

In order to determine the minimum "safe" operating level for the intake, before vortex activity increased to a continuous Type 2 or intermittent Type 3, the water level within the reservoir was slowly lowered while maintaining an intake discharge of 57.2 m^3/s. As the water level within the reservoir was lowered, Type 2 surface vortex activity became more frequent, but Type 3 vortices were not observed. However, at a water level of about El. 617.5 m, the flow was influenced by the sediment excluder sill (crest at El. 615.0 m), with weak standing waves forming over the sill and increased turbulence at the penstock entrance. As the water level was lowered further, flow over the sill became supercritical, and a weak hydraulic jump formed upstream of the penstock entrance. At this stage, a significant volume of air was entrained into the penstock, and the withdrawal discharge was reduced.

3.3.2. Sediment Exclusion

The amount sediment ingested by the intake was found to be approximately 5 percent of the light-weight (gilsonite) sediment that was supplied to the model a short distance upstream of the intake, and the initial design of the sediment excluder (shown in Figure 10) was effective in diverting approximately 60 percent of the sediment that entered the intake. Approximately 20 to 30 percent of the sediment entering the intake passed through the penstock, and the remaining 10 to 20 percent deposited elsewhere within the intake.

Based on the initial design testing observations, modifications to the intake sediment extractor were proposed and successfully examined in the model. The recommended final design consisted of replacing the sediment extractor sill with a simpler vortex tube sediment extractor.
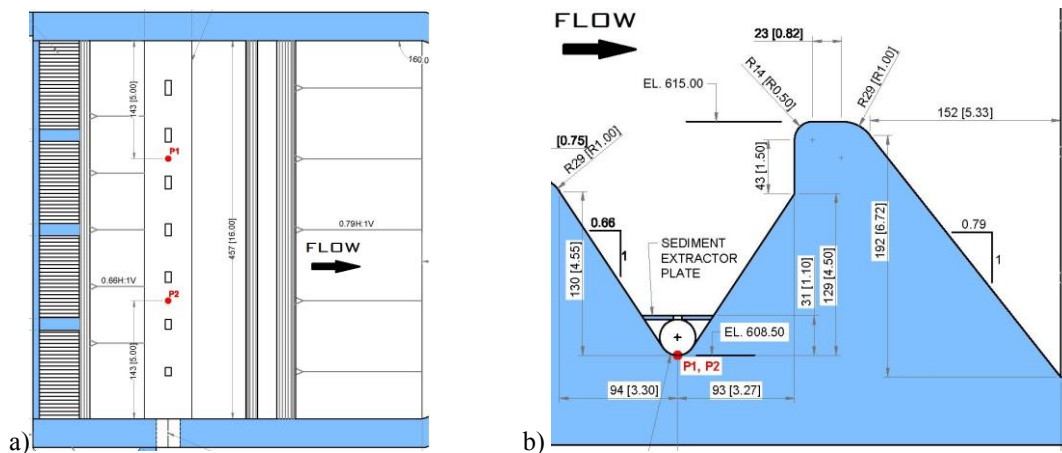
Figure 10. Initial design of the intake sediment extractor; a) plan and b) section views.

3.3.3. Vortex Tube Sediment Extractor

The design for the vortex tube sediment extractor was comprised of a 1.0 m diameter tube aligned at a 7-degree angle to the intake centerline and inset within a lowered sill set at El. 612.90 m, with a 0.5 m high sill constructed immediately downstream of the vortex tube (see Figure 11). Preliminary tests conducted with this design demonstrated that there was almost no flow or sediment being drawn through the vortex tube from the far left side of the intake, resulting in relatively poor performance with respect to sediment exclusion. However, it was determined that adding a slotted plate (similar to the plate used in the initial sediment excluder) was effective at improving the withdrawal of flow and sediment from across the full width of the intake. Furthermore, preliminary testing indicated that it would be feasible to operate the intake at water levels down to El. 616.5 m (1 m lower than determined for the initial intake design) without significantly increasing the surface vortex activity or entraining air into the intake. The hydraulic losses through the intake were found to be similar for the two designs, and the ability to divert the near-

bed sediment entering the intake was also comparable to the original design. Based on these results it was recommended that the vortex tube sediment extractor be incorporated into the final design for the intake.
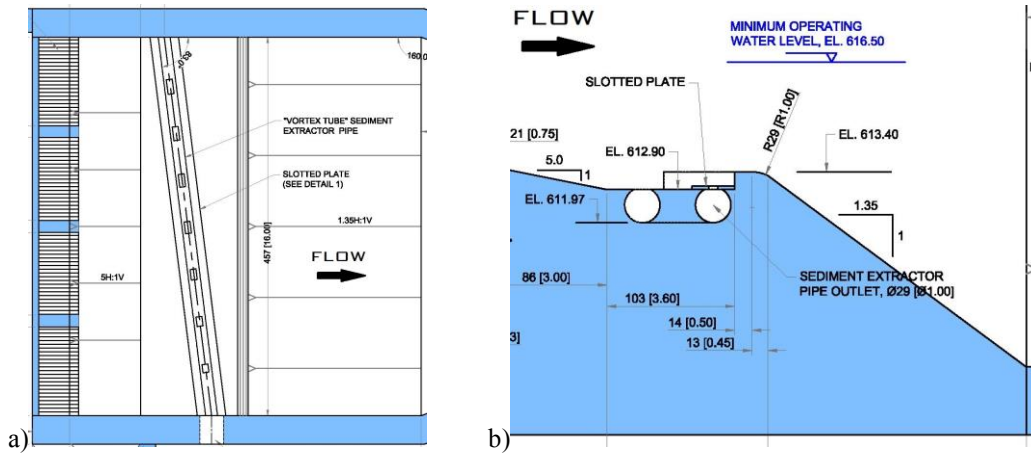
Figure 11. Recommended final design of the intake sediment extractor; a) plan and b) section views.

4. SUMMARY AND CONCLUSIONS

Northwest Hydraulic Consultants Ltd. (NHC) was selected by Hidroalto S.A. to construct and test a 1:35 scale physical hydraulic model of the Due Hydroelectric intake facility, located on the Due River in the Province of Sucumbios, Ecuador. The intake facility will withdraw water from the Due River at a design flow of 57.2 m³/s, with 6.2 m³/s diverted through the sediment excluder pipe and the remaining 51 m³/s entering the 4.8 m diameter power tunnel. The civil works of the project will be comprised of a 133.45 m wide diversion weir with two overflow spillways; six 6.0 m wide gated sluice channels; a four bay intake with sediment excluder; and a 4.8 m diameter power tunnel/penstock leading to a 50 MW powerhouse.

The overall objective of the model study was to confirm the hydraulic performance of the spillway and intake structures and to assess the sediment transport conditions in the vicinity of the intake and diversion weir. Specifically, the study was focused on the improving and optimizing the spillway stilling basin design and minimizing vortex activity and sediment ingestion within the intake. NHC evaluated several modifications to the stilling basins and intake to achieve these objectives.

The recommended modifications within the stilling basin comprised of adding a stilling basin wall between the north spillway and sluice gate 5; shortening the stilling basin length by 5 m; reducing the height of the stilling basin walls by 2 m; reducing the width of the stilling basin walls to 1.25 m using a 1:10 transition; and adding a row of four baffle blocks within the sluice gate stilling basins.

The model was also used to develop operating guidelines for the intake and spillway. It was determined that to avoid excessive sediment entering the intake, operation of the intake should not be permitted at river discharges above 400 m³/s, and to avoid air entrainment into the penstock, operation of the penstock should be halted at a reservoir water level below El. 616.5 m. Furthermore, it was determined that sluice gates 1 to 5 should be operated for river discharges exceeding approximately 800 m³/s in order to maintain reservoir water levels below El. 623.0 m and minimize the potential for damage to the rip rap protection downstream of the spillway stilling basins. A relationship between river discharge and recommended sluice gate operation was developed during the final design tests in the model.

Furthermore, the recommended modifications within the intake included replacing the initial design of the sediment excluder sill with a "vortex tube" sediment extractor, and adding a set of vortex breaker pipes just upstream of the penstock entrance to dissipate surface vortex activity.

5. REFERENCES

American Society of Civil Engineers (2000). Hydraulic Modeling: Concepts and Practice, Manual No. 97.

Heller, V. (2011). "Scale effects in physical hydraulic engineering models." Journal of Hydraulic Research, Vol. 49, No. 3, pp. 293-306.

Hydraulic Institute (2012). American National Standard for Rotodynamic Pumps for Pump Intake Design, Parsippany, New Jersey, ANSI/HI 9.8-2012.

Knauss, J. (1987). *Swirling Flow Problems at Intakes*, IAHR Hydraulic Structures Design Manual, Balkema, Rotterdam, Netherland.

Raudkivi, A.J. (1976). *Loose Boundary Hydraulics*, 2nd Edition, Pergamon Press, New York, USA.

St. Mary Diversion Dam – Case Study of a 100 year Old Diversion

B.J. Heiner[1] and J. Wagner[2]
[1]Hydraulic Investigations and Laboratory Services
U.S. Bureau of Reclamation
Denver, CO 80225
USA
[2]Civil Structures
U.S. Bureau of Reclamation
Denver, CO 80225
USA
E-mail: bheiner@usbr.gov

ABSTRACT

After 100 years of service, the St. Mary Diversion Dam is being replaced with a new design that will provide more effective fish passage and protection. The diversion is located in northern Montana, adjacent to the east side of Glacier National Park. It diverts water from the St. Mary River 1.21 km (0.75 mile) downstream of Lower St. Mary Lake. The existing 60.35-meter-long and 1.83-meter-high (198-foot-long and 6-foot-high) concrete weir diverts up to 24 cubic meters per second (850 cubic feet per second) design flow from the St. Mary River into the North Fork of the Milk River through a 46.67-km (29-mile) long canal, siphon, and drop system. The existing facility, which is maintained and operated by the U.S. Bureau of Reclamation (Reclamation), was completed in 1915 and is in need of replacement. The Endangered Species Act (ESA) listed species that have been adversely affected by limited passage and entrainment into the canal. The St. Mary Diversion and Milk River Irrigation project have been identified as the primary threat to Bull trout habitat in the St. Mary River drainage. Recovery efforts to restore Bull trout habitat in the St. Mary River drainage requires that Reclamation provide effective Bull trout passage and protection at the St. Mary Diversion. This paper presents a short history of the St. Mary Diversion and Milk River Irrigation project, which includes collaborations with all interested parties as well as modeling efforts that were used to enhance the design of the replacement structure to provide the best situation for Bull trout recovery without limiting diversion capability.

Keywords: fish passage, protection, diversion, canal, screen, dam, physical modeling

1. INTRODUCTION

The St. Mary Diversion Dam is part of the Bureau of Reclamation's (Reclamation) Milk River Project in north-central Montana. Located near Babb, Montana, the diversion and canal were constructed in 1915 on the St. Mary River, 1.21 km (0.75 mile) downstream from Lower St. Mary Lake. The dam consists of a 60.35-meter-long and 1.83-meter-high (198-foot-long and 6-foot-high) concrete weir and sluiceway. A design discharge of 24 cubic meters per second (850 cubic feet per second) of water is diverted from the west side of the river upstream of the dam through a 46.67-km (29-mile) long canal. The canal transports the water through two large steel-plated siphons and five large concrete drop structures before it discharges into the North Fork Milk River (Figure 1).

In 1999, the U.S. Fish and Wildlife Service (FWS) listed Bull trout (*Savelinus confluentus*) as a threatened species under the Endangered Species Act (ESA). When listed, FWS concluded that Bull trout native to the St. Mary River drainage are negatively affected by operation of the Reclamation Milk River Irrigation Project (Mogen 2011). More specifically, the St. Mary Diversion dam was cited as a known seasonal barrier to upstream migration of Bull trout (Mogen and Kaeding 2005a, 2005b and 2008) and a threat to the species due to the entrainment of fish during the irrigation season (Wagner and Fitzgerald 1995, Mogen and Kaeding 2000 and 2002). Fish entrained into the canal are either passed to the North Fork of the Milk River or remain in the canal until the gates are shut and the canal is dewatered during the non-irrigation season.
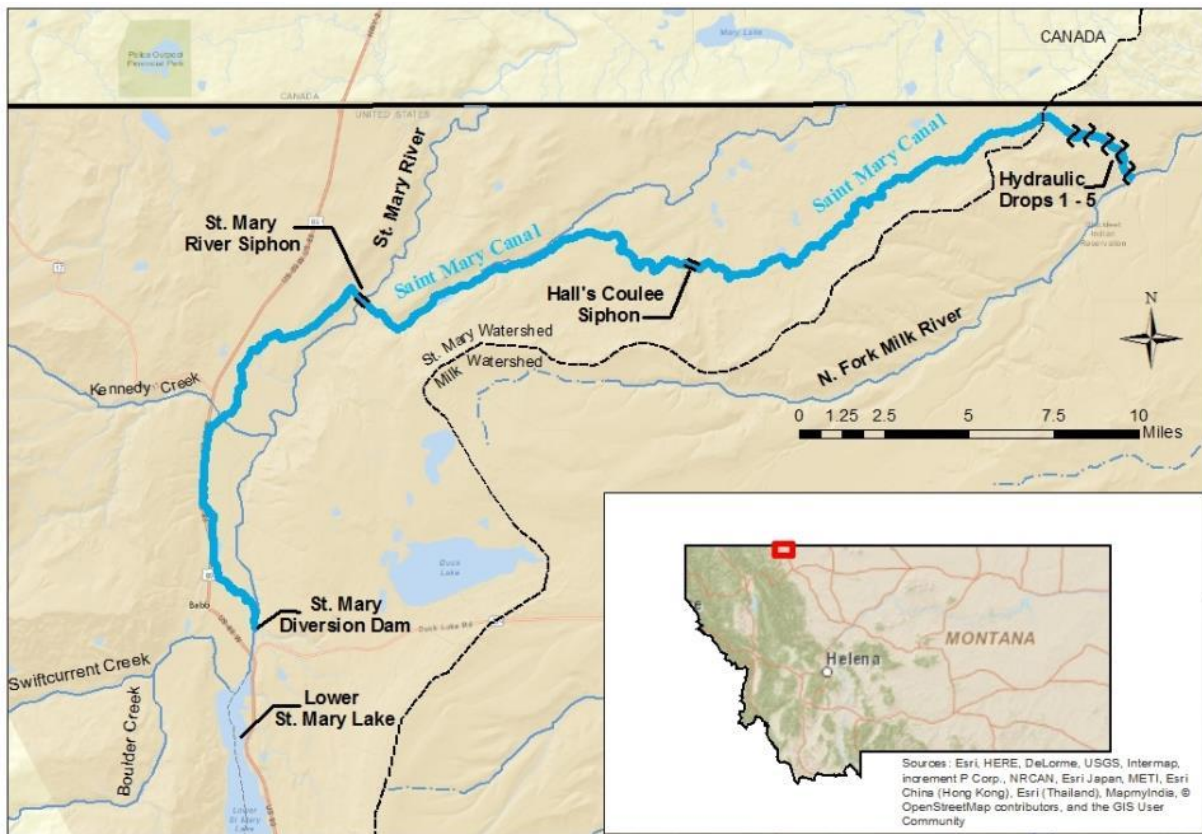
Figure 1. Overview map of the St. Mary Diversion and related features.

To help aid growth of Bull trout and other species in the Milk River System, Reclamation began investigations on how to reduce the impact the St. Mary Diversion Dam and Canal has on Bull trout in the Milk River System. This paper discusses the history of the St. Mary Diversion Dam and Headworks including the condition of the existing facility and several of the recommended mitigation plans to provide fish screening and passage at the facility while still maintaining diversion flow rates. This paper is not a comprehensive list of all design options that have been evaluated over the past 15 years.

2. DESCRIPTION OF EXISTING FACILITY

The St. Mary Diversion Dam is a concrete ogee weir with an overhead abandoned 3-span truss bridge (one span has been removed Figure 2). The spillway is a concrete overflow structure that consists of an uncontrolled weir and downstream horizontal slab. The spillway is ungated and has no mechanical features but is subdivided into two equal sections by a concrete bridge pier on which two abandoned 29.72-meter (97.5-foot) Pratt trusses span the crest of the spillway. Each section of the spillway weir is 28.9 meters wide (94 feet 10 inches). The concrete spillway weir crest is elevation 1362.76 m (4471.0 ft). The weir crest elevation was raised to elevation 1363.07 m (4472.0 ft) by mounting 0.31 m (1 ft) high weir-boards on top of the entire spillway crest. Figure 3 provides an overhead view of the spillway from the upstream channel. The sluiceway is located to the left of the spillway and consists of six openings with inverts at elevation 1361.24 m (4466.0 ft) controlled by 0.1- by 0.1-meter (4- by 4-inch) stop planks (Figure 4). The St. Mary Canal headworks is located on the left abutment and is controlled by eight 1.52- by 1.68-meter (5- by 5.5-foot) headgates with gate sills at elevation 1361.24 m (4466.0 ft) (Figure 6). The headworks are a concrete structure 17.98 meters (59 feet) wide and 6.71 meters (22 feet) long, with an upstream weir in front of the gates with a crest at elevation 1361.54 m (4467.0 ft).

The 46.67-km-long (29-mile) St. Mary Canal was constructed between 1907 and 1915. The unlined canal was designed to convey 24 cubic meters per second (850 cubic feet per second) at a flow depth of 2.74 meters (9 feet). The canal was excavated to a bottom width of 7.92 meters (26 feet) with 2:1 side slopes at a channel invert slope of 0.000095 (Interior 1981). The dam is used to divert water into the canal from March through September. During the non-diversion period, the sluiceways are opened and canal headgates are closed. The canal was designed to convey 24 m^3/s (850 ft^3/s); however, the condition of the canal limits diversion to a

maximum of 18.41 m³/s (650 ft³/s). During March and early April, all river flow in excess of about 2.83 m³/s (100 ft³/s) is typically diverted. From June to August, diversions often reach 75 percent of total river flow. Diversion decreases sharply in late August and September (Mefford 2003).
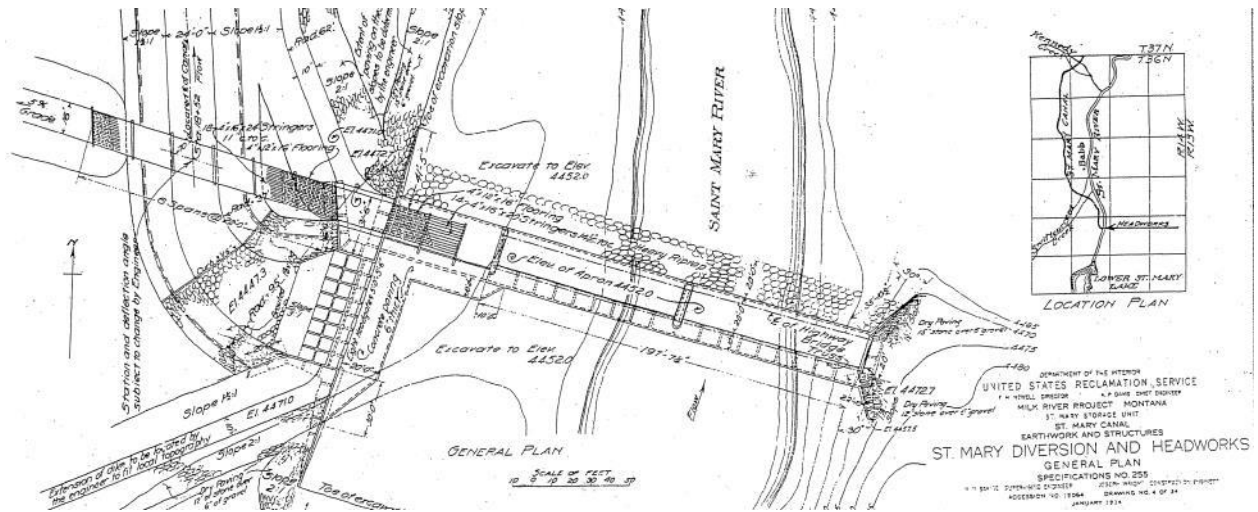
Figure 2. Original plan view drawing of the existing St. Mary Diversion Dam and Headworks (January 1914 – note: elevations are based on project datum that is approximately 4.27 meter (14 feet) lower than NAVD88)

Figure 3. Existing St. Mary Dam Diversion weir, sluiceway and abandoned bridge during low flow fall season (view is from upstream left bank)

Figure 4. St. Mary Diversion sluiceway gates (view is from upstream left bank, standing on top of the headworks structure)

Figure 5. St. Mary Diversion headworks structure (view of from downstream of the headworks, flow is towards reader)

Recent examinations of the 100-year-old diversion dam, headworks, and canal revealed substantial freeze-thaw damage to exposed concrete surfaces. Concrete core samples taken from the piers on the dam and sluiceway indicated that the condition of the concrete is very poor where exposure to ice and frequent freeze-thaw cycles have degraded the strength (Mefford 2003). Based on available inspection data and visits to the structure, the weir (Figure 6), abutments (Figure 7), piers (Figure 8), sluiceways (Figure 9), and diversion headworks will

likely all require demolition and replacement in the near future. Recently, some modifications and repairs to the facility have been made that will prevent catastrophic failure of the structures.

Figure 6. St. Mary Diversion weir concrete failure and exposed rebar.

Figure 7. St. Mary Diversion right abutment damage and exposed rebar.

Figure 8. Concrete degradation on the downstream end of piers surrounding sluice bays.

Figure 9. Concrete degradation upstream end of piers surrounding sluice bays.

3. TIMELINE OF PROJECT DECISIONS

Over the past 15 years, Reclamation has been working with all interested stake holders to help protect the threatened Bull trout at the St. Mary Diversion. This section describes some of the early concepts that were evaluated along with some of the design decisions that have shaped the project. This is not a comprehensive list of events and concepts.

3.1. Early Design Concepts

Mefford (2003) conducted a conceptual design study and outlined two different concepts. Concept 1 recommended rehabilitating the diversion weir and replacing the headworks and sluiceway (Figure 10). Concept 2 recommended replacing all the existing structures (Figure 11). Both concepts included fish screens to prevent entrainment in the canal and a rock type fishway to allow passage over the dam. Both concepts proposed using a flat plate fish screen in the canal with a bypass at the end of the screen to return fish to the river. Main features were intended to maintain approach velocities of 0.12 m/s (0.4 ft/s), provide a 0.31-m (1-ft) sill on the bottom of the screen, and limit fish exposure to the screen to 60 seconds or less. The 0.31 m (1-ft) sill

was meant to provide better protection to the bottom-oriented behavior of Bull trout (Beyers and Bestgen 2002). The rock-type fishway for both options would provide passage on river right by extending a rock fishway at a 3.5 percent slope to approximately 45.72 meters (150 feet) downstream of the weir. The difference between the two options was the extent to which the existing weir structure was rehabilitated or replaced. Each design was sized to allow flows of 18.41 m^3/s (650 ft^3/s) (current canal maximum), 24.07 m^3/s (850 ft^3/s) (original design), and 28.32 m^3/s (1000 ft^3/s) (increased capacity) into the canal. 2003 costs for construction of each concept was estimated to between \$6.9M and \$10M, depending on which was chosen.
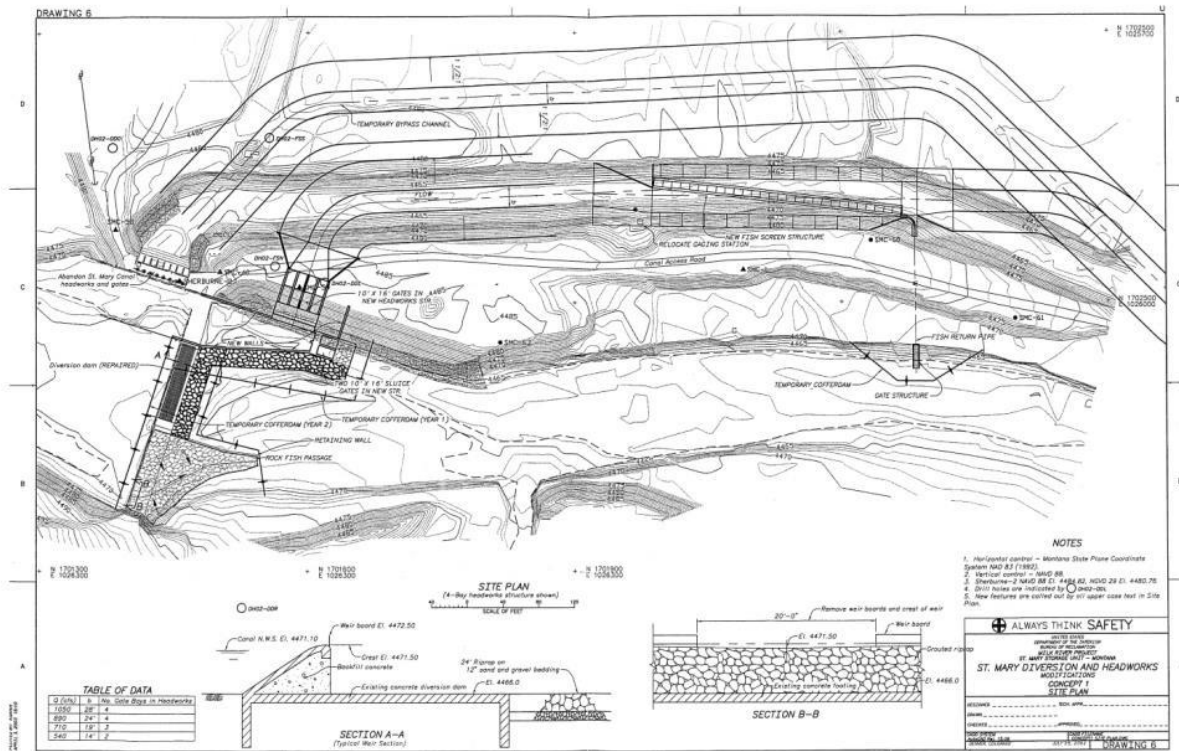
Figure 10. St. Mary Diversion rehabilitation concept 1 as presented by Mefford (2003).
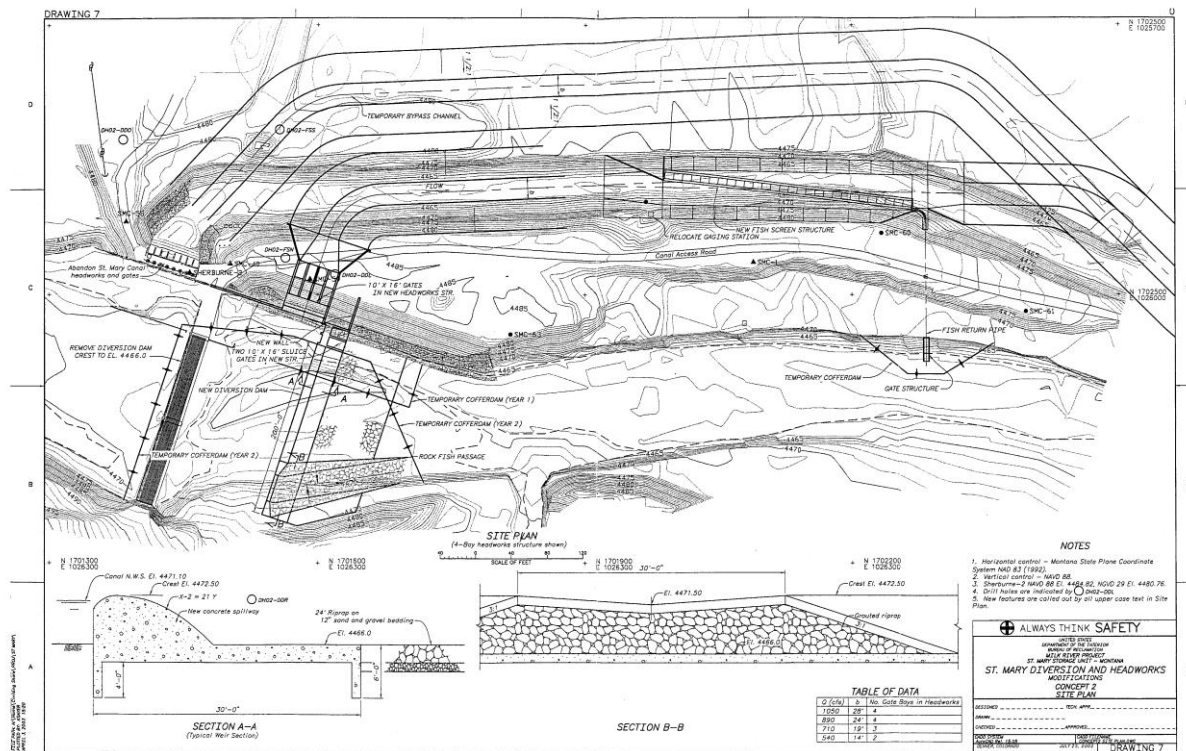
Figure 11. St. Mary Diversion rehabilitation concept 2 as presented by Mefford (2003).

Since the 2003 concepts, many other configurations were investigated by a wide range of individuals and groups. TD&H Engineering Consultants (2006) provided a wide range of alternatives to repair/replace the existing diversion and canal; included in their report are costs and recommendations.

More recently, Reclamation's Montana Area Office (MTAO) funded Reclamation's Technical Service Center (TSC) to develop a 100% design and specification package to allow replacement of the existing diversion facility. The TSC has worked in conjunction with MTAO, FWS, Blackfeet Nation Tribe, Montana Department of Natural Resources and Conservation (DNRC), Milk River Irrigators, St. Mary Rehabilitation Working Group, and many other stake holders to develop a design that met everyone's expectations and requirements. Team discussions and design reviews suggest as many as 6 different diversion and headwork options. Notable designs included a 0.91-meter (3-foot) dam raise, a rock ramp to provide passage, and many different configurations of concrete ladders and fish screen locations.

3.2. Original 60% Design Option – Physical Model 1

In January of 2014, MTAO and other stakeholders met to complete a 60% design review on the to-date plans for the St. Mary Diversion Dam and Headworks. The designs were developed by the TSC with a multidisciplinary team led by Jason Wagner. The 60% design was to be robust, simple, and easy to operate. The fish ladder and fish screen were designed appropriately for juvenile Bull trout. The screens were designed such that a maximum screen approach velocity would not exceed 0.24 m/s (0.80 ft/s) at 30.58 m³/s (1080 ft³/s) flow in the canal. Typical design criteria for salmonids would usually only allow 0.12 m/s (0.4 ft/s) approach velocity, but the multi-agency biological review team obtained an exception due to the species and life stages present at the facility.

Figure 12 provides a plan view drawing of the proposed 60% design. Included in the design are the following features: A) New diversion dam located downstream of the existing structure with a kinked ogee shape and an offset weir height to align flow and allow more flow on the right bank of the river. B) New sluice bays and overshot bays on both the right and left side of the dam adjacent to the abutments to allow sediment and floating debris removal and aid in ladder attraction. C) New headworks that consists of a trashrack with a maximum 0.61 m/s (2 ft/sec) approach velocity and nine 1.52- by 1.68-meter (5- by 5.5-ft) steel slide gates. D) New fish screen 54.86-m long by 2.3-m tall (180-ft long by 7.5-ft tall) and fish bypass to protect fish from entrainment.

E) All species fish ladder located on the right bank of the river. F) New lowered sluice channel on river left to allow non-irrigation flows to pass without inundating the headworks.

Due to the complexity of the project, TSC constructed a 1:12 physical model of the complete structure and several numerical models of individual components of the proposed 60% design to ensure that all the hydraulic and structural components would function as intended and that the project would succeed at both protecting Bull trout and providing the necessary diversion to the St. Mary canal. Figure 13 provides an aerial view of the physical hydraulic model with annotations. Testing the physical model helped the design team identify several areas of concern with the proposed design. The following items were noted from the physical and numerical models: A) The kinked ogee crest dam caused severe scour downstream of the apron, which resulted in an unstable river bed. B) The entrance to the fish ladder was going to be difficult for species to locate due to extreme turbulence and eddies. C) The headworks was too large, resulting in small gate openings to operate the canal at the desired flowrates. D) The overshot bays intended for flushing floating debris over the dam were not in ideal locations and would require excessive operation and maintenance. E) Operation of the facility on two sides of the river would be difficult due to the access limitations on the right bank. F) Having the fish ladder on the opposite side of the river as the headworks required maintaining two thalwegs, which created additional complexity and may increase operation and maintenance costs.
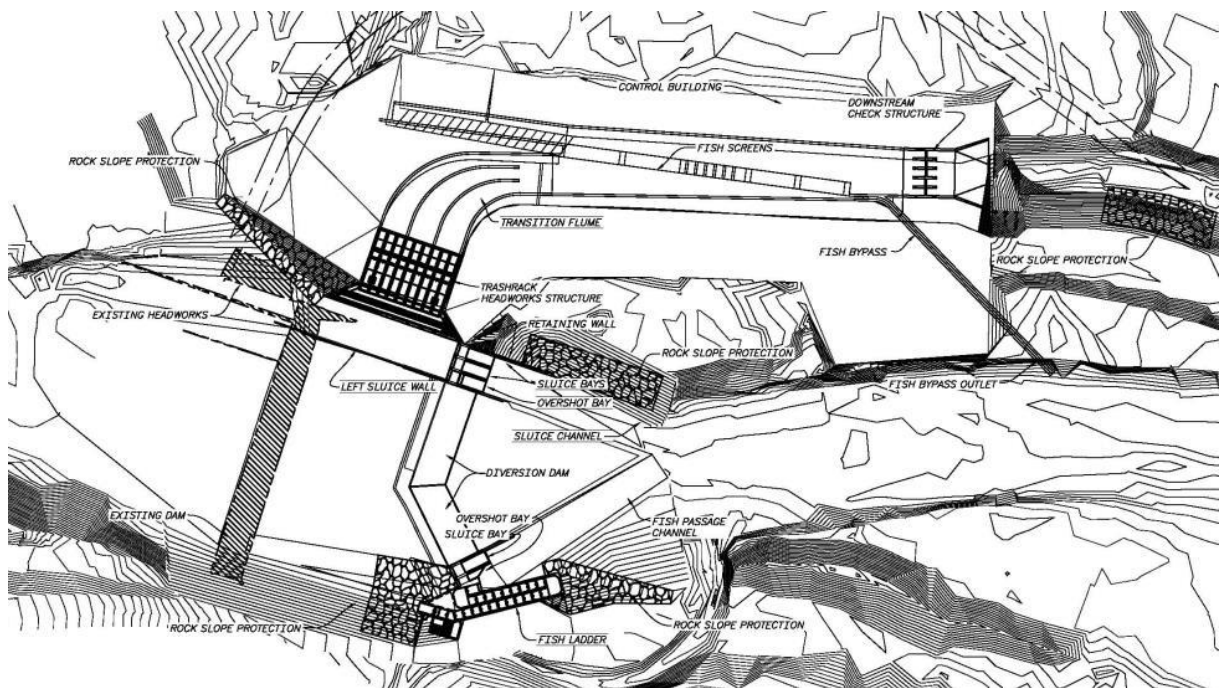
Figure 12. Originally proposed 60% design of the St. Mary Diversion Dam and Headworks.
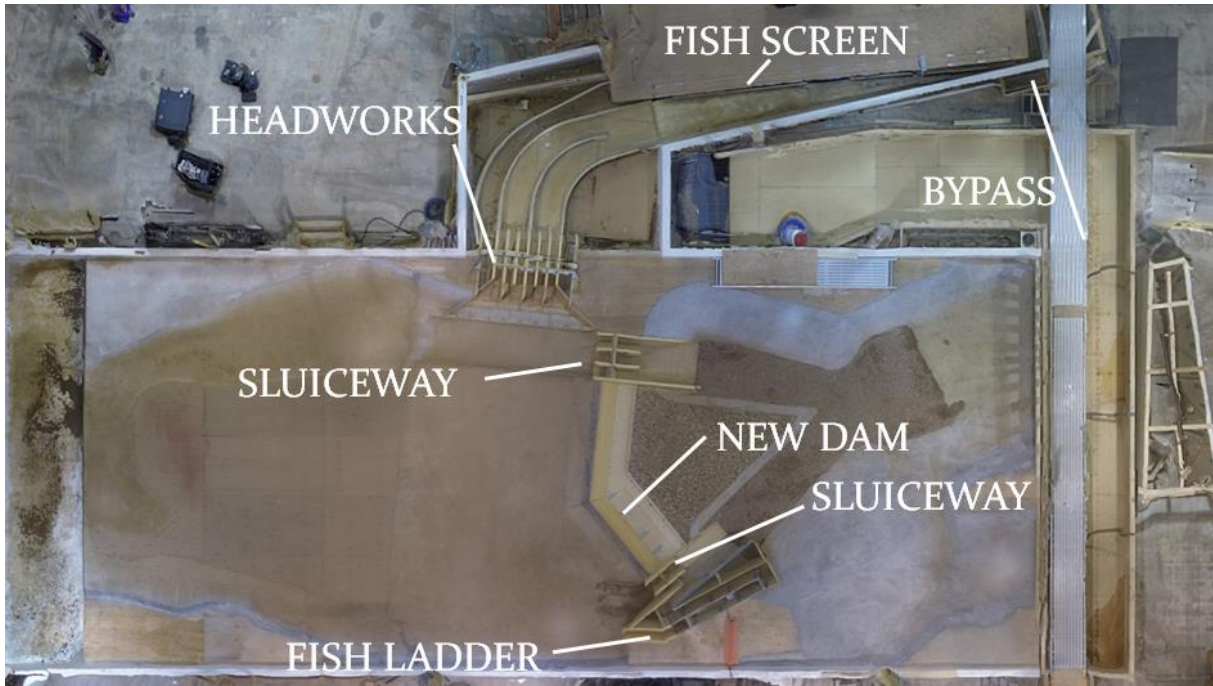
Figure 13. Aerial photograph of the original 60% design of the St. Mary Diversion Dam with annotations.

3.3. Modified 60% Design Option – Physical Model 2

Following the first modeling efforts, project members re-worked the 60% design and incorporated the changes shown in Figure 14. Modifications to the original 60% design include the following: A) A broad crested weir with reduced length (now 55.78-m (183-ft)) and a suitable energy dissipation basin downstream to prevent scour. B) The fish ladder located on river left to allow for easier operation, provide better attraction, and limit the access needed on the right bank. C) The headworks was reduced from nine to six 1.52- by 1.68-m (5- by 5.5-ft) gates. D) The overshot bays were removed on both sides of the diversion dam, and the right bank sluice gate was removed to reduce O&M requirements. Figure 15 provides an aerial view of the modifications to the physical hydraulic model with annotations. Additional information obtained during the model study enabled design team members to A) Set baffle configurations to allow uniform approach velocities for the fish screen at diversion flow rates of 18.41, 24.07, and 30.58 m³/s (650, 850 and 1080 ft³/s). Velocity uniformity was unachievable without baffling due to the screen's close proximity to upstream gates and channel curvature. B) Generate head discharge relationships for the dam with and without the fish ladder and headworks operational to verify that upstream water surface elevations were not too high and to provide a reasonable discharge curve for each structure. C) Verify the amount of headloss produced by the headworks and fish screens to ensure canal discharges could be met with adequate canal depths. D) Confirm that all flow during non-irrigation season can pass through the sluice gates without inundating the headworks with water.
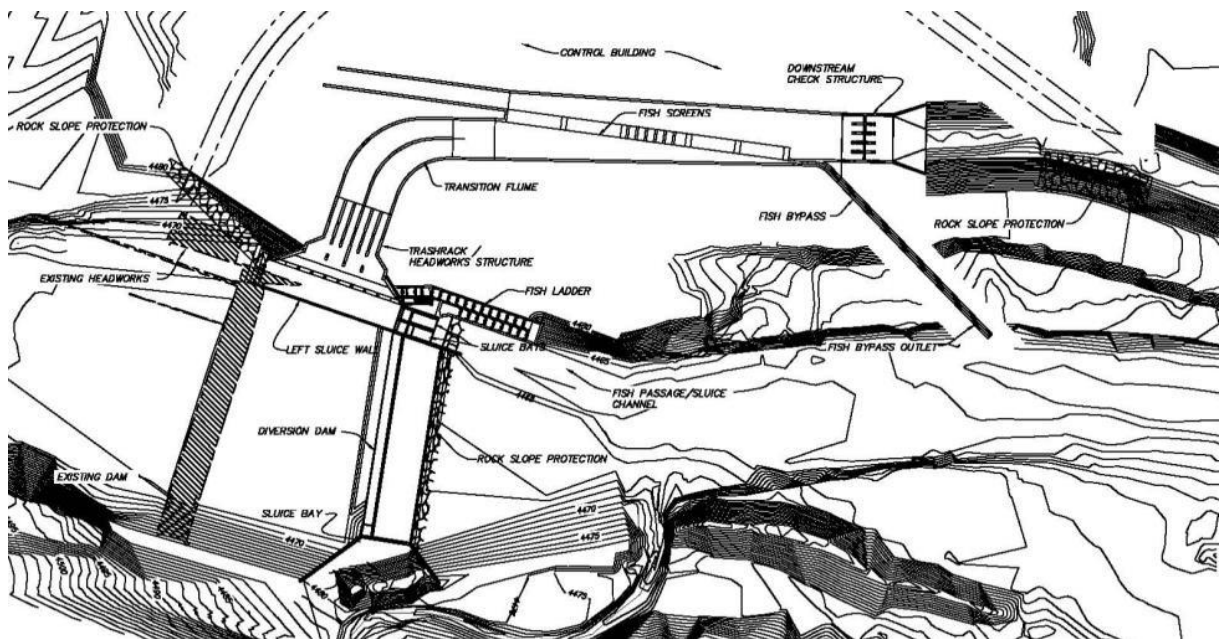
Figure 14. Most recent proposed 60% design of the St. Mary Diversion Dam and Headworks.
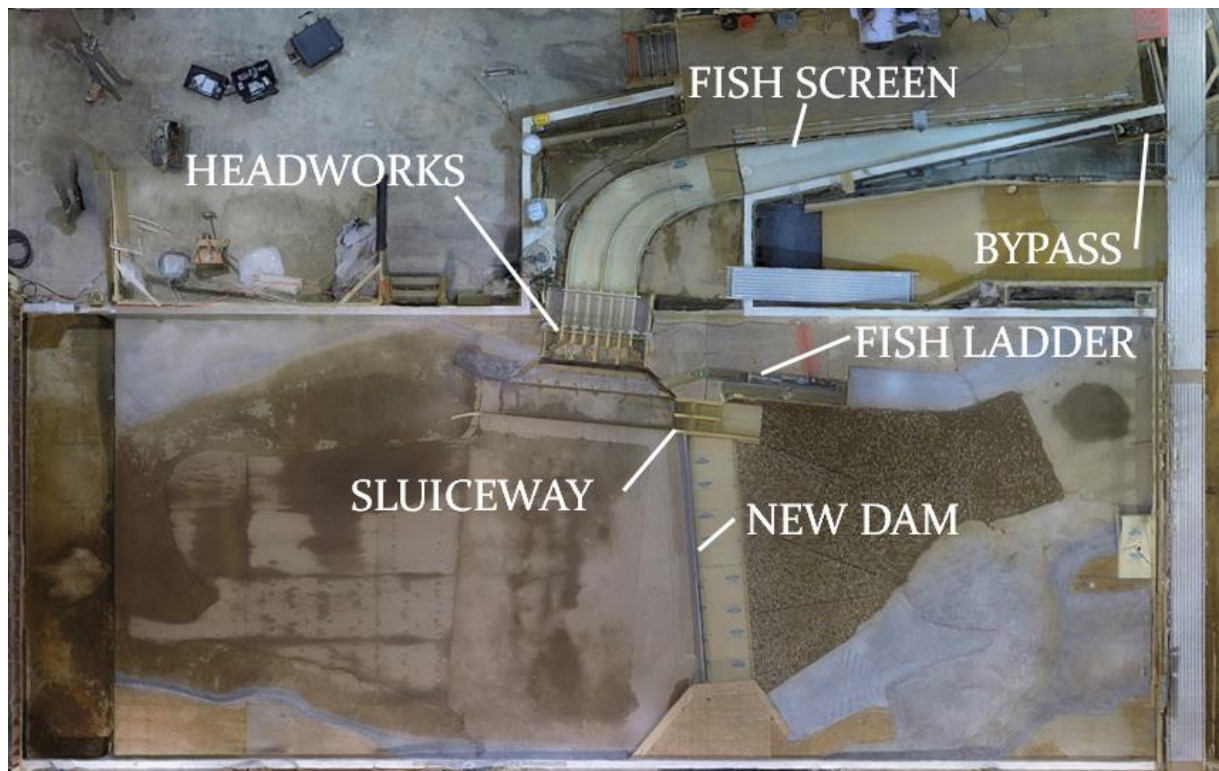
Figure 15. Aerial photograph of the modified 60% design of the St. Mary Diversion Dam with annotations.

4. SUMMARY

In 1999 FWS listed Bull trout as a threatened species. Since then, Reclamation has been engaged in design efforts to provide fish passage and protection from entrainment at the St. Mary Diversion Dam and Headworks. Over the past 15 years, Reclamation has worked with interested parties to develop a rehabilitation plan to address the impact the diversion dam has had on Bull trout recovery. The Reclamation design team at the TSC developed 60% designs of a new facility and constructed physical and numerical models to ensure the facility would operate as intended. Once tested, design team members identified several areas for improvement. Modifications to the original 60% design provided both safe passage and protection to Bull trout while

maintaining the capability of the St. Mary canal to deliver water as desired. The design team and all stake holders are currently working on the completion of a 100% design package.

5. ACKNOWLEDGMENTS

This work was conducted in collaboration with the U.S. Bureau of Reclamation, Department of Interior Montana Area Office, U.S. Fish and Wildlife, Blackfeet Nation Tribe, Montana DNRC, Milk River Irrigators, St. Mary Rehabilitation Working Group, and many other stake holders and interested parties. Thank you to everyone for their feedback and assistance during the design and modeling.

6. REFERENCES

Beyers, D.W., and Bestgen, K.R. (2002). "Bull trout Performance During Passage Over a Horizontal Flat Plate Screen," Larval Fish Laboratory, Department of Fishery and Wildlife Biology, Colorado State University, Fort Collins, Colorado.

Interior, U.S. Department of the. (1981). "Reclamation Data Book" Engineering and Research Center, Denver Colorado 80225.

Mefford, B. Sayer, K., and J. Baysinger. (2003). St. Mary Diversion Dam and Canal Headworks Concept Design Study, St. Mary Diversion and Fish Facilities.

Mogen, J.T. and E. Best. (2011). Fish Entrainment at the Sain Mary Diversion, Montana. Technical Memorandum: 86-68290-10-05. US Bureau of Reclamation, Montana Area Office.

Mogen, J.T. and L.R. Kaeding. (2002). Fish Entrainment Investigations at the St. Mary Diversion Dam, St. Mary River, Montana, a progress report based on field investigations conducted in 2002. Interagency Report. USFWS. Bozeman, MT.

Mogen, J.T. and L.R. Kaeding. (2008). Investigations of Bull trout (*Salvelinus confluentus*) in the St. Mary River Drainage, Montana. Interagency Report. USFWS. Bozeman, MT.

Mogen, J.T., and L.R. Kaeding. (2000). Ecology of Bull trout (*Salvelinus confluentus*) in the St. Mary River Drainage. Interagency Report. USFWS. Bozeman, MT.

Mogen, J.T., and L.R. Kaeding. (2005a). Identification and characterization of migratory and nonmigratory Bull trout populations in the St. Mary River drainage, Montana. Transactions of the American Fisheries Society 134:841–852.

Mogen, J.T., and L.R. Kaeding. (2005b). Large-scale, seasonal movements of radiotagged, adult Bull trout in the St. Mary River drainage, Montana and Alberta. Northwest Science 79:246-253.

TD&H Engineering Consultants, (2006). St. Mary Diversion Facilities Feasibility and Preliminary Engineering Report for Facility Rehabilitation.

Wagner, R. and G.W. FitzGerald. (1995). Fisheries status report: St. Mary storage unit. Final Report 1995. USFWS, Lewistown, Montana.

Investigating Supercritical Flows in Curved Open Channels with Three Dimensional Numerical Modeling

W.K. Brown, PE[1] and B.M. Crookston, PhD, PE[1]
[1]Schnabel Engineering
West Chester, PA 19382
USA
E-mail: KBrown@Schnabel-eng.com

ABSTRACT

The flow patterns observed in supercritical flows at bends in open channels are encountered in spillways, canals, and drainage works – this complex flow condition has been investigated more than 80 years ago, first with hydraulic models and more recently using numerical models. This paper presents a numerical investigation using a selection of experimental data from Dr. A. T. Ippen and a commercially available 3-dimensional CFD solver. A comparison of the numerical results to the physical data is presented, highlighting the ability of the numerical models to reproduce these complex water surface profiles, including the magnitude and location of standing waves. Modeling efforts were of a single fluid and used RNG and LES turbulence models. Furthermore, the observations, findings, and conclusions of this paper are discussed as they relate to open channel design.

Keywords: *Supercritical, Bends, Computational Fluid Dynamics, CFD, Numerical, Modelling*

1. INTRODUCTION

Complex flow behaviors in open channels have been of interest to researchers and practitioners for well over 100 years. One such behavior encountered in spillway and channel applications is the oblique wave patterns occurring in supercritical flow around channel bends, such as is presented in Figure 1 (Henderson 1966). The majority of the empirical relationships commonly used to address this complex behavior resulted from studies performed by researchers such as Ippen (1936), Knapp and Ippen (1938), Von Kármán (1938), Shurkey (1950), Ippen (1951), Knapp (1951), Poggi (1956), Sananes and Acatay (1962), Rakotoarivelo and Sananes (1967), Marchi (1988), and Reinauer and Hager (1997). The United States Army Corps of Engineers summarizes some of these works in their EM 1110-2-1601 (Hydraulic Design of Flood Control Structures, 1991). While experimental results and various calculations (empirical, method of characteristics, etc.) are commonly used to predict water surface profiles, wave amplitudes, and spatial locations around bends, uncertainties can exist when mapping standing waves or computing these parameters for specific channel geometries.
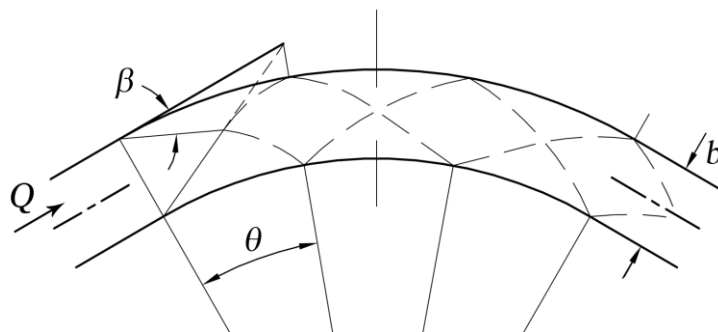
Figure 1. Supercritical Flow in Bends.

Physical hydraulic engineering models have been the preferred tool by practitioners for the design of hydraulic structures and channels. Published literature indicates that numerical modelers began studying flow in curved chutes in the late 1960s and early 1970s. Krause (1970) solved 2D shallow water equations for supercritical flow, although his results appear to be indefinite. As computational fluid dynamic (CFD) solvers evolve and computational power advances, so does the ease with which timely solutions are obtained for complex numerical models. By the early 1990s, works utilizing the 2D shallow water equations were published (Berger and Stockstill (1995), Causon et al. (1999), Elliot and Chaudhry (1992)), and some focused on vertical 2D models (Montes (1994), Valiani and Caleffi (2005), Bhajantri et al. (2007), Ghaeini-Hessaroeyeh et al. (2011), Montazeri-Namin et al. (2012)). The findings of Valiani and Caleffi (2005) indicate that while their shallow water equation (SWE) numerical solutions predict certain characteristics of the flow around bends reasonably well with a low Froude number, the maximum water surface level (i.e., wave extrema) is underestimated. Ghaeini-Hessaroeyeh et al. (2011) and Montazeri-Nemin et al. (2012) compliment Valiani and Caleffi (2005), where Montazeri-Nemin et al. (2012) conclude that the shallow water equations (SWE) using the Godunove type methods (same method as Valiani and Caleffi) can be used in "satisfactorily predicting the reflection pattern of shock waves and the wavelengths along the outer chute wall" yet "the 2D model based on the SWE is however limited to small relative curvature."

For many hydraulic structure applications, CFD models have proven to be a valuable design, analysis, and validation tool, securing a place in the engineer's toolbox with the ability to execute global modification quickly, provide extensive information throughout the flow field, supply qualitative and incremental information and quantities, and compliment physical hydraulic modeling efforts. Of course, it is preferred that a numerical modeler have a thorough understanding of both the actual hydraulics and the chosen numerical methods so as not to be deceived by virtual hydraulic quirks, shortcomings, and erroneous results (Knight 2013).

It is the intent of this paper to explore the complex hydraulics occurring in supercritical flow around bends by juxtaposing the earliest research efforts by Ippen (1936) with 3D numerical simulations via the CFD solver FLOW-3D developed by Flow Science. Results are followed by conclusions and discussion regarding the application of the CFD tool.

2. NUMERICAL MODEL DEVELOPMENT

2.1. Digital Models Based on Ippen (1936)

Ippen (1936) conducted a number of tests for three channel slopes (10%, 3.5%, and 1.5%), three radii of curvature (12.2 m, 6.1 m, and 3.0 m), and two angles of deviation (22.5° and 45°). Additionally, Ippen (1936) investigated means of reducing the magnitude of standing waves by installing longitudinal vanes along the channel bends. Each geometric configuration was tested for a range of discharges, resulting in 93 runs with various corresponding water surface contour maps, water surface profiles, and velocity distributions, though data for some runs appears to be missing. Of the data published, many runs have very limited information available, such as an outside bend profile. A portion of this dataset was selected for numerical modeling and is summarized in Table 1. These selections were based upon water surface data available in Ippen (1936) (for comparison) and also the range of discharges for a given bend geometry.

Development of the digital three dimensional models was accomplished with commercially available CAD software. Two assumptions were required as not all details of the experimental setup were documented by Ippen (1936). First, the model assumed that the radii cited by Ippen (1936) were in the plan view and not in the plane of the slope. Additionally, it was assumed that the flume floor perpendicular to the primary axis was horizontal, that is the floor was horizontal in any given channel cross section. Numerical point gauges were located in alignment with Ippen (1936) data points for experiments summarized in Table 1, as well as at 0.3048 m (1ft) intervals along the chute to provide additional resolution of the computed water surface profile.

Table 1. Investigation Summary

Run	Slope	Discharge	Channel Width (*b*)	Radius of Curvature (*R_a*)	Relative Radii of Curvature ($p_a=b/R_a$)	Angle of Deviation
13	0.0995	57.68 l/s	0.3048 m	3.048 m	1/10	45°
14	0.0995	47.86 l/s	0.3048 m	3.048 m	1/10	45°
15	0.0995	28.74 l/s	0.3048 m	3.048 m	1/10	45°
17	0.0995	9.57 l/s	0.3048 m	3.048 m	1/10	45°
38	0.0345	21.72 l/s	0.3048 m	3.048 m	1/10	45°
39	0.0345	56.07 l/s	0.3048 m	3.048 m	1/10	45°
41	0.0345	33.33 l/s	0.3048 m	3.048 m	1/10	45°
42	0.0345	42.48 l/s	0.3048 m	3.048 m	1/10	45°

2.2. CFD Model

Numerical simulations, as summarized in Table 1, were performed using the commercially available CFD solver FLOW-3D version 11.1. This solver uses a finite-volume approximation to solve continuity and momentum equations in three dimensions. Only one fluid was simulated. The domain was subdivided with a hexahedral single mesh. The 3D digital models representative of Ippen's setups were imported into the CFD software and embedded onto the mesh using the FAVOR method, which allows portions of a cell to be occupied by a solid or obstacle.

Two turbulent closure methods were evaluated: the Re-Normalization Group (RNG) turbulence model and the Large Eddy Simulation (LES) turbulence model, which have various method characteristics and limitations but were viewed as relevant to this case. Turbulence lengths were dynamically computed, and the Split Lagrangian method was used for volume-of-fluid advection and the second order monotonicity preserving solution for momentum advection. Viscous stresses were solved explicitly and pressures were solved implicitly.

Boundary conditions were defined according to the physical model tests using a defined flow rate as the upstream boundary, a free-overfall at the downstream boundary, and solid walls for the remaining boundaries except Z_{max}, which was defined as atmospheric pressure. All simulations were modeled with temporally fixed boundaries with the objective of reaching a steady-state solution of the system.   Three cell sizes were examined for mesh convergence in Run 13 and solutions agreement – 30.5 mm, 15.2mm, and 7.6 mm; the results indicate that solution convergence was obtained with minor differences between the 15.2 and 7.6-mm meshes. Two cell sizes were examined for mesh convergence in Run 39 and solution agreement—30.5 mm and 15.2 mm. At minimum, a third additional refinement is needed to establish a mesh-independent solution for this run; however, this has not been performed to date due to time constraints. Figure 2 presents sample water surface profile (inside and outside bend) solution of the RNG model for Run 1. Figure 3 presents a sample water surface profile (outside bend) solution of the RNG and LES models for Run 39, and. Both figures include the experimental data reported by Ippen (1936).
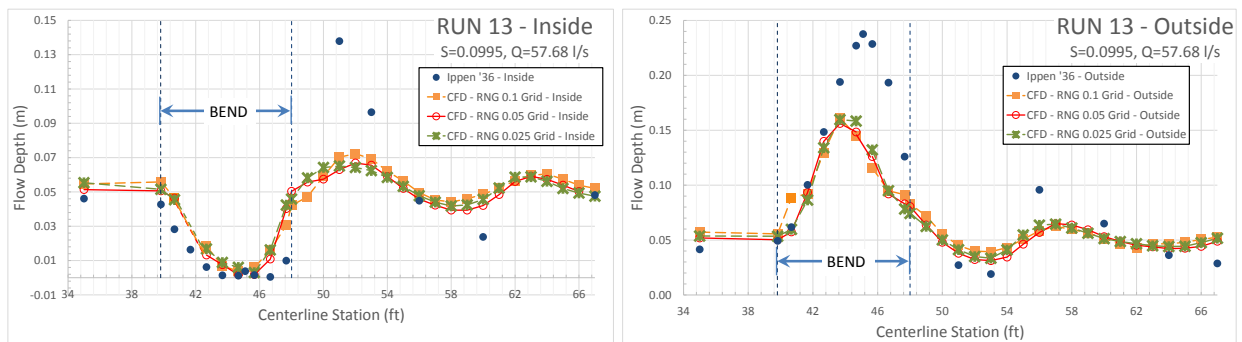
Figure 2. Run 13 Water Surface Profiles (inside and outside bend) for Multiple Mesh Sizes
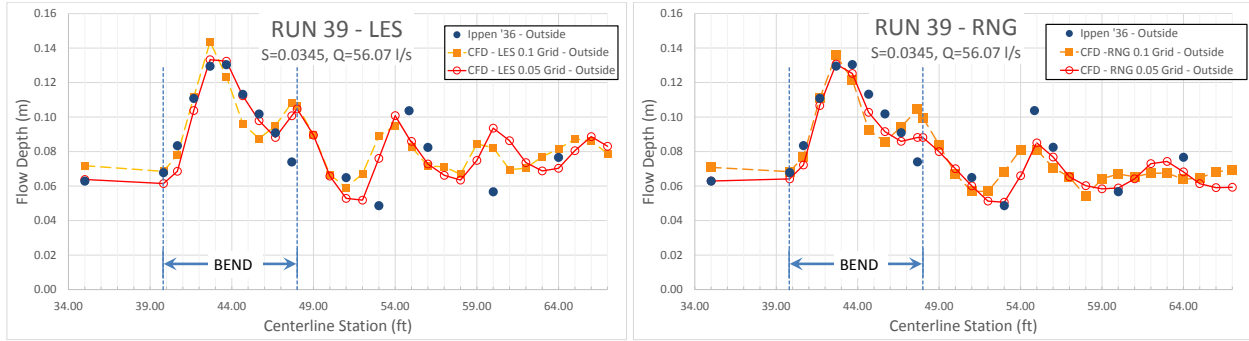
Figure 3. Run 39 Water Surface Profiles (outside bend) for Multiple Mesh Sizes

3. RESULTS

Water surface profiles for the runs identified in Table 1 are presented in Figures 4 through 11. Final numerical solutions from the RNG and LES models are plotted with the experimental results reported by Ippen (1936), with the abscissa maintaining the flume stationing during the experimental investigations. Please note that no profiles are provided for simulations where no physical data was reported in Ippen (1936).
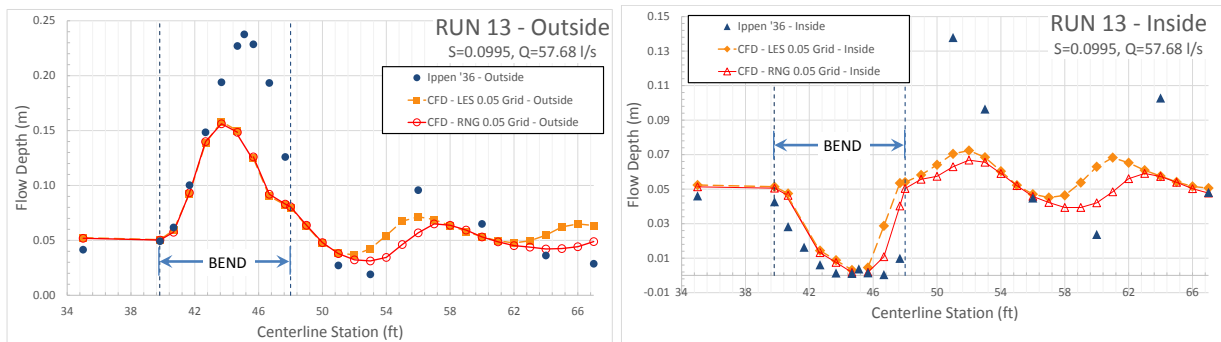
Figure 4. Run 13 CFD and Physical Model Bend Inside and Outside Profile Comparisons.
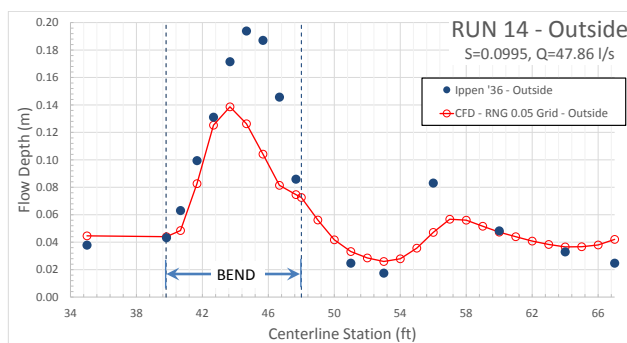
Figure 5. Run 14 CFD and Physical Model Bend Outside Profile Comparison.
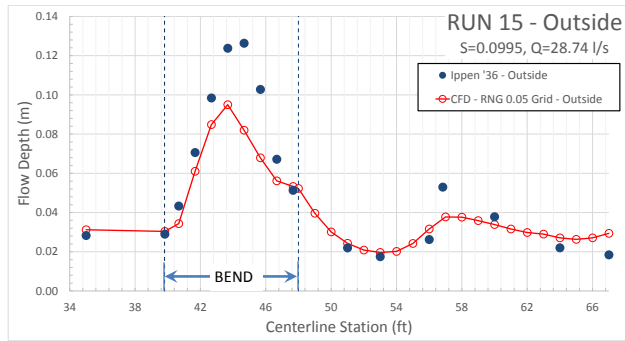
Figure 6. Run 15 CFD and Physical Model Bend Outside Profile Comparison.
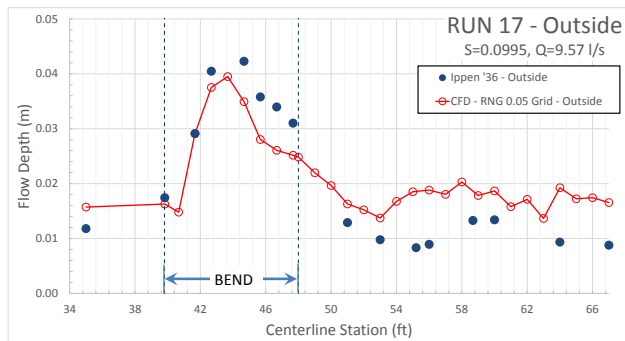
Figure 7. Run 17 CFD and Physical Model Bend Outside Profile Comparisons.
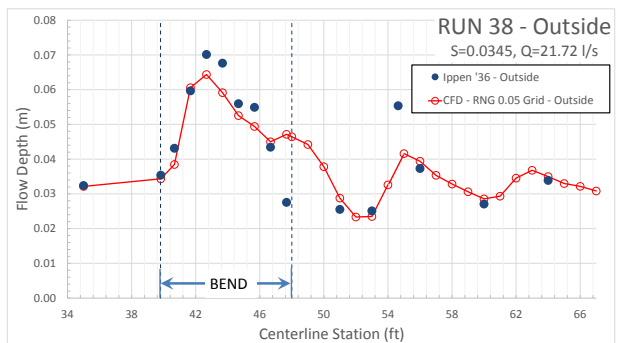
Figure 8. Run 38 CFD and Physical Model Bend Outside Profile Comparisons.
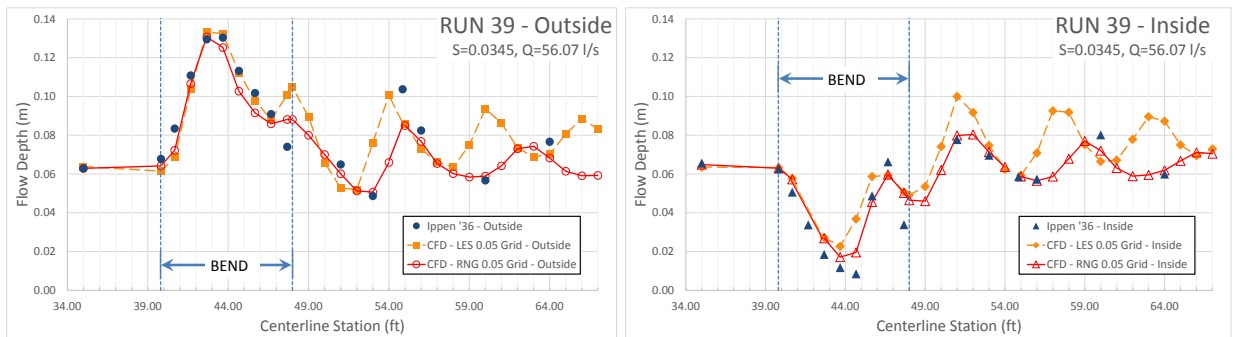
Figure 9. Run 39 CFD and Physical Model Bend Inside and Outside Profile Comparisons.
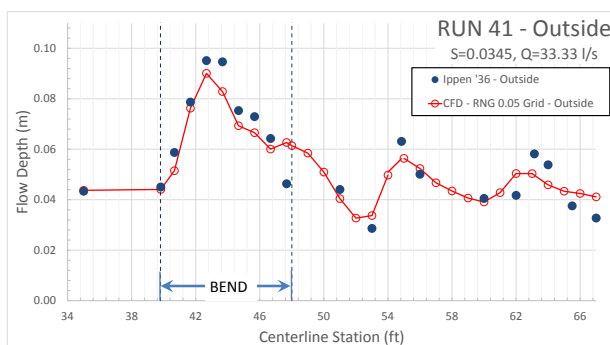
Figure 10. Run 41 CFD and Physical Model Bend Outside Profile Comparison.
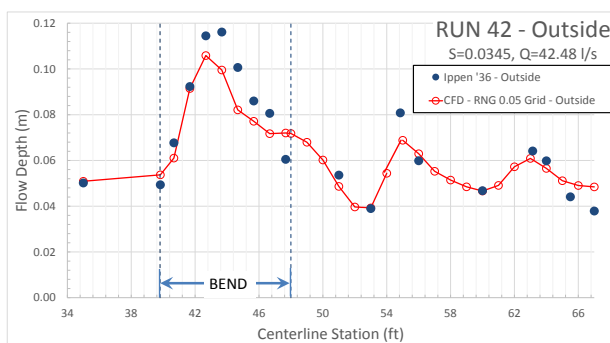
Figure 11. Run 42 CFD and Physical Model Bend Outside Profile Comparison.

Results indicate that the numerical models have good agreement along the outside wall within the bend for each run. No significant differentiator is observed between the LES and RNG turbulence models regarding the water surface along the outside of the channel bend except that, for the milder slope (Runs 38-42), the LES model predicted one additional standing wave in Run 39. In general, the LES model has fairly good agreement with the RNG model; however, the prediction of standing waves in the channel downstream of the bend appears to be phase shifted with a slightly lower frequency.

The numerical results compare most favorably with the experimental results of Runs 38-42, with an average deviation generally within +13% to -12% for Run 38, +5% to -10% for Run 39, +25% to -12% for Run 41, and +20% to -20% for Run 42, depending on the location of the wave in the channel bend. Figure 12 presents plots of the deviation of the RNG models from the experimental data of Ippen (1936) for each simulation, with results summarized in Fig. 13.
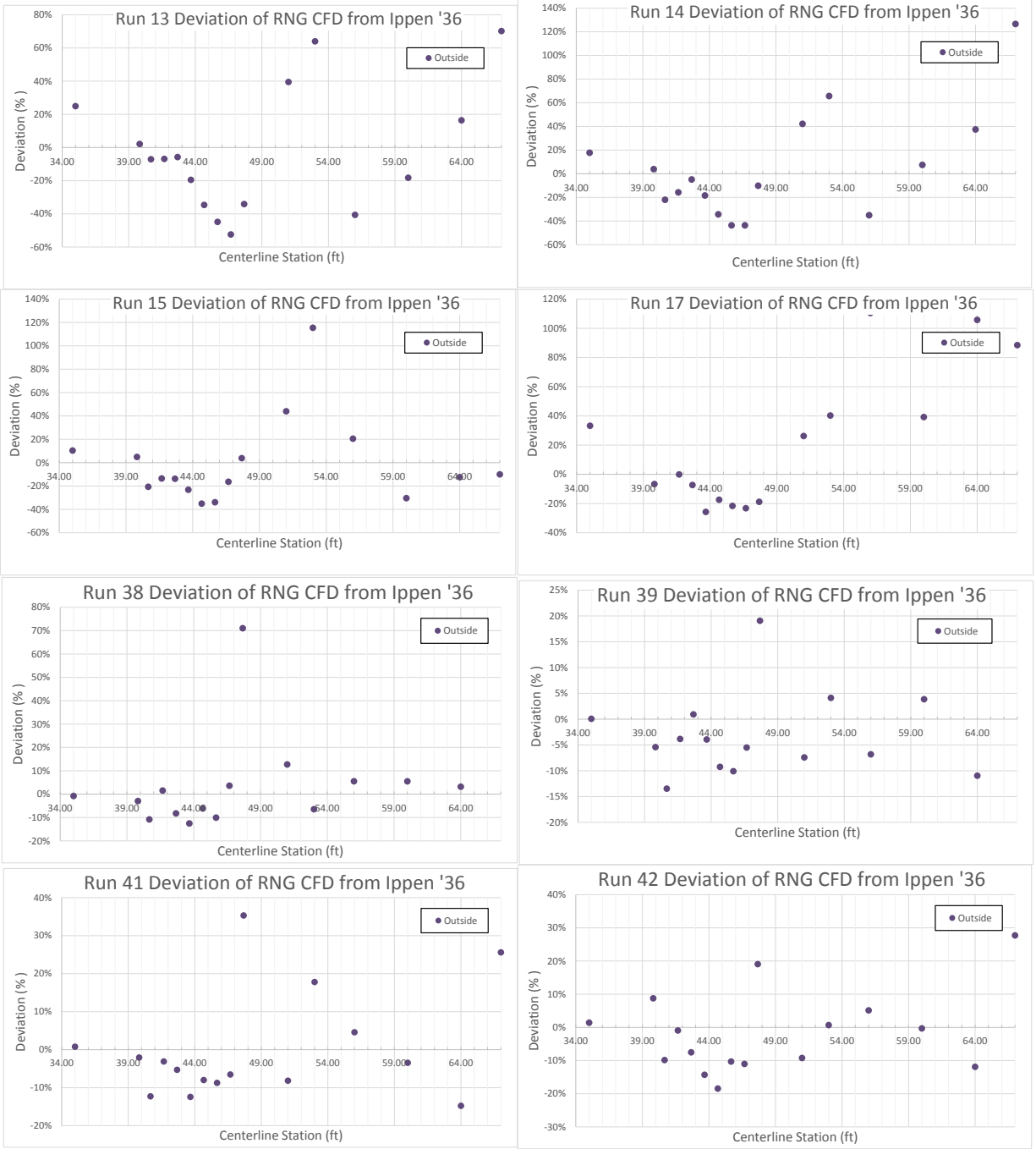
Figure 12. Deviation Plots - Outside of Bend.
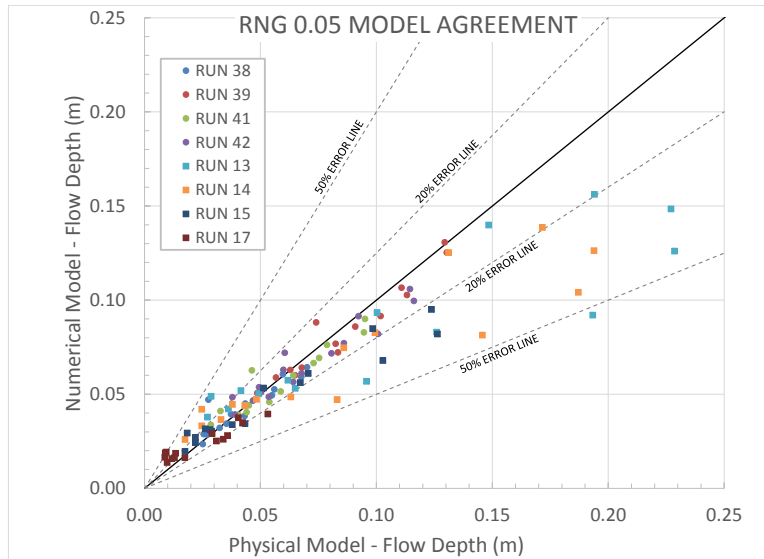
Figure 13. CFD and Ippen (1936) Model Agreement - Outside of Bend.

For a steeper slope and higher Froude number, the general trend of the water surface profile and waves are estimated numerically but differences arise for peak wave magnitudes; better agreement exists along the outside bend (often of more interest in design) with some disagreement along the inside channel bend. Generally, maximum wave heights appear to be underestimated around the channel bends when compared to Ippen (1936).

4. INTERPRETATION OF CFD RESULTS

Flow through a channel is governed by conservation of energy, momentum, and mass. These principles are of necessity approximated numerically by CFD solvers. Therefore, users should be aware of numerical model performance and limitations, including derivations of basic principles of fluid mechanics, closure methods (i.e., numerical methods, algorithms, etc.), coefficients, and any other details applicable to the situation of interest.

As discussed, relatively good agreement (see Figure 13) was generally found between the numerical results and the physical measurements of Ippen (1936). However, there were instances where the numerical point estimations for flow depth were in disagreement by more than 50%, particularly along the inside of the bend (Figures 4 and 9) and downstream of the bend. It is assumed that a small fraction of this error could be attributed to experimental uncertainties, such as measurement accuracy, technique, and temporal variations. Possible sources of numerical error could come from the aforementioned assumptions and approximations of the solver code related to estimation and tracking of the free surface (i.e., free boundary) that, in this case, is quite complex; Volume of Fluid (VOF) technique implemented in the selected solver code; changes in the pressure field; and shear forces. Therefore, it is good practice and strongly recommended that numerical modelers verify the computed results with experimental data to facilitate interpretation of the numerical results for design purposes. An appropriate physical model should be performed when determined to be a beneficial risk-reduction measure for a given project with its corresponding project goals and safety standards.

5. SUMMARY AND RECOMMENDATIONS

The results of this exploration indicate that it is possible to numerically simulate the complex flow patterns created by supercritical flows passing through a bend. In the case of a chute with S=0.0345 and R_a=1/10 (Fr=3.6), the numerical results were generally within approximately 10% to 20% of experimental measurements of Ippen (1936) and considered useful to designers. However, for a steeper slope, S=0.0995 and R_a=1/10 (Fr=6.6), there was general

agreement between the physical and numerical results, but the simulations were not able to replicate the wave magnitudes or peak wave heights within an acceptable level of accuracy. Agreement was observed to decrease with increasing slope and discharge.

Hydraulic optimizations and modeling efforts are leveraged to meet project goals (safety, design, operation, economics, etc.) (Crookston et al 2013). Also, every project does not necessarily justify a quality physical hydraulic model to facilitate an efficient design. For smaller projects, a more conservative design may be preferable. It is also understood that numerical modeling is being used with increasing frequency both alone and in concert with empirical and/or physical modelling. CFD modelling can also be of great value in assessing a range of layouts and channel geometries for supercritical flow through a bend to arrive at one or more design concepts for physical modelling.

Based upon published literature and this investigative effort, it is recommended that a numerical model examining superelevation and standing waves in a supercritical curved channel be calibrated, ideally with experimental results from scaled hydraulic models. Calibration efforts should recognize the experimental accuracies of the physical model data. Quality data sets can also be a valuable source of information in calibration efforts. Until computational advances provide higher levels of consistency with physical model findings, caution should be exercised when interpreting numerical results, as the accuracy of findings will be uncertain.

6. ACKNOWLEDGEMENTS

7. REFERENCES

Berger, R.C., and Stockstill, R.L. (1995). "Finite-Element Model for High-Velocity Channels." *Journal of Hydraulic Engineering,* 121(10), 710-716.

Bhajantri, M.R., et al. (2007). "Numerical modelling of turbulent flow through spillway with gated operation." *International Journal for Numerical Methods in Engineering,* 72, 221-243.

Brown, W.K., et al. (2012). "Revisiting Spillway Discharge Coefficients for Several Weir Shapes." *Proc., 32nd Annual USSD Conference: Innovative Dam and Levee Design and Construction for Sustainable Water Management,* USSD, New Orleans, La., 1317-1334.

Causon, D.M., et al. (1999). "Advances in Calculation Methods for Supercritical Flow in Spillway Channels." *Journal of Hydraulic Engineering,* 125(10), 1039-1050.

Crookston, B.M., Paxson, G.S., and Campbell, D.B. (2013). "Effective Spillways: Harmonizing labyrinth weir hydraulic efficiency and project requirements." in Labyrinth and Piano Key Weirs II – PKW 2013. S. Erpicum, F. Laugier, M. Pfister, M. Pirotton, G Cicéro, A. Schleiss Editors. CRC Press, London, UK.

Elliot, R.C., and Chaudhry, M.H. (1992). "A wave propagation model for two-dimensional dam-break flows." *Journal of Hydraulic Research,* 30(4), 467-483.

Ellis, J. (1985a). "Numerical analysis of Kielder dam spillway." *Journal of the Institution of Water Engineers,* 39, 254-270.

Ellis, J. (1985b). "Numerical modelling of spillway flows." *Proceedings of the 2nd International Conference on the Hydraulics of Floods and Flood Control,* BHRA, Cambridge, England, B(1), 73-90.

Ghaeini-Hessaroeyeh, M., et al. (2011). "Numerical modelling of supercritical flow in rectangular chute bends". *Journal of Hydraulic Research,* 49(5), 685-688.

Ippen, A.T. (1936). *An analytical and experimental study of high velocity flow in curved sections of open channels.* Dissertation (Ph.D.), California Polytechnic University, Ca.

Ippen, A.T., and Knapp, R.T. (1936). "A study of high-velocity flow in curved channels of rectangular cross-section." *Transaction, American Geophysical Union,* 17(2), 516-521.

Ippen, A.T. (1951). "Mechanics of Supercritical Flow." *Transactions, ASCE, 116,* 268-295.

Knapp, R.T. (1951). "Design of Channel Curves for Supercritical Flow." *Transaction, ASCE,* 116, 1318-1347.

Krause, E., and Hirchel, E.H. (1970). "Exact Numerical Solutions for Three-Dimensional Boundary Layers." *Second International Conference on Numerical Methods in Fluid Dynamics,* University of California, Berkeley, Ca.

Marchi, E. (1988). "Correnti veloci in curve a 90° molto strete." *Idrotecnica* 15(6), 439-455.

Montazeri-Namin, M., et al. (2012). "3D Numerical Simulation of Supercritical Flow in Bends of Channel." *International Conference on Mechanical, Automotive and Materials Engineering (ICMAME'2012),* Dubai, United Arab Emirates, 167-171.

Montes, J.S., (1994). "Potential-Flow Solution to 2D Transition from Mild to Steep Slope." *Journal of Hydraulic Engineering, ASCE,* 1(5), 601-621.

Poggi, B. (1956). "Correnti veloci nei canali in curva." *L'Energia Elettrica,* 34, 465-480.

Rakotoarivelo, W., and Sananes, F. (1967). "Etude de l'ècoulement supercritique dans un canal dont la section est en forme de U." *12 IAHR Congress,* Fort Collins 1(38), 1-7.

Reinauer, R., and Hager, W.H. (1997). "Supercritical Bend Flow." *Journal of Hydraulic Engineering,* 123(3), 208-218.

Sananes, F., and Acatay, T. (1962). "Contribution à l'ètude des ècoulements supercritiques dans des canaux coudès." *Comptes Rendus de L'Acadèmie des Sciences,* Paris, France, 255, 471-473.

Shukry, A. (1950). "Flow around bends in an open flume." *Transactions, ASCE,* 115, 751-788.

Valiani, A., and Caleffi, V. (2005). "Brief Analysis of Shallow Water Equations Suitability to Numerically Simulate Supercritical Flow in Sharp Bends." *ASCE, Journal of Hydraulic Engineering*, 131(10), 912-916.

Von Karman, T. (1938). "Eine praktische Anwendung der Analogie zwischen Überschallströmung in Gasen und überkritischer Strömung in offenen Gerinnen." *Zeitschrift für Angewandte Mathematik und Mechanik,* 18(1), 49-56 .

Application of the Optical Flow Method to Velocity Determination in Hydraulic Structure Models

D.B. Bung[1] and D. Valero[1,2]

[1]Hydraulic Engineering Section, Civil Engineering Department
FH Aachen University of Applied Sciences
Bayernallee 9, 52066 Aachen
Germany
[2]Dept. of ArGEnCo, Univ. of Liege (ULg)
Research Group of Hydraulics in Environmental and Civil Engineering (HECE)
Chemin des Chevreuils 1, 4000 Liège
Belgium
E-mail: bung@fh-aachen.de

ABSTRACT

Optical flow estimation is used in Computer Vision for detection of moving obstacles in a sequence of images. The optical flow (OF) is defined as the displacement of brightness patterns between two sequent images. In this paper, this method is applied to high-speed images taken in hydraulic structure models for determination of velocity fields. Water is seeded with tracer particles in two cases and is self-aerated in a third case. It will be shown that the OF method gives valuable results that compare well to other velocity measurements, e.g. by Particle Image Velocimetry. The OF method is generally more time-consuming compared to PIV, but an advantage is given by the density of information when using a so-called global method, as velocity information is obtained at every pixel location.

Keywords: Optical flow, particle image velocimetry, imaging techniques, velocity estimation.

1. INTRODUCTION

Physical modeling of hydraulic structures is still a common technique to elaborate flow patterns, water depths, flow velocities, turbulence, etc. Flow velocities are typically measured by means of intrusive probes, such as anemometers for 1D and ADVs for 3D point measuring in clear water (ASCE 2000) and dual-tip conductivity or fiber-optical probes in bubbly flows (Felder and Chanson 2015). A drawback of these probes is the limitation to a single point, i.e. the velocity is obtained as a local value and the inevitable perturbation of the flow.

If one is interested in instantaneous 2D (or 3D) flow fields, Particle Image Velocimetry (PIV) is a widely accepted technique based on cross-correlation of subsequent frames from a video, which is captured with either a standard or high-speed camera depending on the expected flow velocity (Adrian and Westerweel 2011). To visualize the flow, a tracer material needs to be added to the water. Subsequent frames are divided into so-called interrogation windows of user-defined sizes and 2D cross-correlation in spatial or frequency domain is performed to find the most probable displacements of particles within these windows by using different peak finding methods. The method is thus an integral approach yielding a single statistically determined velocity information for each interrogation window.

Another imaging technique which may be applied to experimental fluid mechanics is given by the Optical Flow method (OF). Coming from computer vision field, it is not yet well-known in the community. To date, this method is mainly used in fields like video compression (motion estimation to predict intermediate frames) or vehicle navigation (autonomous car driving) as reported by Fortun et al. (2015). A first approach for optical flow estimation was presented by Horn and Schunck (1981), defining the optical flow as the movement of brightness (intensity) patterns in a sequence of images. OF aims to approximate a 2D motion or velocity field, which is a projection of generally 3D velocities of surface points onto the imaging surface from spatiotemporal patterns of image intensity. In order to relate the movement of brightness patterns to the movement of an object, it is assumed that the brightness of a moving pixel in the pattern remains constant during the movement. The Horn and Schunck method is a global

method attempting to minimize a global energy function. In addition, local methods have been developed based on optimization of local energy-like expression. For instance, Lucas and Kanade (1981) assume a small, constant optical flow within a neighborhood. By consequence, this method does not allow the determination of optical flow within a region of uniform intensity. Local methods can only provide sparse flow fields in contrast to global methods, which provide dense flow fields with velocity information at every point. Since its original formulation, several improvements and further developments on this basic idea of the optical flow method have been presented and give surprisingly good results although the basic assumption of brightness constancy may be unrealistic in many applications due to shading effects or changes in illumination.

In some recent studies, the Horn and Schunck approach was applied to fluid flows using particle images obtained from PIV measurements (Liu et al. 2015; Liu and Shen 2008). Corpetti et al. (2006) confirm a good agreement with PIV data implementing an approach to account for the continuity equation as well as divergence and vorticity structures of the flow. Liu et al. (2015) state that OF, as a differential approach, is more suitable to images with continuous patterns so that single particles used for PIV are not the best case for OF.

This paper aims to test the Optical Flow method to the field of hydraulic structures modeling for 1) clear water flows being seeded with particles and 2) aerated flows.

2. METHODODOGY

The constancy of brightness $I(X,Y,t)$ of a moving pixel with pixel coordinates X and Y at time t may be expressed as:

$$\frac{dI}{dt} = \frac{\partial I}{\partial t} + \frac{\partial I}{\partial X}\frac{\partial X}{\partial t} + \frac{\partial I}{\partial Y}\frac{\partial Y}{\partial t} = 0 \tag{1}$$

with I_t the temporal derivative, I_X and I_Y the spatial image derivatives in X and Y direction, and U and V the unknown spatial displacements in X and Y directions between two sequent frames. Eq. (1) may be rewritten as

$$I_t + I_X U + I_Y V = 0 \tag{2}$$

Eq. (2) is the spatial term. In order to solve this ill-posed problem (1 equation, 2 variables), a second constraint, i.e. a data term, is required. Horn and Schunck (1981) assumed that neighboring points have a similar velocity by reducing the square of the gradients of the optical flow velocity. Thus, the following objective function needs to be minimized:

$$E = \iint \left[\left(I_X U + I_Y V + I_t\right)^2 + \alpha\left(\left|\nabla U\right|^2 + \left|\nabla V\right|^2\right)\right] dXdY \tag{3}$$

where $\nabla = (\partial/\partial X, \partial/\partial Y)$ is the spatial gradient and α a smoothing factor for the spatial term. This minimization yields (Bruhn et al. 2005):

$$\alpha\Delta U - \left(I_X I_t + I_X{}^2 U + I_X I_Y V\right) = 0 \tag{4a}$$

$$\alpha\Delta U - \left(I_Y I_t + I_Y{}^2 U + I_X I_Y U\right) = 0 \tag{4b}$$

Where ΔU is the spatial Laplace operator over U defined by the scalar product $\nabla \cdot \nabla U$. At image locations with low information from pixel derivatives, no reliable local flow estimate is possible. The Laplace operator fills in information from the neighborhood, α then works as a diffusion coefficient for U and V.

For this paper, an open-source MATLAB® toolbox for Optical Flow determination developed by Sun et al. (2010) is employed. This toolbox implements several different OF methods besides the classical Horn and Schunck method given above as well as different additional image processing techniques, which were developed in the recent past and known to likely improve the results. Bung and Valero (2016) showed that this toolbox can give valuable results in highly aerated flows on stepped spillways when using the air bubbles as seeding. A similar approach was introduced by Ryu et al. (2005) and applied by Bung (2011b), Leandro et al. (2014), and Bung and Valero (2015) using the Bubble Image Velocimetry (BIV) technique, an adapted Particle Image Velocimetry (PIV) technique using the bubbles instead of tracer particles. In order to demonstrate the general applicability of OF to water flows around hydraulic structures, all investigations are limited to the basic Horn and Schunck scheme.

In detail, three test cases are investigated:
1. Dam-break flow being observed in a 30 cm wide flume with an initial water depth of 40 cm in the reservoir (images taken from Oertel and Bung 2012); images of the seeded flow are taken with a high-speed camera at 900 fps and 1280 x 576 px resolution; the OF method is compared to PIV.
2. Wave propagation over a submerged plate (installed at 6 cm below the still water level) being modeled in a 30 cm wide wave flume for a wave height $H = 4$ cm, a wave period $T = 1$ s, and a water depth of 30 cm (images taken from Bung et al. 2008); the water is again seeded with particles, and images are taken with a high-speed camera with only 256 x 256 px resolution at 500 fps; OF is compared to numerical results from a Large Eddy Simulation.
3. Slightly aerated flow over a stepped spillway with 50 cm width, 6 cm step height, 1V:2H slope, and a specific discharge $q = 0.07$ m^2/s; the high-speed video is captured at 732 fps and a resolution of 1920 x 1200 px on step 5, which was found to be the inception point of surface self-aeration by Bung (2011a) (the same setup has been previously used in Bung and Valero (2016) for OF determination for fully aerated flow); water is not seeded in this experiment and, hence, OF is performed on transported air bubbles; OF is compared to BIV results.

MatPIV in its latest version 1.61 is employed for calculation of PIV- and BIV-based velocity fields. MatPIV (Sveen 2004) is another open-source toolbox for MATLAB®, which applies a classical PIV technique allowing variation of several parameter settings, e.g. interrogation window size, window overlap, and different filtering methods for smoothing of the velocity field. The reader may note that the studies were conducted by use of simple halogen spotlights being installed in front of the inspection window and above the flumes. It is acknowledged that the presented results are likely affected by sidewall effects as the applied illumination does not allow to define a thin measuring plane as laser sheets usually do. Thus, particles and bubbles near the sidewall are taken into account as well as those in the rear. This fact may also lead to some distortion affecting the results. Moreover, it is pointed out that 3D flow fields are reduced to 2D for all methods.

3. RESULTS

3.1. Dam Break Flow

This case is analyzed with both methods, OF and PIV using MatPIV. As PIV is a well-established method in hydraulic engineering, this technique is applied to compare and assess the OF capabilities. The PIV calculations are performed with quadratic interrogation windows and 50% overlap. Although MatPIV generally includes several filter options to improve results, all calculations are carried out without any filtering and smoothing.

Figure 1 illustrates the first high-speed image, which was recorded at $t = 0.50$ s after the gate release. In physical scale, the image is roughly 90 cm wide, yielding a pixel density of ~14 px/cm. In combination with the subsequent frame being recorded 1/900 s later, velocities are determined by both imaging techniques and compared to velocity profiles that were visually extracted from the images. For this purpose, four sections of the images were selected with a width of 16 px each, namely at $x = -7$ cm (section 1), $x = 8$ cm (section 2), $x = 23$ cm (section 3), and $x = 38$ cm (section 4) where the gate axis defines the zero position $x = 0$ cm (see Fig. 1). Particles within these sections were tracked by eye from one frame to the next, and their displacements were noted. Due to the high

density of particles, displacement data were obtained with an average distance of roughly 4 px along the water column (e.g. 38 data points were obtained in section 3, where the water depth was given by 160 px).
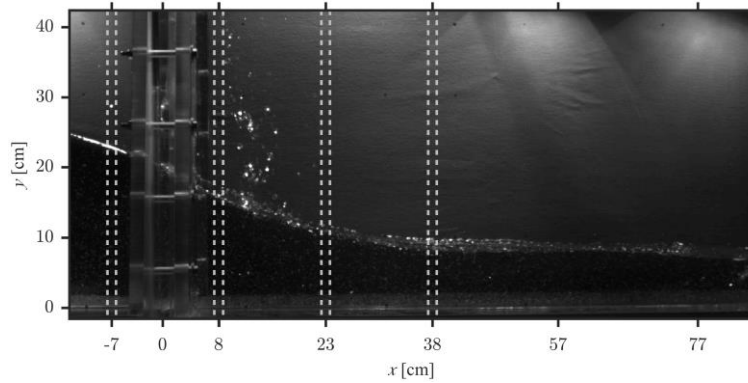
Figure 1. High-speed frame at $t = 0.50$ s after gate opening (from Oertel and Bung, 2012)

The main parameters influencing the quality of calculated results within the two image processing techniques are given by the number of iterations in each warping step for OF and the interrogation window size for PIV. In order to quantify these influences, both parameters have been systematically varied and the resulting mean error defined by

$$meanerror = \frac{1}{n}\sum_{i}^{n}\frac{vel_{im,i} - vel_{vis,i}}{vel_{vis,i}} \tag{5}$$

has been determined. In Eq. (5) n is the total number of visually detected data points in a section, $vel_{vis,i}$ is the ith visually determined velocity magnitude and $vel_{im,i}$ the velocity magnitude in the same elevation from each imaging technique. Using a median filter of size 12 x 12 px for smoothing of the dense data in OF, the mean errors in Fig. 2 were obtained. PIV calculations were run using a multiple approach with three different decreasing interrogation window sizes, i.e. the final pass was run with half of the initial window size.
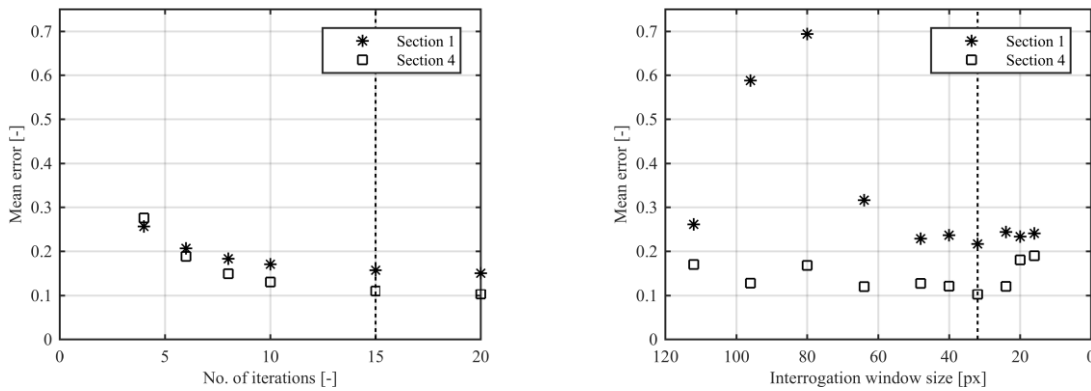
Figure 2. Sensitivity of image processing techniques to parameter settings, exemplarily for section 1 and 4; dashed lines for selected settings; left: number of iterations (OF), right: interrogation window size (PIV).

Obviously, both imaging methods produce results of similar accuracy if settings are properly chosen. In section 1, where there are relatively low velocities, the mean error in PIV is about 0.217 for an initial interrogation window size of 32 x 32 px while it is 0.157 for 15 iterations in OF. The reader may note that the mean error decreases in negligible order for a higher number of iterations. In section 4, with higher flow velocities, both techniques reach the same accuracy with a mean error of 0.103 for PIV again using a 32 x 32 px initial window and 0.110 for OF using 15 iterations. While a clear decreasing trend of the mean error is found in OF with increasing number of iterations, a critical interrogation window size is found in PIV giving the highest accuracy. This fact may be explained by

particle displacements being larger than the final interrogation window size when smaller windows are considered. Particles are then no longer available in the second frame for cross-correlation.

Figure 3 shows the resulting velocity magnitude profiles for sections 1 to 4 using the above detected optimal settings, i.e. 15 iterations for OF and 32 x 32 px for PIV. In order to avoid spurious velocities above the water surface line due to local brightness patterns (Fig. 1), dry areas have been masked before processing. PIV and visual data have been smoothed with a moving average filter in order to get a comparable filtering as it was used for OF. It is found that the velocity data from both techniques compare fairly well. For sections 2 and 4, the differences are very small while for section 1 and 3, some deviation is noted, namely better prediction by OF in section 1 and by PIV in section 3. In any case, PIV supports the calculated shape of the velocity profile. It is observed that both PIV and OF show a lack in accuracy close to the boundaries where an unnatural decrease of velocity is obtained. This decrease may be explained by the smoothing in OF and the overlap of the interrogation window to non-moving areas (masking may support avoiding this error).

a) Section 1

b) Section 2

c) Section 3
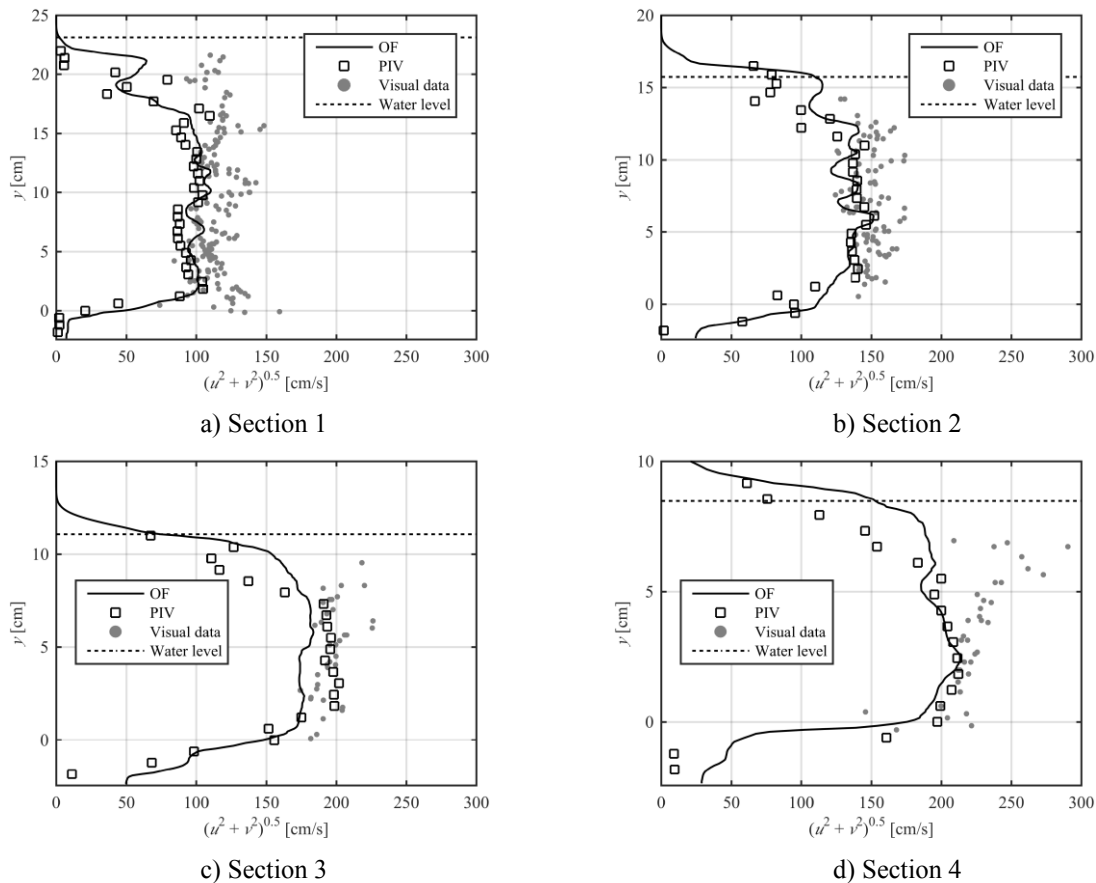
d) Section 4

Figure 3. Velocity magnitude profiles extracted from image processing techniques in comparison to visually determined velocities for four sections (OF data obtained by 15 iterations, PIV data obtained with an interrogation window of 32 x 32 px, note the different scaling of the y-axis)

Figure 4 presents the complete velocity magnitude fields. It must be noted that, for better readability, the OF result displays only every 25th vector, while the PIV result includes every 3rd vector to ease comparison of both plots. In the OF result, some spurious vectors appear in the air region due to fluctuation in the illumination. Those vectors can be eliminated by some image pre-processing, which was not done in the present study. The PIV result shows less spurious vectors. Processing times for OF (Table 1) and PIV (Table 2) are given below. The calculations were performed on a Laptop with a 3.1 GHz Dual-Core Intel i7 processor, 16 GB RAM, and a SSD hard disk. Accordingly, the calculation time in OF takes 28 times the time needed for PIV using the optimal settings (highlighted in gray). However, the absolute time is still acceptable with ~3 minutes regarding the much

higher information density obtained by OF, i.e. 65 times more velocity vectors. Depending on the purpose of a given study, this denser information may be of benefit, e.g. for a vortex flow. However, it is pointed out that the performed averaging (median filter of size 12 x 12 px) is relatively time-consuming. Comparative processing of this case without filtering took only 123.0 s.
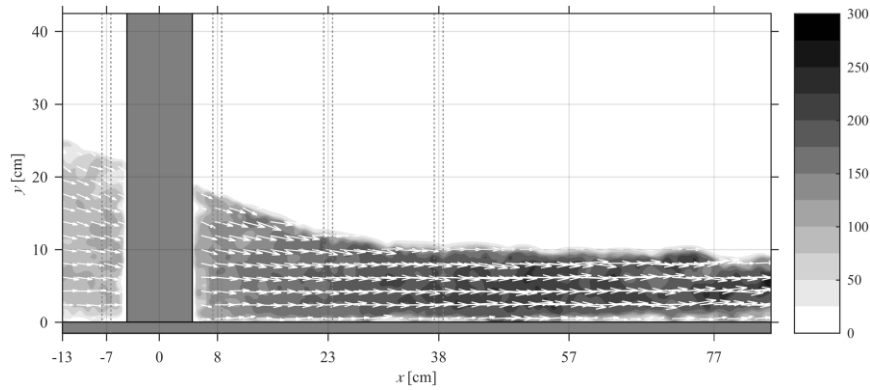
a) Optical Flow for 15 iterations (every 25th vector displayed)
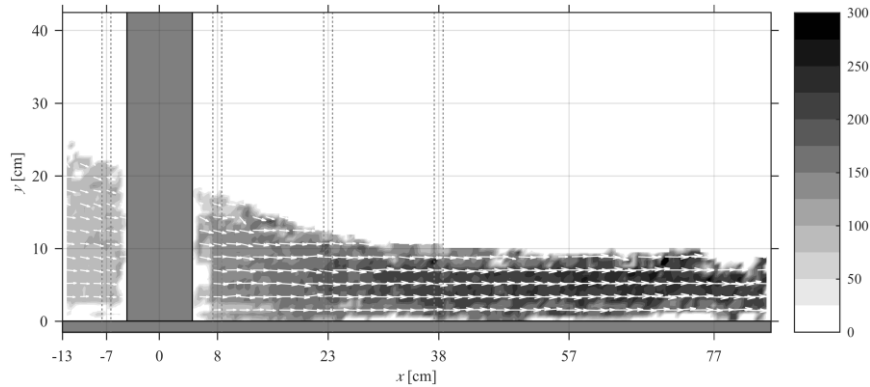
b) Particle Image Velocimetry for 32 x 32 px initial interrogation window size (every 3rd vector displayed)

Figure 4. Resulting velocity magnitude fields (in cm/s)

Table 1. Calculation time for different iteration numbers in OF method (2 to 20 iterations) and resulting size of the velocity field

Method	OF 2	OF 4	Of 6	OF 8	OF 10	OF 15	OF 20
Time (s)	28.8	51.8	75.3	99.8	133.4	183.7	239.9
VF size (px x px)	1280 x 576						

Table 2. Calculation time for different initial interrogation window size in PIV method (112 x 112 px to 16 x 16 px) and resulting size of the velocity field (the final calculation pass used 50 % of the given interrogation window size)

Method	PIV 112	PIV 96	PIV 80	PIV 64	PIV 48	PIV 40	PIV 32	PIV 24	PIV 20	PIV 16
Time (s)	3.2	4.3	5.5	3.9	6.1	8.1	6.5	11.2	15.8	19.0
VF size (px x px)	19 x 44	23 x 52	27 x 63	35 x 79	47 x 105	56 x 127	71 x 159	95 x 212	114 x 255	143 x 319

3.2. Wave Breaking at Artificial Reef

In order to evaluate the performance of the OF method, a regular wave propagating over a submerged plate is investigated in the following. Figure 5 shows the images taken from the high-speed video at six instants over the wave period of 1 s (left column) as well as the results from OF (center column) in comparison with numerical results from a 2D LES simulation obtained by FLOW-3D (right column).

The field of view is limited to the rear end of the submerged plate. The high-speed images cover a range of ~23 x 23 cm with a resolution of 256 x 256 px. The pixel density, i.e. ~11 px/cm, is thus comparable to the previous test case and the same mean averaging filter size of 12 x 12 px is chosen. The time $t = 0$ s was chosen as the moment where the backflow above the plate is just about to set in. Thus, the water is in rest in this moment, and only a small vortex being generated at the end of a wave cycle is still present. A mesh with 5 mm cell size was chosen to resolve the directly simulated large vortices in the LES model.

The flow field in this test case is characterized by several small-scale vortex structures being transported around the plate as well as some aeration after the wave breaking. Generally, the flow velocities, which are obtained by Optical Flow, are in good agreement with the numerical solution. The very complex flow fields consisting of forwards and backwards directed particle displacements are well represented. Moreover, the small vortices at the end of the plate are in good agreement regarding their size and location. It has to be noted that a relatively small interrogation window size would be required to detect these vortex structures with a PIV technique. The OF calculation time for each frame pair was about 10 s on the same computer as in the test case 1 due to the low image resolution. It was found again that the OF method is sensitive to illumination changes leading to high number of spurious vectors above the water surface. For a better readability and comparability, these regions have been masked in the OF result plots.

3.3. Aerated Stepped Spillway Flow

In this section, OF application to slightly aerated flows (with a mean air concentration of 20 %) is tested. Therefore, a high-speed recording of a stepped spillway flow is used. The video is captured with a frame rate of 732 fps and a full resolution of 1920 x 1200 px. Two frames were extracted from the video and rotated by 26.6° to align the pseudo-bottom (connecting the step edges) with the horizontal. The images were cropped to the field of interest, i.e. one single step, yielding an image size of 1270 x 1100 px (Fig. 6a). As the investigated step represents the inception point of self-aeration, clear water is found at the upstream end of the step while flow at the downstream end is aerated. The pixel density is about 90 px/cm in this study, much higher than in the previous cases.

A simple OF estimation as it was performed in the first two cases was found to not provide useful results. For this reason, the image pyramid technique is considered, which is an incremental multi-resolution method. This method is used to apply a single filter to a set of images instead of using different filters to a single image (Adelson et al. 1984, Burt and Adelson1983). Herein, the original image size is reduced by a specified factor yielding a blurred (low-pass filtered) copy of the image when upscaled to its original size. Repeating this step several times, a set of images of different sizes are obtained, forming a pyramid when illustrated above each other. In fact, this pyramid is the spatial-frequency domain of the image. Each level is downsampled from its nearest finer level. The optical flow is estimated at a coarse level in a first step. The coarse scale displacement is then used to correct the sequence at the next finer level (warping) (Sun et al. 2010). The total displacement is then the sum of all increments, resulting in higher accuracy for large displacements (Bruhn et al. 2005).

Naturally, the image pyramid technique is even more time-consuming than the basic Horn and Schunck scheme. For the given sequence of the stepped spillway, the total calculation time was 817.2 s using five pyramid levels with a downsampling factor of 2.5, which yields a minimum image size of 13 x 11 px. The results are illustrated in Fig. 6b in comparison to data from a conductivity probe. This data was gathered by Bung (2011a) in the centreline of a 30 cm wide flume with identical step height, slope and specific discharge. Moreover, an exemplary BIV result is included. For BIV, an interrogation window size of 32 x 32 px with 75 % overlap was applied. The results show that the OF method can give valuable results even in aerated flows, which is known to be difficult by imaging techniques

(Bung 2011b). While BIV commonly tends to provide too low velocities (Bung and Valero 2015), OF is a more robust method in aerated flow analysis.
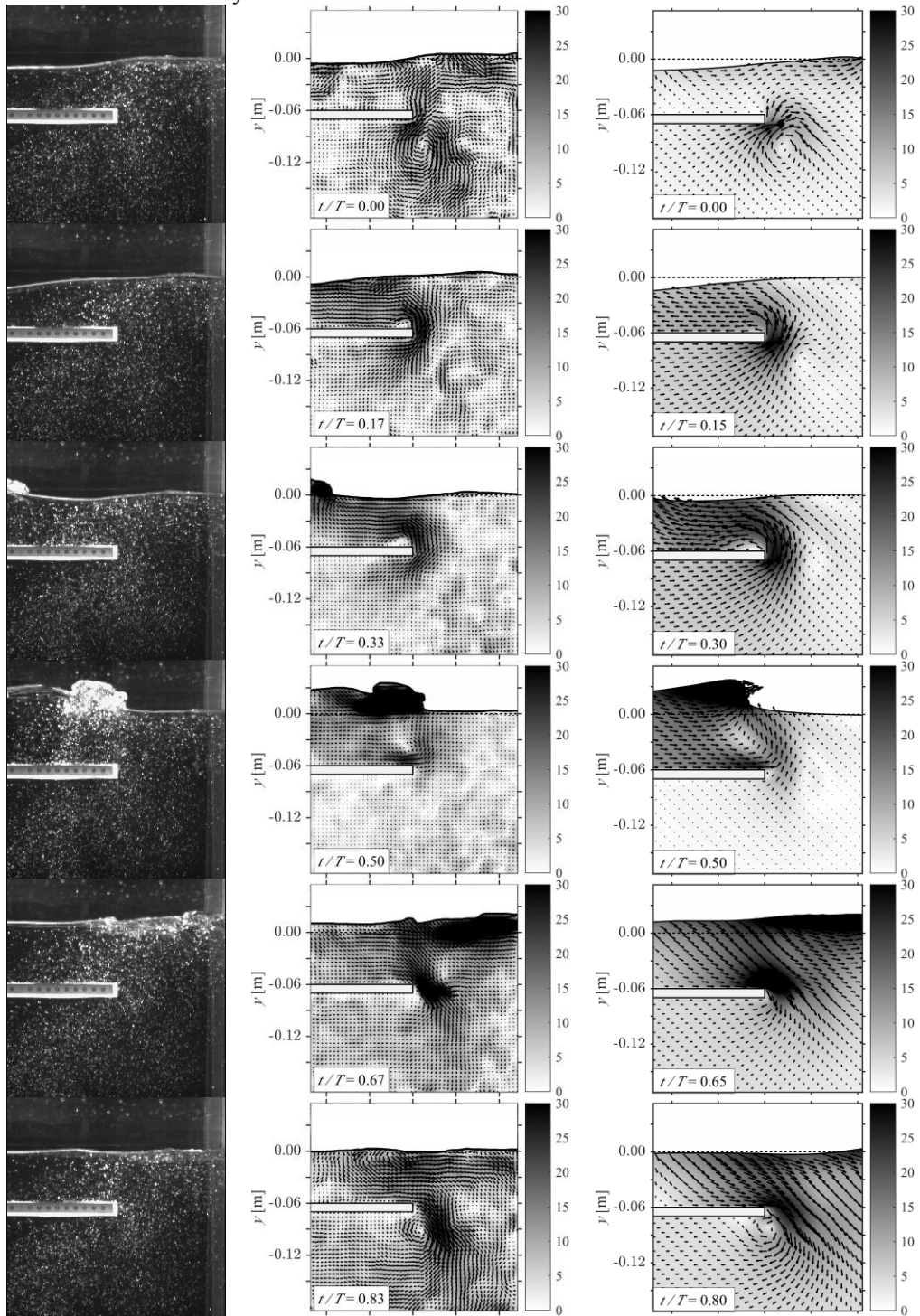
Figure 5. Velocity magnitude fields over one wave period (top to bottom) at the rear end of the submerged plate (in cm/s) obtained from high-speed video frames (left, from Bung et al. 2008) using OF method (center) in comparison to LES simulation (right), note that spurious vectors in OF results have been masked above the free surface

a) High-speed frame captured at step 5, i.e. the inception point of self-aeration with C_{mean} = 20 %, flow direction from left to right

b) Velocity profile obtained by OF method compared to BIV and conductivity probe data (CP) from the centreline (h_{90} is the elevation with a time-averaged air concentration of 90 %)
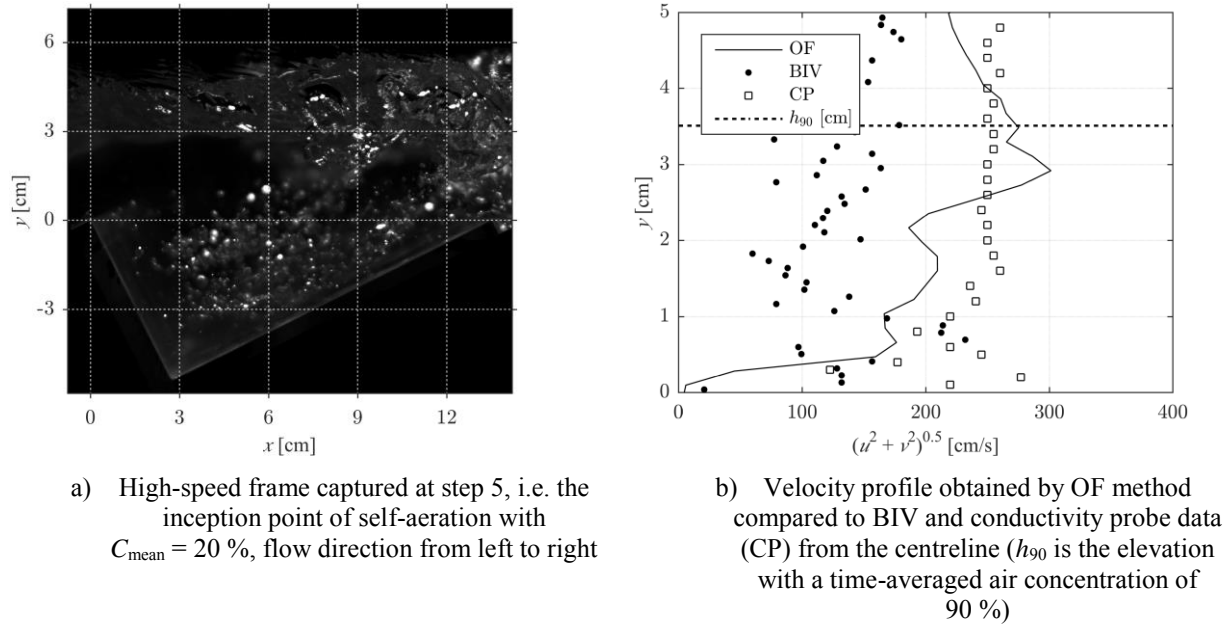
Figure 6. Optical Flow method in slightly aerated stepped spillway flows

3.4. Conclusions

It was shown that the Optical Flow method is fully capable to determine 2D velocity fields in hydraulic structure models. When choosing a global method, e.g. the Horn and Schunck method used in the present paper, a dense velocity field is obtained. Velocity information is then given for every pixel. The calculation time is much longer compared to a classical PIV calculation. However, PIV results are typically of lower resolution and do not allow the determination of such dense velocity fields, except with additional interpolation. The calculation time for OF is still bearable on modern computers and may be reasonable when detection of small-scale rotational flow structures is of interest.

The OF method was successfully applied to seeded and aerated flows although OF, as a differential approach, should be better suitable for continuous objects than for small particles. Moreover, OF is much more sensitive to local illumination changes as it is a differential approach compared to PIV as an integral approach.

In case of aerated flows, calibration of the data is still recommended. Particularly, application of an image pyramid technique helps to improve the results. Application to other types of aerated flows is planned for future research. A detailed benchmark with direct velocity measurements near the wall using an intrusive probe may help in assessing accuracy of the presented method.

References

Adelson, E., Anderson, C. H., Bergen, J. R., Burt, P. J., and Ogden, J. M. (1984). "Pyramid methods in image processing." RCA Engineer, 29(6), 33-41.

Adrian, R.J., and Westerweel, J. (2011). Particle Image Velocimetry, Cambridge University Press, Cambridge.

ASCE (2000). Hydraulic modeling - concepts and practice, ASCE manuals and reports on engineering practice, No. 97, Reston.

Bruhn, A., Weickert, J., and Schnörr, C. (2005). "Lucas/Kanade meets Horn/Schunck: Combining local and global optic flow methods." *International Journal of Computer Vision*, 61(3), 211-231.

Bung, D.B. (2011a). "Developing flow in skimming flow regime on embankment stepped spillways." *Journal of Hydraulic Research*, 49(5), 639-648.

Bung, D.B. (2011b). "Non-intrusive measuring of air-water flow properties in self-aerated stepped spillway flow." 34th IAHR World Congress, Brisbane, 2380-2387.

Bung, D.B., and Valero, D. (2015). "Image processing for Bubble Image Velocimetry in self-aerated flows." *36th IAHR World Congress*, Den Haag.

Bung, D.B., and Valero, D. (2016). "Optical flow estimation in aerated flows." *Journal of Hydraulic Research* (accepted paper)

Bung, D.B., Hildebrandt, A., Oertel, M., Schlenkhoff, A., and Schlurmann, T. (2008). "Bore propagation over a submerged horizontal plate by physical and numerical simulation." *31st International Conference on Coastal Engineering (ICCE)*, Hamburg.

Burt, P. J., & Adelson, E. H. (1983). "The Laplacian pyramid as a compact image code." *IEEE Transactions on Communications*, 31(4), 532-540.

Corpetti, T., Heitz, D., Arroyo, G., Memin, E., and Santa-Cruz, A. (2006). "Fluid experimental flow estimation based on an optical-flow scheme." *Experiments in Fluids*, 40(1), 80-97.

Felder, S., and Chanson, H. (2015). "Phase-detection probe measurements in high-velocity free-surface flows including a discussion of key sampling parameters." *Experimental Thermal and Fluid Science*, 61, 66-78.

Fortun, D., Bouthemy, P., and Kervrann, C. (2015). "Optical flow modeling and computation: A survey." *Computer Vision and Image Understanding*, 134, 1-21.

Horn, B.K.P., and Schunck, B.G. (1981). "Determining optical flow." *Artificial Intelligence*, 17, 185-203.

Leandro, J., Bung, D.B., and Carvalho, R. (2014). "Measuring void fraction and velocity fields of a stepped spillway for skimming flow using non-intrusive methods." *Experiments in Fluids*, 55(5).

Liu, T., Merat, A., Makhmalbaf, M.H.M., Fajardo, C., and Merati, P. (2015). "Comparison between optical flow and cross-correlation methods for extraction of velocity fields from particle images." *Experiments in Fluids*, 56(8).

Liu, T., and Shen, L. (2008). "Fluid flow and optical flow." *Journal of Fluid Mechanics*, 614, 253–291.

Lucas, B.D., and Kanade, T. (1981). "An iterative image registration technique with an application to stereo vision." *Proceedings of imaging understanding workshop*, 121-130.

Oertel, M., and Bung, D.B. (2012). "Initial stage of two-dimensional dam-break waves: Laboratory vs. VOF." *Journal of Hydraulic Research*, 50(1), 89-97.

Ryu, Y., Chang, K.-A., and Lim, H.-J. (2005). "Use of bubble image velocimetry for measurement of plunging wave impinging on structure and associated greenwater." *Meas. Sci. Technol.*, 16 (10), 1945-1953.

Sun, D., Roth, S., & Black, M. J. (2010). "Secrets of optical flow estimation and their principles." *IEEE conf. on computer vision and pattern recognition* (cvpr).

Sveen (2004). "An introduction to MatPIV v.1.6.1." *Department of Mathematics, Mechanics and applied Mathematics, University of Oslo*.

Mouth of the Columbia River North Jetty Erosion Stabilization

C. C. Humphrey[1], B. J. Abel[2], H. R. Moritz[1]
[1]Portland District, US Army Corps of Engineers
Portland, OR 97204
USA
E-mail: christopher.c.humphrey@usace.army.mil
hans.r.moritz@usace.army.mil
[2]Harbor Consulting Engineers, Inc.
Seattle, WA 98102
USA
E-mail: bjabel@harborengineers.com

ABSTRACT

The Mouth of the Columbia River (MCR), located at the river's confluence with the Pacific Ocean between Oregon and Washington, is a critical regional and national gateway for trade and commerce. The MCR is protected and stabilized by three rubble-mound jetties, all of which are in need of major rehabilitation. In 2014, rehabilitation started with construction of the North Jetty Lagoon Fill project.

Soon after construction of the North Jetty in 1917, deposition of sand caused the formation of a wide beach along the north side of the structure, which helped protect much of the north side of the jetty from ocean erosion. However, over time, a linear 'lagoon' feature formed adjacent to the north side of the jetty, primarily caused by erosion and piping through the jetty. This erosion was accelerated by the presence of a small stream that connected with the lagoon and drained through the jetty structure. The erosion was jeopardizing the foundation of the jetty and contributing to ongoing deterioration.

Simply filling the lagoon would not have been a long-term solution without addressing the causes of the erosion. Of the design elements included, three were key: construction of a rock filter adjacent to the jetty, construction of an erosion protection structure near the west end of the lagoon area, and construction of a weir structure to allow stream drainage through the jetty. Construction was completed in June 2015.

Keywords: *Jetty, erosion, sinkhole, breach, stability, Columbia River.*

1. INTRODUCTION

The Mouth of the Columbia River (MCR), or Columbia Bar, is located at the river's confluence with the Pacific Ocean between Oregon and Washington (Figure 1) and is known as one of the most treacherous coastal inlets in the world, with its strong currents, large waves, and extreme tidal influences. The MCR has been linked to the economic future of the Pacific Northwest since settlers first began exploring the region in the late 1700s. Today, about 38 million metric tons of cargo is transported through the MCR each year, with an estimated value of $20 billion (U.S.) (USACE 2012). This level of commerce would not be possible without the deep-draft navigation channel that currently exists through the inlet and which is maintained by nearly continuous dredging operations and the presence of protective jetties at the river's mouth.

The jetty system at the MCR consists of three rubble-mound jetties (North Jetty, South Jetty, and Jetty A) with a total length of about 15.6 km. The jetties were constructed between 1885 and 1939 on massive tidal shoals to secure consistent navigation through the coastal inlet, which historically experienced rapid shifting of sand bars. Since initial construction, these structures have been battered by storms and the jetties have undergone a number of repairs. Today, the jetties are once again in need of major repair, so in 2010, planning and design for rehabilitation began, with construction starting at the North Jetty in 2014. The rehabilitation at the North Jetty is being completed in three phases:

1. Infilling of an eroded lagoon on the landward side of the jetty,
2. Initial 'critical' repair of the jetty from station 85+00 to 98+50 (stationing in U.S. feet), and
3. Construction of a new head cap from station 98+50 to 101+00 and rehabilitation of the jetty truck and root from station 20+00 to 85+00.

The first two phase of the rehabilitation are complete. The third phase is currently being designed, with construction anticipated to begin in 2017. This paper focuses on the first phase of the project, stabilizing the jetty by infilling of the landward lagoon.

Figure 1. North Jetty lagoon aerial photograph looking southwest

2. LAGOON FORMATION

The North Jetty is located in Pacific County, Washington, near the towns of Ilwaco and Long Beach. Originally, the North Jetty was about 3.7 km long, extending from Cape Disappointment west along Peacock Spit, then out to open water (Figure 2). Soon after construction, jetty induced morphological changes to the inlet resulted in the rapid deposition of sand at Peacock Spit and the formation of a wide accreted land mass along the north side of the structure (Benson Beach). This accreted land mass helped protect much of the north side of the jetty from the extreme ocean forces. Since construction, the jetty head has retreated about 610 m, with Benson Beach retreating by a similar amount, but the sand that remains to the north continues to protect the integrity of the jetty trunk and has reduced overall maintenance costs. However, over time, a linear 'lagoon' feature formed adjacent to the north side of the jetty (Figure 1), between station 16+00 and 59+00, primarily as the result of erosion and piping of sand caused by tidal exchange and wave surge through the deteriorated porous structure. This erosion was jeopardizing the foundation of the jetty and contributed to ongoing deterioration. Therefore, the decision was made to fill in the lagoon and construct a landward filter to mitigate for future erosion (USACE 2012).

The initial stages of sand erosion through the jetty likely started soon after formation of Benson Beach. The North Jetty was constructed almost entirely of large jetty stone, originally between 1 and 14 metric tons each. This resulted in a very porous and permeable structure, which allows the free transmission of water through the jetty void space as a result of tidal exchange, wave influence, and stormwater drainage. The tidal range at MCR between mean lower low water (0 m MLLW) and mean higher high water (MHHW) is 2.4 m, with seasonal high tides reaching 3 m MLLW. Mean sea level is at 1.1 m MLLW. During storms, ocean water level along the structure can be surcharged by 0.6 to 1.5 m (above tidal level) due to storm surge effects. Storm wave heights at the seaward extent of the MCR inlet can reach 7.2 m, while wave heights along the channel side of the jetty (within the inlet interior) can range from

Figure 2. Shoreline response north of North Jetty from 1939 to 2002

2.4 to 5.5 m depending upon water level and jetty location. The rapid transmission of water during tidal surcharge and storm wave action results in the piping of erodible material through the jetty and a net degradation of material.

The first indication of erosion was the formation of sinkholes on the landward side of the jetty. Prior to the lagoon formation, the ground surface elevation behind the jetty generally ranged from about 4.3 to 4.9 m, which is higher than most of the significant waves measured at the south side of the jetty. As wave energy propagated through the structure, it initially eroded sands in contact with the jetty side slope below the ground surface. This resulted in development of subsurface voids within the sand deposit. Because the beach and dune sands that make up the Benson Beach complex are essentially non-consolidated and non-cohesive, the ceilings of the voids quickly collapsed, and sand filled the opening like an hour glass. Continued erosion and sand migration through the jetty continued this process until sinkhole depressions formed at the ground surface (Figure 3). The sinkholes enlarged until all the sand had been eroded from near the face of the jetty down to an elevation of approximately 1.2 to 1.5 m (North American Vertical Datum of 1988 - NGVD88), although some areas eroded down to an elevation of 0.3 m (NGVD88).

Wave overtopping contributed to the erosion and enlargement of the lagoon feature. Although actual wave overtopping was determined to be an infrequent event, the impact of such events on the size and shape of the lagoon were significant and likely played a key factor in the formation of the lagoon. Wave overtopping introduces a 'slug' of water into the lagoon from up to 3 m above the ground surface. This force rapidly erodes once stable sands and enters them into suspension. In addition, the slug of water increases the water elevation of the lagoon, creating a steeper hydraulic gradient between the lagoon and south channel, allowing more rapid flow and sediment transport back out into the channel.

Progressive landward recession of Benson Beach contributed to enlargement of the lagoon and undermining of the jetty foundation, primarily during storm surge events. The location of the beach is very much tied to the jetty head location. As the jetty length recedes, the shoreline is exposed to greater wave and storm energy, which impacts the beach. The structure also focuses incoming wave energy to the beach/jetty interface and generates outgoing rip current alongside the north jetty toe that has a negative effect on the stability of the trunk (Figure 4). This focused energy allows storm surge to travel farther inland and has resulted in periodic overtopping and breaching of the foredune near the jetty that separates the beach from the lagoon area. These periodic breaching events significantly accelerated the lagoon formation, especially at its western end.
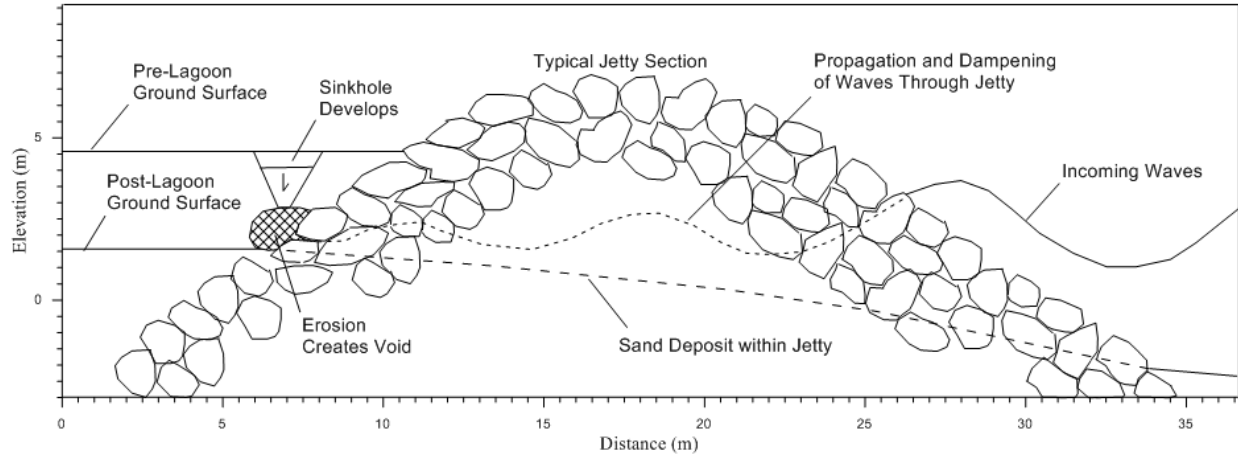
Figure 3. Sketch illustrating the propagation of wave energy through the jetty causing erosion and sinkhole formation.
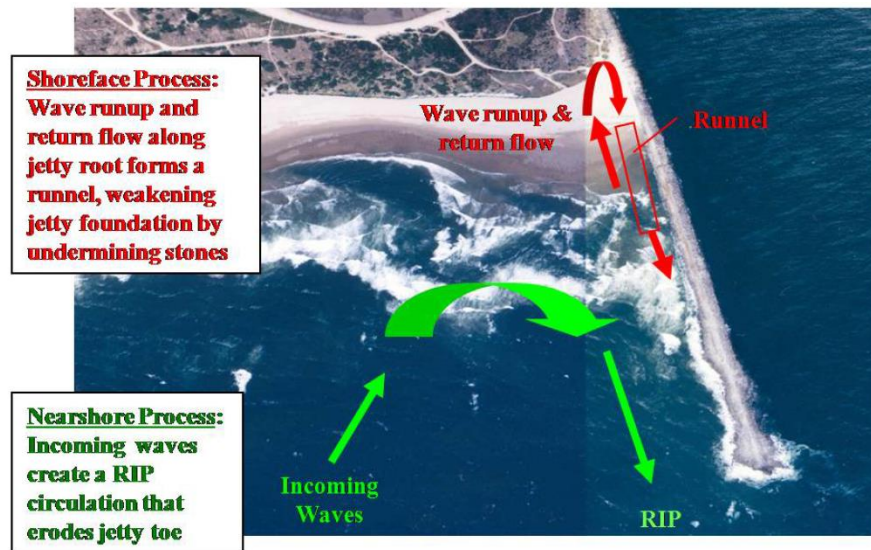
Figure 4. Shoreface and nearshore processes offshore of Benson Beach

Lastly, the formation of the Benson Beach complex also blocked and disrupted natural drainages north of the jetty. As a consequence, an approximately 1.8 km² (450 acre) catchment and lagoon complex formed at the location of the historic, pre-jetty shoreline at the base of McKenzie Head (Figure 5). Surface water no longer discharged directly to the MCR inlet upon reaching the base of McKenzie Head. Instead, runoff was detained in a depositional basin behind Benson Beach. The water that could not be stored or rapidly infiltrated in the basin exited the system by way of a single small stream channel that flowed from the basin south into a broad wetland complex present north of Jetty Road, then flowed south under the road embankment via a 1.2 m (48 inch) culvert towards the North Jetty root where the water simply flowed through the pervious jetty stones and into the inlet channel between Stations 18+00 and 20+00. As the lagoon formed on the landward side, the small stream channel eventually connected with it and contributed fresh water to the more saline intertidal lagoon. This exchanged accelerated the lagoon growth, especially at the south end of the lagoon.
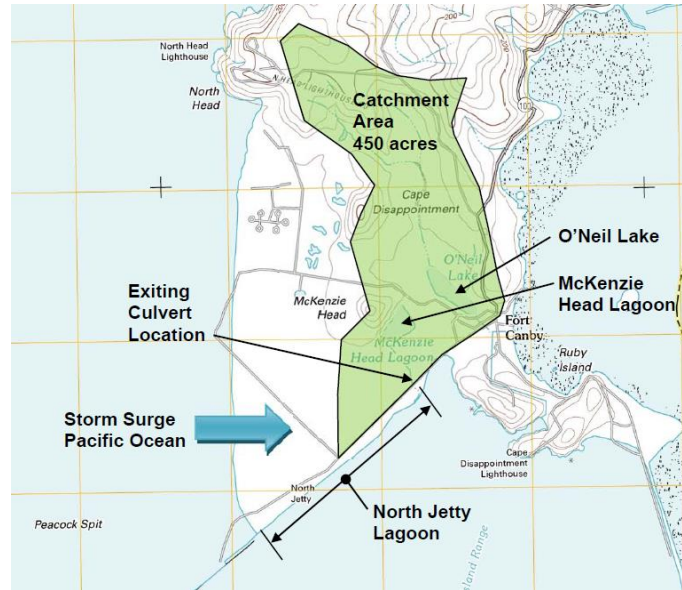
Figure 5. McKenzie Head Lagoon approximated catchment area

The configuration of the lagoon and stream channel, and the elevation of the culvert, also allowed a moderate backflow to occur through the culvert and into the McKenzie Head wetland during extreme high tides (greater than 2.7 m NAVD88). This backflow provided an additional source of water to the wetland complex north of the road. One of the goals of the project was not to significantly impact the McKenzie Head wetland complex or the intertidal exchange during high tides.

3. DESIGN CONCEPTS

The lagoon fill project had a number of technical goals that needed to be incorporated into the design; these included:

- A design life of 50 years with only periodic maintenance.
- No negative impacts to the Benson Beach wetland complex north of Jetty Road.
- Fill design was to address erosion from hydraulic loading associated with; (1) tide, wave, surge, and overtopping loading from the channel side; (2) overland flow from the wetland; and (3) storm surging waves from the Benson Beach side/ocean side of the project.
- Fill design was to maintain sufficient permeability of the jetty.
- Fill design was to provide a sufficient subbase/subgrade surface adequate for future design and construction activities for jetty rehabilitation; including, staging, crane operations, and truck loading.

To achieve these goals, a number of design elements were developed that both helped protect the jetty while maintaining needed tidal exchange through the structure. These included construction of a zoned rock filter adjacent to the north jetty face; construction of a buried, dynamically stable, erosion protection structure near the west end of the lagoon area; and construction of an armored weir structure through the filter zone in the existing stream drainage area to help protect the jetty foundation from erosion while maintaining stream flow and tidal exchange through the jetty in this area. A fourth element was added later in the design process associated with development of a sand borrow pit at the eastern end of the site, which was used to reduce the quantity of import sand material for the lagoon filling. U.S. Army Corps of Engineers Engineering Manuals (EM) were heavily utilized during the design (including EM 1110-2-1100, EM 1110-2-1601, and EM 1110-2-1901).

3.1. Filter Design

To address piping of fine grained sandy fill through the jetty, a filter zone was needed between the jetty stone and the bulk lagoon sand backfill. A three-zone filter rock design was selected, with the coarsest gradation near the jetty and fining outward (Figure 6). The use of geotextile filters was initially considered but was later rejected, primarily due to environmental concerns and concerns related to its long-term performance.
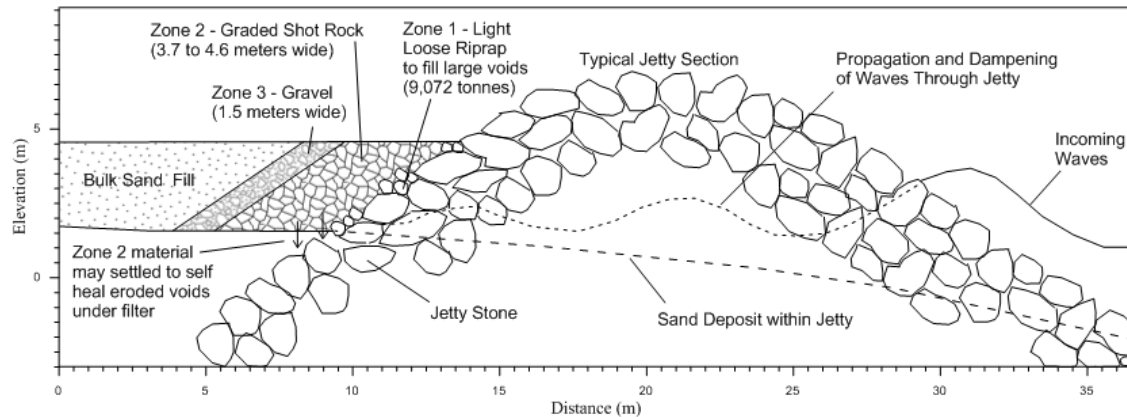
Figure 6. Typical section showing the three zone filter on landward side of jetty designed to help prevent erosion and to filter bulk sand backfill

Zone 1 – The first filter zone (the zone closest to the jetty) consisted of 9,072 metric tons of light loose riprap to be selectively placed on the inside face of the structure to fill major voids in the jetty armoring. A tonnage was specified, rather than a thickness, to simplify the bidding process and contractual oversight. The primary purpose of the Zone 1 riprap was to fill in large voids in the jetty face and to even out the slope, rather than acting as a true filter zone. The Zone 2 shot rock fill (described below) was sized to be able to bridge the jetty stone voids, although some shot rock may have been initially lost within the larger voids. The riprap zone helped reduce the amount of shot rock lose and helped develop a more regular face by which the Zone 2 shot rock could be placed.

Zone 2 – The second zone consisted of a 3.7 to 4.6 m wide zone of graded shot rock, ranging size from about 2 to 40 cm. The 0.9 m tolerance was allowed due to the variable nature of the slope. The purpose of this zone was to provide a filter between the larger jetty stone/Zone 1 riprap and the fine Zone 3 gravel. The shot rock zone also provided a deformable filter that settles and occupies any voids created by piping of the existing underlying fine sand in the lagoon area through the jetty (Figure 6).

Zone 3 – The final filter consisted of a minimum 1.5 m wide zone consisting of graded gravel sized material. This material generally ranged from sand size (min. 35% sand equivalent) to 3.8 cm material. This zone is intended to prevent the lagoon sand fill from piping through the jetty.

3.1.1. General Bulk Lagoon Fill

The required general bulk lagoon fill that was placed landward of the zone 3 filter was generally graded to be in the sand sized range, specifically in the range so that local beach and dune sand material could be utilized. The fill gradation was intended to satisfy filter criteria, provide a stable subbase for future jetty work, be able to support vegetation and promote drainage, and be readily available within the immediate project vicinity.

Initially, the lagoon infilling was to be coordinated with local dredging operations and the dredged sands reused as pump ashore bulk material. However, coordination between multiple contracts proved difficult, and alternative sources were investigated. There were numerous sand and gravel pits in the general vicinity that could provide the required bulk sand. However, costs to transport more than 76,000 m³ of material required to fill in the lagoon proved too excessive. Local borrow sites were then investigated, and a 14,000 m² (3.5 acre) area was identified as a sand

borrow source at the east end of the project to supplement imported sand. This borrow pit provided about 30,000 m³ of sand material and reduced the total cost of the bulk sand material. Additional discussion of the borrow pit and its reclamation is provided in Section 3.4.

3.2. Western Erosion Protection Structure

As previously discussed, during extreme storm surge events along Benson Beach, the foredune protecting the western margin of the lagoon area periodically overtops and breaches. This exposes the lagoon area to more frequent storm induced wave attack. Wave inundation and subsequent backwash would have resulted in channel formation and downcutting along the landward side of the jetty adjacent to the beach without reinforcement. Failure to include erosion protection measures in this area would have resulted in degradation and loss of lagoon infill and filter along its western margin.

To protect the lagoon fill, an erosion protection zone was designed, as shown on Figure 7, which somewhat resembles a buried groin structure. The feature was constructed from jetty station 56+00 and extends northwest for a distance of about 76 m. The skewed angle with respect to the jetty alignment was an attempt to account for possible changes in the orientation of the Benson Beach shoreline resulting from continued recession. The feature was constructed using the Zone 2 shot rock and is intended to be dynamically stable. The stationing of 56+00 was selected, rather than the end of the lagoon fill at 58+00, to minimize disturbance of natural beach and dune deposits and transient features. Water from storm surge waves that overtop the structures would either infiltrate into the lagoon fill, flow over the filter zone and through the jetty, or backflow over the erosion protection structure with minimal erosion to the sand fill.
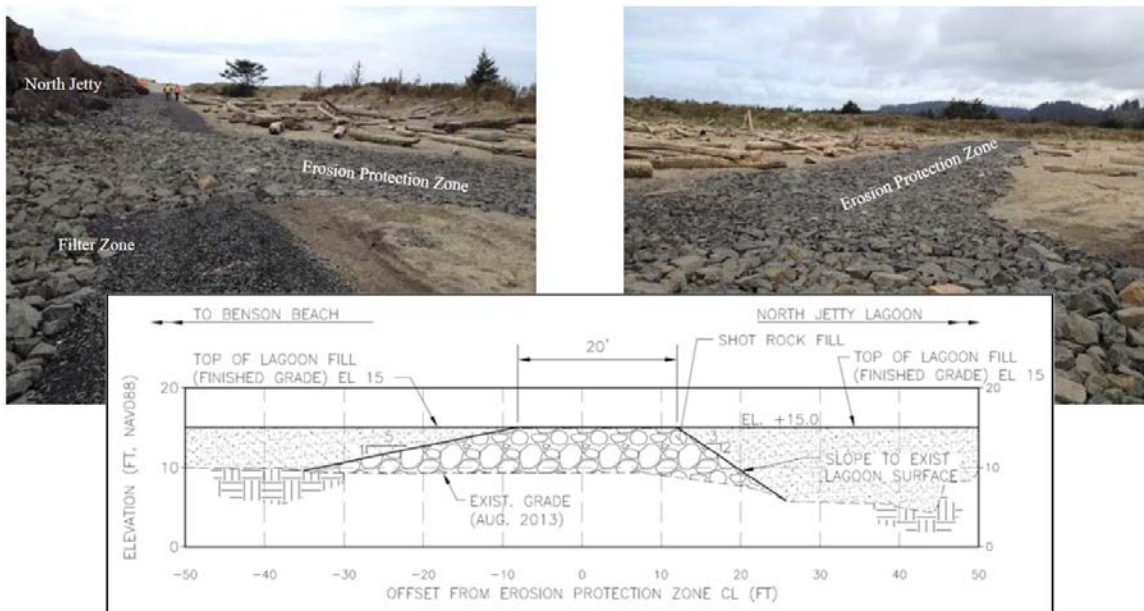
Figure 7. Design section and photographs showing Erosion Protection Zone (1 ft = 0.3048 m). Section Modified from USACE (2014),

3.3. Stream Weir

The presence of an upland drainage path into the lagoon fill project area necessitated a modified design approach in the vicinity of the discharge channel. Design concepts for this area were competing amongst several contradictory

project goals. These included maintaining upland drainage and protecting existing wetlands while eliminating erosion of lagoon formations and maintaining upland drainage while facilitating future equipment access and staging along the jetty.

Analysis of the upland catchment indicated that peak culvert discharge was expected to be about 0.6 m³/s during a 100 year storm event producing 16.5 cm of rain in 24 hours. This relatively low flow rate occurs due in large part to the vast low-lying wetland complex, which formed in the sandy Benson Beach deposits north of Jetty Road. Even in a region that receives an average of 198 cm of rainfall annually, the upstream wetland complex sufficiently dampens peaks flow rates experienced at the culvert.

To address the need for upland drainage and maintained tidal infiltration through the jetty, the lagoon fill template was stopped prior to reaching the discharge channel. In this area, a reduced height fill consisting of shot rock overlaying filter rock was selected. This design effectively created a rock weir that allowed free drainage through the jetty above the crest elevation and partially dampen flow below the crest (Figure 8). The key design considerations for this location were to minimize the mobilization of existing foundation sands underneath the rock weir and to prevent upstream water velocities, which could cause erosion.

The rock weir crest elevation was selected at elevation 1.8 m (NAVD) to

1. Mimic existing hydraulic characteristics and maintain existing wetland hydroperiods both upstream and downstream of the Jetty Road culvert;
2. Provide sufficient elevation to achieve construction vehicle passage across the weir approximately 75% of the time; and
3. Provide a sufficiently large rock section to improve weir stability.

Some excavation of the existing weir foundation sand was necessary for construction, but extensive excavation presented a high risk to jetty stability. For this reason, the project team decided to minimize excavation in favor of a shallower weir section. Ultimately, the top 0.6 to 0.9 m of sand were removed to develop a bench at elevation 0.6 m. Upon this bench, a 0.3 m thickness of filter rock was placed, overlain by an additional 0.9 m of shot rock.

The required length of the weir was calculated based on observed in-situ flow conditions. Hobo gauges placed within the existing lagoon provided historical data relating to the rate of change of the water surface within the lagoon over approximately 6 months of tidal cycles. The average rate of fall was recorded to be -0.25 cm/min with a standard deviation of 0.34 cm/min. A rate of fall of -0.91 cm/min was selected for design to ensure a sufficient margin of water exchange rate through the infiltration area of the jetty in excess of the present condition. The coefficient of permeability (K) was estimated to be 335 cm/sec. Because of the extremely large size and weight of the North Jetty armor stone, infiltration and seepage velocities are not a significant concern. As such, detailed analysis for in-situ conductivity was not considered necessary.

The additional tidally influenced area upland of the jetty resulting from the reclaimed borrow pit (see Section 3.4, below) increased the flow requirements through the weir discharge area. This condition considered the new wetland area connected to the existing culvert discharge channel with a free water surface area of up to 11,000 m² at high tide. A maximum discharge of 1.9 m³/s was calculated resulting from tidal exchange in the new wetland.

Cross-sectional area available for infiltration at the face of the jetty was calculated to be 18.6 m² based on a weir design length of 45.7 m, a crest elevation of 1.8 m, and a tide elevation of 2.3 m (per the continuity equation). An average flow area of 46.5 m² was used to estimate the flow capacity through the infiltration zone and required differential driving head. Assuming a discharge flow rate of 2 m³/s and an assumed flow path length of 15.2 m, a differential head of 19.5 cm was calculated across the North Jetty from the lagoon to the Columbia River channel.

Based on a projected area of 18.6 m², a maximum approach velocity of 10.4 cm/sec was expected. The approach velocity was used in wetland design to confirm the stability of channel features during normal conditions. Grain size analysis performed on samples from the installation of monitoring wells within the proposed borrow area indicates that in-situ sands are poorly graded sands with silt typically ranging from 0.2 to 0.4 mm. At 10.4 cm/sec, water velocities are below the Hjulstrom erosion velocity for sands having a grain size of 0.3 mm.

3.4. Borrow Pit and Reclamation into an Intertidal Wetland

The initial and primary objective of the borrow area was to provide about 30,000 m^3 of bulk backfill material to supplement the total volume of backfill needed for the project; this represented about 1/3 of the total lagoon fill volume. The borrow area is located landward of the jetty between station 20+00 and 26+00. This location was identified as an area where a borrow pit would not compromise the short- or long-term stability of the jetty. The borrow pit was reclaimed as a new intertidal wetland, which has a secondary benefit of improving intertidal habitat within the project site. Layout of the new wetland feature is shown on Figure 8 and was designed both to provide the maximum fill volume while maintaining stability of adjacent features and to optimize hydraulic function in conjunction with the adjacent stream and new rock weir. The new lagoon was appropriately vegetated with Carex Lyngbyei plantings within the emergent march zone (1.7 to 2 m NAVD), suitable native forbs-grass plantings and large woody debris broadcast through the upper marsh zone (2 to 2.4 m NAVD), and sedges with small native tree species within the upland perimeter bordering the new lagoon. The wetland area within the new lagoon (4,000 m^2, below 1.7 m NAVD) was unplanted and expected to colonize native species.

As previously discussed, the intertidal flow in/out of the new wetland is serviced by the porous rock weir that promotes intertidal exchange through the jetty. In addition to providing a secured flow path though the jetty for the new wetland drainage, the rock weir also provides vehicle access for future jetty repairs (to avoid impacting the wetland). Upland drainage (from areas north of Jetty Road) into the new intertidal wetland is serviced by a 1.2 m (48-inch), 15.2 m long culvert passing under Jetty Road.
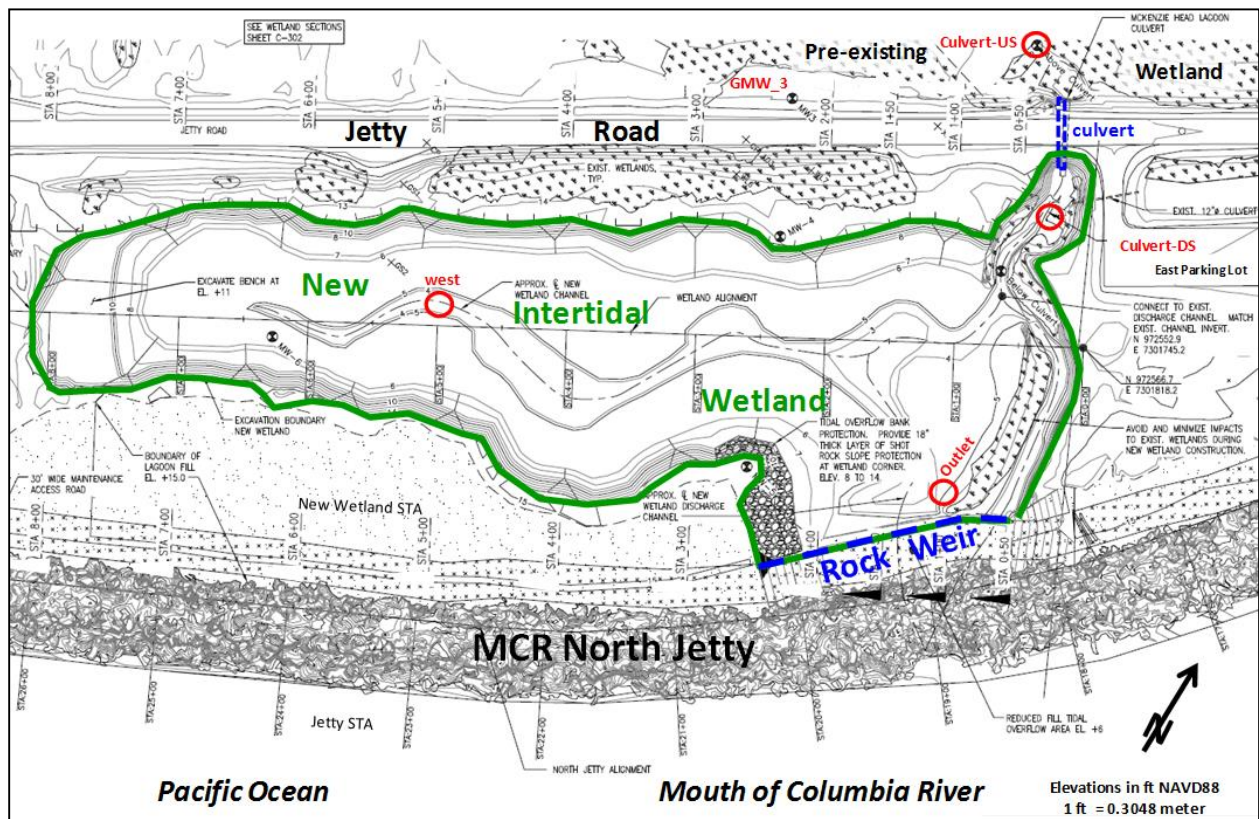
Figure 8. Layout of borrow area reclaimed into a new intertidal wetland lagoon. Modified from USACE (2014).

4. CONCLUSIONS

The majority of the construction work was completed by June 2015, and the zoned filter, weir, erosion protection structure, and new intertidal wetland appear to be functioning as intended (Figure 9). The western end of the lagoon fill area was subsequently used as staging area for initial 'critical' repair efforts for the North Jetty. It is anticipated that the infilled area will be utilized more during the major rehabilitation phase of the project, which will likely start construction in 2017. The newly established intertidal wetland will remain outside the area allowed for future staging activity and will be observed to determine how well it matches a natural wetland environment and to provide data for future reclamation efforts.

Figure 9. Looking west toward lagoon fill filter zone (left), and channel weir and reclaimed borrow pit (right).

5. REFERENCES

USACE (1986), Seepage analysis and control for dams, EM 1110-2-1901, U.S. Army Corps of Engineers (USACE).

USACE (1991), Hydraulic design of flood control channels, EM 1110-2-1601, U.S. Army Corps of Engineers (USACE).

USACE (2002), Coastal engineering manual, EM 1110-2-1100, U.S. Army Corps of Engineers (USACE).

USACE (2012). Major rehabilitation of the jetty system at the Mouth of the Columbia River – Major Rehabilitation Evaluation Report, U.S. Army Corps of Engineers (USACE), Portland District.

USACE (2014). Columbia River MCR North Jetty lagoon fill, Contract Plan Set, U.S. Army Corps of Engineers (USACE), Portland District.

Stepped Chute Training Wall Height Requirements

S.L. Hunt[1] and K.C. Kadavy[1]
[1]Hydraulic Engineering Research Unit
United States Department of Agriculture-Agricultural Research Service
Stillwater, OK 74075
USA
E-mail: Sherry.Hunt@ars.usda.gov

ABSTRACT

Stepped chutes are commonly used for overtopping protection for embankment dams. Aerated flow is commonly associated with stepped chutes if the chute has sufficient length. The aeration and turbulence of the flow can create a significant amount of splash over the training wall if not appropriately accounted for in the design of the structure. According to the United States Department of Agriculture (USDA)-Natural Resources Conservation Service (NRCS) Technical Release 60 Earth Dams and Reservoirs, a structural spillway should be designed to pass the freeboard hydrograph such that it does not cause serious damage to the embankment or the structure itself. For stepped spillways, researchers have suggested the training wall height equal a design factor ranging from 1.4 to 1.5 multiplied by the bulked flow depth, y_{90}. Yet, literature suggests that the design factor is a recommendation with little to no research provided to actually quantify what the design factor should be. Researchers at the USDA-Agricultural Research Service (ARS) Hydraulic Engineering Research Unit (HERU) in Stillwater, OK conducted a series of tests in a near prototype scale stepped chute facility to determine the design factor for training walls necessary to minimize the erosive splash that could result from the aerated flow. Tests were conducted in a stepped chute with a slope of 18.4 degrees for a wide range of skimming flow conditions. Data indicates for a step height, h, to critical flow depth, d_c, ratio of less than 0.4, the design factor for the training wall is 1.4; thus, the training wall height is equal to $1.4y_{90}$. For $h/d_c \geq 0.4$, the design factor increases from 1.4 at $h/d_c = 0.4$ up to 2.0 for $h/d_c = 1.0$. These design factors are recommended for use on chute slopes ranging from 10 to 30 degrees. This research is intended to assist design engineers with appropriately designing stepped chute training walls to minimize the erosive splash that can occur as a result of aerated, turbulent flow.

Keywords: stepped chute, stepped spillway, training walls, energy dissipation, bulked flow depth, physical modeling

1. INTRODUCTION

Aging embankment dams are faced with many challenges including deterioration of structural components, sedimentation encroaching the flood pool, and changing demographics resulting in hazard creep. Stepped chutes are commonly used for embankment overtopping protection of aging flood control structures experiencing hazard creep. Stepped chutes provide significant energy dissipation compared to smooth chute designs (Rice and Kadavy 1997, Boes and Minor 2000, Matos 2003, Hunt et al. 2014, Felder and Chanson 2015). Additionally, stepped chutes provide an alternative to modifying existing earthen auxiliary spillways because stepped chutes may be placed over the top of the dam and provide increased spillway capacity, whereas to achieve the same increased spillway capacity, an earthen auxiliary spillway may have to be significantly modified (i.e. widened) to match the capacity of the stepped chute.

If a stepped chute is of sufficient length, the turbulent boundary layer reaches the free surface and, thus, the air entrainment inception point develops. Downstream of this point, strong air-water interactions occur, creating water droplets that eject from the chute (Chanson 1993, Boes and Minor 2000, Matos 2003, Ohtsu et al. 2004, Felder and Chanson 2015). If the water droplets are not contained by the chute training walls when stepped chutes are applied to existing embankment dams, then scour may occur along the outside of the chute training wall. Excessive scour can undermine the structure and lead to failure of the chute.

Ohtsu et al. (2004) indicated the difficulty of measuring aerated flow depths accurately with a point gage because of the erratic behavior of the water. With the introduction of measuring air concentrations to describe the water droplets and splashing (Ohtsu et al. 2004), researchers (Boes and Minor 2000; Chanson and Toombes 2002; Matos 2003; and Ohtsu et al. 2004) are able to relate air concentration back to flow depth. Today, researchers routinely use the characteristic flow depth with an air concentration of 90%, y_{90}, to describe the bulked flow in stepped chutes. Bulked flow is the increased flow depth due to air introduced in the flow. y_{90} is a measurable term researchers have repeatedly used to relate training wall height for stepped chutes. For instance, Boes and Minor (2000) with concurrence by Matos (2003) suggest setting the training wall height to approximately 1.2 to 1.5 times y_{90} to contain the splash expected as a result of the air-water interactions. Ohtsu et al. (2004) suggest a training wall height of 1.4 times y_{90}. Chanson and Toombes (2002) indicate that the air-water flow depth, y_{90}, may reach 1.4 to 1.6 times d_c, but they do not provide a recommendation on training wall height based on this observation. While many of these researchers (Boes and Minor 2000; Chanson and Toombes 2002; Matos 2003; and Ohtsu et al. 2004) appear to be in agreement with recommended guidance for training wall height design, none of them provide actual data to support these recommendations. The objective of this study is to provide training wall height recommendations that are quantifiable for non-converging stepped chutes over a large range of step chutes slopes (i.e. $10° \leq \theta \leq 30°$) and step height to critical flow depth ratios (i.e. $0.035 \leq h/d_c \leq 1.1$).

2. EXPERIMENTAL SETUP

Testing was conducted in a near prototype scale stepped chute testing facility, as shown in Figure 1, at the USDA-ARS HERU, in Stillwater, OK. Chanson (2002) and Boes and Hager's (2003) recommendations for minimizing the occurrence of major scale effects were followed in model design and construction. The Weber (W) and Reynolds (R) for the original study by Hunt et al. (2014) were $8.1 \times 10^3 \leq W \leq 5.6 \times 10^5$ and $9.5 \times 10^4 \leq R \leq 1.61 \times 10^6$, respectively. Hunt et al. (2014) also indicate that recommendations provided by Pfister and Hager (2011) and Pfister and Chanson (2012) for minimizing scales effects were reasonably met. A subset of testing was conducted in this same flume to examine the training wall height requirements for non-converging stepped chutes. Table 1 summarizes further details of the experimental conditions in terms of chute slope (θ), chute width (B), vertical distance from the chute crest to the stilling basin floor (H_{crest}), unit discharge (q), step height (h), Froude surface roughness (F^*), step height to critical flow depth ratio (h/d_c), Reynolds number (R), Weber number (W), and normalized length (L/L_i).

a).   b).
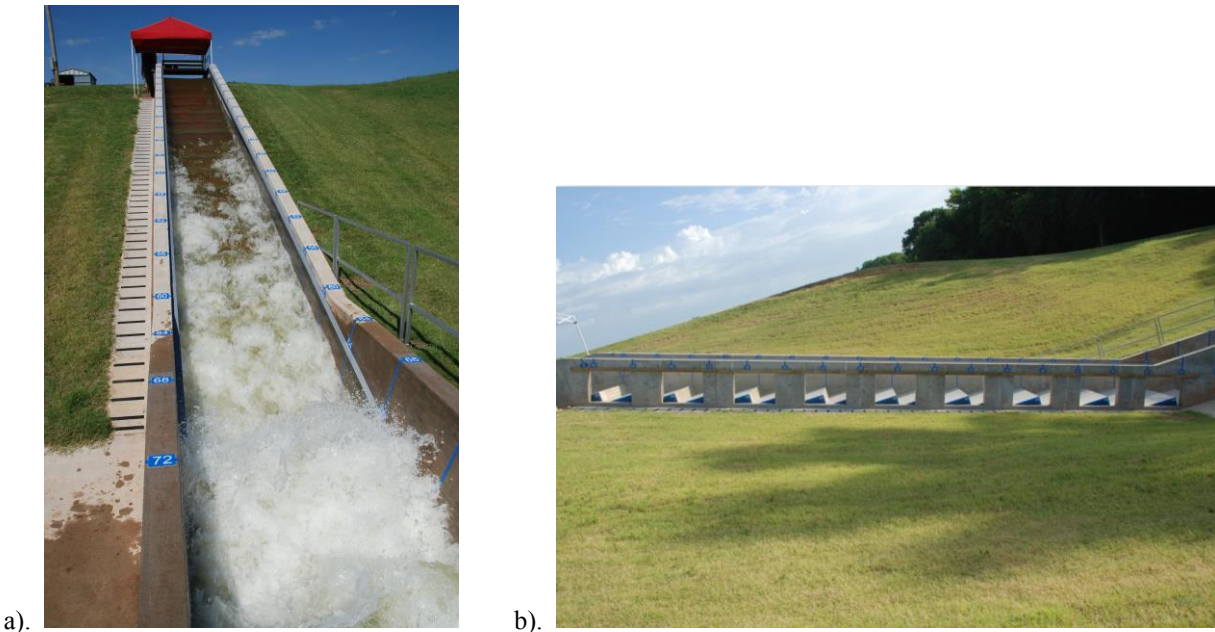
Figure 1. Photographic depiction of stepped chute testing facility at the USDA-ARS HERU: a). stepped chute facility looking from downstream to upstream and b) side view of stepped chute facility.

Table 1. Summary of stepped chute physical model experimental conditions.

Experimental Conditions	
Chute slope, θ	18.4°
Chute width, B	1.83 m
Vertical distance from the chute crest to the stilling basin floor, H_{crest}	5.5 m
Unit discharge, q	0.28 to 1.90 m³/(s•m)
Step height, h	152 mm
Froude surface roughness, $F*$	2.9 to 20
Step height to critical flow depth ratio, h/d_c	0.240 to 0.852
Reynolds number, R	1.3×10^5 to 1.6×10^6
Weber number, W	5.8×10^3 to 1.9×10^5
Normalized length, L/L_i	1.73 to 9.43

The entrance condition to the model consisted of a 3-m long weir that was classified as broad-crested according to Chow (1959). The testing flume consists of a smooth concrete surface with an approximate roughness height of 0.46 mm, which is consistent with Chow (1959). The width of the flume was 1.8 m with a vertical drop of 5.5 m. The original flume was constructed with a chute slope, $\theta = 18.4°$ (3H:1V). Although a large number of tests have been conducted in this facility over a range of chute slopes, step heights, and unit discharges to obtain data of clear and aerated flow depths and air concentrations (i.e. Hunt and Kadavy 2014), an additional seven tests were completed to evaluate the training wall height requirements. Unit discharges ranged from $0.28 \leq q \leq 1.90$ m³/(s•m), indicating flows conditions that were defined as skimming flow conditions according to Chanson (1994) and Ohtsu et al. (2001, 2004).

As outlined by Hunt et al. (2014), flow depth-velocity profiles were measured using a back-flushing Pitot tube coupled with a differential pressure transducer and/or a RBI® dual-tipped fiber optic probe attached to a manually operated point gage. The fiber optic probe tip diameters were approximately 0.08 mm, with a distance of 2.05 mm between them. The sample rate for testing was greater than 300 kHz with a signal response time of 0.033 μs. Sampling was set to 14,000 air bubbles or 30 seconds, whichever came first. To determine the measured flow on or over the training wall, a fixture (Figure 2) was designed to simulate the top of the training wall, y_{sw}, and to collect the splash landing on the top of the wall and outside the wall. The fixture was fabricated from sheet metal with a back to contain splash over the wall and bottom to contain splash on top of the wall. The bottom of the fixture had a triangular groove to convey the collected flow to the downstream end of the section. The fixture was 0.19 m wide and consisted of four 1.5 m long sections for a total length of 6.0 m. It was placed along the concrete wall inside the flume parallel to the pseudo-bottom of the chute floor and was adjusted to depths corresponding to 1.25, 1.50, 1.75, and 2.0 y_{90} for each test flow. Splash on the 1.5 m long downstream section was collected over time through a port located at the downstream end of the fixture and measured as flow per unit length of wall. The three upstream sections of the fixture were used to simulate the top of training wall, but these were not used for flow collection or measurement. To determine the characteristic flow depth with the air concentration of 90%, y_{90}, observed and predicted data were obtained from Hunt et al. (2014). Other data collected during the test were the maximum visually observed splash height, y_{sp}. This information was obtained from scaled digital photos and determined as the maximum level on the training wall that was continuously wetted by the splash. For some of the tests, the existing concrete wall was extended with a plywood wall so the maximum observed splash height could be determined. Figure 3 is a photographic depiction of the visually observed maximum splash height, y_{sp} during one of the tests.

a).

b). c).
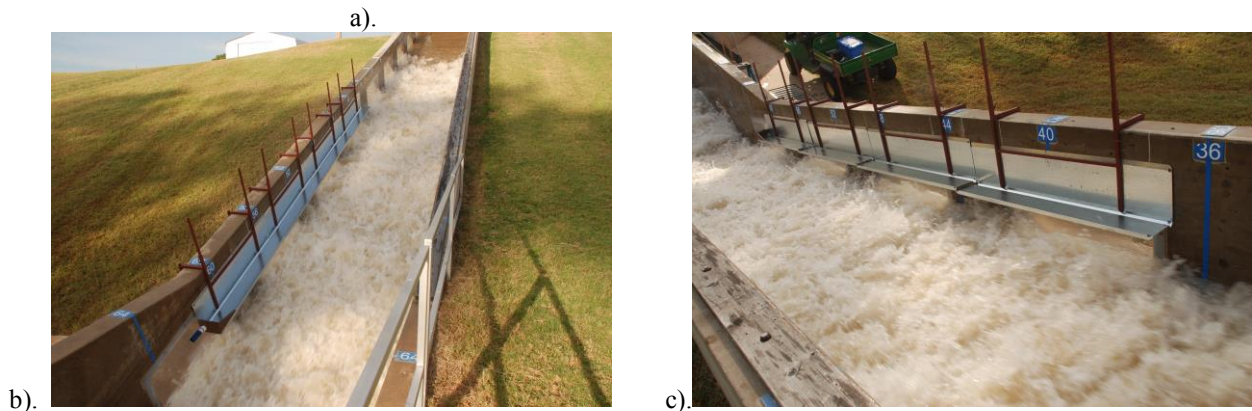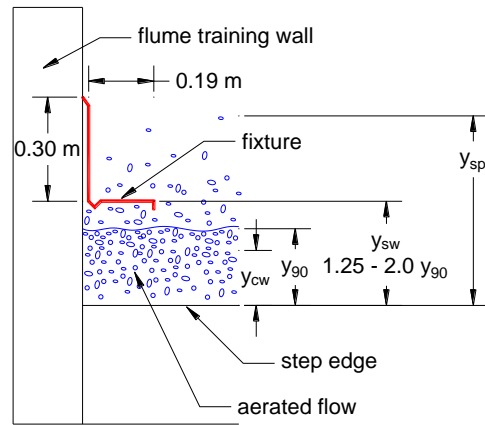
Figure 2. Fixture for measuring flow over or on top of training wall a). schematic, b). fixture simulating top of wall looking upstream, and c). fixture simulating top of wall looking downstream.

Splash line observed on extended wall.
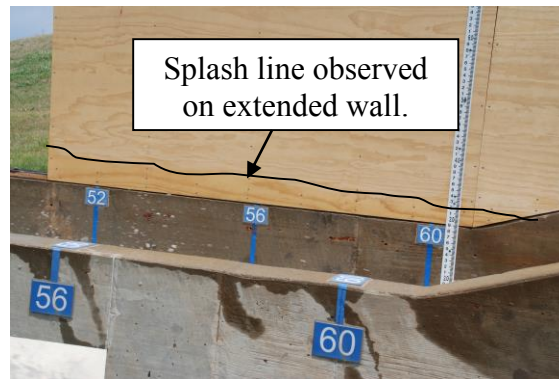
Figure 3. Splash photographically observed during stepped chute test.

3. RESULTS AND DISCUSSION

Boes and Minor (2000), Matos (2003), and Ohtsu el al. (2004) indicate the training wall height should be approximately 1.2 to 1.5 times the characteristic flow depth with an air concentration of 90%, y_{90}, to contain the splash. According to Chanson (2002), y_{90} is a function of the equivalent clear water flow depth, y_{cw}, and mean air concentration, C_{mean}, as shown in Equation 1. The equivalent clear water flow depth, y_{cw}, is the flow depth such that the void fraction (i.e. air concentration) is assumed to equal zero.

$$y_{90} = \frac{y_{cw}}{1 - C_{mean}} \tag{1}$$

While other researchers, including Chanson (2002) and Ohtsu et al. (2004), have provided relationships for determining the clear water flow depth and mean air concentration, Hunt et al. (2013, 2014) provided a more extensive analysis from a large data base developed from their research, resulting in the development of relationships for clear water flow depth, Equations 2 and 3, and mean air concentration, Equations 4 and 5. These relationships are also dependent on the normalized length, L/L_i. Hunt et al. (2014) further validated Equations 2, 3, 4, and 5 with data from literature. Although there are many relationships available for determining the air entrainment inception point for stepped chutes, it is recommended that relationships provided by Hunt and Kadavy (2013) be used in this analysis for consistency purposes. Thus, Equations 6 and 7 are recommended for use in conjunction with Equations 2, 3, 4, and 5.

$$\frac{y_{cw}}{d_c} = 0.34 \left[\frac{h}{d_c} \right]^{0.063} (\cos\theta)^{0.063} (\sin\theta)^{-0.18}$$
$$\text{for } L/L_i \geq 1,\ 0.035 \leq h/d_c \leq 1.1,\ 10° \leq \theta \leq 30° \tag{2}$$

$$\frac{y}{d_c} = \left(\frac{L}{L_i} \right)^{-0.22} \left[0.34 \left(\frac{h}{d_c} \right)^{0.063} (\cos\theta)^{0.063} (\sin\theta)^{-0.18} \right]$$
$$\text{for } 0.1 \leq L/L_i \leq 1,\ 0.035 \leq h/d_c \leq 1.1,\ 10° \leq \theta \leq 30° \tag{3}$$

$$C_{mean} = 0.0645 + 0.216 \left[\frac{h}{d_c} \right] + 0.453(\sin\theta)$$
$$\text{for } L/L_i > 2.0,\ 0.035 \leq h/d_c \leq 1.1,\ 10° \leq \theta \leq 30° \tag{4}$$

$$C_{mean} = 0.11 - \frac{0.22}{\left(\frac{L}{L_i} \right)} + 0.0645 + 0.216 \left[\frac{h}{d_c} \right] + 0.453(\sin\theta) \text{ for } 1.0 \leq L/L_i \leq 2.0 \tag{5}$$

$$\frac{L_i}{k_s} = 5.19 (F_*)^{0.89} \qquad 0.1 < F_* \leq 28 \tag{6}$$

$$\frac{L_i}{k_s} = 7.48 (F_*)^{0.78} \qquad 28 < F_* < 10^5 \tag{7}$$

where h = step height, d_c = critical flow depth, θ = chute slope, L = length from the downstream edge of the broad-crested weir to the point of interest, L_i = characteristic length from the downstream edge of the broad-crested weir to the surface inception point, F_* = Froude number defined in terms of the roughness height: $F_* = q/\sqrt{g(\sin\theta)k_s^3}$, and k_s = the surface roughness = $h \cos(\theta)$.

Based on the visual observations in this study, the maximum splash height, y_{sp}, was noted to range between 2.5 to 5.5 times y_{90}. Although the splash was observed at these heights, it does not necessarily mean that the training walls need to extend to this height since not all of the splash over the top of the wall would exit the chute and be considered erosive in nature. Figure 4 indicates the splash measured as flow per unit length of wall, q_{sw}, decreases exponentially as the ratio of y_{sw} to y_{90} increases. For low values of q_{sw}, the curves tend to level off and are not significantly influenced by the sidewall height. Based on engineering judgement for an acceptable amount of flow over the top of the training wall, a q_{sw} value of 1.24 liter/(min•m) was arbitrarily selected. This value of q_{sw}

corresponds to the transition of the data from exponential to a constant. Values of y_{sw}/y_{90} corresponding to $q_{sw}= 1.24$ liter/(min•m) were determined for each value of h/d_c from the curves in Figure 4 and presented in Figure 5. Figure 5 indicates the required training wall height, assuming a limit of $q_{sw} = 1.24$ liter/(min•m), is approximately 1.4 y_{90} for $h/d_c \leq 0.4$. For $h/d_c > 0.4$, y_{sw}/y_{90} is a function on h/d_c; thus, the training wall height increases to a value of approximately 1.9 y_{90} at $h/d_c = 0.9$. When comparing y_{sw}/y_{90} to h/d$_c$, as shown in Figure 5, y_{sw}/y_{90} appears to be a simple power function of h/d_c for values of h/d_c greater than 0.4 and constant for values of h/d_c less than 0.4; thus, the comparison yields the following empirical yet quantifiable relationships for recommended training wall height:

$$y_{sw}/y_{90} = 1.40 \text{ for } h/d_c \leq 0.4 \qquad (8)$$

And

$$\frac{y_{sw}}{y_{90}} = 2.0\left(\frac{h}{d_c}\right)^{0.37} \text{ for } h/d_c > 0.4 \qquad (9)$$

with a coefficient of determination, R^2, of 0.97. The observations from this study indicate that Chanson (1993), Boes and Minor (2000), Matos (2003), and Ohtsu et al. (2004) provide minimum requirements for training wall height requirements.
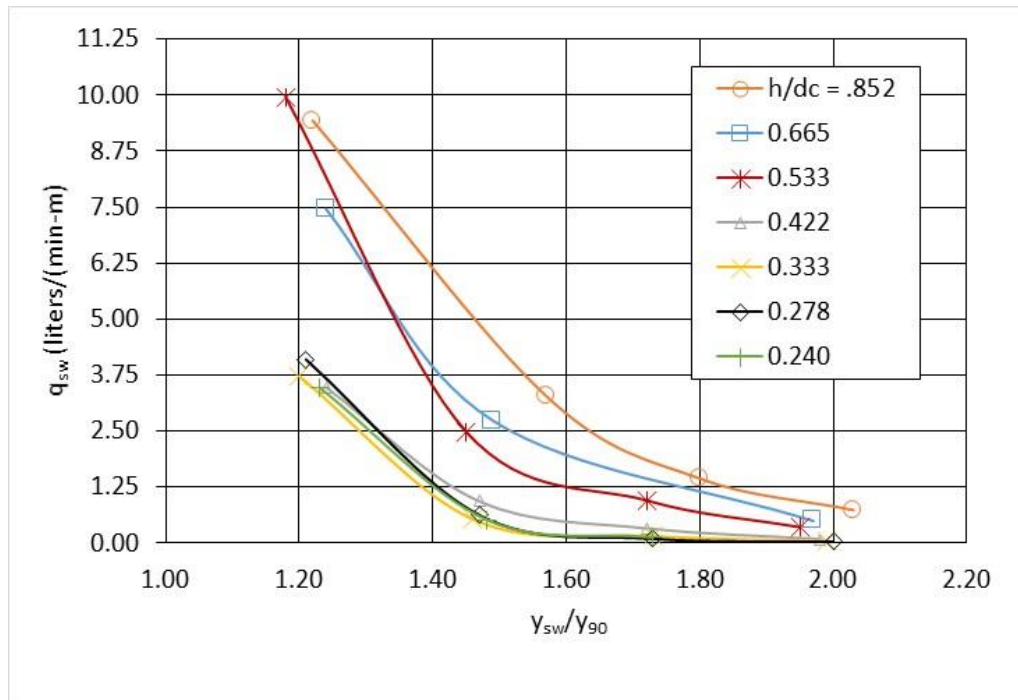
Figure 4. Measured flow per unit of length, q_{sw}, over or on top of training wall versus training wall height, y_{sw}, normalized by characteristic flow depth with air concentration of 90%, y_{90}.
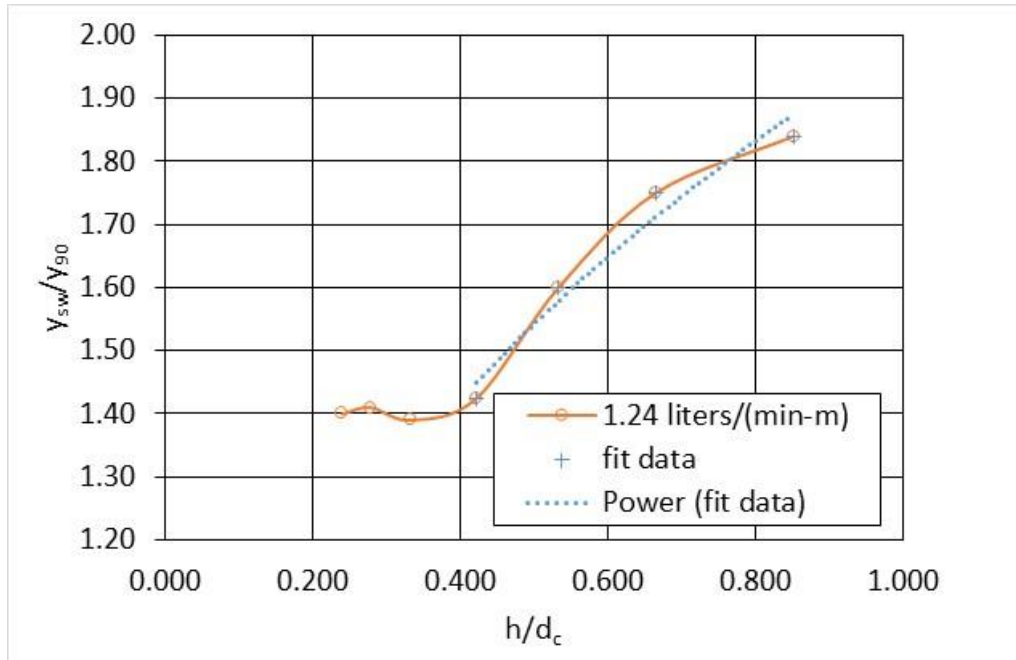
Figure 5. The ratio of training wall height to characteristic flow depth with air concentration of 90%, (y_{sw}/y_{90}) as compared to the ratio of step height to critical flow depth (h/d_c) for a recommended limit on the measured splash flow of 1.24 liters/(min•m) .

Using the relationships as defined in Equations 1 through 7 to determine y_{90}, and by knowing the step height and critical flow depth for a non-converging stepped chute, the design engineer has the tools to estimate the training wall height requirements necessary to contain a significant amount of splash in the chute if the splash flow is minimized to 1.24 liters/(min•m) over or on the top of the training wall. The criteria set forth are recommended for non-converging stepped chutes with skimming flows and chute slopes ranging from $10° \leq \theta \leq 30°$.

4. CONCLUSIONS

An extensive, multi-year, large scale physical model study has been completed at the USDA-ARS Hydraulic Engineering Research Unit in Stillwater, OK. Additional testing to complement the research was conducted for the purposes of providing a quantifiable relationship for training wall height recommendations for non-converging stepped chutes. While Boes and Minor (2000), Matos (2003), and Ohtsu et al. (2004) provide recommendations for training wall height requirements ranging from 1.2 to 1.5 times y_{90}, the maximum splash height, y_{sp}, visually observed in this study ranged between 2.5 to 5.5 times y_{90}. Setting a recommendation for the training wall height to contain the maximum observed splash would be extremely and overly conservative. Based on engineering judgement for an acceptable amount of flow allowed over the top of the training wall, a q_{sw} value of 1.24 liter/(min•m) was arbitrarily selected. This value of q_{sw} corresponds to the transition of the data from exponential to a constant. Allowing flows greater than 1.24 liter/(min•m) to overtop the training wall are expected to be more erosive in nature, creating a higher risk for the structure to fail. Based on the data with the limiting q_{sw} set to 1.24 liter/(min•m), y_{sw}/y_{90} appears to reach a constant of approximately 1.4 for $h/d_c \leq 0.4$, and increases y_{sw}/y_{90} as $h/d_c > 0.4$. The empirical relationships, Equations 8 and 9, provide quantifiable conservative results for determining training wall height. The relationships herein provide design engineers with the tools for determining the required training wall height for non-converging stepped chutes under skimming flow conditions over a range of chute slopes (i.e. $10° \leq \theta \leq 30°$).

5. ACKNOWLEDGMENTS

6. REFERENCES

Boes, R. M. and Hager, W. H. (2003). "Two-phase flow characteristics of stepped spillways." *J. of Hydraul. Eng.,* 129(9):661-670.

Boes, R. M., and Minor, H. R. (2000). "Guidelines for the hydraulic design of stepped spillways." *Proc. Workshop Hydraulics of Stepped Spillways,* Zurich, Switzerland (H.E. Minor and W. H. Hager, eds.) Balkema, Rotterdam, The Netherlands: 163-170.

Chanson, H. (1993). "Stepped spillway flows and air entrainment." *Can. J. Civ. Eng.* 20: 422-435.

Chanson, H. (1994). "Hydraulics of skimming flows over stepped channels and spillways." *J. Hydraul. Res.,* 32(3), 445-460.

Chanson, H. (2002). *The Hydraulics of Stepped Chutes and Spillways.* Steenwijk, The Netherlands: A. A. Balkema Publishers.

Chanson, H., and Toombes, L. (2002). "Experimental investigations of air entrainment in transition and skimming flows down a stepped chute." *Can. J. Civ. Eng.* 29: 145-156.

Chow, V. T. (1959). *Open-channel hydraulics.* McGraw-Hill, Book Company, Inc., Boston, MA.

Felder, S. and Chanson, H. (2015). "Simple design criterion for residual energy on embankment dam stepped spillways. *J. Hydraul. Eng.,* 04015062-1-11

Hunt, S. L. and Kadavy, K. C. (2013). "Inception point for embankment dam stepped spillways." *J. Hydr. Eng.,* 139(1):60-64.

Hunt, S. L., Kadavy, K. C., and Hanson, G. L. (2013). "New flow depth relationships for embankment dam stepped spillway design." *Dam Engineering*, XXIV(1):53-69.

Hunt, S. L, Kadavy, K. C., and Hanson, G. L. (2014). "Simplistic design methods for moderate sloped stepped chutes." *J. Hydraul. Eng.,* 140(12):04014062-1-15.

Matos, J. (2003). "Roller compacted concrete and stepped spillways. From new dams to dam rehabilitation." *Proc. International Congress on Conservation and Rehabilitation of Dams: Dam Maintenance and Rehabilitation,* 553-560.

Ohtsu, I. Yasuda, Y., and Takahashi, M. (2001). "Discussion of 'onset of skimming flow on stepped spillways.'" *J. Hydraul. Eng.,* 10.1061/(ASCE)0733-9429(2001)127:6(519), 519-525.

Ohtsu, I., Yasuda, Y., and Takahashi, M. (2004). "Flow characteristics of skimming flows in stepped channels." *J. Hydraul. Eng.*, 130(9):860-869.

Pfister, M., and Chanson, H. (2012). "Discussion of 'scale effects in physical hydraulic engineering models.'" *J. of Hydraul. Res.* 50(2): 244-246.

Pfister, M., and Hager, W. H. (2011). "Self-entrainment of air on stepped spillways." *Inter. J. of Multiphase Flow,* 37(2):99-107.

Rice, C. E. and Kadavy, K. C. (1997). "Physical model study of the proposed spillway for Cedar Run Site 6 Fauquier County, Virginia." *Trans. ASAE; 13(6):723-729.*

State-of-the-Practice Review of Maintenance Closure Structures for Large Spillway Gates

<u>C.M. Johnson</u>[1], R.T. Indri[1], F.G. Snider[1], S.M. Planck[2] and K.F. De Lapp[2]

[1]Schnabel Engineering
11A Oak Branch Drive
Greensboro, NC 27407
USA
[2]HDR
2365 Iron Point Road, Suite 300
Folsom, CA 95630
USA
E-mail: cjohnson@schnabel-eng.com

ABSTRACT

Maintenance, remediation, and inspection of large spillway gates are best performed in a dry, dewatered state due to reduced overall cost, worker safety, and improved work quality. Provision for gate dewatering has become a key design consideration for new spillways. Unfortunately, many existing spillways were not originally constructed with gate dewatering capabilities. Therefore, maintenance and inspection work has often been scheduled during planned drawdowns or seasonally low reservoir levels. However, for operators of hydroelectric, flood control, water supply, and multi-purpose dams, artificial drawdowns can significantly impact operations, flood protection, downstream habitat, and revenue generation. Aging gates deteriorate and require significant maintenance, rehabilitation, and increased inspection. As dams age and gates deteriorate and require maintenance and rehabilitation, owners are increasingly seeking methods to dewater gate bays while maintaining operational pool levels using maintenance closure structures, such as bulkheads, stoplogs, cofferdams, and caissons. Designing these structures is challenging.

This paper summarizes the findings from a worldwide review of the current state-of-the-practice for various types of maintenance closure structures in use for dewatering large spillway gates. Examples are provided for each maintenance closure type identified. The information presented in this paper will be of benefit to those involved with spillways and dams, especially owners, engineers, and researchers seeking better, safer, inexpensive, and more durable maintenance closure structures that can be installed quickly.

Keywords: maintenance closure structure, hydraulic loadings, bulkhead, cofferdam, dewater, gate rehabilitation

1. INTRODUCTION

Spillway gates are critical components of dams, providing the ability to pass large discharge rates. Spillway gates require routine inspection, maintenance, and periodic remediation to ensure reliable long-term performance. These tasks are usually best performed in the dry due to reduced overall cost, enhanced safety, and improved work quality. Therefore, provision for gate dewatering has become a key design consideration for new spillways. However, many existing spillways were not originally constructed with gate dewatering capabilities. In these cases, inspection and remedial work is often scheduled during planned drawdowns or seasonally low reservoir levels. However, for operators of hydroelectric, flood control, water supply, and multi-purpose dams, artificial drawdowns can significantly impact operations, water supply, downstream habitat, and revenue generation. For large reservoirs, extended reservoir drawdowns may result in millions of dollars (U.S.) annually in lost revenue.

As dams age, gates deteriorate and require maintenance, rehabilitation, and increased inspection. This need, coupled with lost revenue during extended drawdowns, has led many owners to seek methods to dewater gate bays while maintaining operational pool levels. As a result, the industry continues to evolve in response to these needs as engineers develop better, safer, less expensive, and more durable maintenance closure structures (MCS) that can be

installed more quickly to dewater a work area upstream of gates needing attention. Designing retrofit systems can be a major challenge for dams not originally designed with a method to dewater the existing gate bays. This paper draws from worldwide experience in presenting a review of the current state-of-the-practice for various types of structures in use for dewatering large spillway gates.

A summary of an international review of MCS is presented herein, including dams with and without existing dewatering capabilities. MCS are not usually intended to be deployed in emergency situations. However, some information is included regarding which MCS are viable for emergency conditions.

The findings regarding MCS are based on inquiries to the following groups: owners of the 99 largest spillways in the world (based on a search of spillway capacities greater than 28,300m^3/s or 1,000,000cfs according to the International Commission on Large Dams [ICOLD] 2011 World Register of Dams), ICOLD national committee chairs, and major international dam agencies. This research plan met with varying degrees of success. Many organizations were very responsive and helpful, while others were unresponsive to our inquiries or unwilling to allow publishing of information, likely due to security concerns.

For each MCS type identified, key design considerations (including hydraulic loading and overtopping performance), deployment methods (including floating/water ballast bulkheads), installation times, safety considerations, relative costs, and durability concerns are identified. This information, along with recent trends and future design considerations presented in this paper, will be of benefit to those involved with spillways and dams—and, more specifically, to owners and engineers tasked with the selection of an optimal system for their specific site.

2. CURRENT PRACTICE BY SOME MAJOR ORGANIZATIONS AND REGIONS

The type of MCS in use around the world varies based on the specific characteristics of each individual site. However, our research discovered some trends attributable to certain geographical areas or organizations. Several fairly recent publications were found on this topic, including PIANC Working Group 26's Design of Movable Weirs and Storm Surge Barriers (PIANC 2006), Design of Hydraulic Gates (Erbisti 2014), and United States Army Corps of Engineers ERDC/GSL TR-10-44 (Padula 2010) and ERDC/CHL TR-12-8 (USACE 2012). These publications provide an overview of some types of systems employed, case studies, and key design aspects.

Figure 1. Stoplog Install, Itaipu Dam, Brazil/Paraguay (Itaipu Binacional)

For example,

- In Australia and Africa, many areas experience a dry season that lasts about six months. Major gate maintenance is typically scheduled during the dry seasons, in which the reservoir levels are below the bottom of the gates and no MCS is needed.
- For large dams throughout South America, steel stoplogs are very common for dewatering spillway gates and penstocks. For example, on the border of Brazil and Paraguay, upstream stoplogs are used at Itaipu Dam, the second largest hydroelectric production facility in the world. As shown in Figure 1, the stoplog sections are installed using a gantry crane traveling along the spillway crest and lowered vertically into built-in slots in the dam.
- In Russia and other parts of Eastern Europe, it is difficult to schedule major gate maintenance within the short dry season. In such cases, lowering the reservoir by 2-3m (6-9ft) is impractical as it would require operating under the base load curve at most hydropower plants for extended periods of time. Where it is either very difficult to dewater gates using an MCS or difficult to schedule activities during seasonal drawdown, less extensive work is performed underwater by divers. However, the quality and long-term performance of underwater work is often much lower than work performed in the dry. For major gate repairs, a common type of MCS in Russia is steel caissons, which are designed specific to each site. See section 3.2 for a description on steel caissons in Russia.
- In the United States, the U.S. Army Corps of Engineers utilizes a large number of stoplog systems, as well as floating bulkheads and other systems. It is in the process of replacing older, deteriorated maintenance closure systems with safer, more reliable systems. The largest bulkheads identified were approximately 35m wide by 11.6m tall (115-ft wide by 38-ft tall) at the Olmsted Project and 40.5m wide by 8.2m tall (133-ft wide by 27-ft tall) in the Nashville District. The largest bulkheads reported by the Tennessee Valley Authority are 14.6m tall by 14.6m wide by 0.76m thick (48-ft tall by 48-ft wide by 30-in thick) hinged floating bulkheads discussed in section 3.7.
- The U.S. Bureau of Reclamation (Reclamation) has several large dams in the western United States. The largest bulkhead currently in Reclamation's inventory is 16.8m by 16.8m (55-ft by 55-ft). Reclamation's largest circular bulkhead is 6.1m (20-ft) diameter (LaBoon 2014). Other larger dams owned by Reclamation constructed in the early 1900s were not equipped with MCS and have traditionally been serviced during seasonally low reservoir levels or scheduled drawdowns. However, the potential for increased revenue by maintaining high pool levels during maintenance has led to an increased desire for MCS at large dams.

3. MAINTENANCE CLOSURE STRUCTURE TYPES

MCS types found in the research are classified according to the following structure types: historical systems, steel caissons, sheetpile cofferdams, one-piece drop-in bulkheads, operational bulkheads, floating bulkheads, hinged floating bulkheads, stackable blocks, rolling bulkheads, needle and infill systems, arch systems, stoplogs, emergency bulkheads, vertical lift gate bulkheads, and inflatables.

3.1. Historical Systems

MCS designs evolved from concepts of early movable dams. The earliest movable dams were constructed to retain water at canals in China around the year 983 AD (Erbisti 2014). These movable dams consisted of tree trunks, which were raised and lowered into slots cut into opposite sides of the banks using ropes. Movable wood dams evolved into horizontal swinging gates and, later, to metal gates and needle dams (such as Poirée needle dams) around 1830. Early Poirée dams were trapezoidal-framed iron bar structures permanently mounted to the crest of a dam. The frames were raised or lowered by means of chains. Poirée dams rely on interlock with adjacent Poirée dam sections for stability (see Figure 2). Loss of one frame destabilizes all other frames. These types of systems evolved into other similar systems, such as Boulé dams, Parker gates, and bear-trap gates. Bear-trap gates consist of two flat leaves that are hinged horizontally at their lower ends. The two leaves form a chamber that can be filled with water, raising the leaves and forming an inverted v-structure. Water is subsequently drained from the chamber to lower the Bear-trap gate. These systems were well documented by Wegmann (1918). Although these types of MCS are still in use at some

dams around the world, many of them are being replaced by more substantial, durable, and reliable systems. They are not typically considered for new designs, but some of the principles are manifested in modern MCS.

Figure 2. Poirée Needle Dam, Dardanelle Lock and Dam, USA (USACE Little Rock District)

3.2. Steel Caissons

Steel caisson systems consist of steel frames with cladding and watertight chambers filled with air, which are placed against the face of a dam to allow worker access to perform work underwater. One such caisson system was used at Bhakra Dam in India in the 1980s. Two vertical steel columns were installed on the downstream channel. A fully enclosed, multi-level working platform was built to travel vertically on the steel columns to service the full height of the dam. Crews worked within the enclosure while the enclosure was submerged underwater. The face of the enclosure nearest the dam was left open to allow workers access to the face of the dam to make needed concrete repairs. The enclosed chamber required strict pressure and air quality monitoring for worker safety (McDonald 1999).

Steel caissons are commonly used in Russia to perform concrete and gate repairs on the upstream face of a dam, such as Nizhny Novgorod HPP (see Figure 3). The caisson is towed by boat in a horizontal position, using floats for buoyancy, and ballasted to an upright position against the face of the dam. Water is pumped out of the caisson, sealing the caisson against the concrete using hydrostatic pressure and creating an underwater enclosure to make concrete repairs in the dry. A steel caisson, approximately 6m (19.7 ft) tall, was used at the Saratov HPP in Russia. It was towed into place and anchored by divers (see Figure 4). Although other caisson systems have been used against more complex sealing surfaces (e.g., repairing sheetpile with the Acotec DZI Limpet Cofferdam [Acotec 2015]), use of caissons to seal directly against portions of large, irregular-shaped spillway gates presents design and worker safety challenges.

Figure 3. Nizhny Novgorod HPP Caisson, Russia (Hydroproject Institute)
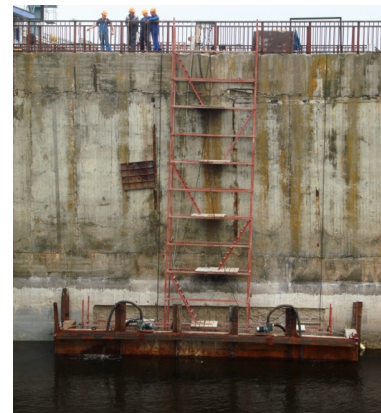
Figure 4. Saratov HPP Caisson, Russia (Hydroproject Institute)

3.3. Sheetpile Cofferdams

Interlocking steel sheetpile has been used for dewatering upstream of spillway gates. Sheetpile works well for low-head facilities where sheetpile can be driven into a soil foundation to form a temporary wall. Other modular or repeating systems consist of built-up sections of vertical tubes and plates that seal together. The sheetpile is driven into the soil so that it acts as a vertically cantilevered system. The material cost for sheetpile systems is relatively low, and its use is fairly common for a wide range of applications. For installations at taller dams, where driving into the upstream channel is impractical, sheetpile may be used on the walls of other structures offering a top support, such as a vertical needle system as described in section 3.10.

3.4. One-Piece Drop-In Bulkheads

One-piece drop-in bulkheads are fabricated and deployed as a single, full-size structure. No field assembly is required. One-piece bulkheads typically consist of one large steel space frame truss, which is lifted by a large crane (or two), with the crane(s) often mounted on a barge. Bulkhead load bearing, similar to a stoplog system, usually transfers hydrostatic load to the piers. The steel framework consists of interconnected horizontal spanning trusses with a steel skin plate on either the upstream or downstream face. Bulkheads tend to be more robust towards the middle (horizontally) to resist maximum bending moments and less so at the supports where moments are small. Bulkheads often bear in slots in the concrete piers. The primary advantage of this type of structure is that it may be installed within a few hours because it is a single unit. However, it may require large cranes for installation. The largest one-piece drop-in bulkhead discovered in our research was at Olmsted Locks and Dam Project in the USACE Louisville District, which is 35.1m long by 11.6m tall (115-feet long by 38-feet tall) and is shown in Figure 5.

Figure 5. Bulkhead Installation at Olmsted Locks and Dam Project, USA (USACE Louisville District)

3.5. Operational Bulkheads

Operational bulkheads are similar to overhead garage doors and are stored in the horizontal position above the bulkheads slots when not in use. The bulkheads can be lowered into slots. For example, the Olmsted Locks and Dam Project in the USACE Louisville District has an operational bulkhead at each of its two lock chambers. The bulkheads allow each lock to go back and forth relatively quickly between "open river" conditions and normal locking conditions. In open river condition, the miter gates are pinned back to the lock walls, and the river flows unimpeded through the locks. The operational bulkheads can be lowered into flowing water typical of open river conditions. Once these bulkheads are set, they can be raised during differential head conditions. Each structure is a massive bulkhead consisting of nine horizontal trusses and an upstream skin plate. Figure 6 (photo courtesy USACE) shows both bulkheads; the bulkhead at the right is in the lowered vertical position and the bulkhead on the left is in the horizontal

open position. Each bulkhead is 34.7m long by 15.2m tall (114-feet long by 50-feet tall). The hoisting equipment is located in machine houses cantilevered out over the lock chambers approximately 27.4m (90 feet) below.

Figure 6. Operational Bulkheads at Olmsted Locks and Dam Project, USA (USACE Louisville District)

3.6. Floating Bulkheads

Floating bulkheads are somewhat similar to docking a ship against the upstream face of the dam. The large steel structures contain internal ballast chambers, which are filled with water to adjust buoyancy. The bulkheads are ballasted to remain partially exposed above the maximum design water level. These structures typically consist of an internal steel framework clad with steel skin plates on all sides. The geometry of the bulkhead is designed to mate with the spillway structure and, typically, seals against the sides and bottom edge of the gate bay. The hydrostatic load is transferred to the skin plates, to the internal steel framing, and then to the concrete piers. Bulkheads are typically towed in a horizontal position using one or two small boats. When the bulkhead arrives near the point of installation, it is partially filled with water to rotate it into a vertical position. Rotation of the bulkhead to vertical typically requires a water depth of at least half the height of the floating bulkhead, which is not possible at many locks. It is then slowly maneuvered into contact with the upstream face of the dam and often tied off to the dam with chains to minimize small movements of the bulkhead. Next, the water downstream of the bulkhead is drained out. As the water drains, the net unbalanced hydrostatic pressure on the bulkheads presses the bulkhead against the dam and provides a seal. The frictional forces on the seals, along with the chains, are usually sufficient to limit movement of the bulkheads to less than one inch under most reservoir conditions. Many of the floating bulkheads discovered in our research were designed for pool fluctuations during installation of less than 1.5m (5 feet). Slightly larger pool fluctuations may be accommodated by operating valves to adjust the amount of internal ballast to keep the bulkhead at a constant elevation. Floating bulkheads are not usually capable of remaining stable in a fully drained condition.

In cases where large pool variations exceed the tolerances of the internal ballast chambers, bulkheads may require provisions for repositioning or mechanical support. Bulkheads are removed by reversing the installation process. Some bulkheads are moved laterally from bay to bay using a truck on the abutments rather than redeploying boats. When the bulkheads are ready to be placed in dry storage, they are usually towed near shore and rolled out of the reservoir. Rollers allow for movement of the massive structures without the need for large cranes (Steve Sembritzky, personal communication, December 31, 2014). Due to the extreme hydrostatic forces and friction caused by small reservoir fluctuations, the seals on these bulkheads wear and may need to be replaced after a few years. Floating bulkheads are typically installed within a few hours and require relatively small boats or crews. Some of the largest floating bulkheads found were the USACE Nashville District's floating bulkhead (or caisson), which is 34.5m-wide by 8.8m-tall (113ft-wide by 29ft-tall) and is shown in Figure 7; at Rocky Reach Dam in Chelan County, WA, USA, which is 18.3m-wide by 21.3m-tall (60 ft-wide by 70ft-tall); and at USACE Portland District's John Day Navigation Lock in Sherman County, OR, USA, which is 30.5m-wide by 9.1m-tall (100ft-wide by 30ft-tall).

Figure 7. Floating Caisson Being Ballasted, USA (USACE Nashville District, ERDC/GSL TR-10-44)

3.7. Hinged Floating Bulkheads

Hinged floating bulkheads operate like an overhead garage door. They consist of parallel steel tubes or built-up sections that have internal ballast chambers and are hinged together between each segment. Bulkheads are foated to the gates from upstream while in the horizontal position. Ballast chambers are filled with water one by one, sinking the individual segments into place against the upstream face of the structure (Lux 1995). Installation of these bulkheads usually requires towing by a small boat (or two). Reservoir levels must be high enough to allow proper placement of the bulkhead after ballasting to the upright position. Expected range of reservoir levels should be accounted for in design of the ballast to ensure placement. Bulkheads are often anchored only at the two top corners with hanger brackets mounted to the face of the spillway to secure the bulkhead in the event the pool is lowered. One advantage of a hinged floating bulkhead over a rigid floating bulkhead is that the individual sections can be designed to be detachable. This allows the number of sections to be tailored to each dam. Also, the small sections are more easily lifted and handled with the use of smaller equipment. The Tennessee Valley Authority in the United States has hinged floating bulkheads for use at twelve of its sites. The floating bulkheads consist of caissons with ballast chambers that may be combined as needed for use at different sites with various gate sizes as shown in Figure 8.

Figure 8. Hinged Floating Bulkhead, USA (Tennessee Valley Authority)

3.8. Stackable Blocks

Stackable concrete blocks have been used to dewater Locks and Dam No. 52 by the U.S. Army Corps of Engineers Louisville District as shown in Figure 9. The blocks are stabilized against overturning by self-weight and against sliding by the horizontal interface friction between blocks. If the weight of the blocks is insufficient for stability, the blocks can be strapped down using vertical pre-stressing straps threaded through the blocks and attached to the top of the dam. All loads are transferred vertically, so the gate width is not a limiting factor on the structural design of the blocks. The blocks are often precast, which allows a high level of construction precision. Uplift pressures on the bottom of the blocks can be reduced by providing open slots in the bottom of each block, effectively eliminating the uplift pressures downstream of the notch. Anchor plates and lifting rods are embedded into the bottom of the base blocks. The blocks are installed with gaps of approximately 51mm (2 inches) between stacks. The gaps are then sealed by using T-shaped vertical seals inserted on the upstream face. The number of required blocks varies based on the height and width of the opening. The downside of dealing with heavy concrete blocks is handling due to their immense weight. For example, one normal-weight concrete cube measuring 2.4m (8-feet) per side weighs nearly 356kN (40 tons). If weight is a design limitation, other materials, such as lightweight concrete, steel boxes with ballast chambers, and fiber reinforced polymer (FRP) composites may be considered. Lighter-weight modular systems, such as Super Sacks® and BoxBarrier® (50 cm height), are options for very low head barriers, but similar technology could be scaled up for taller applications.

Figure 9. Stackable Precast Concrete Blocks, Locks and Dam No. 52, USA
(USACE Louisville District)

3.9. Rolling Bulkheads

Rolling bulkheads are similar to sliding barn doors. They consist of a steel bulkhead mounted to permanent horizontal rails on the upstream face of the spillway. At the push of a button, the bulkheads are rolled along the horizontal rails to any position along the length of the rails. Wheels at the top and bottom of the bulkhead allow the large door to roll horizontally along the length of the rail. When the bulkhead is in place, the wheels retract and the rubber seals placed along the perimeter of the bulkhead seal against the concrete. The bulkhead transfers hydrostatic load horizontally to the piers, minimizing the load requirements on the monorail. The monorail supports the weight of the bulkhead. When the bulkhead is not used, it is rolled and stored past the end gate bay. The concept of rolling systems has been utilized at several lock gates but has been applied recently on a larger scale at the Panama Canal expansion project, which features gates that can be retracted into slots in the lock walls for maintenance. There are a total of 16 steel gates, which were fabricated in Italy, transported to Panama by ship, and offloaded into recesses constructed in the lock walls. The tallest of the gates is 33.04m-high by 57.6m-wide by 10m-deep (108.4ft-high by 189ft-wide by 32.8ft-deep) and weighs 4,234 tons (Panama Canal Authority 2015).

Figure 10. Norfork Dam Rolling Bulkhead, USA (USACE Little Rock District)

Norfork Dam in Arkansas, USA, an example of a rolling bulkhead, is shown in Figure 10. The 578kN (65 ton) maintenance bulkhead runs along a 203.3m (667-foot) long steel monorail beam attached to the dam. The bulkhead was shipped to the site in two halves, which were assembled on site, transported along the length of the dam in the upright position using two trucks travelling parallel (one to each side of a median), and lifted onto the monorail using two cranes placed on top of the dam. Motorized trolleys slide the 7.3m-high by 14.6m-wide (24-foot high by 48-foot wide) bulkhead in front of individual gate bays. As the bay is dewatered, unbalanced pressure pushes the bulkhead against the structure and holds it in place. Bolted connection brackets were fastened to the existing dam pier caps using high-capacity, deep-embedment post-installed concrete anchors (Garver 2012). Within approximately 5 minutes, the bulkhead can be moved from one gate bay to the next.

3.10. Needle and Infill Systems

Needle and infill systems consist of vertical "needle" beams that are supported at the bottom sill by the spillway structure and at the top by a horizontal spanning girder or truss. The needles may be floated in from the upstream in a horizontal position, fastened to the top horizontal beam, and sunk into vertical position or lifted using a crane. Depending on the space available for the working platform between the gates and the needles, the needles may be installed either bearing against the upstream face of the horizontal beam in a seated condition or anchored to the downstream face in an unseated condition (also called a "reverse" needle system). Floating needles may consist of parallel steel tubes or built-up sections that have internal ballast chambers and are hinged together between segments. Other systems use H-shaped steel needles with horizontal wood infill beams placed within the flanges. These systems are common in France and well-suited for low-head, wide-open channels because load is distributed to the structure through each individual needle. These systems consist of many relatively small pieces (except the top horizontal beam), thus requiring minimal equipment. Infill systems are sometimes carried and installed by hand and consist of wood or steel. Other material that may be considered is fiber reinforced polymer composites, which have been commercialized in other applications, such as bridge decks, due to their high strength-to-weight ratios and enhanced corrosion resistance. Needle and infill systems consist of many small pieces and are appealing for lightweight installations where pieces may be installed in a matter of days or weeks.

Figure 11. Needle and Infill Cofferdam, Myllykoski Hydropower Plant, Finland
(Pato Osakeyhtiö)

Myllykoski Hydropower Plant in Finland utilized wide flange steel needles and stacked infill beams (webs horizontal in "H"-orientation). Vertical needles were installed from a small mobile crane 445kN (50-ton) from atop the original bridge completed in 1929. Needles were braced at the top by the bridge. Stacked infill beams were placed within the webs of the needle beams as shown in Figure 11. The system closed a gate bay approximately 5.4m-high by 18m-wide (18ft-high by 59ft-wide). Nearly all material was taken from the owner's storage materials, and the layout of the needles was such that the infill beams did not require cutting. Rubber ribbons were used as seals between the stacked beams at the vertical needles and at the contact with the concrete at the base, resulting in almost no leakage. Despite stringent Finnish safety laws requiring a minimum of three divers working simultaneously, a two-week erection process limited the owner's construction cost to roughly 25,000 to 30,000€.

3.11.   Stoplogs or Stacked Horizontal Trusses

Stoplogs are logs, planks, cut timbers, steel, or concrete beams stacked on top of each other with their ends secured in guides between walls or piers. The logs are usually installed one at a time using a crane with a lifting truss under balanced hydrostatic pressures. Stoplog systems can typically be placed in non-flowing water as they typically have no roller wheels at their ends. The benefits of using this system rather than a large single-piece bulkhead include: increased economic benefit from handling smaller pieces, reduced cranes lifting capacity requirements, increased storage flexibility, and improved transport efficiency. Steel stoplogs utilize a steel skin plate on either the downstream or upstream face to seal water. Rubber seals are placed between each stoplog and at the guide supports. Stoplogs are common at large spillway gates and locks. There are some cases in which stoplogs have been retrofitted to a site and in which slots are cut into the piers. However, new slots require structural analysis of the reduced pier sections, adequate space upstream of the gates for the slots, and sufficient clearance from any overhead bridges. Such modifications are costly. Temporary center posts have been installed at shallow upstream channels to reduce the span and size of the stoplogs, although a more complicated center post installation is required. The largest stoplog project (by orifice size) found was 44.34m-high by 12m-wide (145ft-high by 39ft-wide) for the Runilamu Killam Hydropower Station in Pakistan. It is currently being manufactured by Sinohydro Jiajiang Hydraulic Machinery Company Ltd. in China (JHMW 2015).

The set of six stoplogs at Flix Dam are one of the earliest installations of metal stoplogs found in our research and are still in use today. The stoplogs were fabricated between 1943 and 1948, constructed of iron and rivet materials, and stored in sections above each gate when not in use (ssee Figure 12). The full set of stoplogs measures 12.5m-high by 25.9m-wide (41ft-high by 85-ft wide) and weighs 448kN (100.8 kips). Stoplog systems are used at virtually every inland navigation District of the USACE. For example, Winfield Locks and Dam in the U.S. Army Corps of Engineers Huntington District has a stoplog system on the Kanawha River in Eleanor, West Virginia, USA. The set of six steel trusses was fabricated in Oregon, shipped cross country by train, and offloaded by crane directly from the train to a storage barge on the Kanawha River. The trusses were fabricated from plate sections, which allowed for cutouts for

web openings to be reused as gusset plates. After installation, there was some leakage at the seals (see Figure 13), presumably due to storage directly on their seals, causing permanent compression. In some cases, leaks may be reduced using straw, horse manure, oakum, granite dust, sawdust mixed with oil, or blast furnace slag (Softley 2008). In other cases, repairs or new seals are needed. Leakage at seals should be expected, and tolerable limits should be established depending on the type of work. Environmental regulations should be considered when selecting a method for sealing leaks.

Figure 12. Flix Dam Stoplogs, Spain (Endesa)

Figure 13. Stoplogs at Winfield Locks and Dam, USA (USACE Huntington District)

3.12.   Emergency Bulkheads

Emergency bulkheads have a top and bottom truss, a pair of rollers on each end, and a skin plate (typically on the upstream side). These systems are similar to stoplog systems, but unlike most stoplog systems, emergency bulkheads are designed to be placed in flowing water. In addition, these bulkheads are also used for maintenance activities.

Emergency bulkheads are commonly used by the U.S. Army Corps of Engineers at almost every high lift navigation dam on the Ohio River at tainter gate bays. Each dam typically has four or so (the number varies), and they are typically stored on the tops of the tainter gate piers. Figure 14 (photo courtesy USACE) shows an emergency bulkhead at Cannelton Locks and Dam on the Ohio River, on the border between Indiana and Kentucky. A traveling crane picks each individual bulkhead section up and lowers it into place in the upstream bulkhead slots, one at a time. The lifting beam and hoist cables are visible at the top of the figure on top of the stacked, lowered bulkhead sections. One of the tainter gates, painted white, is shown at the bottom of the figure.

Figure 14. Emergency Bulkhead at Cannelton Locks and Dam, USA (USACE Louisville District)

3.13. Vertical Lift Gate Bulkheads

These bulkheads are often stored in vertical slots in the spillway located upstream of the spillway gates and lowered into place to isolate the spillway gates when needed. In some cases, the bulkhead is a spare gate identical to the permanently installed spillway gates. In other cases, a separate bulkhead is installed upstream of each spillway gate so that each gate may be isolated individually. In cases where the bulkhead is not permanently installed in slots upstream of each gate, the bulkhead is transported using a movable crane that travels along the top of the spillway capable of transporting the bulkhead between bays and lowering it into the vertical slots. These bulkheads are usually part of the original design and construction of the spillway. The bulkheads have a large initial cost and are difficult to retrofit, but they are easily deployed, reliable, and capable of being deployed in emergency situations. Vertical lift gate bulkheads are being used at many new, large spillways, including Folsom Dam Auxiliary Spillway project in California, USA (see Figure 15).

Figure 15. Folsom Spillway Bulkhead, USA (U.S. Bureau of Reclamation/USACE
[Frank 2015])

3.14. Arch Systems

Arch systems are commonly used for the closure of locks. Miter gates are fabricated as two separate doors mounted to the lock sidewalls with hinges on the vertical faces. The gates swing open in the middle like saloon doors. The steel doors are often fabricated with diagonal steel cross-bracing that helps keep the gates from in-plane racking due to self-weight. The vertical edge of the gates is mitered along the vertical face at the middle of the channel. The mitered edge forms a large contact surface that remains in compression due to unbalanced hydrostatic pressure when the downstream is dewatered. This surface seals under hydrostatic pressure without having to swing a full 90 degrees such that the gates are never coplanar. This configuration allows for arching action with a hinge between the two gates, reducing the bending moment in each gate compared to a simple span structure across the entire bay. The hydrostatic pressure is transferred to the gate through bending and in-plane axial force to the hinges and into the concrete sidewalls or piers. This type of system is best suited for bays with a flat upstream channel bottom in order to provide a suitable seal because the sealing plane is V-shaped and not a single plane. USACE proposed a hybrid stoplog and miter gate MCS, which consists of stacked horizontal arches, utilizing the cost savings afforded by arching action while allowing the MCS to be installed in smaller stackable sections. Flow-through baffles would be used to facilitate installation in moving water and would be closed off after the arches are installed (Padula 2010).

3.15. Inflatables

Inflatable rubber fabric dams consist of rubberized fabrics, often with steel reinforcement, inflated with water and/or air to create a cylindrical dam. The dams are anchored to the bottom of the channel and deflated during normal service. The potential advantages of this type of dam are the low material costs and the suitability to very wide channels. The cylindrical nature of these systems makes use impractical for tall channels or channels with very limited space upstream of the gates because the drape of the fabric may encroach on the working area. The drape can be reduced by using an intermediate bracing system, such as steel beams, trusses, or tension cables to essentially reduce the span of the fabric. Puncture resistance of inflatable systems may be enhanced by using steel plates, such as with the Obermeyer gate systems, or by combining multiple layers of fabric to provide an optimal balance of water tightness, strength, ductility, durability, and puncture resistance. Other fabric systems, such as Portadam™ systems, consist of a rubber fabric membrane that conforms to irregular shapes but requires closely-spaced steel backup supports and are limited to hydrostatic heads of approximately 3m (10 feet) (Portadam 2015). Invention of inflatable dams is credited to Prof. Mesnager in France in 1955. In recent years, this technology has been advanced in Japan, the Netherlands, and the United States (Erbisti 2014) and is primarily used for flood control applications.

The Balgstuw bij Ramspol in the Netherlands is, in many ways, a modernized version of a bear-trap gate and resembles a large inner tube of a bicycle tire. A flat membrane dam is inflated with air and water to create a half-round dam (see Figure 16). Obermeyer inflatable dams in the United States may contain multiple air bladders with programmable controllers to facilitate precise flow control, which can be varied along the length.
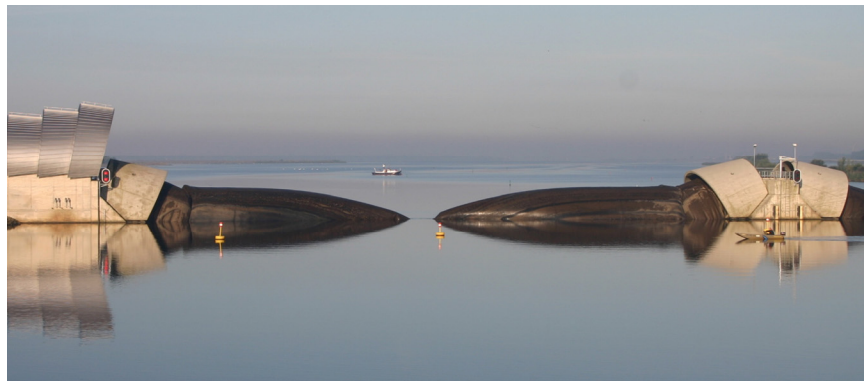
Figure 16. Balgstuw bij Ramspol Inflatable Dam, Netherlands
(BAM Infraconsult BV)

The largest Obermeyer gate installation found was 8m (26.2-feet) high by 60m (197-feet) wide at the Nanming River in Guiyang, China (Figure 17). Current Obermeyer gate production is suited for heights up to 10m (32.8-ft). Taller gates are technically feasible but with increased cost (Robert Eckman, personal communication, January 11, 2016). To date, no installations of inflatables for the sole purpose of dewatering another gate were found. However, inflatable systems are more cost competitive on a per square meter basis with other MCS types if maintenance can be limited to low flow seasons such that the required MCS height is much less than the spillway gate.

Figure 17. Nanming River Obermeyer Gate, China (Obermeyer Hydro)

4. RECENT TRENDS

Maintenance has become part of the design criteria of new dams and a growing concern for existing aging gates. Many relatively new large dams, such as Folsom spillway in the United States and Three Gorges Dam in China, utilize taller and narrower high-head gates such as radial gates and vertical lift gates in lieu of shorter, wider gates such as drum gates and roller gates, which were popular for large dams in the early 1900s. New spillways are constructed with vertical slots within the dam so that a bulkhead or emergency gate may be lowered upstream of each individual gate. However, for existing dams, retrofitting such slots is rarely practical. For dams without heavy installation equipment but with fairly stable water levels, float-in systems are often used.

In addition to scheduled maintenance, there is an increasing desire to develop MCS deployable in emergency situations and in a wider range of environmental conditions, including variable pool levels.

The Design-Build process has been used for many maintenance closure structure projects. This project delivery method is a collaborative process in which the engineer and contractor work together throughout the design and construction process, allowing a shortened overall project schedule and striving to reduce risk and overall project costs to the owner. This method has become more widely accepted by various public and private entities worldwide and is expected to become more prevalent for MCS projects.

5. CONCLUSIONS

A wide variety of maintenance closure structures have been utilized around the world to facilitate maintenance, remediation, and inspection of large spillway gates. Provision for dewatering of gate bays has become a key design consideration for new spillways and an ongoing challenge as existing spillways age and deteriorate. While some MCS types are clearly better suited to a particular site than others, selection of an optimal system requires careful consideration of a variety of factors, such as safety, installation time, durability, and capital and operations costs. The selection process should include close collaboration between owners, engineers, and contractors. The majority of MCS found in our research were traditional steel, concrete, and wood systems; however, technological advancement of other materials, such as fabrics, plastics, and programmable controls offer potential improvements. These technologies may provide such benefits as enhanced corrosion resistance, easier handling, and reduced operator error.

6. ACKNOWLEDGMENTS

7. REFERENCES

Acotec. (2015). "Standard Cofferdams". < http://www.acotec.be/SolutionDetail.aspx?id=01815996-1f2f-4987-988c-993cc8a2da35> (Dec. 12, 2015).

BAM Infraconsult BV. (2015). "Storm Surge Barrier Ramspol, The Netherlands". <http://www.boxbarrier.com/about-us/innovative-projects/item35> (Nov. 28, 2015).

Erbisti, P.C.F. (2014). Design of Hydraulic Gates, CRC Press/Balkema, EH Leiden, The Netherlands.

Frank, S. (2015). "Final Folsom Spillway Gates Installed." <http://www.spk.usace.army.mil/Media/Images.aspx?igphoto=2001005696> (December 12, 2015).

Garver USA. (2012). "Rolling Bulkhead." *Infrastructure Quarterly, Volume 4 Issue 3*, <https://garverusa.com/iq/201243/63/rolling-bulkhead/> (Nov. 28, 2015).

International Commission on Large Dams. (2011). "World Register of Dams". Paris, France.

LaBoon, J.H. (2014). "Appurtenant Structures for Dams (Spillways and Outlet Works". *U.S. Department of the Interior, Bureau of Reclamation Design Standards No. 14, Chapter 3*. Denver, CO.

Lux, F. et al. (1995). "Closure Methods for Large Intakes". *Proceedings of the International Conference on Hydropower, ASCE*. San Francisco, CA.

McDonald, J.E. and Curtis, N.F. (1999). "Repair and Rehabilitation of Dams: Case Studies". *U.S. Army Corps of Engineers Technical Report REMR-CS-63*. Washington, D.C.

Padula, J.A., Abraham, D.D., and Haskins, K.L. (2010). "Emergency Gap Closures". *U.S. Army Corps of Engineers ERDC/GSL TR-10-44*. Washington, D.C.

Panama Canal Authority. (2015). "Steel Giants." <http://micanaldepanama.com/expansion/documents/infographics/#prettyPhoto/0/> (Dec. 12, 2015).

PIANC. (2006). "Design of Movable Weirs and Storm Surge Barriers". *Report of Working Group 26 of the Inland Navigation Commission.* Brussels, Belgium.

Portadam. (2015). "Portadam™ Cofferdam Brochure." <http://www.portadam.com/resources/brochurenew/> (Dec. 12, 2015).

Sinohydro Jiajiang Hydraulic Machinery Company Limited. (2015). "Metal Structure Products" <http://www.jhmw.com/en/Article_Class.asp?ClassID=841&ArticleID=28179> (Dec. 30, 2015).

Softley, P. (2008). "Solution for Sealing Stoplogs." < http://www.hydroworld.com/articles/hr/print/volume-27/issue-6/departments/solution-for-sealing-stoplogs.html> (Dec. 12, 2015).

U.S. Army Corps of Engineers. (2012). "Emergency Closure of Uncontrolled Flow at Locks and Dams". *ERDC/CHL TR-12-8*. Washington, D.C.

U.S. Army Corps of Engineers. (2011). "Pike Island Locks & Dam, Ohio River, 2010 – Dewater Main 110' x 1200' River Lock Chamber." <http://operations.usace.army.mil/nav/11febimts/Szemanski-PI10PresentationSml.pdf> (Nov. 28, 2015).

Wegmann, E. (1918). Design and Construction of Dams, Including Masonry, Earth, Rock-Fill, Timber and Steel Structures, Also the Principal Types of Movable Dams, John Wiley & Sons, New York.

Evaluation of Flexible Barrier and Sabo Sam to Control Effects of Debris Flow in Santo Domingo Ravine

J.W. Cabrera Cabrera[1], and L.F. Castillo Navarro[1]
[1]Facultad de Ingeniería Civil
Universidad Nacional de Ingeniería
Lima, Lima25
PERU
E-mail: juancabrera@uni.edu.pe

ABSTRACT

The coast of Peru is characterized by the presence of ephemeral creeks, which drain water only during the wet season. The extremely dry soil and pebbles combined with precipitation produces debris flows in a seasonal geodynamic. This is the case of Santo Domingo ravine, which is located at eastern Lima and drains its water to Rimac River. In this article, the vulnerability of villages near to Santo Domingo ravine by debris flow and use of flexible barrier and sabo dams are analyzed. In the first stage, the liquid hydrograph of a 100 year return period was built, and a solid hydrograph, a relationship between volume concentration and time, was essayed. Then, both the liquid and the solid hydrograph are calibrated in a debris flow numerical model, and the vulnerability map is built. Finally, this model is coupled to the Rimac River to analyze the possible damming effect. Calibration of a numerical model was done in base to previous estimated volumes by the Japanese International Cooperation Agency (JICA). These first results permitted the definition of high-vulnerability zones, which will be a reference to evaluate efficiency of control measures. In a second stage, mitigation effects of flexible barriers application is simulated in base to Debris Flow Barrier from Geobrugg®. Also, the application of sabo dams was evaluated to by using "Kanako" debris flow simulator from Laboratory of Erosion Control, Division of Forest Science, Graduate School of Agriculture, Kyoto University, & SABO Technical Center. Results permit researchers to evaluate efficiency and select the most economical option.

Keywords: *Debris flow, flexible barriers, floods, sabo dam, vulnerability.*

1.   INTRODUCTION

Chosica is located on the floodplain of the Rimac River, around 850 m.a.s.l. in the Western Chain of the Central Peruvian Andes and surrounded by ephemeral creeks at the both sides. These creeks have normal geodynamic activity that includes debris flow occurrence during wet seasons. One of these ravines is Santo Domingo, which causes damage to population around its stream every year. City Hall tried to reduce their effects by building retaining walls around houses and "sabo" dams along the stream, but these were not a solution because they were undersized. It should be added that the main channel has been reduced to build houses, and it has been deviated in some sections; these changes increase velocity of debris and mudflow and erosion and sedimentation along the channel.

This situation suggests the necessity of research on centennial event magnitude and affected areas to organize a mitigation plan that could prevent future disasters; also, it is necessary to evaluate other alternatives that could be more efficient.

2. STUDY ZONE

2.1. Location

Santo Domingo ravine is located in Lurigancho district, Lima, at coordinates 76°22'35 " - 76°24'07" W and 11° 46'38" - 11°50'20" S. This watershed is part of the Hydrographic Basin of the Pacific and joins the river Rimac at the left bank. It has an extension of 4 Km^2 with a length of main channel of 3.85 Km, approximately. Altitudes vary between 850 m and 1750 m and have an average gradient of 23%.

The watershed consists of three well defined areas: a reception area formed by the slopes that are over 1300 m, this area serves as a funnel, which captures summer rains; a transit area between 1300 m and 950 m; and finally a material deposition area, known as "alluvial fan", which is fully developed.

2.2. Geodynamic

The high watershed contain material presented in the bed gravel-sandy material with a low proportion of silt, which is loose. The slopes of both banks are composed of proluvial material from previous flows discoursed through the gorge; the materials of these ancient deposits have a silty clay matrix with gravel, blocks, and boulders ranging from 0.5 to 2 m in diameter.

In the middle part of the basin, both sides are affected by rill erosion that will undermine and cause landslides on top of the terraces. There lateral erosion undercuts at the base of slopes which causes destabilization. At the low watershed, a narrowing of the channel that is caused by the accumulation of blocks and proluvial material forming small cones is observed; proluvial material has about 5 m of power above the rocky outcrop; it appears the slopes are almost vertical.

Granulometry studies show that the material is low plasticity to non-plastic arenas, ranging from SC (loamy sand) to SM (silty sand) in the scheme of Unified Soil Classification System (USCS). Characteristics of this material make it suitable for the occurrence of possible mud flows against rain from moderate to high intensity.

3. STUDY METHOD

3.1. Data

For this analysis, topography data was based on National Maps from Instituto Geográfico Nacional (IGN) and ASTER information: main channel slope was estimated at 0.23, concentration time at 19.6 min, and lag time at 11.8 min. These values suggest it is almost impossible to organize an early warning system. Figure 1 shows the location of Santo Domingo ravine respective to the Chosica and Rimac Rivers. Simulations will show the affected area of the city.

JICA(1988) realized a vulnerability assessment in Rimac River basin and proposed an equation to estimate probable sediment deposit:

$$V = 14800.1, 2.F.A \tag{1}$$

where F is coefficient of land cover (dimensionless) and A is the sub basin area (in Km^2). To Santo Domingo ravine, F=0.6, which correspond to less 60% of vegetation on sub basin area; their area is 4 Km^2 approximately. The volume estimated with JICA equation is 42624 m^3 and represents the volume of sediment that could fall.

To estimate peak discharge, SCS storm method was used. To estimate infiltration volume, analysis from CESEL (2004) was considered. According to them, Rimac basin headwater shows characteristic like hydrologic soil type "B" and values between 79 to 83 could be assigned like curve number. For this research, 82 was assigned.

To estimate maximum precipitation, data from Santa Eulalia gage station was used. Table 1 summarizes the precipitation analysis to return periods of 20, 50 and 100 years.

Table1. Maximum precipitation (mm)

Gage station	P_{20}	P_{50}	P_{100}
Santa Eulalia	29.40	34.00	38.30

With these values, the peak discharge to return period Tr=100 years was estimated in 9.4m^3/s, and the hydrograph was built. This hydrograph was used to build the solid hydrograph, which represents sediment volume concentration (C_v) at time. In general, a solid hydrograph should maintain the liquid hydrograph shape with the peak volume concentration located a few minutes before the peak of the liquid hydrograph.

For a debris flow event, the range of volume concentration was estimated between 0.22 and 0.45: starting at 0.22, increasing until 0.45, and decreasing again until 0.22. This hydrograph should be calibrated during simulation (values of volume concentration should be modified until one gets approximately estimated volumes by JICA (1988)). The calibrated solid hydrograph is shown in Figure 2.

Figure 1. Santo Domingo ravine. Left, delimited catchment. Right, debris on right side.

3.2.   Hyperconcentrated Flow Model

In normal conditions, rivers and stream flows contain sediments, but these don't affect the properties and behavior of water. However, if the sediment volume is high, water changes its characteristics and behavior like a new fluid. These kinds of flows are called hyperconcentrated flows (Julien, 1991). According to Julien (1991), hyperconcentrated flows could be classified in three categories: floods, mudflows, and debris flows.

Floods are formed by sands and volume concentration of sediments C_v<40%. Mud flows are formed by silts and clays and volume of sediment in the range of 45%<C_v<55%. Finally, debris flow represents a more complex fluid, with pebbles, woods, and with a wide range of diameters. Characteristics of events in Santo Domingo ravine define debris flows.

Debris flow modeling will be performed with the FLO2D software. This model requires topography data, the liquid-solid hydrograph, sediment properties, and rheological parameters. In hyperconcentrated flows, the Bingham plastic model has been widely used with high performance (O'Brien and Julien, 1988). According to these authors, it's generally accepted that viscosity and yield stress are related with volume concentration (C_v) by equations (2) and (3)

$$\eta = 0.0360 e^{22.1 C_v} \tag{2}$$

$$\tau_y = 0.181 e^{25.7 C_v} \tag{3}$$

where η is mixture viscosity (in poises) and τ_y is the yield stress (in dyna/cm^2). This volume concentration varies with discharge during a debris flow, and it should be input as a solid hydrograph (see Figure 2). According to O'Brien and Julien (1988), solid hydrograph peak before the liquid hydrograph peak. Specific gravity was assumed to be 2.65, in accordance with with JICA (1988) and CESEL (2004).
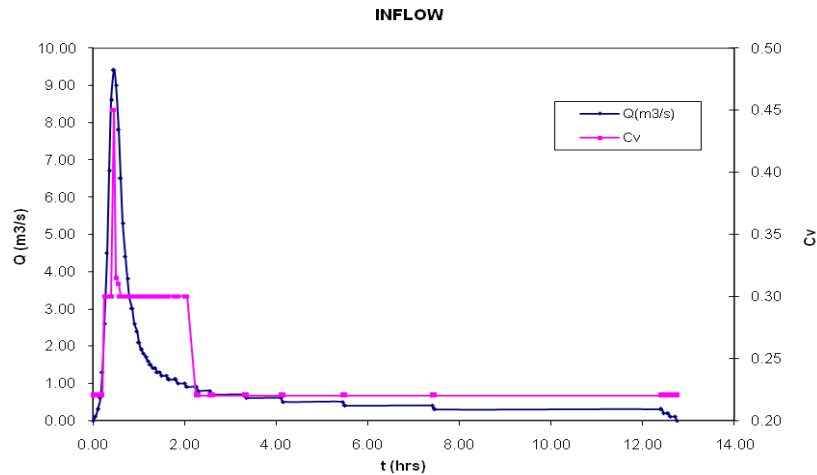
Figure 2. Solid and liquid hydrograph to be input to FLO2D software.

3.3. Hazard Maps

Hazard maps for debris flow events were developed by Garcia et al. (2003) and based in PREVENE (2001). This methodology establishes three hazard levels in similar a way to Swiss and Austrian standards to flood hazard maps (Fiebiger, 1997). More recently, INDECI (2011) have resumed all the related experience and assumed a similar methodology in Peru.

According this frame, Flood hazard risk is a function of both flood intensity and probability. Flood intensity is a function of both flow depth and velocity, as described in Table 2. Maximum depth represents a static analysis and the product of h-v represents a dynamic analysis.

Table 2. Definition of mud or debris flow intensity

Flood Intensity	Maximum depth h (m)		Product of maximum depth h times maximum velocity v (m^2/s)

High	h > 1 m	OR	v.h > 1m^2/s
Medium	h < 1 m	AND	v.h < 1m^2/s
Low	Undefined		Undefined

Flood probability is inversely related to flood magnitude and could be estimated like the inverse of return period. Categories of hazard risk are summarized in Figure 3. Each category is represented by a color to facilitate comprehension of non-technical authorities; each color is related with effects on buildings and structures. Table 3 shows the meaning of every color.

Table 3. Hazard risk levels according to PREVENE(2001).

Hazard Level	Map color	Legend
High	**Red**	People are in danger both inside and outside of structures. Buildings are in danger of being destroyed.
Medium	**Orange**	People are in danger outside of structures. Buildings may suffer damage or possible destruction depending on construction materials.
Low	**Yellow**	Danger to people is low. Buildings may suffer limited damage, but flooding or sedimentation may affect structures.

Hazard maps were built by using the Mapper tool of FLO2D software.
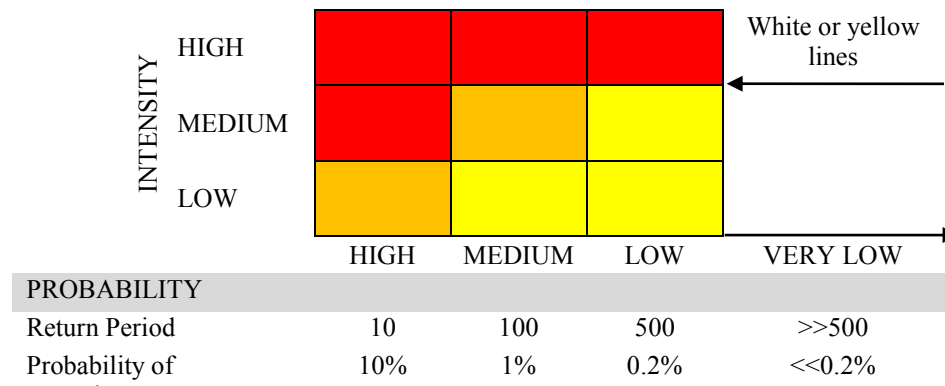
Figure 3. Discrete hazard levels according to PREVENE (2001).

3.4. Control Structures

3.4.1. Sabo Dam

"Sabo dam" is used to describe a group of different structures used to control debris flow; all of these functioning like dam. According to suggestions and experiences of Lien (2003), a check dam (also called "closed dam") was selected for Santo Domingo ravine because material on the zone and characteristics of the ravine. Check dams are closed-type and made of massive concrete and are conform for two dams, a main and a secondary (see Figure 4.a). According with JICA (2010), design discharge correspond to the rainfall of 100 years return period or the maximum rainfall in past records, whichever is larger.

The design discharge of Sabo dam is estimated by considering the ratio of sediment concentration α and using the equation

$$Q = Q'(1+\alpha) \tag{4}$$

where:

        Q = Design flood discharge including sediment (m³/ s)
        Q'= Peak flood discharge to 100 years return period (m³/s)
        α = Ratio of sediment concentration (ordinarily used is 10%)

The height of Sabo dam is defined by the depth of sediment. The opening of Sabo dam has a trapezoidal shape and follows the principles below:

1) The width of opening (B_1) should be at least 3m.
2) The height of the crest opening (H_c) is equal to

$$H_c = h_1 + h_2 \, Ij = Sj + \sigma j \tag{5}$$

where:

        h_1 = Depth of water. Estimated by using the general weir equation. It should be less than 3.0 m.
        h_2 = Freeboard (see Table 4).

Table 4. Proposed freeboard of opening

Proposed Discharge	Freeboard (m)
Below 200 m³/sec	0.6
200 – 500 m³/sec	0.8
500 m³/sec or above	1.0

Source: JICA (2010)

3) The side slope of opening (m^2) is usually 0.5. This typical slope is recommended by JICA (2010) because it provides enough stability.

A typical section is shown in Figure 4. Their operation and efficiency was evaluated with KANAKO debris flow simulator from Laboratory of Erosion Control, Division of Forest Science, Graduate School of Agriculture, Kyoto University, & SABO Technical Center. This software permits the evaluation of operation of check, slit, and grid dams.

3.4.1. Flexible Barrier

A different alternative is the flexible barriers, which are made of high-tensile steel wire netting and mesh. Large-scale field tests developed at the Swiss Federal Institute for Forest, Snow, and Landscape Research WSL (ETH) have shown that "these systems provide efficient, reliable protection against both shallow landslides and rockfalls" (GEOBRUGG, 2009). These kinds of barriers could have a maximum width of 15m without use of brackets (VX barriers), but it could have a width up to 25m with them, as shown in Figure 5 (UX barriers). Flexible barriers withstand high static and dynamic loads and may be installed with little amount of material and labor, which could reduce costs and installation time.

According to Volkwein et al. (2011), to design the barrier, the first step is to estimate a possible debris flow volume (*VDF*). According to Mitzuyama (1992), this *VDF* could be used to estimate the peak discharge (Q_p)

$$Q_P = 0.135 \, VDF^{0.78} \tag{6}$$

and the average flow velocity (v) will be estimated with

$$v = 2.1 Q_P^{0.34} I_s^{0.2} \tag{7}$$

where I_s is the gradient of the torrent.

a)

b)

c)
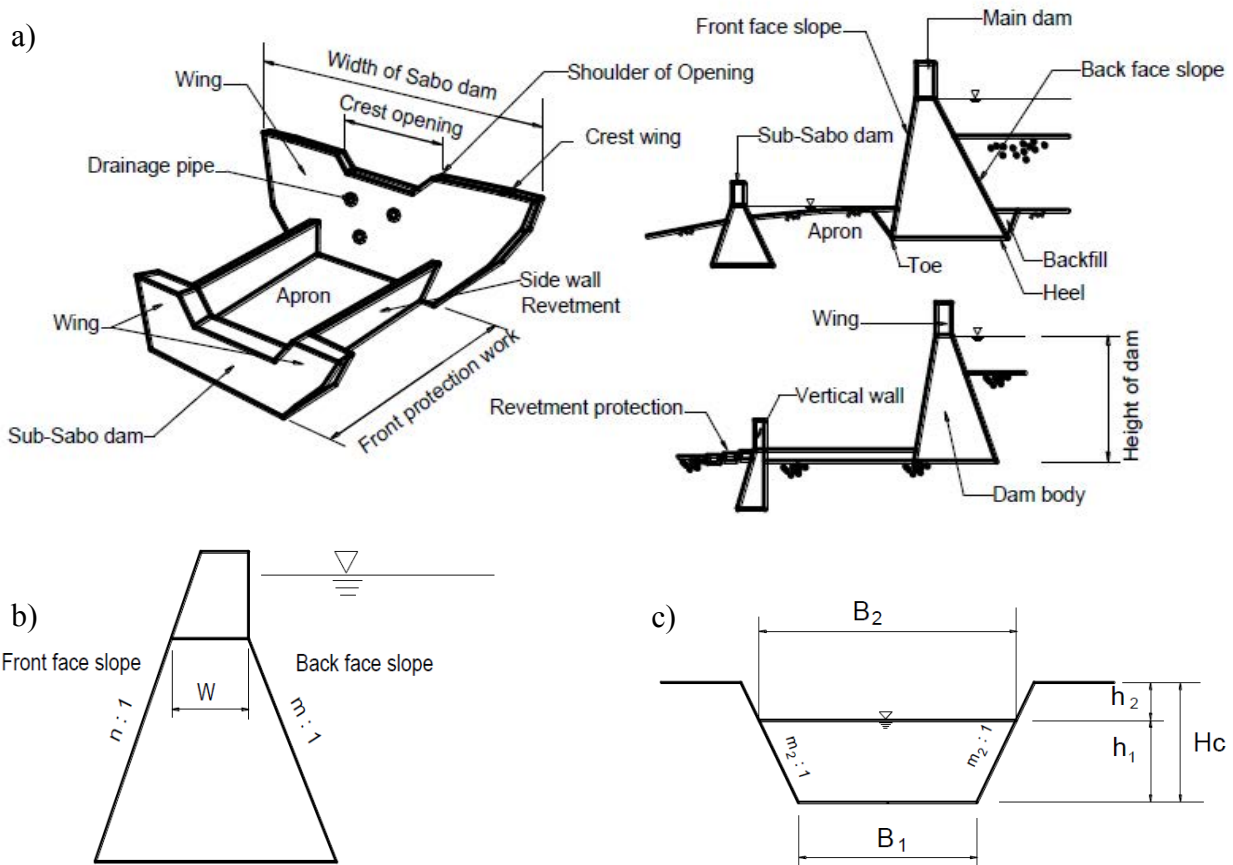
Figure 4. Sabo dam. a) Components of Sabo Dam. b) Thickness of crest. c) Cross Section of opening.

Source: JICA (2010)

The barrier height is estimated assuming a rectangle section and dividing Q_p by $v.b$; however, the post-event height is usually 3/4 of its pre-event height, and the minimum barrier height is determined as follows:

$$h_b = \sqrt{V_R \frac{32}{9} \frac{1}{b_m} \frac{1}{\sin\xi\left(\dfrac{\sin\xi}{\tan(\theta-\theta')}+\cos\xi\right)}} \leq 6m \tag{8}$$

with V_R retention volume, ξ barrier inclination, and θ and θ' the gradient of the material before and after a debris flow event.

A design was realized with the DEBFLOW dimension tool from GEOBRUGG.
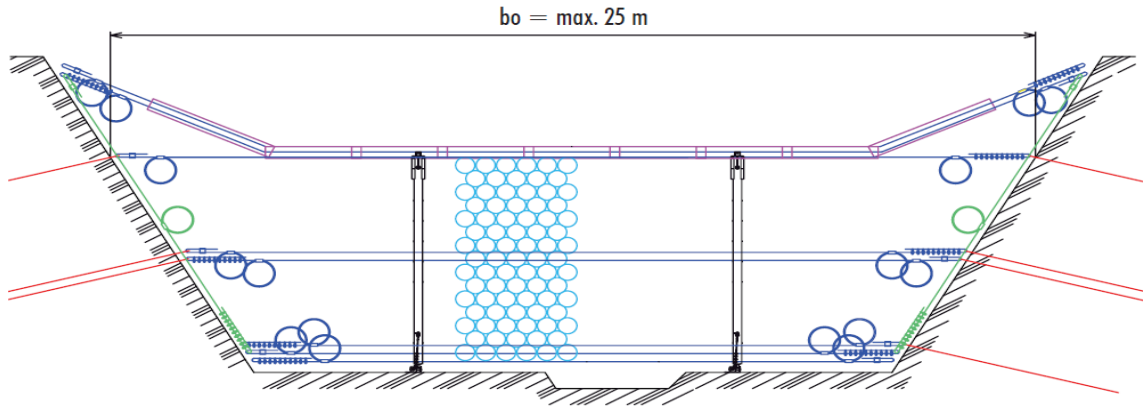
Figure 5. Typical section of flexible barrier type UX.

Source: GEOBRUGG (2009)

4. RESULTS AND DISCUSSION

A bidimensional model was built with a 10m x 10m size grid, peak discharged 9.4m³/s, Manning coefficient of 0.04, and other characteristics described in the last item. Model outflow is summarized in Table 5.

Table 5. Model outflow

Overland Flow	Water (m^3)	Water + sediment (m^3)
Inflow hydrograph	14299.40	22257.70
Floodplain storage	11719.56	18031.50
Floodplain outflow hydrograph	2579.90	4226.20

Table 5 shows that 22257.7 m³ of debris flow is produced and 4226.20 m³ left the model; 2579.90 m³ of this volume is water and 1646.3 m³ is sediment that will be deposited on the ground. This event could affect population at the left side of Rimac River, in 146350 m² approximately. Distribution of sediment will depend on floodplains topography.

Figure 6-left shows the affected area: the maximum depth gets 3.45m and is located on Rimac River stream. Having accounted that the majority of houses have areas between 120m² to 200m², this area represents more than 1000 houses that could be affected by 0.1 to 1.6 meters depth of deposited sediment.

Also, this model suggests the possibility of a damming effect over the Rimac River and a possible secondary effect of floods on the city. To evaluate this secondary effect, a second model with a mean flow in Rimac River was simulated. To this goal, a mean discharge of 33m³/s in Rimac River was assumed.

The model showed that Rimac River is not dammed by debris flow (Figure 6, right); instead, the Rimac River acts like a natural barrier, containing the debris flow. The consequence is an increment of the affected area in 25% approximately, getting 175600m²; however, not all this area could be considered hazardous because part doesn't have enough depth or velocity to represent risk.
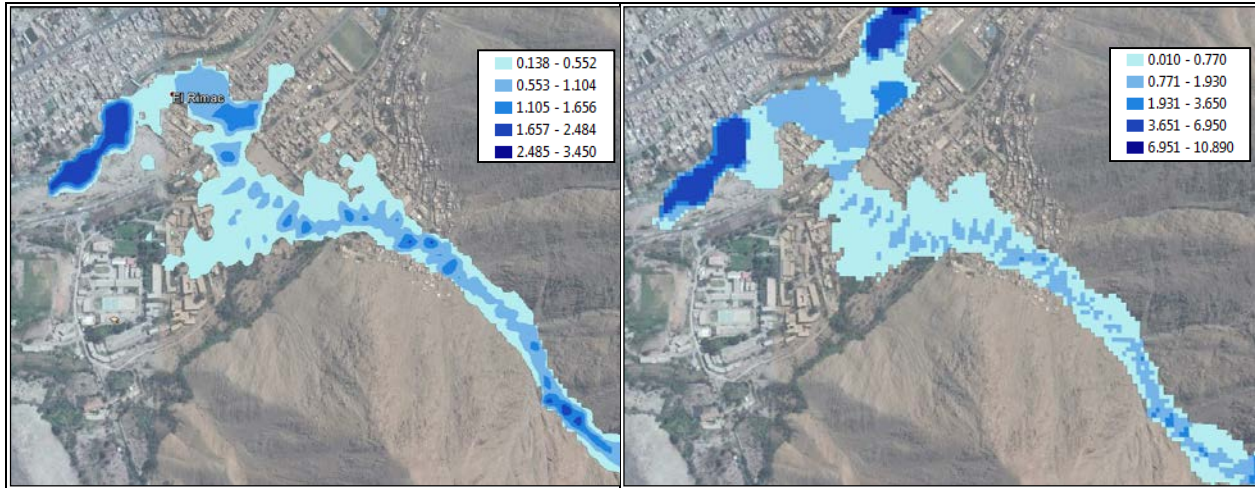
Figure 6. Deposition of Santo Domingo ravine on Rimac River. Left, deposition of debris flow caused by Santo Domingo ravine without consider discharges in Rimac River. Right, deposition of debris flow considering a mean discharge in Rimac River. *Tr*=100 years.

According to this last model, the debris flow hazard map was built (Figure 7). The affected area is estimated to be 103105m^2, and affected houses could be 516 (assuming a mean surface of 200m^2 by house). Also, 220 of these houses are in high risk and could collapse.

Hazard risk	Areas (m2)	Affected houses - 200m2 (approx)
High (red)	43935	220
Medium (orange)	40860	204
Low (yellow)	18310	92
Total	103105	516
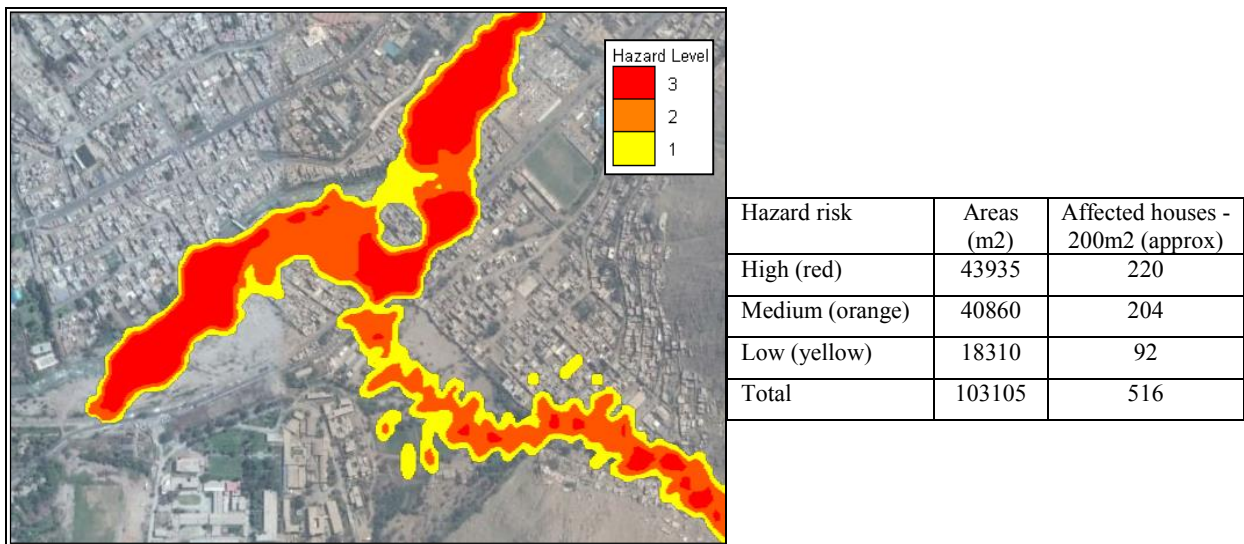
Figure 7. Hazard map to debris flow in Chosica. *Tr*=100 years.

To control debris flow, different heights of sabo dam (*H*) were essayed. For this goal, ineffective flow areas were defined to different heights, according to dimensions of sabo dam. The best selection correspond to *H*= 7.4m. Figure 8 shows effects of this structure on Santo Domingo ravine; sediment volume is absolutely retained.
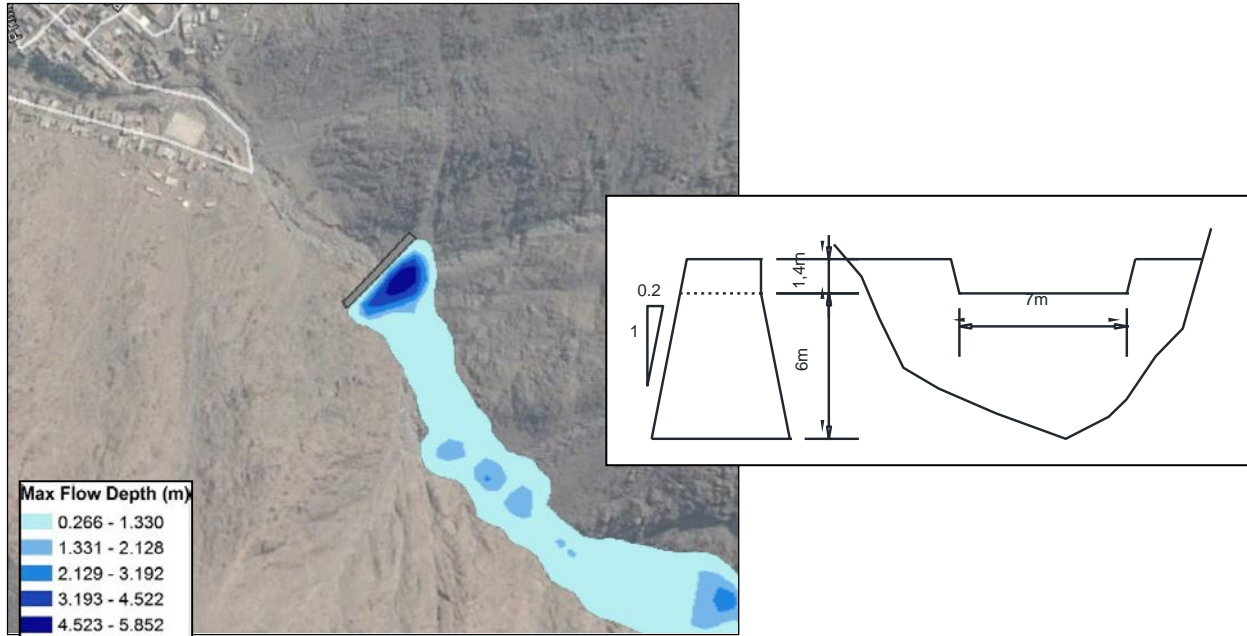
Figure 8. Deposition of Santo Domingo ravine with a sabo dam. Height = 7.4m. *Tr*=100 years.

Operation of sabo dam was evaluated with KANAKO. Results suggest that the best height of sabo dam is 14m, the double of FLO2D (see Figure 9). This result is oversized because KANAKO does not consider effect of banks on retained sediment volume and considers the stream like a rectangle shape.
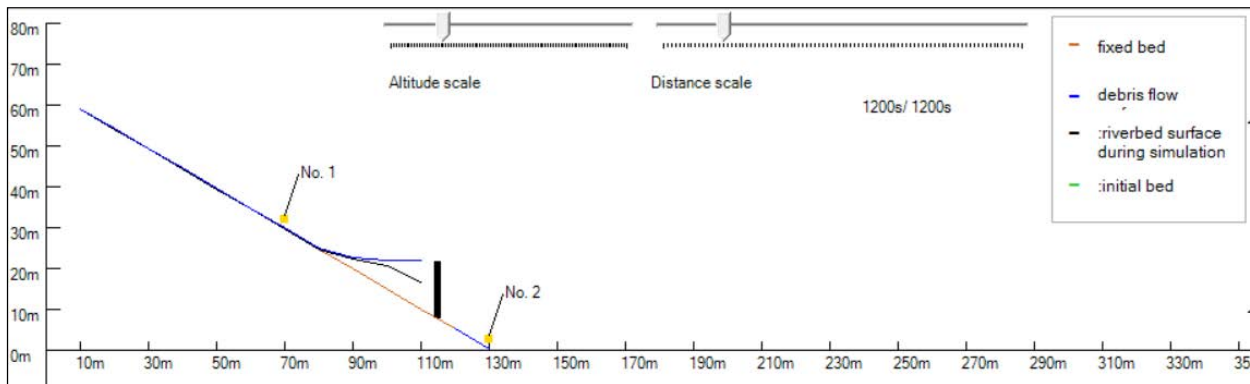
Figure 9. Evaluation of sabo dam with KANAKO. Height = 14m.

To analyze convenience of a flexible barrier, the total volume of sediment estimated with FLO2D was considered (approximately 7800m^3). DEBFLOW shown that it will be necessary 12 flexible barrier type UX180-H6 located along of the stream; every barrier will contain between 861 and 635m^3 of sediment. Steep slopes reduces the retention capability of every barrier and increases the number and the cost of this alternative.

5. CONCLUSIONS

Simulation show that more than 500 families could be affected by debris flow in a centennial event. To avoid this disaster, it is necessary to define evacuation routes and organize the population. The hazard map shows safe areas that could be considered for this goal.

Sabo dam shows the best performance like control measure to these conditions, including high slopes and debris flow. This performance and the possibility of using local material in construction represent an important cost reduction. Flexible barriers show low performance to high slopes and high costs to this conditions and type of barrier. Other products should be tested to verify a better solution.

In respect to software, FLO2D shows the best performance to simulate debris and mudflow, and permits estimation of the optimum height to the sabo dam and its efficiency. On the other hand, KANAKO shows that oversize structures because consider rectangle shape on streams however, could be used in narrow channels.

This methodology could be applied along of the Peruvian coast and mountain where this kind of geodynamic is common in the rainy seasons.

6. REFERENCES

CESEL Ingenieros S. A. (2004) Estudio hidrológico de la quebrada Collana. Lima, Peru.

Fiebiger, G. (1997) Hazard mapping in Austria. Journal of Torrent, Avalanche, Landslide and Rockfall Engineering. 61(134), 121—133.

García, R et al (2003). Hazard mapping for debris-flow events debris flows and warning road traffic at in the alluvial fans of northern Venezuela bridges susceptible to debris-flow. In: Rickenmann, D., Chen, C. (Eds.), 3rd Int. Conf. on Debris-Flow Hazards Mitigation. Millpress, Rotterdam, The Netherlands, pp. 589–599

GEOBRUGG (2011). Barreras flexibles de anillos para retención de flujos de detritos: la solución económica. . Boletin Técnico.

INDECI (2011). Manual de estimación del riesgo ante inundaciones Fluviales. Cuaderno Técnico N°2. INDECI. Marzo 2011.

Japan International Cooperation Agency (1988) The Master Plan Study on the disaster prevention Project in the Rimac basin. Lima-Perú.

Japan International Cooperation Agency (2010) Technical standards and guidelines for planning and design of sabo structures. Tokyo-Japan.

Julien, Pier Y. et al. (1991) Rheology of Hyperconcentrations. Journal of Hydraulic Engineering, Vol. 117, No. 3, March 1991, pp. 346-353. American Society of Civil Engineers (ASCE). Washington – U.S.A. 1991.

Mitzuyama et al (1992) - Prediction of debris flow peak discharge. Proc. Interpraevent, 4: 99-108, Berne.

O'Brien, J. & Julien, P. (1988) Laboratory analysis of mudflow properties. Journal of Hydraulic Engineering 114(8), 877–887. ASCE.

PREVENE (2001) Contribution to "Natural" Disaster Prevention in Venezuela. Technical report Project VEN/00/005. Cooperation: Venezuela—Switzerland—PNUD.

Fish Passage Behavior through Baffled and Nonbaffled Culvert

M.A. Khodier[1] and B.P. Tullis[2]
[1]Dept. of Civil & Environmental Engineering
Utah State University
Logan, UT 84322
USA
[2]Dept. of Civil & Environmental Engineering
Utah State University
Logan, UT 84322
USA
E-mail: m.khodier@aggiemail.usu.edu

ABSTRACT

Culverts can have a negative impact on fish passage. Installing baffles inside culverts can potentially improve culvert fish passage by decreasing the flow velocity and increasing the flow depth. Fish passage behaviors of wild brown trout through a small prototype-scale (0.6 m diameter, 18.3 m in length) baffled, and non-baffled culverts were observed in the laboratory for a variety of discharges and pipe slopes (up to 6%). The baffle height and spacing was 0.15 and 0.9 times the culvert diameter, respectively. The correlation between successful fish passage, sample fish population, and the fish length was evaluated. The influence of baffles installed inside the culvert on fish passage compared to the non-baffled culvert was reported. Resting and staging zones for the fish passing the culvert upstream were observed and reported. A threshold velocity (calculated based on above-baffle flow area) for the fish passage was found to be 1.5 m/s.

Keywords: Fish passage; baffle; culvert; fish length.

1. INTRODUCTION

Maintaining the ability for free movement of many aquatic species, including fish, throughout a river drainage system can be critical with respect to the pursuit of foods or spawning. Some hydraulic structures, including culverts, may create a barrier for these species. Many studies have investigated the influence of culverts on the fish passage as a function of flow condition (Bell 1986; Clay 1995; Pearson et al. 2006). Fish passage through culverts can be improved by installing baffles along the culvert invert at a regular spacing. Baffles have many different designs, but some common ones include weir baffles, slotted-weir baffles, spoiler baffles, and offset baffles. The flow characteristics through different baffle designs were studied by Rajaratnam et al. (1988), Rajaratnam et al. (1989), Rajaratnam and Katopodis (1990), and Rajaratnam et al. (1991). They derived a flow equation that correlates discharge (Q), flow depth (y), culvert slope (S), and gravity acceleration (g). Feurich et al. (2011) investigated numerically the effect of the spoiler baffles on the flow field, and they compared the velocity fields for both baffled and non-baffled culverts. They found a reduction in flow velocities due to baffle installation. No biological tests were conducted in Feutich's study. Morrison et al. (2009) conducted laboratory fish passage tests on juvenile salmon through a spiral-corrugated baffled-culvert of 1.83 m inside diameter at a single culvert slope of 1.14% and different flow rates (Q=43 to 198 L/s). They investigated the correlation between the flow turbulence characteristics and juvenile salmon passage, but no significant relationship was found.

Liao et al. (2003) studied the influence of vortices on Rainbow trout swimming behavior in a small test section. They observed that fish used the vortices to reduce the amount of energy they expended while swimming. Liao's experiment was limited to a small test section. A study by Tritico and Cotel (2010) was conducted to investigate the influence of turbulent eddy diameter and vorticity on the stability and swimming speed of creek chub (*Semotilus atromaculatus*). They found that the turbulent eddies have significant effects on fish behavior and swimming stability. Their study was concise for a small test section of 2.5 m length, 0.6 m width, and 0.55 m height. The influence of flow velocity and turbulence on the fish behavior of juvenile salmonids was studied by Smith et al. (2005). They observed that a flow region of high velocity and low turbulence was a more preferred swimming

environment for fish than a flow region of low velocity and high turbulence. Pearson et al. (2005) conducted fish passage tests on juvenile coho salmon through corrugated, non-baffled culverts with slopes of 1.14% and 4.33% and a variety of flow rates. They observed that juvenile coho preferred to swim in areas of low velocity, which were near the culvert wall. Tillinger and Stein (1996) studied the influence of fish length on the swimming strength. They found that larger fish are typically considered stronger swimmers. Watts (1974) studied the effects of fork length of the fish tail and fish total length on the swimming speed of juvenile fish. They concluded that there is a proportional relationship between the swimming speed and fish total length. Behlke et al. (1991) concluded from their study that larger fish were more likely to pass through culverts than smaller ones. Belford and Gould (1989), however, observed little relationship between fish swimming ability and fish size. Olsen and Tullis (2013) investigated the influence of installing baffles in a culvert on wild brown trout fish passage under a variety of culvert slopes (0% ≤S ≤ 3.5%) and flow rates (28.3-85 L/s). They observed that fish passage through culverts was improved significantly by installing baffles.

The goal of this study was to evaluate the ability of wild brown trout to pass through a weir-baffled culvert at steeper culvert slopes, ranging from 3.0% ≤ S ≤ 6.0%. The preferable swimming zone for the fish is described, and the influence of the fish sample size on the fish passage is reported.

2. EXPERIMENTAL SETUP

A laboratory fish passage was conducted on wild brown trout through a weir-baffled culvert 18.3 m long and 610 mm in diameter. All experiments were carried out at Utah Water Research Laboratory (UWRL) at Utah State University. The culvert and the baffle were made from high-density polyethylene (HDPE). The baffle spacing and height were $0.9D$ and $0.15D$, respectively, where D is the culvert inside diameter. As shown in Figure 1, the upstream end of the culvert was connected to the head tank that supplies flow to the culvert. The downstream end of the culvert was connected to a tail tank where the fish were placed to pass upstream. The weir-baffled culvert was supported by a steel I-beam and adjustable pipe section. In order to provide instrumentation access and a clear visual observation, small rectangular windows were cut into the top of the culvert (Figure 2).

Another observation window was installed in the sidewall near mid-span of the culvert between two adjacent baffles. A flexible sheet of clear Lexan (355-mm-wide and 406-mm-tall) replaced the curved section that was removed from the culvert. In order to eliminate the optical distortion for the video images through the curved windows, an acrylic box of 584×685×635 mm was attached to the observation window, as shown in Figure 2. This box was filled with water. The flow rates were measured using calibrated venturi flow meters with ±0.2% accuracy. The tested flow rates were 28.3, 56.5, and 85 L/s. The corresponding average velocity through the baffled culvert was calculated by dividing the flow rate by the flow area above the baffle ($V=Q/A$). A tank of 350-gallon capacity was used to hold the fish. In an effort to maintain some level of consistency between the fish storage tank and the river environment, the tank was continuously supplied with fresh water from Logan River via a hose/nozzle assembly. The hose-induced jet was used to oxygenate the water in the tank through turbulent mixing at the water surface. A drain was attached to tank to keep the water level constant in the tank. Fish were fed with night crawlers (worms) daily (one per fish). The fish were allowed a minimum of 1 day of rest between tests.
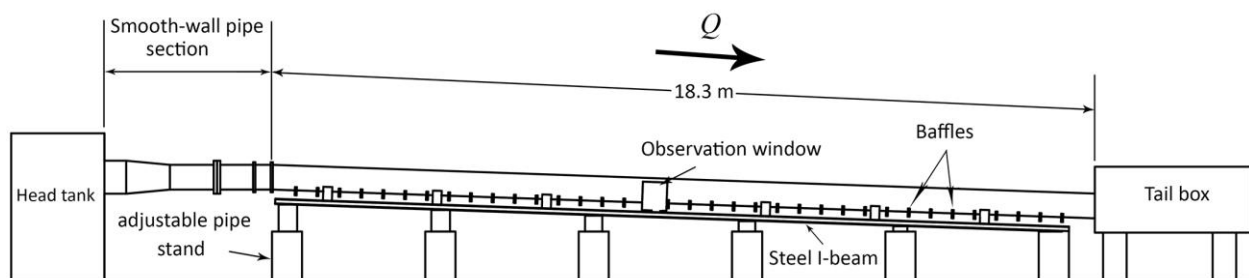
Figure 1. Schematic of baffled culvert fish passage test facility.
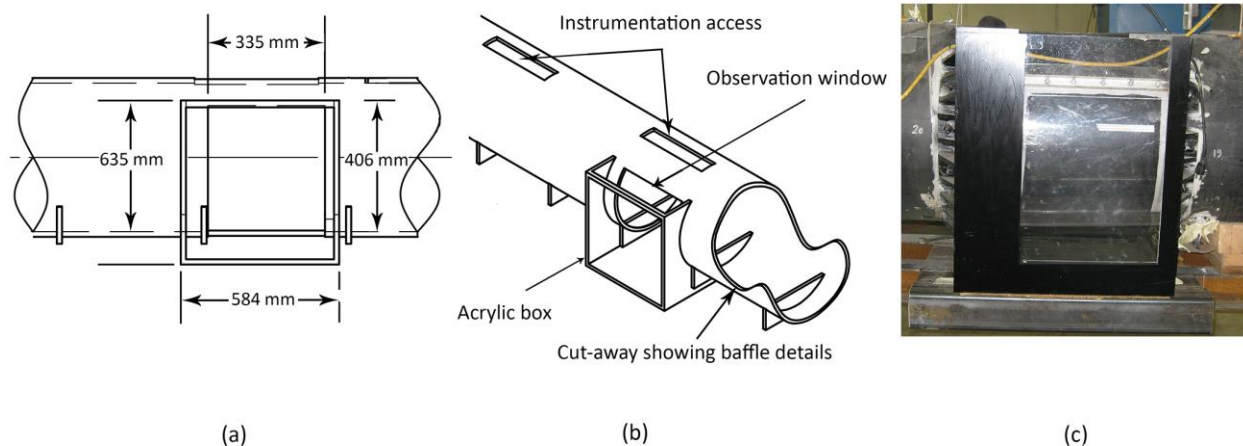
Figure 2. Overviews of baffled culvert observation ports and windows for fish viewing (a) elevation; (b) perspective; (c) photographic

Figure 3. Fish holding tank

3. RESULTS AND DISCUSSION

Wild brown trout passage was evaluated through a non-baffled and baffled culvert of 0.61 m diameter at culvert slopes ranging from 0% to 6% and flow rates of 28.3, 56.5, and 85 L/s. Figure 4 shows the number of fish, percentage of fish passing, and the average flow velocity at each culvert slope and flow rate. The data in Figure 4 shows that the fish percentage passing increased with baffles relative to the non-baffled culverts. In general, the data in Figure 4 show that percentage fish passage decreased as the culvert slope and flow rates increased. Also, Figure 4 shows that for S=3.0 and 4.0%, the percentage of fish passage at small and mild discharge (Q=28.3 and Q=56.5 L/s, respectively) was consistent and the data were not significantly dependent on the culvert slope. However, at larger flow rates (Q=85 L/s), the fish percentage passing was significantly affected by the culvert slope. At culvert slopes S>5.0%, the fish percentage passing significantly decreased for all flow rates. Note that there is a threshold velocity for the fish passing at V>1.5 m/s. The cruising speed, sustained speed, and bursting speed for brown trout fish are

0.674 m/s, 1.884 m/s, and 3.875 m/s, respectively (Bell, 1986). Note that the threshold velocity is between the cruising speed and sustained speed. The influence of the fish sample size on the fish passage results was evaluated at three different sample sizes: 9, 17, and 25. Figure 5 shows the fish percentage passing for three different samples at different culvert slopes and discharges. For $S=3.0\%$, there is a deviation of approximately ±4.0% from the mean and less than ±7.0% for slopes of 5.0 and 6.0%. This indicates that the fish sample size has significant influence on the fish passage at high culvert slopes specifically at $S \geq 5.0\%$.
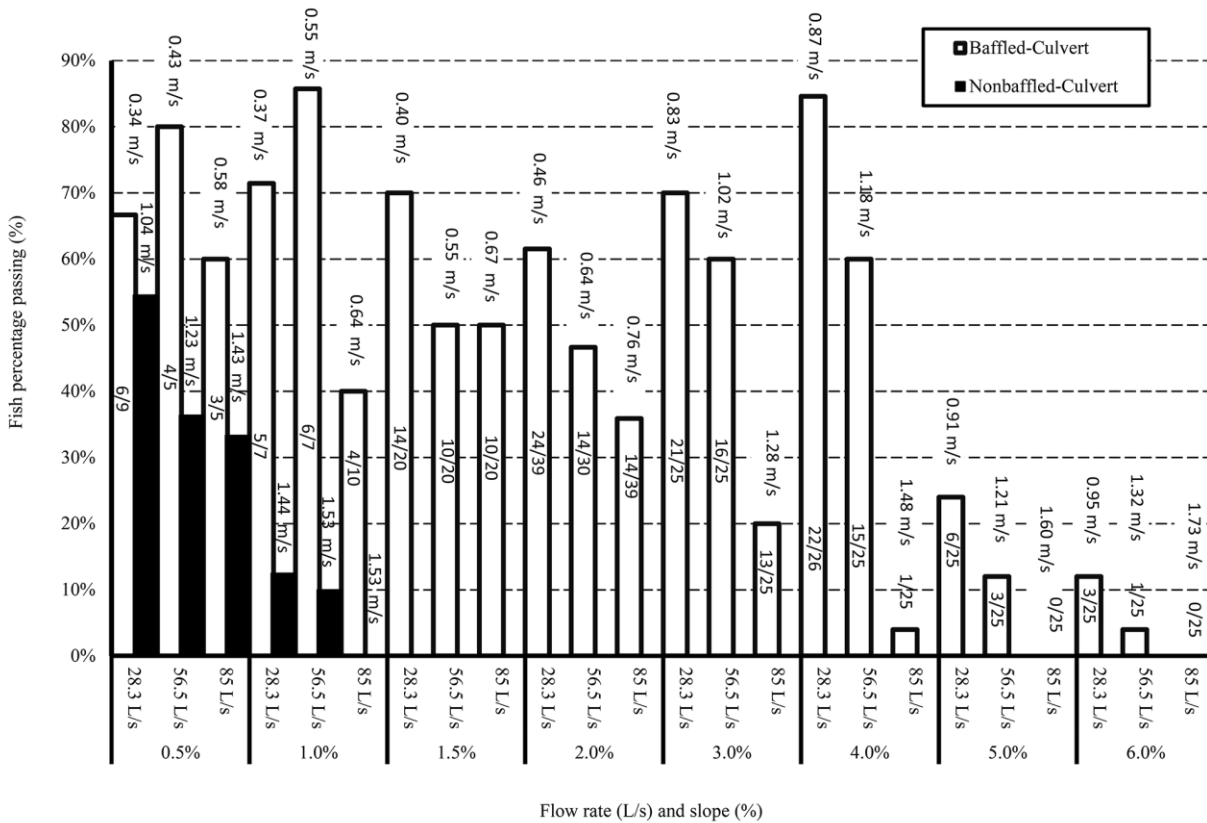
Figure 4. Summary of baffled and non-baffled-culvert fish passage data as a function of S and Q
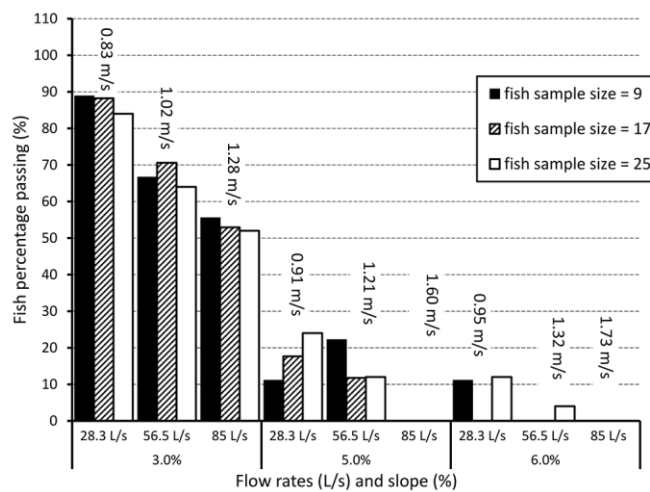
Figure 5. Summary of baffled-culvert fish passage versus fish sample size

Another factor that may influence fish passage is the physical characteristics of the individual fish, such as fish length. Figure 6 shows the ratio of successful total number of passing to the total attempts as a function of the individual fish length. The total number of attempts was fifteen times for all fish. In general, the data in Figure 6 reveal a linear relationship between the ratio of total number of fish passing and the fish length. This observation is consistent with Tillinger and Stein (1996) who found that the swimming ability increases with the size of the fish. Every 5 minutes, the head tank was observed for any successful fish passage, and the number of the fish in the head tank was reported until the end of the experiment. The duration of the experiment was 120 minutes. Figure 7 shows the timeline for the number of fish in the head tank as a function of the elapsed time counted from the last fish entering the culvert. The data in Figure 7 show that at low culvert slope (S=3.0%), more time was required to pass through the culvert and the rate of fish passage success was higher. At the steeper culvert slopes (S=5.0%), the culvert transit time reduced, as did the overall success rate. These results are partly due to the fact that with the more turbulent, higher velocity flow conditions corresponding to the steeper culvert tests, the effectiveness of the fish-resting zones was diminished. Without the ability to rest during transit, fish had to traverse the culvert more quickly before fatiguing.
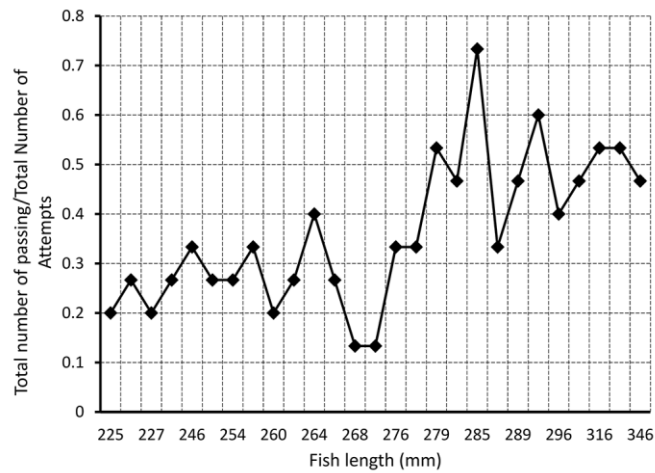
Figure 6. Total number of successful culvert passages to the total number of attempts ratio as a function of fish length (each column represents an individual fish, each fish participated in 15 trials)
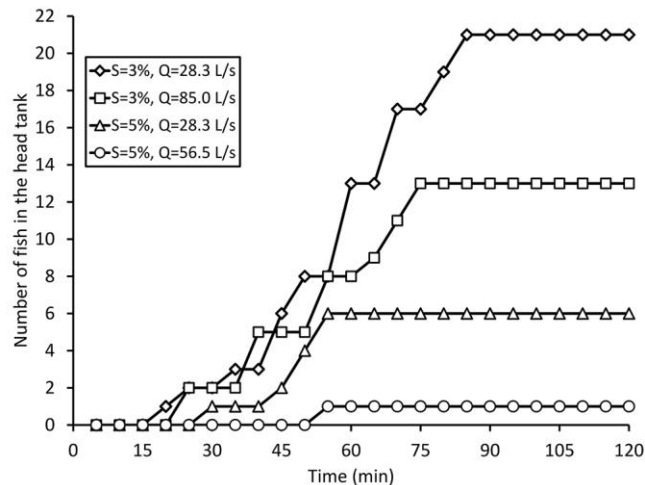
Figure 7. Number of fish in the head tank as a function of elapsed time

In an effort to observe the behavior of the fish passing upstream, a high-definition video camera was used to record the motion of the fish through the observation window located at the mid-span of the culvert. Two zones were preferred by the fish; Zone 1 was located on the downstream side of the baffles, and Zone 2 was located along either

sidewall in between baffles. Figure 8 shows these Zones. Zone 1 was used as resting place for the fish, and Zone 2 was used as a staging area before swimming upstream. Swimming between the two Zones was also observed. Zone 1 and Zone 2 are observed along the whole culvert through the observation rectangular windows cut into the crown of the culvert. In Zone 1, the fish either aligned their bodies parallel to the baffle (Figure 9 a) or aligned themselves with the culvert axis facing the local flow downstream direction (Figure 9b). This illustrates how installing baffles helps to improve the fish passage percentage.
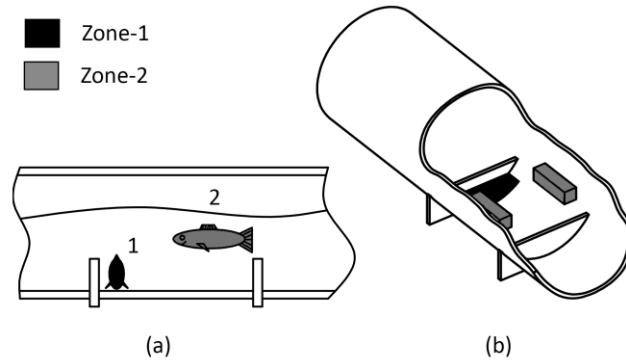
Figure 8. Illustrations of fish zones in the baffled culvert (a) elevation; (b) perspective
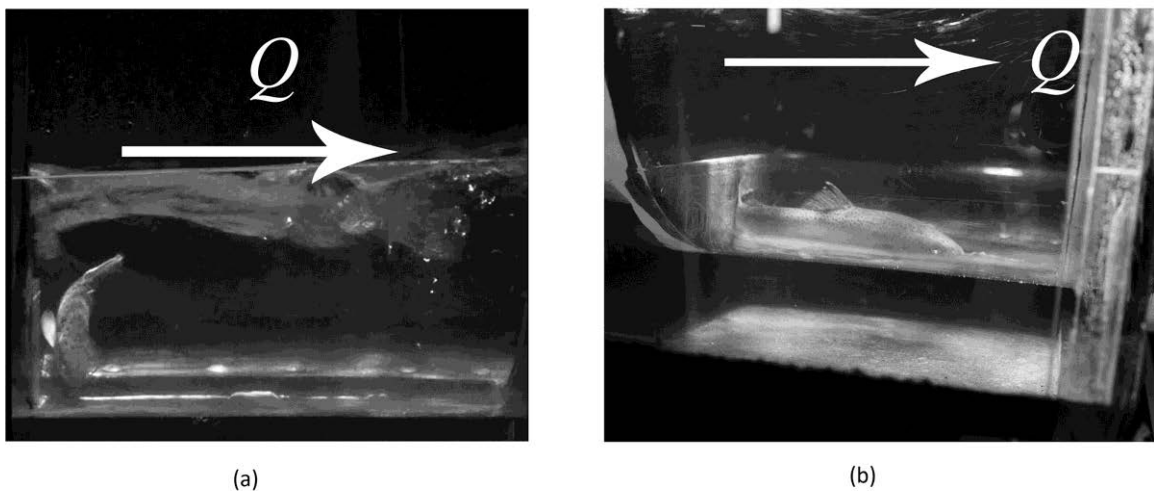
Figure 9. Photographic examples of fish resting: (a) in Zone 1; (b) along the pipe invert facing the between-baffle recirculating eddy flow with its tail braced against a baffle

4. CONCLUSION

Wild brown trout passage was evaluated through baffled prototype-scale culvert (18.3 m long and 0.60 m in diameter) under a variety of culvert slopes and discharge conditions. One can conclude the following:

- The percentage of fish passage is inversely proportional to culvert slope (S) and flow rate (Q), and no successful fish passage was reported for S=5 and 6% at flow rates of 85 L/s.
- For less severe hydraulic conditions, fish sample size showed variation < ±4.0 % from the mean and < ±7.0 % for severe flow condition.
- The swimming ability of the brown trout increased as the length of the fish increased.
- The duration of the overall fish passage process increased as the severity of the hydraulic conditions lessened. Fish that were able to pass with the more severe hydraulic conditions utilized less time.
- Two different Zones were observed for the fish while swimming upstream. Zone 1 was used as a resting area for the fish and Zone 2 was used as a staging area.

5. ACKNOWLEDGMENTS

6. REFERENCES

Behlke, C. E., Kane, D. L., McLeen, R. F., and Travis, M. D. (1991). *Fundamentals of culvert design for passage of weak-swimming fish*, Alaska Dept. of Transportation and Public Facilities, Fairbanks, AK.

Belford, D. A., and Gould, W. (1989). "An evaluation of trout passage through six highway culverts in Montana." *North America Journal of Fisheries Management*, 9(4), 437–445.

Bell, M. C. (1986). Fisheries handbook of engineering requirements and biological criteria, U.S. Army Corps of Engineers, Fish Passage Development and Evaluation Program, North Pacific Division, Portland, OR, 51−176.

Clay, C. H. (1995). Design of fishways and other fish facilities, 2nd Ed., CRC Press, Inc., FL., USA.

Feurich, R., Boubée, J., and Olsen, N. (2011). "Spoiler Baffles in Circular Culverts." *Journal of Environmental Engineering*, 137(9), 854-857.

Liao, J., Beal, D. N. Lauder, G. V. and Triantafyllou, M. S. (2003). "Fish exploiting vortices decrease muscle activity." *Science*, 302(5650), 1556-1569.

Morrison, R., Hotchkiss, R., Stone, M., Thurman, D., and Horner-Devine, A. (2009). "Turbulence characteristics of flow in a spiral corrugated culvert fitted with baffles and implications for fish passage." *Ecological Engineering*, 35(2009), 381-392.

Olsen, A. H., and Tullis, B. P., (2013). "Laboratory Study of Fish Passage and Discharge Capacity in Slip-Lined, Baffled Culverts." *Journal of hydraulic engineering*, 139(4), 424-432.

Pearson, W., Richmond, M., Johnson, G., Sargeant, S., Mueller, R., Cullinan, V., Deng, Z., Dibrani, B., Guensch, G., May, C., O'Rourke, L. Sobocinski, K., and Tritico, H. (2005). Protocals for Evaluation of Upstream Passage of Juvenile Salmonids in an Experimental Culvert Test Bed, Final Report, Washington State Department of Transportation.

Pearson, W.H., Southard S.L., May C.W., Skalski J.R., Townsend R.L., Horner-Devine A.R., Thurman D.R., Hotchkiss R.H., Morrison R.R., RichmondM.C., Deng D. (2006). "Research on the Upstream Passage of Juvenile Salmon through Culverts: Retrofit Baffles", Final Report, Washington State Department of Transportation.

Rajaratnam, N., & Katopodis, C. (1990). "Hydraulics of culvert fishways III: weir baffle culvert fishways." *Can. J. Civ. Eng.*, 17(4), 558-568.

Rajaratnam, N., Katopodis, C., and Lodewyk, S. (1991). "Hydraulics of culvert fishways IV: Spoiler baffle culvert fishways." *Can. J. Civ. Eng.*, 18(1), 76-82.

Rajaratnam, N., Katopodis, C., and Lodewyk, S. (1988). "Hydraulics of offset baffle culvert fish ways." *Can. J. Civ. Eng.*, 15(6), 1043-1051.

Rajaratnam, N., Katopodis, C., and McQuitty, N. (1989). "Hydraulics of culvert fishways II: slotted-weir culvert fishways." *Can. J. Civ. Eng.*, 16(3), 375-383.

Smith, D., Brannon, E., and Odeh, M. (2005). "Response of Juvenile Rainbow trout to Turbulence Produced by Prismatoidal Shapes." Trans. Amer. Fish. Soc., 134, 741-753.

Tillinger, T. N., and Stein, O. R. (1996). "Fish passage through culverts in Montana: A preliminary investigation," Dept. of Civil Engineering, Montana State Univ., Bozeman, MT, 1−20.

Tritico, H., and Cotel, A. (2010). "The effects of turbulent eddies on the stability and critical swimming speed of creek chub (Semotilus atromaculatus)." *The Journal of Experimental Biology*, 213, 2284-2293.

Watts, F. J. (1974). Design of culvert fishways, Water Resources Research Institute, Univ. of Idaho, Moscow, ID.

Effect of River Levee with Geosynthetic-Reinforced Soil against Overflow Erosion and Infiltration

Y. Kurakami[1], Y. Nihei[1], M. Morita[1], S. Futami[1] and M. Itakura[1]
[1]Dept. of Civil Engineering
Tokyo University of Science
2641 Yamazaki, Noda-shi, Chiba, 278-8510
JAPAN
E-mail: 7615701@ed.tus.ac.jp

ABSTRACT

Overflows from huge floods have caused levee breaches in a great number of places, including Japan. To prevent such destruction and thereby increase the resistance of armored levees to overflow erosion, we examined the performance of Geosynthetic-Reinforced Soil (GRS) levees against overflow erosion under various conditions, such as reinforcement, back slopes, and geo-grid layers. In addition, we investigated the effect of geo-grid layers on the infiltration of levees. The model tests revealed that 1) with scour protection in front of the toe of the back slope, the GRS levee exhibits much higher resistance against overflow erosion than the armored levee, and 2) the armored levee with a steep back slope (= 1:0.5) collapsed faster than that with a normal slope (= 1:2). However, the GRS levee with a steep back slope of 1:0.5 maintained high resistance against overflow erosion after the target time. 3) The GRS levee with partial and full reinforcements had a comparably high resistance against overflow erosion. 4) The GRS levee using a small-sized geo-grid maintained a high residual ratio of the cross-sectional area over a long period. 5) The infiltration discharge of the GRS levee was less than that of the levee with no reinforcement due to the reduction in infiltration erosion in the GRS levee. These facts suggest that the GRS levee with partial reinforcement can be applied to the reinforcement of existing levees, and appropriately sized geo-grid layers should be selected.

Keywords: river levee, overflow, infiltration, GRS, erosion, flood

1. INTRODUCTION

River levees are generally designed to protect against scour, infiltration, and earthquakes for water levels below the designated high water level (HWL). Therefore, overflows exceeding the HWL are not generally taken into account. Earthen levees made up of sediments, including sand and clay, are typical in the world because river levees are originally semi-natural structures made of sediments transported from upstream regions. However, earthen levees have the potential of failure due to overtopping flows (e.g., Powledge et al., 1989). Therefore, levee failures have occurred in a great number of places around the world when water levels exceeded the HWL because of severe flooding, tsunamis, and storm surge. On September 10, 2015, an extreme flood by typhoon nos. 1518 caused a levee breach in the Kinugawa River, Japan, mainly due to overflow, thereafter causing huge flood damage in Joso City, Ibaragi Prefecture.

Armored levees, which are covered with concrete panels on the top and side slopes, have been introduced as a measure to protect against overflow erosion (Figure 1 (a), Hughes 2008). However, such levees have still collapsed due to overflow erosion when the panels were swept away by the current created by a flood. In armored levees, the concrete panels maintained their positions thanks to the weight of the panels. To increase the resistance of the armored levee to overflow, it is necessary to increase the weight of the panel, but the stability of the armored levee against earthquakes is reduced with an increase in the panel weight. It is therefore necessary to develop a new reinforcement technology to protect river levees from overflow erosion and earthquakes.

To prevent such destruction and thereby increase the resistance of armored levees to overflow erosion, Kurakami et al. (2013) introduced a river levee with geosynthetic-reinforced soil (GRS; Tatsuoka et al. 1997) in which the
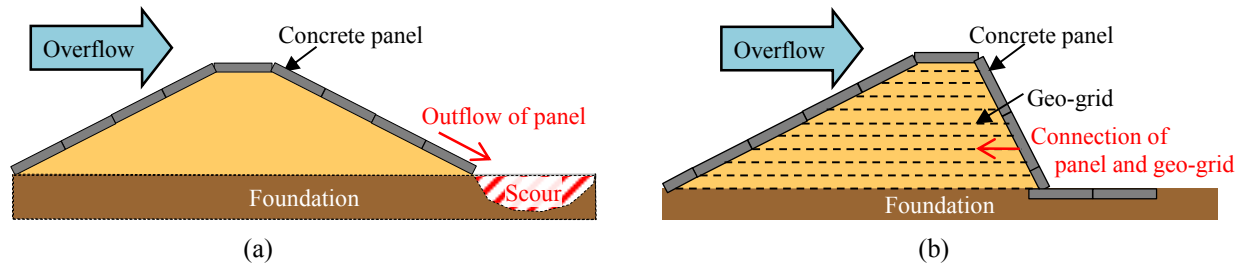
Figure 1. Schematic views of armored levee (a) and GRS levee (b).
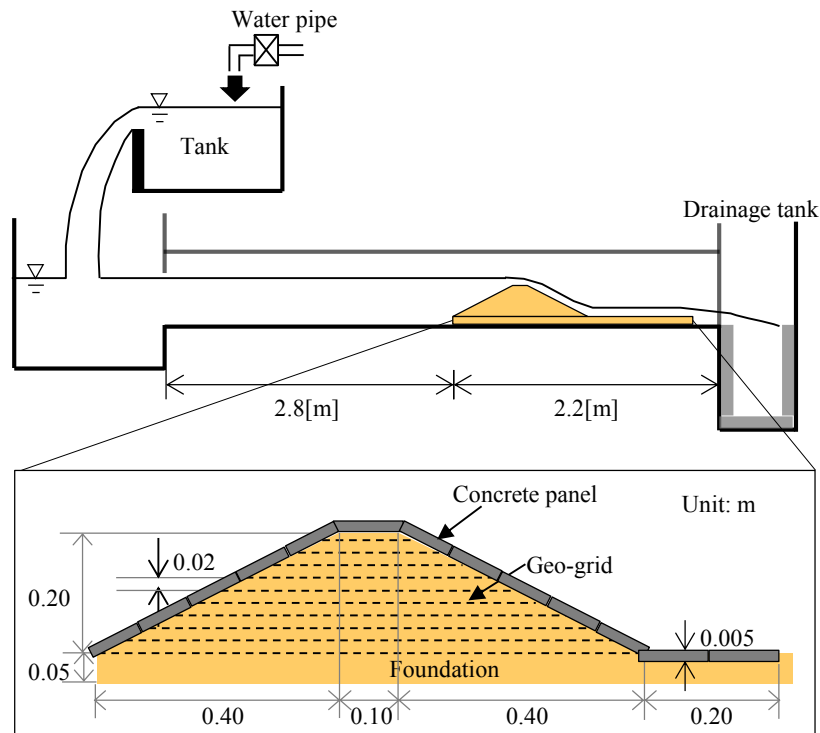
Figure 2. Schematic views of open channel used in overflow model tests and cross-sectional shape of the levee model.

concrete panels are connected to geo-grid layers reinforcing the sand. The geo-grid layers, with their high tensile strength, should help to keep the concrete panels in place and, thus, increase the resistance of the levee to overflow erosion (Figure 1 (b)). GRS structures and walls have been widely used to strengthen levee stability against earthquakes (Tatsuoka et al., 1997; Tatsuoka et al., 1998; Tatsuoka et al., 2009). Kurakami et al. (2013) conducted fundamental tests to evaluate the resistance of the GRS levee to overflow erosion and showed that the GRS levee can survive during prolonged overflow conditions. However, the experimental conditions were limited. Furthermore, it is necessary to confirm the influences of infiltration on the GRS levee because the formation of a water path is a fundamental issue in relation to GRS structures.

In this study, we examined the performance of a GRS levee against overflow erosion under various conditions, such as reinforcement, back slopes, and geo-grid layers. In addition, we investigated the effect of geo-grid layers on the infiltration of levees. For these tests, we conducted a laboratory model test on overflow erosion and infiltration. As the experimental condition to verify the fundamental form of the GRS levee, we tested GRS and conventional armored levees with and without scour protection. In this series, we chose a 1:2 slope, which is used in general levees. In addition, to improve the performance of the GRS levee, we set up three cases: 1) to reduce the area of the cross section of the levees, we tested the GRS levee with a steep back slope (1:0.5 slope), 2) we introduced partial-

Table 1. Experimental conditions of overflow erosion.

No.	Levee	Reinforcement condition	Back slope	Scour protection	Geo-grid size	D_c[%]
1-1	Armored	Panels only	1:2	×	-	85
1-2				○		
1-3			1:0.5			90
2-1	GRS	Full-length reinforcement	1:2	×	Medium	85
2-2				○	Medium	
2-3			1:0.5	○	Coarse	90
2-4					Medium	
2-5					Fine	
3-1		Parial-length reinforcement	1:0.5	○	Coarse	90
3-2					Medium	
3-3					Fine	
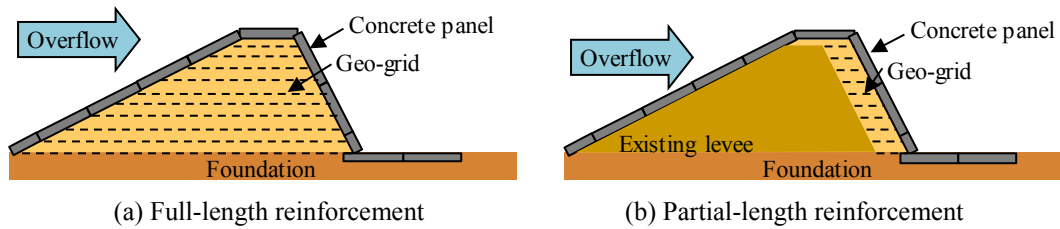
(a) Full-length reinforcement   (b) Partial-length reinforcement
Figure 3. Reinforcement condition
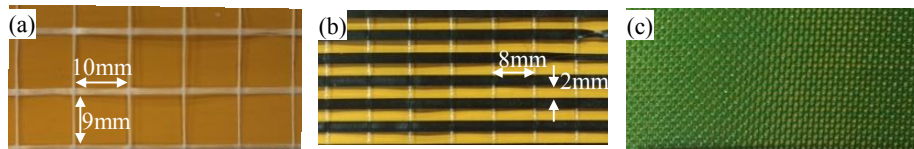
Figure 4. Three grid sizes of geo-grid layer; (a) Coarse (9 * 10 mm, 56 D_{50} * 63 D_{50}), (b) Medium (2 * 8 mm, 12 D_{50} * 50 D_{50}), (c) Fine (0.6 * 0.6 mm, 4 D_{50} * 4 $D_{50)}$

length geo-grid layers to examine the application of the GRS technique to existing levees (Figure 3), and 3) we set three geo-grid sizes to verify the appropriate grid size of the geo-grid layer. In the infiltration experiment, we set the model levee with the same conditions as in the overflow experiment in the water tank, and water level of the waterside land was kept constant.

2. METHODS

2.1. Outline of Overflow Experiments

In this study, we tested a GRS levee against overflow by conducting laboratory model tests in an open channel that was 5 m long, 0.2 m wide, and 0.35 m high, as shown in Figure 2. Model levees at 0.2 m high, with a 0.1 m crest width, and back slopes of 1:2 and 1:0.5 were created by compacting Toyoura sand, which is a well-sorted fine sand in which the mean grain size is 0.16 mm and the optimum water content w_{opt} is 16.0%. The model scale in this test was set to 1/25, and the height of the model levee corresponds to a 5 m prototype levee. The overflow depth on the levees was set to 0.06 m, corresponding to 1.5 m in the prototype using the model scale (= 1/25); Froude similarity was used. The overflow discharge Q was 5.61×10^{-3} m³/s. At this overflow depth, the prototype levee is assumed to take 50 min to collapse based on Yoshikawa (2008). With the Froude similarity, it corresponds to 10 min for the model levee, which is the target overflow time in our experiment. Model levees were set on a 0.05 m thick
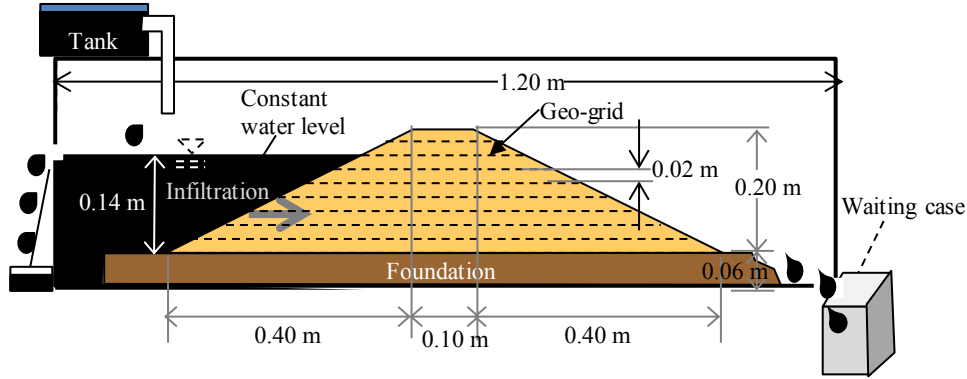
Figure 5. Schematic view of water tank used in infiltration model tests and cross-sectional shape of the levee model.

Table 2. Conditions of infiltration experiments.

No.	Levee	Reinforcement	Back slope	Geo-grid size	D_c[%]
A	Earthen	-		-	
B	GRS	Geo-grid layers without panels	1:2	Coarse	90
C				Medium	
D				Fine	

foundation to account for the effects of scouring at the toe of the back slope of the levee, which is a key factor in the overflow erosion of levees.

Table 1 lists the experimental conditions of overflow erosion. We compared the effects of scour protection for armored and GRS levees with and without scour protection. To improve the performance of the GRS levee, we conducted further model tests. To examine the influence of the back slope of the levees, we compared the armored and GRS levees with 1:2 and 1:0.5 back slopes. To examine the full- and partial-length reinforcements of the GRS levee, we compared the full reinforcements in Case 2-4 and the partial reinforcements in Case 3-2 with 1:0.5 back slopes. Finally, to understand the influences of the grid sizes of geo-gird layers, we used three types of geo-grids: 9 mm * 10 mm, 2 mm * 8 mm, and 0.6 mm * 0.6 mm, corresponding to coarse, medium, and fine sizes, respectively (Figure 4). The full- and partial-length reinforcements with three kinds of geo-grids were set in this experiment. The geo-grid layers were laid at 0.02 m intervals. Digital video (DV) images of the side and top views of the levees were recorded to examine the erosion of the levees. Herein, we used a DV camera (HDR-XR550V, SONY, Ltd.).

2.2.   Outline of Infiltration Experiments

We conducted an infiltration experiment with a model levee to grasp the influence of the geo-grid layer on the infiltration capacity of the levees. The infiltration experiment was conducted using a water tank that was 1.2 m long, 0.2 m wide, and 0.45 m high, as shown in Figure 5. We set the model levee at 0.2 m high, with a 0.1 m crest width and a 1:2 slope, which are the same conditions as in the overflow experiment. The model levee was set on the foundation at 0.06 m thick. The model levee and foundation were created by compacting Silica sand No. 6 ($D_c = 90$ %), which is a well-sorted fine sand (mean grain size 0.26 mm) with the optimum water content: $w_{opt} = 16.0\%$. The infiltration coefficient k of Silica sand No. 6 is 1.70×10^{-4}. To conduct a constant head permeability test, the water level on the river side of the levee remained constant with a depth of $h = 0.14$ m.
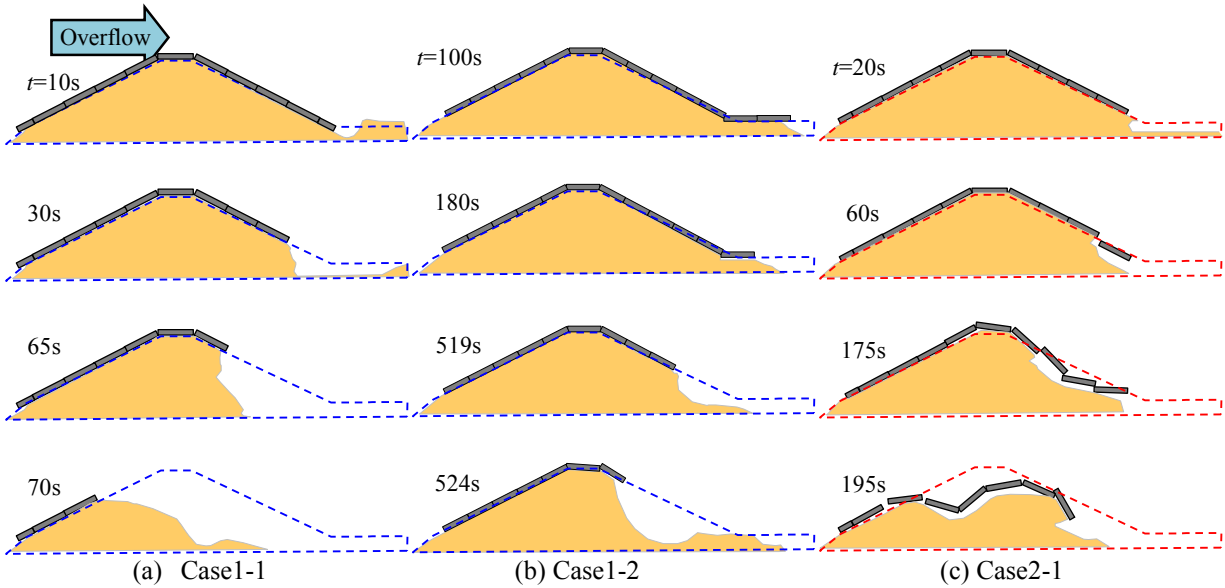
Figure 6. Time variations of the levee shape and position of concrete panels.

Table 2 lists the conditions of the infiltration experiments. An earthen levee and a GRS levee without panels are selected for the reinforcement conditions of the infiltration experiments. For the GRS levees, we used three kinds of geo-grids, where the grid sizes were 9 mm * 10 mm, 2 mm * 8 mm, and 0.6 mm * 0.6 mm, which were the same sizes as in the overflow experiment. The geo-grid layers were laid at 0.02-m intervals. To visualize the infiltration behavior inside the levees, the water was colored using Indian ink. DV images for the side and top views of the levees were recorded to examine the infiltration behavior in the levees and the erosion processes of the levees. To this end, we also used a DV camera (HDR-XR550V, SONY, Ltd.). In addition, to measure the seepage discharge and erosion rate of the levees, we collected the water and sediment at the toe of the back slope of the levees, as shown in Figure 5.

3. RESULTS AND DISCUSSION IN OVERFLOW EXPERIMENT

3.1. Effect of Scour Protection

To verify the effects of scour protection on overflow erosion, Figure 6 indicates the temporal variations in the cross-sectional shapes for the armored levee without scour protection (Case 1-1), the armored levee with scour protection (Case 1-2), and the GRS levee without scour protection (Case 2-1). In the figure, the initial levee surface is drawn with dashed lines. The positions and directions of the concrete panels are also drawn. The geo-grids laying in the GRS levee are omitted from the figure. In addition, note that while the GRS levee with scour protection in Case 2-2 maintained its whole sectional shape beyond the target time, the result of Case 2-2 is omitted from the figure. The result of the armored levee without scour protection indicates the foundation near the toe of the back slope was locally scoured at $t = 10$ s (t: time from start of overflow). Then, the concrete panels near the toe of the levee were swept away and the levee sediments eroded at $t = 30$ s. After the erosion surface reached the crest of the levee at $t = 65$ s, the levee had mostly collapsed at $t = 70$ s. A comparison of the cross-sectional shapes in Cases 1-1 and 1-2 indicates that scour protection can effectively prevent the scour at the toe of the back slope. This means that scour protection improved the resistance of the armored levee against overflow erosion. However, after losing the scour protection, the levee in Case 1-2 was rapidly eroded, showing a pattern similar to that in Case 1-1.
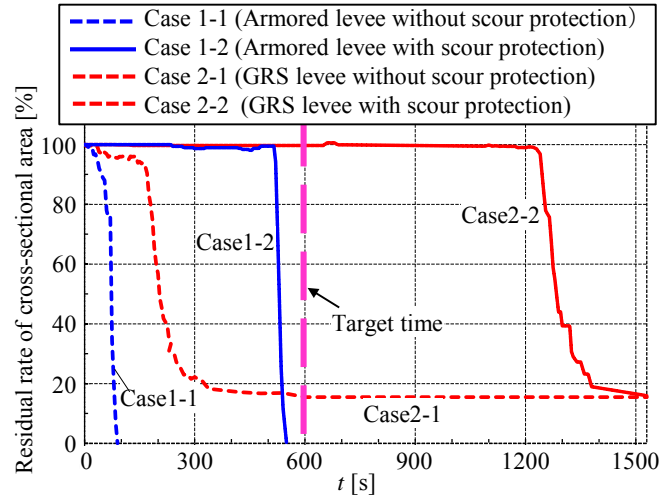
Figure 7. Time variations of residual rate of cross-sectional area in Case 1-1, 1-2, 2-1 and 2-2.
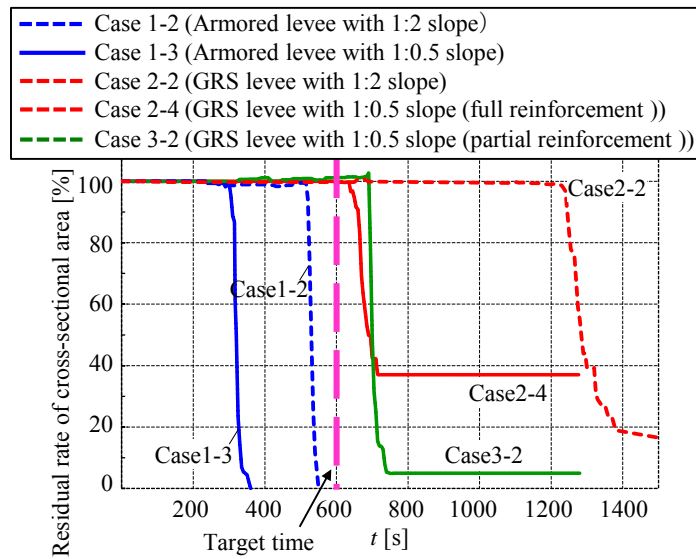
Figure 8. Time series of residual rate of cross-sectional area in Case 1-2, 1-3, 2-2, 2-4 and 3-2.

Figure 7 shows the residual rates of the cross-sectional areas in Cases 1-1, 1-2, 2-1, and 2-2. The residual rate of the cross-sectional area is evaluated with the cross-sectional area at any time divided by the initial cross-sectional area. These results were obtained from the motion picture of the DV camera. The result of the armored levees shows that the residual rates of the cross-sectional areas were 90% in the armored levees with and without scour protection at t = 50 s and 525 s, respectively. This indicates that scour protection can maintain the cross-sectional shape of the levees during lengthy overflow conditions. However, even with scour protection, the armored levee collapsed completely before reaching the target time (= 600 s). On the other hand, in the GRS levee, the scour protection also improved the resistance against overflow erosion. Furthermore, the GRS levee with scour protection maintained its whole sectional shape for 20 min beyond the target time. These facts demonstrate that it is necessary to introduce scour protection to maintain the fundamental form of the GRS levee.

3.2.   Influence of Steep Back Slope and Partial-Length Reinforcement

To examine the influence of back slope on the overflow erosion of the armored and GRS levees, Figure 8 shows the residual rates of the cross-sectional areas of the armored and GRS levees with 1:2 and 1:0.5 slopes. The results in
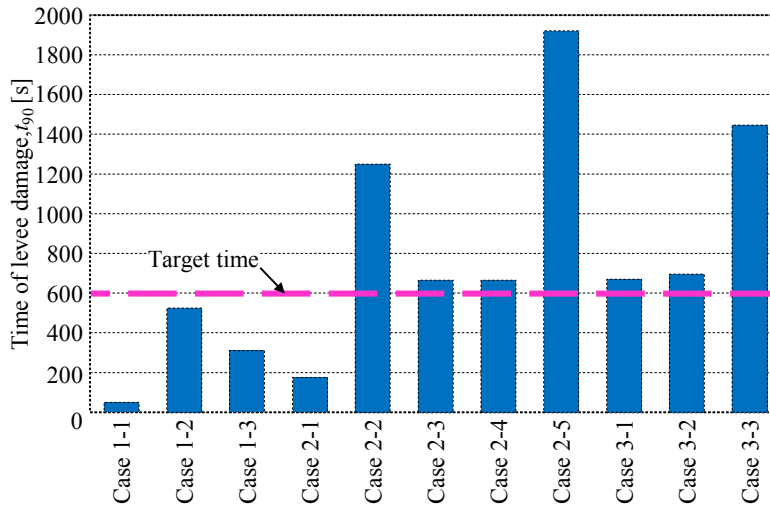
Figure 9. Time of levee damage t_{90} for all of cases.

the GRS levee with a 1:0.5 slope with full- and partial-length reinforcements are shown in the figure. Focusing on the armored levee, the resistance against overflow erosion was reduced by steepening the back slope from 1:2 to 1:0.5. In particular, after losing the scour protection, the residual rates of the cross-sectional areas rapidly decreased in Cases 1-2 and 1-3, and, finally, the armored levee collapsed before the target time. On the other hand, in the GRS levee with a 1:0.5 slope, the residual rate of the cross-sectional shape of the GRS levee was almost 100% even at the target time. This means the GRS levee with a steeper back slope can maintain a high resistance against overflow erosion beyond the target time. Therefore, the GRS levee can significantly improve the resistance against overflow erosion even at a smaller cross section.

A comparison of the results in the GRS levees with full- and partial-length reinforcements shows that the residual rate of the GRS levee with partial-length reinforcement was comparable to that with a full-length reinforcement. The GRS levee with both partial- and full-length reinforcements has a comparably high resistance against overflow erosion, showing that partial reinforcement is also useful to increase the resistance of the levee to overflow erosion. This means the GRS levee with partial reinforcement can be applied to reinforce existing levees.

3.3.   Effect of Grid Size on Geo-Grids

Figure 9 indicates the times of levee damage, t_{90}, for all cases. Here, the time of levee damage t_{90} is defined as the time when the residual rate of the cross-sectional area was 90%. To examine the effects of the grid sizes of geo-grid layers on the resistance against overflow erosion, we here focus on the results of the GRS levees with coarse (Cases 2-3, 3-1), medium (Cases 2-4, 3-2), and fine (Cases 2-5, 3-3) geo-grids. Although the resistance against overflow erosion for the GRS levee with a 1:0.5 slope was lower than that for the 1:2 slope, all cases of GRS levees with a 1:0.5 slope could maintain high resistance against overflow erosion beyond the target time. In the GRS levees with full- and partial-length reinforcements, the t_{90} in the fine geo-grid was larger than those in the coarse and medium geo-grids. The GRS levee using a small-sized geo-grid can maintain a high residual ratio of the cross-sectional area over a long period. Therefore, it is useful to select an appropriate geo-grid layer size for increasing the resistance of the levee to overflow erosion. These results demonstrate that the GRS levee can be a cost-effective measure to increase the resistance against overflow erosion at a small cross-section.
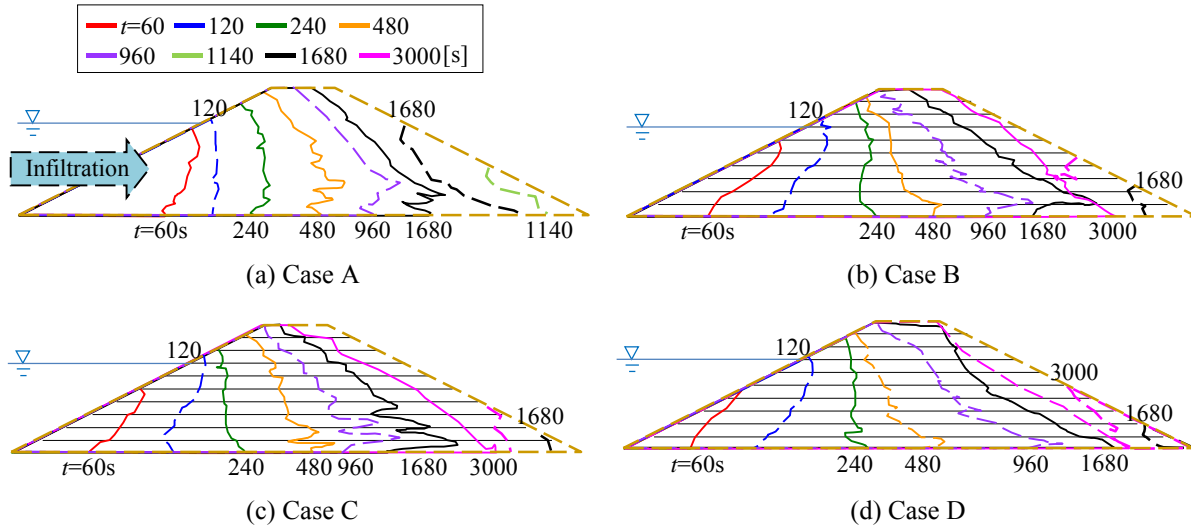
Figure 10. Temporal variation of seepage lines with solid lines and levee erosion with broken lines.
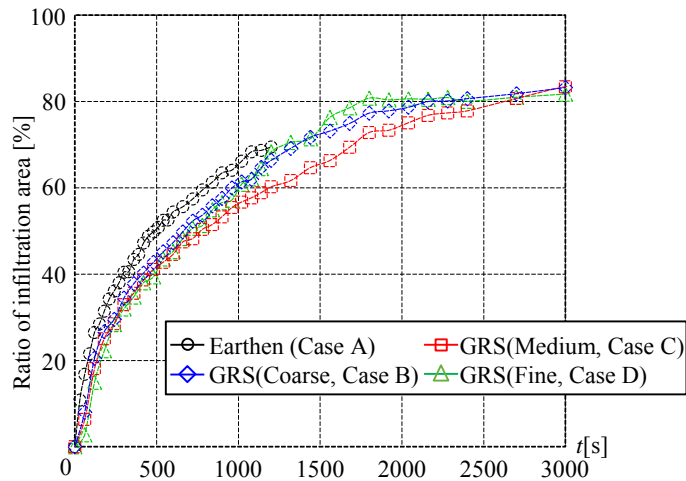
Figure 11. Time series of the ratio of infiltration area.

4. RESULTS AND DISCUSSION IN INFILITRATION EXPERIMENT

To verify the fundamental property of the infiltration into the earthen and GRS levees, Figure 10 shows the temporal variations of seepage lines in all cases of the infiltration experiment. The solid lines show the seepage lines obtained through visualization with Indian ink. The eroded levee shapes are also shown by the broken lines in the figure. The results indicate that the seepage lines were vertically steep initially and transitioned to a milder inclination over time in all cases. This means that the infiltration flows in all cases go toward the toe of the back slope, and the velocity of the infiltration flow is relatively larger near the foundation. The seepage lines were not straight, and the unevenness of the seepage lines appeared not only in the earthen levee, but also in the GRS levees. Furthermore, the height of the unevenness of the seepage lines in the GRS levees did not necessarily correspond to the geo-grid layer. This fact indicates that the water path along the geo-grid layers was not found in this experiment. The eroded area of the earthen levees indicates the erosion near the toe of the back slope started at $t = 1,140$ s and the eroded area increased at 1,680 s. In contrast, the eroded area in the GRS levee with three kinds of geo-grids was smaller than that in the earthen levee, which means the geo-grid layers can function to resist the initial erosion of the levee (Kurakami et al., 2013).
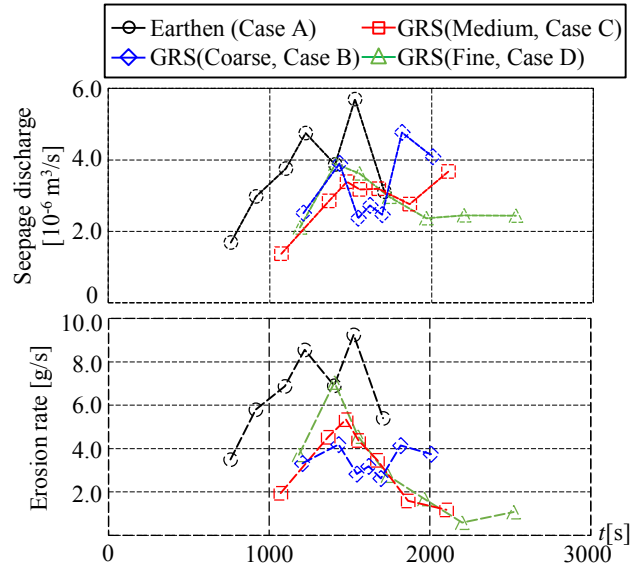
Figure 12. Time series of seepage discharge and erosion rate of the levees.

Figure 11 shows the time series of the ratio of the infiltration area obtained from a motion picture in each case to quantitatively grasp the infiltration property. The ratio of the infiltration area is evaluated with the infiltration area at any time divided by the initial cross-sectional area. These results show that although there were no significant differences in the ratio of the infiltration area among all cases, the ratios of the infiltration areas in the GRS levees were slightly lower than those in the earthen levees, mainly due to the difference in the eroded area.

A time series of the seepage discharge and erosion rate of the levees measured at the downstream end of the water tank is shown in Figure 12. The results indicate that the seepage discharge and erosion rate in the earthen levee were greater than those in the GRS levees. The seepage discharges of the GRS levees were less than those of the earthen levees due to a reduction in the infiltration erosion in the GRS levees.

5. CONCLUSION

In this study, a new type of river levee, a GRS levee, was proposed, and its performance for overflow erosion and infiltration was studied using a series of laboratory model tests. The present study obtained the following conclusions:

1) Scour protection is highly effective both in preventing erosion at the toe of the back slope and in maintaining the stability of the panels covering the levee. Although the armored levee still collapsed before reaching the target time (= 600 s) with scour protection, the GRS levee maintained its whole sectional shape for 20 min, which means the scour protection worked with the GRS levee effectively. Therefore, it is necessary to introduce scour protection to maintain the fundamental form of the GRS levee.

2) The armored levee with a steep back slope (= 1:0.5) collapsed faster than that with a normal slope (= 1:2). However, the GRS levee with a steep back slope maintained a high resistance against overflow erosion after the target time. The GRS levee with partial- and full-length reinforcements has a comparably high resistance against overflow erosion, showing that partial reinforcement is also useful to increasing the resistance of the levee to overflow erosion. This means the GRS levee with partial reinforcement can be applied to reinforce existing levees.

3) The GRS levee using a small-sized geo-grid can maintain a high residual ratio of the cross-sectional area over a long period. Therefore, it is useful to select an appropriate geo-grid layer size for increasing the resistance of the levee against overflow erosion.

4) The infiltration discharge of the GRS levee was less than that of the levee with no reinforcement due to reduction in infiltration erosion in the GRS levee. Introducing a geo-grid was not a disadvantage to making a water path, but it contributed to making the back slope more stable against slope failure.

However, the results shown in this paper were obtained from small-scale model tests, so the reliability of the measured data might not necessarily be exact. More experimental tests under different conditions will be needed to study the details. In addition, it is difficult to satisfy the similarity law completely because in this study, we used various materials composed of concrete panels and geo-grids. Therefore, large-scale model tests with a levee height of more than 1 m should be conducted in the near future.

6. ACKNOWLEDGEMENTS

7. REFERENCES

Powledge, G.R., Ralston, D.C., Miller, P., Chen Y.H., and Clopper, P.E. (1989). "Mechanics of overflow erosion on embankments: I. Research activities." *J. Hydraulic Eng.*, 115(8), 1040-1055.

Hughes, S. (2008). "Levee overtopping design guidance: What we know and what we need." *Solutions to Coastal Disasters*, 867-880. doi: 10.1061/40968(312)78.

Kurakami, K., Nihei, Y., Yada, K., Yamazaki, T., Yamaguchi, S., Kawabe, S., Kikuchi, Y., and Tatsuoka, F. (2013). "Design for River Levee with Increased Resistance against Overflow Erosion." *Proc. of 2013 IAHR World CONGRESS*, 8 pages, USB.

Tatsuoka, F., Tateyama, M., Uchimura, T., and Koseki, J. (1997). "Geosynthetic-reinforced soil retaining walls as important permanent structures, 1996-1997 Mercer Lecture." *Geosynthetic International*, 4(2), 81-136.

Tatsuoka, F., Koseki, J., Tateyama, M., Munaf, Y., and Horii, N. (1998). "Seismic stability against high seismic loads of geosynthetic-reinforced soil retaining structures." *Proc. 6th Int. Conf. on Geosynthetics*, Atlanta, 1, 103-142.

Tatsuoka, F., Hirakawa, D., Nojiri, M., Aizawa, H., Nishikiori, H., Soma, R., Tateyama M., and Watanabe K. (2009). "A new type integral bridge comprising geosynthetic-reinforced soil walls." *Geosynthtetics International, IS Kyushu 2007 Special Issue*, 16(4), 301-326.

Yoshikawa, K. (2008), "Study for River Levee", Gihodo Shuppan, pp.1-270 (in Japanese).

Baffle Designs to Facilitate Fish Passage in Box Culverts: A Preliminary Study

H. Chanson[1] and W. Uys[1]
[1]School of Civil Engineering
The University of Queensland
Brisbane QLD 4072
Australia
E-mail: h.chanson@uq.edu.au

ABSTRACT

Waterway culverts and road crossings are very common structures along water systems, ranging from rural roads to national highways and urban drainage networks. Present expertise in environmental hydraulics of culverts is deficient because of the many empirically-based design guidelines, which are sometimes outdated and often inadequate for fish passage. Engineers and biologists need better, more reliable prediction 'tools' during the design stages to compare the bio-engineering performances of a range of design options. In all the cases, the turbulence of the flowing waters must be optimized efficiently to maximize fish migration. This project focused on the development of simple solutions to retrofit existing box culverts, with the aim to maximize slow flow regions suitable for small fish passage and to minimize the afflux increase. Herein, a physical study of a standard box culvert was performed under controlled flow conditions, and six baffle designs were tested. Two baffle configurations presented promising results: the corner baffles and the streamlined diagonal baffles. The streamlined diagonal baffles assisted with the development of a large recirculation region immediately downstream of each baffle, with a moderate increase in afflux for a given discharge. The optimum design appeared to be the corner baffle system. It produced little additional afflux, while creating excellent recirculation both upstream and downstream of each baffle. However, further testing must be conducted to develop quantitative design guidelines and to assess the impact on real fish passage.

Keywords: Standard box culvert, Small fish passage, Baffles, Physical modelling.

1. INTRODUCTION

Culverts are road crossings that pass under a roadway embankment to allow a continuous flow of water. Numerous waterway culverts are installed worldwide. Culvert designs are diverse, using various shapes and materials determined by stream width, peak flows, stream gradient, and minimum cost (Chanson 2004). For the past two decades, concerns regarding the ecological impact of culvert crossings have led to changes in their design. Although the overall culvert discharge capacity is based on hydrological and hydraulic engineering considerations, large culvert flow velocities may create a fish passage barrier. In some cases, the environmental impact on fish passage may affect the upstream catchment with adverse impact on the stream ecology because the installation of road crossings can limit the longitudinal connectivity of streams for fish movement (Warren and Pardew 1998, Brigg and Galarowicz 2013).

Common culvert fish passage barriers include excessive vertical drop at the culvert outlet (perched outlet), high velocity or inadequate flow depth within the culvert barrel, excessive turbulence, and debris accumulation at the culvert inlet (Olsen and Tullis 2013). The increased velocities in the barrel can also produce reduced flow depths (potentially inadequate flow depths for fish passage) relative to the culvert size. Higher culvert exit velocities may also increase perched outlet fall heights (fish barrier) with increased scour hole development downstream.

One of the primary ecological concerns regarding culvert crossings is the potential velocity barrier to upstream fish passage resulting from the constriction of the channel. In an effort to minimize the impact of culvert crossings on stream ecology, several jurisdictions have developed guidelines to ensure that their design will allow for the upstream passage of fish. In Canada, these guidelines are based on a number of criteria including average flow velocity and minimum embedment depth (Hunt et al. 2012).

For culvert rehabilitation applications where fish passage may be a concern, baffles installed along the invert may provide a more fish-friendly alternative, provided that adequate culvert discharge capacity is maintained (Olsen and Tullis 2013). Baffles would decrease the flow velocity and increase the water depth for fish passage.

Although culvert type may not have a major role influencing the fish longitudinal movement, a general data trend indicated that box culverts were most effective (Brigg and Galarowicz 2013). The culvert length is another important factor in allowing upstream passage of some fish species. For example, in northeastern Kansas streams, fish movement data supported culvert length as an important factor since the culverts limiting upstream fish passage were the longest culverts in the study (Brigg and Galarowicz 2013). The behavioral response by some fish species to culvert length and flow turbulence could play a role in their swimming ability and culvert passage rate. A recent discussion paper recommended that three-dimensional analysis of culvert flows should be considered to gain an understanding of the turbulence and secondary flow motion (Papanicolaou and Talebbeydokhti 2002). The authors recommended an in-depth examination of the spanwise and vertical velocity distributions as well as turbulent intensities and kinetic energy in view of the importance of these parameters to fish passage.

The critical parameters of a culvert in terms of fish passage are the dimensions of the barrel, including its length and cross-sectional characteristics and the slope. These geometric characteristics, together with the water levels upstream and downstream of the structure, determine the hydraulic behavior of the culvert, i.e. the flow discharge, the head loss through the culvert, the flow pattern, and the turbulent velocity field in the barrel (Henderson 1966, Hee 1969, Chanson 2004). The variability of the culvert dimensions is linked to the characteristics and constraints of the site where the road crossing has to be built, the flow discharge passing through the facility, and the compliance with specifications for volumetric power dissipation. This variability results in a wide diversity in flow patterns that can be observed in existing culverts. These flow patterns are one of the elements determining the capacity of the facility to allow the targeted fish species to pass successfully. Indeed, observations in fishways showed that fish behavior was strongly affected by the turbulent flow and its structure (David et al. 2012).

1.1. Designing a Culvert Fish Pass

The selection of the type of culvert fish pass and of the fish pass characteristics depends on the swimming capacities of the fish species. If the fish swimming power is greater than the maximum volumetric power (Bates 2000), the fish will be able to pass the successive baffles and rest in each pool, thus successfully negotiating a fish pass consisting of a large number of pools without difficulty. Currently, there is no simple technical means for measuring the characteristics of turbulence in a fish pass, although it is acknowledged that the turbulence in a fish pass plays a key role in fish behavior (Liu et al. 2006, Yasuda 2011, Bretón et al. 2013). The key turbulence characteristics, which are deemed most important to migrating fish, have been identified as turbulence intensity, Reynolds stresses, turbulent kinetic energy, vorticity, and dissipation (Pavlov et al. 2000. Hotchkiss 2002, Nikora et al. 2003). Recent observations further showed that fish may take advantage of the unsteady character of the turbulent flow (Wang et al. 2010, Tarrade et al. 2011).

In Australia, national guidelines on fish passage requirements for waterway crossings developed in 2003 were based on limited data for native Australian fish. The biological information that underpinned these recommendations was based on research and evaluation of overseas fish species (e.g., salmonids) that display vastly superior swimming capabilities than most Australian native fish. Currently, Australian national recommendations provide little guidance concerning specific culvert design parameters. They merely indicate that water depth should range between 0.2 to 0.5 m with bulk velocity less than 0.3 m/s during base flows, and the culvert cross-sectional area should maximize geometric similarities of the natural waterway profile (Fairfull and Witheridge 2003), thus yielding uneconomical culvert designs. Newer research suggested that bulk velocity maxima should to be revised down to 0.1 m/s for culvert lengths up to 15 m (Rodgers et al. 2014).

In this paper, the hydraulic testing of a range of baffle designs in a standard box culvert was conducted. Physical modelling was conducted in a laboratory under controlled flow conditions to test a variety of baffle designs, with the aim to minimize the afflux increase and to maximize slow flow and recirculation regions suitable to small fish passage. The project focused on the development of simple solutions to retrofit existing box culverts.

2. EXPERIMENTAL FACILITY AND PHYSICAL MODELLING

2.1. Physical Facility

Physical modeling was conducted in a box culvert model located in the AEB hydraulics laboratory at the University of Queensland (Figure 1). All tests were conducted with clear water and without fish. The model culvert had the following barrel internal dimensions: $W = 0.150$ m, $H = 0.105$ m, and $L = 0.50$ m, where W = width, H = height, L = length of the barrel. The barrel invert was aligned with the upstream and downstream channel bed. The design flow conditions of the model were a design discharge: $Q_{des} = 0.010$ m³/s, a tailwater depth at design flow: $d_{tw} = 0.038$ m, with a corresponding afflux: $\Delta h = 0.087$ m. This model was constructed at a scale of 1:7 to 1:20 depending upon the full-scale application.

The model was tested for eight flow rates between $Q = 0.001$ m³/s and 0.014 m³/sec, each with three downstream water depths of 0.020 m, 0.038 m, and 0.045 m. Water was supplied from a constant head tank. The flow rate was measured by a Venturi meter calibrated on site, and the water depths were recorded with a pointer gauge. Visual observation of flow recirculation and flow turbulence was conducted by injecting vegetable blue dye around points of interest. Photographs and video movies were taken to characterize the slow flow motion and recirculation regions.
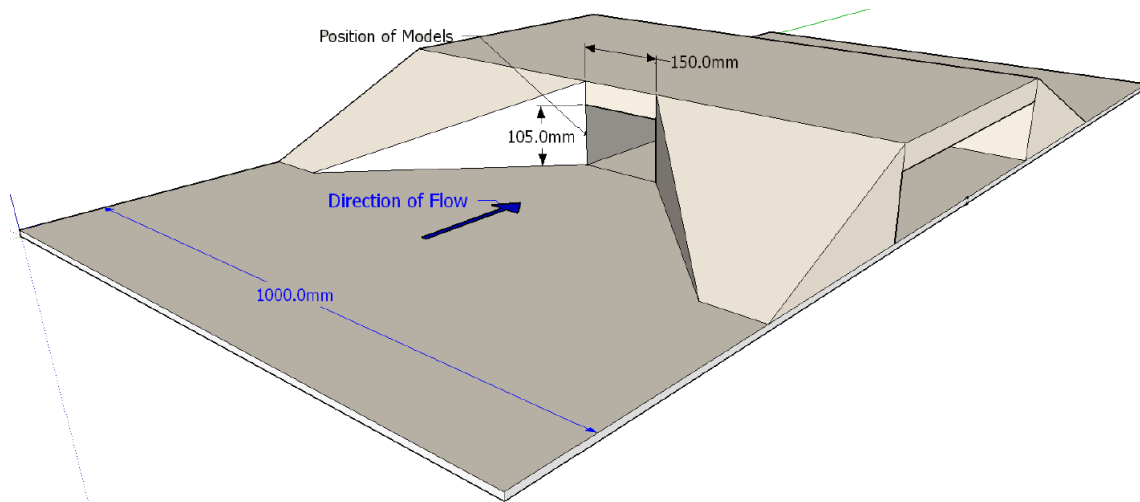
Figure 1. Box culvert model: dimensioned sketch

2.2. Baffle Designs

Six different designs were selected and tested (Figure 2). The corner baffle design and both diagonal baffle designs aimed to generate recirculation in the barrel. The partial pipe system and the rough inverts were designed to reduce the bulk velocity through the culvert barrel. The models were constructed on either a false bottom or a false bottom and sidewall (4 mm thick). This allowed the quick installation and replacement of models, although it is acknowledged that the increase in invert elevation and the narrowing of the barrel caused by the false plates had some impact on the flow.

The corner baffle system (Figure 2e) used the false bottom and side as a base. Triangular baffles were fixed in the bottom left corner of the model to both the false plates. Each triangular baffle was 0.02 m high and wide, and a baffle was positioned every 0.10 m. The most upstream baffle was positioned 0.05 m inside the barrel, and the most downstream baffle was positioned 0.05 m before the barrel outlet.

The partial pipe design (Figure 2b) aimed to slow down the velocity by reducing the hydraulic diameter along the bottom corner. Gaps between rectangular plates were introduced to avoid fish traveling through complete darkness

since fish tend to be attracted to regions of light (Bretón et al. 2013). The system was constructed with a false bottom and side. The rectangular plates were 0.05 m by 0.03 m fixed diagonally at 45°. Seven plates were installed, with a gap of 0.025 m between plates. The first plate was fixed with its leading edge in line with the barrel entrance.

The model with diagonal baffles (Figure 2c) consisted of 0.012 m high baffles fixed to a false bottom. The baffles were oriented to 60° with the streamwise flow direction, and they were positioned with a 0.01 m gap between the barrel sidewalls and the baffles. Each baffle was constructed from 0.012m×0.012m aluminium angle, and all were orientated the same way, with 0.10 m longitudinal spacing between baffles. The leading edge of the most upstream baffle was located 0.0125m inside the barrel.

The streamlined diagonal baffle design (Figure 2d) was based upon the diagonal baffles model. 30° ramps were installed upstream of each baffle to reduce the energy loss.
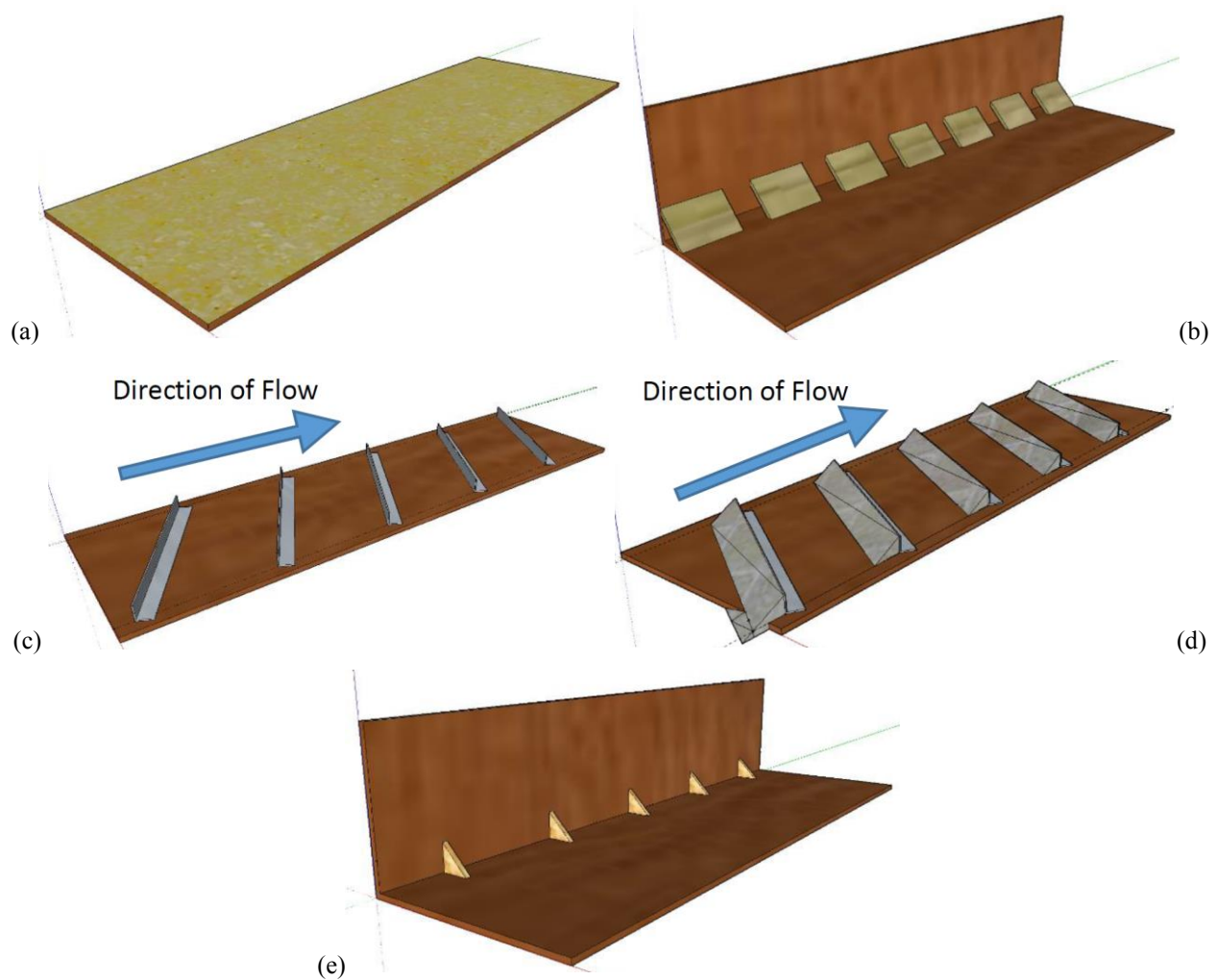
Figure 2. Baffle designs - From top to bottom, left to right: rough sand paper, partial pipe system, diagonal baffles, streamlined diagonal baffles and corner triangular baffles

The last two models used a rough invert (Figure 2a). This aimed to replicate a nature-like stream bed within the barrel. Culverts that had a nature-like invert were thought of as being capable of facilitating fish passage. Each model consisted of a sheet of sandpaper fixed to a false bottom. The first model used grade P40 sandpaper, while the second used grade P60 sandpaper. The rugosity of the sand papers was an average particle size of $k_s = 0.425$ mm and $k_s = 0.269$ mm for the P40 and P60 sandpaper, respectively. (Washington Mills 2015).

3. FLOW PATTERNS AND RECIRCULATIONS

Basic flow patterns were investigated systematically for all discharge and tailwater levels. The followings summarizes the key outcomes.

The rough invert (sand paper) designs slowed the fluid velocity along the surface of the invert. The effect of the P40 sandpaper was greater than that of the P60 sandpaper. In both cases, the effect was restricted to a very thin layer of fluid immediately above the invert (Figure 3, Top). With the partial pipe system, the decrease in velocity did not appear to be significant when compared to the variability in flow velocity within the barrel (Figure 3, 2nd from top). Combined with the lack of flow recirculation, the design was not a practical solution for fish passage.

The diagonal baffle design had different impacts depending upon the discharge. At low flows, the design caused a hydraulic drop immediately downstream of the last baffle, which would be an obstacle for fish passage. At larger flows, the diagonal baffles created regions of helicoidal recirculation (Figure 3, 3rd from top). Although these could act as resting spots for fish, it is unknown whether many fish species could take advantage of such a recirculation motion. Practically, the diagonal baffle system had the potential to cause a debris build-up within the barrel. The effectiveness of the diagonal baffle system was improved by the installation of a ramp in front of each baffle. The ramp reduced the drag caused by a baffle and may reduce the build-up of debris due to the flow streamlining.

The corner baffle design succeeded in creating recirculation eddies. The triangular baffles caused recirculation zones extending both upstream and downstream (Figure 3, Bottom). For the model dimensions, the spacing between baffles allowed the upstream and downstream recirculation zones to connect. The patterns of these recirculation zones were close to those described by Liu et al. (1966). Overall, the corner baffles generated recirculation currents that could allow fish to rest between episodes of burst speed or sustained speed swimming (Baker and Votapka 1990).

4. RELATIONSHIP BETWEEN UPSTREAM WATER LEVEL AND DISCHARGE

For a range of flow conditions, the relationship between upstream water level and discharge was investigated for all six designs and for the (original) un-modified box culvert. Figure 4A presents the results for the original box culvert, with the thick blue line highlighting the design flow conditions. The culvert performed under inlet control for flow rates including and above $Q = 0.0035$ m³/s. At low flow rates, the culvert operated as outlet control. That is, the upstream water height was a function of tailwater depth. The box culvert was also tested with a false bottom model and a false bottom and side model without any baffle. The differences were small to negligible compared to the (original) un-modified box culvert (see for example Figure 5).

For all baffle design configurations, the relationship between headwater level and discharge was tested. Typical results are presented in Figure 4B. The rough sand paper invert designs, corner baffle design, and partial pipe design yielded the smallest increase in afflux for a given discharge and tailwater level. The largest increase in afflux was observed with the diagonal baffle design for all flow conditions, with an increase in afflux of 0.01 m to 0.02 m (Figure 4B). The streamlined diagonal baffle design yielded intermediate results.
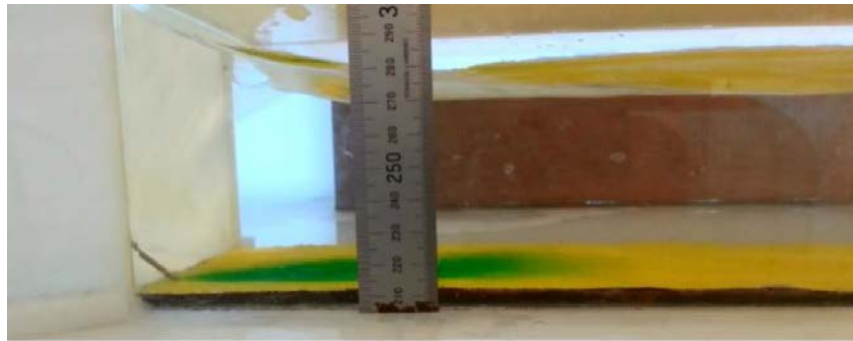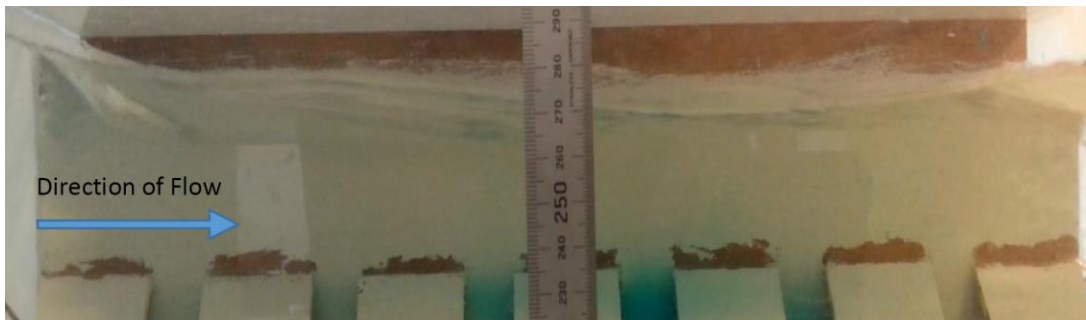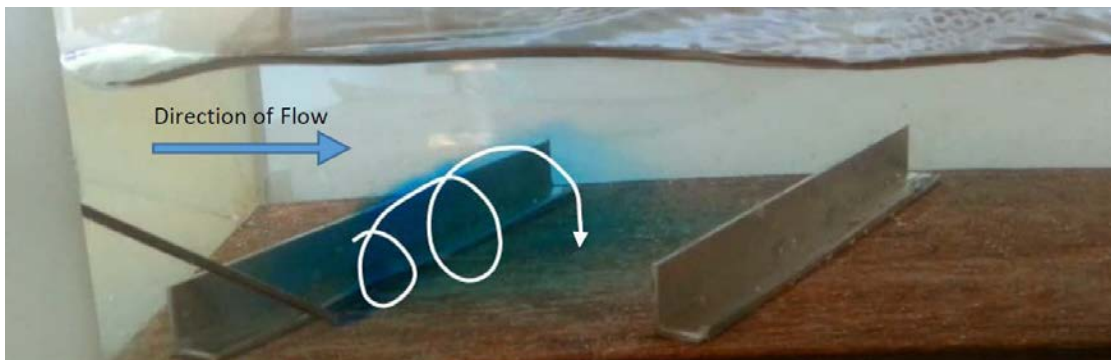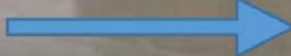
Figure 3. Photographs of slow flow and recirculation regions in the culvert barrel highlighted using dye injection - Flow direction from left to right
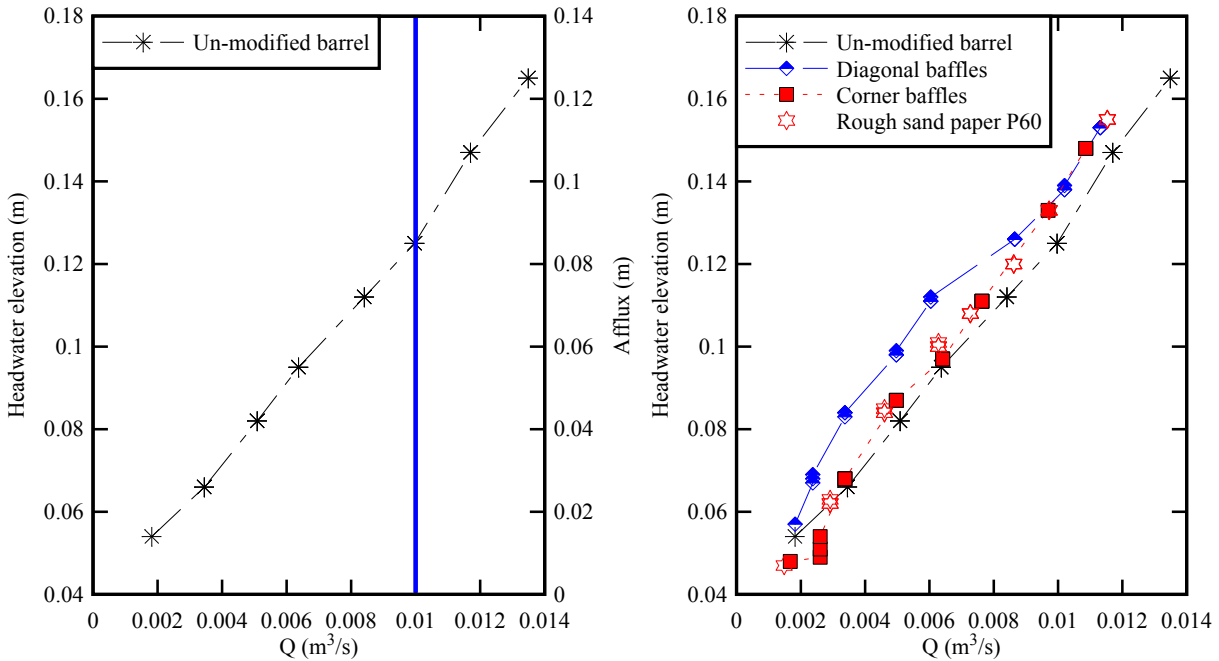
(A, Left) Original, un-modified box culvert - Solid blue line: design discharge

(B, Right) Box culvert equipped with baffle designs

Figure 4. Relationship between upstream water depth and discharge

5. DISCUSSION

With the diagonal baffle design, two different flow regimes were present within the barrel for flow rates larger than $Q = 0.00935$ m³/s: drowned conditions and un-drowned conditions (Figure 6). Figure 6A presents an un-drowned flow motion and Figure 6B a drowned flow condition (flow from left to right). The barrel was un-drowned at small flow rates. When the flow rate increased slowly, the barrel changed flow regimes into drowned conditions (Fig. 6B). In order to retain the initial un-drowned condition, the flow rate needed to increase relatively rapidly to the new flow conditions (Figure 6A). In practice, the transition between the two states of barrel flow might be abrupt as discussed by Montes (1997) and might lead to large pressure and pressure fluctuations on the obvert, which should be avoided.

Interestingly, the afflux Δh was smaller under drowned conditions for a given discharge $Q > 0.00935$ m³/s (Fig. 5). This is illustrated in Figure 5 where the upstream water level is presented as a function of the discharge, the drowned flow conditions being shown with red colored symbols. The lower value for afflux, developed from the drowned barrel conditions, should not be used to design box culverts with diagonal baffles, however. The results were unrelated to the tailwater level, within $0.020 < d_{tw} < 0.045$ m.

Lastly, the present laboratory experiments were conducted for Reynolds numbers ranging from 3×10^4 to 1×10^5. The laboratory flow conditions corresponded to turbulent flows, in line with the literature recommending that the physical model flows be turbulent, with the same relative roughness as for the prototype (Novak and Cabelka 1981, Hughes 1993, Chanson 2004). Any extrapolation of the results to full-scale must, however, be conducted with care, and full-scale testing should be considered.
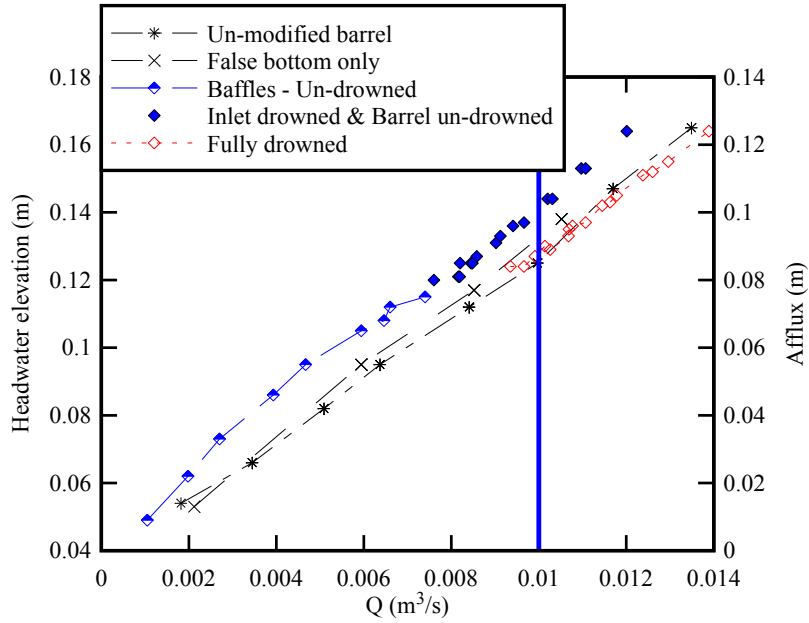
Figure 5. Relationship between upstream water depth and discharge for diagonal baffle design: effect of barrel flow conditions - Thick blue line: design discharge

(A) Un-drowned barrel flow conditions for $Q = 0.012$ m³/s, $\Delta h = 0.126$ m

(B) Drowned barrel flow conditions for $Q = 0.0139$ m³/s, $\Delta h = 0.126$ m
Figure 6. Operation of box culvert with diagonal baffle design at large discharges - Flow direction from left to right

6. CONCLUSION

Physical modelling of a standard box culvert was performed with a range of baffle designs. The study aimed to minimize the increase in afflux and to maximize slow flow and recirculation regions, which might facilitate the passage of fish with small body mass, upstream migration in particular. A total of six configurations plus the un-modified box culvert were tested.

Two baffle configurations presented promising results: the corner baffle design and the streamlined diagonal baffle design. The streamlined diagonal baffles assisted with the development of a large recirculation region immediately downstream of each baffle, with a moderate increase in afflux for a given discharge. However, it should not be used until further investigation is conducted on both fish behavior in the helicoidal recirculation and development of drowned conditions. Overall, and based upon physical modelling, the optimum design appeared to be the corner baffle system. It produced little additional afflux while creating excellent recirculation regions both upstream and downstream of each baffle, which might be suitable to small fish typical of Australian streams.

It must be acknowledged that the present findings are preliminary. Further design testing must be conducted to develop quantitative design guidelines with optimum baffle dimensions and spacing. Tests must further encompass impact on real fish passage: that is, in a laboratory using fish-friendly facilities and complemented by field monitoring of prototype structures.

7. ACKNOWLEDGMENTS

8. REFERENCES

Baker, C.O., and Votapka, F.E. (1990). Fish passage through culverts. Dept. of Transportation, Federal Highway Administration, United States Department of Agriculture, Forest Service, Washington, D.C., USA.

Bates. K. (2000). Fishway guidelines for Washington State. Washington Department of Fish and Wildlife, 57 pages.

Bretón, F., Baki, A.B.M., Link, O., Zhu, D.Z., and Rajaratnam, N. (2013). Flow in nature-like fishway and its relation to fish behaviour. *Canadian Journal of Civil Engineering*, Vol. 40, No. 6, pp. 567-573(DOI: 10.1139/cjce-2012-0311).

Briggs, A.S., and Galarowicz, T.L. (2013). Fish Passage through Culverts in Central Michigan Warmwater Streams. *North American Journal of Fisheries Management*, Vol. 33, No. 3, pp. 652-664 (DOI: 10.1080/02755947.2013.788589).

Chanson, H. (2004). The Hydraulics of Open Channel Flow: An Introduction. Butterworth-Heinemann, 2nd edition, Oxford, UK, 630 pages.

Fairfull, S., and Witheridge, G. (2003). Why do fish need to cross the road? Fish passage requirements for waterway crossings. NSW Fisheries, Cronulla NSW, Australia, 14 pages.

David, L., Calluaud, D., Pineau, G., and Texier, A. (2012). Fishway Hydrodynamics and Global Approaches for insuring the Upstream Migration around Dams. *Proc. 4th IAHR International Symposium on Hydraulic Structures*, APRH - Associação Portuguesa dos Recursos Hídricos (Portuguese Water Resources Association), J. Matos, S. Pagliara & I. Meireles Editors, 9-11 February 2012, Porto, Portugal, Paper 4, 15 pages (CD-ROM).

Hee, M. (1969). Hydraulics of Culvert Design Including Constant Energy Concept. *Proc. 20th Conf. of Local Authority Engineers*, Dept. of Local Govt, Queensland, Australia, paper 9, pp. 1-27.

Henderson, F.M. (1966). Open Channel Flow. MacMillan Company, New York, USA.

Hotchkiss, R. (2002). Turbulence investigation and reproduction for assisting downstream migrating juvenile salmonids, Part I. BPA Report DOE/BP-00004633-I, Bonneville Power administration, Portland, Oregon, 138 pages.

Hughes, S.A. (1993). Physical Models and Laboratory Techniques in Coastal Engineering. Advanced Series on Ocean Engineering, Vol. 7, World Scientific Publ., Singapore, 568 pages.

Hunt, M., Clark, S., and Tkach, R. (2012). Velocity distributions near the inlet of corrugated steel pipe culverts. *Canadian Journal of Civil Engineering*, Vol. 39, No. 12, pp. 1243-1251 (DOI: 10.1139/l2012-112).

Liu, C.K., Kline, S.J., and Johnston, J.P. (1966). An Experimental Study of Turbulent Boundary Layer on Rough Walls. Report ND-15, Stanford University, Dept of Mechanical Engineering, 171 pages.

Liu, M.M., Rajaratnam, N., and Zhu, D,Z. (2006). Mean flow and turbulence structure in vertical slot fishways. *Journal of Hydraulic Engineering*, ASCE, Vol. 139, No. 4, pp. 424-432.

Montes, J.S. (1997). Transition to a Free-Surface Flow at End of a Horizontal Conduit. Journal of Hydraulic Research, IAHR, Vol. 35, No. 2, pp. 225-241.

Nikora, V., Aberle, J., Biggs, B., Jowett, I., and Sykes, J. (2003). Effects of fish size, time-to-fatigue and turbulence on swimming performance: a case study of Galaxias maculatus. *Journal of Fish Biology*, Vol. 63, pp. 1365-1382.

Novak, P., and Cabelka, J. (1981). Models in Hydraulic Engineering. Physical Principles and Design Applications. Pitman Publ., London, UK, 459 pages.

Olsen, A.H., and Tullis, B.P. (2013). Laboratory Study of Fish Passage and Discharge Capacity in Slip- Lined, Baffled Culverts. *Journal of Hydraulic Engineering*, Vol. 139, No. 4, pp. 424-432 (DOI: 10.1061/(ASCE)HY.1943-7900.0000697).

Papanicolaou, A.N., and Talebbeydokhti, N. (2002). Discussion of Turbulent open-channel flow in circular corrugated culverts. *Journal of Hydraulic Engineering*, Vol. 128, No. 5, pp. 548–549.

Pavlov, D.S., Lupandin, I.A., and Skorobogatov, M.A. (2000). The effects of flow turbulence on the behavior and distribution of fish. *Jl Ichthyol*, Vol. 40, pp. S232–S261.

Rodgers, E.M., Cramp, R.L., Gordos, M., Weier, A., Fairfall, S., Riches, M., and Franklin, C.E. (2014). Facilitating upstream passage of small-bodied fishes: linking the thermal dependence of swimming ability to culvert design. *Marine and Freshwater Research*, Vol. 65, pp. 710-719 (DOI: 10.1071/MF13170).

Tarrade, L., Manceau, R., Texier, A., David, L., and Larinier, M. (2005). Etude numérique des écoulements hydrodynamiques turbulents dans une passe à poissons. *Proceedings of the 17ème Congrès Français de Mécanique*, Troyes, France, 6 pages (in French).

Wang, R.W., David, L., and Larinier, M. (2010). Contribution of experimental fluid mechanics to the design of vertical slot fish passes. *Knowledge and Management of Aquatic Ecosystems*, Vol. 396, No. 2, 21 pages (DOI: 10.1051/kmae/2010002).

Warren, M.L., Jr., and Pardew, M.G. (1998). Road crossings as barriers to small-stream fish movement. *Transactions of the American Fisheries Society*, Vol. 127, pp. 637–644.

Washington Mills. (2015). Particle Size Conversion Chart - ANSI. <http://www.washingtonmills.com/guides/grit-sizes-ansi/particle-size-conversion-chart-ansi/> (Retrieved 5th June, 2015).

Yasuda, Y. (2011). Guideline of Fishway for Engineers. Corona Publishing, NPO Society for Fishway in Hokkaido, Japan, 154 pages (in Japanese).

Steady and Unsteady Turbulent Velocity Profiling in Open Channel Flows Using the ADV Vectrino II Profiler

X. Leng[1] and H. Chanson[1]
[1]School of Civil Engineering
The University of Queensland
Brisbane QLD 4072
Australia
E-mail: h.chanson@uq.edu.au

ABSTRACT

The Nortek Vectrino II profiler acoustic Doppler velocimeter (ADV) was developed for velocity profiling. Herein, the study aims to 1) demonstrate the applicability of the ADV profiler to steady and rapidly-varied unsteady open channel flows, 2) check the data quality, based upon a new systematically comparative analysis with traditional ADV data, and 3) conduct a sensitivity analysis on ensemble-averaged data collection in a positive surge. This was achieved by systematically performing steady and unsteady velocity measurements under controlled flow conditions in a relatively large laboratory facility. All experiments were repeated 25 to 50 times for each controlled flow condition and the results were ensemble-averaged. Steady and unsteady velocity measurements highlighted a number of instrumental errors using the ADV Profiler. Overall, the study demonstrated that the propagation of positive surges was a highly unsteady turbulent process, and the performance of ADV Profiler in such an unsteady turbulent flow could be satisfactory provided that careful validation was undertaken for all ADV Profiler outputs.

Keywords: *ADV Vectrino II profiler, Instrumentation, Steady and unsteady flows, Positive surge, Validation process.*

1. INTRODUCTION

In an open channel, steady flow conditions may be achieved when the discharge and boundary conditions remain constant for a reasonable period of time. The operation of any regulation device, such as a gate, is associated with unsteady flow motions: positive and negative surges (Liggett 1994, Chanson 2004). Geophysical applications include tidal bores and tsunami propagating into river systems. Turbulence in open channel flows has been studied for decades (Nakagawa and Nezu 1977, Nezu 2005). Most data were obtained in steady flows: e.g., using laser Doppler anemometry, particle image velocimetry, or acoustic Doppler velocimetry. Measurements in rapidly-varied unsteady flows are less common (Hornung et al. 1995, Koch and Chanson 2009, Leng and Chanson 2015). Herein, new unsteady velocity measurements were performed systematically under controlled flow conditions using a Nortek[TM] acoustic Doppler velocimeter Vectrino II Profiler equipped with a fixed-probe down-looking head. Both steady and unsteady measurements were performed in a relatively large laboratory facility. The quality and accuracy of the present data set obtained using the Profiler were validated against data collected with an Nortek[TM] acoustic Doppler velocimeter Vectrino+.

2. VELOCITY MEASUREMENTS

Two velocimeters were deployed in the present study: a Nortek[TM] acoustic Doppler velocimeter Vectrino II Profiler (Serial number P27338, Hardware ID VNO 1366) and a Nortek[TM] acoustic Doppler velocimeter (ADV) Vectrino+(Serial No. VNO 0436). The latter, referred to as ADV, was used to validate the Profiler data. The Vectrino II Profiler is a high-resolution acoustic Doppler velocimeter used to measure turbulence and three-dimensional water velocity (Nortek 2012). The basic measurement technology is coherent Doppler processing (Zedel and Hay 2011, Nortek 2012). Herein, the Profiler was equipped with a fixed downward-looking head, one central emitter, and four receivers. The Profiler was capable of recording velocity components simultaneously in a vertical profile of up to 35 mm in height (Figure 1-left). The minimum distance from the emitter was 40 mm to the first point of the profile. Two profiling ranges were tested: 30 and 35 mm. The height of each sampling cell was 1 mm: e.g., a profiling range of 35 mm consisted of 35 sampling cells sampled simultaneously. The velocity range was ±1.0 m/s, and the sampling frequency was 100 Hz. The Profiler was located at x = 2.0, 7.87 m, or 8.5 m, where x was the longitudinal distance measured from the channel upstream end. The ADV was

equipped with a three-dimensional side-looking head (Figure 1-right). The ADV was set up with a velocity range ±1.0 m/s , a transmit length of 0.3 mm, a sampling volume of 1.5 mm height, and power setting High. Two sampling frequencies were used: in the steady flow measurements, the ADV was sampled at 200 Hz; during the unsteady flow experiments, the ADV was sampled at 100 Hz. The Profiler output data were post-processed with the Matlab program VTMT version 1.1 (Becker 2014). In steady flows, the post-processing included the removal of data with average correlation values less than 90% and average signal to noise ratio less than 5 dB. In addition, the phase-space thresholding technique developed by Goring and Nikora (2002) was applied to removal spurious points in the data set. In the unsteady flows, the above post-processing technique was not applicable (Nikora 2004, *Person. Comm.*, Chanson 2008, Koch and Chanson 2009), and raw data was used directly for analysis.
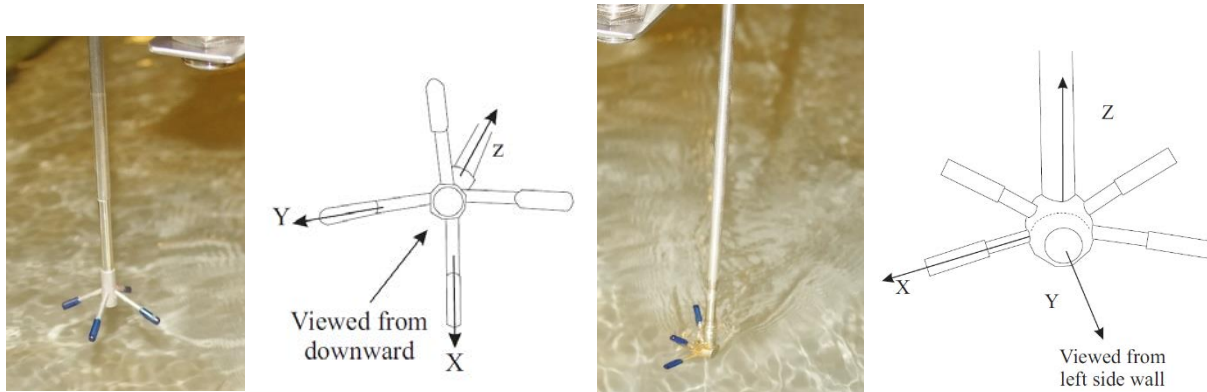
Figure 1. Photographs and coordinated sketches of ADV Vectrino II Profiler and ADV Vectrino+. (Far Left) Profiler photograph; (Left) Profiler definition sketch; (Right) ADV photograph (Far Right) ADV definition sketch.

3. EXPERIMENTAL SETUP AND FLOW CONDITIONS

The experimental channel was 19 m long and 0.7 m wide, made of glass side walls and a smooth PVC horizontal bed. The initially steady flow was supplied by the upstream water tank leading to the glass-sidewall test section through a smooth convergent intake. The discharge provided by the tank was measured by a magneto flowmeter with an accuracy of 10^{-5} m³/s and was checked against the brink depth d_b at the flume's downstream end. A fast-closing Tainter gate was located next to the channel's downstream end at $x = 18.1$ m. The positive surges were generated by rapidly closing the Tainter gate and the bore propagated upstream. A radial gate was located at $x = 18.88$ m to control the initial water depth. Unsteady free-surface measurements were performed using a series of acoustic displacements meters (ADMs) located at various positions, most importantly at $x = 18.17$ m, 8.5 m and 7.93 m. All ADMs were calibrated against point gauge measurements in steady flows and sampled at 200 Hz on the channel centerline. The ADMs and were synchronized within 1 ms with the ADV and Profiler.

First, steady flow velocity measurements were performed using the Profiler over a wide range of flow conditions (Table 1). The data was compared to measurements using the ADV sampled simultaneously. Both ADV and Profiler were located at $x = 7.87$ m. The Profiling range was 30 mm, and the ADV control volume was located at the centre of the Profiling range. Figure 2 presents an overview of the experimental channel and instrumental setup. Second, unsteady ensemble-averaged velocity measurements were performed using the Profiler, with validation against ADV data (Table 1). In the unsteady flow, the experiments were repeated 50 times to obtain the ensemble-averaged median velocity properties. A sensitivity analysis was performed to find the appropriate number of repeats (less than or equal to 50) to characterise accurately the rapidly-fluctuating velocity characteristics. Two instrumental setups were used during the ensemble-averaged measurements (Figure 3) to minimise instrument interferences between Profiler and ADV. In Setup 1, the Profiler was sampled alone at $x = 8.5$ m, with a profiling range of 35 mm. In Setup 2, the Profiler was located at $x = 8.5$ m, sampled simultaneously with an ADV located 0.57 m upstream. The control volume of the ADV was placed at the bottom of the profiling range.

The experimental flow conditions were summarized in Table 1, where Q is flow discharge, d_1 is the initial steady flow depth at the velocity sampling location, x is the location of the Profiler measured from the upstream end of the flume, Fr_o and Fr_1 are the Froude numbers for the initially steady flow and of the positive surge, respectively, h is the Tainter gate opening after closure, and z/d_1 is the dimensionless vertical elevation where velocity measurements were conducted, with z being the sampling volume elevation above the invert. The radial gate opening height is denoted N/A when it is fully opened. Table 2 lists the setup, used to test the combinations of Profiler and ADV. Herein, Brisbane tap water was used, and no seeding was applied. Further details were reported by Leng and Chanson (2016a).

(A) Side view
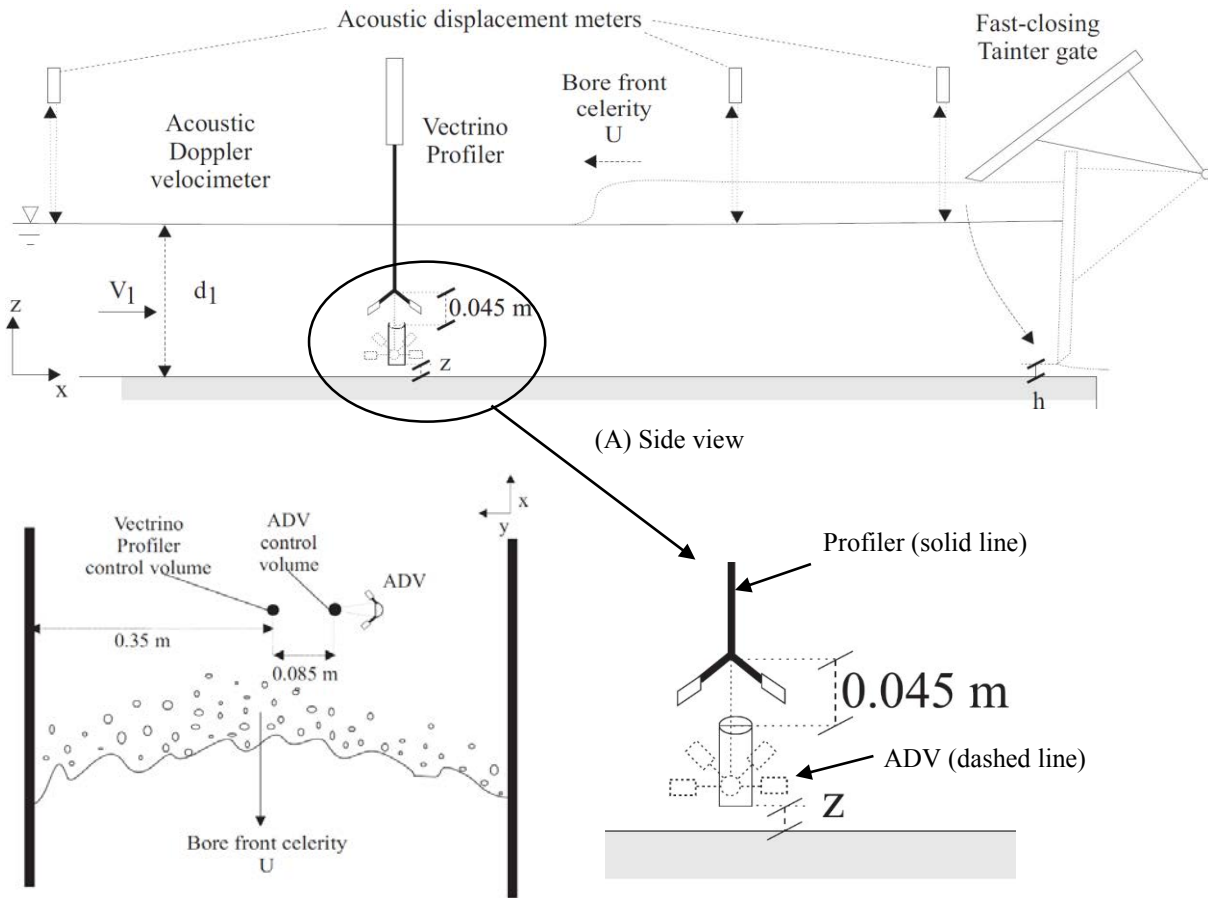
(B, left) Top view of the setup. (C, right) Zoomed view of the relative vertical elevations of the ADV and Profiler

Figure 2. Sketches of the experimental channel and instrument setup (thick black line indicates channel side walls) during the preliminary velocity measurements.

Table 1. Experimental flow conditions.

Q (m³/s)	d_1 (m)	x (m)	Fr_o	Fr_1	Radial gate opening (m)	h (m)	z/d_1	Instrumentation	Remark
0.100	0.177	2, 7.87, 8.5	0.60	1.58	N/A	0	0.00-0.73	ADV & Profiler	Steady flow & ensemble-averaged unsteady velocity measurements
0.085	0.161	7.87	0.60	--	N/A	N/A	0.00-0.60	ADV & Profiler	Steady flow
0.071	0.144	7.87	0.59	--	N/A	N/A	0.00-0.63	ADV & Profiler	Steady flow.
0.100	0.215	7.87	0.45	--	0.112	N/A	0.00-0.70	ADV & Profiler	Steady flow.
0.086	0.211	7.87	0.40	--	0.090	N/A	0.00-0.71	ADV & Profiler	Steady flow.
0.071	0.21	7.87	0.33	--	0.670	N/A	0.00-0.71	ADV & Profiler	Steady flow.
0.055	0.201	2	0.27	--	0.05	N/A	0.00-0.75	ADV & Profiler	Steady flow.

Table 2. Descriptions of instrumental setups

Setup	Instrumentation	Profiler location	ADV location	Remarks
1	Profiler only	x = 8.5 m, y = 0.35 m	N/A	
2	Profiler and ADV	x = 8.5 m, y = 0.35 m	x = 7.93 m, y = 0.225 m	ADV emitter facing right sidewall
3	Profiler and ADV	x = 8.5 m, y = 0.35 m	x = 8.5 m, y = 0.215 m	ADV emitter facing right sidewall
4	Profiler and ADV	x = 8.5 m, y = 0.35 m	x = 7.93 m, y = 0.225 m	ADV emitter facing Profiler
5	ADV only	N/A	x = 8.5 m, y = 0.35 m	
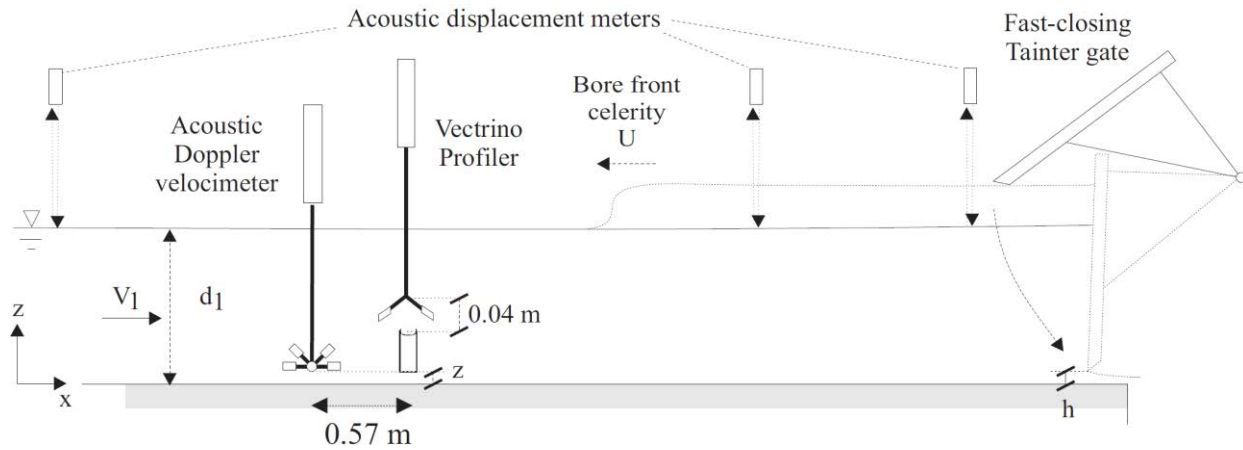
(A) Setup 1 (Profiler only, marked by solid outline) and 2 (with ADV, marked by dashed outline) side view
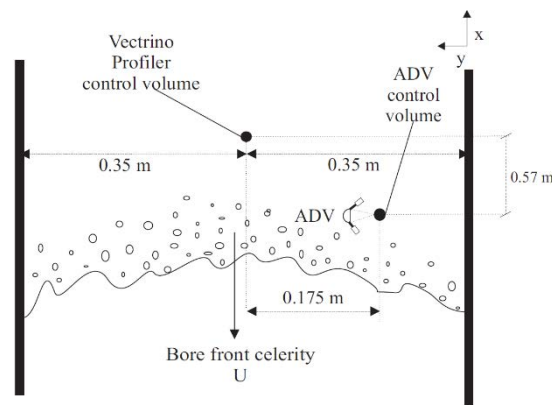
(B) Setup 2 (Profiler working with ADV) elevation view

Figure 3. Experimental channel and instrument setup of the ensemble-averaged measurements.

4.   STEADY FLOW MEASUREMENTS USING VECTRINO II PROFILER

4.1. Steady Flow Velocity Measurements

For all flow conditions (Table 1), steady flow velocity measurements showed a close agreement between Profiler and ADV data in terms of time-averaged velocity components. This was consistent with the findings of Craig et al. (2011), Zedel and Hay (2011), and Macvicar et al. (2014). However, some outlying points occurred slightly above the outer edge of the boundary layer. This is illustrated in Figure 4, showing typical vertical profiles of time-averaged longitudinal velocity V_x and velocity fluctuations at two longitudinal locations. The occurrence of such suspicious points was consistent with all velocity components: i.e. if the longitudinal velocity showed outlying data at particular vertical elevations, similar outliers would be observed at the same vertical elevations for the other velocity components. The velocity fluctuations were characterized by the standard deviation of velocity data v'. Figure 4 highlights some inconsistent vertical pattern in terms velocity fluctuation data throughout the water column, especially in a thin boundary layer (Figure 4, right). Zedel and Hay (2011) and Macvicar et al. (2014) also showed errors in velocity variance using a Profiler. Larger differences were observed in terms of vertical velocity fluctuations, compared to other velocity components. This could be some effect of the bed proximity on the receiver for the vertical velocity component, as previously observed with ADVs (Martin et al. 2002, Chanson et al. 2007). The experiments were conducted at two longitudinal locations $x = 7.87$ m (Figure 4-left) and $x = 2$ m (Figure 4-right) to examine the occurrence of error points in relation to the boundary layer thickness. The results suggested no obvious difference in terms of both locations and quantity. However, the number of error points was significantly larger with measurements conducted with the smaller discharge ($Q = 0.055$ m^3/s) at both locations.

Overall, the steady flow velocity measurements highlighted a number of advantages and issues with the Profiler. The Profiler was reliable for the measurements of mean velocity profile in the longitudinal, transverse, and vertical directions in a turbulent flow with high temporal resolution (100 Hz), together with the ability to simultaneously sample velocity characteristics at up to 35 closely-spaced locations. Some error points existed in the sampling profile for which the recorded velocity values were not meaningful. The error points were typically located outside the outer edge of the boundary layer. Although their occurrences seemed to be random and discontinuous, their locations in a single profile at fixed vertical elevation were consistent and can be reproduced by repetition; therefore, such locations are relatively easy to avoid. The presence of error points in the Profiler measurements was related to flow discharge and vertical elevation rather than turbulent flow properties.
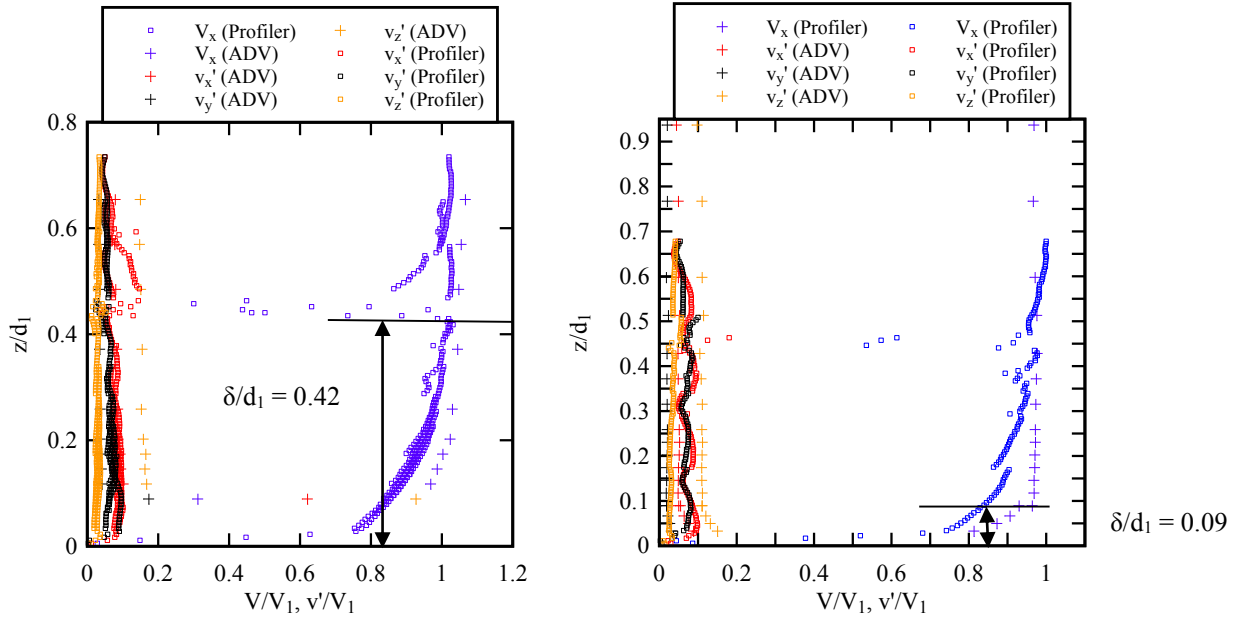
Figure 4. Vertical profile of the time-averaged longitudinal velocity and velocity fluctuations in steady flow: comparison between ADV and Profiler data - $Q = 0.100$ m^3/s, $d_1 = 0.177$ m, $x = 7.87$ m (left) and 2 m (right).

4.2. Discussion: Interactions Between ADV and Profiler

During the steady flow measurements, interactions between ADV and Profiler units were observed and their effects in terms data magnitude and quality were investigated. Five instrumental setups were experimented under the same flow condition ($Q = 0.100$ m^3/s, $d_1 = 0.177$ m) for the same vertical range ($z/d_1 = 0.09$ to 0.28). This vertical range was selected based on preliminary measurements, during which a zero error point was found within the range. Table 2 describes the five setups, where y is the transverse distance positive towards the left sidewall. Figure 5 presents typical velocity statistics with different setups. The results clearly showed some interactions between ADV and Profiler units when both instruments were sampled simultaneously. While they did not affect the values of the mean velocity for the majority of the profile, the interactions had more impacts on the velocity fluctuations. The velocity fluctuations at the upper and lower portions of the profiler were most adversely affected. The interactions between the instruments and impacts on the data quality were reduced by simply rotating the ADV emitter by 180º to face the side wall instead of facing the Profiler control volume, as in Setups 2 and 3. Further improvements were achieved by moving the ADV longitudinally and transversely away from the Profiler, as in Setup 2. In summary, Setups 1 and 2 provided data that were best compared to the ADV data (Setup 5) among all setups.
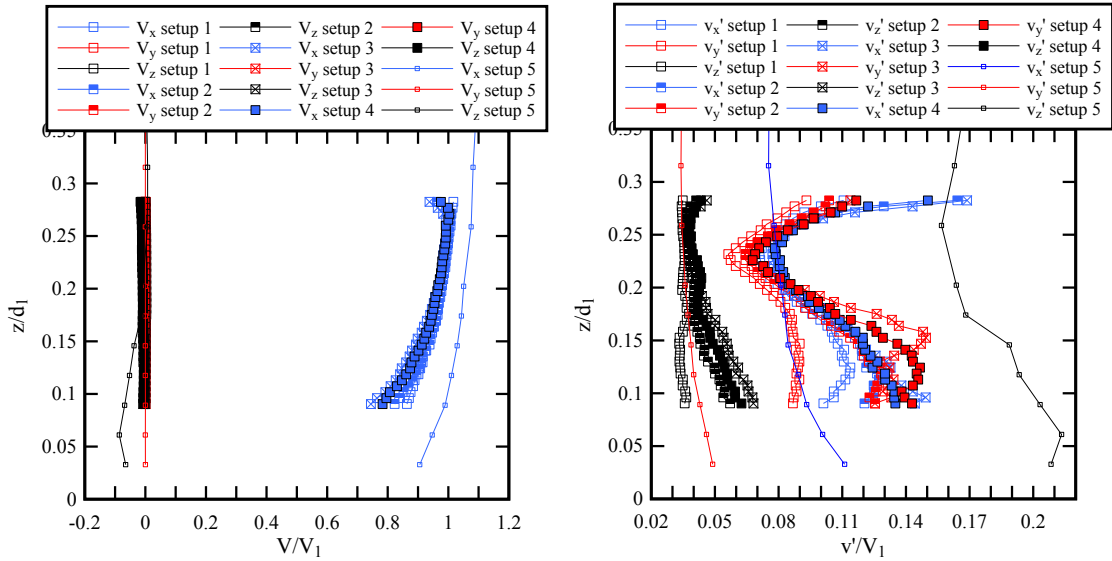
(A) Time-averaged velocity profiles

(B) Time-averaged velocity fluctuations
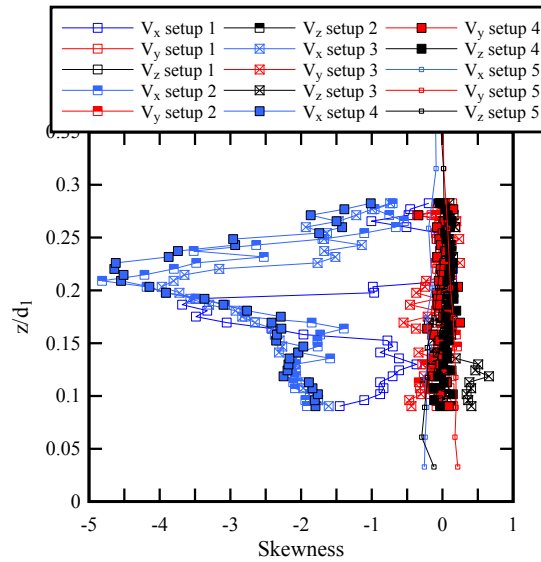
(C) Skewness of velocity data

Figure 5. Velocity statistics measured by Profiler sampling alone (setup 1), sampling with ADV using Setups 2, 3 and 4 (denoted "setup 2/3/4") compared to ADV measurements sampling alone (setup 5).

5. ENSEMBLE-AVERAGED MEASUREMENTS AND SENSITIVITY ANALYSIS

5.1. Presentation

The positive surge propagation was highly repeatable and reproducible in the current experimental setup. The free-surface and velocity characteristics were analyzed by repeating the experiment for a number of times and obtaining the median of the instantaneous data (i.e. the ensemble-average) at a point at an instant, which can be used to represent the mean property of the relevant parameters (Docherty and Chanson 2012). The synchronization between different runs for a single flow condition was critical. This was done by taking the ADM located downstream of the gate as a reference. When the gate was closed, it generated a negative surge propagating downstream, which was characterized as a sudden drop of water elevations at the same time as the generation of the bore. All 50 runs were synchronized according to the time at which the leading edge of the negative surge reached the ADM sensor located downstream of the gate. Mathematically, this time is equal to

the instance at which the first derivative of the free-surface elevation with respect to time becomes non-zero. The ensemble-averaged velocity measurements were performed using Setups 1 and 2 (Fig. 3, Table 2) because they produced the least instrumental interference. The results were ensemble-averaged over the total 50 runs, as well as over 35 runs with some data overlapping, 25 runs, 15 runs, 10 runs, and 5 runs with no data overlapping.

A number of characteristic unsteady turbulent fluctuating properties were examined. Previous experimental analysis suggested that these properties were characteristics associated with the turbulent flow nature (Leng and Chanson 2016b). Thus, the sensitivity analysis focused on the following properties: the maximum longitudinal velocity fluctuations occurring shortly after the passage of the bore, the time lag for the maximum longitudinal velocity fluctuation to occur after the bore passage, and the longitudinal recirculation velocity (Figure 6). In Figure 6, t_{bore} denotes the time at which the free-surface started to rise. Mathematically, this time is equal to the instance at which the first derivative of the free-surface elevation with respect to time becomes non-zero. The longitudinal velocity fluctuations were quantified by the difference between the third and first quartile of the total ensemble (V_{75}-V_{25}). The maximum velocity fluctuations (V_{75}-V_{25})$_{max}$ were found to occur shortly after the passage of the bore, and the associated time lag Δt_V was quantified as the delay relative to the time when the free-surface elevation started to rise up. The longitudinal recirculation velocity V_{recirc} marked the minimum velocity reached at the end of the longitudinal deceleration, typically a negative value for the experimental flow conditions. Such a negative velocity indicated a transient flow reversal and recirculation beneath the surge front. A definition sketch of the above fluctuating properties is illustrated in Figure 6.
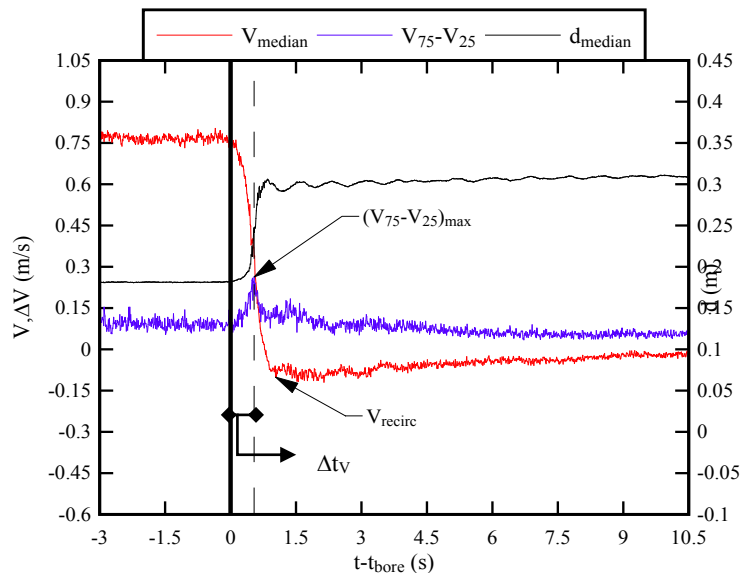
Figure 6. Definition sketch of characteristic unsteady turbulent fluctuating properties during a positive surge propagation.

5.2. Ensemble-Averaged Unsteady Velocity Measurements

Overall, the ensemble-averaged unsteady velocity measurements showed a close agreement between Profiler and ADV velocity data for the same flow and vertical elevation. Figure 7 presents the time-variations of ensemble-averaged longitudinal velocity measured by the ADV (left) and Profiler (right) at a similar vertical elevation, both calculated based on 50 runs. The results showed close agreement in terms of shape and magnitude of the ensemble-median velocity measured by the two instruments. The velocity fluctuations in terms of (V_{75}-V_{25}) produced by both instruments showed marked peaks shortly after the passage of the surge front (t-t_{bore} > 0). The Profiler data seemed to show a more pronounced recirculation zone in comparison to the ADV data, as highlighted by negative velocity of larger magnitudes reached at the end of the longitudinal deceleration, indicating a stronger flow reversal. Altogether, the time-variations of the unsteady velocity measured by the Profiler, instantaneous or ensemble-average, were very similar to those measured by the ADV for all three components. Table 3 compares the turbulent fluctuating characteristics measured by Profiler and ADV at similar vertical elevations. The Profiler measurements are presented for two setups, ensemble-averaged over 50 runs. The ADV measurements included present data (Setup 2) ensemble-averaged over 50 runs, and data by Leng and Chanson (2016b) ensemble-averaged over 25 runs. The results showed a close agreement between the Profiler data, working alone or with the ADV, and ADV data, working alone or with the Profiler, at a given elevation. Clearly, the Profiler was suitable to conduct

high-frequency measurements in highly unsteady turbulent flows and captured rapidly fluctuating characteristics with good accuracy, provided that the measurements were taken at vertical elevations where no spurious points existed.
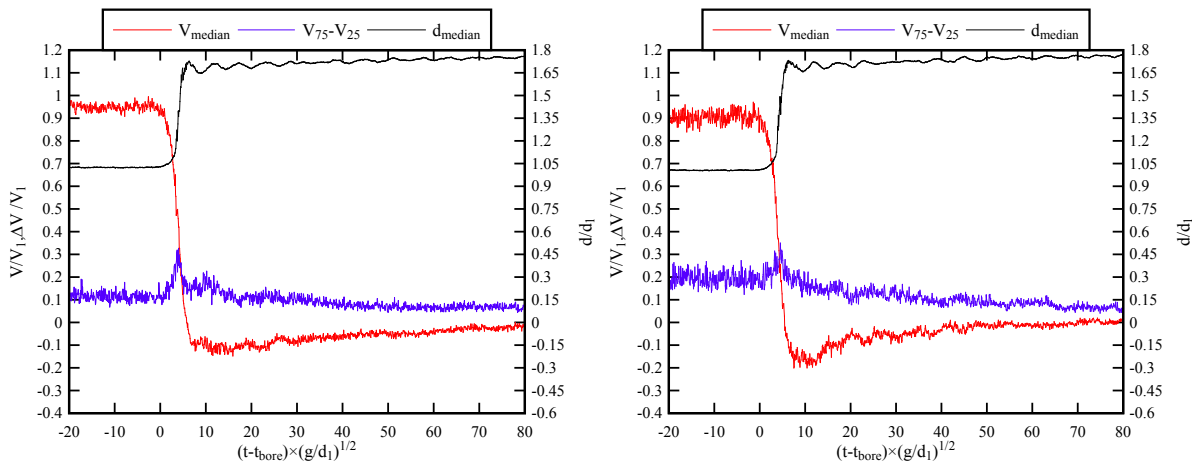
Figure 7. Ensemble-averaged time-variations of the longitudinal velocity and free-surface elevation at the velocity sampling point during a positive surge: comparison between ADV data (left, Setup 2) and Profiler data (right, Setup 1), both calculated from 50 runs - Flow conditions: $Q = 0.100$ m^3/s, no radial gate, $h = 0$ m, $z/d_1 = 0.12$ for ADV and Profiler.

Table 3. Comparison of turbulent fluctuating characteristics in a positive surge between instruments and setups

Instrument and setup	z/d_1 (m)	$(V_{75}-V_{25})_{max}$ (m/s) Ensemble-averaged	Δt_V (s) Ensemble-averaged	V_{recirc} (m/s) Ensemble-averaged
Profiler with ADV Setup 2	0.13	0.305	0.52	-0.146
ADV Setup 2	0.12	0.263	0.54	-0.119
Profiler alone (Setup 1)	0.13	0.282	0.61	-0.162
ADV_2016 [1]	0.10	0.215	0.61	-0.239

Remarks: [1] ADV measurements collected by Leng and Chanson (2016b) at $x = 8.5$ m on channel centreline for the same flow condition. Results were ensemble-averaged over 25 runs.

5.3. Sensitivity Analysis

The longitudinal velocity data at 7 vertical elevations, that is 1 in 5 measuring points out of 35 points in a profile, were analyzed to examine the effect of number of runs on the fluctuating characteristics ($(V_{75}-V_{25})_{max}$, Δt_V, and V_{recirc}. Figure 8 presents typical results for Setup 1 (Profiler only), each for two vertical elevations ($z/d_1 = 0.27$ and 0.10). For all flow conditions, the turbulent characteristics showed asymmetrical envelopes of data distribution when the number of runs varied from 50 down to 5. The maximum fluctuations calculated based upon 50 runs tended to be smaller than the average of the results calculated from 35 or 25 runs. The time delay Δt_V obtained from a total ensemble of 50 runs was very close to the average of the time delay obtained from 35 and 25 runs, with 25 runs producing results that were closer to that of the 50 runs at some elevations. The magnitude of the recirculation velocity tended to decrease on average as the number of runs increased. The longitudinal deceleration took place in typically less than 0.8 s, a period within which the flow was highly unsteady and intensive turbulent mixing occurred, and the turbulence was likely anisotropic. The time of occurrence of the peak velocity fluctuation was different, although only by a few milliseconds, in every single run, and the recirculation velocity, defined as the minimum velocity reached at the end of the deceleration phase, occurred at slightly different time as well. Hence, the ensemble-averaging over a large number of runs tended to 'smooth' the maximum velocity fluctuation and recirculation velocity. In practice, the number of runs must be large enough to accurately represent the turbulent fluctuating quantities in the rapidly varied flow but not too large so that the attenuation is minimized. Herein, 25 and 35 runs were considered most suitable for ensemble-average velocity measurements using the Profiler, with 25 runs being selected because of time limitations.
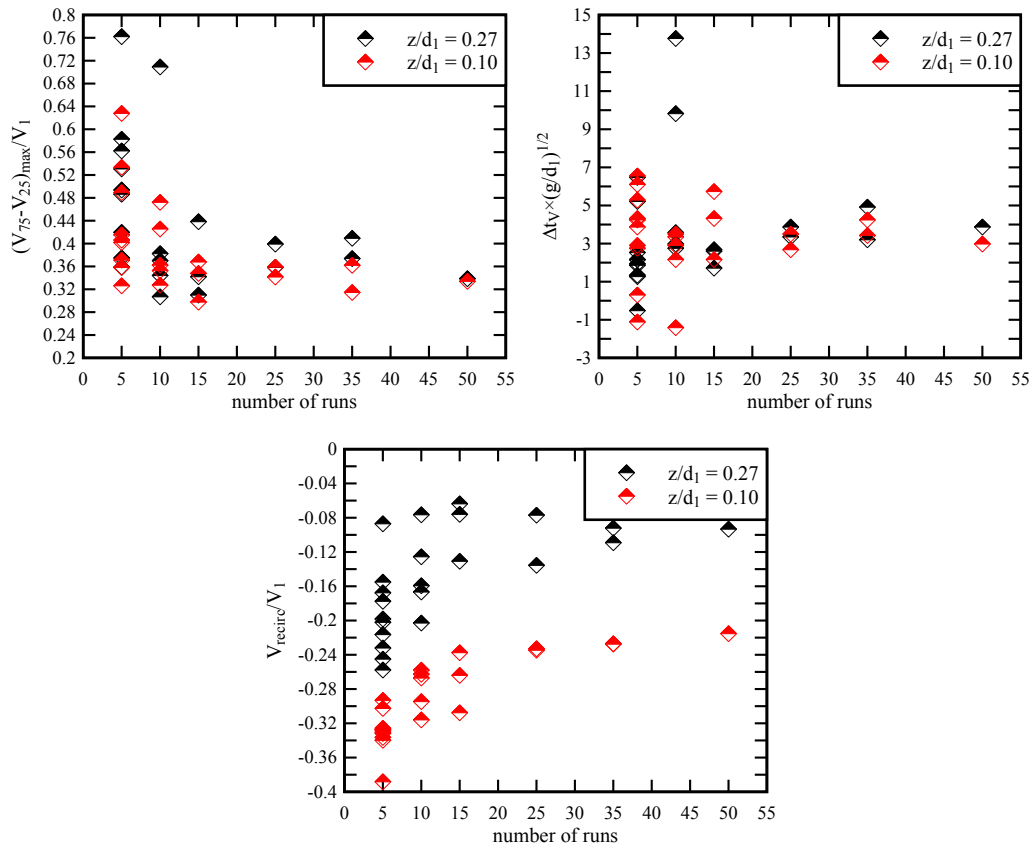
Figure 8. Sensitivity analysis of the characteristic turbulent fluctuating properties in a positive surge at two vertical elevations: ensemble-averaged results over different number of runs; Profiler sampling alone (Setup 1).

6. CONCLUSION

New steady and unsteady velocity measurements were conducted in open channel flows using a Nortek[TM] ADV Vectrino II Profiler equipped with a fixed stem and down-looking head. Steady and unsteady velocity measurements using the Profiler showed a close agreement with experimental results obtained using a Nortek[TM] ADV Vectrino+ for the same flow conditions, in terms of the instantaneous median velocity and velocity fluctuations, longitudinal velocity recirculation, longitudinal velocity deceleration, etc. The instantaneous velocity fluctuations were of the same order of magnitude between the Profiler and ADV results. A careful sensitivity analysis was conducted to test the number of runs appropriate for ensemble-averaging. The results indicated that the selection of 25 runs was suitable. Some instrumental error was observed. Outside the boundary layer, the Profiler tended to produce errors in terms time-averaged velocity data and velocity fluctuations for a number of points in a profile. Even at vertical elevations where the time-averaged velocity was meaningful, the vertical distribution of the velocity fluctuations contained errors.

Overall, the study demonstrated that the propagation of positive surges is a highly unsteady turbulent process, and the performance of ADV Vectrino II Profiler in such an unsteady turbulent flow was satisfactory, provided that a careful validation was undertaken for all Profiler outputs.

8. REFERENCES

Becker, J. (2014). VTMT (Version 1.1) [Computer software]. Federal Waterways Engineering and Research Institute (BAW), Karlsruhe. <http://sdrv.ms/12eHgvw/> (accessed on 19 Nov. 2014).

Chanson, H. (2004). The Hydraulics of Open Channel Flow: An Introduction. Butterworth-Heinemann, 2nd edition, Oxford, UK, 630 pages.

Chanson, H. (2008). Acoustic Doppler Velocimetry (ADV) in the Field and in Laboratory: Practical Experiences. Proceedings of the International Meeting on Measurements and Hydraulics of Sewers IMMHS'08, Summer School GEMCEA/LCPC, 19-21 Aug. 2008, Bouguenais, Frédérique Larrarte and Hubert Chanson Eds., Hydraulic Model Report No. CH70/08, Div. of Civil Engineering, The University of Queensland, Brisbane, Australia, Dec., pp. 49-66.

Chanson, H., Trevethan, M., and Koch, C. (2007). Turbulence Measurements with Acoustic Doppler Velocimeters. Discussion. Journal of Hydraulic Engineering, ASCE, Vol. 133, No. 11, pp. 1283-1286 (DOI: 10.1061/(ASCE)0733-9429(2005)131:12(1062))

Craig, R. G. A., Loadman, C., Clement, B., Ruesello, P. J., and Siegel, E. (2011). Characterization and Testing of a new Bistatic Profiling Acoustic Doppler Velocimeter: The Vectrino-II. Proc. IEEE/OES/CWTM 10th Working Conference on Current, Waves and Turbulence Measurement (CWTM), Monterey, Canada, 20-23 March, pp. 246-252 (DOI: 10.1109/CWTM.2011.5759559).

Docherty, N.J., and Chanson, H. (2012). Physical Modelling of Unsteady Turbulence in Breaking Tidal Bores. Journal of Hydraulic Engineering, ASCE, Vol. 138, No. 5, pp. 412-419 (DOI: 10.1061/(ASCE)HY.1943-7900.0000542)

Goring, D.G., and Nikora, V.I. (2002). Despiking Acoustic Doppler Velocimeter Data. Journal of Hydraulic Engineering, ASCE, Vol. 128, No. 1, pp. 117-126. Discussion: Vol. 129, No. 6, pp. 484-489.

Hornung, H.G., Willert, C., and Turner, S. (1995). The Flow Field Downstream of a Hydraulic Jump. Journal of Fluid Mechanics, Vol. 287, pp. 299-316.

Koch, C., and Chanson, H. (2009). Turbulence Measurements in Positive Surges and Bores. Journal of Hydraulic Research, IAHR, Vol. 47, No. 1, pp. 29-40 (DOI: 10.3826/jhr.2009.2954).

Leng, X., and Chanson, H. (2015). Unsteady Turbulence in Expansion Waves in Rivers and Estuaries: an Experimental Study. Environmental Fluid Mechanics, Vol. 15, No. 5, pp. 905-922 (DOI: 10.1007/s10652-014-9385-9).

Leng, X., and Chanson, H. (2016a). Unsteady Turbulent Velocity Profiling in Open Channel Flows and Tidal Bores using a Vectrino Profiler. Hydraulic Model Report No. CH101/15, School of Civil Engineering, The University of Queensland, Brisbane, Australia, 118 pages (ISBN 978-1-74272-145-3).

Leng, X., and Chanson, H. (2016b). Coupling between Free-surface Fluctuations, Velocity Fluctuations and Turbulent Reynolds Stresses during the Upstream Propagation of Positive Surges, Bores and Compression Waves. Environmental Fluid Mechanics (DOI: 10.1007/s10652-015-9438-8). (In Print)

Liggett, J.A. (1994). Fluid Mechanics. McGraw-Hill, New York, USA.

Macvicar, B., Dilling, S., Lacey, J., and Hipel, K. (2014). A Quality Analysis of the Vectrino II Instrument using a New Open-source MATLAB Toolbox and 2D ARMA Models to Detect and Replace Spikes. Proc. 7th International Conference on Fluvial Hydraulics (River Flow), Lausanne, Switzerland, 3-5 Sept., pp. 1951-1959.

Martin, V., Fisher, T. S. R., Millar, R. G., and Quick, M. C. (2002). ADV data analysis for turbulent flows: Low correlation problem. Proceedings of Conference on Hydraulic Measurements and Experimental Methods, ASCE-EWRI & IAHR, Reston Va, USA (CD-ROM).

Nakagawa, H., and Nezu, I. (1977). Prediction of the contributions to the Reynolds stress from the bursting events in open-channel flows. Journal of Fluid Mechanics, Vol. 80, pp. 99-128.

Nezu, I. (2005). Open-Channel Flow Turbulence and its Research prospect in the 21st Century. Journal of Hydraulic Engineering, ASCE, Vol. 131, No. 4, pp. 229-246.

Nortek (2012). Vectrino Profiler: User Guide, Nortek Scientific Acoustic Development Group Inc., User Manual.

Zedel, L., and Hay, A. (2011). Turbulence Measurements in a Jet: Comparing the Vectrino and Vectrino II. Proc. IEEE/OES/CWTM 10th Working Conference on Current, Waves and Turbulence Measurements (CWTM), Monterey, Canada, 20-23 March, pp. 173-178 (DOI: 10.1109/CWTM.2011.5759547).

Determining Optimal Discharge and Optimal Penstock Diameter in Water Turbines

Arturo S. Leon
School of Civil & Construction Engineering
Oregon State University
Corvallis, OR 97331
USA
E-mail:arturo.leon@oregonstate.edu

ABSTRACT

Minimizing water consumption for producing hydropower is critical given that overuse of flows for energy production may result in a shortage of flows for other purposes such as irrigation and navigation. This paper presents a dimensional analysis for finding optimal flow discharge and optimal penstock diameter when designing impulse and reaction water turbines for hydropower systems. The objective of this analysis is to provide general insights for minimizing water consumption when producing hydropower. This analysis is based on the geometric and hydraulic characteristics of the penstock, the total hydraulic head, and the desired power production. As part of this analysis, various dimensionless relationships between power production, flow discharge, and head losses were derived. These relationships were used to draw general insights on determining optimal flow discharge and optimal penstock diameter. For instance, it was found that for minimizing water consumption, the ratio of head loss to gross head should not exceed about 15%. An example of application is presented to illustrate the procedure for determining optimal flow discharge and optimal penstock diameter for an impulse turbine. It is worth mentioning that this paper presents part of the material published by the author in Leon and Zhu (2014).

Keywords: Design, dimensional analysis, efficiency, hydropower, optimal power, turbine

1. INTRODUCTION

The world energy consumption will grow by 56% between 2010 and 2040 (U.S. Energy Information Administration 2013). As world population continues to grow and the limited amount of fossil fuels begins to diminish, there is an increasing demand to exploit renewable sources of energy. In the United States, about 9% of all energy consumed in 2012 was from renewable sources (U.S. Institute for Energy Research 2012). While this is a relatively small fraction of the U.S. energy supply, in 2012, the United States was the world's largest consumer of renewable energy from geothermal, solar, wood, wind, and waste for electric power generation, producing almost 25% of the world's total (U.S. Institute for Energy Research 2012). This institute also reports that in 2012, 30% of the renewable energy in the U.S. was from hydropower. This means that only about 3% of all energy consumed in the United States was from hydropower.

Globally, hydropower accounted for 16% of all global electricity production in 2007, with other renewable energy sources totaling 3% (Schumann et al. 2010). Hence, it is not surprising that when options are evaluated for new energy developments, there is a strong impulse toward fossil fuel or nuclear energy as opposed to renewable sources. However, as hydropower schemes are often part of a multipurpose water resources development project, they can often help to finance other important functions of the project (IEA Hydro, 2000). In addition, hydropower provides benefits that are rarely found in other sources of energy. In fact, dams built for hydropower schemes, and their associated reservoirs, provide human well-being benefits such as securing water supply, flood control, and irrigation for food production and societal benefits such as increased recreational activities and improved navigation (IEA Hydro, 2000).

Furthermore, hydropower, due to its associated reservoir storage, can provide flexibility and reliability for energy production in integrated energy systems. The storage capability of hydropower systems can be seen as a regulating mechanism by which other diffuse and variable renewable energy sources (wind, wave, solar) can play a larger role in providing electric power of commercial quality (Schumann et al. 2010). While development of all the remaining hydroelectric potential could not hope to cover total future world demand for electricity, implementation of the remaining potential can make a vast contribution to improving living standards in the developing world (South America, Asia and Africa), where the greatest potential still exists (U.S. Institute for Energy Research 2012).

Minimizing water consumption for producing hydropower is critical given that overuse of flows for energy production may result in a shortage of flows for other purposes such as irrigation or navigation (Leon and Zhu 2014). The present work was motivated when the author was unable to find in literature a theoretical framework for determining optimal flow discharge and optimal penstock diameter for the design of impulse and reaction turbines. Recently, Pelz (2011) provided a theoretical approach for determining the upper limit for hydropower gained by a water wheel or turbine per unit width in a rectangular open-channel. This is somewhat different for impulse and reaction turbines, as in the latter turbines, the flow in the penstock is pressurized.

This paper aims to provide general insights on determining optimal flows and optimal penstock diameters when designing impulse and reaction turbines for hydropower systems. This paper is divided as follows. First, dimensionless relationships between power production, flow discharge, and head losses are derived. Second, these relationships are used to draw general insights on determining optimal flow discharge and optimal penstock diameter. Third, an example of application for determining optimal flows when designing impulse turbines is presented. Finally, the key results are summarized in the conclusion.

2. DIMENSIONAL ANALYSIS FOR OPTIMAL FLOW DISCHARGE, OPTIMAL HEAD LOSSES, AND OPTIMAL POWER

The electric power, P, in Watts (W), can be determined by the following equation:

$$P = \eta \gamma Q \left(H_g - h_L \right) \tag{1}$$

where $\gamma \, (= \rho \, g)$ is the specific weight of water in kg/(m^2 s^2), Q is flow discharge in m^3/s, H_g is gross head in m, h_L is sum of head losses in m, ρ is water density in kg/m^3, g is acceleration of gravity in m/s^2, and η is overall hydroelectric unit efficiency, which in turn is the product of turbine efficiency (η_t) and generator efficiency (η_g). In all derivations presented in this paper, it is assumed that $\eta \, (= \eta_t \, \eta_g)$ is constant.

For an impulse turbine (see Figure 1), the sum of head losses can be written as

$$h_L = \frac{Q}{2 g A_2{}^2} \left[f \frac{L}{D_2} + \sum k_{1-2} + k_N \left(\frac{A_2}{A_N} \right)^2 \right] \tag{2}$$

where L, D_2, and A_2 are length, diameter, and cross-sectional area of penstock, respectively. In addition, f is friction factor, Σk_{1-2} is the sum of local losses in penstock due to entrance, bends, penstock fittings and gates, A_N is nozzle area at its exit (section 3 in Figure 1), and k_N is nozzle head loss coefficient, which is given by (e.g., Brater and King 1976)

$$k_N = \frac{1}{C_V{}^2} - 1 \tag{3}$$

where C_V is nozzle velocity coefficient. According to Dixon (2005), C_V varies between 0.98 and 0.99 for a typical Pelton turbine nozzle.

For a reaction turbine (see Leon and Zhu 2014), the sum of head losses can be written as

$$h_L = \frac{Q}{2gA_2{}^2}\left[f\frac{L}{D_2} + \sum k_{1-2} + k_N\left(\frac{A_2}{A_d}\right)^2 \right] \qquad (4)$$

where A_d is the draft tube cross-sectional area at its outlet (section Leon and Zhu 2014). The expression inside the brackets in Eqs. (2) and (4) is dimensionless, and it is denoted herein as

$$C_L = \begin{cases} f\dfrac{L}{D_2} + \sum k_{1-2} + k_N\left(\dfrac{A_2}{A_N}\right)^2 & \text{for an impulse turbine} \\[2em] f\dfrac{L}{D_2} + \sum k_{1-2} + \left(\dfrac{A_2}{A_d}\right)^2 & \text{for a reaction t urbine} \end{cases} \qquad (5)$$
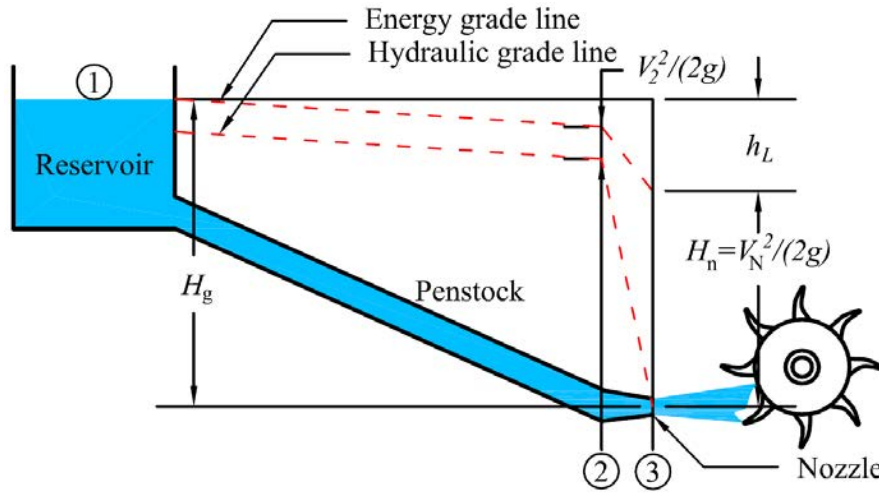
Figure 1. Sketch of an impulse turbine

Hence, the total head losses in Eq. (2) and Eq. (4) is equal to the product of C_L and $Q^2/(2g(A_2)^2)$ and, thus, Eq. (1) can be written as

$$P = \eta\gamma Q\left(H_g - C_L\frac{Q^2}{2gA_2^2}\right) \qquad (6)$$

For generalizing the findings in this paper, a dimensionless relationship between power and flow discharge is sought. To achieve this, Eq. (6) is divided by a reference power (P_r). P_r is assumed to be the maximum power that can be generated using a reference discharge (Q_r) and a fixed gross head and penstock geometry (constant C_L). For maximum power, the turbine and generator efficiencies need to be 100% (i.e., $\eta_t = 100\%$ and $\eta_g = 100\%$). Also, maximum power for a fixed penstock geometry can be obtained by setting dP/dQ in Eq. (6) equal to zero, which gives

$$h_L = H_g/3 \qquad (7)$$

The reference flow discharge Q_r can be obtained by using Eq. (7) and the energy equation between the reservoir and the nozzle exit for an impulse turbine or between the reservoir and the tailrace for a reaction turbine, which gives

$$Q_r = 2A_3\sqrt{\frac{1}{3}gH_g}$$

(8)

where A_3 is given by

$$A_3 = \begin{cases} A_N & \text{for an impulse turbine} \\ A_d & \text{for a reaction turbine} \end{cases}$$

(9)

Substituting Eq. (7) and Eq. (8) into Eq. (1) gives the following relation for the reference power (P_r):

$$P_r = \frac{4}{3}\gamma H_g A_3\sqrt{\frac{1}{3}gH_g}$$

(10)

Note that Q_r and P_r (Eqs. 8 and 10) are a function of the penstock properties and the gross head only. Dividing each side of Eq. (6) by P_r (Eq. 10) and defining P/P_r as P_+ and Q/Q_r as Q_+, and after some algebra, the following dimensionless relationship between power and discharge is obtained:

$$P_+ = \eta\left[\frac{3}{2}Q_+ - C_L\left(\frac{A_3}{A_2}\right)^2 Q_+^3\right]$$

(11)

Denoting with β the product of C_L and $(A_3/A_2)^2$, Eq. (11) can be rewritten as

$$P_+ = \eta\left(\frac{3}{2}Q_+ - \beta Q_+^3\right)$$

(12)

where

$$\beta = \begin{cases} \left(\frac{A_N}{A_2}\right)^2\left(f\frac{L}{D_2} + \sum k_{1-2} + k_N\left(\frac{A_2}{A_N}\right)^2\right) & \text{for an impulse turbine} \\ \left(\frac{A_d}{A_2}\right)^2\left(f\frac{L}{D_2} + \sum k_{1-2} + \left(\frac{A_2}{A_d}\right)^2\right) & \text{for a reaction turbine} \end{cases}$$

(13)

In practice, the ratios A_N/A_2 and A_d/A_2 in Eq. (13) are typically kept constant, which means that β varies as a function of f, L, D_2, and the coefficients of local head losses (Σk). In most applications, friction losses are more important than local head losses, that is $f L/D_2 \gg \Sigma k$. Also, L is typically constant as it is restricted by topographic conditions. In addition, f does not show significant variation as a function of discharge or penstock diameter. Recall that for a given penstock diameter, f is independent of the Reynolds number for fully developed turbulent flows, which is the case of most penstock flows. Hence, β is more or less inversely proportional to the penstock diameter. The variation of P_+ with respect to Q_+ for a fixed β can be obtained by differentiating P_+ with respect to Q_+ in Eq. (12), which gives

$$\frac{dP_+}{dQ_+} = \eta\left(\frac{3}{2} - 3\beta Q_+^2\right)$$

(14)

The maximum dimensionless power for a fixed β can be obtained by setting dP_+/dQ_+ in Eq. (14) equal to zero. The maximum power occurs when

$$(Q_+)_{max} = \sqrt{\frac{1}{2\beta}}$$

(15)

The maximum dimensionless power for a fixed β is obtained by substituting Q_+ from Eq. (15) in Eq. (12), which gives

$$(P_+)_{max} = \eta\sqrt{\frac{1}{2\beta}}$$

(16)

In most applications, β should range between 0.01 and 1.0 for impulse turbines and between 10 and 1000 for reaction turbines. Likewise, C_L should range between 1 and 100 for both impulse and reaction turbines. Even though β is used throughout the entire paper, as shown later, only C_L is needed for design purposes. Figures 2 and 3 plot Q_+ versus P_+ in Eq. (12) for typical ranges of β for impulse and reaction turbines, respectively. An overall hydroelectric unit efficiency (η) of 0.8 was used for plotting these figures. As can be observed in Figures 2 and 3, the change in power production in relation to change in flow discharge ($\Delta P_+/\Delta Q_+$) for each dimensionless curve has a positive and negative gradient. For optimizing power production, only the positive gradient is of interest ($\Delta P_+/\Delta Q_+ > 0$). To visualize changes in power production in relation to changes in flow discharge, five ratios of dP_+/dQ_+ in Eq. (14) are plotted in Figures 2 and 3. Note in Figures 2 and 3 that for a given β, the positive range of dP_+/dQ_+ varies from $(3/2)\eta$ to 0. Note also that dP_+/dQ_+ changes rapidly near $(Q_+)_{max}$ and that in the positive range of dP_+/dQ_+, the maximum relative power P_+ occurs for the maximum relative flow discharge Q_+.
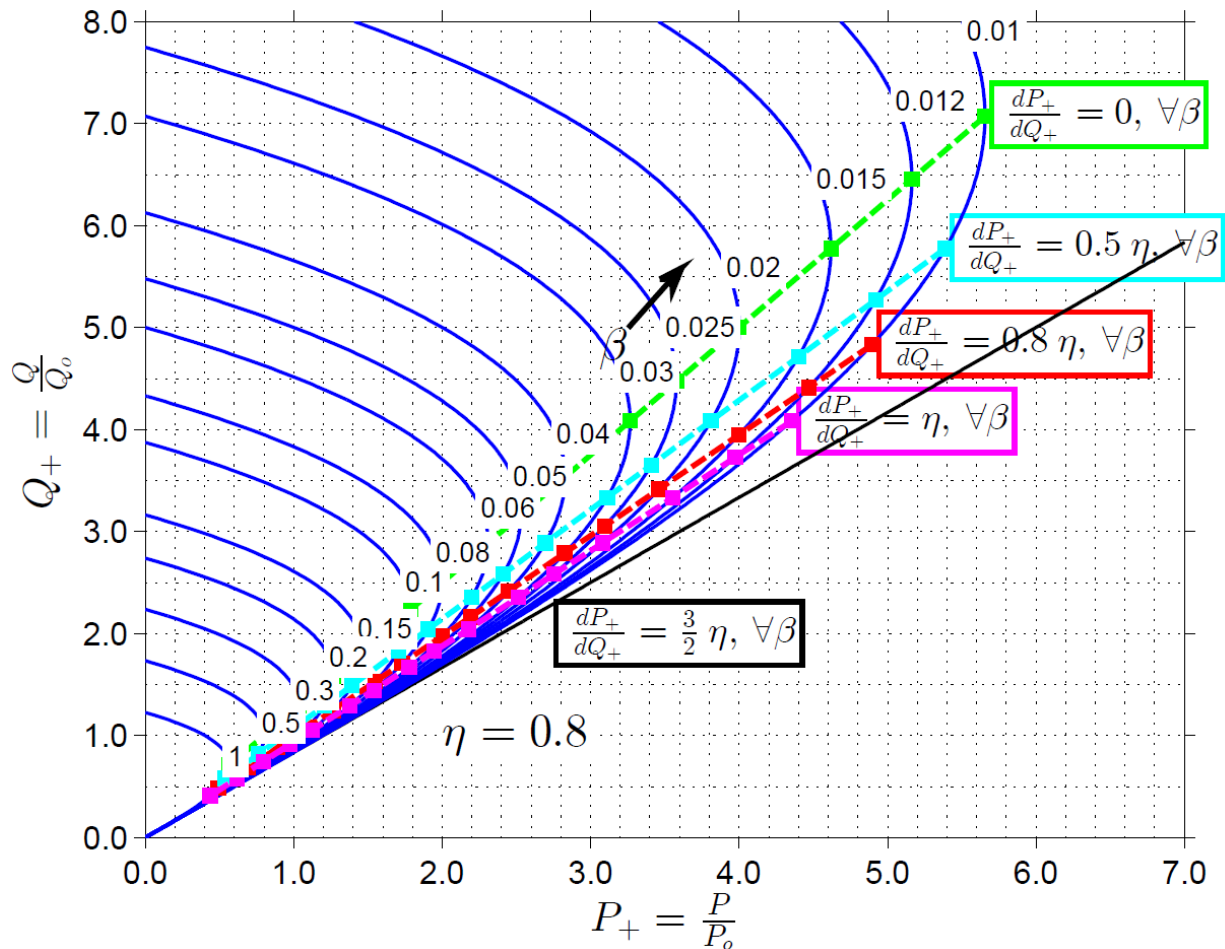
Figure 2. Dimensionless discharge (Q_+) versus dimensionless power (P_+) for $\eta = 0.8$ and a typical range of β for impulse turbines

For minimizing water consumption to produce a given amount of hydropower, it is necessary that dP_+/dQ_+ in Eq. (14) is close to its maximum value $(3/2)\eta$. Note in Figures 2 and 3 that for each curve between approximately $dP_+/dQ_+ = (3/2)\eta$ and $dP_+/dQ_+ = 0.8\eta$, the increase in dimensionless power (P_+) is approximately linear with increase in dimensionless discharge (Q_+). Note also in these figures that for dP_+/dQ_+ smaller than about 0.8η, the increase in P_+ is small compared to the increase in Q_+. Herein, to minimize water consumption, the optimal lower

limit of dP_+/dQ_+ is set to 0.8η. Substituting $dP_+/dQ_+ = 0.8\eta$ into Eq. (14) gives the following upper limit for the dimensionless flow discharge:

$$(Q_+)_{\text{opt upper}} = \sqrt{\frac{7}{30\beta}}$$

(17)

The corresponding upper limit for the dimensionless power is

$$(P_+)_{\text{opt upper}} = \eta\frac{19}{15}\sqrt{\frac{7}{30\beta}}$$

(18)
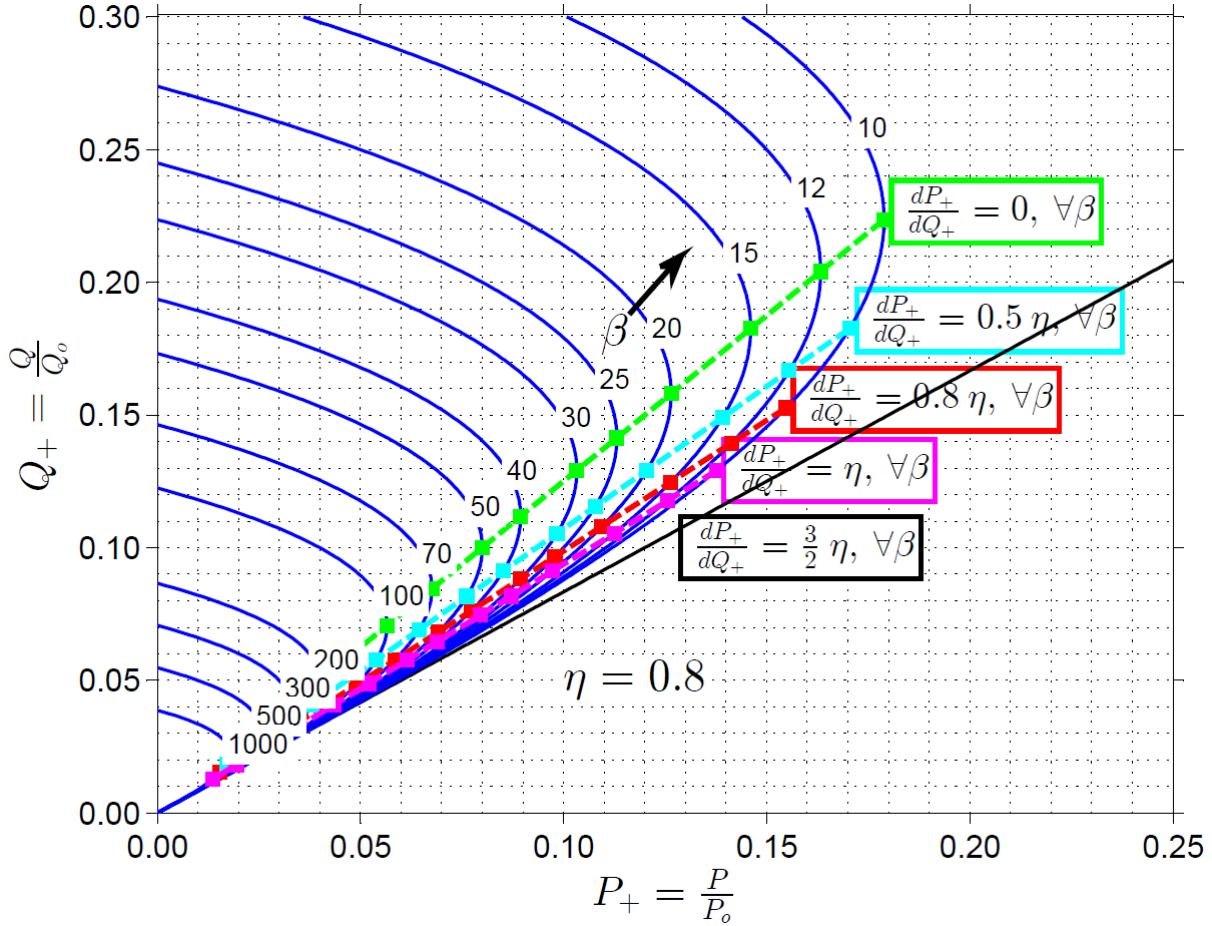
Figure 3. Dimensionless discharge (Q+) versus dimensionless power (P+) for $\eta = 0.8$ and a typical range of β for reaction turbines

The optimal dimensionless head loss ($h_{L+} = h_L/H_g$) can be obtained by assuming that the optimal upper limit for the flow discharge is $Q_+ = [7/(30\beta)]^{1/2}$ (Eq. 17). In Eq. (12), dividing the second term of the right-hand side (RHS) by the first term of the RHS gives

$$h_{L+} \leq \frac{2}{3}\beta Q_+^2$$

(19)

Substituting $(Q_+)_{\text{opt upper}} = [7/(30\beta)]^{1/2}$ into Eq. (19) gives

$$h_{L+} \leq \frac{7}{45}$$

(20)

Eq. (20) shows that for minimizing water consumption, the ratio of head loss to gross head ($h_{L+} = h_L/H_g$) should not exceed 15.6%. The 15.6% ratio also provides the threshold for the optimal penstock diameter. Losses higher than 15.6% mean that a small penstock diameter is used. The 15.6% ratio is about half of that derived for maximum power and maximum flow discharge, which is 33.3%. This means that the optimal conditions for producing power do not correspond to those that use maximum flow discharge for a given β. This can be better understood by observing Figures 2 and 3, in which dP_+/dQ_+ decreases rapidly near $(P_+)_{max}$ for all β. So far the analysis assumed that β is constant, and, hence, the penstock diameter (D_2). For the influence of changing the penstock diameter on power production, the reader is referred to Leon and Zhu (2014).

For practical applications, the derived dimensionless relationships are made non-dimensionless. For instance, the optimal upper limit of the flow discharge can be obtained by combining Eqs. (8) and (17), which, after some algebra, gives

$$Q_{\text{opt}} = \frac{2}{3} A_2 \sqrt{\frac{7}{10} \frac{gH_g}{C_L}}$$

(21)

Similarly, the optimal upper limit of the power can be obtained by combining Eqs. (10) and (18), which, after some algebra, gives

$$P_{\text{opt}} = \frac{76}{135} \eta \gamma H_g A_2 \sqrt{\frac{7}{10} \frac{gH_g}{C_L}}$$

(22)

When designing a turbine, it is necessary to specify either the flow discharge to use or the desired electric power. These cases are presented below.

2.1. *P* is Specified

If *P* is specified, the optimal upper limit of the flow discharge can be obtained by combining Eqs. (21) and (22), which gives

$$Q_{\text{opt}} = \frac{45}{38} \left(\frac{P}{\eta \gamma H_g} \right)$$

(23)

The optimal penstock diameter (or C_L) can be determined from Eq. (21), which gives

$$\frac{(C_L)_{\text{opt}}}{A_2^2} \leq \frac{14}{45} \frac{gH_g}{Q^2}$$

(24)

where *Q* in Eq. (24) is the same as Q_{opt} in Eq. (23).

2.2. *Q* is Specified

If *Q* is specified, the optimal upper limit of the power can be obtained by combining Eqs. (21) and (22), which gives

$$P_{\text{opt}} = \frac{38}{45} \eta \gamma H_g Q$$

(25)

In this case, the optimal penstock diameter can still be determined using Eq. (24). It is pointed out that the proposed methodology for determining the optimal flow discharge and optimal penstock diameter does not account for

cavitation. Reaction turbines (not impulse turbines) are subjected to cavitation. In reaction turbines, cavitation may occur at the outlet of the runner or at the inlet of the draft tube where the pressure is considerably reduced (Dixon 2005). In order to determine whether cavitation will occur in any portion of a reaction turbine, the Thoma's cavitation factor (σ) is compared with the critical cavitation factor (σ_c). If the value of σ is greater than σ_c, cavitation will not occur in the turbine under analysis, where σ_c is a function of the specific speed of the turbine (N_s). Because N_s is not used in the proposed methodology, the occurrence of cavitation cannot be determined using the utilized parameters. The occurrence of cavitation in reaction turbines needs be checked after using the proposed methodology. Following, an example of application for determining optimal flow discharge and optimal penstock diameter for an impulse turbine is presented. For an example of application of reaction turbines, the reader is referred to Leon and Zhu (2014).

3. EXAMPLE OF APPLICATION FOR AN IMPULSE TURBINE

The site, penstock and nozzle characteristics for this example are as follows:
1. Gross head (H_g) = 200 m
2. Penstock length (L) = 500 m
3. Ratio of penstock cross-sectional area to nozzle cross-sectional area at its outlet (A_2/A_N) = 16
4. Nozzle velocity coefficient (C_V) = 0.985
5. Sum of local losses in penstock due to entrance, bends, penstock fittings and gates (Σk_{1-2}) = 1.5
6. Roughness height of penstock material (ε) = 0.045 mm (commercial steel)
7. Kinematic viscosity (ν) = 10^{-6} m^2/s
8. Turbine efficiency (η_t) = 82%
9. Generator efficiency (η_g) = 90%

3.1. Case A1: Q is Specified

In this case, it is assumed that the design flow Q is 0.6 m^3/s, and it is desired to know the optimal hydropower that can be extracted using this flow. First, it is necessary to determine the optimal penstock diameter. From Eq. (24),

$$\frac{(C_L)_{\text{opt}}}{A_2^2} = 1693.8272 \text{ m}^{-4} \tag{26}$$

where $C_L = 500f/D_2 + 1.5 + k_N(16^2)$.

The nozzle coefficient is determined using Eq. (3), which gives $k_N = 0.0307$. The friction factor (f) is determined using the explicit Swamee-Jain equation, which is given by

$$f = \frac{0.25}{\left[\log_{10} \left(\frac{\epsilon}{3.7D_2} + \frac{5.74}{\text{Re}^{0.9}} \right) \right]^2} \tag{27}$$

where ε is the roughness height and Re is the Reynolds number. The Reynolds number is defined as VD_2/ν, where V is the flow velocity. Note that when Q is known, f and C_L are functions of D_2 only. Solving for D_2 in Eq. (26) gives D_2 = 0.3968 m. In practice, a penstock with an internal diameter equal or slightly larger than 0.3968 m (397 mm) would be selected. Assuming that a schedule 80 steel pipe is required due to structural considerations, an 18-in outside diameter pipe would be selected. For this pipe, the wall thickness is 0.938 in, and, hence, the internal diameter is 16.124 in (409.5 mm). For this pipe diameter, the value of C_L is 25.35. This value can be used to determine the dimensionless head loss as follows (e.g., see Eq. 6).

$$h_{L+} = C_L \frac{Q^2}{2gH_gA_2^2} = 0.134 \text{ or } 13.4\%$$

(28)

which satisfies the inequality in Eq. (20) (< 15.6%). The electric power that can be extracted from this system can be determined using Eq. (6), which gives,

$$P = 0.82 \times 0.90 \times 1000 \times 9.8 \times 0.6 \times \left(200 - 25.35 \times \frac{0.6^2}{2 \times 9.8 \times 0.1317^2}\right) = 751421 \text{ W} = 751.4 \text{ kW}$$

3.2. Case A2: *P* is Specified

In this case, assume that *P* is 100 kW, and it is desired to determine the optimal flow discharge and optimal penstock diameter to produce this power. In this case, first, the optimal discharge is determined using Eq. (23) as follows:

$$Q_{\text{opt}} = \frac{45}{38}\left(\frac{100,000}{0.82 \times 0.90 \times 1000 \times 9.8 \times 200}\right) = 0.082 \text{ m}^3/\text{s (82 L/s)}$$

The optimal pipe diameter (inside diameter) can be determined in a similar way to Case A1, which gives 0.176 m.

To facilitate the calculations, a MATLAB hydropower calculator was developed for which the graphical user interface (GUI) is shown in Figure 4. As can be observed in this figure, the consumption of flow is optimized in the linear region because the amount of power is proportional to the amount of flow used. Right before the large positive gradient in each curve, both the flow discharge and the penstock diameter are optimized. The hydropower calculator is available at http://web.engr.oregonstate.edu/~leona/Codes/Hydropower/.

Optimal flow discharge and optimal penstock diameter - Arturo Leon, Oregon State University

Optimal discharge and optimal penstock diameter for impulse and reaction turbines

Author: Arturo Leon, Oregon State University   **e-mail:** arturo.leon@oregonstate.edu

Disclaimer: This program is distributed in the hope that it will be useful, but WITHOUT ANY WARRANTY; without even the implied warranty of MERCHANTABILITY or FITNESS FOR A PARTICULAR PURPOSE.

Data Input

Specify the type of turbine — Impulse Turbine

Enter variable that is known — Only flow discharge...

Flow discharge in m^3/s — 0.6

Penstock length [m] — 500

Gross head [m] — 200

Ratio of penstock area to nozzle area [no units] — 16

Nozzle velocity coefficient [no units] — 0.985

Sum of local losses in penstock due to entrance, bends, penstock fittings and gates [no units] — 1.5

Roughness height of penstock material [mm] — 0.045

Kinematic Viscosity [m^2/s] — 1.000e-06

Turbine efficiency (%) — 82

Generator efficiency (%) — 90

Calculate and Plot

Results

Optimal electrical power [kW] — 732.88

Head loss (%) — 15.56   Optimal diameter [mm] — 396.80

Comments: The calculation did not produce errors

Plot legend:
- $\beta = 0.050592$
- $\beta = 0.10118$ (Data)
- $\beta = 0.20237$
- $dP_+/dQ_+ = 0$
- $dP_+/dQ_+ = 0.8\eta$

Vertical axis: $Q_+ = \frac{Q}{Q_0}$
Horizontal axis: $P_+ = \frac{P}{P_0}$

Your data places here
$\eta = \eta_t \times \eta_g = 73.8\%$

OSU Oregon State University

This program is based on the paper:
Leon, A. S. and Zhu, L. (2014), "A dimensional analysis for determining optimal discharge and penstock diameter in impulse and reaction water turbines", Journal of Renewable Energy.

Click here to download paper

Figure 4. Graphical User Interface (GUI) of hydropower calculator

4. CONCLUSIONS

This paper presents a dimensional analysis for determining optimal flow discharge and optimal penstock diameter when designing impulse and reaction turbines for hydropower systems. The aim of this analysis is to provide general insights for minimizing water consumption when producing hydropower. The key findings are as follows:

1. The analysis is based on the geometric and hydraulic characteristics of the penstock, the total hydraulic head, and the desired power production. This analysis resulted in various dimensionless relationships between power production, flow discharge, and head losses.

2. The derived relationships were used to draw general insights on determining optimal flow discharge and optimal penstock diameter. For instance, it was found that for minimizing water consumption, the ratio of head loss to gross head (h_L/H_g) should not exceed about 15%.

3. To facilitate the calculations, a MATLAB hydropower calculator was developed which is available at http://web.engr.oregonstate.edu/~leona/Codes/Hydropower/.

4. Overall, the present analysis is general and can be used for determining optimal design flow and penstock diameter when designing impulse and reaction turbines.

5. ACKNOWLEDGMENTS

6. REFERENCES

Brater, E.F. and King, H.W. (1976). Handbook of Hydraulics, McGraw-Hill, New York.

Dixon, S.L. (2005). Fluid Mechanics and Thermodynamics of Turbomachinery, 5th ed., Elsevier, Burlinton, Massachusetts.

International Energy Agency Implementing Agreement for Hydropower Technologies and Programmes - IEA Hydro (2000). "Hydropower and the world's energy future. The Role of hydropower in bringing clean, renewable energy to the world 2000", <http://www.ieahydro.org/reports/Hydrofut.pdf> (Nov. 30, 2013).

Leon, A.S. and Zhu, L. (2014). "A dimensional analysis for determining optimal discharge and penstock diameter in impulse and reaction water turbines." *Renewable Energy*, 71, 609–615

Pelz, P. (2011). Upper Limit for Hydropower in an Open-channel Flow. *J. Hydraul. Eng*., 137(11), 1536-1542.

Schumann, K., Saili, L., Taylor. R., and Abdel-Malek. R. (2010). "Hydropower and Sustainable Development: A Journey." *Proc., 21st World Energy Congress*, World Energy Council, Montreal, CA.

U.S. Energy Information Administration – USEIA (2013). "World Energy Demand and Economic Outlook". *International Energy Outlook 2013*, <http://www.eia.doe.gov/oiaf/ieo/world.html> (Nov. 30, 2013).

U.S. Institute for Energy Research – USIER (2012). "Renewable energy in the U.S." <http://www.instituteforenergyresearch.org/energy-overview/renewable-energy/#_ednref4> (Nov. 30, 2013).

Spillway Rock Scour Analysis - Composite of Physical & Numerical Modelling, Paradise Dam, Australia

E J Lesleighter[1], E F R Bollaert[2], B L McPherson[3] and D C Scriven[4]

[1]Director, Lesleighter Consulting Pty Ltd, NSW
[2]Principal, AquaVision Engineering Sàrl, Ecublens
Switzerland
[3]Principal Engineer, Specialist Services NSW Public Works
[4]Principal Civil Design Engineer, SunWater Limited, Queensland
Australia

E-mail: lesleighter@yahoo.com

ABSTRACT

A number of problems and solutions of rock scour downstream of spillways have been evaluated using a composite approach based on the gathering of detailed data from a physical model and utilizing those data in a sequence of calibration and application of numerical modeling of the scour. This paper will describe the application of the Computational Scour Model (CSM - Bollaert, 2002 and subsequent) as the numerical procedure that makes the composite approach a proven methodology for such problems. The paper will focus on a case study application of the procedure based on the experiences of flooding and scour at the Paradise Dam, Queensland, Australia.

Flooding in 2013 caused substantial scour downstream of the primary spillway. The occurrence led to a series of studies for the evaluation of the geology and the evident hydraulics behaviour, using a well-instrumented physical model to capture pressure and velocity transients, all as part of a process to determine the scour mechanism and to determine the response of the spillway and areas downstream to future floods of larger magnitude. Utilizing the transient data from approximately 60 pressure transducers, ADV measurements for transient velocities, and a detailed geologic assessment, the comprehensive scour modeling procedures developed by Bollaert were applied for calibration of the numerical model and its application for possible discharge scenarios.

The paper will discuss the design and construction of the physical model and instrumentation as a key part of securing adequate data for the composite procedure, and goes on to illustrate the outcomes of the CSM procedures.

Keywords: *Spillways, flood hydraulics, hydraulic modelling, numerical modelling, rock scour, transients, numerical analysis, energy dissipation.*

1. INTRODUCTION

Since 2010, a succession of floods in eastern Australia, and particularly in Queensland, brought about spillway operation with return periods in the region of Annual Exceedance Probabilities (AEP) of 1 in 2,000 or more. Rock erosion at Wivenhoe Dam (near Brisbane) has been discussed in a number of publications (Lesleighter, Andaroodi & Stratford (2012); Lesleighter, Stratford & Bollaert (2013); Bollaert & Lesleighter (2014); and Bollaert, Stratford & Lesleighter (2014)).

Paradise Dam, Queensland, is a RCC dam with a 315 m long stepped primary spillway with an ogee crest level of EL 67.6 m. A flood with a peak discharge having an AEP of 1 in 30 occurred in December 2010-January 2011. This caused a certain amount of re-adjustment of the loose rock and alluvium and some damage to the stilling basin apron due to ball milling effects from rock in motion. The focus of the present paper is an appreciably larger flood (AEP in 1 in 170) in January 2013, which caused extensive and deep scour downstream of the apron as well as removal of a 1-metre-high end sill.

Following that flood, investigations comprising the geology downstream of the spillway, detailed surveys, and concrete works to repair and enhance the stilling basin apron have been directed towards investigation of the rock scour and its possible occurrence in the future. A key thrust of the studies has been the use of a physical model to quantify the hydraulics and hydrodynamics of the primary spillway and numerical modelling to evaluate the possible rock scour for future discharge scenarios. The paper provides detail according to the following:

- A description of the scour
- The geology of the areas prone to scour
- The flood characteristics
- The design of the physical model
- The application of geologic and model data for processes of calibration and application of Comprehensive Scour Modeling, (CSM – Bollaert (2004)), and
- The modeling outcomes and preliminary investigation of types of remedies.

2. PARADISE DAM PRIMARY SPILLWAY

The primary spillway is 315 m long with an ogee crest at EL 67.6 m and maximum height of 36.1 m. The crest is constructed in conventional reinforced concrete, and the downstream stepped face is capped with reinforced concrete anchored into 620 mm tall RCC steps. At the base of the steps, spillway flows meet a horizontal apron approximately 20 m in length with a vertical end sill 1 m in height. At the left end of the spillway, the original apron was at a level of EL 37.6 m, and at the right end, the apron was at EL 30.9 m. Figure 1 is a photograph of the dam and spillway. Figure 2 shows some detail of the primary spillway.

Figure 1. Paradise Dam primary spillway (2007)
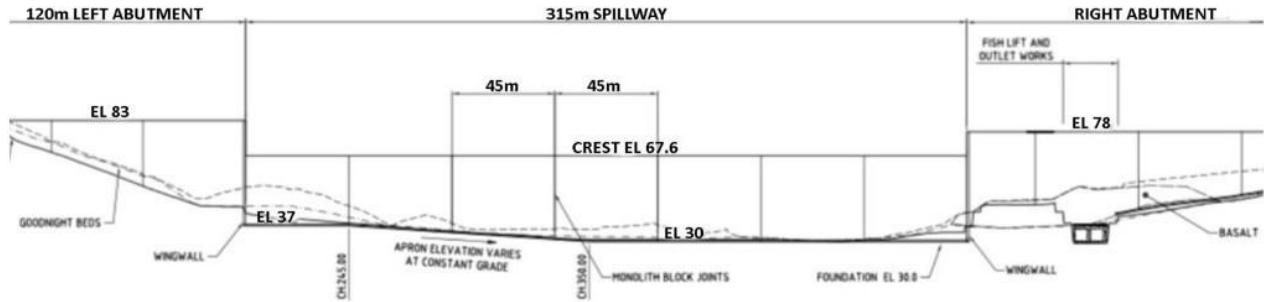
Figure 2. Transverse section of primary spillway (from upstream)

3. THE FLOOD OF 2013

The primary spillway was overtopped by 6 m on 29 December 2010. The reservoir level peaking at EL 73.6 m and remained above the crest level for more than three weeks. The peak discharge was equivalent to approximately 9,600 m^3/s, or a unit discharge, q, of 30.48 m^2/s. Table 1 presents the AEP discharges up to the AEP 1 in 10,000. Of much more consequence was a flood in January 2013. The peak reservoir level was EL 76.2 m, 8.6 m above the crest, and the corresponding discharge was 17,090 m^3/s, a unit discharge of 54.3 m^2/s. The Paradise outflow hydrograph is shown in Figure 3.

Table 1. Paradise Dam AEP Discharges

AEP (1 in year)	Discharge (m^3/s)
50	12,840
100	15,410
200	17,490
500	20,820
700	22,330
1,000	24,440
2,000	28,180
3,000	31,950
10,000	48,740
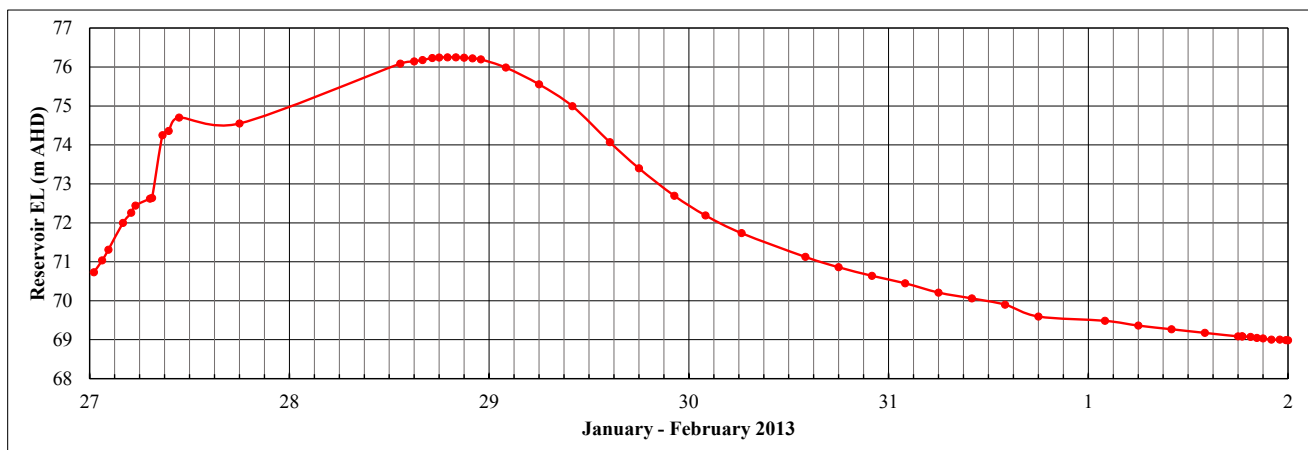
Figure 3. Paradise primary spillway stage hydrograph January 2013

The earlier flood produced some scour of material downstream of the spillway – mainly removal of alluvium and some movement of loose rock and rip rap. The 2013 flood, however, produced scour right across the length of the

primary spillway, some deep scour adjacent to the apron, and removal of the end sill. Figure 4 is a photograph of the flood behavior, and Figure 5 illustrates the scoured surface over the area downstream of the spillway.

The damage was judged sufficiently extensive to warrant a certain amount of repair concrete works in the interim and led to a series of activities to fully investigate what the event meant in relation to future floods. Those activities broadly comprised more detailed geologic investigations, and a model testing and scour modeling program – the latter being the emphasis of the present paper.

4. GEOLOGY

The scour from the 2013 flood (Figure 5) demonstrated a geologic condition that provided scant resistance to the energy dissipated during the four-to-five day 2013 flood event. The dam is generally founded on metasediments known as the "Goodnight Beds" except on the right side where it is founded on basalt. Following the flood of 2013 and subsequent scour, further geotechnical investigations were undertaken. Features of particular note are faults, termed the "Paradise Fault" and the apron faults.

The Paradise fault, located downstream of the dissipator slab, is a zone of Goodnight Beds that has been subjected to intense structural deformity. The zone is characterised by a series of closely spaced shears, dykes, and faults. These features are steeply dipping. The apron faults are a series of major thrust faults that meander between outcropping downstream of the dissipator slab or concealment under the slab. These faults dip moderately underneath the dissipator slab.

Figure 4. Flood behaviour January 2013

Figure 5. 2013 flood scour downstream of the primary spillway

The deep scour that occurred in the 2013 flood, relatively close to the apron, including the removal of the vertical end sill, led to a series of investigations and analyses related to dam stability and the part that the geologic conditions played in the dam's integrity. It was necessary to augment the geologic knowledge of the site by extensive site investigations and mapping.

The safety evaluations included not only the depth of scour that had occurred – up to 13 m below apron level in one location – and the geologic investigations, but also investigation of the integrity of the concrete in the spillway apron. At an early stage following the 2013 flood, concrete works were implemented immediately downstream of the apron and included a capping slab on the apron itself. These measures were simply a precaution while the more detailed studies were being carried out.

As it was clear that future floods might lead to more extensive scour of the apron and rock downstream of the apron, the dam owner, SunWater, defined and initiated additional studies of the geology and evaluations of the stability of the dam as well as the program of hydraulic modeling and numerical scour modeling, which are the subject of the present paper.

5. PHYSICAL MODEL

A three-dimensional hydraulic model was commissioned by SunWater. It was built and tested by the Manly Hydraulics Laboratory (MHL), Sydney NSW for detailed studies of the Paradise Dam spillways. The hydraulic modeling was one part of a two-part hybrid approach to the rock scour investigation – the other part being the application of a numerical modeling calibration and analysis procedure.

The model was built to a scale of 1:70, with the ability to test for discharges up to the AEP 1 in 10,000. It was set up to investigate the spillway's as-built condition, the post-2011 flood condition, the post-2013 flood condition including interim works mentioned above, and studies of the secondary spillway overflow of the right abutment of the dam. Figure 6 provides a general view of a portion of the model with some of the flush-diaphragm transducers. Figure 7 shows the model operating at a mid-range discharge. Model instrumentation included more than 60 pressure transducers, a large number of piezometers, and an Acoustic Doppler Velocimeter (ADV) with electromagnetic flow metering up to model discharges of 1,200 L/s. Figure 8 illustrates the pressure transducer coverage on several lines.
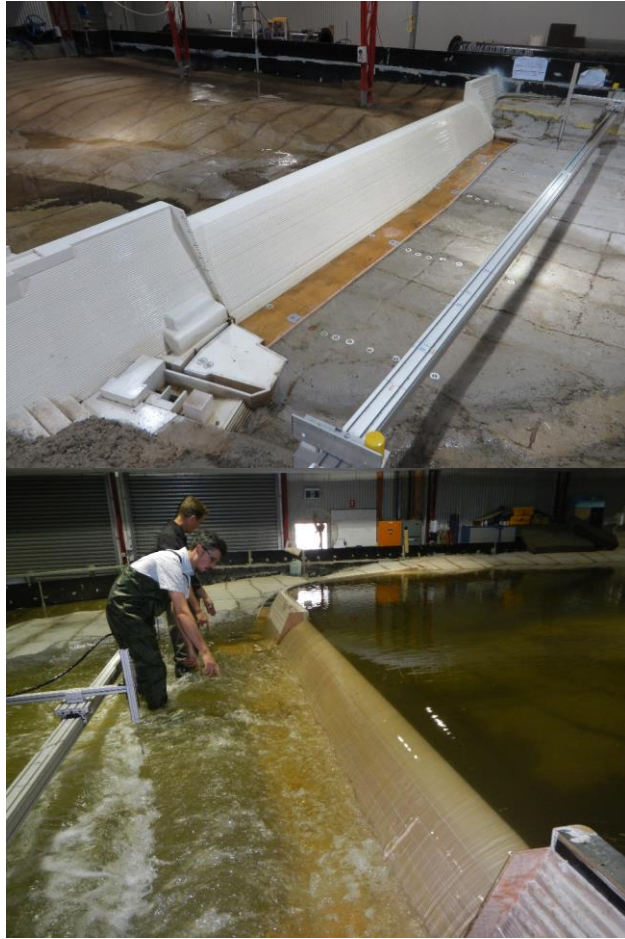
Figure 6. Model showing pressure transducer lines   Figure 7. Paradise Dam physical model
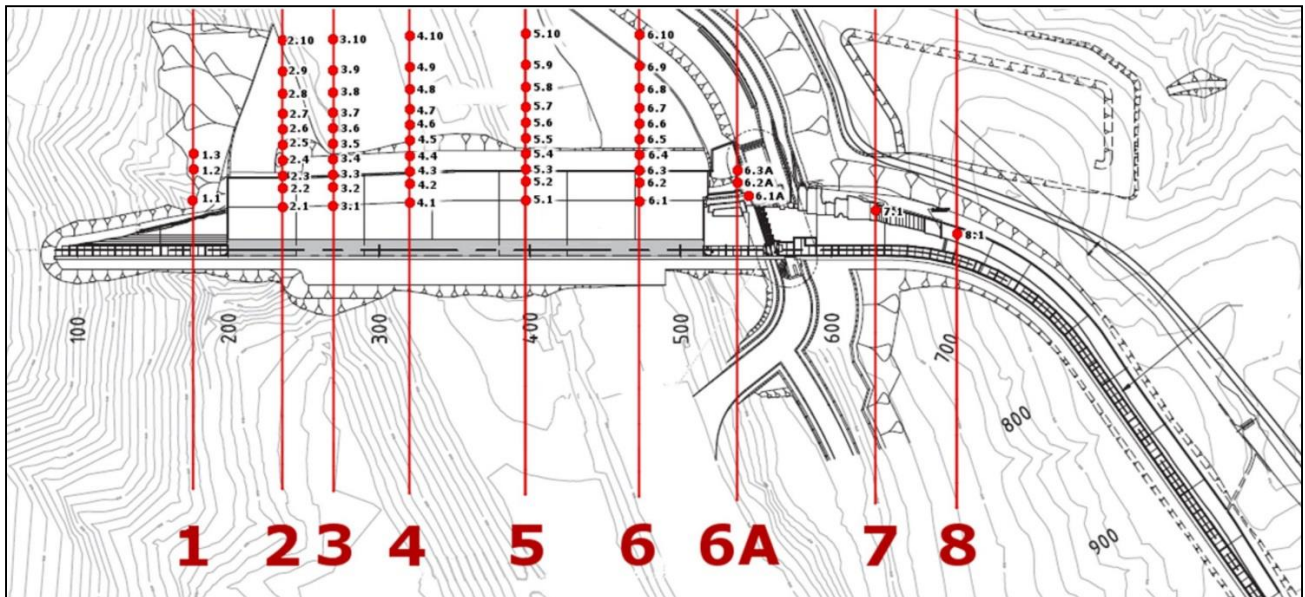
Figure 8. Paradise model pressure transducer coverage

The sensors used were Keller Series 25 flush diaphragm temperature-compensated vented-gauge transmitters, factory-adjusted to provide a single-ended high level linear output from -30 to +200 mbar. Velocity measurements were made using a SonTek 10-MHz ADV. Velocities at each measurement location (subject to the water depth) were recorded at four or five heights for each flow test in the x, y, z directions. All ADV velocity measurements were recorded at a sampling rate of 20 Hz for a 60-second period. The transient pressures at 58 locations in the spillway apron and downstream were measured at a sampling rate of 400 Hz for a period of 150 s (60,000 values).

6. FACTORS AFFECTING ROCK SCOUR

In evaluating the factors which affect rock scour, it becomes clear that it is not simply a case of velocity, however high the velocity may be, but it is the characteristics of turbulence and the intensity of turbulence in the energy dissipation process, which is going on in dissipators and plunge pools. Furthermore, the presence of entrained air is important because of the physics of what is going on in flows impacting rock bodies containing an array of fissures. Vital to the erodibility issue is the particular geology of the plunge areas. The character of the rock mass with its variability and low strength character is key to the manner in which the rock will respond to the flows impacting it. The velocities impacting the deep tailwater at Paradise would be generally less than about 25 m/s, and at the rock surfaces, the impact velocities due to a certain amount of decay would be appreciably lower. Of particular relevance to the ability of a plunging jet and hydraulic jump to fracture the rock is the way pressure transients impact the rock surface and penetrate the rock defects and bedding.

The scour that occurred at Paradise Dam primary spillway resulted from discharges that had a difference in head between the reservoir level and the tailwater level of less than 30 m – a difference that can be classed as modest when compared with many spillways operating under much greater heads.

For a long time, the design of stilling basins was based on velocities and sufficient depths to retain a hydraulic jump. Bowers and Toso, 1988, reported as follows: "*many of the large dams in the United States utilize ... structures designed before information was available on the magnitude of fluctuating pressures in the hydraulic jump ... turbulent pressure fluctuations in the hydraulic jump should be considered in the design of stilling basins…*" It is the key effect of the transient behavior that is encompassed in the numerical procedures to estimate rock scour as described below.

The hydrodynamics of situations like those at Paradise Dam show that it becomes not simply the velocities, or even the pressures impacting the rock surfaces, but also the transient behavior in the turbulent flow and in addition a mechanism of amplification of pressures within the rock defects and fissures. The transients play a vital and often neglected part.

7. BOLLAERT COMPREHENSIVE SCOUR MODEL (CSM)

The Comprehensive Scour Model comprises three methods that describe failure of jointed rock. The Comprehensive Fracture Mechanics (CFM) method determines the ultimate scour depth by expressing instantaneous or time-dependent joint propagation due to water pressures inside the joint. The Dynamic Impulsion (DI) method describes the ejection of rock blocks from their mass due to sudden uplift pressures. The Quasi-Steady Impulsion Model (QSI) describes peeling off of rock blocks from their mass by quasi-steady wall jet flows. The structure of the Comprehensive Scour Model consists of three modules: the falling jet, the plunge pool and the rock mass. The latter module implements the aforementioned failure criteria. More details on equations that describe the hydrodynamics can be found in Bollaert (2004).

The 'falling jet' module describes how the hydraulic and geometric characteristics of the jet are transformed from dam issuance down to the tailwater pool. The 'plunge pool' module describes the characteristics of the jet when traversing the pool into which the jet impinges and defines the water pressures at the water-rock interface. In the Paradise situation, the overflow jet impacts the tailwater and spreads to then be deflected by the apron into the tailwater on the way to impacting the rock, generating in this way a sort of semi-submerged hydraulic jump turbulence. Finally, the 'rock mass' module contains the aforementioned rock break-up methods. The main

hydrodynamic parameters used by the CSM are the bottom flow velocities and the fluctuating and maximum dynamic pressures. In this study, these were recorded firstly on a physical model for different discharge scenarios, and then used as input by the CSM. Full details of the numerical rock break-up modules are outside the scope of this paper, and a comprehensive discussion of the components of the methodology and their direct relevance to the dynamics of rock scour is described by Bollaert et al, 2014 (ICSE Perth).

The detailed analyses that have applied the CSM procedures passed through two stages of calibration using the actual flood hydrograph in histogram format and use of the calibrated model to estimate various scour flood discharge scenarios. The calibration, for the most part, used the actual hydrographs of the 2013 flood. The calibration analyses for one of the profiles downstream of the spillway, Line 2 (see Figure 8), are shown in Figure 9.
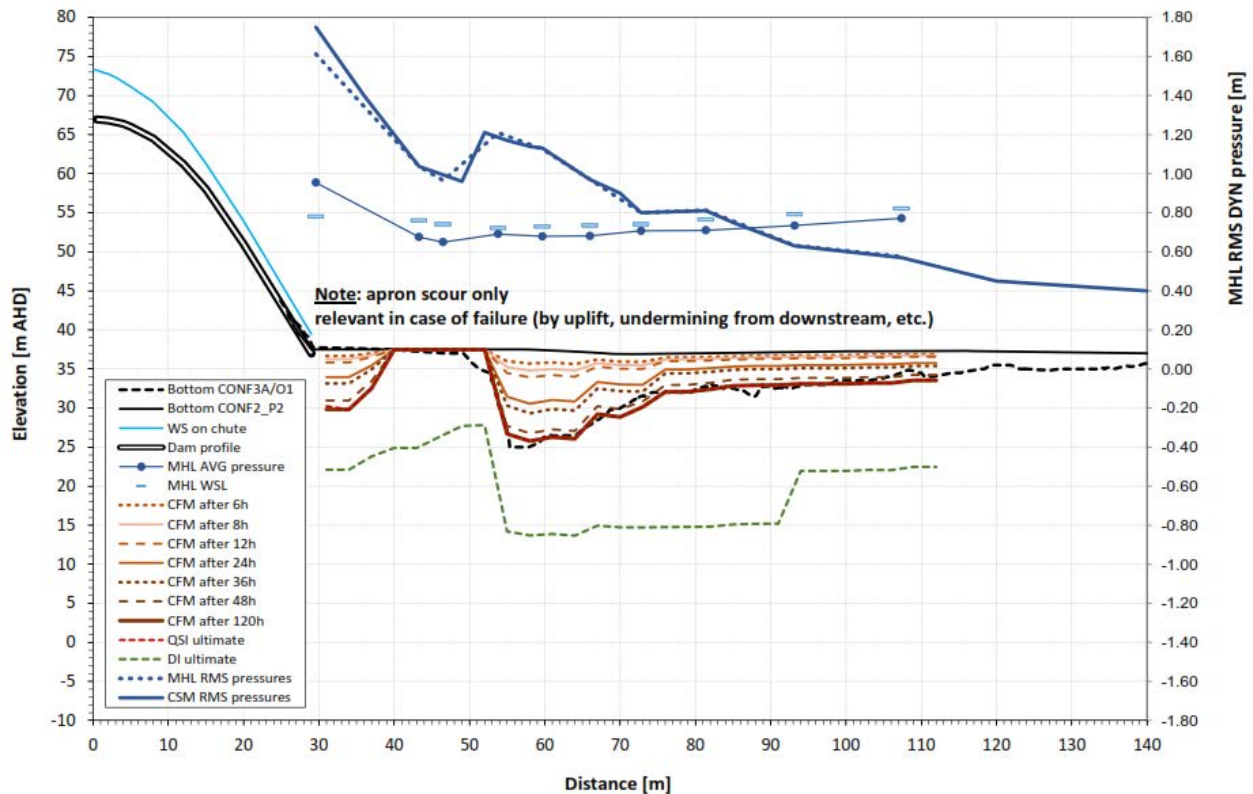
Figure 9. CSM calibration for the 2013 flood hydrograph

The profiles show the analysis of scour for the three modules described above (CFM, QSI, and DI). In this flood, the rock scour was extensive. There are some key profiles to note. In light blue, the average of the dynamic pressures elevation from the transducers is shown. In heavy blue, the standard deviation of the measured and CSM calculated fluctuations is shown (read right). Other key profiles are in brown and show the estimate of progressive scour with exposure times for 6 to 120 hours. These may be compared to the black dashed profile, which is the surveyed profile following the 2013 flood.

On the basis of a successful calibration, as adjudged from the profiles exemplified in Figure 9, the CSM procedure was in a position to proceed to analysis of future scour. For those procedures, it was necessary to determine a long-term series of flood discharges that could be applied to determine on a time or year basis the expected scour that could occur downstream of the primary spillway. Using the selected discharge scenarios and the dynamic pressures and flow velocities as measured on the physical model, the CSM was set up also to investigate possible works if they were determined to be required.

Figure 10 is an example of the estimated potential scour downstream of the existing apron for a range of discharges devised to represent a scenario of six floods with discharges ranging from an AEP of 100 to and AEP of 1 in 10,000. While each module of the CSM procedure is shown (brown, red dashed, and green dashed), the time estimate of

scour using the Comprehensive Fracture Mechanics module, shown in brown, is deemed to represent the possible scour progress for the selected hypothetical range of floods and discharges. As noted on the figure, the scour profiles "under" the apron (distance 30m to 50m) apply to the possible scour in the event that the apron was actually removed.
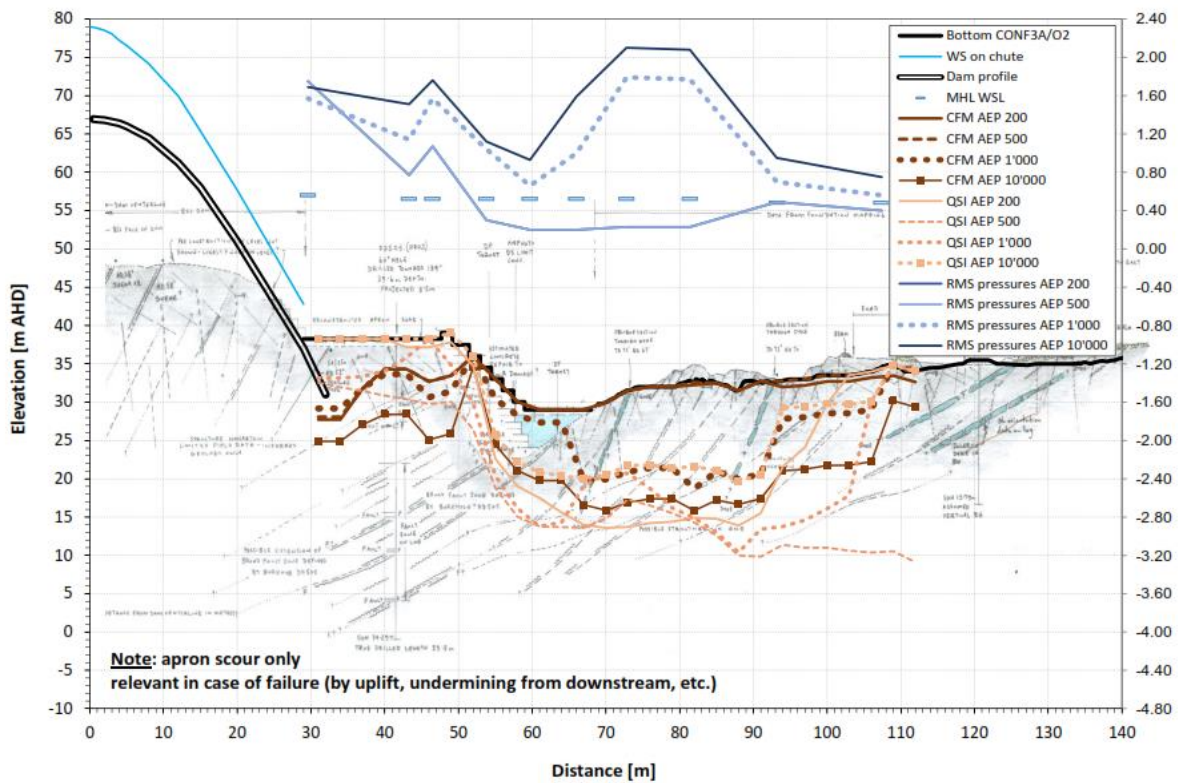
Figure 10. Estimate of future scour progress for a range of large flood discharges

8. CONCLUSIONS

The paper uses a real situation of flood-induced scour to illustrate an advanced composite methodology to evaluate the factors in hydraulics and energy dissipation that cause the scour of rock around dams and spillways. The Paradise Dam experience is a notable example, similar to many others in different types of spillways, of how high-power flows are able to scour rock – even rock that is apparently or seemingly hard and durable. The methodology described herein illustrates two key components, in addition to a proper and full understanding of the local geology, namely (1) a well-scaled and instrumented physical hydraulic model and (2) a comprehensive, physics-based application of the data to the numerical analysis of pressure and pressure amplification to the breaking up and scour of rock. Composite application of both components allowed sound calibration of the numerical model and estimates of future scour progress for different discharge scenarios.

9. ACKNOWLEDGEMENTS

10. REFERENCES

Bollaert, E F R. (2004). A comprehensive model to evaluate scour formation in plunge pools, Int. J. Hydropower & Dams, 2004(1), pp 94-101.

Bollaert, E F R, and Lesleighter, E J. (2014). Spillway rock scour experiences and analysis – the Australian scene over the past four decades, Int. Symp. on Hydraulic Structures, Brisbane, June.

Bollaert, E F R, Stratford, C E, and Lesleighter, E J. (2014). Numerical modelling of rock scour, Case study of Wivenhoe Dam, Int. Conf. Scour and Erosion, Perth, December.

Bowers, C E, and Toso, J. (1988). Karnafuli project, model studies of spillway damage, ASCE Jl. of Hydraulic Division, May.

Lesleighter, E J, Andaroodi, P, and Stratford, C E. (2012). Rock erosion experiences in the Wivenhoe Dam Spillway, ANCOLD, October.

Lesleighter, E J, Stratford, C E, and Bollaert, E F R. (2013). Plunge pool rock scour experiences and analysis techniques, IAHR Congress, Chengdu, China, September.

Experimental Study of Sequent Depths Ratios of Hydraulic Jump in Sloped Trapezoidal Channels

Sonia Cherhabil[1], Mahmoud Debabeche[2]
[1&2]Research Laboratory in Civil and Hydraulic Engineering,
Sustainable Development and Environment (LARGHYDE)
University of Biskra, BP145 RP07000
ALGERIA
E-mail : soniacherhabil@hotmail.fr

ABSTRACT

The hydraulic jump in a sloped trapezoidal channel of 72.68° sidewall inclination angle was experimentally examined. The study aimed to determine the effect of channel slope on the sequent depths ratio of the jump. An experimental analysis is proposed to determine experimental relationships of the inflow Froude number as a function of the sequent depth ratio of the jump and the channel slope. For this purpose, positive and negative slopes were tested.

Keywords: Hydraulic jump, trapezoidal channel, positive slope, adverse slope, open channels, stilling basins.

1. INTRODUCTION

Hydraulic jumps are formed during the abrupt transition from supercritical to subcritical flow, when energy is dissipated. This phenomenon is invoked generally either downstream of a dam in order to dissipate the hydraulic energy or in water conveyance channels to rise the stream level. The hydraulic jump has been studied by many researchers such as Bradley and Peterka (1957), Hager and Bretz (1987), Hager (1992), and Ead and Rajaratnam (2002). Most studies focused on the hydraulic jump in horizontal rectangular channels. However, the first detailed study on the hydraulic jump in a rectangular channel with positive slope was carried out by Bakhmeteff and Matzke (1938), who examined the surface profile, the jump length, and the jump speeds distribution. Additionally, Kindsvater (1944) classified the sloped hydraulic jump, according to the position of the upstream edge of the jump with regard to the end of the slope, into four types: A-jump, in which the toe of the jump coincides with the downstream extremity of the slope; B-jump, in which the toe of the jump is between the A-jump and the C-jump; C-jump, in which the end of the jump roller coincides with the downstream extremity of the slope; and D-jump, in which the jump roller appears completely in the sloped portion. The D-jump was analyzed by Wilson (1970), Ohatsi and al (1973), Rajaratnam and Murahari (1974), and Mikhalev and Hoang (1976). Debabeche et al. (2009) have studied the hydraulic jump with positive slope in a triangular channel. Cherhabil (2010) subsequently developed, in her PhD thesis, the hydraulic jump with a positive slope in triangular and U-shaped channels. The most recent work on the hydraulic jump in a trapezoidal channel is that of Kateb (2014).

This study proposed an experimental research on the hydraulic jump in a sloped trapezoidal channel. The configuration adopted in this article corresponds to the D-jump type according to the classification of Kindsvater (1944). The objective is to determine the effect of the channel slope on the upstream sequent depth h_1 and downstream sequent depth h_2 for this jump configuration experimentally. However, empirical relationships are proposed relating the sequent depth ratio (Y) to the inflow Froude (F_1) and the channel slope (i).

2. EXPERIMENTAL SET-UP

Experimentation was carried out in a trapezoidal channel of 6 m length, 20 cm width, and 72.68° sidewall inclination with regard to the horizontal [see Figure 1]. Initial flow was generated by a set of five load boxes [see Figure 2] for which the opening heights correspond to the upstream sequent depths: h_1(mm) = 20, 30, 40, 50, and 60. For each chosen height h_1, six positive and two negative (adverse) slopes were tested so that the channel slope takes the following values, i(%): 0.005; 0.01; 0.015; 0.02; 0.00;-0.005 ;-0.01. Additionally, 22 thin

sills of different heights *s* varying from 5 to 26 cm were used to control the hydraulic jump [see Fig. 3]. A practical range of inflow Froude numbers was obtained ($1\leq F_1\leq 14$).

Figure 1. Trapezoidal channel

Figure 2. Load boxes

Figure 3. Thin sills

3. Sequent Depth Ratio

Figures 4, 5, 6, 7, and 8 show the variation of the sequent depth ratio $Y = h_2/h_1$ as function of the inflow Froude number F_1 for seven slopes. Data analysis showed that a linear equation is possible for each value of the slope channel. This latter follows the form of $y = a\ i + b$.

Upstream Sequent Depth : h_1=20mm
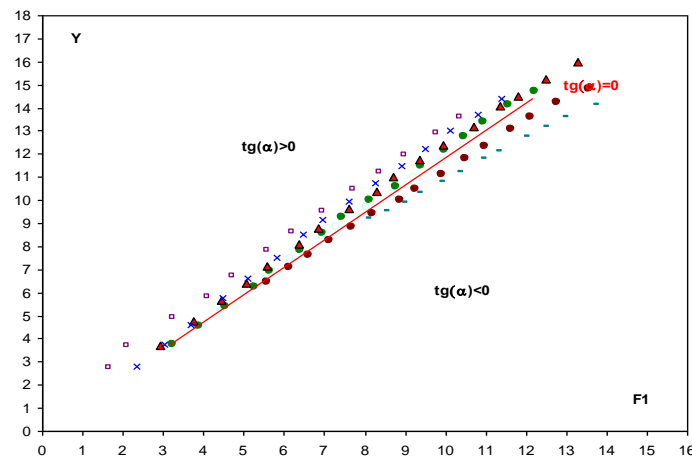
Figure 4. Variation of the sequent depth ratio as function the inflow Froude number for seven values of the channel slope *i=(●)0.005,(Δ) 0.01, (×) 0.015,(□) 0.02;(○) 0.00,(●)-0.005,(-)-0.01(———)Trend Curve for (◆) 0.00.*

Upstream Sequent Depth : h_1=30mm
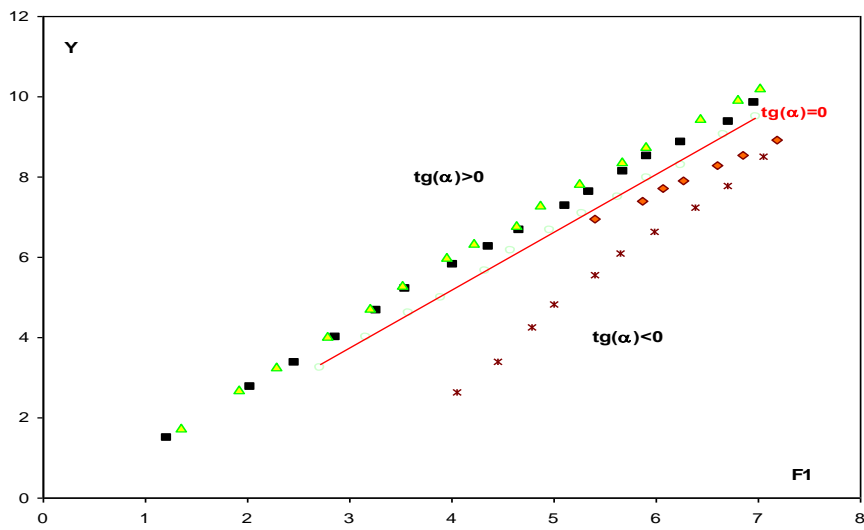
Figure 5. Variation of sequent depth ratio as function of the inflow Froude number for five values of the channel slope, such as $i=tg(\alpha)$ = (□)0.005, (Δ) 0.01, (○) 0.00,(◆)-0.005,(*)-0.01. (——)Trend Curve for (◆) 0.00.

Upstream Sequent Depth : h_1=40mm
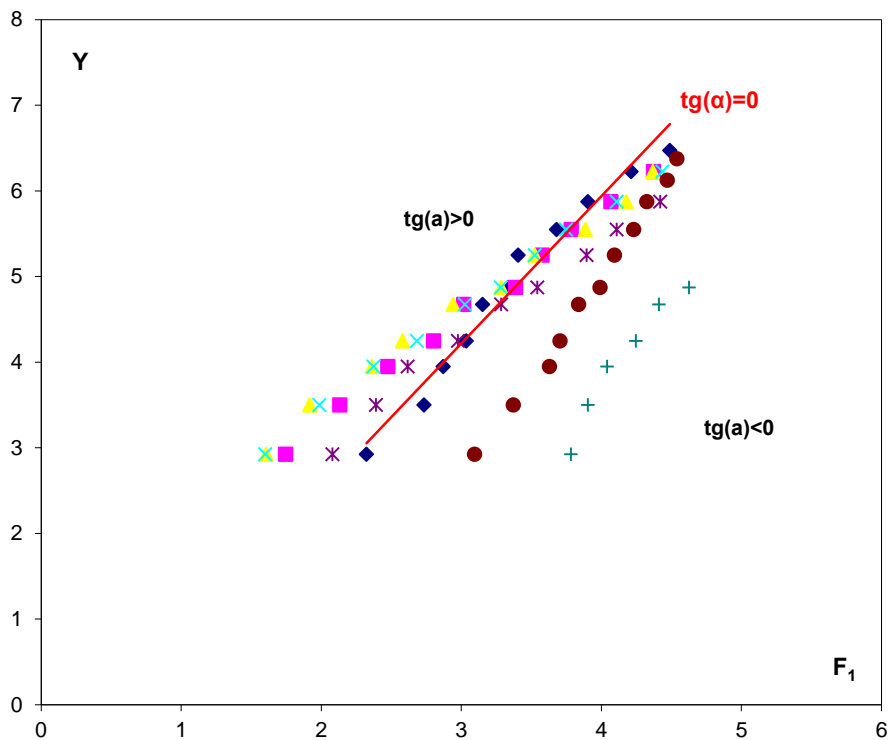
Figure 6. Variation of the sequent depth ratio as function of the inflow Froude number for seven values of the channel slope, such as $i=tg(\alpha)$ = (*)0.005,(□) 0.01, (×) 0.015,(Δ) 0.02;(◆) 0.00,(●)0.005,(+)-0.0 . (——)Trend Curve for (◆) 0.00.

Upstream Sequent Depth : h₁=50mm
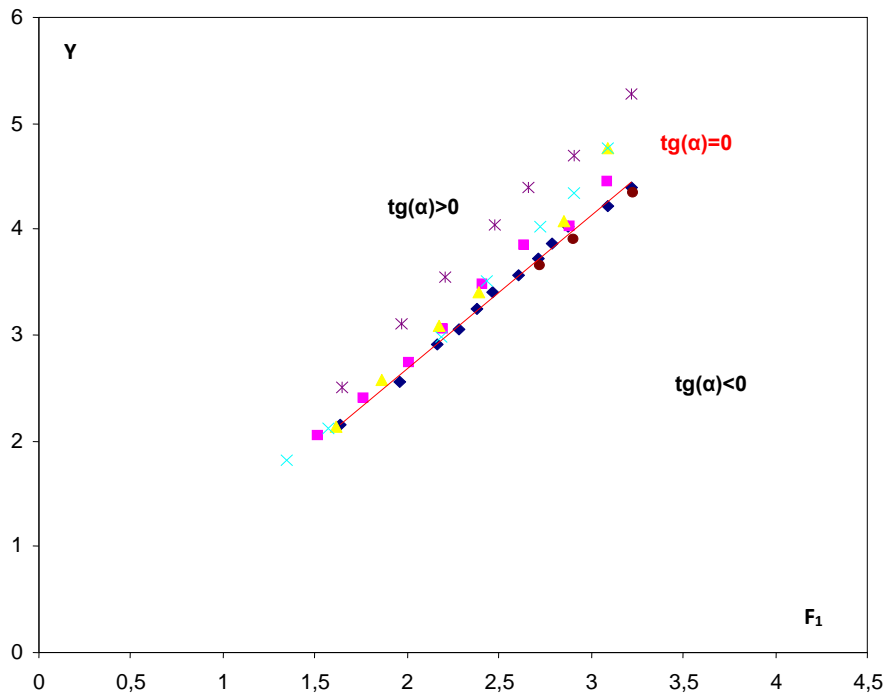
Figure 7. Variation of the sequent depth ratio as function of the inflow Froude number for six values of the channel slope *i=(□)0.005,(Δ) 0.01, (×) 0.015,(*) 0.02;(◆) 0.00,(●)0.005. (—)Trend Curve for (◆) 0.00.*

Upstream Sequent Depth : *h₁=60mm*
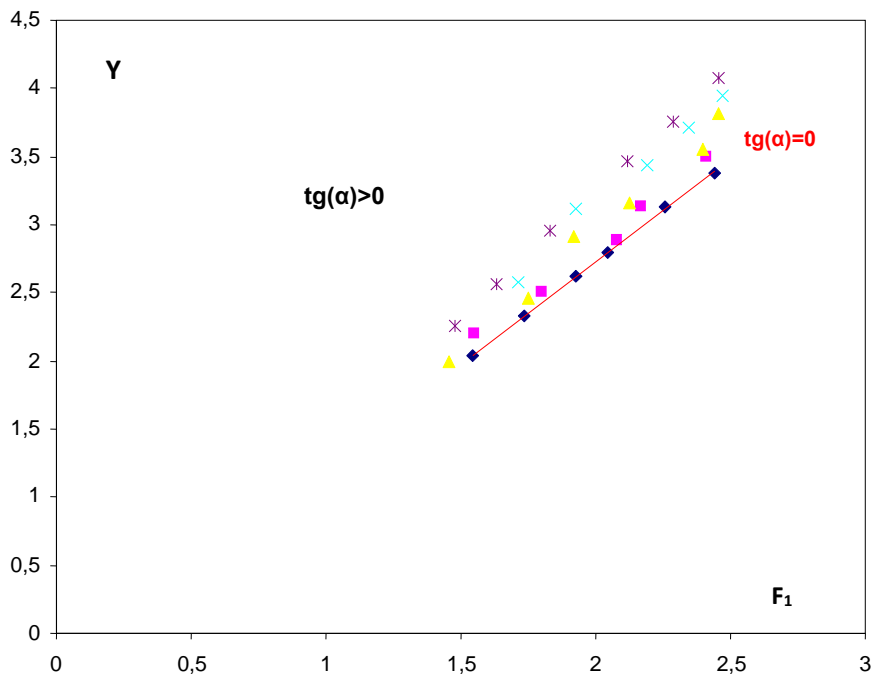
Figure 8. Variation of the sequent depth ratio as function of the inflow Froude number for five values of the channel slope, such as *i=tg(α) = (□)0.005,(Δ) 0.01, (×) 0.015,(*) 0.02;(◆) 0.00. (—)Trend Curve for (◆) 0.00 .*

Table 1. Explicit relationships of variation of the sequent depth ratio, as function of the inflow Froude number and channel slope.

Initial depth h_1	Relation of Y_{app}	$i=tg\ \alpha$ (%)	F_1
20 mm	$Y_{app}= (3.25\ tg(\alpha)+1.17)\ F_1 + 39.65\ tg(\alpha) + 0.09$	[0 - 2]	[3.1 - 3.6]
	$Y_{app}= (13.1\ tg(\alpha)+1.156)\ F_1 + 0.395$	[-1 - 0]	[3.1 - 3.6]
30 mm	$Y_{app}=(\ 5,535\ \ tg\ (\alpha) + 1,446)F_1+(\ 3,331\ tg\ (\alpha) + 0,082)$	[0 - 2]	[4 - 8]
	$Y_{app}=1,4/4F_1 -1,545$	[-1 - 0]	[4 - 8]
40 mm	$Y_{app}=(8,2\ tg\ (\alpha)+ 1,032)F_1 -65,1\ tg\ (\alpha) +2,006$	[0 - 2]	[1 - 5]
	$Y_{app}=1,4/4F_1 -1,545$	[-1 - 0]	[3 - 5]
50 mm	$Y_{app}= (\ 11,177\ tg\ (\alpha)\ +\ 1,521)\ F_1 + (\ 24,7\ tg\ (\alpha)\ - 0,858)$	[0 - 2]	[1 - 4]
60 m	$Y_{app}= 17,134\ tg\ (\alpha)\ + 1,4789)\ F_1 - 15,243\ tg\ (\alpha)\ - 0,1152$	[0 - 2]	[1 - 3]

Explicit relationships provide a simple way for determining the ratio of the combined heights Y by knowing the inflow Froude number F_1 and the value of the channel slope.

4. CONCLUSION

The hydraulic jump in a sloped trapezoidal channel was experimentally studied. The configuration of the jump adopted in this study corresponds to the D-jump. The experimental study focused on the variation of the relative height Y. The generalized relations obtained, express the sequent depth ratio Y as a function to the inflow Froude number F_1 and the channel slope i.

5. REFERENCES

Argyropoulos, P., A., (1962), General solution of the hydraulic jump in sloping channels, Proc. ASCE, J. Hydraulic Division, Vol. 88, HY4, pp. 61-75.

Beiram, M., K., Chamani, M.,R., (2006), Hydraulic Jumps in Sloping Channels: Sequent Depth Ratio, J. Hydraulic Engrg., vol 32(10), pp. 1061-1068.

Bradley, J.N., Peterka, A.J., (1957), The hydraulic design of stilling basins : Hydraulic jumps on a horizontal apron, paper 1401, proc. Amer. Soc. Civ. Engnrs., J. Hydraulic. Division, Vol.83, HY5.

Cherhabil, S., (2010) Le ressaut hydraulique dans les canaux prismatiques à pente variable, Thèse de doctorat en sciences, département de génie-civil et hydraulique, de l'université Mohamed Khider, Biskra, Algérie.

Debabeche, M., Cherhabil, S., Hafnaoui, A., Achour, B., (2009) hydraulic jump in a sloped triangular channel, canadian journal of civil engineering, 36(4), pp. 655-658.

Forster, J.W, Skrinde, R.A (1950), Control of the hydraulic jump by sills, Trans Asce, 115, 973-1022.

Hager, W.H., Sinniger, R., (1987), Construction hydraulique, Ecoulement stationnaire, Edition suisse romande.

Hager, W.H, and Nicola V.Bretz (1988à, Sill-Controlled stilling basin, the international symposium on hydraulics for high dams, 273-280.

Kateb,S., (2014) etude théorique et experimentale de quelques types de ressauts hydrauliques dans un canal trapezoidal. Thèse de doctorat en sciences, département de génie-civil et hydraulique, de l'université Mohamed Khider, Biskra, Algérie.

King, S., and Delatte, N.J. (2004). "Collapse of 2000 Commonwealth Avenue: Punching shear case study." *J. Perf. Constr. Facil.,* 18(1), 54-61.

Mc Corcodal, 1994, Journal of Hydraulic Research, VOL. 32, 1994, NO.1; 119-130.

Noor Afzal, A. Bushra (2002), structure of the turbulent hydraulic jump in trapezoidal channel. Journal of hydraulic Research 40(2), 205-214.

Ohashi et al. (1973) :Design of Combined Hydraulic Jump and Ski-Jump Energy Dissipator of Flood Spillway. XIII ICOLD Congress Madrid Q.41, R.19: 311-333.

Okada, A., et Aki, S. (1955). Experimental study of hydraulic jump on reversed slope apron. J. Tech. Lab., 5(6), Tokyo (in Japanese).

Pagliara, S. Peruginelli, A. 2000, Journal of Hydraulic Engineering/ November 2000/ 847-850.

Posey, C.J and Hasing, P.S, (1938), Hydraulic jump in trapezoidal channel, Engineering News Record, Vol.121, Des.22 nd, 797-798.

Press, M.T, (1961), The hydraulic jump Engineering honors thesis, University of western Australia, Nodlands, Australia.

Rajaratnam, N. (1963): Discussion to "General Solution of the Hydraulic Jump in sloping Channels"

Rajaratnam, N., (1965), Hydraulic Jump in horizontal conduit, Water Power, 17, pp. 80-83.

Rajaratnam, N (1967), hydraulic jumps. Advances in Hydroscience. Vol4. Academic Press, New York, 197-280.

Silvester, R (1964), Hydraulic jump in all shapes of horizontal channel, Journal of hydraulic division, ASCE (HY1), 23-55.

Sinniger, R.O, Hager W.H -1988), Ecoulement stationnaire, Presses Polytechniques Romandes, 439p.

Wanoschek, R. Hager, W.H (1989), Hydraulic jump in trapezoidal channel, Journal of Hydraulic Research 27(3), 429-446.

6. LIST OF SYMBOLS

D Diameter of the channel [m]

F_1 inflow Froude number [-]

g acceleration of gravity [m.s^{-2}]

h_1 upstream sequent depth [m]

h_2 downstream sequent depth [m]

i channel slope ($i=tg(\alpha)$)

Q flow discharge [m^3.s^{-1}]

Y sequent depth ratio

α angle of inclination of the channel with regard to the horizontal [rad]

Nappe Vibration Mitigation Techniques for Free-overfall Structures

M. Lodomez[1], B. M. Crookston[2], B. P. Tullis[3], M. Pirotton[1], S. Erpicum[1]
[1]Dept. of Hydraulics in Environmental and Civil Engineering
University of Liège
Quartier Polytech - Allée de la Découverte, 9 (B52/3), Liege 4000
BELGIUM
[2]Schnabel Engineering, Inc.
1380 Willmington Pike, Suite 100, West Chester, Pennsylvania 19382
USA
[3]Utah Water Research Laboratory
Utah State University
8200 Old Main Hill, Logan, Utah 84322-8200
USA
E-mail: m.lodomez@ulg.ac.be

ABSTRACT

Nappe vibration is a phenomenon that has been witnessed in the field for a variety of different free-overflow hydraulic structures operating at low heads, such as fountains, crest gates, and weirs. This phenomenon is visually characterized by oscillations in the thin nappe cascading downstream of the control structure. These oscillations can produce a significant level of noise and acoustic pressure waves, which can increase the environmental and societal impacts of the hydraulic structure. As a result, a detailed investigation has been undertaken to identify practical and effective mitigation solutions for free-overfall structures where nappe vibration may be of concern. Research is being performed with a prototype-scale linear weir (weir length of 3.5 m and fall height of 3 m) located at the Engineering Hydraulics laboratory of the University of Liège to assess the effectiveness of various crest modifications and any corresponding impacts to hydraulic efficiency (i.e., flow rate). The test matrix includes the optimization (position and spacing of elements) of three mitigation solutions, which are projecting bolts, deflectors, and step. In addition, a high-speed camera and audio equipment have been used to evaluate effectiveness of the configurations in reducing nappe vibration. Finally, this practical study has identified countermeasures that are suitable for retrofits and new construction, easy to construct, durable, hydraulically efficient, and that have minimal potential for debris collection.

Keywords: Spillway, nappe vibration, nappe oscillations, physical modelling, flow acoustics.

1. INTRODUCTION

Nappe vibrations have been identified as an undesirable and potentially dangerous phenomenon in the case of flow over a gate (Naudascher and Rockwell 1994; USBR 1964). The occurrence of nappe vibration on this widespread type of structure has been attributed in part to the interaction between the flow and the enclosed air pocket between the gate and the nappe (Naudascher and Rockwell 1994). Indeed, adding splitters to the gate crest to divide the nappe, thus venting the air pocket, has been successful in mitigating nappe vibration problems in some instances.
In addition to gates, nappe vibrations have also been observed on free surface weirs, including labyrinth weirs, even with an aerated air pocket behind the nappe (Crookston et al. 2014; Crookston and Tullis 2012; Metropolitan water and board 1980; Schwartz 1966). However, such dam safety structures typically operate less frequently than overflow gates, which are usually used as regulating structures and, therefore, operate regularly. As a consequence of this lack of documentation for operating conditions, the low number of free surface weirs leading to nappe vibration has promoted the implementation of case-by-case countermeasures, such as an increase in the crest roughness or a modification of the crest profile (Metropolitan water and board 1980).

Beside these practical considerations, a review of the scientific literature shows that over the last 80 years, a lack of consensus exists on the causes and source of the oscillations or vibration development (Charles Knisely personal

communications 2015). The most commonly suggested theory behind the mechanism is based on Kelvin-Helmholtz instabilities at the interface between falling water and air (Casperson 1993), with a source of the vibrations distributed along the nappe. However, this theory requires an appreciable velocity differential between the air and the falling water, which is likely not reached at the crest. Others point to the pressure discontinuity at the weir crest as the cause of the phenomenon (Chanson 1996), with an origin of the vibrations at the crest. The resonance with the air pocket entrapped behind the nappe is, in that case, described as a cause of amplification of nappes oscillation (Naudascher and Rockwell 1994). Twenty years after these early works, following the nappe vibration problems experienced after the rehabilitation of the Linville Land Harbor Dam, new investigations were conducted at the Utah Water Research Laboratory (Utah State University) (Anderson 2014; Crookston et al. 2014). They suggest that the initiation of the instability most likely occurs at the weir crest. Indeed, the waves resulting in the vibrations are observed directly after the flow separation from the weir crest (even for unconfined nappe models), and the roughness modification of the weir affects the vibration. In addition to these results, significant scale effects have been shown to affect the phenomenon, especially on the function of the air pocket entrapped behind the nappe. It can be concluded from literature that this is a complex hydraulic behavior where more than one mechanism might initiate vibration, provide feedback, and/or sustain the vibration, with an enclosed air cavity serving as an amplifier and not as an absolute requisite attribute for occurrence (Rockwell and Knisely 1979; Sato et al. 2007).

The current experimental study was undertaken to develop generic scientific conclusions regarding the physical processes and, especially, appropriate mitigation techniques by means of an experimental study on a large-scale model, including a means of quantifying the vibrations and the level of mitigation provided by crest modifications. This paper provides an overview of the preliminary results regarding the mitigations techniques.

2. EXPERIMENTAL SETUP

The experimental apparatus used in this study is located at the Engineering Hydraulics laboratory of the Université de Liège. It is illustrated in Figure 1. This large-scale model is a confined prototype-scale linear weir with a 3.46-m long crest and a 3.04-m high chute. The fall of water from the weir is confined between two lateral walls and a back wall, one lateral confinement wall being transparent (Plexiglas) and the others black multiplex panels.

Figure 1. Prototype-scale model

Flow is supplied to the model via two pipes, as shown in Figure 2, which are connected to two regulated pumps. Flows enter through perforated pipes parallel to the crest, which are located on the bottom of the reservoir. The maximum unit discharge is 7.22×10^{-2} m²/s (250 l/s in the model). The discharge is measured with an electromagnetic flow meter located in the supply piping (accuracy of 0.5% FS). In the reservoir, a baffle wall of synthetic membranes further assists in providing flow velocities as uniform as possible upstream of the crest (Figure 2).

The weir crest is a 15-cm radius quarter-round followed by a flat 15-cm long horizontal element. This geometry is patterned after typical prototype dimensions of reinforced concrete weirs. The goal of the study being to identify suitable mitigation solutions to nappe vibrations, three types of crest modifications, i.e., projecting bolts, deflectors, and step, were tested as illustrated and listed in Table 1.
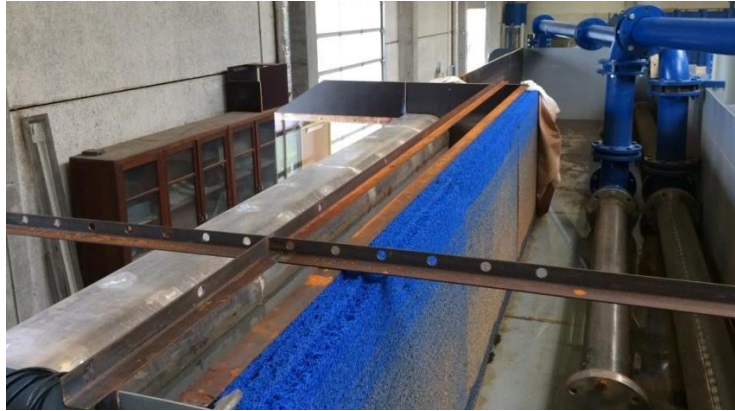
Figure 2. View of the reservoir, water supply pipes, and the baffle wall

The following equipment is used in the experiments for data acquisition:
- high-speed video camera to capture images of the falling water. The camera records 240 frames per second,
- microphone in front of the falling nappe to characterize the nappe vibration phenomenon in terms of sound peak frequency following a Fourier transform of the audio signal.
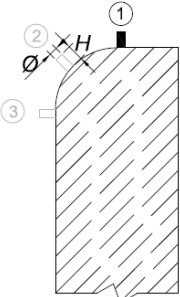
3. RESULTS AND DISCUSSION
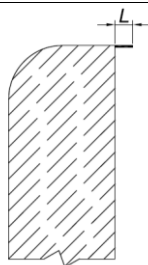
3.1. Base Configuration Analysis
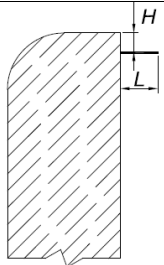
A preliminary study has been conducted on the non-modified quarter-round crest to establish the flow range that induces nappe vibrations and to characterize nappe vibration acoustics. This characterization is based on acoustic measurements and flow visualization. Audio and image recordings with a microphone and a high-speed camera (240 fps) have been made for various flow rates. A Fourier transform has been applied to the acoustic signal in order to isolate the dominant frequencies, and the lens distortion of the extracted images has been corrected. High-speed camera images in combination with Fourier transform of sound recording are illustrated in Figure 3 for a range of unit discharges.

For unit discharges between 0.01 m²/s and 0.07 m²/s, measurements give a dominant frequency that varies between 30.75 Hz and 35.5 Hz. The associated sound level reported as a function of the discharge in Figure 4, combined with the visualization of nodal lines, allowed researchers to detect nappe vibration regions. Three distinct areas can be observed and distinguished from a hypothetical behavior without vibration (dashed line). Indeed, a significant increase of the sound level that exceeds 80 decibels (the mean sound level) occurs as the discharge increases up to 0.025 m²/s. Then, the sound level remains steady in the range of 100 dB for discharges ranging from 0.025 m²/s to 0.045 m²/s. Finally, as the nappe oscillation visually disappears, the sound level decreases and tends to stabilize at 80 dB. This base configuration analysis documents a baseline range of nappe vibration for unit discharges between 0.015 m²/s to 0.05 m²/s.

Table 1. List of mitigation techniques

PROJECTING BOLTS					
 3 possible positions of bolts as represented.	N°	Characteristics (cm)			
		Diameter, Ø	Height, H	Spacing, s	Position
	PB1	2	1.5	10	1
	PB2		2.5		
	PB3		3.5		
	PB4		4		
	PB5		2.5	20	
	PB6		4		
	PB7		4	40	
	PB8		4	80	
	PB9		4	10	2
	PB10		8	20	
	PB11		4	20	
	PB12		8		3
DEFLECTORS					
	N°	Characteristics (cm)			
		Length, L	Width, W		Spacing, s
	D1	5	50		100-200
	D2	10			
	D3	15			
	D4	5	20		20
	D5	5	30		30
STEP					
	N°	Characteristics (cm)			
		Length, L	Height, H		Width, W
	S1	10	5		346
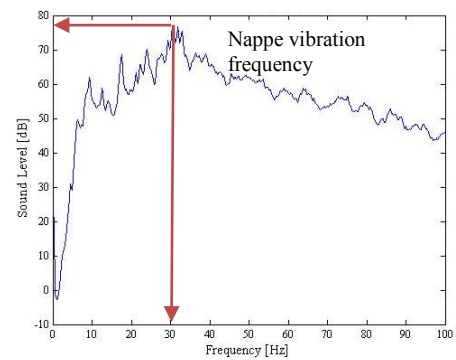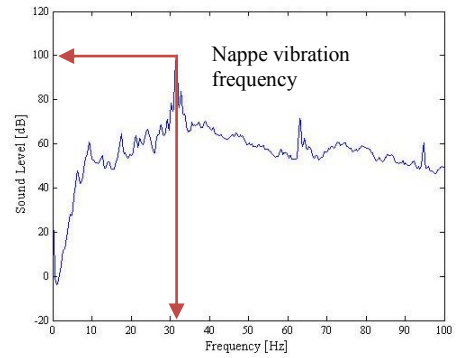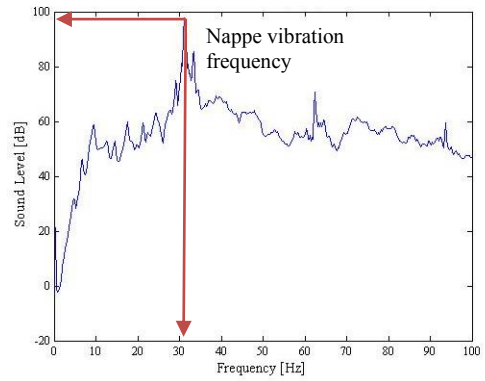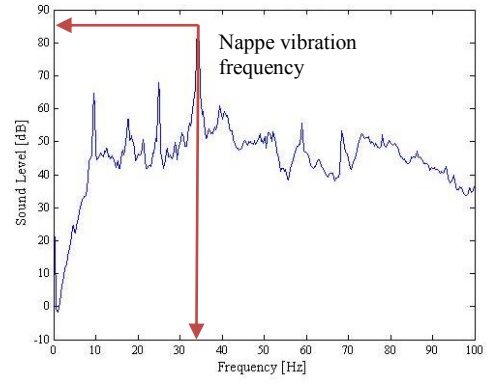
Figure 3. Nappe vibration visualization and associated Fourier transform of sound recording for (a) 0.015 m²/s, (b) 0.03 m²/s, (c) 0.045 m²/s and (d) 0.06 m²/s
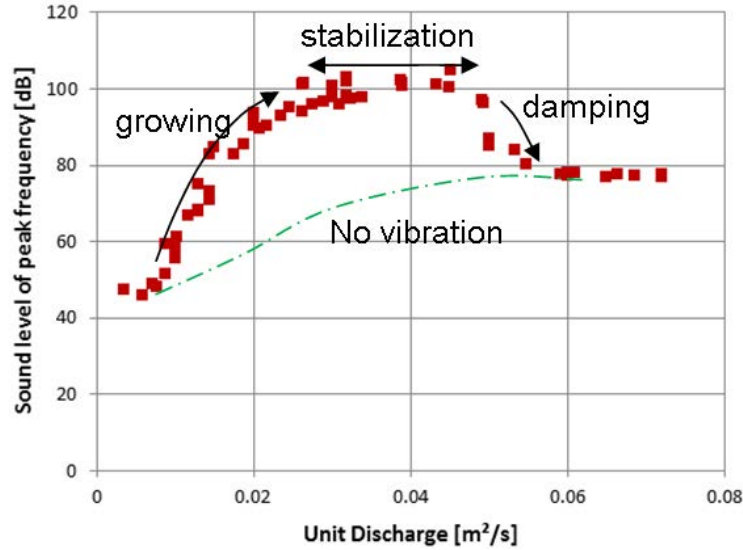
Figure 4. Detection of nappe vibration region using Fourier transform of sound recording

3.2. Mitigation Solutions

As listed in Table 1, the test matrix includes 18 configurations. The mitigation techniques have been tested for the discharges generating the most intense noise disturbances in the case of the smooth quarter-round crest, i.e., 0.03 m²/s, 0.04 m²/s, and 0.05 m²/s. The chronology of these experiments is related to the optimization of the mitigation techniques.

For projecting bolts, the first stage was research into the minimum bolt height required for a specific spacing and position, e.g., 10 cm and position 1 (configurations PB1 to PB4). Then, the bolt spacing was optimized for a fixed bolt height (configurations PB4 to PB8). The results of this first stage of experiments are illustrated in Figure 5 and show that the optimal configuration of projecting bolts is the configuration PB 6. Finally, in order to reduce the potential for debris collection, two additional positions (2 and 3) have been tested and optimized (configurations PB9 to PB12). The results of this second stage of experiments is illustrated in Figure 6; unfortunately, neither position was very effective.
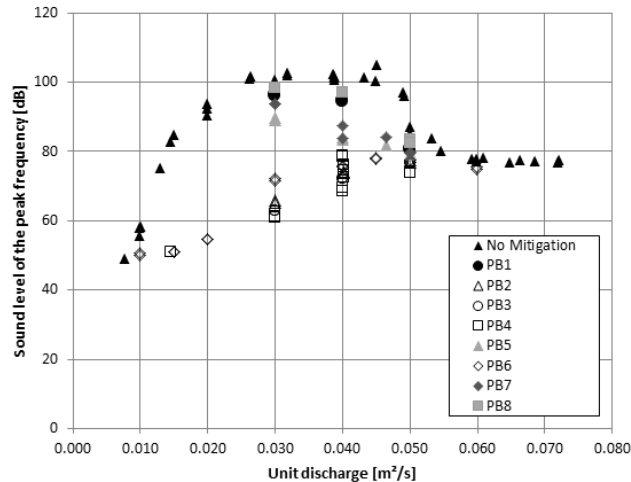
Figure 6. Evolution of sound level at the peak frequency with unit discharge: configurations PB9 to PB12 (projecting bolts mitigation technique)

For deflectors, initial experiments focused on a deflector width of 50 cm located 1 m from the right bank of the weir and 1.96 m from the left bank (configurations D1 to D3). Considering the results gained with a single 50-cm wide deflector as well as the results of the tests for projecting bolts, which concluded that a bolt spacing of 20 cm is necessary to avoid audible nappe vibration, 5 cm long deflectors of 20 cm and 30 cm widths have been tested with a spacing equal to the deflector width (configurations D4 to D5). The results of these experiments are illustrated in Figure 7 and show the effectiveness of configuration D4.

Finally, the results of the experiment for a continuous step along the entire length of the weir and a minimum length of the step (determined from the trajectory of the nappe in the case of smooth crest) are illustrated in Figure 7. This mitigation technique was found to be effective and would likely be a preferred approach for field installations.
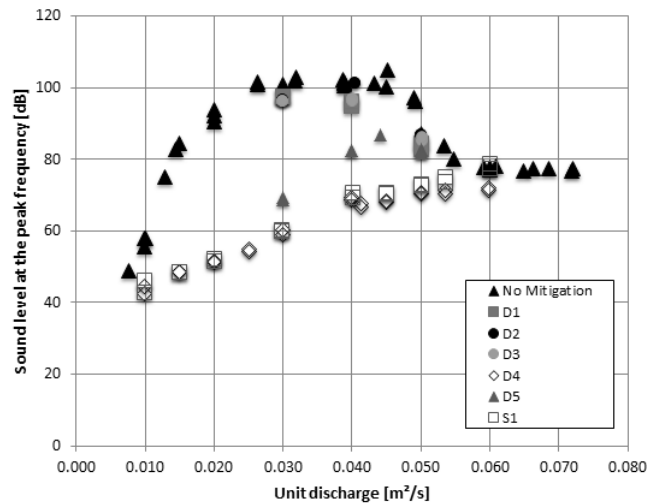
Figure 7. Evolution of sound level at the peak frequency with unit discharge: configurations D1 to S1 (deflectors and step mitigation techniques)

3 CONCLUSIONS

The primary goal of this study was to develop practical countermeasures for nappe vibration that are suitable for retrofits and new construction, easy to construct, durable, hydraulically efficient, and have minimal potential for debris collection. In the current experimental study, three mitigations techniques have been tested and turned out to be effective. Indeed, if the nappe dividing does not exceed 20 cm for projecting bolt and deflectors, the nappe dividing led to a significant decrease of sound level frequency peak. Foremost, the optimization procedure shows that the spacing length required for projection bolts and deflectors is a fundamental parameter and leads to optimal configuration PB6 and D4. Nappe visualization of these optimal configurations still displays nappe oscillations, which are yet phase shifted. Also, the efficiency of the step, as well as the optimal position of the projection bolt (position 1), indicates the sensitivity of the nappe vibration phenomenon to turbulence and upstream hydrodynamic conditions.

A step placed along the whole crest that modifies the flow conditions also proves to be effective and easy to construct since the length of the step is the sole setting. In contrast, projecting bolts, which require the choice of diameter, spacing and, transversal position, seem to be the least suitable solution. The findings of this study should be of interest to owners, operators, practitioners, and researchers involved with free-overfall hydraulic structures.

4 ACKNOWLEDGMENTS

5 REFERENCES

Anderson, A. A. (2014). "Master thesis : causes and countermesures for nappe oscillation." Utah State University.

Casperson, L. W. (1993). "Fluttering fountains." *Journal of Sound and Vibration*, 162(2), 251–262.

Chanson, H. (1996). *Some hydraulic aspects during overflow above inflatable flexible membrane dam*. The CH47/86, Department of Civil Engineering, The University of Queensland.

Crookston, B. M., Anderson, A., Shearin-Feimster, L., and Tullis, B. P. (2014). "Mitigation investigation of flow-induced vibrations at a rehabilitated spillway." *ISHS 2014 - Hydraulic Structures and Society - Engineering Challenges and Extremes: Proceedings of the 5th IAHR International Symposium on Hydraulic Structures.*

Crookston, B., and Tullis, B. (2012). "Hydraulic design and analysis of labyrinth weirs. I: Discharge relationships." *Journal of Irrigation and Drainage Engineering, American Society of Civil Engineers*, 139(5), 363–370.

Metropolitan water, sewerage, and board, sydney drainage. (1980). "Investigation into spillway discharge noise at Avon Dam." *Ancold bulletin*.

Naudascher, E., and Rockwell, D. (1994). *Flow-induced vibrations: an engineering guide. Balke*ma.

Rockwell, D., and Knisely, C. (1979). "The organized nature of flow impingement upon a corner." *Journal of Fluid Mechanics*, Cambridge Univ Press, 93(03), 413–432.

Sato, Y., Miura, S., Nagamine, T., Morii, S., and Ohkubo, S. (2007). "Behavior of a falling water sheet." *Journal of Environment and Engineering*, The Japan Society of Mechanical Engineers, 2(2), 394–406.

Schwartz, H. I. (1966). "Edgetones and nappe oscillation." *Journal of the Acoustical Society of America*, 39(3), 579.

USBR. (1964). *Experience of the Bureau of Reclamation with flow-induced vibrations*. Hydraulics branch.

Influence of Some Geometrical Parameters on Piano Key Weir Discharge Efficiency

G.M. Cicero[1], J. Vermeulen[2] and F. Laugier[2]
[1]National Hydraulics and Environment Laboratory
EDF LAB
Chatou, 78406
FRANCE
[2]Hydro Engineering Center
EDF CIH
Le Bourget, 73370
FRANCE
E-mail: guy-michel.cicero@edf.fr

ABSTRACT

The Piano Key Weir (PKW) is a type of labyrinth weir with efficient hydraulic performance, especially at low heads. Since the primary parameters were extensively studied, Electricité De France (EDF) launched a new experimental program to improve the knowledge of some secondary parameters such as the overhangs, the crest shape, and the dam height. This program included the testing of a trapezoidal shape and of PKWs under submerged conditions. The data measured under free-flow conditions were also used to validate empirical correlations and FLOW-3D numerical models. This paper gives an overview of the program and highlights the main experimental and numerical results.

Keywords: Hydraulic, Piano-key-weir, Discharge, free-flow, submerged flow.

1. INTRODUCTION

The PKW (Figure 1, left) is a type of labyrinth weir (Tullis et al., 2007) with efficient hydraulic performance, especially at low heads. The reduced footprint due to the overhangs allows installing PKWs on the top of the crest of existing gravity dams, and since the first prototype of Goulours (2006), many of them (St Marc, Etroit, Malarce, etc.) were installed by EDF to upgrade the spillway capacity of these dams (Vermeulen et al., 2011).

For about ten years, many experimental and numerical studies have contributed to identify the primary parameters influencing hydraulic performance, such as the width ratio of the inlet and outlet keys (W_i/W_o), the developed length to width ratio (L/W), and the weir height (P). Figure 1 (left) shows the main geometric parameters of a classical rectangular PKW with the standard notation defined by Pralong et al. (2011).

In 2011, Electricité De France (EDF) started a new experimental program at the National and Environmental Hydraulic Laboratory (LNHE) in Chatou to expand the knowledge on some secondary parameters effects such as the overhangs, the crest shape, and the dam height (P_d). This program included the testing of a trapezoidal shape with a side-wall angle of the lateral walls to compare the hydraulic performance to the classical rectangular shape. Furthermore, since most of the experiments were carried out under free-flow conditions, the rectangular PKWs were tested under submerged conditions (Belaabed et al., 2011), (Dabling and Tullis, 2012).

The experimental data under free-flow conditions were used to validate empirical correlations and FLOW-3D numerical models.

This paper gives an overview of the experimental program and a synthesis of the results already presented (Cicero et al., 2012, 2013a, 2013b, 2013c) and of complementary tests at various dam heights.

2. EXPERIMENTAL SET-UP

2.1. Testing Apparatus

The PKW testing was conducted in a 2-m wide, 1-m deep, and 25-m long rectangular channel with discharge capacity measurements up to 500 L/s. The weir discharge (Q) was measured by an electromagnetic flow-meter of 1% accuracy and the piezometric heads were measured at ~ 6 m upstream (h_u) and ~ 3 m downstream (h_d) of the PKW with an accuracy of +/-0.18 mm. The total upstream (H_u) and downstream (H_d) heads were calculated by adding the velocity head corresponding to the average cross-sectional velocity at the level measurement locations of h_u and h_d. The discharge and the water levels were recorded for a 3 min period at a 0.5 Hz frequency. As a result, the measurements used for analysis were the average and standard deviation of 90 temporal values at steady state conditions.

2.2. PKW Design

The PKWs were fabricated of PVC, following common design principles (Cicero and Delisle, 2013a). The width (W) was the total channel width to avoid side effects and maximize the number of PKW units, which was $N_u = 6.5$, with half an inlet key and half an outlet key on each end.

The side wall thickness ($T_s = 2$ cm) was chosen to be wide enough to enable the testing of various crest shapes on the type A PKW. According to the recommended value (~35 cm) for prototypes (Vermeulen et al. 2011), the geometric scale of the models was around 1/20. The PKWs were installed on top of a platform in concrete without noses underneath the upstream overhangs. The PKWs were tested at three dam heights: $P_d = 0.6P, 1.5P, 2P$.
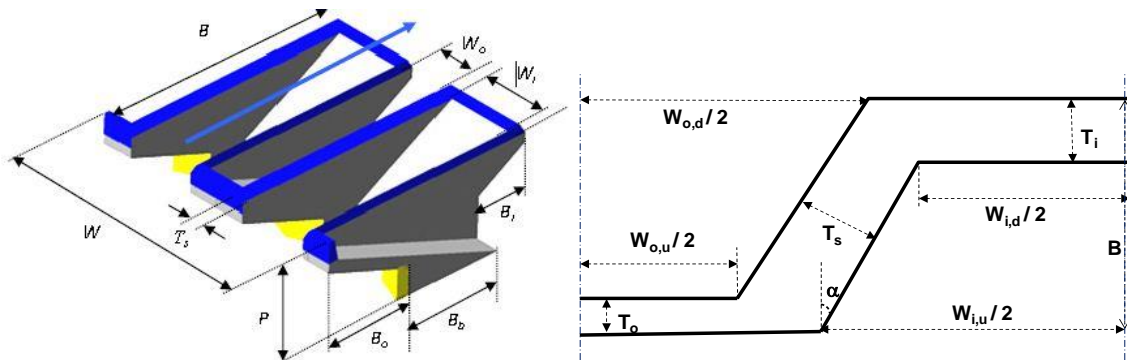
Figure 1. Geometric parameters of a classical rectangular PKW (left) Half-element unit of a trapezoidal PKW in plan view (right).

2.2.1. Rectangular PKWs

The geometry of the three PKWs types A, B and C was the design recommended by Lemperiere et al. (2011) for the type B, i.e. with the same inlet and outlet key widths ($W_i = W_0$). As a result, the type C design (without upstream overhang) was the same as type B (without downstream overhang), but with a reversed placement in the channel. The main geometric parameters (Cicero et al., 2013a) are strictly the same except for the lengths of the upstream and downstream overhangs (B_o, B_i) and, consequently, for the bottom slopes of the outlet and the inlet keys (S_o, S_i).

2.2.2. Crest Shapes Tested on the PKW Type A

Four geometries (Cicero et al., 2013b) were tested on the lateral walls: a flat-top, a half-round, and a quarter-round crest, with the rounded face in both the inlet and the outlet keys. Four geometries were also tested on the upstream and the downstream crests: a flat-topp, a half-round, and both rounded shapes in horizontal and also vertical.

2.2.3. Trapezoidal PKWs

Two trapezoidal PKWs (Figure 1, right) with a sidewall angle (α) were designed, keeping the main geometric parameters of the rectangular type A with the flat-top crest. The common parameters maintained were P, B_b, T_s, T_i, T_o and the widths of the inlet ($W_{i,d}$) and outlet ($W_{o,d}$) keys at the downstream edge, (i.e. $W_{i,d} = W_i$, and $W_{o,d} = W_o$). The resulting geometric parameters were calculated (Cicero et al., 2013c) according to the design constraints. The first design constraint (trapezoidal 1) was to maximize the sidewall angle keeping constant L_u/W_u, the main relevant parameter on PKW hydraulic performance. The maximum sidewall angle was found to be $\alpha = 5°$.

The second design constraint (trapezoidal 2) was to maintain the upstream-downstream length (B), which is a parameter that influences the building cost of PKWs. So, the inlet (B_o) and outlet (B_i) overhang lengths were the same as the rectangular type A. Although the maximum sidewall angle was found to be $\alpha = 6°$, we kept $\alpha = 5°$ to allow comparisons with the trapezoidal 1.

The trapezoidal 1 (non-symmetric in planned view) was experimentally tested at LNHE, in the "design position" when the inlets are larger than the outlets at the upstream edge ($W_{i,u} > W_{o,u}$), and in the "reverse position" ($W_{i,u} < W_{o,u}$). The tests performed on the type A and the trapezoidal 1 (in both positions) were used to validate FLOW-3D models. Then, the hydraulic performance of the trapezoidal 2 was predicted with the validated numerical model.

3. HYDRAULIC EFFICIENCY UNDER FREE FLOW CONDITIONS

3.1. Testing Procedure and Measurement Analysis

For tests under free flow conditions, the discharge (Q) was increased step by step to measure the piezometric upstream level (h_u) when the flow conditions were stabilized. The discharge efficiency of the various geometries (PKW, dam height and crest shape) was characterized by the non-dimensional rating curves $C_w(H_u/P)$ where

$$C_W = \frac{Q}{W\sqrt{2g}H_u^{1.5}} \tag{1}$$

The experimental data $C_w(H_u/P)$ were correlated by polynomial interpolations, which allowed a comparison between the discharge of the various geometries at the same upstream head. As recommended by Leite Ribeiro et al. (2012), these equations were used for $H_u > 3$cm, since we observed a wide range of measurement deviations due to viscosity and surface tension scale effects. This comparison also took into account the measurements error on C_w (Cicero et al., 2013b), which were usually greater than 2%. Consequently, the discharge differences lower than 4% are considered negligible.

3.2. Overhang Effects

3.2.1. Experimental Results
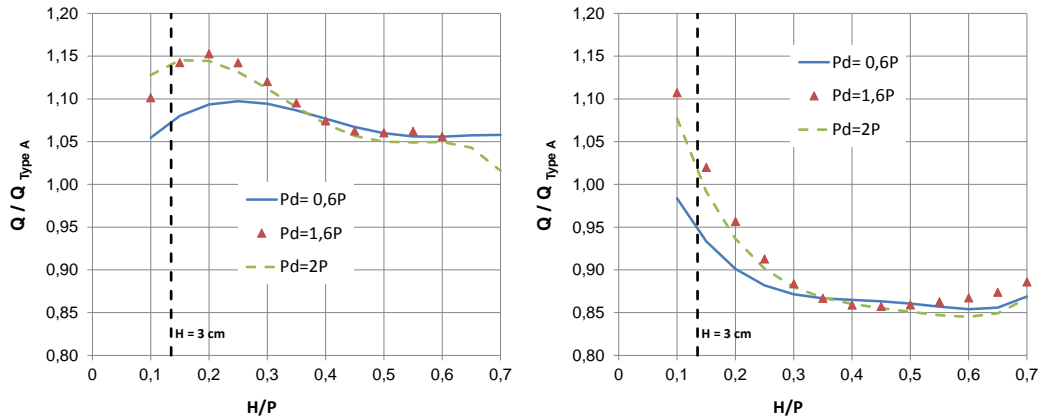
Figure 2. Dam height effect on the discharges of the type B (left) and the type C (right), compared to the type A.

The types A, B, and C were tested at 3 dam heights, and the first results observed at low dam height (Cicero et al., 2013a) were confirmed at higher dam heights. The type B was 5% to 15% more efficient than the type A, according to the upstream head and the dam height (Figure 2). The type A was up to 15% more efficient than the type C. These results are consistent with the first PKW experiments of Ouamane and Lemperiere (2006), who observed that the type B was 9% to 12% more efficient than the type A. An explanation can be given thanks to Machiels (2012) experiments on a large scale model of type A. The latter observed a control section in the inlet key, which reduces the effective developed length and moves downstream for increasing heads. Thus, for the same upstream head, the effective length will be greater for type B than for type A and type C.

The effects of the dam height were found to be the same for all PKW types. The major effect on C_w was observed at low heads ($H_u <$ 3cm) when scale effects are not negligible. For $H_u >$ 3cm, we measured the same curves $C_w(H_u/P)$ at low and intermediate dam heights and a decrease of C_w at the highest dam height. This latter result was rather unexpected since Leite Ribeiro et al. (2011) and Machiels (2012) observed an increase of the discharge efficiency with the dam height. That could be due to a higher units number ($N_u = 6.5$ instead of 1.5 to 3) of the PKWs tested at LNHE.

3.3. Crest Shape Effects

The first tests performed at low (10 tests) and intermediate dam heights (4 tests) were presented in Chatou (Cicero et al., 2013b). (The various geometries characterized by the dam height and the shape of the lateral, upstream and downstream crests were detailed in a table). This program was completed by testing the 4 "uniform" crest configurations at the highest dam height. The whole tests analysis highlights the following results:

- The influence of the crest shape is mainly due to the lateral crest and strongly decreases with increasing upstream head when the lateral jets coming from the inlet keys begin to cross into the outlet keys.
- The half-round and the quarter-round shapes have better hydraulic performance than the flat-top shape, with a gain in discharge decreasing from 20 to 25% for $H_u = 3$ cm to 5% for $H_u/P > 0.4$. Anderson (2012), who also compared the half round and the flat-top shapes on a type A, found similar results: the gain in discharge decreased from 22 to 4% for $0.1 < H_u/P < 0.6$.
- The quarter-round on the lateral crest provides the same discharge efficiency whatever the position of the rounded face (in the inlet or the outlet).

- The dam height has negligible effect when scale effects became negligible (H_u >3 cm). For each "uniform" crest (Figure 3), the differences on C_w measured at the 3 dam heights were lower than the measurement uncertainties.
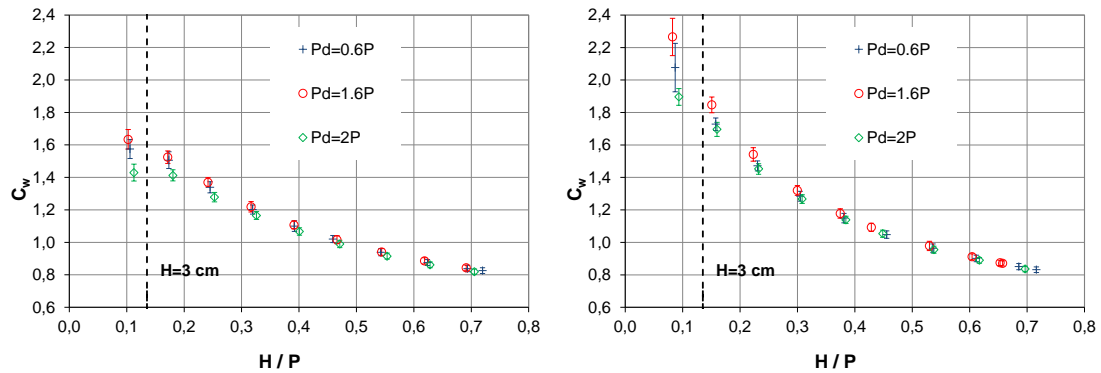
Figure 3. Effect of the dam height on the hydraulic efficiency of the type A with the flat-top crest (left) and the half-round crest (right).

As a result, it is recommended to design PKWs with a half-round or a quarter-round shape on the lateral crest and a flat–top shape on the upstream and the downstream crest.

3.4. Validation of Empirical Correlations

The LNHE experiments were used (Cicero et al., 2013b) to validate both empirical correlations published by Leite - Ribeiro et al. (2012) for type A and by Machiels (2012) for general PKW geometries.

The "type A correlation" is based on a geometrical parametric study of PKWs tested with a half-round crest and with noses under the upstream overhangs. The predictions were compared to the measurements of the type A with the half-round crest (regardless of dam height since it has no effects). Within its limitations ($H > 0.05$ m), this correlation overestimated the discharge by 7% to 18%. Note that Anderson (2011) observed a beneficial effects (~3%) of the noses, which could reduce this relative error.

The "Machiels correlation" is more based on a physical analysis of the various geometrical effect, including the overhang and the dam height. The PKWs were tested with a flat-top crest and without noses. For the types A and C, this correlation underestimated the discharge with a maximum error of 10%. For the type B, the discharge was predicted with an error of +/- 15%, depending on the upstream head and the dam height.

3.5. Effect of a Trapezoidal PKW

3.5.1. Experimental Results

These tests were performed on the trapezoidal 1 only, with intermediate dam height tests presented in Chatou (Cicero et al., 2013c). Since then, the trapezoidal 1 was tested in both positions at high dam height and in the design position at low dam height only.

In the design position (Figure 4 left), the trapezoidal 1 was more efficient than the rectangular type A regardless of dam height. The gain in discharge decreased with the head and the dam height. The maximal gain was respectively 30% (low), 20% (intermediate), and 10% (high dam height). As for the rectangular PKWs (see 3.2.1): for $H_u > 3$cm, the curves $C_w(H_u/P)$ were the same at low and intermediate dam heights (Figure 5 left) and decreased at the highest dam height.

In the reverse position (Figure 4 right), the trapezoidal 1 was less efficient than the rectangular, and the loss of discharge increased with the head and the dam height. The discharge efficiency $C_w(H_u/P)$ decreased from the intermediate to the high dam height (Figure 5 right) and significantly for $H_u/P < 0.4$.
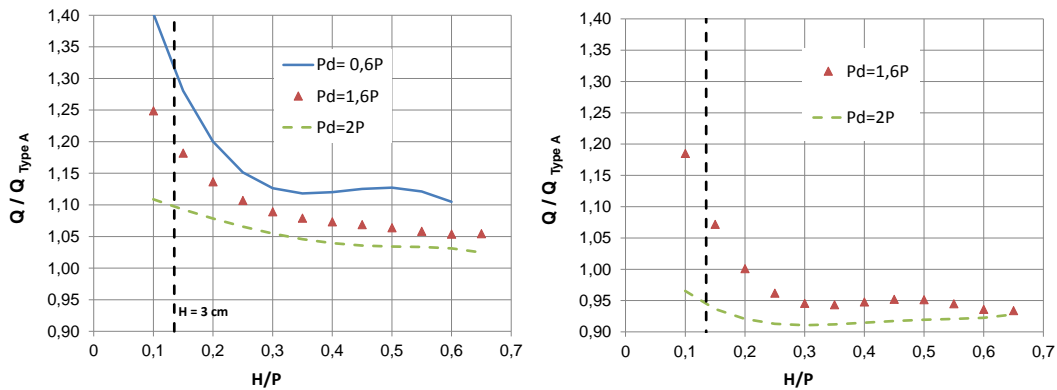
Figure 4. Dam height effect on the discharges of the trapezoidal 1 in the design (left) and reverse (right) positions, compared to the type A.
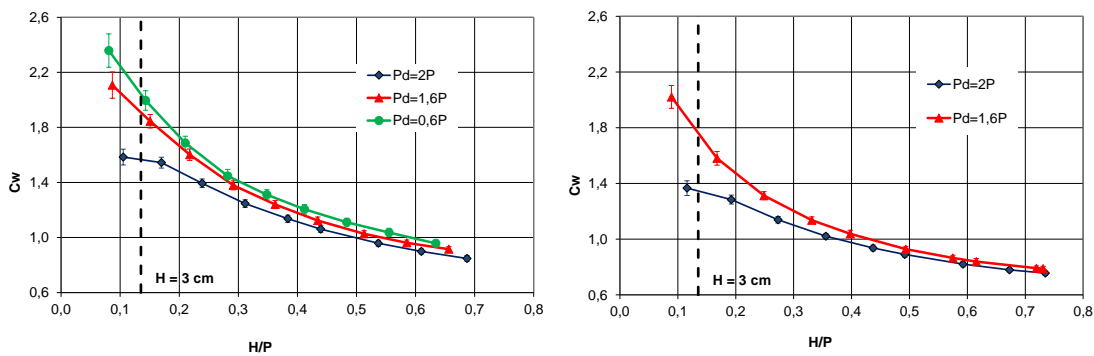
Figure 5. Effect of the dam height on the hydraulic efficiency of the trapezoidal 1 in the design (left) and in the reverse position (right).

3.5.2. FLOW-3D Numerical Results

The numerical simulations of the rectangular type A and of both trapezoidal 1 and 2 were presented in Chatou (Cicero et al., 2013c). For the rectangular and the trapezoidal 1, the numerical results of the FLOW-3D® simulations were in rather good agreement with the physical model outcomes: the mean deviation between both models was about 8% for the rectangular PKW, 2% for the trapezoidal 1 in the design position, and 8% in the reverse position. However, the gain in discharge could be underestimated by more than 5% due to the maximal computations errors (~5% for the rectangular and 15% for the trapezoidal 1).

The FLOW-3D® model so validated allowed predicting the discharge capacities of the trapezoidal 2. Globally, this configuration was around 2% less efficient than the trapezoidal 1 due to its shorter developed crest length.

4. HYDRAULIC EFFICIENCY UNDER SUBMERGED CONDITIONS

These tests were performed on the 3 PKW types at the lowest dam height ($P_d = 0.6P$). This chapter summarises the previous results (Cicero et al., 2013a) and presents a new application in § 4.3.2. (See notations in Figure 6).

4.1. Testing Procedure and Measurement Analysis

For submerged testing, the tailwater level was increased step by step while maintaining a constant flow rate to measure the discharge (Q_s) and both the upstream (h_u) and the downstream (h_d) piezometric levels at stabilized flow conditions. For each constant discharge, we started from free-flow conditions with a tailwater level below the crest elevation. First, the downstream level was raised by increments of 2 cm to isolate the modular submergence limit, when the free-flow conditions still applies (i.e., $H_u = H_0$) whereas the downstream level exceeds the crest elevation ($H_d > 0$). Above this modular limit, the downstream level was raised by steps of 5 cm.

The measurements were analysed by the method of Tullis et al. (2007) previously used by Belaabed and Ouamane (2011) and Dabling and Tullis (2012). This method is based on the use of the total upstream (H_u) and downstream (H_d) heads normalized by (H_0) the total upstream head for the same discharge under free-flow conditions.
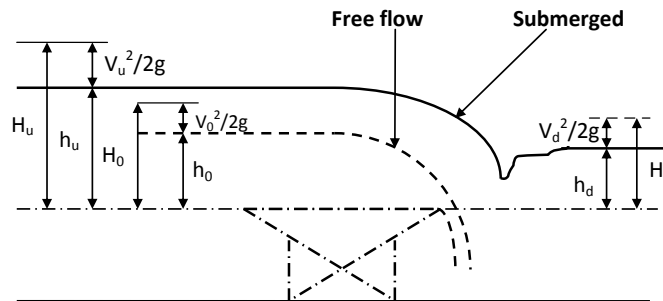
Figure 6. Hydraulic parameters under free-flow and submerged conditions

4.2. Sensitivity to Submergence

This "sensitivity to submergence" characterizes the behaviour of a weir under submerged flow conditions. For the 3 PKW types, these conditions occurred when the downstream level exceeded the crest level and the modular submergence limit increased with the flow rate. For each PKW type, the experimental data sets were correlated by exponential interpolations given by the general Eq. (2):

$$\frac{H_0}{H_u} = 1 - 0.01e^{\alpha(S - S_m)} \tag{2}$$

$S = H_d/H_u$ is the submergence factor, and S_m the modular submergence limit which can be defined, according to this equation, by $H_0 < 0.99H_u$ for $S > S_m$.

This equation is not valid when the submergence factor S tends to 1, since the PKW no more acts as a control structure and the discharge becomes undefined. For each PKW type, the parameters (α, S_m) and the limitations were given in (Cicero et al., 2013a), as well as the correlation coefficient R^2.

Within the limitations of S, these equations could predict the measured ratio H_0/H_u with an average error of 2% for type A and of 3% for types B and C. Then, the discharge $Q_s(H_0)$ were predicted by the free-flow equations, for the measured values of H_u and H_d, with an average error of 3% for types A and B and of 5% for type C.

Eq. (2) allowed for comparisons between the "sensitivity to submergence" of the 3 PKWs (Figure 7 left). At constant S, the ratio H_0/H_u decreased from type C to type A, meaning that the type C was less sensitive than the type A, which was less sensitive than the type B. The PKWs were also compared to linear weirs of same width ($W = 2$ m) and same crest elevation ($P + P_d = 0.355$ m) for identical submerged conditions (H_u, H_d).

Tullis (2011) measured the curves Q_s/Q_f (S) of a submerged Ogee crest, at constant discharge (Q_s), for different values of P_{uo} and P_{do}, the vertical distances from the upstream and downstream aprons to the weir crest. We used (Figure 7 right) the Tullis measurements at $Q_s = Q_{design}$ for $H_{OD}/P_{uo} = H_{OD}/P_{do} = 0.46$. With $P_{uo} = P_{do} = 0.355$ m; these data can be used for an Ogee crest profiled at a design head $H_{OD} = 0.163$ m. The free-flow discharge Q_f was computed by Eq. (1) with the classical empirical correlation $C_W = 0.495(H_u/H_{OD})^{0.12}$.

For sharp and broad crested weirs, Q_s/Q_f (S) were computed by the Hager (1986) equations detailed in Cicero et al. (2013a), and Q_f was computed by Eq. (1) with $C_W = 0.42$ (sharp crest) and $C_W = 0.327$ (broad crest).

As a result (Figure 7 left), the sharp crested weir is the most sensitive, and the broad crested weir is the least sensitive. The Ogee crest weir and the PKW of type C have the same sensitivity to submergence.
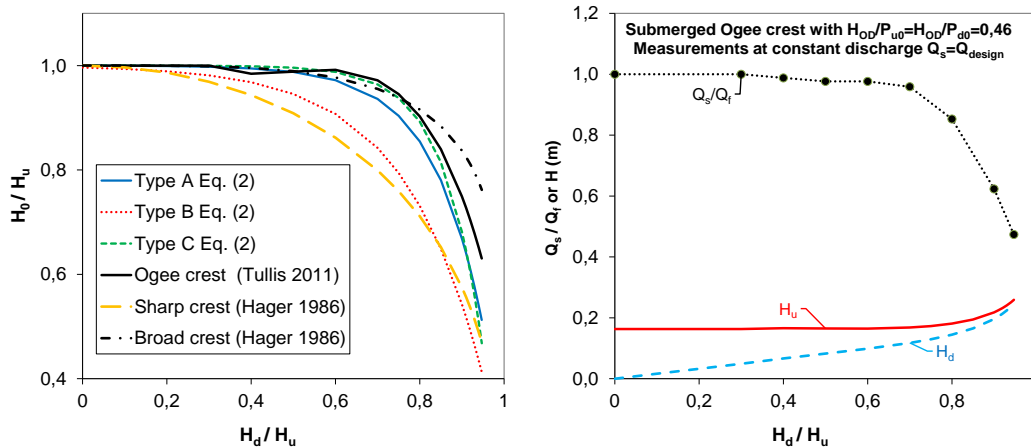
Figure 7. Sensitivity to submergence of PK and linear weirs (left) for identical upstream (H_u) and downstream (H_d) heads given by Ogee crest Tullis measurements (right).

4.3. Hydraulic Efficiency

The submerged hydraulic efficiency depends on both the sensitivity to submergence and the free-flow hydraulic efficiency. Both applications are shown in § 4.3.1 and 4.3.2, respectively, to compare the 3 PKW types to linear weirs of same width and same crest elevation.

4.3.1. Discharge Efficiency at Identical Submerged Conditions

In this first application, we compare the discharges of PK and linear weirs for identical submerged conditions (H_u and H_d) given in Figure 7, right. For PKWs, first we calculate H_0 by the sensitivity equations $H_0/H_u(S)$, then Q_s (H_u) by the free-flow equations. For linear weirs, Q_s (H_u) is directly computed by the sensitivity equations $Q_s/Q_f(S)$ and the free-flow equations $Q_f(H_u)$.

Figure 8 left compares the weir discharges to the Ogee crest discharge, which is constant ($Q_{Ogee} = Q_{design}$). The hydraulic performance of PK and linear weir under submergence depends on the downstream head. For the chosen values of H_u and H_d,
- The type C is less efficient than the type A. The type B is more efficient than the type A for $S > 0.6$ and more than the type C for $S < 0.8$.
- The Ogee crest is more efficient than the sharp and the broad crested weirs. The PKWs are more efficient than the Ogee crest by 30% to 60% for the type A, 10 to 70% for the type B, and 5 to 45% for the type C.

4.3.2. Upstream Level Rise at Constant Discharge

The goal of this second application is to compare, with the previous hypotheses and data, the impact on the upstream level rise (H_u - H_d) of submerged weirs. The flood discharge Q_s =0,290 m³/s is equal to the design discharge of the Ogee crest computed for H_{OD} = 0,163 m.

We compute H_u according to S at constant discharge Q_s. For PKWs, we first calculate H_0 (Q_s) by the free-flow equations then H_u by the sensitivity equations $H_0/H_u(S)$. For linear weirs, we first calculate Q_f by the sensitivity equations $Q_s/Q_f(S)$ then $H_u(Q_f)$ by the free-flow discharge equations.

Figure 8, right compares the rise of the upstream level (H_u - H_d) computed versus H_d = SH_u:
- The PKWs have less impact than the Ogee crest weir, which has less impact than the sharp and the broad crest weirs.
- The impact of the PK and linear weirs depends on the downstream level associated to the discharge Q_s. For this application, both types A and B are similar and have less impact than type C for H_d < 0.1 m. The sharp crest weir has less impact than the broad crest weir for H_d < 0.15 m.

Since the scale factor of the PKWs was around 1/20 (see § 2.2), the prototype data of this "fictional" application are Q_s = 517 m³/s, W = 40 m, and P_{uo} = P_{do} =7.1 m. If the downstream level was H_d = 2 m (~0.1 m in Figure 8 right), a type A PKW should lower the upstream level by 0.90 m, 1.60 m, and 2 m compared respectively to an Ogee crest, a sharp crest, and a broad crest weir.
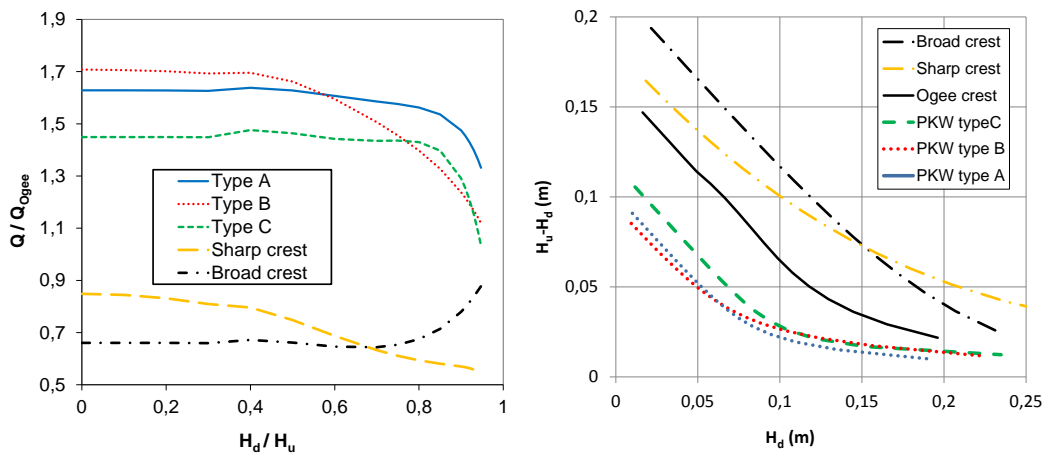
Figure 8. Discharge at identical upstream and downstream heads (left). Upstream level rise at constant discharge (right).

5. CONCLUSIONS

These LNHE experiments based on PKWs of the channel width (2 m) allowed us to isolate the effects of some secondary parameters on the hydraulic performance under free flow and submerged conditions.

Under free-flow conditions:
- The overhang effect was confirmed, and the type B was from 5 to 15% more efficient than the type A, which was 15% more efficient than the type C.
- Both the sidewall angle and a round shape on the lateral crest could increase the discharge efficiency at low heads by 20 to 30%. These beneficial effects decreased down to 5% with the upstream head.
- The discharge efficiency was the same at low and intermediate dam heights and decreased at the highest dam height. Although unexpected, this latter result was clearly observed for rectangular as well as trapezoidal PKWs.

- The type A correlation overestimated the discharge by 7 to 18% without taking into account the beneficial effects of the noses (~3%).
- The general Machiels correlation underestimated the discharge of the types A and C up to 10%, and it predicted the discharge of the type B with a maximal error of +/- 15%.
- The numerical simulations with FLOW-3D models allowed predictions of the hydraulic performance of the type A and the trapezoidal 1 with an error lower than 8%.

Under submerged conditions:
- The "sensitivity to submergence" of the 3 PKW types were characterized by the general Eq. (2). The type C was less sensitive than the type A, which was less sensitive than the type B.
- The hydraulic performance of PK and linear weirs were compared on both "fictional" applications:
  o At identical submerged conditions, the type C is less efficient than the type A, which is less efficient than the type B for $S > 0.6$. The PKWs are more efficient than the linear weirs.
  o At constant discharge, the PKWs have much less impact than the linear weirs on the upstream level rise. With a PKW type A, the latter could be lowered by 0.90 m, 1.60 m, and 2 m compared respectively to an Ogee crest, a sharp crest, and a broad crest weir.

6. REFERENCES

Anderson, R.M. (2011). "Piano Key Weir Head Discharge Relationships." M.S. Thesis, Utah State University, Logan, Utah.

Belaabed, F. and Ouamane, A. (2011). "Contibution to the study of the Piano Key Weir submerged by the downstream level." *Proc. International Workshop on Labyrinths and Piano Key Weirs PKW 2011, CRC Press,* 89-96.

Cicero, G.M., Delisle, J.R. (2013a). "Discharge characteristics of PK weirs under submerged flow." *Proc. International Workshop on Labyrinths and Piano Key Weirs PKW 2013, CRC Press, 101-*109.

Cicero, G.M., Delisle, J.R. (2013b). "Effect of the crest shape on the discharge characteristics of a type A PKW." *Proc. International Workshop on Labyrinths and Piano Key Weirs PKW 2013, CRC Press, 41-*48.

Cicero, G.M, Delisle, J.R, Lefebvre, V., Vermeulen, J. (2013c). "Experimental and numerical study of the hydraulic performance of a trapezoidal PKW." *Proc. International Workshop on Labyrinths and Piano Key Weirs PKW 2013, CRC Press, 265-*272.

Dabling, M.R. and Tullis, B.P. (2012). "Piano Key Weir submergence in channel applications." *Proc. International Workshop on Piano Key Weir for In-Stream Storage and Safety, New Delhi, India.* 13-23.

Hager, W.H. (1986). "Discharge Measurements Structures." *Communication1,R. Sinniger, ed. Chaire de Constructions hydrauliques,* Dep. de Génie Civil. EPFL, Lausanne, Switzerland.

Leite Ribeiro, Boillat, J.L, Schleiss, A.J., Le Doucen O. and Laugier F. (2011). "Experimental parametric study for hydraulic design." *Proc. International Workshop on Labyrinths and Piano Key Weirs PKW 2011, CRC Press, 183-*190.

Leite Ribeiro, M., Pfister, M.., Schleiss, A.J. and Boillat, J.L. (2012). "Hydraulic design of A-type Piano Key Weirs." *Journal of Hydraulic Research,* 50(4), 400-408.

Lemperiere, F., Vigny, J.P. and Ouamane, A. (2011). "General comments on Piano Kew Weirs: The past and present." *Proc., International Workshop on Labyrinths and Piano Key Weirs PKW 2011, CRC Press,* 17-25.

Machiels, O. (2012). "Experimental study of the hydraulic behaviour of Piano Key Weirs."M.S. Thesis, Université de Liege, Liege, Belgium.

Ouamane, A., and Lemperiere, F. (2006). "Design of a new economic shape of weir." *Proc., International Symposium on Dams in the Societies of the 21st Century, Barcelona,* 463-470.

Pralong, J., Vermeulen, J., Blancher, B., Laugier, F., Erpicum, S., Machiels, O., Pirotton, M., Boillat, J.L., Leite Ribeiro, M. and Schleiss, A.J. (2011). "A naming convention for the Piano Key Weirs geometrical parameters." *Proc., International Workshop on Labyrinths and Piano Key Weirs PKW 2011, CRC Press,* 271-278.

Tullis, B.P., Young, J.C. and Chandler, M.A. (2007). "Head-Discharge Relationships for Submerged Labyrinth Weirs." *Journal of Hydraulic Engineering,* 133(3): 248-254.

Tullis, B.P. (2011). "Behavior of Submerged Ogee Crest Weir Discharge Coefficients." *Journal of Irrigation and Drainage Engineering,* 133(3): 677-681.

Vermeulen, J., Laugier, F., Faramond, L. and Gilles, C. (2011). "Lessons learnt from design and construction of EDF first Piano Key Weirs." *Proc., International Workshop on Labyrinths and Piano Key Weirs PKW 2011, CRC Press,* 215-224.

Confined Disposal Facility Improved Weir Designs

C.K. Maglio, and B.M. Scully
U.S. Army Corps of Engineers (USACE) Engineer Research and Development Center (ERDC)
3909 Halls Ferry Road
Vicksburg, MS 39180-6199
USA
E-mail: coraggio.maglio@usace.army.mil

ABSTRACT

One of the initial constraints of any dredging project is deciding where to place dredged material. When placed upland, materials can be used beneficially, as beach nourishment or for habitat restoration, or can be placed in an upland confined disposal facility (CDF). Several times the solids volume in water is required to fluidize and hydraulically pump the materials. Once in the CDF, materials settle out of suspension, with clarified water decanted. This paper describes in general a current weir design used by the U.S. Army Corps of Engineers (USACE) and illustrates the innovations of the new Jacksonville District standard weir. The new outfall structure is safer, easier to construct, and has inherent environmental protection features. It also has a longer lifecycle and lower lifecycle cost than traditional structures. This paper also discusses a new composite weir system that is in the patent and construction phase. These new corrosion-resistant systems have the capability of revolutionizing and standardizing water control structures due to basic changes in material selection and operational controls. The construction, management, and maintenance of weir systems are a significant cost incurred by USACE navigation projects; improved systems are available that can reduce maintenance costs while improving the safety of personnel who operate them.

Keywords: *Dredging, water control structure, box riser, composite weir, dredged material disposal.*

1. INTRODUCTION

The ability to control fluid levels in a system is a fundamental aspect of water management, whether in the form of stormwater detention, raw water holding, wastewater treatment, industrial, agricultural, or other applications, instances where retaining variable head volumes of fluid are common. This is true also for nearly every port or waterfront facility around the world with confined disposal facilities (CDF) for dredged material. In the continental United States of America, the U.S. Army Corps of Engineers (USACE) maintains over one thousand CDFs, and within the Department of Defense (DoD), other state and federal agencies, and the private sector, thousands of water control structures within CDFs are in operation.

A CDF normally includes a water control structure in the form of a weir to separate water from dredged material. The supernatant water returns to the natural water body from which it was entrained by the dredge. In general, CDF weirs are designed with three objectives: to retain all of the dredged sediment solids within the CDF, to return clarified water from the CDF to the natural water body, and to control the release of water in such a way that turbidity, sediment resuspension, and scour are minimized.

One of the primary decisions made during any dredging project is where to place the dredged material. In basic terms there are only two alternatives; place the material in the water or place it on land. When dredged material is placed on land in a CDF, it is typically placed using a hydraulic pumping method that entrains sediment in a slurry with roughly four times as much water. Separating water from dredged material frequently employs an outlet weir structure to decant supernatant water back to the receiving water body. The outlet structure is usually a weir box (see Figure 1), half-pipe riser (see Figure 2), or other water control apparatus.

These facilities are often placed in very remote locations (disposal islands); thus, any construction that occurs at these sites is often at a premium. Maintenance of these facilities is also often neglected due to the inherent operation

difficulties and funding constraints. In coastal areas, the dredged material pumped into these CDFs evaporates and leaves behind highly saline and dissolved oxygen deficient liquids, creating extreme corrosion conditions. These structures are normally built out of coal-tar coated steel and/or sheet metal and wood and are highly susceptible to degradation and corrosion if the protective coatings have the slightest scratch or defect. Traditional alternatives to controlling fluid at variable heights include designs with materials such as concrete, steel, and wood and mechanisms such as weirs, sluice gates, and fixed orifices.

The relatively rapid degradation of materials within and adjacent to coastal environments are common throughout the world with significant damage caused by chloride-induced corrosion, chemical attack, physical deterioration (e.g., abrasion and erosion), thermal and freeze/thaw cycling, and biological and UV degradation. In many cases, the use of new, non-corrosive materials and designs can reduce initial construction costs and greatly reduce the life-cycle costs of these facilities.

Figure 1. Box riser weir crevice corrosion at water-air interface after one use cycle.

Figure 2. Half-pipe riser weir's sheet metal skin experiencing pitting corrosion after one use cycle with protective asphaltic coating.

Most weir structure designs have not evolved and still require operators to climb into the structures to manually alter the weir elevation (see Figure 3). The usefulness of a CDF is dependent on the ability of the weir structure to decant water at varying elevations during and after the dredge material placement event. Elevation control of the pool in the CDF is crucial for maximizing disposal capacity and adhering to water quality standards. For a weir to decant at varying elevations, the most common method involves stacking timber boards into vertical slots along the face of the weir, starting at the bottom, until the weir stack reaches the desired decanting elevation. Adding weir boards increases the pool elevation of dredge slurry in the CDF, which increases retention time and settling efficiency. Clean water remaining at the top of the water column after entrained solids have settled are released over the weir crest. The frequency with which crest heights need adjustment depends on several variables. It is not uncommon to adjust elevation several times each day during a dredging operation. Adjustments made to the weir board stack after material placement are usually much less frequent and depend on the level of material management intensity.

Figure 3. Traditional USACE fluid control operation (removing timber weir boards) with harnesses within confined disposal area (front view - left) and (plan view - right).

Historically, weir structures averaged 2.5-3.5 m (8-10 ft) in height but have grown as CDFs are incrementally raised to match dredging needs. Currently, weir structures between 8 and 10 m (25 and 35 ft) in height are commonly found. Operators are required to wear fall protection gear to make adjustments to the weir crest (decanting) elevation. To make elevation adjustments, the operator generally enters into the weir structure at the top, climbing through a tight lattice work of steel structural members to reach the face of the box. Once the operator climbs down to the top board of each stack, they must continuously secure their fall protection gear and brace themselves within the structural members in order to physically remove or install the boards. Wooden boards frequently swell into the slots and require the operator to dislodge them by swinging a claw hammer or pick-axe into the face of the board, which may be submerged several inches below the surface of the pool. In a worst case scenario, the operator must use a chainsaw to cut the boards into pieces for removal.

Given the dangerous working conditions and level of effort needed to keep the stack of boards at the optimum elevation during and after a dredge event, weirs may be operated improperly. Improper operation of the weir has negative impacts relating to adherence to outflow water quality standards and the overall operational inefficiency of the site. In most cases across the nation, CDF capacities are at a premium given their vicinity to port growth and

other valuable uses of land along waterways. Inefficient uses of CDFs due to improper operations of a weir box can usually be traced to the difficulties relating to removing or adding weir boards. To address operational life-safety and greatly improve the life-cycle of CDF weirs while lowering initial costs, the following designs were developed.

2. NEW JACKSONVILLE DISTRICT STANDARD WEIR

The new Jacksonville District standard weir design was developed to resolve lifecycle concerns while increasing overall functionality. This redesign of a standard system looked at all of the competing issues and maintained three basic design tenets that guided the process: simplicity, flexibility, and redundancy. The result of this process was a new outlet structure design that uses a wrap-around floating dock to access the dual coal-tar epoxy coated steel box riser weirs on a single concrete slab foundation, as shown in Figure 4 (Maglio, et al. 2014).

Figure 4. Set of 4.9 m (16 ft) tall 1.2X1.2 m (4x4 ft) Box Riser Weirs with floating dock access, Buck Island, Jacksonville, Florida. (Maglio et al. 2014).

This new weir design uses composite weir boards that are lighter, stronger, more dimensionally accurate, and tighter fitting than traditional treated timber weir boards. The wrap-around floating dock allows for safe and easy access for the installation or removal and storage of the weir boards, as shown in Figure 5. An internal emergency flap gate is installed within the box at the discharge pipe, as a redundant environmental safety feature. The modular nature of this system allows the design to be easily adapted for a particular application without significant alterations (Maglio 2014).

Figure 5. Bartram Island Cell F floating dock in use with composite weir boards removed and stacked on the docks deck from two sides of each box riser (Maglio et al. 2014).

Another significant improvement of this design over previous systems is the fact that these weirs are installed in pairs. This ensures that dredging can continue in the event that a single weir becomes compromised during the course of a dredging event. The risers are connected to continuously fused, high-density polyethylene (HDPE) outfall pipes that are permanently installed, as shown in Figure 6 (Maglio 2014). This type of plastic, continuously fused pipe has far less lifecycle issues than other pipeline materials.

Figure 6. Permanently installed and elevated 30 inch outfall pipes to minimize wetland impacts Bartram Island Cell B2 (Maglio et al. 2014).

The approximate total construction cost for a set of coal-tar epoxy coated steel box riser weirs on a concrete spread foundation with HDPE return outfall pipe is $350,000 in 2014 U.S. dollars. This includes all associated earthwork, fabrication, and material costs (Maglio 2014).

This design solved the vast majority of issues related to traditional CDF weirs associated with safety and lifecycle; however, it did not address the construction cost and practices, especially in remote locations. It also employed structural steel in a highly corrosive environment with only a thin protective coating.

3. INCREMENTALLY ADJUSTABLE FLUID CONTROL MECHANISM

The Jacksonville District weir re-design overcame two critical issues through material selection and general arrangement. The first critical issue was environmental compliance and safety shortcomings that arise from the mating issues inherent in the use of wood in a steel guide channel. Dimensional inconsistency in the wood results in leakage or difficulty in operation. Neither improved the function of the system. System performance benefitted from the selection of a dimensionally stable, corrosion-resistant composite material, in that leakage was reduced. The second critical issue was operator safety, which was also improved by selection of lighter material that was less prone to jamming in the guide channel. Operators no longer require the use of hammers, pick-axes, or chain saws to remove flashboards. Safety was further improved by the use of a floating dock, which enables users to access flashboards without entering the riser; fall protection is no longer necessary to operate weirs safely.

Despite these improvements, it was recognized that further operational gains could be achieved. Owing to the composite material's shape and strength, it is possible to lift individual or multiple boards using a simple lifting mechanism inserted into the open face of a board, which has been modified from a rectangular cross section to a c-shaped cross section. By lifting boards in this manner, it is possible to create a weir crest or orifice anywhere within the stack of weir boards. By enclosing the riser box and affixing the operation mechanism to its exterior, the need to approach the weir face during operation can be eliminated, as can the necessity and cost of floating docks used for that purpose.

Recognizing the available benefits, the USACE applied for a patent for the incrementally adjustable fluid control mechanism. The mechanism combines the function of both a weir and an orifice, traditionally used independently, enabling flexible fluid height control and operation modes over a varying head range, limited only by the strength of riser boards and the lifting mechanism connection members, see Figure 7.
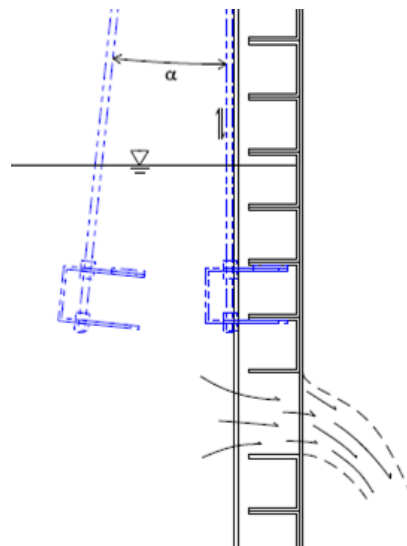
Figure 7. Side view - incrementally adjustable fluid control mechanism concept, employing a stack of composite c-channels and a picking mechanism.

The picking mechanism is lowered to the desired elevation of fluid withdrawal, usually just below the water surface, then inserted into the flange of the C-channels. This picking mechanism is similar to a picking beam utilized for evenly lifting heavy loads. The vertical lifting force can be produced by an actuator, winch, jack, or similar

mechanism. The withdrawal depth can be determined by measuring the inserted length of the picking mechanism using pre-determined marks or a line counting system.

4. COMPOSITE WEIR SYSTEM

USACE is currently working to develop a fully composite weir system that takes advantage of the incrementally adjustable fluid control mechanism. The primary benefits of the proposed Complete Composite Box Weir System is the ability to open a window at any elevation from the top of the structure using the picking system (see Figure 7). The removal of boards is no longer necessary when using this system as the guide channel can be fabricated to account for the required "window opening" height, rather than removing all the stop logs to the desired elevation. The structure can be entirely fabricated out of available composites and plastics products, and can also be easily excavated and moved to a new location and reinstalled because it does not require a typical concrete or pile foundation due to its light weight.

The complete composite weir system is a conceptual design for a 7.9 m (26 ft) tall adjustable weir with composite C-channels and an integral spread foundation using composite beams, timber, and granular backfill to distribute the structural load and to counter uplift buoyancy forces. One of the benefits of this proposed system is the elimination of the need for external ladders, floating docks to pull boards, or other access methods because water withdrawal control is handled from the top of the structure. The system functions by using a picking mechanism controlled from the top of the riser to regulate the weir crest elevation on all sides of the riser at any elevation. Removal of boards is no longer necessary when using this system as all weir boards remain in the channel permanently (Maglio 2014).
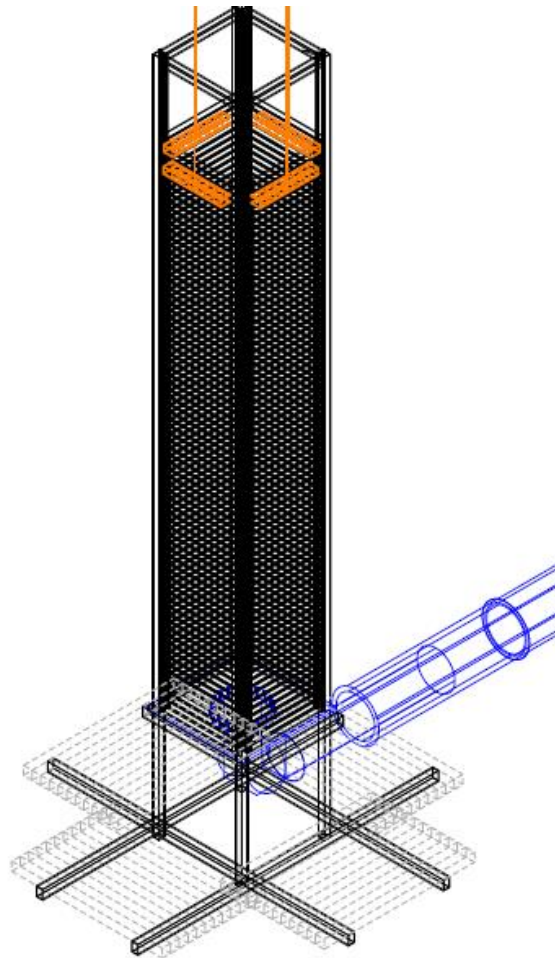
Figure 8. Isometric view of conceptual Complete Composite Weir.

The system is entirely fabricated from fiberglass reinforced composites and plastics. It includes a slip joint of HDPE pipe to preclude forces due to settlement of the adjacent dike from transferring along the outfall and causing the weir to lean or connections to fail. This slip joint also allows for easy extraction of the riser structure so that it can easily be moved to a new location and reinstalled in the event that the structure must be relocated for material management purposes. Extending the foundation of the structure downward into the subgrade and the use of onsite granular backfill for stability and to offset floatation or settlement forces provides a relatively inexpensive and more expedient construction option compared to typical foundation systems (Maglio 2014).

This concept is intended to provide an improvement in terms of design lifecycle, operations, and costs to common existing systems. It consists of vertical guide channels containing a stack of C-channel members that make up a vertical wall. The C-channels are oriented such that their flanges are exposed to the working fluid, while the c-channel webs make up the vertical retaining wall. The flanges of the C-channels provide an easy lip for raising the C-channels to create a window at any level.
The composite weir system design characteristics:

- C-channel composite shapes are lightweight when compared timber or steel.
- Fiberglass reinforced composite materials are non-corrosive, can be made UV resistant, and with the proper resin, can be manufactured to be heavier than seawater, and they can have a 50 year design life.
- The C-channel shape is such that there is an easy picking lip that in integral to the structures design.
- The stack of C-channels with their flange's out looking provides a flat matting wall surface against the back guide channel flanges.
- The C-channel composite shapes are able to withstand large hydrostatic forces.
- Flexibility due to the composite c-channels inherent strength; these gate systems can be made wider or taller depending on the application needs.

The total initial cost of one of these systems is relatively similar to traditional steel frame designs if fabrication and installation cost are included.

5. CONCLUSIONS

A weir is a barrier that operates like a small dam, pooling fluid behind the structure while also allowing it to flow steadily over their tops at a semi-adjustable elevation. Common uses of weir stacks include altering the flow of rivers to prevent flooding, measuring fluid discharge, and rendering rivers navigable. Traditional weir stacks consist of a stack of "stop logs" fabricated out of timber or aluminum and held into place with vertical channels. Water flows over the top, with stop logs removed or added to control the water level upstream of the weir stack. There are several limitations inherent to weir structures. One of the design problems is that the buoyant stop logs can float, compromising the control of the stack. Additionally, water level control is only possibly from the top, by removing logs from or adding logs to the stack.

Incorporating materials from other industries to improve standard systems design can reap huge benefits in terms of lifecycle management and long-term project costs. The implementation of such an initiative was conducted within the USACE Jacksonville District. This has led to initial and long-term cost savings as well as many other benefits. This improved system has been embraced by project Sponsors and their consultants, and numerous installations have been completed. The primary drawback of the Jacksonville District's new standard design is the use of carbon steel, which in the marine environment, is easily corroded if the coating system is compromised. However, this material selection issue has been addressed by the conceptual full composite weir system design. This concept removes the issue of corrosion and lifecycle concerns by the use of composites to replace the steel members. The concept also allows for easier relocation of these structures by dispensing with a solid foundation in favor of an easily excavatable, granular backfill. The floating weir system employs standard marine materials and a constant withdrawal depth to achieve production efficiencies while maintaining an extended life cycle (Maglio 2014).

6. ACKNOWLEDGMENTS

7. REFERENCES

Maglio, C.K. (2014). "Dredged Material Management Area – Weir Design, the State of the Art". *Proceedings of the Western Dredging Association and Texas A&M University Center for Dredging Studies' "Dredging Summit and Expo 2014"*. WEDA 34 and TAMU 45. Toronto, Canada June 15-18, 2014.

Maglio, C.K., Bearce, J.W., Presley, M.A. and Grover, J.L. (2014). "New standard weir design for dredged material management area, Jacksonville District." *DOTS Technical Notes Collection. ERDC TN-DOTS-14-01* Vicksburg, MS: U.S. Army Engineer Research and Development Center. June 2014.

Optimizing A New Flow Diversion Structure For The Planned Expanding Of The Spillway For The Malter Dam In Germany Using A Physical Hydraulic Model

J. Schmidt[1], J. Wieland[1] and J. Jensen[1]
[1]Research Institute for Water and Environment (fwu)
University of Siegen
Paul-Bonatz-Str. 9-11
57076 Siegen
Germany
E-mail: jessica.schmidt@uni-siegen.de

ABSTRACT

The State Reservoir Administration of Saxony is planning to expand the spillway discharge capacity of the 102-year-old Malter Dam. After a catastrophic flood in 2002, updated hydrologic modeling indicated that the design discharges for the dam had increased significantly. As a result, the original spillway discharge capacity was insufficient to pass the revised design flows. A design concept was developed to add a second spillway and stilling basin to the dam, and to pass flow into this spillway using a novel vertical flow separator. The design and performance of this system was evaluated using a 1:25-scale physical model. The modeling activities were performed by the Research Institute for Water and Environment located at the University of Siegen. The modeling effort led to an improved design of the vertical flow separator, which meets the needs of the project and will allow for an increase in the spillway discharge capacity to satisfy dam safety concerns.

Keywords: diversion structure, physical modeling, spillway, dam, flood safety

1. INTRODUCTION

The State Reservoir Administration of Saxony (LTV) is planning to expand the spillway of the 102 year old Malter Dam. This is necessary to reinstate the flooding safety of the dam, which has currently not been given due to an adaptation of the hydrological design discharges. As part of this project, the LTV commissioned the Research Institute Water and Environment (fwu) of the University of Siegen to perform a hydraulic model test for review and optimization of the hydraulic functionality.
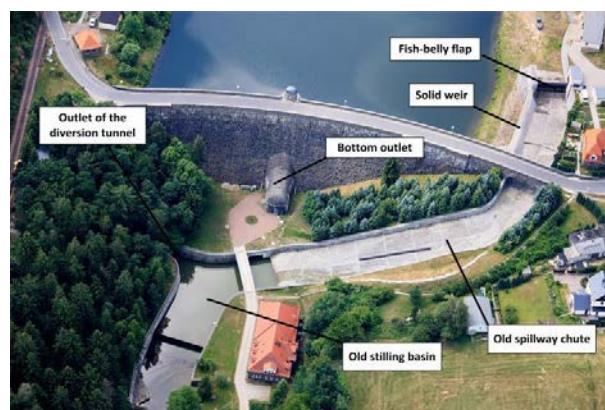
Figure 1. Aerial view of the Malter Dam in 2008 (Source: LTV)

The Malter Dam was built from 1908 to 1913 in the valley of the river "Rote Weißeritz" and has a storage volume of 8.78 million m³. The 193 m long curved dam consists of quarry stone masonry. The dam serves mainly for flood

protection, as well as for recreational activities and industrial water supply. Furthermore, an annual average of 1.7 million kWh of electricity from hydropower is gained at the Malter Dam. In normal operation, the water of the dam is released through the bottom outlet (two pipelines, each with DN 1,000) of the dam into the riverbed. If a flood is expected, the 200 m long diversion tunnel by the right side of the slope can be used for pre-release. In case of floods, the flow discharges through the spillway, which lies on the left side of the slope in the form of a fish-belly flap that is arranged laterally to a masonry weir with an overflow threshold, through the wall passage over the old spillway chute, and down to the old stilling basin below the dam (Figure 1).

The extreme flood event in August 2002 resulted in damage and overloading of the spillway of the Malter Dam, causing extensive flooding at the lower reaches of the "Rote Weißeritz". The flood also lead to huge damages in Dresden at the Elbe river, which is only about 20 km away from the Malter Dam. The total damage of the flood event in Germany amounted to about 10 billion euros. The extreme flood event at the Malter Dam is shown in Figure 2. On the left side is the view from the dam into the old spillway chute. On the right side is the view from the dam to the fish-belly flap and the masonry weir.

Figure 2. Extreme flood event at the Malter Dam in 2002 (Source: LTV)

In 2006, new design discharges were determined on the basis of new rainfall-runoff models. The comparison of the last design discharges of the Malter Dam in 1983 and of the new design discharges in 2014 show that the design discharges have increased about 131% for the flood discharge $HQ_{1,000}$ (= BHQ_1 = design flood event, that statistically occurs every 1,000-years) from 125 m³/s to 289 m³/s and about 137% for the flood discharge $HQ_{10,000}$ (= BHQ_2 = design flood event, that statistically occurs every 10,000-years) from 166 m³/s to 393 m³/s. The spillway of the Malter Dam was not originally designed for these increased design discharges. Therefore, the flooding safety of the Malter Dam is no longer guaranteed. For this reason, the LTV is currently planning the expansion of the spillway to restore the flood safety the Malter Dam.

Figure 3. Spillway of the Malter Dam 2014 (left) (Source: LTV); Evened bottom slope in the hydraulic model (right)

As part of the development plans, the expansion of the existing spillway with an additional spillway chute with a new stilling basin has turned out to be the preferred option for an economically viable capacity improvement of the spillway. The expansion of the spillway also includes a lowering of the sole of the wall passage to about 1.5 m with a bed slope of 3.5 % to prevent over-fill (Figure 3). The application of the two spillways occurs behind the wall passage by a new kind of flow diversion structure with a vertical flow separation. Furthermore, the hydraulic performance of the diversion tunnel is increased by replacing the existing slide valves with more efficient slide valves (3 x 2 slide valves in two levels in closed type w/h = 1,000/1,000 mm). Due to the mutual flow influence of the individual components and complex geometries, for which no hydraulic boundary conditions or calibration measurements are presently available, a physical hydraulic model test was required (Kobus 1980).

2. HYDRAULIC MODEL TEST

2.1. Model Features and Measuring Technique

The hydraulic model (1:25) of the Malter Dam was built due to the dominant gravity and inertial force as a Froude model and includes a part of the water storage area, the dam, the existing spillway, the planned expansion of the spillway (diversion structure, new spillway chute, new stilling basin), the bottom outlet, the diversion tunnel, the old stilling basin, and a part of the below lying river, "Rote Weißeritz" (Figure 4). The model extends over a length of 19.60 m, with a maximum width of 7.20 m within an area of 85 m². The water area of the storage space in the model comprises about 22 m²; the storage volume in a flood event is about 14 m³. The largest hydraulic height difference ranges about 1.58 m. The hydraulic model has been designed with a concrete surface.
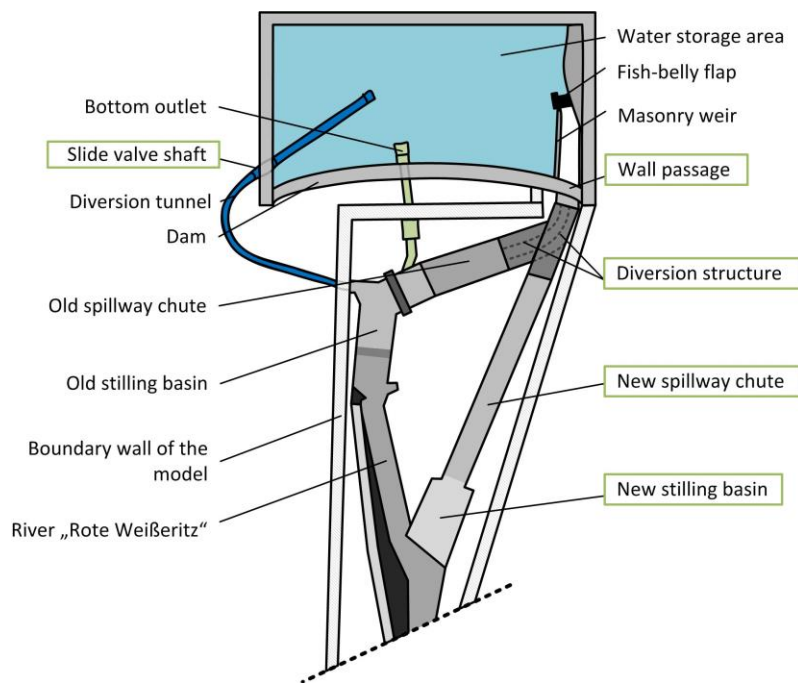
Figure 4. Schematic sketch of the hydraulic model of the Malter Dam; outlined in green are the components that are newly built or rebuilt in the context of the expansion

The control of the outflow amount, the settings of the valves (2 x bottom outlet, 3 x diversion tunnel, 1 x fish-belly flap), and the setting of the lower water level at the end of the model was performed fully automatic and computer controlled by servomotors that achieve a positioning accuracy of 0.1 mm. The inflow into the model was measured by an inductive flowmeter (IDM) in the supply line, whereby the accuracy of the discharge measurement was achieved within 0.1% of full scale. The maximum load to be examined in nature PMF (= probable maximum flood = HQ_{max}) = 461 m³/s has been examined as an inflow of PMF = 147.5 l/s in the model. For the investigations, the water

level was recorded at six positions with ultrasound measuring probes in real-time. These data were supplemented and densified by further measured water levels and velocity profiles. Furthermore, differential pressure measurements were performed for qualitative statements, and video and image materials were recorded. With the used measurement technology, highly precise measurements and an optimum reproducibility of the measurement results were guaranteed.

2.2. Optimization and Investigation Aspects

Special optimization and examination aspects in the model test included the outflow distribution into the diversion structure, the hydraulic performance of the new spillway chute, the dimensions of the new stilling basin, and the impact of the planned increase in the hydraulic performance of the diversion tunnel with simultaneous operation of the spillway. To optimally utilize the existing building stock and to prevent overloading of the existing spillway, the flow behavior in the diversion structure was analyzed to optimize the loading of the two spillways. In the hydraulic model test, seven load cases (HQ_{80}, HQ_{100}, HQ_{200}, HQ_{500}, $HQ_{1,000}$, $HQ_{10,000}$ and PMF) of $HQ_{80} = 36.8$ m³/s to PMF = 461 m³/s with the respective settings of the operating facilities (1 to 2 opened slide valves of the bottom outlet, 1 to 3 opened slide valves of the diversion tunnel, upper edge of the fish-belly flap from 333.0 to 330.5 mNN) were examined. According to the investigation concept, all objects of study have been investigated for the planned state (Jensen et al. 2015). Since individual conversion measures, in turn, have effects on the entire outflow behavior of the model experiment, the hydraulic model was rebuilt from the plan state to optimization state (optimized end state) using the recommended conversion measures; subsequently, all the objects of the investigation were examined again.

A particular challenge is the hydraulic performance and the optimization of the outflow process in both closed and curved components diversion tunnel and diversion structure, because of the supercritical flow and complex transitions from free-surface to pressure drain in conjunction with air entry (Schmidt et al. 2015a). In addition, the outflow processes in the diversion tunnel and in the diversion structure depend decisively on the boundary conditions above and below.

3. INVESTIGATIONS OF THE DIVERSION STRUCTURE IN THE MODEL TEST

3.1. Proof of the Functional Principle of the Diversion Structure (Planned Geometry)

Behind the wall passage, the construction of a transition channel is planned, which leads to the diversion structure. On the upper level, the new spillway chute and stilling basin are connected. In the case of a flood, the runoff is first discharged through an opening in the sole of the diversion structure on the lower level into the old spillway chute (Figure 5, left). Due to the optimal design, the hydraulic efficiency of the opening and of the old stilling basin should correspond, taking into account inflows into the stilling basin from the bottom outlet and diversion tunnel, preventing an overloading of the old stilling basin. When the flood discharge exceeds the hydraulic performance of the opening, and thus of the old stilling basin, there is an overflowing of the opening and the remaining flood discharge is passed onto the upper level of the diversion structure into the new spillway chute (Figure 5, right).

The functionality of the planned diversion structure could be demonstrated in a first-test series. However, there was a splashing phenomenon from the sole opening to the upper level into the new spillway chute whereby the uneven inflow of new spillway chute and the associated cross wave formation were amplified (Figure 6, left). Even at the old spillway chute, a cross wave formation could be observed. But this resulted from the supercritical flow through the three curved channels of the diversion structure below the sole opening (Figure 7, left). The optimization of the cross waves was subordinate to the overarching goal of safe dissipation of the flood runoff (Schmidt et al. 2015a).

Due to the increased efficiency of the diversion tunnel by the new valves in the slide valve shaft and through the operational recommendations by Jensen et al. (2015) for operation without ventilation in pressure drain, the old stilling basin was overloaded in the design load cases $HQ_{1,000}$ and $HQ_{10,000}$ in the planned state. To avoid this, several geometries and the opening width of the vertical separator were investigated and optimized in five experimental test series. For these tests, discharge and pressure measurements, as well as video and image recordings, were used.
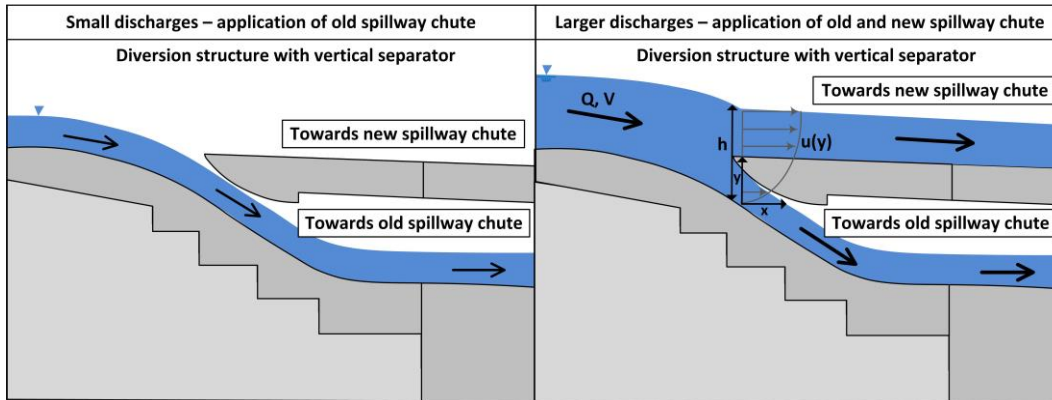
Figure 5. Functional principle of the diversion structure during smaller and larger outflows

Figure 6. Comparison of the splashing effect in experiment series 4 and 5 (optimized geometry), $Q = 100$ m³/s

Figure 7. View into the three channels of the lower diversion structure (left) and at the upper diversion structure (right) in the optimized state in the hydraulic model, load case $HQ_{1,000}$

3.2. Optimization of the Vertical Separator Geometry (experiment series 1 to 5)

According to the investigations of the plan state (experiment series 1), first the partial discharge into the old spillway chute should be reduced by shifting the vertical separator horizontally to shrink the opening width from 0.80 m to 0.64 m (experiment series 2). Due to the uneven flow in the wall passage in the planned state, the discharge flows unevenly over the vertical separator, and, hence, the new spillway chute is unevenly applied so that cross waves arise. This negative effect was even stronger in experiment series 2 because the lowered surface curve collides with the edge of the vertical separator. To optimize this issue, the rounding of the vertical separator was adjusted in experiment series 3 so that the inlet gap again corresponds approximately to the original length of the planned geometry (3.17 m). The reduction of the opening of the vertical separator (0.64 m) has been preserved. It became

apparent that this geometry leads to an increased splashing effect. To avoid the splashing effect, the vertical separator was adjusted in experiment series 4 so that the edge is more pointed. But in experiment series 4, the splashing effect was considerably strengthened (Figure 6, left). Based on these observations, was concluded that the splashing effect is not due to the collision of the water with the edge of the vertical separator.

The splashing phenomenon could be explained after four extensive experiment series: Due to the larger opening of the inlet gap of the vertical separator compared to the control section below, more water is discharged as the control section of the vertical separator can absorb under the given pressure conditions. In the vicinity of the expansion behind the control section, a negative pressure temporarily occurs in the area of the control section, so additional runoff is pressed in the diversion structure by the atmospheric air pressure. This increases the performance of the diversion structure but also the risk of cavitation. The rounding of the vertical separator is therefore not necessary, and even a hindrance, as the water jet is in contact with the rounding of the vertical separator and the cross-section, which adjusts pressure drain, is increased. To avoid the negative impact of the rounded vertical separator, an optimization geometry in wedge shape was constructed and examined in experiment series 5 (Schmidt et al. 2015b). Deviating to the planned geometry, the control section was set without rounding directly into the inlet gap of the vertical separator (Figure 8, right).
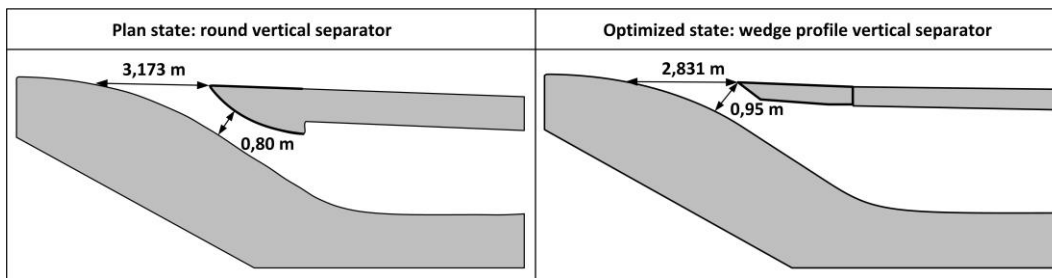
Figure 8. Schematic sketch of the geometry of the vertical separator in the plan state (left) and in the optimized state (right), longitudinal section

The flow now breaks off directly at the wedged edge control section so that the discharge is no longer in contact with the vertical separator and no pressure drain in this field may develop anymore. The runoff is now discharged below the vertical separator completely as free surface discharge, and there is no splashing effect at the inlet gap. Due to the free surface discharge, the flow velocity in the three curved channels is lower than in the state plan. Therefore, the water level deflection is smaller, the discharge flows more uniformly into the old spillway chute, and the expression of the cross waves is reduced. An utter prevention of cross wave formation is impossible due to the geometry of the diversion structure and of the old spillway chute (Schmidt et al. 2015a). Nevertheless, the new geometry of the vertical separator, as can be seen in Figure 9, generates an even more equal diversion of the flow. Due to the narrow design of the vertical separator, generous underwater ventilation is ensured and the structural complexity is significantly reduced. The risk of cavitation in the area of deduction is now minimal.
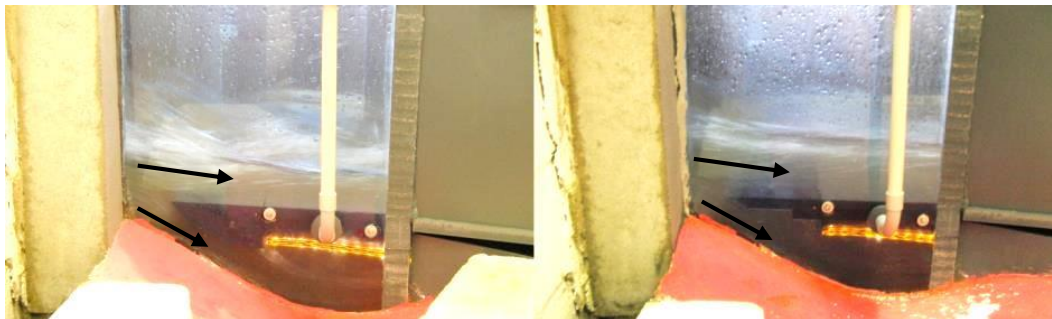
Figure 9. Geometry of the vertical separator in the planned state (left) and in the optimized state (right) in the hydraulic model, load case $HQ_{1,000}$

4. NUMERICAL INVESTIGATIONS OF THE OPTIMIZED DIVERSION STRUCTURE

For the numerical description of the discharge partition by the diversion structure, additional measurements of the water level h (Figure 5) at the edge of the vertical separator for 12 outflows (Q = 50, 60, 70, 80, 90, 100, 110, 120, 130, 140, 150 and 200 m³/s) were recorded. From the measured data, the mean water level h, the mean water level under the vertical separator y (Figure 5), and the mean velocity in the whole flow cross-section V (Figure 5) were determined for each load case. To calculate the mean velocity under the vertical separator $u_{mean,lo}$ and thereby the partial discharges into the old and the new spillway chute, the velocity profiles and the shear stress distribution were determined both for the simplified consideration of a predominantly two-dimensional flow and the three-dimensional flow of the measured partial discharges in the hydraulic model.

4.1. Simplified Consideration as a Predominantly Two-Dimensional Flow

Due to the change in slope behind the wall passage into the diversion structure, there is a non-uniform channel flow. Jirka and Lang (2009) say that local speed profiles of non-uniform channel flow are in a first approximation, similar to those in uniform flow. So for open channel flow with a large width ($w \gg h$) and a small bed slope, a linear shear stress distribution may approximatively be assumed. The maximum shear stress at the sole τ_0 ($y = 0$) is described as

$$\tau_0 = \gamma \cdot I_0 \cdot h = \rho \cdot g \cdot I_0 \cdot h \tag{1}$$

where ρ is the density of water (1,000 kg/m³), g is the constant of gravitation (9.81 m/s²), I_0 is the bottom slope, and h is the water level. The shear stress is in kinematic form, expressed as the shear stress velocity or friction velocity u_*.

$$u_* = \sqrt{\frac{\tau_0}{\rho}} \tag{2}$$

From the measured values of the water depth h at the edge of the vertical separator, the turbulence parameter u_*/V was determined for each load case and shown in Figure 11 (red line). The values range from 0.125 to 0.168 and, thus, lie all in the rough area. Also, the Reynolds number confirms that it is a fully rough open channel flow (100 > Re) (Chanson 2004). The current flow is characterized by turbulent momentum exchange operations in the form of fluctuating vortex motions, which are superposed on the mean velocity profile $u(y)$. These internal turbulence mechanisms control the shape of the resulting velocity profile $u(y)$ because the logarithmic velocity profile results from the friction velocity and depends on the sole roughness k_s. The turbulent channel flow corresponds to a boundary layer flow that is over the entire water depth fully developed. For turbulent flows with a fixed boundary, the logarithmic law of the velocity distribution is applicable (Jirka and Lang 2009, Chaudhry 2008):

$$\frac{u}{u_*} = \frac{1}{\kappa} \cdot ln(y) + C \tag{3}$$

where κ is the Karman constant Kappa ($\cong 0.40$), C is a function of the boundary conditions of the respective flow subzone, y is the partial water depth in which the velocity is to be determined, and u is the velocity at the water depth y. The simplified velocity profile can be represented dimensionless (normalized) by the mean velocity in the main flow direction V (Jirka and Lang 2009).

$$\frac{u}{V} = 1 + 2.5 \cdot \frac{u_*}{V} \cdot \left(1 + ln\frac{y}{h}\right) <=> u = V \cdot \left(1 + 2.5 \cdot \frac{u_*}{V} \cdot \left(1 + ln\frac{y}{h}\right)\right) \tag{4}$$

Eq. (4) shows the dependence of the velocity profile of the turbulence parameter u_*/V, which is a measure for the out of the frictional resistance arising turbulent vortex motions. The velocity profiles at the vertical separator could be determined as a function of y/h (= 0.05 to 1.0) from the turbulence parameters u_*/V and the mean velocities in the whole flow cross-section V, calculated from the measured. Figure 12 (left) shows the velocity profiles for each load case. The velocity u at the water level under the vertical separator y is also marked. For each load case, the integral over the curve up to the measured value of y/h has been calculated, and by the mean value theorem of the integral calculus, the mean velocity of the partial discharge under the vertical separator $u_{mean, lo}$ has been determined (Eq. (5)). The mean velocity above the vertical separator has been determined correspondingly. From the mean velocities

above and below the vertical separator, the partial discharges into the old and the new spillway chute could be calculated using the continuity equation.

$$u_{mean,lo} = \frac{1}{\frac{y}{h}-0.05} \cdot \int_{0.05}^{y/h} \left(V \cdot \left(1 + 2.5 \cdot \frac{u_*}{V} \cdot \left(1 + ln\frac{y}{h}\right)\right)\right) \tag{5}$$

Figure 10 shows the comparison of the calculated and the in the model test measured partial discharges in the old and the new spillway chute. The calculated partial discharges show a good agreement to the measured discharges for the load cases $Q = 50$ and 60 m³/s when the discharge flows completely under the vertical separator in the old spillway chute. But for all other load cases, there are very high differences. A possible reason is the assumption of a linear shear stress distribution in the turbulent flow when the flow is divided into the old and new spillway chutes. Thus, the simplified assumption of a predominantly two-dimensional flow before the division structure is not effective for these load cases. A mere numerical calculation of the partial discharges with this approach is not possible. The three-dimensionality of the flow has to be considered, which is why a hydraulic model test for determining the partial outflows is imperative.
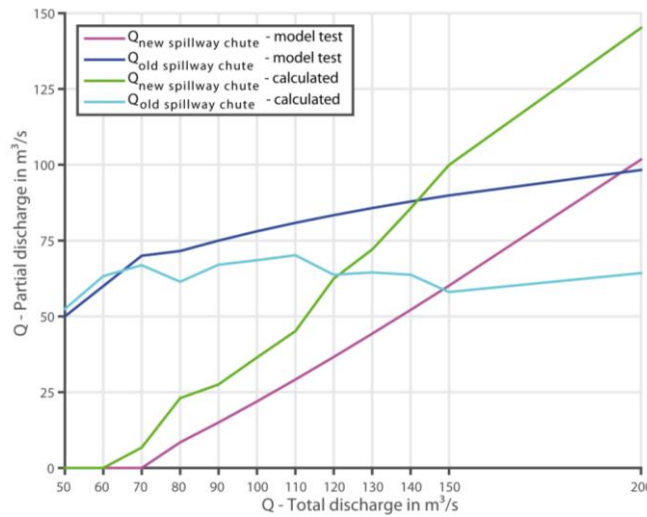
Figure 10. Partial discharges on the old and the new spillway chute (calculated and measured in the model test)

4.2. Three-Dimensional Flow of the Measured Partial Discharges

According to Bollrich (2013), the shear stress due to turbulence results from the product of the density with the temporal mean value of the product of the velocity fluctuation components in flow direction v_s' and transverse v_n'.

$$\tau = \rho \cdot \overline{v_s' \cdot v_n'} \tag{6}$$

Accordingly, the shear stress velocity results to

$$u_* = \sqrt{\frac{\tau}{\rho}} = \sqrt{v_s' \cdot v_n'} \tag{7}$$

The shear stress due to turbulence is thus proportional to the square of a velocity.

$$\tau = \rho \cdot u_*^2 \tag{8}$$

From the partial discharges measured in the model test, a formula for the partial discharge below the vertical separator $Q_{old\ spillway\ chute}$ could be determined, valid for the total discharges $Q_{total} > 70$ m³/s (Figure 10).

$$Q_{old\ spillway\ chute} = 29.158 \cdot ln(Q_{total}) - 56.213 \tag{9}$$

For $Q_{total} \leq 70$ m³/s applies $Q_{total} = Q_{old\ spillway\ chute}$ because up to this discharge, the whole discharge is drained under the vertical separator into the old spillway chute. With the calculated partial discharges $Q_{old\ spillway\ chute}$ and the continuity equation (Eq. (10)), the mean velocity under the vertical separator u was determined.

$$u = \frac{Q_{old\ spillway\ chute}}{w \cdot y} \tag{10}$$

The shear stress velocity u_* was calculated with Eq. (4) dissolved to u_*, and the shear stress due to turbulence was calculated with Eq. (8). The turbulence parameter u_*/V calculated from Eq. (2) (red) and from Eq. (4) (blue) are shown in Figure 11. The blue line shows that the shear stress velocity cannot be calculated for $h \leq 1$, because the shear stress velocity is then zero (e.g. $h = y = 0.87$ for $Q = 50$ m³/s and $h = y = 1.05$ for $Q = 60$ m³/s).
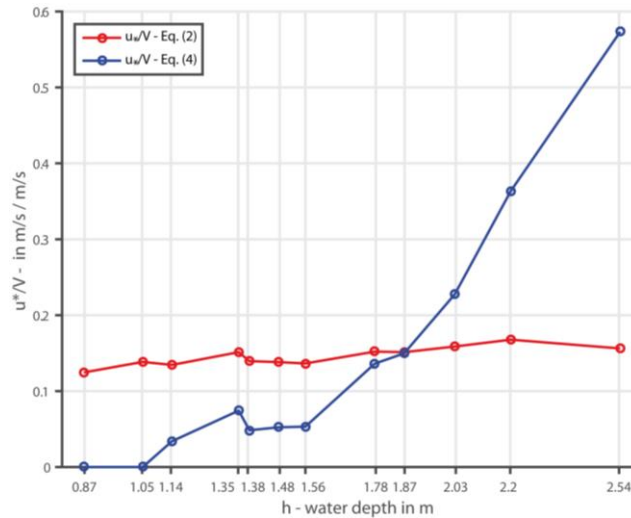
Figure 11. Turbulence parameter u_*/V for the measured water depth at the vertical separator of the diversion structure for the load cases $Q = 50$ to 200 m³/s calculated from Eq. (2) (red) and Eq. (4) (blue)
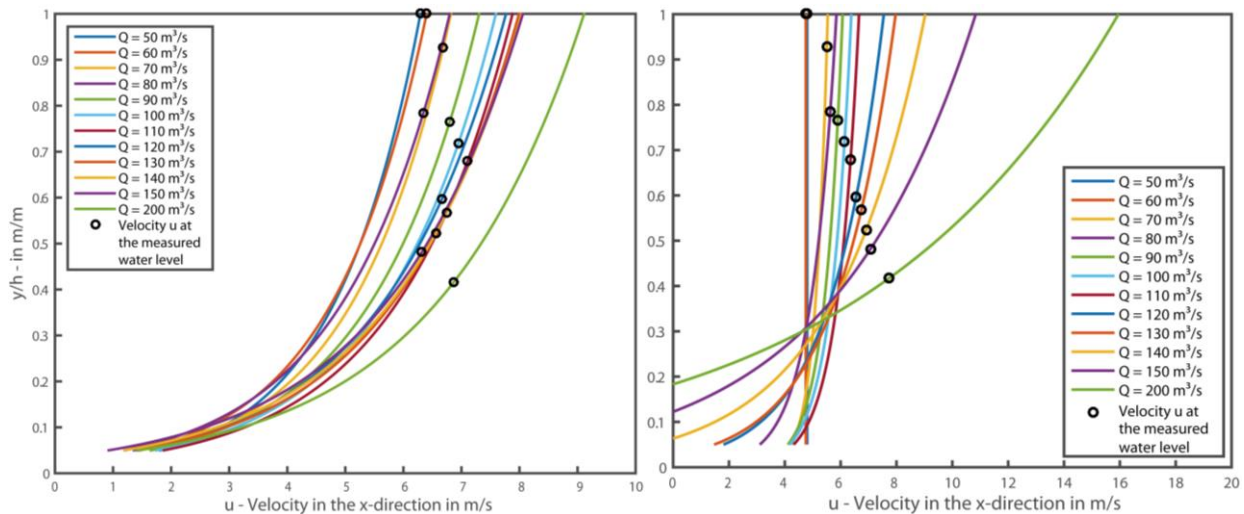
Figure 12. Velocity profiles as a function of y/h, load cases $Q = 50$ to 200 m³/s, Left: 2-D flow, Right: 3-D flow

The shear stress velocity u_* used in Eq. (4) yield to the velocity distributions for each load case, shown in Figure 12, right. These velocity distributions consequently result for the measured partial discharges. Again, it can be seen that this method is not applicable for $h \leq 1$ ($Q = 50$ and 60 m³/s).

5. CONCLUSION

With the hydraulic model test for the Malter Dam, the hydraulic performance and reliability of the preliminary draft were examined, optimized, and verified. The planned geometry of the vertical separator of the diversion structure was rounded with a control section lying below the opening. However, the studies on the planning geometry showed heterogeneous hydraulic phenomena. A vacuum formed in the area of the control section, which led to an increased risk of cavitation, an accelerated outflow with suction effect, and a splashing effect from the vertical separator in the above located new spillway chute. The rounding of the vertical separator, on which the discharge was abutted, was finally removed, and the vertical separator could be adjusted to a wedge shape. The control section is now lying directly in the sole opening. The discharge in the lower diversion structure now flows with a completely free surface. Vacuum and the associated negative hydraulic consequences no longer occur with the optimized geometry of the vertical separator in a wedge shape. As another side effect, the uneven inflow over the vertical separator into the new spillway chute is now more even because of the prevented splashing effect, whereby, the cross waves on the new spillway chute have been considerably reduced. In this contribution, it was also shown that numerical calculations of the partial discharges in the diversion structure using the simplified assumption of a two-dimensional flow are not effective, and, thus, a hydraulic model test is essential for the safe design of the diversion structure.

The challenge of enlargement of the spillway of the Malter Dam consisted primarily in making optimum use of the existing building stock so that overloading of the old spillway is excluded. By using the hydraulic model test, reliable statements on the runoff process for a worldwide new diversion structure could be made. As a result, the division structure was optimized so that the operational reliability and hydraulic efficiency, even in extreme flood events (PMF), is ensured. Thus, a safe and economic design could be achieved with this hydraulic model test.

6. ACKNOWLEDGMENTS

7. REFERENCES

Bollrich, G. (2013). Technische Hydromechanik 1. 7th Edition, Beuth Verlag GmbH, Berlin, Germany, 2013.

Chanson, H. (2004). The Hydraulics of Open Channel Flow: An Introduction. 2nd Edition, Elsevier, Oxford, Great Britain, 2004.

Chaudry, H. (2008). Open-Channel Flow. 2nd Edition, Springer Science+Business Media, New York, USA, 2008.

Jensen, J., Schmidt, J., and Wieland, J. (2015). Endbericht. Hydraulischer Modellversuch zum Projekt „Talsperre Malter – Erweiterung der Hochwasserentlastungsanlage". Unpublished project final report. University of Siegen, Germany, 6th July 2015.

Jirka, G. H., and Lang, C. (2009). Einführung in die Gerinnehydraulik. 2nd Edition, Universitätsverlag Karlsruhe, Karlsruhe, Germany, 2009.

Kobus, H. (1980). Hydraulic modelling. Bulletin / DVWK 7, Paul Parey Verlag, Hamburg, Germany, 1980.

Schmidt, J., Wieland, J., Jensen, J., Findeisen, B., and Haufe, H. (2015a). "Hydraulischer Modellversuch Talsperre Malter – Herausforderungen infolge von schießendem Abfluss in gekrümmten Bauteilen." *Proc., 38. Dresdner Wasserbaukolloquium „Messen und Überwachen im Wasserbau und am Gewässer"*, Dresdner Wasserbauliche Mitteilungen, Issue 53, Dresden, Germany, 109–118.

Schmidt, J., Wieland, J., and Jensen, J. (2015b). "Hydraulischer Modellversuch Talsperre Malter – Optimierung eines Teilungsbauwerkes mit vertikaler Strömungstrennung." *Proc., 17. JuWi-Treffen*, Dresdner Wasserbauliche Mitteilungen, Issue 57, Dresden, Germany, 25–32.

Unsteady-Flow Modeling for Emergency Shutdown of the CAP Canal

Bert Clemmens[1], Brian Wahlin[1] , Marcus Shapiro[2] and Patrick Dent[2]
[1]WEST Consultants, Inc.
Tempe, AZ 85284
USA
[2]Central Arizona Water Conservancy District
Phoenix, AZ 85024
USA
E-mail: bwhalin@westconsultants.com

ABSTRACT

The Central Arizona Project (CAP) is designed to bring about 1.9 ML of Colorado River water per year to Maricopa, Pima, and Pinal counties in Arizona. CAP carries water from the Colorado River at Lake Havasu to Tucson. The CAP canal system is a 540 km long system of conveyance system aqueducts, tunnels, pumping plants, pipelines, and a large reservoir (just north of Phoenix, AZ). Water is pumped uphill from the Colorado River. This study was conducted for the Hayden-Rhodes Aqueduct of the Central Arizona Project (CAP), which starts at the afterbay of the Bouse Hill Pumping Plant and extends to the forebay of the Salt-Gila Pumping Plant, which is just south of the Salt River, east of Phoenix. Additional pumping plants downstream lift water uphill to Tucson. The canal between adjacent pumping plants defines a canal segment. A sloping lined canal with check structures carries water between power plants. The canal between adjacent check structures defines a canal pool. The Pumping Plants use electric motors to power the pumps. Power outages could cause the canal to overtop at the forebay of these power plants, since the flow in the canal would not stop with a power outage. The check structures in between the power plants can be closed with battery-operated electric motors. This was intended to contain water within each canal pool if power is lost. Stopping the pumping plants and closing the check gates causes surge waves in the canal. Some additional freeboard at the downstream end of each canal pool was provided to contain these surge waves. Increases in frictional resistance in the canal have reduced the available canal freeboard from design conditions. This study evaluated the available freeboard in the canal during steady conditions and during unsteady conditions associated with a power outage. HEC-RAS was used to determine water surface elevations and available freeboard under both steady and unsteady conditions.

Keywords: Irrigation systems, canal and diversion structures, canal management, operator training

1. INTRODUCTION

1.1. The Central Arizona Project

The Central Arizona Project (CAP) is Arizona's largest renewable water supply and was constructed to help the state conserve its groundwater by importing surface water from the Colorado River. CAP was designed to deliver an average of 1.9 ML of water per year to residents of Maricopa, Pima, and Pinal counties (see Figure 1), making it a critical economic lynchpin for the region. CAP delivers untreated water to three major types of customers: municipal and industrial, agricultural, and Native American users. The customers are then responsible for their own water treatment. The CAP canal travels 540 km across the state of Arizona. The canal begins at Lake Havasu, continues through the Phoenix metropolitan area, and ends in Tucson. CAP consists of 14 pumping plants, 1 pump/generating plant, 10 siphons, 3 tunnels, and more than 45 turnouts for customer deliveries. During its travels across the state of Arizona, water is pumped more than 850 vertical meters and flows through the canal via gravity following the natural contours of the land. Construction of the system began in 1973 and was substantially complete in 1993. The CAP Canal System is operated by the Central Arizona Water Conservancy District (CAWCD).
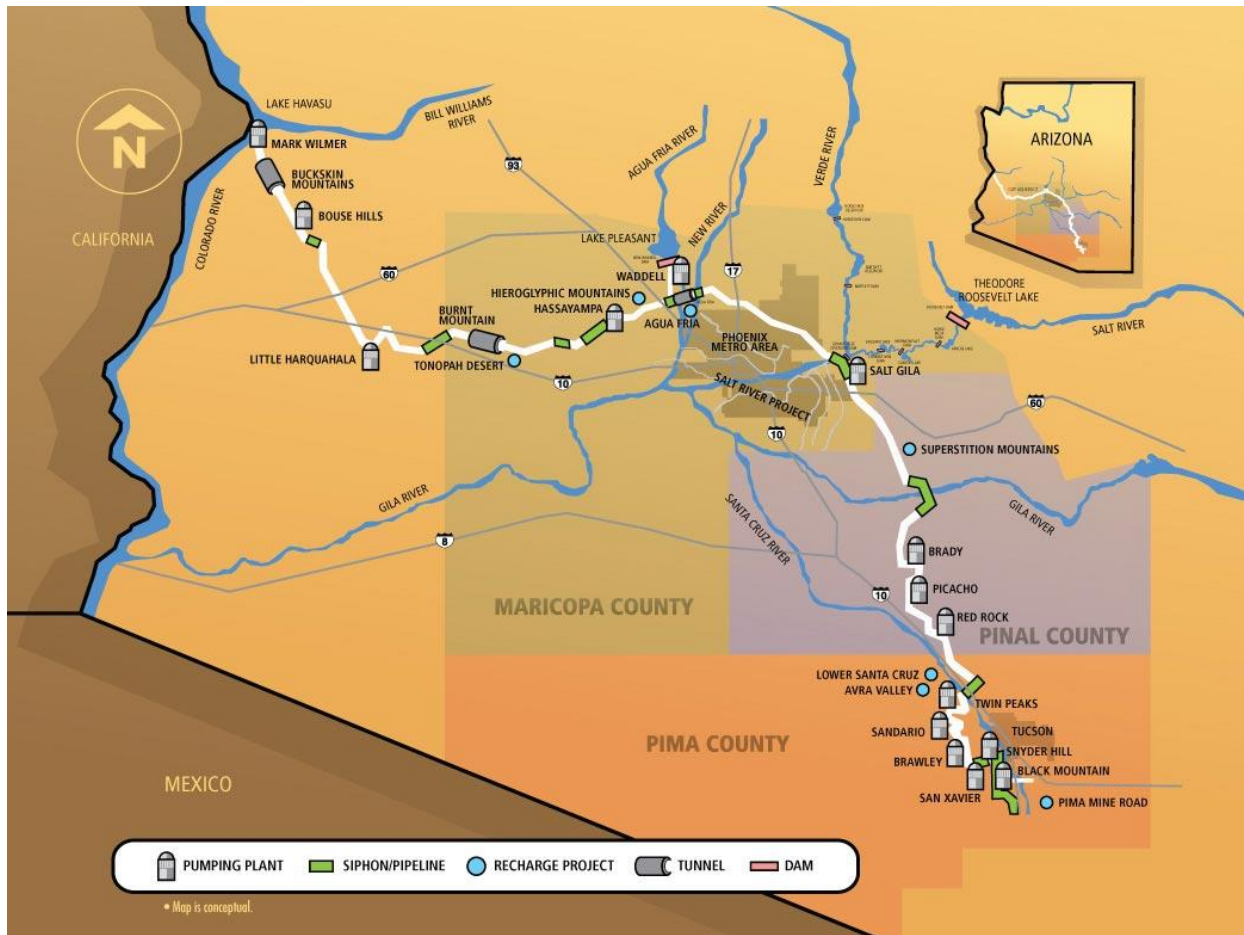
Figure 1. Schematic diagram of the CAP canal system

1.2. The Hayden-Rhodes Aqueduct

The Hayden-Rhodes Aqueduct portion of the CAP starts at the afterbay of the Bouse Hill Pumping Plant and extends to the forebay of the Salt-Gila Pumping Plant, which is just south of the Salt River, east of Phoenix. The aqueduct has two additional pumping plants, the Little Harquahala Pumping Plant and the Hassayampa Pumping Plant. These two pumping plants lift the water roughly 60 m vertically. Additional pumping plants downstream lift water uphill to Tucson. The canal between adjacent pumping plants defines a canal segment. A sloping lined canal with check structures carries water between power plants. The aqueduct has 7 inverted siphons under river beds and 2 tunnels. The profile of the canal invert is shown in Figure 2, along with labels for the pumping plants and major siphons.

- Segment 1 is the canal between the Bouse Hill Pumping Plant and the Little Harquahala Pumping Plant.
- Segment 2 is the canal between the Little Harquahala Pumping Plant and the Hassayampa Pumping Plant.
- Segment 3 is the canal between the Hassayampa Pumping Plant and the Salt-Gila Pumping Plant.

Segment 1 includes four check structures, CS-01 to CS-04. The canal between adjacent check structures or between a check structure and a pumping plant defines a canal pool. Thus Segment 1 has 5 pools. Segment 2 has 9 check structures, CS-05 to CS-13, and 10 pools. Segment 3 has 12 check structures, CS-14 to CS-25, and 13 pools. The pumping plants use electric motors to power the pumps. Power outages could cause the canal to overtop at the forebay of these power plants since the flow in the canal would not stop with a power outage. The check structures in between the power plants can be closed with battery-operated electric motors. This was intended to contain water

within each canal pool. Stopping the pumping plants and closing the check gates causes surge waves in the canal. Some additional freeboard at the downstream end of each canal pool was provided to contain these surge waves. Increases in frictional resistance in the canal have reduced the available canal freeboard from design conditions and might cause canal and/or check gate overtopping during power outages. These check gates were designed to overtop in an emergency.

The Hayden-Rhodes Aqueduct also includes the Waddell Canal, which connects Waddell Dam to Segment 3 between the Agua Fria Siphon and the New River siphon. The canal from Waddell Dam to the Salt-Gila Pumping Plant was called Segment 3M. Unsteady hydraulic simulation results for Segment 3M and the Waddell Canal are not discussed in this paper. The section of Segment 3 upstream of the Waddell Canal is called Segment 3 upper, and the section of Segment 3 downstream of the Waddell Canal is called Segment 3 lower.

Separate HEC-RAS (2010) models were developed for each Segment. In some cases, additional cross sections were added for the unsteady portion of the model to increase model stability. This effectively resulted in separate models for steady and unsteady flow.
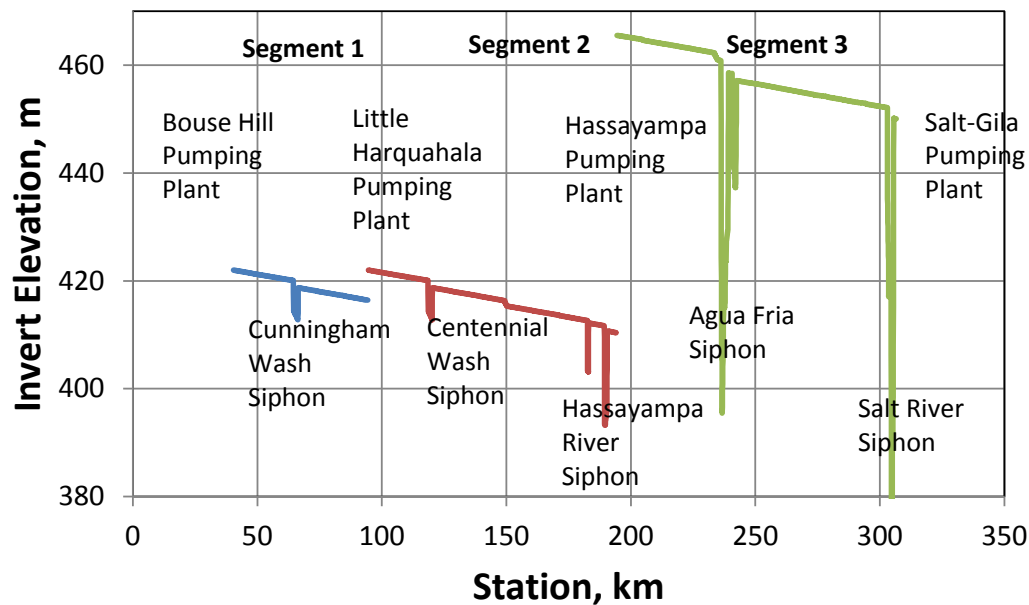
Figure 2. Profile of the Hayden-Rhodes Aqueduct.

2. STEADY-STATE WATER SURFACE PROFILES

The design capacity of the Hayden-Rhodes Aqueduct was 935 m^3/s. The canal was designed so that the water was at normal depth at all locations when flow was at capacity; there is no backwater from the check gates. In fact, at high flows, operators often take the check gates out of the water. The design water depth was 5.0 m, for a design Manning n value of 0.016. The design freeboard was approximately 0.67 m, for a lining height of roughly 5.67 m. This lining height was increased to 5.94 m just upstream from check gates to contain surge waves, which are discussed in the section on emergency shutdown. (Note that these dimensions varied for a few canal pools.) As-built construction drawings were available, from which the cross sections and structure details were developed for HEC-RAS. In addition to this information, development of steady state profiles with HEC-RAS requires knowledge of Manning n values for the canal sections, Manning n values for the inverted siphons, and calibration of the check structure gates. Steady state profiles were developed for 935 m^3/s, 966 m^3/s, 997 m^3/s, and 1028 m^3/s.

2.1. Canal Manning n Values

The discharges at the pumping plants are measured in the outlet pipes with multipath ultrasonic meters. Under steady conditions, it is possible to approximate the discharge in each canal pool, from which estimates of Manning n can be determined. CAWCD staff had compiled many years' worth of data from which they estimated Manning n values for each canal pool. These estimates were provided as input to this study. For pools 1 through 6, the Manning n value was set to 0.018. Manning n values for pools 7 through 18 and the Waddell Canal were 0.0175. Manning n values for pool 19 through the Salt-Gila Pumping Plant were set to 0.017. Note that these are above the design value of 0.016.

2.2. Siphon Manning n Values

Siphons and tunnels were modeled in HEC-RAS as channels with lidded cross sections. Preissman slots were added to the top of these cross sections to account for water pressure above the top of the siphon or tunnel. These models were calibrated at 935 m^3/s as follows: Manning n values for siphons and tunnels were determined through trial and error with both the steady and unsteady HEC-RAS models to match the head losses provided by CAWCD at 935 m^3/s. The resulting Manning n values are given in Table 1. Minor differences in Manning n values were found for the steady and unsteady models.

Table 1. Manning n values for siphons and tunnels at 935 m^3/s.

Site	Measured Head Loss (m)	Manning n values from CAWCD	Manning n values from calibrated steady flow	Manning n values from calibrated unsteady flow
Cunningham Wash	1.07	0.0159	0.0159	0.0159
Centennial Wash	1.29	0.0145	0.0137	0.0141
Burnt Mt Tunnel	0.63	0.0130	0.0124	0.0122
Jackrabbit Wash	0.47	0.0179	0.0169	0.0162
Hassayampa River	0.84	0.0149	0.0143	0.0141
Agua Fria Tunnel	0.85	0.0130	0.0119	0.0117
Agua Fria River	1.98	0.0141	0.0135	0.0134
New River	1.15	0.0139	0.0135	0.0127
Salt River	1.74	0.0134	0.0135	0.0134
Waddell Siphon	0.60	0.0161	0.0149	0.0150

2.3. Check Structure Calibrations

CAWCD staff had developed relationships for each check structure gate with discharge over gate openings plotted against the difference in the upstream and downstream depths. This function sometimes had positive discharge even when the depth difference was negative. The upstream and downstream depths had not been reconciled to express elevation difference, so the functions developed did not match physical conditions. These relationships were useful for gate operations, but attempts to use them in HEC-RAS were not successful. WEST and CAWCD agreed on the following method to determine gate openings and gate calibrations:

- The standard HEC-RAS equations for gates were used to compute discharge in the model. The submerged discharge coefficient was set to 1.0.
- For gates without siphons or tunnels, the gate opening was adjusted to provide a drop in water surface elevation of roughly 0.046 m. (In most cases, this was approximately the same as the drop in energy head).
- For gates with siphons or tunnels, the gate opening was adjusted to provide a minimum drop in energy head of roughly 0.037 m. For lower flows, meeting the target water level resulted in much higher energy differences. At high flow, the change in energy head was often the governing criteria.

2.4. Steady-State Profile Results

With the above Manning n values and gate calibrations, gate openings were determined by trial and error. The depth upstream from the checks with a siphon was the maximum of normal depth or 5.33 m, with a head loss greater than 0.037 m. The depth upstream from other checks was based on the elevation drop of roughly 0.046 m. These criteria were sufficient to determine water surface profiles. Water surface profiles were generated for 935 m³/s, 966 m³/s, 997 m³/s, and 1,028 m³/s. Figure 3. shows the steady-state profile for segment 3 at the design discharge of 935 m³/s. The increase in lining height just upstream from check structures can be seen as a stair-step in the lining. Additional lining increases can be seen between CS-22 and CS-24, where the lining was increased due to subsidence.
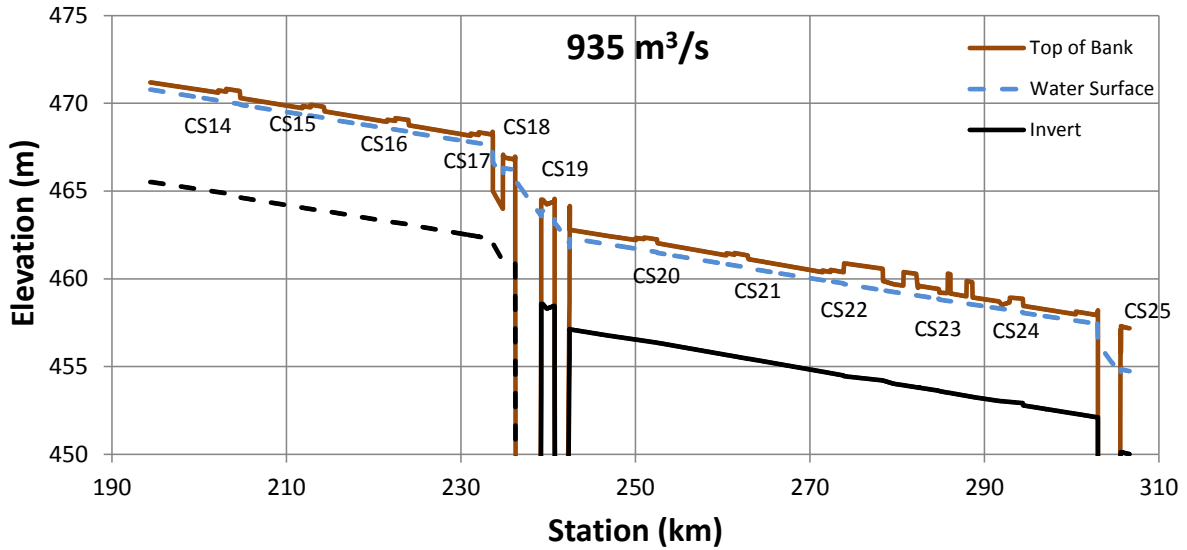
Figure 3. Steady-state profile for Segment 3 at design discharge of 935 m³/s.

Figure 4 shows the freeboard for Segment 3 at design discharge. One location below the allowable freeboard of 0.304 m can be seen just upstream from CS-24. This is likely an area of subsidence.
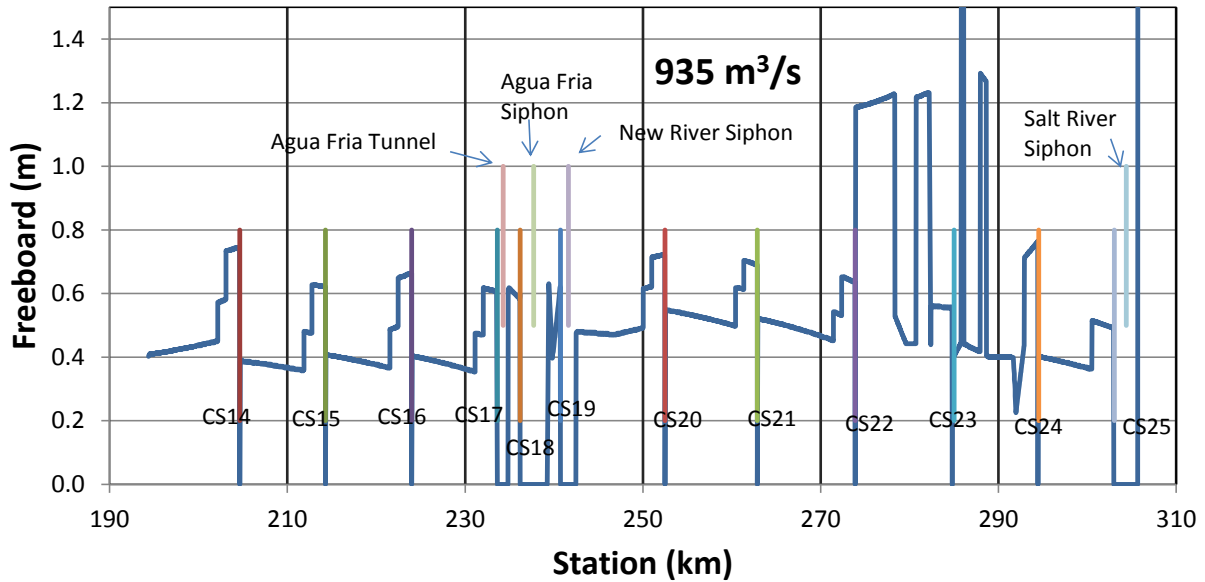
Figure 4. Freeboard for Segment 3 at design discharge.

2.5. Steady State Freeboard Results

Operational freeboard was defined by CAWCD as 0.305 m. The freeboard under steady flow was used to determine capacity. For some segments, the minimum freeboard was essentially equal to the required freeboard at one of the modelled discharges. In one case, the capacity could be determined from the Manning n value. In other cases, it was below 935 m^3/s, and capacity could only be determined by trial and error. This was not deemed necessary for this study. The distance over which the canal did not meet operational freeboard for the specified discharge was also determined for each canal segment. These results are given in Table 2. The lining deficiency often went from zero to a few centimeters.

Table 2. Length of canal (km) where lining needs to be increased to meet operational freeboard.

Canal	@ 935 m^3/s (km)	@ 966 m^3/s (km)	@ 997 m^3/s (km)	@ 1028 m^3/s (km)	Capacity (m^3/s)
Segment 1	6.1	24.0	40.1	43.8	916
Segment 2	0.0	17.2	50.9	75.3	935
Segment 3 upper	0.0	0.0	22.0	31.5	966
Segment 3 lower	0.5	0.6	1.3	48.0	< 935
Waddell Canal	0.8	1.6	4.0	6.3	< 935
Total	7.4	43.5	118.3	204.9	

At 1028 m^3/s, the water surface is above the canal lining at CS-01 in Segment 1 and CS-05 and CS-06 in Segment 2 (negative freeboard).

402

3. EMERGENCY SHUTDOWN

With the unsteady-flow HEC-RAS models, pump discharge at the upstream and downstream end of these canal segments was stopped for one minute, and gates were closed over a 10-minute period to simulate an emergency shutdown. The reduction of inflow and outflow in each canal pool caused a surge in the water levels of the pool and reflection waves that traveled both upstream and downstream. As discussed earlier, the lining height at the check structures was increased (to 5.94 m at most pools to accommodate the maximum water height from this surge wave. With higher resistance (Manning n and larger flow, it was expected that the water would exceed the lining height during these surges. The design elevation of the top of the road was 0.67 m above the top of the lining. In many pools, this was the top of the embankment that contained water in the canal. The hope was that the water surface elevation during surges would be contained within the canal and not spill. The current elevations of these roads/embankments were not surveyed, so these results rely on the design intent.

Each check structure contains two check gates. The height of the check gates is 5.94 m, the nominal height of the lining for most canal pools at the check gate. Thus, if the surge wave exceeded the lining height, it was usually higher than the check gate height, resulting in flow over the check gates. This could be a concern since water might accumulate in the most downstream pool of a segment. Fortunately, the lining height at the forebay to pump stations was 6.55 m. With the gates closed, the lined canal section is supposed to contain the water within each pool. The water depths for each pool were examined 16 hrs after shutdown to see if this occurred.

3.1. Surge Wave Heights

In general, the maximum water surface elevation was at the downstream end of each canal pool, at the gate forebay. By design, the lining at the downstream end of each pool was increased to accommodate this surge. These increases in lining height generally matched the surge height fairly well. However, the highest water surface elevation relative to the top of lining elevation was generally upstream at one of the transitions in lining height. Usually the highest water surface elevation relative to the top of lining elevation was where the increase in lining height first started. In a few cases, it was where the second stair-step in lining height occurred.

At the design discharge of 935 m^3/s, the maximum water surface elevation exceeded the lining height at the downstream end of all pools even though additional lining height had been provided to accommodate these surges during original construction. This is caused by operational water depths that are greater than the design values, mostly resulting from Manning n values that are greater than the design value. These short-duration surge waves that exceed the top of the lining are not a concern, since the velocity is mostly vertical and does not appear to cause scour. The maximum water surface elevations from emergency shut down at 935 m^3/s in Segment 1 are shown in Figure 5.
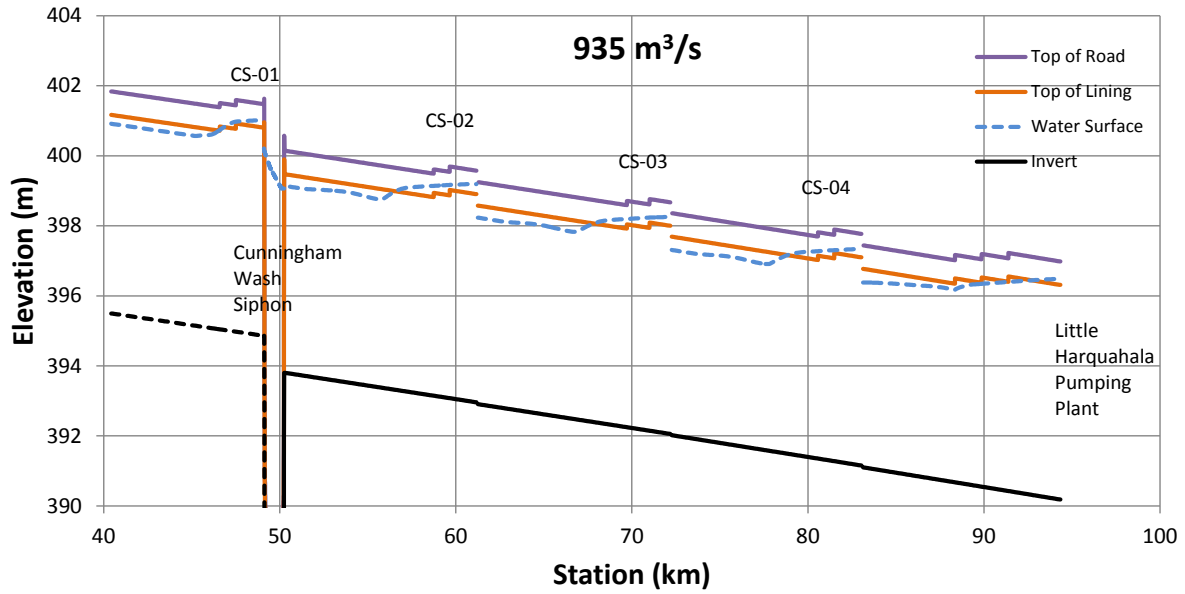
Figure 5. Maximum water surface elevation resulting from emergency shut down in Segment 1 at 935 m³/s.

Up to 997 m³/s, the maximum water surface elevation did not exceed the top of the road in any cases. At 1,028 m³/s, the top of the road was exceeded at Segment 2, CS-06. The depth was within 0.02 m of the top of road at CS-01, CS-05, and CS-11. Thus, increasing the discharge above the design discharge has the potential for aqueduct overtopping during an emergency shut down. The maximum water surface elevations from emergency shut down in Segment 1 are shown in Figure 6. At the scale of these figures, it is hard to determine how close the water level is to the top of the road.

3.2. Ability to Contain Pool Volume

For design conditions with an initial flow of 935 m³/s, some flow did pass over the gates during the surge waves from emergency shutdown, but the water after 16 hrs was below the top of all the gates in all the segments and below the top of the lining. The water surface profile 16 hours after shut down for Segment 2 is shown in Figure 7. Note that the water surfaces are below the top of lining, and thus below the top of the check gates. In this case, no significant oscillations remain in the water surface.
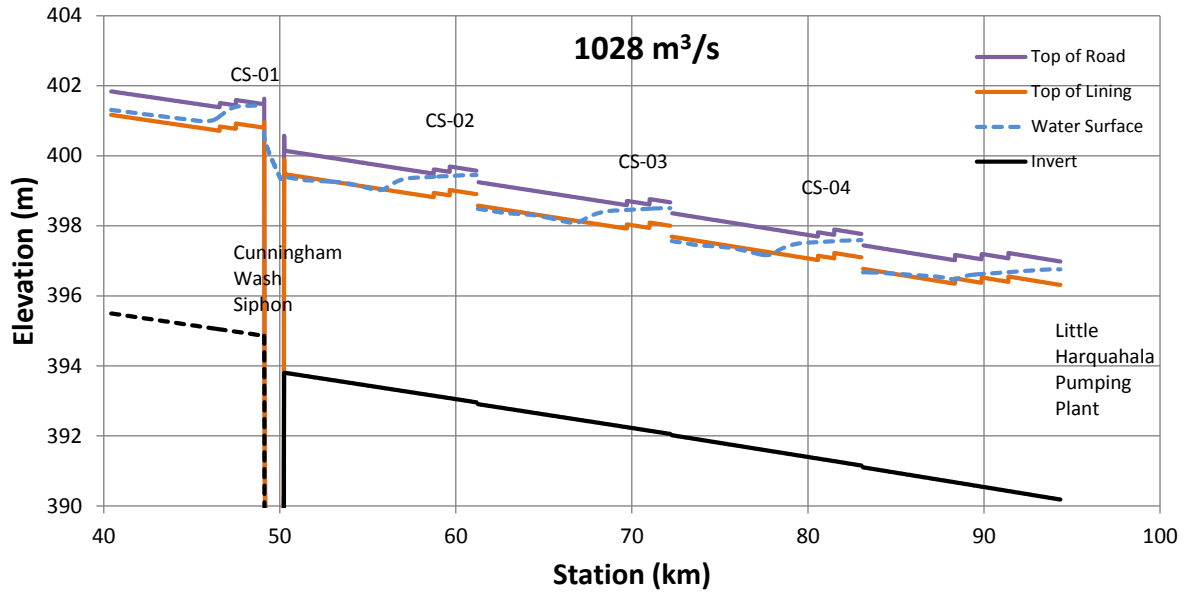
Figure 6. Maximum water surface elevation resulting from emergency shut down in Segment 1 at 1,028 m^3/s.
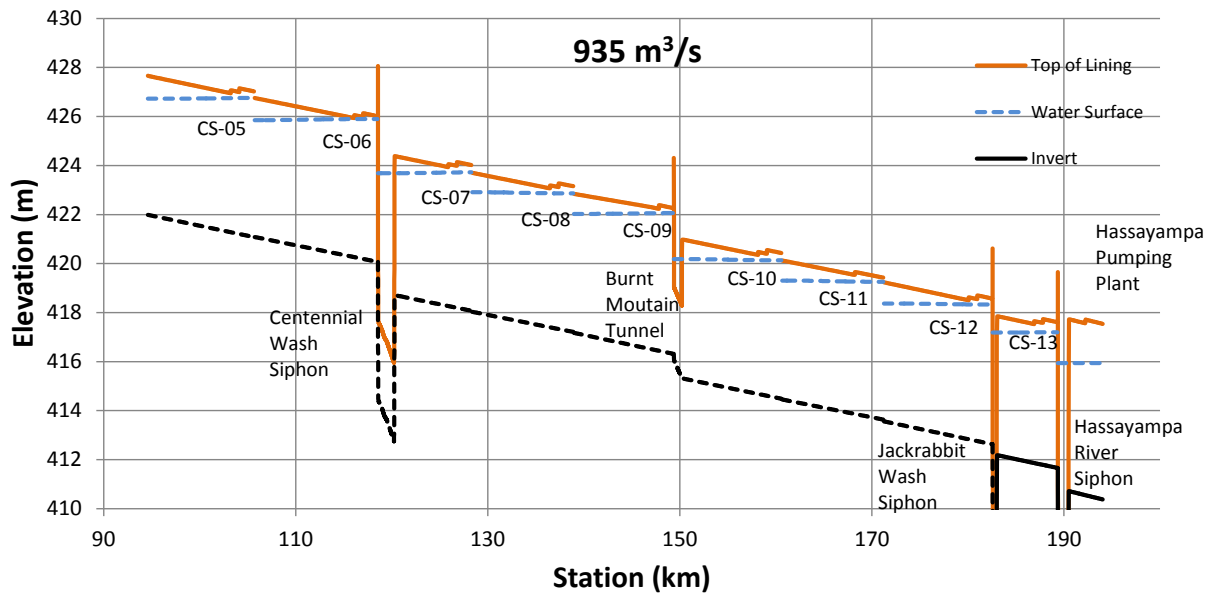
Figure 7. Water surface profile in Segment 2 after emergency shutdown from 935 m^3/s.

At 1,028 m^3/s, the depth at 16 hrs exceeded the top of the radial gates at three checks in Segment 1, 3 checks in Segment 2, and 0 checks in Segment 3. The hydrograph for flow over the gates at 1,028 m^3/s shows water cycling over about a 12 hr period as the water depth in the pool continues to cycle, as shown in Figure 8 for Segment 2. For most gates, the flow dropped to zero as the waves were on the low side at the gate. Two check gates showed flow over the gates continuously. Some pools had lining heights that were lower than the top of the gates. The water depth was above the lining height but below the top of the gates at 16 hrs in 1 pool each for Segments 1 and 2 (these were just upstream from the pumping plants) and for 3 pools in Segment 3. Water depths exceeding the lining height for extended time periods are a concern since this could lead to embankment failure and spill.
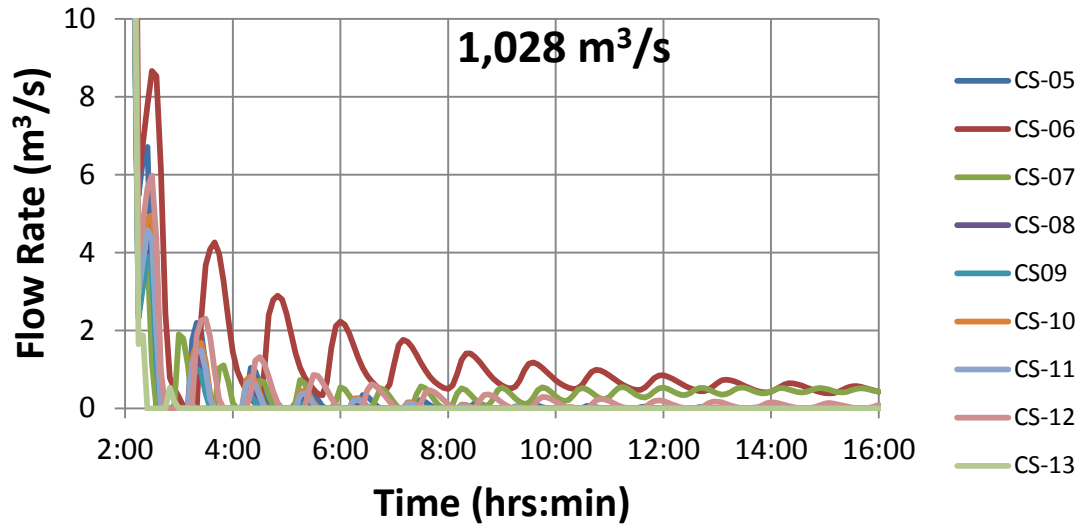
Figure 8. Flow over the top of check gates as the result of shut down from 1,028 m³/s for segment 2.

4. SUMMARY

The HEC-RAS models were able to determine steady state profiles, available capacity, and available freeboard for the Hayden-Rhodes Aqueduct. The discharge capacity of the aqueduct was sufficiently close to the design discharge, such that the design discharge could be provided with only modest reductions in freeboard. These estimates are highly influenced by frictional resistance and highlight the need for CAWCD to be diligent in keeping frictional resistance on the canal walls within acceptable values. Additional lining is needed in a few key locations, but increasing the lining height by a decimeter or less over many kilometres is impractical.

With flow at the design discharge of 935 m³/s, the Hayden-Rhodes Aqueduct has slightly less than 0.305 m (1 ft) of freeboard. At 110% of the design capacity (1028 m³/s), water will overtop the canal lining in Segments 1 and 2. This highlights the importance of maintaining the canal walls to reduce friction.

During emergency shutdown from the design discharge of 935 m³/s, the maximum water surface elevation exceeds the canal lining within all canal pools. At 110% of the design discharge, the maximum water surface elevation overtop the canal roadway at several locations during emergency shutdown. Further analysis would have to be done to determine if these water surface elevations would cause canal embankment overtopping and spill.

During emergency shutdown from the design discharge of 935 m³/s, the canal water volume is contained within each canal pool even though some water spills temporarily over some check gates. At 110% of the design discharge, the canal water volume continues to flow downstream over check gates and possibly over the canal embankment. It is unclear whether or not the canal volume is contained within the canal if an emergency shut down occurs at this discharge.

5. REFERENCES

HEC-RAS (2010). HEC-RAS River Analysis System Version 4.1. Hydrologic Engineering Center, US Army Corps of Engineers, Davis, CA

Hydraulics of Submerged Offset-jets

G. Ravi Kishore[1] and Subhasish Dey[1]
[1]Department of Civil Engineering, E-mail: kisore20105@gmail.com; sdey@iitkgp.ac.in
Indian Institute of Technology
Kharagpur 721302, West Bengal
India
E-mail: kisore20105@gmail.com

ABSTRACT

This study presents an experimental investigation of hydraulic characteristics of submerged offset jets. The instantaneous velocity was captured by an acoustic Doppler velocimeter (ADV). A total of 20 runs were carried out by varying different parameters: Reynolds number (28475–80730), offset ratio (3.16–6.2), jet Froude number (1.9–3), submergence parameter (0.65–2.82) and sluice gate openings (3, 3.5, 4, 4.5 and 5 cm). It is observed that the length of the reattachment depends on the relative offset height and the tail water depth. A mathematical formulation is developed for the submerged offset jet assuming a submerged jump in a drop structure to find the back-up depth and subcritical sequent depth by applying the momentum and continuity equations at the inlet and at tail water depth respectively. A mathematical equation is also developed for the back-up depth at the efflux section, which is experimentally verified for the range of supercritical Froude numbers from 1.1 to 10 and submergence factor. The jet trajectories (lower layer of jet, upper layer of jet and maximum jet velocity layer) are also derived applying the boundary conditions. The computed jet trajectories of the submerged offset jet show a satisfactory agreement with the experimental data.

Keywords: offset jet, coanda effect, rough bed, recirculation region, open channel flow, boundary layer.

1. INTRODUCTION

The topic of submerged wall jets has been the focus of many investigators due to their engineering application in energy dissipation downstream of hydraulic structures including drop structures, spillways, barrages and weirs. The submerged jumps can be considered as a transitional phenomenon between wall jets and free jumps. A submerged offset jet is formed when a fluid jet is issued from an elevated opening. This high-velocity jet over an abrupt drop creates a complex flow pattern following reattachment to a solid boundary and, hence, is called a reattaching offset jet (ROJ). The flow consists of a deflecting free jet and the evolving wall jet past reattachment. Figure 1 shows the flow pattern in a reattached offset jet.

An offset jet is formed when a jet discharges into a medium above a wall that is parallel to the axis of the jet but offset by a certain height. The flow field of an offset jet is complex and is encountered in many engineering applications. As the fluid jet is issued from an elevated opening, it is deflected towards the solid boundary due to the reduced pressure from the bottom of the jet. This phenomenon is known as Coanda effect (Rajaratnam and Subramanya 1968; Miozzi et al 2010), and the reattaching offset jet is known as a Coanda jet after the Romanian aerodynamicist Henri Marie Coanda (1886–1972). The flow velocity reduces as the jet approaches the boundary, and, as a consequence, the pressure inside the jet increases.

The reattaching offset jet encloses a zone where a reverse eddy is formed. Upon reattaching, the jet behaves like an impinging jet, which results in the formation of pressure greater than hydrostatic pressure, with the maximum value at the impinging point. This provides the pressure gradient to accelerate the flow. As the impinging zone ends, the acceleration ceases establishing a turbulent wall jet condition. The thickness of the wall jet region increases due to the presence of solid boundary and turbulent diffusion. Surface rollers or large reverse flow regions are formed near the free surface, which is influenced by the tailwater depth conditions. Further downstream, the flow recovers the normal subcritical open channel flow.

2. THEORY OF SUBMERGED OFFSET JET

When a fluid jet is issued from an elevated opening, an offset jet is formed. The flow consists of a deflecting free jet and a submerged wall jet after reattachment to the solid boundary. The flow zones in a submerged offset jet are depicted in figure 1. The flow in the region below the maximum velocity point, characterized by a boundary layer
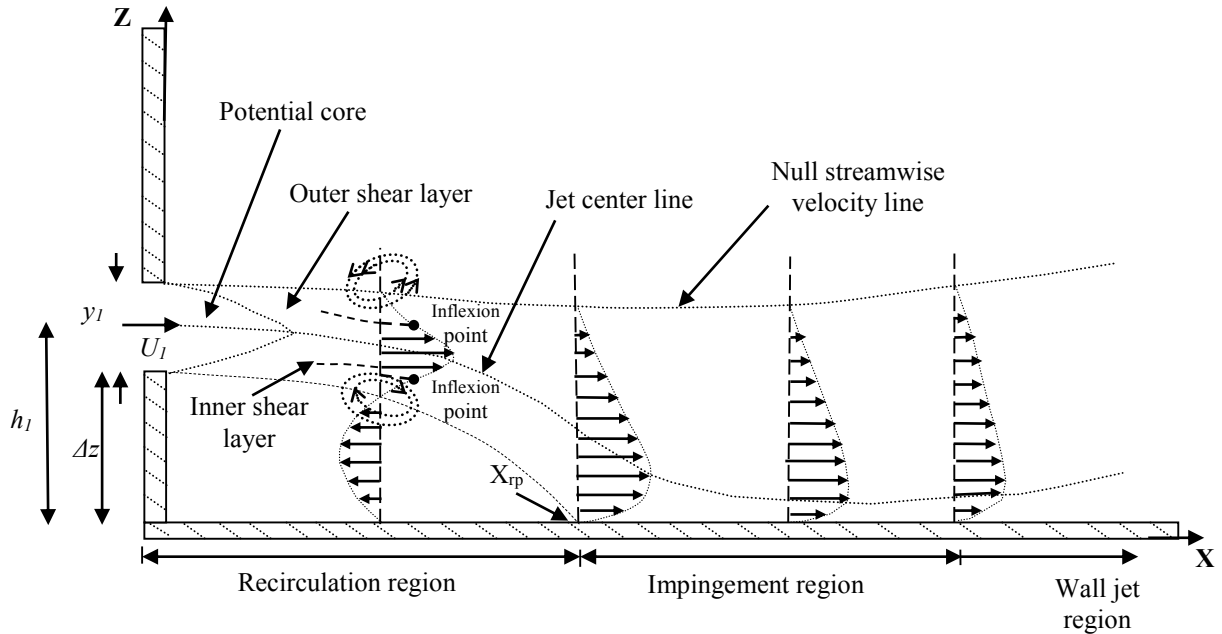
Figure 1. Schematic diagram of flow zones in submerged offset jet and its coordinate system.

Flow, is called inner layer of shear flow. The problem of an offset jet interacting with an adjacent parallel boundary has been previously described along with the important flow parameters that must be considered. This particular problem is relatively new, the first reported study being that of Bourque and Newman (1960). Since then, several investigators attempted to study various aspects of the problem. Earlier work by Rajaratnam (1967) identified the effects of wall jets in a water channel. Bourque and Newman (1960) studied the effects of Reynolds number and offset ratio on the reattachment length and distribution of the wall static pressure in the recirculation region. They considered the offset ratios in the range 4−48.5 and Reynolds number in the range 2760−7750. The flow field solution of an offset jet in the presence of a free stream motion is provided by Hoch and Jiji (1981). They considered offset ratios in the range 3−8.7 and Reynolds number of 16,000. Pelfrey and Liburdy (1986) reported the mean flow characteristics for the offset ratio 7 and the Reynolds number 15,000 using Laser Doppler Anemometry (LDA). Later on, Holland and Liburdy (1990) experimentally investigated the thermal characteristics of the heated offset jet over adiabatic impingement surface. They considered the flow geometry similar to that of Pelfrey and Liburdy (1986) and three offset ratios viz. 3, 7 and 11. Yoon et al. (1995) investigated the flow characteristics of a two dimensional offset jet (offset ratio viz. 5) discharged parallel to a rough wall and the distributions of the mean velocity, and turbulent stresses in the flow field were obtained and compared with those of the wall attaching offset jet on a smooth wall. It has been observed that the reattachment region on the rough wall is longer than on the smooth wall for the same offset height and jet speed. Nasr and Lai (1997) studied the mean velocities and turbulence characteristics of a turbulent plane offset jet with a small offset ratio of 2.125 using LDA. The LDA results were used to examine the capability of three different turbulence models in predicting the velocity field of the jet. Dey and Sarkar (2008) investigated the conditions of submerged jumps having different submergence factors and jet Froude numbers over different rough beds. It was found that the rate of decay of jet velocity in a submerged jump increases with increase in bed roughness, the most important observation being the flow in fully developed zone is self-preserving in general. Dey et al. (2010) compared the flow field in the fully rough and smooth submerged wall jets and observed that the rate of decay of jet-velocity on fully rough walls is greater than that on smooth wall, but it is less than that on transitionally rough walls due to the presence of roughness sub-layer on the fully rough walls. Bhuiyan et al. (2011) studied the characteristics of reattached offset jets on rough beds under the influence of limited

tailwater depth. The influence of roughness on reattached offset jets was found to be less than that in submerged wall jets on a similar rough bed. Agelin-Chaab and Tachie (2011) experimentally investigated the three-dimensional offset jet using a particle image velocimetry technique. They have performed experiments for four different offset ratios viz. 0.5, 1.0, 2.0 and 4.0, and three nozzle exit Reynolds numbers of 5,000, 10,000 and 20,000. The reattachment lengths are independent of Reynolds number but increase with offset height.

3. EXPERIMENTAL SETUP AND PROCEDURE

The experiments presented in this paper were performed in the Hydraulic and Water Resources Engineering laboratory, Department of Civil Engineering, Indian Institute of Technology Kharagpur, India.
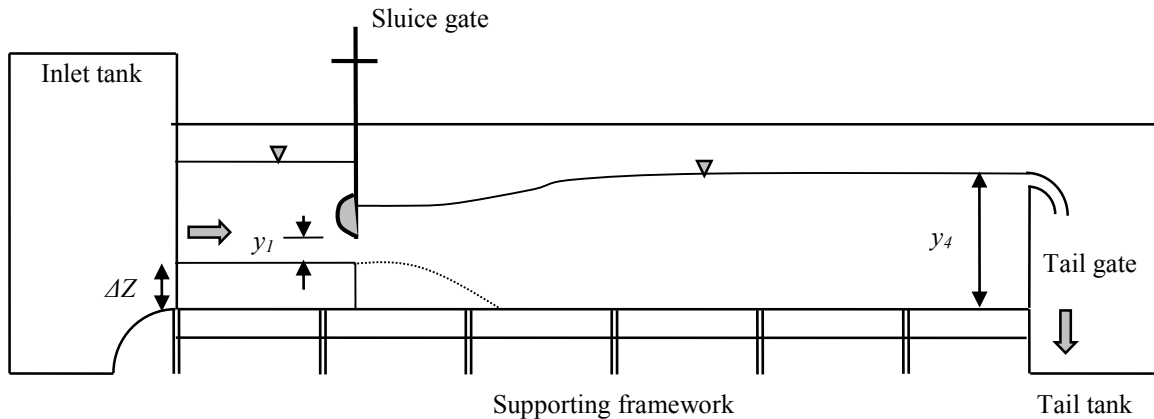
Figure 2. Schematic view of the experimental setup

Experiments were carried out in an open channel flume. Submerged offset jets were tested on a horizontal rigid rough bed. Figure 2 shows a schematic view of the experimental setup to study the hydraulic characteristics of submerged offset jets over rough bed. The flume was 0.6m wide, 0.71m deep, and 12m long. The sidewalls of the flume were made of transparent glass to facilitate optical access. A Perspex vertical sluice gate, which had a streamlined lip to produce a supercritical stream with a thickness equal to the gate opening, was fitted over the bed. Different sluice gate openings y_1 (= 3.0, 3.5, 4.0, 4.5 and 5 cm) were achieved by adjusting the gate vertically. The water discharge at the inlet, controlled by an inlet valve, was measured by a calibrated V-notch weir. An adjustable tailgate downstream of the flume controlled the tailwater depth y_4. The free-surface profile was measured by a point gauge. Table 1 furnishes the important experimental parameters of different runs for various combinations of jet Froude number F_1 (= $U_1/(gy_1)^{0.5}$) where, U_1 is the jet velocity, Reynolds number R (=U_1y_1/V), where V is the coefficient of kinematic viscosity and g acceleration due to gravity.

Velocity profiles were measured by a 4-beam down-looking Acoustic Doppler Velocimeter (ADV), named *Vectrino,* used to capture the instantaneous velocity components, which had a sampling rate and volume of 100 Hz and 0.09 cm^3, respectively. The sampling duration was 4 min in order to have a statistically time-independent average velocity. Near the bed, the sampling durations were relatively long. The closest vertical spacing of the ADV measurements was 0.25 cm. The ADV measurements were taken in the central vertical plane (CVP), which is along the centerline of the flume in vertical lines at different streamwise distances from the sluice gate.

4. TIME-AVERAGED FLOW FIELD

Figure 3 schematically illustrates the different flow zones in a submerged offset jet. The time-averaged velocity components in (x, z) are represented by (u, v). The origin of the coordinate axes is located at the junction of the sluice gate and the horizontal wall. Here, x and z are the horizontal and vertical distances, respectively. The flow characteristics are plotted on a nondimensional $\hat{x}\ \hat{z}$ -plane, where $\hat{x}$ is x/y_1 and $\hat{z}$ is z/y_1. Velocity measurements

help to understand the flow field. Vertical profiles of horizontal velocities were measured at selected sections of the channel, covering pre-attached and attached part of and up to the section where the reversed velocity occurs. The jet is observed to curve down slowly through the first half of the recirculation region and then sharply downward to the attachment point. Jet velocity starts to recover slightly in the impingement region, and after attachment, the decay of maximum velocity with distance follows the same pattern as that of a wall jet.

Table 1. Experimental parameters

Run. no	y_1 (m)	U_1 (m/s)	y_4 (m)	ΔZ (m)	F_1	R	OFFSET RATIO (OR) (h_1/y_1)
1	0.025	1.139	0.540	0.10	2.3	28475	4.50
2	0.030	1.356	0.540	0.12	2.5	40680	4.50
3	0.045	1.328	0.555	0.12	2.0	59798	3.16
4	0.050	1.400	0.550	0.14	2.0	70000	3.30
5	0.040	1.566	0.495	0.15	2.5	62640	4.25
6	0.045	1.528	0.515	0.15	2.3	68767	3.83
7	0.030	1.627	0.495	0.16	3.0	48810	5.83
8	0.040	1.190	0.485	0.18	1.9	47600	5.00
9	0.035	1.758	0.480	0.20	3.0	61525	6.20
10	0.045	1.794	0.480	0.20	2.7	80730	4.90

(a)

(b)
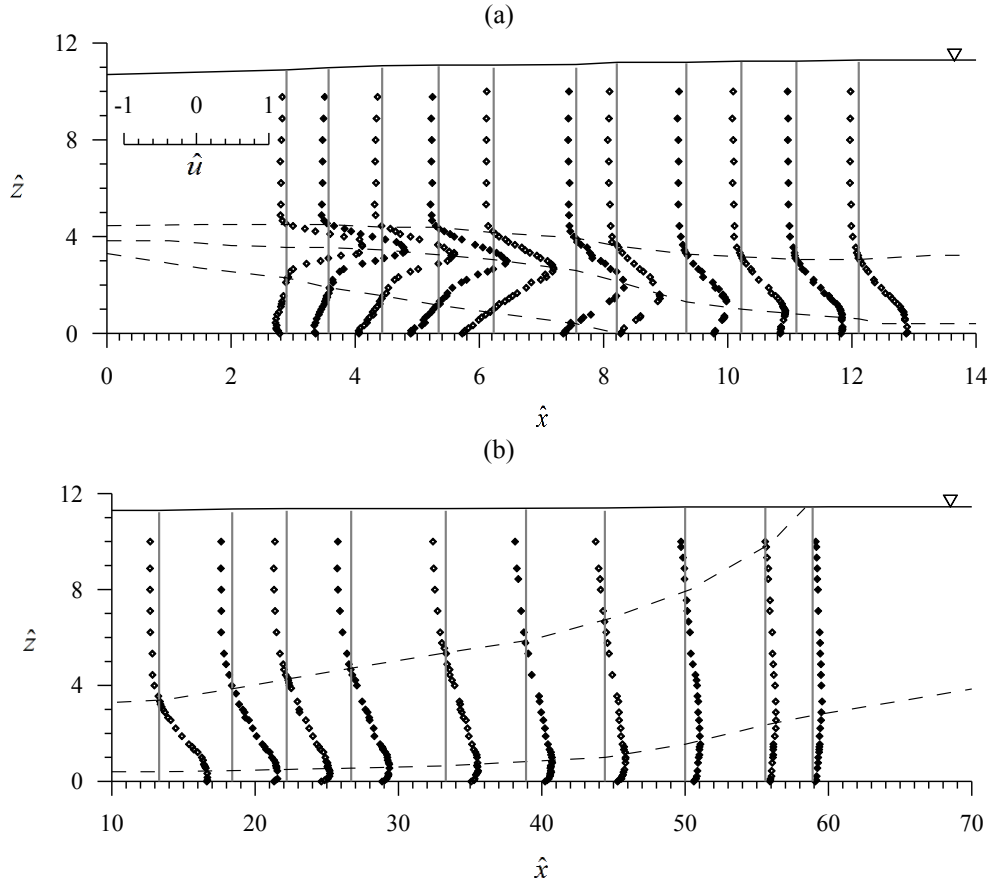
Figure 3. Vertical distribution of $\hat{u}$ (a) up to minimum jet thickness and (b) from minimum jet thickness to the wall jet region for $U_1 = 1.528$ m s^{-1} and $y_1 = 0.045$ m in submerged offset jet subjected to offset ratio $h_1/y_1 = 3.83$

5. SUBMERGED JUMP AT DROP IN A RECTANGULAR CHANNEL

For a supercritical stream discharging from a slot with offset height ΔZ, if a normal jump is to be formed at the efflux section where the depth is y_1 and the Froude number is F_1, the tail water depth y_4 should be equal to the subcritical sequent depth y_2 given by the momentum equation. If y_4 is less than y_2, the jump is swept downstream and is known as a repelled jump.

If, however, y_4 is greater than y_2, the jump gets submerged or drowned jump, simply called the submerged jump. Based on the experimental data obtained, a definition sketch for the submerged jump is presented in figures 4 & 5, which defines the average flow field of a submerged jump in a rectangular prismatic channel. Usually y_1 and y_4 are depths at the toe and at the end of jump, y_3 is the back up near the gate, and y_2 is the minimum flow depth.
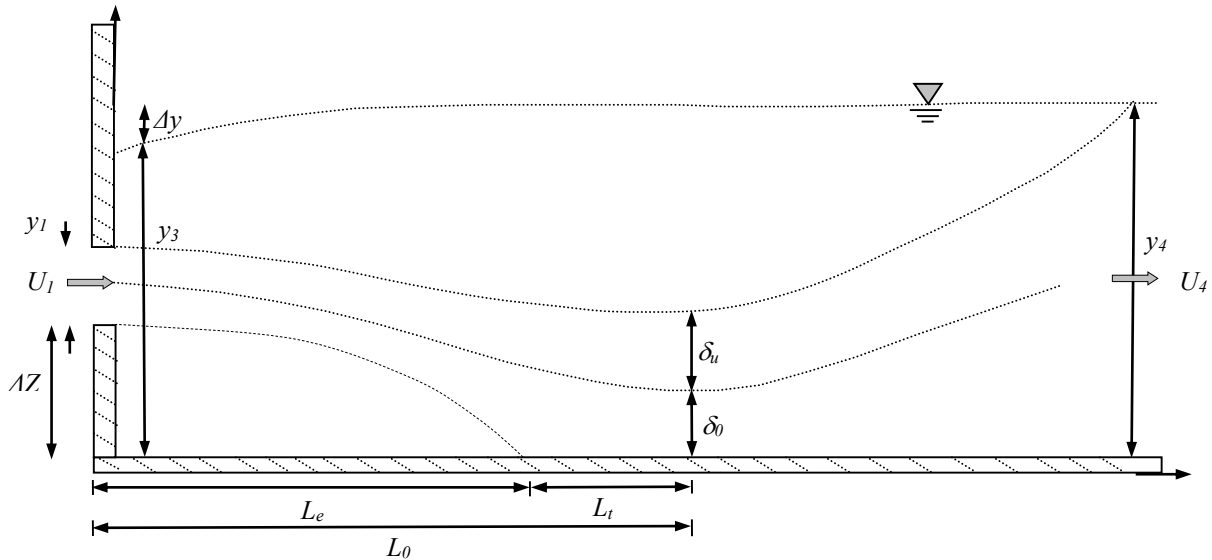
Figure 4. Definition sketch for the submerged jump at drop in a rectangular channel

A supercritical stream of depth y_1 and Froude number F_1 comes out of a slot with parallel boundaries. As the tailwater depth y_4 is greater than y_2, the jump is submerged. At the inlet section, there is backing up, and the depth is y_3. From this section forward, there is a continuous increase in water surface up to tailwater depth y_4. The submergence factor s for a submerged jump of supercritical depth y_1 and Froude number F_1 is defined as

$$s = \frac{y_4 - y_2}{y_2} \implies y_4 = (s+1)y_2 \tag{1}$$

Referring to the definition sketch, the ratio of the backed-up depth y_3 to the supercritical depth y_1, found using the principles of continuity and momentum equation y_3/y_1, can be shown to be a function of only F_1 and s. Applying the momentum equation to the efflux section and the end of jump,

$$Q = U_1 y_1 = U_4 y_4 \tag{2a}$$

$$\frac{\rho g}{2} y_3^2 - \frac{\rho g}{2} y_4^2 = \rho Q (U_4 - U_1) = \rho U_1^2 y_1 \left(\frac{y_1}{y_4} - 1 \right) \tag{2b}$$

Substituting Eq. (1) into Eq. (2) using equation of continuity and simplifying,

411

$$\left(\frac{y_3}{y_1}\right)^2 - \left(\frac{y_2}{y_1}\right)^2 (s+1)^2 = 2F_1^2\left(\frac{y_1}{y_4}-1\right) \tag{3a}$$

$$\frac{y_3}{y_1} = \left[(s+1)^2\left(\frac{y_2}{y_1}\right)^2 - 2F_1^2 + \frac{2F_1^2}{(s+1)}\left(\frac{y_2}{y_1}\right)^{-1}\right]^{0.5} \tag{3b}$$

The free surface profiles of submerged offset jets were measured by a point gauge with a Vernier least count of ±0.1 mm. The flow rate at the flume inlet controlled by an inlet valve was measured by a calibrated V-notch weir. In Table 2, the submergence ratio s and the jet Froude number F_1 are defined. In this study, the y_4 was measured at the location where the free surface profile became parallel to the flume bottom. The sequent depth y_2 of a B-jump is obtained from Eq. (6).

The theoretical equation above is developed for the back-up depth at the efflux section; Table 2 shows calculated and experimental values of back-up depth.

Table 2. Calculated and experimental values of back-up depth, submergence factor and sequent depth

Run no	F_1	ΔZ (m)	y_1 (m)	U_1 (m/s)	OR	y_4 (m)	y_2 (m)	s	y_3 (Cal)	y_3 (Exp)	Δ_y (Cal)	Δ_y (Exp)
1	2.3	0.10	0.025	1.139	4.50	0.555	0.144	2.82	0.5490	0.5500	0.00571	0.0050
2	2.5	0.12	0.030	1.356	4.50	0.540	0.176	2.02	0.5300	0.5330	0.00992	0.0070
3	2.0	0.12	0.045	1.328	3.16	0.555	0.199	1.78	0.5414	0.5360	0.01357	0.0190
4	2.0	0.14	0.050	1.400	3.30	0.535	0.227	1.35	0.5177	0.5160	0.01722	0.0190
5	2.5	0.15	0.040	1.566	4.25	0.495	0.229	1.16	0.4760	0.4760	0.01893	0.0190
6*	2.3	0.15	0.045	1.528	3.83	0.515	0.234	1.19	0.4956	0.4940	0.01934	0.0210
7	3.0	0.16	0.030	1.627	5.83	0.495	0.223	1.21	0.4793	0.4860	0.01561	0.0090
8	1.9	0.18	0.040	1.190	5.00	0.485	0.241	1.01	0.4739	0.4650	0.01105	0.0200
9	3.0	0.20	0.035	1.757	6.20	0.480	0.272	0.76	0.4582	0.4600	0.02178	0.0200
10	2.7	0.20	0.045	1.794	4.90	0.480	0.291	0.65	0.4512	0.4550	0.02873	0.0250

5.1. Hydraulic Jump in Drop Structure
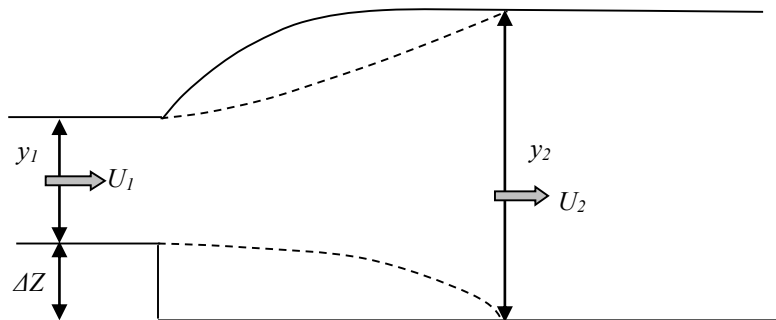
Figure 5. Sequent depth at drop structure in a rectangular channel

By applying a momentum equation and continuity equation at the inlet y_1 and at sequent depth y_2, we get a depressed cubic equation, as follows:

$$\frac{\rho g}{2}(y_1 + \Delta Z)^2 - \frac{\rho g}{2}y_2^2 = \rho Q(U_2 - U_1) = \rho U_1^2 y_1\left(\frac{y_1}{y_2} - 1\right) \tag{4a}$$

$$(\Delta Z + y_1)^2 - y_2^2 = 2\frac{U_1^2}{gy_1}y_1^2\left(\frac{y_1}{y_2} - 1\right) = 2F_1^2 y_1^2\left(\frac{y_1}{y_2} - 1\right) \tag{4b}$$

$$\left(\frac{y_2}{y_1}\right)^3 + \left[-2F_1^2 - \left(\frac{\Delta Z}{y_1} + 1\right)^2\right]\left(\frac{y_2}{y_1}\right) + 2F_1^2 = 0 \ Ij = Sj + \sigma j \tag{5}$$

$Y^3 + aY + b = 0$, Where, $y_2 / y_1 = Y$ and $C = (a^3 / 27 + b^2 / 4)$

$$Y = 2\left(-\frac{a}{3}\right)^{0.5}\cos\left(\frac{\theta + 2k\pi}{3}\right) \tag{6}$$

where $k = 0$, 1, 2 and $\theta = \arccos(3b / 2a)(-3/a)$, was adopted in the present study with three real roots $y_2/y_1 = 2(-a/3)^{0.5}\cos(\theta/3)$. Hence, Eq. (3) and (5) have been used to give a chart for $\Delta y/y_1$ for values of F_1 to 10 and values of s to 5 as shown in Figure 6. Using this chart, the back-up depth for any particular case could easily be obtained.
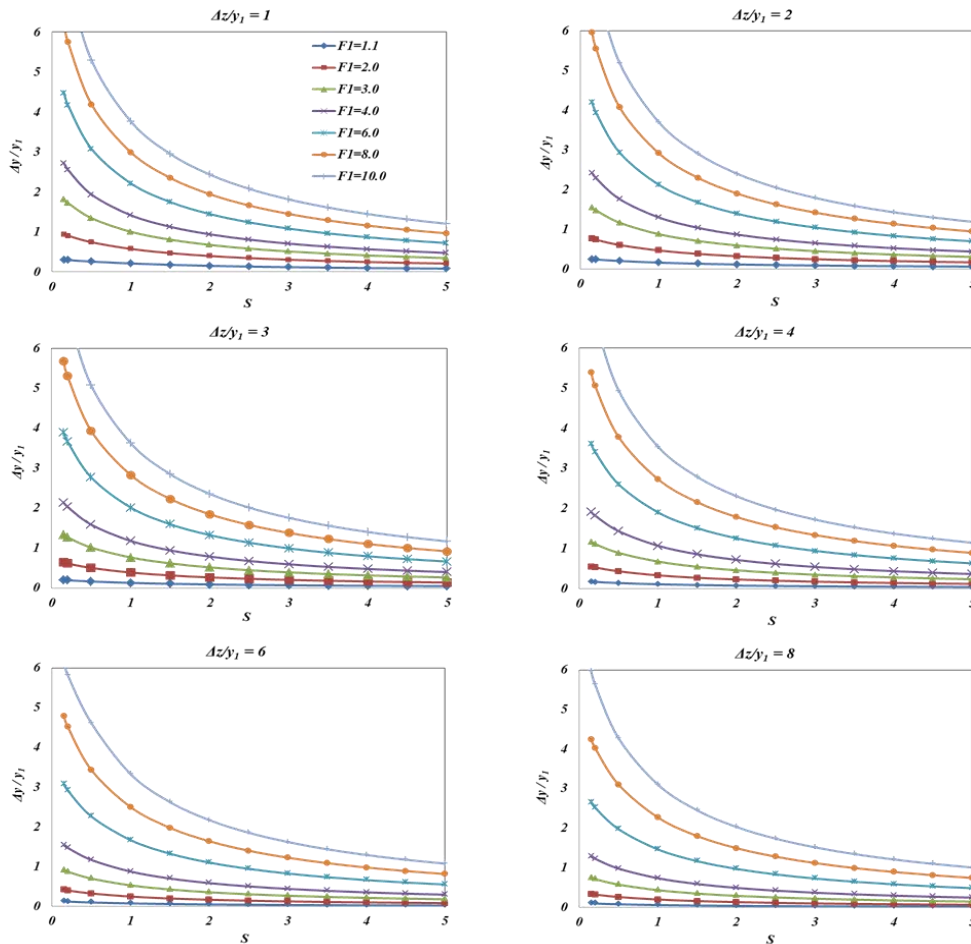
Figure 6. Back-up depth with Froude number 1.1 to 10 and submergence factor at different $\Delta Z / y_1$

5.2. Trajectories of Offset Jet

Theoretical equations are also developed for jet trajectories (lower layer of jet, upper layer of jet and maximum jet velocity layer) based on the boundary conditions by taking the input values of reattachment length (L_e), horizontal distance at minimum jet thickness (L_0), and the vertical distances (δ_u and δ_0) at minimum jet thickness from experimental data as shown in figure 4.

$$Z = a + bx + cx^2 + dx^3 \tag{7}$$

Applying the boundary conditions: (i) $Z\,(x = 0) = \Delta Z$, (ii) $dZ/dx\,(x = 0) = 0$ (iii) $Z\,(x = L_e) = 0$ and $d^2Z/dx^2\,(x = L_e) = 0$, we get

$$\frac{Z}{\Delta Z} = 1 - \frac{3}{2}\left(\frac{x}{L_e}\right)^2 + \frac{1}{2}\left(\frac{x}{L_e}\right)^3 \tag{8}$$

Similarly for maximum velocity layer, let

$$Z = a + bx + cx^2 + dx^3 + ex^4 \tag{9}$$

By applying the boundary conditions (i) $Z\,(x = 0) = \Delta Z + y_1/2$, (ii) $dZ/dx\,(x = 0) = 0$ (iii) $d^2Z/dx^2\,(x = L_e) = 0$ (iv) $Z\,(x = L_0) = \delta_0$ and $dZ/dx\,(x = L_0) = 0$, we get

$$\frac{Z}{\Delta Z + \dfrac{y_1}{2}} = 1 + \frac{1 - \dfrac{\delta_0}{\Delta Z + \dfrac{y_1}{2}}}{1 - 6\dfrac{L_e}{L_0} + 6\left(\dfrac{L_e}{L_0}\right)^2}\left(\frac{x}{L_0}\right)^2\left\{6\frac{L_e}{L_0}\left(2 - 3\frac{L_e}{L_0}\right) + 4\left[3\left(\frac{L_e}{L_0}\right)^2 - 1\right]\left(\frac{x}{L_0}\right) + 3\left(1 - 2\frac{L_e}{L_0}\right)\left(\frac{x}{L_0}\right)^2\right\} \tag{10}$$

For upper layer of jet trajectory, replace $(\Delta Z + y_1 / 2) / \delta_0$ with $(\Delta Z + y_1) / (\delta_0 + \delta_u)$ and $\Delta Z + y_1/2$ with $\Delta Z + y_1$

$$\frac{Z}{\Delta Z + y_1} = 1 + \frac{1 - \dfrac{\delta_0 + \delta_u}{\Delta Z + y_1}}{1 - 6\dfrac{L_e}{L_0} + 6\left(\dfrac{L_e}{L_0}\right)^2}\left(\frac{x}{L_0}\right)^2\left\{6\frac{L_e}{L_0}\left(2 - 3\frac{L_e}{L_0}\right) + 4\left[3\left(\frac{L_e}{L_0}\right)^2 - 1\right]\left(\frac{x}{L_0}\right) + 3\left(1 - 2\frac{L_e}{L_0}\right)\left(\frac{x}{L_0}\right)^2\right\} \tag{11}$$

Pre-attachment length L_e is one of the important parameters of offset jet. Experimental data of L_e is a function of offset ratio (OR). Importantly, the L_e remains almost independent of jet Froude number F_1 and submergence ratio s. Another important parameter is the length L_0 ($= L_e + L_t$) required for the initiation of a wall jet region. It can be expressed as a function of F_1, OR, and s. The vertical distance δ_0 of the occurrence of jet velocity at $x = L_0$ and the thicknesses δ_u of the upper layer at $x = L_0$ were important for performing a multiple regression analysis, which showed regression coefficients as 0.99, 0.97, 0.75 and 0.95.

It is important to determine the trajectories of the submerged offset jet and the jet velocity. The submerged offset jet in the pre-attachment region is bounded by the inner and the outer separation lines forming the lower and upper profiles of the jet (figure 1). Note that for Run 6, the experimental analysis is shown in figure 7. The computed lower profile of the submerged offset jet in the pre-attachment region corresponds with the experimental profiles more in flow zone toward the boundary than toward the issuing jet, where the experimental profiles are underestimated as shown in figure 7(a). On the other hand, the computed upper profiles of submerged offset jets in

the pre-attachment region have satisfactory agreement with the experimental profiles in the falling portion but underestimate the experimental profiles near the issuing zone of the jet. The reason of this discrepancy is attributed to the fact that the jet near the issuing zone spreads over a short horizontal distance due to its abounding momentum before it curves down as shown in figure 7(c). Lastly, the trajectory of maximum jet velocity layer in the pre-attachment region show a good agreement with the experimental profiles as shown in figure 7(b).
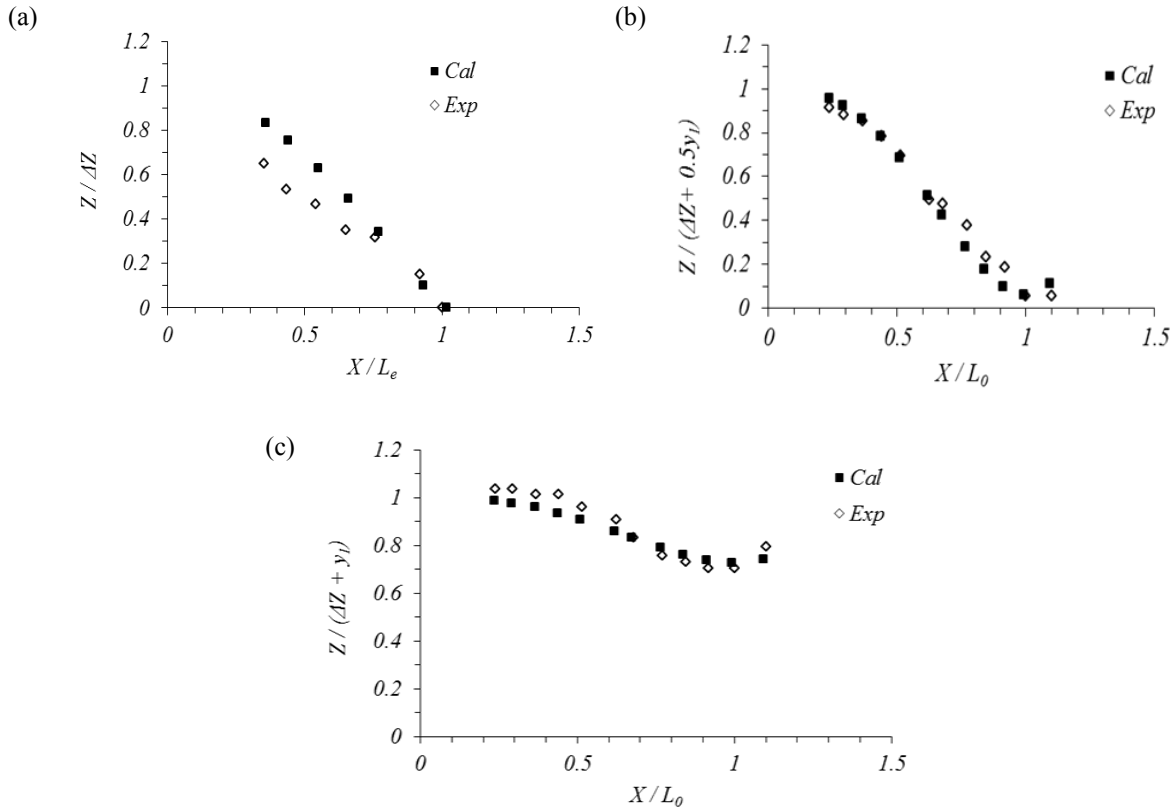
Figure 7. (a) Trajectory of lower null velocity, (b) Trajectory of maximum velocity and (c) Trajectory of upper null velocity

6. CONCLUSIONS

The streamwise velocity profiles in the submerged offset jet were measured at different sections to study the jet characteristics. The vertical position of the upper null streamwise velocity point goes down initially but moves upward as soon as the reattachment of the deflected jet occurs. It meets the water surface as the flow changes to the normal subcritical open channel flow. The maximum horizontal velocity occurring within the jet layer has been found to decrease along the flow direction. The limited tailwater depth and surface roughness can accelerate the decay. The vertical position of maximum streamwise jet velocity moves down almost abruptly until the offset jet reattaches to the wall and then gradually along the reattachment region until the wall jet is developed. After that, the boundary layer grows upward as the jet thickness increases. After attachment, the jet centreline velocity drops to its lowest value due to pressure increase resulting from impingement where the slope of the curve changes its sign and the jet velocity starts to recover slightly and the decay of maximum velocity with distance follows the same pattern as that of a wall jet. A theoretical equation is developed for the back-up depth at the efflux section, which is experimentally verified for the range of supercritical Froude numbers and submergence factor. Experimental results agree well with the mathematical predictions. Theoretical equations are also developed for jet trajectories (lower layer of jet, upper layer of jet and maximum jet velocity layer) based on the boundary conditions by taking the input values of reattachment length, horizontal distance at minimum jet thickness and the vertical distances at minimum

jet thickness from experimental data. The predicted jet trajectories of submerged offset jet are in good agreement with the experimental results.

7. REFERENCES

Agelin-Chaab, M., Tachie, M.F., (2011) Characteristics of Turbulent Three-Dimensional Offset Jets, *Journal of Fluids Engineering*, Vol.133 (5),051203-1-9.

Agelin-Chaab, M., Tachie, M.F., (2011) Characteristics and structure of turbulent 3D offset jets, *International Journal of Heat and Fluid Flow* 32 (3), 608-620.

Bhuiyan, F., Habibzadeh, A., Rajaratnam, N., Zhu, D.Z., (2011) Reattached turbulent submerged offset jets on rough beds with shallow tailwater , *Journal of Hydraulic Engineering,* ASCE, Vol.137(12), 1636-1648.

Bourque, C., Newman, B. G., (1960). Reattachment of two-dimensional incompressible jet to an adjacent plate. *Aeronautical Quarterly* 11, 201–232.

Dey, S., Nath, T.K, Bose, S.K, (2010) submerged wall jets subjected to injection and suction from the wall, *Journal of Fluid Mech.,* 653, 57-97, doi:10.1017/s0022112010000182.

Dey, S., Sarkar, A., (2008) Characteristics of Turbulent Flow in Submerged Jumps on Rough Beds, *Journal of Engineering Mechanics, ASCE* Vol.134 (1), 49-59.

Gao, N., and Ewing, E. (2007). "Experimental investigation of planar offset attaching jets with small offset distances." Exp. Fluids, 42(6), 941–954.

Govinda Rao, N.S, (1963). "the submerged hydraulic jump." *J. Hydraul. Div.,* 89(HY1), 139–162.

Gu, R. (1996). "Modeling two-dimensional turbulent offset jets." J. Hydraul. Eng., 122(11), 617–624.

Hoch, J., and Jiji, L. M. (1981). "Two-dimensional turbulent offset jet boundary interaction." *Trans. of ASME J., Fluids Eng.,* 103(1), 154–161.

Holland, J. T., and Liburdy, J. A., (1990).Measurements of the thermal characteristics of a turbulent heated offset jets. *International Journal of Heat and Mass Transfer* 33 (1), 69–78.

Long, D., Steffler, P.M, Rajaratnam, N. (1990). "LDA study of flow structure in submerged hydraulic jump." *J. Hydraul. Res.,* 28(4), 437–458

Nasr, A., Lai, J. C. S., October (1997). Comparison of flow characteristics in the near field of two parallel plane jets and an offset jet. *Physics of Fluids* 9 (10), 2919–2931.

Nasr, A., Lai, J.C.S., (1998) A turbulent plane offset jet with small offset ratio, *Experiments in fluids 24(1),* 47-57

Pelfrey, J.R .R, Liburdy J.A, (1986) Mean flow characteristics of a turbulent offset jet. *Journal of fluid engineering*, 108:82-88, doi:10.1115/1.3242548.

Rajaratman, N. (1976). Turbulent jets. *Elsevier Scientific, Amsterdam.*

Rajaratnam, N., and Subrarnanya, K. (1968). "Plane turbulent reattached wall jets." *J. Hydraul. Div.,* 94(1), 95–112.

Sawyer, R. A., (1960). The flow due to a two-dimensional jet issuing parallel to a flat plate. *Journal of Fluid Mechanics* 9, 543–559.

Yoon, S. H., Kim, K. C., Kim, D. S., and Chung, M. K. (1993). "Comparative study of a turbulent wall-attaching offset jet and a plane wall jet." *KSME J.,* 7(2), 101–112.

Yoon, S.H, Kim, K.C, Kim, D.S, Chung, M.K, (1995) Effect of surface roughness on a turbulent wall-attaching offset jet, *Experiments in fluids* 19 (1), 38-42

Spillway Deflector Design Using Physical and Numerical Models

<u>M. Politano</u>[1], T. Lyons[1], K. Anderson[2], S. Parkinson[2] and L. Weber[1]
[1]IIHR – Hydroscience & Engineering
The University of Iowa
Iowa City, IA 52242
USA
[2]Idaho Power Company
P.O. Box 70
Boise, ID 83707
USA
E-mail: marcela-politano@uiowa.edu

ABSTRACT

Elevated total dissolved gas (TDG) can be a serious threat to migrating fish. Gas supersaturation downstream of a dam occurs due to bubble dissolution in deep high-pressure regions in the tailrace. TDG production depends on both air entrainment and depth of entrained bubbles. Deflectors installed at the spillway face are designed to change the regular plunging jets into surface jets, where bubbles are transported in a thin surface layer minimizing dissolution. Distinct flow conditions may, however, occur depending on the deflector geometry, spillway flowrate, and tailwater elevation. Deflectors are commonly designed based on jet regimes observed in physical and CFD models. Since bubbles are not scaled in the physical models and most commonly used CFD models do not predict the TDG field, deflector performance cannot be fully evaluated with this methodology.

This paper presents the design of spillway deflectors at Hells Canyon Dam using a 1:48 scale laboratory model and a two-phase flow model capable of predicting TDG production, dilution, and downstream mixing. The numerical model was validated against jet regimes observed in the laboratory and TDG field data. After a deflector was selected, possible fish injury due to pressure and acceleration changes near the deflector was estimated with a particle tracking technique.

Keywords: deflectors, total dissolved gas, physical model, CFD model, supersaturation, jet regime.

1. INTRODUCTION

Spill, considered one of the safest fish passage strategies, was historically used to enhance fish survival. However, large spill volumes can be harmful for fish since they can increase TDG, which may lead to gas bubble disease. TDG levels are usually reported relative to atmospheric pressure. Current regulation limits TDG levels to 110%. Washington and Oregon have granted waivers for the Columbia and Snake hydropower facilities to facilitate fish migration that allow 120% TDG downstream of a dam and 115% in the downstream dam's forebay when spill occurs. Hells Canyon Dam (HCD) can neither meet Idaho nor Oregon state standards for TDG during spill in excess of about 71 m³/s. In order to meet state and federal regulations, Idaho Power Company developed a TDG study plan that includes the design of spillway deflectors (Myers et al. 1999).

Gas supersaturation occurs when bubbles are carried to deep regions where solubility is enhanced by high pressure. TDG production depends on gas volume fraction, bubble interfacial area, and bubble depth. Figure 1 shows the main TDG processes downstream of a spillway. TDG concentration depends on extremely complex processes such as air entrainment, breakup and coalescence of entrained bubbles, bubble dissolution, degasification at the free surface, and bubble and TDG transport. In addition, powerhouse flows might be attracted towards the spillway region, increasing the volume of water exposed to bubbles modifying TDG production and dilution.

One alternative to minimize TDG supersaturation is to install deflectors on the spillway face to change the regular plunging into surface jets with most of the spilling momentum tangential to the free surface (Figure 2). In this regime, bubbles are transported in a thin surface layer minimizing dissolution. Distinct flow conditions may, however, occur depending on the deflector geometry, spillway flowrate, and tailwater elevation. Deflectors are commonly designed based on the capability of producing surface jets under a wide range of spillway flowrates and tailwater elevations. Figures 1 and 2 show a schematic of the flow pattern observed downstream of spillways; deflector and spillway shape in the figures do not reflect the particular geometry of HDC.
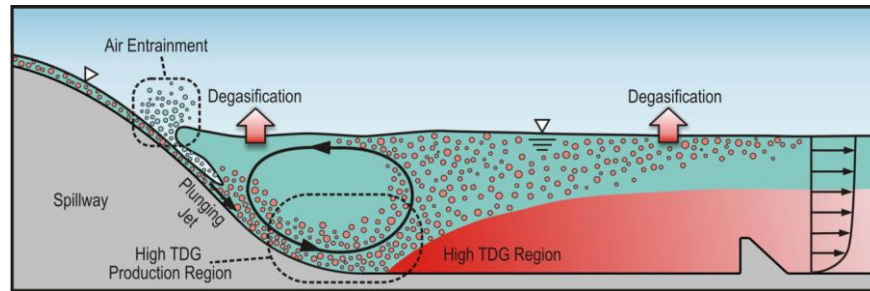
Figure 1. Air entrainment and TDG processes downstream of a spillway
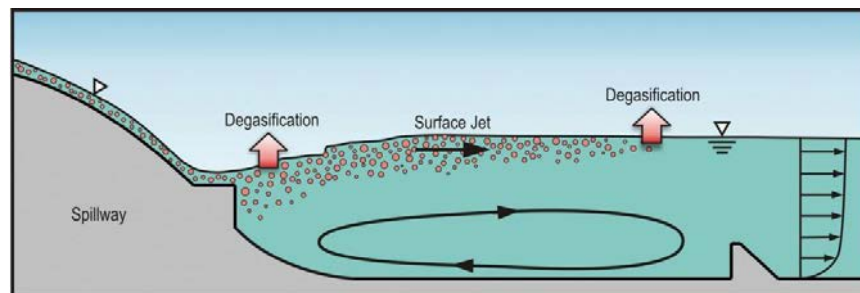
Figure 2. Surface jet in a spillway retrofitted with deflector on the spillway face

Deflector performance is usually tested in a physical model before installation in the field. Empirical models to predict TDG downstream of spillways have been developed and widely used to evaluate TDG production or refine the deflector design in several dams in the Columbia River Basin (Hibbs and Gulliver 1997, Shaw 1998, Geldert et al. 1998, Orlins and Gulliver 2000, Urban et al. 2008, Li et al. 2009, Schneider and Hamilton 2009, among others). In the past 15 years, CFD models emerged as a tool to simultaneously predict the hydrodynamics and TDG distribution downstream of dams (Weber at al. 2004, Gulliver et al. 2009, Politano et al. 2009, Feng et al. 2013). Most commonly used CFD models neglect the effect of the bubbles on the flow field and assume isotropic turbulence. Since the most important source of TDG is the gas transferred from the bubbles, a proper model for TDG prediction must account for the two-phase flow in the stilling basin and the mass transfer between bubbles and water. Moreover, bubbles modify the effective density and viscosity, changing the jet regime downstream of the deflector. Turbulence modeling also plays an important role since turbulence levels near the free surface are over-predicted by isotropic models, resulting in ineffectual prediction of spillway jet regimes (Turan et al. 2007). Advances in computer technology have made the use of three-dimensional two-phase flow modeling possible to optimize the design of spillway deflectors and complement physical models. In this paper, various configurations of deflectors in the sluiceways of HCD were evaluated, and a deflector design was selected using physical and two-phase flow models. Fish injury was then estimated based on acceleration and strain rate down the sluiceway.

2. HELLS CANYON DAM

HCD is located at river mile 247.7 on the Snake River. Figure 3 shows the dam structures and tailrace bathymetry. The dam comprises three upper crest gates, two lower level or sluice gates, nappe deflectors, left and right training walls, three powerhouse units, non-overflow sections, a left bank guidewall, and a diversion tunnel outlet. Data from

multi-beam and single beam bathymetry and photogrammetry supplied by Idaho Power were used to generate the riverbed downstream of the dam.
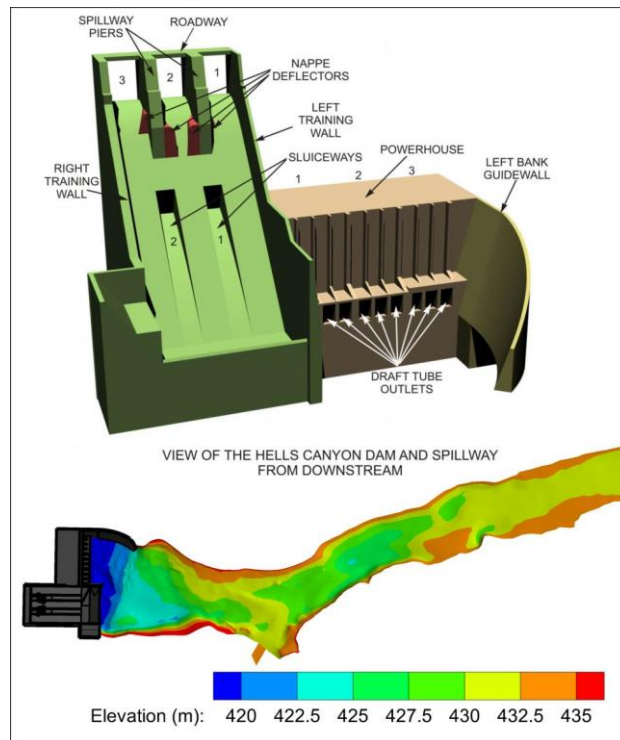
Figure 3. Hells Canyon Dam

3. PHYSICAL MODEL

Since gravitational forces are predominant, Froude similarity was used for the physical model (White 1999). A 1:48 model scale was selected based on discernable flow characteristics, available laboratory space, and construction cost. Scaling ratios based on Froude similarity for the flowrate, Reynolds number, and Weber number are 1:15963, 1:332.6, and 1:2304, respectively. Smaller levels of turbulence and smaller and larger bubbles (in dimensionless terms) in the physical model prevent the capture of bubble behavior and TDG production. However, although the Reynolds-number similarity is violated, conditions simulated in the laboratory corresponded to fully turbulent flow, and the model is expected to reproduce the spillway jet regime and general flow pattern in the tailrace. The original physical model recreated the entire spillway section and was used to develop the deflector performance curves. This sectional model consisted of a large head tank, a spillway section, and an open-channel flume. A Plexiglas wall as one side of the downstream flume permitted flow visualization for the various deflector designs. The model was later modified for investigation of potential erosion impacts and three-dimensional flow characteristics. The spillway section, powerhouse units, left and right bank training walls, forebay area, and about 1 km of downstream tailrace were included in the model

Potential for erosion was evaluated only with the physical model. Deflectors significantly changed the tailrace flow pattern and increased tailrace erosion potential at flowrates above 425 m^3/s per sluiceway bay. Model observations indicated that spill operations should change after deflector installation to minimize erosion. For total spill flowrates of 850 m^3/s or less, only sluiceways should be opened evenly. At spill flowrates between 850 and 5600 m^3/s, only upper crest gates should be opened evenly. Above 5600 m^3/s, both fully opened crest gates and evenly opened sluiceway gates should be used.

4. TWO-PHASE FLOW MODEL

The study area used for the CFD model includes about 11.4 km of the Snake River, beginning at HCD and extending downstream to just below to Wild Sheep rapids. The model is based in the commercial CFD code ANSYS FLUENT. The free-surface shape in the 300 m downstream of the dam was obtained with a VOF method assuming a negligible effect from the bubbles. Mike 11 was used to predict the water elevation in the river downstream.

A rigid-lid grid conformal to the predicted free surface was created, and a slip mixture two-phase flow model with attenuation of normal velocity fluctuation at the free surface was used for the hydrodynamics and TDG prediction. The model accounts for buoyancy, pressure, drag, and turbulent dispersion forces. A transport equation for the bubble number density was used to predict the local bubble size, which can change with dissolution and pressure. The model uses a Reynolds Stress Model to provide anisotropic turbulence closure. In order to capture the turbulence structure and attraction of powerhouse flows by spillway jets, zero normal fluctuations at the free surface are enforced. A modified bubble-induced turbulence term is used to account for suppression and production of turbulence by the bubbles. The TDG field is calculated with a two-phase scalar transport equation in which the source is the bubble/liquid mass transfer, function of the gas volume fraction, and bubble size. Details of the mathematical model, model limitations, numerical schemes, and implementation using User Defined Functions in FLUENT are presented in Politano et al. (2009).

Fish mechanical injury due to spillway deflectors was analyzed using a particle tracking technique. The history of accelerations and strain rate on particles released from the sluiceways gates was recorded and linked to injury values reported in the literature. Fish are assumed to be passive, neutrally buoyant particles with no behavioral responses, which is expected to be valid at the high velocity found in the sluiceway.

5. DEFLECTOR PERFORMANCE CURVES

Deflector design at HCD is challenging due to the unique project characteristics such as high head, upper nappe deflectors, lower level sluiceways, and a short, deep stilling basin. Initial laboratory tests demonstrated that upper nappe deflectors would be problematic since the flow is deflected away from the concrete spillway surface. Dam operation flexibility could be maintained if an acceptable deflector design could be developed for the lower level sluiceways. A balance between energy dissipation and bubble entrainment must be achieved for acceptable flow deflector design. The lower level sluiceways could then be operated when TDG levels are important, and the upper spillway gates could be operated for high spill discharges when energy dissipation and dam safety become important.

The jet regime depends on the spillway discharge per bay and tailwater elevation. Figure 4 shows different spillway regimes observed in the laboratory. Figure 4 shows the jet regime for a spillway flowrate of 141.5 m^3/s using a deflector 4.88 m long with 5° lip angle at an elevation 448 m. A surface jump occurs during high tailwater elevations. A hydraulic roller forms above the jet, aerating the downstream water surface with potential of TDG production (Figure 4a). The most efficient regime to prevent TDG production is the surface jet (Figure 4b) in which the jet remains tangential to the free surface, minimizing the bubble transport to depth and TDG production. In the vented surface jet (Figure 4c), the jet is still surface oriented but the nappe begins to intermittently aerate. At low tailwater elevations, water flowing over the spillway plunges deep into the stilling basin, resulting in a plunging regime with the highest TDG production (Figure 4d).

Primary flow deflector design components include elevation, length, transition radius, and lip angle. Deflector elevation must remain below the tailwater level to prevent vented surface and plunging flows and high enough to keep performance within the surface jet flow regime for high tailwater. Deflectors must be long enough to deflect flow but short enough to minimize construction cost. Cavitation is also a factor of concern in flow deflector length. Sluiceway bay deflectors at HCD could cause cavitation problems if they extend beyond the spillway face. The transition radius is the radius of an arc connecting the sluiceway face to the horizontal deflector face. A 4.5 m transition radius was used initially to minimize fish injury. Three positive lip angles were then examined over the course of the model.

A performance curve shows flow regimes regions for different sluiceway unit discharges and tailwater elevations for a given deflector geometry. These plots are used to compare deflector designs and to optimize operating conditions once a deflected is selected. The curve was created in the physical model first setting a given discharge in each sluiceway. After the forebay was stabilized, which took approximately 15 minutes, the tailwater elevation was set to approximately 450 m, providing deep deflector submergence. The corresponding flow regime for this tailwater was observed and recorded. The tailwater was gradually lowered until a flow regime change was observed. The discharge, tailwater elevation, and flow regime were then recorded. This procedure was repeated until plunging flow regime was observed. This process was implemented for different flows per sluiceway bay for various deflector designs (length from 4.3 to 5.57 m, elevation from 446.2 to 447.4 m, lip angle: 0, 10 and 15 degrees). Figure 5 shows the performance curve for a deflector 4.87 m long with a 5° lip angle set at elevation 447.4 m. This deflector demonstrated the highest potential for minimizing TDG of all tested deflectors in the laboratory,.
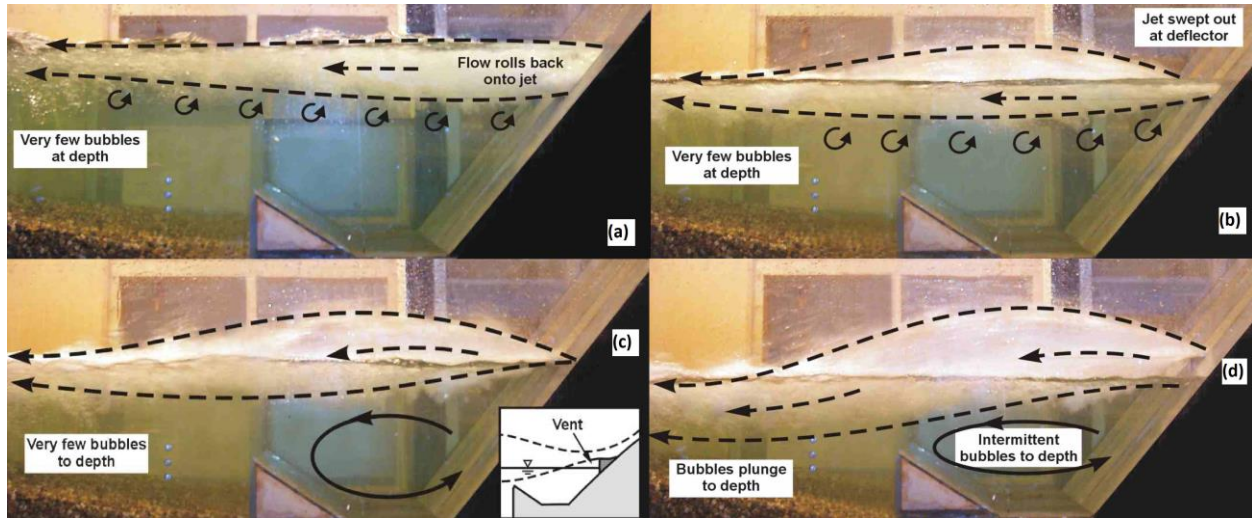
Figure 4. Jet regimes observed in the laboratory model. Surface jump (a), surface jet (b), vented surface jet (c) and plunging flow (d)
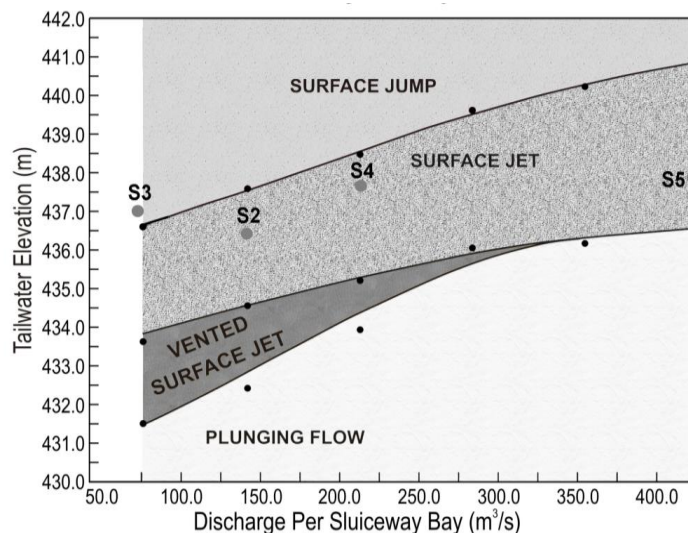
Figure 5. Deflector performance curve

Four numerical simulations were performed for the deflector selected in the laboratory to compare predicted jet regimes with those observed in the physical model. For unit discharges of about 100 m³/s, the model predicted a surface jet similar to that observed in the laboratory (Figure 6). Also consistent with the laboratory results, a surface

jump with waves at the impact region was predicted at the lowest discharge per bay (simulation S3). Figure 6 shows the surface jump predicted in slices through the middle of the low-level sluice gates SG1 and SG2 for simulation S3. White lines represent the free surface location. Velocity vectors above the free surface show air velocity. Note that 3D effects predicted with the numerical model are not captured by a sectional model. Lateral powerhouse flows reduce the performance of the deflector. This effect is more important at low spillway flows, and it was observed in both the numerical model and laboratory model with the powerhouse and tailrace included.
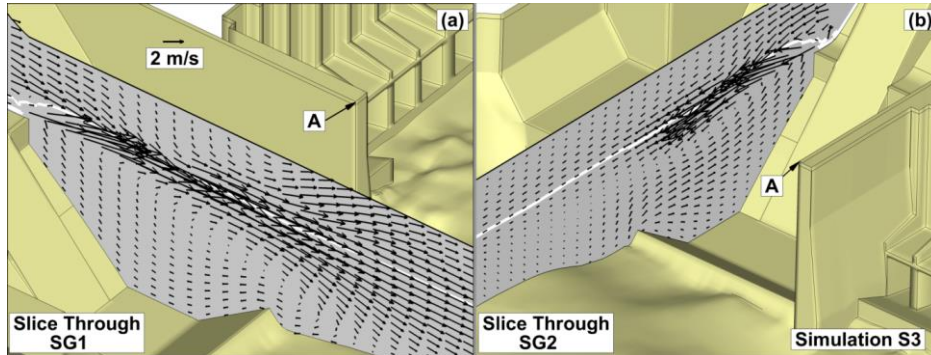
Figure 6. Predicted jet regimes for simulation S3. Velocity vectors in a slide passing through SG1 (a) and SG2 (b)

6. CALIBRATION AND VALIDATION OF TDG MODEL

Inputs of the two-phase model are bubble diameter and gas volume fraction at the spillway inflows, representing the air entrainment. Different bubble sizes and gas volume fractions were used to determine the parameters that produced the least error between modeled TDG and field data collected on May 21, 1998 and May 4, 2006. Three gas volume fractions, $\alpha = 0.03$, 0.04, and 0.045, and two bubble diameters, 0.5, and 0.8 mm, were tested. The parameters that produced the smallest difference with the field data were $\alpha = 0.03$ and bubble diameter 0.8 mm. The entrained gas volume fraction and bubble size distribution are expected to change with flow conditions and spillway geometry. Unfortunately, TDG data at HCD were insufficient to obtain model parameters for different spillway flow regimes. However, the values obtained for HCD are comparable to those used at other hydropower projects with and without deflectors (Politano et al. 2009, Politano et al. 2011). Table 1 shows the percent of saturation of TDG measured in the field at the forebay and tailrace as well as the results of the model. The model matched the results of the field measurements with an error smaller than +/- 3%.

Table 1. Measured and predicted TDG concentrations

| | TDG Saturation | | | | | | | | |
| | Field Data | | | Model | | | | Error % | |
	Forebay	RM 246.87	RM 246.38	Forebay	RM 246.87 Average	RM 246.87 Near Oregon	RM 246.38 Average	RM 246.87	RM 246.38
May 21, 1998	1.170	1.268		1.170	1.358	1.280		0.950	
May 4, 2006	1.224	1.321	1.366	1.224	1.349	1.304	1.329	-1.290	-2.710

Figures 7a and 7b show gas volume fraction contours predicted by the model in vertical slices on May 21, 1998 and May 4, 2006. Bubbles are transported to deep regions in the tailrace due to the plunging jets created by spillway and sluiceway flows. High velocity water plunges deep into the stilling basin, creating a vertical recirculation upstream of the roller bucket. This recirculation moves bubbles up near the free surface to regions of low pressure with lower dissolution rate. Bubbles are present within 200 m downstream of the dam. The percentage of spill on May 21, 1998 and May 4, 2006 were 54% and 49%, respectively, and river flowrates were comparable. Larger spills favor plunging, resulting in a slightly higher concentration of bubbles at depth on May 4, 2006. According to the model, surface spill flows move towards the powerhouse region, transporting some bubbles to this region. This phenomenon is more pronounced for smaller spill flowrates. The TDG model assumes that no air is entrained with turbine flows, which explains the low gas volume fraction close to the powerhouse. TDG isosurfaces presented in

Figures 7(c) and 7(d) display a similar TDG field for May 21, 1998 and May 4, 2006. Maximum TDG values are found within 100 m from the dam as a consequence of bubble dissolution. High TDG concentrations, of the order of 180%, are predicted near the stilling basin.
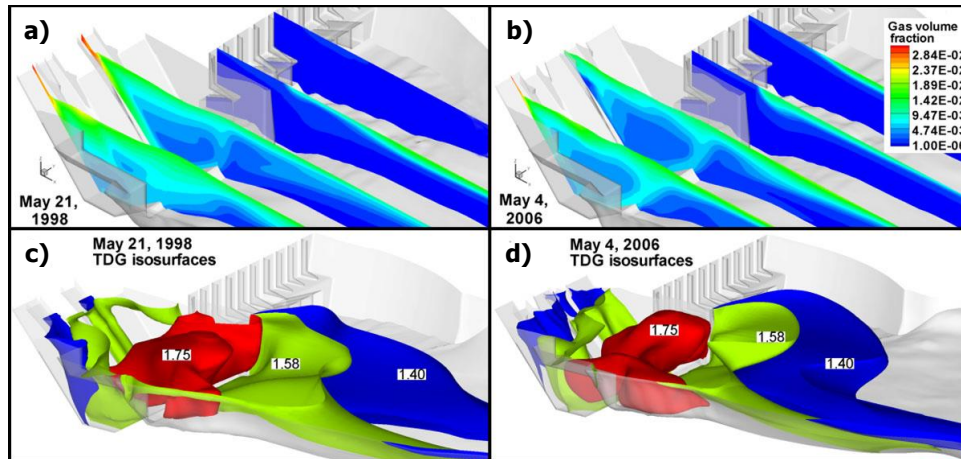
Figure 7. TDG model results. May 21, 1998 (left) and May 4, 2006 (right). Slices with gas volume fraction contours (a) and (b) and TDG isosurfaces (c) and (d)

7.   HYDRODYNAMICS AND TDG CONCENTRATION

The flow pattern obtained with the numerical model compared qualitatively well with that observed in the physical model. Figure 8 shows the simulated and observed free surface for the selected deflector at a river flowrate of 1274 m^3/s. Sluice surface jets created by deflectors generate a local depression in the water elevation near the spillway that depends on the flowrate and tailwater elevation. Spillway flow travels through the pool alongside the powerhouse wall, creating one clockwise recirculation near the right bank training wall. A counterclockwise recirculation near the fish trap is also predicted in the simulations with moderated and elevated spill flowrates. For this simulation, surface jets generate waves near the spillway with amplitude of approximately 0.60 m. The wave amplitude is significantly smaller than predicted for plunging flows without deflectors, but the waves propagate farther downstream impacting a larger region of the tailrace. Comparisons at additional flowrates are found in Politano and Carbone (2012).
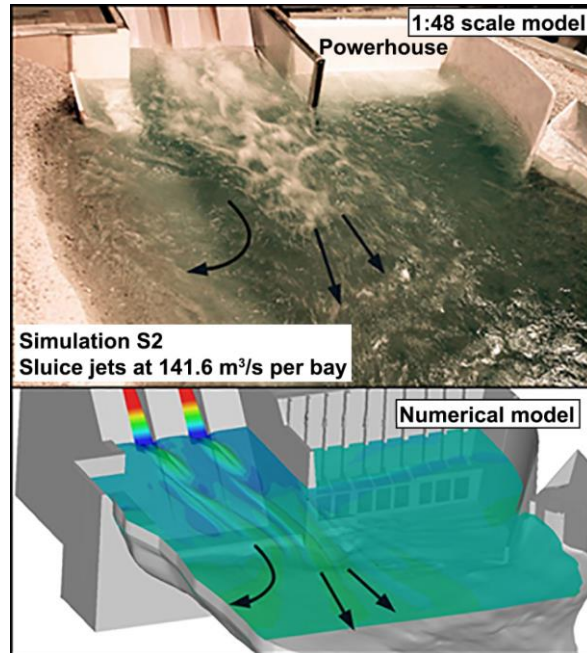
Figure 8. Flow pattern in the tailrace observed in the physical model (top) and predicted with the model (bottom)

Eight additional numerical simulations (SI to SVIII) were performed to test different deflector geometries for river flowrates of 707 (odd number simulations) and 1274 m^3/s (even number simulations). These simulations assumed a constant flow of 212.4 m^3/s passing through each of the sluiceways and no flow through the upper spillway gates. Two simulations with the highest average flow that occurs for a period of seven days in a once in ten years period (7Q10 flow) were also carried out to estimate possible fish injury due to inclusion of deflectors.

Streamlines colored by TDG for different deflector geometries are shown in Figure 9. Simulations SI and SII are for the deflector selected in the physical model, SIII and SIV a deflector 0.3 m higher, SV and SVI a deflector 0.3 m shorter, and SVII and SVIII comprise a 7.6 m curvature radius. Figures 9(a-d) are for a river flowrate of 707 m^3/s and Figure 9(e-h) are for river flows of 1274 m^3/s. An important recirculating zone near the left bank, which might affect the efficiency of the fish trap, is predicted by the simulations with a river flow of 707 m^3/s. This recirculation is created by attraction of ambient water beneath the surface jets created by deflectors. According to Turan et al. (2007), this phenomenon can be explained by acceleration of the surrounding fluid as the jet decelerates, surface currents, and the Coanda effect. For simulations with a river flow of 1274 m^3/s, this flow patterns is observed only in simulation SIV, which has the deflector placed at the highest elevation and is able to maintain a surface jet for higher tailwater elevations. Simulations with a river flow of 1274 m^3/s have three times more powerhouse flow than those with a total river flow of 707 m^3/s, and, therefore, downstream TDG dilution is more important. According to the simulations, the shorter deflector produces a weaker surface jet and favors some plunging downstream. Note that, as an additional factor, a weaker surface jet entrains less water from the powerhouse region, which results in more bubbles falling deeper and earlier in the tailrace the highest values of TDG. Maximum values of TDG production are predicted for the simulation with the greatest transition radius. However, this case also predicts higher degasification near the free surface, and the resulting TDG concentration is smaller than the case with shorter deflector.
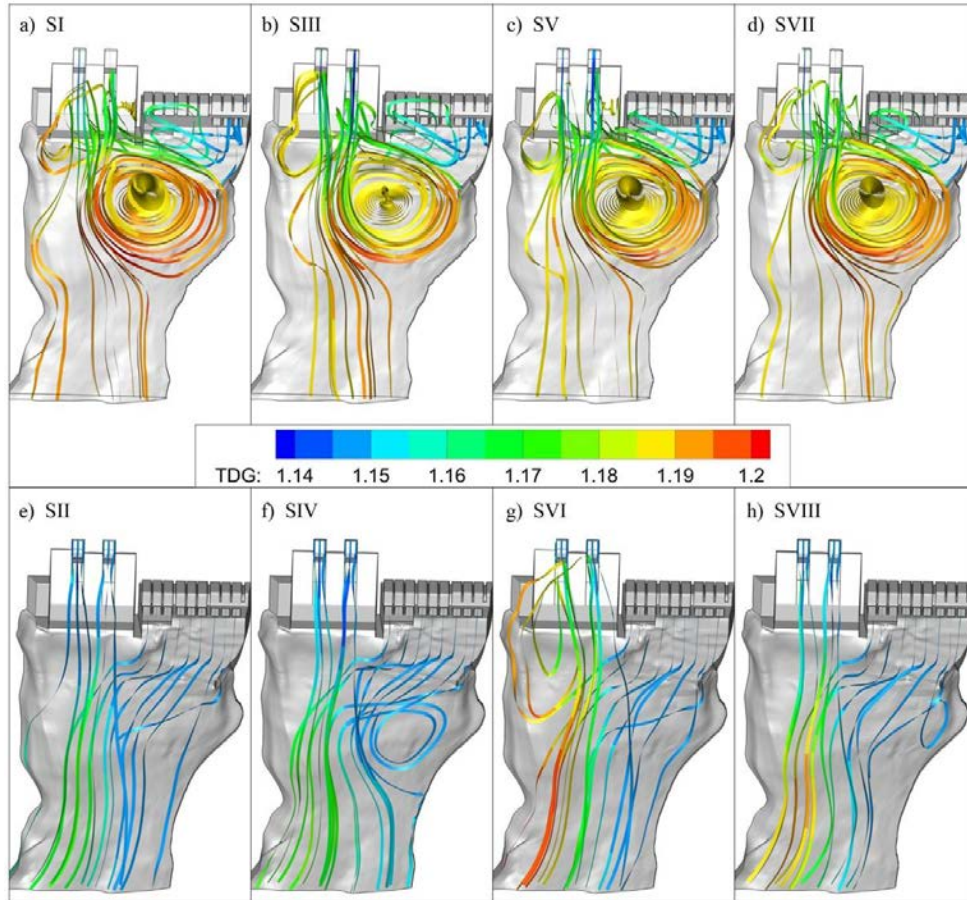
Figure 9. Streamlines colored by TDG for 707 m^3/s (top) and 1274 m^3/s (bottom)

8. FISH INJURY

Results from the VOF model for a 7Q10 flow with and without deflectors were used to analyze fish injury. For each operating condition, 6000 particles were released. Figure 10 shows values of flow acceleration and strain rate when the deflector is included (averaged every 0.5 m). Particles moving downstream over the sluiceways are exposed to a space-averaged maximum acceleration of 165 m/s^2. Maximum values of space-averaged acceleration coincide with changes in flow direction due to inclusion of the deflector in the sluiceway. When particles move over the spillway without deflectors, the space-averaged maximum acceleration is 76.2 m/s^2. In this case, the maximum acceleration occurs when flow plunges the basin pool.

The averages of the particle maximum accelerations for the cases with and without deflectors are 180.6 and 170.2 m/s^2, respectively. According to Deng et al. (2005), maximum accelerations experienced by the particles in the simulation with deflector have, on average, probabilities of 0.095 and 0.028 of causing minor and major injuries in fish, respectively. The probabilities of minor and major injuries without the deflector are 0.088 and 0.026. It is important to note that the experiment presented in Deng et al. (2005) introduced fish into a submerged jet with different water velocities. Fish injuries reported by this experiment could also be caused by the elevated shear present at the moment fish were introduced into the jet. Fish passing over the sluiceway and spillway are expected to be accelerated with the flow, and, thus, they may not be exposed to the same levels of shear as fish in the experiment. The average of the particle maximum strain rates are 20.3 and 28.6 s^{-1} for the simulations with and without the deflector, respectively. Maximum values recorded for a single particle are 47.6 and 210.8 s^{-1}, respectively. These values of strain rate are below the value of 360 s^{-1} reported by Foust et al. (2010) as detrimental to fish life.
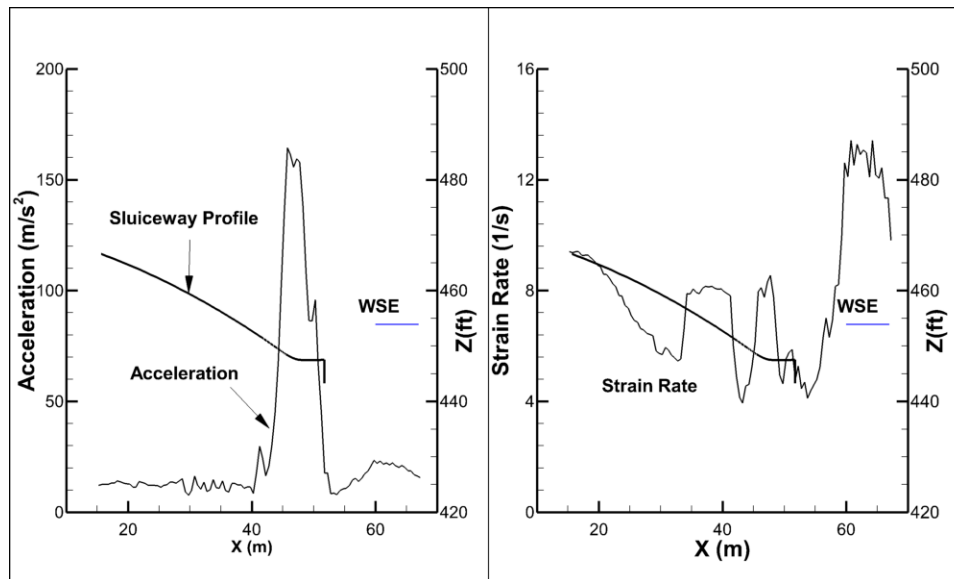
Figure 10. Space-averaged acceleration (left) and strain rate (right) for 7Q10 flow

9. CONCLUSIONS

Spillway deflectors that meet the specified design goals to reduce TDG concentration downstream of HCD were recommended using a 1:48 laboratory scale and two-phase flow models. Numerical model results agreed with observations at the physical model. A 4.87-m deflector with a 5° lip angle at elevation 447.4 m has the highest potential to minimize TDG and avoid negative flow patterns that could affect the operation of the fish trap. The recommended sluiceway deflectors retain operational flexibility to pass spill flows larger than 849.5 m^3/s through the upper spill gates while dissipating enough energy to maintain the structural integrity of the dam. The numerical model was used to further exploration of deflector performance, flow deflector effects on general flow patterns in the tailrace, and possible fish injury. Results show that with the recommended deflector, a negligible amount of bubbles is transported to depth and TDG field meet the standards for all tested conditions. Particle tracking simulations were performed to evaluate possible fish injury. On average, particles moving over the sluiceways with deflectors were exposed to higher accelerations than particles moving over the spillways. According to the values presented in Deng et al. (2005) and the results of the model, fish passing downstream of HCD are not likely to suffer severe mechanical injuries.

10. REFERENCES

Deng, Z., Guensch, G,R., McKinstry, C.A., Mueller, R.P., Dauble, D.D., and Richmond M.C. (2005). "Evaluation of fish-injury mechanisms during exposure to turbulent shear flow." Can. J. of Fisheries and Aquatic Sciences, 62(7): 1513-1522.

Feng, J., Li R., Yang, H., and Li, J. (2013). "A laterally averaged two-dimensional simulation of unsteady supersaturated total dissolved gas in deep reservoir." J. of Hydrodynamics 25: 396-403.Foust, J.M., Coulson, S., Hecker, G.E., Allen, G.S., and Dixon D.A. (2010). "Design considerations for the Alden fish friendly hydro turbine". Proc. Hydrovision International, Charlotte, NC, USA

Geldert, D.A., Gulliver, J.S., and Wilhelms, S.C. (1998). "Modeling dissolved gas supersaturation below spillway plunge pools." J. Hyd. Eng., 124(5): 513-521.

Gulliver, J.S., Groeneveld, J., and Paul, G.E. (2009). "Prediction of total dissolved gas below the Cabinet Gorge Spillway." Proceedings, XXXIII Congress of IAHR, August 9–14, 2009, Vancouver, B.C.

Hibbs, D.E., and Gulliver, J.S. (1997). "Prediction of effective saturation concentration at spillway plunge pools." J. Hyd. Eng., 123(11): 940-949.

Li, R., Li, J., Li K., Deng, Y., and Feng, J. (2009). "Prediction for supersaturated total dissolved gas in high-dam hydropower projects." Science in China Series E: Technological Sciences, 52(12), 3661-3667.

Myers, Ralph, Stan Pierce, and Mark Stute. (1999) "Hells Canyon Complex Total Dissolved Gas Study." Project Progress Report. Idaho Power Company.

Orlins, J.J., and Gulliver J.S. (2000). "Dissolved gas supersaturation downstream of a spillway II: computational model." J. Hyd. Res., 38(2): 151-159.

Politano, M., Carrica, P., and Weber, L. (2009). "A multiphase model for the hydrodynamics and total dissolved gas in tailraces." Int. J. Multiphase Flow, 35(11): 1036-1050.

Politano, M. S., Arenas Amado A., Bickford, S., Murauskas J., and Hay D. (2011). "Investigation into the total dissolved gas dynamics of Wells Dam using a two-phase flow model." J. Hydraulic Engineering, 137(10): 1257-1268.

Politano M. and Carbone M. 2012. Numerical model in the tailrace of Hells Canyon Dam. Phase V: Deflector optimization. IIHR LDR No 378.

Schneider, M. and Hamilton, L. (2009). "SYSTDG manual". U.S. Army Corps of Engineers Report.

Shaw, P. (1998). "Gas generation equations for CRiSP 1.6". University of Washington, Seattle, Washington. <http://www.cbr.washington.edu/d_gas/tdg_manual.pdf.> (Aug. 2015).

Turan, C., Politano, M.S., Carrica, P.M., and Weber, L. (2007). "Water entrainment due to spillway surface jets." Int. J. Computational Fluid Dynamics, 21 (3-4): 137-153. Urban, A.L., Gulliver, J.S., and Johnson, D.W. (2008). "Modelling total dissolved gas concentration downstream of spillways." J. Hyd. Eng. 134: 550-561.

Weber, L., Huang, H., Lai, Y., and McCoy, A. (2004). "Modeling total dissolved gas production and transport downstream of spillways: three-dimensional development and applications." J. River Basin Management 109: 157-167.

White, Frank M. (1999) Fluid Mechanics. 4th ed. Boston: WCW/McGraw-Hill.

Technical Developments in Fish Exclusion, Guidance, and Collection Materials

A. L. Peters
Pacific Netting Products
2553 United Road Northeast
Kingston, WA 98346
USA
E-mail:andy@pacificnettingproducts.com

ABSTRACT

Construction of mills, dams and other structures in rivers and streams and the withdrawal of water for irrigation or cooling industrial facilities vital to social and economic progress have impacted the survival of marine life. Barriers and guidance or collection nets can protect fish and aquatic species while allowing water to flow unimpeded for commercial and industrial use. However, nets can attract aquatic growth, fill with debris, degrade with environmental stress, and be expensive to operate and maintain. A closer look at the technical developments of materials and net designs in diverse settings can offer guidance that will be of use to engineers and community stakeholders in varied environments who are striving to meet similar challenges. With careful consideration of bathymetry, topography, pool fluctuation, water flow, debris, weather, and deployment, the principles and materials outlined can be adapted to environments around the world. Successful implementation will allow humans to continue to harness our most valuable resource with respect for the wider social and economic health of the planet.

Keywords: Pacific Netting, UHMWPE, fish exclusion, downstream fish passage, barrier net, guidance net, collection net, Dyneema®

1. INTRODUCTION

For almost as long as humans have been harnessing water to perform work, industrial and agricultural applications have been in conflict with those who depend on continued healthy populations of fish and aquatic life. Construction of mills, dams, and other structures in rivers and streams and the withdrawal of water for irrigation or cooling industrial facilities have impacted the survival rate of marine life that is vital to related social and economic progress. In 1872, the U.S. Supreme Court required persons who own or build dams to construct fish ways to enable fish migration and required compensation from upstream riparian land owners for loss of fishery and related property value (Holyoke Co. v. Lyman, 1872).

Ideally, a barrier, guidance, or collection net could allow water to flow unimpeded while protecting fish and aquatic species from harm. However, nets tend to attract aquatic growth, get filled with debris, be destroyed by ice, and require costly maintenance and operation time. The challenge is to design a fish exclusion system that not only maintains sufficient population but successfully repels debris and other stressors and can be installed and maintained economically and efficiently.

In this paper, the author will take a closer look at the technical developments of material used in fish exclusion, guidance, and collection netting systems and review three installation designs that successfully deploy these nets in diverse settings, offering guidance that will be of use to engineers and community stakeholders around the world who are striving to meet similar challenges.

2. ADVANCES IN NETTING MATERIALS

Until the early 1880s, nets were woven from natural plant fiber including manila, hemp, linen, cotton, coir, jute, straw, and sisal. The fiber was twisted or braided to a line and sewn into the form of a net. Joseph Swan, while

searching for a better carbon filament for his light bulb, discovered a method for creating an artificial fiber that was ultimately used by the textile industry for clothing and domestic products.

Beginning in the 1940s, DuPont's nylon was introduced and quickly became the preferred material for rope manufacture. Nylon is a polyamide, a macromolecule with repeating units linked by amide bonds. It offers several advantages over natural fiber rope. It is stronger for a given diameter, more elastic, more consistent in quality, and immune to dry rot. Although nylon tends to lose some of its strength when it is wet, it remains shock absorbent. However, it is weakened by exposure to acid and extreme sunlight. DuPont next introduced Dacron®, a polyethylene terephthalate fiber, in 1953. Dacron® ropes stretch much less, remain strong when wet, are more abrasion-resistant than nylon, and are also immune to most acids and alkalis. However, they do not absorb energy very well, nor can this rope be manipulated as easily as rope made from nylon (Wolfe 2008).

Another fiber, discovered in 1951, was found ideal for many marine applications. "In 1951, while attempting to convert propylene into gasoline, J. Paul Hogan and Robert L. Banks of Phillips Petroleum Company discovered polypropylene, a high-melting crystalline aliphatic hydrocarbon" (American Chemical Society, 1999, 2). When used for ropes and lines, polypropylene stretches a considerable distance under load. Though its breaking strength is considerably less than nylon or polyester, this relatively cheap fiber is lightweight and buoyant, making it suitable for numerous uses.

Each of these materials have played important roles in the development of modern nets for fishing, safety, security, and now fish protection. Engineers and designers try to match the properties of a particular fiber to a specific application. For instance, it may be that nylon is the best fiber for a safety net if elasticity and elongation are a critical part of a design. In an environment with acids or alkalis, a polyester fiber might prove a better choice.

The most modern development in construction of large barrier nets is due in large part to the development of a gel-spun, multi-filament fiber produced from ultra-high molecular weight polyethylene (UHMWPE). First commercialized as Dyneema® in the late 1970s by the Dutch science-based company DSM, UHMWPE provides the characteristics of high strength, low weight, low elongation at break, and resistance to most chemicals. Today, other manufacturers of UHMWPE include Honeywell (Spectra®), Quadrant EPP, Inc. (TIVAAR®), and Röchling Engineering Plastics (Polystone-M®).

DSM testing indicates that UHMWPE rope is seven times stronger than steel wire rope, based on comparative weight. Two of the reasons for its strength are its molecular weight and orientation. "Normal" polyethylene has a low molecular orientation and low molecular weight. By untangling these molecules through a gel spinning process and aligning them all in one direction through a drawing process, UHMWPE fiber has very long molecular chains with very high molecular weight (between 2 and 6 million) and very high molecular orientation. UHMWPE is lighter than water and extremely durable. It is four times stronger than polyester fibers, and yet its mechanical elongation at load is substantially less.
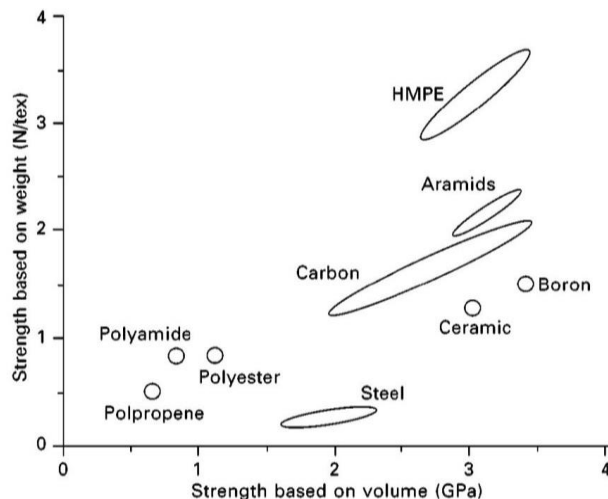
Figure 1. Strength Based on Weight and Volume, Courtesy of DSM
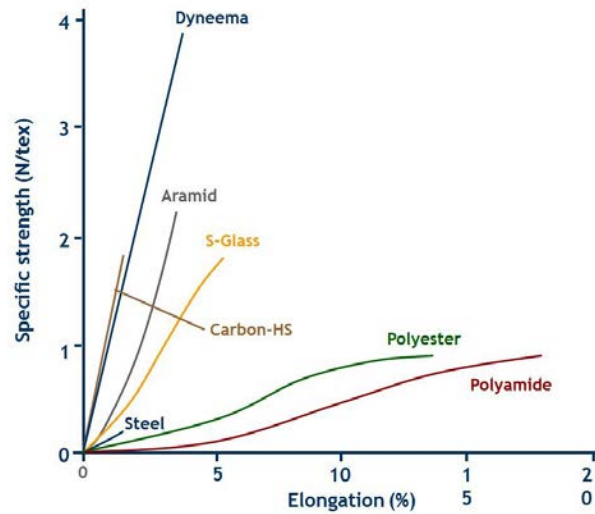
Figure 2. Elongation at Load, Courtesy of DSM

In addition, the fiber offers excellent abrasion, cut, and tear resistance even if the loading is partly in compression, as in repeated bending of rope applications. The fibers are flexible and have a long flexural fatigue life. Because of the low friction coefficient and good abrasion resistance, internal abrasion of ropes is usually negligible. The fiber has high resistance to chemicals and excellent UV resistance, described as the ratio of the retention of strength to exposure time. When comparing Dyneema® to a polyester fiber, its UV resistance is nearly three times higher. Of tremendous value for fish passage applications, UHMWPE has excellent biological resistance. The fiber neither stimulates undesired growth nor is it sensitive to attack by microorganisms. It is regarded as biologically inert and is IARC classified 3 (not classifiable carcinogenic to humans) based upon its length-weighted geometric mean diameter.
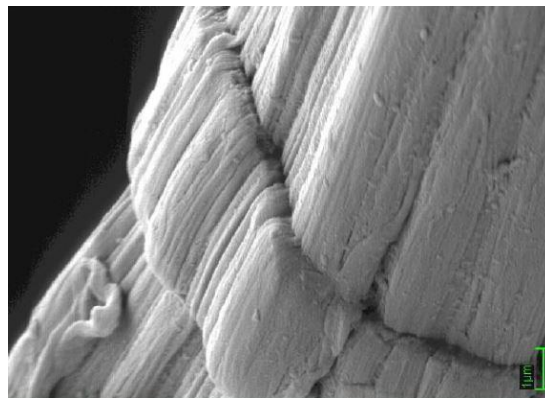
Figure 3. Electron Microscope View of UHMWPE, courtesy of DSM

According to Dave Erickson, a partner at Pacific Netting Products, "It is the combination of these fiber properties: strength, longevity, surface area, biological resistance, fatigue, and low friction coefficient, which have allowed engineers and designers to build modern fish guidance, barrier, and collection structures that are larger, stronger, last longer, and cost less to operate than anything built before."

3. ADVANCES IN DEBRIS CONTROL MATERIALS

Log booms have been used for years to protect facilities from debris, ice, and water borne traffic. Trees, often plentiful, were inexpensive and easily replaced. Constructed in a daisy chain method, the strength of log boom

systems was limited by the chain, wire rope and fittings and attachment methods used. Over time, log booms become waterlogged, and during their life, they will attract a variety of biological growth.

More recently, barriers for fish guidance and collection systems, as well as facility protection, visibility and demarcation, have been built using colorful, foam-filled plastic floats strung on a wire like a necklace. The floats are fabricated with rotational molding, or rotomolding, a casting process that is ideal for making hollow articles. When designed to be used as debris booms, the finished product can be filled with foam for floatation. Inexpensive, lightweight and easy to ship, these type of floats are similar to those that protect swimmers from boat traffic.

However, the end product can be adversely affected by such variables as ambient temperature, humidity, types of mold, material specification, and powder quality (Engineers India Research In, 2009). In addition, for heavy debris applications, the excessive amount of moving hardware and lack of continuity in the boom surface (gaps between floats), when combined with a lack of UV protection and minimal impact resistance, has resulted in limited life span and costly deployments.

Multi-Function Booms™, built by Pacific Netting Products (PNP), are built with custom extruded, high-density polyethylene. They are corrosion-free, rot-resistant, able to withstand temperatures to 140 degrees below zero, and feature excellent UV resistance, flexibility in design, and tremendous strength. A September 2015 pull test on a 24" diameter Multi-Function Boom, designed for medium debris applications, showed a safe working load of 34,000 Kg with an ultimate break of nearly 135,900 Kg on the HDPE floats.

The booms come standard with a keel for attachment of a debris curtain, temperature curtains, Dyneema Fish Barrier curtain, or a combination of these options. To enhance efficiency of operations and maintenance, especially in installations where fine mesh or wedge wire screens are installed, the booms are fitted with a debris splash guard. Access within a closed area is provided by means of a manually operated boat gate. To allow ease of shipping, configuration, and installation, booms are provided in 15 M sections with flanged ends for connection to other sections. They are anchored to the shore by embedment anchors, with the ability to attach mid-barrier bottom anchors as necessary.
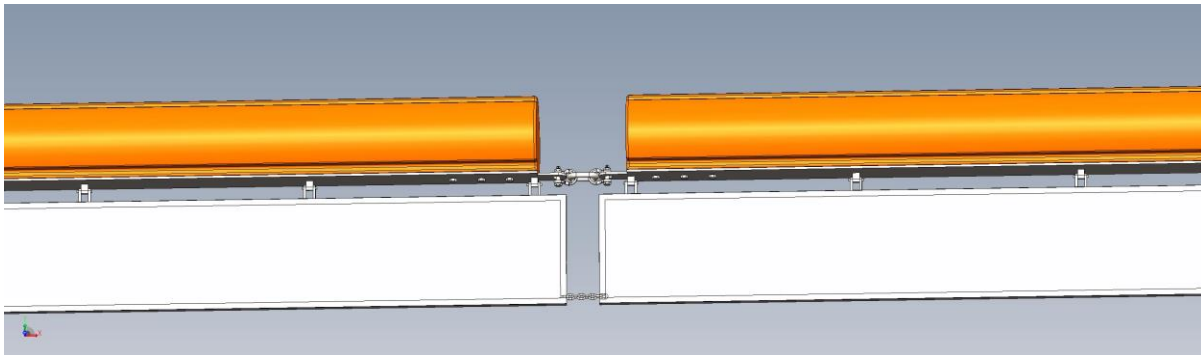
Figure 4. Typical rotomolded float boom with excessive moving hardware, as described above. Illustration: Pacific Netting Products

Figure 5: Degraded rotational molded boom. Photo: Andrew Peters, Pacific Netting Products

Figure 6. Multi-Function Boom™. Illustration: Pacific Netting Products

In a December 2015 installation at Portland General Electric's North Clackamas facility, a Multi-Function boom was installed to replace an existing log boom. The PNP boom was chosen to better protect the downstream fish passage collection system, which includes a floating surface collector and guide nets built of Dyneema®. To reduce operations and maintenance cost, the boom was aligned to guide debris to one side of the river for efficient removal of collected debris. With fewer moving parts, anchored securely to shore by embedment anchors, bolted together to form a long continuous surface, and built of a thick walled high density polyethylene, the expected operating life of the boom is 50 years with periodic maintenance.
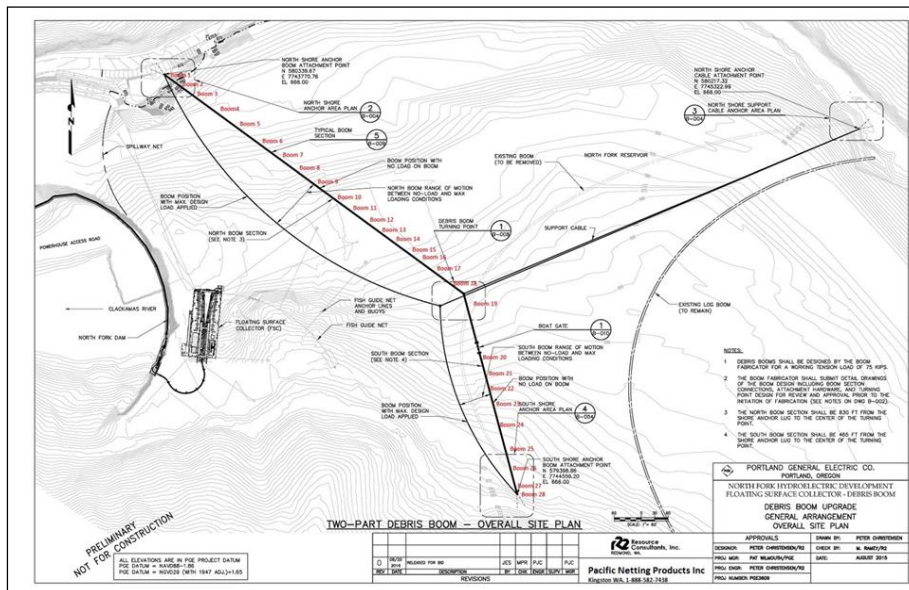
Figure 7. North Fork Clackamas Arrangement of Floating Surface Collector and PNP Multi-Function Boom

4. IMPROVED DESIGN AND CONSTRUCTION TECHNIQUES

Advances in materials for netting, flotation, and debris control has allowed designers the flexibility to install exclusion, guidance, and collection systems that demonstrate dramatic improvements in operations and maintenance. The lightness of the UHMWPE netting aids not only in shipping and installation logistics, but in deployment as well. Lighter weight means installations can be accomplished with fewer people and smaller, less costly equipment. A UHMWPE barrier net, with its specific gravity of less than 1.0 (DSM), can easily be anchored to the bottom of a waterbody with the net floating to the head rope. As a result, pool fluctuations can be accommodated so that the barrier net maintains a smooth shape and holds its position when the elevation of a reservoir changes. The result is a full exclusion net that provides complete fish passage protection.

The smaller surface area of UHMWPE fiber means a smaller size twine can be used to get a similar strength when compared to other fibers. The reduction provides less area for attachment of aquatic growth, and therefore, less material to clean. In addition, once attached, the UHMWPE smooth surface and natural abrasion resistant properties makes marine growth easier to remove.

Aquatic growth factors vary from site to site, influenced by water depth, bottom type, water clarity, and variables in the watershed (rainfall, snowmelt, or groundwater, topsoil, fertilizer). Generally, in cold, deep water, there will be little growth compared to warmer, shallow water. Net cleaning techniques and equipment will therefore depend on site considerations. In some applications where the net panel is flat and strung tight, machines can be used to maintain the netting. In other areas, sonic devices or manual brushing are more practical.

Figure 8: 731 M wide, 91 M deep guide net built of Dyneema®

5. CASE STUDIES

5.1. Puget Sound Energy, Upper and Lower Baker Lakes, Concrete Washington

The construction of two dams (Upper Baker: 95 M high, Lower Baker: 87 Mhigh) for the Baker River Hydroelectric Project, in the state of Washington created challenges for fish passage in that watershed. Baker river sockeye (O. nerka) are native to Baker Lake and Baker River, the tributary to the Skagit River. Artificial enhancement began in 1896 when the state of Washington built a hatchery on Baker Lake. The natural run at that time was estimated to be approximately 20,000 fish. Lower Baker Dam, which was constructed in 1925, creating Lake Shannon, blocked access to the lake. A ladder and "elevating contrivance" was constructed to provide passage. Adults were released above the dam to spawn naturally. Construction of the Upper Baker Dam was completed in 1959 and inundated the valley that included the natural Baker Lake (Washington Department of Fish and Wildlife).

In the late 1950s, Puget Sound Energy (PSE) built the world's first floating system to simulate swift river current behind a large, deep-water dam in order to attract and capture young salmon and transport them downstream. However, by 1980, just 99 fish returned to spawn. In the late 1980s, PSE modified commercial fishing nets to create partial depth fish guidance net systems. The enhanced system allowed downstream migration to steadily rise, reaching a record 20,225 fish in 2003. While showing promise, the materials and engineering were not suitable for long term, low cost deployment. Fluctuating pool levels made it difficult to keep the net in an effective shape. Debris tore the nets, and once a tear started, it could rip from side to side.

PSE and stakeholders enacted a number of strategies to support the watershed's fish populations. Pacific Netting Products installed full exclusion netting at both the upper and lower Baker Lake Dams in 2012. The 47000 Sq M nets were built of .635 cm- and .3175 cm mesh, 731 M in length, with an average depth of 91 M. One was built with Dyneema®, the other with a nylon fiber. Both were anchored to shore by embedment anchors, weighted down with chain and anchored to the bottom by ship's anchors. Both were built in a square-mesh design to maintain load and to accommodate pool fluctuations of up to 24 M. Supported with flotation, and protected by debris booms, the "v" shaped net "worked like an extension of the shoreline" to help guide the fish toward the floating surface collector (FSC) according to Ed Meyer, Senior Hydraulic Engineer for the National Oceanographic service (October 10, 2015 phone conversation).

The PSE exclusion barriers are deployed year-round. The effectiveness of the design of the full barrier net was proven dramatically in its first year of operations, as shown in the chart below. By 2014, over 1,000,000 downstream migrating salmon were counted, with returns of 60,000 to 100,000 adult fish expected in 2016. The anticipated lifespan of the Dyneema® exclusion barrier is 10 years. Operators report that aquatic growth is slow in the cold, deep water, and with excellent debris protection, there is minimal maintenance.

5.2. Bagnell Dam, Osage River, Camden County, Missouri

Bagnell Dam impounds the Osage River in south-central Missouri, creating the Lake of the Ozarks. The 45 M tall concrete gravity dam was built by Union Electric Company in 1931 for the purpose of hydroelectric power generation and is now owned and operated by the Ameren Corporation.

The presence of the dam and hydroelectric facility offered a number of challenges to fish and wildlife resource managers, including fish mortality at the dam. Of particular concern was the protection of American paddlefish (Polyodon spathula), which are endemic to the Mississippi River basin. Paddlefish are a basal Chondrostean ray-finned primitive fish that have evolved with few morphological changes since their earliest fossil records seventy to seventy-five million years ago (Oxford University Press).

Figure 10. Gated spillway at Bagnella Dam, Osage River, Camden

"One of the primary reasons for the decline in paddlefish populations is the loss of spawning and rearing habitat due to environmental alteration. Dam construction has eliminated spawning sites, interrupted natural spawning migrations, altered water flow, and eliminated backwaters that were important as nursery and feeding areas. Industrial contaminants, illegal fishing, and overexploitation by commercial and recreational anglers have also contributed to the decline. Unfortunately, population problems are not always immediately recognized because

paddlefish are long-lived and highly mobile, and their presence is sometimes construed as an indication that the species has not been adversely affected" (U.S. Fish and Wildlife Service).

In December of 2003, Alden Labs conducted studies of behavioral and physical deterrents to prevent paddlefish from impingement. Researchers investigated the effects of behavioral restraints such as low frequency transducers, strobe lights, and air bubble curtains. They also researched physical barriers including bar racks and barrier nets. The study showed paddlefish did not respond to behavioral interference but were effectively restricted by bar racks and exclusion barriers. Following an economic evaluation, the operators of the Ameren facility chose to install barrier nets.

Two exclusion nets built of Dyneema® were installed at the Bagnell Dam. A 366 M exclusion barrier, 36 M deep, built of 2.54 cm and 5.08 cm square mesh sufficient to prevent fish from being caught in it, was installed three meters in front of one of the turbine intakes on the lake side of the dam. 3.5 M upstream, a debris barrier net, 259 M long and 6 M deep, was installed to prevent damage to the fish exclusion nets. The nets were designed for single direction flow and periodic reverse directional currents with water velocities from 0.3 M to 1 MPS. They are anchored by concrete blocks and permanently installed.

Phillip Thompson, Ameren UE plant supervisor, Lake Ozark, MO, noted, "… it is very critical that the right material be chosen to make sure that you don't have a net failure that ultimately ends up impacting your operation of the turbine." Today, this installation successfully protects adult paddlefish from passing through the turbines, diverting their passage to safe routes, and allows Ameren to satisfy its regulatory obligations and deliver power to its customers.

5.3. Consumers Energy, Ludington, Michigan

The Ludington Pumped Storage Plant was built between 1969 and 1973. It sits along the Lake Michigan shoreline. The plant, jointly owned by Consumers Energy and Detroit Edison, is operated by Consumers Energy. It is one of the world's biggest pumped storage facilities. A 27-billion gallon reservoir feeds a set of six turbines that drive electric generators, which double as pumps to fill the reservoir again with water from Lake Michigan. At night, when electric demand is low, Ludington's reversible turbines pump water 110 M uphill from Lake Michigan. The water is pumped through six penstocks, to the 842-acre reservoir. During the day, when electric demand is high, the reservoir releases water to flow downhill through the penstocks (Consumers Energy).
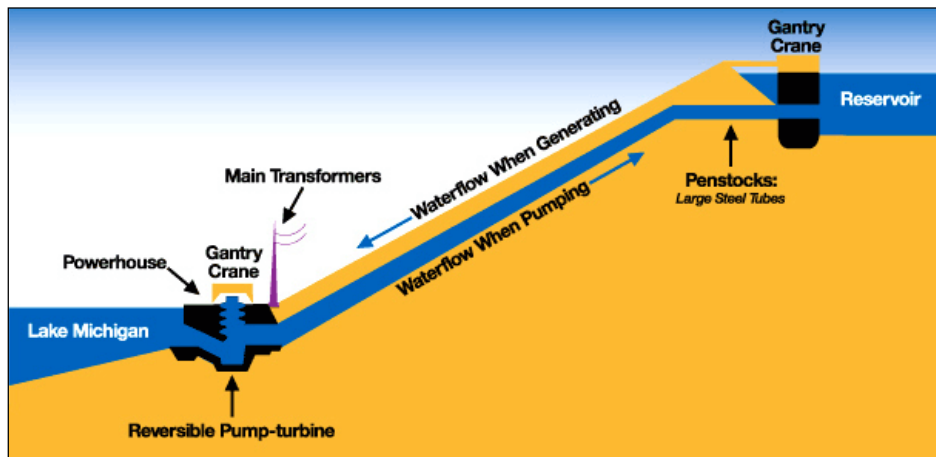
Figure 9. Luddington Pumped Storage Facility. Illustration: Consumers Energy

To protect alewives, yellow perch, salmon, and trout from being impinged and entrained during plant operations, Consumers Energy installed a 2.5 mile long barrier net in 1998. The 56,000 Sq. M barrier, which averages about 17 M in depth, was built in 62 sections using 1.27 cm and 1.9 cm Dyneema® netting. Anchored from subsurface steel

embedment anchors, it is designed for bidirectional currents and water velocities of 1.0 – 3.0 fps in ocean-like conditions with rolling surf. As velocities increase, the net floats release pressure while maintaining the net's position and effectiveness. Late each fall, the net is removed for Michigan's severe winter season when fewer fish are active. Each spring it is redeployed.

This barrier, which requires continual maintenance, is the longest in the world of its type. The installation design has proved effective in protecting fish while enabling Ludington to continue as an economical generator of electricity (Consumers Energy).

6. CONCLUSION

The ultimate goal of allowing the most efficient and economical use of water power without adversely impacting marine life is within reach thanks to the development of modern materials and advances in engineering. Using ultra high molecular weight polyethylene and modern flotation and debris booms, engineers can now design massive fish exclusion, guidance, and collection structures in locations previously unserved by viable options for fish protection. Current technology allows standard mesh sizes as low as .635 cm, preventing the impingement and entrainment of important or threatened species.

The principles and materials outlined in this paper can be adapted to environments around the world. Of course, each facility's unique site conditions, which include consideration of bathymetry, shoreline topography, pool fluctuation, water flow, size and type of debris, boat traffic, icing, weather, seasonal or permanent deployment, as well as consideration of impacted aquatic species, must be addressed in the design and installation of each system. With careful consideration and implementation, humans will be able to continue to harness our most valuable resource with respect for the wider social and economic health of the planet.

7. REFERENCES

Consumers Energy, https://www.consumersenergy.com (October 8, 2015).

DSM Company, http://www.dsm.com/products (October 15, 2015).

Encyclopedia Britannica, http://www.britannica.com/biography/Joseph-Wilson-Swan (October 15, 2015).

Engineers India Research In, (2009). "Rotational Moulding Technology Handbook."

Oxford University Press, http://gbe.oxfordjournals.org (November 1, 2015).

Phillips Petroleum Company (1999). "Discovery of Polypropylene and the Development of a New High-Density Polyethylene." American Chemical Society, Washington, DC.

U.S. Fish and Wildlife Service, https://www.fws.gov/midwest/fisheries (October 10, 2015)

Washington Department of Fish and Wildlife. <http://wdfw.wa.gov/fishing/salmon/sockeye/baker_river.html> (October 15, 2015).

Wolfe, A.J. (2008). "Nylon: A Revolution in Textiles." Chemical Heritage Foundation.

Junction Chamber at Vortex Drop Shaft: Case Study of Cossonay

G. Crispino[1,3], D. Dorthe[2], T. Fuchsmann[2], C. Gisonni[1] and <u>M. Pfister</u>[3]
[1]Dept. of Civil Engineering, Design, Building and Environment (DICDEA)
Second University of Naples (SUN)
Aversa, CE 81031,
Italy
[2] Ribi SA Ingénieurs Hydrauliciens
Lausanne, CH 1015,
Switzerland
[3] Laboratory of Hydraulic Constructions (LCH)
École Polytechnique Fédérale de Lausanne (EPFL)
Lausanne, CH 1015,
Switzerland
E-mail: michael.pfister@epfl.ch

ABSTRACT

The drainage network of the city of Cossonay (Switzerland) is currently being adapted for future needs. In particular, it is required to drain increased storm discharges due to a population augmentation and to provide an adequate concept to overcome unfavorable geotechnical conditions. Vortex drop shafts are sewer manholes commonly applied in steep urbanized topographies to connect conduits across large elevation differences. In Cossonay, the existing 48 m high vortex drop shaft, with a diameter of 1.5 m, allowed the storm discharge to flow from the city to a watercourse issued at half of the valley height. The discharge capacity was initially assumed as 4.1 m³/s, but frequent pulsations and choking phenomena implied a reduced effective capacity of around 3.0 m³/s. A new planned vortex drop shaft will collect the supercritical inflows of four collectors in the old City Centre and spill them through a shaft of roughly 120 m height, restituting the flow at the valley bottom. It was pre-designed using FLOW-3D simulations to estimate the hydraulic features of the incoming flows and to predict the hydraulic behavior of the upper elements (before the water enters the shaft). The simulation thus included a novel junction chamber type and a steep inlet channel before the spiral intake. The numerical simulations provided a first layout of the structure that was then validated by physical model tests. The physical model was built at the Laboratory of Hydraulic Constructions (LCH) of École Polytechnique Fédérale de Lausanne (EPFL).

Keywords: Sewer. Fall manhole. Vortex drop shaft. Physical model. Numerical model. Design discharge.

1. INTRODUCTION

Fall manholes are commonly used in drainage systems of steep topographies. They convey discharges by connecting collectors at considerably different elevations to dissipate energy and generate adequate flow conditions in the drainage systems. Depending on the elevation difference between upper and lower collectors, two fall manhole types exist. For smaller differences of elevation, up to 7 m, a classical drop manhole (SIA 1980) is adopted. Conversely, if drop height results are larger than 5 m, vortex drop shafts are applied (Gisonni and Hager 2012).

Vortex drop shafts efficiently dissipate the flow energy. They consist of three components: intake structure, vertical shaft, and outlet structure. The intake structure orientates the flow, among others, from horizontal to vertical. Furthermore, it produces an annular stable vortex flow in the shaft. For supercritical flows, Kellenberger (1988) proposed a spiral intake type in which the flow is forced to adhere to the walls. Drag along the shaft is responsible for the relevant energy dissipation.

Herein, the authors describe the vortex drop shaft that is to be added to the storm water net of Cossonay. The new structure will replace the existing vortex drop shaft to meet geotechnical and hydraulic requirements. In particular, the old vortex drop shaft has to be substituted for the following reasons:

- The air transport was not secured because of the presence of an orifice at the toe, and, consequently, choking and pulsations phenomena occurred.
- The growth of the population and the larger storm water flows required the vortex drop shaft design to increase discharge capabilities to 12.61 m^3/s.
- The tailwater gallery placed at the toe of the old vertical shaft returned the storm water flow in the water course "Rochettes". This stream flows along a slow landslide, resulting in the erosion of river bed and banks. Possible river restoration works were discarded because they cannot guarantee that the water course will be stabilized. Conversely, a new and higher vortex drop shaft allows for overstep of the entire landslide area.
-

The new concept (Fuchsmann and Périsset 2013) considers a vortex drop shaft with a larger drop height of 120 m located outside of the landslide area. It will be placed in the city centre where both storm water collectors and sewers arrive. The necessity to minimize the construction volume and to ensure adequate flow conditions entering the inlet structure (Pfister et al. 2013) provided motivation for a common junction chamber for all arriving collectors. This solution allows for a steep and short inlet channel to accelerate the flow before entering the spiral intake. This concept seems novel and no design rules are available, so it was necessary to carry out a comprehensive design. The design was composed by three phases:

1. A preliminary hydraulic design of the individual components;
2. A FLOW-3D simulation of the inlet structure (Dorthe 2013, 2014), including the junction chamber and the inlet channel (Figure 1); and
3. Physical model tests at the Laboratory of Hydraulic Constructions (LCH) of École Polytechnique Fédérale de Lausanne (EPFL).
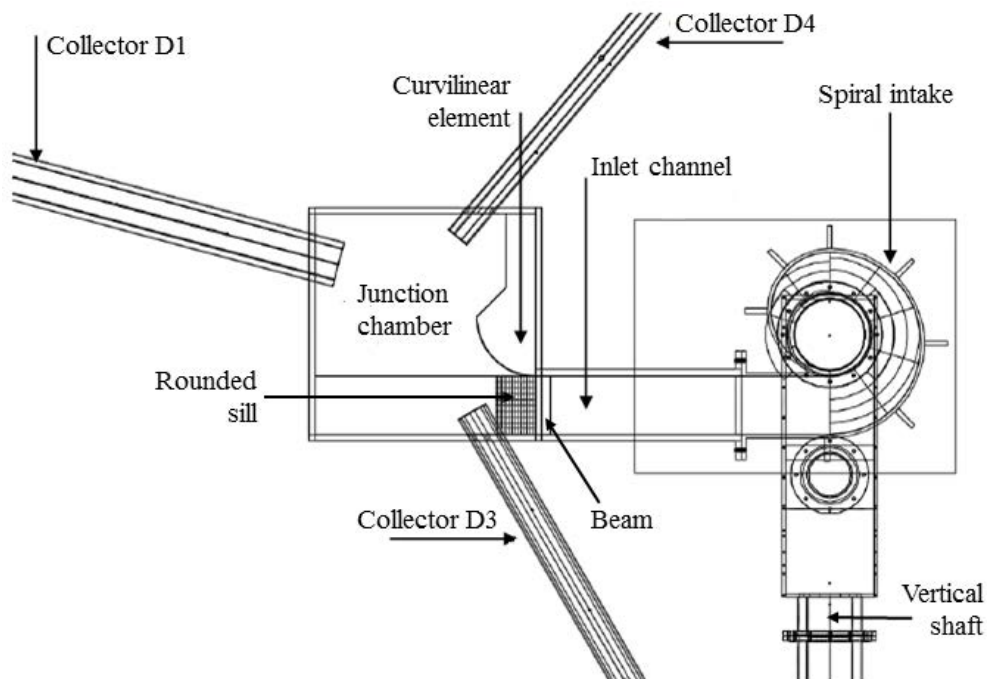
Figure 1. Plan view of the inlet structure (modified from Fuchsmann et al. 2015)

2. PRELIMINARY HYDRAULIC DESIGN

A preliminary hydraulic design (Dorthe 2013, 2014) was performed to assign minimum dimensions to the individual components of the vortex drop shaft. This stage was preparatory for further numerical and physical model tests.

Shape and dimensions of the junction chamber were chosen to guarantee an adequate volume to join the incoming flows. The chamber is almost square-shaped (Figure 2a), and it was orientated to facilitate the flow inlet towards the steep inlet channel. Moreover, a curvilinear element was added in proximity to the channel inlet to orient the flow. The first draft of the curvilinear element was shaped according to Army Engineer Waterways Experiment Station (WES) "entrance with roof curve" (ASCE 1957). The position of junction chamber with reference to the collectors was defined so that all the inflows merged at one point and no jet was directly oriented towards the inlet channel. The inlet channel allows the establishment of a stable supercritical flow needed to homogenize the flows, prevent hydraulic singularities, and ensure stable annular flow along the vertical shaft (Kellenberger 1988). This recommendation implies that Froude numbers should be larger than $\mathsf{F} = 2.50$ at the outlet cross-section. The channel length L_c and width b were 10.0 m and 2.0 m, respectively, and the slope was $S_c = 20\%$.

The supercritical spiral intake (Figure 2b) was designed according to the standard of Kellenberger (1988). Hager (1990) recommends uniform and stable free-surface flow at the entrance of the spiral. The elevation difference between the intake and the outlet structures gives the shaft height. The required shaft diameter D_s is related to the discharge capacity, herein with $Q_M = 12.61$ m³/s as (Kellenberger 1988)

$$Q_M = [g \cdot (D_s/1.25)^5]^{0.5} \tag{1}$$

Equation (1) results in D_s=2.18 m. After that, a shaft diameter D_s=2.40 m was chosen to assign a discharge margin to the vortex drop shaft.

The dissipation chamber (Figure 2c) dissipates the remaining flow energy and de-aerates the flow. Flow pulsations and breakdown of the air circulation should be avoided by designing adequate chamber dimensions. Thus, the standard configuration according to Kellenberger (1988) is foreseen. The dissipation chamber resulted as 10.0 m long, 3.0 m wide, and 5.0 m high. The chamber was also equipped with a de-aeration system consisting in an aeration pipe placed on the chamber top. The aeration pipe diameter was $D_a = 1.40$ m.
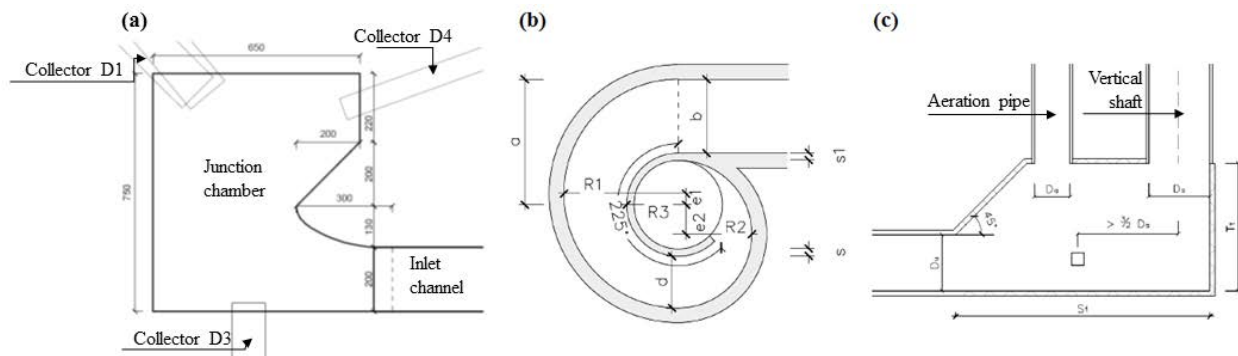
Figure 2. Sketches of vortex drop shaft components for the hydraulic preliminary design: (a) junction chamber, (b) spiral intake and (c) dissipation chamber (modified from Dorthe 2014)

3. NUMERICAL SIMULATION

A numerical FLOW-3D simulation was performed (Dorthe 2013, 2014) to verify the hydraulic behaviour of the structure resulting from the preliminary hydraulic design. The numerical model involved the collectors, the junction chamber, and the inlet channel. The junction chamber joins flows delivered by four collectors. The spiral intake, the vertical shaft, and the outlet structure were not simulated. Their performance depends strictly on the approach flow

conditions generated by the end of the inlet channel. If the simulated upper part of the system works adequately, then assume that the lower part will also operate as foreseen.

At first, numerical simulation did not show an optimal operation of the inlet structure derived by the preliminary design process. The free-surface in the junction chamber was irregular, and shock waves occurred along the inlet channel. Consequently, the flow orientation towards the spiral intake was poor, and Froude numbers of the flow entering the spiral intake were not in the achieved range. For these reasons, some modifications were introduced and tested by further simulations. In particular, the following changes were included:

- The curvilinear element in the junction chamber was simplified to a circular shape.
- An ogee-like sill (Fig. 1) was inserted to generate a critical section at the channel inlet and to increase the water volume in the junction chamber. The profile was designed to avoid sediment deposition in the chamber.
- A horizontal beam (Fig. 1) was inserted with the goal to break the flow rotation.
- The inlet channel slope was increased to 30% to accelerate the flow and, thereby, make the free-surface more regular.
- The altitude of the chamber invert was raised to tranquilize the flow in the junction chamber and to gain adequate flow acceleration along the inlet channel.
- The global inlet structure was rotated by 30° with reference to three collectors to optimize the flow stability at the inlet channel.
-

The above modifications were partially combined so that four set-ups were tested:

(1). Corresponding to the initial set-up. Its hydraulic performance results were not optimal.
(2). Including modifications of the junction chamber and the inlet channel but without any global rotation. The modelling highlighted an improvement in terms of free-surface flow pattern.
(3). As (1) but with a global rotation. The hydraulic behavior was better than in set-up (1).
(4). As (2) but with a global rotation. A pronounced improvement regarding flow stability and regularity was observed in the junction chamber and the inlet channel.

Figure 3 shows a comparison of the set-ups (1) and (4). The inlet cross-section of the channel is affected by a shock wave on the right channel wall for set-up (1) (Fig. 3a). This shock wave is absent in set-up (4), among others, due to the horizontal beam (Fig. 3b). Similarly, the middle and outlet cross-sections were initially characterized by the occurrence of surface irregularities (Fig. 3c, e), which were reduced in set-up (4) (Fig. 3d, f).

These qualitative impressions are supported by comparison criteria considering the free-surface regularity, the flow orientation, and the hydraulic stability. The first criterion relates to the transverse flow depth standard deviation. This parameter was used for quantifying the dispersion of flow depths around the average value by considering three inlet channel cross-sections. The second criterion includes the flow orientation by means of the velocity vectors angle α at the channel outlet with reference to the channel axis. The third criterion was based on the Froude number F_u at the channel outlet cross-section. The corresponding values of these criteria are listed in Table 1. As visible, the modifications included in set-up (2) allowed homogenizing the free-surface in comparison with the un-modified set-up (1). At the same time, the global rotation employed in set-up (3) improved the flow orientation. Overall, the set-up (4) seems most preferable, being characterized by sufficient a Froude number F_u. Accordingly, set-up (4) was retained for further investigations.
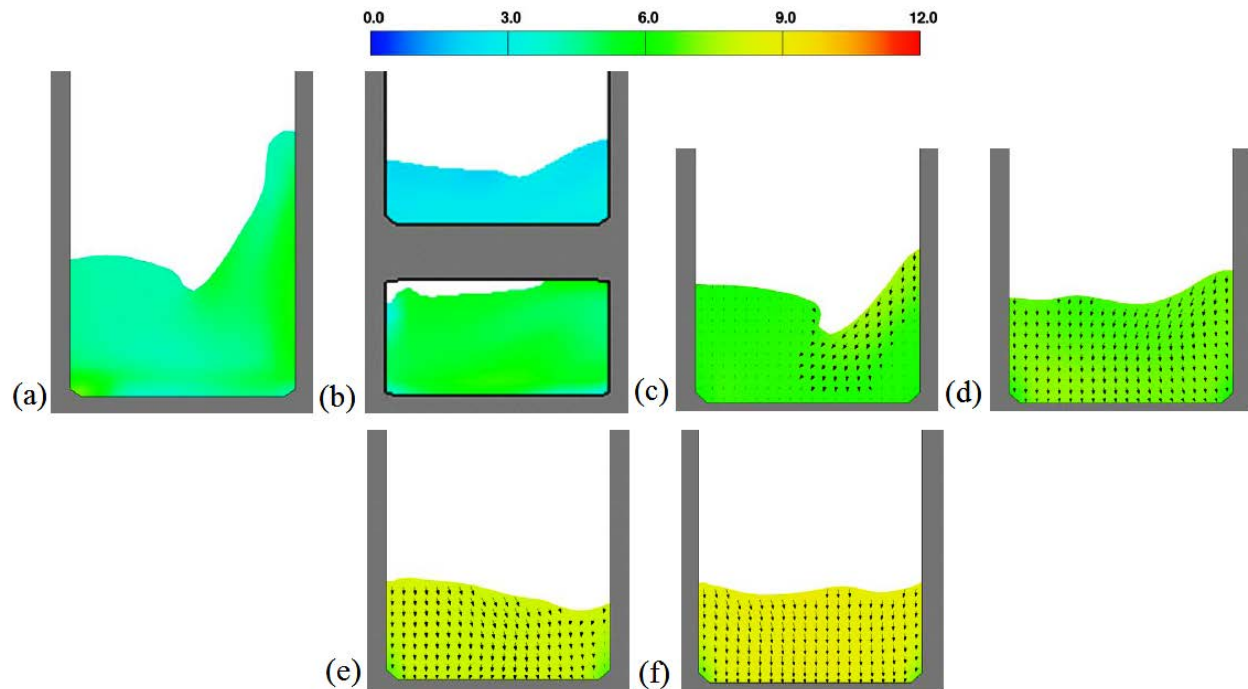
Figure 3. Simulated transverse velocity and free-surface profiles at different inlet channel cross-sections for set-ups (1) and (4), namely (a) and (b) inlet cross-section for set-ups (1) and (4), (c) and (d) middle cross-section for set-ups (1) and (4), and (e) and (f) outlet cross- section for set-ups (1) and (4) (modified from Dorthe 2014)

Table 1. Numerical values of criteria used for comparing set-ups for a discharge of Q = 12.61 m³/s (from Dorthe 2014)

Criteria	Set-up (1)	Set-up (2)	Set-up (3)	Set-up (4)
Free-surface regularity, standard deviation				
at the channel outlet (at $1.00 \cdot L$)	0.07 m	0.05 m	0.06 m	0.03 m
at $0.75 \cdot L$	0.14 m	0.08 m	0.11 m	0.06 m
at $0.50 \cdot L$	0.15 m	0.11 m	0.12 m	0.09 m
Flow orientation				
α	1.8°	1.5°	1.1°	1.1°
Hydraulic stability				
F_u	2.8	3.1	2.9	3.1

4. PHYSICAL MODEL INVESTIGATION

The significance and complexity of the vortex drop shaft – including aspects related to air transport along the shaft – requested for a verification of its hydraulic comportment in physical model tests. Thus, a physical model was built at the *Laboratory of Hydraulic Constructions* (LCH) of EPFL Lausanne (Fig. 4). The model reproduced the complete structure (set-up (4) from numerical simulations). The Froude similarity was applied as typical for gravity driven free-surface flows. A geometrical scale factor of 1:7.82 was chosen.

The experimental set-up (Fig. 4) consisted of the junction chamber and the inlet channel (made of painted formwork plates). Three (out of four) transparent PVC pipes (collectors) spilled their discharges into the chamber. The fourth collector was not physically modelled, being considered not relevant due to its small discharge. Thus, the discharge conveyed by this collector was summed proportionally to the other three. The collector lengths were equal to $15 \cdot D$ to ensure adequate flow conditions at the chamber. A supercritical spiral-type intake was provided at the end of the inlet channel. The vertical shaft was made up with a transparent PVC pipe. At the toe of the shaft, the dissipation chamber

made of PVC was provided. The chamber was equipped with an aeration pipe to secure adequate de-aeration of the flow. Finally, a PVC tailwater conduit with a slope $S_o = 1.5\%$ was the tailwater gallery.

The main hydraulic parameters were measured and recorded for each run. In particular, the total discharge in the individual collectors was measured by using electromagnetic flowmeters with a full scale accuracy (FS) of 0.5%. The flow depths in the junction chamber and along the inlet channel were measured by point gauges. A micro-propeller was used to record the velocities along the inlet channel and the spiral intake. Free-surface profiles along the spiral intake were discretized by using a point gauge. The rotational flow angles along the vertical shaft were also recorded. The dynamic pressures were recorded in the dissipation chamber with piezometers. Flow depths were measured inside the dissipation chamber and along the tailwater conduit. Finally, air velocities in the aeration pipe were measured by an anemometer.

Several discharges Q were tested. Herein, the scenarios included in Table 2 are considered. These values correspond to discharges between 50% to 140% of the design discharge Q_d. The discharge of scenario D exceeds the vortex drop shaft discharge capacity, $Q = 16.00$ m³/s according to Eq. (1). For this "overload" scenario, which is of interest regarding the reliability of the structure, no particular phenomena (such as pulsations, choking, or insufficient de-aeration) occurred, and the annular air-water flow in the vertical shaft was preserved. This evidence seems to suggest that vortex drop shafts designed following the literature recommendations may guarantee a safety in terms of discharge capacity.
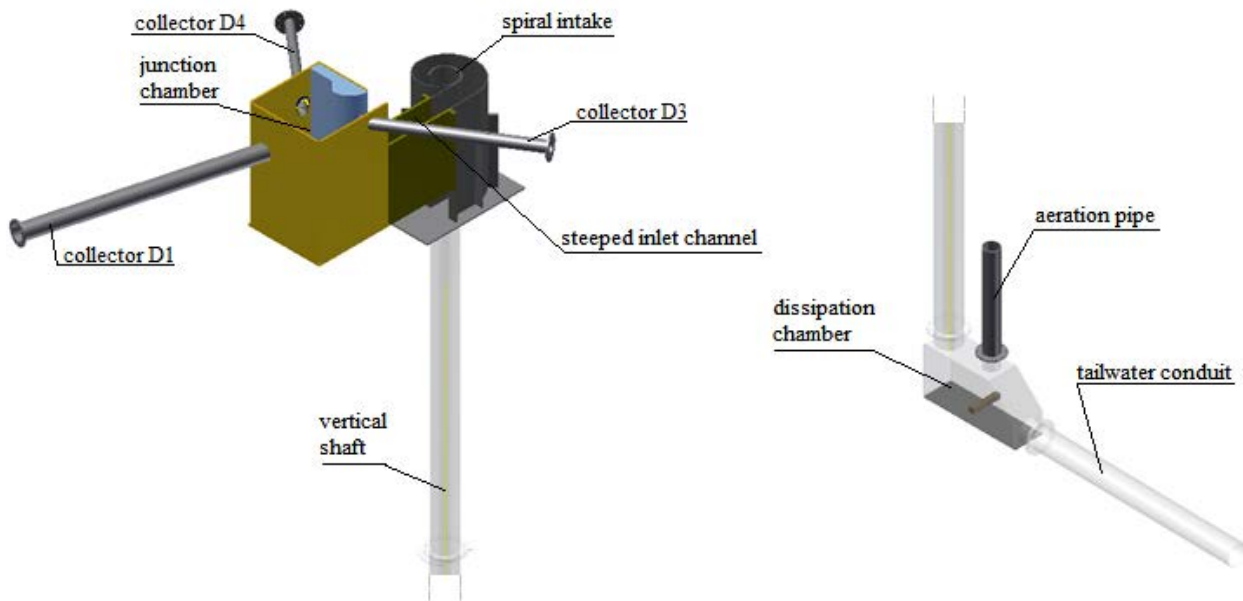
Figure 4. Sketch of the physical model (modified from LCH 2015)

Table 2. Test program

Scenario	Discharge [m³/s]
A: 50%·Q_d	6.43
B: 75%·Q_d	9.54
C: 100%·Q_d	12.70
D: 140%·Q_d	17.39

4.1. Hydraulic performance

4.1.1. Junction chamber and inlet channel

Figure 5a shows the free-surface profiles for scenarios A to D. No data are recorded below the collectors because their presence hindered the instrumentation placement. The free-surface appears regular, being almost horizontal from point D to point G (Fig. 5b), confirming the results of the numerical simulation corresponding to the set-up (4). Water surface level differences are below some 0.6 m in scenario D when ignoring the area near the curvilinear element (point B). There, the free-surface was affected by a swell induced by the impact of flow on the curvilinear element. Nonetheless, the swell height was such that it remained in the chamber. More importantly, the flow coming from the collector D1 was not affected (no hydraulic jump was observed) despite the water level being close to its top. This is due to the large momentum of the collector flow, requiring a larger conjugated depth than available.
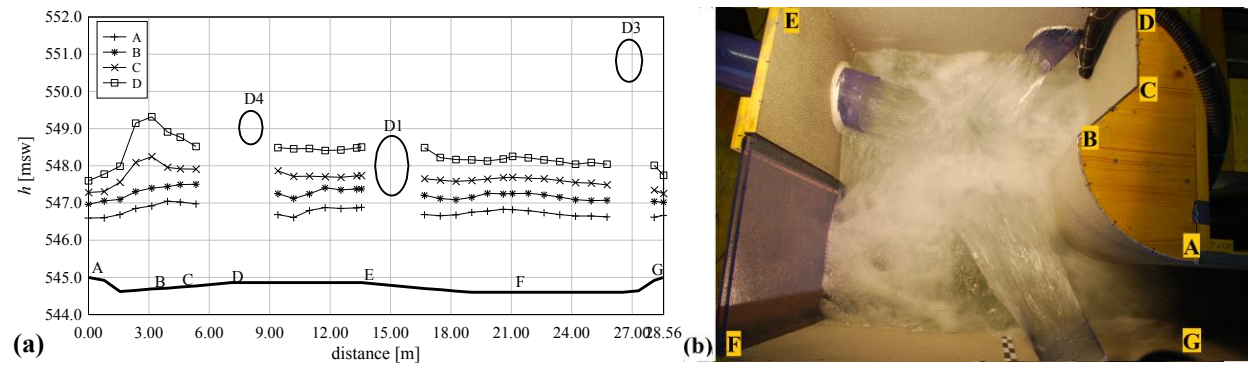
Figure 5. (a): Free-surface profiles detected in the junction chamber perimeter, (b) top view of the junction chamber flow pattern for scenario C

A supercritical flow profile was observed along the inlet channel. Flows are mainly accelerating along the first half of the channel and almost in the uniform flow regime along the second half (Figure 6). It is noticeable that the inlet flow depths at the inlet cross-section exceed the beam elevation and overtop it, at least for the herein presented discharges. The beam acts as a combination of a gate and a broad-crested weir. Froude numbers $F_u = V_u/(g \cdot h_u)^{0.5}$ between 2.42 (scenario D) and 4.10 (scenario A) were derived at the channel end. These values roughly support the outcomes of the numerical simulations, according to which the Froude number related to the design scenario was $F_u = 3.10$ (Table 1) against the physical model Froude value of $F_u = 2.70$.
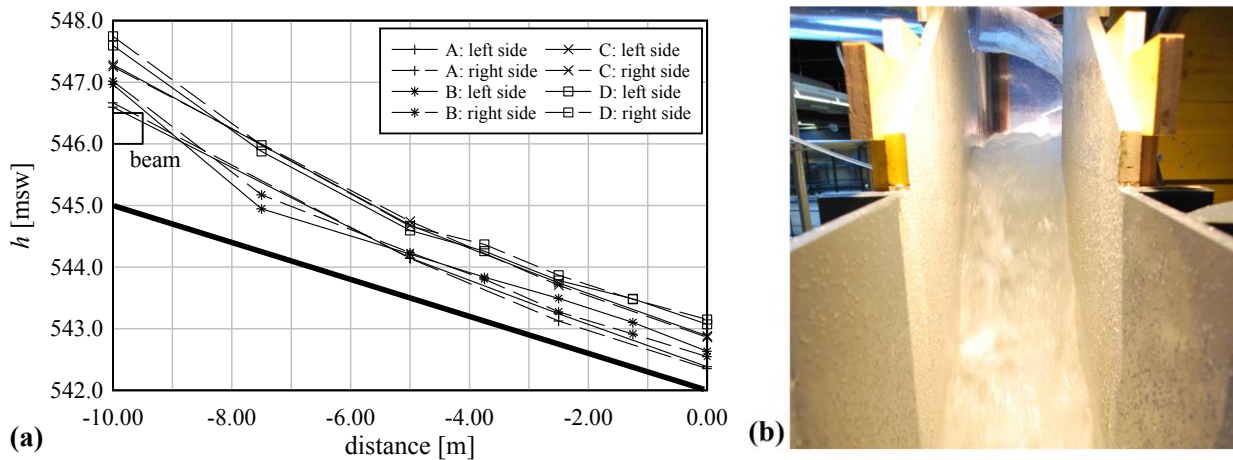
Figure 6. (a): Free-surface profiles along left and right sidewall of the inlet channel, and (b) view of the inlet channel flow under scenario D

Figure 7 shows the free-surface profiles along the external sidewall of the spiral intake. The supercritical approach flow generates a pronounced shock wave because of the abrupt deviation at the spiral intake. Hager (1990) observed only one, single-standing shock wave for highly supercritical approach flow ($F_o = 5.70$), whereas two maxima were observed for $F_o = 1.80$. Here, approached Froude numbers F_o were between 2.42 and 4.10, and two maxima were observed.
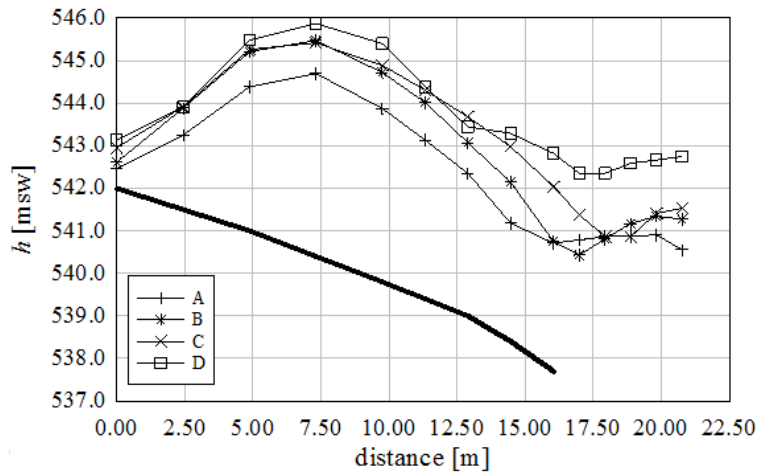
Figure 7. Free-surface profiles along the external sidewall of the spiral intake

4.1.2. Vertical drop shaft

The annular flow along the shaft was stable even under scenario D with a discharge exceeding the design value (Fig. 8). No collapse of the central air core or pulsations was observed. The approach flow was set in rotation by the spiral intake, producing the achieved annular flow in the shaft.

Figure 8. side view of the central air core at the inlet of the vertical drop shaft for scenario D

4.1.3. Outlet structure

The vertical jet issued by the shaft impinges on the dissipation chamber bottom and abruptly changes its direction to the horizontal. If the outlet structure works adequately, the energy of the impinging water mostly disperses, and the flow entering the tailwater gallery is subcritical.

The dissipation chamber showed an adequate performance. Pulsations or a breakdown of the air circulation was not observed, and the outflow from the shaft was never submerged despite the overload discharge in scenario D (Fig. 9b). Mixture air-water flow depth and pressure measurements were carried out in the dissipation chamber. Fig. 9a shows the average free-surface water levels inside the dissipation chamber for scenarios A to D. Obviously, the large inflows generated a relevant turbulence in the chamber, with flow depths touching the 45°-sloped chamber top.
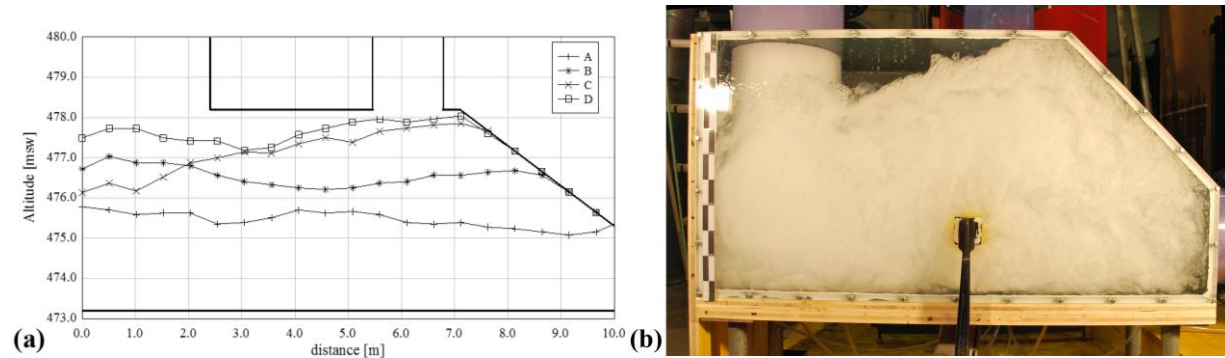
Figure 9. (a): Free-surface profiles in the dissipation chamber, and (b) mixture flow pattern for scenario D

5. CONCLUSIONS

A new vortex drop shaft is planned in Cossonay (Switzerland) with a design discharge of 12.61 m^3/s, a total drop height of around 120 m, and a shaft diameter of 2.40 m. It replaces the existing vortex drop shaft, which was affected by several hydraulic and geotechnical constraints. The proposed concept herein combines several inflow collectors arriving at various elevations with a standard vortex drop shaft. A common junction chamber merges four collectors, minimizing the construction volume and providing only one single inlet channel. This technical solution has never been discussed systematically in the literature, so a detailed hydraulic design was required.

A preliminary "manual" hydraulic design indicated the geometry of all individual components according to the standard recommendations. In the frame of a numerical simulation, the hydraulic behavior of the inlet structure elements (collectors, junction chamber, inlet channel) was verified. The simulations showed which modifications to the inlet structure geometry were required, namely a global rotation of the structure to improve the flow features in the chamber, the set-up of the chamber with a sill and a beam, and the slope of the inlet channel.

Physical tests in a scale model (1:7.82) were carried out to verify the design of the entire structure. The overall performance of the vortex drop shaft was adequate. Choking and pulsations phenomena were absent during the design discharge run. Furthermore, the physical model results showed that vortex drop shaft discharge capacity was larger than the design value.

6. REFERENCES

ASCE (1957). "Sluice entrances flared on four sides pressure-drop coefficients". WES, *US Corps of Civil Engineers*, Vicksburg, MS, 211-1-211-1/2.

Dorthe, D. (2013). "Conception et dimensionnement d'un puits à vortex" (Concept and design of a vortex drop shaft). Projet de Master, Ecole Polytechnique Fédérale de Lausanne (EPFL), Lausanne (Switzerland). [in French].

Dorthe, D. (2014). "Dimensionnement d'un puits à vortex combinant quatre conduites d'arrivées" (Design of vortex drop shaft combined with a junction chamber merging four collectors). M.Sc. thesis, Laboratory of Hydraulic Constructions (LCH), Ecole Polytechnique Fédérale de Lausanne (EPFL), Lausanne (Switzerland). [in French].

Fuchsmann, T., and Périsset, P. (2013). "Etude du vortex existant et de solutions d'évacuation des eaux - rapport technique" (Hydraulic study of the existing vertical drop shaft and analysis of the alternative solutions – technical report). Ribi SA, Lausanne (Switzerland). [in French].

Fuchsmann, T., Dorthe, D., Pfister, M. (2015). "Exemples de projet: Le nouveau puits à vortex de la ville de Cossonay" (Design example: The new vortex drop shaft in the City of Cossonay). *Séminaire Hydraulique des canalisations*, VSA/EPFL, Lausanne (Switzerland), in press. [in French].

Gisonni, C., and Hager, W.H. (2012). Idraulica dei sistemi fognari: Dalla teoria alla pratica, Springer-Verlag, Milan (Italy). [in Italian].

Hager, W.H. (1990). "Vortex drop inlet for supercritical approaching flow". *J. Hydraul. Eng.*, 116(8), 1048–1054.

Kellenberger, M. (1988). "Wirbelfallschächte in der kanalisationstechnik" (Vortex drops in sewers). Mitteilung 98. Versuchsanstalt für Wasserbau, Hydrologie und Glaziologie (VAW), ETH: Zürich (Switzerland). [in German].

LCH (2015). Puits à vortex – Commune de Cossonay; Etude sur modèle physique (Vortex drop shaft – City of Cossonay; Physical model study). Rapport intermédiaire 3/2015, LCH, EPFL, Lausanne (Switzerland). [in French].

Pfister, M., Gökok, T., and Gisonni, C. (2013). "Les jonctions avec des écoulements torrentiels" (Free-surface junctions). *Séminaire Hydraulique des canalisations*, VSA/EPFL, Lausanne (Switzerland), 107-124. [in French].

SIA (1980). "Sonderbauwerke der Kanalisationstechnik" (Special structures in sewer techniques). SIA-*Dokumentation 40*, Schweizerischer Ingenieur- und Architektenverein, Zurich (Switzerland). [in German].

Piano Key Weir for Enlargement of the West Fork of Eno River Reservoir

B.M. Crookston[1], L. Crowley[1] and M. Pfister[2]
[1]Schnabel Engineering, LLC.
11-A Oak Branch Drive
Greensboro, NC 27407
USA
[2]Laboratory of Hydraulic Constructions (LCH), Ecole Polytechnique Fédéral de Lausanne (EPFL)
CH-1015, Lausanne
Switzerland
E-mail: bcrookston@gmail.com

ABSTRACT

The West Fork of Eno River Reservoir Dam is located near Hillsborough, North Carolina, USA. The earthen embankment dam provides an impoundment used by the town for water supply. The project was originally completed in 2000 with forethought by the owner for an expansion, which was anticipated in the original design. Currently, the design of that expansion to raise the reservoir level for increased water supply is underway. Following a detailed analysis of viable upgrades, a piano key (PK) weir (anticipated as the first to be constructed in the USA) was selected by the owner due to its effectiveness in meeting project requirements. Presented in this paper are the site-specific characteristics of the existing auxiliary chute spillway, the proposed PK weir, and additional modifications to the chute. This paper also presents site-specific information including the existing auxiliary chute spillway, the new PK weir, and additional modifications to the auxiliary chute. The results include the comparison of four PK weir hydraulic design methods for sizing the spillway. Details and results of a CFD model are also included. Finally, additional significant design considerations are presented, which include anticipated hydraulic conditions in the downstream chute and identified existing structure deficiencies; estimated spillway design flood hydraulic force distributions taken from the CFD model; the PK key weir stability summary; and other important project aspects including embankment modifications and seepage control measures. It is anticipated that this project will be of interest to those concerned with dam safety and will further encourage the consideration of PK weirs in the USA.

Keywords: Piano Key Weir, Spillway Upgrade, Water Supply, Lateral Spillway, CFD

1. INTRODUCTION

It is not uncommon for passive spillways (i.e., various weir types) to be implemented as a risk reduction measure to address dam safety issues related to spillways. Such concerns may be related to spillway capacity, hydrologic loadings on the system including hydraulic structures, or operations and maintenance. New dams, levee networks, and upgrades related to water supply also regularly make use of these hydraulic structures. Weirs may be among the oldest and most ubiquitous control structures used in water supply systems.

In North Carolina, USA, the Town of Hillsborough uses the West Fork of Eno River Reservoir (surface area of 0.9 km²) for water supply. Originally constructed in 2000, water is impounded by a 760-m (2,500 ft) long, 18.9-m (64-ft) high earthen embankment. The dam features two spillways; the primary spillway is the intake tower. The auxiliary spillway (see Figures 1 and 2) is an atypical lateral or side-channel spillway – the control section is a 65.5-m (215-ft) long, 4.6-m (15-ft) wide broad-crested weir immediately followed by a converging chute with a 70° bend left (oriented downstream) that reduces the chute width by over 60%. The 24.4-m (80-ft) wide chute terminates with a small hydraulic jump stilling basin.

Figure 1. The Existing Auxiliary Spillway for West Fork of Eno River Reservoir Dam looking upstream at control section (A), control section (B), and chute (C)
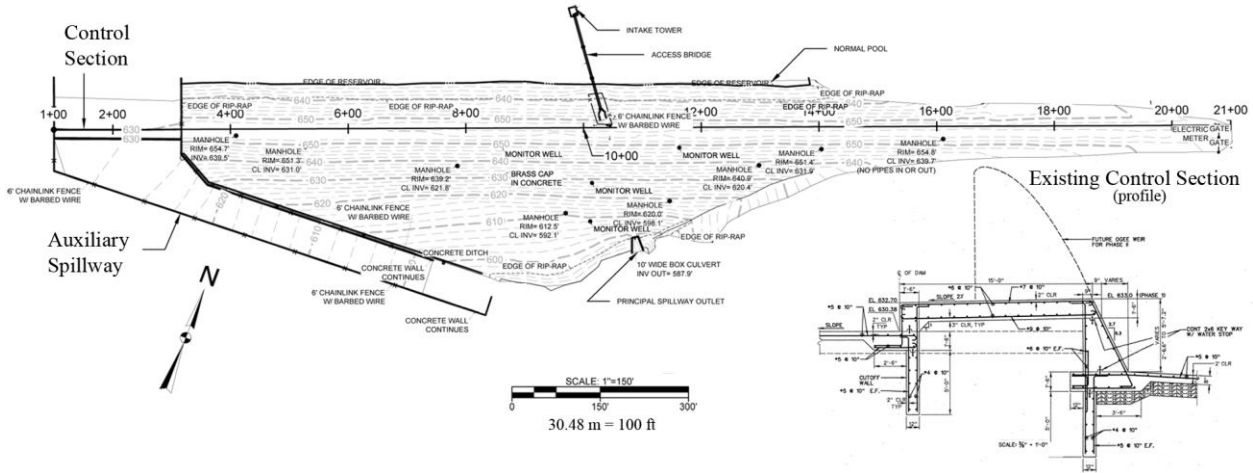
Figure 2. Schematic of existing auxiliary spillway for West Fork of Eno River Reservoir Dam and detail of broad crest and originally proposed ogee for raise

1.1. Project Requirements

The original design of the dam and necessary permits included a two-phased development plan. Phase 1 included constructing the existing dam and spillway structures. Phase 2 was planned to include construction of a 3.05-m (10-ft) high ogee weir in the auxiliary spillway to allow the normal reservoir pool to be raised, thereby clearing vegetation along the reservoir rim between the Phase 1 and Phase 2 normal pool elevations and raising roadway embankments to provide adequate freeboard between the reservoir surface and adjacent roadways. It was anticipated that construction of Phase 2 would be completed by the end of 2018.

During the preliminary engineering phase of Phase 2, a number of design details (shown on Record Drawings) that could result in potential distress during flood loading or less than desirable performance over the life of the structure were identified on Record Drawings. One deficiency related to the spillway hydraulics was the height of the auxiliary spillway chute walls downstream of the control section. The change in direction of flow in the chute combined with the reduction in spillway width is expected to create both flow bulking on the right side of the spillway channel where the chute changes directions and standing waves. In addition, overtopping of the chute walls could lead to erosion of the soil adjacent to the spillway chute, which in its current condition, would likely lead to a structural failure.

The other deficiencies included insufficient slab thickness and improper configuration of seepage cutoffs. The Record Drawings show that the typical thickness of the spillway slab is generally a mere 20 cm (8 inches). The impacts of high-velocity flows at the base of the proposed ogee weir section and in the stilling basin are expected to

provide a significant stress to the spillway chute slab. The stress associated with these high-velocity flows impacting the slab would be expected to damage a concrete slab of this thickness. The current configuration for seepage mitigation below the control section includes two reinforced concrete cutoff walls, one installed at the upstream edge of the control section and one installed at the downstream edge of the control section. The downstream cutoff wall extends about 1 m (3.5 ft) lower than the upstream cutoff wall. This configuration could result in water pressures building below the control section, i.e., between the two cutoff walls, which is undesirable.

As a result of the multiple deficiencies identified and to more effectively and cost-efficiently address these deficiencies, alternative spillway configurations to the originally planned ogee weir were considered. The two other options considered were a labyrinth and PK weir. The labyrinth weir was eliminated as a cost-effective alternative due to the anticipated upstream-downstream depth of the weir being much larger than the existing control section depth [12.2 m (40 ft) versus 4.6 m (15 ft)]. A PK weir could be constructed within the footprint of the existing control section, and the existing spillway width could be narrowed by 45%. A narrower control section would result in construction cost savings due to less concrete being required for spillway slab overlays and a narrower seepage cut-off (Robblee et al. 2016).

2. PIANO KEY WEIR HYDRAULICS

The PK weir is a type of labyrinth weir with a non-linear weir geometry to increase the crest length within a channel (Crookston and Tullis 2013). The additional length in a compact spillway footprint provides additional discharge capacity relative to a broad-crested weir for the same channel width. Therefore, the ability to reduce the channel width while still safely passing the design flow with non-linear spillways (e.g. traditional labyrinth weirs) often results in economically attractive, viable solutions and, consequently, is commonly implemented in the USA for rehabilitations, upgrades, and new dams (Crookston et al. 2015). The authors have no knowledge of any PK weirs having been constructed in the USA to date.

PK weirs are characterized by rectangular 'keys' and ramps and commonly have a sidewall angle (α) of 0° (i.e., parallel sidewalls); however, a number of geometric variations exist that are grouped into four general types (Lempérière et al. 2011). A representation of a Type-A PK weir is presented in Figure 3. Since 1998, many studies have been performed in various laboratories such as in France, Belgium, Algeria, India, China, Vietnam, Switzerland, and the USA, among others, to characterize hydraulic performance and behaviors of PK weirs.
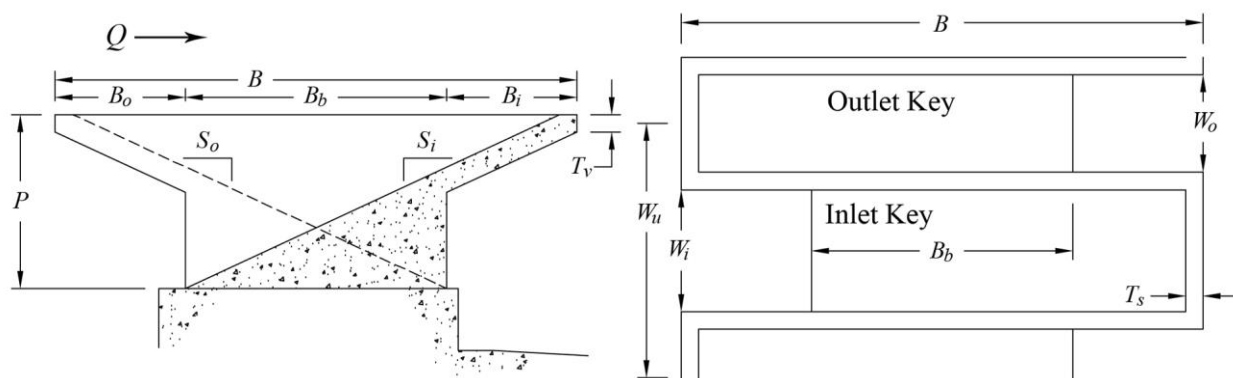
Figure 3. PK weir geometric parameters (Pralong et al. 2011)

2.1. Proposed PK Weir Geometry

The reservoir, spillways, and downstream river were analyzed as a system to select an appropriate PK weir geometry. This included maximum allowable pool elevation in the reservoir, inflow hydrographs, and attenuation provided by reservoir storage. It also allowed examination of potential downstream hazards associated with larger discharges and facilitated a comparison of anticipated peak outflows (during a given flood event) of the existing

auxiliary spillway and the proposed PK weir. Depending on risks assumed by the owner, a non-linear spillway outflow hydrograph can be modified by placing weir crest segments at two or more elevations. These 'staged' labyrinth spillways (Dabling et al. 2013) can generally match existing peak outflows in an outflow hydrograph for more frequently occurring storms while still providing the needed discharge capacity for the spillway design storm (e.g., the probable maximum flood or an approved ratio thereof). However, a staged labyrinth spillway with the higher stage above normal pool frequently requires additional crest length compared to a single-stage labyrinth weir (crest set at normal pool) and, therefore, incurs additional construction expenses.

In the instance of West Fork of Eno River Reservoir Dam, the hydrologic and hydraulic routings indicated that a two-stage 9-key PK weir (0.3 m vertical offset) would generally match peak outflows of the existing auxiliary spillway (with broad-crested weir) for the 100-year frequency flood. For the same event, a single-stage 8-key PK weir would increase peak outflows by about 25% (equivalent upstream head) from the two-stage 9-key weir; however, no additional hazards downstream (i.e., due to additional flow) were observed in the river model. Also, the 100-year peak discharge of the 8-key PK weir was less than the estimated outflow for the 100-year frequency flood by FEMA for the West Fork of Eno River (FEMA 2007). For the spillway design flood (SDF), which is estimated as the ¾ probable maximum precipitation (PMP), the PK weir peak discharge would be 15% less than the peak discharge of the existing auxiliary spillway. This is due to the increased hydraulic efficiency of the proposed weir (more flow is conveyed at a given pool elevation during the rising limb of the hydrograph, reserving reservoir storage when the flood is most intense). Based upon these results and supporting information, the owner selected a single-stage PK weir configuration. Estimation of the PK weir rating curve is discussed in the following section.

The PK weir will be installed on an upgraded concrete platform where the existing broad-crested weir is located, with a bottom elevation at 192.69 m a.s.l. The PK weir crest has a "broad-crested" shape and is installed at elevation 195.74 m a.s.l., so that a height of P=3.05 m (10.0 ft) results. It consists of eight full cycles. The characteristic geometrical parameters are the linear transversal channel width W=35.60 m (116.8 ft), the developed PK weir crest length L=177.02 m (580.8 ft), the streamwise PK weir length B=9.14 m (30.0 ft), the inlet key width W_i=2.13 m (7.0 ft), the outlet key width W_o=1.71 m (5.6 ft), and the streamwise overhang lengths $B_{i,o}$=2.29 m (7.5 ft). Accordingly, the magnification ratio is L/W=4.97, the key depth ratio is B/P=3.00, the key width ratio is W_i/W_o=1.25, and the overhang ratio is $B_{i,o}/B$=0.25.

2.2. PK Weir Discharge Rating Curve

The rating curve was estimated with two approaches. First, four empirical PK weir hydraulic design methods provided in literature were considered. Second, data derived from a sectional physical model test (Anderson 2011) were used, taking into account that the model did not exactly represent the considered PK weir geometry. Note that the design point of H_d=2.26 m (7.4 ft) is based upon allowable maximum reservoir pool elevation.

For the first approach, the rating curves according to Kabiri-Samani and Javaheri (2012), Leite Ribeiro et al. (2012), Machiels et al. (2014) Machiels et al. (2015) with a correction, and Anderson and Tullis (2013, personal communication 2015) were computed. However, these involve different crest types; namely, a sharp-crested type for Kabiri-Samani and Javaheri (2012), a cylindrical crest for Leite Ribeiro et al. (2012), and a broad-crested type for Machiels et al. (2014) and Anderson and Tullis (2013). The rating curves were thus computed according to the proposed equations of the afore-mentioned studies and then adapted as required to the broad-crested weir, as proposed for the discussed prototype. This adjustment was done by multiplying the discharge for a certain head with the discharge coefficient ratio of the considered crest types with the broad-crested type as reference. The discharge coefficients C_d were derived per crest type based on

- Hager and Schwalt (1994) for the broad-crested weir, where C_d tends from C_d=0.33 for H<0.2 m to C_d=0.42 for H>1 m,
- Hager and Schleiss (2009) for the sharp-crested weir, where C_d=0.42 for all H, and
- Castro-Orgaz (2012) for cylindrical weir crests if H<0.5 m (C_d=0.54 at H=0.5 m), then linearly approaching C_d=0.42 at H=4.4 m as observed by Ramamurthy and Vo (1993), and finally C_d=0.42 for all H>4.4 m.

For the second approach, the data points derived from a particular physical model tests performed by Anderson and Tullis (2013) were analyzed. The aforementioned rating curve estimation included a series of tests with different PK weir geometries, whereas for the second approach only that closest to the prototype PK weir was retained. Given that the model set-up (L/W=5.06, B/P=3.0, W_i/W_o=1.25 and B_i/B=0.25) was not identical with the PK weir prototype configuration, two discharge conversions were used to up-scale the model values to prototype discharges:

- The C_d development in function of H/P of the model was applied on the prototype, and
- A geometrical scale factor referring to P was defined, resulting in λ=15.5. The discharge was then up-scaled based on the Froude similitude. Considering other characteristic lengths (e.g., W_i or B) would result in slightly different values of λ. Following Leite Ribeiro et al. (2012), P has a dominant effect on the rating curve, whereas the other lengths are of secondary importance.

A comparison of both approaches to estimate the rating curve of the considered prototype is shown in Figure 4. Most of the rating curves collapse and, for a design head of H_d=2.26 m (7.4 ft), closely predict the design discharge Q_d=445 m³/s (15,720 ft³/s). The curve of Machiels et al. (2014) predicts smaller discharges for a given head if H>1.5 m, given that this equation explicitly takes the effect of the approach flow depth into account. None of the other approaches do. Nevertheless, this effect becomes relevant if H_d>0.5P, i.e. for H>1.5 m being similar to Q>300 m³/s. The equation of Kabiri-Samani and Javaheri (2012) clearly overestimates the discharge capacity, as observed previously (Pfister et al. 2012).
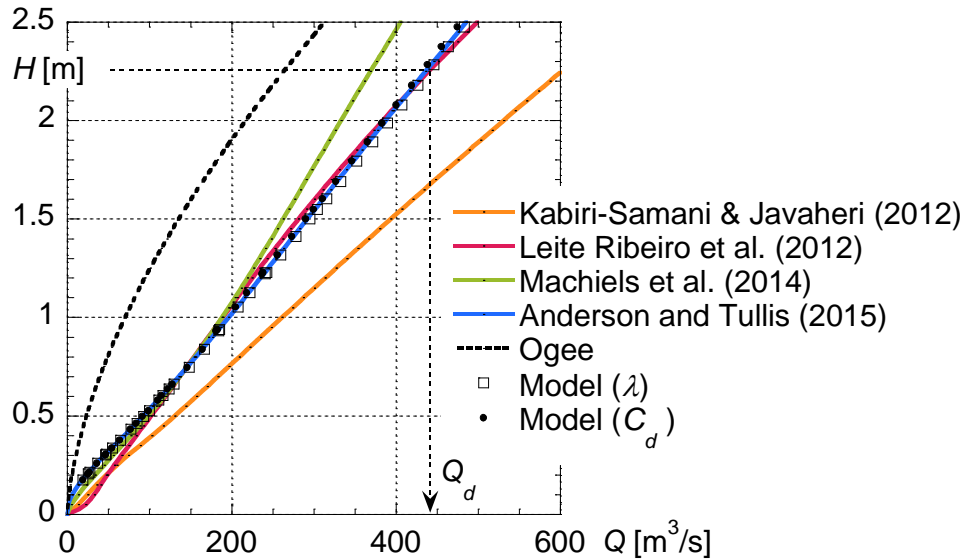
Figure 4. Comparison of Rating Curves from Literature and based upon Physical Model Tests

2.3. Numerical Modeling of Spillway

The primary objective of the numerical model was to simulate site-specific conditions with a focus on the PK weir and the rapidly varied flow region immediately downstream of the control section. A computational fluid dynamics (CFD) model of the control section and chute, basin, and portion of the reservoir was developed using a commercially available CFD solver. The majority of simulations utilized the Reynolds-Averaged Navier-Stokes (RANS) equations with the Renormalized-Group (RNG) turbulence model (Yakhot et al. 1992). This solver uses a finite volume method with conservation of mass and momentum via Eqs. (1) and (2).

$$\mathrm{V}_F \frac{\partial \rho}{\partial t} + \frac{\partial}{\partial x}\left(\rho u A_x\right) + \frac{\partial}{\partial y}\left(\rho v A_y\right) + \frac{\partial}{\partial z}\left(\rho w A_z\right) + \xi \frac{\rho u A_x}{s} = R_{DIF} \tag{1}$$

$$\frac{\partial U_i}{\partial t} + \frac{1}{V_F}\left(U_j A_j \frac{\partial u_i}{\partial x_j} \right) = -\frac{1}{\rho}\frac{\partial P'}{\partial x_i} + g_i + f_i \qquad (2)$$

The simulation matrix included existing conditions, an ogee crest alternative (not selected for design; results not included herein), and the proposed PK weir. The domain was discretized into hexahedral cells with select mesh planes defined based upon geometries, which were drafted as three-dimensional solids. To improve simulation efficiency, solids that represented domain-removing volumes or initial water geometry (i.e., conditions within reservoir and adjacent to control section) were included.

This project did not include a Froude-scaled hydraulic model of the spillway and site-specific conditions. However, calibration efforts utilized experimental data provided by Utah State University for PK weir geometries tested in a laboratory flume. Limitations and uncertainties are associated with hydraulic physical and numerical models (Heller 2011, Pfister and Chanson 2012, Freitas 1993); results require experience and expertise for interpretation (Knight 2013). Simulations are summarized in Tables 1 and 2.

Table 1. CFD Model Discharge Calibration Results

Simulation	H/P	Mesh Size		$C_{d\text{-}cfd}$	$C_{d\text{-}cfd}/C_{d\text{-}exp}$	$C_{d\text{-}cfd}/C_{d\text{-}emp}$	Turbulence Model
		(mm)	(ft)				
7	0.2	8.47	1/36	0.501	7.27%	6.47%	RNG / 0.07 P
8	0.2	8.47	1/36	0.501	7.27%	6.47%	RNG / 0.07 H
9	0.2	8.47	1/36	0.497	6.28%	5.49%	RNG / Dynamic
10	0.2	6.35	1/48	0.504	7.78%	6.98%	RNG / Dynamic
11	0.2	5.08	1/60	0.494	5.70%	4.91%	RNG / Dynamic
12	0.2	8.47	1/36	0.500	6.97%	6.18%	LES
13	0.2	5.08	1/48	0.501	7.30%	6.50%	LES
14	0.3	8.47	1/36	0.414	7.57%	6.30%	RNG / Dynamic
15	0.3	5.08	1/60	0.400	3.99%	2.76%	RNG / Dynamic
16	0.4	8.47	1/36	0.351	4.99%	3.81%	RNG / Dynamic
17	0.4	5.08	1/60	0.345	3.13%	1.98%	RNG / Dynamic
18	0.5	8.47	1/36	0.316	6.53%	5.18%	RNG / Dynamic
19	0.5	5.08	1/60	0.305	2.65%	1.34%	RNG / Dynamic
20	0.7	8.47	1/36	0.256	1.24%	0.82%	RNG / Dynamic
21	0.7	5.08	1/60	0.253	0.10%	-0.31%	RNG / Dynamic
22	0.9	8.47	1/36	0.229	3.98%	2.32%	RNG / Dynamic
23	0.9	6.35	1/48	0.231	4.64%	2.97%	RNG / Dynamic
24	0.9	5.08	1/60	0.229	3.89%	2.23%	RNG / Dynamic

As can be seen in Figures 5 and 6, good agreement regarding discharge capacity was established between the experimental results of Anderson (2011) and a geometrically duplicate numerical model. The RNG turbulence model with dynamically computed turbulence mixing length and second order monotonicity preserving momentum advection produced the closest agreement, with final simulations accurate from 0.1% to 5.7%, with a 3.2% mean. Figure 6 shows the general matching of flow structure, with some differences occurring primarily where the flow is more turbulent and highly aerated.
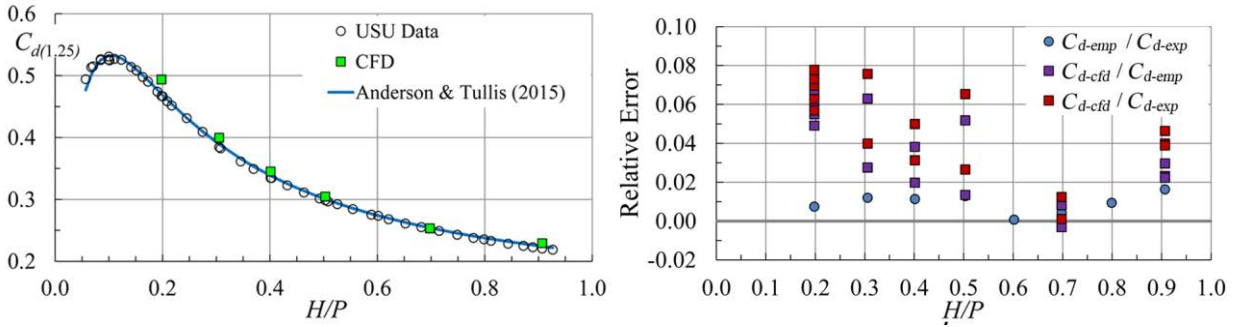
Figure 5. Agreement between Numerical Results and USU Experimental Results for Type-A PK Weir
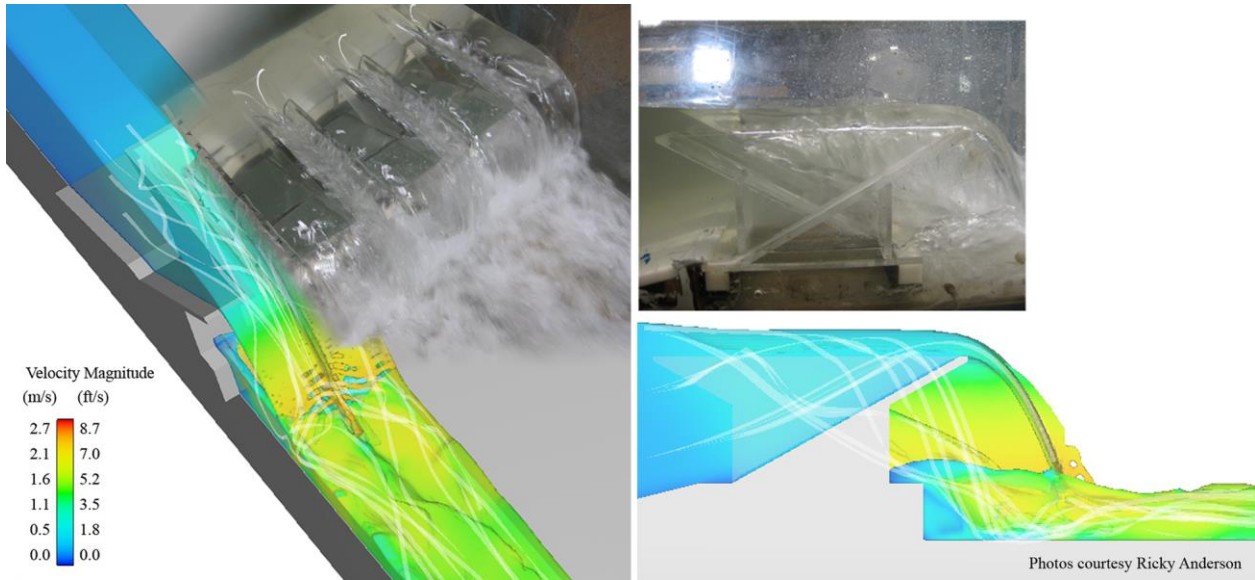
Figure 6. Comparison of physical and numerical model flow structure

Table 2. CFD Modeling Test Matrix – Hillsborough

Hillsborough Model Simulation		Turbulence Model
1	Existing – 100 yr	RNG / Dynamic
2	Existing – ¾ PMP	RNG / Dynamic
3	PK weir – 100 yr	RNG / Dynamic
4	PK weir – ¾ PMP	RNG / Dynamic
5	Ogee – 100 yr	RNG / Dynamic
6	Ogee – ¾ PMP	RNG / Dynamic

With an increased understanding of the numerical model performance regarding PK weirs, a location model of the existing proposed PK weir and original ogee-weir concept were simulated for the 3/4 PMP and the 100-year frequency storm. Although not verified, it was understood that the CFD model could provide qualitative and quantitative information and incremental quantities useful to the designers, such as estimated flow depths downstream of the three control sections (Figure 7), the pressure field acting on the PK weir (Figure 8), and also identify potential problematic areas as the flow enters the lateral chute and is conveyed to the stilling basin. Please note that in Figure 7a, flow overtops the existing chute but is partially confined due to the domain limits.
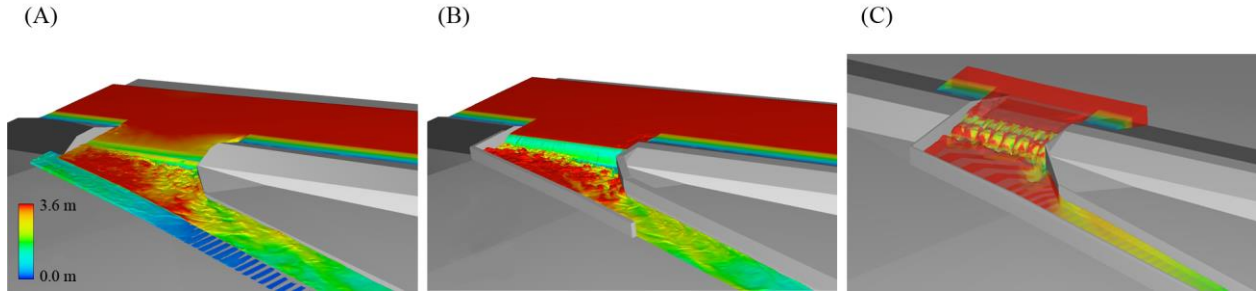
Figure 7. Estimated flow depths for SDF for existing conditions (A), ogee weir (b), and proposed PK weir (C)
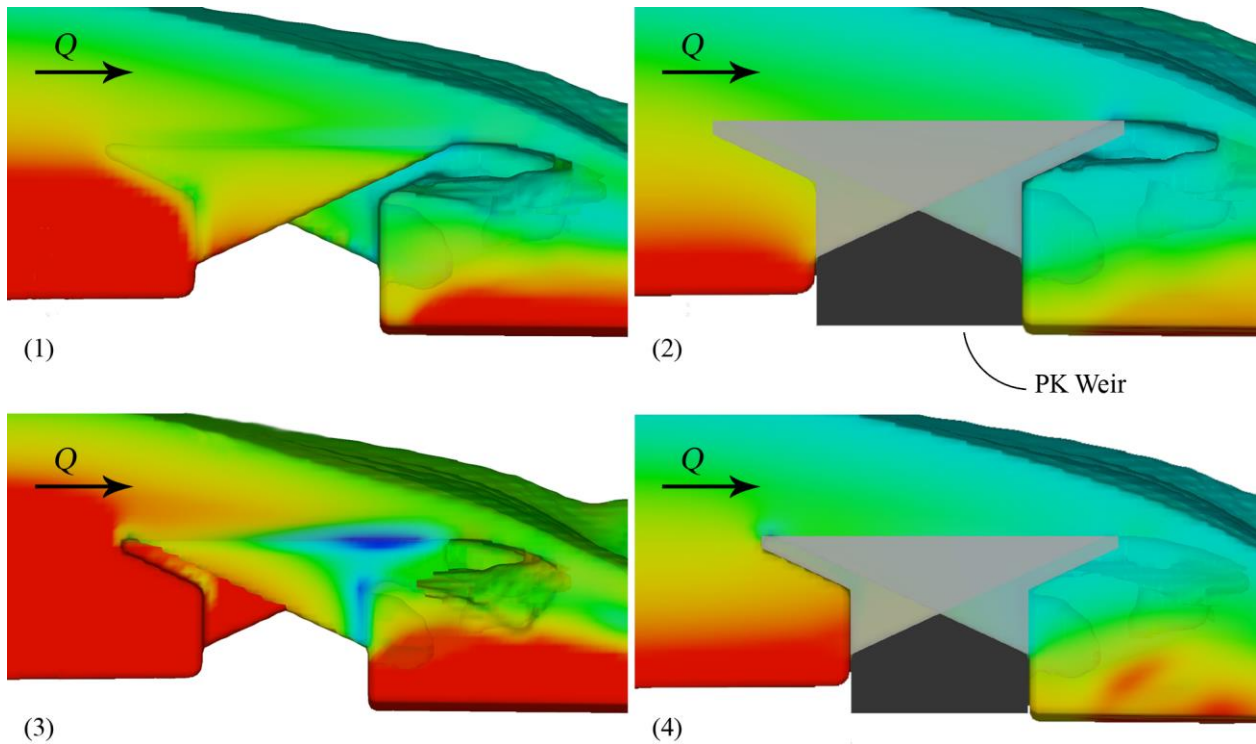
Figure 8. Estimated pressure field at four locations across the PK weir at Q_d=445 m³/s (15,720 ft³/s)

For the existing broad-crested weir, the downstream chute wall was estimated to overtop by about 2.4 m (8 ft). The numerical results predict a hydraulic jump in all cases immediately downstream of the control sections; however, the PK weir provides additional energy dissipation relative to the ogee-weir, and the additional turbulence appears to provide some benefit within the transition portion of the chute. A comparison to the numerical results was performed via a short estimation of the hydraulic jump and shock wave. Assuming no energy dissipation exclusive to the hydraulic jump (a computed F_1=2.95 assuming a 2D channel), the sequent depth at the impact wall is approximately 4.9 m for stagnant water. Furthermore, an estimation of the shockwave height via Hager (1992) indicates that that a hydraulic jump is expected with no shockwave (θ=70°, β_s=90°), which agrees with the numerical simulations. An oblique standing wave forms at the end of the transition or chute entrance followed by anticipated shockwave patterns in the supercritical flowing chute.

Replacement of the existing 2.4-m high (8-ft) wall with a 5-m high wall (about 16 ft) in the downstream chute is required to adequately contain the flow from the SDF. During such an extreme event, some local splash and spray may exit the channel. The maximum headwater ratio for this PK weir is H/P=0.74, which is approximately twice

the typical ratios for PK weirs built in France. To ensure stability, additional cutoff walls will be constructed at the control section and drainage added to reduce uplift pressures. Also, the PK weir will be structurally connected to the new base slab.

3. CONCLUSIONS

The design of the West Fork of Eno River Reservoir Dam expansion is currently underway, and preliminary engineering analyses identified several design inadequacies related to spillway capacity and structural integrity of the existing chute. An alternatives analysis identified a PK weir to be the optimal economic solution that met all project requirements. To estimate the spillway rating curve, four empirical methods were evaluated with close agreement found between Leite Ribeiro et al. (2012) and Anderson and Tullis (2012, personal communication 2015). Further hydraulic analyses used CFD modeling, which was validated using experimental results by Anderson (2011). The CFD provided qualitative and quantitative information that assisted with design of the chute transition region, including chute wall heights and stability of the PK weir.

4. ACKNOWLEDGEMENTS

5. REFERENCES

Anderson R.M. (2011). "Piano Key Weir Head Discharge Relationships." M.S. *Thesis*, Utah State University, Logan, Utah.

Anderson, R.M. Tullis, B.P. (2013). Piano Key Hydraulics and Labyrinth Weir Comparisons. *J. Irrig. Drain. Engng.*, 139(3):246-253.

Castro-Orgaz, O. (2012). Discussion Overflow characteristics of circular-crested weirs. *J. Hydraulic Res.* 50(2): 241–243.

Crookston, B.M. Tullis, B.P. (2013). Hydraulic Design and Analysis of Labyrinth Weirs. 1: Discharge Relationships. *J. Irrig. Drain. Engng.*, 139(5):363-370

Freitas, C.J. (1993). Journal of fluids engineering editorial policy statement on the control of numerical accuracy. *Journal of Fluids Engineering*-Transactions of the ASME 115(3): 339-340.

Crookston, B.M., Mortensen, D., Stanard, T., Tullis, B.P., Vasquez, V. (2015). Debris and Maintenance of Labyrinth Spillways." *Proc. of the 35th Annual USSD Conference,* Louisville, Kentucky. CD-ROM.

Dabling, M.R., Tullis, B.P., Crookston, B.M. (2013). Staged Labyrinth Weir Hydraulics. *J. Irrig. Drain. Engng.*, 139(11):955-960.

FEMA (20017). Federal Emergency Management Agency, Flood Insurance Study: A Report of Flood Hazards in Orange County, North Carolina and Incorporated Areas (FIS Study Number 37135CV001A), February, 2, 2007.

Hager, W.H. (1992). Spillways-shockwaves and air entrainment. ICOLD Bulletin, Vol. 81 International Commission on Large Dams, Paris, France.

Hager, W.H., Schleiss, A.J. (2009). Constructions hydrauliques, Ecoulements stationnaires. *Traité de Génie Civil*, Vol. 15, Presses Polytechniques et Universitaires Romandes, Lausanne, Switzerland.

Hager, W.H., Schwalt, M. (1994). Broad-crested weir. *J. Irrig. Drain. Engng.* 120(1): 13-26.

Heller, V. (2011). Scale effects in physical hydraulic engineering models. *J. Hydraulic Res.* 49(3), 293-306.

Kabiri-Samani, A., Javaheri, A. (2012). Discharge coefficient for free and submerged flow over Piano Key weirs. *J. Hydraulic Res.* 50(1), 114-120.

Knight, D.W. (2013). River hydraulics—A view from midstream. *J. Hydraulic Res.* 51(1):2–18

Leite Ribeiro, M., Pfister, M., Schleiss, A.J., Boillat, J.-L. (2012). Hydraulic design of A-type Piano Key weirs. *J. Hydraulic Res.* 50(4): 400–408.

Lempérière, F., Vigny, J.P., Ouamane, A. (2011). General comments on Piano Kew Weirs: The past and present. Proc. Intl *Workshop on Labyrinths and Piano Key Weirs* PKW 2011, CRC Press, 17-25.

Machiels, O., Pirotton, M., Archambeau, P., Dewals, B., Erpicum, S. (2014). Experimental parametric study and design of Piano Key Weirs. *J. Hydraulic Res.* 52(3): 326–335.

Machiels, O., Pirotton, M., Archambeau, P., Dewals, B., Erpicum, S. (2015). Closure to Experimental parametric study and design of Piano Key Weirs. *J. Hydraulic Res.* 53(4): 545.

Pfister, M., Chanson, H. (2012). Scale Effects in Physical Hydraulic Engineering Models. Discussion. *J. Hydraulic Res*. 50(2): 244-246

Pfister, M., Erpicum, S., Machiels, O., Schleiss, A., Pirotton, M. (2012). Discussion to Discharge coefficients for free and submerged flow over Piano Key Weirs. *J. Hydraulic Res.* 50(6): 642-645.

Pralong, J., Vermeulen, J., Blancher, B., Laugier, F., Machiels, O., Erpicum S., Pirotton, M. Leite Ribeiro, M., Boillat, J.L. and Schleiss, A.J. (2011). "A naming convention for the piano key weirs and geometrical parameters." in Labyrinth and piano key weirs. Erpicum, S., Laugier, F., Boillat, J.-L., Pirotton, M., Reverchon, B., Schleiss, A.J. (eds.) CRC Press, Boca Raton, FL.

Ramamurthy, A.R., Vo, N.D. (1993). Characteristics of circular-crested weir. *J. Hydraulic Engng.* 119(9), 1055-1062

Yakhot, V., Orszag, S.A., Thangam, S., Gatski, T.B. & Speziale, C.G. (1992), Development of turbulence models for shear flows by a double expansion technique, *Physics of Fluids A*, 4:7 pp1510-1520.

Cross-Section Influence on Velocity Distribution & Energy Dissipation of a Moderately Sloped Spillway Chute Flow

A.Tohidi[1], and F. S. Maleki[2]
[1]Glenn Dept. of Civil Engineering,
Clemson University,
Clemson, SC, 29634,
USA

[2]Assistant Professor of Engineering
Massachusetts Maritime Academy,
Buzzards Bay, MA, 02532,
USA
E-mail: fmaleki@maritime.edu

ABSTRACT

Erosion at the dam toe due to potential to kinetic energy conversion of the outlet release is a complex yet fascinating engineering challenge. The energy dissipation due to flow separation at sharp cornered geometries affects the flow stream and causes the lower velocity at the dam's toe. To date, many of the conventional dam engineering techniques consider the dam toe as the examination point. In this research, by the use of OpenFOAM numerical model, the water flow in the spillway chute is modeled. The velocity profile of the chute flow in three different cross-sections is considered for the same outlet boundary conditions. The effect of geometry on kinetic energy (velocity) reduction has been studied in order to find a trend for this type of energy cascade. Simulation results show that lateral eddies form due to generation of translatory waves and aeration processes in trapezoidal and curved edge rectangular cross sections. While these type of cross sections might be of use from the energy dissipation perspective, the higher velocities may deliver higher stagnation or uplift pressures in cases of vertical offset on the spillway's slab (bed).

Keywords: Erosion, Energy Dissipation, Spillway Chute, OpenFOAM, Numerical Modeling.

1. INTRODUCTION

Dams play a significant role in efficient control of a flood from extreme hydrological events. A rise in the reservoir's water level will be induced by the substantial inflow during intense rainfalls. Hence, spillways are designed to convey the excess water in a controlled and non-destructive fashion. On this matter, a key aspect of spillway design is energy dissipation. The energy dissipation system in most of the dams consists of a spillway crest, a water conveying part, and a terminal structure at the downstream. A poor design in any part of the spillway may cause dam failure (Christodoulou 1993; Lempérière et al. 2012; Chanson 2015).

The enormous energy release of large inflows over spillways necessitates a design such that energy cascades without considerable damage to the hydraulic structures, facilities downstream, and surrounding environment. This process is strongly dependent on the geometry and design of the water conveying part of the dissipater system. With regard to this, the water conveying part of spillways should be designed in order to deliver a stable free surface flow and lower the risk of localized failure due to defects and anomalies on the bed surface. One of the common designs, especially in concrete gravity dams, is chute spillways as they are usually not intended to dissipate energy like stepped spillways (Tanchev 2014). Design characteristics of this type of spillways are very well documented; see for example (Ippen and others 1951; Reinauer and Hager 1998). Yet, the main objective of this study is to investigate the effects of cross section geometry on the energy dissipation behavior of the smooth (without baffle blocks) chute spillways. Although there has been some studies on the effects of geometry on the free surface flow through chute spillways (Ellis and Pender 1982; Montes 1994; Song and Zhou 1999), the influence of various cross section geometries on the energy dissipation behavior is less considered. This could be an arduous task with costly testing

prototypes. However, with recent advancements both in computational fluid dynamics (CFD) algorithms and high performance scientific computing, it is now possible to model a full-scale chute spillway with different geometries in 3D and observe the effects.

In the present study, three cross sections, i.e. rectangular, trapezoidal, and rectangular with curved edges, are examined numerically by simulating multiphase (air-water) flow through chute spillways. The main motive behind adopting the initial conditions and geometric parameters is the failure of Big Sandy Dam's spillway due to pressure stagnation (Billington et al. 2005). This document particularly deals with simulation of the transport processes through the aforementioned cross sections and studies the distribution of velocity, water phase fraction, and pressure across the depth of the downstream end of the spillway. Since the final design depends on many different parameters, this study just presents the exploratory results, which are not conclusive for engineering practice. Section two presents the adopted numerical model and solution procedure. Section three presents the results and relevant discussions, and, finally, section four delivers the concluding remarks.

2. NUMERICAL MODEL

Supercritical flow in the chute spillway along with certain geometric characteristics of the cross section may lead to cavitation, shock (interface) waves, translatory waves, and aeration of the flow (Abbasoglu and Okay 1992; Kökpinar and Göugücs 2002; Novák et al. 2007; Tanchev 2014). In order to capture the essential physics behind these phenomena, the turbulent flow and flow separation processes should be taken into account. This is done by solving Reynolds Averaged Navier-Stokes (RANS) equations for a case that serves as a close approximation to the chute spillway of Big Sandy Dam with three different cross section configurations (see section 3) by utilizing an open source computational fluid dynamics C++ library called OpenFOAM (Jasak et al. 2007). The following subsections present the governing equations, numerical solution method, and simulation parameters, respectively.

2.1. Governing Equations & Computational Domain

Navier-Stokes equations are fundamental governing equations of the fluid motion given the fluid is a continuum medium. The governing partial differential equations, for incompressible isothermal fluids at relatively low Mach numbers (less than one), are conservation of momentum and conservation of mass. They, respectively, read as

$$\rho \frac{D\boldsymbol{U}}{Dt} = -\nabla p + \mu \nabla^2 \boldsymbol{U} + \rho \boldsymbol{g} \tag{1}$$

$$\nabla \cdot \boldsymbol{U} = 0 \tag{2}$$

where D is material derivative, $\boldsymbol{U}$ is instantaneous velocity vector, p is pressure, μ is dynamic viscosity, and ρ is the fluid's density. Also, $\boldsymbol{g}$ is the gravity acceleration vector. Through this study, instead of modeling the actual slope of the steeped chute spillway, the complete geometry is considered in the Cartesian coordinates where the gravity acceleration vector is decomposed in three dimensions as $(gsin(\theta), 0, -gcos(\theta))$; Figure 1 shows schematic view of the computational domain and geometric outline of the cross sections. For complete derivation of the governing equations, see Kundu et al. (2002).
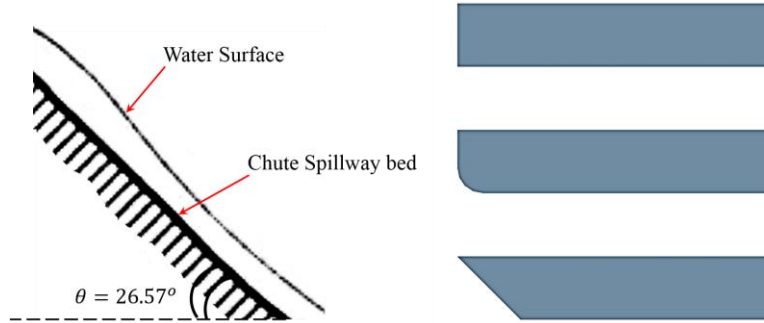
Figure 1. (Left) Side view schematic of the chute spillway and (Right) outline of cross sections from front view.

2.2. Numerical Solution Method

The solution domain is discretized into a finite number of small control volumes, mostly hexahedron shapes, and the governing equations are averaged over each control volume. For details of this method, that is finite volume method (FVM), see (Ferziger and Peric 2012). The feature of the flow in the chute spillways is the unsteady transport of air and water by a recognizable interface. This is resolved using volume of fluid (VOF) method in which a specie transport equation is used to determine the relative volume fraction of the air and water (Hirt and Nichols 1981). The volume fraction of water to the control volume is shown by α throughout this work. The phase fraction can be any value between 0 and 1 (totally water), and the solver (interFoam) uses a multi-dimensional universal limiter for explicit solution (MULES) method to maintain boundedness of each phase fraction independent of the time marching schemes. The convection terms in momentum equations are discretized using the Gauss Linear Upwind method. Also, the phase fraction convection term is resolved by Gauss Van Leer scheme to ensure stability. For the rest of the terms in governing equations, Gauss Linear Corrected scheme is adopted. Going to the details of the solver, particularly time marching algorithms, in not within the scope of this study. Therefore, see the OpenFOAM programmer's guide for a thorough explanation.

2.3. Turbulent Flow Model

According to the Bureau of Reclamation's report, the chute spillway at Big Sandy Dam failed due to uplift stagnation pressure at failure velocity of $U=9.45\ ^m/_S$. This leads to the fact that Reynolds' number of the flow is of the order of $O(10^6 - 10^7)$ in this case. Hence, the flow is fully turbulent, and velocity and pressure fluctuations need to be taken into account.

Both Direct Numerical Simulations (DNS) and Large Eddy Simulations (LES) give a fine time-varying turbulent velocity field (Pope 2000). However, their computational cost is significantly higher than RANS methods. For engineering purposes in which the range of 5% error is acceptable and high resolution of the flow is not needed, RANS models work perfectly for describing the flow behavior. Several surveys such as that conducted by Bombardelli et al. (2011) & Valero and Bung (2015) provide more information on applications, capabilities, and limitations of RANS models in simulating spillway flows. In RANS methodology, time-averaging of governing equations introduces a nonlinear term called Reynolds' stress term into momentum equations (Pope 2000). In order to model this term, manifold RANS closures models are proposed (Pope 2000). Here, the well-known standard κ-ε model is employed since the flow is fully turbulent and effects of molecular viscosity are negligible. Basically, in addition to the time-averaged governing equation, two more equations for turbulent kinetic energy ($k = 1/2\ \overline{u_i'u_i'}$) and dissipation rate of kinetic energy (ε) should be solved. Overbar notation denotes the time-averaged quantities of each term. The equations for turbulent kinetic energy and dissipation rate are as follows if overbar notation is ignored for simplicity.

$$\frac{\partial k}{\partial t} + U_j \frac{\partial k}{\partial x_j} = \frac{\partial}{\partial x_j}\left[\left(\nu + \frac{\nu_t}{\sigma_k}\right)\frac{\partial k}{\partial x_j}\right] + \tau_{ij}\frac{\partial U_i}{\partial x_j} - \varepsilon \tag{3}$$

$$\frac{\partial \varepsilon}{\partial t} + U_j \frac{\partial \varepsilon}{\partial x_j} = \frac{\partial}{\partial x_j}\left[\left(\nu + \nu_t/\sigma_\varepsilon\right)\frac{\partial \varepsilon}{\partial x_j}\right] + C_{\varepsilon 1}\frac{\varepsilon}{k}\tau_{ij}\frac{\partial U_i}{\partial x_j} - C_{\varepsilon 2} \tag{4}$$

$$\nu_t = C_\mu k^2/\varepsilon \tag{5}$$

$$C_{\varepsilon 1} = 1.44, \ C_{\varepsilon 2} = 1.92, \ C_\mu = 0.09, \ \sigma_k = 1.0, \ \sigma_\varepsilon = 1.3 \tag{6}$$

where U is now the time-averaged velocity, ν is kinematic viscosity, and ν_t is the eddy viscosity. Also, subscripts i, j represent the coordinate system directions in Einstein notation. In addition, τ_{ij} is the Reynolds' shear stress tensor. Details of the κ-ε model in multiphase flow simulations are very well documented (Jones and Launder 1972). In this work, standard coefficients of the κ-ε model, as shown above, are used. Performance validation of κ-ε model and two-phase flow solvers of OpenFOAM are beyond the scope of this study although the failure depth and velocity of the Big Sandy Dam is obtained within a narrow error margin; see section 3. However, for supplementary details on validation of OpenFOAM solvers over various length and time scales, see Deshpande et al. (2012) and Lopes (2013).

2.4. Simulation Parameters

As mentioned before, the goal of this study is to investigate the energy dissipation behavior with change in cross section geometry while the failure conditions of Big Sandy Dam's spillway are reached. Based on the available characteristics of the Big Sandy Dam (Reclamation Magazine 2012), the failure discharge is 11.33 m^3/s, with uniform failure velocity of 9.45 m/s in a rectangular cross section. Therefore, the failure initial depth for the flow inside the chute spillway is 0.09-m. The slope of the spillway, i.e. θ, is considered to be 26.57° with horizon, which is a relatively moderate slope for chute spillways. Specifics of the chute spillway's simulation models are presented in Table 1.

On this matter, the minimum mesh size is found through a mesh convergence analysis that will be presented in next section. Implemented boundary conditions on the computational domain are also shown in Figure 2.

Table 1. Specifics of the chute spillway simulation models.

Cross section	Dimensions (m)	Minimum mesh size (m) – Mesh type
Rectangular	$20 \times 13.32 \times 0.5$	$0.1 \times 0.1 \times 0.05 -$ structured Hexahedron
Rectangular with curved side edges at bed	$20 \times 13.32 \times 0.5*$	$0.1 \times 0.1 \times 0.05 -$ unstructured Hexahedron
Trapezoidal	20×12.32 with 45° slope up to 13.32 at the top $\times$ 0.5	$0.1 \times 0.1 \times 0.05 -$ unstructured Hexahedron

* Curved edges have 0.2-m radius
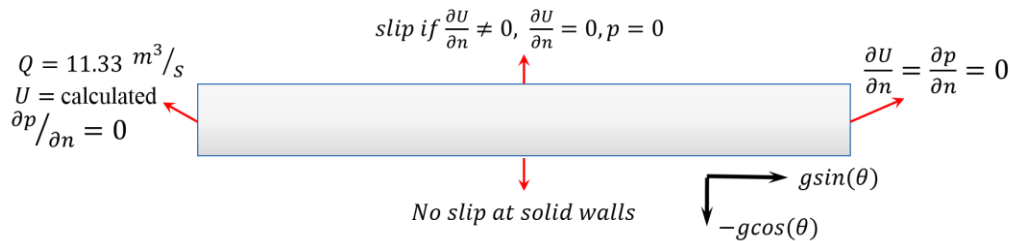
Figure 2. Schematic, side view (X-Z plane), diagram of implemented boundary conditions for pressure and velocity at the inlet in left, solid walls at the bottom and sides of the domain, atmosphere on top, and outlet at right.

As for of the turbulence model initial conditions at the inlet, the flow height is chosen such that it satisfies two conditions. Firstly, the inflow remains constant and equal to the critical failure discharge of Big Sandy Dam, at least in the rectangular section. Secondly, the hydraulic radius of the cross sections remains in the same order. Turbulent mixing length is considered to be 7% of the hydraulic radius of the cross sections. Additional inlet details are given in Table 2, assuming that the turbulence intensity for all cases is 5%.

Table 2. Inlet values of the turbulence model.

Turbulence parameters	Rectangular	Rectangular with curved edges	Trapezoidal
$l = 0.07 R_h$	0.0630	0.0600	0.1310
$k = 1.5(UI)^2$	0.0920	0.0110	0.0170
$\varepsilon = C_\mu k^{1.5} / l$	0.0399	0.0017	0.0009
$\nu_t = C_\mu k^2 / \varepsilon$	0.0191	0.0660	0.0142

The simulations are conducted with 380 Intel Xeon E5-2665 cores on Clemson University's Palmetto cluster. The initial time step is chosen such that the Courant Number in each case is less than 1, i.e. $\delta t = 0.001 \ (s)$. However, OpenFOAM's interFom solver has this ability to adapt the time step with the maximum allowable Courant number, which is introduced to be 0.7 in all simulations.

3. RESULTS & DISCUSSIONS

The first set of analysis examined the convergence of solutions by decreasing the mesh size in Z direction. Figure 3, illustrates the velocity profiles through water and air depth with increments of 0.1, 0.08, and 0.05 m. Considering symmetry of the flow, the profiles are extracted from the centerline of the rectangular cross section at the outlet. The difference between 0.08-m and 0.05-m mesh size is less than 5% and is in the acceptable range for engineering applications. Therefore, for the rest of simulations $dz = 0.05 \ m$ is adopted.

Energy dissipation behavior including processes like cavitation, interface waves, translator waves, and aeration can be understood from the quasi-steady state of the water surface through the domain. Thus, the kinetic energy of the simulations is recorded through the simulations to determine when the average flow is relatively steady. Figure 4, demonstrates time history of the turbulent kinetic energy during 15 seconds of the simulations at a point with coordinates of (15, 6.66, 0.01) meters through the water phase.
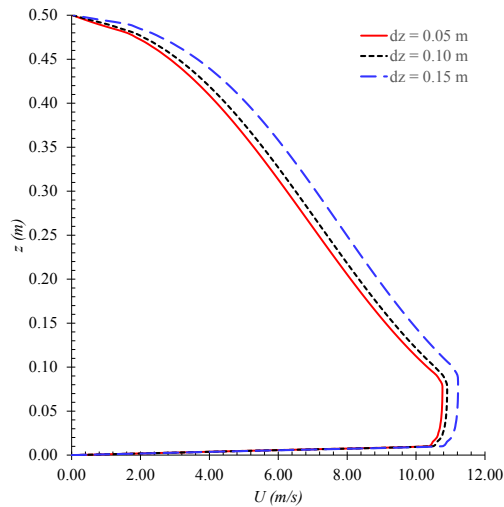
Figure 3. Mesh convergence analysis based on the velocity distribution over two phases, i.e. water and air in rectangular cross section. The velocity profiles are extracted from the centerline of the domain at the outlet.

Since it is shown that after 15 seconds the chute spillway flow is quasi-steady, discussions will be based on the results at 15 seconds. In order to validate the simulation outputs, results of the rectangular cross section are compared with the failure state of the Big Sandy Dam's chute spillway (Billington et al. 2005; Reclamation Magazine 2012). The simulation results extracted at 10 m downstream from the inlet. Results show a fully turbulent velocity profile with maximum value of 9.11 $m/_s$, which delivers only 3.7% error compared to the reported failure velocity in the Big Sandy Dam case; see Figure 5. Note that markers in all figures are for visualization purposes and don't correspond to the face or cell-center values of the mesh in simulations. Also, Figure 5 shows phase fraction distribution of water through the depth, and, as can be seen, the failure depth of water is captured almost exactly equal to 0.09 m.
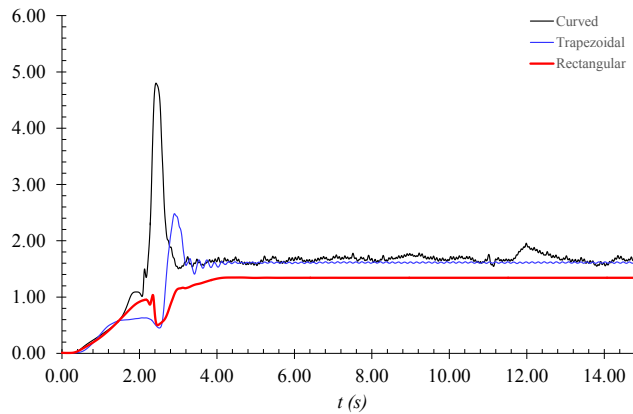
Figure 4. Time history of the turbulent kinetic energy at a point with coordinates of (15, 6.66, 0.01) meters through the water phase.
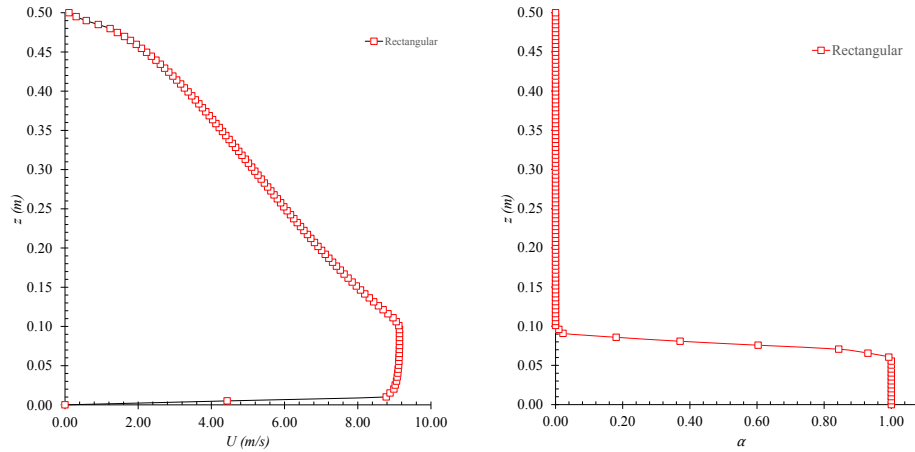
Figure 5. (Left) Vertical velocity profile of the chute spillway with rectangular cross section at the center-line of the cross section in 10-m downstream. (Right) Corresponding water phase fraction distribution through the depth of the flow.

Figure 6 shows the contour plots of the water surface corresponding to phase volume fraction of water, $\alpha = 0.99$. The α is chosen only for visualization purposes to provide a smooth surface translator waves. Considering the energy dissipation of the flow through different cross sections by lateral eddies, three observations can be noted. First, formation of a stationary interface wave (not shown here) due to considerable inflow inside the chute spillway domain. Since this type of wave is immediately convected downstream of the spillway, it doesn't interfere with the energy dissipation process (Tanchev 2014). Second, generation of translatory waves that move along the flow towards the terminal structure. These waves are observed mainly in curved edge rectangular and trapezoidal cross sections and cause non-stationary impulses into the main dissipator structure at downstream end. As shown in Figure 6, translatory waves are propagated through the entire width of the curved edge rectangular cross section whereas in the trapezoidal cross section, they are localized on the sides. Although these waves may dissipate energy early and well before the main dissipator structure, they may cause overflowing of water. The third observation is the aeration, which contributes to the energy dissipation (Tanchev 2014). Aeration develops where turbulent boundary layer starts to penetrate the full depth of the flow in spillway (Tanchev 2014). The approximate aeration length can be calculated using Hickot's equation (Novák et al. 2007), $14.7q^{0.53}$, where q is the unit discharge per width. The aeration length for the trapezoidal and curved edge rectangular cross sections, with 0.795 and 0.854 m^2/s unit discharge, is 13.05-m and 13.54-m downstream, respectively. This shows that the aeration point and location of non-stationary impulses of translatory waves occur adjacent to each other. Therefore, the energy dissipation due to aeration and energy loss on the water surface starts earlier inside the chute spillway channel for trapezoidal and curved edge rectangular cross sections compared to rectangular cross sections.
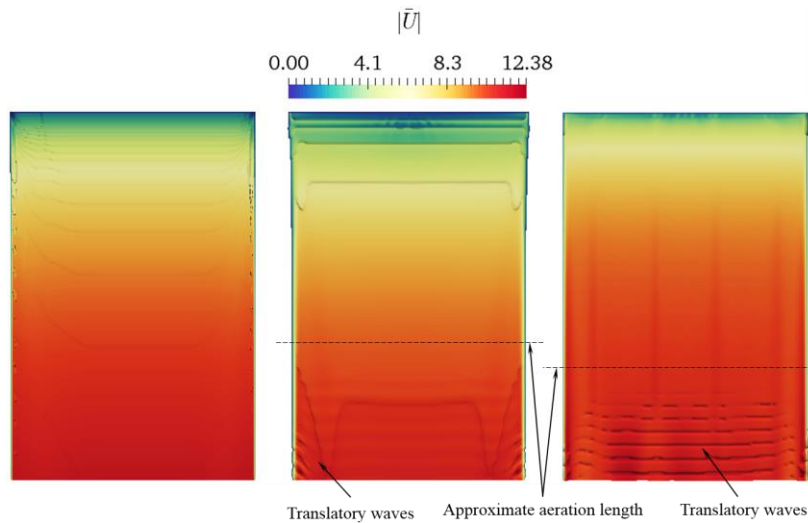
Figure 6. Contour plots of water surface with phase volume fraction of $\alpha = 0.99$ overlaid with contours of time-averaged velocity magnitude. On the left is rectangular section, in the middle is the chute spillway with trapezoidal cross section, and at the right is the spillway with rectangular yet curved edges at bottom cross section.
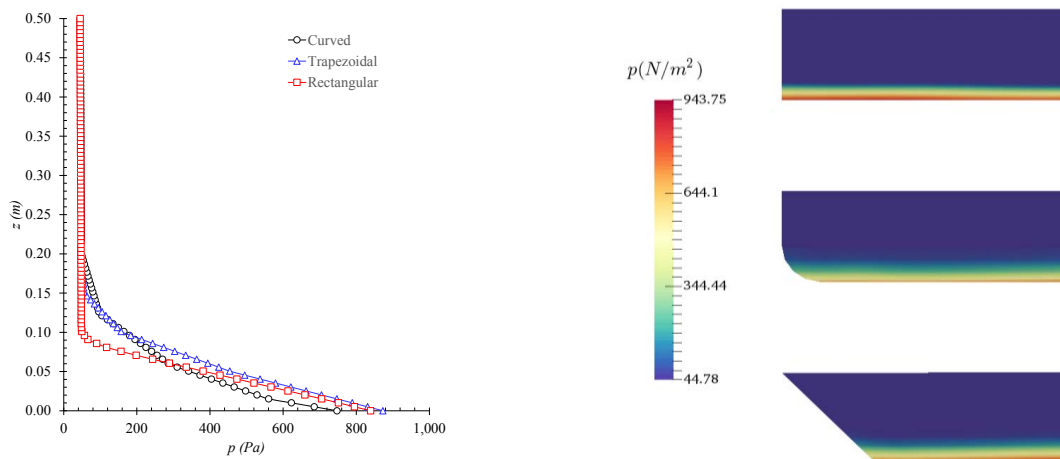
Figure 7. (Left) Pressure distribution across the depth of the domain and along the center-line of the cross sections at 10 m downstream in $t = 15\ (s)$. Pressure is calculated relative to the reference point (0, 0, 0.5) where p = 0. (Right) Corresponding pressure contours close to the side walls.

Results suggest that the early energy dissipation is more intense through curved edge rectangular cross sections compared to trapezoidal forms.

Although a curved edge rectangular cross section might have better performance at starting the energy dissipation process, pressure and velocity distributions suggest that this type of cross section is not only impractical to build but also more likely to damage the spillway slab due to uplift/stagnant pressure incidents induced by vertical offsets in bed; see Figure 7 and Figure 8.

Figure 8 shows velocity distributions at 10 and 20 m downstream. It is illustrated that the curved edge rectangular and trapezoidal cross sections causes more velocity at 10 m downstream, i.e. middle of the spillway's slab.
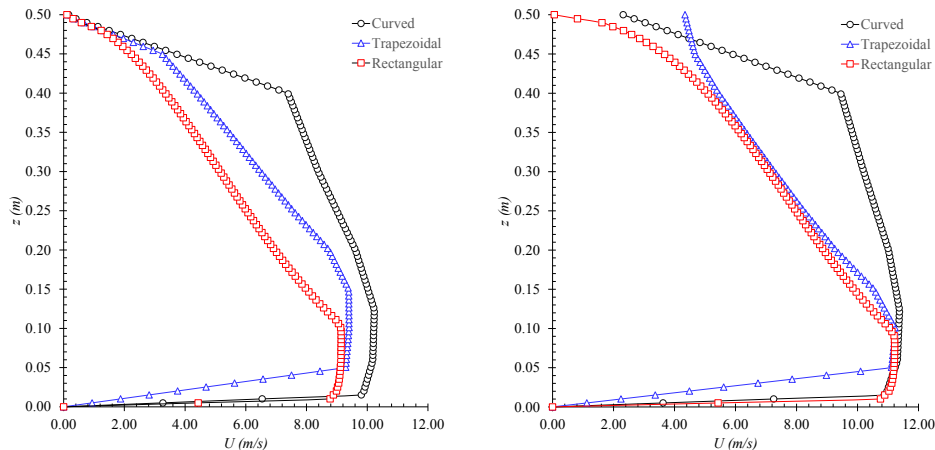
Figure 8. Stream-wise velocity profiles at 10 m (left), and 20 m (right) downstream extracted from the centerline of the cross-sections.

Hence, in cases of forward vertical offset of the bed, they may lead to higher stagnation pressure. Also, at the outlet it is shown that the three flows reach to the same maximum velocity. However, translatory waves and aeration process in trapezoidal and curved edge rectangular section can cause a varying velocity at the upper surface of the air phase. This is mainly an air-water phase interaction caused by translatory waves leading the energy dissipation.

4. CONCLUDING REMARKS

Effects of different types of cross sections on the energy dissipation procedure through smooth chute spillways are studied numerically. The multiphase flow of water and air through half a meter depth of the spillway is modeled with OpenFOAM solvers. The failure state of the Big Sandy Dam's spillway is simulated with 3.7% error in predicting the maximum stream-wise velocity and almost no error in water-air interface depth at 10 m downstream section. Horizontal velocity and phase fraction profiles across the depth of the channel suggest mixing with generated bubbles and formation of translatory waves. From the early presence of such processes in smooth spillways with trapezoidal and curved edge rectangular cross sections, it can be inferred that energy dissipation starts earlier upstream for these sections relative to the rectangular section. In addition, results imply that while these types of geometric configuration maybe of use for energy cascade purposes, they may lead to higher velocities, which delivers higher risk of stagnation or uplift pressure due to vertical offsets in the slab.

5. REFERENCES

Abbasoglu, C., and Okay, G. (1992). "The remedial structures on the spillway of Keban dam." International water power & dam construction, Wilmington Business Publishing, 44(12), 22–27.

Billington, D. P., Jackson, D. C., and Melosi, M. V. (2005). The history of large federal dams: planning, design, and construction in the era of big dams. Government Printing Office.

Bombardelli, F. A., Meireles, I., and Matos, J. (2011). "Laboratory measurements and multi-block numerical simulations of the mean flow and turbulence in the non-aerated skimming flow region of steep stepped spillways." Environmental Fluid Mechanics, Springer, 11(3), 263–288.

Chanson, H. (2015). Energy Dissipation in Hydraulic Structures. Igarss 2014, Taylor & Francis, London, UK.

Christodoulou, G. C. (1993). "Energy dissipation on stepped spillways." Journal of Hydraulic Engineering, American Society of Civil Engineers, 119(5), 644–650.

Deshpande, S. S., Anumolu, L., and Trujillo, M. F. (2012). "Evaluating the performance of the two-phase flow solver interFoam." Computational Science & Discovery, 5(1), 14016.

Ellis, J., and Pender, G. (1982). "Chute spillway design calculations." ICE Proceedings, 299–312.

Ferziger, J. H., and Peric, M. (2012). Computational methods for fluid dynamics. Springer Science & Business Media.

Hirt, C. W., and Nichols, B. D. (1981). "Volume of fluid (VOF) method for the dynamics of free boundaries." Journal of computational physics, Elsevier, 39(1), 201–225.

Ippen, A. T., and others. (1951). "Proceedings of a Symposium on High-Velocity Flow in Open Channel." Trans. ASCE, 116, 265–400.

Jasak, H., Tukovic, Z., and Jemcov, A. (2007). "OpenFOAM : A C ++ Library for Complex Physics Simulations ˇ." nternational Workshop on Coupled Methods in Numerical Dynamics, Dubrovnik, Croatia, 1–20.

Jones, W. P., and Launder, Be. (1972). "The prediction of laminarization with a two-equation model of turbulence." International journal of heat and mass transfer, Elsevier, 15(2), 301–314.

Kökp\inar, M. A., and Gö\ugü\cs, M. (2002). "High-speed jet flows over spillway aerators." Canadian Journal of Civil Engineering, NRC Research Press, 29(6), 885–898.

Kundu, P. K., Cohen, I. M., Hu, H. H., and Publishers, E. S. (2002). Fluid mechanics. Academic Press, San Diego.

Lempérière, F., Vigny, J. P., and Deroo, L. (2012). "New methods and criteria for designing spillways could reduce risks and costs significantly." Hydropower & Dams, (3), 120–128.

Lopes, P. (2013). "Free-surface flow interface and air-entrainment modelling using OpenFOAM."

Montes, J. S. (1994). "Potential-flow solution to 2D transition from mild to steep slope." Journal of Hydraulic Engineering, American Society of Civil Engineers, 120(5), 601–621.

Novák, P., Moffat, A. I. B., Nalluri, C., and Narayanan, R. (2007). Hydraulic structures. CRC Press.

Pope, S. B. (2000). Turbulent Flows. Cambridge University Press.

Reclamation, B. of. (2012). "Water Operation and Maintenance Bulletin." Reclamation Managing Water in the west, 229.

Reinauer, R., and Hager, W. H. (1998). "Supercritical flow in chute contraction." Journal of hydraulic Engineering, American Society of Civil Engineers, 124(1), 55–64.

Song, C. C. S., and Zhou, F. (1999). "Simulation of free surface flow over spillway." Journal of Hydraulic Engineering, American Society of Civil Engineers, 125(9), 959–967.

Tanchev, L. (2014). Dams and appurtenant hydraulic structures. CRC Press.

Valero, D., and Bung, D. (2015). "Hybrid investigation of air transport processes in moderately sloped stepped spillway flows." E-proceedings of the 36th IAHR World Congress, 28 June - 3 July, The Hague, the Netherlands, 1–10.

Assessment of Equilibrium Scour by a Submerged Circular Turbulent Impinging Jet in Cohesive Soils

M.R. Amin[1] and K.A. Mazurek[1]
[1]Dept. of Civil and Geological Engineering
University of Saskatchewan
Saskatoon, SK S7N 5A9
Canada
E-mail: Kerry.Mazurek@usask.ca

ABSTRACT

In this paper, results from a study where detailed measurements of the time development of the scour holes produced by a submerged circular vertical impinging jet in cohesive soils from long-term scour tests are presented. This is the type of jet used in the ASTM standard Jet Erodiblity Test, which relies on measurements of the time development of scour for prediction of soil erodibility parameters. In the experiments, measurements of the entire scour hole were taken after scouring times of 5 min, 10 min, 15 min, 20 min, 30 min, 40 min, 50 min, 1 h, 1.5 h, 2 h, 4 h, 8 h, 16 h, 24 h, and then at an interval of 24 h thereafter until the scour hole was considered to have reached equilibrium. The measurements were taken on a 2 mm grid using a computer-controlled laser displacement meter. For the tests, two types of manufactured pottery clays were used. The growth of the maximum depth of scour, average scour hole radii, centerline depth of scour, and scour hole volume were evaluated. It was seen that the characteristic dimensions of the scour hole that have been typically been used to assess equilibrium state, namely, the maximum and centerline scour holes, come to equilibrium more quickly than other locations in the scour hole. Results also showed the Sumer et al. (1993) model for predicting the time development of scour worked well for the present tests.

Keywords: cohesive soils, clays, impinging jets, scour, erosion, time development.

1. INTRODUCTION

Understanding the time development of scour of soils below hydraulic structures is important due to the potential losses associated with the undermining of the foundations of these structures. Most often the flows issuing over, through, or below hydraulic structures are in the form of turbulent jets. As such, scour by jets has been a topic of active research over the last 80 years. Further, results from tests assessing the scour produced by vertical impinging jets are also used to assess the erodibility of soils. The jet erodibility test developed by Greg Hanson and his colleagues of the Agriculture Research Service of the US Department of Agriculture (Hanson 1990, Hanson 1991, Hanson and Cook 1997, Hanson and Cook 2004) is an ASTM standard test for erodibility (ASTM D5852, 2007).

Often experiments of scour by jets are run until the scour hole has reached its final or largest size, called the equilibrium, ultimate, or asymptotic state. The equilibrium state is used to help determine the largest size a scour hole might get under particular hydraulic conditions of flow for a given soil. It is thought by some that a scour hole never actually reaches a final size due to the potential for large turbulent fluctuations, and, therefore, some treat this state as a "practical" largest size. Additionally, there has been uncertainty in deciding how to assess when a scour hole has reached equilibrium.

Equilibrium scour has been defined differently in different studies. According to Chabert and Engeldinger (1956), the depth of scour does not change "appreciably" with time at equilibrium condition. Ettema (1980) distinguished three phases of scour and indicated that the scour depth remains "practically" unchanged with time in the last phase, known as the equilibrium phase. Coleman *et al.* (2003) inferred that at equilibrium condition, the scour depth might continue to increase at a "relatively slow rate." The interpretation of equilibrium scour is different by the selection of the words "appreciably," "practically," and "relatively slow rate" in these studies (Simarro *et al.* 2011), and a quantifiable definition of the equilibrium scour is required. Lauchlan (1999) adopted a uniform period of only 24 hours for bridge pier scour experiments. Coleman *et al.* (2003) considered that the equilibrium condition is achieved

when the rate of scour had reduced to 5% of the minimum dimension of the structure (e.g., pier diameter, abutment length, etc.) in a 24-hour period. Sheppard *et al.* (2004) followed a similar approach for local scour experiments with circular piles in cohesionless sediments. Ahmed and Rajaratnam (1998) adopted a relatively conservative approach and ran experiments with cylindrical pipers in cohesionless sediments for 2-3 weeks until the incremental increase in scour depths were less than 1 mm in 24 hours. Grimaldi (2005) identified the equilibrium condition when the scour rate is reduced to 5% of one-third of the pier diameter in 24 hours. Fael *et al.* (2006) proposed to consider the reduction of scour rate in 24 hours to two times of the mean diameter of the cohesionless sediment after they conducted local scour experiments at vertical-wall abutments. However, Simarro *et al.* (2011) and Chreties *et al.* (2008) criticized such quantifications of equilibrium scour because these values are arbitrary, and any change in these arbitrary values may produce significant change in measured equilibrium dimensions and time.

A graphical approach has been used in many studies in scour experiments with turbulent wall jets and circular impinging jets to reduce arbitrariness in assessing equilibrium scour (e.g., Rajaratnam and Berry 1977, Rajaratnam and Beltaos 1977, Rajaratnam 1982, Rajaratnam 1981). In this method, the scour depth is plotted against the logarithm of time to observe the change of gradient in the resulting curve. When the gradient approaches zero, the system is considered to be in equilibrium. Cardoso and Bettess (1999) utilized the graphical approach in experiments of local scour at bridge abutments in a sand bed.

In these previous studies, the equilibrium condition was assessed using the time development of the maximum or centerline depth of scour. In cohesionless soils, these two depths generally coincide in scour by vertically impinging circular jets. However, in clayey soils, this is often not the case (Mazurek *et al.* 2001). Because of mass erosion in clayey soils, the scour hole may not be at equilibrium although the maximum and centerline scour depths may have appeared to reach this state. In this paper, results for the time development of scour from two long-duration tests of scour by submerged, vertical turbulent impinging jets in cohesive soils are reported. The entire scour hole was measured at different intervals during testing to assess whether equilibrium was in fact reached. Additionally, time development of scour results are compared to predictions from four models.

2. EXPERIMENTAL SETUP AND EXPERIMENTS

The scour testing was performed inside an octagonal Plexiglas tank of 1.2 m depth and 1.1 m height. Figure 1 shows the experimental setup. A 0.95 m long plenum was centered above the tank and hung vertically to an iron frame with hinges so that the plenum could be moved sideways along a vertical plane. A circular nozzle with a diameter d of 8 mm was attached at the bottom of this plenum. The nozzle was designed following the standards laid out in ASME (1990) so that the flow contraction occurred smoothly without any significant head loss, and the velocity across the nozzle would be uniform. City of Saskatoon tap water was pumped to the jet plenum from a constant head tank. Flow rates were measured using both an ultrasonic flow meter and a mercury U-tube manometer. A device was constructed to ensure that the jet impinged vertically on the soil sample set below the jet. The jet was set at a height H of 85 mm of the sample so that the relative impingement height H/d = 10.6. For the first test (clay sample P300), the jet velocity U_o was 8.99 m/s so that the jet Reynolds number at the nozzle, $R=U_o d/\nu$, was 71625, where ν is the kinematic viscosity of water at test temperature. For the second test (clay sample M370), the jet velocity was 10.69 m/s with a jet Reynolds number of 85152.

For each measurement of the shape of the scour hole, the flow was diverted back to the constant head tank and the jet plenum was moved away from the sample. The scour hole was then measured using a laser optical profiler mounted on a two-dimensional (in the horizontal plane), computer-controlled traverse system set above the jet tank. The traverse system was operated using National Instruments LabVIEW 5.5. The profiler moved on a 2 mm fine grid over the sample. The sample was kept under water during profiling so that the sample would not crack due to shrinkage as it dried. Therefore, the depth recorded was less than the actual depth due to refraction. The depths were corrected later to take this into account. The measurements were taken at 5 min, 10 min, 15 min, 20 min, 30 min, 40 min, 50 min, 1 h, 1.5 h, 2 h, 4 h, 8 h, 16 h, 24 h and then after every 24 h until the equilibrium condition was achieved. During the test, the eroded volume was plotted against the logarithm of time to see whether the resulting curve had started to become parallel to the *x*-axis, which was an indication that the scour hole was in equilibrium. The test duration for Test 1 (P300 clay) was 168 h, while the Test 2 (M370 clay) ended after 312 h of testing.
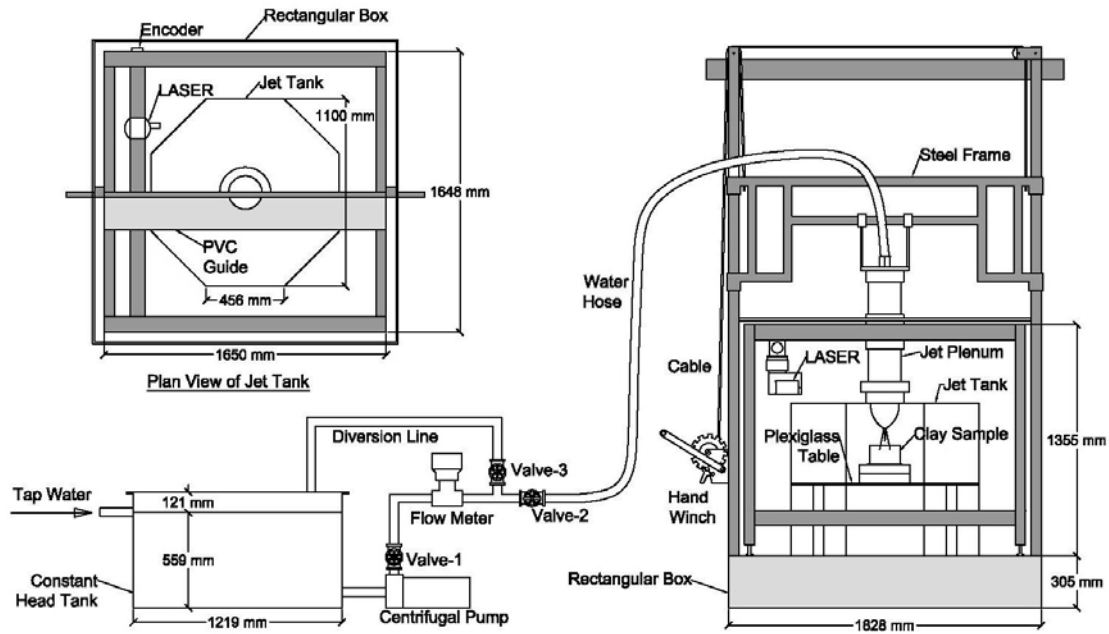
Figure 1. Experimental setup

The P300 and M370 soil samples were manufactured pottery clays from Plainsman Clays of Medicine Hat, Alberta, Canada. These were used instead of the natural soil samples since disturbances due to sampling in natural samples can have a strong influence on the development of scour in clayey soils. The P300 soil sample contained 50% clay, 47% silt, and 2% fine sand, while the M370 soil sample contained 55% clay, 43% silt, and 2% fine sand. Table 1 gives the soil properties of each sample, which were determined following the ASTM standards D854-14 (2014), D2216-10 (2010), D4318-10 (2010), and D7263-09 (2009).

Table 1. Properties of the clay samples used in scour testing experiments.

Clay Sample	Specific Gravity, G_s	Average Water Content, w_c (%)	Liquid Limit, LL (%)	Plastic Limit, PL (%)	Bulk Density, ρ_b (kg/m^3)	Dry Density, ρ_d (kg/m^3)	Degree of Saturation, S_w (%)
P300	2.70	31.3	34.0	18.5	1916	1686	98
M370	2.69	28.9	43.3	15.1	1951	1788	100

3. OBSERVATIONS OF THE TIME DEVELOPMENT OF SCOUR

The time developments of the characteristic dimensions of the scour hole are plotted in Figure 2. The dimensions used for assessing equilibrium were scour hole volume (V), cubic root of scour hole volume or the average scour hole depth (ε_{avg}), depth of scour hole along the jet centerline (ε_{cl}), maximum depth of scour hole (ε_m), the maximum depth found along a section (ε_{ms}), average radius of scour hole (r_{avg}), average half-width of scour hole for scour depth on the jet centerline (b_{cl}), and average half-width of the scour hole for the maximum depth (b_m). The half-width of the scour hole is the radial distance from jet centerline to the location where b_{cl} = ½ ε_{cl} for the centerline depth, or b_m = ½ ε_{ms} for the maximum depth. The average values of scour hole radii and half-widths were determined by averaging these dimensions from four different sections of the scour hole for a particular measurement. The maximum scour depth of the section that took the longest time to reach equilibrium was used as ε_{ms}. For assessing the time to reach equilibrium, the graphical approach was used. First, the aforesaid dimensions of the scour hole were plotted against the logarithm of time in individual graphs. A "plateau" or potion of the curve parallel to the time axis was identified near the final stage of scouring, and a tangent was drawn to that plateau. The co-ordinates of the point of tangency gave the equilibrium scour dimension and time to reach equilibrium.

From Figure 2, it can be seen that for a significant portion of scouring before the equilibrium condition, the scour hole volume and depths increased linearly with the logarithm of time (Fig 2a to 2e) in scour testing in clayey soils with vertical impinging jets in cohesive soils, which is consistent with the observations of Mazurek (2001), Mazurek *et al*. (2001), and Moore and Masch (1962). However, this relationship was not seen clearly in the case of scour hole radii (Fig. 2f to 2h). Particularly in Fig. 2g, b_{cl} for Test 2 first decreased before coming into equilibrium. One of the reasons for such a behavior is the removal of large soil chunks, which resulted in skewed scour hole shape during the initial phase of the scouring process. As the scouring went on, the scour hole took a more symmetrical shape.

The removal of large soil chunks also resulted in some parallel plateaus in the development of the scour hole radius, which can be best seen in Test 1 in Fig. 2f. This happened because when a large chunk was removed, the radius did not change for few subsequent measurements. The temporal development of the average radii of the scour hole was affected most by the large chunk removal.

A comparison of time to reach equilibrium, determined from the graphical approach among different dimensions of the scour hole for Tests 1 and 2, is given in Table 2. In Test 1, the volume, average depth, and maximum depth reached equilibrium condition at the same time. The centerline took the shortest amount of time, and section-wise maximum depths took the longest to reach equilibrium state. Also, the half-widths took a considerable amount of time to reach equilibrium. This indicates in this particular test, while the maximum and centerline scour depths were not changing and the average radius of the scour hole was also constant, the side slope of the scour hole was still eroding. In Test 2, the average radius of the scour hole came to equilibrium condition considerably earlier than the section-wise maximum depth, similar to Test 1. This contrasts with the development of scour hole radius in cohesionless soils, where the radius continues to grow even after the depth reaches equilibrium state (Rajaratnam and Beltaos 1977).

Table 2. Equilibrium size and time to reach equilibrium for different characteristic dimensions of the scour hole.

Dimensions considered to test equilibrium condition	Test 1		Test 2	
	Time to Equilibrium (h)	Equilibrium Size (mm³ for V, mm for others)	Time to Equilibrium (h)	Equilibrium Size (mm³ for V, mm for others)
Volume, V	48	260241	16	351977
Average depth ((volume)$^{1/3}$), ε_{avg}	48	63.85	16	70.61
Centerline depth, ε_{cl}	48	31.68	240	37.82
Maximum depth, ε_m	48	36.88	16	40.52
Sectional maximum depth, ε_{ms}	48	36.85	312	38.68
Average radius, r_{avg}	16	72.00	48	74.00
Average half-width for centerline depth, b_{cl}	72	45.67	144	45.00
Average half-width for maximum depth, b_{max}	72	43.73	96	44.40

For Test 2, there was a large difference in equilibrium time considering the scoured volume and section-wise maximum depths. The volume came to equilibrium quickly, as little changes in volume could not be identified using the graphical approach. This is also true for the average scour depth, which was derived directly from the scour hole volume.

Though the observations of the time development of scour hole dimensions can vary from test to test, assessing the equilibrium using the section-wise or sectional maximum scour depth seems appropriate. The equilibrium time assessed using the sectional maximum scour depths was long enough for other dimensions of the scour hole to reach equilibrium as well.
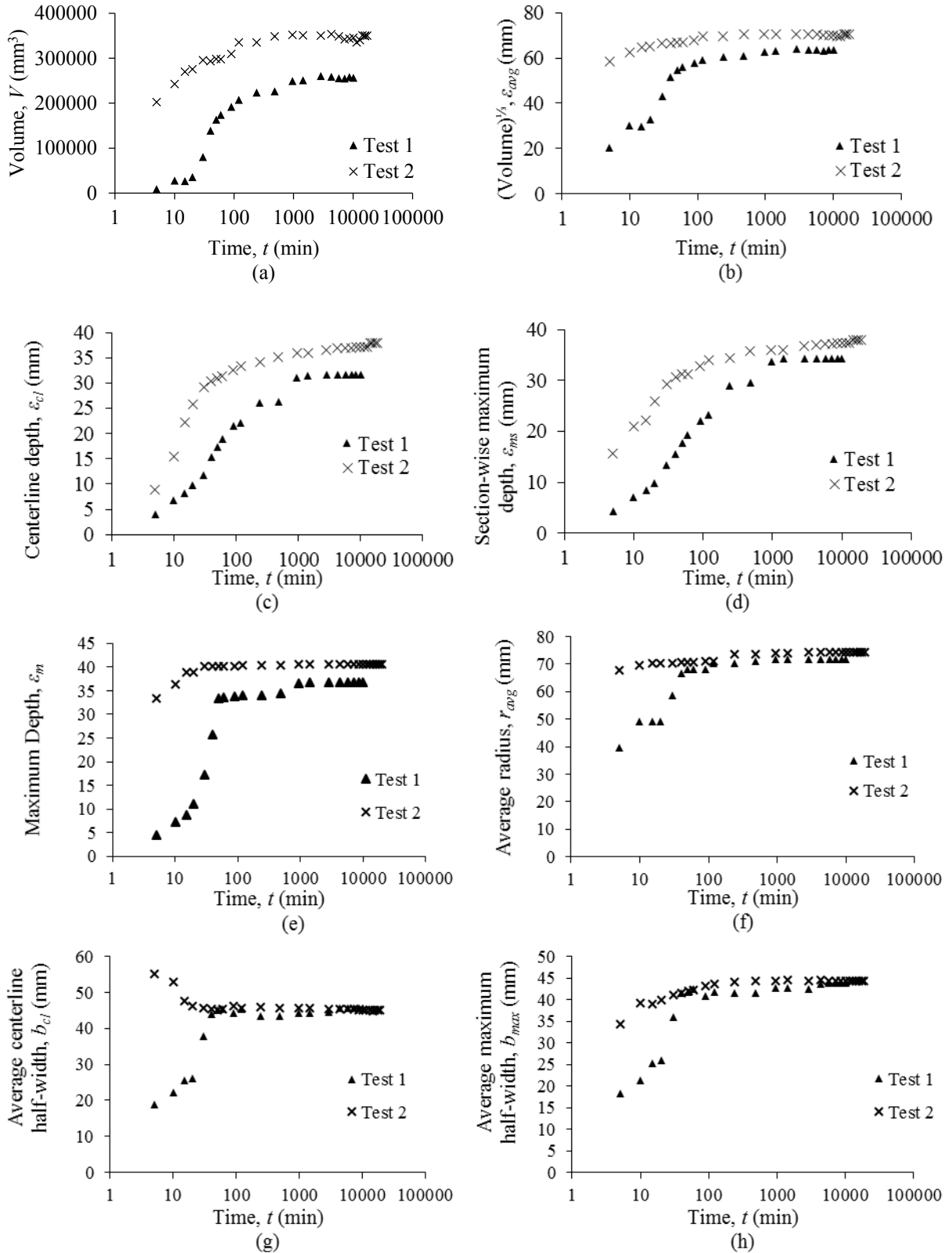
Figure 2. Time development of (a) volume, (b) average depth, (c) centreline depth, (d) sectional maximum depth, (e) maximum scour depth, (f) average radius (g) average centreline half-width, and (h) average maximum half-width of scour hole in Test 1 and Test 2.

The measurement of the maximum scour depths and other dimensions were subjected to measurement errors. These errors could produce a wrong outcome using the graphical approach, as this approach considers no visible change of time development plot at equilibrium condition. In reality, the dimension might still be in equilibrium if the changes in that dimension with time were within the margin of error. Therefore, the sectional maximum scour depths for Test 1 and Test 2 were again assessed for equilibrium time using the instrumental error of the laser optical profiler with traverse system. From analysis, it was found that the measurement system had an instrument error of ±0.25 mm for each measurement. Hence, the equilibrium time was defined when two successive depth measurements did not change by 0.25 mm in 24 h. The equilibrium time assessed by this definition using the section-wise maximum scour depths were found to be 48 h and 288 h for Test 1 and Test 2, respectively, whereas from a graphical approach, these values were 48 h and 312 h, respectively.

4. METHODS FOR DETERMINING THE EQUILIBRIUM SCOUR DEPTH

The determination of equilibrium scour depth requires the knowledge of time development of scour. Among several models for time development of scour, four of them are described briefly in this section.

Blaisdell et al. (1981) produced a hyperbolic function for the temporal development of scour hole for local scour downstream of a cantilevered pipe or culvert outlet. Hanson and Cook (1997 and 2004) later used this model for scouring by normal impingement of submerged circular jet. The hyperbolic function can be shown as follows:

$$(f - f_0)^2 - x^2 = A^2 \tag{1}$$

where $f = \ln(H/d) - \ln(U_o t/d)$, $f_o = \ln(H_e/d)$, and $x = \ln(U_o t/d)$; in which A is the semi-transverse axis of the hyperbola, H is the height of the jet origin from the soil surface, H_e is the vertical distance of the scour hole from the jet nozzle at equilibrium, d is the jet diameter at its origin, and U_o is the jet velocity at its origin. The observed scour data is fitted with the hyperbolic function using A and f_o as parameters.

Sumer *et al.* (1993) performed a series of scour experiments with circular and square piers in cohesionless sediments and developed a general equation for time development of scour hole:

$$\varepsilon_{cl} = \varepsilon_e \left(1 - e^{-t/T_1} \right) \tag{2}$$

where ε_{cl} is the centerline scour depth at time t, ε_e is the scour depth at equilibrium condition, and T_1 is the time scale of scour process. T_1 represents the time at which "significant" amount of scour occurs. Quantitatively, T_1 is the intercept from the asymptote of the scour depth versus time curve by the gradient of the curve at the initiation of scour. Using T_1 and ε_e as parameters, Eq. (2) is fitted to the observed scour data.

Mazurek (2001) showed that the plot of the dimensionless centerline scour depths against dimensionless time collapses into one single curve for the same soil under different hydraulic conditions. The following equation was developed for the time development of scour hole in the tested clayey soils:

$$\frac{\varepsilon_{cl}}{\varepsilon_{cl\infty}} = 0.10 ln\left(\frac{t}{t_{80}} \right) + 0.79 \tag{3}$$

where $\varepsilon_{cl\infty}$ is the centerline scour depth at equilibrium condition and t_{80} is the time to reach 80% of the equilibrium scour depth. This model assumes the time development of the centerline scour hole depth is logarithmic. However, this relationship was not tested for other scour hole dimensions, such as the cubic root of the scour volume, the maximum scour depth, and radius of the scour hole.

Daly et al. (2013) suggested a method of solving the excess shear stress equation (Eq. (7)) to analyze the experimental results of scour testing of cohesive sediments by jets:

$$\dot{E} = k_d \left(\tau_o - \tau_c \right)^m \tag{4}$$

where $\dot{E}$ is the erosion rate of the sediment during scour testing, k_d is the erodibility parameter, τ_o is the applied maximum shear stress on the soil surface by the jet, τ_c is the critical shear stress, and m is an empirical exponent. τ_c represents the threshold shear stress of the soil, below which no erosion can occur. The applied shear stress is computed using the following equation:

$$\tau_o = C_f \rho \left(C_d U_o \frac{d}{H} \right)^2 \tag{5}$$

where C_f is the skin friction coefficient, ρ is the density of water at test temperature, and C_d is the jet diffusion constant. From experiments with circular impinging jets on smooth and flat surfaces, Hanson et al. (1990) obtained $C_f = 0.00416$. Rajaratnam (1976) gives $C_d = 6.3$. Following Hanson (1990) and Hanson and Cook (1997 and 2004), Daly adopted $m = 1$ for cohesive sediments. The proposed method for the solution of Eq. (4) is straightforward. k_d and τ_c are considered as solution parameters. Using an equation solver, the values of these parameters are adjusted to optimize the solution for each data point. For equilibrium condition, the applied shear stress on the soil reduces to the threshold value, critical shear stress and corresponding jet height is the equilibrium jet impinging height, H_e. Then the equilibrium depth can be simply derived by deducting the initial jet impinging height, H_i from the equilibrium jet impinging height.

5. ANALYSIS AND DISCUSSION

The time development of the maximum scour depth along a section of the scour hole (ε_{ms}) was computed using the aforesaid four different models for the entire test durations of Test 1 and Test 2 to see how well these models fit the experimental data and how correctly they can predict the maximum equilibrium scour depths (ε_{me}). Table 3 shows the estimated equilibrium scour depths using different approaches.

The equilibrium scour depths predicted by the Blaisdell et al. (1981) curve fitting procedure were significantly larger than the observed equilibrium scour depth. This indicates that either the curve fitting approach overestimated the equilibrium scour depths or the experiments were not conducted up to the equilibrium condition. However, previous studies (Laursen 1952, Rajaratnam and Beltaos 1977, Rajaratnam and Berry 1977) suggested that the depth of scour increases linearly with logarithm of time and suddenly starts to become parallel with the time axis when equilibrium phase initiates. From experimental results, it can be inferred that the performed scour tests actually reached equilibrium phase, and, hence, that the curve fitting approach overestimated the equilibrium scour depths.

The general equation developed by Sumer et al. (1993) was solved for the observed data points. The solutions fit well for the observed data points with correlation coefficients $r^2 = 0.98$ for Test 1 and $r^2 = 0.99$ for Test 2. Figure 3 shows the accuracy of the Summer et al. (1993) approach. Though for both tests the curve fits were good, the predicted equilibrium scour depths were slightly underestimated.

The Mazurek (2001) model for time development of scour reasonably fit the data for both the tests. However, this model assumes the time development of scour depth is linear with the logarithm of time for the whole scouring process, which is not the case in reality. Therefore, instead of fitting the observed scour data near the equilibrium state, the predicted curve was increasing logarithmically. As a result, maximum scour depths were overestimated.

Table 3: Estimation of equilibrium depths of scour using different methods.

Analysis Methods	Equilibrium Depth, ε_{ms} (mm) for Test 1	Goodness of fit		Equilibrium Depth, ε_{ms} (mm) for Test 2	Goodness of fit	
		Correlation coefficient, r^2	Root Mean Square Error, RMSE (mm)		Correlation coefficient, r^2	Root Mean Square Error, RMSE (mm)
Graphical Approach	36.85	-	-	38.68	-	-
Blaisdell *et al.* (1981)	134.31	0.83	10.61	50.18	0.58	10.62
Sumer *et al.* (1993)	35.86	0.98	2.01	37.60	0.99	1.01
Mazurek (2001)	40.32	0.77	7.90	42.90	0.52	3.69
Daly *et al.* (2013), *m*=1	36.79	0.76	9.07	37.92	0.16	23.07
Daly *et al.* (2003), *m*=2.5	37.16	0.84	6.79	38.33	0.73	5.87
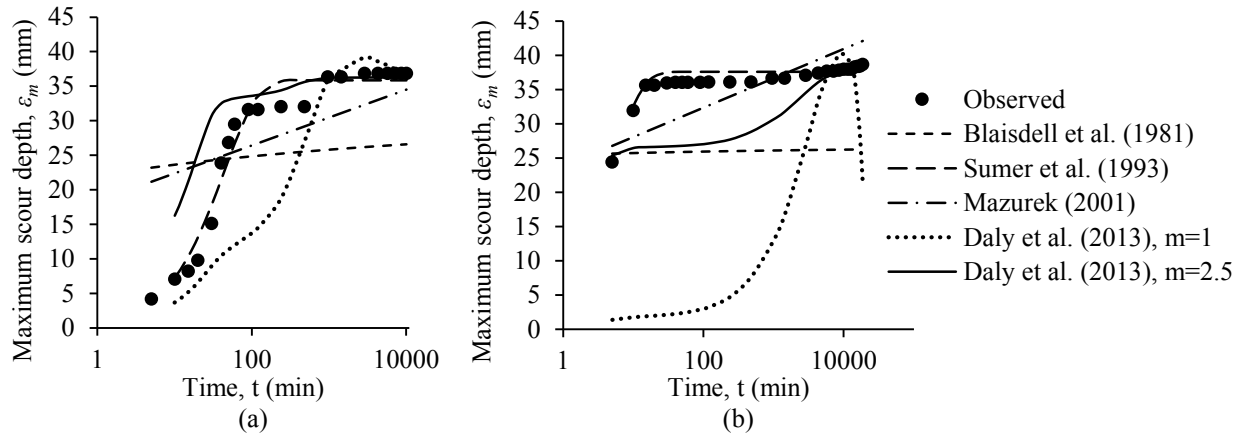
Figure 3: The performance of different time development models for fitting experimental data of (a) Test 1, and (b) Test 2.

Using the Daly *et al.* (2013) approach, the excess shear stress equation was fitted with the observed data for *m*=1. Like the Blaisdell curve fitting approach, multiple solutions were possible. Therefore, the solutions were again optimized to minimize the curve fitting errors. For P300 soil sample, estimated values of k_d and τ_c were 1.4×10^{-7} m^3/N-s and 49.3 N/m^2, respectively. For the M370 sample, these values were 1.0×10^{-7} m^3/N-s and 68.2 N/m^2, respectively. For both samples, the estimated equilibrium scour depths were very close to those obtained by the graphical approach. However, the curve fitting was poor. This implies that if experimental data with less data points were used instead of full scouring data till equilibrium, the predicted scour depth would be much different than the observed one. The same analysis was performed again for erosion exponent *m*=2.5, as suggested by Walder (2015). This time, k_d and τ_c for the P300 sample were 2.1×10^{-9} m^3/N-s and 49.0 N/m^2, respectively, and 5.6×10^{-9} m^3/N-s and 67.4 N/m^2 for the M370 sample, respectively. The model fit the experimental data well, and the predicted scour depths were close to the scour depths obtained using graphical approach.

Apart from the above four time development model of scour, another model developed by Ansari (2003) was also considered for scour depth prediction and fitting of experimental results. However, the Ansari (2003) scour model requires three unknowns to solve for the curve fitting, i.e., the equilibrium scour depth, the time to reach equilibrium, and an exponent. Therefore, it was not possible to use that model to predict equilibrium scour depth. Rather, using observed equilibrium depth and equilibrium time, Ansari's (2003) time development equation was solved for the exponent, and then the equation was used to find the goodness of fit. This model showed reasonable fit with r^2=0.71 for Test 1 and r^2=0.51 for Test 2. The obtained exponent values were 0.12 and 0.02 for Test 1 and Test 2, respectively.

6. CONCLUSIONS

Time development of entire scour hole shape was observed from scour testing of two clayey soils by circular impinging jets. Using the graphical approach, the time to reach equilibrium for each dimension was obtained. The results showed that the radius of the scour hole in clayey soils reached equilibrium soonest, and this observation is different from previous studies of cohesionless soils scouring, where the radius continued to grow after the depth reached equilibrium. In this work, since the entire scour hole was measured with time, it also was seen that although the centerline scour depth and overall maximum scour depth reached equilibrium, the scour hole was still growing. Four different analytical models were evaluated for their ability in equilibrium scour prediction by fitting experimental data. Among the models, the Sumer *et al.* (1993) model predicted the equilibrium scour depth quite accurately and offered best fit with the observed data.

7. REFERENCES

Ahmed, F., and Rajaratnam, N. (1998). "Flow around bridge piers". *Journal of Hydraulic Engineering*, 124(3), 288-300.

Anderson, C.L. (1975). Chapter II. Sediment Transportation Mechanics; Section C, Erosion of Sediment- Local Scour. Sedimentation Engineering, Manual No. 54. Vanoni, Vito A. (Ed.), ASCE, USA.

Ansari, S.A., Kothyari, U.C., and Raju, K.G.R. (2003). "Influence of cohesion on scour under submerged circular vertical jets*". Journal of Hydraulic Engineering*, 129(12), 1014–1019.

ASME (American Society of Mechanical Engineers). (1990). Measurement of Fluid Flow in Pipes Using Orifice, Nozzle, and Venturi. ASME, New York. (ASME MFC-3M-1990).

ASTM (American Society of Testing and Materials) D2216-10(2010), Standard Test Methods for Laboratory Determination of Water Content of Soil and Rock by Mass, ASTM International, West Conshohocken, PA.

ASTM D422-63(2007)e2, Standard Test Method for Particle-Size Analysis of Soils, ASTM International, West Conshohocken, PA.

ASTM D4318-10(2010)e1, Standard Test Methods for Liquid Limit, Plastic Limit, and Plasticity Index of Soils, ASTM International, West Conshohocken, PA.

ASTM D5852-00(2007)e1, Standard Test Method for Erodibility Determination of Soil in the Field or in the Laboratory by the Jet Index Method, ASTM International, West Conshohocken, PA

Blaisdell, F.W., Anderson, C.L., and Hebaus, G.G. (1981). "Ultimate dimensions of local scour". *Journal of the Hydraulics Division*, 107(3), 327–337.

Cardoso, A.H., and Bettess, R. (1999). "Effects of time and channel geometry on scour at bridge abutments". *Journal of Hydraulic Engineering*, 125(4), 388–399.

Chabert, J., and Engeldinger, P. (1956). Etude des affouillements autour des piles de ponts. Serie A. Laboratoire National d'Hydraulique, 6, Qui Watier, Chtou, France (in French).

Chreties, C., Simarro, G., and Teixeira, L. (2008). "New experimental method to find equilibrium scour at bridge piers". *Journal of Hydraulic Engineering*, 134(10), 1491–1495.

Coleman, S.E., Lauchlan, C.S., and Melville, B.W. (2003). "Clear-water scour development at bridge abutments". *Journal of Hydraulic Research*, 41(5), 521–531.

Daly, E.R., Fox, G.A., and Miller, R.B. (2013). "A scour depth approach for deriving erodibility parameters from jet erosion tests". *Transactions of the ASABE*, 56(6), 1343–1351.

Ettema, R. (1980). Scour at bridge piers. Report No. 216, School of Engineering, University of Auckland, Auckland, New Zealand.

Fael, C.M.S., Simarro-Grande, G., Martín-Vide, J.P., and Cardoso, A.H. (2006). "Local scour at vertical-wall abutments under clear-water flow conditions". *Water Resources Research*, 42(10), 1–12.

Grimaldi, C. (2005). Non-conventional countermeasures against local scouring at bridge piers. Ph.D. Thesis. Hydraulic Engineering for Environment and Territory. University of Calabria, Cosenza, Italy.

Hanson, G.J. (1990). "Surface erodibility of earthen channels at high stresses. Part II-developing an in situ testing device". *Transactions of the ASAE*, 33(1), 132–137.

Hanson, G.J. (1991). "Development of a jet index to characterize erosion resistance of soils in earthen spillways". *Transactions of the ASABE*, 34(5), 2015–2020.

Hanson, G.J., and Cook, K.R. (1997). "Development of excess shear stress parameters for circular jet testing". *ASAE Paper No. 972227*, 21p.

Hanson, G.J., and Cook, K.R. (2004). "Apparatus, test procedures, and analytical methods to measure soil erodibility in situ". *Applied Engineering in Agriculture*, 20(4), 455–462.

Hanson, G.J., Robinson, K.M., and Temple, D.M. (1990). "Pressure and stress distributions due to a submerged impinging jet". *Proc., National Conference on Hydraulic Engineering*, ASCE, Stillwater, United States, 525-530.

Hanson, G.J., Robinson, K.M., and Temple, D.M. (1990). "Pressure and stress distributions due to a submerged impinging jet". *Proc. ASCE National Conference on Hydraulic Engineering*, USDA ARS, Hydraulic Engineering Research Unit, Stillwater, United States, 525-530.

Lauchlan, C.S. (1999). Countermeasures for pier scour. Ph.D. Thesis. University of Auckland, Auckland, New Zealand.

Mazurek, K.A. (2001). Scour of Clay by Jets. Ph.D. Thesis, Department of Civil Engineering, University of Alberta, Edmonton, Alberta.

Mazurek, K.A., Rajaratnam, N., and Sego, D.C. (2001). "Scour of cohesive soil by submerged circular turbulent impinging jets". *Journal of Hydraulic Engineering,* 127(7), 598–606.

Moore, W.L., and Masch, F.D. (1962). "Experiments on the Scour Resistance of Cohesive Sediments". *Journal of Geophysical Research*, 67(4), 1437–1446.

Rajaratnam, N. (1976). Turbulent Jets. Elsevier, New York, 304p.

Rajaratnam, N. (1981). "Erosion by plane turbulent jets". *Journal of Hydraulic Research*, 19(4), 339–358.

Rajaratnam, N. (1982). "Erosion by submerged circular jets". *Journal of the Hydraulics Division*, 108(2), 262–267.

Rajaratnam, N., and Beltaos, S. (1977). "Erosion by impinging circular turbulent jets". *Journal of the Hydraulics Division*, 103(10), 1313–1328.

Rajaratnam, N., and Berry, B. (1977). "Erosion by circular turbulent wall jets. *Journal of Hydraulic Research*, 15(3), 277–289.

Sheppard, D.M., Odeh, M., and Glasser, T. (2004). "Large scale clear-water local pier scour experiments". *Journal of Hydraulic Engineering*, 130(10), 957–963.

Simarro, G., Fael, C.M.S., and Cardoso, A.H. (2011). "Estimating equilibrium scour depth at cylindrical piers in experimental studies. *Journal of Hydraulic Engineering*, 137(9), 1089–1093.

Sumer, B.M., Christiansen, N., and Fredsoe, J. (1993). "Influence of cross-section on wave scour around piles". *Journal of Waterway Port Coastal and Ocean Engineering*, 119(5), 477–495.

Walder, J.S. (2015). "Dimensionless erosion laws for cohesive sediment". *Journal of Hydraulic Engineering*, 10.1061/(ASCE)HY.1943-7900.0001068 , 04015047.

Cabinet Gorge Dam Spillway Modifications for TDG Abatement - Design Evolution and Field Performance

S. L. Dunlop[1], I. A. Willig[1], and G. E. Paul[2]

[1]Alden Research Laboratory, Inc.
Portland, OR 97205
USA
[2]Avista Utilities
Clark Fork, ID 83811USA
E-mail: sdunlop@aldenlab.com

ABSTRACT

Avista is implementing spillway modifications to reduce Total Dissolved Gas (TDG) supersaturation downstream of Cabinet Gorge Dam. The key feature of the modifications is the addition of roughness elements, similar to supercavitating baffle blocks, to break up the spillway jet, thereby reducing the depth of plunge and TDG supersaturation. The work is progressing in a step-wise manner. A single bay was modified in 2012 and field tested in 2013. Following the initial field tests, a CFD model was developed to aid in design refinements for the prototype and to improve the design prior to modification of subsequent spillway bays. The prototype demonstrated that spillway modifications are an effective method to reduce TDG downstream of a spillway discharging freely into a deep plunge pool. The CFD model has allowed the design to be simplified while both maintaining the plunge depth improvements of the initial prototype and reducing the effect of the modifications on spillway capacity. This paper presents the prototype design and the design that will be implemented for the next two bays, summarizes the results from the prototype field tests, and describes the CFD model and results.

Keywords: Spillways, Total Dissolved Gas, Computational Fluid Dynamics, Jets, Plunge Pools, Cavitation

1. INTRODUCTION

Elevated levels of Total Dissolved Gas (TDG) in spillway discharge is a significant water quality concern at many dams due to the potential for TDG supersaturated water to induce Gas Bubble Trauma (GBT) in endangered fish species. Water quality standards typically limit TDG to 110% of saturation. At Cabinet Gorge Dam, TDG often exceeds 130% during spill.

Avista Utilities owns and operates Cabinet Gorge Dam and is actively implementing modifications to reduce TDG generated by spill releases. Cabinet Gorge Dam is located on the Clark Fork River in Idaho, approximately 16 kilometers (10 miles) upstream of Lake Pend Oreille. The dam was constructed in 1952. It has eight gated spillways that release water over very short chutes before the jets fall freely into a deep plunge pool. The spillway configuration allows the jets to entrain air and plunge to depth, where increased pressure forces the air into solution, resulting in the potential to elevate TDG concentrations in the river downstream. Avista is pursuing structural spillway modifications that will break up the jet to reduce the depth of plunge and the length of time that the aerated water is held at depth, thereby reducing TDG levels downstream. The scientific literature includes considerable research about TDG and GBT. The focus of this paper is to document a new method to reduce TDG downstream of spillways with freely plunging spillway jets. For general information about TDG and GBT, the reader is referred to other sources such as Maynard (2008), Weitkamp (2008), Johnson (1975).

Avista's approach to the spillway modification design, construction, and monitoring has been incremental, with a goal to learn from each installation and to use site-specific performance data to guide the design for a full build-out of the concept. In 2012, Avista modified a single bay, the design of which was based upon extrapolation of studies conducted for other facilities and applications. In 2015, two additional bays are being modified; the design for these bays was developed with the benefit of site-specific Computational Fluid Dynamics (CFD) modeling to estimate plunge depth and the effect of the modifications on spillway capacity. This paper presents the two designs, the

numerical modeling used for design development, and the field performance of the spillway modifications, which are the first full-scale application of this TDG abatement measure.

2.   LAYOUT OF THE SPILLWAY MODIFICATIONS

Cabinet Gorge Dam has eight spillway bays and a four-unit powerplant with a hydraulic capacity of 1,100 m³/s (38,800 cfs). Flow release from the spillway bays is controlled by 12.2-meter wide by 10.7-meter high (40-foot by 35-foot) vertical-lift roller gates, which are numbered sequentially from the right bank to the left bank (looking downstream). The drop from the end of the spillway to the downstream water surface varies with tailwater depth but is on the order of 12 meters (40 feet). The plunge pool is lined with a 1.5 meter (5 foot) thick concrete apron that generally follows the natural bathymetry at the time of construction, which varied substantially in elevation. The apron below Bays 5-8 has its invert at elevation 626 meters (2055 feet) and drops up to 4.6 meters (15 feet) at its end. The plunge pool invert is up to 20 meters (65 feet) lower below spillway bays 1-4, and there is a splitter wall dividing the two sides of the plunge pool. The shallow-side apron provides a physical constraint to the depth that a jet from Bays 5-8 may plunge. The plunge pool geometry, coupled with the interaction between spillway and powerplant discharge, creates complex flow patterns that likely affects the degree of TDG supersaturation in the plunge pool and river downstream. See Figure 1 for the general layout of the spillway and plunge pool.
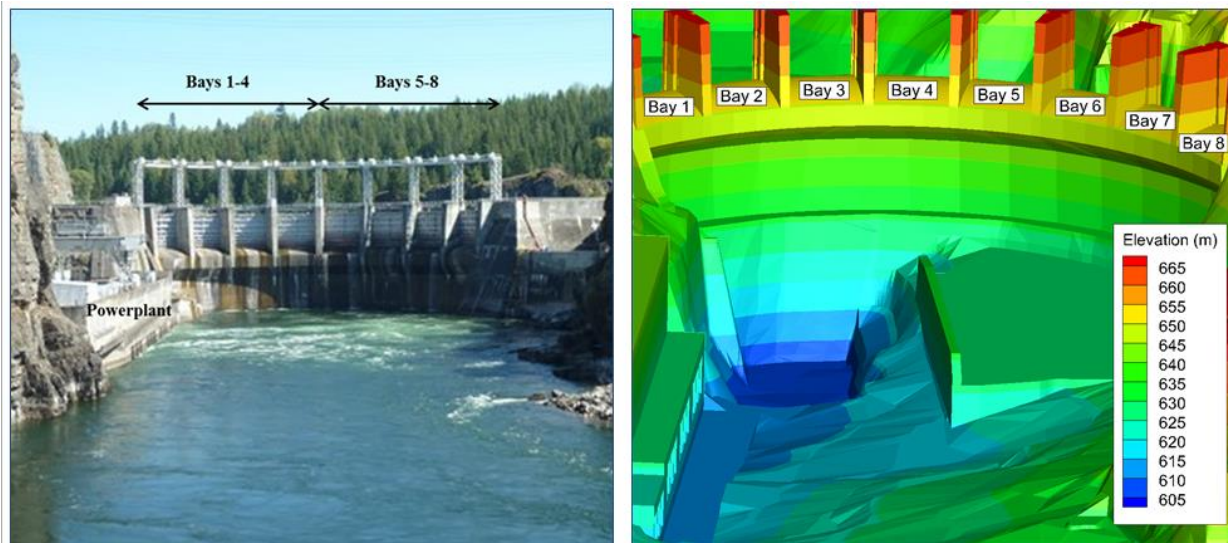
Figure 1. Cabinet Gorge Dam Layout and Plunge Pool Bathymetry

2.1. Spillway Bay 2 Prototype Modifications

The first spillway bay to be modified (Bay 2) features two rows of roughness elements and a flip bucket addition at the spillway terminus. The shape of the roughness elements is intended to mimic the supercavitating blocks studied by the United States Bureau of Reclamation (USBR) (Frizell 2009); however, the function and location of the roughness elements is different for the Cabinet Gorge application. The USBR sought to develop baffle blocks to dissipate energy in a stilling basin, whereas the roughness elements implemented at Cabinet Gorge seek to break up the spillway jet, thereby reducing the depth to which it will penetrate within the plunge pool. A ramp, 25.4 centimeters (10 inches) in height, is located immediately upstream of the first row of roughness elements. The Bay 2 ramp serves two purposes: to lift the tails of horseshoe vortices that form upstream of the roughness elements and to provide a conduit for air, which is supplied to reduce the potential for cavitation damage on the downstream row of roughness elements. Figure 2 shows the layout of the Bay 2 spillway modifications. As illustrated in the photo, the Bay 2 roughness elements have different designs; this was done to evaluate constructability and physical performance in anticipation of future construction on additional bays, but because the differences are all downstream of the roughness elements' faces, these variations do not affect TDG performance.
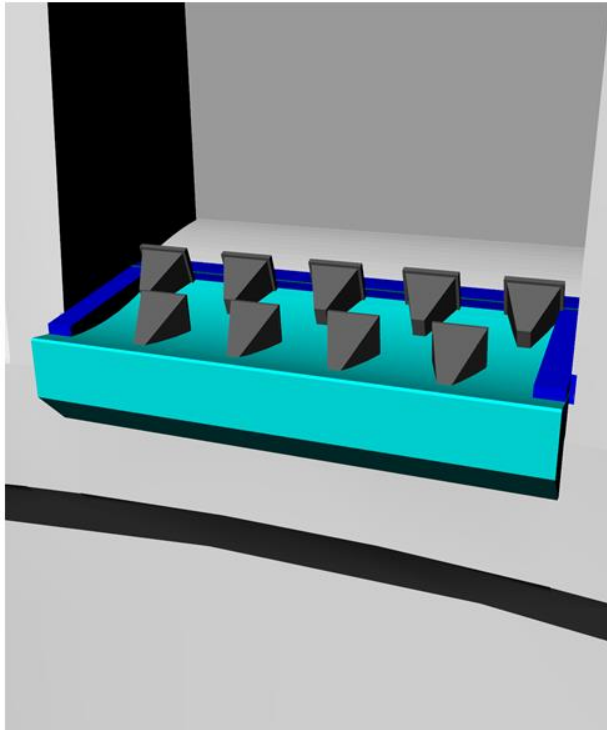
CFD Isometric   As-Constructed

Figure 2. Bay 2 Final Design

TDG supersaturation was measured in controlled field tests before and after Bay 2 was modified. In addition, field tests were run using Bay 7 to allow comparison between spillway discharges into the shallow and deep sides of the plunge pool. The controlled field tests produced the peak TDG measurements shown in Table 1.

Table 1. Bay 2 Modification TDG Performance, Spillway Only Operation

	Peak TDG (% Saturation)		
	Q = 156 m³/s (5,500 cfs)	Q = 217 m³/s (7,660 cfs)	Q = 302 m³/s (10,660 cfs)
Bay 2 Before Modification	116.7	123.0	127.9
Bay 2 After Modification	110.5	115.2	120.3
Bay 7 Unmodified	110.7	112.6	114.5

Similar controlled tests were conducted with the powerplant operating. These tests were conducted with a total facility discharge of 434 m³/s (15,320 cfs) evenly split between the spillway and the powerplant, i.e., 217 m³/s from the spillway and 217 m³/s from the powerplant. This set of tests attempted to determine if there was any effect of flow interaction between the spillway and powerplant discharges and whether the location of the powerplant discharge affected TDG supersaturation. The results are presented in Table 2.

479

Table 2. Bay 2 Modification TDG Performance, Combined Spillway and Powerplant Operation

Powerplant Unit and Spillway Bay Operating	TDG (% Saturation)					
	Average Forebay TDG		Peak Downstream TDG		TDG Increase	
	Powerplant Unit 1	Powerplant Unit 4	Powerplant Unit 1	Powerplant Unit 4	Powerplant Unit 1	Powerplant Unit 4
Bay 2 After Modification	99.9	101.2	107.7	111.5	7.8	10.3
Bay 7 Unmodified	101.3	100.1	108.2	109.5	6.9	9.4
Bay 3 Unmodified	100.7	101	123.1	135.7	22.4	34.7

Comparing the results of the modified Bay 2 versus unmodified Bay 3 tests clearly demonstrates that the modifications are effective at reducing TDG generated by a spillway bay discharging into the deep side of the plunge pool. Comparing the results for modified Bay 2 and unmodified Bay 7 indicates that the modifications applied to a deep bay may approach, or even exceed, the performance associated with spillway releases from a shallow bay, depending on operations. Finally, the results indicate that the interaction between flow released from the powerplant draft tubes, flow released from the spillway, and the resulting plunge pool circulation patterns affect TDG supersaturation measured at the downstream TDG monitoring gauge.

Prior to implementing spillway modifications, spillway discharge was released preferentially through Bays 5-8 to minimize TDG supersaturation downstream. After completion of the Bay 2 prototype modifications, Avista changed the operating sequence as follows: the powerplant discharge was maximized, then the first 170 m^3/s (6,000 cfs) of spillway flow was released via modified Bay 2, and any remaining spillway discharge was evenly distributed between the four shallow spillway bays (Bays 5-8). Late in the season, the historic preferential operation in which flow was released only through Bays 5-8 was resumed; this allowed "opportunistic" testing of both operational regimes, which is summarized in Figure 3. Figure 3a indicates that the use of modified Bay 2 discharging up to 170 m^3/s (6,000 cfs) produces lower TDG supersaturation for a given spillway discharge than the historic preferential operation. Figure 3b directly compares the TDG measured upstream and downstream of Cabinet Gorge Dam for different spillway operations on a given day.

The foregoing tests validated the theory that breaking up the spillway jet through the use of roughness elements resulted in a measureable reduction in TDG.
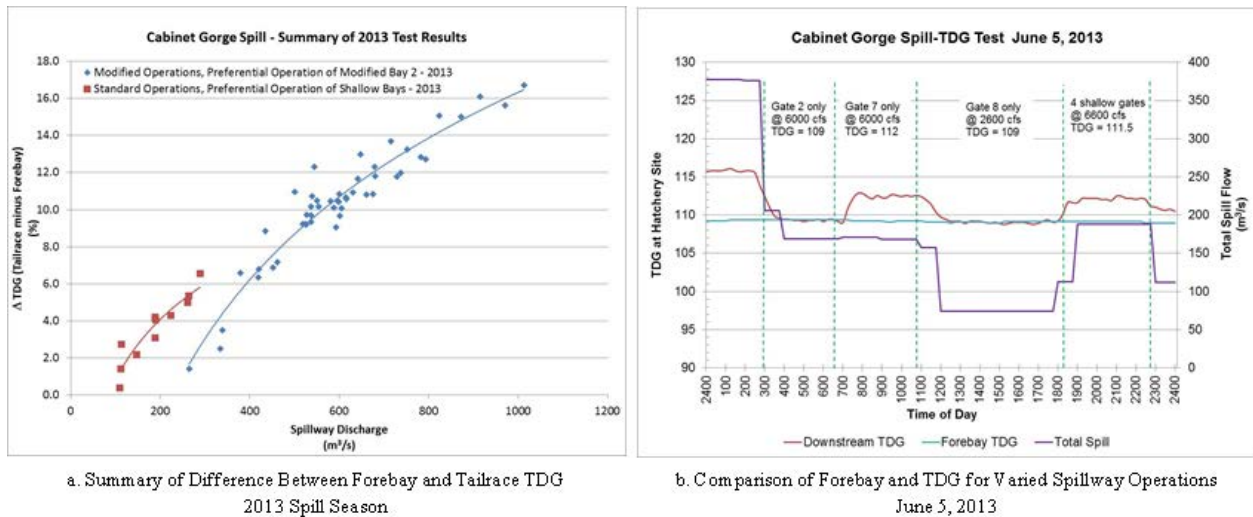
a. Summary of Difference Between Forebay and Tailrace TDG 2013 Spill Season

b. Comparison of Forebay and TDG for Varied Spillway Operations June 5, 2013

Figure 3. Operations Testing, 2013 Spill Season

2.2. Spillway Bays 4 and 5 Modifications

The next two spillway bays to be modified (Bays 4 and 5) feature a single row of roughness elements, a ramp without air supply, and a straight tangential spillway end extension. Figure 4 shows the layouts of Bays 4 and 5. CFD modeling (as described below) was used to develop the design and to evaluate a range of constructible alternatives with the goal of minimizing the effect of the roughness elements on spillway capacity while still reducing TDG levels downstream of the dam. The new design is comparatively straightforward and is expected to treat a higher volume of spill flow per bay than the Bay 2 modifications. Bay 4 (deep plunge pool) and Bay 5 (shallow plunge pool) will be field tested in early 2016, and the results of those tests will guide the selection of which spillway bays to modify for the full TDG abatement project build-out.

C   sometric   As-Constructed
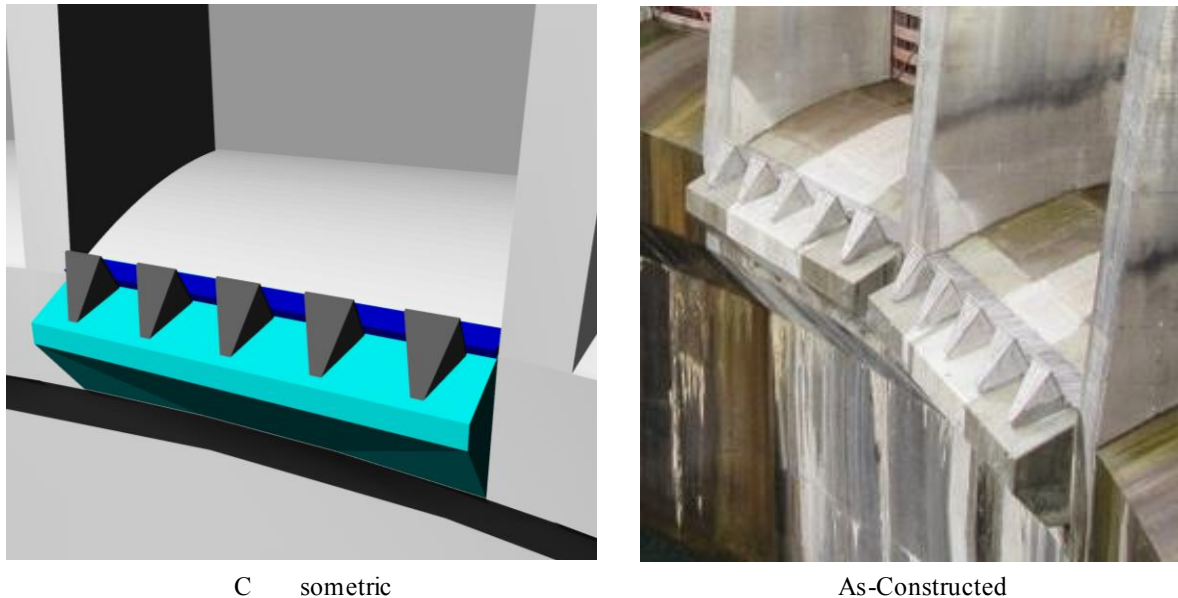
Figure 4. Bays 4 and 5 Final Design

3. SPILLWAY BAY MODIFICATIONS - DESIGN DEVELOPMENT

The hydraulic design of the Bay 2 modifications was guided by physical and computational modeling that were in progress for a similar approach to TDG abatement being analyzed for Seattle City Light's Boundary Dam (Dunlop *et. al.* 2014), and on work performed by the USBR to develop the stilling basin for Folsom Dam (Frizell 2009). The layout of the Bay 2 roughness elements was established to fit the geometry of the Cabinet Gorge spillway but was not verified using site-specific modeling. The Bay 2 modifications were evaluated for TDG performance during controlled field tests, then Bay 2 was operated continuously for 26 days during the first spill season after construction. The field data validated the theory that roughening the spillway surface to break up the jet is an effective TDG abatement measure; however, cavitation damage to the spillway surface and roughness elements was observed. In response, a CFD model of a single spillway bay was developed to aid the refinement of the Bay 2 configuration. The final Bay 2 modifications (as seen in Figure 2) were field tested for 26 days in 2014. An inspection conducted by Avista after spillway operation confirmed that the revised design successfully mitigated cavitation damage.

Avista subsequently proceeded with implementing spillway modifications for two additional bays. The design for the additional bays was developed with the benefit of the single-bay CFD model. The model was used to the following purposes:

- Quantify any effect of the roughness elements on spillway capacity during passage of the Probable Maximum Flood (PMF)

- Refine the spillway modifications' design to minimize capacity effects while maintaining the reduction in jet plunge depth
- Reduce design and construction complexity, to the extent possible

The design development considered these goals in parallel, *i.e.* for a given layout, input on constructability was obtained prior to modeling, and modeling of the effect on discharge capacity and plunge depth were each considered. In addition, the design development process used the results of each run and the knowledge gained to guide the configuration of the subsequent runs.

3.1. CFD Model Description

The numerical modeling design tool selected for this study was the FLOW-3D software, developed by Flow Science Inc. The software solves the Reynolds-averaged Navier-Stokes equations to predict steady-state and transient flow fields in the model domain. In FLOW-3D, free surfaces are modeled with the volume of fluid (VOF) technique (Hirt and Nichols, 1981). The VOF method consists of three components: a scheme to locate the surface, an algorithm to track the surface as a sharp interface moving through a computational grid, and a means of applying boundary conditions at the surface. The software is also able to model air entrainment by turbulence at the free surface (Hirt, 2012). This capability was used to compare relative air entrainment depth in the plunge pool across the alternatives investigated for this study.

Two discrete computational domains were used for this study. The model domain used for the PMF investigations consisted of a single bay and a limited portion of the forebay. The mesh extended almost a full bay width on either side of the operational bay and included the full pier geometry. The model domain used for the assessment of plunge depth consisted of a single bay, a limited portion of the forebay, and approximately 150 meters (500 feet) of the plunge pool. The exact bathymetry of the forebay and plunge pool were not included in either model; instead, a flat surface at the approximate elevation of the invert at the dam was used. The upstream and lateral forebay boundary conditions were modeled as pressure boundaries. The downstream boundary in the PMF model was simulated as an outlet, allowing free discharge. The downstream boundary in the plunge depth model was simulated as a pressure boundary set to the tailwater elevation. Bay 2 was used as the representative bay for the study, and the corresponding tailrace invert elevation was set to 606.6 meters (1990 feet). This approach allowed the design development for Bays 4 and 5 to build on the modeling work completed for the Bay 2 final design and provided a representative bay for assessing plunge depth into a deep bay.

The computational mesh for the PMF model domain consisted of approximately 2.2 million cells with cell size ranging from 1 meter in the forebay to 8 centimeters in the vicinity of the roughness elements. The computational mesh for the plunge depth model domain was made up of roughly 2.6 million cells with cell size spanning from 1.5 meters in the tailrace to 15 centimeters in the vicinity of the roughness elements.

The air entrainment model estimates the rate at which gas is entrained into the flow by balancing the stabilizing forces (gravity and surface tension) and destabilizing forces (turbulence) (Flow Science, 2014). The air entrainment model setup used the default settings as no field data were available for refinement of the coefficients. Bulking and buoyancy were both included in the air entrainment model, and the renormalized group (RNG) k-ε turbulence model was used based on its robustness and on the advice of Flow Science.

Ten configurations were simulated using the CFD model. These included the baseline (no modifications), the existing Bay 2 geometry, a flip bucket without any roughness elements, and seven different layouts of roughness elements and end treatments. The seven alternative layouts considered changes to the following parameters:

- Roughness element height
- Position of the upstream row of roughness elements
- Spillway end extension configurations
- Roughness element number, orientation, and relative positioning
- Number of rows of roughness elements
- Number of roughness elements per row

3.2. Spillway Capacity during Passage of the PMF

The Bay 2 roughness elements are located in a zone of supercritical flow downstream from the critical flow control at the spillway crest, but they are located high on the spillway, and the flip bucket changes the trajectory of the flow downstream of the roughness elements; therefore, the effect of the roughness elements on spillway capacity could not be conclusively determined using hydraulic theory alone. The CFD model was used to evaluate what effect, if any, the spillway modifications would have on spillway capacity during passage of the PMF.

The following conditions were imposed in the CFD model for the simulation of the PMF discharge capacity: the spillway gate was removed completely from the computational domain, the forebay water surface elevation was set to the PMF peak static reservoir level, and the model was run to simulate 60 seconds of operation in order to capture the range of turbulent flow variation. The discharge through the spillway bay was estimated by monitoring the flow rate at six vertical planes (computational baffles) placed along the spillway. The six baffles were used to improve the accuracy of the computed discharge and to provide accurate comparison across the different spillway geometries.

The discharge during passage of the PMF was determined using the CFD model for each of the spillway modification layouts presented in Table 3. The results were compared to the discharge computed by the CFD model for an unmodified bay. The CFD results for the baseline condition at the design flow rate showed good agreement with the spillway rating curves (within 1%).

Table 3. Effect of Spillway Modifications on Spillway Capacity during Passage of the PMF

Layout	PMF Capacity Reduction from Baseline (%)	Details
Baseline (Unmodified)	N/A	Pre-Modification Baseline
Layout 1	8.1	Max. Block Height (2 rows h=1.22 meters (48 inches))
Existing (Bay 2 Prototype)	6.7	Bay 2 Prototype (2 rows – U/S h=1.02 meters (40 inches), D/S h=0.94 meters (37 inches))
Flip Bucket Only	5.4	Flip Bucket Only
Layout 2	2.5	Single Row h=0.94 meters (37 inches), Tangential End Ext.
Layout 3	3.2	Single Row h=1.22 meters (48 inches), Tangential End Ext.
Layout 4	4.0	Single Row h=1.52 meters (60 inches), Tangential End Ext.
Layout 6	3.0	Single Row h=0.94 meters (37 inches), 5 Blocks Rotated, Tangential End Ext.
Layout 7	3.0	Single row h=1.14 meters (45 inches), Tangential End Ext.

Layout 1 resulted in a decrease of 8.1 percent in the capacity of a single bay, as compared to the baseline (unmodified) spillway bay capacity. The geometry of Layout 1 represents the largest roughness element that could be physically constructed given the available space.

The next run documented the performance of the Bay 2 prototype and concluded that the as-constructed geometry reduced the discharge of that bay during passage of the PMF by 6.7 percent.

The third run isolated the primary factors causing the reduction in capacity. The geometry of the Bay 2 prototype was simulated with the roughness elements removed, *i.e.*, the only change from the baseline condition was the addition of the flip bucket end extension. The capacity reduction associated with the Bay 2 prototype geometry (6.7 percent) compared with the flip bucket only geometry (5.4 percent) demonstrates that the flip bucket end extension is a primary variable affecting spillway capacity. Based on this finding, the flip bucket end extension was removed from further consideration, and subsequent alternatives were developed using a tangential end extension.

The purpose of the next simulation (Layout 2) was to determine the PMF effect of roughness elements placed as far downstream on the tangential end extension as possible. The maximum length of the end extension and the location

of the roughness elements were dictated by structural design and constructability requirements. The roughness element height was set equal to the height of the downstream row of roughness elements in the Bay 2 prototype (0.94 meters). This produced a reduction in discharge capacity during the PMF of 2.5 percent. Simulation of the effect of the change in geometry on plunge depth was conducted in parallel with the PMF analysis and indicated that a single row of roughness elements on a tangential end extension could provide satisfactory TDG performance.

The next four simulations (Layouts 3-6) investigated a range of roughness element heights and arrangements.

The final simulation (Layout 7) was performed in response to a change in the design discharge from 170 m^3/s (6,000 cfs) to 204 m^3/s (7,200 cfs), which was implemented to maintain the desired total TDG abatement design flow while reducing the number of bays that would be modified for full build-out from seven to six.

Layout 7, the preferred alternative, was subsequently analyzed using HEC-HMS to determine the change in peak reservoir elevation that would result from the reduction in spillway capacity. This analysis confirmed that although the amount of freeboard would be reduced, the peak water surface would remain below the critical reservoir elevation for dam safety during passage of the PMF.

3.3. TDG Performance

A primary variable driving TDG production is the depth that entrained air bubbles are carried into the tailwater by the plunging spillway jet(s). Other factors include the duration at which the air bubbles are held at depth and potential mixing of air with powerhouse discharge due to plunge pool circulation patterns. Plunge depth was used as a surrogate for TDG performance to develop the Bay 4 and 5 design. The single-bay model and its simplified tailrace did not allow consideration of the effects of time for gas transfer and plunge pool circulation patterns on TDG; however, for a comparative analysis, plunge depth was considered an acceptable method to estimate relative TDG performance.

The CFD model was run for a range of alternatives, and the results were post-processed to analyze air entrainment at depth. The post-processing procedure provides a simplified representation of the transient and three-dimensional aspects of the plunging spillway jet and TDG generation process. The maximum plunge depth associated with the different spillway modification geometries may occur in different locations and will change for each computational time step. The post-processing procedure addresses this by accounting for both the areal and temporal variation in air concentration by including both area and time in the analysis. The plunge pool region was "sliced" horizontally at a constant elevation from the invert (elevation 606.6 meters) to above the water surface elevation (elevation 633.8 meters) at 1.5 meter increments, and the air concentration for each elevation (or slice) was averaged. This was completed for each time step; then, the air concentration was averaged over 30 seconds of data (31 time steps) to develop an air concentration profile spanning the water column. The region to which the post-processing analysis was applied encompassed the jet impact area in the tailrace, as shown in Figure 5.
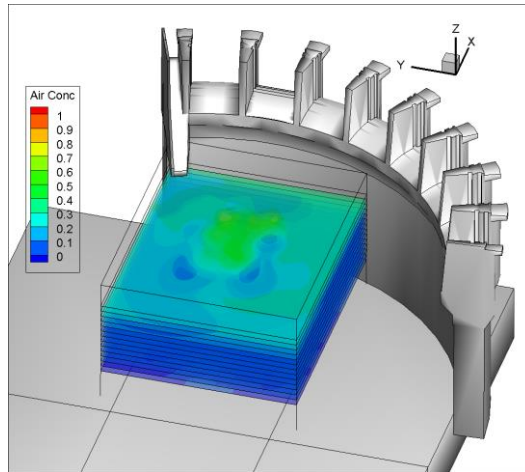
Figure 5. Area used in Plunge Depth Analysis with Slices (Baseline)

For the purposes of comparison, the maximum depth of plunge was assumed to be represented by the depth at which the air concentration was equal to 1 percent. The elevation at which the air concentration would diminish to 1 percent was calculated by linearly interpolating between the two elevations at which the air concentration data went from more than 1 percent to less than 1 percent. The resulting values are presented in Table 4.

Table 4. Plunge Depth Results for 1 Percent Air Concentration

| Layout | 1% Air Concentration | | Details |
	Difference Compared to Baseline (m)	Percent of Baseline Plunge Depth (%)	
Baseline (Unmodified)	NA	NA	Pre-Modification Baseline
Layout 1	-4.4	62.3	Max. Block Height (2 rows @ 1.22 meters)
Existing (Bay 2 Prototype)	-4.7	59.7	Bay 2 Prototype Geometry
Layout 2	-5.9	49.7	Single Row @ 0.94 meters, Tangential End Ext.
Layout 3	-5.8	50.5	Single Row @ 1.22 meters, Tangential End Ext.
Layout 4	-5.5	52.6	Single Row @ 1.52 meters, Tangential End Ext.
Layout 5	-4.9	57.9	Single Row @ 0.94 meters, 4 Blocks Rotated, Tangential End Ext.
Layout 6	-5.8	50.0	Single Row @ 0.94 meters, 5 Blocks Rotated, Tangential End Ext.
Layout 7[1]	-5.9	49.2	Single Row @ 1.14 meters, Tangential End Ext.

1. All runs were completed for a discharge of 170 m^3/s except Layout 7, which was run for 204 m^3/s.

Layout 7 produces the shallowest depth of plunge despite having been run for a higher design discharge; however, given the assumptions and limitations of the plunge depth modeling approach, the observed variations for the all of the alternatives except baseline are within the accuracy of the estimate. Importantly, Layout 7 has less effect on discharge capacity while achieving plunge depths that are comparable to Bay 2, which has been proven effective for TDG reduction through field testing.

4. CONCLUSIONS AND APPLICATION OF RESULTS

Avista is implementing modifications to reduce TDG downstream of Cabinet Gorge Dam using an incremental approach of analysis and field study. The initial prototype installation has demonstrated, through field operation and monitoring, that modifying a spillway through addition of roughness elements to break up the jet is an effective means to reduce plunge depth and the associated TDG production. CFD modeling was an effective method to improve upon the prototype design and achieve performance and constructability improvements for the modification of subsequent bays.

The purpose of the CFD modeling for design development was to provide a basis upon which to choose how to modify two additional spillway bays and to select which bays to modify. The Bay 2 modifications with two rows of roughness elements have been field tested and shown to reduce TDG downstream of Cabinet Gorge Dam. However, the two-row design requires a mechanism to introduce air in order to limit the potential for cavitation damage to the downstream row. In addition, CFD modeling indicates that the Bay 2 design reduces the spillway discharge capacity by 6.7 percent. For these reasons, Avista sought an alternative design that would provide a measureable reduction in plunge depth with a limited effect on discharge capacity during passage of the PMF. The finding that the two-row configurations had adverse effects on spillway capacity led to the development of a tangential end extension that would permit construction of a single row of roughness elements as far downstream from and below the spillway crest as possible. Several variations of a single row configuration were evaluated in the CFD model, and a layout was developed that would balance TDG reduction, effect on spillway capacity, and ease of construction.

Keeping with the step-wise design development philosophy, Avista will implement the recommended design on two spillway bays, then field monitor the performance before deciding which bays to modify for the full build-out condition. This intent was known when the simplified, single-bay modeling approach was adopted. A notable unknown is how the jet interaction with the shallow concrete apron will affect TDG after modification. In addition, the interaction of jets from adjacent bays has not yet been evaluated. For these reasons, the modifications will be implemented on Bays 4 and 5, which are located to either side of the training wall that separates the shallow and deep sides of the plunge pool, thereby allowing the aforementioned variables to be examined through field testing.

5. FUTURE WORK

Construction of the modifications to Bays 4 and 5 began during the Fall of 2015 and are scheduled to be complete in early 2016 prior to spill season. Avista intends to execute controlled testing to measure the TDG performance of Bays 4 and 5 singly and in combination prior to the spring freshet. During the spill season, Avista will continuously collect TDG data upstream and downstream of Cabinet Gorge Dam and will record all facility operations. These data will be analyzed during the summer of 2016, and based on the results of the field tests, Avista will decide whether to further refine the design of the spillway modifications or implement the present design on additional bays.

6. ACKNOWLEDGMENTS

7. REFERENCES

Dunlop, S., Paul, G. and Pate, K. (2014). "Partnering to Mitigate T G through Spillway Modifications" Hydro Review, 33(2), 16-24.

 lo w Science (2014). " lo w-3   User Manual".

 riz ell, K. W. (2009). "Cavitation Potential of the o lsom Auxiliary Spillway Basin Baffle Blocks." prepared for U.S. Bureau of Reclamation, Hydraulic Laboratory Report No. HL-1009-06.

Hirt, C.W., and Nichols, . B. (1981). "Volume of fluid (VO) method for the dynamics of free boundaries." Journal of Computational Physics, 39, 210-225.

Hirt, C.W. (2012). "Modeling Turbulent Entrainment of Air at a re e Surface" low Science Report 01-12.

Johnson, P.L. (1975). "Prediction of is solved Gas at Hydraulic Structures", United States Bureau of Reclamation Report No. GR-8-75, Denver, CO.

Maynard, C. (2008). "Evaluation of Total Dissolved Gas Criteria (TDG) Biological Effects Research: A Literature Review", Washington State epartment of Ecology Water Quality Program, Publication Number 08-10-059.

Weitkamp, . E. (2008). "Total is solved Gas Literature 1980 – 2007, An Annotated Bibliography", prepared for Parametrix, Bellevue, WA.

Design and Monitoring of a Small Living Shoreline Scaled for Private Properties on Exposed, Rapidly-Eroding Coasts

D. D. McGehee
Emerald Ocean Engineering LLC
Pensacola Beach, FL 32561
USA
E-mail: Bigwave@EmeraldOE.com

ABSTRACT

Living shoreline projects in exposed sites are unusual unless sponsored by a government agency or a foundation with adequate resources; these tend toward larger scale for obvious economic reasons. Small projects, on the scale of individual private lots, are almost exclusively built at sites with reduced exposure. This paper describes the design and post construction monitoring of a residential property scale living shoreline project on a rapidly eroding, exposed shoreline. The final design was modelled on the award-winning (and much larger) Project Greenshores Phase II built in 2007 in nearby Pensacola Bay, FL. The novel feature for both projects is a constructed salt marsh behind a unique broad-crested, offshore submerged breakwater/oyster reef for wave protection. The project site is on the north-eastern side of Mobile Bay, AL, with a maximum fetch of 129 km. Pre-construction shoreline retreat has averaged -80 cm/year since 1997. The project was constructed in the spring and summer of 2014 and is halfway through a 3-year post construction monitoring program. This paper will describe the site analysis, design process, and the owner's self-imposed adaptive management plan - an equally unique feature for a small-scale project. Results of the monitoring effort and its impact on implementation of the AMP are presented. To date, the design has been successful at eliminating erosion without the usual deleterious effects to adjacent properties associated with traditional shore protection schemes.

Keywords: *living shoreline, erosion, shore protection, reef breakwater, oyster reef, salt-marsh.*

1. INTRODUCTION

Because of both actual and perceived negative impacts, the traditional shoreline protection options for small projects – bulkheads (seawalls), revetments, and groins - have fallen out of favour with regulatory agencies in coastal states and are becoming increasingly harder to permit. A relatively new alternative is a popular, if loosely defined, concept that combines shore protection with at least some habitat restoration. A living shoreline is a "management practice that provides erosion control benefits; protects, restores, or enhances natural shoreline habitat; and maintains coastal processes through the strategic placement of plants, stone, sand fill, and other structural organic materials" (NOAA 2013a). At sites already experiencing significant erosion, vegetation alone has a limited chance of long-term survival unless protected by some sort of wave attenuation feature. Typical layouts use offshore emergent or low crested stone breakwaters in front of replanted subaquatic, intertidal, and/or upland vegetation. Living shoreline projects at exposed, high-energy sites require robust breakwaters and are usually sponsored by a government agency or a foundation with adequate resources to build a larger project. Small living shoreline projects, on the scale of individual residential lots, have been exclusively built at sites with reduced exposure.

The project described in this paper is located on private property southeast of Point Clear on the eastern shore of Mobile Bay, AL (Figure 1) with a maximum fetch of 29 km. Mean tidal range is only 0.4 m, but the region is susceptible to extreme hurricane-induced surges; even a thunderstorm can generate surges exceeding the tidal range. In addition, the property is located near the peak erosional hot spot for this stretch of the bay. Pre-construction shoreline retreat at the site has averaged -80 cm/year since 1997. The client's goals for the shore project were as follows:

- Prevent or significantly reduce erosion of the upland property
- Avoid or minimize interruption of normal LST and negative impacts to neighboring properties.
- Maintain or enhance recreational and swimming access and aesthetic functions of the shoreline
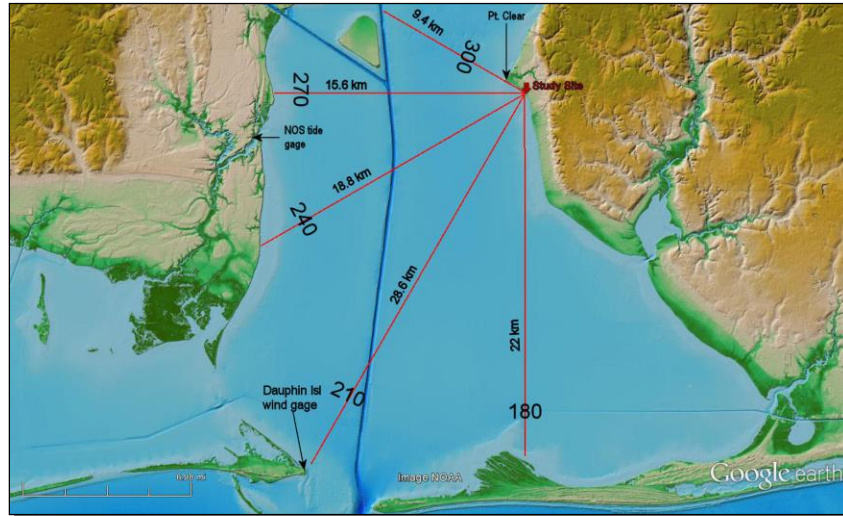
Figure 1. Project Site and Location

The approach selected by the client to achieve these goals was a living shoreline combined with adaptive management practices. The design used in this project is based on concepts developed and implemented by the author that have proven successful under more energetic environmental conditions - the highly successful, award-winning (and much larger) Project Greenshores in nearby Pensacola Bay, FL. The significant and novel feature for both projects is a broad-crested, submerged breakwater/oyster reef. Phase I was completed in 2002 and survived a direct hit by Hurricane Ivan without damage; Phase II was built in 2007 (McGehee 2008).

2. SITE ANALYSIS

The mid-term (scale of years to decades) shore processes at this site are dominated by wind-driven waves. Long-shore transport (LST) i.e., movement of sand parallel to the shoreline, is controlled by the cumulative effect of normal, seasonal winds. The typical annual pattern of dominant winds on the northern Gulf coast is bi-modal – somewhat east of southerly in the summer season and somewhat west of northerly in the winter season, so LST stress on the eastern shore is generally northward in the summer months and southward in the winter months. The shoreline south of the study site is aligned roughly north-south and is protected from southeasterly winds but exposed to winds from the south through the west northwest. The shoreline bends to roughly northwest-southeast at the project site and is sheltered from the northwest but exposed to winds from the southeast through the west northwest.

Wind waves offshore of the project site were hindcast using methods of Bretschneider, including shoaling and reduction in wave height caused by bottom friction according to Miche (IKM Engineering 2013). Setup due to wind stress on the bay was calculated for the various wind conditions, using the additional coefficient of 0.5 for enclosed basins. LST potential was estimated from the hindcast wave statistics by way of the CERC formula, as modified by Kamphuis and Readshaw (Smith et al. 2009). Calculated average net LST potential is on the order of several hundred m³/yr to the north at the southern end of the study site. It decreases in magnitude going north until it is essentially negligible near the project site. Continuing northward, LST potential reverses direction to south easterly transport and increases to a few hundred m³/yr near Point Clear.

All of the unprotected shorelines in the general vicinity are retreating, but the most severe erosion observed in the study area, about 60-90 cm/yr, is just south of the project (Figure 2). The obvious question that arises from the LST calculation is this: if net LST comes from both directions toward this site (a LST node), why is it eroding at the fastest rate instead of accreting? Three other factors need addressing to explain the erosion:

First, the LST formulas provide the sediment transport *potential*. This is the maximum amount of sediment that would be transported given an unlimited supply of sediment updrift. At this site, there is effectively no nearshore sediment available south and north of the study area to feed the LST in between due to the extensive groin fields and bulkheading of the shoreline. That is why the central portion does not accumulate sediment in the long term, but that does not explain the significant shoreline retreat.

Figure 2. Project site on aerial photo from 11/02/2013 with historical shorelines from 1997, 2008, 7 2010

The second factor is cross-shore transport (CST), i.e., movement of sand perpendicular to the shoreline. Offshore-directed CST is episodic and occurs almost exclusively during higher wave events; it is insignificant below some energy threshold. Storms produce larger, steeper waves that pull sand from the shoreline offshore to create bars (sometimes called "storm bars"). On an open ocean coastline, swell waves – lower waves with longer periods – occur after and between storms. Swell transports the sediments on the bar shoreward, so in the long-term (and with a constant sea level), cross shore transport is in equilibrium. Mobile Bay often experiences high enough winds and the site has sufficient fetch to produce highly erosive, steep, short-period waves. However, there is insufficient fetch to generate the long-period swell that moves the bars shoreward. Thus, the shoreline retreats with each high wave event and does not fully recover in between. Quantitatively, comparison of the eroded upland volumes with measured offshore profiles taken during the site analysis phase showed that all of the sediment volume lost from the upland shoreline between 1997 and 2013 can be accounted for in the underwater bars within 61 m (200 ft) of the shoreline.

The third factor is sea-level rise. Under rising sea levels, all shorelines retreat landward; it is the dominant influence on the scale of decades to centuries. The Bruun rule is a simple model for quantifying the eventual response of a shoreline to sea-level rise. Using the 3 mm/yr rate of sea level rise at Mobile between 1966 and 2012 (NOAA 2013b), the predicted shoreline retreat over the 16 years covered in the historical shoreline analysis is about 2.1 m (7 ft).

3. DESIGN

The design condition is a wind of 20 m/s with a direction band of 220º to 250º True (*T*). Winds greater than this threshold occurred just 0.03% of the time, an average of less than 3 hours per year, between 1997 and 2008 (NDBC 2013). For this wind speed, the wave hindcast/transformation analysis produced the maximum incident wave condition of 0.8 m wave height, H_D, with a period, T_D, of 4.1 sec. Inside the 1 m contour, the incident direction band of the design wave was from 215º to 240º True (*T*), and the wavelength, L_D, was about 13 m. The wind setup for these conditions is 35 cm. The design water level is the occurrence of the design conditions at mean high tide for a total water level of 75 cm MLLW. The design water depth, h_D, for a structure with a toe about 50 m offshore, is 1.2 m. The maximum wave height in that water depth (for braking index, $\gamma = 0.6$) is 0.7 m, so the design wave is conservative for structural response considerations. Figure 3 is the profile of the design used to meet the client's goals under these design conditions. Figure 4 is an aerial photograph of the project taken 01/30/2015, 6 months after completion. Profile lines described in the Monitoring section are also shown. Elements of the design are discussed in the following sections.
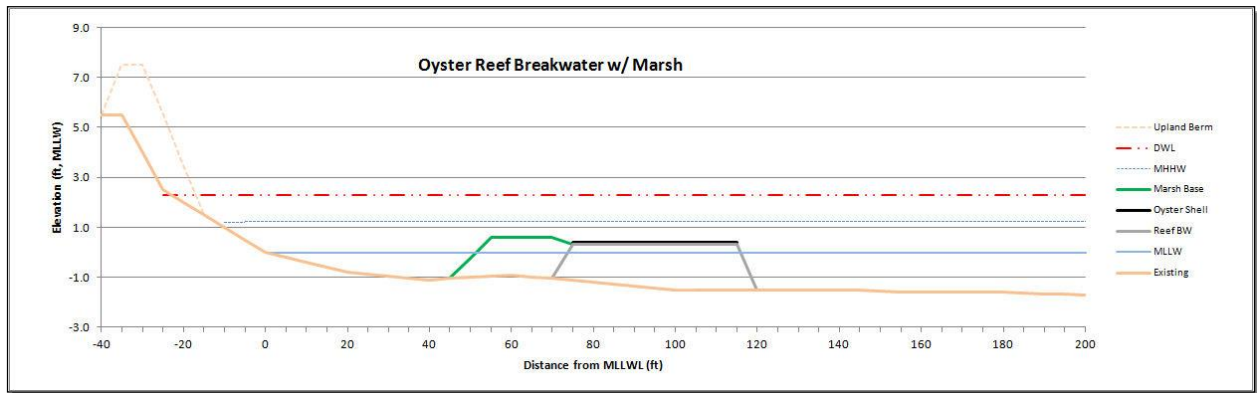
Figure 3. Project design profile

Figure 4. Project post construction, 1/30/2015, with survey profiles 5S through 5N

3.1. Submerged Reef Breakwater

Living shorelines in general, and submerged reef breakwaters specifically, are relatively new engineering approaches with little data and guidance for design. Typical living shorelines utilize either shore-connected or detached breakwaters with narrow-crested trapezoidal cross-section designs refined over the previous century. These function well in protecting harbors from incident wave energy, but there are two major drawbacks to this choice for protecting sandy shorelines, depending upon the crest height of the breakwater.

If the breakwater is an emergent structure that is rarely overtopped, it completely interrupts LST behind it. Sediment that settles in the lee of the breakwater forms a dry beach bulge in the shoreline that reaches either partially (a salient) or completely (a tombolo) to the back side of the breakwater. In either case, all LST is captured and the "starvation" of the sediment to the downdrift beach results in a localized erosional hot spot - the so called "groin effect" (Department of the Army 1992); see the lower right portion of Figure 2 for an example near the project due to a groin. If the crest is low or submerged so that it is routinely overtopped, the overtopping waves produce a set-up of the mean water level in the lee of the structure. Under higher wave conditions, the return flow of the elevated water can produce significant gyres in the lee to each side of the structure that result in erosion to the adjacent shorelines (Stauble et al. 2003; Pilarczyk 2003).

By contrast, a submerged, broad-crested breakwater reduces wave energy by friction and dissipation, like a natural reef, rather than by reflecting the incident wave energy. However, because it is broad crested, the transmission coefficient is not a constant – it is a function of frequency. Steep, higher frequency waves that cause nearshore and backshore erosion due to offshore-directed CST are highly attenuated by friction during the breaking process. Low-steepness, longer period waves that tend to move sediment shoreward are less attenuated. It is, in effect, a low-pass filter for wave energy, not a wave barrier. For example, the reef is completely transparent to tides (and their

associated currents), which facilitates natural flushing and promotes water quality. Making the reef broad-crested solves the setup drawback as well. Since the setup takes place on the reef, and not behind it, the return flow is directed toward the sides of the reef that are stable under these currents, not near the highly erodible sand in the nearshore.

Finally, the reef breakwater can reduce or even eliminate the groin effect. Since it is routinely overtopped, even under mild wave conditions, some wave energy is still transmitted shoreward, especially under storm conditions with associated surges. Thus, LST can continue in the lee of the structure, though at a reduced rate. As much as half of the total LST on a shoreline takes place in the swash zone by waves that are too small to break further offshore or have already broken and reformed. Since the potential transport rate is much greater than the actual rate at this site, even a much reduced LST rate can bypass the quantities that normally move downdrift.

The main quantitative performance criterion of the breakwater is to reduce the incident wave, H_i, to a transmitted wave, H_t, which will allow the emergent salt marsh to thrive. Douglass and Stout (2004) established a maximum wave climate for non-eroding marsh shorelines along Mobile Bay based on the wave height, H_x, exceeding an x percent occurrence: $H_{50} < 0.15$ m and $H_{80} < 0.25$ m. The marsh will be newly planted, so a more restrictive criterion was selected for reducing the transmitted design wave height, $H_{t,D} < 0.25$ m. There is limited engineering guidance on three-dimensional design of submerged porous structures; in this case, property boundaries controlled the plan dimensions. Desire for a recreational, swimming beach established dimensions for the inner edge, and navigational access to an existing boat dock established the outer edge, while regulations mandated a 3 m (10 ft) side setback from the owner's riparian boundary. The breakwater was placed essentially within these constraints.

As is true for other aspects of reef breakwater design, there is little guidance on stone size for stability. The classic Hudson formula was derived for emergent breakwaters with relatively steep slopes. Using a horizontal slope in the formula forces the stone size to 0. Stability under the design wave is predicted for randomly placed angular stone ($\rho = 2,400$ kg/m^3 or 150 lb/ft^3) with a median weight, w_{50}, of 5 kg (11 lb) and median diameter, D_{50}, of about 15.2 cm (6 in)[1] if placed on a 1:20 slope, so it should be a conservative choice for a horizontal surface. The material is limestone, though clean, graded, crushed concrete would have also worked. The outer face of the structure is anticipated to respond to waves above the design condition dynamically by readjusting to a more stable, s-shaped profile.

In most living shoreline designs, the marsh or subaquatic vegetation is the intended "living" component – the breakwater is merely functional. This reef's second major role is to serve as a significant additional submerged habitat – in fact, the largest portion of the living shoreline created. A single, thin layer of oyster shell, either fossilized or air dried and quarantined for at least 3 months, was placed on the top surface of the reef to provide substrate for oyster spat colonization. Data on natural oyster reef growth rates in the bay are limited, but it is likely that a thriving reef could grow vertically with SLR, providing long-term resilience to the project. No foundation was designed, but allowance for 10.2 cm (4 in) of settlement was made during construction by advance placement of this much additional stone.

3.2. Marsh

The marsh primarily serves as a highly functional habitat with a secondary aesthetic role of blocking the view of the exposed reef from the shore when water levels are below the crest elevation. It also provides some additional wave attenuation effects, but due to lack of published guidance, this will not be considered in the performance of the project. Previous experience in similar conditions has verified that the sand base for the marsh should be near mid tide elevation, or 0.6 ft MLLW[2]. Placing the outer edge of the marsh directly behind the reef makes it a perched beach, which enhances its stability. By keeping the inner edge of the marsh within the -0.3 m (1 f)t contour, a protected water swimming area was achieved with a maximum depth of 0.7 m (2.2 ft)at high tide, a depth considered safe for small children. Emergent marsh sprigs, including *Spartina alterniflora* (smooth cordgrass), *Scirpus validus* (soft-stem bulrush), and *Juncus romerianus* (black needlerush) were manually installed on 60 cm

---

[1] This is the same size and material used at the Project Greenshores Phase II submerged reef, which has shown no degradation in 8 years.
[2] This is consistent with the marsh elevation used in Project Greenshores Phase I and II, which have proven highly viable and stable for 13 years.

centers. The marsh accumulates sediment and grows upward, so it may be able to maintain its elevation under rising sea levels.

3.3. Upland Berm

The upland berm provides vegetated upland habitat and reduces additional backshore during energetic conditions. As it erodes, it will provide easily replaced feeder material for the littoral zone. The face and crest was planted with native vegetation including *Spartina patens* (marsh hay), *Panicum amarum* (bitter panicgrass), *Ammophila breviligulata* (American beachgrass), and *Scirpus robustus* (salt marsh bulrush) on 60 cm centers.

Adaptive Management Plan

Localized negative impacts on adjacent unprotected shorelines are practically assured for traditional shore protection options such as bulkheads, revetments, and groins at this site and frequently lead to disputes or legal actions between neighbours. Because of both the variability in the seasonal and annual wave climate and the limited prior data available on reef breakwater performance, it is conceivable that this project will as well. The client agreed to proactively include a mitigating response in this instance and included it in the permit application. However, it is important to distinguish impacts related to the project from either the pre-existing and ongoing regional shoreline retreat or from temporary, small scale waterline undulations that occur routinely on unprotected shorelines and that are often self-correcting. Negative impacts related to the project could occur to the downdrift shoreline only if the project significantly captures the net LST that would have transited the property. As described earlier, while the long term downdrift shoreline is to the north, the direction may reverse from year to year, so the impact could be felt on either side of the project. This effect will be recognizable if the following two symptoms occur in synchrony:

1. Localized shoreline retreat on one side of the project that is significantly greater than the existing 0.6-0.9 m/yr (2-3 ft/yr).
2. Accumulation of an equivalent volume of sediment on the upstream side and/or behind the project.

If these symptoms persist, the accumulated sediment above the MHWL will be mechanically transported (bypassed) at the client's expense to the affected shoreline and deposited where it can re-enter the littoral zone. A small skid loader could move several years' worth of captured LST in a day. This option would not be nearly as practical if there were groins, a revetment, or a bulkhead blocking access to the sediment near the waterline.

4. MONITORING

Permits for the project were received in February of 2014, and construction commenced the following May. In June, the Alabama Department of Conservation and Natural Resources issued a unique requirement to conduct semiannual monitoring for three years following project completion. Eleven profiles extending up to 61 m (200 ft) offshore and photographic documentation are required each spring and fall. Three profiles cover the north, center, and south bounds of the project, and four pairs of profiles are spaced 7.6 m, 15.2 m, 30 m, and 75 m north and south of the project bounds. Figure 4 shows the location of the profiles, numbered consecutively from the center of the project (profile 0) outward to the south and north (profiles 1S - 5S & 1N - 5N, respectively). Each profile was measured using wading survey methods and local instantaneous water levels as a datum. Elevations were adjusted to MLLW using measured water levels at the time of each profile from nearby National Ocean Service tide gages (Figure 1). To date, surveys have been made on October 8, 2014; May 2, 2015; and September 19, 2015. Additional site visits were photo documented in July of 2013; in June, July, August and December of 2014; and in August, September, and October of 2015.

Figure 5 provides sample profiles from the first three surveys. The most obvious change is the expected growth of the salient directly behind the breakwater at profile 0. However, the trend of shoreline advancement was consistent (except for localized undulations due to debris in the swash zone) along the entire study area, as evidenced by the average of all the profiles. It is even seen at profiles 5S and 5N, well outside any possible impacts from the project

over this time period. The implication is that the period since the monitoring program began has been unusually mild in terms of erosive wave conditions.
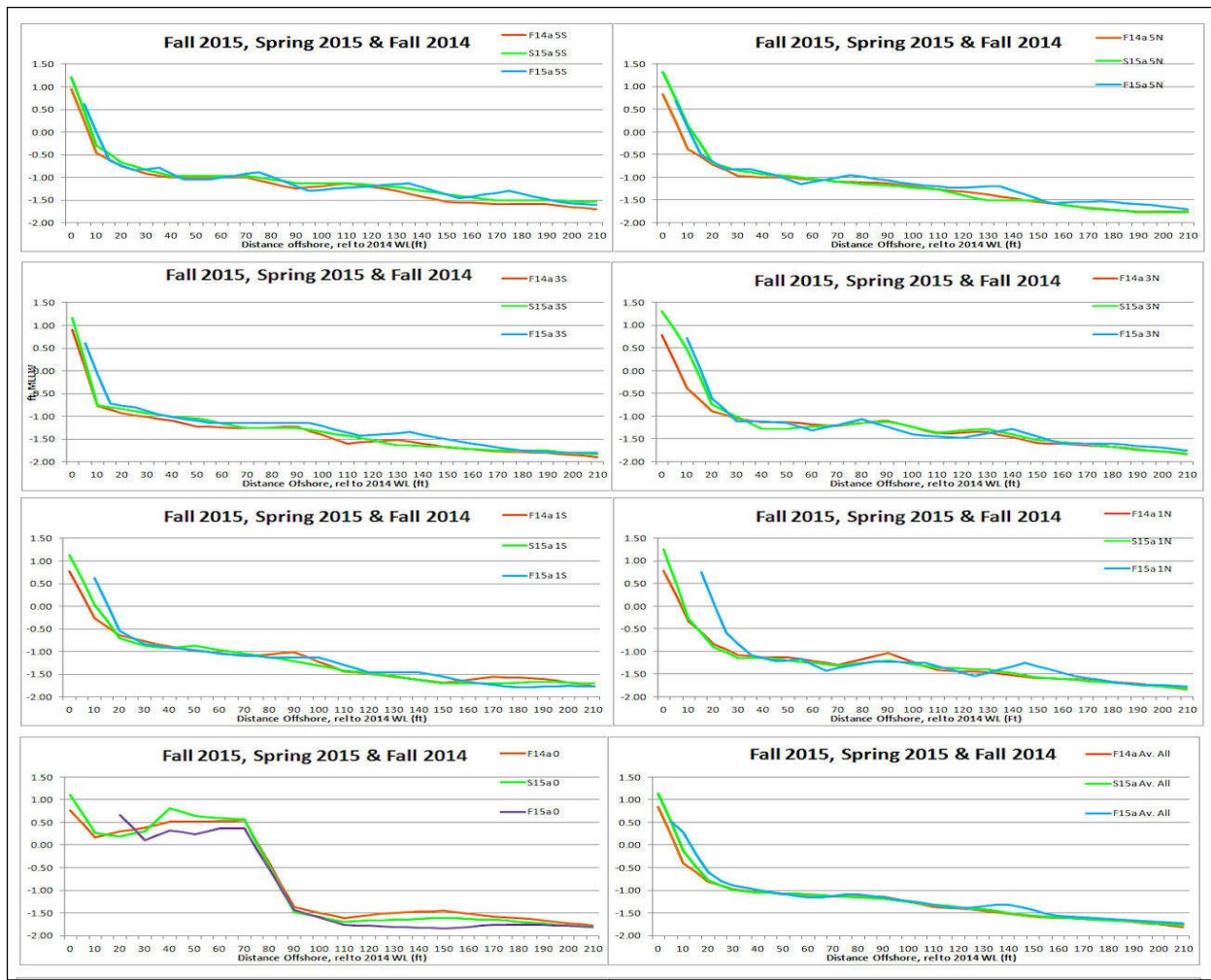
Figure 5. Measured underwater profiles from fall 2014, spring, 2015, and fall 2015.

Figure 6 is a sequence of ground-level photos of the project and nearby shorelines. Figure 6(a) was taken one week after construction of the offshore portion but before the berm was vegetated. A minor salient has already begun to form. Figure 6(b) was taken about one year after construction. The salient has prograded to a tombolo, but neither the photo nor the surveys in Figure 5 reveal observable erosion of the adjacent shorelines. Material for the tombolo could also be coming from the pre-placed sand in front of the berm and/or from deeper water offshore of the breakwater. Implementation of the adaptive management plan was discussed at this time, but it was decided to wait until the following spring to see if higher wave conditions would reduce the tombolo. It is apparent that the emergent marsh is thriving.

A moderate storm occurred on October 25, shortly after the fall 2015 survey, that produced winds from the southeast near the design conditions and water levels exceeding the design water level. Incident waves were not measured but probably did not exceed the design wave because of the reduced fetch to the southeast. No post-storm surveys were conducted, but a site inspection showed that shorelines to the south were noticeably eroded (Figure 6(c)). Figure 6(d), taken two days after the peak of the storm shows remnant waves passing over the reef and through the marsh before impinging, much attenuated, on the shoreline. There were no impacts to the marsh or the backshore, but the tombolo that formed under mild wave conditions had been reduced considerably (Figure 6(e)). Figure 6(f), looking northward from the project site, illustrates how a significant portion of the tombolo was transported northward and deposited on the adjacent foreshore, verifying that LST continues under higher wave conditions. Subsequent surveys will determine if the effect is persistent and quantify volume of sediment transported in the longer term.

Figure 6. Sequence of ground level photos of the completed project and adjacent shorelines.

5. CONCLUSIONS

A novel, small-scale living shoreline designed for an exposed, eroding shoreline has been shown to be stable and functional under conditions exceeding the design wind and water levels. The submerged, broad-crested reef breakwater greatly increases the amount of habitat created – the "living" portion – compared to traditional narrow crested sections while, to date, avoiding some of the negative impacts typical of more traditional hard solutions. By eliminating structure near the waterline, it maintains aesthetic and recreational features of a natural beach while allowing for affordable mitigation if the self-imposed adaptive management plan is required. Halfway through a 3-year monitoring plan, the project appears to be functioning as designed.

6. ACKNOWLEDGMENTS

7. REFERENCES

Department of the Army (1992). "Coastal Groins and Nearshore Breakwaters," Engineer Manual 1110-2-1617, U.S. Army Corps of Engineers, Washington, DC

Douglass, S.L. and Stout, Judy, 2004, "An Estimate of the Upper Limit of Wave Level Tolerance for Spartina alterniflora in Coastal Alabama," University of Southern Alabama, March 31, 2004.

IKM Engineering BV. "CRESS (Coastal and River Engineering Support System" <http://www.cress.nl/About.aspx> (Sep. 15, 2013)

McGehee, D. D., (2008). "GreenShores vs. Ivan: Response of a Created Saltmarsh to a Major Hurricane", Gulf Coast Hurricane Preparedness, Response, Recovery & Rebuilding Conference, PIANC, Brussels, Belgium.

NDBC (National Data Buoy Center) (2013). "National Data Buoy Center." https://ndbc.noaa.gov (Sep. 15, 2013)

NOAA (National Oceanic and Atmospheric Administration (NOAA) (2013a). "NOAA Shoreline Webite; Glossary." < http://shoreline.noaa.gov/glossary.html> (Sep. 15, 2013)

NOAA (National Oceanic and Atmospheric Administration (NOAA) (2013b). "Updated Mean Sea Level Trends." <http://tidesandcurrents.noaa.gov/sltrends/sltrends_update.shtml?stnid=8735180> (Sep. 15, 2013)

Pilarczyk, K. W. (2003). "Design of low-crested (submerged) structures – an overview." Proc., 6th International Conference on Coastal and Port Engineering in Developing Countries, Copedec, Colombo, Sri Lanka 1-19

Smith, E.R., Ping Wang, Ebersole, B, and Jun Zhang (2009). "Dependence of Total Longshore Sediment Transport Rates on Incident Wave Parameters and Breaker Type," Journal of Coastal Research, 25(3) 52-61.

Stauble, D. K. and Tabar, J. R. (2003). "The Use of Submerged Narrow-Crested Breakwaters for Shoreline Erosion Control." Journal of Coastal Research, 19(3), 684–722.

Numerical Modeling of the Spillways for the Dam Raise at Isabella Dam

L.L. Ebner[1], S.K. Askelson[1], E.A. Thompson[2] and N.C. Cox[3]
[1]Portland District Corps of Engineers
US Amy Corps of Engineers
PO Box 2946
Portland, OR 97208-2946
USA
[2] Sacramento District Corps of Engineers
US Amy Corps of Engineers
1325 J Street
Sacramento, CA 95814
USA
[3]McMillen Jacobs Associates
1401 Shoreline Drive, Suite 100
Boise, ID 83702
USA
E-mail: Laurie.L.Ebner@usace.army.mil

ABSTRACT

The Sacramento District Corps of Engineers is designing modifications to the Isabella Dam located on the Kern River in the Tulare Lake Basin in the southern portion of the San Joaquin Basin, in Kern County, California. These modifications include raising the elevation of two high head dams (56.4 m or 185 ft and 30.5 m or 100 ft) by 4.88 m (16 ft); modifying a service spillway to better suit the needs of flood capacity, and creating a new labyrinth weir emergency spillway. To aid in the design of both spillways, a series of three-dimensional (3D) computational fluid dynamics (CFD) models of the Isabella Reservoir and outlet works were developed.

The design process for the emergency spillway has been streamlined using a composite modeling approach with physical and CFD modeling of the labyrinth weir. The CFD models of the Isabella Dam forebay, the main and auxiliary dams, and service and emergency spillways provide an efficient test bed for design alternatives of the spillways, support for rating curve development, and validation of the information obtained in the physical model. CFD model results were also used to evaluate hydraulic conditions in and down the spillway chute. Velocity, water surface elevation, and stream power were computed so that appropriate measures could be taken to protect the chutes from damaging erosion.

Keywords: CFD, Labyrinth Weir, Rating Curve, Physical Model, Stream Power

1. INTRODUCTION

Isabella Lake Reservoir is located on the Kern River in Kern County, California and lies within the Sacramento District's (CESPK) area of responsibility. The project is approximately 67.6 km (42 miles) northeast of the city of Bakersfield and one mile upstream of the town of Lake Isabella. Isabella Lake Reservoir is formed by two earthen embankment dams: a main dam located where the Kern River once was and an auxiliary dam located in the hot springs valley (there is no historic evidence of an old riverbed in this valley). The two dams are separated by a natural topographic feature called Engineer Point, which runs perpendicular to the dams where the Kern County Fault is located. Figure 1 shows the layout of the two dams; the main dam with an ungated overflow spillway is on the left and the auxiliary dam is on the right.

Figure 1. Isabella Main Dam and Auxillary Dam

Spillway adequacy studies were performed, revising the Probable Maximum Flood with the current peak inflow PMF of 16,452 m³/s (581 Kcfs). These studies concluded that the Isabella Dam, as constructed, could not safely pass the revised PMF. The new PMF is 67 percent larger (by volume) than the original spillway design flood. Routing of the PMF through Isabella Lake while assuming any reasonable starting storage level produces overtopping of the dam. Only about 50 percent of the PMF can be routed through the project before the dam is overtopped, assuming the reservoir is at gross pool at the beginning of the flood. It is estimated that overtopping of the dam currently has about a probability of 1 in 4,100 annual chance exceedance. In order to pass the revised PMF, modifications to the project have been proposed.

The proposed design will increase the height of the existing dams by 4.88 m (16 ft). The existing service spillway crest elevation will remain unchanged at 795.3 m (2609.26 ft). The revised capacity of the service spillway will not pass the flood flows; therefore, additional capacity will be provided with a new emergency spillway. In order to optimize use of existing space while minimizing the required construction and excavation, the new emergency spillway is being designed as an arced labyrinth weir design, allowing for increased spillway crest length in a smaller footprint than a traditional spillway design. See Figure 2.

The design has been developed by Sacramento District Corps of Engineers (CESPK). Portland District Corps of Engineers (CENWP) supported CESPK by performing Computational Fluid Dynamics (CFD) Modeling of the proposed configuration. The CFD effort was done in conjunction with a 1:45 scale physical model performed by Utah State University, Utah Water Research Laboratory.

Figure 2. Proposed Spillway Configuration for Isabella Dam

2. NUMERICAL MODELS

CENWP selected Star-CCM+, a commercially available software package, as the computational code for the CFD portion of the analysis. Star-CCM+ has the ability to model rigid lid flows (defined water surface, single fluid analysis) and free surface flows (CFD calculated interaction between air and water, two fluid analysis), plus the ability to "map" a solution from one model to another to provide initial conditions and/or boundary conditions for the subsequent models.

A series of models were built:

- A CFD sectional model of a labyrinth spillway evaluated in a physical model (Crookston, 2012). It was developed to identify appropriate modeling techniques (minimum cell size, cell growth away from the labyrinth, relaxation coefficient, etc) for the labyrinth weir. The sectional model was validated against the physical model studies.
- A large coarse grid model (CFD_1) was developed to evaluate the flow direction from the reservoir into the spillway approach channels for two scenarios: service spillway operation only and service and emergency spillway operations in tandem. CFD_1 was a rigid lid model that included portions of the North Fork and the South Fork Kern River and both the Main Dam and Auxiliary Dam. CFD_1 was used to generate boundary conditions for CFD_3, a transient free-surface model of the service and emergency spillways.
- CFD_3 is a free surface CFD model of the forebay just upstream of the emergency spillway, service spillway, and channels. CFD_3 was used to describe the approach conditions such as approach flow distribution and flow bulking along the weir crest, as well as define the spillway rating curve, and evaluate effective crest length of the spillways. CFD_3 was also used to describe the hydraulic conditions in the spillway chutes.
- A CFD_{PM} model of the physical model was also produced. This model was used to evaluate concerns associated with physical model footprint and potential scale effects.

2.1. Model Geometry, Grid, and Boundary Conditions

As the first step in CFD model development, a solid model of the Isabella Reservoir bathymetry and structures was created. The bathymetry was generated from topographic maps developed prior to dam construction, a limited number of soundings, and photogrammetric data representing the existing reservoir bathymetry. The assortment of survey data was combined using ArcGIS, a subset of data points representing bathymetry data was triangulated into multiple surfaces (required due to file size constraints) in Microstation V8. Those bathymetry surfaces were combined into a single surface and imported into StarCCM+, where a simulated water surface and upstream boundary surfaces were added to create a 3D volume representing the computational domain of CFD.

The existing reservoir bathymetry was then altered to represent design conditions using files provided by CESPK. The alterations to the existing bathymetry included the following:
- Raising of the main and auxiliary dams;
- Addition of a spur dike to the main dam;
- Modifications to the right wall of the service spillway, the spillway crest, and the left wall;
- Excavation of the emergency spillway area and channel; and
- Addition of the labyrinth weir and abutment walls

The point (*.txt) files provided by CESPK were turned into surfaces in Microstation V8, which were then turned into 3D volumes in StarCCM+. These 3D volumes along with the service spillway and emergency spillway 3D solids were then subtracted from or added to the original bathymetry volume in StarCCM+.

An arc surface was included in the model approximately 304.8 m (1000 ft) upstream of the labyrinth weir apexes to allow mapping of CFD_1 solution data to the upstream boundary of CFD_3. Horizontal planes were also included at Engineer Point to allow flexibility in applying and monitoring flow conditions over Engineer Point.

The grids for the CFD$_1$ model runs were created in Star-CCM+ version 8.02. The development of the model grid parameters to be used for CFD$_1$ model runs was an iterative process that involved testing and adjusting grid development strategies. The same general cell resolution settings were used to develop the grids for all of the models:

- Base grid: 10 m cells, one 1m thick prism layer
- Refinement within ~200 m of spillways: 3 m cells, one 0.5 m thick prism layer
- Refinement within ~100 m of spillways: 1 m cells, two prism layers (0.5 m total thickness – notionally 1/3 and 2/3 thickness)
- Service Spillway water surface refinement ~100 m upstream and downstream of ogee: 0.5 m cells
- Emergency Weir refinement: 0.1 m min, 1 m target size, two prism layers (0.2 m total thickness)

Figure 3 shows the resolution of the CFD$_1$ grid near the service and emergency spillways. The yellow arc surface is the surface from which CFD$_1$ run data is mapped to the CFD$_3$ upstream boundary.
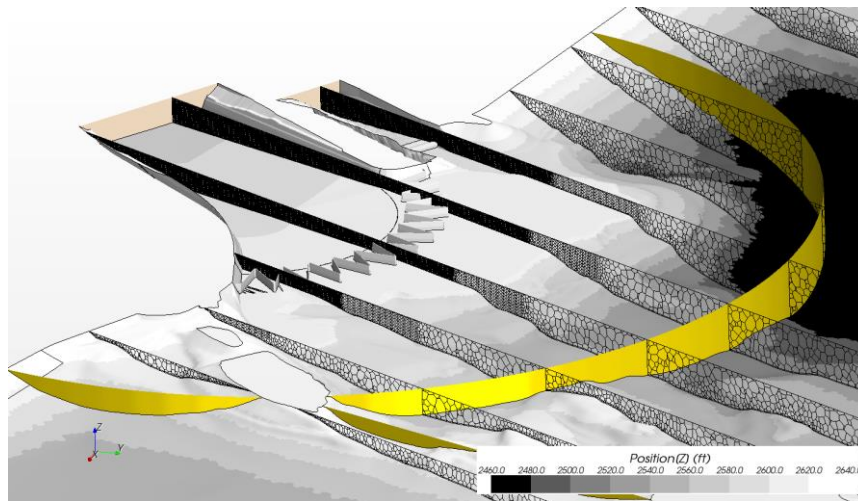
Figure 3. Grid Resolution CFD$_1$

The single CFD$_3$ upstream boundary was set as a velocity inlet with the velocity magnitudes and directions mapped from the results of corresponding CFD$_1$ runs. Upstream boundary air/water interface elevations for all runs were set at the rigid lid of corresponding CFD$_1$ runs. At the upstream boundary, only air can move in above the air/water interface and only water can move in below the air/water interface. The interface was only prescribed on the boundary, and the free surface allowed the air water interface to adjust as needed away from the boundary.

The downstream boundary conditions for both the Service and Emergency Spillways was a "stagnation inlet" in Star CCM+ terminology, which is an outlet where flow moves out of the model. The flow split (between air and water) is defined by a field function; only water is allowed to leave the model below the specified tailwater elevation, and only air is allowed to leave the model above the specified tailwater elevation. The physical model results were used to estimate the tailwater elevation at the downstream boundary. A second field function is used to apply hydrostatic pressure boundary based on the fluid type/depth (air or water) on the downstream boundary surface.

The boundary at the top of the model domain was set as a pressure boundary allowing air to enter and exit freely. Interface boundaries that do not influence the computation were included in the model just downstream of the service spillway crest and at the crest of each labyrinth weir cycle as locations to monitor discharge. All other region boundaries were set as default wall boundaries, including the bathymetry, concrete structures, and inactive flow outlets.

In addition to mapping CFD_1 velocity results to the CFD_3 upstream boundary, initial velocities and water surface elevations throughout the CFD_3 model domain were also mapped. For all runs, initial pressures were hydrostatic based on a constant 101,325 Pascal (1.0 atm, 14.7 psi). Other initial conditions were left at StarCCM+ default values.

The same model geometry was applied for all of the models: CFD_1, CFD_3, and the physical model. Figure 4 shows the geometry truncated by the footprint of the physical model.
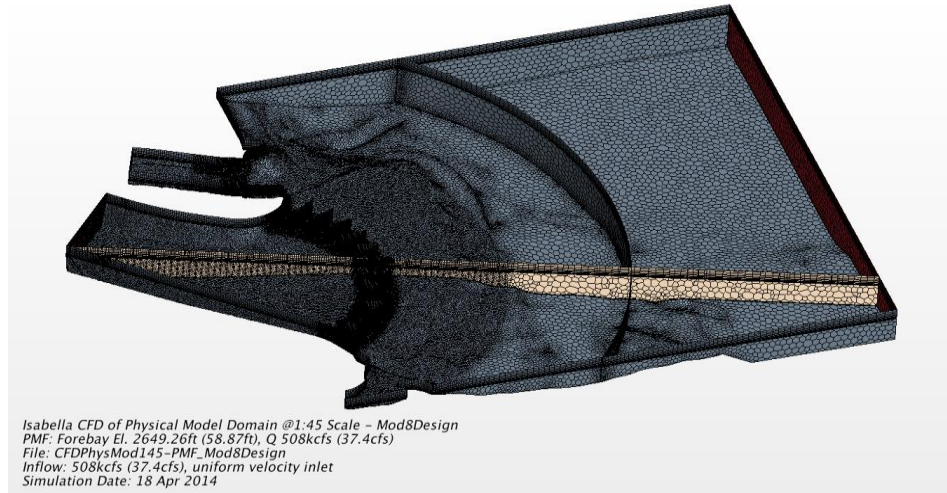
Figure 3. CFD Model of Physical Model

2.2. Model Results

The CFD model results are shown in Figure 5. Figure 5 shows an early version of the labyrinth weir in which both the physical and numerical model showed that the labyrinth was submerged on the right side of the image. The design was modified and tested in both the physical and numerical model.
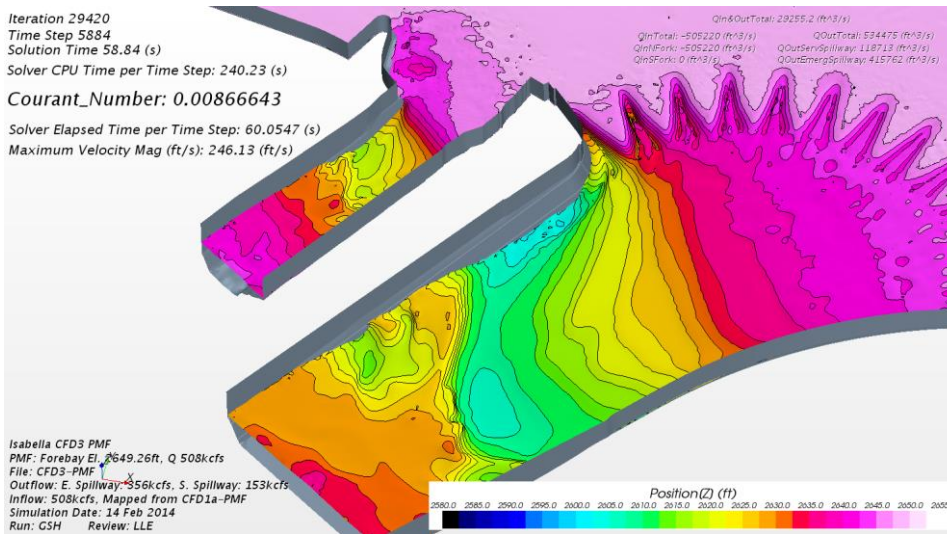
Figure 4. Sample CFD Output

502

Physical and CFD model results were compared at similar locations. Details on data collection in the physical model are defined in Utah Water Research Report Number 2999, 2014. Comparisons were made between the results from the CFD_{PM} model at physical model scale, CFD_{PM} model at prototype scale, and the Physical Model; see Figure 6 for a sample comparison. Scale effects for the PMF were not evident when the physical model results of the CFD_{PM} model at physical model scale and prototype scale are compared. The physical model discharge was 14,640 m^3/s (517 Kcfs) versus the 15263 m^3/s (539 Kcfs) discharge for the CFD_{PM} model scale, approximately a 4% difference. The comparison of the various rating curves is depicted in Figure 7.
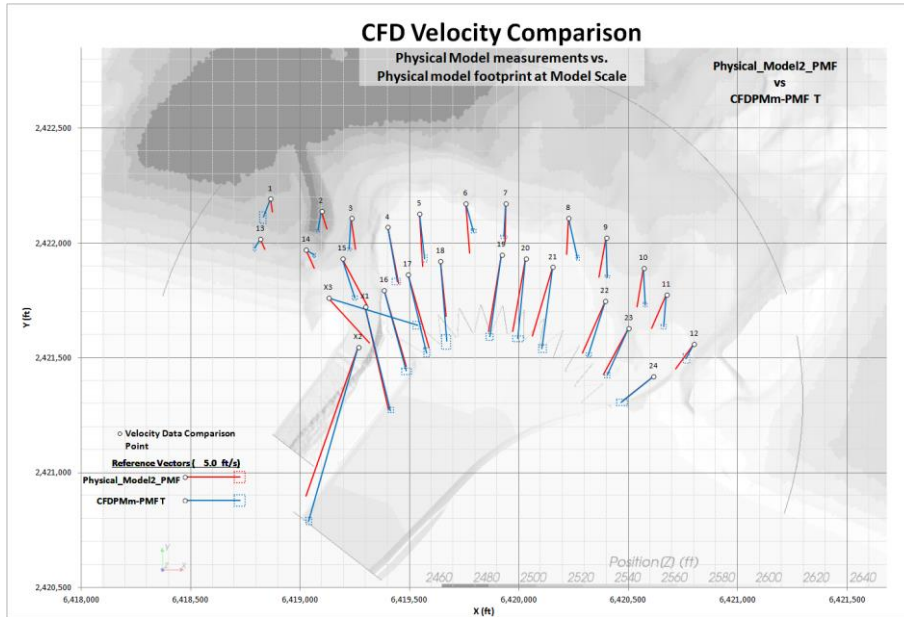
Figure 5. Physical Model Measurements Compared to CFD of Physical Model at Model Scale. Plan View of Velocity Vectors
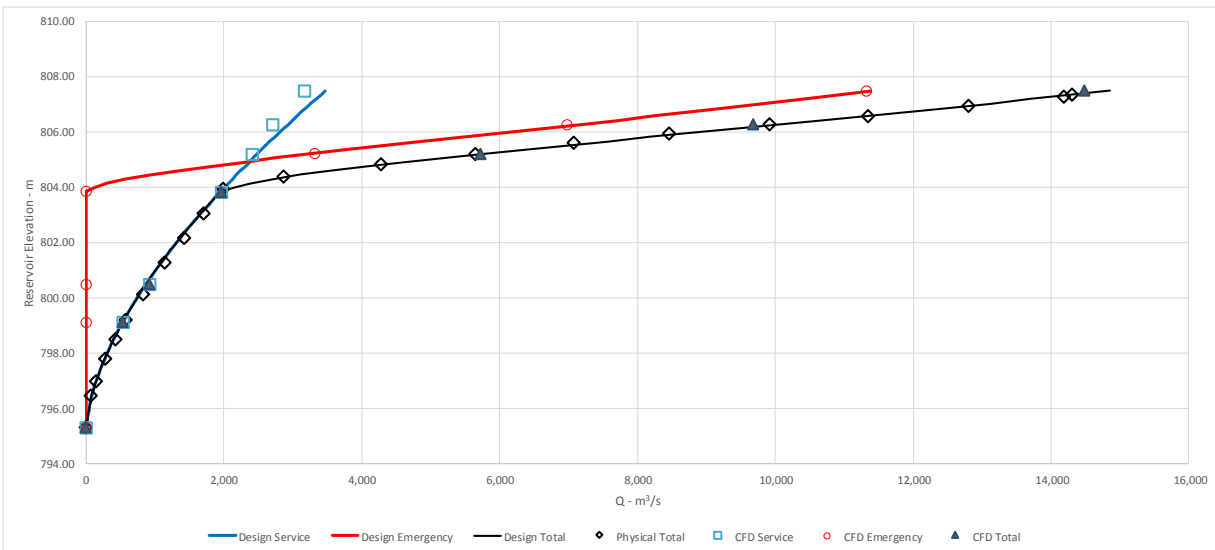
Figure 6 . Isabella Spillway Rating Curves

3. DESIGN DATA

The modeling effort (physical and numerical) has confirmed that the rating curve developed using traditional methods (discharge coefficients, velocity head, etc.) are accurate and that the current configuration of the service spillway and labyrinth weir (mod 10) will pass the PMF at a forebay elevation of less than 807.5 m (2649.26 ft).

The CFD model results were probed to provide additional information to the designers. In particular velocities, pressures and stream power were extracted from the model results. Several profiles and cross sections were placed in the model. All of the model nodes with cells that the sections touched were exported to a text file. Figure 8 shows all of the profiles/cross sections taken from the CFD models.
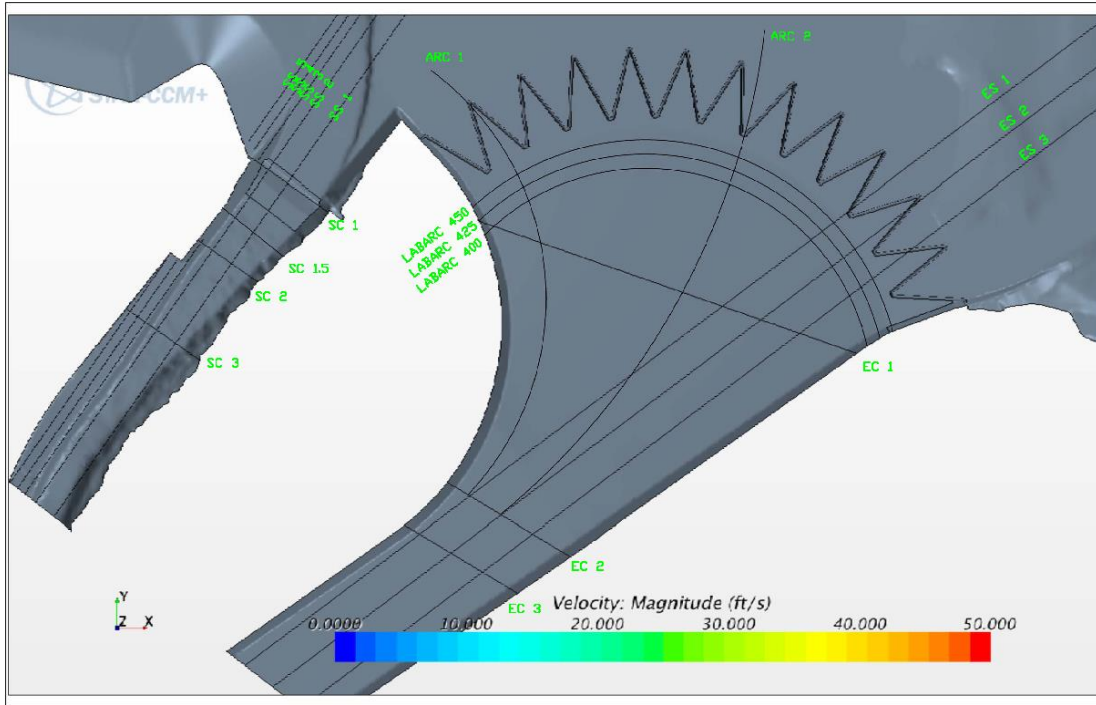
Figure 7. Location of Profiles and Cross Sections

Stream power can be used to evaluate the potential for erosion to occur. Stream Power is one variable that is combined by specific rock properties. Stream Power is computed from the dimensional equation:

$$SP = \gamma * q * Sf \tag{1}$$

where SP = Stream Power (kW/m²), γ = unit weight of water (kN/m³) and equal to 9.807 kN/m³, Sf = energy slope, (m/m), and q = unit discharge, (m³/s/m).

Stream power was computed for profiles where an energy slope was available. Stream power was also computed for the three labyrinth arcs shown in Figure 8 where stream power was computed for the center arc with the energy slope being defined between the outer arcs.

Figures 9 and 10 show the water surface elevation down the service spillway and emergency spillway for different CFD model runs. The legend is total Q for the project, not Q through the specific spillway.
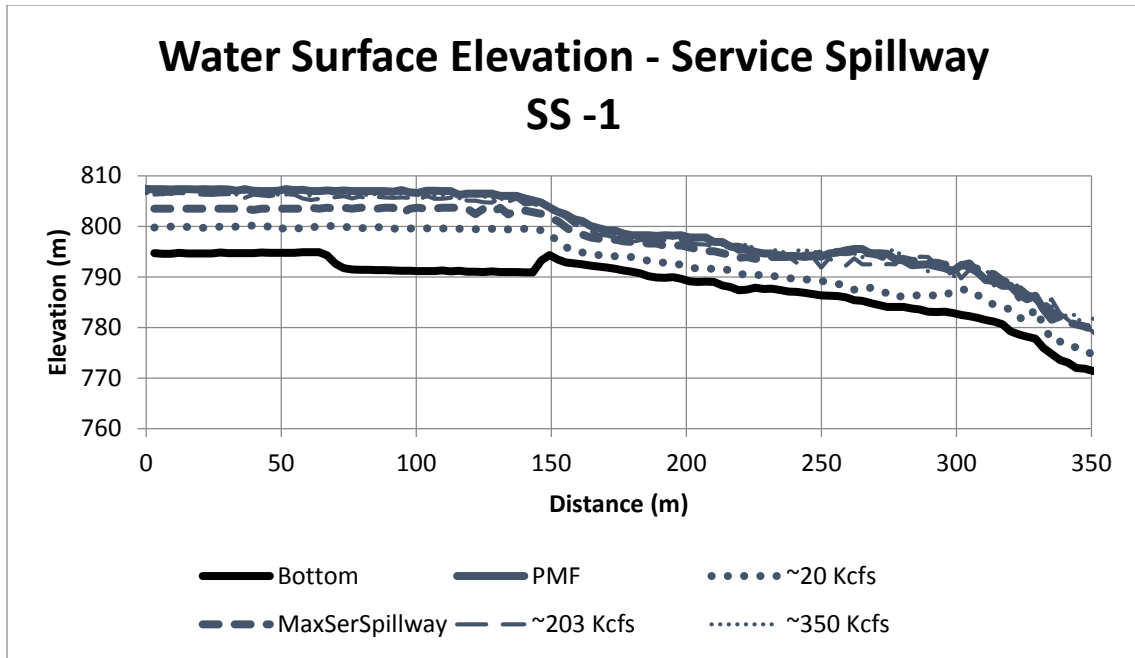
Figure 8. Water Surface Elevation – Service Spillway
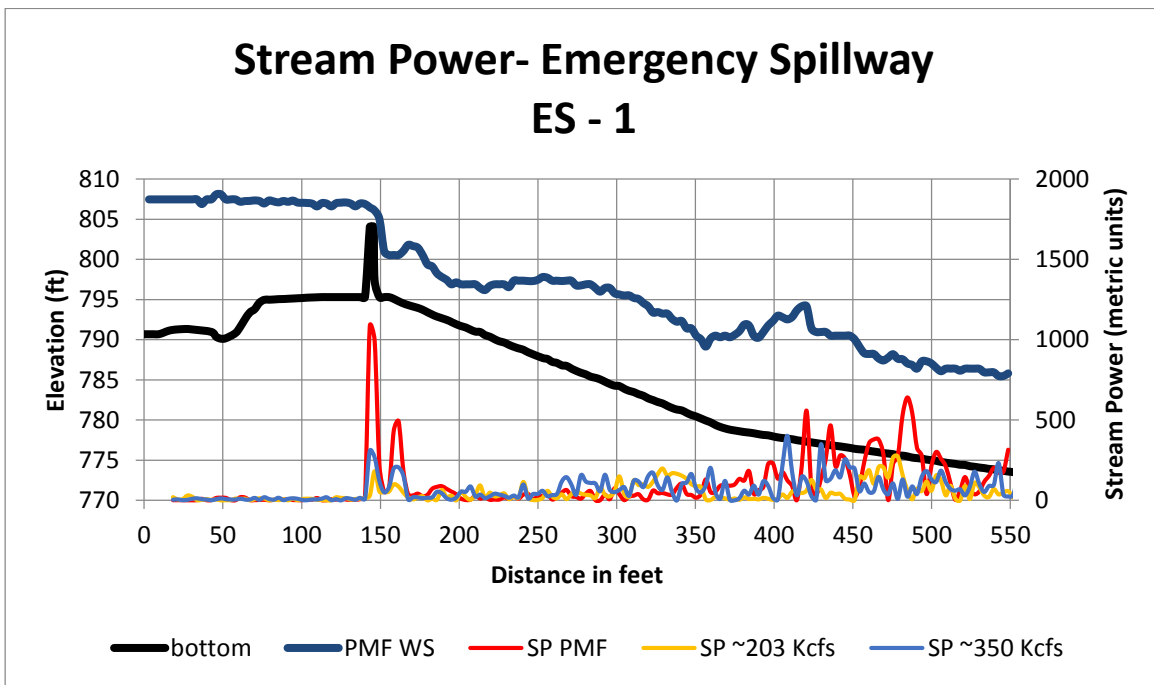
Figure 9. Water Surface Elevation – Emergency Spillway

Figures 11 and 12 show stream power for the same conditions plotted in Figures 9 and 10. The PMF water surface is included in the figures. The stream power plots are all shown with a scale of 0 to 2000. There is a spike in stream power at the spillway crest (significant change in energy slope). The magnitude of stream power at the spillway crest is large, but the crest is also concrete. In the service spillway, the stream power values spike at the downstream end of the chute where the slope of the chute is extremely steep. In the emergency spillway, the stream power

values tend to be higher at the lower end of the chute right downstream of the change in the invert slope. The spikes in stream power occur well downstream of the dam's crest.
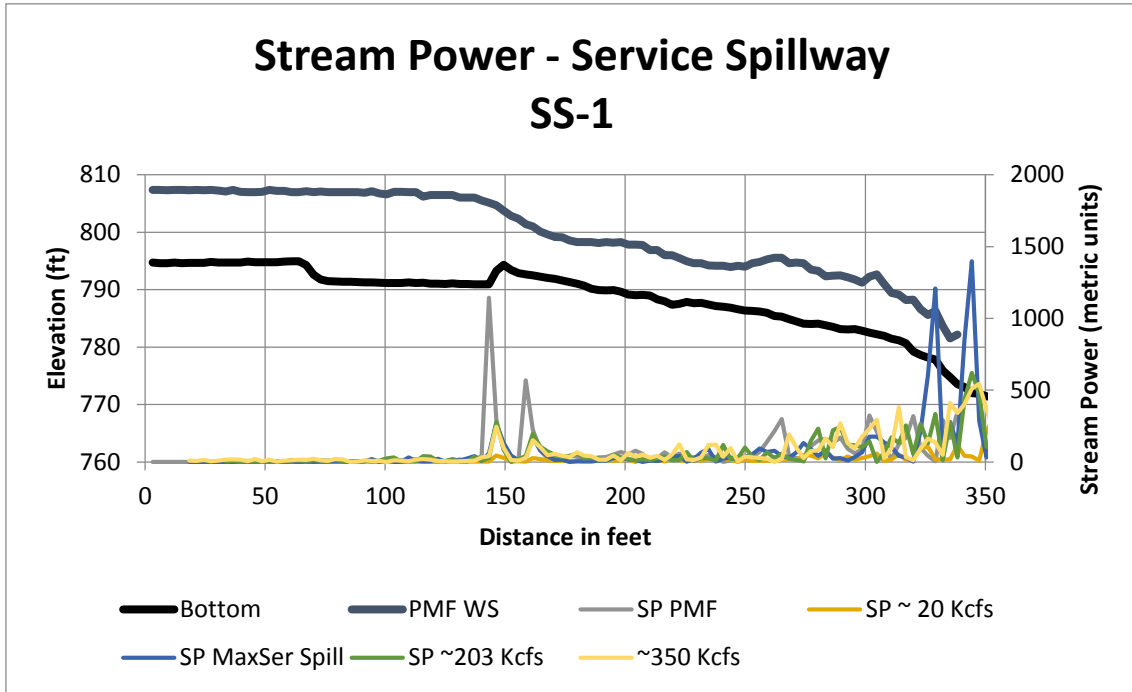
Figure 10. Stream Power – Service Spillway
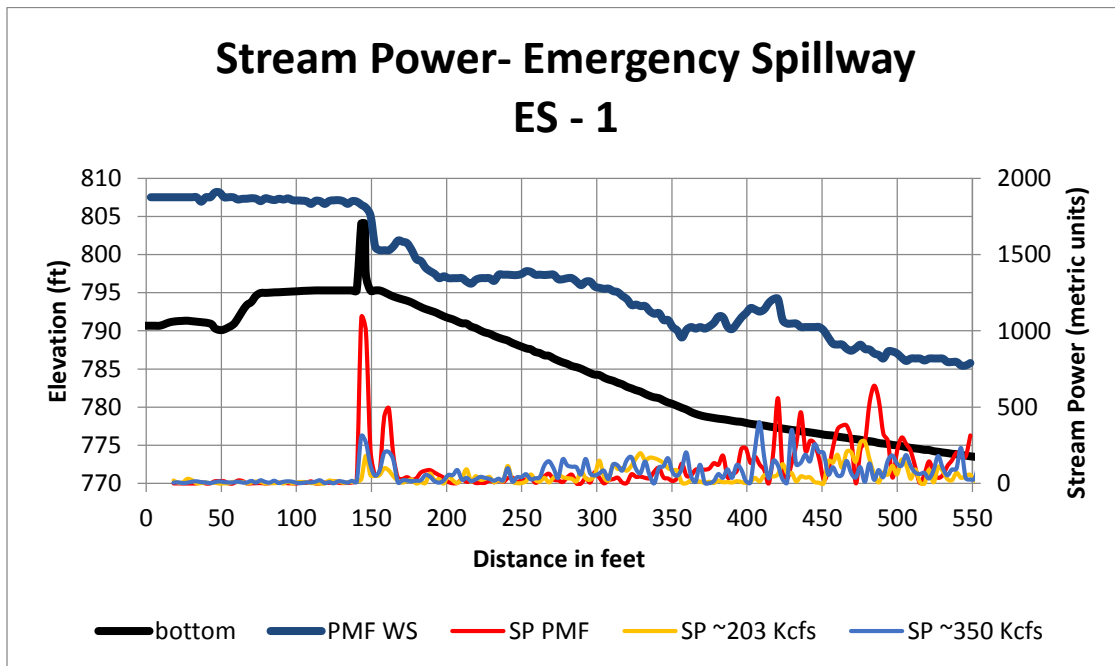
Figure 11. Stream Power of Emergency Spillway

4. CONCLUSIONS

The design process for the emergency spillway was streamlined using a composite modeling approach employing both physical and CFD modeling of the labyrinth weir. Utah State University, UtahWater Research Laboratory constructed a 1:45 scale physical model of a portion of the main dam forebay, emergency spillway, and service spillway. CENWP hydraulic engineers developed CFD models of the Isabella Dam forebay, auxiliary dam, and service and emergency spillways to provide an efficient test bed for design alternatives for the spillways, support rating curve development, and to validate information obtained in the physical model.

5. REFERENCES

Crookston, B.M. and B.P. Tullis (2012). "Arced Labyrinth Weirs." *J. Hydraul. Eng.*, 138(6), pp. 555-562.

Tullis, B. P. and Z. Sharp, (2014). "Isabella Dam Spillway Model." UWRL Report No. 2999, Utah Water Research Laboratory, Utah State University, Logan Utah.

USACE (2015). "Isabella Dam Service and Emergency Spillways – Computational Fluid Dynamics Modeling." US Army Corps of Engineers, Portland District, Hydraulic Design Section, Portland Oregon.

Managing Dam Safety Risks Related to Hydraulic Structures

W.R. Fiedler[1]

[1]Geotechincal Services Division (86-68300), Technical Service Center
Bureau of Reclamation
Denver, CO 80225
USA
E-mail: wfiedler@usbr.gov

ABSTRACT

The Bureau of Reclamation's Dam Safety Program manages risk for over 300 high and significant hazard dams. When risk estimates for potential failure modes indicate increasing justification for taking action to reduce risk, dam safety recommendations are typically made. The dam safety recommendations can focus on collecting additional data and performing studies to better quantify risk, or on initiating corrective actions to address well-defined risks. Dam safety recommendations within Reclamation's inventory address a number of different issues, such as those related to internal erosion, flood overtopping of dams, and seismic stability of dams. Dam safety recommendations related to hydraulic structure potential failure modes also represent a significant portion of the recommendations within Reclamation's inventory. This paper will focus on the methodology used to estimate risks for some of the more common hydraulic structure potential failure modes and will summarize the relative contribution of the risk posed by hydraulic structures to the overall risk within Reclamation's inventory of dams. Potential failure modes related to hydraulic structures include overtopping of chute walls, stagnation pressure failure of spillway chute slabs, cavitation damage of concrete flow surfaces leading to loss of concrete lining, structural failure of spillway gates, and erosion of the foundation and scour and headcutting in the downstream channel or dam/spillway foundations. The paper also includes examples of dam safety modifications related to hydraulic structure potential failure modes.

Keywords: Hydraulic Structures, Risk, Dam Safety, Modification.

1. INTRODUCTION

Ensuring that dams are safe and do not pose an unacceptable risk to the public are essential goals for a dam owner. Dam safety should be a key consideration during the design of a new dam and is reflected in both the design loads selected for the dam and redundant features included in the design. Once a dam is in operation, dam safety continues to be a key consideration and can be impacted by changes in the physical condition of the dam or waterways and changes in the potential loads at the dam. The Bureau of Reclamation has a robust dam safety program that utilizes risk analysis and risk assessment as foundational pieces for evaluating the safety of its dams.

Dams are evaluated thoroughly on an eight-year cycle as part of a Comprehensive Review (CR). Some of the elements of a CR include an inspection of the dam; a review of the static, hydrologic, and seismic hazard at the dam; a re-evaluation of the critical potential failure modes (PFM) at the dam; and an estimation of risk for the critical PFMs. During CRs, dam safety recommendations are often made if risks for a PFM are above the threshold values for increasing justification to take action to reduce risk (Reclamation 2011). Dam safety recommendations can also be made at the conclusion of higher level studies. Dam safety recommendations can initiate higher level analysis or studies or, if they are generated from a higher-level study, can initiate corrective action studies to evaluate modification alternatives that will reduce risk.

In 2015, there were 185 outstanding dam safety recommendations within Reclamation's dam safety program. Of these, 31 percent were related to the hydraulic structures in some way (e.g. flood overtopping of the dam or issues with the hydraulic structures). Seventeen percent of the outstanding dam safety recommendations in 2015 were specifically tied to the hydraulic structures (related to hydraulic issues associated with the spillway or structural capacity issues with the spillway during earthquakes). Dam safety risks related to the hydraulic structures make up a

significant percentage of the efforts within the dam safety program. The most common issues have been related to overtopping of chute walls, stagnation pressure failure of spillway chute slabs, cavitation damage of concrete flow surfaces, and structural failure of spillway gates. Each of these common potential failure modes is discussed in the following sections. If the risk for any PFM is high enough, and if the confidence in the risk estimates is good, corrective actions to reduce the risk related to the PFM is typically pursued by Reclamation. All of the PFMs addressed in this paper have resulted in modifications to several Reclamation spillways. The type of modification and the details will vary with each dam. Examples of modifications are provided in the following sections.

2. CHUTE WALL OVERTOPPING

Spillway structures often rely on a concrete chute to safely convey spillway releases from the crest structure to an energy dissipation structure near the river channel. The spillway chute forms a rectangular or sometimes trapezoidal open channel. Spillway chute walls were typically sized for the flow depths that would occur during the design spillway discharge, plus some freeboard to accommodate variations in flow depths due to air bulking (air entrainment) and cross-waves. If the spillway chute is subjected to discharges larger than the design discharge, or if air bulking or cross waves were not incorporated properly into the design, flow depths in the chute will increase and the walls may overtop. Overtopping flows will likely initiate erosion in the wall backfill, which has the potential to progress to the point of undermining the spillway chute slab and failing the invert of the spillway. Once this occurs, headcutting can initiate and progress upstream, possibly leading to a breach of the reservoir.

2.1. Spillway Design Discharge

The discharge that the spillway was designed for will determine the flow capacity of the spillway chute and stilling basin. If current flood loadings indicate that the spillway design discharge will be exceeded for some flood events, then the flow depths in the spillway chute and stilling basin will increase and wall overtopping becomes more likely for those floods. Whether the walls actually overtop during a given flood will be influenced by both the freeboard provided in the original design and factors that may not have been accounted for in the original design, including air bulking, cross waves, or variations in boundary roughness. If the current flood loadings indicate that the spillway design capacity will not be exceeded, and if a review of the design documentation indicates that the design methods were adequate, overtopping of the chute walls will generally not be a concern.

2.2. Spillway Discharges (Depths and Durations)

Water surface profiles in the spillway can be estimated for discharges that are obtained from the routings of frequency floods. A range of discharges that correspond to given frequency floods should be evaluated to provide flow depths and velocities at selected stations in the chute and can be completed with either models or boundary layer theory calculations. Flood routings will provide information on the duration of certain discharge levels. If durations of spillway flows are limited, failure of a spillway chute that has overtopped may initiate but may not have time to fully develop into a breach of the reservoir.

2.3. Other Factors That Can Affect Flow Depths

There are a number of additional factors that can affect flow depths in a spillway chute, and these should be considered when evaluating the potential for chute walls to overtop. These factors include converging and diverging chute walls, air bulking of the flow, and cross waves in a spillway chute. The best hydraulic performance of a spillway chute is obtained when the confining sidewalls are parallel to the flow direction and the distribution of flow across the channel is relatively uniform. In order to optimize a spillway design, however, it may have been desirable to make the chute narrower or wider than either the crest structure or the terminal structure. Sidewall convergence must be made gradual to avoid cross waves, wave run-up on the walls, and uneven distribution of flow within the chute. In a similar manner, the divergence of spillway chute walls should be limited, or the flow will not spread to

uniformly fill the chute. Guidance on acceptable angular variation of the flow boundaries is provided in Reclamation (1987).

Air bulking occurs where the turbulent water boundary reaches the water surface and air is introduced into the flow (entrained air) as a result of this turbulence. Under certain conditions, air bulking can significantly increase the flow depths in a spillway chute. Procedures that can be used to account for air bulking are provided in Reclamation and USACE (2015).

Cross waves can form in a spillway chute from a variety of sources: non-symmetrical entrance conditions into the spillway control structure, chute walls that converge too rapidly, piers that are introduced into the flow and then terminate, or curved chute walls. Cross waves will be superimposed on the flow depths that would occur under normal conditions and could lead to wall overtopping. For trapezoidal channels, cross waves can lead to run-up and wall overtopping sooner than for rectangular sections.

2.4. El Guapo Dam Spillway

El Guapo Dam is located on the Rio Guapo, 5 km south of the city of El Guapo, in the state of Miranda, Venezuela. The reservoir volume is 40 million m^3. The dam was constructed from 1975 to 1980. The original spillway at El Guapo Dam consisted of an uncontrolled ogee crest, located on the left abutment of the dam, a concrete chute, and a concrete hydraulic jump stilling basin. The spillway had a width of 12 m, a length of 282 m, and a design discharge capacity of 102 m^3/s. Initial hydrologic studies were based on a basin similar to the Rio Guapo basin. During construction of the spillway, the chute walls were overtopped, which triggered a new flood study. A tunnel spillway was constructed through the dam's left abutment, 250 m from original spillway.

On December 14, 1999, the reservoir was 1 m above the normal pool and 5 m below the dam crest. The radial gate on the tunnel spillway was fully open; both spillways were operating normally. Early on the morning of December 15th, the reservoir rose quickly and was 0.8 m below the dam crest. Early the next morning, the reservoir was 20 cm below the dam crest; the spillway chute walls just below the spillway crest began to overtop, and erosion of the adjacent fill initiated. By 4:30 a.m. on December 16th, cities below the dam were evacuated. At 9:00 a.m., the dam was inspected by helicopter, and the reservoir level had subsided (0.8 m below crest); people believed that flood had crested and the crisis was over. At 4:00 p.m. on December 16th, the reservoir rose again quickly; the bridge over the spillway collapsed; erosion of spillway backfill accelerated and the reinforced concrete chute, basin, and crest structure failed; but the concrete lined approach channel remained intact and controlled flows through the spillway. At 5:00 p.m., the approach channel failed and the reservoir was breached through the spillway area. El Guapo Dam never overtopped. Overtopping of the spillway chute walls initiated erosion of backfill behind chute walls and undermining and failure of the spillway chute. Headcutting progressed upstream and lead to reservoir breach. The spillway foundation consisted of decomposed rock, which was erodible (Villar 2002).

2.5. Modifications to Reduce Chute Wall Overtopping Potential

If the potential for overtopping of the chute walls exists, the solution is usually simple. The walls can be raised to contain the desired spillway flows, and the extent of the wall raise will typically be limited to only a portion of the chute. This type of modification was implemented at Reclamation's A.R. Bowman Dam in central Oregon. Based on a hydraulic model study, there was a concern for spillway wall overtopping under the increased flows above the original design discharge. Modification to address this issue consisted of installing flashboards over a 41-m length of the spillway chute. These flashboards were fabricated from 1.2-m by 2.4-m by 1-cm thick steel plates bolted to the inside face near the top of the walls. These panels extend upward 0.6 m (normal to the sloping top of wall) above the top of the walls.

3. STAGNATION PRESSURE RELATED FAILURE

Stagnation pressure related spillway failures can occur as a result of water flowing into cracks and joints within a spillway chute during spillway releases. A portion of the velocity head from the flow can be converted to an uplift pressure under the chute slab if vertical offsets exist, and water can pass through a joint without functional waterstops. If water entering a joint or a crack reaches the foundation, failure can result from excessive pressure and/or flow into the foundation.   If no drainage exists, or if the drainage is inadequate, and if the slab is insufficiently tied down, the build-up of uplift pressure under a concrete slab can cause hydraulic jacking. If drainage paths are available but are not adequately filtered, erosion of foundation material is possible, and structural collapse may occur. Figure 1 depicts the development of stagnation pressures under a spillway chute slab.
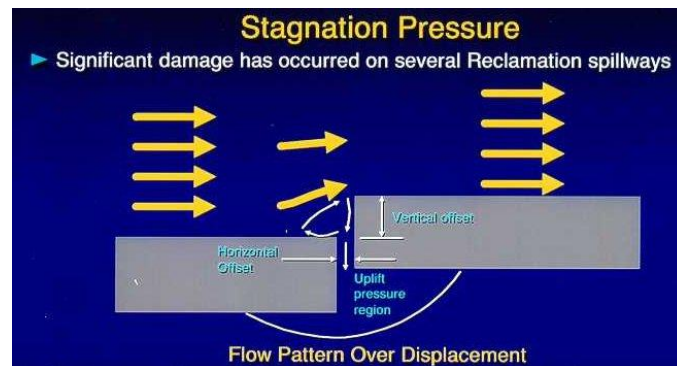
Figure 1. Development of Stagnation Pressures

Failure of a spillway chute slab, due to either hydraulic jacking or as a result of collapse after the supporting foundation is removed, can lead to scour of the spillway chute foundation, headcutting, and breach of the reservoir through the spillway crest structure.

3.1. Defensive Design Measures

Defensive design measures can prevent the failure mode from initiating or developing. Defensive design measures include the following (listed in order of decreasing effectiveness): waterstops, which can block path for water flow through joints in slabs; transverse cutoffs, which prevent vertical offsets at transverse joints and limit path for water from inside of chute to foundation; longitudinal reinforcement/dowels across chute floor joints, which minimize width of cracks and openings at joints and may prevent offsets; anchor bars, which provide resistance to uplift pressures lifting slabs off foundation; filtered underdrains, which relieve uplift pressures that can be generated under slabs (filtering prevents movement of foundation materials into the drainage system and initiation of foundation erosion); and insulation, which insulates the drainage system and prevents it from freezing and also prevents frost heave locally. An absence of or inadequate defensive design measures can allow initiation and progression of this failure mode.

3.2. Reclamation Research on Stagnation Pressure Potential

Reclamation conducted research in 2007 to evaluate different spillway chute transverse joint geometries and their effects on the stagnation pressures that could be generated beneath a spillway chute slab, as well as the flows that could be transmitted underneath the slab (Reclamation 2007).   Both drained and undrained conditions were evaluated. Figure 2 is an example of the testing results, which depict uplift pressures that were generated for a transverse joint with a 1.3-cm gap, sharp edged geometry and drained conditions for a variety of offset dimensions that encroach into the flow from the channel boundary (downstream slab raised with respect to upstream slab).

3.3. Big Sandy Dam Spillway

Big Sandy Dam is located on the Big Sandy Creek, 72 km north of Rock Springs, Wyoming. The earthfill embankment dam was completed in 1952. The spillway is located on the right abutment of the dam and consists of an uncontrolled concrete side-channel crest structure and a concrete chute and stilling basin. The spillway is founded on thinly bedded to massive siltstone and sandstone. A zone in the foundation below the spillway inlet structure contains open joints and bedding planes, which allowed reservoir water to seep under the spillway chute floor. The spillway chute was designed with an underdrain system and anchor bars grouted into the foundation rock, but waterstops and continuous reinforcement were not provided across the contraction joints. Deterioration of the concrete slab occurred shortly after the dam was put into service. Cracking occurred in the chute slabs due to excessive water and ice pressures along the foundation-concrete slab interface, and some of the slabs heaved and were displaced off the foundation, creating offsets into the flow. The spillway operated from 1957 to 1982 without incident, but a chute floor slab failed in June 1983 due to uplift pressures from flows of 11 m³/s (Hepler and Johnson 1988). The potential failure mode did not progress beyond the spillway slab jacking, primarily due to the erosion resistance of the underlying foundation relative to the energy of the spillway release flows. Calculations were performed to confirm that the failure was the result of stagnation pressures being generated under the chute slab. The calculations also showed that with fully effective anchor bars, the slab would not have failed. The uplift pressures assumed in the calculations were estimated from extrapolated laboratory tests (Hepler and Johnson 1988). From observations after the failure, it was noted that the anchor bars exposed beneath the slab were not coated with grout, indicating that the anchor bar capacity was not fully developed. This case history illustrates that both well thought out details and good construction procedures are needed to achieve performance.
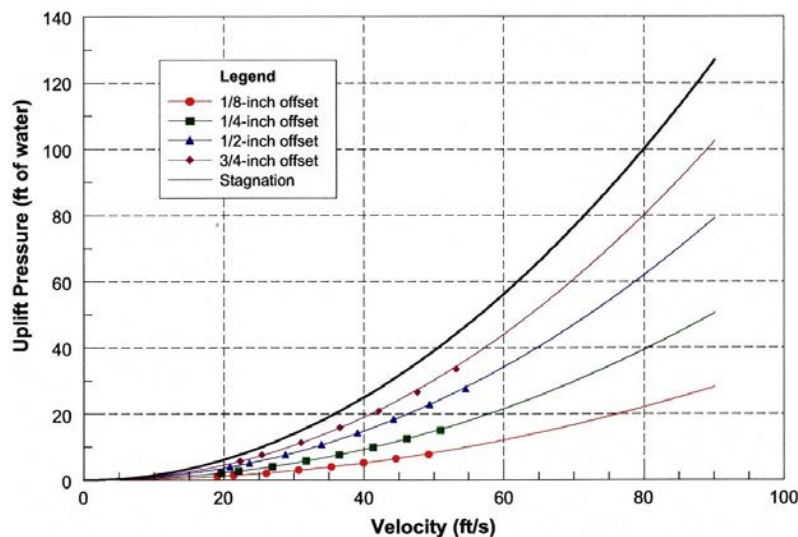
Figure 2. Mean uplift pressure, sharp-edged geometry, vented cavity, 1.3 cm (1/2-inch) gap (Reclamation 2007)

3.4. Modifications to Reduce Stagnation Pressure Failure Potential

Modifications to prevent a stagnation pressure failure along a spillway chute typically involve replacing a portion or all of the spillway chute and incorporating defensive design measures into the spillway chute. Figure 3 shows the typical design details that are beneficial in reducing the potential for stagnation pressure failure. These design details were implemented in spillway chute modifications at Reclamation's Hyrum Dam in Utah and Big Sandy Dam in Wyoming.
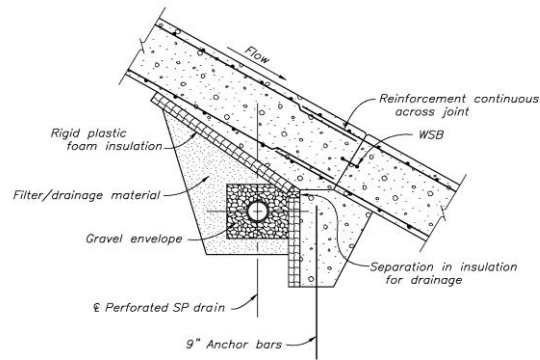
Figure 3. Defensive Design Measures for Stagnation Pressures

4. CAVITATION DAMAGE

Cavitation is the formation of vapor cavities in a liquid. Cavitation occurs in high-velocity flow, where the water pressure is reduced locally because of an irregularity in the flow surface. As the vapor cavities move into a zone of higher pressure, they collapse, sending out high-pressure shock waves (see Figure 4). If the cavities collapse near a flow boundary, there will be damage to the material at the boundary. Cracks, offsets, and surface roughness can increase the potential for cavitation damage. The extent of cavitation damage will be a function of the cavitation indices at key locations in the spillway chute or tunnel and the duration of flow. If the spillway lining is completely failed, the spillway foundation will be exposed, which can lead to scour and headcutting or expansion of the eroded area. These mechanisms could lead to breach of the reservoir. In most cases, this failure mode is unlikely to progress to the point where dam failure occurs due to the long flow durations that are required to cause major damage to concrete linings.

Figure 4. Cavitation Created in Low Ambient Pressure Chamber

4.1. Condition of Concrete in Spillway

Cracks, offsets, surface irregularities, and/or open joints in chute slabs (or tunnel linings) and the lower portions of chute walls exposed to flow may allow this failure mode to initiate. The geometry of the flow surface irregularities will affect the initiation of cavitation. The more abrupt the irregularity, the more prone the spillway will be to the initiation of cavitation. Concrete deterioration in the form of alkali-silica reaction, freeze thaw damage, and sulfate attack can exacerbate this PFM by creating surface irregularities and/or offsets at damaged areas.

4.2. Cavitation Indices

Cavitation indices can be used to evaluate the potential for cavitation damage in a spillway chute or tunnel. The cavitation index is defined as follows:

$$\sigma = \frac{P - P_v}{\frac{\rho V^2}{2}} \tag{1}$$

where P = pressure at flow surface (atmospheric pressure + pressure related to flow depth), P_v = vapor pressure of water, ρ = density of water, and V = average flow velocity.

There is the potential for cavitation damage to initiate when the cavitation index, σ, is between 0.2 and 0.5 for typical concrete, but significant damage is typically associated with cavitation indices less than 0.2 and long durations of spillway operation. For large features that are introduced into the flow abruptly (such as stilling basin baffle blocks or splitter walls), cavitation damage can occur when the σ is as high as 1.0 or greater. Additional information on the potential for cavitation damage can be found in Falvey (1980).

4.3. Aeration of Flow

The introduction of air into spillway flows reduces the potential for cavitation to damage concrete surfaces. Aeration reduces the damage that occurs from collapsing vapor cavities. If the flow is not naturally aerated, measures can be taken to introduce air into the flow at critical locations along a spillway.

4.4. Glen Canyon Dam Spillway

Glen Canyon Dam is located on the Colorado River in northern Arizona. The dam, completed in 1964, is a constant radius, thick-arch concrete structure. Spillways are located at each abutment, and each consists of a gated intake structure regulated by radial gates, a concrete lined tunnel through the soft sandstone abutments, and a deflector bucket at the downstream end. Each spillway tunnel is inclined at 55 degrees, with a vertical bend and a horizontal section. The spillways experienced significant cavitation damage during operation in June and July, 1983 during flooding on the Colorado River system, when the reservoir filled completely for the first time and releases were required. The cavitation damage was initiated by offsets formed by calcite deposits on the tunnel invert at the upstream end of the elbow. Both spillways were operated at discharges up to about 850 m³/s. Cavitation indices of the flow in the area where damage initiated in the left spillway ranged from about 0.13 to 0.14. The cavitation indices of the deposits along the tunnel (indices at which cavitation was likely to occur) ranged from 0.64 to 0.73. The worst damage occurred in the left tunnel spillway: a hole 11-m deep, 41-m long, and 15-m wide was eroded at the elbow into the soft sandstone (Burgi and Eckley 1987).

4.5. Modifications to Mitigate Potential for Cavitation Damage

An effective means of mitigating the potential for cavitation damage is to entrain air into the flow. This dramatically reduces the damage that can occur on flow surfaces. This is typically accomplished by separating the flow from the flow surface (through the use of a ramp) and then introducing air on the underside of the flow jet. An example of this is shown in Figure 5, which shows the air slot installed at Glen Canyon Dam.

Figure 5. Air Slot at Glen Canyon Dam

The 1.2- by 1.2-meter air slot at Glen Canyon Dam extends over the lower three-quarters of the tunnel circumference, which ensures that adequate air entrainment and good distribution of the entrained air occurs in the flow.

5. SPILLWAY RADIAL GATE FAILURE

Gated spillways can create a vulnerability during floods if the gates cannot be reliably operated to their full capacity. Gate reliability can be impacted by failure of power supplies, binding of gates, or failure of components of the hoist system. While gate reliability issues can increase the probability of a dam overtopping during a flood, this paper focuses on spillway gate structural issues that can lead to an uncontrolled release of the reservoir. The most common type of spillway gate in Reclamation's inventory is a radial gate. Radial gates consist of a cylindrical skinplate reinforced by vertical or horizontal support ribs, horizontal or vertical girders, and the radial arm struts that transfer the hydraulic loads to the gate trunnions. Radial gates rotate about their horizontal axis during opening/ closing operations. These gates are generally large, and the capacity through a failed radial gate can often generate large uncontrolled releases. If the ultimate capacity of the gate is exceeded, a radial gate can fail rapidly. Most of the load on a radial gate is from the reservoir, but additional loads can be generated from trunnion pin friction for a gate that is being operated or from hydrodynamic and inertial effects during an earthquake. Reclamation has documented procedures for estimating risk from radial gate failure both during normal conditions and seismic conditions (Reclamation and USACE 2015).

5.1. Interaction Ratio

A key consideration in evaluating the potential for a radial gate to fail is the interaction ratio (IR), which is used to assess the stability of a structural member subjected to axial compression and bi-axial bending. Instability of the member will occur in accordance to AISC (AISC 2011) when the loadings result in the interaction ratio exceeding 1.0. When evaluating stability for a risk analysis, all load and resistance factors are equal to 1.0 so the actual load carrying capacity of the structure is evaluated. The following equations can be used to calculate the IR for a radial gate element:

$$IR = \frac{P_u}{P_n} + \frac{8}{9}\left(\frac{M_{ux}}{M_{nx}} + \frac{M_{uy}}{M_{ny}}\right) \qquad for \; \frac{P_u}{P_n} \geq 0.2 \tag{2}$$

$$IR = \frac{P_u}{2P_n} + \left(\frac{M_{ux}}{M_{nx}} + \frac{M_{uy}}{M_{ny}}\right) \qquad for \; \frac{P_u}{P_n} < 0.2 \tag{3}$$

where P_u – required axial strength, P_n – the available axial strength equals the nominal compressive strength, M_u – required flexural strength, M_n – the available flexural strength equals the nominal flexural strength, and subscripts x and y relating to strong and weak axis bending, respectively

5.2. Other Considerations for Radial Gate Failure

In addition to the IR, other factors should be considered in a risk analysis evaluating radial gate failure. These include the gate arrangement and structural conditions, the frequency of inspecting and exercising the radial gates, and the potential for the radial gate bushings to fail and lead to increased trunnion friction. All of these factors have the potential for either reducing the structural capacity of the gates or increasing the loading on the gates. Guidance on how to incorporate these elements into a risk analysis is provided in Reclamation and USACE (2015).

5.3. Failure of Radial Gate at Folsom Dam

Folsom Dam was designed and constructed by the U.S. Army Corps of Engineers between 1948 and 1956. The dam was transferred to the Bureau of Reclamation for operation and maintenance in 1956. The dam consists of a concrete gravity section across the river channel, flanked by long earth fill wing dams. The concrete dam has a gated overflow spillway section that is regulated by eight radial gates: five service gates and three emergency gates. One of eight large spillway radial gates failed at Folsom Dam in California during reservoir releases on July 17, 1995. The gate failure occurred with a nearly full reservoir releasing a peak flow of about 1130 m³/s. No injuries or fatalities occurred as a result of the gate failure.

Gate No. 3 was being operated at approximately 8 a.m. on July 17, 1995, to maintain flow in the river during a powerplant shutdown. As the gate was opened, it was allowed to stop at 15 cm automatically and again at 30 cm. The auto-stop function was overridden (normal procedure) with no stop being made at the 60-cm level. As the gate opening approached 73 cm, the gate operator felt an "unusual vibration" and he stopped the gate hoist motor. As the operator turned to check the gate, he saw the right side of the gate swing open slowly, like a door hinged on the left side, and saw water pouring around both sides of the gate leaf (see Figure 6). The time from the operator's initial awareness of the vibration to observing gate displacement and uncontrolled flow of water was estimated to be no more than 5 seconds.

Figure 6 – Failure of Radial Gate No.3 at Folsom Dam

Following the failure of Gate No.3, a multi-disciplinary, multi-agency forensic team was formed to investigate and determine the cause of the failure. The team identified the two main causes of the gate failure as insufficient stiffness and strength in critical structural gate arm members and increased trunnion friction by corrosion of the steel trunnion pins.

5.4. Modifications to Reduce Structural Failure of Spillway Radial Gates Potential

There are several options for reducing the potential of spillway radial gate failure. If the issue is driven by trunnion pin friction, the bushings can be replaced with bushings that reduce the trunnion pin friction. If the structural capacity of key gate elements is lacking, gate elements can be modified by increasing the steel section. At Reclamation's Bradbury Dam in California, the flanges of the WF beams that form the radial gate arms were thickened by welding steel plates onto the existing flanges. This increased the section of the beams and increased their structural capacities.

6. CONCLUSIONS

Risk analysis and risk assessment are key elements of Reclamation's Dam Safety Program. This approach has allowed Reclamation to identify the most critical issues within its inventory and to focus efforts to reduce overall dam safety risks. This process has identified a number of deficiencies associated with the hydraulic structures at Reclamation dams. Modifications have been implemented to address these issues and reduce the chance of a hydraulic structure contributing to dam failure.

7. REFERENCES

American Institute of Steel Construction (2011). Specification for Structural Steel Buildings, AISC Standard 360-10, Chicago, Il.

Bureau of Reclamation (1987). Design of Small Dams, Bureau of Reclamation, Third Edition, Denver, Co.

Bureau of Reclamation (2007). *Uplift and Crack Flow Resulting from High Velocity Discharges over Open Offset Joints, Report DSO-07-07*, Denver Co.

Bureau of Reclamation (2011). *Interim Dam Safety Public Protection Guidelines: A Risk Framework to Support Dam-Safety Decision Making*, Denver, Co.

Bureau of Reclamation & USACE (2015). *Best Practices in Dam and Levee Safety Risk Analysis*. Training manual jointly prepared by the Bureau of Reclamation Technical Service Center and the U.S. Army Corps of Engineers Risk Management Center, Denver, Co. Version 4.0.

Burgi, P.H. and Eckley, M. S. (1987). "Repairs at Glen Canyon Dam." *Concrete International Design and Construction*, Vol 9, Issue 3, American Concrete Institute, Detroit, Mi.

Falvey, H.T. (1980). Cavitation in Chutes and Spillways, Engineering Monograph No. 42, Bureau of Reclamation, Denver, Co.

Hepler, T.E., and Johnson, P.L (1988), "Analysis of Spillway Failures Caused by Uplift Pressure," *Proceedings of National Conference on Hydraulic Engineering and International Symposium on Model-Prototype Correlations*, ASCE, Colorado Springs, Co.

Villar, L.M.S. (2002), Incidentes en las Presas de Venezuela, Problemas, Soluciones y Lecciones, Venezuela.

Advanced Gate Operation Strategies in HEC-RAS 5.0

C.R. Goodell[1]
[1]WEST Consultants, Inc.
Portland, OR 97223
USA
E-mail: cgoodell@westconsultants.com

ABSTRACT

The Hydrologic Engineering Center's River Analysis System (HEC-RAS) is designed for computing water surface profiles and inundation maps, but it is also able to handle flow through gated structures using a variety of equations and techniques. HEC-RAS has a small selection of built-in gate types, representing some of the more common gates that are used for controlling flow at dams and canal structures. Each gate type in HEC-RAS has a set of empirical equations that are used to compute head loss through the structure for a given flow. There are also two operational schemes that can be chosen for gates: Time Series Gate Openings, and Elevation Controlled Gates.

While the built-in gate types and operational schemes in HEC-RAS might be appropriate for some of the more common gate structures, it is quite common to have a gate system or other flow control device that simply does not fit within the confines of the built-in techniques in HEC-RAS. In these cases, the user has the option to take advantage of some lesser known techniques both within HEC-RAS and by external applications.

This paper will discuss four gate and operation strategies that can be used with HEC-RAS that allow the user to handle any flow control scheme possible. These include Navigation Dams, User Defined Curves, Rules, and the HECRASController API.

Keywords: *HEC-RAS, Gate, Operation, Rules, Automation, Rating Curve*

1. INTRODUCTION

HEC-RAS is a software application designed to perform one and two-dimensional hydraulic calculations for a full network of natural and constructed channels. Although its original and primary intent is to develop water surface profiles and inundation maps in rivers and streams, additional functionality added over the years has allowed HEC-RAS to be used successfully in simulating reservoir operations, specifically the operation of different types of flow control gates. HEC-RAS computes unsteady flow water surface profiles using conservation equations developed for gradually varied flow conditions. The rapidly varied flow that occurs in and around gate structures cannot be explicitly modeled using the HEC-RAS unsteady flow solver. Therefore, in HEC-RAS, modelers typically use built-in gate equations and/or rating curves to determine energy loss through gate structures.

HEC-RAS's built-in gate types are limited to sluice gates, radial gates (i.e. tainter gates), and overflow gates (both open air and closed top). Specific equations are used for each of these gates at three different flow regimes: low flow, free flow, transitionary flow, and fully submerged flow. If these built-in gates and their associated equations do not fit a specific gate type that needs to be modeled, the user has the option of defining the "non-standard" gate using a series of rating curves (User Defined Curves); each curve representing a specific gate opening. As long as the gate can be described with rating curves and it remains tailwater independent throughout the simulation, this option provides a useable method for modeling any type of hydraulic control at a dam. At certain low-head dams, tailwater may play a very important role in the discharge of flow through a gate and the User-Defined Curves will not work. In this case, the user can implement scripts to further define the characteristics of the gate. Gate Rules are technically a boundary condition and are meant for describing the operation of gates. However, there are some script commands that will allow the user to either explicitly define the flow through the gates under a range of conditions or access an unlimited number of rating curves (i.e. one family set for each tailwater condition) that can be changed automatically during run-time, based on conditions at the reference points.

Operation of the built-in gates and gates defined by User Defined Curves is handled in the boundary condition editor in HEC-RAS, which consists of four boundary condition types. Two relatively unsophisticated control options include Time Series, where a gate opening is set by the user for each computation interval, and Elevation Control, based on either the water surface elevation at a reference location or the difference in stage between two reference locations. Navigation Dams is another available boundary condition type for gates and is specifically used for optimizing gate settings in simulation time in order to maintain a target water surface elevation, or range of elevations, during an event. If complex operations are required, scripting can be implemented using the Gate Rules boundary condition.

It is quite possible that none of the standard features included in HEC-RAS can properly simulate either the gate type or the operation the user wishes to implement into the model. The HECRASController API is a library of programming procedures that can be called from programming code in external applications. This gives the user flexibility to simulate just about any flow control device and operational scheme that can be conceived. The HECRASController capabilities in modeling gate types and gate operations is limited only by the programming skill of the user.

In any computational model, it is important to construct the model to provide the user an appropriate level of confidence in the results but not to make the model unnecessarily complex. As Albert Einstein is purported to have said, "Everything should be as simple as it can be, but no simpler." This is a skill that typically takes years of experience to develop. HEC-RAS provides functionality to allow the user to simulate gates and gate operations with either very simple and easy-to-use methods or very complex and wide-ranging methods, depending on the user's objectives.

2. GATE TYPES

2.1. Standard gates

Radial gates and sluice gates use essentially the same equations. The difference is that for the free flow condition, the radial gate will use a version of the orifice equation that is heavily dependent on the shape and position of the gate relative to its opening.

$$Q = C\sqrt{2g}\,WT^{TE}B^{BE}H^{HE} \qquad\qquad Q = CWB\sqrt{2gH}$$
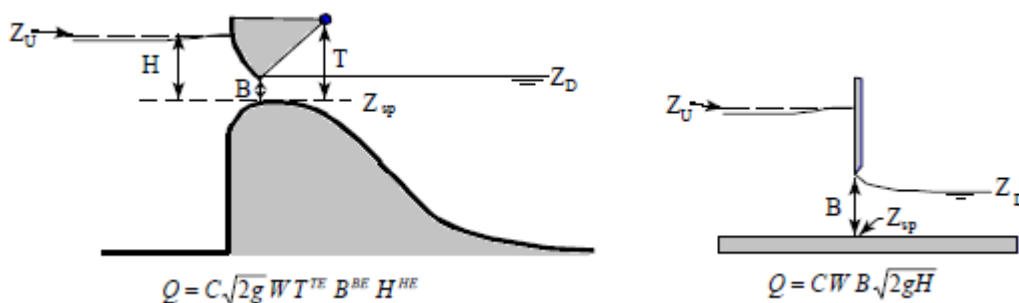
Figure 1. Free flow gate equations for radial and sluice gates.

In Figure 1, Eqs. (1) and (2) are presented where Q is the discharge, C is the sluice gate discharge coefficient, W is the crest length, B is the gate opening, and T is the radial gate trunnion axis height. The head, H, is measured from the headwater energy level, Z_U, to the gate seat elevation, Z_{sp}. HEC-RAS provides the option to instead measure H from the headwater energy level to the center of the gate opening if the user desires. The HEC-RAS default exponent values are $TE = 0$, $BE = 1$, and $HE = 0.5$. With these defaults, the equation for radial gate flow and sluice gate flow become the same.

Submergence on the gate is defined as the tailwater depth ($Z_D = Z_{sp}$) divided by the headwater energy depth ($Z_U - Z_{sp}$). Once the submergence on the gate increases to 67%, HEC-RAS will begin to transition from free flow gate equations to the fully submerged gate flow equation. At 80% submergence, HEC-RAS uses the fully submerged orifice equation for both gate types:

$$Q = C_{sub}WB\sqrt{2gH_{sub}} \tag{3}$$

where C_{sub} is the submerged orifice discharge coefficient and H_{sub} is the head differential between the headwater energy, Z_U, and the tailwater elevation, Z_D.

Under low flow conditions, the gate is raised higher than the upstream water surface elevation, and HEC-RAS will use the weir equation:

$$Q = C_{weir}WH^{3/2} \tag{4}$$

where C_{weir} is the weir discharge coefficient.

Overflow gates are also available in HEC-RAS. Overflow gates can either be set as "open air," or "closed top." Open air overflow gates only use the weir coefficient Eq. (4). However, as the gate crest (Z_{sp}) moves up and down, H will change accordingly. Closed top overflow gates work the same as sluice gates, only the gate crest (Zsp) with a corresponding top will move up and down, rather than the gate lip.
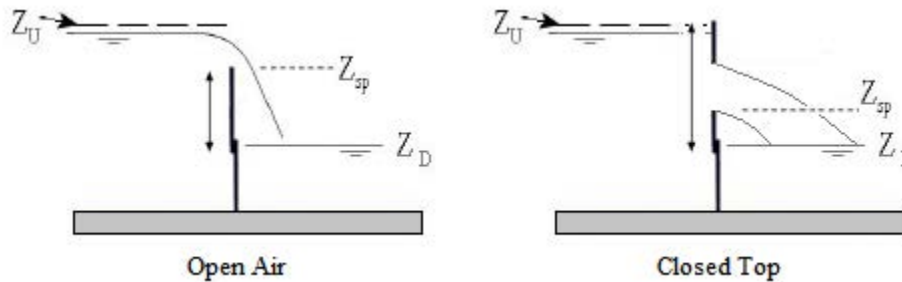
Figure 2. Open air and closed top overflow gates.

Note that in HEC-RAS under standard operational boundary conditions, C, C_{sub}, and C_{weir} are fixed for all hydraulic conditions for the entire simulation. This is a limitation in HEC-RAS when using the standard gate operations, since discharge coefficients are known to vary over a range of heads.

2.2. User-Defined Curves

If the user intends to simulate a hydraulic control structure that is not simulated properly with any of the standard gates, User-Defined Curves can be used instead. This option allows the user to enter in a family of rating curves (one per gate opening) that are used in place of the gate equations. This option only works when tailwater does not have a submergence effect on the flow through the gate. Figure 3 provides an example of a typical family of rating curves for a gate. Note that in HEC-RAS, the free discharge curve is called "Low Flow," but, ironically, this is typically anything but low flow.

Although User-Defined Curves are technically a gate "type," they can be used to simulate any hydraulic control structure for which one could generate a rating curve as long as flow control remains independent of tailwater. This feature has been used successfully to simulate flow over spillway structures whose discharge coefficients and/or crest lengths change significantly with different head levels. Labyrinth weirs and piano key weirs are examples where this is the case. User-Defined Curves can also be used quite easily to simulate hydraulic structures that

exhibit distinctly different flow controls for varying head levels, such as morning glory spillways. Morning glory (shaft) spillways are unique flow control structures with two different, distinct flow controls: a free overfall, where the circular crest controls flow, and the submerged condition, where the shaft controls flow.
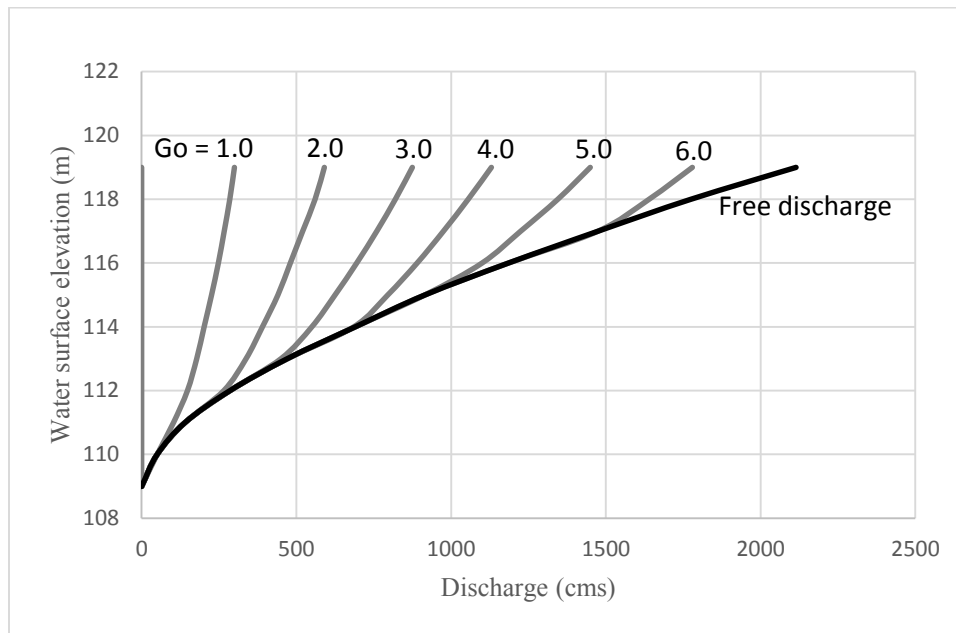
Figure 3. Typical gate rating curve.

3. GATE OPERATION

HEC-RAS comes with four boundary conditions that can be applied to gates: Time Series Gate Openings, Elevation Controlled Gates, Navigation Dams, and Rules. Time Series and Elevation Control are simple, unsophisticated methods for describing gate operations, while Navigation Dams is an optimization scheme that determines the best sequence of gate openings to meet a target water surface elevation (or range of water surface elevations) at a reference point in the model. Rules is a scripting tool that allows the user to operate the gate in almost any way desired.

3.1. Standard Operational Schemes

Time Series Gate Openings is very easy to use and simply requires a gate opening height for each prescribed time interval over the entire model simulation period. The gate settings are determined prior to the run by the user and are set as they are, for the entire simulation (i.e. there is no feedback applied to the settings). With Elevation Controlled Gates, HEC-RAS will monitor one or two reference locations and open or close the gates based on the water surface elevations at those locations. Figure 4 shows the HEC-RAS Elevation Controlled Gates input dialog with the gate set to operate based on a single reference cross section just upstream of the gate. The user sets when the gate opens and when it closes, as well as the opening and closing rates. Based on the reference point, HEC-RAS will determine what the gate setting should be for each computation interval. Although simple to use, elevation control is limited to control based on one location's water surface elevation or a head difference between two reference points. Beyond this, there is no logic programmed into the gate's operation. For example, if a user desires the gate to operate to maintain a certain water surface elevation in the reservoir, or would like to have more control on how the gate operates, either navigation dams or rules must be used. Alternatively, the HECRASController API can provide near limitless operational control (discussed in Section 4).
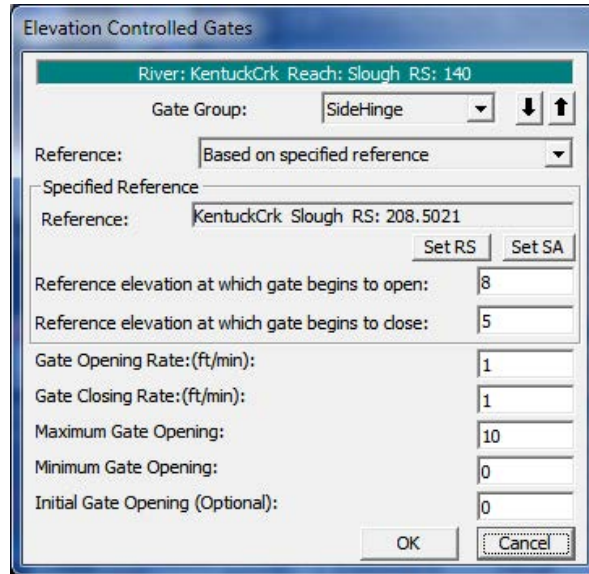
Figure 4. Elevation Controlled Gates Input Dialog

3.2. Navigation Dams

When Navigation Dams is used as a gate boundary condition, HEC-RAS will attempt, during run-time, to maintain a minimum and maximum water surface elevation at some reference point by opening or closing the gate. As the name implies, this feature is advantageous when trying to maintain a certain draft upstream of a dam for navigation traffic. The user enters a target water surface elevation along with some rather obscure calibration data, and HEC-RAS will try to meet the target as closely as possible. This technique frequently requires a number of iterative runs to achieve the desired results. There are four optimization methods available for Navigation Dams: Pool Only Control, Hinge Point Only Control, Hinge Point and Minimum Pool Operations, and Hinge Point and Minimum and Maximum Pool Control. Each method is progressively more complicated. Pool Only Control is discussed herein.

Pool Only Control attempts to maintain a user-specified target water surface just upstream of the gate structure. Since there is some delay between the arrival of a flood wave and the pool elevation change from a gate setting, HEC-RAS needs to forecast the flow rate at the gate structure. This is done by monitoring flow at some point further upstream of the gate structure. The user specifies this flow monitor location and frequently requires some iteration to achieve the proper response. A good initial guess is to select a flow monitor location so that the river travel time between the monitor location and the gate structure is similar to the normal gate change time increment (Brunner, et al. 2010a).

The Pool Control dialog gives the user some calibration control over how the target is met. The user enters in a series of water surface elevations that set the desired target as well as the "urgency" of gate operation at various water surface elevations away from the target. First, a primary water surface elevation range is bracketed around the target water surface elevation by selecting a target high and target low. As long as the water surface elevation is within this range, HEC-RAS will simply use the average flow rate between the gate structure and the monitor location and set the gate opening accordingly to achieve the target water surface elevation. As the pool elevation moves outside of this range, the average discharge between the gate structure and the reference location is multiplied by factors (also provided by the user). Once the flow in the river exceeds the user-specified "Flow Open River," HEC-RAS will open the gates to their maximum opening. If the flow falls below the user-specified "Flow Minimum," the gates will be set to the gate minimum opening. Figure 5 shows the Navigation Dams boundary condition dialog using Pool Only Control. Aside from the Target Water Surface Elevation and the Flow Open River and Flow Minimum, the water surface elevations and flow factors are largely calibration parameters. The user must run the program, evaluate the results, and adjust these parameters accordingly until the target water surface elevation range is met for the entire simulation.
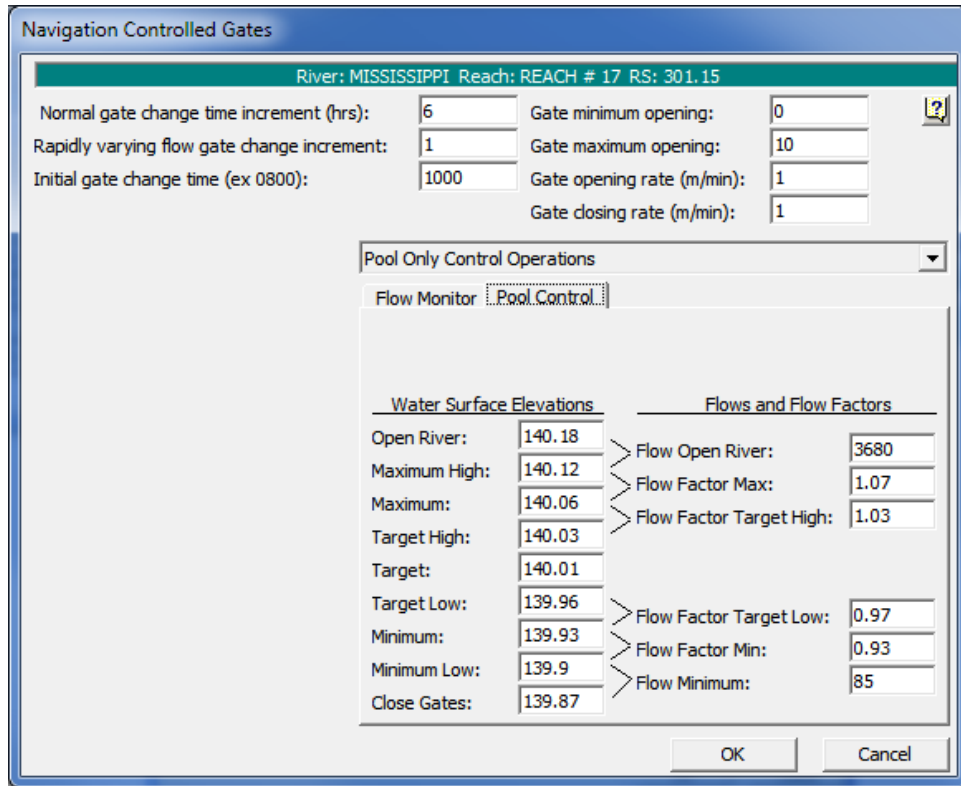
Figure 5. Navigation Dams Gate Operation - Pool Only Control

3.3. Rules

Rule Based Operations is an embedded scripting feature in HEC-RAS meant to offer a high degree of flexibility and customization of gate operations beyond what is available in the standard gate boundary conditions and navigation dams. With Rules, the user can give HEC-RAS the ability to operate gate openings or override the standard gate openings by specifying flows at a gate structure. The user can script operations based on input or computed variables at various locations including current and previously computed flows, water surface elevations, and even based on time considerations such as time of day or season. The user also has the ability to change input parameters during run time such as weir/gate coefficients or rating curve tables based on computed output. Basic math and conditional operations provide the user a great deal of flexibility in simulating complex gate operational procedures. All of these controls are pre-programmed into the Rules Operations Editor as shown in Figure 6.

Unlike typical programming code, Rules are scripted inside the Rules Operations Editor by clicking buttons and filling out input and dropdown boxes. With this editor, the user can define new variables, retrieve simulation values, set operational parameters, program conditional statements, perform mathematical computations, and set up tables of paired data.

A simple Rules operation might be set up to open or close a gate based on a computed flow at a reference location. If a certain flow rate is exceeded, the gates will open by a predetermined amount. On the other hand, if the computed flow is less than an input value, the gates will close by a predetermined amount. Figure 7 demonstrates the conditional scripting statement required to handle this simple operation in the Rules Operations Editor.
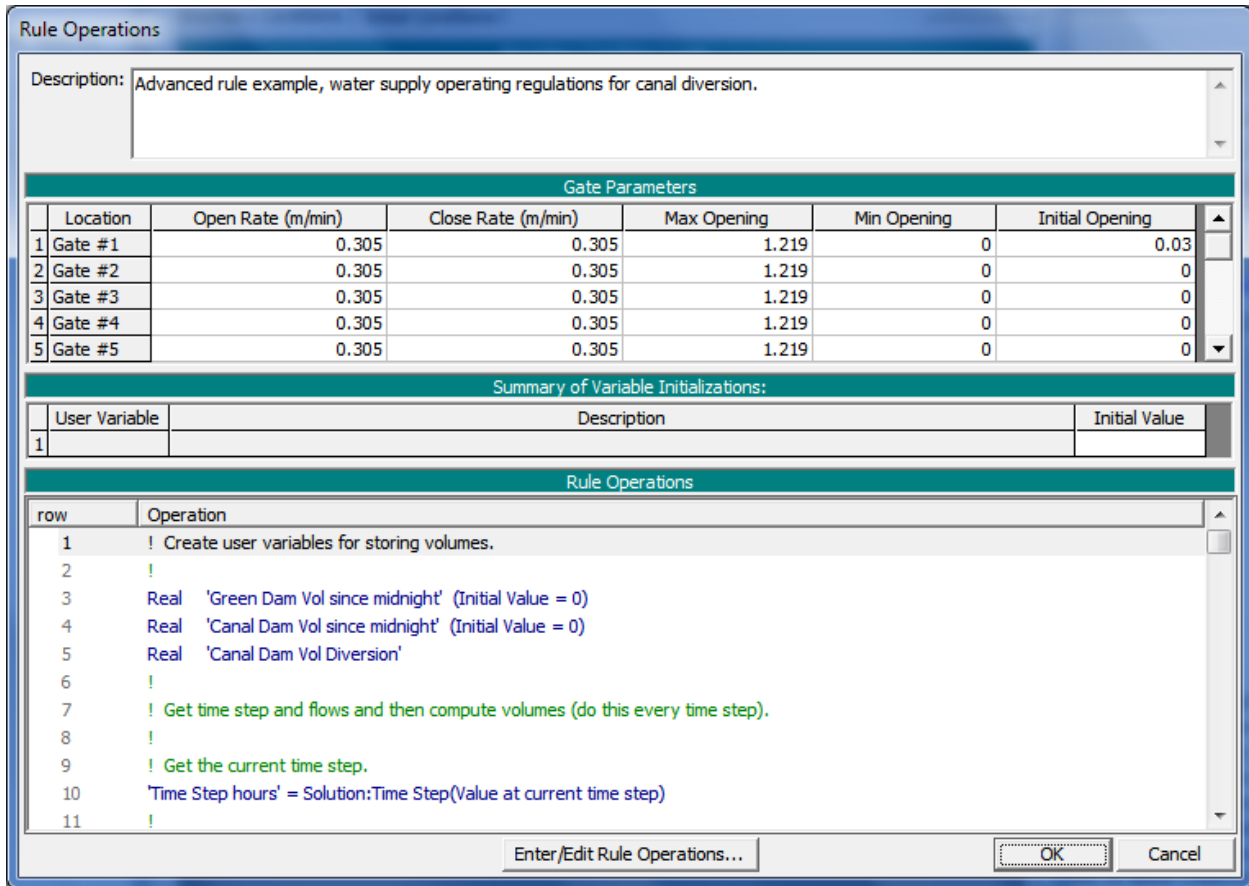
Figure 6. Rules Operations Editor
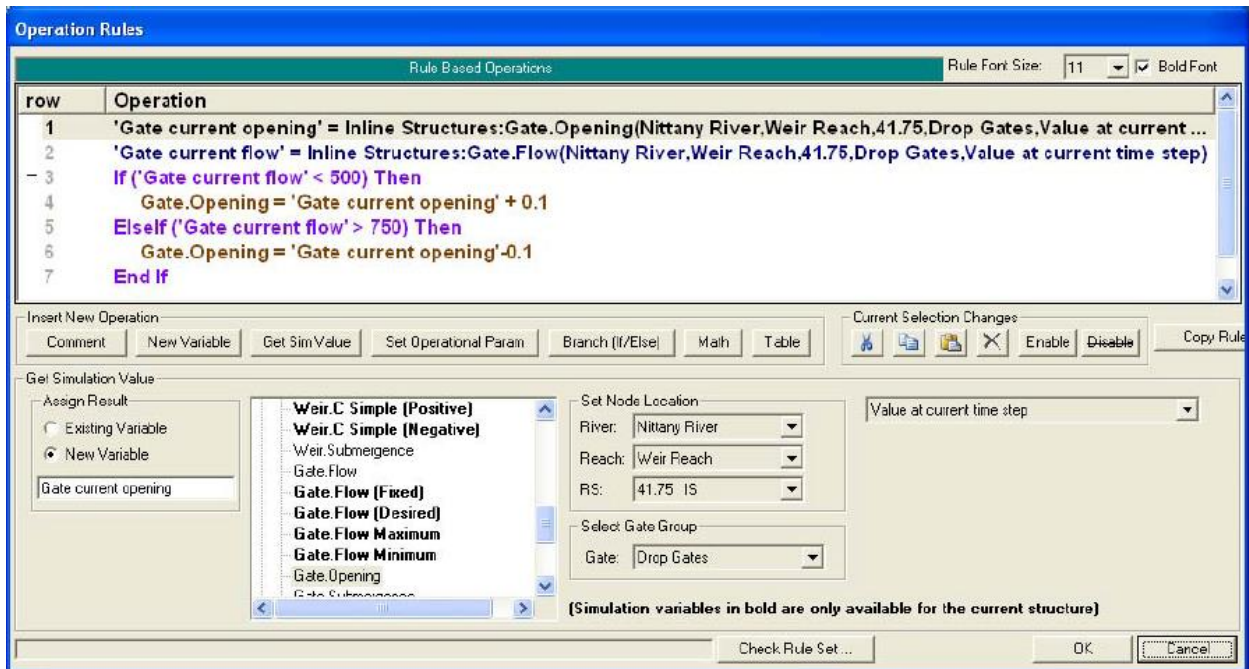
Figure 7. Conditional Statements in the Rules Operations Editor.

While the Rules Operations Editor is designed to offer the user a great deal of flexibility and control over gate operations, it is somewhat limited in that the user can only apply changes to gate structures and it only works for structures connected to cross sections and storage areas (not 2D areas). Furthermore, the user must use the somewhat restrictive buttons and dropdown boxes provided in the Rules Operations Editor. This can be an advantage for users that are new to or otherwise unfamiliar with programming code, as the editor will effectively write the code for the user. For the seasoned programmer; however, scripting rules in the Rules Operation Editor will feel archaic and cumbersome. Programming gate operations in an external programming platform can provide the user even more operational control and a wider range of applications, and it also offers the scripting elegance sought after by experienced programmers.

4. HECRASCONTROLLER API

A relatively unknown but powerful feature embedded in HEC-RAS is the HECRASController. The HECRASController is part of an application programming interface (API) that includes a library of programming procedures that work directly with HEC-RAS from any external programming platform that can read in component object module (COM) version of a dynamic link library (DLL) (Goodell, 2014).

The HECRASController comes with the installation of HEC-RAS and can be used to control the functions of HEC-RAS, manipulate input, and retrieve output, all during run-time. With regard to gate structures, this gives the user near limitless options for operational control and physical characteristic definition. "Breaking the HEC-RAS Code" (Goodell, 2014) is a book that explains how to use the HECRASController both to read and write to HEC-RAS input files and to read results from the output file. To do this during run-time for gate operation requires the user to make use of a "pausing" technique. The pausing technique is described in "Breaking the HEC-RAS Code" on page 116 and follows these steps:

1. Set your simulation window to one day (or whatever increment suits your needs).
2. Set your model to create a restart file at the end of the run. This is done in the Output Options menu item under Options in the unsteady flow analysis window. Run the model once to create the first restart file; then set the unsteady flow editor to read that restart file as its initial conditions.
3. Run the one-day simulation through the programming code using the HECRASController procedures.
4. Using programming code and the HECRASController, read the output file and then make changes to the flow file based on computed results at specific output locations.
5. Repeat steps 3 and 4 for a full (multiple-day) simulation.

In this manner, gate settings can be chosen based on water surface elevations, velocity, flow rates, or any HEC-RAS output at any reference point or points during the simulation. Furthermore, gate characteristics can also be changed during runtime, such as the gate discharge coefficient or the gate rating curve. Describing and setting the gate operations and characteristics are really only limited by the programming skill and creativity of the user.

5. CONCLUSIONS

Methods for defining and operating gates in HEC-RAS are presented. They range from simple and easy-to-use methods, like the built-in standard gate types and standard operational boundary conditions, to the rather complex Navigation Dams and Rules operations editor. The HECRASController API makes gate definition and operation schemes near limitless and applicable during run-time. With these options, just about any gate type and operation can be simulated in HEC-RAS.

It is prudent to acknowledge that HEC-RAS is first and foremost a model designed to simulate rivers with an objective of evaluating reach-wide conditions, such as increases in flood risk, extents of inundation, and changes in velocity and flow patterns. HEC-RAS should be used to assess the reach-wide implications of various alternatives over existing conditions, rather than near-field design activities. To gain a true understanding of the hydraulics in and around different types of gates and gate structures, a more sophisticated computer model (e.g. 3D or computational fluid dynamics (CFD)), physical model, or combination of both should be used.

6. REFERENCES

Brunner, G. et al. (2010a). *HEC-RAS River Analysis System User's Manual Version 4.1*, Hydrologic Engineering Center, Davis California.

Brunner, G. et al. (2010b). *HEC-RAS River Analysis System Hydraulic Reference Manual Version 4.1*, Hydrologic Engineering Center, Davis California.

Goodell, C. (2013). "Advanced Rules for Unsteady Flow." *The RAS Solution,* <http://www.hecrasmodel.blogspot.com> (Sep. 24, 2013).

Goodell, C. (2014). *Breaking the HEC-RAS Code*, h2ls, Portland Oregon.

Piper, S. (undated). *Advanced Rules for Unsteady Flow,* Hydrologic Engineering Center, Davis California.

Effects of Hydraulic Jump Motion on Air Entrainment in Closed Conduits

J.D. Mortensen and J.P. Kubitschek
Hydraulic Investigations and Laboratory Services
United States Bureau of Reclamation
Denver, CO 80225
USA
E-mail: jmortensen@usbr.gov

ABSTRACT

Air vent systems are designed to protect hydropower penstocks and reservoir outlets under various operating conditions. During an emergency closure of an upstream gate, the hydraulic jump that forms downstream of the gate is not stationary and may advance downstream, potentially increasing the total air demand. A lab-scale physical model of a general outlet works piping configuration was constructed at Reclamation's Hydraulics Laboratory in Denver, CO to observe hydraulic jump behavior during emergency gate closures. Parameters including gate discharge, gate closure rate, air vent size, and downstream pipe pressure were tested at two different pipe slopes. Results indicate that the hydraulic jump travel speed is dependent on air vent size as well as gate closure rate, both of which affect the internal pressure in the pipe near the vent connection. For a shallow-sloped pipe, the jump speed remains steady throughout the entire pipe length if the air supply is sufficient. However, if air flow is significantly reduced due to an undersized air vent, unsteady travel speeds and pressure surges were observed. This was not the case for a steep-sloped pipe, which produced steady jump speeds for all vent sizes. Once completed, these results are expected to be applicable for prediction of hydraulic jump travel speed and its effects on air demand for vent sizing considerations based on hydraulic operating conditions.

Keywords: air entrainment, air vent, emergency gate closure, hydraulic jump, outlet works, penstock.

1. INTRODUCTION

Air vent systems are designed to protect penstocks and low-level outlet pipes from excessively low pressures during emergency gate closures. An adequate air supply is necessary to allow smooth gate operation, prevent cavitation damage, and, in some cases, prevent pipe collapse. As the emergency gate closes, a hydraulic jump (jump) forms in the pipe, which may then travel downstream, drawing air as it moves due to entrainment and the air volume change in the pipe. Extensive work has been done on air entrainment for stationary jumps in closed conduits, including Kalinske & Robertson (1943), Sharma (1976), Falvey (1980), Escarameia (2007), and Mortensen et al (2011). Also, Parvaresh et al (2006) and Nasvi et al (2010) have conducted experiments on moving jumps in rectangular open channels. However, there is limited information in the literature that addresses moving jumps in closed conduits.

The main objective of this study is to determine the travel speed of jumps in closed conduits due to an upstream gate closure and its effect on the total air demand. For this study, total air demand is defined as the air flowrate entrained by the jump plus the air flowrate required to fill the evacuated pipe volume as the jump moves downstream. This study focuses on the latter component, which will further aid in the design and sizing of air vent systems for penstocks and outlet pipes. As infrastructure ages and operational requirements change, it becomes increasingly important to accurately predict air demand for adequate sizing of air vent systems. Improvements in predicting jump movement are necessary to reduce the uncertainty of existing air demand prediction methods.

The results presented in this paper were obtained using a lab-scale physical model as part of an ongoing study at the Bureau of Reclamation's Hydraulics Laboratory in Denver, CO to improve analyses of air vent systems. The study includes collections of physical data from both the lab-scale model and future field testing at a Reclamation facility (not included in this paper). Data collection and analyses are expected to be completed in 2016. These data will be used to improve analytical methods (Falvey, 1980) and (Frizell, 1993) for air demand prediction to support optimized air vent sizing and design.

2. EXPERIMENTAL SETUP

The laboratory physical model is comprised of a 30.48 cm diameter pipe on 0.55- and 26.0-percent slopes as illustrated in Figure 1 and Figure 2. The arrangement consists of a slide (emergency) gate at the upstream end, which is operated with a variable speed motor, followed by a 7.62 cm clear PVC air vent pipe immediately downstream. The main section is approximately 45 pipe diameters in length and made of clear PVC for flow visualization. Back pressure in the pipe was provided by a butterfly valve at the downstream end of the pipe.
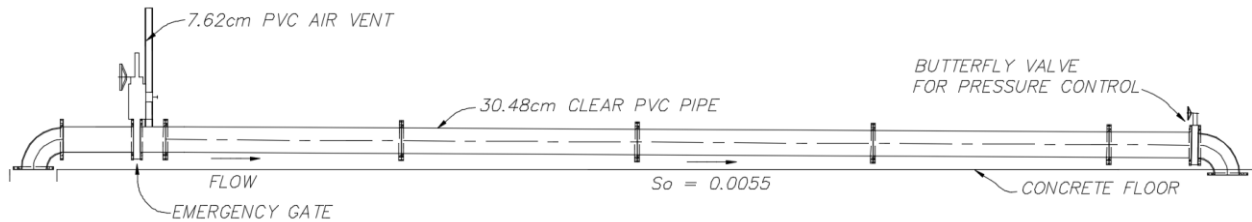
Figure 1. Profile view of 0.55-percent slope model.
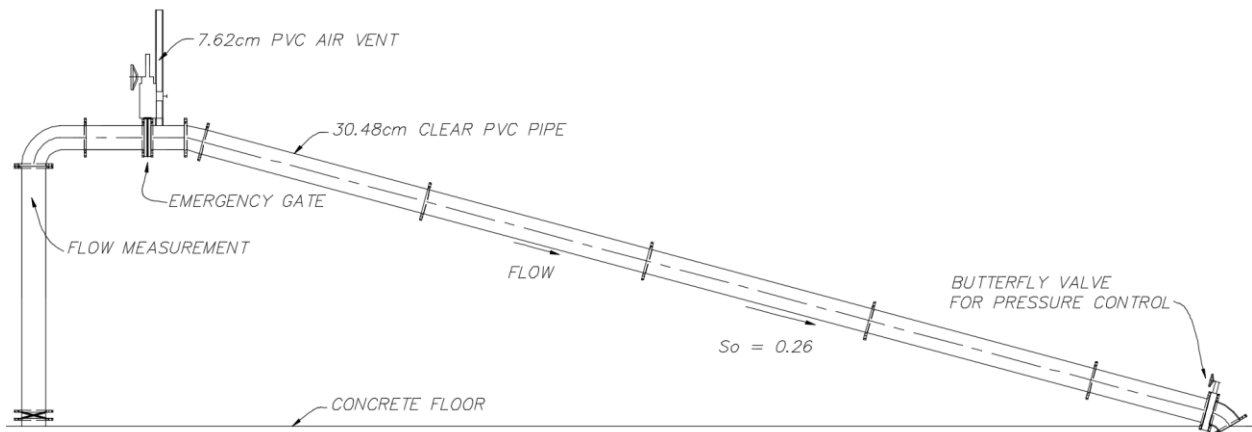
Figure 2. Profile view of 26-percent slope model.

Initial water flowrates, vent sizes, and gate closure rates were varied at each pipe slope as shown in Table 1. Flowrates were controlled with the lab's PLC pump control system. Initial laboratory tests produced maximum flowrates that were limited as a result of the steep pipe slope and higher inlet elevation, which increased head on the pump. Additional flowrates at the steep slope are currently being tested, and results will be available in the near future. The air vent size was varied by inserting a fitting with different orifice sizes at the top of the air vent pipe. Gate closure rates were controlled using the variable speed motor.

2.1. Test Procedure

Each test run began with a steady-state flow rate in the pipe before the emergency gate started to close. As the gate closed, the air vent was manually opened to allow air to flow into the pipe when the internal pressure downstream of the gate was sufficiently low to initiate venting. The pressure upstream of the gate was held constant throughout the test by adjusting the variable frequency drive on the pump as the gate closed to represent a constant reservoir head. As the gate continued to close, a jump would form downstream of the gate and eventually move downstream and out of the pipe. The downstream butterfly valve was left in a set position throughout each test run.

The instrumentation setup included an acoustic flowmeter (±2% accuracy) to measure water flowrate entering the laboratory setup, a string transducer (±0.25% accuracy) to measure gate position, an anemometer (±1.5% accuracy)

to measure air velocity in the vent pipe, and absolute pressure transducers (±0.25% accuracy) to measure pipe pressures immediately upstream and downstream of the gate as well as at the downstream end of the pipe near the butterfly valve. All measurements were recorded at a sample rate of 500 samples per second. Local atmospheric pressure was obtained using a mercury barometer during each testing period. The average jump travel speeds were estimated using an HD video camera (30 frames per second) and visible station markers located along the test pipe.

Table 1. Operational parameters tested with the physical pipe model.

Pipe Slope	Vent Diameter Ratio	Gate Closure Rate	*Q_{stand}
cm / cm	*(D_{vent} / D_{pipe})*	*(% Open) / sec*	*Q_{water}^2 / (gD^5)*
0.0055	0.25	0.76, 0.60, 0.34, & 0.10	3.94, 2.45, 1.30, & 0.52
	0.125	0.76, 0.60, 0.34, & 0.10	3.94, 2.45, 1.30, & 0.52
	0.094	0.76, 0.60, 0.34, & 0.10	3.94, 2.45, 1.30, & 0.52
	0.063	0.76, 0.60, 0.34, & 0.10	3.94, 2.45, 1.30, & 0.52
	0.042	0.76, 0.60, 0.34, & 0.10	3.94, 2.45, 1.30, & 0.52
0.26	0.25	0.76, 0.60, 0.34, & 0.10	3.09, 2.75, 1.83, & 1.27
	0.094	0.76, 0.60, 0.34, & 0.10	3.09, 2.75, 1.83, & 1.27
	0.063	0.76, 0.60, 0.34, & 0.10	3.09, 2.75, 1.83, & 1.27
	0.042	0.76, 0.60, 0.34, & 0.10	3.09, 2.75, 1.83, & 1.27

Standardized water discharge at full gate opening - dimensionless flowrate equation and parameters are further defined on pg. 51 of Falvey (1980)

3. RESULTS & DISCUSSION

3.1. Shallow Slope Pipe

Results show that air vent size has a significant effect on both internal pipe pressure at the vent connection and air flowrate through the vent, as expected (Figures 3 and 4). Figure 5 shows that air vent size and gate closure rate also influence the travel speed of the moving jump. Vent ratios larger than 0.1 had an influence on travel speed by allowing the jump to move slightly faster in the larger vent sizes. This is most likely due to higher internal pipe pressures upstream of the jump due to the adequately-sized (prevents negative pipe pressure) air vent, effectively reducing the pressure differential across the jump and thereby reducing the resistance of the jump to move downstream. In this scenario, jump speeds were steady (no acceleration) from the time the jump formed in the upstream pipe near the gate until it left the end of the pipe downstream.

For vent ratios less than 0.10, the jump travel speed increased significantly (Figure 5). Under such conditions, the jump would hold at a stationary point, usually near the upstream end of the pipe, until it finally released and rapidly moved down the pipe. Video documentation showed that the jump started to move when air that had previously accumulated downstream of the jump flowed back upstream, forcing the jump to quickly move downstream. The delay of the jump, and then its release and movement, were caused by initially negative upstream pressures caused by an undersized air vent. This process is shown in the time series photos in Figure 6.

Since air flow travelled back upstream, the incoming air flow through the vent decreased temporarily in the same gate position range for which jump movement occurred (Figure 4). Also, the upstream pressure increased temporarily during initial jump movement (Figure 3). Jump movement was often erratic and unsteady both before and after the burst of downstream movement. Data scatter in Figure 5 may be attributed somewhat to the difficulty in manually controlling pump pressure upstream of the gate but is largely due to the inherently erratic nature of jumps.
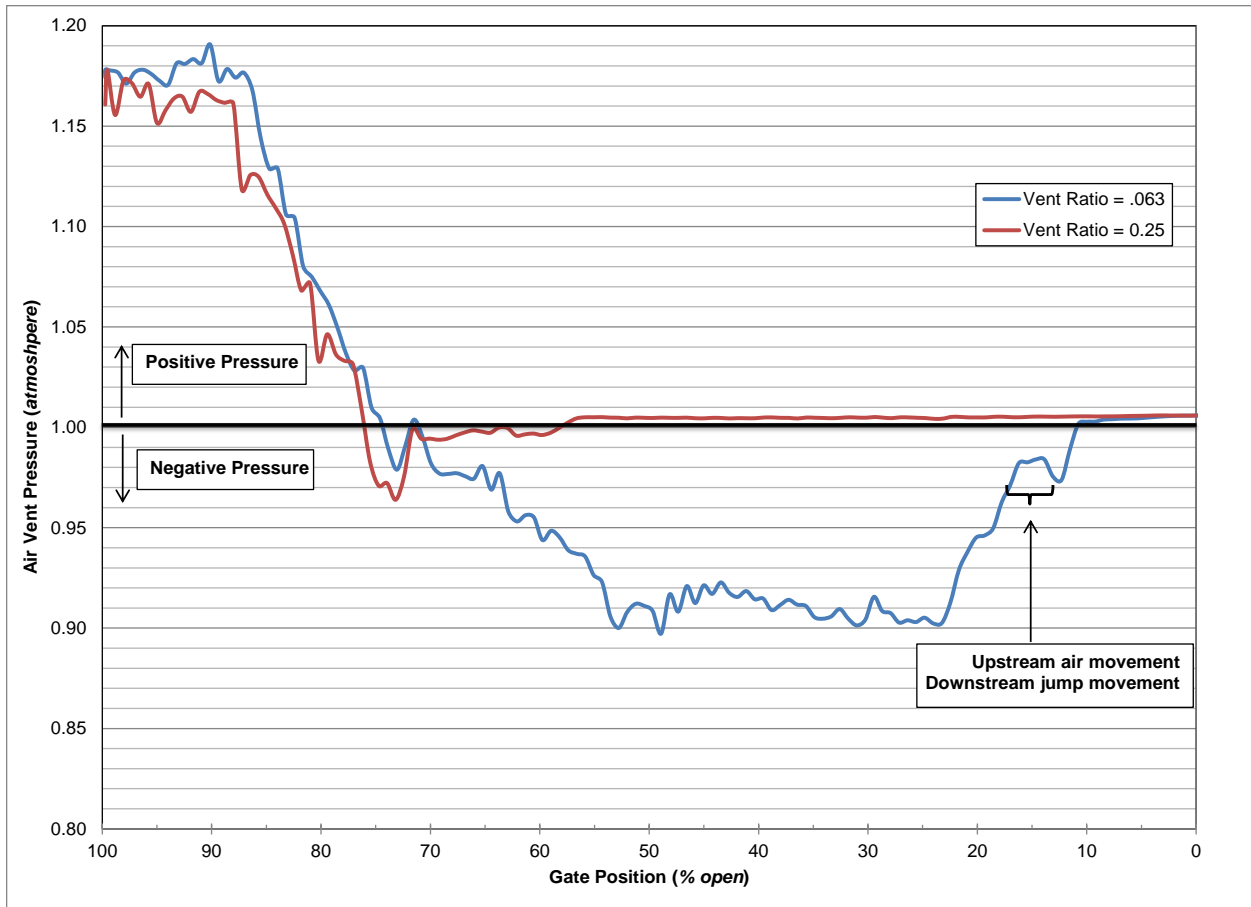
Figure 3. Air vent pressure vs. Gate position comparison of an adequately-sized (red) and undersized (blue) air vent. Pressure is standardized to local atmosphere indicating that pressure less than 1 atmosphere is negative.
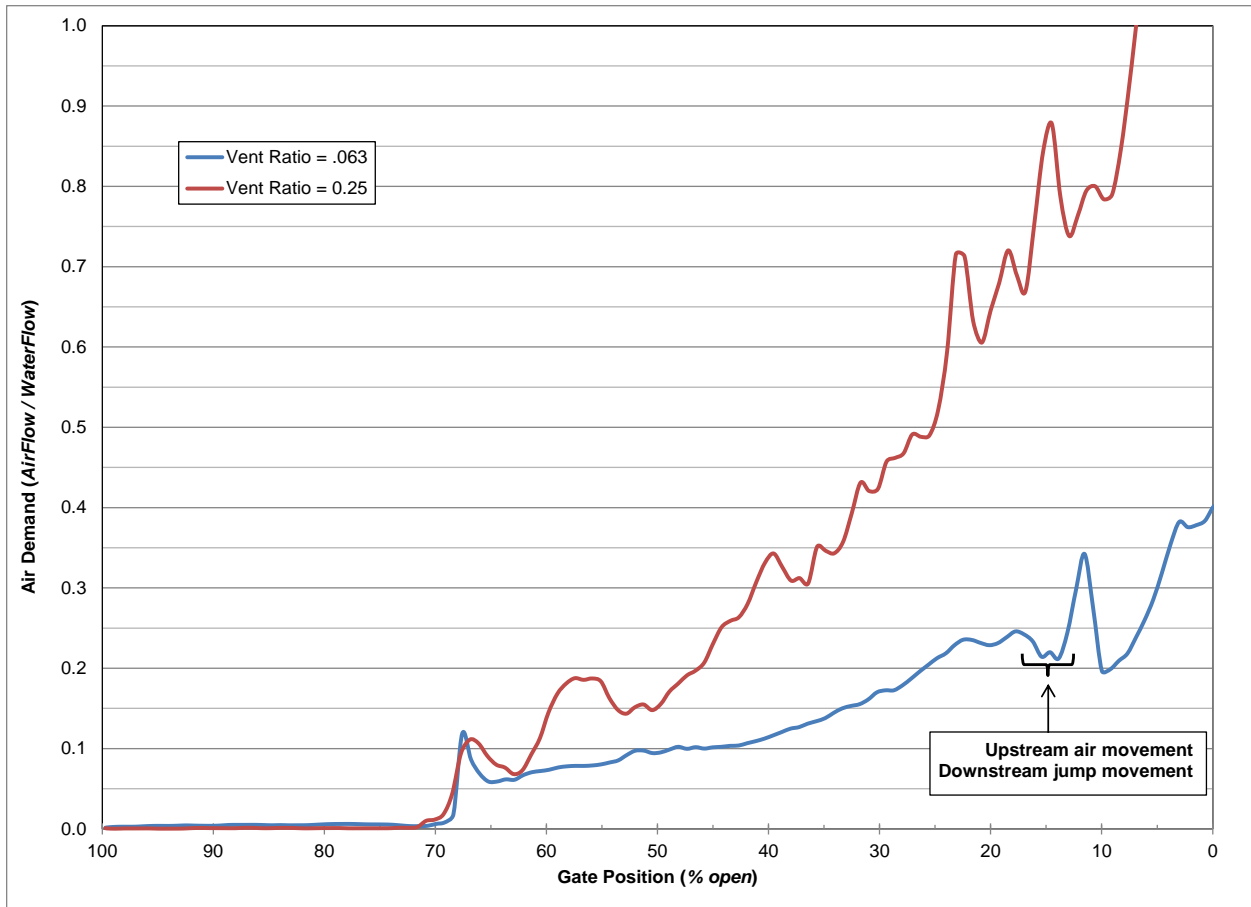
Figure 4 Air demand vs. Gate position comparison of an adequately-sized (red) and undersized (blue) air vent.
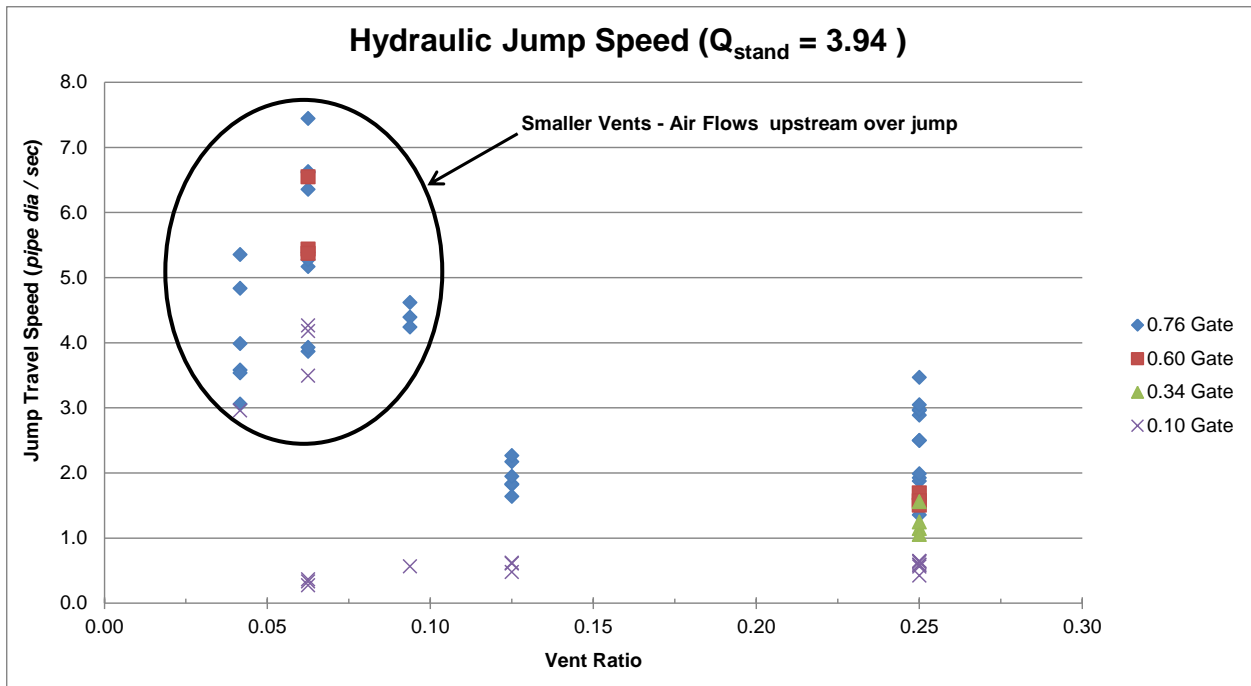
Figure 5. Jump travel speed vs. vent ratio for various gate closure rates on the shallow slope pipe.

(a)

(b)

(c)
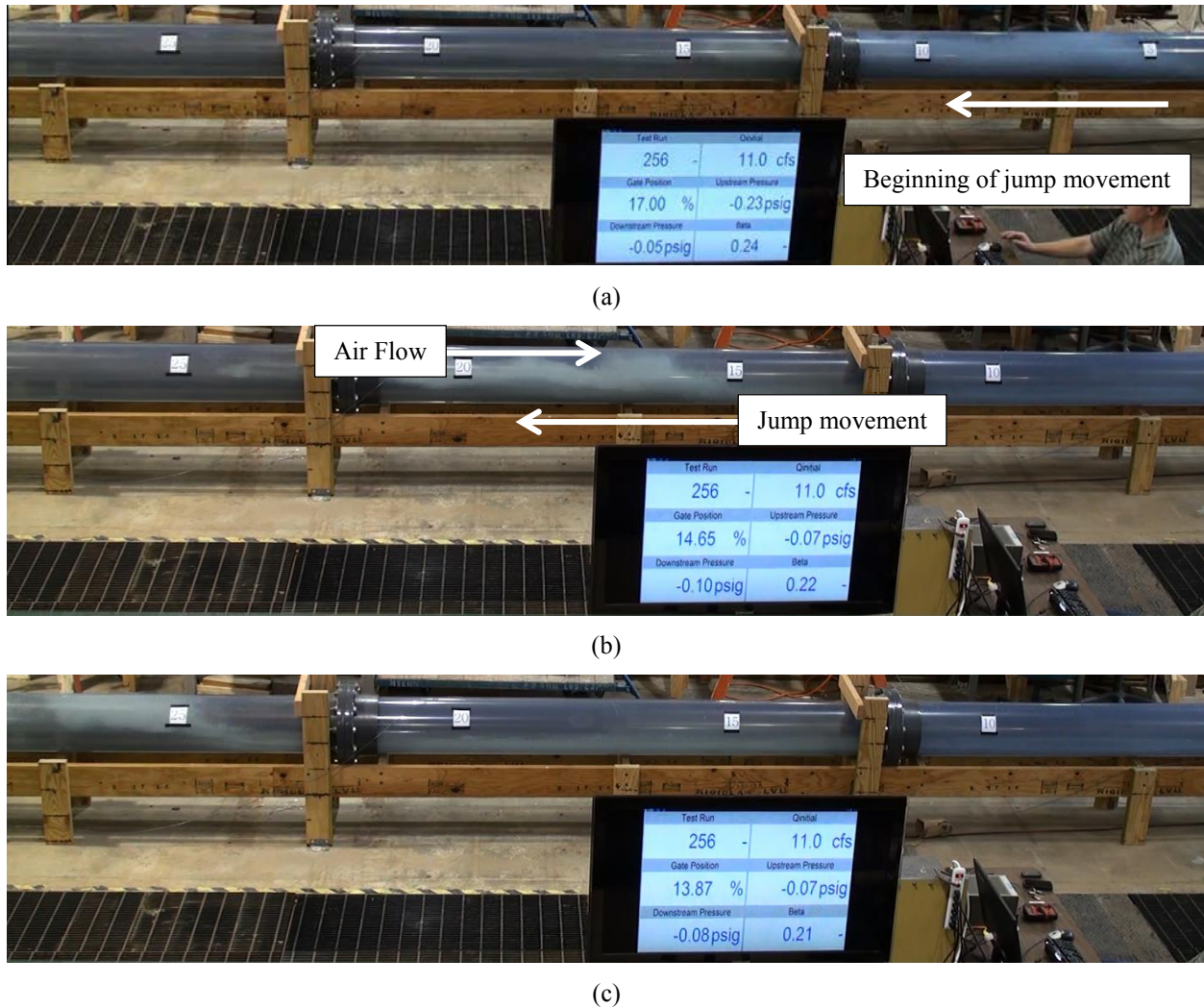
Figure 6. Time series photographs of jump motion with an undersized air vent: (a) Jump is released and begins movement, (b) Jump moves downstream with air flowing back upstream, and (c) Jump is halted again further downstream in the pipe. Water flow and jump movement are from right to left.

3.2. Steep-Slope Pipe

As with the shallow slope, air vent size and gate closure rate also influenced the jump travel speed in a steep-sloped pipe, though there is still data scatter. Figure 7 shows the correlation of travel speed to vent size for all gate closure rates tested. The average of these data groups (Figure 8) helps clarify the effect of vent size for each gate closure rate tested. The most drastic change in jump travel speed occurs for vent ratios less than 0.10 except for the lowest gate closure rate where vent size has very little influence on travel speed.

A spike in travel speed at the smaller vent ratios has not been observed with the steep-slope. One explanation for this may be that the weight of the water column in and downstream of the jump at a steeper slope becomes a significant factor in the total momentum of the jump. The increased weight component of the momentum then overcomes the pressure differential component, which is large for smaller vent sizes, allowing continuous jump movement without halting. For data collected so far, the jump travel speed does not exceed 4 pipe diameters per second, which is similar to jump speeds measured at the shallow slope with adequately sized air vents. This information will be useful in estimating the total air demand by accounting for the air flowrate required to fill the pipe volume as the jump travels down the pipe.
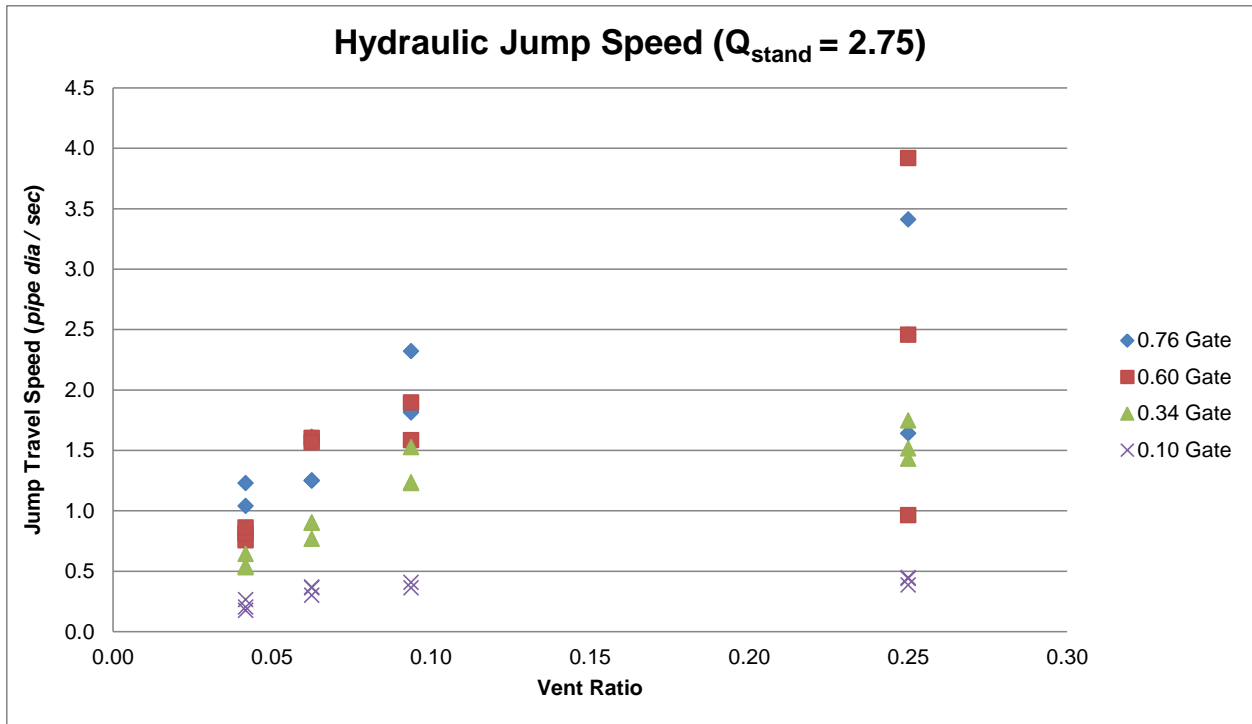
Figure 7. Hydraulic jump travel speed vs. vent ratio for various gate speeds on the steep-slope pipe.
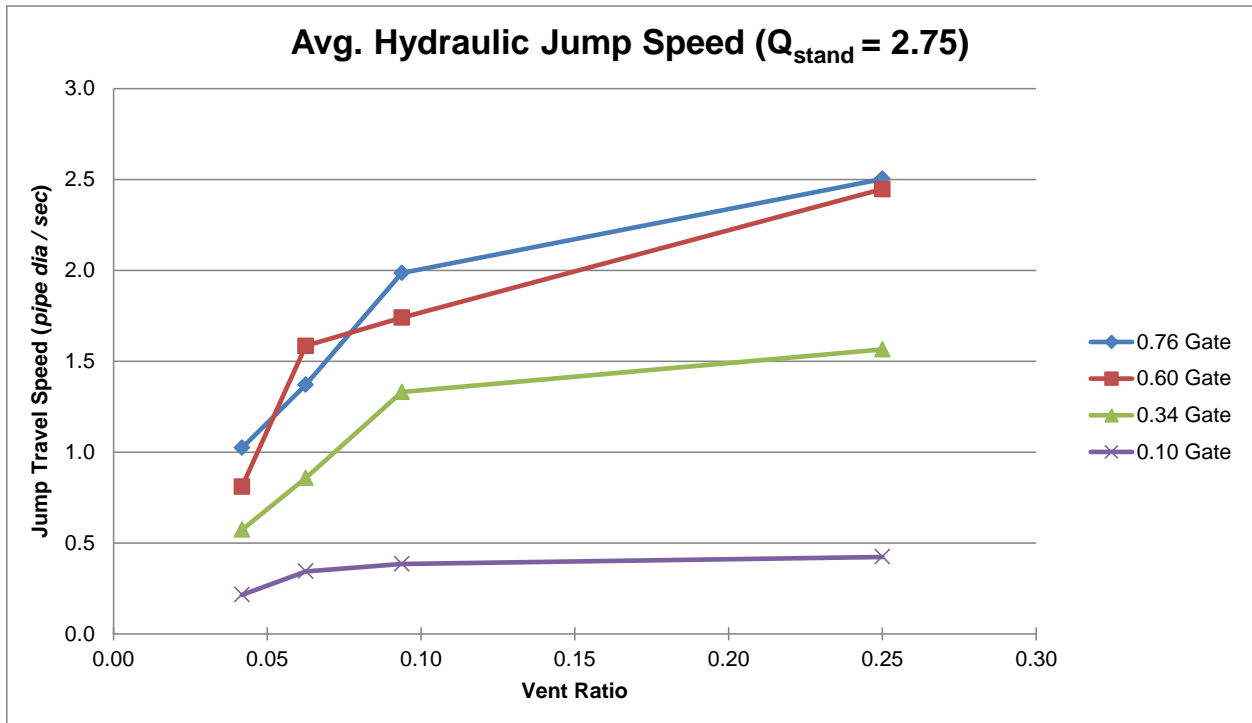
Figure 8. Average hydraulic jump travel speed from Figure 7 vs. vent ratio for various gate speeds on the steep-slope pipe.

4. CONCLUSIONS

The preliminary results of the laboratory physical modeling provide insight into the effects of hydraulic jump travel speed on the total air demand:

- Faster gate closing rates produced increased jump travel speed for both pipe slopes.
- For the shallow-slope pipe, adequately-sized air vents allowed faster jump travel speeds that remained steady (no acceleration) through the entire pipe length.
- For the shallow-slope pipe, jump speed was irregular and increased significantly when air flow was reduced by an undersized vent. This produced a large pressure difference across the jump, which caused accumulated air downstream of the jump to intermittently flow back upstream, causing the jump to release and move downstream at high speed. Air flow through the vent was decreased for this case despite increased jump speed.
- For the steep-slope pipe, jump speed remained steady for all vent sizes and the spike in jump travel speed observed in the shallow-slope pipe did not occur. Jump travel speed increased with both air vent size and gate closing rate.
- For both pipe slopes, jump travel speed never exceeded 4 pipe diameters per second.

Additional data collection from both the physical model and a field testing of an emergency gate closure are planned for later in 2016. The results are expected to help improve current analytical methods for air demand prediction in air vent sizing and design.

5. ACKNOWLEDGMENTS

6. REFERENCES

Escarameia, M. (2007). Investigating hydraulic removal of air from water pipelines. *The Institution of Civil Engineers Water Management I60, issue WMI*, pg. 25-34.

Falvey, H. T. (1980). *Air-Flow in Hydraulic Structures.* Denver, CO: Bureau of Reclamation.

Frizell, K. W. (1993). *Emergency Closures of Guard Gates with Unbalanced Heads.* Denver, CO: Bureau of Reclamation.

Kalinske, A., & Robertson, J. (1943). Closed-conduit flow. *Trans. ASCE 108*, 1435-1447.

Mortensen, J., Barfuss, S., & Johnson, M. (2011). Scale effects of air entrained by hydraulic jumps within closed conduits. *Journal of Hydraulic Research, 49:1*, 90-95.

Nasvi, M., Asmeer, Z., Mowsoom, F., & Pathirana, K. (2010). Correlation among Hydraulic Parameters of Moving Hydraulic Jump in a Rectangular Open Channel. *ENGINEER - Vol. XXXXIII, No.03*, pg. 20-25.

Parvaresh Rizi, A., Kouchakzadeh, S., & Omid, M. H. (2006). A Study of Moving Hydraulic Jumps in Rectangular Channel. *Journal of Applied Sciences 6 (5)*, pg. 1192-1198.

Sharma., H. (1976). Air-Entrainnent in high head gated conduits. *J. Hydraulics Division ASCE 102(HY11)*, 1629-1646.

Optimization of Air Entrained Grout Enriched Roller Compacted Concrete for Improving Freeze-Thaw Resistance of Hydraulic Structures

E.S. Musselman, PE[1]; R.J. Flynn[1]; G.J. Zimmer[1]; and J.R. Young, PE[2]

[1]Dept. of Civil & Environmental Engineering
Villanova University
Villanova, PA 19085
USA

[2]Schnabel Engineering
1380 Wilmington Pike, Suite 100
West Chester, PA 19382
USA
E-mail: eric.musselman@villanova.edu

ABSTRACT

Roller compacted concrete (RCC) is frequently used to construct both gravity dams and stepped spillways and to armor earthen embankments for passing extreme floods. Early experiments on RCC dam applications in the 1980s showed a tendency for seepage to develop along the lift lines. Therefore, RCC dam designers started including an upstream facing system as a watertight barrier. An alternative facing material that has been used extensively overseas and is starting to gain more widespread acceptance in the United States is Grout Enriched RCC (GERCC). The grout enriched method of face construction has been shown to be less expensive than other facing options, particularly on larger dam projects. However, in the United States, the use of GERCC technology has been fairly limited, primarily due to concern over the material's freeze-thaw resistance. The objective of this project is to develop a grout formulation and construction technique that allows the production of air entrained GERCC. The study includes four phases to systemically achieve this objective: optimizing grout formulation including type and dosage of chemical admixtures, evaluation of small scale laboratory samples of RCC and grout combined in a mixer, evaluation of large scale laboratory samples of RCC and grout combined using field construction techniques, and conducting a field trial. The results show that when the grout and RCC are combined in a mixer, good freeze-thaw resistance can be achieved; however, when combined using field techniques, the amount of vibration must be carefully controlled to avoid loss of performance.

Keywords: Roller Compacted Concrete, Overtopping Protection, Stepped Spillways, Freeze-Thaw Resistance

1. INTRODUCTION

Roller compacted concrete (RCC) is frequently used to construct gravity dams and stepped spillways and to armor earthen embankments for passing extreme floods. RCC is a no-slump concrete that is typically spread and compacted in lifts with conventional earthmoving equipment. Early experiments on RCC dam applications in the 1980s showed a tendency for seepage to develop along the lift lines. Therefore, RCC dam designers started including an upstream facing system as a watertight barrier, typically constructed of conventional concrete, an exposed geomembrane liner system, or geomembrane-faced precast concrete panels.

An alternative facing material that has been used extensively overseas (in areas having limited freeze-thaw cycles) and is starting to gain more widespread acceptance in the United States is Grout Enriched RCC (GERCC). This innovative process includes the addition of a neat cement grout to the uncompacted RCC at each lift along the upstream and/or downstream face. After the grout has soaked into the RCC, immersion vibrators are used to mix and to consolidate the grout and RCC to produce a seamless zone that is similar to conventional concrete. The grout enriched method of face construction has been shown to be less expensive than other facing options, particularly on larger dam projects (Fitzgerald, 2013). However, in the United States, the use of GERCC technology has been fairly limited, primarily due to concern over the material's freeze-thaw resistance.

1.1. Background

Studies conducted by Cannon (1993) and Hazaree et al (2011) have shown that it is possible to entrain air in standard RCC and achieve reasonable freeze-thaw resistance. However, researchers and contractors attempting to integrate air entraining admixtures into GERCC to improve freeze-thaw resistance have not been successful to date. Forbes (1999) cited an early example at the Horseshoe Bend dam in New Zealand where a freeze-thaw resistant facing was desired. In order to achieve this, the grout was heavily dosed with an air entraining admixture to achieve 3-4% residual air in the GERCC facing. The initial trials using the air entrainer were unsuccessful since the grout became highly foamy and would not soak through the spread RCC layer. McDonald (2002) described the most detailed studies in air entrained GERCC to date. The study consisted of laboratory tests that evaluated the grout formulation, dosage rate, and techniques to combine the grout with the RCC, as well as field trials. The laboratory tests showed that it is very difficult to produce a homogenous mixture by placing the grout on the top and/or bottom of the RCC. In addition, when internal vibrators are used to combine the grout and RCC, the air content of the mixture and, therefore, the freeze thaw resistance decreases substantially. Similar conclusions could also be drawn based upon the field trial, as well as field trials conducted in a separate study conducted by Tatro et al (2008). These two observations highlight the difficulty of using air entrained GERCC: current construction techniques require significant vibration energy to produce a homogenous mixture, but that vibration energy removes much of the entrained air from the grout, reducing the freeze-thaw resistance.

1.2. Research Objective

The objective of this research program is to advance the use of GERCC and promote more cost effective and technically viable construction of gravity dams, stepped spillways, armored earthen embankments, and other hydraulic structures in climates subject to freeze-thaw cycles. Achieving cost-effective GERCC air entrainment and consolidation can significantly advance the competitiveness of RCC versus other alternatives.

2. EXPERIMENTAL PROGRAM

The research program was divided into 4 phases to systemically achieve the research objectives. The first two phases will be described in this paper, as the third and fourth phases are currently in progress. Phase 1 consists of optimizing the grout mixture design, with a focus on evaluating the effect of multiple chemical admixtures. Phase 2 combines the grout mixtures with the RCC in a standard drum mixer and evaluates the properties of the resulting GERCC. Phase 3 combines the grout mixtures with the RCC using both standard and novel techniques that could be applied in the field. Phase 4 consists of a field trial to further evaluate the performance of the grout mixture designs developed in Phases 1 and 2 and the construction techniques developed in Phase 3.

2.1. Phase 1: Grout Optimization

To evaluate the changes in properties of grout with the addition of chemical admixtures, a uniform method of mixing grout was put in place. The water-to-cement ratio for all grout mixes was 0.95, except those containing a water reducing admixture. This value was recommended by the research sponsors (Schnabel Engineering) based on their experience with GERCC. The admixtures were first mixed into the water for a short period of time, after which cement was slowly added. As the cement was added to the batch, a paddle mixer attached to a 1,600 RPM drill was used to agitate the mixture. Once all of the cement was added, the drill was operated at full speed for four minutes.

Once the four minutes of mixing were complete, a standard Marsh Funnel (ASTM D6910) test was performed to measure the fluidity of each mixture. The time for 946 mL of grout to pass through the Marsh funnel was measured and recorded. The Marsh Funnel test was followed by the determination of the air content of the mix, as per ASTM C231/C231M-10. The standard pressure method was used with a Type-B meter. It is important to note that the standard procedure was modified slightly to provide a representative air content by minimizing the amount of foam in the pressure meter during testing. When the grout was added to the pressure meter, it was allowed to overflow the

container, removing some foam. Then, a steel rod was used to strike off the excess foam still present on the surface. This procedure was repeated twice for each sample, then tested according to the ASTM standard.

The remainder of the original grout was allowed to sit for 30 minutes. After 30 minutes, the remaining grout was placed on a shake table and subjected to the maximum intensity vibration for 1 minute. This method simulated the internal vibration of concrete enriched with grout after placement. After vibration, the identical air pressure method was used to determine the air content of the mix.

Six different admixtures were evaluated during this phase including organic air entraining admixture (AEA), synthetic AEA, polycarboxylate water reducing admixture (WRA), latex-based water repelling and efflorescence controlling admixture, saline-based efflorescence reducing and water repelling admixture, and powder water resisting and superplasticizing admixture. The water repelling admixtures were added to evaluate their effect on the stability of the air void system and because reducing permeability is another method of increasing the freeze-thaw resistance. Initially, the admixtures were examined individually with multiple dosage rates being evaluated. Then, the admixtures were combined to evaluate the interactions between them and the effects on the stability of the air matrix. A total of 37 grout formulations were evaluated using this procedure.

2.2. Phase 2: Small Scale Laboratory GERCC

Phase 2 determined multiple fresh and hardened properties for the RCC mix, grout and GERCC resulting from a combination of the RCC and grout. Numerous tests were run including flow, air content, bleed, and compressive strength. Samples from each individual mix were also created for freeze-thaw resistance testing. Seven chemical admixture combinations for the grout were individually tested, as well as one series of tests that included grout without any chemical admixtures. The chemical admixture combinations tested in Phase 2 were selected based on their performance during Phase 1.

The first step for this phase consisted of weighing out the materials to produce the RCC mixture, which had been developed based on the mixture design procedures outlined in ACI 211.3R-02, "Guide for Selecting Proportions for No-Slump Concrete," and refined through a series of trial mixes. The RCC was designed to have a Vebe time of around 30 seconds, and for each mix, the Vebe test was run to evaluate the mixture's consistency. Following Vebe testing, the unit weight of the RCC was determined. After determining the unit weight of the RCC, the next step was to cast 150 mm by 300 mm cylinders to be tested for 28-day compressive strength. In order to simulate roller-compaction, the cylinders were filled in thirds with a Hilti TE 805 demolition hammer drill used at three intervals to fully compact the concrete inside of the cylinder as per ASTM C1435. Two RCC cylinders were cast for each mix. Aside from cylinders, a 75 mm by 100 mm by 400 mm rectangular prism was also cast in a steel mould to later be used for freeze-thaw resistance testing. To simulate roller-compaction in the rectangular mold, a square block of steel was struck with about ten blows of a rubber mallet at one-quarter intervals down the length of the mold.

The grout was mixed in a heavy duty, high volume colloidal mixing grout plant, ChemGrout CG-600 colloidal series. The amount of cement used for each grout mix was 42.6 kg, and the dosage of both water and chemical admixtures were determined from the results of Phase 1. After an initial four minutes of mixing, the grout was transferred from the mixing tank to the holding tank, where it could be pumped into two 5-gallon buckets to be used for fresh property testing. The first bucket was tested immediately while the second bucket sat for thirty minutes before testing, following the procedure described for Phase 1. The temperature of the grout was immediately determined and recorded. The first bucket of grout was tested for flow, specific gravity, and air content. A Marsh Funnel flow cone test was performed as per ASTM D6910, with the time it took for 946 mL of grout to pour out of the bottom of the cone monitored and recorded as the initial flow.

Following the flow cone test, a mud balance was performed to determine the specific gravity of the grout. The specific gravity was evaluated as a consistency check with the results of air content tests. The test is simple to perform and is commonly used in post-tensioned grouting applications. Following the mud balance test, the air content of the grout was determined as per ASTM C231/C231M-10, using a Type B meter with a vertical air chamber. The same air content method as described in Phase 1 was performed.

Another test was performed to determine the initial bleed of the grout as per ASTM C1741-12, "Standard Test Method for Bleed Stability of Cementitious Post-Tensioning Tendon Grout." A filtration funnel was filled with fresh grout within 5 minutes of mixing. The funnel was connected to an air supply, and air was pumped into the funnel at a pressure of 172 kPa for five minutes while bleed water travelled through a stem on the bottom of the funnel into a graduated cylinder. After five minutes, the pressure was released and the funnel was tipped in order to remove any excess bleed water to exit the stem. The volume of the collected bleed water in the graduated cylinder was measured to the nearest 0.2 mL.

Thirty minutes after the initial grout mix, the grout previously set aside was placed on a shake table for one minute. It was then tested using the mud balance and air content meter. The specific gravity and air content for the grout after thirty minutes was recorded and evaluated against the grout that was tested immediately after mixing. In order to simulate the conditions that may be found in the field, grout was also circulated through the grout mixing plant itself. For three minutes, grout was pumped through the grout plant at full speed with a valve constricted to generate a pressure of about 345 kPa at the outlet of the pump. The grout was poured into a 5-gallon bucket and once again tested for specific gravity and air content to be evaluated against previous fresh property results.

Following all of the fresh property tests, a pre-calculated amount of grout from the material collected after recirculating through the pump was added to 79.4 kg of the remaining original RCC mix. The grout and RCC were mixed together in a concrete mixer for one minute to form grout-enriched RCC. Once successfully mixed, a Vebe test was performed on the grout-enriched concrete to determine its Vebe time. The unit weight of the grout-enriched concrete was determined using the same method as described for the RCC mix. Two grout-enriched concrete cylinders were created following standard ASTM C31 procedures. Three rectangular freeze-thaw samples were also created using a tamping rod to compact the grout-enriched concrete in two lifts.

Four 75mm by 100 mm by 400 mm freeze-thaw samples resulted from each mix in Phase Three. Three of the samples were enriched with grout and one was standard RCC. As previously stated, these samples were tested for freeze-thaw durability as per ASTM-C666. The specimens were allowed to cure for 14 days while sitting in lime water. At the 14 day curing period, each of the specimens was weighed and tested for fundamental transverse frequency. This process was repeated for every 30 cycles in a freeze-thaw cabinet.

3. RESULTS

3.1. Phase 1: Grout Optimization

The data obtained from Phase 1 included the Marsh Funnel flow times and the air contents of the grout both immediately after mixing and after 30 minutes of rest and one minute of vibration. The flow times for the mixtures without water reducing admixtures were fairly consistent, falling between 26-38 seconds for all the mixtures, which was consistent with the target of 30 seconds. In general, the longer flow times tended to result from mixtures with higher air contents. This makes physical sense as an increase in air content reduces the unit weight of the grout, which reduces pressure within the grout as it exits the funnel, reducing the velocity and increasing the flow time. For the mixtures with water reducer, the flow times varied more significantly until the dosage of admixture and the corresponding reduction in water content were better understood. The final mixture had flow times ranging from 34-38 seconds, depending on the presence of other admixtures.

The average air contents obtained for select tests are shown in Figure 1 and Figure 2. Figure 1 shows the average air content for the samples containing the organic AEA at what was determined to be the optimal dosage. The optimal dosage was the dosage that produced an air content of between 15 and 20%. This target air content was determined based on two criteria. The first criterion was the behaviour of the grout during this study, primarily the amount of foam produced and the stability of the resulting air void matrix. The second criterion was calculations based on the required air content in the GERCC and the typical dosage rates of grout based on existing literature and experience.

Figure 1 also shows the effect of other chemical admixtures on the air content of grouts containing the organic AEA and seems to indicate that the latex based water repelling admixture may increase the effectiveness and the stability of the organic AEA, while the powder water resisting admixture has a significant negative impact. Figure 2 shows

the same results for the synthetic AEA at its optimum dosage. By examining these data, it is apparent that the water reducer and the powder water resisting admixture significantly decrease the stability of the air void system, while the latex-based water repelling admixture seems to have little effect. Comparing the performance of the two AEAs, it appears that the synthetic AEA is slightly more stable and can maintain its stability at slightly higher air contents. Therefore, moving forward into Phase 2, more emphasis was placed on the synthetic AEA, and the powder water resisting admixture was excluded from further testing based on its detrimental interaction with both AEAs.
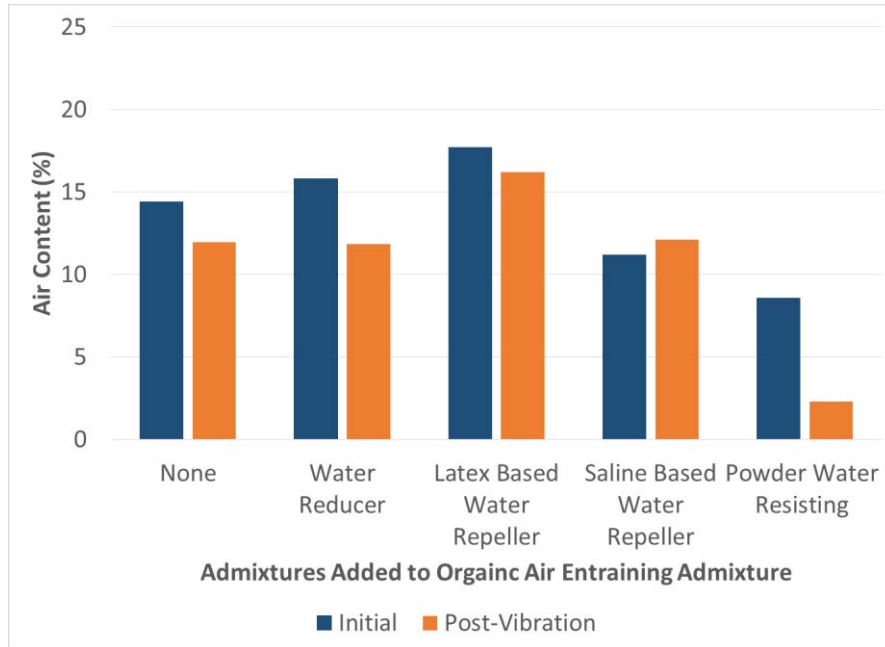
Figure 1. Average Air Content for Grout Containing Organic Air Entraining Admixture
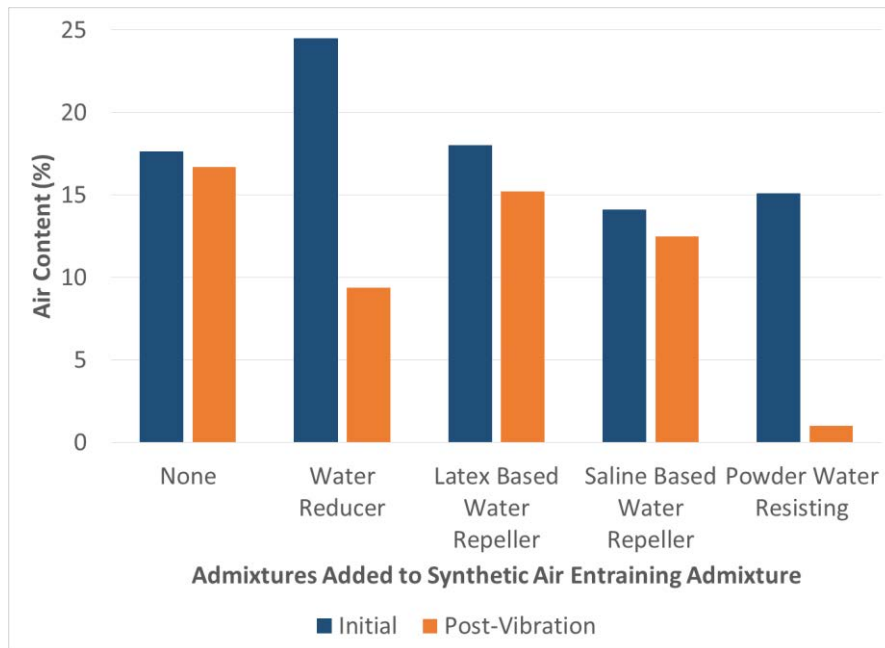
Figure 2. Average Air Content for Grout Containing Synthetic Air Entraining Admixture

3.2. Phase 2: Small Scale Laboratory GERCC

During Phase 2, properties of the grout, RCC, and GERCC were determined. For the grout, the flow times were recorded immediately after mixing and were typically within the same range of 26-38 seconds for all grouts, with the exception of the grout with the water reducing admixture, which had a significantly higher flow time. This may have been the result of the thixotropic nature of the grout when a WRA is added, which would result in a higher flow time when measured by the Marsh Funnel method. The bleed of the grout was also measured, and due to the high water to cement ratio, the amount of bleed was substantial. The average bleed of all the grouts was 82 mL, with the lowest being 42 mL from the grout containing the WRA, which is the result of a reduced water to cement ratio in this grout. The air content of the grout was measured immediately after mixing, after 30 minutes of rest and 1 minute of vibration, and after recirculation under pressure through the pump for 3 minutes. These results are shown in Figure 3.
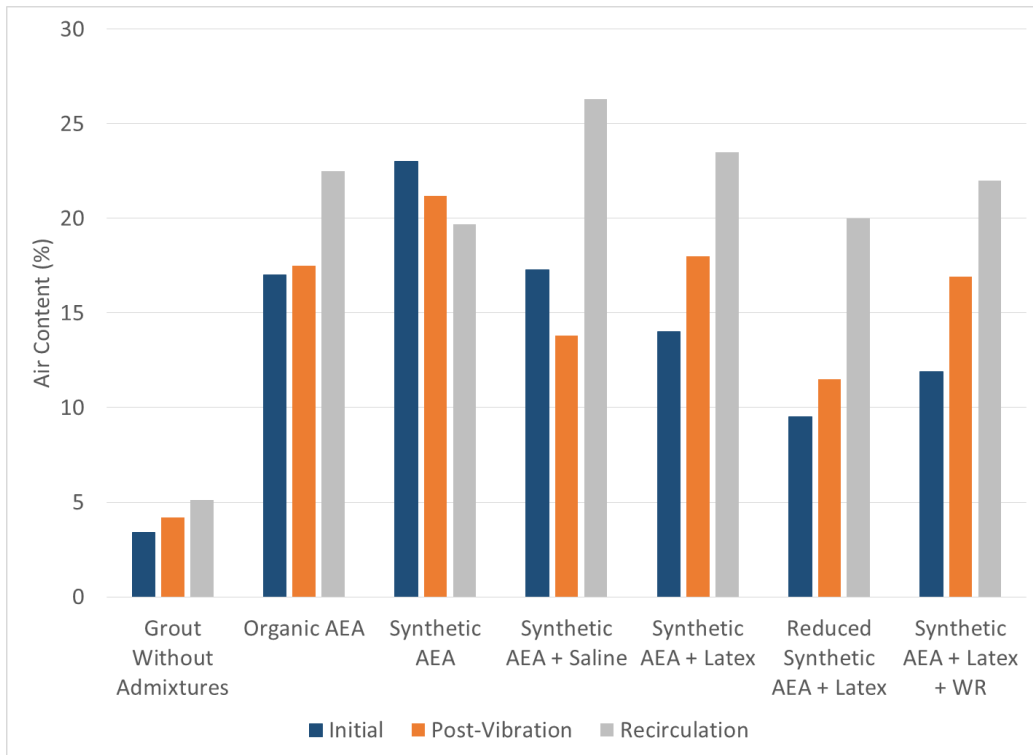
Figure 3. Grout Air Content during Large Scale Testing

Some interesting observations can be made from the air content data from Phase 2. The recirculation of the grout through the pump does not negatively affect the air content of the grout; in fact, for most materials, recirculation increased the air content. This is likely because after the grout was pumped under pressure, it was reintroduced into the holding tank containing the grout where it splashed around, allowing more air to be introduced into the grout. Additionally, the material for the initial air content was removed from the holding tank first, followed by the grout used to determine the 30 minute air content. The pump is setup so that it removes material from the bottom of the holding tank; therefore, if the lighter material with the higher air content rises to the top, it would be used for the recirculated air content and may be the reason for the higher air contents. The same justification could be used to explain why for many of the samples, the grout allowed to sit for 30 minutes and subjected to vibration has a slightly higher air content.

When comparing the different materials, the synthetic AEA exhibited the highest performance with the highest initial air content and produced air contents that were the most consistent, indicating an ability of the mixture to remain homogeneous. This was the primary justification for using the synthetic AEA for evaluating the other admixtures. The other admixtures generally had a negative effect on the initial air content, with the saline having the least effect. It should be noted that one sample, labeled as "Reduced Synthetic AEA + Latex," had a reduced

dose of AEA added to evaluate if the high air content of the grout was necessary to achieve acceptable freeze-thaw resistance.

The air content of the GERCC was also measured for each grout formulation and is shown in Figure 4. The air contents correlate well with the expected values calculated based on the measure air content of the grout and the dosage, and they also largely achieve the target of 4-5% that is needed for reasonable freeze-thaw resistance. The once exception is the grout with the water reducing admixture, where the measured air content was much higher than expected. One possible explanation for this anomaly is that, as indicated earlier, the grout with the water reducer had a significantly higher flow time, indicating it was less fluid than the other grouts. The meter used to measure the air will report the percent of all air within the meter, including any voids within the sample. So, if a less fluid grout resulted in a sample with poor compaction, the air content measured would be artificially high.
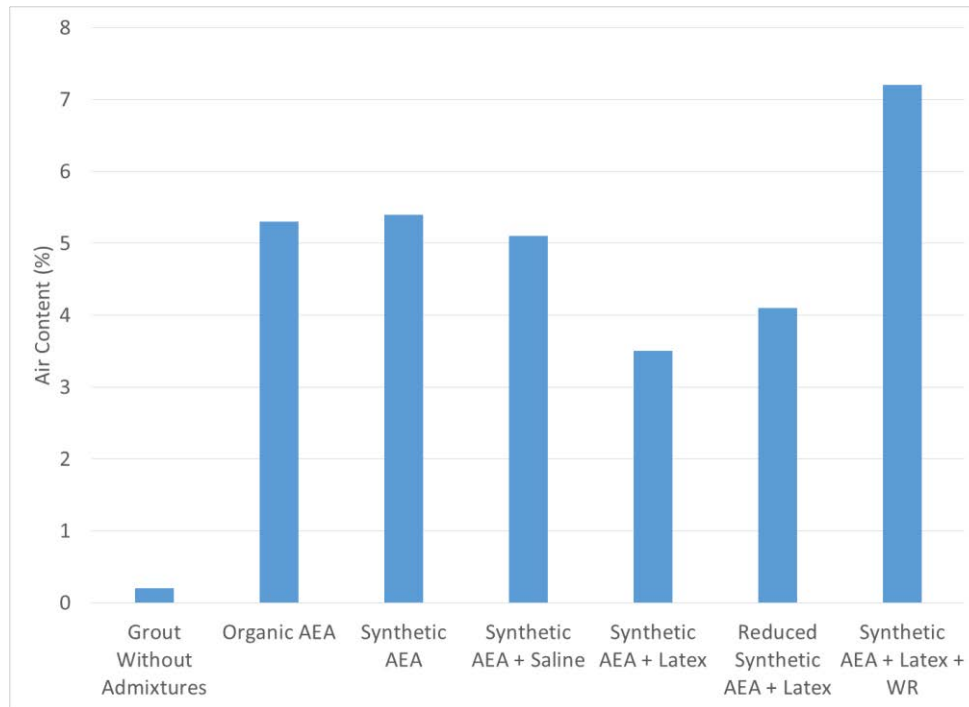
Figure 4. Air Content of GERCC

The results of the freeze-thaw tests are shown in Figures 5 and 6, as well as Table 1. Figure 5 shows the change in modulus of elasticity versus the number of freeze-thaw cycles. The only samples to fail the test (exhibit a drop in dynamic modulus below 60% of original) were the plain RCC samples shown in black and the grout without admixtures shown in light blue. All samples containing an AEA maintained at least 75% of their initial modulus. Table 1 shows the average mass loss and percent of original dynamic modulus for each set of samples. The samples with the highest freeze-thaw resistance were the synthetic AEA with the saline water repelling admixture, which retained 96.8% of its initial modulus. The remaining mixtures all preformed similarly and satisfactorily. Figure 6 shows the samples containing the synthetic AEA and saline water repelling admixtures as well as the corresponding RCC sample after 300 cycles and clearly shows the greatly improved durability when the air entrained grout is added.
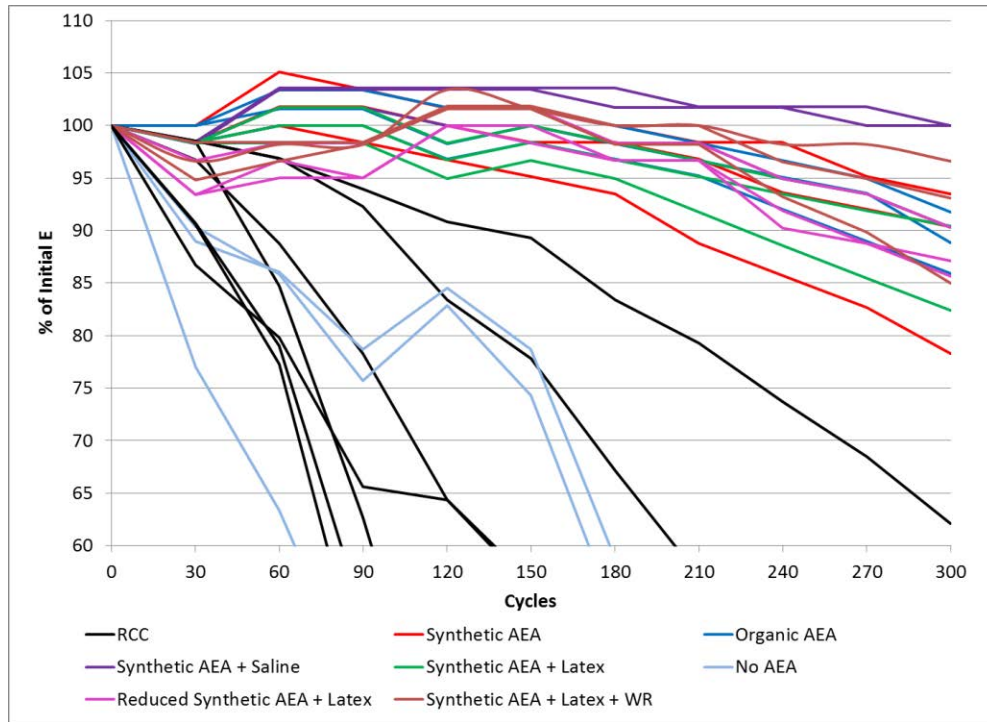
Figure 5. Freeze Thaw Resistance of GERCC

Table 1. Freeze Thaw Resistance of GERCC

GERCC	Average % of Original E After 300 Cycles	Average % of Mass Lost After 300 Cycles
Synthetic AEA + Saline	96.8	0.29
Synthetic AEA + Latex + WR	91.6	0.39
Organic AEA	88.8	0.49
Synthetic AEA + Latex	87.7	0.00
Reduced Synthetic AEA + Latex	87.7	0.48
Synthetic AEA	87.4	0.67
No AEA	12.9	3.76

Figure 6. Freeze Thaw Samples After 300 Cycles

4. CONCLUSIONS

Based on the results of the research program, the following conclusions can be drawn:

- Both the organic and synthetic air-entraining admixtures were capable of successfully achieving an air content between 15% and 25% when added at their respective maximum recommended dosages. The most successful air-entrainer with the most stable air content readings and superior freeze-thaw resistance was the synthetic air-entrainer.
- Although the water-reducing admixture was beneficial in reducing bleed and permeability, its addition resulted in a greater variance in air content. Therefore, the use of a water reducing admixture is not recommended for use in air entrained GERCC at this time.
- Both water-repelling and efflorescence controlling admixtures proved to be beneficial to the performance of air-entrained grout, with the saline-based admixture exhibiting superior freeze-thaw resistance. The powder water resisting admixture negatively impacted the air entrainment and is not recommended for use in air entrained GERCC.

The ongoing research is focused on evaluating different construction techniques and their effect on the distribution of grout within the RCC and the freeze-thaw resistance of the resulting air entrained GERCC with the goal of recommending a placement technique and vibration level that optimizes performance in these two competing criteria. Future research could evaluate these parameters for different RCC mixtures. Additionally, an automated process for grout placement, mixing of the grout with the RCC, and consolidation of the resulting mixture could be developed to improve the quality and consistency of the GERCC.

5. ACKNOWLEDGMENTS

6. REFERENCES

ACI Committee 211 (2002). Guide for Selecting Proportions for No-Slump Concrete. (ACI 211.3R-02), American Concrete Institute. Farmington Hills, MI.

Cannon, Robert W. (1993). "Air-entrained roller compacted concrete." Concrete International, 15(4), 49-54.

Fitzgerald, T., Basinger, D., Cannon, R., Rogers, G. (2013). "Grout Enriched RCC at Deep Creek." *International Water Power and Dam Construction Magazine*, 65(7), 30-33.

Forbes, B.A. (1999) "Grout enriched RCC: A History and Future.*" International Water Power and Dam Construction Journal*, 51(6) p. 4.

Hazaree, C., Ceylan, H., Wang, K. (2011). "Influences of mixture composition on properties and freeze-thaw resistance of RCC." *Construction and Building Materials*, 25(1), 313-319.

McDonald, J.E. (2002). "Grout Enriched Roller-Compacted Concrete – Phase I Investigation." High Performance Materials and Systems Research Program, US Army Corps of Engineers, Research and Development Center.

Tatro, S.B., Hinds, J.K., West, J.L. (2008) "Final Report: Properties of Air Entrained Grout Enriched Roller Compacted Concrete." *Proc. United States Society on Dams Annual Conference*, Portland, OR, 197-211.

Articulating Concrete Blocks: The Long and Winding Road

J. A. Nadeau[1]

[1] National Engineered Erosion Control Product Manager
ACF Environmental
Richmond, VA 23234
USA
E-mail: jnadeau@acfenv.com

ABSTRACT:

This paper will provide an overview of Articulating Concrete Blocks (ACBs) from three perspectives: 1. the Manufacturer, 2. the Engineer, and 3. the Researcher and will discuss how these independent entities interact with each other and the regulatory community to further the scientific understanding and use of ACB systems. Since their development in the late 1970s, ACBs represent a growing choice of design engineers in economically solving their critical erosion prevention problems as well as in a variety of other non-hydraulic applications. Typical applications of ACBs are found in protecting channels and canals, dam spillways and embankments, bridge piers and abutments, river bank stabilization projects, boat ramps, and wet stream crossings. The ACB manufacturers work closely with both the ACB design engineer, dam safety and environmental regulators, and ACB researchers. Design challenges faced by the engineering and regulatory communities include but are not limited to non-linear flow paths, converging flows, and hydraulic jump. By working with manufacturers, the research community has developed much data and insight into ACB performance and limitations since standardized testing started in the mid-1980s; however, each manufacturer "owns" this information and is reluctant to share with other manufacturers. Recent testing extending the length of the ACB revetment being evaluated has shown the consistent development of aerated flows and potential for stone drainage layer movement, which need to be further researched along with hydraulic jump performance.

Conference Topics: Spillway Weirs and Flumes, Slope Protection

Keywords: Articulating Concrete Blocks (ACB's), Erosion Prevention, Overtopping Protection, Slope Protection, ASTM, FHWA, Factor of Safety Determination

1. INTRODUCTION

ACBs were developed in the 1970s in an effort to improve the performance and reliability of existing erosion control systems, mainly riprap. In 1987, what is considered the first comprehensive study of ACBs was conducted by the Construction Industry and Research Information Association (CIRIA) in the United Kingdom at Jackhouse Reservoir (Hewlett et al 1987). This study was followed by the Federal Highway Administration's 1988 and 1989 studies on embankment overtopping protection countermeasures at Colorado State University (CSU) in Fort Collins, Colorado. With the FHWA 1988 and 1989 (FHWA 1988, FHWA 1989) testing also came a derived Factor of Safety (FOS) methodology from Paul Clopper (Clopper 1991) and Dr. Amanda Cox (Cox 2010) updated the FOS methodology both of which will be discussed in this paper. The results of the FHWA studies showed ACBs to be a promising technology for erosion prevention of earthen embankments subjected to overtopping flows.

2. ACB MANUFACTURERS, DESIGNERS, REGULATORS, AND RESEARCHERS

Three main groups have played major roles in the development and implementation of ACB Revetment Systems, and these include
1. The Manufacturers of ACB Revetment Systems
2. The Researchers and Research Facilities where ACB Revetment Systems are tested
3. The Design Engineers and Regulators of Erosion Control Projects

2.1. The Manufacturers of ACB Revetment Systems

The Manufacturers of ACBs have been the primary source of information on ACB performance since the CIRIA and FHWA studies in the mid to late 1980s. Due to the competitive nature of the ACB marketplace, much of this information has remained private and not available for inclusion into a large research database. Innovations in ACBs, such as the introduction of tapered ACB revetment systems and a system where the gravel drainage layer under the ACB system is stabilized, have been at the hands of the manufacturers investing in the development and testing of these ideas. Due to the significant investment required to test an ACB system, innovation has been slow in this market. The Manufacturers of ACB revetment systems, to varying degrees, provide technical assistance, design guidance, and serve as a conduit of information for the Engineering and Regulatory communities. The information possessed by the Manufacturers is typically conveyed in person through working on a specific design project or in a seminar or Lunch n' Learn setting where the Manufacturer is addressing a small focused group of individuals and may include topics delivered by members of the Research community.

2.2. Research Community and Test Facilities

Research facilities focusing on ACB revetment testing and research are a very specialized and small group. Several Universities and associated hydraulic laboratories have run ACB full-scale flume tests over the years; however, at present, the majority of the testing is being conducted at Colorado State University (CSU) on the outdoor steep slope flume. This flume is built on a 2:1 slope, is 3.05 m wide, 30.5 m long, and can be set up to deliver in excess of 1.8 m of overtopping flow, which is approximately 0.345 $m^3/m/s$. It has the ability to expose ACB revetment systems to velocities and shear stresses in excess of 12.2 m/s and 1150 Pa, respectively. Scale model testing of ACB systems has not produced reliable results to date.

The FHWA testing was completed in a horizontal flume where the embankment elevation needed to be built within the flume, and there is typically a height restriction within the limits of the flume that restricts the velocity and shears that can be generated. Typically, a maximum vertical drop of 1.83 m can be attained in a horizontal flume, which would allow for a maximum velocity of approximately 6.7 m/s and a shear stress of 335 Pa at a 4-foot overtopping depth. Generation of the velocities and shear stresses the steep slope flume is capable of producing has proven a difficult challenge for research laboratories with horizontal flumes to remain relevant in the overtopping flow test arena for tapered ACB systems in which the focus is on generating high water velocities.

2.3. Design Engineers and Regulators

Design engineers and regulators have embraced ACB revetment systems with varying degrees of openness and acceptance. The first dams saw ACB revetments in the early 1990s, and now it is estimated that several hundred dams (Nadeau 2015) in the United States have had ACB revetment systems installed to armour the auxiliary spillways or to protect the embankment from an overtopping event. Acceptance of the performance of ACB revetment systems among the design engineers and regulators has grown over the past 30 years, as has the understanding of ACB performance limitations and failure modes. Any new technology has a group of "early adopters" who clearly see the benefits the new technology offers in terms of economics and performance, and there is also a group known as the "late adopters" who prefer to wait and let the technology become proven. Acceptance of the ACB revetment technology, especially when used in potential high-risk scenarios like dam overtopping and spillways applications, were sometimes slow to evolve over the first 15 or so years of product introduction, but they have gained significant momentum in the last 10 years. The Manufacturers, working with the early adopters of the design and regulatory community, have helped widen ACB acceptance in high-risk applications by sharing the latest test results, product innovations, and documented case studies from the field where actual real life performance data has been collected. A growing number of design engineers and regulators are compiling field experiences and subsequent analyses of ACB revetment systems that have experienced flow and sharing this information with their peers at local, national, and international conferences on hydraulic structures and revetment technology.

3. A BRIEF HISTORY OF EROSION CONTROL AND HARD ARMOR SOLUTIONS

The control of unwanted erosion has been a challenge for humans for several millennia. For the purpose of this paper, erosion control practices will be limited to a discussion on channelized flows, sheet flows, and high velocity flows and will not address the issues experienced by the agricultural community relating to farmland as a whole. Since antiquity, man has utilized natural vegetation, flow interruption devices, and rocks (riprap) as measures to stop the ravages of unwanted erosion and has learned each has its range of applicability for successful results. Many products have been invented and tested to improve resistance to erosion of soils when compared to natural vegetation or riprap, and ACBs will be discussed below.

3.1. Definition of Failure of an ACB System

The threshold of system performance for any erosion control countermeasure is a critical term for design engineers and regulators to fully understand as they are undertaking erosion control countermeasure projects. The definition of failure for ACB systems is defined as "the hydraulic conditions (velocity and shear stress) at which the onset of erosion occurs" (ASTM D7277 2008). This is considered a very conservative definition of failure, thus making ACBs suitable for a wide variety of applications. When properly designed, ACBs will require little long term maintenance. Other countermeasures may have different definitions of "failure," and it is important to read and understand each different definition when working at evaluating multiple revetment technologies.

3.2. Riprap, Grouted Riprap, and the Development of Articulating Concrete Blocks

Rock riprap has been used for years to control erosion without reliance on vegetation. The size of the rocks employed is directly related to the hydraulic forces that can be withstood. Quarried rocks, in which flat surfaces are present, were the next logical step in the use of riprap. This was followed by grouting these flat topped surfaces together to form a relatively smooth surface for the water to flow over, thus eliminating many of the moment arms created with angular rocks (as shown in Figure 1) and, thereby, increasing performance of these systems. The USACE developed a "cable tied" concrete mat system in the 1970s, consisting of concrete "blocks" approximately 0.61 m by 1.22 m cast on steel cables and rolled up, which were commonly deployed from barges along rivers to slow down erosion from seasonal flooding (shown in Figure 2). This appears to be the first time individual blocks were connected via cables and can be considered the forerunner of the modern ACB revetment systems seen today.

Figure 1. Grouted riprap

Figure 2. USACE Cable Tied Concrete

ACBs present in today's market are typically cabled systems of varying geometric shapes and have varying hydraulic performance thresholds. Typical modern ACB units range in area from 0.093 m^2 to approximately 0.28 m^2, in thickness from 7.62 cm to 22.9 cm, and in unit weights from 98 kg/m^2 to 440 kg/m^2. Modern ACB systems can be manufactured either by the dry cast or wet cast method. ACB revetment systems can have the individual blocks arranged within the mats in a linear or staggered format, can have the individual units interlocked, and may have the cable either cast into the blocks or inserted after the block has been manufactured. ACB revetments can have "dome"

tops or flat tops, and its thickness can vary by 12.5 mm along the direction of flow (tapered ACB). Examples of modern ACBs are shown in Figure 3. Every ACB system is unique and needs to have full-scale flume testing results to determine the performance parameters that can be reliably used by the design engineer.

Figure 3. Typical ACB Systems currently available on the open market

3.3. FHWA Testing and Analysis

The test programs funded by the FHWA and run at CSU in 1988 and 1989 are considered by many as the birth of controlled, measurable, and repeatable testing on ACBs and other such revetment systems. The test procedures employed during this testing were exactly that, a procedure to provide consistent testing and results. From the results of these tests, it is empirically known that on a 1.82 m tall embankment with a 2:1 (H:1V) slope, an overtopping event of a specified depth either failed the system or the ACB revetment system resisted the erosive forces of the flowing water. The test data was analysed, and velocity and shear values calculated based on the hydraulic forces for the given system geometry the revetment system was able to resist the erosive forces applied. Specifically, the most important value determined for each revetment system tested was the critical shear value τ_c, which is defined as the maximum shear the revetment was exposed to that did not fail the system, corrected to a flat surface (0 degree slope). These design parameters, determined through the full-scale flume tests, are of little value unless there is a set of equations or a procedure developed to determine the factor of safety. These formulas are mathematical representations of the physical forces acting on the block, which divides the sum of the stabilizing forces by the sum of the destabilizing forces.

3.4. Factor of Safety Equations

The original FOS equations and currently the industry standard FOS methodology can be found in the NCMA publication "Design Manual for Articulating Concrete Block (ACB) Revetment Systems" (NCMA 2010). A proposed set of improved FOS equations is found in the PhD dissertation of Dr. Amanda Cox "Moment Stability Analysis Method For Determining Safety Factors For Articulated Concrete Blocks" (Cox 2010). The reader is encouraged to review these documents for a more thorough understanding of each of these methodologies, including the underlying assumptions made in their respective development.

3.5. Setting the Factor of Safety for a Project

The methodologies developed to determine the FOS of an ACB revetment system for a given project allow the designer to place a cushion of performance for the system in the given design. The result of these FOS equations is a

mathematical interpretation of this cushion. The target FOS for each project needs to be set, and, typically, this is done by the design engineer and/or regulatory community. A typical industry "default" FOS for ACB applications with well-defined hydraulic conditions is 1.5; however, other levels can be set for any given design. When setting the FOS for a project, engineering judgement is exercised to set an acceptable minimum FOS based on risks associated with failure of the ACB revetment system, uncertainty in the hydraulic model employed to determine the flows, and overall project costs. There are no widely accepted methodologies to set the minimum FOS for a project; however, a guide is presented HEC-23 (FHWA 2009). A practical approach to setting the FOS is to look at a range of flow conditions, as illustrated in Table 1. In examining the FOS presented in this example, one can readily see that the relationship between flow and FOS is not linear. If the FOS for this sample project had been set at 2.0 for a design flow of 0.086 m^3/sec m, there would still be a FOS of 1.5 if the actual flow doubled. The Natural Resources Conservation Service (NRCS) will specify in many designs two FOS targets for the design, one typically set at 2.0 for a highly probable flow event (stability hydrograph) and another (typically 1.0) for an extreme flow event (freeboard hydrograph). The rationale behind this approach is that they do not want to have any maintenance issues associated with the highly probable flow event, and in the case that the extreme flow event is realized, they want to ensure the dam is not breached.

Table 1. Factor of Safety Comparison at Various Flow Rates NCMA (2006)

FLOW (m^3/s/m)	VELOCITY (m/s)	SHEAR (Pa)	FACTOR OF SAFETY
0.0431	4.84	316	2.96
0.0863	6.40	474	2.12
0.1726	8.44	718	1.47

Note: FOS Values based bed slope of 3:1 (_H:1V) and Side Slope of 20:1. FOS via NCMA Methodology and Shoreblock SD 475 OCT ACB System. Velocity and shear values at uniform flow state.

4. IMPROVEMENTS IN TESTING, DATA ANALYSIS, INSTALLATION, MANUFACTURING AND FOS DETERMINATION

FHWA test and analysis protocols set in motion the growth of ACB revetment systems being designed and specified by the engineering and regulatory communities. The 25 years since these protocols were introduced have led to significant changes and improvements proposed and adopted by the ACB user community at large, and these changes are outlined below. These updated protocols are important to be aware of so that the current ACB revetment designs are completed with the best information and methodologies available to the designer. We have learned a lot from history and need to ensure we do not repeat past oversights moving forward.

4.1. ASTM

Currently there are 4 ASTM standards that pertain to ACB systems:
1. ASTM D6684 – Standard Specification for Materials and Manufacture of Articulating Concrete Block (ACB) Revetment Systems
2. ASTM D6884 – Standard Practice for Installation of Articulating Concrete Block (ACB) Revetment Systems
3. ASTM D7276 – Standard Guide for Analysis and Interpretation of Test Data for Articulating Concrete Block (ACB) Revetment Systems in Open Channel Flow
4. ASTM D7277 – Standard Test Method for Articulating Concrete Block (ACB) Revetment Systems for Hydraulic Stability in Open Channel Flow

Use of these standards by designers and regulators has led to improved system reliability for ACB revetments, with ASTM 7276 and 7277 being the basis upon which the biggest impact has been seen. The data analysis methodology employed on the FHWA involved taking the measured test data from the full scale flume test, calculating the energy grade line (EGL), setting a best fit line to the EGL data, and then calculating the threshold velocity and shear stress values for the given dataset. While, technically, this method will ultimately arrive at velocity and shear stress values, it is very dependent upon who is running the analysis. Stated directly, two individuals can run the analysis on the same data set and come up with different values of velocity and shear, yet both could technically defend their

analysis. Additionally, this methodology sometimes violated the fundamental laws of thermodynamics where energy appeared to be created. ASTM 7276 was first adopted in 2008, and it allowed the data generated during a full-scale flume test of an ACB system to be more consistently and accurately analysed. Now, there is a methodology where several people can analyse the same data set and obtain results that are reasonably close. This method employs the stepforewater methodology in which the measured water surface profile data is statistically fit to known hydraulic equations. Dr. Cox showed in her dissertation that FHWA shear stress values were overstated by as much as 70% (Cox 2010).

4.2. CSU FOS Methodology

The development of a new set of FOS equations was undertaken because in the original FOS equations, the lift forces were assumed to be equal to the drag forces. In the original NCMA FOS equations, velocity has no impact on the calculated FOS for a tapered ACB system where the projection height (ΔZ) is set to 0. The CSU methodology treats lift and drag forces separately. When analysing a total of 24 data sets generated in full-scale flume tests on ACB blocks, the CSU methodology was able to correctly predict threshold performance in 23 of the 24 data sets, while the existing NCMA (2006) methodology correctly predicted only 11 of the 24 data sets. A comparison of the results presented in Table 1 with the NCMA (2010) methodology to the CSU FOS results is presented in Table 2. Of particular note is that at the highest flow rate presented, the FOS with the CSU methodology falls under the 1.5 typical minimum value, which is due to the inclusion of velocity in the equations. The CSU methodology returns 4 FOS calculations, the lowest of which is set at the FOS for the project.

Table 2. NCMA (2006) and CSU FOS Methodologies FOS Comparison

FLOW (m³/s/m)	VELOCITY (m/s)	SHEAR (Pa)	FOS NCMA (2006)	SF_O CSU	SF_P CSU	SF_M CSU	SF_{BED} CSU
0.0431	4.84	316	2.96	7.33	2.80	3.85	2.80
0.0863	6.40	474	2.12	4.40	1.92	2.56	1.93
0.1726	8.44	718	1.47	2.60	1.27	1.64	1.27

Note: FOS Values based bed slope of 3:1 (_H:1V) and Side Slope of 20:1. FOS via NCMA (2006) and CSU Methodologies and Shoreblock SD 475 OCT ACB System. Velocity and shear values at normal flow state.

Again, we note in Table 2 that the FOS is not linearly related to the flow. We also note that the CSU methodology, taking into account both velocity and shear in the FOS determination, produces more conservative and presumed accurate values. Dr. Cox, showed in her dissertation that at velocities in excess of 3.05 m/s, the lift forces dominate compared to the drag forces in destabilizing an ACB system (Cox 2010). The effect of velocity on the FOS determined with both the NCMA (2010) and CSU methodologies is presented in Table 3. For this exercise, shear was held constant at 316 Pa.

Table 3. FOS comparison between NCMA (2006) and CSU Methodologies showing effect of velocity

VELOCITY (m/s)	SHEAR (Pa)	FOS NCMA (2006)	SF_O CSU	SF_P CSU	SF_M CSU	SF_{BED} CSU
4.84	316	2.96	7.33	2.80	3.85	2.80
6.40	316	2.96	4.40	2.23	2.85	2.23
8.44	316	2.96	2.60	1.65	1.97	1.65

Note: FOS Values based bed slope of 3:1 (_H:1V) and Side Slope of 20:1. FOS via NCMA (2006) and CSU Methodologies and Shoreblock SD 475 OCT ACB System.

5. HISTORY AS A TEACHER

ACB revetment systems have been utilized for erosion prevention since the late 1970s, thus providing the industry and designer a large database of experiences to draw upon. The philosopher George Santayana stated, "Those who do not learn from history are doomed to repeat it." Approaching the understanding of ACB performance from past

experience has been a recently emerging theme and is one that is gaining momentum. In recent years, Paul Schweiger P.E. and Darin Shaffer have begun the compilation of field performance results of ACB applications specific to dam overtopping and emergency spillway applications and have written papers for national conferences (Schweiger & Shaffer 2013). This theme has been followed at other technical gatherings of Dam Safety engineers with the database and understanding learned growing every year. The study of past performance of ACB systems has led to some of the innovations discussed later in this paper.

5.1. Current State of ACBs in the Market

ACB systems are currently manufactured in both hand placed and cabled mat systems, interlocked and non-interlocked, and wet cast and dry cast offerings. There are several manufacturers actively selling and promoting ACBs to the engineering community, and each brings strengths and weaknesses in terms of technical knowledge, regional manufacturing capabilities, sales and installation support, as well as testing of the ACB systems to current ASTM standards. Design engineers need to obtain, read, and understand the test data and installation details of each ACB manufacturer they choose to work with. The quality of the ACB product in terms of physical properties as well as performance for a given set of project design parameters vary widely, and the designer should insist on adherence to ASTM specifications and work with more than one manufacturer on their design projects. The designers and regulators need to be diligent in reading technical test reports provided they often are not what they appear.

5.2. Innovations in ACB Systems

The process of innovation and modifications to ACB blocks began soon after the initial product development. Each innovation needs to be evaluated for its merits in improving the performance of ACB systems, and it must be noted that not all modifications made to ACB blocks have resulted in positive improvements on performance. The basic shape of the original ACB block was rectangular and arranged in a linear fashion within mats. The following innovations are discussed briefly as to their role in the furthering of ACB revetment performance

5.2.1. Interlocking Blocks

Interlocking and in some cases staggering every other row of ACB blocks within a mat are innovations that have been widely employed and have seen varying degrees of success in improving the performance and reliability of ACB revetment systems and are depicted in Figure 4. Some interlocking systems are positive interlocking, which means they contain projections similar to those seen in jigsaw puzzle pieces. These projections can cause binding or break if the ratio of block thickness to projection length is not adequate. Should a positive interlocking piece break, the ACB unit will no longer have the representative design characteristics determined from the flume test, potentially putting the revetment at risk of failure.

5.2.2. Dome top ACBs

Roughening of the top surface of the blocks led to an observed increase in Manning's n as determined from water surface profiles measured during full scale flume tests are shown in Figure 5, while Figure 6 shows a flat top ACB. This roughening was accomplished by adding a "dome" to the top of many ACBs. This had the effect of reducing the velocity and increasing the shear during the full scale flume test, and at that time when this innovation was introduced, it was thought that shear really controlled the ACB performance, so seeing the increased shear was very welcomed by the ACB manufacturers. Thanks to both the dome top and the slower velocities seen due to higher Manning's n, the effect of the projecting block in the FOS equations was reduced.

Figure 5. Interlocking Dome Top ACBs   Figure 6. Interlocking Flat Top ACBs

5.2.3. Tapered ACBs

The introduction of tapered ACBs led to a major improvement in hydraulic performance for revetments utilizing these products. Tapered ACB systems have been tested to 1.52 m of steady state overtopping depth on a 2:1 (H:V) slope and have not reached the onset of erosion, but they have experienced significant movement of the drainage stone required for adequate hydraulic performance. Early testing showed that tapered ACB systems saw dramatic improvement in performance when a 10 cm stone drainage layer of AASHTO #57 stone with a d_{50} of 19 mm was placed beneath the ACBs on top of the geotextile. Tapered ACBs are the predominant ACB system utilized for dam overtopping and emergency spillway applications.

5.2.4. Length of Flume used in Testing

The original FHWA testing and subsequent tests for at least the following 10 years typically ran a flume set up on a 2:1 (H:V) slope with a 1.83 m to 1.98 m tall embankment (~ 4.6 m of slope length). Starting around 2007, the slope lengths tested on a 2:1 (H:V) slope were extended, initially to 12.2 m, then 21.3 m and, finally, in 2013 to 30.5 m for tapered ACB systems. Typically, untapered ACB systems are run on a flume 15.2 m or less in length as, typically, the threshold of performance is reached for these products at lower velocities; thus, the longer flume lengths are not necessary. Tapered ACB systems have not reached the threshold of performance (onset of erosion) in steady state overtopping flows, even with a 30.5 m flume length. What has been observed with the 30.5 m flume length is that the stone drainage layer becomes unstable and moves, causing the ACB revetment surface to deform at overtopping depths of 0.91 m or more. Basically with this observation, designs of tapered ACB systems have become limited to velocities approximately 6.4 – 7.9 m/sec or less on a 2:1 (H:V) slope. This limitation on velocity is to avoid maintenance that would be required of the ACB system should flows of this magnitude be experienced. ACB systems have experienced in excess of 5 cm of vertical movement in flume testing (CSU 2014). Maintenance would be required to level the stone drainage layer, thus removing any projecting ACB blocks due to this stone movement. Table 4 shows the effect of this projection height on the FOS of tapered ACB systems. As can be noted, the FOS decreases very rapidly with increasing projection height.

One manufacturer is developing a system to stabilize the stone drainage layer, and this will be described in the next section. It should be noted that the exact mechanism that causes this stone movement is not completely understood. Testing of tapered ACBs in 21.3 m flume run to 1.22 m of steady state overtopping depth with a 10 cm stone drainage layer showed no stone movement.

Table 4. Effect of Projection Height on Tapered ACB Calculated FOS

PROJECTION HEIGHT (mm)	VELOCITY (m/s)	SHEAR (Pa)	NCMA (2006)	SF$_O$ CSU	SF$_P$ CSU	SF$_M$ CSU	SF$_{BED}$ CSU
0	6.40	316	2.96	4.4	2.23	2.85	2.23
6.35	6.40	316	1.27	1.75	1.02	1.25	1.02
12.7	6.40	316	0.81	1.10	0.66	0.80	0.66
25.4	6.40	316	0.47	0.63	0.49	0.47	0.39

Note: FOS values Shoreblock SD 475 OCT on 3:1 slope (_H:1V) with a Side Slope of 20:1 (_H:1V) and a Unit Flow of 0.0863 m3/s/m at normal flow state.

5.2.5. Stabilized Stone Layer

As a result of the discovery of shifting stone drainage layer under higher velocities generated with longer test flume construction, a system has been developed, and is currently being tested, that aims to stabilize the stone and keep the ACB revetment system from deforming. The system involves a cellular confinement system similar to the Presto Geoweb system placed within the stone drainage layer beneath the ACB system.

5.2.6. Elimination of Half Blocks

Since the introduction of staggered ACB block mats, half-blocks have been present to keep the manufactured mats rectangular. Half blocks are not truly tested because when they are used in the flume, they are retained by an angle iron bar along the edge; thus, the focus of the testing is the free-floating full blocks. FOS calculations only use the design parameters developed for full blocks, and there is no accepted extrapolation to estimate the performance of the smaller half blocks utilized in the industry. Additionally, half blocks in most staggered interlocking ACB mat systems are secured with only one cable; thus, there is a potential for the half block to roll on this single cable, compromising the revetment system.

One option for eliminating the use of half blocks has been dubbed the "lacing detail." This installation technique involves omitting the half blocks during the ACB mat fabrication process, placing the mats adjacently such that a void is created, running an additional cable through the cable duct then backfilling the void with grout. A schematic is shown in Figure 7. In addition to not using half blocks in the revetment, the potential for linear flow paths between adjacent mats has been eliminated, and the entire ACB system is one contiguous revetment.
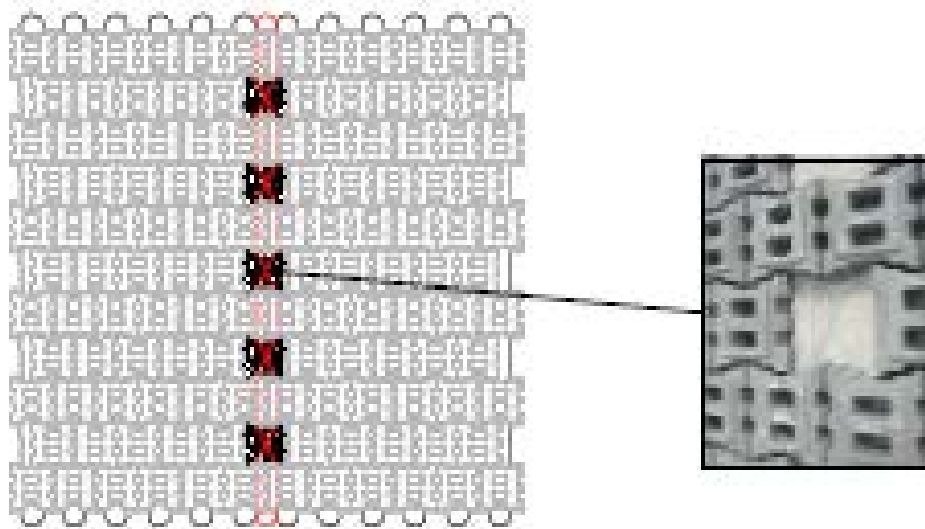
Figure 7. ACB Lacing Detail Schematic

6. AREAS FOR FUTURE RESEARCH AND TESTING

Research, testing, and application of this knowledge gained has led to the continued use of ACB systems for high velocity erosion control applications in risk prone environments. While much has been learned, many topics of future research have been identified through flume testing and in-field performance results. Areas requiring further research include a better understanding of ACB system stability under varying hydraulic jump conditions, rollers caused by converging flow scenarios such as seen in a tapered channel or spillway application, aerated flows and the implications for ACB system performance, and the impact of non-linear flow scenarios on tapered ACB systems.

7. CONCLUSIONS

Since their introduction in the 1970s and with the promising results seen in the early flume testing, ACB revetment systems have proven themselves in terms of hydraulic performance and economics in thousands of field installations. Improvements in flume test protocols, test data analysis, field installation, consistency of manufacturing, and new product offerings will lead to ACBs being used in a wider range of hydraulic applications. The work undertaken in the past 30 years in this field has led to an increased scientific understanding of how and why ACB revetment systems perform and serves as the basis for future research avenues to gain deeper knowledge and confidence in design methodologies employed.

Many manufacturers of ACB systems have entered the market with new ones showing up periodically, which has had both positive and negative impacts on the ACBs systems available. On the positive side for the project owners, ACB prices have been on a downward trend with more product offerings, while on the negative side, more product offerings have led to products not being adequately tested and evaluated in real-time field applications, potentially putting the installed system at risk due to oversights on the part of the manufacturer lacking practical experience and on the part of the specifying engineer in relying on the word of the manufacturer. In an effort to overcome some of the inconsistencies and negatives stated above, ASTM has developed a series of standards and guides that are viewed as the benchmark for the current manufacturers and users of ACB revetment systems. Design guidance for the engineering community is offered in several places including HEC-23, NCMA ACB Design Manual (2006 & 2010) and the CSU FOS methodology of Dr. Amanda Cox. All of these systems have been peer reviewed, and any new system of equations proposed to determine the FOS for an ACB revetment should also undergo this peer review process before being utilized by the designer. Currently, there is a wealth of information, standards and guidance for the engineering community to successfully and economically design an effective ACB revetment system; however, if these standards are not followed, the chances of a successful installation are diminished.

8. REFERENCES

ASTM D7276 (2008). Standard Guide for Analysis and Interpretation of Test Data for Articulating Concrete Block (ACB) Revetment Systems in Open Channel Flow.
ASTM D7277 (2008). Standard Test Method for Performance Testing of Articulating Concrete Block (ACB) Revetment Systems for Hydraulic Stability in Open Channel Flow.
ASTM D6884 (2010). Standard Practice for Installation of Articulating Concrete Block (ACB) Revetment Systems.
ASTM D6684 (2010). Standard Specification for Materials and Manufacture of Articulating Concrete Block (ACB) Revetment Systems.
Colorado State University (CSU) (2014) Hydraulic Testing and Data Report for Armortec Class 40T ACB
Cox, A.L. (2010) Ph.D. Dissertation, "Moment Stability Analysis Method For Determining Safety Factors For Articulated Concrete Blocks" Colorado State University
FHWA (2009) FHWA-NHI-09-111 HEC-23, Bridge Scour and Stream Instability Countermeasures: Experiences, Selection and Design Guidance, Third Edition
FHWA (1988) RD 88-181 Minimizing Embankment Damage During Overtopping Flow
FHWA (1989) RD 89-199 Hydraulic Stability of Articulating Concrete Block Revetment Systems During Overtopping Flow
Hewlett, H.W.M., Borman, L.A., Bramley, M.E. (1987). Design of Reinforced Grass Waterways. Construction Industry Research and Information Association, Report 116, London, UK.

Nadeau, J.A. (2015) – Unpublished marketing research

National Concrete Masonry Association (NCMA) (2006 & 2010). Design Manual for Articulating Concrete Block (ACB) Revetment Systems.

Schweiger, P.G., and Darin Shaffer (2013), *The ABCs of ACBs – What Have We Learned 12 Years Later, Armoring Embankment Dams and Earth-Cut Spillways with ACBs*, 2013 ASDSO National Conference, Rhode Island.

Sensitivity Analysis for Discharge Coefficients of Piano Key Weirs

M. Oertel[1]
[1]Hydraulic Engineering Section, Civil Engineering
Department Lübeck University of Applied Sciences
23562
Lübeck
Germany
E-mail: mario.oertel@fh-luebeck.de

ABSTRACT

Piano Key Weirs are relatively new weir structures that can be used as a flood release structure at the top of a dam or as a regular weir structure within a river system. The benefit of a PKW is an increased discharge capacity and, hence, lower free surface heads at the upstream reservoir. During the last few years, several experimental and numerical research investigations were carried out to analyze discharge coefficients for various PKW types. Therefore, numerical 3D CFD codes and small-scaled experimental models were used. To identify discharge coefficients, the Poleni formula can be used. By measuring the total discharge and the weir head, discharge coefficients can be calculated. However, results will be sensitive due to the weir head because basically the total energy head includes the velocity head. Hence, the position of the measuring point for the weir head and the associated velocity head must be selected carefully. To show the variation of results for discharge coefficients due to the measurement point and measurement accuracy, a sensitivity analysis for PKW discharge coefficients is given. Measurement data were collected from experimental models at Lübeck University of Applied Sciences' Water Research Laboratory.

Keywords: *PKW, Piano Key Weir, discharge coefficients, sensitivity analysis, weir head, velocity head*

1. INTRODUCTION AND STATE OF THE ART

Blanc and Lempérière (2001) and Lempérière and Ouamane (2003) developed a general Piano Key Weir design, which is a nonlinear weir type. PKWs can be used as in-channel structures or for top-of-dam spillway control structure to increase discharge capacity (Oertel and Tullis 2014). During the last decades, a significant amount of research investigations were carried out to identify PKW's discharge coefficients (e.g. Anderson 2011, Machiels et al. 2011 and many more).

Generally, PKWs are classified into four main geometric types (Type A, B, C, and D). A Type A PKW features symmetrical keys relative to a transverse centerline axis. Type B has cantilevered apexes on the upstream end and vertical apex walls on the downstream end. Type C is the opposite of Type B. A rectangular labyrinth weir with vertical apex walls is presented by Type D. Primary (crest length, head) and secondary (ratio of inlet and outlet key width and height, overhang length, height of parapet walls) parameters with significant influence on PKW Type A discharge capacity were identified by Ribeiro et al. (2012). Kabiri-Samani and Javaheri (2012) determined discharge coefficients for free and submerged flow over PKWs. Dabling and Tullis (2012) evaluated and compared submerged head-discharge relationships for Type A PKWs and labyrinth weirs. General flow characteristics over a PKW were investigated by Machiels et al. (2011) within a scaled experimental model. Anderson (2011) and Anderson and Tullis (2012) investigated several PKW geometries and discharge efficiencies for in-channel and reservoir-approach flow conditions. Erpicum et al. (2014) analyzed geometric parameter influence on PKW performances and mentioned e.g. the weir height's primary importance. Experimentally determined discharge coefficients for several PKW types were compared with those from a numerical 3D VOF model by Oertel and Tullis (2014); a good agreement and applicability of the VOF code was found. Additional variations of PKW Type A geometries with

semi-circle and triangle expansions were analyzed by Oertel (2015). In summary, PKW (2011) and PKW (2013) gives an overview about PKW research investigations.

Generally, discharge coefficients C_d for a PKW are in the focus of interest. Figure 1 gives example results for various PKW discharge coefficients (experimental and numerical models) from Anderson and Tullis (2012) and Oertel (2015). It can be shown that the basic development of C_d follows a comparable trend: for small discharges ($H_T P_0 < 0.07$ to 0.11) an increase of C_d can be found; for increasing discharges (after reaching the maximum C_d value, $H_T P_0^{-1} > 0.07$ to 0.11) a continuous decrease of C_d can be observed.
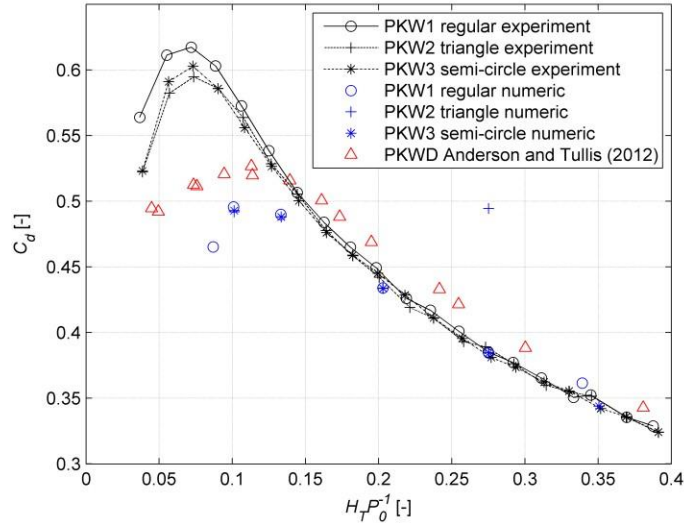
Figure 1. Exemplary discharge coefficients from experimental and numerical models (Oertel 2015).

Using numerical or experimental models, discharge coefficients can be calculated by measuring the upstream water surface level h_T (above weir crest) and calculating the associated velocity head v_T averaged over total flow depth ($h_T + P$, where P is the total weir height for in-channel approach). Figure 2 gives a schematic plot. Subsequently, C_d values can be determined by Poleni formula:

$$Q = \frac{2}{3} C_d L (2g)^{0.5} H_T^{1.5} = C' L H_T^{1.5} \tag{1}$$

where Q = discharge, C_d = dimensionless discharge coefficient, C' = coefficient including 2/3 and C_d and $(2g)^{0.5}$, L = total centerline crest length, g = acceleration due to gravity, H_T = total upstream energy head including velocity head = $h_T + v_T^2/(2g)$

Aigner (2008) additionally defines discharge coefficient C_d for regular weirs as a function of various influencing parameters; for PKWs, $C_{d,0}$ to $C_{d,3}$ might be of interest:

$$C_d = C_{d,0} \cdot C_{d,1} \cdot C_{d,2} \cdot C_{d,3} \cdot C_{d,4} \cdot C_{d,5} \cdot C_{d,6} \tag{2}$$

where $C_{d,0}$ = basic coefficient (Euler equation), $C_{d,1}$ = inflow velocity coefficient (kinetic energy), $C_{d,2}$ = constriction loss coefficient (head losses), $C_{d,3}$ = jet shape coefficient (velocity distribution), $C_{d,4}$ = backwater coefficient, $C_{d,5}$ = inclined inflow coefficient, and $C_{d,6}$ = pile coefficient.

Since the upstream velocity profile, and hence the water surface level (WSL), will not be uniform, the distance of measurement x_m (ultrasonic sensors for h_T) from the PKW's centerline will influence results for discharge coefficients. Also, the accuracy of measurement techniques might influence investigation results (ultrasonic probes

and magnetic inductive flow meters). Consequently, this paper deals with influencing parameters for discharge coefficient results and their accuracy.
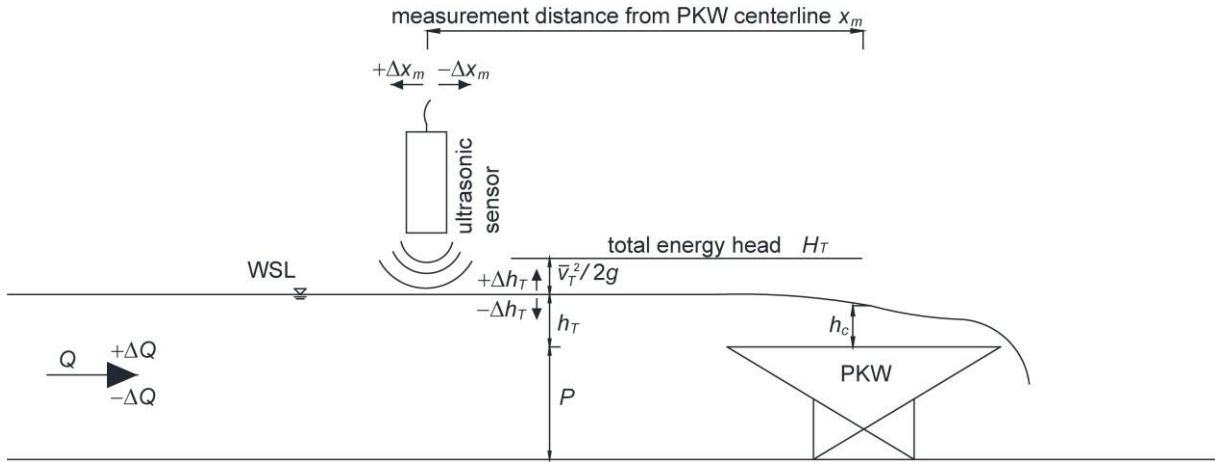
Figure 2. Schematic plot for total energy head (inlet key section, in-channel approach).

2. EXPERIMENTAL MODEL

2.1. Scaled Physical Model and Measurement Technique

To analyze discharge coefficients for PKWs and their accuracy, an experimental model was built up at Lübeck University of Applied Sciences' Water Research Laboratory. The in-channel PKW was fabricated using 5 mm thick acrylic sheeting (PT_s = 39.4). The flattop weir crest was machined using a CNC (computerized numerical control) mill to ensure an accurate PKW structure. The as-built dimensions presented in Table 1 were used for all analyses. Parameters are given in Figure 3. The in-channel PKW experiments were conducted in a 0.80 m wide by 0.80 m deep by 10.0 m long rectangular tilting flume. A schematic plot of the experimental model is presented in Figure 4. Flow was supplied into the test flume via piping containing calibrated magnetic inductive flow meters for flow measurement (MID, manufacturer: Krohne, model: Optiflux 2000, accurate to ±0.1 l/s). An ultrasonic sensor upstream the PKW was used to determine h_T (USS, manufacturer: General Acoustics, model: USS60350, accurate to ±1 mm). An automatic positioning system performs a predefined measurement program in the x-axis (main flow direction) with approximately 250 measurement points on a 1 cm grid (manufacturer: isel, model: step motor, accurate to ≤1 mm). Mean flow velocities were calculated analytically by continuity equation. The total upstream energy head finally is $H_T = h_T + v^2_T(2g)^{-1}$. Using the experimental H_T and Q data, C_d coefficients were calculated using Eq. (1).

Scale effects for PKWs are rarely discussed within the literature (e.g. Machiels et al 2011, Erpicum et al. 2014). Limits for water depths to upscale laboratory-scale results can be found to be approx. 3 cm (see e. g. USDI 1980 or Ribeiro et al. 2012). Since not all experimental model runs were conducted with minimum overtopping water depths of 3 cm, some scale effects for small discharges can be expected due to viscosity or surface tension but without significant influence due to the paper's outcome.

Table 1. Summary of laboratory-scale PKW model dimensions.

Test Weir Dimensions [mm]			
P	196.9	L	4667.2
W	796.0	B_b	230.7

W_i	105.0	$B_o = B_i$	129.1
W_o	84.0	T_s	5.0
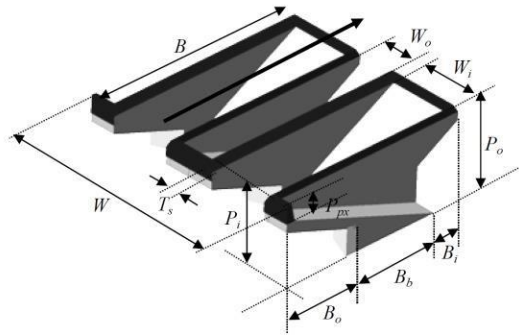
Figure 3. PKW parameters (Pralong et al. 2011)
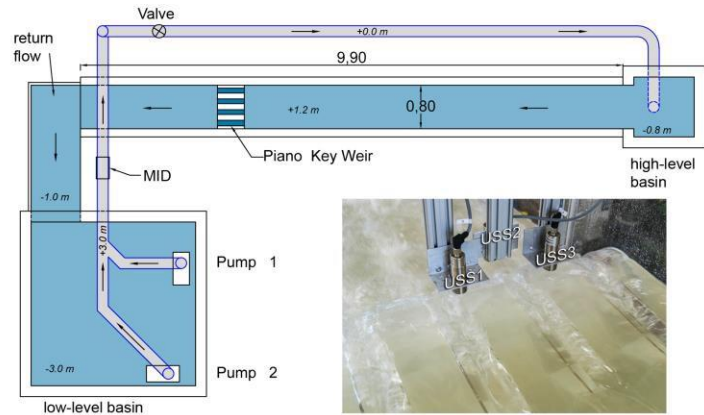
Figure 4. Schematic plan view of exp. Water circulation system and ultrasonic sensors above PKW (Oertel 2015).

2.2. Investigation Program

For the present investigation, 18 model runs were performed with a regular (symmetrical) PKW Type A geometry (see Figure 3). Discharges were selected from Q = 2.0 to 100 l/s (q = 2.5 to 125 l(sm)$^{-1}$). For all discharges, water surface levels were measured each centimeter upstream the PKW's centerline (inlet key section) on a total length of 2.5 m for approximately 10 to 20 seconds (sample rate 75 Hz). Results for each measurement point were averaged over time, and outliers were removed using a standard deviation criterion (outlier if: $d > m + 2 \times s$ or $d < m - 2 \times s$, where d = time depended flow depth data point, m = mean time averaged flow depth, s = standard deviation). With the chosen investigation program, flow depths for calculating total energy heads can be selected on a wide range.

Data analysis will focus on a sensitivity study due to various parameter variations and their influence on discharge coefficients:

1. measurement distance x_m
   → influence of measurement point

2. measurement point vs. averaged measurement area
   → influence of standing waves

3. measurement accuracy h_T
   → influence of ultrasonic probe's accuracy

4. measurement accuracy Q
   → influence of MID's accuracy

5. velocity head $v_T^2(2g)^{-1}$
   → influence of included velocity head

3. RESULTS AND DISCUSSION

3.1. Water Surface Elevation (WSL)

Water surface elevations/levels (WSL) for all investigated discharges are produced by averaging measurements over measuring time (see Section 2.2). All resulting WSL are given in Figure 5. For increasing discharges, a progressive change of the water surface profile directly above the PKW, along with an accelerated flow, can be observed.
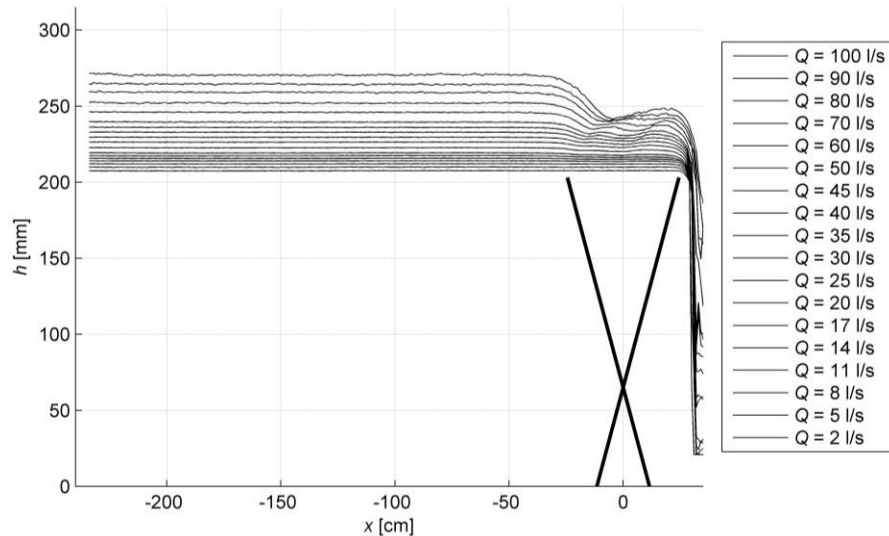
Figure 5. WSL for all investigated discharges at flume's centerline (inlet key section), exaggerated plot.

3.2. Measurement Distance x_m

Model runs are analyzed due to their selected distance of the measurement point, located at a defined distance x_m upstream of the PKW's centerline (see Figure 2). Bollrich (2007) mentioned a measurement distance for overflown hydraulic structures of $x_m = 3 \times h_T$ to $4 \times h_T$. Since the flow depth above the weir is variable due to changing discharges, the measurement point will change.

Figure 6 presents results for various selected measurement distances between $0.5 \times P$ and $3 \times P$ for channelized PKW applications. Since P is a fixed value, the measurement distance will not change with increasing flow depths above the weir for the present investigation. It can be shown that an absolute distance of $2.0 \times P \leq x_m \leq 3.0 \times P$ will be acceptable for result analyses since discharge coefficients can be reproduced with high accuracy (Figure 6 right).

3.3. Measurement Point x_m vs. Averaged Measurement Area $x_{m,1..2}$

Within an experimental model, small standing waves may occur as a result of small flume lengths or of time-averaged flow depth values. To describe the influence of possible standing waves, C_d values will be calculated on the one hand by measured flow depths at one single location x_m and in contrast by averaged flow depths along a defined measurement area $x_{m,1..2}$. Figure 7 shows results for both approaches. It can be noticed that no major difference in C_d values can be observed, and, hence, no standing waves occur for investigated discharges. Consequently, only the absolute measurement distance x_m is of interest for C_d calculation.
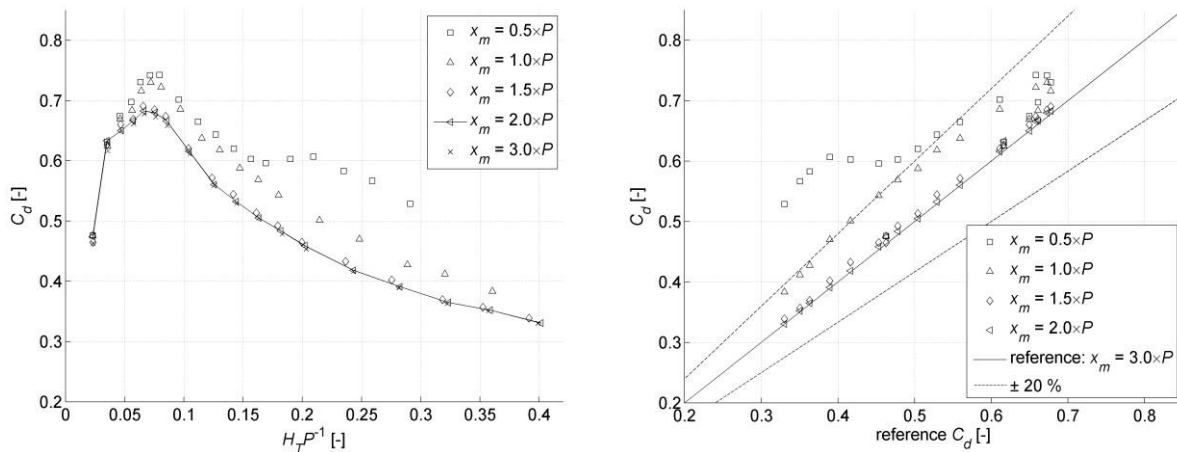
Figure 6. Influence of measurement distance x_m on discharge coefficients C_d, left: absolute values, right: direct comparison.
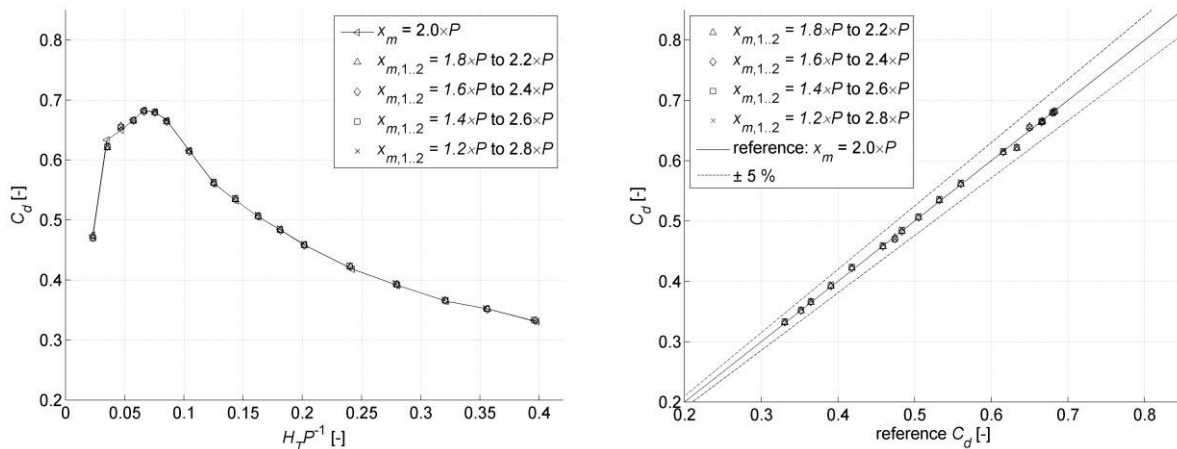
Figure 7. Influence of measurement point x_m vs. averaged measuring area $x_{m,1..2}$ on discharge coefficients C_d, left: absolute values, right: direct comparison.

3.4. Measurement Accuracy of h_T and Q

Ultrasonic probes and MIDs are accurate measurement devices to measure flow depths and discharges within experimental models. The accuracy of used ultrasonic probes can be assumed to be better than 1 mm; for MIDs 0.1l/s. However, results also depend on calibration and offset data. Analogous sensors transfer a defined voltage as output to an AD converter. This converter creates digital values for measurement software products. Hence, a measured voltage represents an exactly associated flow depth or discharge. Therefore, a calibration is necessary to identify the measurement boundary areas.

The ultrasonic probes used provide a voltage range of 0 to 10 V and a measurement distance is 60 to 350 mm. An offset data set allows an identification of the initial flume bed, since the probe is installed somewhere within its measurement range. This may generate some measurement errors or uncertainties.

For results analysis, the original data set will be manipulated. Therefore, the measured flow depths will be increased by Δh_T = 0.5 or 1.0 mm and decreased by Δh_T = –0.5 or –1.0 mm. With these new flow depths, new discharge coefficients C_d *will* be calculated.

Figure 8 gives results for an original data set at $x_m = 2 \times h_T$ as well as for four Δh_T manipulated results. It can be shown that especially for small discharges, (larger C_d values, $H_T P^{-1} < 0.2$) the influence is significant. Already for very small changes in measured flow depths discharge coefficients will be influenced majorly (perhaps partly due to scale effects, which must be quantitatively analyzed in further studies).

Another data set will be manipulated due to measured discharges. Here, the discharge will be increased by 1% or 5% and decreased by –1% or –5%. Plots will be generated using these manipulated values. Results for discharge coefficients with manipulated discharges can be found in Figure 9. Discharge coefficients are calculated using Eq. (1). Consequently, C_d directly depends on Q, and, hence, the percentage accuracy of the discharge measurement device directly leads to the accuracy of discharge coefficient results. Generally, the influence of h_T on resulting discharge coefficients will be increased for increasing discharges (the denominator becomes more important). Thus, the effect of manipulated discharges is larger for small discharges ($H_T P^{-1} < 0.1$).
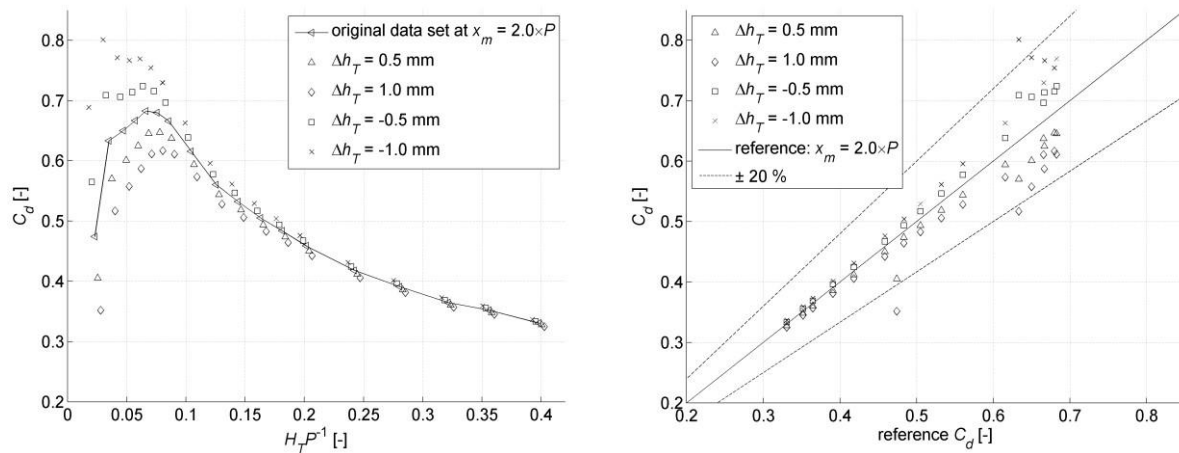
Figure 8. Influence of measurement accuracy h_T on discharge coefficients C_d, left: absolute values, right: direct comparison.
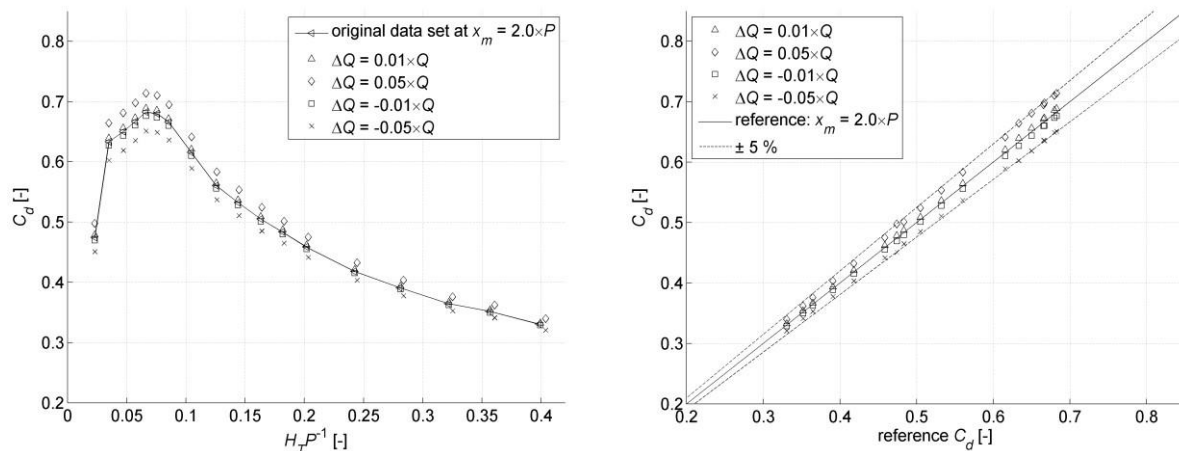
Figure 9. Influence of measurement accuracy Q on discharge coefficients C_d, left: absolute values, right: direct comparison.

3.5. Velocity Head

The literature definitively suggests the inclusion of velocity head into the total energy head for discharge coefficient calculations. To confirm this statement, C_d values will be calculated with and without included velocity heads. Figure 10 clearly shows the difference. Discharge coefficients will be overestimated by up to 20% for nearly all discharges ($H_T P^{-1} > 0.05$). Only for very small flow depths above the PKW ($H_T P^{-1} < 0.03$) are the influence of the velocity head negligible.
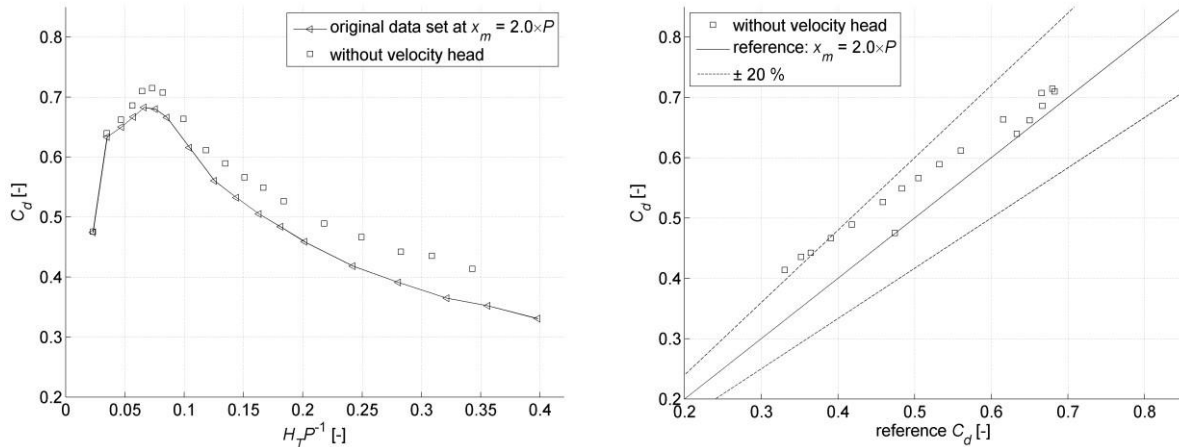
Figure 9. Influence of velocity head $v_T^2 \ (2g)^{-1}$ on discharge coefficients C_d, left: absolute values, right: direct comparison.

4. SUMMARY AND CONCLUSIONS

In the present paper, a sensitivity analysis for Piano Key Weir discharge coefficients was performed for a selected experimental PKW model at Lübeck University of Applied Sciences' Water Research Laboratory. Five influencing parameters were successively investigated, and their influence on calculated discharge coefficients was quantified for centerline axis (inlet key section).

Main results will be summarized within the following itemization:
- The measurement distance x_m majorly influences calculated discharge coefficients C_d for small x_m values. It is suggested to use values of $x_m = 2 \times P$ for measurement purposes for channelized PKW applications.
- Since no major standing waves occur upstream the PKW within the experimental model, an averaged measurement area will lead to no significant change of C_d values. Hence, a single measurement point at $x_m = 2 \times P$ can be used for accurate results.
- The accuracy of ultrasonic probes majorly influences C_d results. Also, less than 1 mm deviation will increase or decrease discharge coefficients significantly, especially for small discharges.
- The accuracy of discharge meters (MID) has less influence on C_d values since the discharge directly influences results within the Poleni approach. Consequently, the accuracy of calculated C_d values directly comes along with the accuracy of MID measurements.
- Neglecting the velocity head during C_d calculation will generate a difference of up to 20%. Generally, when publishing research works on discharge coefficients, it is essential to mention whether velocity heads were included or not to make own results comparable with values from literature.

The present paper and its sensitivity analysis should provide a guideline for measurement purposes on experimental PKW models within hydraulic laboratories to guarantee comparable results by various researchers and authors.

5. REFERENCES

Aigner, D. (2008). "Überfälle". *Dresdner Wasserbauliche Mitteilungen*, No. 36, Technical University of Dresden, 162-176 [in German].

Anderson, R. M. (2011). "Piano Key Weir Head Discharge Relationships". *All Graduate Theses and Dissertations*, Paper 880, Utah State University.Anderson, R. M., and Tullis, B. P. (2012). "Piano Key Weir: Reservoir versus Channel Application". *Journal of Irrigation and Drainage Engineering*, 138, 773-776.

Blanc, P., and Lempérière, F. (2001). "Labyrinth spillways have a promising future". *Hydropower & Dams*, 8(4), 129-131.

Bollrich, G. (2007). "Technische Hydromechanik". Part 1, 6th edition, huss, Berlin [in German].

Dabling, M. R., and Tullis, B. P. (2012). "Piano Key Weir Submergence in Channel Applications". *Journal of Hydraulic Engineering*, 138(7), 661-666.

Erpicum, S., Archambeau, P., Pirotton, M., and Dewals, B. J. (2014). "Geometric Parameters influence on Piano Key Weir hydraulic performances", *Proc. 5th International Symposium on Hydraulic Structures*, Brisbane, Australia.

Kabiri-Samani, A., and Javaheri, A. (2012). "Discharge coefficients for free and submerged flow over Piano Key weirs". *Journal of Hydraulic Research*, 50(1), 114-120.

Lempérière, F., and Ouamane, A. (2003). "The piano key weir: a new cost-effective solution for spillways". *Hydropower & Dams*, 10(5), 144-149.

Machiels, O., Erpicum, S., Dewals, B., Archambeau, P., and Pirotton, M. (2011). "Experimental observation of flow characteristics over a Piano Key Weir". *Journal of Hydraulic Research*, 49(3), 359-366.

Oertel, M., and Tullis, B. P. (2014). "Comparison of Piano Key Weir Discharge Coefficients from experimental and numerical models". *Proc. 3rd IAHR European Congress*, Porto, Portugal.

Oertel, M. (2015). "Discharge coefficients of Piano Key Weirs from experimental and numerical model". *Proc. 36th IAHR World Congress*, The Hague, the Netherlands.

PKW (2011). "Workshop on Labyrinth and Piano Key Weirs", *Proc. 1st International Workshop on Labyrinth and Piano Key Weirs*, Liège, Belgium.

PKW (2013). "Workshop on Labyrinth and Piano Key Weirs", *Proc.2nd International Workshop on Labyrinth and Piano Key Weirs*, Paris, France.

Pralong, J., Vermeulen, J., Blancher, B., Laugier, F., Erpicum, S., Machiels, O., Pirotton, M., Boillat, J. L., Leite Ribeiro, M., and Schleiss, A. J. (2011). "A naming convention for the Piano Key weirs geometrical parameters". *Proc. Intl. Conf. Labyrinth and Piano Key Weirs*, Liege, Belgium.

Ribeiro, M. L., Pfister, M., Schleiss, A., and Boillat, J.-L. (2012). "Hydraulic design of A-type Piano Key Weirs". *Journal of Hydraulic Research*, 50(4), 400-408.

USDI (1980). "Hydraulic Laboratory Techniques". *A Water Resources Technical Publication*, U.S. Department of the Interior, Water and Power Resources Service, Denver, Colorado.

Scouring Processes Downstream a Crossbar Block Ramp

M. Oertel[1] and D. B. Bung[2]
[1]Hydraulic Engineering Section, Civil Engineering Department
Lübeck University of Applied Sciences
23562 Lübeck
Germany
[2] Hydraulic Engineering Section, Civil Engineering Department
Aachen University of Applied Sciences
52066 Aachen
Germany
E-mail: mario.oertel@fh-luebeck.de

ABSTRACT

Crossbar block ramps are hydraulic structures used to conquer large river bottom steps via several pool-step-systems. Due to reduced velocities and increased flow depths, fish climbing capability can be given. Several authors have investigated crossbar block ramp variations to determine flow resistance, energy dissipation, and bed stability features on the structure. But the downstream end of the structure must also be taken into account concerning scouring processes to guarantee the structure's stability and to reduce damage during flood events. The present paper presents a comprehensive experimental investigation program dealing with scouring processes downstream a crossbar block ramp. Influences by ramp slope, discharge, and the structure's geometry are tested. Particularly, for larger discharges and steep slopes, massive scouring takes place. With increasing tailwater depth scouring is reduced and hence the structure's stability is less affected.

Keywords: *Crossbar block ramp, scour, stability, flow regimes.*

1.   INTRODUCTION AND STATE-OF-THE-ART

Crossbar block ramps are low head hydraulic structures used to conquer large river bottom steps via several pool-step-systems. These structures thus reduce flow velocities and increase flow depths to guarantee fish climbing capability. Usually, lower openings within the crossbars are used to create the fish passage corridor for low to medium discharges. Crossbar block ramps can be designed as bypasses next to hydropower plants or as full replacements for weir structures within the original river bed. Generally, their design depends on following parameters: (1) flow conditions accounting for the needs of local fish species, (2) bed stability criteria, and (3) ecological aspects (Oertel, 2012). Crossbar block ramps are structured ramps and part of the block cluster design (Fig. 1).
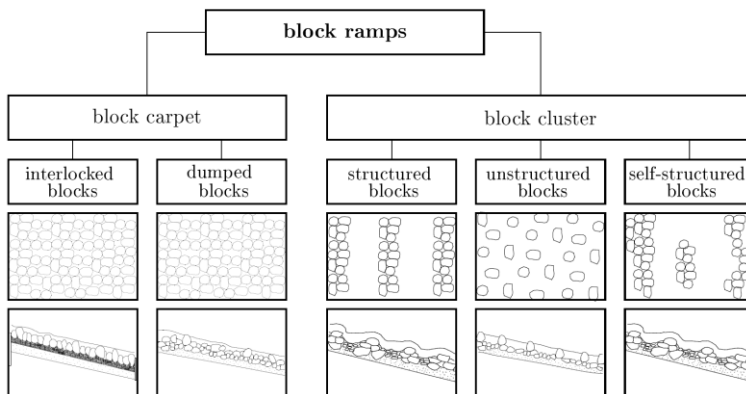
Figure 1. Block ramp design (Oertel 2012, Tamagni et al. 2010).

Due to the European Water Framework Directive (EU-WFD 2000), the design of block ramps became more and more popular. A detailed state of the art review regarding flow resistance and energy dissipation processes can be found in Oertel (2012) or Tamagni et al. (2014). Crossbar block ramps were also investigated in Oertel (2012) and Oertel and Schlenkhoff (2012a). To describe the hydraulic processes on the structure, three main flow regimes must be taken into account: (1) basin flow regime, (2) waved flow regime, and (3) channel flow regime. While limited research is available for the waved flow regime, the basin flow regime ($h < \sim 1.2 \times h_B$, where h = flow depth, h_B = large boulder height) can be clearly described by using the standard Poleni formula (see in-situ measurements in Oertel and Schlenkhoff 2012b). For the channel flow regime (see Fig. 2), the flow becomes quasi-uniform and flow depth can be calculated using the Darcy approach:

$$U = \sqrt{\frac{8}{f}} \sqrt{gRS} \tag{1}$$

where: U = mean flow velocity, f = Darcy-Weisbach friction factor, g = acceleration due to gravity, $R = A/U_p$ = hydraulic radius, A = flow area, U_p = flow perimeter, S = channel slope.

According to Oertel and Schlenkhoff (2012a), friction factors may be estimated by:

$$\sqrt{\frac{8}{f}} = \left(4.4 + \frac{0.09}{S}\right)\log\left(\frac{h}{h_B}\right) + \left(2.2 - \frac{0.0023}{S}\right) \tag{2}$$

General stability investigations for rough channels and ramps are given by Hartung and Scheuerlein (1970), Knauss (1979), Whittaker and Jäggi (1986), Hassinger (1991), Aberle (2000), or Palt (2001). Stability processes on block ramps are essential to guarantee sustainable structures. Therefore, three main criteria must be considered: (1) single boulder's stability, (2) bed material stability along the structure, and (3) bed material stability at the downstream end of the ramp. The single boulder's stability depends on drag coefficients of installed boulders, which varies due to interaction processes (Oertel et al. 2011).

Several authors discussed sediment transport processes on block ramps. For the special case of crossbar block ramps, Oertel and Bung (2015) investigated sediment transport within the formed basins and developed formulas to calculate critical discharge condition for major bed erosion. Recently, the downstream area of block ramps has also been investigated concerning scouring processes (e. g. Pagliara 2007, Pagliara 2009, Pagliara et al. 2015). Measures to avoid and control scouring were analyzed (e. g. Pagliara and Palermo 2008) as well as tailwater influences (Pagliara and Palermo 2010).

Generally, scouring is a flow induced, time dependent change in the riverbed (DIN 4047 1989). Scouring downstream a block ramp can influence the structure's stability due to regressive erosion processes. Figure 2 presents a typical scour profile and useful parameters for scour description. Eroded material will be deposited downstream, forming a new bed profile, which also changes hydraulic processes. DIN 4048 (1987) gives measures to protect the downstream riverbed with boulders and filter material. Downstream of the scour control measures, the riverbed should be protected for another 3 to 5 m or twice the channel width (for non-erosive river beds).

For scour sensitive materials (sand, silt) the assumed scour profile should be pre-formed with a protected riverbed (scour depth approx. 1/3 or 1/2 of ramp height, DWA 509 2010). Then, downstream of the bed scour protection measures, the continuous protection should be applied to the riverbed for distances up to 10 times the ramp height.
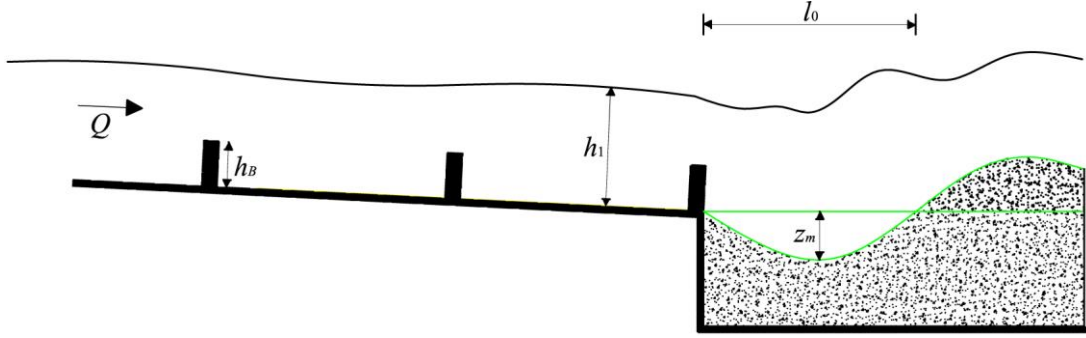
Figure 2. Parameters for scouring (according to Pagliara 2007).

Pagliara (2007) defines downstream scouring as a result of supercritical flow conditions on the block ramp. Parameters like ramp slope, discharge and material influence scour development. Two flow situations can occur: (1) "free" hydraulic jump and (2) submerged hydraulic jump in mobile bed. While for the free hydraulic jump scouring ends at approx. 30 min for the given test conditions, for the submerged hydraulic jump scour profiles change continuously. Additionally, the tailwater depth majorly influences the scouring process, which also will be identified within the present study.

Dimensionless scour depth downstream a block ramp without crossbars can be calculated with (Pagliara 2007):

$$Z_m = 0.58 S^{0.75} \mathsf{F}_{d,90}^{1.8} \tag{3}$$

where: $Z_m = z_m/h_1$ = dimensionless mean scour depth, z_m = mean scour depth, h_1 = flow depth at ramp toe, S = ramp slope, $\mathsf{F}_{d,90} = v_1/(g'd_{90})^{0.5}$ = particle densimetric Froude number, v_1 = mean flow velocity at ramp toe, d_{90} = particle diameter for which 90% of sediment is finer, $g' = [(\rho_s-\rho)/\rho]g$ = reduced gravitational acceleration, ρ = water density, ρ_s = sediment density, g = acceleration due to gravity.

The dimensionless scour length depends on the known dimensionless scour depth and can be calculated with:

$$L_0 = 3.75 S^{-0.5} Z_m^{0.8} \tag{4}$$

where: $L_0 = l_0/h_1$ = dimensionless scour length, l_0 = scour length.

Parameters z_m and l_0 are shown in Fig. 2. Eqs. (3) and (4) are valid for 1:12 < S < 1:4 and 1.0 < $\mathsf{F}_{d,90}$ < 3.75.

2. EXPERIMENTAL MODEL

A physical model was built up at the University of Wuppertal's Hydraulic Engineering Section. The model scale was approximately 1:15 and consisted of a lower tank, a head tank, a tilting flume, a guiding channel and different measurement devices (see Fig. 3). The pump (Grundfos inline pumps) and pipe (DN 125) system allows discharges up to Q = 45 l/s. The tilting flume is made of aluminum with transparent sidewalls (Plexiglas). The crossbar block ramp geometry was formed by synthetic material with the following dimensions: crossbar height h_B = 6 cm, crossbar width in longitudinal direction L_B = 6 cm, crossbar width = ramp width W = 100 cm. Two distances of crossbars were investigated: $l_b = 5 \times h_B$ = 30 cm and $l_b = 7 \times h_B$ = 42 cm. The length of the total ramp is L_R = 300 cm. Slopes were adjusted to 1:20, 1:30, 1:50.

Within the sediment basin, two different mixtures were installed: (1) stratified material layer and (2) mixed material layer (see Table 1 and 2). Materials were selected based on BAW (1989) and the Terzhagi's filter rule $D_{15}/D_{85} \leq 4$.
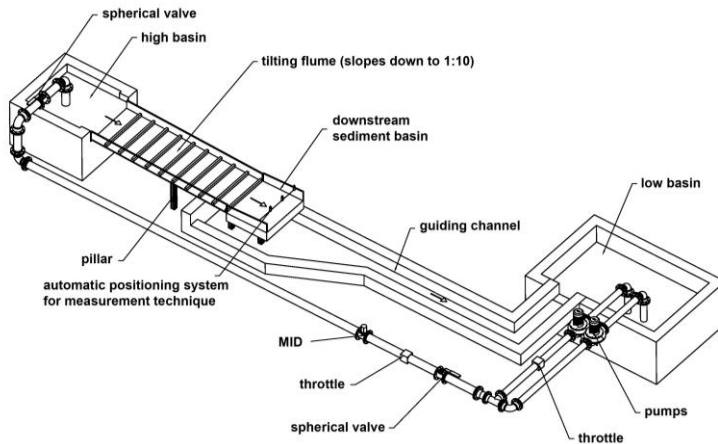
(a) Schematic plot of water circulation system   (b) Photograph
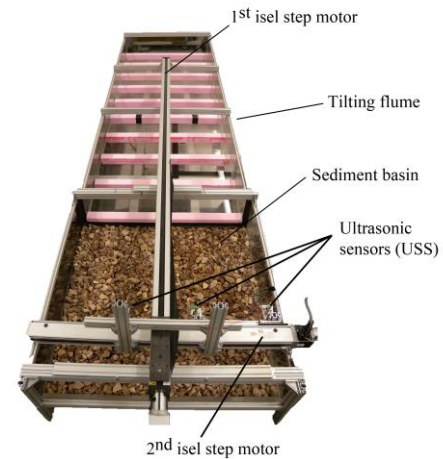
Figure 3. Experimental model.

Table 1. Characteristics of stratified material layer.

	ρ_S [kg/m³]	D_{15} [mm]	D_{85} [mm]	Thickness [mm]	
1st layer (top)	1720	~16.0	~32.0	55	
2nd layer (middle)	2720	~2.00	~4.00	35	
3rd layer (bottom)	~2700	~0.25	~1.00	110	

Table 2. Characteristics of mixed material layer.

	ρ_S [kg/m³]	D_{15} [mm]	D_{50} [mm]	D_{75} [mm]	D_{85} [mm]	D_{95} [mm]	Thickness [mm]	
mixed layer	~2700	~4.00	~7.0	~12.0	~22.0	~35.0	200	

Discharges were measured by magnetic inductive flow meters (MID, fabricate: Krohne, model: Optiflux 2000, accuracy: ± 0.1 l/s). Water surface elevations on the ramp and within the sediment basin were recorded using ultrasonic sensors (fabricate: General Acoustics, model: 60350, accuracy: ± 1 mm). An automatic positioning system performed a pre-defined measurement program in x-axis and y-axis with approximately 2000 measurement points in total (fabricate: isel, model: step motor, accuracy: < 1 mm). Scour surface measurements were carried out in the dry bed following the prescribed test time. In total 54 model runs were performed for the stratified material layer (Table 2) and 42 model runs for the mixed material layer (Table 3). Main investigation parameters were discharge and slope. Additional model runs focus on material variations, tailwater flow depth, basin length, and model run times (for stationary scouring development). Especially for small discharges in combination with higher tailwater depth within the sediment basin, less scouring occurs. Hence, some investigation programs were shortened to reduce investigation time and costs.

Table 3. Performed model runs and results for stratified material layer.

S = 1: ...	Q [l/s]	W	l_b [cm]	T [min]	z_m [cm]	l_0 [cm]	h_1 [cm]	Z_m [-]	L_0 [-]	$F_{d,90}$ [-]
50	5	0	30	0	0.0	0.0	1.2	0.000	0.000	0.567
50	5	0	30	30	0.0	0.0	1.2	0.000	0.000	0.567
50	5	1	30	0	0.0	0.0	1.3	0.000	0.000	0.523
50	5	1	30	30	0.0	0.0	1.3	0.000	0.000	0.523
50	10	0	30	0	0.0	0.0	1.7	0.000	0.000	0.801
50	10	0	30	30	0.0	0.0	1.7	0.000	0.000	0.801
50	10	1	30	0	0.0	0.0	1.3	0.000	0.000	1.047
50	10	1	30	30	0.0	0.0	1.3	0.000	0.000	1.047
50	15	1	30	0	0.0	0.0	3.0	0.000	0.000	0.680
50	15	1	30	30	0.0	0.0	3.0	0.000	0.000	0.680
50	20	0	30	0	0.0	0.0	3.5	0.000	0.000	0.778
50	20	0	30	30	0.8	20.0	3.5	0.229	5.714	0.778
50	20	1	30	0	0.0	0.0	3.3	0.000	0.000	0.825
50	20	1	30	30	0.0	0.0	3.3	0.000	0.000	0.825
50	40	0	30	0	0.0	0.0	5.5	0.000	0.000	0.990
50	40	0	30	30	3.0	32.0	5.5	0.545	5.818	0.990
50	45	1	30	0	0.0	0.0	6.5	0.000	0.000	0.942
50	45	1	30	30	0.0	0.0	6.5	0.000	0.000	0.942
30	15	0	30	0	0.0	0.0	2.8	0.000	0.000	0.729
30	15	0	30	30	0.5	15.0	2.8	0.179	5.357	0.729
30	20	0	30	0	0.0	0.0	3.3	0.000	0.000	0.825
30	20	0	30	30	0.6	16.0	3.3	0.182	4.848	0.825
30	25	0	30	0	0.0	0.0	3.8	0.000	0.000	0.895
30	25	0	30	30	1.2	18.0	3.8	0.316	4.737	0.895
30	35	0	30	0	0.0	0.0	5.0	0.000	0.000	0.953
30	35	0	30	30	2.2	22.0	5.0	0.440	4.400	0.953
30	35	1	30	0	0.0	0.0	5.2	0.000	0.000	0.916
30	35	1	30	30	0.0	0.0	5.2	0.000	0.000	0.916
30	40	0	30	0	0.0	0.0	5.5	0.000	0.000	0.990
30	40	0	30	30	3.8	32.0	5.5	0.691	5.818	0.990
30	40	0	30	210	4.8	40.0	5.5	0.873	7.273	0.990
30	40	0	30	390	6.7	47.0	5.5	1.218	8.545	0.990
30	45	1	30	0	0.0	0.0	6.5	0.000	0.000	0.942
30	45	1	30	30	0.2	10.0	6.5	0.031	1.538	0.942
20	15	0	30	0	0.0	0.0	3.0	0.000	0.000	0.680
20	15	0	30	30	0.8	16.0	3.0	0.267	5.333	0.680
20	20	0	30	0	0.0	0.0	2.9	0.000	0.000	0.939
20	20	0	30	30	1.6	18.0	2.9	0.552	6.207	0.939
20	25	0	30	0	0.0	0.0	3.7	0.000	0.000	0.920
20	25	0	30	30	2.7	22.0	3.7	0.730	5.946	0.920
20	30	0	30	0	0.0	0.0	4.7	0.000	0.000	0.869
20	30	0	30	30	3.9	26.0	4.7	0.830	5.532	0.869
20	35	0	30	0	0.0	0.0	5.0	0.000	0.000	0.953
20	35	0	30	30	6.7	40.0	5.0	1.340	8.000	0.953
20	35	1	30	0	0.0	0.0	5.5	0.000	0.000	0.866
20	35	1	30	30	0.0	0.0	5.5	0.000	0.000	0.866
20	40	0	30	0	0.0	0.0	5.5	0.000	0.000	0.990
20	40	0	30	30	7.5	47.0	5.5	1.364	8.545	0.990
20	40	0	30	210	8.0	53.0	5.5	1.455	9.636	0.990
20	40	0	30	390	8.2	54.0	5.5	1.491	9.818	0.990
20	45	1	30	0	0.0	0.0	7.0	0.000	0.000	0.875
20	45	1	30	30	0.5	25.0	7.0	0.071	3.571	0.875

Table 4. Performed model runs and results for mixed material layer.

$S = 1: ...$	Q [l/s]	W	l_b [cm]	T [min]	z_m [cm]	l_0 [cm]	h_1 [cm]	Z_m [-]	L_0 [-]	$F_{d,90}$ [-]
30	10	0	30	0.0	0.0	0.0	2.3	0.000	0.000	0.595
30	10	0	30	30.0	2.0	15.0	2.3	0.870	6.522	0.595
30	10	0	42	0.0	0.0	0.0	2.5	0.000	0.000	0.548
30	10	0	42	30.0	0.7	13.0	2.5	0.280	5.200	0.548
30	15	0	30	0.0	0.0	0.0	2.8	0.000	0.000	0.733
30	15	0	30	30.0	3.3	21.0	2.8	1.179	7.500	0.733
30	15	0	42	0.0	0.0	0.0	3.0	0.000	0.000	0.684
30	15	0	42	30.0	1.8	17.0	3.0	0.600	5.667	0.684
30	20	0	30	0.0	0.0	0.0	3.3	0.000	0.000	0.83
30	20	0	30	5.0	4.0	26.0	3.3	1.212	7.879	0.83
30	20	0	30	10.0	4.4	27.0	3.3	1.333	8.182	0.83
30	20	0	30	20.0	4.4	27.0	3.3	1.333	8.182	0.83
30	20	0	30	30.0	4.7	28.0	3.3	1.424	8.485	0.83
30	20	0	30	60.0	5.3	29.0	3.3	1.606	8.788	0.83
30	20	0	30	120.0	5.3	29.0	3.3	1.606	8.788	0.83
30	20	0	42	0.0	0.0	0.0	3.4	0.000	0.000	0.805
30	20	0	42	5.0	2.6	23.0	3.4	0.765	6.765	0.805
30	20	0	42	10.0	3.5	23.0	3.4	1.029	6.765	0.805
30	20	0	42	20.0	3.5	23.0	3.4	1.029	6.765	0.805
30	20	0	42	30.0	3.5	23.0	3.4	1.029	6.765	0.805
30	20	0	42	60.0	3.5	23.0	3.4	1.029	6.765	0.805
30	20	0	42	120.0	3.5	23.0	3.4	1.029	6.765	0.805
30	30	0	30	0.0	0.0	0.0	3.8	0.000	0.000	1.081
30	30	0	30	5.0	6.2	36.0	3.8	1.632	9.474	1.081
30	30	0	30	10.0	6.3	36.0	3.8	1.658	9.474	1.081
30	30	0	30	20.0	7.2	41.0	3.8	1.895	10.789	1.081
30	30	0	30	30.0	8.4	47.0	3.8	2.211	12.368	1.081
30	30	0	30	60.0	9.3	57.0	3.8	2.447	15.000	1.081
30	30	0	30	120.0	9.7	57.0	3.8	2.553	15.000	1.081
30	30	0	42	0.0	0.0	0.0	4.6	0.000	0.000	0.893
30	30	0	42	5.0	4.2	32.0	4.6	0.913	6.957	0.893
30	30	0	42	10.0	5.0	36.0	4.6	1.087	7.826	0.893
30	30	0	42	20.0	8.5	42.0	4.6	1.848	9.130	0.893
30	30	0	42	30.0	8.5	42.0	4.6	1.848	9.130	0.893
30	30	0	42	60.0	8.5	43.0	4.6	1.848	9.348	0.893
30	30	0	42	120.0	7.5	46.0	4.6	1.630	10.000	0.893
30	40	0	30	0.0	0.0	0.0	5.5	0.000	0.000	0.996
30	40	0	30	5.0	7.2	46.0	5.5	1.309	8.364	0.996
30	40	0	30	10.0	10.2	60.0	5.5	1.855	10.909	0.996
30	40	0	30	20.0	11.3	65.0	5.5	2.055	11.818	0.996
30	40	0	30	30.0	11.3	65.0	5.5	2.055	11.818	0.996
30	40	0	30	60.0	11.3	65.0	5.5	2.055	11.818	0.996
30	40	0	30	120.0	12.0	66.0	5.5	2.182	12.000	0.996
30	45	1	30	0.0	0.0	0.0	7.0	0.000	0.000	0.88
30	45	1	30	30.0	1.7	52.0	7.0	0.243	7.429	0.88
30	45	1	42	0.0	0.0	0.0	5.7	0.000	0.000	1.081
30	45	1	42	30.0	0.5	30.0	5.7	0.088	5.263	1.081

3. RESULTS AND DISCUSSION

3.1. General

Flow depths at the ramp toe were determined by ultrasonic probes at the flume's centerline (see Fig. 4a). Additional 3D CFD simulations (96 numerical model runs) were performed in FLOW-3D to confirm experimental model results for downstream flow depths at the ramp toe. As a result, rating curves for all modeled discharges were developed to identify flow depths on the last downstream crossbar (h_1, see Eqs. (3) and (4)).

Table 3 and 4 give model results for all investigated configurations (measured mean scour depth z_m, measured scour length l_0, flow depth at ramp toe h_1, dimensionless mean scour depth Z_m, dimensionless scour length L_0, dimensionless particle densimetric Froude number $F_{d,90}$).

3.2. Scour development

With increasing slopes and increasing discharges, scour development processes within the stilling basin changed. Figure 4 gives a schematic plot of three varying flow conditions. While the straight flow into the downstream sediment basin will generate no major scour development, induced vortexes will impact the initial bed and form the scour profile. For large flow depths at the structure's toe, an additional recirculating vortex will be generated and scouring increase (Fig. 4c). Figures 5 and 6 give additional graphical results for scour profiles of various model runs. An exemplary scour development for various discharges on a crossbar block ramp with a slope of $S = 1:20$ is shown in Fig. 5a. It was found that both the mean scour depth and the scour length will increase with increasing discharges (compare Eqs. (3) and (4)). It also can be shown, that the formation of the scour profile occurs faster for steep ramp slopes ($S = 1:20$) – see Figures 5b and 6. Especially for high discharges and small slopes the scour formation process takes longer than 30 min. Results are taken from the latest measurement time when the scour was fully developed.

(a) Straight flow   (b) Vortex   (c) Vortex and recirculation
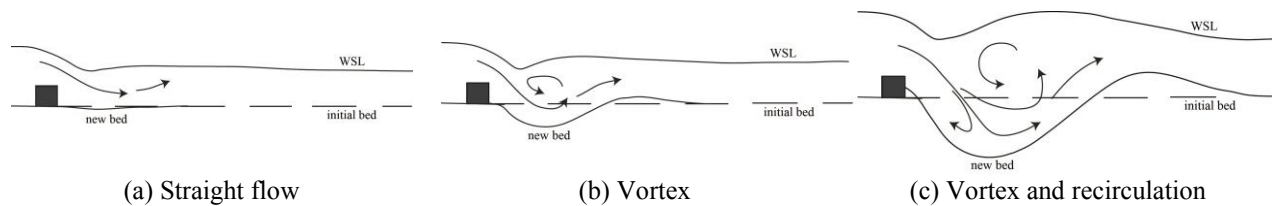
Figure 4. Schematic plot of hydraulic processes influencing scouring.

(a) $S = 1:30$, $T = 30$ min   (b) $Q = 40$ l/s
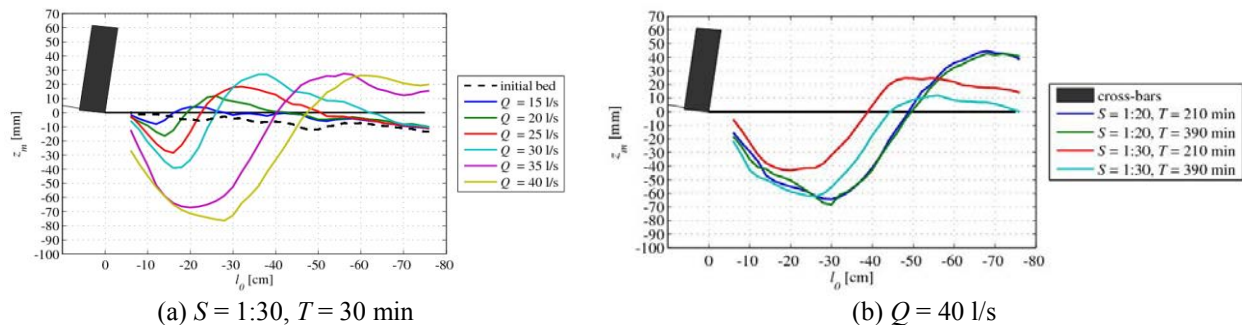
Figure 5. Mean scour profiles (averaged over width) for various ramp slopes, discharges and times, stratified material layer.
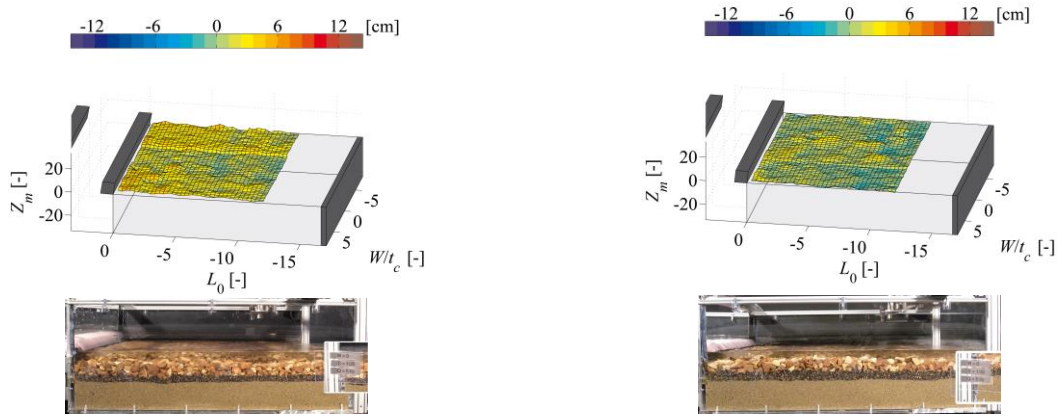
(a) *t* = 0 min, initial bed
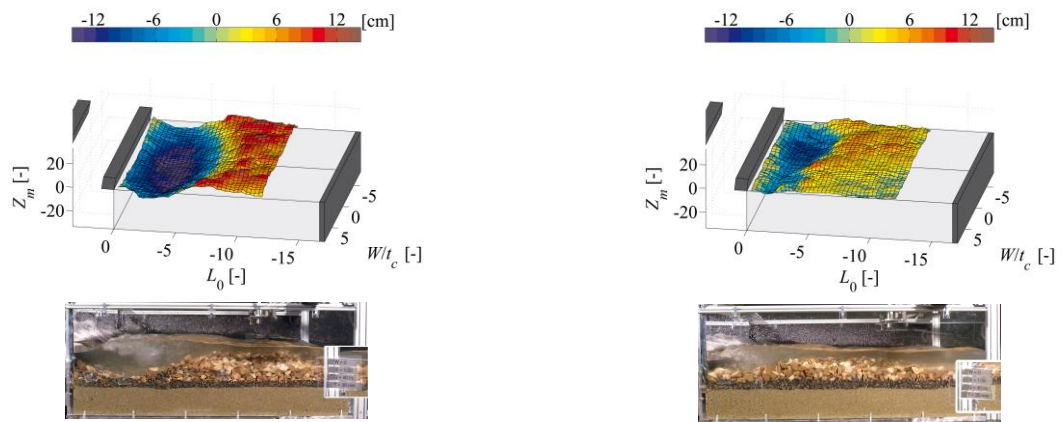
(b) *t* = 30 min
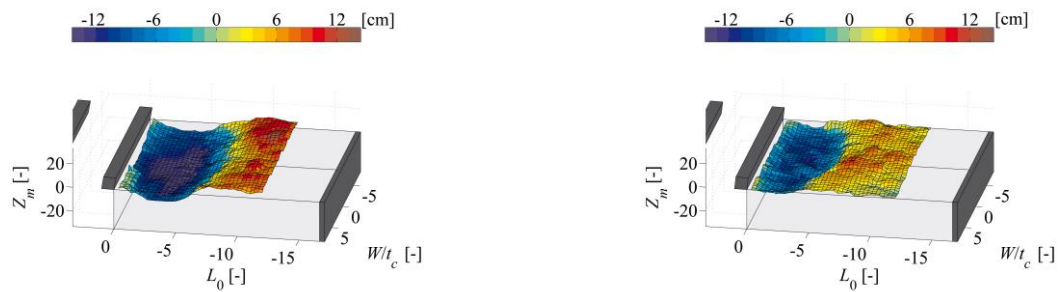
(c) *t* = 210 min
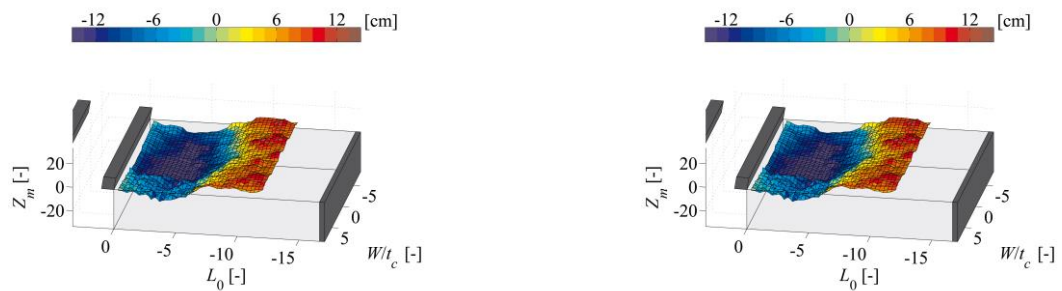
(d) *t* = 390 min

Figure 6. Exemplary scour development for various time steps, stratified layer,
left: S = 1:20, Q = 40 l/s (h_c/H = 0.5467), right: S = 1:30, Q = 40 l/s (h_c/H = 0.3647).

3.3. Data fitting

New formulas are developed to calculate scouring downstream of crossbar block ramps. The dimensionless mean scour depth for stratified material layer can be calculated by (see Fig. 7a):

$$Z_m = 1.13 F_{d,90}^{6.14} \qquad (5a)$$

For the mixed material layer, scouring will be increased. Experiments were only adapted for slopes of $S = 1{:}30$. For this slope the dimensionless mean scour depth for the mixed material layer can be calculated by (see Fig. 7a):

$$Z_m = 1.78 F_{d,90}^{1.90} \qquad (5b)$$

It can be shown, that the ramp slope will impact scour depth development, but a detailed analysis of quantities is not possible within the given investigation. Hence, only a separation for stratified and mixed layers is given with Eqs. (5a) and (5b) with a model quality ± 20 to 30% for most measurement points. Eqs. (5a) and (5b) are valid for $0.5 < F_{d,90} < 1.1$.

For fitting the scour length L_0 it is not necessary to include the slope as well. The dimensionless scour length can be calculated by a simple exponential approach (see Fig. 7b):

$$L_0 = 0.4 \exp(0.53 Z_m) \qquad (6)$$

The accuracy of Eq. (6) is almost better than $\pm 20\%$.

4. SUMMARY AND CONCLUSION

Crossbar block ramps are nature-oriented structures used to conquer large river bottom steps. These hydraulic systems are well suited to fish climb capabilities. But to design structures that will remain stable even during flood events, knowledge of scouring processes is essential. Scouring occurs on the structure within the basins and downstream the ramp. Both can affect the ramp's stability and must be investigated. The present paper dealt with scouring processes downstream crossbar block ramps and analyzes several experimental model setups with various discharges and slopes.

Scouring occurs due to three different hydraulic processes and generally ends within a time period of 30 minutes; except model runs with small slopes and large discharges. Scouring profiles were identified and compared for various discharges in the experimental model. It could be shown, that the scour length follows a simple exponential approach; depending on the scour depth. The scour depth itself majorly depends on a particle densimetric Froude number.

Subsequently, general findings will be itemized for scouring processes downstream crossbar block ramps:
- Three hydraulic processes influence downstream scouring processes.
- Final scour results took less time for steep slopes.
- Decreased mean scour depth occurred with increased crossbar distances.
- Increased mean scour depths with increased slopes.
- Generally scouring finalized after 30 min (in the experimental model) – only for small slopes and large discharges it takes longer time.
- Increased discharge will increase both mean scour depth and scour length.
- The ramp's slope will affect the scouring process – but these influences cannot be quantified in detail.
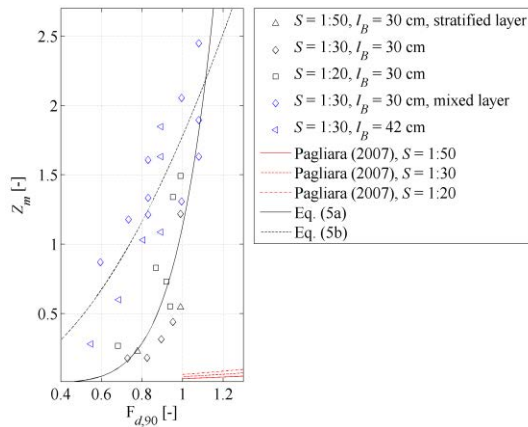
(a1) Mean scour depth Z_m (b1) Scour length L_0
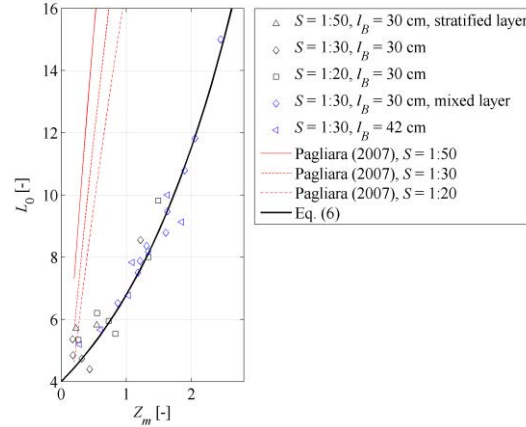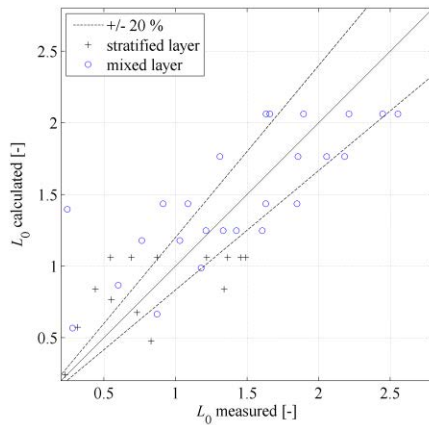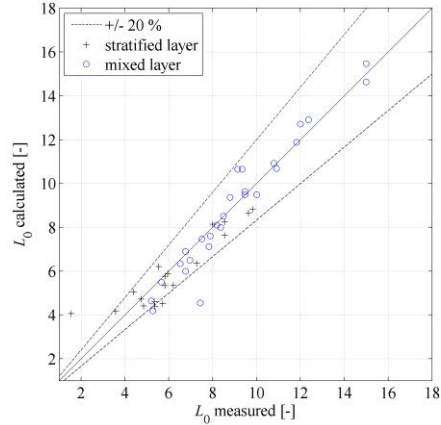
(a2) Model quality   (b2) Model quality

Figure 7. Comparison of new formulas with laboratory data and literature.

5. ACKNOWLEDGMENTS

6. REFERENCES

Aberle, J. (2000). "Untersuchung der Rauheitsstruktur zur Bestimmung des Fließwiderstandes in Gebirgsbächen unter Klarwasserabfluss". *Mitteilungen des Instituts für Wasserwirtschaft und Kulturtechnik*, Vol. 207, University of Karlsruhe, Germany [in German].

BAW (1989). "Anwendung von Kornfiltern an Wasserstraßen", Technical Bulletin, Bundesanstalt für Wasserbau – Federal Waterways Engineering and Research Institute, Karlsruhe [in German].

Ben Meftah, M., and Mossa, M. (2006). "Scour holes downstream of bed sills in low-gradient channels", *J. Hydr. Res.* 44(4), 497-509.

DIN 4047 (1989). "Wasserbau – Teil 5: Begriffe, Ausbau und Unterhaltung von Gewässern". *Deutsches Institut für Normung e. V.*, Berlin, Germany [in German].

DIN 4048 (1987). "Landwirtschaftlicher Wasserbau – Teil 1: Begriffe, Stauanlagen". *Deutsches Institut für Normung e. V.*, Berlin, Germany [in German].

EU-WFD (2000). "Directive 2000/60/EC of the European Parliament and of the Council". 23. October 2000, establishing a framework for Community action in the field of water policy.

Hartung, F.; Scheuerlein, H. (1970). "Design of Overflow Rockfill Dams". *Dam Congress, Montreal*, Article No. R.25 of Q.36, Canada.

Hassinger, R. (1991). "Beitrag zur Hydraulik und Bemessung von Blocksteinrampen in flexibler Bauweise". *Mitteilungen des Instituts für Wasserbau*, Vol. 74, University of Stuttgart, Germany [in German].

Knauss, J. (1979). "Flachgeneigte Abstürze, glatte und rauhe Sohlrampen". *Berichte der Versuchsanstalt für Wasserbau*, Vol. 41, TU Munich, Germany [in German].

Oertel, M., Petersein, S., and Schlenkhoff. A. (2011). "Drag coefficients of boulders on a block ramp due to interaction processes". *J. Hyd. Res.*, 49(3), 372-377.

Oertel, M. (2012). "Cross-Bar Block Ramps – Flow Regimes, Flow Resistance, Energy Dissipation, Stability", Habilitation Thesis, ISBN 978-3-8440-1225-5, Shaker.

Oertel, M., and Schlenkhoff, A. (2012a). "Crossbar Block Ramps: Flow Regimes, Energy Dissipation, Friction Factors, and Drag Forces", *J. Hydr. Engng.*, 138(5), 440-448.

Oertel, M., and Schlenkhoff, A. (2012b). "Scour Development in Basins of Cross-Bar Block Ramps", *Proc. 2nd IAHR European Conference*, Munich, Germany.

Oertel, M. (2013). "In-Situ Measurements on Cross-Bar Block Ramps", *Proc. Intern. Workshop on Hydraulics Design of Low-Head Structures (IWLHS)*, Aachen, Germany, 111-119.

Oertel, M., and Bung, D. B. (2015). "Stability of Bed Material on Crossbar Block Ramps", *J. Sed. Res.*, in press.

Pagliara, S. (2007). "Influence of Sediment Gradiation on Scour Downstream of Block Ramps", *J. Hydr. Engng.*, 133(11), 1241-1248.

Pagliara, S., and Palermo, M. (2008). "Scour control and surface sediment distribution downstream of block ramps", *J. Hydr. Res.*, 46(3), 334-343.

Pagliara, S., Palermo, M., and Carnacina, I. (2009). "Scour and hydraulic jump downstream of block ramps in expanding stilling basins", *J. Hydr. Res.*, 47(4), 503-511.

Pagliara, S., and Palermo, M. (2010). "Influence of Tailwater Depth and Pile Position on Scour Downstream of Block Ramps", *J. Irr. and Drainage Engng.*, 136(2), 120-130.

Pagliara, S., Palermo, M., Kurdistani, S. M., and Hassanabadi, L. S. (2015). "Erosive and hydrodynamic processes downstream of low-head control structures", *J. Applied Water Engng. and Res.*, 3(2), 122-131.

Tamagni, S., Weitbrecht, V., and Boes, R. (2010). "Design of unstructured block ramps: A state-of-the-art review". *Proc. River Flow*, Braunschweig, Germany, 729-736.

Tamagni, S., Weitbrecht, V., and Boes, R. (2014). "Experimental study on the flow characteristics of unstructured block ramps". *J. Hydr. Res.*, 52(5), 600-613.

Whittaker, J.; Jäggi, M. (1986). "Blockschwellen. Wasserbau, Hydrologie und Glaziologie, Vol. 91, TH Zurich, Switzerland [in German].

Decision-making through Sustainability

F. Pardo-Bosch[1] and A. Aguado[2]
[1]Dept. of Political Science, UC Berkeley – Civil Engineering Department, BcnTech
UC Berkeley - Universitat Politècnica de Catalunya (BcnTech)
Berkeley, CA 94720 – Barcelona 08034
USA - SPAIN
[2] Civil Engineering Department
Universitat Politècnica de Catalunya (BcnTech)
Barcelona, 08034
SPAIN
E-mail: francesc.pardo@berkeley.edu – francesc.pardo@upc.edu

ABSTRACT

From immemorial time, dams have contributed significantly for the progress of civilizations. For this reason, nowadays, there is a vast engineering heritage. Over the years, these infrastructures can present some ordinary maintenance issues associated with their normal operation or with ageing processes.

Normally, these problems do not represent an important risk for the structure, but they have to be attended. To do it, owners of dams have to finance many ordinary interventions. As it is impossible to carry out all of them at the same time, managers have to make a decision and select the most "important" ones. However, it is not easy because interventions usually have very different natures (for example: repair a bottom outlet, change gates, seal a crack...) and they cannot use a classical risk analysis for these type of interventions.

The authors, who are aware this problem, present, in this paper, a multi-criteria decision-making system to prioritize these interventions with the aim of providing engineers a useful tool, with which they can prioritize the interventions from the most important to the least. To do it, the authors have used MIVES. This tool defines the Prioritization Index for the Management of Hydraulic Structures (PIMHS), which assesses, in two phases, the contribution to sustainability of each intervention. The first phase measures the damage of the dam, and the second measures the social, environmental and economic impacts. At the end of the paper, a case of study is presented where some interventions are evaluated with PIMHS.

Keywords: Sustainability, decision-making, MIVES, MCDM, Dams, Prioritization.

1. INTRODUCTION

Dams are considered fundamental structures for the development of nations in providing numerous socio-economic and environmental advantages (ICOLD, 2007). Their main functions are water supply, irrigation, flood control throughout the whole year, power generation, navigation, fishing, and even leisure. At the same time, these structures generate obvious environmental and social impacts caused by their construction (ICOLD, 1997). Given the evidence that society cannot live without the benefits which dams provide, it is necessary to maximize the utility of the dams that are already in operation.

Over the years, these infrastructures can present some ordinary maintenance problems associated with their normal operation or with ageing processes. Due to these problems, dams can lose resistance capacity, while, as a general rule, the solicitations, at least, are equal or even bigger than when they started to work. For this reason, direct managers of each structure suggest to their superiors some maintenance interventions to re-establish or to improve functional, mechanical and/or safety aspects of each dam. As it is impossible to carry out all of these interventions (budgets are usually very important) at the same time, general managers have to make a decision and select the most "important" ones. However, it is not easy because interventions usually are very different (for example: repair a bottom outlet, change a gate, seal a crack...) and they cannot use a classical risk analysis for these type of

interventions because they are used to studying events or loads that can provoke the failure of the dam. Moreover, these kinds of studies need sophisticate calculations that required month of work. Thus, it is important to develop a decision support system that ranks, prioritizes, and selects the required maintenance interventions.

Given this need, this communication aims to present the Prioritization Index for the Management of Hydraulic Structures (PIMHS) a multi-criteria decision-making system, based on Integrated Model for Sustainable Value Assessments (MIVES for its name in Spanish) and on Analytic Hierarchy Process (AHP), which orders and prioritizes non-similar maintenance investments in hydraulic structures. The final and most important objective is that *n* maintenance and conservation actions, which have no common characteristics, may be compared, in order to select the ones with best global result to deliver the most benefit to all citizens (Pardo-Bosch 2014, Pardo-Bosch & Aguado 2015).

2. BACKGROUND

2.1. Management classic systems on the hydraulic field

According to ICOLD (1987), a structure is safe when it is free of any condition that may lead to deterioration or destruction. To measure the distance between the real condition of the structure and a state regarded as not safe, the technical community has developed two types of methodologies: Condition Index and Risk Analysis.

Infrastructures management methodologies, which use a condition index, are based on the Pavement Condition Index (Sahin et al. 1977), was developed to study the condition of pavements on airfields. This index assesses the type, the amount, and the severity of damage to obtain a value from 0 to 100, where 100 is assigned to a perfect pavement. Despite the technological advances developed since the 80s, this method remains as the reference system for the air industry (Broten and De Sombre 2001). Using PCI as a reference, the US Army Corps of Engineers developed a Condition Index (CI) to assess the state of the concrete of dams, including spillways (Bullock and Folz 1995), and another one to assess the state of the gates (Greimann *et al.* 1995), because they understood that it was impossible to develop a single system to evaluate all cases. These methods and those that have followed them only focus on the study of the structure, so it is impossible, by their nature, to assess the consequences that the detected damage can cause in other elements, such as the dam or the environment.

Risk analysis, which can also be used to manage hydraulic structures, can be divided in two different groups: stochastic and deterministic. The stochastic group is used to study events or loads that can provoke the failure of the dam, so it is not adapted to the current needs of daily management of dams (ICOLD, 2005). Due to this fact, the Bureau of Reclamation and Army Corps of Engineers (2010) have converted the stochastic approach into a deterministic one, using qualitative or semi-quantitative methods. In this case, risk severity is calculated through Eq. (1), where P(failure) may be low, moderate, high or very high; and the Consequences can be Level 1 (minimum), Level 2, Level 3 and Level 4 (maximum). As the methodology is so general, the problem is that many damages can be located in the same group of preferences. So, it is fantastic to define a first approximation, it is not possible to classify a large number of very similar interventions in order to select only the most important ones.

$$Risk=P(failure) * Consequences \tag{1}$$

2.2. Integrated Model for Sustainable Value Assessments (MIVES)

In civil engineering, as in other fields, multi-criteria decision-making (MCDM) methodologies have been incorporated on the decision making process in order to assist those who have to make decisions. These systems usually assess a set of variables to compare the benefits and damages of different alternatives. Among them, there is the Integrated Model for Sustainable Value Assessments (MIVES) a methodology developed in Spain within the field of industrial construction (San-José and Cuadrado 2010, Aguado *et al.* 2012, Pons and Aguado 2012).

MIVES has the particularity that combines multi-criteria decision-making and multi-attribute utility theory (MCDM, MAUT) with the concept of value function (Alarcon, 2010) in order to standardize the indicators with different units

(very typical for a global comparison); this process is more qualitative than quantitative in nature,. Its first applications were within the field of industrial construction, but over the years it has been adapted to any construction typology, in aspects such as localization, materials, energy and water consumption, construction solutions, etc.

The MIVES method has special features that are lacking in other sustainability assessment methods. It not only focuses on costs or product data, because it offers the possibility of incorporating other types of requirements, for example, social or environmental impacts, and doing so at any stage of the life cycle of a construction. MIVES encompasses the upward process of assessing indicators and weighing sub-levels, effectively integrating the set of indicators, criteria, requirements and fields of assessment proposed, and thus emerging as a dynamic and convenient method. To reflect the relative importance and prioritization of each requirement, criterion, and indicator level weights are assigned by decision-makers using the Analytic Hierarchy Process (AHP), developed by Saaty (1980).

Until this project, MIVES had been used to comparing homogeneous alternatives (for example, to decide the location of a factory between two different cities), but now the problem is much more complex because the alternatives are not homogenous, and as a result, it will be necessary to introduce a modification in the regular structure of MIVES.

3.   SUSTAINABILITY AS A GUIDE TO DECIDE

As seen on section 2, MCDM have been and are a reference as methodologies to assist the decisions makers. The only problem, which is not so trivial, is to find, among stakeholders, consensus on the definition of the concepts to be measured, either by variables or attributes.

Sustainability has been introduced firmly, despite being a recent discipline (United Nations World Commission on Environment and Development used this concept for the first time in the Brundtland Report in 1987), as a valid argument when it is necessary to create consensus to define the variables that have to be measured in some areas of the civil engineering sector. Sustainability, according the World Commission on Environment and Development (1987), is the capacity to meet the needs of the present without compromising the ability of future generations to meet their own needs. The concept of sustainable development does imply limits - not absolute limits but limitations imposed by the present state of technology and social organization on environmental resources." Any sustainable development is based on a long-term approach, taking into account the inseparable nature of environmental, social and economic impacts of human actions, as shown in Figure 1 (United Nations 2013).
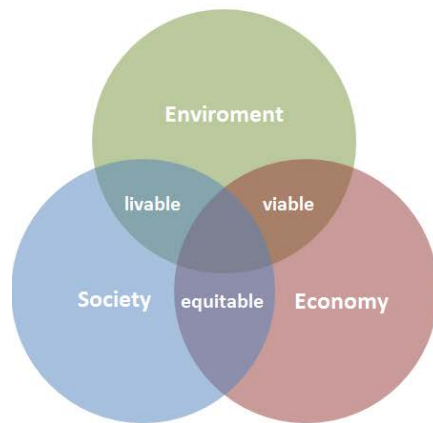
Figure 1. Axioms of sustainability

The *Economic* area assesses the use given to the limited economic resources of the decision-makers, either to perform a new project or to maintain it in operation. Executing a project 'A' can mean not executing project 'B', so companies (public or private) should strive to achieve maximum yield. The *Environmental* area considers the capacity of the project to preserve the environment (natural and constructed) in which the new project should be

located. The goal is to promote those projects that encourage this preservation. Finally, the *Social* area evaluates the consequences (direct or indirect) that a project could generate on people that use or live with it.

Despite its transcendence, in civil engineering, sustainability as a main argument of a multi-criteria analysis has only been used to select, in a specific project, the most convenient alternative among a finite number of homogeneous alternatives, as shown in Shang et al. (2004), Abrishamchi et al. (2005), Comisión Permanente del Hormigón (2008), Koo and Ariaratnam (2008), and Ariaratnam et al. (2013), among others. Due to the existing hole in this field, the decision model will use the axioms of the sustainability as main guidelines.

4. NEW DECISION-MAKING MODEL

In a dam, it is possible to find structural units (*SU*) as different as: the body of the dam (*BD*), the abutments (*Ab*), the foundation (*Fd*), the reservoir (*Rv*) and auxiliary structures (*AS*). Each of them has its functions, all essential for the development of the hydraulic activity. These structures can present very different types of damage, associated with different causes that must be repaired in order to keep operating the dam. Given the evidence that the interventions needed will correct the damages will be also very different, it is necessary, according to Pardo-Bosch and Aguado (2015), to divide the analysis and evaluation process in two phases (see Figure 2).
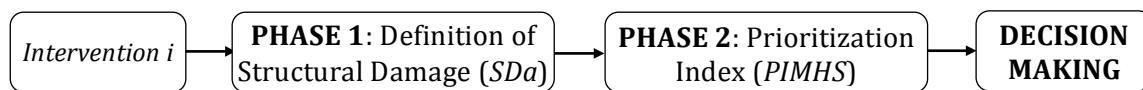
Figure 2. Decision Model

4.1. Structural damage (phase 1)

To understand the benefits of an intervention, it is essential to know the damage that affects the structure, because severe damage means severe consequences, and it is important to remember that the mission of owners and managers is to avoid negative consequences. In order to assess the damage that affects the structure, a new engineering concept called Structural Damage (*SDa*) has been defined, which is a universal system (valid for all structural typologies) to perform a semi-quantitative evaluation of the capacity of the structure to operate without compromising the safety. As equivalent units, *SDa* allows technicians to compare the condition of different structural units, which is basic in order to compare the consequences in the next phase.

SDa, as it shown in Figure 2, is evaluated through 4 independent and complementary variables that ensure the rigor and quality needed with that this type of analysis. These variables are defined to answer strategic questions (see Figure 2). All of them are assigned a score, which ranges from one (very low) to five (very high/ very significant) points as recommended in Williams (2009). As all variables are independent, each score is not conditional upon the values of others. The 4 variables are Degree of Damage (*DeD*), Location of Damage (*LoD*), Extension of Damage (*ExD*) and Evolution of Damage (*EvD*).

- Degree of Damage (*DeD*), which answers the question "*what is the severity of the damage?*" This defines the intrinsic seriousness of the damage. It means that *DeD* assesses the physical condition of the structure after it has been modified by the action of the damage. The decision maker will assign 5 points when the damage compromises the ultimate limit-state of the structure, and 1 point when the problem (damage) be simply aesthetic

- Location of Damage (*LoD*), which answers the question "*where does the damage happen?*" This defines the relative position where damage appears. The importance of damage will vary in accordance with the relevance of its location on the structural unit.

- Extension of Damage (*ExD*), which answers the question "*what is the extent of the damage?*" This defines which part of the structure is affected by the damage. To obtain the punctuation of the variable easily, the measurement is done in percentage.

- Evolution of Damage (*EvD*), which answers the question "*how the damage is evolving?*" This defines the potential capacity of the pathological process to increase the damage in the immediate future.

To obtain the final value of the *SDa*, these 4 variables are related through a summation [see Eq. (2)], where they are weighted according to their relative importance as determined by a group of experts using the Analytic Hierarchy Process (Saaty 1980).

$$StD(A_x)=0.35DeD(A_x)*0.35LoD(A_x)*0.10ExD(A_x)*0.20EvD(A_x) \qquad (2)$$

4.2. Prioritization Index for the Management of Hydraulic Structures (phase 2)

Phase 2 of the decision model develops, through MIVES, the Prioritization Index for the Management of Hydraulic Structures (*PIMHS*). *PIMHS* is an index that assesses the degree of sustainability associated with a proposed maintenance intervention. The evaluation is semi-quantitative and uses the value of *SDa* to relate the damage and the consequences. The degree of sustainability depends on the social, environmental and economic consequences, for this reason the decision model is articulated through the 3 axioms of sustainability, as it shown in Table 1, which, in this case, are defined as:

Table 1: Decision framework for the Investment Prioritization Index

	Requirements	Criteria	Indicators
PIMHS	R1. Social (50%)	C1. Physical people (60%)	I1. Population Exposed to Risk* (70%)
			I2. Collective Perception of Risk (30%)
		C2. Effects (40%)	I3. Essential Services Affected* (50%)
			I4. Material-Economic loses* (50%)
	R2. Environmental (15%)	C3. Environmental impact (100%)	I5. Negative Impact of Damage* (65%)
			I6. Value Added Actions (35%)
	R1. Economic (35%)	C4. Service change (50%)	I7. Annual Unitary Cost* (100%)
		C5. Return on investments (50%)	I8. Maintenance Supervision Savings (30%)
			I9. Estimation Increase in Production (70%)

* Indicators conditioned by SDa

- The Social requirement assesses the affects that damage can cause on people. The health and welfare of people are prioritized above any other consideration. The requirement is divided into two criteria: Individuals, which evaluates direct damages that a person may suffer; and conditions, which assesses the indirect damage that may alter the normal activity of people or companies.

- The Environmental requirement assesses the negative impacts that damage can generate on the natural surroundings of the dam. Also, it assesses the positive impacts that interventions generate on that environment. Usually, these kinds of impacts are not very important (the most important impact was occasioned by the construction of the dam) so the weight of this requirement should be pretty small.

- The Economic requirement aims to maximize the yield of every dollar invested in eliminating damages, which is not the same as to prioritize those actions that will increase the owner's benefits. This requirement breaks down into two criteria to complete the economic study of the project to be carried out: the first one analyzes the initial investment, and the second one the potential impact of that investment.

The final result of the *PIMHS* for each investment project is calculated according to Eq (30 as the weighted sum of each indicator, $IV_j(A_{i,x})$. As previously mentioned in section 2, the relative weights of each indicator (w_{I_j}), criteria

(w_{C_y}) and requirement (w_{R_t}) were calculated by the Analytic Hierarchy Process (AHP), and the indicator $IVj(Pi,x)$ with the function value of each indicator.

$$PIMHS(A_x) = \sum w_{R_t} \cdot w_{c_y} \cdot w_{I_j} \cdot IV_j(A_{i,x})$$

(3)

PIMHS value goes from 0 (low priority) to 1 (high priority). A qualitative assessment may be assigned to each project according to the *PIMHS* five category levels presented in Table 2 (ICE 2010, ASCE 2013). Projects will likely be classified among the B, C and D level due to the high demanding requirements of the multi-criteria analysis. The maximum and minimum contributions to sustainability are represented by levels A and E, respectively. According to Pardo-Bosch and Aguado (2015), investment projects may hardly score over 0.8 due to the highly demanding requirements of a multi-criteria analysis. At the same time, it is unlikely to get projects with an E level score, as those are directly rejected beforehand for its obvious lack of contribution to sustainability.

Table 2. PIMSH levels to classify the projects (ICE, 2010; and ASCE, 2013)

Level A	Level B	Level C	Level D	Level E
$0 \leq PIMHS < 0.8$	$0.8 \leq PIMHS < 0.6$	$0.6 \leq PIMHS < 0.4$	$0.4 \leq PIMHS < 0.2$	$0.2 \leq PIMHS < 0$

This paper, because of its length, cannot explain the details of the calculation of the indicators presented in Table 1. The reader can find complete information either on Pardo-Bosch (2014) or Pardo-Bosch and Aguado (2015).

5. CASE OF STUDY

This section aims to present a real case in which the decision-maker could use *PIMHS* to prioritize its maintenance investments. Nine (9) different interventions have been selected to show the usefulness of this tool. All of them were projected by a private hydroelectric company in 6 different dams. The prioritized interventions are described below:

A1.- Treatment and sealing of cracks which affect two thirds of the dam, mainly the left abutment.

A2.- Building a wall to reinforce the rock mass where the dam is supported. The aim is to increase the safety factors, and thus prevent slippage.

A3.- Reparation and reinforcement of a land retaining wall on the road access to hydroelectric power station, where it is registered low displacements.

A4.- Replacing valves of bottom outlets to adapt them to the design criteria. The current ones suffer a widespread deterioration due to aging. Furthermore water leaks are considerable.

A5.- Grout injections to waterproof the dam body, with the aim of halting: the loss of cohesion, increased porosity and surface erosion.

A6.- Injection of cold joints in the dam body where has appeared some water leaks.

A7.- Reconstruction of a side compartment (10m high) collapsed by an avenue. There is no risk for people or environment.

A8.- Stabilizing a rock mass to avoid a landslide, which could generate a wave that would affect the dam crest, as well as the dam body.

A9.- Injection of cold joints in dam body. They have been opened by the combined action of concrete expansion and uplift pressure.

5.1. Prioritization

Due to the limited extent of this communication, it is not possible to present the evaluation of each variable of the decision model (the reader can find more information on Pardo-Bosch 2014). In order to present the results, Figure 3

shows, for each of the 9 interventions, the value (from 0 to 1) of each indicator, before applying their weight. It is easy to see that the value of each indicator varies significantly depending on the intervention, which means that all of them are important to generate discrimination among the interventions.
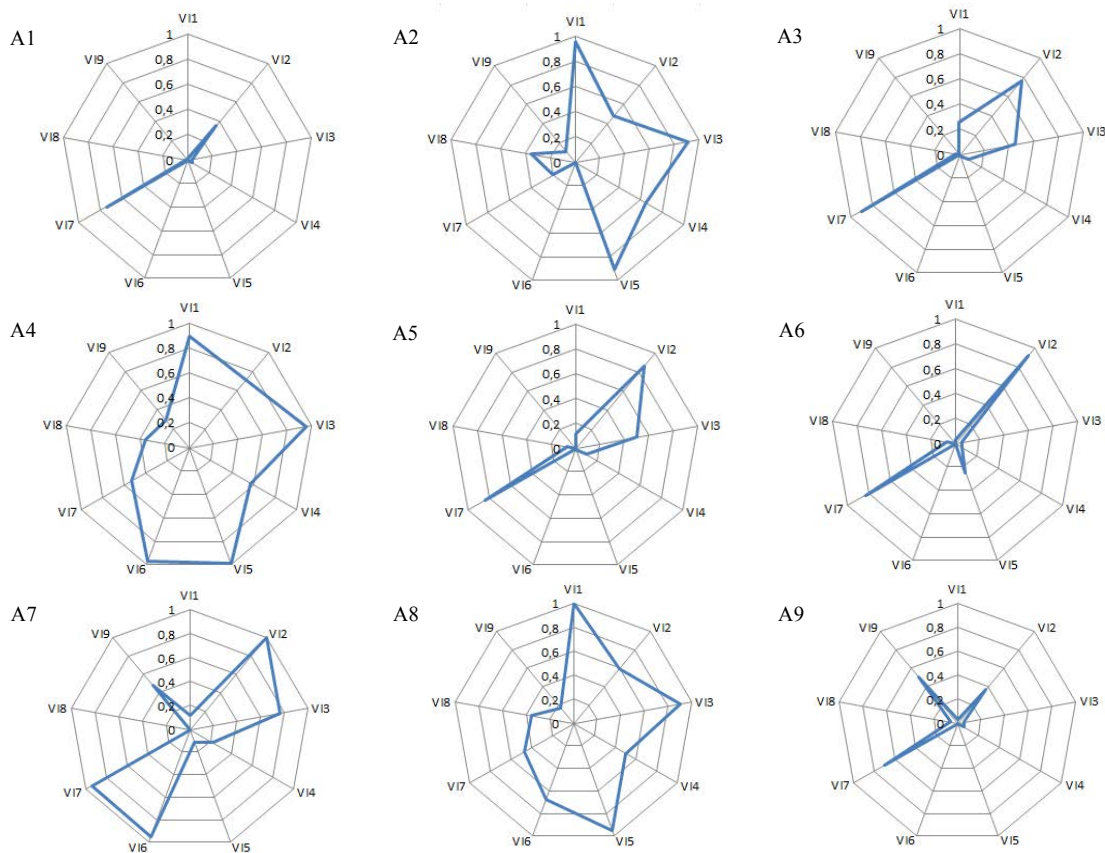
Figure 3. Indicators value (from 0 to 1) for each project

The prioritization is presented in Table 3. As the reader can see, the variability of the PIMSH values for the intervention options (values are ranged between 0.22 and 0.77) is sufficient to help identify the more important options. It's also important to remark regarding three different aspects. First, the order that we obtain with PIMSH is not the same as would be obtained if using only the *SDa* parameter (as an example, intervention A2 is located on the 3rd position using *PIMHS*, while it would have been located on the 5th position only using *SDa*), so we need to use both phases of the decision model. Another relevant aspect is that the cost of the operation does not determine the result of the classification. The first two prioritized interventions are much more expensive than the third, for example. Finally, it's important to say the all of structural units are ordered randomly, so none of them determine the result.

5.2. Sensitivity analysis

Sensitivity analyses are essential in any multi-criteria decision-making tool. These studies involve changing the value of variables to determine the impact that they can have on the final outcome (French 2003). In this case, to do this study, three new alternatives are presented, which were obtained by changing the weight of the requirements in the decision tree (see Table 4). Variation 1 and Variation 2 represent two combinations with weights that are considered consistent (possible).

On Variation 1, the weight of social requirement is reduced by 20%, so it goes from 50% to 40%. The remaining 10% is divided in two equal parts between the other two requirements. On variation 2, the weight of social

requirement is increased by 20%, so it goes from 50% to 60%. In that case, the additional 10% was obtained from the economic, as it is not possible to reduce more weight from the environmental requirement. Moreover, in Variation 3, the *SDa* was removed, but the weight remained the same as in the original decision model. The aim of this Variation is to show the significance of the *SDa*.

Table 3. Interventions classification obtained by PIMSH

Classification	Actuation	*PIMSH*	*SDa*	Level	*SU*	Cost ($)
1	A4	0,70	4,25	B	*AS*	4,500,000
2	A8	0,66	4,35	B	*Rv*	5,500,000
3	A2	0,57	3,35	C	*AS*	160,000
4	A7	0,48	4,2	C	*DB*	470,000
5	A3	0,34	2,95	D	*Ab*	7,500,000
6	A5	0,31	3,45	D	*DB*	330,000
7	A6	0,27	2,65	D	*DB*	270,000
8	A9	0,22	2,65	D	*DB*	330,000
9	A1	0,17	2,05	E	*DB*	220,000

Table 4. Weight of the requirements in each alternative

	Social	**Environmental**	**Economic**
Initial Weight (%)	50	15	35
Variation 1 (%)	40	20	40
Variation 2 (%)	60	15	25
Variation 3	Initial Weight, without StD		

In Figure 4a, the reader can see that the results of Variations 1 and 2 do not introduce big changes in the valuation for the interventions, and for this reason the prioritization order is exactly the same that was obtained by the original weight. These results demonstrate the robustness of the model.

The case of the Variation 3 (V3) is quite different. Without the *SDa*, the evaluation of the interventions, in some cases, is different enough to change the order of the prioritization (see Figure 4a and 4b). This result reinforced the indivisible nature of the two phases of the decision model.
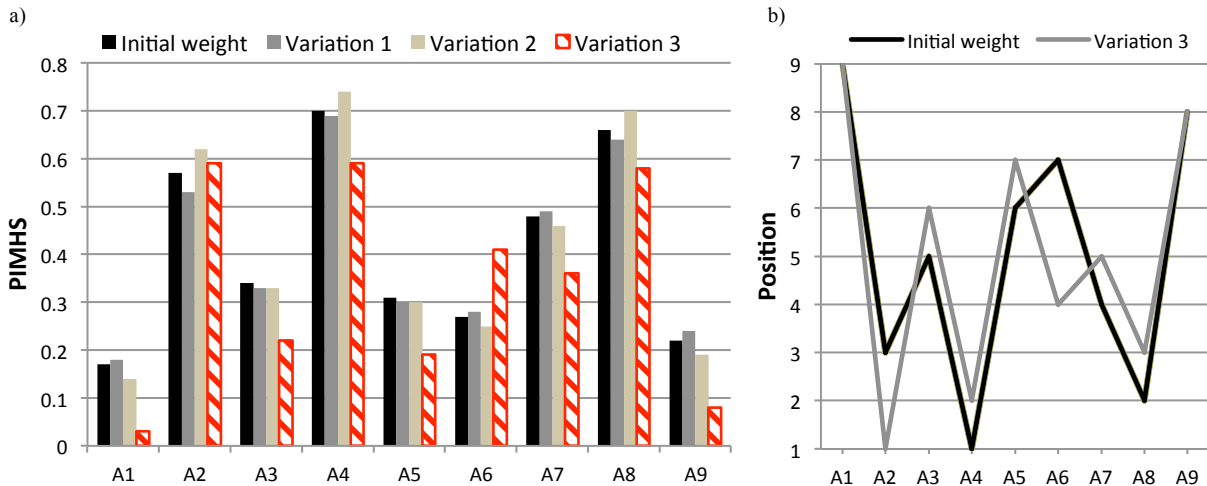
Figure 4. a) Value for each intervention in each variation of weight; b) Classification order Initial Weight vs V3

6. CONCLUSIONS

PIMHS allows prioritizing maintenance interventions in hydraulic structures with technical rigor. The main contribution of PIMSH is that it allows comparing different interventions, which would take place in very different hydraulic structures. The definition of the Structural Damage (*SDa*) is essential in order to allow comparisons between different interventions. Another advantage is that an expert can assess a large number of interventions in a few hours because the analysis is very simple, but at the same time, it is also very accurate.

This multi-criteria decision model based on MIVES will minimize the subjectivity in the entire decision-making process, and it will help companies and public administrations to explain their policies. Sustainable development is, at all times, the main argument that guides the process through the decision three requirements: economic, environmental, and social.

Once the model is defined, each institution can change the weight of any variable to introduce its philosophy or the citizens' demands in the decision-making process.

7. ACKNOWLEDGMENTS

8. REFERENCES

Abrishamchi, A.; Ebrahimian, A.; Tajrishi, M.; and Mariño, M. (2005). "Case Study: Application of Multicriteria Decision Making to Urban Water Supply." Journal of Water Resources Planning and Management, 131(4), 326–335. DOI: 10.1061/(ASCE)0733-9496(2005)131:4(326).

Aguado A.; del Caño A.; de la Cruz P.; Gómez P.J. and Josa, A. (2012). "Sustainability assessment of concrete structures within the Spanish structural concrete code". J Constr Eng M ASCE 2012;138(2):268–76.

Alarcón, B.; Aguado, A.; Manga, R. and Josa, A. (2010). "A Value Function for Assessing Sustainability: Application to Industrial Buildings". Sustainability, 3(1), 35-50; Doi:10.3390/su3010035.

Ariaratnam, S.; Piratla, K.; Cohen, A.; and Olson, M. (2013). "Quantification of Sustainability Index for Underground Utility Infrastructure Projects". Journal Construction Engineering and Management. DOI: 10.1061/(ASCE)CO.1943-7862.0000763.

ASCE (2013). "Report card for America's infrastructure". American Society of Civil Enginyers, Virgina, 74 p.

Broten, M. and De Sombre, R. (2001). "The Airfield Pavement Condition Index (PCI) valuation Procedure: Advantages, Common Misapplications, and Potential Pitfalls". 5th International Conference on Managing Pavements, Seattle, 9 p.

Bullock, R.E. and Foltz, S.D. (1995). "REMR Management Systems – Navigation and Reservoir Structures Condition Rating Procedures for Concrete in Gravity Dams, Retaining Walls, and Spillways". Repair, Evaluation, Maintenance, and Rehabilitation Research Program, Technical Report REMR-OM-16. U.S. Army Corps of Engineers, Washington, DC, 73 p.

Comisión Permanente del Hormigón (2008). "Instrucción de hormigón estructural EHE-08". Ministerio de Fomento, España, 722 p.

de la Fuente, A.; Pons, O.; Aguado, A. and Josa, A. (2016). "Multicriteria-decision making in the sustainability assessment of sewerage pipe systems". Journal of Cleaner Production, 112(5): 4762-4770. doi: 10.1016 / j.jclepro.2015.07.002

Greimann, L.; Stecker, J. and Nop, M. (1995). "REMR Management Systems—Navigation Structures, Condition Rating Procedures for Tainter Dam and Lock Gates" . Repair, Evaluation, Maintenance, and Rehabilitation Research Program,Technical Report REMR-OM-17. U.S. Army Corps of Engineers, Ames, Iwoa, 80 p.

ICE (2010). "The state of the nation infrastructure. Infrastructure 2010". Institution o Civil Engineers, London, 23 p.

ICOLD (1997). "Dams and the Environment". 16 p.

ICOLD (2007). "Las presas y el agua en el mundo". París, 68 p.

Koo, D. and Ariaratnam, S. (2008). "Application of a Sustainability Model for Assessing Water Main Replacement Options". Journal Construction Engineering and Management, 134 (8), 563–574. Doi: 10.1061/_ASCE_0733-9364_2008_134:8_563.

Pardo-Bosch, F (2014), "Gestión integral de obras hidráulicas: del diagnóstico a la inversión". Tesis doctoral. ETSICCP. Barcelona. UPC

Pardo-Bosch, F. and Aguado, A. (2015). "Investment priorities for the management of hydraulic structures". Structure and Infrastructure Engineering: Maintenance, Management, Life-Cycle Design and Performance, 11(10), 1338-1351. doi: 10.1080 / 15732479.2014.964267

Pardo-Bosch, F. and Aguado, A. (2016). "Sustainability as the key to prioritize investments in public infrastructures". Environmental Impact Assessment Review. *Under review*.

Pons, O. and Aguado A. (2012). "Integrated value model for sustainable assessment applied to technologies used to build schools in Catalonia, Spain". Build Environ 2012;53:49–58.

Saaty, TL. (1980). "The Analytic Hierarchy Process". McGraw-Hill. New York, USA. ISBN:0-07-054371-2

San-José JT and Cuadrado J. (2010). "Industrial building design stage based on a system approach to their environmental sustainability". Constr Build Mater 2010;24(4):438–47.

Sahin, M. Y.; Darter, M. I. and Kohn, S. D. (1977). "Development of a Pavement Maintenance Management System, Vol. I-V". U.S. Air Force Engineering Services Center, Tyndall AFB.

Shang, J.; Tjader, Y. and Ding, Y. (2004). "A Unified Framework for Multicriteria Evaluation of Transportation Projects". IEEE Transactions on Engineering Management, 51 (3), pp. 300-313.

United Nations (2013). "Sustainable Development Challenges. World Economic and Social Survey 2013". U. N. Publication. New York. 181 p. ISBN 978-92-1-109167-0.

Williams, M. (2009). "Introducción a la Gestión de proyectos" [The principles of project management]. Anaya, Madrid, Spain, 224 pp.

South Channel Dam Rehabilitation Project: Successfully Addressing Dam Rehabilitation Challenges

M.D. Graeser[1] and M.C. Jensen[2]
[1]Alden Research Laboratory, Inc.
Fort Collins, CO 80525
USA
[2]Avista Utilities
Spokane, WA 99220
USA
E-mail: mgraeser@aldenlab.com

ABSTRACT

The Post Falls South Channel Dam is located on the Spokane River in Post Falls, Idaho. The concrete gravity dam was constructed in 1906 and was recently rehabilitated. The rehabilitation project included several design elements; the primary objectives were the replacement of the six spillway gates and hoists and significant rehabilitation of the concrete. The South Channel Dam rehabilitation encountered several challenges due to the age and condition of the existing structure, the large scale of the rehabilitation, and the location of the project. The concrete rehabilitation addressed several challenges, which are presented in detail. The existing concrete consisted of cyclopean concrete; concrete demolition and surface preparation also revealed large voids and substantial areas of low strength material. This paper presents lessons learned along with procedural methods implemented for effective change management during construction. The project was ultimately a success in a large part due to the team approach and practices implemented during construction.

Keywords: *Construction Management, Cyclopean Concrete, Dam Rehabilitation, Dam Safety*

1. INTRODUCTION

South Channel Dam is one of three dams within the Post Falls Hydroelectric Development (HED) owned and operated by Avista Utilities. The dam was built in 1906 and has recently undergone extensive rehabilitation to improve its durability, safety, maintenance, and operation. Originally conceived as a gate refurbishment project, the scope evolved to include significant structural rehabilitation and ultimately included spill gate and hoist replacement, structural improvements to address deteriorated concrete, rock stabilization, and temporary works including dredging and cofferdam construction. Although a relatively small dam, the rehabilitation was a complex project that included mechanical, electrical, structural, and geotechnical design and required environmental permitting and monitoring during construction. The project is also located in a high-visibility area within a public park that remained in active use during construction.

Due to the age of the structure and the location of the project, several challenges were encountered. The challenges and solutions developed for the existing concrete are presented. Based on data collected prior to construction, the original concrete was known to consist of cyclopean concrete with voids, seams, and cold joints. The condition of the concrete, however, was worse than expected. The concrete demolition revealed that the concrete was in poor condition not only at the surface, but also at depth, with alternating layers of high and low cement content and pockets of low strength material. The observed condition of the original concrete necessitated adjustments to the design and detailing during the construction phase.

This paper presents technical and procedural methods used to resolve challenges typical in dam rehabilitation projects. This paper also presents lessons learned along with procedural methods implemented for effective change management during construction. The owner, design engineers, consultants, inspector, and contractor worked as a

unified team to effectively adapt the design as needed, while maintaining balance between documentation needs and construction schedule, resulting in successful project execution.

1.1. DESCRIPTION OF THE FACILITY

Avista Utilities owns and operates the Post Falls Hydroelectric Development (HED), located on the Spokane River in Post Falls, Idaho. The Post Falls HED consists of three concrete gravity dams spanning three separate channels of the river. North Channel Dam is the primary spillway structure, Middle Channel Dam contains an integral powerhouse, and South Channel Dam is the secondary spillway structure.

South Channel Dam is a concrete gravity structure approximately 40 meters (130 feet) long and 11 meters (35 feet) high. The dam includes a 23 meter (76 foot) long gated spillway section and an overflow section. Prior to the rehabilitation, the South Channel Dam spillway gate system consisted of six vertical slide gates (each approximately 1.8 meters wide by 4.0 meters high) that were manually operated by means of a crest mounted rack and pinion type hoisting system. Significant modifications and upgrades to South Channel Dam (prior to the recent rehabilitation project) included replacement of the original wooden gate panels with steel gates in the late 1980s and installation of six post-tension anchors in 1992 to improve global stability.

1.2. PROJECT SCOPE

The Post Falls South Channel Dam rehabilitation project was originally expected to only include gate refurbishment (gate surface preparation and gate recoating). Prior to design, further evaluation by the owner and engineer of the existing gates and the existing concrete determined that more extensive rehabilitation was needed.

The objective of the South Channel Dam Rehabilitation Project was to replace the six spillway gates and rehabilitate the concrete dam. The project included geotechnical engineering, structural engineering, mechanical engineering, and electrical engineering. The spillway gates and associated hoist mechanism were removed and replaced with six new spillway gates; each were 2.1 meters wide by 4.2 meters high (6.8 feet wide by 13.7 feet high). The new gates are of a modern steel roller-gate design with wire rope hoists. Deteriorated concrete was removed over much of the exposed surfaces and replaced with new concrete. A consolidation grouting program was also included in the dam rehabilitation. The existing mule house was replaced with a new concrete masonry structure that houses a new motor control center and controls for the gate hoists. Figure 1 shows photographs of South Channel Dam before and after the rehabiliation project. Figure 2 shows a general rehabilitated dam section at the spillway gate.

Figure 1. South Channel Dam, Before and After Rehabilitation
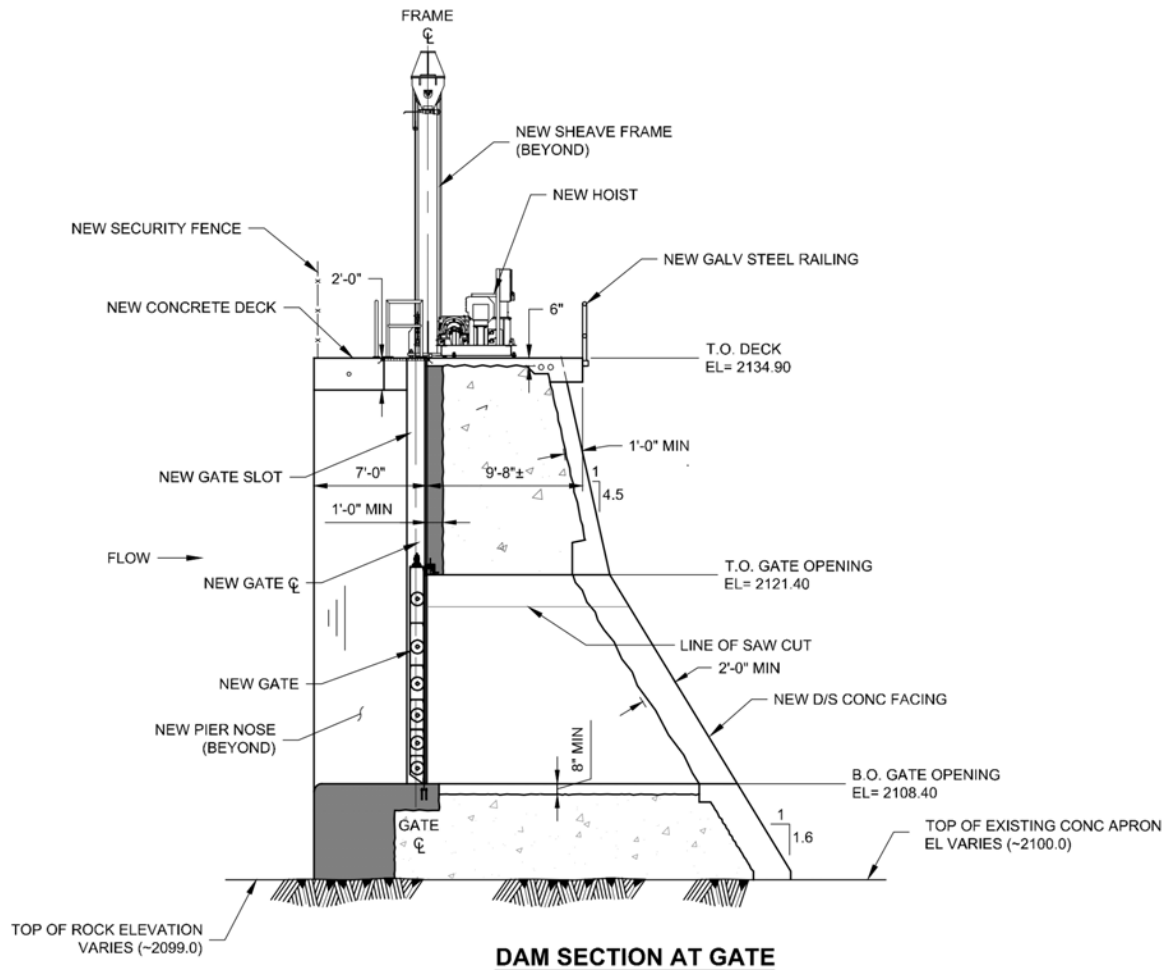
Figure 2. General Dam Rehabiliation Section at Gate

2. CHALLENGES

Challenges and changes were expected for the South Channel Dam rehabilitation project due to the age and condition of the existing structure and the large scale of the rehabilitation. The design addressed the challenges as much as possible and anticipated the features that were most likely to be affected by change due to conditions discovered during construction. Specific challenges encountered during the rehabilitation construction of the South Channel Dam include the following:

- Construction within the boundary of Q'emiln Park with continued public access in close proximity of the dam.
- Flooding the toe of the mechanically stabilized embankment crane pad due to unforecasted stream flows into Lake Coeur d'Alene.
- Turbidity from dredging affecting diver visibility.
- Discovery of an old grenade near the base of the cofferdam.
- North abutment rock upstream of the dam was severely undercut below the normal water level, impacting the cofferdam construction and requiring the design and construction of an additional concrete wall.

- North abutment rock stabilization required for worker safety.
- Settling of the cofferdam structural fill during the dewatering process.
- Cofferdam seepage due to bedrock fissures at the bottom and sides and interface with the cofferdam.
- Incorrect as-built drawings from the original construction.
- Poor quality of the existing concrete.
- Unexpected bedrock outcropping upstream of Spill Gate 1.
- Weak zones and heterogeneous sections of bedrock at the dam foundation.
- Electrical conduit congestion at the new concrete top deck.

This paper will present the general approach used to address the challenges and changes encountered during construction. The challenges and associated solutions developed for the rehabilitation of the existing concrete will be described in detail; other challenges identified above will not be covered.

2.1. GENERAL APPROACH

By nature, rehabilitation projects are challenging and often require adjustments due to actual conditions encountered during construction. Due to the nature of the project, the team recognized from the beginning that there would be change and expected challenges during construction. As a result, a team approach was emphasized and efficient change management was implemented early in construction.

2.1.1. Team Approach

The owner, design engineers, inspector, and contractor worked as a team to successfully complete the project. All members of the team had a common understanding of expectations, design intent, etc. Clearly defined roles, responsibilities, and lines of communication were also established.

The design intent was effectively communicated to all levels during construction. The design engineers placed an emphasis on explaining the design intent to the team. This helped everyone understand the important aspects of the design, and it also fostered a cooperative atmosphere. The existing post-tension anchors are an example of an item that everyone had to understand and respect; 4,180 kN (940 kips) of post-tension load is a substantial compressive force during concrete demolition.

In the spirit of this team approach, not only the inspector, but also the construction workers were looking out for the quality of the project. For example, after the structural engineer explained the importance of eliminating and avoiding feathered edges at the interface between the new facing concrete and the rock abutments to the construction team, one of the demolition subcontractor workers noticed a similar situation at a different location. The demolition worker notified the structural engineer, and the correct adjustment was made in the field.

In addition to weekly construction meetings, the project also implemented numerous onsite pre-construction meetings to discuss key construction steps well ahead of the event. This is often standard practice, but it is critical to rehabilitation projects. The pre-construction meetings ensured that everyone was prepared and knew what to expect before the busy construction activities began. The South Channel Dam rehabilitation project included pre-construction meetings regarding the access road rock blasting, cofferdam, concrete demolition, concrete placement, cold weather concrete, consolidation grouting, gate installation, and the hoisting equipment.

2.1.2 Efficient Change Management

The team recognized from the beginning that there would be challenges and changes; therefore, the team developed a process for efficient change management during construction to reduce potential impacts to schedule and expense that might occur using a traditional RFI process. The Engineer Supplemental Information (ESI) process was developed. An ESI is basically a fast-track Request for Information (RFI) process. The ESIs were numbered

(similar to RFIs) for documentation. The typical RFI process is shown below in Figure 3. The implemented ESI process is shown below in Figure 4.
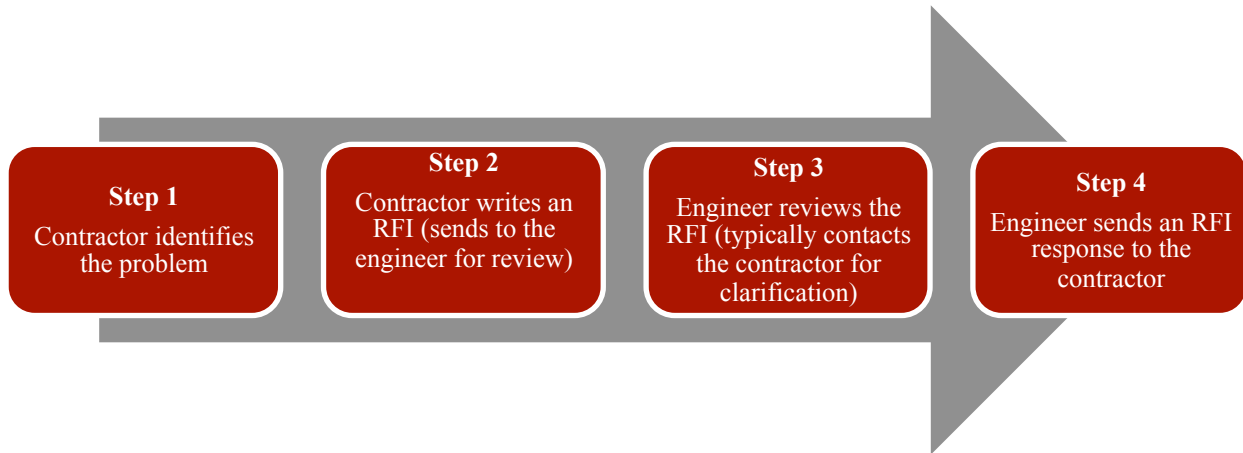
Figure 3. Typical RFI Process

Figure 4. Implemented ESI Process

The ESI process eliminates Step 2 in the typical RFI process. ESIs are also helpful when the engineer identifies the need for clarification or minor design changes prior to a question from the Contractor. An example may be a site visit where the design engineer notices a unique field condition that may warrant an additional detail for clarification. An ESI can help the design engineer get ahead of contractor questions or RFIs, therefore reducing schedule and cost impacts. The ESIs speed up the time required to determine a corrective action and implement it in the field.

The condition of the existing concrete is an application where the above general approach was implemented, as detailed in the following section.

2.2. EXISTING CONCRETE REHABILITATION

2.2.1.   Existing Concrete

The condition/quality of the existing concrete was a driver for several proposed modifications for the project. Prior to design, investigations and condition assessments were completed for the existing concrete. The concrete data included full-depth core logs through the dam, concrete test results, and petrographic analysis. The geotechnical report (GCI 1990) for the existing post-tension anchor design provided a detailed description and evaluation of the condition of the existing concrete. The investigation included logs for three full-depth cores taken at the dam. Concrete testing revealed a surprisingly high average unconfined compressive strength of 42,600 kN/m^2 (6,180 psi) and a high average concrete permeability of 1.1×10^{-3} cm/s (GCI 1990). Petrographic analysis was performed on three existing concrete cores; the overall presence of alkali-silica reactivity (ASR) in the concrete was judged to be minor, and air content was estimated between 0 and 4% (CTL, 2013). The overall data for the existing concrete indicated cyclopean concrete with minor voids, seams, and cold joints, but with adequate compressive strength and limited chemical reaction concerns.

Prior to design, a dive inspection (AUS 2012) was performed for the upstream face of the dam, and a structural condition survey was also performed for the gate tunnels and the downstream face of the dam. The dive inspection and the structural condition survey had similar findings. The existing concrete was in poor condition with concrete spalling, cracking, and voids over a substantial area of the exterior of the dam.

2.2.2.   Concrete Rehabilitation Design

Due to the observed condition of the existing concrete, consolidation grouting was included in the dam rehabilitation design in order to improve the existing South Channel Dam concrete. The consolidation grouting program was designed to fill the voids in the concrete with a structural material to decrease permeability and improve the structural integrity of the existing concrete.

Based on data collected and field observations, it was determined that the upstream and downstream deteriorated concrete surfaces should be replaced with new concrete (facing concrete) rather than implementing local concrete repairs. The dam rehabilitation design included facing concrete to reduce upstream permeability and to improve freeze-thaw resistance. The new concrete was designed per the guidelines of ACI 350 (ACI 2006). The specified facing concrete included Type I/II Portland cement and a 28-day minimum design compressive strength of 31,000 kN/m^2 (4,500 psi). The upstream facing concrete also included a crystalline waterproofing admixture to further reduce upstream permeability. The new facing concrete was a minimum of 12 inches thick to develop the dowel reinforcement and to provide enough mass to improve the durability of the concrete repair. The new concrete facing construction included air-entrained concrete with reinforcement.   The facing concrete was drilled and epoxy doweled into the existing concrete. The facing concrete dowels and concrete reinforcement consisted of #4 and #6 ASTM A615/A615M Grade 60 deformed steel bars. The condition of the existing concrete was not expected to improve significantly with depth. Therefore, the demolition was detailed to a fixed depth rather than extending the demolition down to "sound" concrete.

Due to the condition of the existing concrete and the significant lock-off loading (as high as 4,180 kN (940 kips)) for the existing mulit-strand post tension anchors (Black & Veatch 1993), the minimum clearance for demolition limits and drilling locations in the proximity of the existing post-tension anchors was determined using conservative assumptions. A minimum clearance radius of 0.71 meters (2.33 feet) was specified at each existing post tension anchor location. The minimum required clearance from the existing post tension anchors was determined based on the minimum unreinforced column size needed to support the maximum anchor loading, and it accounted for the potential inclination of the existing post-tensioned anchors.

2.2.1. Modifications during Construction

Based on data collected prior to construction, the existing concrete in the historic dam was known to consist of cyclopean concrete with voids, seams, and cold joints. The condition of the existing concrete encountered during construction, however, was worse than expected. Concrete demolition and surface preparation revealed large voids and substantial areas of low strength material. Extending the demolition was not an option because there were no indications that the concrete would improve with depth. The observed condition of the original concrete necessitated adjustments to the design and detailing during the construction phase. The design modifications for the concrete rehabilitation included the following:

- Surface preparation and local repairs to facilitate the facing concrete
- Facing concrete drill and epoxy dowels
- Consolidation grouting

Low strength material was observed at several locations in the dam. The following questions were discussed during construction:

- How much material should be removed?
- How should the soft material be removed?
- How should the resulting voids be repaired?

Ultimately, high-pressure water was used to remove the low strength material. Test sections were performed; the team all agreed to proceed with high-pressure water to remove the areas with low strength material. The extent of low strength material removal was limited to what the high pressure water could remove. Figure 5 shows the concrete surface preparation with high pressure water and the downstream face of the dam after concrete demolition and surface preparation.

Figure 5. Concrete Demolition and Surface Preparation

High-pressure washing the concrete surfaces of the dam revealed several concrete voids. The voids ranged in size from 0.15 meters (0.5 feet) wide by 0.15 meters (0.5 feet) deep to up to 1.2 meters (4 feet) wide by 0.6 meters (2 feet) deep. The concrete voids were prepared to ensure that the voids could be filled as part of the facing concrete placement. The facing concrete was a flowable concrete mix with a water-reducing admixture and 19 mm (¾-inch)

maximum aggregate size. Each void area was inspected, and additional local demolition was performed with hand tools as needed to remove obstructions. Hard to reach deep sections were repaired with dry pack grout (Portland cement and sand) to build the void out to a depth that could be filled as part of the new facing concrete placement. The implemented void repair detail to facilitate filling with the facing concrete is shown in Figure 6.
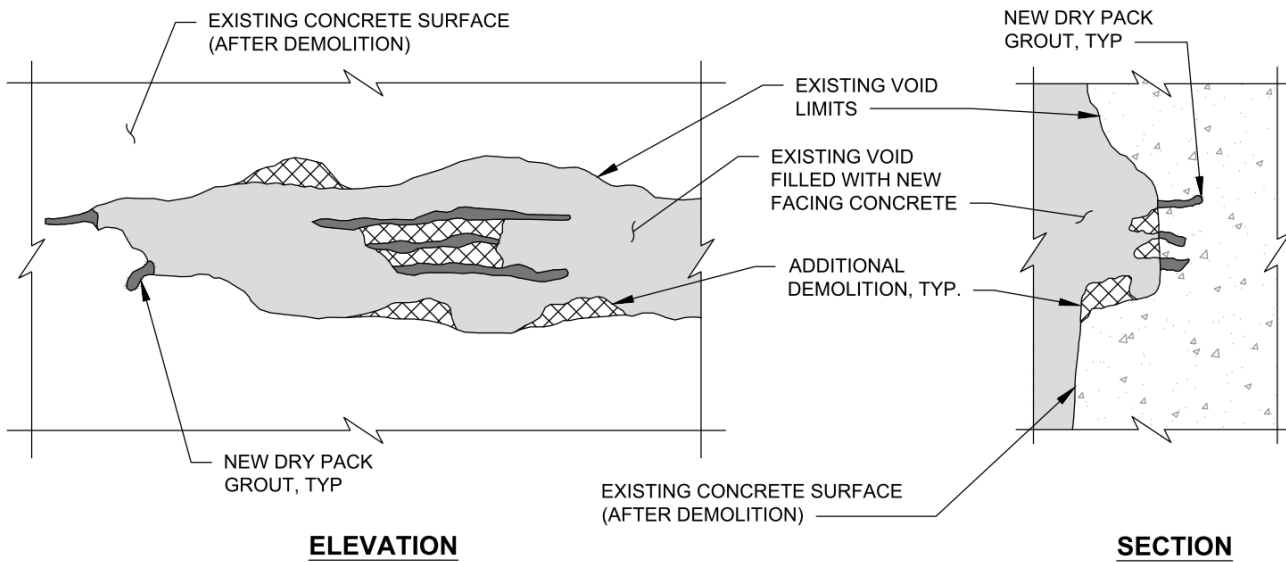
Figure 6. Concrete Void Repair Detail

Due to the extent of the concrete voids and the zones of low strength material, the reinforcement dowel design was revised. The reinforcement dowel size was increased, and the embedment into existing concrete was increased to provide more confidence in the facing concrete anchorage. The grid spacing was also increased to allow for field adjustment in order to properly locate the reinforcement dowels to anchor into the more competent concrete locations and into void areas. The existing concrete voids and the reinforcement dowel installation are shown in Figure 7 below.

Figure 7. Existing Concrete Voids, Drill and Epoxy Dowel Installation, and Facing Concrete Reinforcement

The consolidation grouting program was also adjusted after the concrete demolition was completed. Due to the condition of the existing concrete, the grouting at the upstream and downstream dam faces was moved to the gate tunnel walls. The consolidation grouting was also modified due to a change in construction sequence to expedite the schedule. The gate tunnel wall grouting was performed after the new facing concrete was installed. The primary change was a reduction in grouting pressures in order to avoid overstressing of the new facing concrete. Seventy-two locations (six per tunnel wall face) were drilled and grouted within the tunnel walls. The grout mix consisted of 1:1 water content/superfine cement ratio with 0.75% water-reducer and 0.06% diutan gum admixtures (Budinger 2015). A total of 787 liters (208 gallons) of grout was placed for tunnel grouting. Grout injection pressure ranged between 6.89 and 82.7 kN/m^2 (1 and 12 psi); grouting was continued on each hole until the grout injection pressure reached the design cut-off pressure of 82.7 kN/m^2 (12 psi) and could be maintained within 15% for two minutes.

Originally, the grouting program for the overflow section of the dam included horizontal grouting at the upstream and downstream faces of the existing overflow section. Due to the condition of the existing concrete, especially the alternating layers of low cement concrete, the grouting for the overflow section was changed to vertical grouting. The vertical grouting allowed the grouting to cross several layers of poorly consolidated concrete. The vertical grouting at the overflow section included significantly higher grout pressures due to the static head pressures (vertical column) of grout; therefore, vertical grouting was performed prior to the placement of the facing concrete in order to avoid overstressing the new facing concrete. The overflow section vertical grouting was performed on the upstream side of the overflow centerline. The grouting program featured split-spacing grouting with primary holes (3 meters on-center) and secondary holes (1.5 meters on-center) along the overflow section. The grout mix design for the overflow grouting was 1:1 water/superfine cement with superplasticizer at 2% by weight of the cement (Budinger 2015). A total of 1912 liters (505 gallons) of grout was injected in four primary holes, four secondary holes, and three tertiary holes. The maximum depth of the grout holes was 6.1 meters (20 feet), and the estimated radius of travel of grout was 0.9 to 1.5 meters (3 to 5 feet). Grout pressures ranged between 6.89 and 55.2 kN/m^2 (1 and 8 psi) and were based on the static head of grout due to the depth to the packer and an additional pressure not to exceed 5.64 kN/m^2 per meter (0.25 psi per foot) of depth below the overflow crest. Grouting was continued on each hole until the grout injection pressure reached the design cut-off pressure and could be maintained for five minutes.

2.3. LESSONS LEARNED

Several valuable lessons came out of all of the challenges encountered throughout the project. Notable lessons learned are as follows:

- Verification of As-Built Drawings for the Existing Structure: An extensive survey of the existing structure is important to verify the accuracy of the existing as-built drawings prior to construction and ideally before final design is completed. Verifying the accuracy of the as-built drawings will limit change orders, aids in accurate design drawings and specifications, and gives the team up-front knowledge of what they are dealing with.

- Investigative Work during Construction: Substantial data was collected during the design phase of the project to determine the quality of the existing concrete. Typically, this data is limited to visual inspection and non-destructive testing. This information is important, but additional investigative work at the beginning of construction should also be considered. Depending on the quality of the existing concrete, test areas for partial concrete demolition, evaluation, and surface prep may give valuable insight into existing conditions. Even the core logs for South Channel Dam were not representative of the actual conditions

encountered after concrete demolition and surface preparation. The voids around the cyclopean concrete and the extents of the weak concrete material were substantially more than what was expected based on the core logs. If demolition test panels are planned into the project, the contractor can schedule accordingly, and the design engineer can identify early in the construction project if design modifications are needed.

- Design Engineer and Contractor Coordination for Ordering of Construction Materials: The general contractor is responsible for the timing and ordering of the construction materials in order to meet the construction schedule. However, there may be materials that should be ordered in smaller batches or on an as-needed basis. The design engineer and contractor should discuss the risk and likelihood of change prior to ordering materials. Early on, it is important for the design engineer to identify materials that may be subject to change and communicate these potential issues and concerns to the contractor. An example is the drilled and epoxy reinforcement dowels for the facing concrete. The reinforcement was revised to meet the conditions encountered during construction. It may be more cost efficient to order concrete reinforcement only after enough of the demolition is completed and in small batches so that design changes can be made if needed. This may reduce the potential for change orders.

Several aspects of the project worked well and could be applied to other rehabilitation projects. These include the following:

- Team Approach: In the beginning of a project, it is beneficial for the design engineers to explain the basis for the design and the design intent to the design team; this fosters a cooperative construction environment. Pre-construction meetings and team workshops worked well to make sure that everyone was on the same page ahead of critical construction steps.

- Anticipate Change: In rehabilitation projects, even the best design may require adjustments due to actual conditions encountered. Identify areas that may change and prepare to make provisions for change. ESIs worked well for efficient change management; the process met the needs for quality and schedule.

- Be Prepared to Adapt: Understand the existing structure and have realistic expectations. For example, typical standard practice for concrete repair is to remove the concrete down to sound concrete. The quality of the existing concrete at South Channel Dam was questionable. As a result, the concrete demolition was adjusted to a fixed depth rather than down to "sound" concrete. High pressure washing the concrete was a project-specific solution for surface preparation of the existing concrete.

3. CONCLUSION

The Post Falls South Channel Dam Rehabilitation Project consisted of multiple challenges throughout the project. Most of these challenges could not be avoided. The challenges were well understood and tools/procedures/plans were established to meet the needs of the project. This included identifying areas of uncertainty and notifying the contractor of them.

The project was ultimately a success in a large part due to the approach and practices implemented during construction. Some of these best practices include the ability to adapt the design as needed due to site conditions encountered, maintaining a proper balance between documentation needs and the construction schedule, and the importance of a unified team approach between owner, design engineers, inspector, and contractor.

4. REFERENCES

American Concrete Institute (ACI). (2006), "350-06 Code Requirements for Environmental Engineering Concrete Structures"

Associated Underwater Services (AUS). (2012). "Post Falls – South Channel Dam Dive Inspection Report." June 27, 2012.

ASTM A615/A615M. "Standard Specification for Deformed and Plain Carbon-Steel Bars for Concrete Reinforcement"

Black & Veatch. (1993). "Post Falls Final Stabilization Report." January 1993.

Budinger & Associates. (2015). "Grouting Work Plan and Grouting Summary Report".

CTL Group. (2013). "Petrographic Examination, ASTM C856, of Concrete Cores from Avista Dams - ASR Assessment, Long Lake, Washington and Post Falls, Idaho." February 21, 2013.

Gifford Consulting, Inc. (GCI). (1990). "Geotechnical Report for Post Falls Explorations – FERC Project 2545." November 15, 1990.

The Role of Physical and Numerical Modeling in Design Development of the Priest Rapids Fish Bypass

T.C. Lyons [1], M. Politano [1], C. Dotson [2], L.J. Weber[1] and D. Hay[3]

[1]IIHR – Hydroscience & Engineering
University of Iowa
Iowa City, IA 52242
USA
[2]Public Utility No. 2 of Grant County
Ephrata, WA 98823
USA
[3]Oakwood Consulting Inc.
Belcarra, BC V3H4P3
CANADA
E-mail: troy-lyons@uiowa.edu

ABSTRACT

This paper describes a number of years of physical and numerical modelling that were instrumental in the development of the final fish bypass design at Priest Rapids Dam. Three physical models and multiple numerical models were used to guide the design of the fish bypass including its location on the dam, impact on forebay and tailrace flow patterns, intake configuration, design flow rates, flow control scheme, tailrace egress, potential for scour near the dam, potential impacts on total dissolved gas (TDG), impacts on spillway and powerhouse operation, and overall fish friendliness of the bypass.

Throughout those years of design work, results from actively tagged salmonid smolt studies were used to guide and validate each step of the design process. In 2011, a construction contract was awarded, and the Priest Rapids Fish Bypass facility was completed in the early spring of 2014. Final validation of this newly constructed facility came in the spring of 2014 with a survival and behavior study conducted using acoustic tagged yearling Chinook and juvenile steelhead smolts to evaluate the salmonid smolt survival rate through the bypass along with the fish passage efficiency (FPE) of the bypass facility.

This paper discusses the physical models plus CFD models used to support the design development of a non-turbine fish bypass and presents the results of the survival and behaviour studies conducted after the fish bypass was installed at Priest Rapids Dam.

Keywords: *Fish passage, modeling, dams, fish bypass, salmonids, spillway.*

1. INTRODUCTION

Priest Rapids Dam is a large hydroelectric dam on the Columbia River in central Washington, USA, owned and operated by Public Utility District No. 2 of Grant County, Washington (The District). Construction of the dam was completed in 1959. It creates a reservoir that extends 29 km (18 miles) upstream to the spillway of Wanapum Dam. Figure 1 shows the project site and an aerial view of the dam. The dam consists of a ten-unit powerhouse and a twenty-two bay spillway. The total powerhouse capacity is 955.6 MW.

Two fish ladders incorporated into the design of Priest Rapids Dam have been successful in passing adult salmonids upstream past the dam, but concerns related to the survival of juvenile salmonids passing the dam on their downstream migration led to a number of studies and field tests in the 1980s to assess various means of collecting juvenile salmonids in the forebay and transporting them downstream. Concerns regarding the use of screens to

collect the juvenile fish led to examining whether an efficient passage route could be designed that allowed juvenile fish to bypass the turbines and pass the dam directly into the tailrace without resorting to large flow releases through the spillway.

As part of regulatory requirements associated with its FERC (Federal Energy Regulatory Commission) license and other agreements, the District was required to design and install a non-turbine fish passage for downstream migrating juvenile salmonids at the dam in order to help meet its pre-established survival standards for salmonid smolts passing through the Priest Rapids Hydroelectric Project during their downstream migration. The standards include a 93% juvenile dam and reservoir survival.

In 2002, a study was undertaken to identify a number of fish passage alternatives for Priest Rapids Dam including screening systems, use of the spillways, and collecting and bypassing fish through surface-oriented openings and/or through modified turbine passages (Voskuilen et al. 2003). This fish passage alternatives study (FPAS) suggested several options that had the potential to provide high fish passage efficiency and survival in a manner different and more efficient than high-volume tainter-gate spill programs. Options that made use of existing spillbays and released flow from the surface rather than from the underside of the radial gates were selected for field-testing as prototypes. This decision was based upon observations of fish passage from other projects where flow released from the surface appeared to be associated with a greater efficiency of smolt passage than flow released from depth.

Figure 1. Priest Rapids Dam perspective photo, map, and satellite view.

2. APPROACH

To facilitate the study and design development of a fish bypass, IIHR-Hydroscience & Engineering (IIHR) developed comprehensive three-dimensional physical models of the forebay and tailrace of Priest Rapids Dam and a model of spillbays 19-22 and powerhouse unit 1. The three physical models were used in conjunction with computational fluid dynamics (CFD) models and a numerical fish surrogate (NFS) model to develop and test various aspects of the fish bypass design. The NFS model was developed by the Engineering Research and Development Center (ERDC) of the US Army Corps of Engineers (USACE).

The physical and CFD models were used in conjunction with prototype tests to advance the design of a non-turbine passage route. Field data on the percent passage and the percent survival through the turbine and non-turbine route was obtained through prototype tests conducted at the dam over a period of several years. The field data and CFD and laboratory models were used to design prototype tests and, ultimately, the final bypass design.

The laboratory and numerical models helped define the following hydraulic characteristics that were incorporated in evaluation of various bypass options, along with other parameters:
- Proximity of the non-turbine passage opening to where the highest density of salmonids was expected to be;
- The degree to which there was competition between flow through the powerhouse and flow through the non-turbine passage route;
- The stability of the flow and acceleration field upstream of the non-turbine passage route;
- The source of bypass water and zone of influence of the bypass;
- The egress of the bypass water in the tailrace with respect to proximity to areas of potential high predation; and,
- The egress of the bypass water with respect to minimizing the uptake of gas in the tailrace.

3. PHYSICAL MODEL DESCRIPTIONS

The three physical models used for the design development and final design of the fish bypass included a forebay model, a tailrace model, and a spillway sectional model. The scale models were built at the University of Iowa over a period of several years. A general description of each model is provided below:
- The 1:64 scale forebay model replicated a portion of the Priest Rapids forebay over an area 1,768 meters (5,800 feet) wide by 1,745 meters (5,725 feet) long upstream of the dam to Goose Island. The model included a fully operational spillway, powerhouse, and left and right bank fish facilities that could be set to match prototype operating conditions. Structural details included spillway piers, ogee profiles, radial tainter gates, and powerhouse intakes. The model replicated prototype river flows up to 11,327 cms (400,000 cfs).
- The 1:64 scale tailrace model replicated a portion of the Priest Rapids tailrace over an area approximately 853 meters (2,800 feet) wide by 2,316 meters (7,600 feet) long downstream of the dam as shown in Figure 2. The model included a fully operational spillway, powerhouse, and left and right bank fish facilities which could be set to match prototype operating conditions. Structural details included spillway piers, ogee profiles, radial tainter gates, and powerhouse draft tubes. The model replicated prototype river flows up to the probable maximum flood (PMF) flow rate of approximately 39,644 cms (1.4 million cfs).
- The 1:20 scale sectional model replicated a portion of the Priest Rapids tailrace over an area approximately 91 meters (300 feet) wide by 244 meters (800 feet) long downstream of the dam. The model included fully operational spillbays 19-22 and powerhouse unit 1 exterior features. The model replicated prototype flows up to the PMF flow through a full-open single spillbay.

Figure 2. Hydraulic model of the Priest Rapids Dam and tailrace.

4. CFD MODEL DESCRIPTIONS

The four numerical models used for the design development of the fish bypass at Priest Rapids Dam include a forebay model, a top spill model, an ogee shaped bypass model, and a numerical fish surrogate (NFS) model. The first three models were implemented in the CFD solver ANSYS FLUENT. The NFS model utilized the results of the forebay model to predict the behavior of outmigrating salmonid smolts in the forebay of Priest Rapids Dam. Each model is described briefly below:

- The forebay model comprised approximately 5,182 meters (17,000 feet) of the forebay of Priest Rapids Dam and used a flat rigid-lid approach. The forebay model included the river bathymetry, 10 powerhouse units with 3 intakes per unit, 22 spillway bays, and an ice-trash sluiceway located in the tainter gate of spillbay 22. Spillbays 19 and 20 were initially modeled as top spill, the other spillbays as bottom spill. The model also included Goose Island. The forebay model grid contained roughly 2 million grid points.

- The top spill model predicted the flow conditions downstream of spillways 19 to 22. This model used a VOF (Volume of Fluid) method to predict the free surface and calculate pressures and accelerations associated with flows through the fish bypass prototypes in spillbays 19 and 20. The model of the prototype top spill bays was developed to assess the hydraulics in the tailrace immediately downstream of the top spills. Figure 3 provides an illustration of this model. This model simulated flow through bays 19 and 20 and was used to determine the pressure loads on particles (fish) traveling through the bays. The VOF method allowed the water surface profile in the forebay, tailrace, and nappe to be obtained by the simulation for an incoming flow rate.

- The ogee shaped bypass model also used the VOF method, and it was developed to compute cavitation indices and total hydraulic loads on the fish bypass surfaces of the final design. The VOF method was used to simulate the flow field over the spillbays for the final design. To reduce computing time and grid size, instead of simulating the entire geometry, simplified geometries were used. Simulations with spillbays 21 and 22 required the modeling of one full bay and a half bay resulting in a grid with about 3.1×10^6 cells. A small region of the tailrace was incorporated into the model to account for the effect of the bypass submergence condition.

- The NFS model, which is based on a particle tracking algorithm, was used to predict the distribution of smolts passing the dam for given flow releases. This model used the hydrodynamic data results obtained with the forebay model as inputs. IIHR worked with the USACE for many years to develop a method for predicting the movement and behavior of migratory salmon by providing the hydrodynamic data obtained by computational fluid dynamics (CFD) simulations of a given waterway. This collaborative effort led to the development an Eulerian-Lagrangian-Agent Method (ELAM) that tracks fish as particles in the waterway and moves the fish according to certain "behavior rules." The behavior rules are a function of fluid properties such as acceleration, strain, velocity, and velocity gradients. This particular ELAM is known as the NFS model. The USACE took the lead in the development of the biological responses of the salmonids that ultimately comprised the NFS model (Nestler et al. 2001, Goodwin et al. 2004).
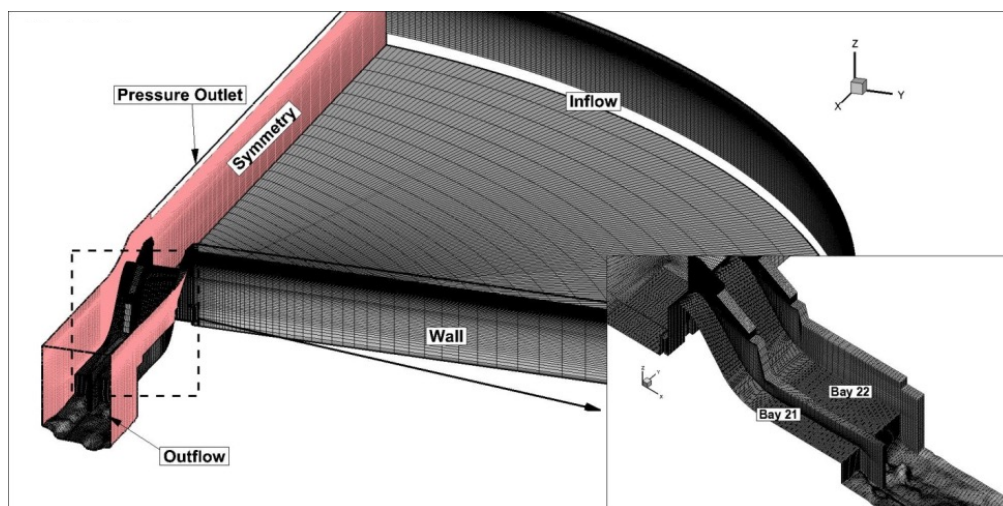
Figure 3. Ogee shaped model.

5. FISH BYPASS DESIGN DEVELOPMENT

The District began work at Priest Rapids Dam in 2002 by commencing the FPAS and also prototype testing of spillway gate 17 fully open. The hydraulic model test program at IIHR began in earnest in 2002 with the construction of the 1:64 scale forebay model followed by construction of the tailrace model and development of the forebay CFD model. The CFD and laboratory models supported investigations and decisions related to field-testing of prototypes. Over the next eight years, the District used a variety of tools in the design and evaluation process of the fish bypass, including the following:

- Acoustic tagged fish;
- CFD models of forebay and tailrace;
- Physical models of forebay, tailrace, and bypass;
- The numerical fish surrogate model.

Observations from the fully opened spillbay tests in 2002 together with the CFD and hydraulic modeling of top spills led to the decision to prototype test top spills in spillbays 19 and 20 starting in 2006. As a result, extensive work was undertaken in 2004-2005 to develop a top spill fish bypass concept, which was field-tested in 2006 and 2007 (Fig. 4).

To develop the top spill concept, the forebay and tailrace hydraulic models were used to evaluate bulkheads that released flow from the surface of the forebay. The forebay model was primarily used to examine approach-flow conditions, entrance characteristics such as shockwaves and flow separations, and measure tainter gate clearance. The tailrace model was used to examine nappe characteristics such as trajectory and impact location, test various bulkhead sill shapes, examine stilling basin hydraulics, develop a bypass flow rating, and document egress flow patterns. Approach flow to the topspill bypass was also studied using the forebay CFD model to observe the zone in the forebay that was influenced by the flow withdrawal for various conditions. The CFD model was also used to define flow patterns, examine where the water passing the fish bypass originated in the forebay, and examine the velocities and accelerations of flow approaching the bypass. The CFD top spill model was also used to calculate sectional nappe profiles along the spillbay centerline to determine the nappe clearance beneath the tainter gate and to determine the jet impact location.

Figure 4. Topspill bulkheads tests at Priest Rapids in 2006 and 2007.

The prototype testing in 2006 and 2007 was undertaken in conjunction with studies of acoustically tagged fish to determine the effectiveness of the top spills. While prototyping proved successful in assessing the effectiveness of attracting and passing juvenile salmonids through top spills, it raised the concern that pressures and accelerations experienced by fish might result in injury or mortality that would render free-fall top spills unsuitable for a permanent fish bypass design. Two initiatives were undertaken to assess these concerns; a field study by Battelle (Duncan 2009) using sensor fish and the development of the ogee shaped bypass CFD model, from which accelerations and pressures along streamlines could be extracted.

Ultimately, the percent of fish using the top spills in 2006 and 2007 to bypass the powerhouse did not appear to be adequate to achieve the survival goal for the project. This led to two study initiatives which started in 2007; one initiative was to study and assess the benefits of increasing the rate of bypass flow and/or changing the bypass location; the second initiative was to study and assess whether more fish could be guided to bypass the powerhouse through the use of training walls or training velocities.

The concept of using training walls to guide outmigrating fish had been prototyped by the US Army Corps of Engineers (USACE) at the Lower Granite Lock and Dam on the Snake River, and it was being prototyped at the second powerhouse at Bonneville Dam when consideration was being given to prototype tests at Priest Rapids Dam in 2008 and 2009.

The concept of guiding fish through the use of submerged water jets was advanced by Mr. Gordon C. Burns and patented in May 2004 as a Flow Velocity Enhancement System. The system envisaged the placement of nozzles in low velocity areas within a river, lake, or reservoir "as a method to create water flow velocities that fish are reluctant to pass through for a barrier or curtain to further guide the fish" (Burns 2004).

The hydraulic modeling of the training walls and jets was undertaken in concert with CFD/NFS modeling, with the physical modeling used to gain some qualitative visual insights and the numerical modeling used to define velocities, accelerations, and the source of bypassed water. The CFD forebay model was used to estimate the hydrodynamic loads on training walls that might be used to enhance the number of fish using the bypass. It was also used to examine the effectiveness of using jets of pumped water to guide fish to a bypass. Insights from the tests and numerical modeling, along with an assessment of the costs and effectiveness of these measures elsewhere, were used to decide whether training walls or jets would be prototyped.

The modeling led to the decision in 2008 to increase the amount of bypass flow by leaving the topspill bulkheads in spillbays 19 and 20 but adding a bottom release in spillbay 21 and a release from the sluiceway in spillbay 22. It was observed in the models that the increase in total bypass flow created a stronger draw from the forebay to the bypass routes, and releasing flow through spillbays 21 and 22 enhanced flow conditions in the tailrace for egress of the

smolts. Also based on the model tests, inadvertent spill was released through the higher numbered spillbays in 2008. The 2008 prototype testing condition is shown in Figure 5.

Figure 5. Topspill in bays 19, 20, and 22 and bottom spill in bay 21 as tested in 2008.

As was the case for the 2006 and 2007 prototype tests, it was decided to leave the 2008 bypass configuration in place for the 2009 season in order to obtain an additional year of fish passage data without making any changes to the prototype. There was no prototyping of training walls or velocity enhancement jets undertaken; instead, these techniques were left as potential additional measures that might be considered for implementation should the survival goal not be achieved following construction and commissioning of the final bypass design.

Throughout the design process, the NFS model was useful in comparing the percent of fish using a non-turbine passage for various bypass configurations, bypass enhancements, and plant loadings on a relative basis to give indications as to which configurations were most likely to produce the best bypass efficiencies. Results indicated that bypass efficiency would be greater with the bypass located close to the powerhouse rather than at a more central position on the spillway. They also supported the observation from the field that the bypass efficiency could be higher with bypass flows drawn from the surface. All the modeled configurations indicated that location of the bypass and withdrawals from the surface were more important parameters than the total bypass flow alone.

Prototype testing guided by laboratory and CFD modeling proved successful, with an increase in percent fish passage over a period of five years. The percent fish passage by year of prototype testing is summarized in Table 1.

Table 1. Topspill bulkhead percent fish passage

Year	Chinook	Steelhead	Sockeye
2006	12%	15%	20%
2007	13%	19%	12%
2008	23%	33%	22%
2009	n/a	50%	39%
2010	n/a	64%	52%

6. THE FINAL FISH BYPASS DESIGN

In 2010, the final design of a production bypass was initiated. The primary factors that determined the design characteristics were as follows:
- The bypass entrance should be located near a high concentration of fish approaching the project;
- The bypass exit should be near additional flows and away from areas of high concentrations of predators;
- No deceleration or upwelling should be present at the entrance;
- Bypass flow should be selected to achieve the required survival goal through top spill or combination of top and bottom spill;

- Bypass flow of a single bay should be limited to 283 cms (10 Kcfs) to minimize total dissolved gas and maximize tailrace survival;
- To minimize mortality, impacts and shear should be minimized at the exit;
- To minimize uptake of dissolved gas, plunging flow should be avoided at the exit;
- The dam must be able to pass probable maximum flood after the bypass is installed; and
- Installation of the bypass must not result in a reduction of dam stability.

These factors resulted in the following decisions:
- The bypass will be located adjacent to the powerhouse;
- The bypass will be installed in spillbays 20, 21, and 22;
- There is no need for special control of accelerations at the entrance; and
- The target flowrate is 255 cms (9 Kcfs) per bay.

Based on an analysis of the four years (2006 – 2009) of fish passage data, it was estimated that a total bypass top spill flow of 765 cms (27 kcfs) would be required from spillbays close to the powerhouse in order to meet the target of at least 95% survival of smolts passing the dam with the assumption of 99% survival through the top spill.

A review of the probable maximum flood (PMF) that would be required to pass Priest Rapids Dam, together with a review of the hydraulic capacity of the spillway (Larry Weber, personal communication, 2010), indicated that three spillbays, each with a design bypass flow of 255 cms (9 kcfs), could be dedicated to fish passage while still maintaining sufficient hydraulic capacity in the spillway to pass the PMF.

For the final design, the NFS model was used to give an estimate of the three-spillbay bypass route efficiencies, and CFD work was undertaken using the ogee shaped model to compute pressures and cavitation indices. The hydraulic loads and center of pressure on the spillway face for the various simulations were provided for use in structural engineering and stability analysis of the fish bypass.

The physical models were used extensively to test the final design. For example, the models were used to analyze approach conditions in the forebay for various river flows and powerhouse loadings, perform a flow rating, determine water surface profiles through the bypass, measure pressures on the ogee surface, determine maximum velocity on the apron, determine the optimum apron elevation and length, assess pier extension heights and lengths, characterize jet performance over a range of tailwater elevations, examine egress flow patterns, and assess downstream scour potential. In addition, the tailrace model was used to assess wave and velocity characteristics in the fish bypass construction zone that were likely to be encountered by crews and equipment during construction. A number of tests were also conducted on the 1:64 scale tailrace model to help determine the appropriate apron elevation when releasing bypass flows. It became apparent that it would be necessary to raise the invert elevation of the stilling basin and extend the spillway pier tails downstream over the apron in order to preclude the bypass flow from plunging to depth in the tailrace. Subsequent tests indicated it was necessary to extend the pier tails beyond the end of the spillway apron to curtail return flow from the tailrace moving upstream on the apron along the walls of the pier, creating a condition of turbulence and shear that was potentially adverse for fish. Testing of the final apron design is shown in Figure 6. Figure 7 shows a photograph of the final design being tested in the tailrace model. Figure 8 is a photograph of the final bypass in operation on the dam.

Figure 6. Fish bypass apron design being tested on the tailrace model.

Figure 7. The final fish bypass design in the tailrace model.

Figure 8. Photograph of the final fish bypass in operation.

7. SURVIVAL AND BEHAVIOUR STUDY RESULTS

Final validation of the newly constructed facility came in the spring of 2014 with a survival and behavior study conducted using acoustic tagged yearling Chinook and juvenile steelhead smolts to evaluate both the salmonid smolt survival rate through the bypass and the fish passage efficiency (FPE) of the bypass facility. Results showed that 47.2% of steelhead and 38.1% of yearling Chinook used the fish bypass (Hatch et al. 2015). The selection of passage routes for both species is shown in Figure 9. Steelhead had slightly higher passage rates through the bypass compared to yearling Chinook, with similar passage rates through the spillway and powerhouse. Survival rates through the bypass for steelhead and yearling Chinook were 99.6 and 99.8%, respectively.
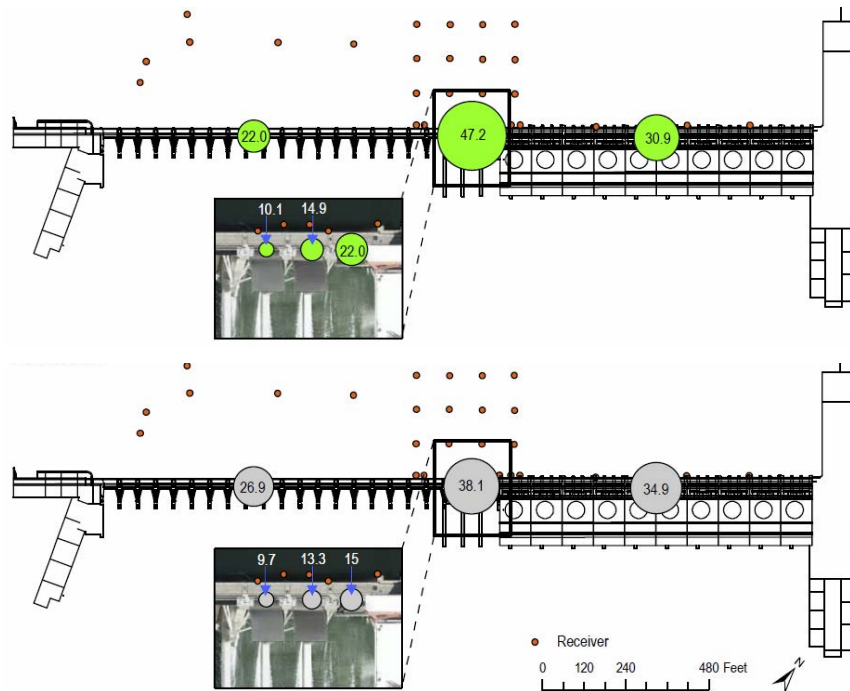
Figure 9. Passage rates for Chinook (top panel) and steelhead (bottom panel) for 2014.

8. ACKNOWLEDGMENTS

9. REFERENCES

Burns, G.C., Flow Velocity Enhancement System. United States, Patent 6,729,800. May 04, 2004.

Duncan, J.P. (2009). Use of an Electronic Sensor Fish to Estimate Hydraulic Conditions and Characterize Fish Passage Conditions over a Top-Spill Bulkhead at Priest Rapids Dam. Report by Battelle, Pacific Northwest Division for Public Utility District No. 2 of Grant County.

Goodwin, R.A., Nestler, J.M., Anderson, J.J., and Weber, L.J. (2004). *Virtual fish to evaluate bypass structures for endangered species.* Proceedings of the 5th International Symposium on Ecohydraulics, 12 - 17 September 2004, Madrid, Spain.

Hatch, K.B., Timko, M.A., Sullivan, L.S., Rizor, S.E., Skalski, J.R., Townsend, R.L., and Dotson, C.L. (2015). Behavior and Survival Analysis of Juvenile Steelhead and Yearling Chinook Salmon through the Priest Rapids Hydroelectric Project in 2014. Report prepared for Public Utility District No. 2 of Grant County, Washington by Blue Leaf Environmental, Inc., Ellensburg, Washington.

Nestler, J., Goodwin, R., Weber, L.J., & Lai, Y. (2001). *Theoretical and Computational Templates for Juvenile Salmon Swim Path Selection in the Complex Hydrodynamic Environments of Rivers and Designed Hydraulic Structures.* ERDC/EL TR-00: US Army Corps of Engineers.

Voskuilen, M.R. (2003). Fish Passage Alternatives Study. Prepared for Public Utility District No. 2 of Grant County by Jacobs, IIHR, and Oakwood Consulting Inc. January 31, 2003.

Physical Modeling of an Aerating Stepped Spillway

S. Erpicum[1], M. Lodomez[1], J. Savatier[2], P. Archambeau[1], B. J. Dewals[1], M. Pirotton[1]
[1]Dept. of Architecture, Geology, Environment and Constructions (ArGEnCo)
Liege University
Liege, 4000
Belgium
[2]ISL Ingénierie
Saint Jean de Luz, 64500
France
E-mail: S.Erpicum@ulg.ac.be

ABSTRACT

To mitigate the negative effects on the water quality in the downstream river of a projected large dam, and in particular to increase the dissolved oxygen concentration during low flow periods within the first 10 years of dam operation, an aerating weir has been designed and tested on a physical model at the Laboratory of Engineering Hydraulics (HECE) of the Liege University. The design of the structure considers data from the literature. The selected solution is a 3 m high stepped spillway designed to operate in nappe flow conditions within the range of design discharges (25 – 100 m³/s). To validate the design, a physical model representing a section of the weir at a 1:1 scale has been built and operated in the laboratory. A chemical dissolved oxygen removal technique has been applied upstream of the model to be able to measure the weir aerating efficiency. The physical model results show that the proposed structure is able to maintain, in the range of discharge in the river from 25 to 100 m³/s, a minimum 5 mg/l oxygen concentration downstream, whatever the upstream oxygen concentration. The paper presents the design process of the weir, the scale model features and the results of the validation tests on the physical model. The prototype construction will take place in 2017 and the water quality will be monitored.

Keywords: Physical modeling, aeration, water quality, oxygen deficiency, aerating weir

1. INTRODUCTION

Vegetation decomposition taking place in artificial reservoirs of tropical regions may significantly alter the water quality by consuming dissolved oxygen and producing methane. If released without sufficient aeration, for instance through the turbines of a power plant, this poor quality water is likely to have a significant impact on the downstream river life. This phenomenon is particularly important during the first years following the first filling of large reservoirs, when flooded vegetation volume is important and the reservoir water renewal limited.

A few dams are known to experience this problem and specific structures have been built downstream to increase the dissolved oxygen concentration (aeration) while degassing methane. Two examples include

- Petit Saut dam in French Guiana, where a steel weir with two successive chutes have been placed (Gosse and Grégoire, 1997);
- Nam Theun 2 project, where various specific structures such as a hollow jet valve, concrete tooth and an aerating weir have been designed (Descloux et al. 2015).

Several systems, using labyrinth weirs, have also been designed and tested by the Tennessee Valley Authority (Hauser and Morris, 1995).

Generally, hydraulic structures such as weirs and stepped spillways may be very effective in increasing the oxygen concentration and degassing methane. This efficiency may be characterized by the deficit ratio r or the aeration efficiency E. These parameters depend on the temperature T and are defined as

$$E_T = 1 - \frac{1}{r_T} = \frac{C_d - C_u}{C_s - C_u} \tag{1}$$

where C_d is the downstream dissolved oxygen concentration, C_u is the upstream dissolved oxygen concentration and C_s is the saturation oxygen concentration.

Among the works published to date, Nakasone (1987) proposed design equations to predict the deficit ratio r from side to side of a chute depending on the chute height D, the specific discharge q, the critical depth h_c and the tailwater depth h_d. For specific discharges higher than 0.0653 m²/s, they are

$$\ln r_{20} = 5.39 \left(D + 1.5h_c \right)^{1.31} q^{-0.363} h_d^{0.310} \text{ for } D + 1.5h_c \leq 1.2m \tag{2a}$$

$$\ln r_{20} = 5.92 \left(D + 1.5h_c \right)^{0.816} q^{-0.363} h_d^{0.310} \text{ for } D + 1.5h_c > 1.2m \tag{2b}$$

Nakasone formula is based on laboratory tests and has been validated regarding other researchers' results and field measurements, as detailed in Nakasone (1987). Essery et al. (1978) and more recently Bayar et al. (2007) studied the aeration efficiency of stepped spillways. Using data from experimental tests considering 1 and 2 m high chutes with steps .05 to .5 m high, slope from 11.3 to 45°, and discharge ranging from 0.0116 m²/s to 0.1447 m²/s, Essery et al. (1978) equation writes

$$\ln r_{20} = \frac{D}{\sqrt{gh_s}} \left(0.427 - 0.310 \ln \frac{h_c}{h_s} \right) \tag{3}$$

with h_s as the step height. This equation does not depend on the flow regime. On the contrary, Bayar et al. (2007) equations depend on the flow regime. Also set up from experimental results (2.5 and 1.25 m high chutes, steps .05, 0.1 and 0.15 m high, slope from 14.48 to 50°, and discharge from 0.0167 m²/s to 0.1667 m²/s), Bayar et al. (2007) equation for nappe flow regime writes

$$\ln r_{20} = \left(1 - 0.265 \left(\sin \theta \right)^{-2.661} \left(\frac{h_c}{h_s} \right)^{0.007} L_a^{-2.057} \right)^{1.575} \tag{4}$$

with θ the chute angle and $L_a = \frac{D}{\sin \theta} - 6.834 h_s^{0.749} q^{0.205} \left(\cos \theta \right)^{0.915}$.

In this paper, the solution designed to aerate the flow from a large dam reservoir under first filling is presented in details. In particular, the solution has been validated using laboratory tests on a 1:1 physical model of a section of the aerating structure. Section 2 presents the project constraints and the preliminary design of the solution. The physical model used for validation and the methodology of the tests are depicted in section 3, while the results and their discussion are given in section 4.

2. PROJECT CONSTRAINTS AND PRELIMINARY DESIGN

2.1. Project Features

The target oxygen concentration in the river downstream of the aerating structure is 5 mg/l for discharges up to 100 m³/s. It is expected to reach a zero concentration of dissolved oxygen in the water released through the turbines during the first years of reservoir operation. The water temperature in the river varies from 20 to 30°C along the

year. At 20°C and atmospheric pressure, oxygen saturation concentration is equal to 9.09 mg/l. The objective of the structure is thus to reach aeration efficiency at 20°C E_{20} equal to 0.55.

It has been verified that the water in the river doesn't contain any specific element which could act against oxygen transfer. Only "natural" oxygen consumption is thus present. In addition, high methane concentrations are expected. The aerating structure has to release this dissolved gas in the atmosphere.

Because of economic and time constraints as well as a difficult access to the construction site (natural reserve), the aeration structure has to be simple and made as much as possible from materials available on site. It has also to be easily dismantled as it will impact the operation of the dam's powerplant while the quality of the reservoir water is expected to become "good" after some years of operation. In particular, a specific first filling plan lasting over several years will be applied to control and mitigate negative impact on the water quality. The requested life time of the structure is thus around 10 years. Regarding the planned operation of the dam during the first years following first filling, key discharges are 25 and 50 m³/s.

A river survey suggested locating the aerating structure at a place where rocks show on the surface (natural chute), a few kilometers downstream of the dam. The river width at this place is around 160 m. Depending on the operation of the upstream powerplant, the chute can be 3 m high.

2.2. Preliminary design

Regarding the river width and the prototype discharge range, the aerating structure has to be effective in the range of specific discharges from 0.159 to 0.637 m³/s/m. The maximum chute height is 3 m. In this context, two main solutions for the aeration structure have been analyzed:
- One or two successive overflow chutes with a downstream basin, where aeration occurs in the downstream basin thanks to the air entrained by the jet at impact;
- A stepped spillway, where aeration occurs on each step along the structure, depending on the flow regime.

Considering the equations available in the literature, and in particular the ones mentioned in section 1, it is possible to propose a structure geometry able to provide enough aeration in the whole range of project discharge, while not exceeding the maximum chute height for both solutions.

Considering technical reasons including availability of materials on the dam work site and easier decommissioning, the stepped spillway solution has been preferred by the Designer (ISL Ingénierie). In such a case, nappe flow is the flow regime providing most effective aeration (Baylar et al., 2007). Different criteria can be found in the literature to get such a flow regime. Ohtsu et al. (2001), cited by Baylar et al. (2007), propose the following limit

$$\frac{h_s}{h_c} > 0.57 \left(\tan \alpha \right)^3 + 1.3 \text{ for } 5.7° < \alpha < 55° \tag{5}$$

while André et al. (2008) propose

$$\frac{h_s}{h_c} > 1.356 \left(\tan \alpha \right)^{0.244} \text{ for } 18.6° < \alpha < 30° \tag{6}$$

Application of the most restrictive of these two formulae to the discharge range of the project and considering a 15° slope compatible with construction and stability constraints leads to choose 50 cm high steps.

Given these geometric and flow parameters, the aeration efficiency E_{20} of the system has been assessed using equations 3 and 4. E_{20} values predicted by Essery et al. (1978) equation range from 0.67 to 0.52, with increasing discharge. An almost constant value of 0.75 is predicted by Baylar et al. (2007) equation, whatever the discharge. These values are better or close to the target E_{20} value of the project. It has to be noticed that some of the present

project characteristics fall outside the range of parameters considered in the researches by Essery et al. (1978) and Baylar et al. (2007).

2.3.   Aerating Structure Geometry

Based on the above-mentioned considerations, the aeration structure geometry has been defined as follows: 3 m high and 157 m wide weir with a smooth upstream face inclined by 26.5°, a 3-m long horizontal broad crest and a downstream face made of six 50-cm high and 1.87 m long steps (15° slope). The weir will be built on an existing rock bar using rubble masonry (CIDB, 2015).

3.   PHYSICAL MODELING

3.1.   Model Features

In order to validate the design of the aerating weir, a physical model has been built and operated at the Laboratory of Engineering Hydraulics (HECE) of the University of Liege.

To avoid scale effects on the oxygen transfer mechanisms and thanks to the limited chute of the prototype, the model has been built at prototype scale (1:1 scale factor). Indeed, even with large scale factors, it has been shown (Chanson, 2009; Felder and Chanson, 2015) that bubbles size is not properly scaled on hydraulic scale models. The bubbles size, and thus the surface of oxygen exchange between water and air, is a key parameter in the aeration process.
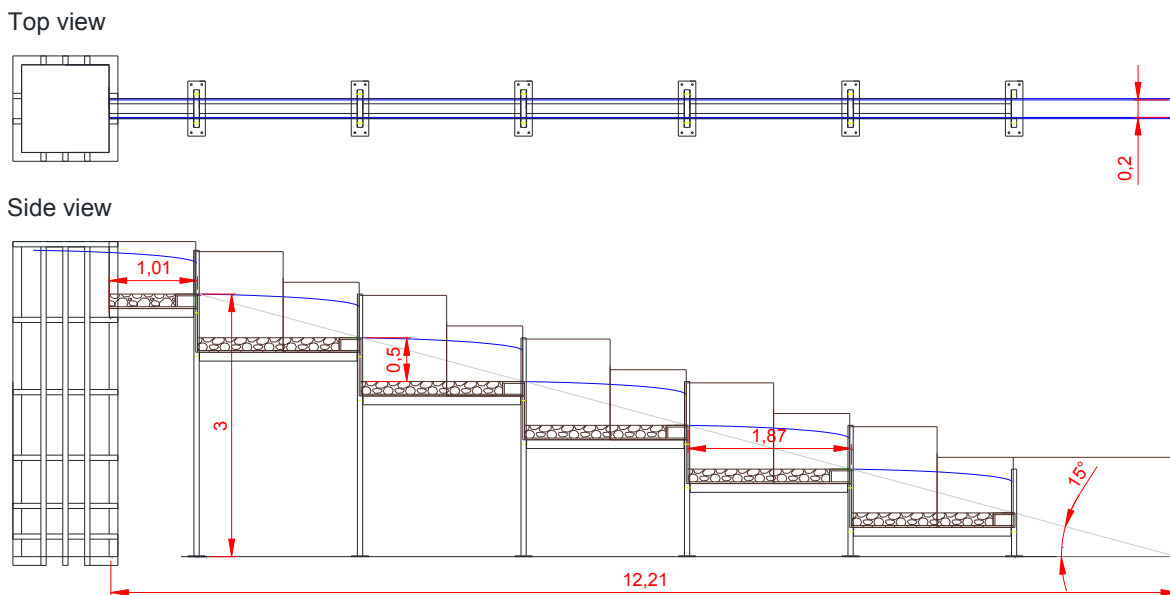
Figure 1. Sketch of the physical model – Dimensions in m

With a 1:1 scale factor, the discharge is a limiting parameter for the tests. As the aerating weir will be horizontal and built perpendicular to the main river reach, the discharge will most probably be uniformly distributed over the weir width. Therefore, the physical model focused on a limited section of the weir (2D vertical model – Fig. 1). The model width has been chosen considering available water volume and discharge considerations. Indeed, to study the aeration process on the weir, it is necessary to remove the oxygen from the upstream water. As the water supply system of the laboratory is a closed loop with pumps, pressurized conduits and an underground reservoir, it is

necessary to remove the dissolved oxygen from the water stored in the reservoir. As a consequence, the duration of a test is directly linked to the available water volume and to the discharge. To enable tens of minutes long tests with 4 discharge levels (25, 50, 75 and 100 m³/s on the prototype), a 20 cm wide physical model has been built. Resulting maximum discharge in the physical model is 127.5 l/s.

With such a limited width, strong wall effects may affect the physical model results. In order to limit side friction effects, the model side walls have been made of Plexiglas and PVC (smooth materials). In addition, all the measurements have been done along the model centerline. Finally, air entrainment and aeration will probably be less in the 2D model than in the 3D prototype flow, especially because transverse flow fluctuations development will be limited by the side walls. It is thus believed that the model is conservative in terms of aeration efficiency.

The physical model represents the weir crest and the whole downstream face. The crest and steps bottom are made of rubble masonry, as on the prototype (Fig. 2 - left). Steps face is made of PVC on the physical model (formed concrete on the prototype).

During the test, the upstream discharge has been measured using an electromagnetic discharge meter on the supply pipe (accuracy of 0.5% FS). Dissolved oxygen concentration has been measured continuously in the upstream reservoir, in the downstream collecting channel and on several steps using 6 optical oximeters. On the steps, the oximeters have been placed along the channel centerline and just upstream of the jet impact area, in order to try to avoid perturbations of the measurement by the high air bubbles content at the impact and downstream (Fig. 2 - right). In addition, some Winkler tests have been done to validate the measures from the oximeters.

Figure 2. Rubble masonry on the steps (left) and oximeter (right)

3.2.   Tests Characteristics

The tests have been carried out with water almost completely deoxygenated (oxygen concentration close to 0 upstream of the model). As the water supply system upstream of the model is completely pressurized (submerged pipe in the model upstream reservoir), the whole water volume of the laboratory reservoir (350 m³) has been deoxygenated.

To remove the dissolved oxygen from the reservoir, Cobalt chloride and sulfite have been mixed with the water. By a careful control of the sulfite volume, the dissolved oxygen concentration in the reservoir has been brought very close to zero. Sulfite excess has to be avoided to not affect the reaeration process on the aerating structure.

During a test, the deoxygenated water is first pumped into the model and upstream oxygen concentration is close to 0. After some minutes, because of mixing of the remaining deoxygenated water with the (aerated) water coming back from the model, oxygen concentration upstream of the model increases slowly. To limit this increase, when this concentration approaches 1 mg/l, sulfite is added in the free surface collecting channel downstream of the model, just before return to the laboratory reservoir. This sulfite, together with the Cobalt chloride still present in the

water, consumes the oxygen. To control this sulfite injection during the tests, continuous control of oxygen concentration took place just upstream of the first step (model inlet).

Because of negative effects on the global water quality during the deoxygenation process (in particular, increase of the water conductivity), the number of deoxygenation operations has been limited to three. Each test has been conducted with increasing or decreasing discharge, with stabilization to each of the target discharge values (25, 50, 75 and 100 m³/s at prototype scale).

The experimental conditions and the chronology of the three tests are given in Table 1. Given the discharges considered and the model dimensions, Reynolds number $Re = q/\nu$, with ν the kinematic viscosity, varies from 1.6 10^5 to 6.4 10^5 while Weber number $We = \rho q^2/h_c\sigma$, with ρ the water density and σ the water surface tension, varies from 2.5 10^3 to 1.6 10^4.

Table 1. Experimental conditions and tests chronology

	Water temperature	Atmospheric pressure	pH start/end	Conductivity start/end	Time	Stage duration	Model discharge	Prototype discharge
	[°C]	[hPa]	[-]	[μS/cm]	[min]	[min]	[l/s]	[m³/s]
Test 1	20.0	998.0	8.4/8.5	365/480	0	-	0.0	0
					3 to 13	10	31.8	25
					15 to 22	7	63.7	50
					24 to 30	6	95.5	75
					30	-	0.0	0
Test 2	19.0	990.0	8.5/8.5	490/590	0	-	0.0	0
					3 to 13	10	121.0	95
					15 to 27	12	95.5	75
					30 to 40	10	63.7	50
					41 to 65	24	31.8	25
					65	-	0.0	0
Test 3	18.9	984.0	8.6/8.6	590/770	0	-	0.0	0
					3 to 18	15	31.8	25
					28 to 38	10	63.7	50
					41 to 51	10	95.5	75
					53 to 63	10	127.4	100
					65	-	0.0	0

4. RESULTS AND DISCUSSION

4.1. General Flow Features

Instantaneous pictures of the flow are given in Figure 3 for discharges of 25, 50, 75 and 100 m³/s at prototype scale. Nappe flow regime occurs for all discharges on all steps except on step 1 for discharges higher than 25 m³/s. On step 1 and for discharges higher than 25 m³/s, no jet and impact are observed on the downstream step and flow aeration seems consequently very weak compared to what is observed on the same step for smaller discharge (Fig. 4).
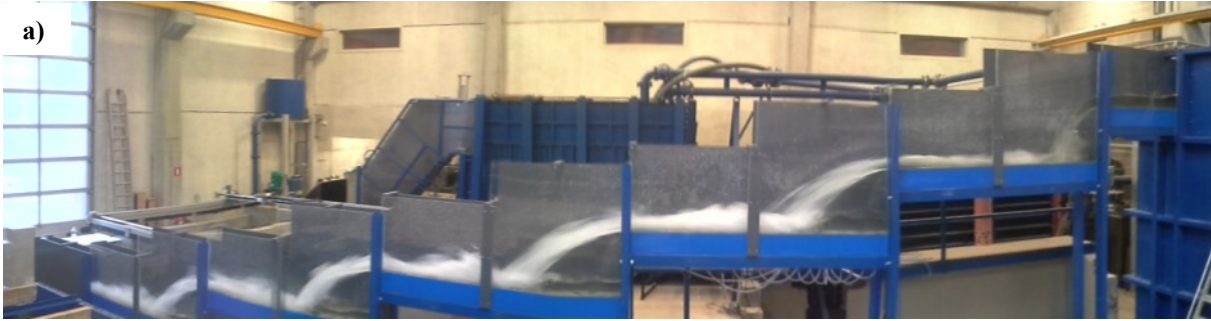
Figure 3. General view of the model – Prototype discharge of a) 25 m³/s, b) 50 m³/s, c) 75 m³/s and d) 100 m³/s
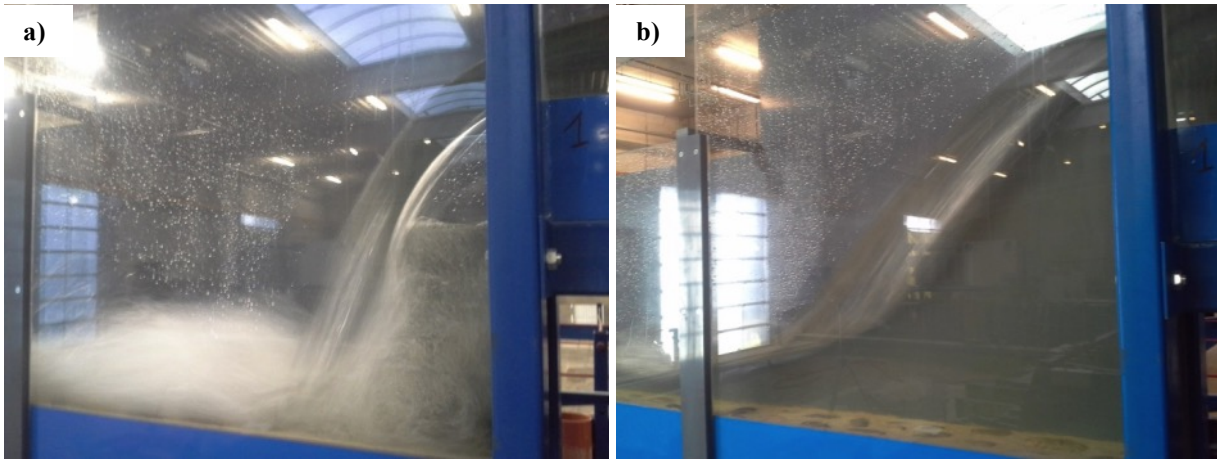
Figure 4. Flow over step 1 - Prototype discharge of a) 25 m³/s and b) 75 m³/s

4.2. Aeration efficiency

The graphs in figure 5 show the evolution of the aeration along the aerating structure depending on the discharge. The results from each test are similar. They show a continuous increase in oxygen concentration along the structure. Each step contributes significantly to the aeration efficiency.
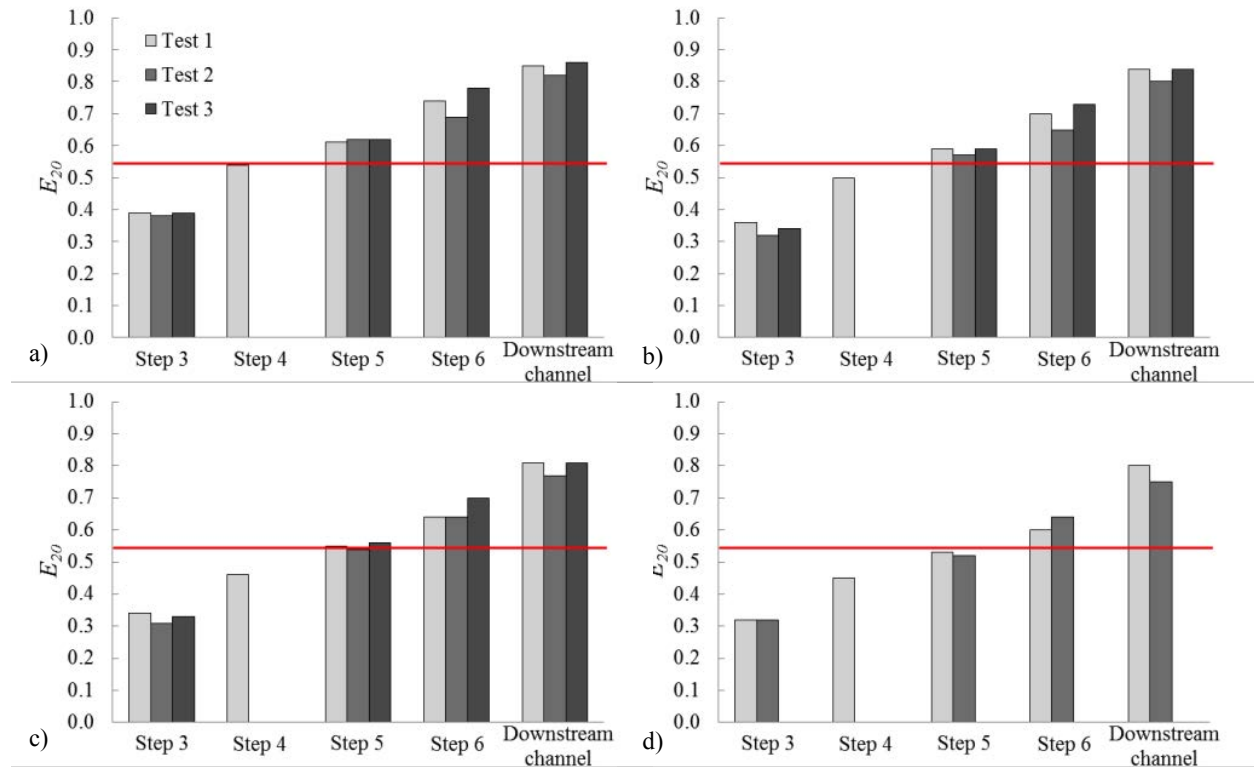
Figure 5. Aeration efficiency at 20°C E_{20} measured along the model for each test – Prototype discharge of a) 25 m³/s, b) 50 m³/s, c) 75 m³/s and d) 100 m³/s

Mean aeration efficiency computed from the results of the 3 tests is displayed in figure 6. Whatever the discharge, the target aeration efficiency is reached after step 6, i.e. a chute of 3 m. For discharges of 25 and 50 m³/s, the target efficiency is reached after step 5. The proposed structure is thus able to meet the project objective.
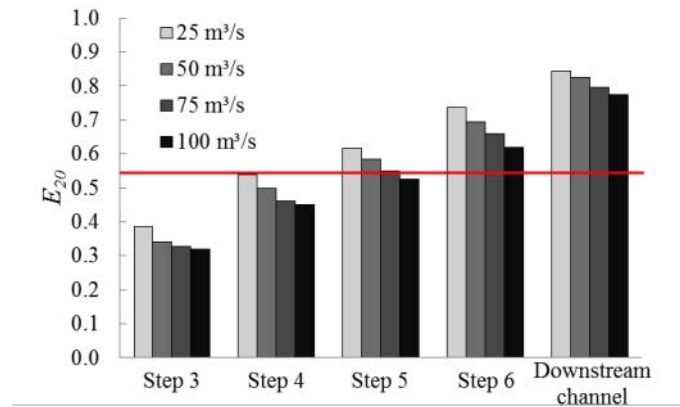
Figure 6. Mean aeration efficiency at 20°C E_{20} measured along the model

Comparison of predicted values from Equations 3 and 4 to measured values given in Table 2 shows similar values, with physical model results bounded by the empirical equations. However, the influence of the discharge is more important in the model than what is predicted by Baylar et al. (2007) formula (Eq. 3), which provides overestimated values. Essery et al. (1978) formula (Eq. 4) predicts well the effect of the discharge variation but provides underestimated aeration efficiencies.

Table 2. Predicted and measured aeration efficiency E_{20} for the structure proposed in this paper

q	h_c	h_c/h_s	E_{20}		
[m³/s/m]	[m]	[-]	Baylar et al. 2007	Essery et al. 1978	Phys model
0.159	0.14	0.27	0.75	0.67	0.74
0.318	0.22	0.44	0.75	0.60	0.69
0.478	0.29	0.57	0.75	0.56	0.66
0.637	0.35	0.69	0.74	0.52	0.62

5. CONCLUSIONS AND PERSPECTIVES

An aerating system using a stepped spillway has been designed to improve the water quality downstream of a large dam. The efficiency of the proposed structure has been validated by means of a 1:1 physical model of a section of the spillway. Experimental results show that target oxygen concentration is reached downstream of the proposed structure in the range of relevant discharges.

Comparison of the measured aeration efficiency with results from the literature shows similarities but also differences. The study is still in progress with

- additional tests on the physical model to increase the reliability of the results and better quantify the gain in oxygen concentration given by each step in order to derive improved design equation;
- a study of scale and geometry effects by building and operation of a scale physical model with a variable width (scaled width or larger width than the one of the physical model presented in this paper).

6. ACKNOWLEDGMENTS

7. REFERENCES

André S., Boillat J.-L. and Schleiss A. (2008). "Ecoulements aérés sur évacuateurs en marches d'escalier équipées de macro-rugosités – Partie I : caractéristiques hydrauliques". *La Houille Blanche*, 2008(1), 91-100. (in French).

Baylar, A., Bagatur, T. and Emiroglu, M.E. (2007). "Prediction of oxygen content of nappe, transition and skimming flow regimes in stepped-channel chutes". *J. Environ. Eng. Sci.* 6, 201–208.

CIDB (2015) *Labour-based methods and technologies for employment-intensive construction works – Best practice guideline – Part 1*, Construction Industry Development Board, Pretoria, South Africa.

Chanson, H. (2009) "Turbulent air-water flows in hydraulic structures: dynamic similarity and scale effects". *Environ. Fluid Mech.* 9, 125-142

Descloux S., Chanudet V., Taquet B., Rode W., Guédant P., Serça D., Deshmukh C. and Guerin F. (2015) "Efficiency of the Nam Theun 2 hydraulic structures on water aeration and methane degassing". *Hydroécol. Appl.* Published online on 25 March 2015.

Essery, I.T.S., Tebbutt, T.H.Y. and Rajaratnam, S.K. (1978). *Design of spillways for re-aeration of polluted waters*. Construction Industry Research and Information Association, Report 72, London, UK.

Felder, S. and Chanson, H. (2015). "Scale effects in high-velocity air-water flows on a stepped spillway". *E-proc. of the 36th IAHR World Congress*, 28 June – 3 July 2015, The Hague, the Netherland, 1-8.

Gosse Ph. and Grégoire A. (1997) "Artificial re-oxygenation of the Sinnamary, downstream of Petit-Saut dam (French Guiana)." *Hydroécol. Appl.* 9(1-2), 23-56. (in French)

Hauser G.E. and Morris D.I. (1995). "High-performance aerating weirs for dissolved oxygen improvement." *Proc., Waterpower'95: Int. Conf. on Hydropower*, ASCE, Reston, Va., 1696-1705.

Nakasone H. (1987). "Study of aeration at weirs and cascades." *J. Environ. Eng.* 113, 64-81.

Ohtsu, I., Yasuda, Y. and Takahashi, M. (2001). "Onset of skimming flow on stepped spillways". *J. Hydraul. Eng.* 127(6), 519-525.

USACE Portland District Spillway Gate Rehabilitation Program

L.L. Ebner[1]; W.B. Fortuny[1]; D.R.Hamernik[1]; M.K. Hess [1]; M.J. Sawka[1]
[1]US Army Corps of Engineers - Portland District
333 SW 1st Ave
Portland, OR 97204-3440 USA
E-mail: david.r.hamernik@usace.army.mil; matthew.k.hess@usace.army.mil

ABSTRACT

The U.S. Army Corps of Engineers (USACE) Portland District has 90 spillway radial Tainter gates. There are 42 gates at the 11 Willamette Valley Basin projects, 5 gates at the two Rogue Basin projects, and 43 gates at the two Columbia River projects. Since 2001, there have been various studies, inspections, and incidents that have prompted the Portland District to become concerned about the structural integrity and mechanical and electrical reliability of these gates. In 2008, load induced buckling was observed on three of the four Tainter gate end frames at Foster Dam, which led to emergency repairs. Additional observations of buckled Tainter gate strut arms at Dexter Dam in December 2009 required repairs and created urgency with respect to documenting the risk to the downstream population at all District projects. These events led to a comprehensive assessment of the Tainter gates in the Willamette Valley and Rogue Basin projects, which was implemented in 2010. The comprehensive assessment included a gates specific potential failure modes analysis (PFMA); structural, mechanical, and electrical assessments; identification of interim risk reduction measures (IRRMs); and analysis of impacts of the interim risk reduction measures. As part of this assessment, the District developed a tool for prioritizing projects for gate repair based on the results of the assessment. Since identifying the issues with Tainter gates, Portland District has implemented IRRMs, taken a systems-based approach to repairs, and implemented a capitalization program to improve gate reliability. Repairs are complete or underway at 36 of the 42 Tainter gates in the Willamette Valley. A study is underway to address reliability of regulating outlets, and future studies are planned for Columbia River spillway gates.

Keywords: *Spillway, Gates, Risk, Rehabilitation, Tainter, Radial.*

1. INTRODUCTION

The US Army Corps of Engineers (USACE) Portland District has 90 spillway Tainter gates. There are 42 gates at the Willamette Valley projects, 5 gates at the Rogue Valley projects, and 43 gates at the Columbia River projects. Table 1 provides an inventory of Portland District's Tainter Gates. Since 2001, there have been various studies, inspections, and incidents that have prompted the Portland District to become concerned about the structural integrity and mechanical and electrical reliability of these gates. There are several factors that led to this conclusion:

- The consequences, both life safety and economic, of an unreliable spillway Tainter gate system are significant.

  - Life safety consequences are greatest at the Willamette and Rogue River projects where a full pool release through a spillway bay exceeds downstream channel capacity. These projects have large volume reservoirs and little or no other means to evacuate the reservoir.

  - Economic consequences dominate on the Columbia River projects due to lost hydropower and navigation. Life safety consequences are considered minimal on the Columbia River projects.

- Design criteria have been updated as knowledge expanded due to operational experience. The majority of the District's gates are deficient when evaluated under the current design guidance. New guidance includes effects of loads such as trunnion friction and single sided hoisting. Structural analysis indicates that the gates are overstressed when operated, even under normal pool levels.

- Spillway Tainter gate trunnions across the US have had issues with seized or "frozen" trunnion bearings. This has also been experienced in the Portland District. Seized trunnion bearings are the result of deferred maintenance and have resulted in sheared keeper plate bolts and increased trunnion friction.

- Fabrication deficiencies have been identified during inspections. The primary fabrication deficiency is poor weld quality, which has resulted in cracked welds.

- Operational use changes have occurred. These operational changes include spilling with small gate openings (1 to 2 foot gate opening of a 30 to 40 foot gate) for improvements to water quality (temperature control), spilling for fish passage, and spilling for power load balancing resulting from wind power generation being added to the grid.

- Inspections have identified numerous deficiencies including: localized buckled members, wire rope failures, seized trunnion pins, cracks in steel in gate members, and deformed members.

Table 1 - Portland District Tainter Gates and Status.

Project	Total Number of Gates	Placed In Service	Status
Willamette Valley Basin Projects			
North Santiam Subbasin			
Detroit	6	1950	In Design
Big Cliff	3	1951	Repairs Complete
South Santiam Subbasin			
Green Peter	2	1962	Repairs Complete
Foster	4	1964	Repairs Complete
McKenzie River Subbasin			
Cougar	2	1959	Construction to start in 2016
Blue River	2	1965	In Design
Middle Fork Willamette Subbasin			
Hills Creek	3	1957	In Construction
Lookout Point	5	1951	In Construction
Dexter	7	1953	Repairs Complete
Fall Creek	2	1963	Repairs Complete
Coast Fork Willamette and Long Tom Subbasins			
Fern Ridge	6	1940	Structural Repairs not Required Mechanical and Electrical Repairs are Planned
Rogue Valley Projects			
Applegate	2	1988	Repairs not Required
Lost Creek	3	1976	Structural Repairs not Required Mechanical and Electrical Repairs are Planned
Columbia River Projects			
The Dalles	23	1952	Future Work
John Day	20	1966	Future Work

1.1. Tainter Gate Assessment

In 2010, the current reliability and safety of Portland District Spillway Gate Systems was assessed due to recent events:

2008 – buckled Tainter gate strut arms at three of the four Tainter gates at Foster Dam led to emergency Tainter gate repairs.

2009 – wire rope failure at two of three gates at Big Cliff led to emergency wire rope replacement.

2009 – buckled Tainter gate strut arms at Dexter Dam where emergency Tainter gate repairs were implemented.

The assessment was done using risk-based tools and a risk-informed decision making process. The goal of this analysis was to inform the Portland District about the risk associated with the operability and dependability of spillway Tainter gates. By establishing the relative risk at each of these projects, a prioritization of risk mitigation and IRRMs can be established. IRRMs are a temporary approach to reduce Dam Safety risks while long-term solutions are being pursued. In establishing IRRMs, the prevention of loss of life is the first and foremost objective, followed by prevention of catastrophic economic or environmental losses. A systems-based repair and capitalization program was implemented to improve gate reliability. Repairs are complete or underway at 30 of the 42 Tainter gates in the Willamette Valley.

2. INTERIM RISK REDUCTION MEASURES

To reduce risk associated with failure of the Tainter gates, gate operating restrictions were implemented at 9 projects on an interim basis until the gates could be rehabilitated. Operation of the gates with the pool near the top of the gate can mobilize large friction forces within the trunnion, resulting in additional bending in the struts. If these forces are large enough, the gate structure could catastrophically fail, resulting in a sudden release of water from behind the gate.

Analysis showed that operating the gates at these 9 projects with the pool above the upper girder on the gate could overstress the struts. Gate operating restrictions were implemented that prevented the gate from being operated if the pool was above a certain elevation on the skin plate. Typically, the elevation was at the upper girder. Implementing the gate operating restrictions significantly reduces the likelihood that the Tainter gates would be operated with the pool above the upper girder. However, it is possible to operate at a higher pool elevation than the elevation of the upper girder by raising the gates as the pool rises (the gates would need to track with the pool). Gate operating restrictions remain in place until rehabilitation work on the Tainter gates is completed.

3. GATE REPAIR PROGRAM

Although structural concerns initiated the spillway gate rehabilitation program effort, Portland District realized through the PFMA process that a systems based approach was necessary for spillway gate rehabilitation. Portland District focused on four factors to ensure reliability and safety:
- Structural strengthening
- Improving mechanical reliability
- Improving electrical reliability
- Implementing a regular operational testing, maintenance, and inspection program

3.1. Structural Strengthening

The structural problem encountered was that spillway Tainter gates required strengthening due to unaccounted loads (typically trunnion friction) and new design criteria. The objective of the program was to strengthen the gates to meet the current design criteria. Typically, the overstressed members were the struts, ribs, and horizontal girders. The criteria used to strengthen the gates came from USACE EM 1110-2-2702 and USACE ETL 1110-2-584.

Finite element models (FEM) were built for each gate including separate models for quality control purposes. Load combinations were run from the criteria to determine the worst case loading and to ultimately determine which members were overstressed. At the same time, steel samples were taken from gates in order to verify yield and ultimate strengths as well as chemical composition for weldability determination.

The most significant issue involved in the strengthening program was to address the large machinery load (Q) that occurs in a few of the load combinations as seen in Table 2. The maximum applied machinery load is generally two to five times larger than the required lifting load. This load is a force applied to the gate from the lifting hoists and occurs when the gate is jammed within its bay in a non-moving, single-sided hoisting event (LC 5) or when the gate is completely open bearing against its gate stops (LC 6) while the hoist is still operating. To overcome this issue, a load limiting device (LLD) was incorporated into the design, which limited the hoisting load to what was required to operate the gate under its worst case loading (LC 3, single-sided hoisting, gate moving) in order to achieve the flood control mission.

Welding and fabrication issues from the 1950s and '60s needed to be addressed. Typically, complete joint penetration welds were not back-gouged, which left a line of indications at the joint's mid-depth and effectively made them partial penetration welds. Back-gouging is a process that removes imperfections from a partially welded joint to assure complete fusion upon subsequent welding. Therefore, a fit-for-service weld analysis was performed to ascertain if the joint had adequate capacity. Intersecting welds that cause restraint within the joint and that can lead to fracture were drilled out to eliminate a brittle failure mode (Figure 1).

Table 2 - Load Factors for Tainter Gates.

Load Cases			Loads/Load Factors							
			D	G	Hs	Hd	Q	EV	IM	EQ
Limit State	Description	Case	γD	γG	γHs	γHd	γQ	γEV	γIM	γEQ
Strength I	Gate Closed	1	1.2	1.6	1.4Hs2	0	1.2Q1	0	0	0
Strength I	Gate Closed	1	1.2	1.6	1.4Hs2	1.2(1)	1.2Q2	0	1.6(1)	0
Strength II	Usual Operation	2.a	1.2	1.6	1.4Hs3	0	1.4QFs2+ 1.0QFt2	0	0	0
Strength II	Usual Operation	2.b	1.2	1.6	1.4Hs2	1.2(1)	1.4QFs2+ 1.0QFt2	0	1.6(1)	0
Strength II	Unusual Operation	3	1.2	1.6	1.4Hs2	0	1.4QFs2+ 1.0QFt2	0	0	0
Extreme I	Gate Closed	4.a	1.2	1.6	1.4Hs3	0	1.2Q2	0	0	0
Extreme I	Gate Closed	4.b	1.2	1.6	1.4Hs1	0	0	0	0	1.0EQ
Extreme I	Gate Jammed	5	1.2	1.6	1.4Hs2	0	1.2Q3	0	0	0
Extreme I	Gate Opened	6	γD2(2)	γG2(2)	0	0	1.2Q3(1)	1.3W(1)	0	1.0EQ(1)

Notes: (1) Select one at a time
      (2) Use max or min values, whichever produces maximum effects

D – dead loads; G – gravity loads (silt, debris, ice); Hs – hydrostatic; Hd – hydrodynamic; Q – machinery load; EV – environmental loads (wind); IM – impact loads; EQ – earthquake load; γ – load factor to be applied to loads as indicated in table.
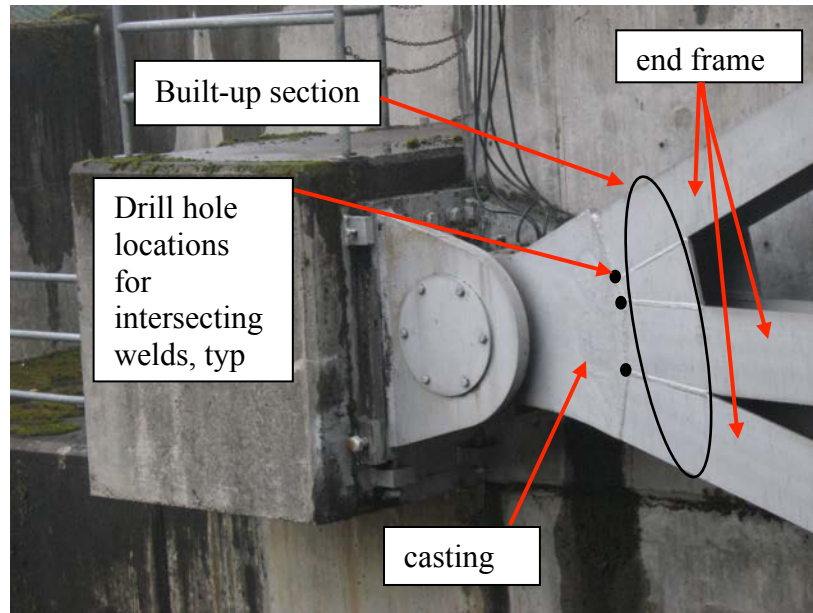
Figure 1. End Frame at Casting Intersecting Welds, Fall Creek Dam, Lowell, Oregon.

Various repair options were considered for each individual project, taking into account scheduling, cost, constructability, and the risk of unknown field conditions that have been experienced on similar jobs performed in the past. Generally, the strut arms, ribs, and horizontal girders required strengthening. The ribs and girders were reinforced by either additional bracing or increasing the section. Repair options considered for strengthening of the strut arms included cover plates, complete end frame replacement (struts and strut bracing), and additional bracing. The addition of bracing (to decrease the effective length of the strut arms) was typically not a viable option. The strut arms see significant axial and weak axis bending forces and relatively small strong axis bending forces. Therefore, even if the strong axis of the strut arms could be effectively braced, the additional capacity gained would not do very much to bring down the stress level in the section. Bracing would be required to cross the width of the spillway to the gate's adjacent end frame or attach to the horizontal girders, making strong axis bracing impractical. The location of the existing weak axis bracing from the original design is typically at its optimal location. Therefore, the strut arm section's axial capacity is 'capped off' and any additional bracing that would decrease the strut's effective length would not increase section axial capacity.

There are numerous benefits associated with a repair that reinforces the strut arms with cover plates. This lessens work scope, saves time and cost, and lessens the impact on other disciplines as opposed to a greater work scope such as replacing end frames. Cover plates have been implemented at Willamette Valley projects such as Fall Creek and Lookout Point Dams outside of Lowell, Oregon, and Foster Dam outside Sweet Home, Oregon. The strengthening of the Fall Creek Dam spillway gates may be seen in Figure 2. However, there are issues that need to be evaluated if this option is to be implemented. For instance, cover plate termination before the casting was required for the Fall Creek project. It is not desirable to weld to the castings due to potential cracking concerns and melting of the trunnion bushing from welding heat. An analysis was performed in order to determine if the built-up section immediately upstream of the steel casting (not reinforced with a cover plate) had adequate strength (Figure 1 and Figure 2). Fatigue is an issue that needs to be addressed for cover plates. Welded cover plate terminations have an undesirable fatigue category associated with them, which can ultimately lead to fracture of the base metal member.
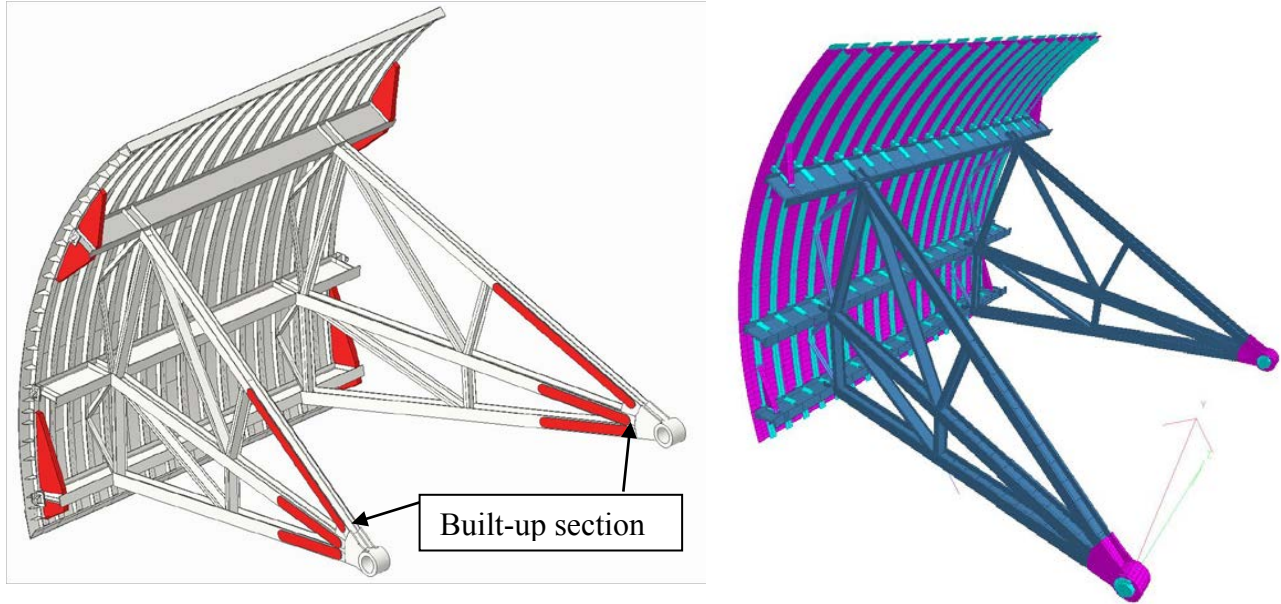
Figure 2. Strengthening (Red Highlights) of Fall Creek Dam Spillway Gates. Drawing Isometric Left and FEM Isometric Right.

Complete end frame replacement, including the trunnion hub, is another strengthening option which was implemented at Dexter Dam Spillway gates outside of Lowell, Oregon (Figure 3), Big Cliff Dam outside of Detroit, Oregon, and Green Peter and Foster Dams outside of Sweet Home, Oregon. This option is obviously more expensive than cover plates and also requires additional work and schedule considerations since the gate will be taken off seal. However, this option minimizes the risk of unexpected field conditions and results in a new end frame that utilizes modern steel and welding techniques, increasing long term reliability.

Figure 3. New End Frame at Dexter Dam Spillway Gates, Lowell, Oregon.

3.2. Electrical Modifications for Reliability

The electrical assessment was conducted to establish a probability of failure for the electrical components associated with the operation of spillway Tainter gates at Portland District projects. For the purposes of the electrical assessment, the probability of failure is defined as the probability that an individual gate will not operate the next time operation is attempted. It does not take into account the reasons behind the necessity for operation, the consequences of inoperability, or the timeframe required to troubleshoot and repair the failed component. The goal is to obtain a probability of failure below 1.0E-04 for each gate individually and also for the gate system at each project. This reliability metric was developed by Jack Lewin in the evaluation "Reliability Assessment of Spillway Gate Installations" written in November 2001.

At each project, the electrical equipment was subdivided into three primary categories: (1) power sources; (2) power distribution; and (3) control equipment. A probability of failure for each category was derived by developing a fault tree based on the project's electrical configuration and distribution system, as well as its local control equipment. The three individual values were then summed to provide an overall project spillway electrical probability of failure.

From the results of the Portland District reliability study, it was observed that the dominant probability of failure lies with the local control equipment, which is also the easiest and least expensive to repair or replace. The second most likely to cause a failure of the gate to operate is the loss of distribution equipment due to the lack of redundancy in dam power feeders at most of Portland District sites. The least likely to cause a failure to operate is the loss of all power sources, which includes utility power, loss of medium voltage switchgear in the powerhouse, and emergency backup generators.

In order to increase the reliability of the Portland District spillway gate electrical systems, the following modifications have been made to the gate systems as part of the gate rehab projects:

Controls: Replace entire control systems for all spillway gates, which were all original and at or nearing the end of their 50yr design life. Convert all local spillway gate control systems to deadman style pendant controls and provide multiple pendants for each site that can be used on all new gate systems across Portland District's sites. This pendant style system provides redundant pushbutton controls and thus increases reliability. Also, by converting to the deadman style controls, the controls were simplified and the number of components used in the control systems was reduced by eliminating incremental limit switches and timing relays, which reduces the overall probability of failure. Deadman controls, as implemented on Portland District spillway gates, are defined as controls designed to return the system to a safe or neutral state in the absence of continuous input from a human operator, i.e. the operator must press and hold the raise or lower button during the entire gate operation; if released, the operation stops.

Power Distribution: Replace existing dam feeder and install/replace redundant dam feeder. It is also important to ensure each dam feeder is physically separated from one another, i.e. each feeder either takes different route to the dam or is in a separate raceway. For example, two feeders fed from the same distribution panel with a single bus are not considered to be redundant. The goal is to ensure that a single fault in a piece of distribution equipment or physical damage to a single raceway will not cause a loss of both feeders.

Power Supply: Replace switchgear and/or associated feeder breakers for main and redundant dam feeders. Replacing or rehabilitating the emergency backup generators is also considered on each of the rehab projects. In addition to these changes, adding a portable generator supply receptacle at the spillway decks, which allows the ability to utilize trailer mounted generators for emergency spillway operation, has also been done, thus adding a fourth available source of power.

One other recommendation to come out of the electrical reliability assessment, which has not been addressed due to operational constraints at a majority of the Portland District's sites, is increasing the frequency of operations. An increase in operations would improve the reliability of the gate systems, but there are operational constraints that do not enable the gates to operate except when the reservoir levels are down below spillway crest, which is typically only during flood season.

In addition to increasing the reliability of the spillway gate systems, the modifications that have been made greatly increase the operability and maintenance of the systems. The reduced hardware and simplified controls systems

have decreased the time it takes for operators to be trained on these systems. Additionally, troubleshooting these systems is simplified as a result of the reduced amount of hardware.

3.3. Mechanical Modifications for Reliability

The mechanical objective of each gate rehab project has been ensuring the hoist and trunnion bearing systems are in a condition that will result in safe and reliable gate operation for the next 50 years of service. To obtain this objective, each system has been evaluated for compliance with current design criteria and the potential for continued reliable operation. The scope required to obtain this objective at each site has been full replacement of the mechanical hoisting and trunnion bearing systems.

Replacement of some hoist systems has been necessitated by gate weight increases from the structural retrofit. However, even locations with negligible weight increase have required replacement to ensure compliance with more conservative, updated mechanical criteria. In addition, most original hoist systems have met or exceeded their intended service life, are starting to show signs of degraded reliability, and are not expected to provide continued reliable service for a 50 year lifecycle. Full system replacements have dramatically increased the reliability of Portland District spillway gate systems. In addition, other improvements, such as designing to more conservative criteria, improved material selections, and design simplifications have also resulted in reliability improvements.

The main design criteria changes that have occurred since original Portland District gate systems were installed have been the assumptions of how overload hoisting forces are distributed between sides of a gate. Original systems were designed assuming that a maximum overload condition would result in a 50/50 load split between sides of the gate. Gate operating experiences have shown this assumption is not valid. When gates are jammed between piers, they tend to flex and skew, resulting in differential hoisting loads between sides of the gate. Current USACE criteria requires designing for overloads with a 70/30 load split between sides of a gate. Portland District designers have gone a step further and have been designing Portland District hoist systems for a 100/0 load split to match the structural design criteria. Designing to this more conservative overload assumption has been made feasible with the use of load limiting devices, which are discussed below.

Other design changes have helped to improve assembly, alignment, and installation of the new hoist systems. This includes C-face mounting of drive system components and skid mounting hoist assemblies with electrical controls. Both of these changes have helped facilitate shop assembly/alignment and have minimized the onsite installation time where the gate is out of service, Figure 4.

Figure 4. Shop Assembly and Testing of Skid Mounted Hoists.

The largest change in material selections have been on trunnion bearing systems. Portland District has utilized fabric, reinforced, composite, self-lubricated trunnion bearing materials to improve the reliability of the trunnion bearing lubrication. Spillway Tainter gate trunnions across the US have had issues with seized or "frozen" trunnion

bearings. This often results from insufficient grease being pumped across the full running surface of the bearing. Self-lubricated materials have the primary lubricant (solid lubricants) incorporated into the parent bearing material. The lubrication is always present on the bearing running surface and does not rely on grease pumps, grease lines, maintenance funding, and other external factors for successful performance. PTFE seals have been utilized with the self-lubricated materials to exclude water and contaminants and ensure low coefficients of friction, Figure 5.

Figure 5. Self-Lubricated Trunnion Bearing and Thrust Washer.

3.4. Load Limiting Devices

Changes to more conservative structural and mechanical design criteria have driven a need to optimize how the hoist system is controlled in overload cases. The purpose of a spillway gate is to control flow. When an overload condition is experienced, a gate is still capable of performing the function of controlling flow until it becomes jammed between piers. When a gate jams, there is no value added in subjecting the gate to additional load. Portland District has been able to optimize hoist and gate sizing by utilizing load limiting devices (LLD) to prevent unnecessary load after a gate becomes jammed.

To determine appropriate load limits for a hoist system, Portland District has investigated each gate being rehabbed with a 3D FEM of the gate. Gates are modeled under single sided lifting to quantify deflections. The reaction forces to keep the gate deflection constrained within the pier widths are then quantified. Next, a coefficient of friction is applied to the pier reaction forces, resulting in a drag force that is used to solve the theoretical maximum single-sided hoisting load required to operate the gate. An uncertainty factor is then applied to the theoretical hoist load to account for efficiencies of the mechanical system as well considering the accuracy range of the LLD.

Portland District has performed this analysis on many gate systems and found that most require a motor overload limit between 130%-140% of the motor full load torque (FLT) to prevent unnecessary hoist loads. Motors used for hoisting application are typically selected as a NEMA design B or D. Per NEMA MG-1, design D motors are required to have a max torque no less than 275% of the full load torque with actual values commonly between 300%-350% of FLT. Design B motors are required to have a max torque no less than 205%-225% of the FLT (depending on hp rating and RPM for sizes common to spillway gates) with actual values commonly between 250% - 275% of FLT. These common hoist motor designs have a tremendous amount of overload potential. Portland District has started utilizing LLDs to lower the max torque the system can deliver and keep designs feasible and economical.

Portland District has investigated various LLDs for spillway Tainter gate hoist systems and has authored a White Paper on this subject. Key features of these devices include:

- Reliable operation

- Overload protection for 100% of the operating time (no protection at inrush is unacceptable)
- No disengagement of the load (devices are load holding and never disconnect the motor or brake from the load which could potentially drop the gate)
- Fast reaction time (time between sensing overload and system shut down are minimal)

After evaluating LLDs against a typical spillway gate application, there were three devices that had clear advantages over others:

- Custom wound motors – A motor with a custom winding design that meets the normal operating and overload characteristics specific to the application. The motor is designed with a reduced overload value that prevents overload of the system.
- Torque Transducers – A device that measures drive train torque and triggers a relay to shut the hoist system down when allowable values are exceeded.
- Torque Switch – A shaft coupling with a ball detent system calibrated to move a coupling plate axially when a critical torque value is reached (without disengagement of power-train load). The axial movement of the plate can be used to activate a switch or proximity sensor to shut the hoist system down when allowable values are exceeded.

Portland District has successfully installed custom wound motors and is evaluating them for long term use. In addition, Portland District is also in the process of installing and evaluating torque transducers for successful performance.

4. OPERATION AND MAINTENANCE CHANGES

USACE Northwest Division introduced a policy (Corps of Engineers, Northwestern Division, Operational Testing and Inspections, Periodic Inspections, and Evaluations of CENWP Spillway Gates) in 2012. This policy requires regular trunnion bushing lubrication, full cycle open/close tests, full mechanical/electrical component inspections, and hands-on structural inspections. This has been fully implemented across Portland District to ensure gate reliability and safe operation.   Results of the testing and inspection are included in project Periodic Inspection reports.

5. PRIORITIZATION OF REHABILITATION WORK

In order to develop a long-term plan for repairing the Portland District's spillway gates, a process to prioritize gate repair at the project level was developed. A matrix was developed to consider the various criteria that would be used to prioritize repairs and provided a tool to rank the projects based on these criteria. Each criterion had a metric defined for it, and a score was given for each project. It was decided that the various criteria should not all have the same weight in terms of determining the priority of repair; sensitivity analyses were performed to assess the impact of varying the weight of each of the factors. The criteria for prioritization included:

Engineering Reliability: these criteria were based on the results of structural, mechanical, and electrical reliability assessments. Rehabilitation of projects with lower reliability systems were prioritized over higher reliability projects.

Economic Impacts: these criteria were based on the economic impacts of the gate operating restrictions to the project missions (flood damage reduction, hydropower and recreation). Rehabilitation of projects with high economic impacts were prioritized over those with lower impacts.

Operations Impacts: these criteria were based on the operation's manpower impacts of existing mechanical and electrical reliability deficiencies and from the gate operating restrictions. Rehabilitation of projects with larger operation impacts were prioritized over those with lower impacts.

Environmental Impacts: these criteria were based on the impacts of the gate operating restrictions on the ability to refill the reservoirs in the spring, fish and wildlife habitat, and water quality. Rehabilitation of projects with larger environmental impacts were prioritized over those with lower impacts.

Weights were assigned to the various criteria used to prioritize gate repair to reflect this. The criteria that were linked to life safety issues were given highest weights. Gate reliability (structural, mechanical and electrical) has life loss consequences; therefore, these criteria were given large weights. Flood damage reduction is a primary authorized purpose for these dams, and reduction in this capability due to gate operating restrictions may result in economic consequences; therefore, this criterion was weighted relatively high.   The weights of the remaining criteria were smaller and tended to be grouped within a relatively small range.   The relative magnitude of the weights of these criteria was debated, and it was found that small changes to these weights do not result in dramatically different project priorities.

6. REHABILITATION PROGRAM

Portland District initiated a capitalization program to rehabilitate all spillway gates in the Willamette Valley in 2009. Table 1 provides the progress to date of Portland District's rehabilitation program.

7. FUTURE WORK

7.1. Columbia River Spillway Gates

Once the Willamette and Rogue projects are complete, the effort will be expanded to include the Columbia River projects. Although potential life safety consequences at these projects are unlikely since the instantaneous change in discharge would not be significant, the potential economic consequences are greatest at the Columbia River projects, where hydropower and navigation capabilities could be impacted in the event of Tainter gate failure.

7.2. Regulating Outlets Reliability

There are 34 reservoir regulating outlets (ROs) in the Willamette and Rogue Basin Projects. The regulating outlets, just as the spillway gates, are integral to the flood damage risk reduction mission. Recent work on ROs within the Portland District revealed a high likelihood of systemic reliability issues. Inability for the gates to function as designed could lead to dam safety, and consequently, life safety issues for downstream stakeholders. The regulating outlets are operated under hydraulic pressure. Any oil leaks could have significant environmental impacts. Additionally, the ROs may be used for downstream temperature control as an interim measure as part of the fish passage improvement plan. Loss of use would severely impact fish listed under the Endangered Species Act in the Willamette and Rogue River Basins. Effort has just begun to assess the condition of each RO and provide a comprehensive evaluation and report on their condition.

7.3. Trunnion Anchors

The trunnion is often anchored to the concrete through steel anchor rods. USACE is currently researching and developing means to test the integrity of these anchors.

8. CONCLUSIONS

Significant conclusions as a result of the CENWP spillway gate program are as follows:

- Although the program initiated out of structural concerns and local buckling at Foster Dam, the potential failure modes analysis and comprehensive inspections indicated a holistic approach was needed. Mechanical and electrical reliability, as well as regular operational testing and inspections, needed to be addressed to minimize risk.
- The initial assessment of CENWP spillway gates that documented findings, the PFMA, inspections, prioritization, reliability, and risk, served as an excellent account and vision and led to a successful and well-funded program.
- The initial spillway gate assessment did not address planning of construction at the 11 projects within the Willamette Valley. Emergency and routine vehicular use of the spillway deck, lack of bulkheads at some projects, and confined construction windows challenged the ability to schedule implementation. A systems approach was developed to coordinate the construction over the entire Willamette River system.
- Extreme machinery loads are challenging to implement structurally, and this led to the investigation of load limiting devices.
- The program needed to be broadened to include other water discharge structures such as regulating outlets.

9. REFERENCES

Lewin, J. and G. Ballard. *Preliminary Reliability Assessment of Spillway Gate*. (2001)

U.S. Army Corps of Engineers. Load Limiting Device White Paper. U.S. Army Corps of Engineers: Portland District, Portland, OR, January 2016.

National Electrical Manufacturers Association. *ANSI/NEMA MG 1-2011*. 7 July 2012. American National Standards Institute, Inc. Washington D.C.

U.S. Army Corps of Engineers. *Design of Hydraulic Steel Structures*. ETL 1110-2-584. Washington, DC: U.S. Army Corps of Engineers, April 30, 2014.

U.S. Army Corps of Engineers. *Design of Spillway Tainter Gates*. EM 1110-2-2702. Washington, DC: U.S. Army Corps of Engineers, January 1, 2000.

U.S. Army Corps of Engineers. *Mechanical and Electrical Design for Lock and Dam Operating Equipment*. EM 1110-2-2610. Washington, DC: U.S. Army Corps of Engineers, June 30, 2013.

U.S. Army Corps of Engineers. *Operational Testing and Inspections, Periodic Inspections, and Evaluations of CENWP Spillway Gates*. Regulation No. 1130-2-8. U.S. Army Corps of Engineers: Northwestern Division, Portland, OR: U.S. Army Corps of Engineers, 2014.

A Risk Based Framework for Evaluating Gated Spillway Operations

G.S. Paxson[1], M.W. McCann, Jr.[2], M.E. Landis[3]
[1]Schnabel Engineering
West Chester, PA 19382
USA
[2]National Performance of Dams Program and
Department of Civil and Environmental Engineering,
Stanford University
Stanford, CA 94305
USA
[3]Schnabel Engineering
Greensboro, NC 27407
USA
Email: gpaxson@schnabel-eng.com

ABSTRACT

Gated spillways are often necessary to provide both operational flexibility and discharge capacity to pass large flood events. However, gated spillways present operational challenges to dam owners and operators, often necessitating development of a flood operations plan (FOP) that is used in tandem with the dam's emergency action plan (EAP). Even a well-intentioned and robust FOP/EAP can require personnel to predict flooding, use judgment particular to the requirements of the plan, and react quickly. In addition, all of the equipment required to operate the gates needs to function as designed and be operated in accordance with the FOP.

This paper presents a framework for evaluating the risks related to gate operations during floods, considering operations in accordance with the FOP, as well as operations that deviate from the FOP/EAP due to operator (human) error or system (mechanical/electrical/structural) malfunction. Case studies are presented to evaluate the downstream impacts of gate operations (or misoperation) for a range of flood events. A basis for quantitative evaluation of risks is included. Considerations for improving operation plans and replacement of spillway gates with more reliable passive systems are presented in the context of risk framework.

Keywords: *Risk Management, Risk Analysis, Spillway Gates, Flood Operations*

1. INTRODUCTION

Gated spillway systems are often necessary for dams where regulation of the pool level is required, outflows must be controlled to prevent downstream flooding, and when significant discharge capacity is required to pass large inflow flood events. According to the National Inventory of Dams (USACE 2015), there are over 8,500 dams in the United States with "controlled" spillways. This is about 10 percent of the dams included in the inventory. A similar search indicates that about 20 percent of the 3,800 Federal dams have controlled spillways. Of the 8,500 dams with "controlled" spillways, nearly 3,500 (about 40 percent) have a primary purpose of "Flood Control" or "Hydroelectric."

Spillway gates include both underflow gates (examples include radial or Tainter gates and vertical lift gates) and overflow, or crest, gates. Underflow gates result in larger "surges" in outflow when operated under full head, whereas crest gates are typically better suited to control outflows.

Gated spillways offer specific advantages over fixed crest spillways, including significant discharge capacity within a given spillway width and the ability to provide surcharge (flood) storage with little to no outflow until the gates are operated to provide discharge capacity. The primary disadvantage of gated spillway systems is their vulnerability and reliability, particularly during large storms.

The US Army Corps of Engineers (USACE) acknowledges the advantages of a fixed crest spillway, noting "the value of an uncontrolled fixed crest spillway in providing an extremely reliable operation and a very low cost maintenance facility is undeniable" (USACE, 1990). However, USACE (1990) also recognizes the need for spillway gates in certain circumstances and provides guidance for these scenarios, noting that fixed crest spillways should be incorporated into designs when watershed response time (time of concentration) is relatively short (less than 12 to 24 hours), and they also suggest the use of at least two gates to "satisfy safety concerns." The latter requirement is likely to provide redundancy for situations where a gate cannot be operated.

As presented in Paxson et al. (2015), dam safety and flooding risks related to spillway gates can result from two primary sources:

1. Unintended and/or uncontrolled releases resulting from
    a. accidental or improper gate operations
    b. structural failure of the gate(s)
    c. inability to close gate(s) after operation
2. Reduction in spillway capacity, resulting in overtopping failure of the dam from
    a. Inability to properly operate the gates
    b. Blockage of spillway gate openings from debris

Item 2 is often addressed in traditional dam safety potential failure mode and risk analyses; the risks related to item 1 can be more difficult to quantify. Effective use of spillway gates during floods often requires actions by the dam owner/operator. This not only includes operating the gates, but also making decisions to predict flooding and the impacts of gate operations.

1.1. Impacts of Gated Spillway Operations

The National Performance of Dams Program (NPDP 2016a) website includes documentation of 65 dam safety incidents related to gated systems, including structural failure, operator error, and issues with gate operation systems (mechanical, hoisting, cables, and chains). Incidents could include an uncontrolled release resulting from structural failure of the gate (e.g., Folsom Dam, see ASDSO/EPRI 2000), failure of the dam during a flood due to inability to operate gates (e.g., Delhi Dam, see Fiedler et al. 2011), or unintended releases due to gate misoperation. This paper focuses on the issues related to gate operations as opposed to failures of the dam or components of the dam.

Two 2014 events in India demonstrate the potentially catastrophic impacts of spillway gate operations. In June, at the Larij Hydropower Project, the spillway gates were operated, reportedly increasing spillway outflows from 20 cubic meters per second (cumecs) to 450 cumecs over the course of an hour (NDTV 2014). The flooding resulted in the deaths of 24 students and a tour guide on an excursion in the Beas River downstream of the dam. An inquiry into the incident led blame to the dam authorities for the tragedy, noting that standard procedures for releasing water were ignored. Less than a month after this incident, ten boys were nearly drowned after gate operations at Tenughat Dam, which reportedly caused significant flooding (The Telegraph 2014).

In addition to cases where downstream flooding occurs as a result of releases associated with gate operations, there are many situations where the dam operator was criticized for the gate operations even though the releases may not have caused the downstream flooding or certainly did not increase flooding over what would have occurred if the dam were not in place. In July 2014, the US Army Corps of Engineers was criticized for operations at Coralville Reservoir in Iowa, which included allegations from residents of 1) not releasing enough water prior to the flood and 2) releasing too much water during the flood (O'Leary 2014).

The Washington Suburban Sanitary Commission (WSSC) came under similar scrutiny related to flooding in Laurel, Maryland, downstream of Duckett Dam during a storm in April 2014. Residents and politicians suggested that

WSSC had "manufactured" the flood (Shaver 2014) and questioned whether releases at the dam could have been controlled to reduce the flooding (Pichaske 2014). WSSC and residents defended the operations, noting that the gate operations were necessary to address a potential dam safety concern (Johnson 2014). It should be noted that unlike Coralville Dam, the Duckett Dam was not constructed to provide downstream flood risk reduction; the structure impounds a water supply reservoir. Nonetheless, the dam likely provides some level of flood protection.

The 2015 floods in South Carolina were reported to have been roughly a 1,000 year event, and more than 30 dams failed (NPDP 2016b). South Carolina Electric and Gas (SCE&G) owns and operates Saluda Dam (impounding Lake Murray) to provide hydroelectric power. During the 2015 floods, SCE&G operated the spillway gates, resulting not only in criticism, but lawsuits from downstream residents (Ham 2015). Claims from residents ranged from, "[SCE&G] mishandled the rain event," to, "[they] had no right to create a flood," and had "no easement to flood [neighborhoods]." In addition to claims that SCE&G caused the flooding, the utility was criticized for not providing sufficient warning, even though they reportedly issued press releases noting the need to open the gates as much as two days prior (Smith, 2015). Of note, SCE&G faced a lawsuit in the 1960s related to releases in June 1965; the federal judge dismissed the lawsuit with a conclusion that the flooding would have occurred even without the dam (Smith 2015).

These, and numerous other case histories, document not only the potential for loss of life or property damage resulting from gate operations, but also the likelihood that the owner will face criticism and lawsuits for gate operations, resulting in significant costs to defend themselves against claims.

1.2. Flood Operations Plans

Most dams with gated spillways commonly have some type of flood operations plan (FOP) that is used to assist the operator during flood events. Even projects without a formal FOP usually have set up some guidance to maintain the reservoir pool at a target elevation by opening gates as inflow increases. More formal plans may require monitoring precipitation forecasts, stream gauge data, and lake levels. Based on observed conditions, the operator opens or closes gates and continues monitoring. In addition to reliable electrical, mechanical, and structural systems, the effective execution of an FOP requires an available operator who may need to make difficult decisions during an emergency situation in which he/she may have other responsibilities.

2. EVALUATING SPILLWAY GATE OPERATIONAL RISKS

A framework for evaluating the risks related to spillway gate operations needs to consider a variety of systems and scenarios, including management decision-making and operator actions with regard to operations and implementation of the FOP. Each project is different, and the flood scenarios that may be experienced could have a complex sequence of events during a flood. An example project is used to illustrate such a scenario.

2.1. Example Project

The example project is a 40-m (130-ft) high dam impounding a water supply reservoir. The spillway is a concrete chute equipped with three Tainter gates, each about 5.5 m (18-ft) high, located in 5.5 m (18-ft) wide bays. This is the only spillway at the dam, which is located on a 56.8 square km (22 square mile) mountainous watershed. A city with a population of about 90,000 is located 19 km (12 miles) downstream of the dam. The dam is classified as "high hazard," and the regulatory spillway design flood (SDF) is the Probable Maximum Flood (PMF). The gated spillway was found to have a capacity of about 65 percent of the PMF, assuming a starting reservoir elevation of 791.9 m (2,598 ft). The gates are operated to maintain this elevation until they are fully opened. If the gates are inoperable (closed), flow would overtop the gates at reservoir EL 792.9 m (2,601.5 ft) and the spillway would have capacity to pass a flood with an estimated return period of about 1,250 years without overtopping the embankment dam (top of dam EL 796.3 m (2,612.5 ft)). The PMF has been estimated to have a return period between 100,000 and 200,000 years. Based on the requirement to pass the PMF, the owner is constructing a new auxiliary spillway

through an abutment, requiring significant investment. As part of this project, the owner is considering options to reduce reliance on the gated spillway to pass floods.

2.1.1. Flood Operations

This project has a formal FOP, which includes guidance for gate operations that is tied to precipitation forecasts, upstream stream gauge data, and reservoir level before and during the flood event, as follows:

- The FOP includes monthly target "normal" reservoir levels, selected based on anticipated water supply needs balanced with reducing reliance on gate operations.
- The operator may be required to open gates when significant rainfall (greater than 15.2 cm (6 inches) over 24 hours) is predicted, depending on the reservoir elevation.
- If the reservoir is below EL 789.4 m (2590 ft), the gates remain closed.
- If the reservoir is above EL 789.4 m but below the monthly target, one to three of the gates are opened between 0.15 and 0.3 m (0.5 to 1.5 ft) based on flows reported at a stream gauge located upstream of the reservoir.
- If the reservoir is above the monthly target, one to three of the gates are opened between 0.15 and 0.46 m (0.5 to 1.5 ft) based on the rate of rise in the reservoir.
- The gates are opened such that the gates do not overtop.
- The FOP includes guidance to enact the dam's EAP if rainfall, inflow, or reservoir rise reach given threshold values related to anticipated flooding of downstream structures.

To follow the FOP guidance, the gate hoisting systems (mechanical, electrical, structural) must be operational and the onsite operator is required to make decisions based on predicted and actual flooding conditions.

2.1.2. Risk Analysis Framework

To support the owner's efforts to reduce reliance on a gated spillway system, a risk-informed evaluation is carried out. The first step in this process is the development of a risk model for the project in its current configuration with the gated spillway system. A component of the risk model is an event tree that is used to evaluate the possible sequence of events that may occur during inflow floods and the outflows that may occur as a result of these sequences that may include overtopping and failure of the dam, unplanned releases due to operator error, or gate system failure. The development of the event tree was guided by the steps and guidance in the FOP. Of particular interest are the flood releases during events significantly smaller than the PMF, particularly since the PMF is estimated to have such a low probability.

For purposes of this evaluation, failure modes (structural, geotechnical, etc.) associated with the dam are not explicitly evaluated. Instead, a "dam fails" event was included to consider all failure modes. The general sequence of events evaluated is presented in Figure 1.

Each of the events shown in Figure 1 can have multiple branches to simulate conditions and result in different estimates of outflow and reservoir stage. Some examples include:

- If the precipitation forecast is greater than the actual rainfall, it is possible the gates would be opened more than needed, resulting in a greater outflow than if the forecast were accurate.
- The stream gauge that is used for flood prediction only represents a portion of the watershed; therefore, it is possible that actual inflow could be lower or higher than anticipated, representing uncertainty in flow releases.
- Gate operations require interpretation of several factors, including estimating reservoir rise and anticipating whether overtopping of the gates is imminent. In addition, decision making during a large flood is stressful, and an operator may elect to deviate from the FOP.

Figure 1. Event sequence, based on Flood Operations Plan
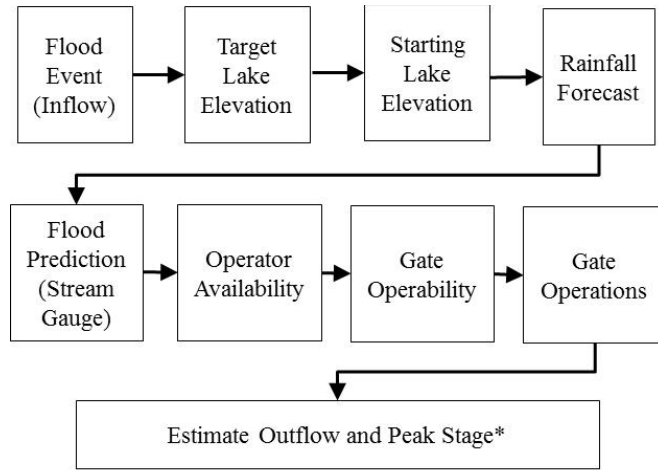
* Peak Stage can be used to estimate dam failure probability

The event tree is presented in Figure 2. Three event trees were developed for each flood evaluated, corresponding to the three target reservoir elevations included in the FOP. Several branches of the event tree are not expanded. The probabilities at each node were estimated by the authors, but in a real example, these probabilities would be estimated based on statistical analysis or expert elicitation.
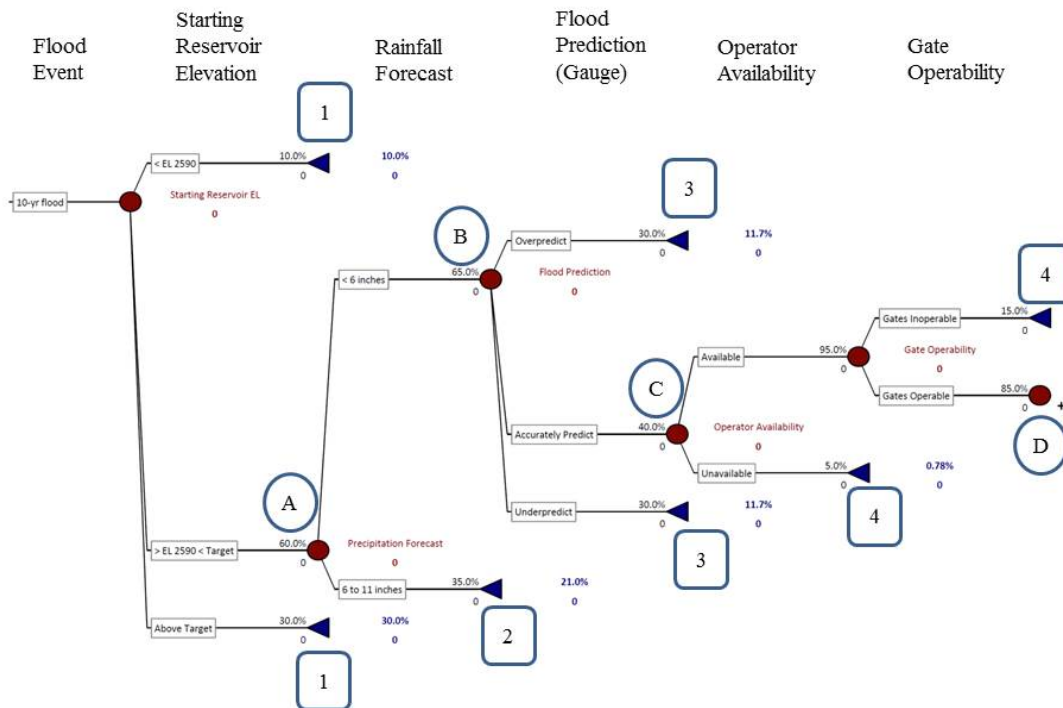

Figure 2. Gate operations event tree

The results at the various branches, quantitative and qualitative, are as follows:

1. These nodes would be expanded similar to node A. Probabilities at each node may differ.
2. If the precipitation forecast is greater than actual precipitation, the spillway gates would be opened at the start of the storm. This would result in an initial release of about 14 to 28 cumecs (500 to 1,000 cfs). This node would be expanded similar to node B.
3. If inflow is greater than predicted by the upstream gauge (underprediction), gates would be operated later in the storm. If inflow is less than predicted by the gauge (overprediction), gates would be operated earlier in the storm. These nodes would be expanded similar to node C.
4. If the operator is unavailable or the gates cannot be operated, the gates would be overtopped, resulting in an estimated peak stage of 793.8 m (2,604.3 ft) and peak outflow of about 23 cumecs (800 cfs). This node could be expanded to also include branches representing a gate failure and a dam failure.

As noted above, a "dam fails" node can be included the end of each branch of the tree. For this model, the probability of failure was explicitly related to hydrologic loading, with an estimated failure probability of 5×10^{-6} for reservoir elevation of 789.4 m (2590 ft) and 1×10^{-5} for reservoir elevation of 795.5 m (2610 ft). Figure 3 shows the expansion of node D, illustrating gate operation scenarios relative to the FOP.
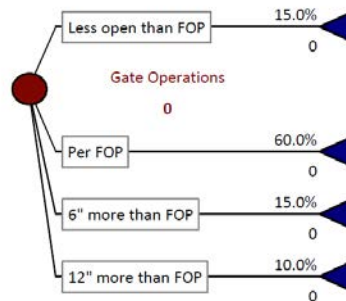
Figure 3. Gate operation scenarios event tree branches

Hydrologic modeling for various hypothetical storms (2- through 1,000-year estimated return periods) was performed using the HEC-HMS computer program. Inflow hydrographs were then input into spreadsheet model that was developed to perform reservoir storage routings, and estimate outflow and peak stage. This model can be used to simulate operations according to the FOP or manually revised to consider various scenarios, including those identified in Figure 3.

A baseline model was developed to simulate operations per the FOP, which also considers that precipitation and inflow estimates are accurate, an operator is available, and the gates can be operated according to the FOP. Three scenarios were modeled to consider each of the target reservoir elevations included in the FOP. The modeling assumes the reservoir is at the target elevation at the start of the storm. The results of the modeling of the gate operations per the FOP for these storms are presented in Table 1. The 10- and 100-year 24-hour rainfall are 13.5 cm (5.3 inches) and 20.5 cm (8.1 inches), respectively, and the estimated inflows are 171 cumecs (6,030 cfs) and 337 cumecs (11,900 cfs), respectively.

The results in Table 1 show that outflows are significantly less than the flood inflow, illustrating that the dam, while not constructed for the purpose of flood protection, provides significant reduction in outflows over what would occur without the dam in place. The results also show the sensitivity of outflow to the target elevation. The downstream area is particularly sensitive to flooding, with flooding of structures occurring at a flow of about 45 cumecs (1,600 cfs).

Table 1. Results – Gate Operations per FOP for Reservoir Targets

Storm	Parameter	Result for Target Reservoir EL:		
		790.6m (2594 ft)	791.3 m (2596 ft)	791.9 m (2598 ft)
10-year	Outflow (cumecs/cfs)	27.1 / 960	31.2 / 1100	47.3 / 1670
	Peak Stage (m/ft)	792.9 / 2601.5	793.1 / 2602.0	793.3 / 2602.6
	Gate Opening (m/ft)*	0.30 / 1.0	0.3 m / 1.0	0.46 m / 1.5
100-year	Outflow (cumecs/cfs)	80.2 / 2830	97.3 / 3440	130.2 / 4600
	Peak Stage (m/ft)	793.6 / 2603.7	793.8 / 2604.4	794.0 / 2605.0
	Gate Opening (m/ft)*	0.76 / 2.5	0.91 / 3.0	1.22 / 4.0

* Maximum gate opening per FOP or to prevent overtopping of gates

Three event trees were constructed (one for each target elevation), and outflows were estimated using the spreadsheet program for each branch of the event tree. Probability distributions were developed for each reservoir target elevation for both the 10- and 100-year flood, presented in Figure 4.
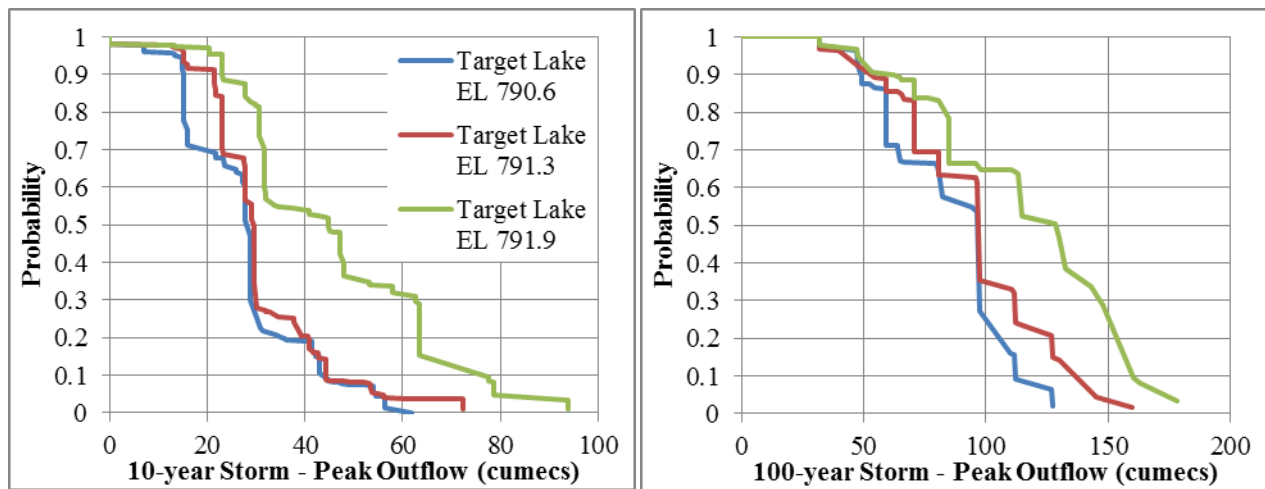

Figure 4. Probability distribution of peak outflows (10- and 100-year flood)

To develop a single probability distribution that considers the three different target reservoir elevations, the probability of a given target elevation for a given event is estimated. The target reservoir elevations vary by season, with the lowest target from November to January, the highest target from April to July, and the middle target for the remaining months. The probability of a given flood event occurring in a given month can be estimated using Seasonality Analysis, which is provided as part of the NOAA Precipitation Frequency Data Server (NOAA, 2016). Since each month corresponds to a given target reservoir elevation, the probability can be estimated for a given storm event. Using this data, the low, middle and high targets were estimated to have respective 7, 61, and 32 percent probabilities for the 10-year storm and respective 1, 80, and 19 percent probabilities for the 100-year storm. This data was used to combine the probability distributions shown in Figure 4 into a single distribution for each of the storm events, as presented in Figure 5.

In addition to estimating peak outflows, the event tree model can be used to estimate probability of a gate overtopping and dam failure for a given storm event. The probability of gate overtopping was estimated to be 19 and 27 percent for the 10- and 100-year floods, respectively. To estimate a dam failure, a simplified linear relationship between peak stage and dam failure probability was developed, with a failure probability (given an event) of 5×10^{-6} for peak stage EL 789.4 m (2590 ft) and 1×10^{-5} for peak stage EL 795.5 m (2610 ft). Using this relationship, the probability of failure given 10- and 100-year events were estimated to be 8.1×10^{-6} and 8.7×10^{-6}, respectively.
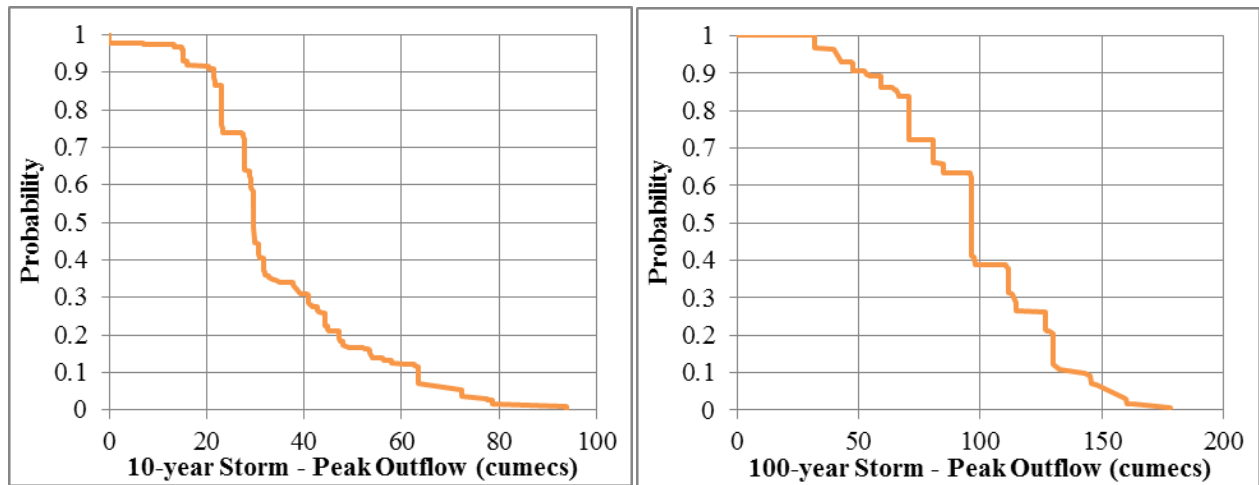
Figure 5. Combined probability distribution of peak reservoir stage (10- and 100-year flood)

2.2. Addressing Risks

As presented in Paxson et al. (2015), there are numerous approaches to reduce risks related to gated spillway operations, including:

- Regular inspection, maintenance, and testing of gates and operating systems to improve reliability.
- Development and implementation of an effective and easy to follow FOP, including operator training and FOP testing.
- Replacement of manually operated systems with automated systems.
- Replacement of some or all of the spillway gates with a fixed crest spillway, such as a labyrinth or piano key weir.

2.2.1. Case Histories

There have been several projects where gated spillway systems were replaced with more reliable spillways, often as part of a project to address other dam safety deficiencies. Several examples follow.

The original spillway at Sugar Hollow Dam in Virginia consisted of an ogee crest equipped with eight 1.5 m (5 ft) high vertical lift gates, which were operated manually using a hoisting system mounted on rails across a bridge over the spillway. In at least one instance, the operator had to open the gates while there was flow over the bridge, making operations very difficult. This gated system was replaced with a rubber bladder, which provided more efficient hydraulic performance and better debris passage than the original spillway. The new "gate" includes an automated system, which is operated based on water level control. This system has operated reliably for nearly 15 years. For additional information on the Sugar Hollow Dam and modeling and programming of the automated operation systems, refer to Paxson et al, 1999.

Tipping Fusegates are considered more reliable than manually operated gate systems. These "gates" typically only "operate" during extreme events (in excess of 500 or 1,000 year storms). At Canton Lake Dam in Oklahoma, the US Army Corps of Engineers selected Fusegates over more traditional Tainter gates (Hydroplus 2014a). Similarly, Fusegates were used at Jindabyne Dam in Australia (Hydroplus 2014b).

Examples of labyrinth spillways being used to replace gated structures include the Brazos Dam in Texas (Vasquez et al. 2009), the New London Dam in Minnesota (Minnesota DNR 2014), and the Lake Townsend and Linville Land Harbor Dams, both in North Carolina (Paxson et al. 2015). In all of these cases, the owner had difficulties related to maintenance and operations of the previous gated spillways.

At Malarce Dam in France, a piano key weir was constructed to provide spillway capacity in tandem with the existing large spillway gates. The piano key weir flows during floods prior to gate operations, providing twice as much time for the dam operator to travel to the dam to open gates, which was particularly important given the rapid watershed response time (Laugier et al. 2014).

2.2.2. Example Project – Gated Spillway Replacement

To address the risks related to the gated spillway in the example project, replacement of the gated spillway with a fixed crest weir is considered. As noted, the dam rehabilitation project will include construction of a large auxiliary spillway to provide hydraulic capacity to pass the PMF. The crest of this auxiliary spillway will be set at EL 795.5 m (2,610 ft), which corresponds to the estimated 200-year flood elevation if the gated primary spillway were replaced with a fixed crest weir, with a crest EL 792.9 m (2,601.5 ft). This is similar to the peak stage for the existing spillway if the gates were not operated and were overtopped. Replacing the gated spillway with a fixed crest weir will result in a larger auxiliary spillway depending on the assumption regarding gate operations during the PMF. If full opening of all gates is considered, the capacity of the existing primary spillway with the reservoir at top of dam is about 671 cumecs (23,700 cfs) compared to a capacity of 178 cumecs (6,300 cfs) for the fixed crest weir primary spillway. The computed PMF outflow is about 2,150 cumecs (76,000 cfs). Therefore, the additional capacity provided by the gates does not significantly impact the sizing of the auxiliary spillway. In addition, conservatism in design is typically recommended to provide redundancy in gates (i.e., provide more than the required capacity if all gates are operable).

If the gated primary spillway is replaced by a fixed crest weir in tandem with the new auxiliary spillway, operations during floods are simplified. Instead, the dam operator can focus on observing conditions (reservoir level, condition of dam and spillway, downstream flows, etc.) and coordinating with local emergency management agencies, as required with regard to either downstream flooding or a potential dam safety issue. In addition, the design can eliminate the need to set lowered monthly lake levels, increasing reservoir safe yield. When normal inflows are sufficient and exceed water supply withdrawals, the pool will be maintained at EL 792.9 m (2,601.5 ft).

2.2.3. Example Project - Risk Model for Proposed Modifications

For the project that is the subject of this paper, replacing the gated primary spillway system with a fixed crest weir eliminates a number of steps/actions in the FOP; the need to predict rainfall and inflows, operator onsite, and gate operations. As a result, the scenarios to model flooding for the fixed crest weir are simplified significantly. Only the starting reservoir elevation impacts the outflows and peak stage for an inflow flood event. To estimate probabilities for the fixed crest weir, an exceedance plot of reservoir elevation was developed based on historical reservoir levels prior to implementation of the FOP reservoir targets.

To illustrate the reduction in risk related to outflows, the probability distributions of peak outflow for the existing gated primary spillway and the proposed replacement fixed-crest weir are plotted in Figure 6.

Figure 6 shows that there is potential for increased peak outflow with the fixed crest weir for the 10-year flood. This is likely due to the application of the target reservoir elevations in the FOP. Even if the reservoir isn't at the target elevation at the start of the storm, implementing the target elevation into the FOP results in a release at the start of the storm, providing a drawdown of the reservoir which results in additional flood attenuation. If this potential for increased flooding is a concern for the dam owner, the new spillway could include some form of gates to accommodate an initial drawdown or release at the start of the storm. For the 100-year flood, the impact of attenuation is less, resulting in lower computed peak outflows for the fixed crest weir than the gated spillway.

The computed peak stage for the fixed crest weir is typically higher than for the existing gated spillway, and this increased hydrologic loading (reservoir levels) could result in an increased risk of dam failure. The probability of failure is estimated using the same simplified procedures as for the gated spillway, resulting in a failure probability of 8.2×10^{-6} and 9.0×10^{-6} for the 10- and 100-year floods, respectively. This represents a relatively small increase in risk.
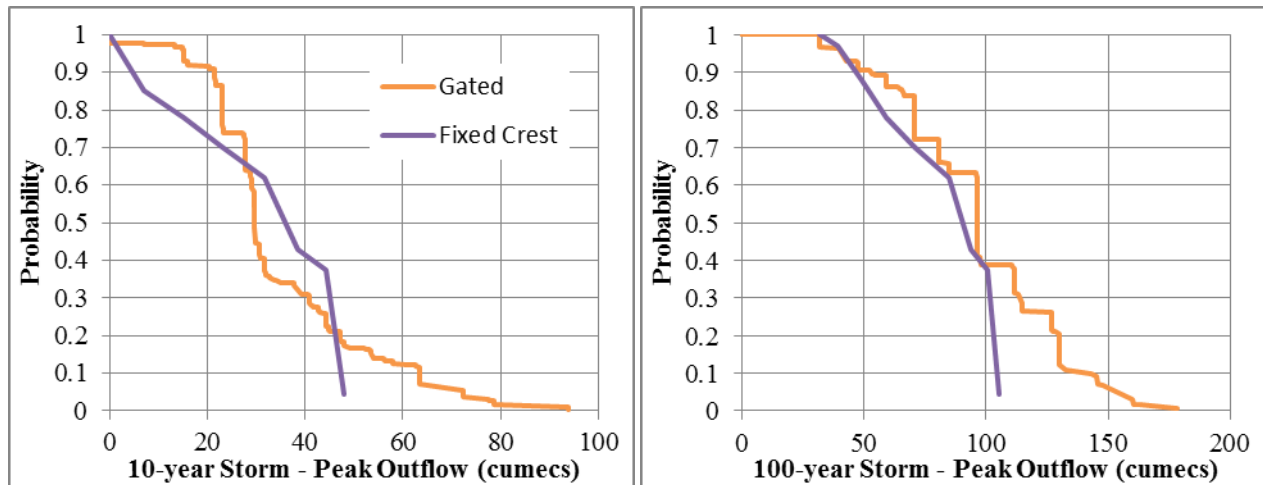
Figure 6. Probability distributions of peak outflow for gated and fixed crest spillways

3. CONCLUSIONS

Gated spillway systems are often necessary to meet specific project requirements. However, these systems present challenges with regard to reliability of operations and the potential for operations (mechanical, electrical, and human) to result in adverse consequences. While reduced operability or inoperability of gates increases risks related to passage of very large floods, potentially resulting in a dam failure, operations during more "routine" flood events could result in higher risks related to downstream flooding (i.e., while the consequences may be less, the probability of damage could be significant higher than a dam failure scenario).

The development of a framework to evaluate the risks of a gated spillway system should consider all aspects of the operations, including flood prediction, operator availability, reliability of the gated system, and operator error. An event tree can be used to model this framework and develop probability distributions for outflow. These distributions can be used to evaluate options for replacement of the system.

4. REFERENCES

ASDSO/EPRI. (2000). "Association of State Dam Safety Officials (ASDSO)/ EPRI Spillway Gate Workshop: January 5 & 6, 2000." EPRI, Palo Alto, Ca., and the Association of State Dam Safety Officials, Lexington, Ky.

Fiedler, W., King, W., Schwanz, N., Garton, J., and McDaniel, L. (2011). "Dam Safety: What Happened to Lake Delhi Dam?" *Hydroworld*, 30 (Sept.), 8-15.

Ham, R. (2015). "Lawsuits mount against SCE&G after dozens lose homes during floods." *Cola Daily*, <http://coladaily.com/> (October).

Hydroplus. (2014a). "Canton Dam." Information sheet provide to authors by email from Hasan Kocahan, Hydroplus representative, Dec. 2014.

Hydroplus. (2014b). "Jindabayne Dam." Information sheet provide to authors by email from Hasan Kocahan, Hydroplus representative, Dec. 2014.

Johnson, J. N. (2014). "Duckett Dam was operated responsibly during heavy rainstorm [Commentary]." *Baltimore Sun*, <http://baltimoresun.com> (Jan. 4, 2016).

Laugier, F., Vermeulen, J. and Lefebvre, V. (2014). "Overview of Piano Key Weirs experience developed at EDF during the past few years." *Labyrinth and Piano Key Weirs II*, PKW 2013, CRC Press, Taylor and Francis Group, Boca Raton, Fl.

Minnesota DNR. (2014). "New London Dam Reconstruction." <http://www.dnr.state.mn.us/waters/surfacewater_section/damsafety/new_london_dam.html> (Oct. 14, 2014).

National Performance of Dams Program (2016a). "Performance of Hydraulic Systems." < http://npdp.stanford.edu/sites/default/files/reports/performance_of_hydraulic_systems.pdf>. Stanford University, Stanford Ca.

National Performance of Dams Program (2016b). "October 2015 South Carolina Dam Failures" <http://npdp.stanford.edu/2015_SC_Flood_Failures>. Stanford University, Stanford Ca.

NDTV. (2014). "Inquiry Report Blames Hydropower Project Authorities for Beas River Tragedy." <www.ndtv.com> (June 20, 2014).

NOAA (2016). National Weather Service, Hydrometeorological Design Studies Center, Precipitation Frequency Data Server, <http://hdsc.nws.noaa.gov/hdsc/pfds/> (January 2016)

O'Leary, J. (2014). "Residents call for new dam outflow schedule." Iowa City Press-Citizen, <http://www.press-citizen.com> (Jan. 4, 2016).Paxson, G., Harrison, J., and Campbell, D. (1999). "Hydraulic Assessment of Rubber Dam Spillway Crest Control." *Dam Safety 1999, the 16th annual conference of the Association of State Dam Safety Officials*, ASDSO, St. Louis, Mo.

Paxson, G., Indri, R., and Landis, M. (2015). "Addressing Operational Risks and Uncertainties for Gated Spillways." *USSD 2015 Annual Conference*, USSD, Louisville, Ky.

Pichaske, P. (2014). "WSSC under fire after another major flooding of Laurel*."* Baltimore Sun, <http://baltimoresun.com> (Jan. 4, 2016).

Shaver, K. (2014). "Laurel officials, businesses say WSSC should pay for Duckett Dam's flood damage." Washington Post, <http://www.washingtonpost.com> (Jan. 4, 2016).

Smith, T. (2015). "Residents question decisions made with released water." Greenville News, <http://www.greenvilleonline.com> (Jan. 4, 2016).

The Telegraph (2015). "Marooned 10 saved in the dead of night." The Telegraph <http://www.telegraphindia.com>.(Jun 22, 2014)

U.S. Army Corps of Engineers. (1990). "Hydraulic Design of Spillways." Engineering Manual 1110-2-1603, Washington, D.C.

U.S. Army Corps of Engineers. (2015). "CorpsMap, National Inventory of Dams" < http://nid.usace.army.mil/cm_apex/f?p=838:12>. (Dec 16, 2015)

Vasquez, Victor, M., Wolfhope, J.S. and Garrett, R. (2009). "An Elegant Solution: The Lake Brazos Labyrinth Weir." *Civil Engineering Magazine*, 7(1), 48-55.

Discharge Correlations for Spillways with Radial Gates

G.A. Schohl
River Operations and Renewables
Tennessee Valley Authority
Knoxville, TN 37902
USA
E-mail: gaschohl@tva.gov

ABSTRACT

Equations used at the Tennessee Valley Authority (TVA) to compute free and gated (orifice) discharges through spillways with radial gates are presented along with correlations based on TVA model test data for discharge coefficients and submergence factors. The correlations and data may be applicable for estimating discharges through gated spillways that are similar to those at TVA and for which specific model test data are unavailable. Included in this paper, perhaps for the first time in the literature, are correlations and data indicating the headwater at which flow begins the transition from free discharge to gated discharge, the variation in the orifice discharge coefficient as headwater rises above the transition point, and the effect of tailwater submergence on gated discharge for given gate openings.

Keywords: spillway, discharge, radial gate.

1. INTRODUCTION

In recent years, the Tennessee Valley Authority (TVA) has developed or revised discharge rating curves, or "dam rating curves" (DRCs), for every dam in their river system for use in probable maximum flood (PMF) routing studies. Literature searches during this work revealed the lack of publicly available data for predicting discharges through spillways with radial gates. For a given gate opening, flow over a gated spillway may be free discharge or gated discharge, depending on headwater elevation, and may also be affected by tailwater submergence. Correlations for predicting free discharge and the effects of tailwater submergence on free discharge are available, at least for spillways with standard or ogee crests (e.g., USBR, 1987; USACE, 1988), but no data were found indicating the headwater at which flow begins the transition from free discharge to gated discharge or the discharge coefficients in the transition region. A curve showing a discharge coefficient as a function of radial gate opening for headwaters well above the transition region is available (USACE, 1988), but no data were found indicating submergence effects on radial gated flows.

For many of its spillways, the Tennessee Valley Authority (TVA) has model test data from which relationships between discharge, headwater, tailwater, and gate opening have been developed and used to generate spillway discharge tables specifying gate arrangements (gate openings and combinations of gates) for achieving desired discharges at various headwater and tailwater combinations. Normalized correlations developed using model test data from several of the tested spillways have been used to generate spillway discharge tables for TVA dams without specific model test data and without tailwater submergence effects. The normalized correlations, especially those for specifying orifice discharge coefficients for gated flows, may be useful for application to other spillways for which model test data are unavailable. Model test data from two spillways (Nickajack and Tellico) where tailwater submergence affects gated discharges under normal operating conditions have also been put into normalized form, making them at least helpful for estimating submergence effects on gated flows at dams for which model test data are unavailable.

Kirkpatrick (1957) presented model test data collected for eleven TVA spillways and plotted the free discharge coefficient data for nine of them against normalized head, using the "design head" for a standard crest as the reference head. As shown by the examples in Figure 1, in which several TVA spillway crests are compared with a standard crest as specified by the USACE (1988), most TVA crests are not standard, typically having a milder

downstream slope than a standard crest to prevent negative pressures at moderately low discharges. Kirkpatrick estimated a standard crest design head, H_o, for each spillway after comparing its shape with that of a standard crest. This technique was later applied to estimate design heads for additional spillways for which model test data were available. The design heads were used to develop normalized correlations for the head at which the overflowing nappe first touches the lip of a partially opened gate and for the orifice flow discharge coefficients for heads above the gate lip (Harshbarger et. al., 1985).
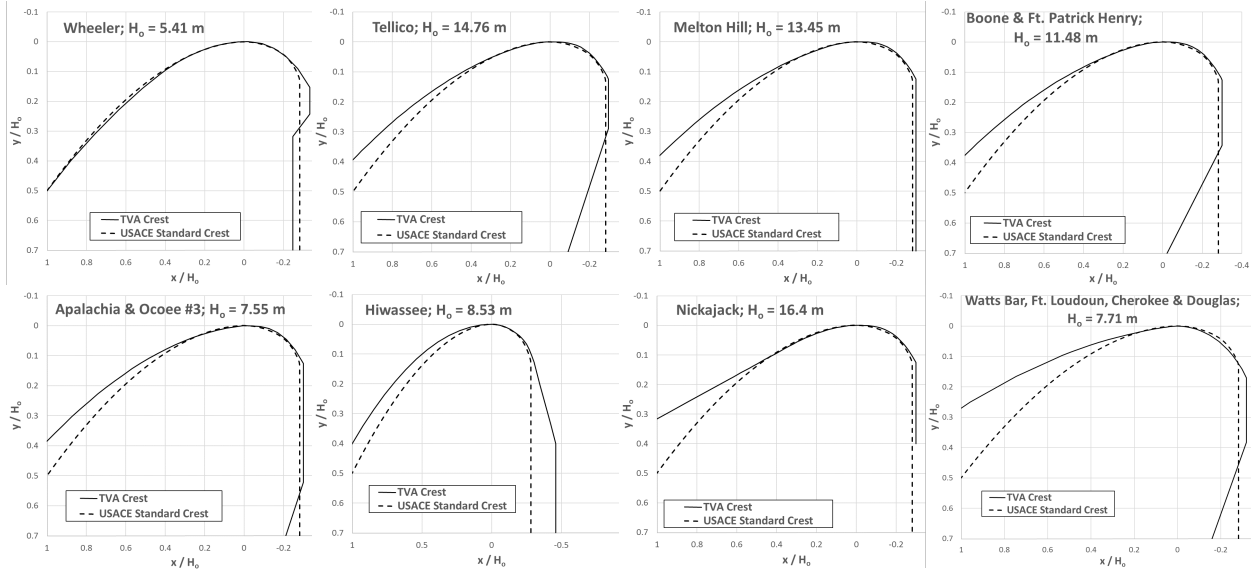

Figure 1. TVA Crests Compared to USACE Standard Crest

2. EQUATIONS FOR FLOW OVER A GATED SPILLWAY

Figure 2 illustrates radial gate geometry and defines variables indicating gate position. Gate opening, G, may be indicated by the vertical distance between the gate lip and the spillway surface, G_v; or by the minimum, or normal-to-the-spillway surface, distance between the gate lip and the spillway surface, G_n. Gate position may be indicated by the vertical opening above the crest centerline, V, by G, or by angle β or ϕ.

Figure 3 illustrates discharge under a partially opened radial gate on a spillway for conditions where the overflowing nappe just touches the lower lip of the gate. This condition occurs when $H_c = H_{L1}$ where $H_{L1} = H_{L1}(G)$ = value of H_c at which a rising, overflowing nappe first impinges on the lip of a gate opened to position G. The discharge under the gate is free discharge for $H_c <= H_{L1}$ and gated (or orifice) discharge for $H_c > H_{L1}$.

Free discharge is computed using a weir-type equation as follows (neglecting pier contraction and abutment effects):

$$Q_f = S_f C_f L_c H_c^{3/2} \tag{1}$$

in which Q_f = free discharge, $S_f = S_f(d/H_c)$ = tailwater submergence factor, $C_f = C_f(H_c)$ = discharge coefficient, $H_c = HW - z_c$ = total energy head on overflowing crest, z_c = crest elevation, HW = headwater elevation, TW = tailwater elevation, $d = TW - z_c$ = tailwater submergence, and L_c = length of overflowing crest (width of spillway bay). The TVA physical models typically included three to five spillway bays and the piers between them, with a half-pier at each bounding wall in the flume. Consequently, the effects of pier contractions are implicitly included in the discharge coefficients derived from the model test data.

Figure 4 depicts flow under a partially opened radial gate with headwater elevation well above the gate lip. For tailwater submergence, d, less than a transition value, d_1, gated discharge is computed using an orifice equation as follows:
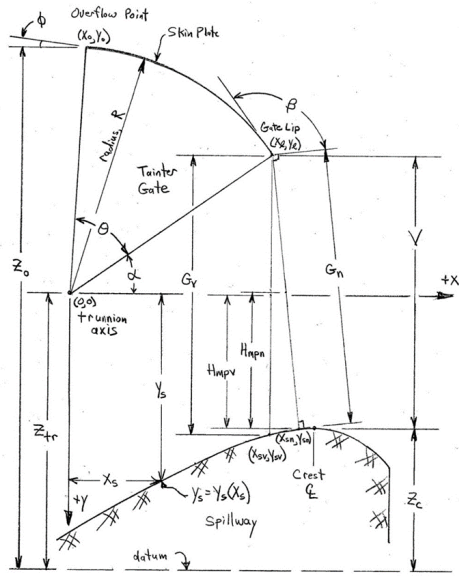
Figure 1. Definition Sketch for Radial Gate Geometry

$$Q_{g1} = C_{g1} S_{g1} G L_c \sqrt{2g(H_c - H_{mp})} \tag{2}$$

in which Q_{g1} = gated discharge; $d_1 = d_1(G, H_c)$ = transition value of tailwater submergence, d; $G = G_v$ or G_n = gate opening for current gate setting as used in the determination of C_{g1} from model test data; $C_{g1} = C_{g1}(G, H_c - H_{L1})$ = discharge coefficient; $S_{g1} = S_{g1}(G, d/H_c, H_c)$ = tailwater submergence factor; g = acceleration of gravity; and $H_{mp} = H_{mpv}$ or H_{mpn} = the elevation of the midpoint of the opening G_v or G_n minus the crest elevation z_c as used in the determination of C_{g1} from model test data.

For d greater than d_1, gated discharge is computed using the alternate equation:

$$Q_{g2} = C_{g2} G L_c \sqrt{2g(H_c - d)} \tag{3}$$

in which Q_{g2} = gated discharge; and $C_{g2} = C_{g2}(G)$ = discharge coefficient.

In the presentations below, H_{L1} and C_{g1} are based on G_v and H_{mpv} as the physical and normalization parameters to be consistent with the correlations provided by Harshbarger et. al (1985). However, d_1, C_{g2}, and S_{g1} are based on G_n and H_{mpn} as the physical and normalization parameters to be consistent with the definitions of these relationships in TVA software for computing spillway discharge.
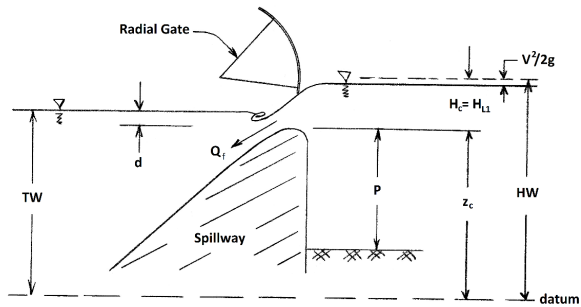

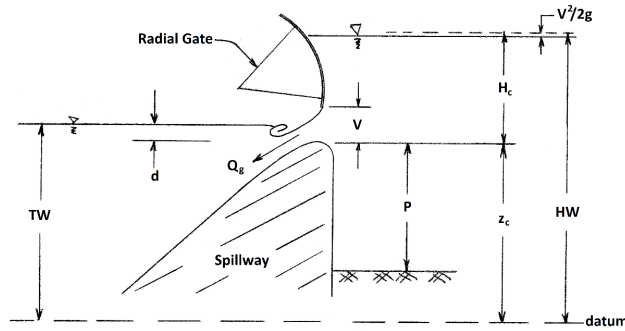Figure 2. Transition HW between Free and Gated Discharge

Figure 4. Gated Discharge under Spillway Gate

3. COEFFICIENTS FOR FREE DISCHARGE

The free discharge coefficient and submergence factor relationships, $C_f(H_c)$ and $S_f(d/H_c)$, are both significantly affected by variations in crest shape and upstream depth, P. In addition, the submergence factor relationship is also affected by downstream depth and apron details. The TVA model test data are not sufficient to define general correlations for these relationships, but a few examples are illustrated here.

Figure 5 compares $C_f(H_c/H_o)$ for several TVA dams at which $P/H_o > 2.5$ with $C_f(H_c/H_o)$ for "high overflow dams" (large P/H_o) of standard crest shape. The TVA curves are fits to the model test data for each dam. The legend lists the dams in order of increasing deviation of crest shape from the standard shape. As expected for crest shapes with higher downstream elevations, the discharge coefficients are lower than those for a standard crest. For the TVA crests, the reduction in C_f generally increases with increasing deviation of the crest shape from standard. All curves inFigure 5 represent conditions with adjacent bays open, without abutment effects. As mentioned above, the TVA model test data implicitly include the effects of pier contractions. It is unclear whether or not the same can be said for the USACE curve.

Figure 6 compares $S_f(d/H_c)$ curve fits to model test data for three TVA dams with a curve for an ogee crest with equal upstream and downstream bed elevations (USACE, 1988). Although it may not be obvious from the plot, effects of submergence occur for $d/H_c > 0.2$ for Tellico, $d/H_c > 0.4$ for Watts Bar, and $d/H_c > 0.6$ for Nickajack. Additional free discharge and submergence relationships for TVA Dams were reported by Kirkpatrick (1957).
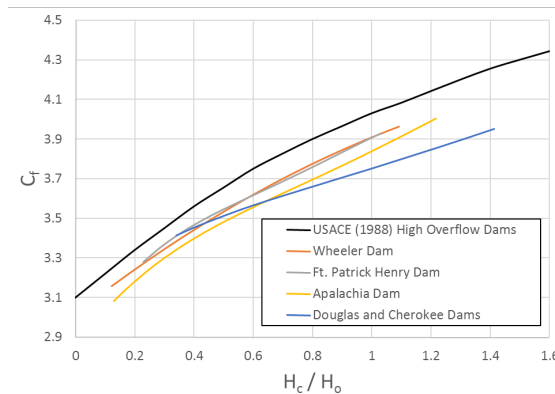

Figure 3. Free Discharge Coefficient Relationships
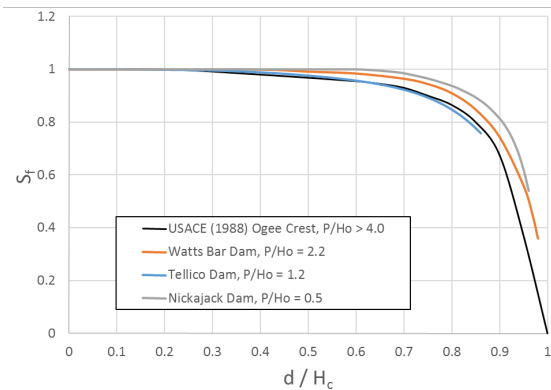
Figure 4. Submergence Factor Relationships

4. TRANSITION HEAD BETWEEN FREE AND ORIFICE DISCHARGE

Figure 7 shows a correlation provided in Harshbarger et. al (1985) for the relationship $H_{L1}/H_o(G_v/H_o)$ compared to the model test data for the five TVA dams from which it was derived. Figure 7 also shows data for Hiwassee Dam, which was not included in the correlation development. The correlation is defined as follows:

$$\frac{H_{L1}}{H_o} = \begin{cases} 1.648\frac{G_v}{H_o} & \cdots for \ \frac{G_v}{H_o} \leq 0.088 \\ 0.145 + 1.183\left(\frac{G_v}{H_o} - .088\right) & \cdots for \ \frac{G_v}{H_o} > 0.088 \end{cases} \tag{4}$$

The consistency of the data is impressive considering the differences among the spillways as quantified in Table 1, in which R = gate radius (see Figure 2) and x_{seat} = distance between the spillway crest centerline and the gate seat (the location of the gate lip on the spillway surface when the gate is closed). Comparison of the parameters suggests little difference between the Hiwassee Dam spillway and the other TVA spillways listed, but, as shown in Figure 7, the correlation for H_{L1} does not fit the model test data for Hiwassee as well as it fits the model test data for the other dams. Figure 1 illustrates that the upstream face of the Hiwassee spillway is sloped while the upstream faces of the other TVA spillways are vertical, which apparently affects the slope of the $H_{L1}/H_o(G_v/H_o)$ relationship. These results suggest that the correlation defined by Equation 6 is most useful for spillways with vertical upstream faces.

Figure 7. Transition Head, H_{L1}, between Free Discharge and Orifice Discharge

Table 1. Parameter Comparison for TVA Spillways

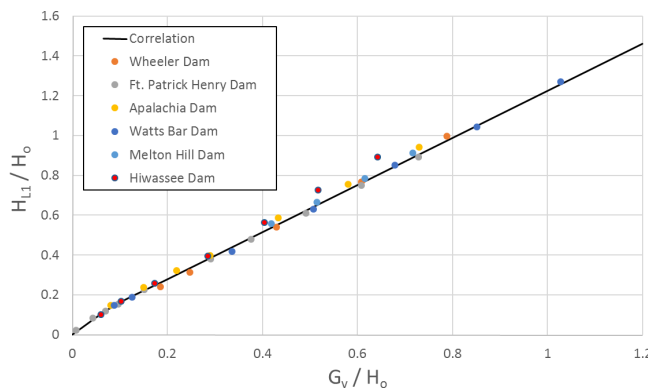| Dam	H_o (m)	P/H_o	R (m)	L_c (m)	x_{seat}/H_o
Wheeler	5.03	2.6	5.33	12.19	0
Ft. Patrick Henry	10.67	3.2	10.97	10.67	0.152
Apalachia	7.01	4.2	9.75	9.75	0.173
Watts Bar	7.16	2.2	12.19	12.19	0.146
Melton Hill	12.5	0.65	12.5	12.19	0.165
Hiwassee	7.93	4.0	6.86	9.75	0.212

5. DISCHARGE COEFFICIENTS FOR GATED FLOW

Figure 8 and Table 2 show correlations provided by Harshbarger et. al (1985) for the relationship $C_{g1v}(G_v/H_o, H_c-H_{L1}/H_o)$ as estimated from TVA model test data for Wheeler, Ft. Patrick Henry, Apalachia, Watts Bar, and Melton Hill Dams. Subscript v on C_{g1} indicates that its definition is based on use of G_v and H_{mpv} in Equation 2. The dashed line for $H_c-H_{L1}/H_o = 0$ is not unique but is determined for any given spillway by equating gated discharge from Equation 2 to free discharge from Equation 1 with $H_c = H_{L1}(G_v/H_o)$. Depending on its shape, it may be necessary to adjust the other curves to ensure that C_{g1v} for all values of $H_c-H_{L1}/H_o > 0$ are less than those indicated by the dashed line. Because the data for a given G_v indicate that C_{g1v} tends to a constant as H_c-H_{L1} increases, the correlation for $H_c-H_{L1}/H_o = 0.1$ is used for $H_c-H_{L1}/H_o \geq 0.1$. For the range $0.1 \geq H_c-H_{L1}/H_o \geq 0$, Harshbarger et. al claim a maximum deviation in C_{g1v} of ±2 percent for the dams from which the correlations were developed.

For comparison, Figure 9 shows the relationship $C_{g1v}(G_v/H_o, H_c-H_{L1}/H_o)$ as developed from specific model test data for six TVA dams. These relationships [in the form $C_{g1n}(V, H_c-H_{L1})$ where subscript n on C_{g1} indicates that its definition is based on use of G_n and H_{mpn} in Equation 2], with linear interpolation between the specified curves, are used in TVA's spillway discharge calculation software to determine values of C_{g1} for use in computing gated discharges at each dam.
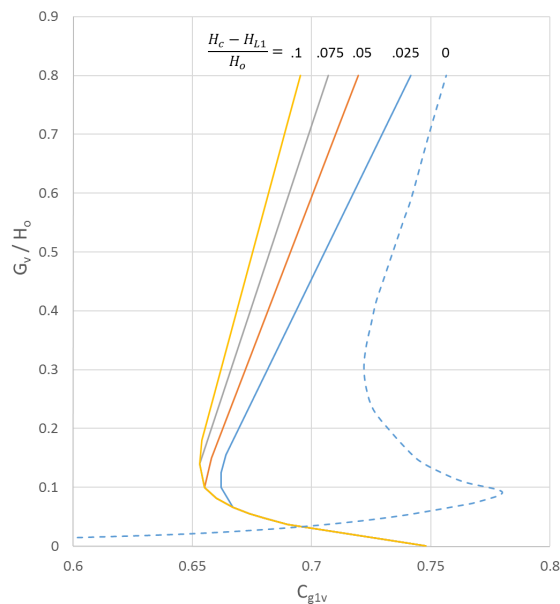
Figure 8. General Correlation for Discharge Coefficient, C_{g1v}

Table 2. Discharge coefficient

H_c-H_{L1}/H_o=0.1		H_c-H_{L1}/H_o=0.075		H_c-H_{L1}/H_o=0.05		H_c-H_{L1}/H_o=0.025	
G_v/H_o	C_{glv}	G_v/H_o	C_{glv}	G_v/H_o	C_{glv}	G_v/H_o	C_{glv}
0	0.748	0	0.748	0	0.748	0	0.748
0.03	0.7	0.03	0.7	0.03	0.7	0.03	0.7
0.037	0.69	0.037	0.69	0.037	0.69	0.037	0.69
0.0475	0.68	0.0475	0.68	0.0475	0.68	0.0475	0.68
0.055	0.674	0.055	0.674	0.055	0.674	0.055	0.674
0.066	0.667	0.066	0.667	0.066	0.667	0.066	0.667
0.081	0.66	0.081	0.66	0.081	0.66	0.1	0.662
0.1	0.655	0.1	0.655	0.1	0.655	0.125	0.662
0.14	0.653	0.14	0.653	0.15	0.658	0.155	0.664
0.18	0.654	0.8	0.707	0.8	0.720	0.8	0.742
0.8	0.695						
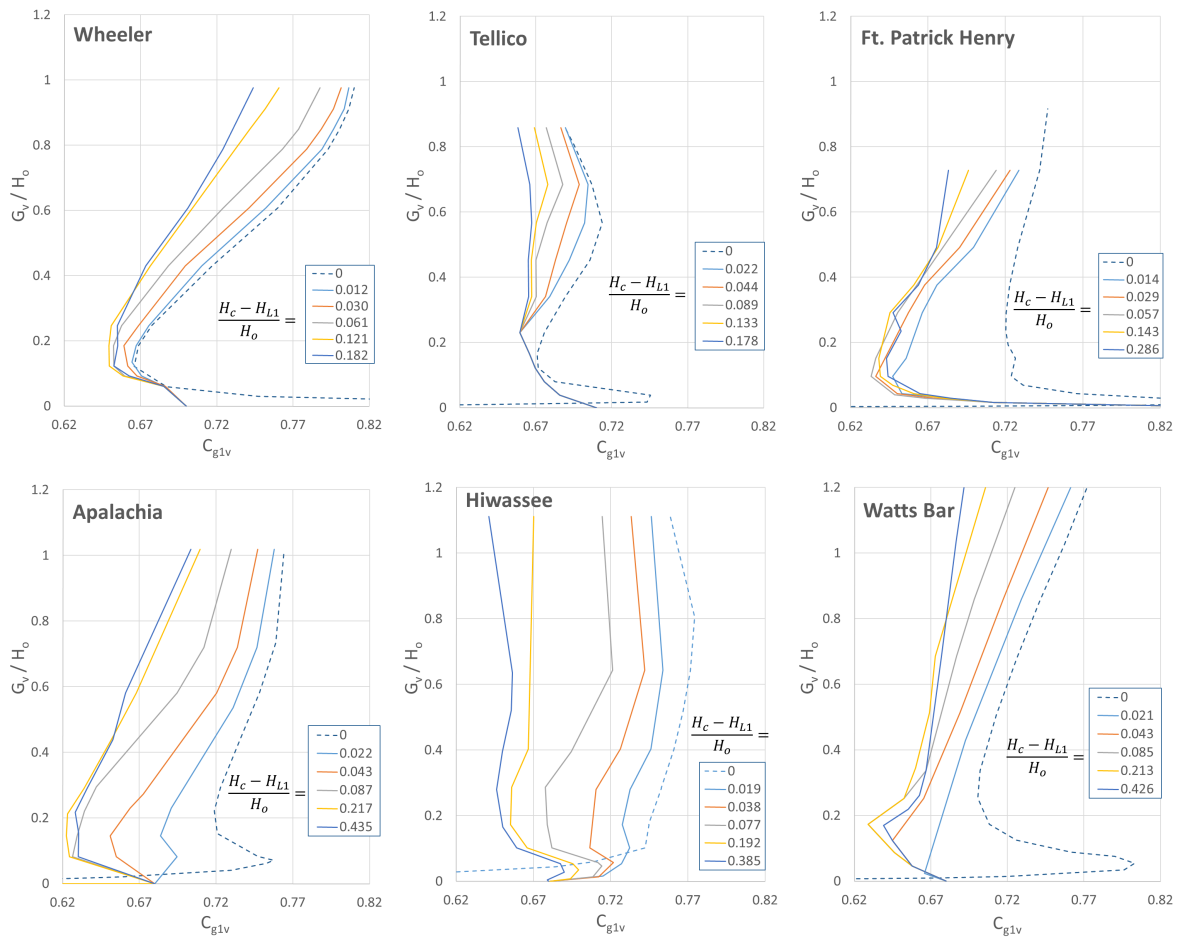
Figure 9. C_{glv} Relationships for TVA Dams

Figure 10 compares curves developed from TVA model data for $C_{gln}(\beta)$ (β is defined in Figure 2) at high values of H_c-H_{L1}/H_o with suggested design curves for the same conditions on a standard crest (USACE, 1988). The USACE curve for $x_{seat}/H_o = 0$ agrees reasonably well with the curve for Wheeler spillway, which is the only represented TVA spillway with $x_{seat}/H_o = 0$ and is the spillway illustrated in Figure 1 that most resembles a standard crest. However, the USACE curve for $0.3 \geq x_{seat}/H_o \geq 0.1$ specifies values of C_{gln} that are 5 to 10 percent higher at large

openings (large β) than those for the TVA curves. For a standard crest, the suggested design curves indicate that moving the valve seat downstream from the crest increases the values of C_{g1n}. However, for crests that are not standard, the TVA data suggest the opposite. It is also noted that, as mentioned earlier, the TVA model data implicitly include spillway pier effects, whereas the published data are unclear on this point.
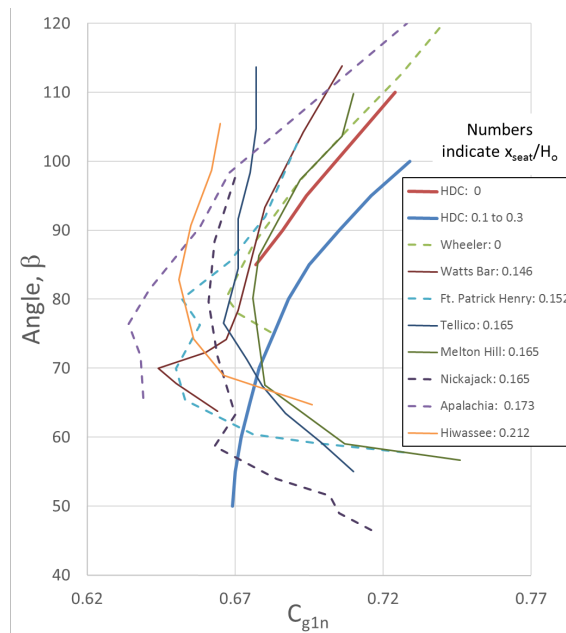
Figure 10. TVA C_{g1n} Compared with Curves from Hydraulic Design Criteria (USACE, 1988)

6. SUBMERGENCE EFFECTS ON GATED DISCHARGE

The model test data for Tellico and Nickajack spillways, which are the only TVA spillways for which data were collected with tailwater submergence affecting gated discharges, indicate that Equation 3, with a value of C_{g2} that is constant or slightly variable with head, is valid for tailwater submergence, d, greater than a transition value, d_1, which may vary with head, H_c. For tailwater submergence below the transition value ($d < d_1$), discharge is computed using Equation 2 with submergence factor $S_{g1} = S_{g1}(G, d/H_c, H_c)$ defined from the model test data.

For three example gate openings, two for Nickajack and one for Tellico, Figure 11 shows the variation of C_{g2n} with both d/G_n and d/H_c for all values of positive d included in the model test data. For the smaller openings (1.024 m and 2.13 m), C_{g2n} becomes approximately constant for values of d exceeding both a minimum d and a minimum value of d/H_c, these two criteria defining d_1. The plots for Nickajack with $V = 6.76$ m show that the model test data range, limited to the expected operating range, was not wide enough at the largest gate openings to determine either d_1 or C_{g2n}. The scatter in these plots also illustrate the reason that C_{g2n} is not simply specified as a function of d/G_n or d/H_c for all values of d greater than zero, but instead, for better precision in computing discharge, S_{g1} is defined and Equation 2 is used to compute discharge for $d < d_1$.

For various gate openings, V, Figure 12 shows the estimated minimum values of d/G_n and d/H_c for which Equation 3 with C_{g2n} is valid for computing gated discharge. For TVA's spillway discharge calculation software, the curves in Figure 12 are extrapolated in order to estimate values for gate openings above those for which values are shown even though they are not needed under normal operating conditions. The transition value of d, d_1, is determined from Equation 5. Figure 13 shows the variation of C_{g2n} with gate opening, V, as estimated from the model test data.

$$d_1(G_n, H_c) = \begin{cases} G_n \left(\frac{d}{G_n}\right)_{min} & \cdots for \; \frac{G_n}{H_c}\left(\frac{d}{H_c}\right) \geq \left(\frac{d}{H_c}\right)_{min} \\ H_c \left(\frac{d}{H_c}\right)_{min} & \cdots for \; \frac{G_n}{H_c}\left(\frac{d}{H_c}\right) < \left(\frac{d}{H_c}\right)_{min} \end{cases} \quad (5)$$

Analysis of the model test data indicates that for any given value of H_c/G_n, a $S_{g1}(d/H_c)$ relationship developed from data for one gate opening can be applied for $d < d_1$ to another gate opening as a reasonable approximation for extrapolation and interpolation purposes. Figure 14 illustrates $S_{g1}(d/H_c, H_c/G_n)$ as developed for gate opening $V = 2.13$ m at Tellico Dam. The "free discharge" curve is the $S_f(d/H_c)$ relationship, as shown in Figure 6, extended smoothly to $d/H_c = 1$. For this curve and $V = 2.13$ m, $H_c/G_n = H_{L1}/G_n = 1.44$. The $S_{g1}(d/H_c)$ relationships for $H_c/G_n = 3$ and $H_c/G_n = 6.5$ were determined from the model test data, which are all in the range $3 < H_c/G_n < 6.5$. The range of valid C_{g2n} is below the curved portion and to the right of the vertical portion of the dashed curve representing $d_1(H_c)$. The additional $S_{g1}(d/H_c)$ relationships from other gate openings are added for completeness and to cover the range of unusual operating conditions. The $S_{g1}(d/H_c)$ relationship for $H_c/G_n = 2$ is a composite curve developed from data for several other openings. The $S_{g1}(d/H_c)$ relationship for $H_c/G_n = 8.6$ was developed from the data for $V = 1.52$ m. For TVA's spillway discharge calculation software, linear interpolation between the curves in Figure 14 is used to determine in-between values for the $V = 2.13$ m gate opening at Tellico.
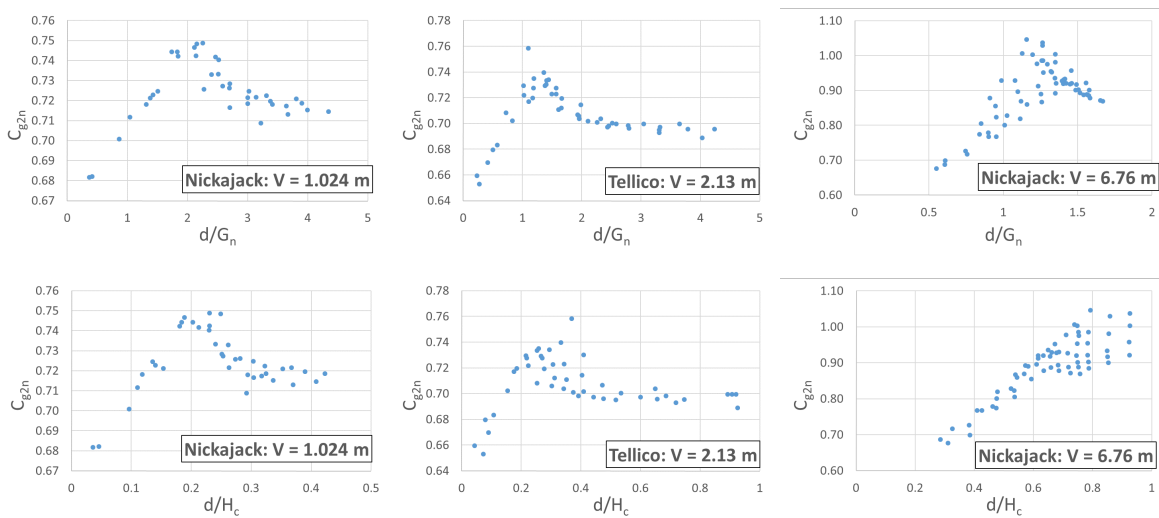
Figure 11. Variation of C_{g2n} with d/G_n and d/H_c
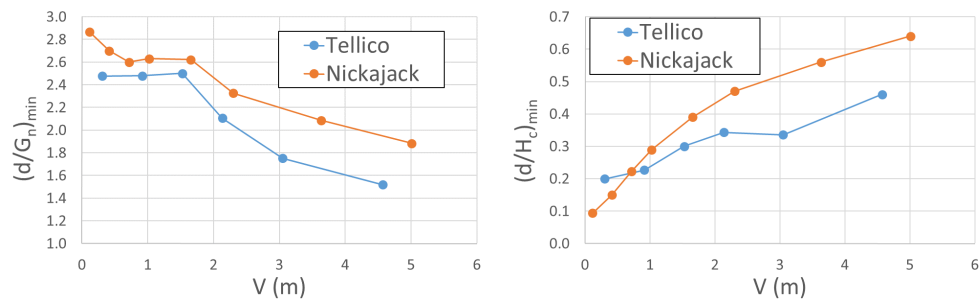
Figure 12. Minimum Values of d for use of C_{g2n}
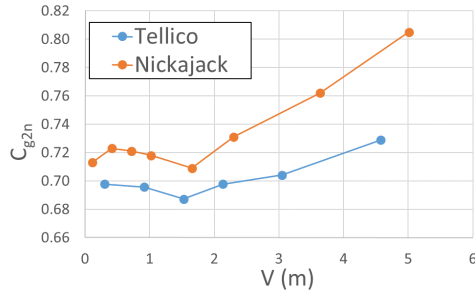
Figure 13. Variation of C_{g2n} with V
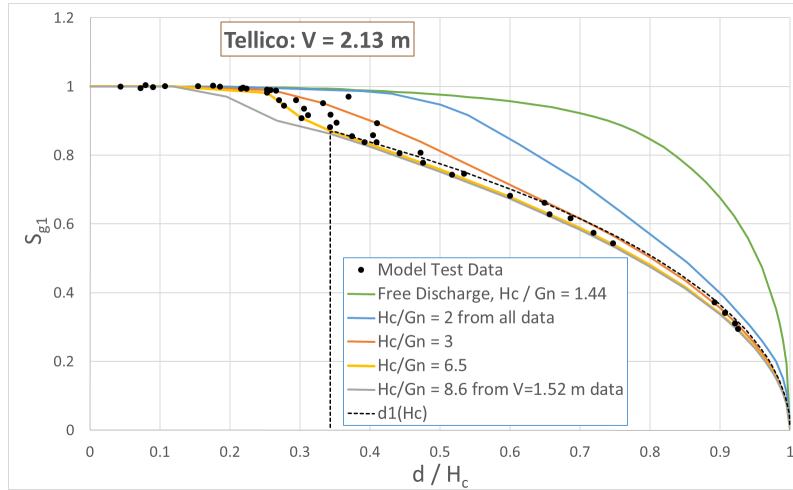
Figure 14. S_{g1} for V = 2.13 m at Tellico Spillway

Figure 15 shows a selection of $S_{g1}(d/H_c)$ relationships for Tellico and Nickajack Dams. The curves labeled "composite" were developed using data from two or more gate openings. The other curves are specific examples for particular gate openings. The lower portions of the curves for $H_c/G_n > 2.3$ were generated using constant values of C_{g2n} to compute S_{g1} from Equations 2 and 3. Figure 15 also illustrates a significant difference between two $S_{g1}(d/H_c)$ relationships for different gate openings at nearly the same value H_c/G_n (3.1 and 3.2). The difference is consistent with the observation that the minimum d/H_c value for submergence effects varies widely with gate opening at Nickajack, from about 0.1 for $V = 0.411$ m to about 0.6 for $V > \approx 6.7$ m.
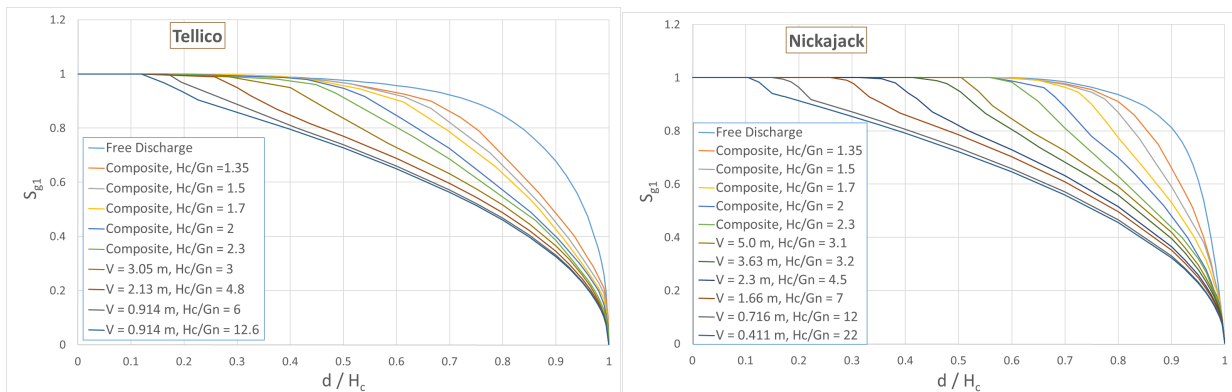
Figure 15. S_{g1} for Tellico and Nickajack Spillways

650

7. CONCLUSIONS

Data and correlations are presented for radially gated spillway discharge with possible submergence effects based on TVA model test data. The correlations for the transition head, H_{L1}, between free and gated discharge (Figure 7 and Equation 4) and for the gated discharge coefficient, C_{g1}, as a function of gate opening and head (Figure 8 and Figure 9) should provide reasonable estimates of discharge (within 5 percent) for gated spillways that are similar to TVA spillways but for which specific model test data are unavailable. Applicability of data for two TVA dams on submergence effects (Figure 12, Figure 13, Figure 14, and Figure 15) to other spillways is less certain, but it may still be useful when no other data are available. For large gate openings (low H_c/G_n) at other TVA dams, TVA has used the data shown in Figure 15 for the purpose of developing dam rating curves applicable to probable maximum flood conditions. In those cases, the submergence relationship for free discharge was known and was used as the bounding free discharge submergence relationship. For gated discharge submergence, the Tellico data were used for dams at which submergence affects free discharge for $d/H_c > \approx 0.2$, the Nickajack data were used for dams at which submergence affects free discharge for $d/H_c > \approx 0.6$, and an average between the two was used for dams at which submergence affects free discharge for $d/H_c > \approx 0.4$. The accuracy of this approach is uncertain, but for the unusual flood conditions under which gated discharge at large openings is affected by submergence at these dams, the approximation is considered acceptable. For smaller gate openings, a more reasonable approach for estimating submergence effects on gated discharge may be to specify C_{g2} using the data in Figure 13 as a guide and use Equation 3 to compute discharge for all $H_c > H_{L1}$. A drawback of this approach is that the discharge function $Q\ (H_c)$ will have a discontinuity at $H_c = H_{L1}$. Depending on the requirements of the application, this approximation and discontinuity may be acceptable.

8. ACKNOWLEDGMENTS

9. REFERENCES

Creager, W. P. and J. D. Justin, 1950, Hydroelectric Handbook, 2nd Edition, John Wiley & Sons, New York.

Harshbarger, E. D., B. J. Clift, and J. W. Boyd, 1985, "Method for Estimating Discharge at Overflow Spillways with Curved Crests and Radial Gates," TVA (Tennessee Valley Authority) Report WR28-2-900-123, January.

Kirkpatrick, K. W., 1957, "Discharge Coefficients for Spillways at TVA Dams," Trans. American Society of Civil Engineers, Paper No. 2855, vol. 22, pp. 190-210.

USACE (U. S. Army Engineer Waterways Experiment Station), 1988, Hydraulic Design Criteria, Eighteenth issue, Vicksburg, MS.

USBR (U. S. Bureau of Reclamation), 1987, Design of Small Dams, United Stated Department of the Interior, 3rd Edition, Washington DC.

Numerical Investigation of USBR Type III Stilling Basin Performance Downstream of Smooth and Stepped Spillways

D. Valero[1, 2], D.B. Bung[1], B.M. Crookston[3], and J. Matos[4]
[1]Hydraulic Engineering Section, Civil Engineering Department
FH Aachen University of Applied Sciences
Aachen, 52066
Germany
[2]Dept. of ArGEnCo, Research Group of Hydraulics in Environmental and Civil Engineering (HECE)
University of Liege (ULg)
Chemin des Chevreuils 1, Bat B52/3 +1, B-4000 Liège
Belgium
[3]Schnabel Engineering
West Chester, PA, 19382
USA
[4]Department of Civil Engineering, Architecture and Georesources
Instituto Superior Técnico, Universidade de Lisboa
Av. Rovisco Pais, 1049-001 Lisboa
Portugal

E-mail: valero@fh-aachen.de

ABSTRACT

Recent systematic studies on air-water flows have included stepped spillways. However, to date, little has been investigated about how the hydraulic conditions on the stepped spillway may affect the design of traditional energy dissipation structures. In this paper, both smooth chute and stepped chute configurations terminating with the USBR type III stilling basin are tested by means of numerical modelling, allowing a qualitative comparison. Unsteady RANS equations have been employed together with VOF and RNG k-ε for free surface tracking and turbulence modeling, respectively. Eight different Froude numbers (F) ranging from 3.1 to 9.5 have been analyzed for a type III basin designed for F = 8, following recent studies conducted in a physical model by Reclamation. The basin flow structure is discussed for both smooth chute and stepped chute cases. Additionally, the modelled basin has been tested for design and adverse hydraulic conditions, obtaining a detailed insight of the role of each basin element and their adapting roles when insufficient tail water conditions exist.

Keywords: Stepped chute, RANS, hydraulic jump energy dissipators, CFD, velocity decay, USBR type III stilling basin.

1. INTRODUCTION

A stilling basin is a hydraulic structure located between the outlet works and the tail-water, intended to return flows safely to the downstream channel by dissipating excess kinetic energy (Vischer and Hager 1998, Chanson 2015). Its performance is directly linked to the inlet flow characteristics, which are influenced by the spillway geometry. In classic studies, a smooth invert chute has been considered ideal (Peterka, 1978); however, recent knowledge on stepped spillways (Chanson 2002, Amador et al. 2009, Meireles and Matos 2009, Bung 2011, Felder and Chanson 2013, Hunt et al. 2014, Matos and Meireles 2014) has encouraged practitioners to consider this type of hydraulic structure. A smooth chute provides little energy dissipation, therefore requiring concentrated energy dissipation in the stilling basin; whereas the stepped spillway works as a continuous dissipater, thus potentially reducing required stilling basin dimensions while also improving flow aeration conditions.

When a stepped spillway is considered, the stilling basin's chute blocks may be dispensable, thus altering the original and widely tested designs of USBR basins II and III (Peterka 1978, Hager 1992). These chute blocks are small baffles at the basin entrance, intended to mix the flow via jet trajectory modification in order to shorten the hydraulic jump without requiring additional tail-water (Peterka 1978, Vischer and Hager 1998). The effects of chute blocks, including a shortened and more stable hydraulic jump, were recently numerically analyzed in Valero et al. (2015) for both design and adverse conditions (i.e., insufficient tail-water).

In addition to shortening the hydraulic jump, basin accessories exert a stabilizing effect and, when correctly designed, can greatly improve stilling basin performance and economics. Omitting the chute blocks in the design could alter the performance of the baffle block in the USBR type III basin and reduce jump stability, yet omission may be compensated by the spillway steps. A USBR type III basin, as modeled in the present work, is sketched in Figure 1. Depending on project objectives, anticipated risks, and economics, stilling basins are sometimes designed to contain the entire length of the hydraulic jump for the selected design discharge of the stilling basin; consequently, any change in the flow conditions from this design point can be critical for satisfactory stilling basin performance for a range of anticipated flows. The recent study by Reclamation (Frizell and Svoboda 2012) focused on this issue by analyzing conjugate depths ratios for a USBR type III basin with a stepped spillway at the inlet. Likewise, pressure heads for similar configurations have also been presented (e.g., Meireles et al. 2010, Bung et al. 2012). Frizell et al. (2009) suggested that additional research was needed to optimize the design of stilling basins. Indeed, inlet flow properties caused by stepped chutes can vary, and little is known about the new hydraulic jump flow structure or the quantitative effect of each basin element. Use of Computational Fluid Dynamics (CFD) tools may help to gain insight into the effect that a stepped chute may have on stilling basins, including basin geometry and tail-water (Shearin-Feimester et al. 2015), given the intrinsic limitations of experimental measurements. However, lack of validation and verification is still an issue noted by several researchers (Chanson and Lubin, 2010; Chanson, 2013). Therefore, physical models of stepped chutes with stilling basins at medium and large scales (e.g.: Frizell and Svoboda 2012) may constitute an enlightening workbench for numerical models.

Different options are available for numerical models, which depend on the part of turbulence that is calculated or simulated; it is RANS modelling with eddy viscosity models that remains most commonly used for high-velocity and large domain engineering applications (Davidson 2015). More complex and time consuming methods exist; however, it is often not recommended to expend additional computational costs to obtain average forces, distributions, and velocity fields (Bradshaw et al. 1996). However, given the complexity of turbulence, no single turbulence model can reproduce all turbulent problems (Bradshaw et al. 1996, Pope 2000, Wilcox 2006, Hirsch 2007). Despite existence of models that are more complex than eddy viscosity based models (i.e., Reynolds-Stress Transport models or RST), the continued use of one and two-equation turbulence models is expected (Slotnick et al. 2014). Also, RST models lack robustness and are, on occasion, less accurate than standard RANS models (Slotnick et al. 2014).
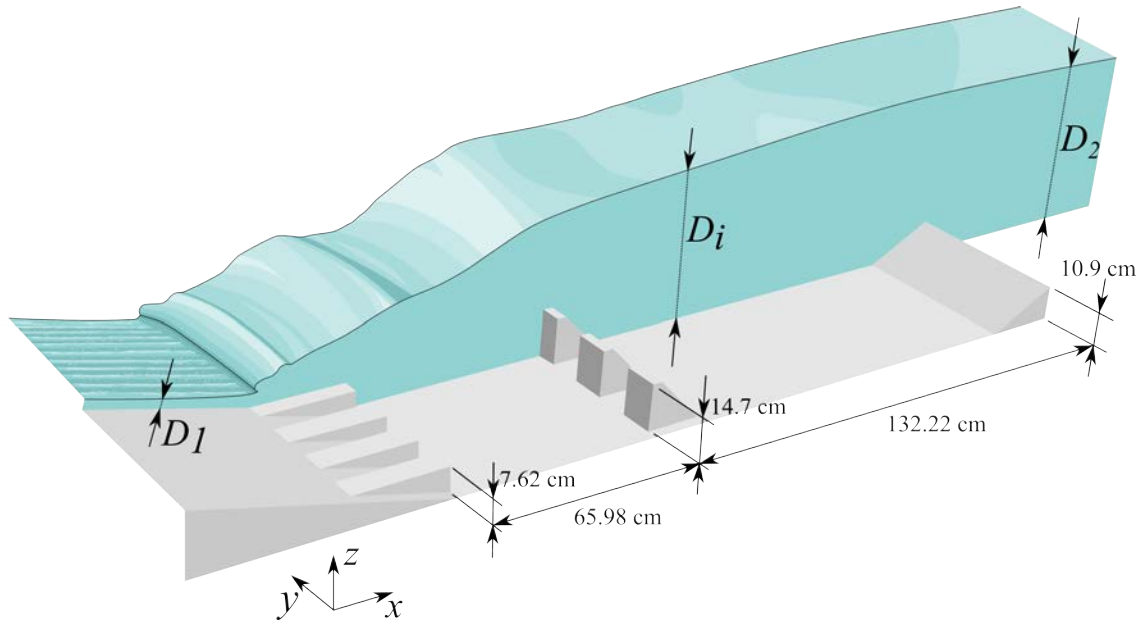
Figure 1. USBR type III basin half section and main geometrical parameters. Definition of the upstream section (S_1), intermediate section (S_i) and downstream section (S_2) with corresponding flow depths D_1, D_i and D_2.

Concerning RANS applications in related hydraulic engineering problems, Bombardelli et al. (2011) studied the accuracy of k-ε closure for RANS modelling of steep, stepped spillways using a 2D VOF single fluid approach, obtaining a good approximation of the inception point location and the non-aerated flow velocity profiles. Likewise, Valero and Bung (2015) studied the accuracy of RNG k-ε with similar conclusions for the non-aerated region with a full 3D approach. However, they noticed some difficulties for the aerated region even when using a calibrated subscale model for the air entrainment modelling (Valero and García-Bartual 2016). Wang et al. (2015) studied jet regimes downstream of a spillway flow by means of Spalart-Allmaras (SA)-DES (Detached Eddy Simulation with one transport equation for eddy viscosity) and compared their results to a 1:25 physical model. They highlighted the importance of numerical inlet conditions over the whole flow behaviour. Carvalho et al. (2008), based on a 2D RANS model and RNG k-ε for turbulence modelling, stated that RANS is appropriate for hydraulic jump problems despite its limitations (i.e., observed differences in velocities and free surface profile). Later, Valero et al. (2015) found good qualitative agreement with the study of Peterka (1978) for USBR type I and type II basins, and the study of Kawagoshi and Hager (1990) for the B-jump case , and the study of Ohtsu and Yasuda (1991) using a 3D RANS model with RNG k-ε closure. Recently, Witt et al (2015) studied accuracy of realizable k-ε for three Froude number hydraulic jumps simulations, noticing important mesh sensitivity.

In this study, eight different numerical models were developed to study the effects of a smooth chute and a stepped chute on the USBR type III stilling basin. The RNG k-ε model, which can present some advantages over other $k - \varepsilon$ models (Bradshaw, 1997), and the VOF method as described by Hirt and Nichols (1981) - used extensively for hydraulic engineering problems (Carvalho et al. 2008, Bombardelli et al. 2011, Oertel and Bung 2012) - have been employed using FLOW-3D® to properly reproduce turbulence and free surface effect upon the mean flow. First, a thorough mesh sensitivity study has been performed. Model geometry (as shown in Figure 1) and flow boundary conditions are based on the previous experimental study of Frizell and Svoboda (2012). The aim of the present work is to provide the following:

- Description and analysis of USBR type III basin performance downstream of stepped spillways under design and adverse conditions.
- Comparison with smooth spillway classical case, focused on stilling basin performance in response to a stepped chute inlet and the influence of each basin element on the hydraulic jump.

2. NUMERICAL MODEL

2.1. General Settings

The stilling basin geometry corresponds to the experimental study of Frizell and Svoboda (2012), designed for Froude number $F = 8$ with incoming supercritical flow clear water depth D_1 of 0.0762 m. Two geometric cases are investigated: a smooth chute and a stepped chute located upstream of the basin. Also, two inlet chute slopes have been considered: 4H:1V and 0.8H:1V. For the stepped chute, a constant step height $h = 38.1$ mm has been considered. In order to better observe 3D effects, the chute width has been expanded to 1.056 m (+60 %) instead of the original width used in the study of Frizell and Svoboda (2012). Main basin dimensions are shown in Figure 1. The range of simulated Froude numbers (3.1 to 9.5) is similar to the range of specific flow discharges and flow depths of Frizell and Svoboda (2012). Further details of the simulated cases can be found in Table 1.

Downstream water level (D_2) is set to the value provided by the Bélanger equation ($D_2{}^*$), which is based on the upstream water level and Froude number (Chanson 2009) in order to be similar to design conditions, and it is held for 2 seconds after asteady state condition is achieved. Then, D_2 is decreased exponentially, up to 40% of its initial value during 30 additional seconds, forcing the hydraulic jump to sweep out at some intermediate instant, allowing for an assessment of the corresponding D_2 level, which causes sweep out of the hydraulic jump for adverse conditions.

Table 1. Description of conducted simulations, each ID corresponds to two simulations: the design (steady) conditions and also the adverse (transient) conditions.

ID	Inlet chute	F	D_1 [m]	Slope [H:V]
S01		3.72	0.082	4:1
S02	smooth	6.37	0.065	4:1
S03		6.17	0.064	0.8:1
S04		9.52	0.066	0.8:1
R01		3.12	0.103	4:1
R02	stepped	4.20	0.093	4:1
R03		6.47	0.080	0.8:1
R04		8.27	0.072	0.8:1

For all simulations, the RNG k-ε turbulence model has been employed (Yakhot and Orszag 1986, Yakhot et al. 1992) with the VOF method, as defined by Hirt and Nichols (1981), for free surface tracking. In addition, a single fluid approach for free surface flows was selected, thus not explicitly considering the effect of air on the water surface (Prosperetti and Tryggvason 2007). Additionally, an air entrainment routine was not considered; thus self-aeration via bubble entrainment was not considered; however, the numerical models do include the effects of any entrapped air due to free surface roughness. Solids are represented as obstacles by means of the FAVOR porosity-based technique (Hirt and Sicilian 1985). Advection is computed with a second order scheme with a slope limiter that ensures proper gradient conservation (Van Leer 1977, Hirsch 2007), which was found to be very sensitive to initial flow conditions in the stepped chutes cases. Numerical stability was ensured by setting $CFL = 0.75$ so that no flow property can be advected further than 0.75 cells (Hirsch 2007). Linear systems are numerically solved by using the projection based algorithm GMRES (Saad 2003) with a Krylov subspace dimension of 15. This value affects computational time but not accuracy and is chosen based on the authors' experience.

2.2. Meshing and Boundary Conditions

Flow rate has been imposed in the upstream mesh plane (inlet boundary) with a thin plate that simulates the effect of a gate (to approximate the jet box utilized by Frizell and Svoboda 2012). This plate is located a sufficient distance upstream of the stilling basin to guarantee that a fully developed flow is established upstream of the stilling basin (i.e., upstream of the chute blocks for the smooth chute case). In the downstream mesh plane (outlet boundary), a pressure condition is imposed that allows the establishing of a flow depth value with a hydrostatic pressure distribution. Lateral planes are considered as smooth walls, similar to the physical model geometry surface of Frizell and Svoboda (2012).

For the mesh sensitivity analysis, two meshing strategies have been studied: first, uniform regular cubic cells ($\Delta x = \Delta y = \Delta z$) and second, mesh refinement over the basin blocks with three linked meshes. In the second approach, one mesh block was defined for the inlet region, a second mesh block was defined for the outlet region and downstream boundary condition, and the intermediate block comprised the main region of interest with finer cells near to the basin floor. Cell counts increased structurally following the suggestion of Celik et al. (2008) regarding mesh refinement. As shown in Figure 2, the second meshing strategy considerably reduced uncertainty of the numerical solution (implicitly shown in the scattering and trend of the results). This procedure has been carried out both for case S01 and S02 obtaining similar results; for clarity reasons, only case S01 is presented herein. Results from the mesh sensitivity analysis are shown in Figure 2. Detailed descriptions of employed meshes can be found in Table 2. For the remaining cases, lengths of the meshes have been modified to cover the entire flow region and the number of cells have been adjusted to remain with same minimum, maximum, and mean cell sizes.
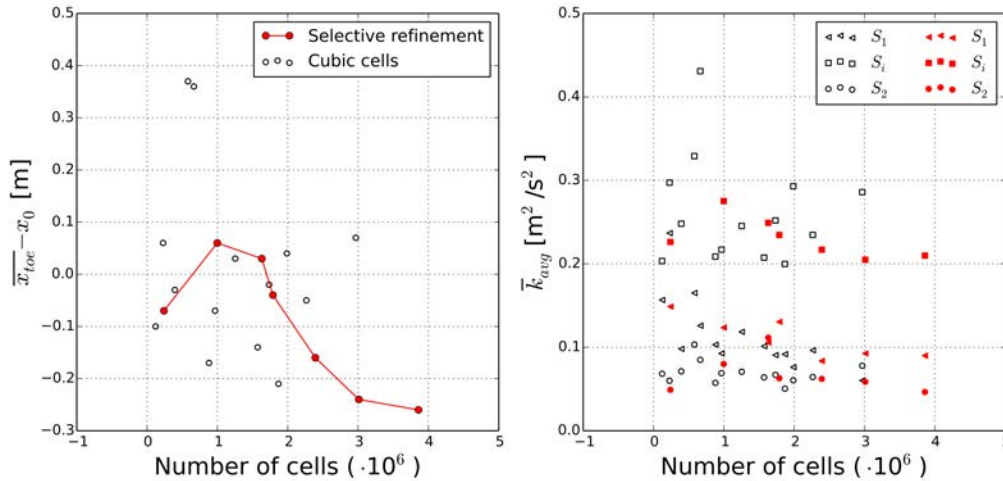
Figure 2. Time averaged hydraulic jump toe location $\overline{x_{toe}}$ relative to the inlet-basin junction location x_o and time and depth averaged turbulent kinetic energy $\overline{k}_{avg}$. White markers correspond to regular cubic cells mesh whereas red markers correspond to the multiblock refined meshing strategy for case S01.

Table 2. Main characteristics of the employed meshes for case S01, resulting from the Figure 2 sensitivity analysis.

	x		y	z		
	Length [m]	Δx [m]	Δy [m]	min(Δz) [m]	max(Δz) [m]	mean(Δz) [m]
Mesh 1	1.5	0.012	0.012	0.012	0.012	0.012
Mesh 2	3.5	0.012	0.012	0.003	0.020	0.011
Mesh 3	1.2	0.015	0.015	0.006	0.025	0.015

3. RESULTS AND DISCUSSION

3.1. General Remarks

For each case, a simulation has been conducted for $t = 15$ seconds in order to obtain the steady solution. Later, a new simulation has been set using the original simulation as the initial conditions. The initial two seconds of the new simulation are run with a constant downstream level $D_2 = D_2^*$, similar to design conditions. The solution is averaged with a temporal window $\Delta t = 0.05$ s, which allows for proper accounting of the naturally occurring oscillations effect of Unsteady RANS simulations (Spalart 2000). After those initial two seconds, the tail-water level is smoothly reduced for another $t=30$ seconds, procuring different solutions for adverse hydraulic conditions ($D_2 < D_2^*$).

Integration over a plane perpendicular to the flow was performed to obtain the real Froude number and the section representative flow depth. This becomes more important for the stepped spillway cases (R01-R04), which display greater free surface roughness.

3.2. Flow Structure

Supercritical flow enters the stilling basin and forms a roller and a shear region, similar to a classic hydraulic jump (Chanson and Brattberg 2000), as shown in Figure 3. However, it has sometimes been reported that hydraulic jumps over sloping aprons can, under certain conditions, behave more similarly to the classic wall jet. Nevertheless, some differences might be pointed out.

When the high-velocity flow impinges the roller and a smooth chute is considered, the chute blocks immediately downstream affect the flow by increasing turbulence, which can surpass the turbulence generated in the hydraulic jump impingement point. When a stepped chute is considered, the flow is continuously fed with turbulence throughout the spillway and the turbulence generated in the impingement is smaller than in the previously mentioned case.

For both types of simulated aprons, the majority of turbulent kinetic energy is held between the basin inlet and the baffle blocks or baffle piers. Additionally, the roller and its spatial location are influenced by flow impacting the baffle blocks. The end sill has proven to be effective in protecting the adjacent channel bed via flow uplift, as in the USBR type II basin numerical study of Valero et al. (2015). Note that the geometry of the USBR type III end sill is altogether different (spatially uniform) than the type II, which mimics the shape of the baffle blocks with vertical faces and angled dentations.
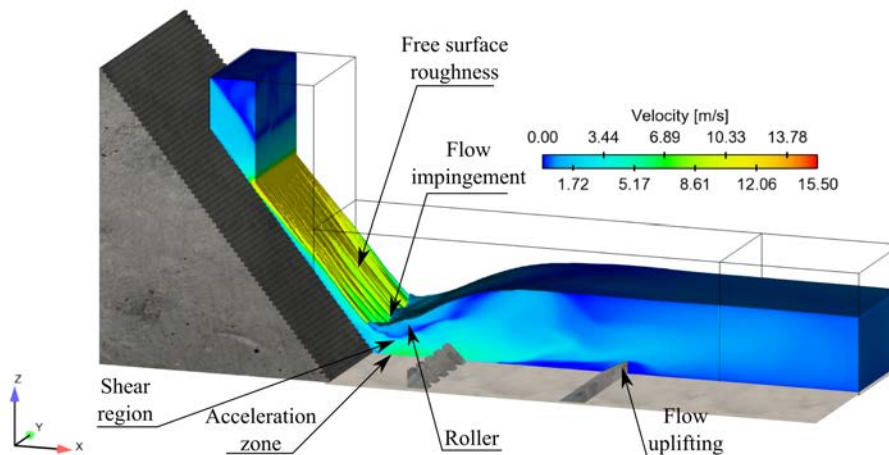
Figure 3. Instantaneous flow structure for case R03. Downstream water level set to D_2^*. Meshes are shown with black solid lines

As noted in published literature, chute blocks provide a minor jet deflection and create small but intense shear regions. Baffle blocks are more influential as an obstruction, with fluid impact magnifying 3D flow patterns and turbulence.

3.3. Velocity Decay

High velocities in the chute are rapidly reduced when flow enters the basin. Given the diffusive nature of the flow equations, it is more likely that the maximum velocity within the profile would be more resistant to velocity reduction; thus, it has been previously studied in many works as a descriptor of the flow structure.

Figure 4 shows the decay of the maximum velocity obtained at the numerical model for the studied configurations after a previous averaging in time of the velocity field. Herein, $\bar{v}_{max}$ is the maximum velocity of the averaged velocity distribution in the inlet section and, for ease of notation, $\bar{v}$ directly corresponds to the maximum velocity located at a transversal section placed in x. For context, other similar flows have been added to Figure 3 of type I and type II USBR basins from previous works with F noted. Empty markers correspond to the smooth chute at the basin inlet and filled markers to stepped chute. Although differences in velocity decay can be caused by differences in the numerical model settings, it is clearly acknowledged that a significant gap exists (as expected) between the USBR type I or II basin and the case considered herein. Baffle blocks appear to provide an improvement in the jet velocity dissipation for the USBR type III basin.

The numerical simulations identified the acceleration zone after the jet impacts the basin floor, which was also noted in the physical model study of Ohtsu and Yasuda (1991). However, when the jet impacts the baffle blocks, a more appreciable abrupt "step" is produced in the velocity decay. Within this short zone, the maximum velocity is held between the blocks and the decaying velocity trend is located immediately downstream of the baffle blocks. Considering the stepped chute, there is a noticeable effect from the steps that caused an even higher decay of the maximum velocity, possibly driven by the fact that the inlet flow is considerably more turbulent with a greater rate of energy dissipation. This is more pronounced for lower Froude numbers and can have an appreciable influence on basin performance under adverse conditions, as discussed in the following section.
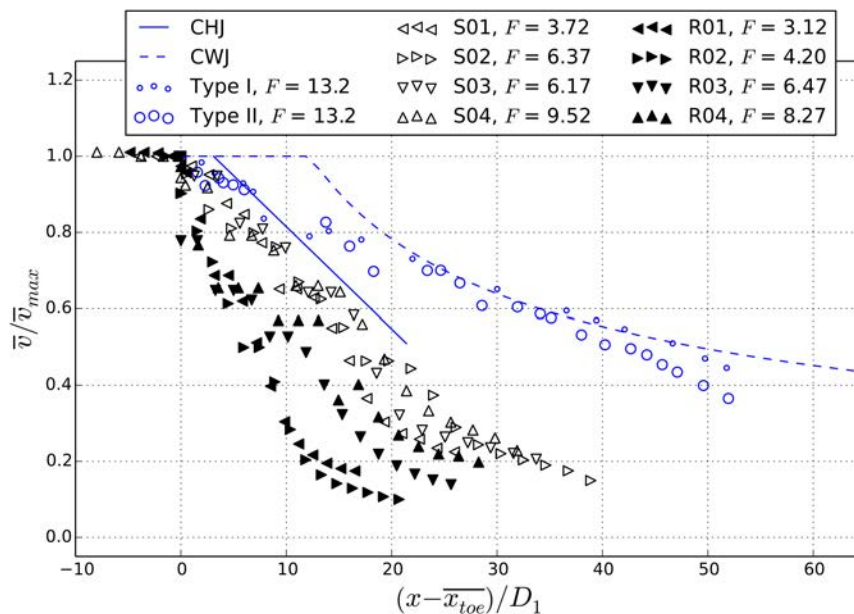

Figure 4. Decay of the maximum mean velocity for simulated cases, classic hydraulic jump (CHJ) according to Chanson and Brattberg (2000), classic wall jet (CWJ) according to Rajaratnam (1976) and the numerical simulations

3.4. Stilling Basin Performance Under Adverse Conditions

The flow structure changes in response to a reduction in tail-water ($D_2 < D_2{}^*$), and as previously mentioned, the flow structure is also influenced by basin elements. Herein, an analysis is conducted of what are considered the most influential basin elements.

When applying Newton's second law to a control volume around the hydraulic jump, the following equation for horizontal forces balance can be obtained:

$$\iint p_1 \, dA_{1,x} + \iint \rho \, v_1{}^2 \, dA_{1,x} = \iint p_2 \, dA_{2,x} + \iint \rho \, v_2{}^2 \, dA_{2,x} + F_x \tag{1}$$

where ρ is the fluid density, $dA_{1,x}$ and $dA_{2,x}$ are the horizontal component of the area differential at sections S_1 and S_2, respectively (see Figure 1), p is the pressure at each section, and F_x is the horizontal contribution of all the other forces; for instance, the resulting baffle blocks force (F_b), the force opposed by the end sill (F_{es}) or the force exerted by the basin bed (F_w), among others. For a control volume over a slope, gravity may also contribute. F_x could also be considered the force caused by the chute blocks or the lateral walls; however, they have not been considered in this study.

P_1 and P_2 are used to represent the resulting horizontal pressure forces. For the momentum contribution, F_{m1} and F_{m2} are employed. Then, the inlet flow contribution can be written as $P_1 + F_{m1}$ and, when no other force is considered, $P_2 + F_{m2}$ may be an equivalent sum when a classical hydraulic jump is considered.
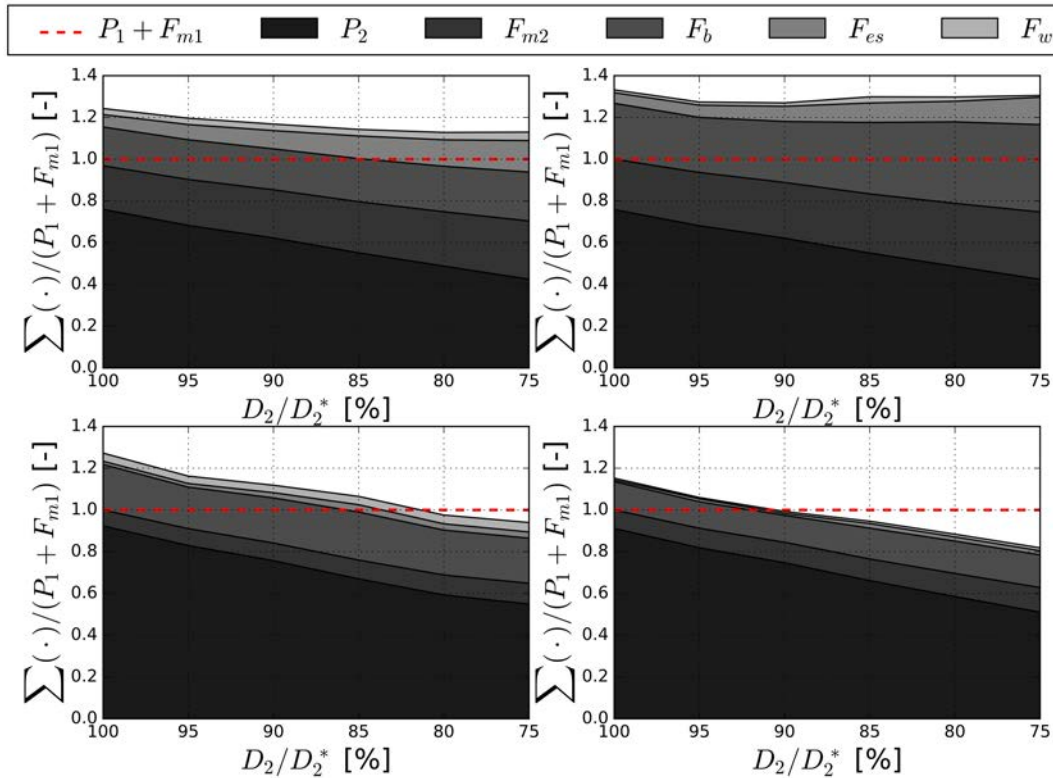
Figure 5. Relative contribution of each basin element to the stability of the hydraulic jump for different adverse tail-water levels, up to 75% of design downstream depth D_2^*. Case S01 (upper left), R01 (upper right), S04 (lower left), R04 (lower right). Red dashed line represents inlet flow contribution.

Figure 5 shows the comparative importance (relative to the inlet flow characteristics) of each element for the lower and higher studied Froude numbers. The effect of each term is presented in a cumulative way for each D_2/D_2^* considered. Please note the significant importance of the baffle blocks term in all cases, which can contribute more than the downstream momentum. When tail-water is decreased, flow over the baffle block provides an increased contribution to the total force, especially for the lower Froude number cases. This phenomenon is of special interest when combined with the stepped spillway since the baffle block term helps to overcome the contribution of the inlet flow. This may be caused by the important velocity decay observed for this configuration in Figure 4. As a consequence, total downstream forces remain higher than $P_1 + F_{m1}$ for high reductions of tail-water level; this might explain the highly stable hydraulic jump observed by Frizell and Svoboda (2012) for Froude numbers below 6. The effect of basin bed friction is slightly smaller for the stepped spillway cases, which may be due to the steps elevating the centroid of the velocity profiles (and resulting in lower gradients close to the channel bed).

4. CONCLUSIONS

CFD may be utilized to analyze the complex behaviors of flows within a hydraulic jump stilling basin, providing qualitative and quantitative information to practitioners, in part through comparative analyses. Unsteady RANS equations have been employed with VOF and RNG k-ε for free surface tracking and turbulence modeling, respectively. Eight different Froude numbers (F) ranging from 3.1 to 9.5 have been analyzed for a stilling basin designed for $F = 8$, following recent studies conducted by Reclamation. The basin flow structure was investigated for both smooth chute and stepped chute cases, each at two slopes. Additionally, the modelled basin has been tested for design and adverse hydraulic conditions, obtaining a detailed insight of the role of each basin element and their adapting roles when insufficient tail-water conditions exist.

When a stepped chute is considered, the flow is continuously fed with turbulence throughout the spillway chute, and the turbulence generated via impingement is smaller than for a smooth chute. The steps cause an even higher decay of the maximum velocity within the basin, possibly driven by the fact that the inlet flow is considerably more turbulent relative to a smooth chute. This decrease is more pronounced for smaller Froude numbers. Also, baffle blocks promote maximum velocity decay. The acceleration zone immediately downstream of the basin entrance is more significant in the profile when the jet impacts baffle blocks.

In Figure 5, the relative importance (relative to the inlet flow characteristics) is shown for each stilling basin element for the lower and higher studied Froude numbers. The effect of each term is presented in a cumulative way for each D_2/D_2^* considered. The influence of baffle blocks was found to exceed that of the other stilling basin elements.

5. REFERENCES

Amador, A., Sánchez-Juny, M., and Dolz, J. (2009). "Developing flow region and pressure fluctuations on steeply sloping stepped spillways". *Journal of Hydraulic Engineering,* 135(12), 1092-1100.

Bombardelli, F.A., Meireles, I., and Matos, J. (2011). "Laboratory measurements and multi-block numerical simulations of the mean flow and turbulence in the non-aerated skimming flow region of steep stepped spillways". *Environmental Fluid Mechanics*, 11(3), 263-288.

Bradshaw, P., Launder, B. E., and Lumley, J.L. (1996). "Collaborative testing of turbulence models". *Journal of Fluids Engineering,* 118(2), 243-247.

Bradshaw, P. (1997). "Understanding and prediction of turbulent flow—1996". *International journal of heat and fluid flow,* 18(1), 45-54.

Bung, D.B., Sun, Q., Meireles, I., Viseu, T. and Matos, J. (2012). "USBR type III stilling basin performance for steep stepped spillways". *Proc., 4th IAHR International Symposium on Hydraulic Structures*, 9-11 February 2012, Porto, Portugal, ISBN: 978-989-8509-01-7.

Carvalho, R.F., Lemos, C.M., and Ramos, C.M. (2008). "Numerical computation of the flow in hydraulic jump stilling basins". *Journal of Hydraulic Research*, 46(6), 739-752.

Chanson, H. (2002). The Hydraulics of Stepped Chutes and Spillways, Balkema, Lisse, the Netherlands.

Chanson, H (2009). "Development of the Bélanger equation and backwater equation by Jean-Baptiste Bélanger (1828)". *Journal of Hydraulic Engineering,* 135(3), 159-163.

Chanson, H. (2013). "Hydraulics of aerated flows: qui pro quo?". *Journal of Hydraulic Research*, 51(3), 223-243.

Chanson, H. (2015). Energy Dissipation in Hydraulic Structures. IAHR Monographs, CRC Press/Balkema, Taylor & Francis Group. ISBN: 978-1-138-02755-8

Chanson, H., and Brattberg, T. (2000). "Experimental study of the air–water shear flow in a hydraulic jump". *International Journal of Multiphase Flow*, 26(4), 583-607.

Chanson, H. and Lubin, P. (2010). Discussion on "Verification and validation of a Computational Fluid Dynamics (CFD) model for air entrainment at spillway aerators". *Can. J. Civil Eng.*, 37(1), 135-138. DOI:10.1139/L09-133

Celik, I.B., Ghia, U., and Roache, P.J. (2008). "Procedure for estimation and reporting of uncertainty due to discretization in CFD applications". *Journal of Fluids Engineering,* ASME, 130(7), 1-4.

Davidson, P. (2015). "Turbulence: an introduction for scientists and engineers". Oxford University Press, USA.

Felder, S., and Chanson, H. (2013). "Aeration, flow instabilities, and residual energy on pooled stepped spillways of embankment dams." *J. Irrig. Drain Eng.*, 139(10), 880–887

Frizell, K. W., Kubitschek, J. P. and Matos, J. (2009). "Stilling basin performance for stepped spillways of mild to steep slopes – Type III Basins". Proceedings of the 33rd IAHR Congress: Water Engineering for a Sustainable Environment. ISBN: 978-94-90365-01-1

Frizell, K.W. and Svoboda, C.D. (2012). "Performance of Type III Stilling Basins – Stepped Spillway Studies. Do Stepped Spillways Affect Traditional Design Parameters?" *U.S. Department of Interior, Bureau of Reclamation, HL-2012-02*.

Hager, W. H. (1992). Energy dissipators and hydraulic jump. Water Science and Technology Library, Kluwer Academic Publishers. ISBN: 0-7923-1508-1.

Hirsch, C. (2007). Numerical Computation of Internal and External Flows: The Fundamentals of Computational Fluid Dynamics: The Fundamentals of Computational Fluid Dynamics. Butterworth-Heinemann.

Hirt, C.W., and Nichols, B.D. (1981). "Volume of fluid (VOF) method for the dynamics of free boundaries". *Journal of computational physics,* 39(1), 201-225.

Hirt, C.W., and Sicilian, J.M. (1985). "A porosity technique for the definition of obstacles in rectangular cell meshes". *Proc., Fourth International Conf. Ship Hydro* (pp. 1-19).

Hunt S.L., Kadavy, K.C., and Hanson, G.J. (2014): "Simplistic design methods for moderate-sloped stepped chutes" *Jour. of Hydr. Eng.*, ASCE, Vol. 140, No. 12, pp. 04014062-1 to 04014062-15.

Kawagoshi, N., and Hager, W.H. (1990). "B-jump in sloping channel, II." *Journal of Hydraulic Research*, 28(4), 461-480.

Matos, J. and Meireles, I. (2014). "Hydraulics of Stepped Weirs and Dam Spillways: Engineering Challenges, Labyrinths of Research". In Chanson, H. and Toombes, L., Hydraulic structures and society - Engineering challenges and extremes, *Proc, 5th IAHR International Symposium on Hydraulic Structures*, Brisbane, Australia, 1-30. DOI: 10.14264/uql.2014.11

Meireles, I., Matos, J. and Silva-Afonso, A. (2010). "Flow characteristics along a USBR type III stilling basin downstream of steep stepped spillways". *Proc. 3rd Int. Junior Researcher and Engineer Workshop on Hydraulic Structures*, Edinburgh, Scotland, Hydraulic Model Report CH80/10, The University of Queensland, Brisbane, Australia, pp. 57-64.

Meireles, I. and Matos, J. (2009). "Skimming Flow in the Nonaerated Region of Stepped Spillways over Embankment Dams". *J. Hydraul. Eng.*, 10.1061/(ASCE)HY.1943-7900.0000047, 685-689.

Oertel, M. and Bung, D.B. (2012). "Initial stage of two-dimensional dam-break waves: Laboratory versus VOF." *Journal of Hydraulic Research,* 50(1), 89-97.

Ohtsu, I. and Yasuda, Y. (1991). "Hydraulic jump in sloping channels". *Journal of Hydraulic Engineering*, 117(7), 905-921.

Peterka, A.J. (1978). Hydraulic design of spillways and energy dissipators. A Water Resources Technical Publication, Engineering Monograph, (25).

Pope, S.B. (2000). Turbulent flows. Cambridge University Press.

Prosperetti, A., and Tryggvason, G. (2007). Computational methods for multiphase flow. Cambridge University Press.

Rajaratnam, N. (1976). Turbulent jets. Elsevier.

Saad, Y. (2003). Iterative methods for sparse linear systems. Siam.

Shearin-Feimster, L.E., Crookston, B.M. and Felder, S. (2015). "Design approaches and numerical modeling of a stepped spillway under high tailwater conditions." *Proc. of the 35th Annual USSD Conference*, Louisville, Kentucky. CD-ROM.

Slotnik, J., Khodadoust, A., Alonso, J., Darmofal, D., Gropp, W., Lurie, E., & Mavriplis, D. (2014). "CFD vision 2030 study: a path to revolutionary computational aerosciences". *NASA/CR–2014-218178*

Spalart, P.R. (2000). "Strategies for turbulence modelling and simulations". *International Journal of Heat and Fluid Flow,* 21(3), 252-263.

Valero, D., and García-Bartual, R. (2016). "Calibration of an air entrainment model for CFD spillway applications". *Advances in Hydroinformatics*. Springer Singapore. 571-582.

Valero, D. and Bung, D.B. (2015). "Hybrid Investigations of Air Transport Processes in Moderately Sloped Stepped Spillway Flows". *Proc., 36th IAHR World Congress*, 28 June – 3 July, 2015, The Hague, the Netherlands.

Valero, D., García-Bartual, R., and Marco, J. (2015). "Optimisation of Stilling Basin Chute Blocks Using a Calibrated Multiphase RANS Model". *Proc, 5th International Junior Researcher and Engineer Workshop on Hydraulic Structures*. Spa, Belgium, 28-30 August, 2014.

Van Leer, B. (1977). "Towards the ultimate conservative difference scheme. IV. A new approach to numerical convection". *Journal of Computational Physics*, 23(3), 276-299.

Vischer, D.L. and Hager, W.H., (1998). Dam Hydraulics. Wiley Series in Water Resources Engineering.

Wang, Y., Politano, M., Laughery, R., and Weber, L. (2015). "Model development in OpenFOAM to predict spillway jet regimes". *Journal of Applied Water Engineering and Research*, 3:2, 80-94. DOI: 10.1080/23249676.2015.1025442

Wilcox, D.C., (2006). Turbulence modelling for CFD. DCW Industries, 3rd edition. ISBN: 978-1-928729-08-8

Witt, A., Gulliver, J., and Shen, L. (2015). "Simulating air entrainment and vortex dynamics in a hydraulic jump". *International Journal of Multiphase Flow*, 72, 165-180. doi: http://dx.doi.org/10.1016/j.ijmultiphaseflow.

2015.02.012

Yakhot, V., and Orszag, S.A. (1986). "Renormalization group analysis of turbulence. I. Basic theory". *Journal of Scientific Computing*, 1(1), 3-51.

Yakhot, V., Orszag, S.A., Thangam, S., Gatski, T.B., and Speziale, C.G. (1992). "Development of turbulence models for shear flows by a double expansion technique". *Physics of Fluids A: Fluid Dynamics* (1989-1993), 4(7), 1510-1520.

A Regulatory Perspective on Implementing
Risk-Informed Decision Making in Dam Safety

Douglas Boyer, PE, CEG[1], William Allerton, PE[2]

[1]Chief, Risk-informed Deccision Making Branch, FERC, Division of Dam Safety and Inspections
850 SW Broadway, Suite 550
Portland, OR 97205
USA
[2]Director, FERC, Division of Dam Safety and Inspections
888 First Street, NE
Washington, DC 20426
USA
E-mail: Douglas.Boyer@ferc.gov

EXTENDED ABSTRACT

Risk, if used properly, can be a very powerful tool to aid in understanding in more detail the critical aspects of a dam's design, construction, analysis, and performance, and the potential consequences of a dam failure. The correct approach to risk analysis can improve the prioritization of dam safety actions to focus limited resources on what is important, direct risk reduction evaluations to those measures that are more effective, and better inform routine dam safety activities, such as dam safety inspections, surveillance and monitoring, emergency action plans, and others.

The Federal Energy Regulatory Commission (FERC) is currently developing risk-informed decision making (RIDM) concepts to integrate risk into our dam safety program. This concept was initiated in 2009 and was a specifically identified objective in the 2010 FERC Strategic Plan. This strategy continues to be included in FERC's most recent (2014) strategic plan. Risk methodologies and experiences have matured to the point where, as a dam safety regulator, FERC is able to apply these concepts in a regulatory environment.

A number of other federal agencies have developed and are actively using risk-informed approaches in their dam safety programs, including the Bureau of Reclamation and US Army Corps of Engineers. For the most part, these dam owning agencies use in-house resources to perform risk analyses, risk assessments, and risk management. FERC's role is as a regulator and not an owner; therefore, the approach and execution of risk, among other things, will be different than other federal agencies.

Many challenges exist to integrating RIDM into the FERC dam safety program, including development of risk guidelines; training of risk policies, procedures, and methodologies; and communication. Risk pilot studies will be used to help evaluate the RIDM policies and processes, including identifying potential shortcomings in the interim guidelines and obtaining input from licensees and consultants on the overall RIDM processes and methodologies.

Keywords: *Risk, Dam Safety, RIDM, FERC*

Interaction of Hydraulic Structures with Air, Water, and Rock: The Challenge of Researchers and Designers

Anton J. Schleiss
Laboratory of Hydraulic Constructions (LCH)
Ecole polytechnique fédérale de Lausanne (EPFL)
Station 18, CH-1015 Lausanne
Switzerland
E-mail: anton.schleiss@epfl.ch

KEYNOTE - EXTENDED ABSTRACT

1. THE IMPORTANCE OF HYDRAULIC STRUCTURES AND SCHEMES FOR THE WORLD ECONOMY

Since the last ten years, financial crisis has strongly impacted the global economy, which was mainly the result of un-controlled financial speculations at the stock markets highlighted by the revelations regarding offshore companies. Fortunately, the field of construction of large infrastructures, such as hydraulic schemes, has been left relatively untouched by this crisis. In order to stimulate their economies, many governments across the world have injected significant sums into sustainable infrastructures development.

This progress in the field of hydraulic structures and schemes is not astonishing since it has to be kept in mind that the soundness of the world economy is founded mainly on investments and particularly by the creation of infrastructures. Among the last ones, hydraulic schemes play an important role. During several thousand years, man has continuously developed techniques to use water and at the same time to protect himself against water. History shows that the economic prosperity of a society and its cultural wealth have always been closely related to the level of the development of the hydraulic schemes (Schleiss 2000).

The term *hydraulic schemes* includes all measures and human interventions aiming to the control and exploitation of the water cycle. A vital element of our environment, water also presents an important destructive potential. Thus, hydraulic schemes can be divided, according to their objectives, into two groups (Fig. 1):

- schemes for water utilization
- schemes for protection against water

The hydraulic structures designed for water utilization are multipurpose, ensuring water supply, irrigation, hydropower production, and navigation. The structures designed for protection against water are also used for sewage treatment, drainage, flood protection, and erosion protection measures.
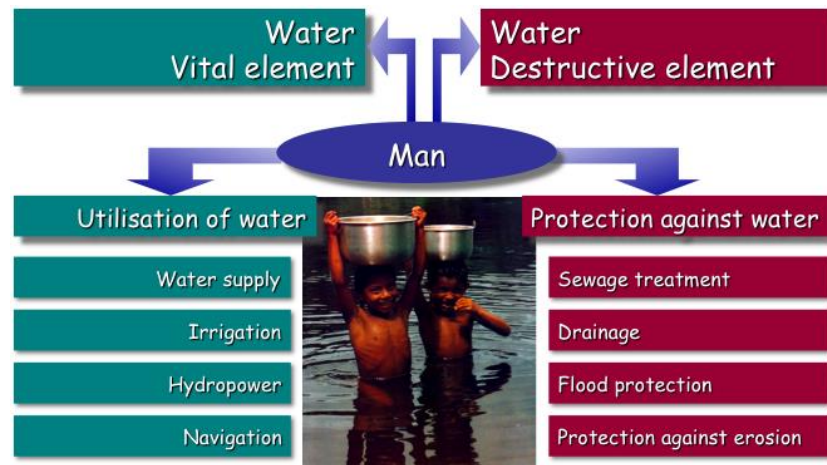
Figure 1. Application of hydraulic structures and schemes (Schleiss 2000)

Hydraulic structures can be grouped as follows:

- Storage structures: water supply reservoirs, artificial lakes created by dams, flood retention basins, a.s.o.
- Withdrawal structures: intakes at lakes and rivers, weirs, ogee crests, desilting basins, orifices, a.s.o.
- Conveying and diversion structures: channels, galleries, pressure tunnels and shafts, surge tanks, chutes, bank and bed erosion protections, a.s.o.
- Restitution and energy dissipation structures: stilling basins, plunge pools, flip buckets, vortex and drop shafts, a.s.o.
- Appurtenant hydraulic structures of dams: spillways, bottom outlets, river diversion channels and tunnels, a.s.o.
- Special structures: syphons, aqueducts, a.s.o.

2. CHALLENGES IN THE WORLDWIDE DEVELOPMENT OF HYDRAULIC STRUCTURES AND SCHEMES

The major problems of the world population in this century will certainly be the safe supply of ecological and renewable energy and the supply of good quality water and a sufficient quantity in order to fight against famine, poverty, and disease in the world. These problems must be solved, above all, by investments in the development of new hydraulic structures and schemes, as well as in their maintenance and refurbishment, which is briefly discussed in the following sections.

2.1. Water for Domestic, Industrial, and Agricultural Use

At the beginning of the 21st century, water supply and sanitation services left much to be desired; two thirds of the world population still suffered from the lack of safe water (insufficient quantity) or from the lack of safe sanitation (inappropriate quality). Besides harnessing available resources and improving management of existing resources, the usable potential has to be increased by hydraulic schemes mainly for storage and transportation of water. Even in developed countries, failure of sewer systems due to insufficient hydraulic design causes flooding and pollution of adjacent areas.

2.2. Irrigation

An important part of the world population is still threatened with famine. This risk could be considerably lessened by the irrigation of arid areas not cultivable today. For an efficient irrigation, the creation of reservoirs and the construction of hydraulic structures, such as dams, waterways, and transfer system, as well as restitution structures is absolutely necessary. Furthermore, climate change will contribute to the diminution of today's arable lands in some areas. It has to be feared that the lack of freshwater could be an increasing source of local wars in this century.

2.3. Hydropower and Electricity Production

Since 1950, the growth of the hydropower production has strongly accelerated, a tendency that still continues today. All energy scenarios forecast that the speed of the development of hydropower in the next 50 years will be equal to that of the last 50 years. Less than 20% of the technically feasible hydropower potential has been developed worldwide so far. In South America, only one third of the economically feasible potential is in operation; in Asia (including Russia and Turkey), it is only one fifth. In Africa, a very small portion, namely about 7%, of the economically feasible potential is exploited today. However, in Europe more than 70% and in North America more than 75% of this potential are used. The worldwide remaining economically feasible hydro potential would be high enough to replace the generation by nuclear power plants as well as an important part of the electricity produced by fossil fuels. Furthermore, hydropower from storage schemes can regulate the high volatile production of such new renewable energies as wind and solar.

2.4. Navigation

Most of the goods exchanged and their transportation in the world are ensured by sea and river navigation. This will also be the case in the future as the transportation of goods by road has already reached, in some regions, its bearable limits. There remains a considerable amount of work to be done in the field of navigation, especially in regions where the rivers are not thoroughly navigable. To allow navigation, the construction of hydraulic structures such as dams, canals, ship locks, and harbors is necessary.

2.5. Flood Protection

The population growth combined with the greenhouse effect considerably increases the risk of floods including tsunamis with the danger of disastrous damages as experienced several times recently. Therefore, flood protection measures are an important application of hydraulic structures and become more and more vital for many regions of the world, mainly for densely populated areas.

Concluding this list of applications of hydraulic structures, it is not exaggerated to say that hydraulic schemes will be of fundamental importance in the development of the world society since they can satisfy the vital needs of water-energy-food, and this respecting the environment and the sustainable development of resources.

3. RESEARCH CHALLENGES IN THE FIELD OF HYDRAULIC STRUCTURES AND SYSTEMS

Although a classic branch of civil engineering already theoretically advanced, hydraulic engineering still presents research challenges ensuing from varied reasons. The arise of new measuring and computational capabilities allow the assessment of variables with more detail and precision; a deeper insight in the mechanics of the flows is now possible, allowing a breakthrough on the interpretation of results, which, in the fields of research covered by hydraulic engineering, ensue seldom from empirical approaches based on bulk observations, practical assumptions, or inference from similar studies. Research challenges arise also from new needs claimed by the society, related

mainly to economic (need for optimization and upgrading of water resources exploitation), safety (increased public awareness of the risk associated with built infrastructures and natural elements), and ecologic (increased public awareness on environmental conservation) concerns.

The construction of new and the rehabilitation of existing infrastructure for the use of water and protection against its natural hazards will be a main challenge all over the world. Since the hydraulic schemes have to be realized in a more complex environment, the design and implementation of such schemes are much further demanding, and research is required to answer complex questions.

Hydraulic schemes are in interaction with the environment where, physically spoken, interaction of structures with water, air, and underground is a main issue. This interaction involves multi-phase flows (water, air, sediment) in a 3D environment bounded by complex structures. Even if the numerical models have been strongly improved over the last decade, and if this progress will continue, there will always be new complex problems, which have to be assessed by physical modelling. Furthermore, the latter will always be required to further develop and validate the numerical models. Experience over the last 20 years showed that in parallel with a strong development of numerical models and simulations, the demand in physical modelling was continuing to grow. Today, high competences in physical modelling combined with advanced measurement technologies are required which need a long experience and development in the hydraulic laboratories.

4. THE CHALLENGE TO ASSESS THE INTERACTIONS OF HYDRAULIC STRUCTURES WITH AIR, WATER, AND ROCK

The interaction of hydraulic structures with air, water, and rock results often at interface problems between hydraulic engineering on one side and geotechnical and structural engineering on the other side. These interface problems have to be treated with an interdisciplinary approach, which should be led by the hydraulic engineer.

In the following sections, the challenges for researchers and designers when treating such interface problems involving air, water, and rock are highlighted with some examples.

4.1. Design of Pervious Pressure Tunnel Linings

Pressure tunnels that are not steel lined or not sealed with plastic membranes are essentially permeable. Even not cracked concrete linings are not absolutely tight. Reinforced concrete linings crack under internal water pressure. The task of the reinforcement is to distribute the cracks in such a way that the crack widths remain below a certain limit value. A seepage flow through the lining into the rock inevitably results in the case of permeable linings. The corresponding seepage forces affect both the deformation of the lining and rock. In contrast to an absolutely tight lining, the internal water pressure thus acts both as a uniformly distributed load at the inner side of the lining as well as a hydraulic body force inside the lining and rock. This body force resulting from the hydraulic gradient of the seepage flow causes deformations, which exert an effect on the lining and rock mainly in the form of a change in the crack and fissure widths.

This results in a change in their permeability, which in turn influences the seepage flow forces. Consequently, the mechanical and hydraulic states of a permeable waterway system mutually influence each other through hydraulic-mechanical interactions, as is shown in Figure 2. In order to take this physical characteristic of permeable linings sufficiently into account, the following must be considered when determining stresses and deformations in lining and rock (Schleiss, 1986, 1988):

- forces caused by seepage flow through the lining into the rock (or vice versa) = statics of porous media
- changes in permeability due to lining and rock deformations = rock/groundwater hydraulics

The influence of seepage flow in concrete lining and rock on the design of permeable pressure tunnels is considerable and cannot be neglected in the design (Schleiss 1986, 1988, 1997).
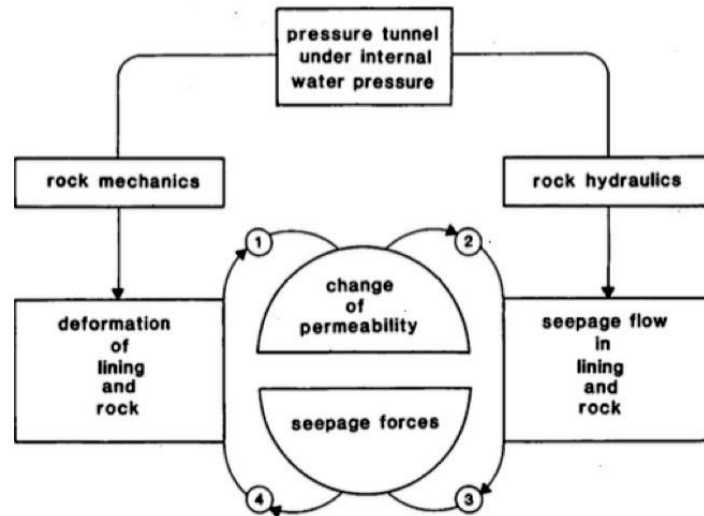
Figure 2. Hydraulic-mechanical interactions and pervious pressure tunnels (Schleiss, 1988)

4.2. Pressure Relief Valves for Protection of Steel-lined Pressure Shafts against Buckling during Emptying

Using high-strength steels for pressure shafts and tunnel liners and taking into account significant rock mass participation allows the design of comparatively thin steel liners in hydropower projects. Nevertheless, during emptying of the waterways, these steel linings may be endangered by buckling. Compared with traditional measures such as increased steel liner thickness and stiffeners, pressure relief valves are a very economical solution for the protection of steel liners against critical external pressure and, therefore, buckling during emptying. A calculation procedure has been developed for the design of the required number and arrangement of pressure relief valves, and this has been used successfully in practice (Schleiss and Manso 2012). Systematic model tests enabled the assumptions of the design method to be verified. The pressure relief valves in the steel liner have to drain the seepage flow from the rock mass in such a way that the external water pressure does not exceed the tolerable value for a certain steel liner thickness. Assuming radial-symmetrical permeability conditions, the discharge through the pressure relief valves is influenced by the head losses of the seepage flow across the a) far field rock mass; b) grouted or loosened rock zone around the pressure shaft or tunnel (if present); c) backfill concrete (non-reinforced, cracked); d) gap between steel liner and backfill concrete (opening depends on external water pressure); e) pressure relief valves. Since the opening of the gap between the steel liner and the backfill concrete depends on the external water pressure, a mechanical hydraulically-coupled system is obtained, which has to be solved with an iterative approach.

4.3. Interaction of Bend Flow in a Channel with Bank Roughness, Bed Morphology and Air Bubble Screens

Practical experience with flood protection projects showed that the scour along outer bank protection walls can be considerably reduced by placing macro-roughness on the bank protection wall. This allows for the reduction of the depth of the foundations, which, in turn, has a reducing impact on the cost of the project. In the framework of a research project, systematic tests were performed to establish the basis for dimensioning vertical ribs, which served as macro-roughness (Hersberger et al. 2016). Experiments showed that the macro-rough outer bank changed considerably the bed morphology under equilibrium conditions. Ribs, appropriately placed along the outer wall, may reduce the maximum scour depth up to 40% in comparison with the scour depth along a smooth (outer) wall. The two prominent scour holes in a 90° bend almost disappear and the erosion is distributed over the whole bend.

Other experiments in a laboratory flume demonstrated that a bubble screen along the outer bank of curved channel can modify the flow patterns and the bed morphology, i.e. reduce bend scour under conditions of live-bed sediment transport and subcritical flow (Dugué et al. 2013, 2015). Air bubbles generated by a pressurized porous tube situated on the bed can entrain the surrounding water and induce a secondary flow perpendicular to the porous tube. In the investigated range of conditions, based on both theoretical considerations and experimental results, the vertical velocity of the entrained water was estimated to be about 25% of the rising velocity of the air bubbles, which defines the water entrainment efficiency. The bubble-induced secondary flow can redistribute the pattern of the longitudinal velocity, which results in less scour at the outer and less deposition at the inner channel bank under mobile-bed conditions. Such bubble screen may be a promising mitigation measure to ensure an almost uniform flow depth across bends in navigation channels.

4.4. Interaction of Turbidity Currents in Reservoirs with Fixed and Permeable Obstacles

In order to ensure the sustainable use of man-made reservoirs, the management of sedimentation is a challenge for designers and dam operators. Very often, turbidity currents are the main process for the transport and deposit of suspended sediments in reservoirs. Systematic physical and numerical investigations showed that turbidity currents can be slowed down by obstacles or permeable screens and most of the sediments can be retained upstream of them (Oehy and Schleiss, 2007). For turbidity currents with heights of 10 m to 20 m, as they occur in narrow alpine reservoirs, the obstacle shows efficient blocking if the approaching flow is subcritical and if the height of the obstacle is at least equal to twice the height of the approaching flow. The blocking effect of the permeable screen or geotextile depends mainly on its porosity and is efficient in both sub- and supercritical flows. To obtain a significant blocking effect, the screen should have a height of twice the height of the approaching flow and a porosity smaller than 30%. Fixed obstacles can be built as embankment dams, which should always be submerged during reservoir operation. During each flood event in which a turbidity current occurs, the storage volume upstream of the obstacle is reduced somewhat. The case study in Grimsel reservoir (Oehy and Schleiss, 2001) showed that obstacles with heights of 20m will lose their retaining capacity only after about 50 years. A more sustainable solution could be the construction of several obstacles along the reservoir.

Screens or geotextile curtains have similar applications in reservoirs as obstacles. Nevertheless, compared to embankment dams or concrete walls, the installation of geotextile screens is less time consuming and requires only a short lowering of the reservoir level. Installing several screens in series can increase the sediment retention efficiency. The screens can be made of fiber-reinforced geotextile bands. They can then be fixed at horizontal steel cables spanned over the reservoir valley and/or fixed with vertical steel cables and floats.

4.5. Rock Scour due to High-velocity Jet Impact Downstream of Dams on Rocky River Bed

In the case of high head spillways at dams, one main issue is the challenge of energy dissipation and scour control downstream (Schleiss 2002). High-velocity jets can occur, which are guided by the releasing structures into the tail-water at a certain distance from the dam. At the zone of impact of these high-energy jets, the riverbed will be scoured. Since scour due to plunging jets can reach considerable depth even in rocky river beds, instability of the valley slopes has to be feared, which, in some cases, can endanger the foundation and the abutment of the dam itself. Such scour problems occur especially at concrete dams were the spillways are combined with the dam structure itself, and, consequently, the impact zone of the high-velocity falling jets is relatively close to the dam. Scour in jointed media is a very complex process that has to consider all involved physical parameters which can be related to the three phases: water, rock, and air. Bollaert (2002) measured for the first time the transient pressures in rock joints due to high-velocity jet impact with systematic laboratory tests with and experimental set-up reproducing near prototype conditions and reproduced them in a numerical model. New phenomena could be observed and explained as the reflection and superposition of pressure waves, resonance pressures, and quasi-instantaneous air release and resolution due to pressure drops in the joint. The analysis revealed that the pressure wave velocity is highly influenced by the presence of free air bubbles in the joints. These bubbles can be transported by flow from the plunge pool into the joint but also be released from the water during sudden pressure drop below atmospheric pressure.

In open-end joints, instantaneous net uplift pressures of 0.8 to 1.6 times the incoming kinetic energy of the impacting jet has been measured. Based on the experimental results and the numerical simulation, a new model for the evaluation of the ultimate scour depth has been developed, the so-called Comprehensive Scour Method (CSM), which represents a comprehensive assessment of the two physical processes: hydrodynamic fracturing of closed-end rock joints and dynamic uplift of rock blocks (Bollaert 2002, 2004, Bollaert and Schleiss 2003a, 2003b, 2005). All relevant processes as the characteristics of the free falling jet (velocity and diameter at issuance, initial jet turbulence intensity), the pressure fluctuations at the plunge pool bottom, and the hydrodynamic loading inside rock joints are dealt with and compared with the resistance of the rock against crack propagation. The CSM model was further enhanced by considering geometry of plunge pool and lateral confinement of plunging jet (Manso et al. 2009) as well as the dynamic response of a rock block due to fluid-structure interaction (Federspiel 2011, Asadollahi et al. 2011). In a recent research study, the influence of jet aeration was investigated and implemented in the CSM model (Duarte et al. 2015, 2016).

5. REFERENCES

Asadollahi, P., F. Tonon, M. Federspiel, M. and A. J. Schleiss, (2011). Prediction of rock block stability and scour depth in plunge pools. Journal of Hydraulic Research, 49(5): 750-756.

Bollaert, E. (2002). Transient water pressures in joints and formation of rock scour due to high-velocity jet impact. Communication N° 13 of the Laboratory of Hydraulic Constructions (LCH), EPFL, Lausanne. (Ed. By A. Schleiss).

Bollaert E. and A. J. Schleiss. (2003a). Scour of rock due to the impact of plunging high velocity jets - Part I: A state-of-the-art review. Journal of Hydraulic Research, 41(5): 451-464.

Bollaert E. and A. J. Schleiss. (2003b). Scour of rock due to the impact of plunging high velocity jets. Part II: Experimental results of dynamic pressures at pool bottoms and in one- and two-dimensional closed end rock joints. Journal of Hydraulic Research, 41(5): 465-480.

Bollaert, E. (2004). A comprehensive model to evaluate scour formation in plunge pools. International Journal of Hydropower and Dams 11(1): 94-101.

Bollaert E. and A. J. Schleiss. (2005). Physically based model for evaluation of rock scour due to high-velocity jet impact. Journal of Hydraulic Engineering ASCE, March 2005, pp.153-165

Duarte, R., Schleiss A.J. and Pinheiro, A. (2015). Influence of jet aeration on pressures around a block embedded in a plunge pool bottom". Environmental Fluid Mechanics, (15)3, p. 673-693.

Duarte, R., Schleiss A.J., Pinheiro, A. (2016). Effect of pool confinement on pressures around a block impacted by plunging aerated jets, Canadian Journal of Civil Engineering, 43:(3), 201 - 210.

Dugué, V. , Blanckaert, K. , Chen, Q. , and Schleiss, A. J. (2013). Reduction of bend scour with an air-bubble screen - Morphology and flow patterns. Int. J. Sediment Res. , 28 (1), 15–23.

Dugué, V., Blanckaert, K., Chen, Q., and Schleiss, A.J. (2015). Influencing Flow Patterns and Bed Morphology in Open Channels and Rivers by Means of an Air-Bubble Screen. J. Hydraul. Eng., 141(2), 04014070.

Federspiel, M.P.E.A., 2011. Response of an embedded block impacted by high-velocity jets. Communication 47 of Laboratory of Hydraulic Constructions, Lausanne, Switzerland, ISSN 161-1179 (Ed. Schleiss A.).

Federspiel, M., Bollaert, E., Schleiss, A. J. (2011). Dynamic response of a rock block in a plunge pool due to asymmetrical impact of a high-velocity jet. Proc. of 34th IAHR World Congress, 26 June - 1st July 2011, Brisbane, Australia, CD-Rom, ISBN 978-0-85825-868-6, pp. 2404-2411

Manso, P. A., Bollaert, E. F. R., Schleiss, A. J. (2009) Influence of Plunge Pool Geometry on High-Velocity Jet Impact Pressures and Pressure Propagation inside Fissured Rock Media. Journal of Hydraulic Engineering, 135(10): 783-792.

Oehy C.D., Schleiss, A.J. (2001). Numerical modelling of a turbidity current passing over an obstacle – practical application in the Lake Grimsel, Switzerland. Proceedings of the 2001 International Symposium on Environmental Hydraulics, Tempe, 5-8 December 2001, 6 pages, CD-ROM.

Oehy Ch., Schleiss, A.J. (2007). Control of Turbidity Currents in Reservoirs by Solid and Permeable Obstacles. Journal of Hydraulic Engineering, 133(6): 637-648.

Hersberger, D., Franca, M., and Schleiss, A.J. (2016). Wall-Roughness Effects on Flow and Scouring in Curved Channels with Gravel Beds. Journal of Hydraulic Engineering, 10.1061/(ASCE)HY.1943-7900.0001039, 04015032.

Schleiss A. J. (1986). Design of previous pressure tunnels. Water Power and Dam Construction, 38(5): 21–26

Schleiss A.J. (1988). Design criteria applied for the lower pressure tunnel of the North Fork Stanislaus River Hydroelectric Project in California. Rock Mechanics and Rock Engineering, 21, 161-181.

Schleiss A. J. (1997). Design of reinforced concrete linings of pressure tunnels and shafts. Hydropower and Dams. 4(3): 88–94

Schleiss A. J. (2000). The importance of hydraulic schemes for sustainable development in the 21st century. Hydropower and Dams 7(1): 19 – 24.

Schleiss, A.J. (2002). Scour evaluation in space and time – the challenge of dam designers, Proc. of Int. Workshop on Rock Scour due to falling high-velocity jets, Lausanne, Switzerland, 25-28 September, (Ed. Schleiss and Bollaert), pp 3-22.

Schleiss, A. J. and Manso P. (2012). Design of pressure relief valves for protection of steel-lined pressure shafts and tunnels against buckling during emptying. Rock Mechanics and Rock Engineering 45 (1): 11–20

Reconfiguring, Replumbing and Repurposing Hydraulic Structures - Responding to New Realities

Thomas North, P.E., F. ASCE/SEI[1],
[1]U.S. Army Corps of Engineers
1201 NE Lloyd Blvd Suite 400
Portland, OR 97232-1257
USA
E-mail: Thomas.L.North@usace.army.mil

KEYNOTE - EXTENDED ABSTRACT

Keywords: *Hydraulic design, Government policies, Economics, Optimization, Risk analysis*

The state of the art of design of hydraulic structures is changing rapidly. Although hydraulic structures include a broad spectrum of applications, there is an increasing need for specialization in planning, design, materials, construction, risk and hazard assessment, aging infrastructure, and lifecycle maintenance.

Today's role of hydraulic structures involves improving water management practices, water quality, and environmental restoration and protection. Hydraulic design has expanded to include water planning as well as improvements in the design, construction, operation, and maintenance of locks, dams, spillways, and outlet works. The challenges affecting planning and design involve understanding the role of government policies, economics, optimization, and risk analysis for a wide range of uses that include flood control, irrigation, power generation, navigation, domestic and municipal supply, environmental, and recreation.

Given the enormous problems in water engineering, design of hydraulic structures will remain relevant in the future. Hydraulic structural design is complex. It requires significant coordination of multiple disciplines, three-dimensional analysis, a complex and time-consuming contractual process, and extensive plans and specifications packages. For existing hydraulic structures, the concern for safety and risk evaluation of existing structures is becoming a growing area of need as materials age, hydrologic methods improve, and the technology for evaluations improve.

In order for hydraulic design to meet the needs of the future, there needs to be discussion on how to bridge the gap between research and practice, identification of knowledge gaps, providing experience, encouraging continuing education, development of competent data bases, and promoting collaboration with other organizations in the advancement and understanding of hydraulic structures.

To accomplish these goals, engineers need to step up as leaders to turn ideas into solutions, to adapt innovation, to influence governments and societies in a meaningful way, to solve the problems of an aging infrastructure through sustainability and resilience, and to meet current environmental needs. Engineers must be engaged, involved, and proactive in shaping the future of global engineering of hydraulic structures.

Reconfiguring, Replumbing and Repurposing Hydraulic Structures - Responding to New Realities

P.H. Burgi[1],
[1]Consultant – Hydraulics and Water Resources Engineering
3940 Dover St
Wheat Ridge, CO 80033
USA
E-mail: philipburgi@aol.com

KEYNOTE - EXTENDED ABSTRACT

Keywords: *reconfigure, infrastructure, innovation, resilient, collaboration, hydraulics*

We look into an ever-changing future filled with challenges to continue developing new water resources but with an increased emphasis on water conservation and preserving our natural environment. This is a different approach to that of the 20th century, where the emphasis was generally on development of water resources. As water engineers and managers facing an increasingly limited water supply, our challenge is to build, and in some cases change, infrastructure for a resilient future. The built infrastructure for water systems must protect life and provide a safe living environment, including an adequate supply and quality of fresh water. Skills and technologies adaptable to the new societal realities of the 21st century will be needed. This presentation will focus on the possibilities of reconfiguring, replumbing, and repurposing hydraulic structures even as we look to develop new water resources and face the growing water needs of an ever changing future. The paper is based on several case studies that concentrate on "Doing Things Differently."

The case studies will include the following:
- Reconfiguring: Rearranging the elements of a structure
  - Las Vegas new water tunnel from Lake Mead
  - Shasta Dam Raise
- Re-plumbing: Reforming Water Conveyance Systems that connect water supply to users
  - Bay Delta -Twin Tunnels
  - Pueblo Dam- Water for Colorado Springs
- Repurposing: Amending the original purpose of a hydraulic structure
  - Glen Canyon - Environmental Flows
  - Reauthorization for hydropower
- Removal: Abolishing structures that outlasted their intended purpose
  - Elwha Dam
  - Klamath River Dams

Resilience is becoming an important factor in the design and operation of hydraulic structures. As public values continue to change and concerns develop over environmental and societal consequences of water development, it is imperative that we as water resource engineers learn the skills necessary to articulate in the public arena the importance of hydraulic structures to a sustained quality of life. We are finding that the water infrastructure built in the 20th century is not necessarily going to serve us in the 21st century. To provide the resilience we desire, we will have to do things differently.

As we strive to do things differently, innovation will play an important role in our ability to impact our future. Innovation speaks to shared thinking and informal collaboration as key components of problem solving and affecting change. As hydraulic engineers, we have always looked to innovative approaches and creative designs to solve problems. However, as the complexities of modern society create new challenges, we find the need to work as a

community. This often involves the need to invite a more diverse group to the collaboration table. Such a group would include, but not be limited to, other engineering professionals, environmentalists, architects, economist, and political leaders.

This keynote will focus on the challenge of "doing things differently" by looking at reconfiguring, replumbing, and repurposing hydraulic structures, and, in a limited number of cases, removing existing hydraulic structures. Water projects, whether new or reconfigured, are often massive, expensive, politically fraught—and an indication of things to come. In most cases, this study will look at existing structures in which something has been added to the facility over its original planned design and purpose.

Only by changing today's approach to future water management and development can we ensure a prosperous future. This path – one that is resilient and sustainable – will help ensure a better world for future generations. The good news is that real progress is being made in responding to these new realities.

Tsallis Entropy Theory for Hydraulic Modeling

Vijay P. Singh[1],
[1]Department of Biological & Agricultural Engineering &
Zachry Department of Civil Engineering
Texas A&M University
College Station, Texas 77843-2117
USA
E-mail: vsingh@tamu.edu

KEYNOTE - EXTENDED ABSTRACT

Keywords: *Entropy, Principle of maximum entropy, Entropy number, Lagrangian function, Probability distribution function, Flux-concentration relation*

Hydraulic structures serve a multitude of human needs. They are needed for water supply, water transfer, water diversion, irrigation, land reclamation, drainage, flood control, hydropower generation, river training, navigation, coastal protection, pollution abatement, and transportation. Many of the structures, such as channels, culverts, and impoundments, have been with us since the birth of human civilization; some, such as spillways, dams, and levees, are more than two centuries old; and some are of more recent origin. In the beginning, structures were designed more or less empirically. Then, engineering and economics constituted the sole foundation of design. Nearly fifty years ago, planning and design of hydraulic structures went through a dramatic metamorphosis. These days, designs are based on both engineering and non-engineering aspects. The engineering aspects encompass planning, development, design, operation and management; and non-engineering aspects include environmental impact assessment, socio-economic analysis, policy making, and impact on society.

For designing hydraulic structures such as channels, reservoirs, levees, bridge piers, dams, and spillways, some key questions that need to be addressed relate to velocity distribution, sediment concentration and discharge, pollutant concentration and transport, river bed profile, hydraulic geometry relations, flow routing, and seepage through a dam. For water supply hydraulic systems, the key questions deal with the reliability, loss of energy in the distribution system, and pipe sizes. Likewise, pollution and pollutant transport, and pollution abatement are now essential components of hydraulic design.

In a similar manner, because of increased public awareness primarily triggered by environmental movement, non-engineering aspects of hydraulic design, dubbed under "socio-economic analyses" play a critical role. Besides engineering feasibility and economic viability, issues related to public health, political support, legal and judicial restrictions, and social acceptability determine to a large extent if the hydraulic project will go off the ground.

Survey of water engineering literature shows that there is a myriad of techniques for addressing questions pertaining to the design of hydraulic structures. For example, different techniques, ranging from empirical to semi-empirical to physically-based, have been employed for computing velocity distributions, sediment concentration and discharge, hydraulic geometry, and reliability. The techniques are based on different hypotheses and assumptions. The large diversity of techniques makes it difficult to present the subject matter in a unified coherent manner. This becomes particularly challenging when teaching hydraulic engineering design at the undergraduate level. There are, of course, some theories that do apply to a wide variety of problems, such as kinematic wave theory and diffusion wave theory. These theories can be applied to solve a wide variety of questions where the movement of water, sediment, and/or pollutant is involved. These aspects have been dealt with in the literature using different techniques that are based on different concepts and assumptions and that vary in complexity. The question we ask is: Can we develop a unifying theory for addressing these and related issues? To that end, the second law of thermodynamics permits us to develop such a theory that helps address these issues in a unified manner. This theory can be referred to as entropy theory.

The thermodynamic entropy theory is analogous to Shannon entropy or information theory. Perhaps the most popular generalization of the Shannon entropy is the Tsallis entropy that has been applied to a broad range of scientific areas, including hydraulics. This paper discusses rudimentary aspects of the Tsallis entropy theory and illustrates its potential for application in hydraulic engineering. Furthermore, many problems in hydraulic design, however, require a statistical treatment, which is afforded by the entropy theory as well.

Management of River System Flows

Keil Neff, P.E.
Water Resources Engineer
TVA River Operations Hydrology and Hydraulics
Tennessee River Valley Authority
Knoxville, Tennessee
USA
Email: kjneff@tva.gov

SPECIALTY SESSION - EXTENDED ABSTRACT

The Tennessee Valley Authority (TVA) operates a system of 49 dams and reservoirs in the Tennessee River and Cumberland River watersheds of the southeastern United States. TVA operates this system for the purposes of navigation, flood control and power production; management of water supply, water quality and aquatic habitat; and recreation and other public benefits. TVA, created by the U.S. Congress under the TVA Act of 1933, is the largest public power supplier in the U.S. and is fully self-financed with no federal appropriations. The Tennessee River is the only basin in the U.S. that is operated by a single agency, TVA, to achieve basin-wide water management objectives. TVA implements a reservoir operations policy that integrates the entire 110,000-square-kilometer basin through balancing competing demands on the system and overall value to the public. The operating guide, most recently established in the 2004 Reservoir Operations Study, provides seasonal variations in flood storage and guides river management decisions in all hydrologic conditions throughout the year.

Figure 1. Tennessee Valley Authority

TVA operates a system of 30 hydropower projects comprising 29 conventional plants and one pumped storage plant, with a total of 113 hydro units. TVA's hydropower system has a net dependable capacity of approximately 5,500 MW, and typically generates about 15,000 GWH per year. For real-time plant optimization, WaterView is used to increase plant efficiency, generation and revenue. WaterView receives process data, scheduling inputs and constraints from the automation control system, and optimizes this information to provide necessary inputs for forecasting and system scheduling.
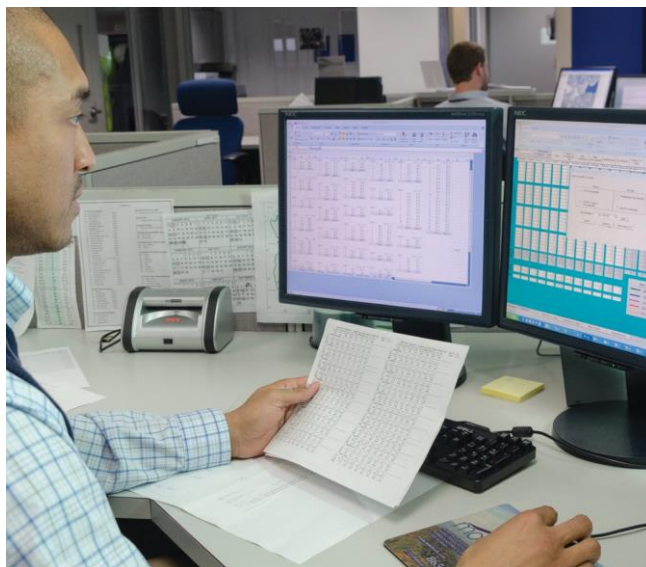

Figure 2. TVA River Forecasting, Scheduling, and Monitoring

TVA is currently improving its river forecasting and scheduling tools by modernizing and developing new runoff, reservoir routing and hydraulic models, and integrating these models with observed and forecasted time series data into an open data handling platform developed for hydrologic forecasting. This system will provide a central platform for data management, visualization, model integration and reporting.

Discharge rating curves (DRCs) for many of TVA's dams provide good estimates of discharge for various hydraulic conditions and a range of flows including extreme floods. Historically, this included developing specific spillway discharges from scaled physical models for several TVA dams, and more recently used statistical relationships to develop DRCs for other TVA projects. Results from these analyses have been incorporated into a Spillway Calculator tool utilized by river forecasters to facilitate their modeling efforts and ultimately provide balanced river scheduling decisions.

The Spillway Calculator is a critical component of supporting flood reduction and dam safety by optimizing spillway releases to be effectively scheduled using ensembles of forecasted flows with respect to available storage and spillway capacity. The benefits of appropriate reservoir operations prior to and during floods will likely reduce flood risks and avert loss of life and economic consequences downstream of dams
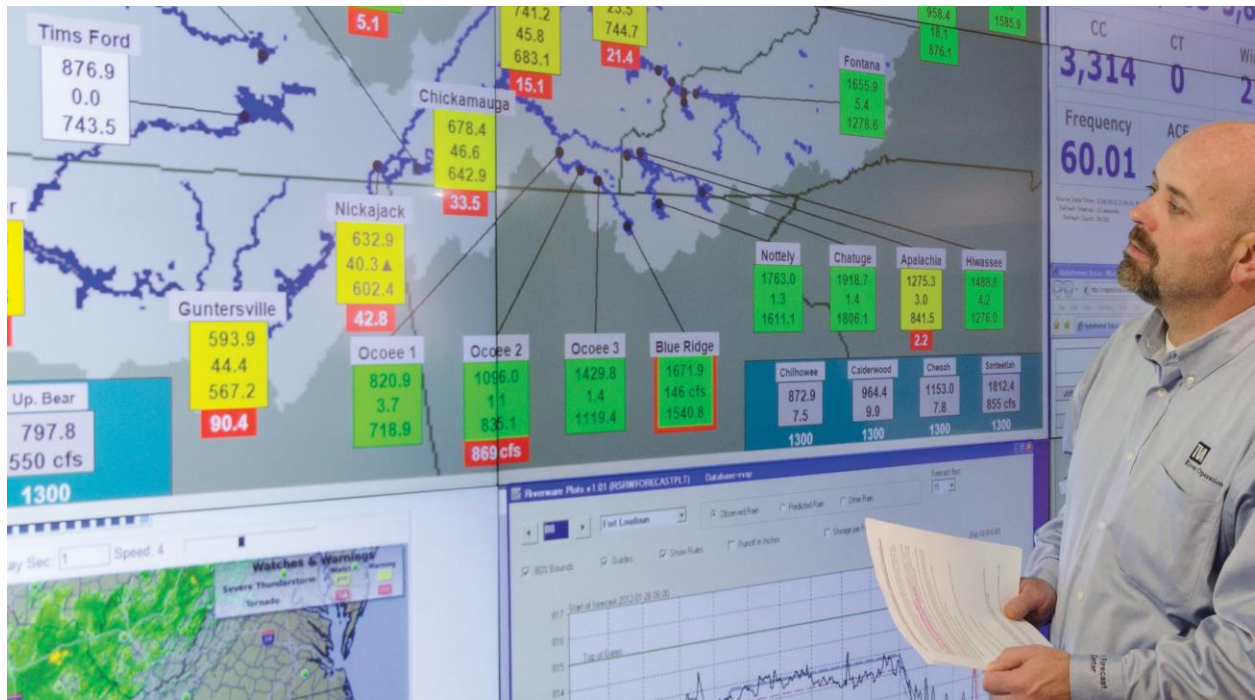
Figure 3. TVA Monitoring System Performance

Columbia River Treaty and System Reservoir Operations

Pete Dickerson, P.E.
Columbia River Treaty 2024 Program Manager
U.S. Army Corps of Engineers, Northwestern Division
Portland, Oregon
USA
Email: Peter.D.Dickerson@usace.army.mil

SPECIALTY SESSION - EXTENDED ABSTRACT

Keywords: *Columbia River Treaty, Flood Risk Management, Columbia River Basin, Hydropower, Ecosystem Function*

1. THE COLUMBIA RIVER BASIN

The river headwaters of the Columbia River originate in British Columbia and ultimately enter the Pacific Ocean near Astoria, Oregon (1,214 miles). About 15% of the basin is in Canada, and 35% of the average annual flow comes from Canada (as measured at The Dalles, Oregon). Historically, the largest flood run-offs occur in the spring, primarily driven by snowmelt. The basin has the most hydropower capacity, ~37 GW, in North America. U.S. federal projects are authorized to meet multiple purposes: flood risk, hydropower, fish and wildlife, navigation, irrigation, recreation, and municipal and water supply.

Figure 1. The Columbia River Basin

2. THE COLUMBIA RIVER TREATY

The Treaty required Canada to construct and operate three large dams (Mica, Arrow, and Duncan) with 15.5 million acre-feet (Maf) of storage in the upper Columbia River basin in Canada "for improving the flow of the Columbia River." 8.95 Maf (of the 15.5 Maf) of the Canadian Treaty storage is operated for flood control in Canada and the U.S. by the U.S. Army Corps of Engineers.

The entire 15.5 Maf of Treaty storage in Canada is operated for optimum power generation within flood control constraints. The Treaty allowed the U.S. to construct and operate Libby Dam, with 5 Maf of storage on the Kootenai River in Montana, for "flood control and other purposes." U.S. and Canada are to share equally the downstream power benefits produced in the U.S. from the operation of Canadian Treaty storage. Reservoir storage is operated to reduce flood flows and shift energy from low-value time periods to high-value time periods.

3. FLOOD RISK MANAGEMENT

Current Treaty: Canadian Entity is obligated for the first 60 years to operate 8.95 Maf of reservoir storage according to the Flood Control Operating Plan prepared by the Corps for the U.S. Entity (pre-paid by the U.S.). Canadian Entity must also operate all additional storage on an on-call basis as requested and paid for by the U.S. In September 2024, the coordinated operation of 8.95 Maf of flood control storage ends and is replaced with an undefined called upon operation.
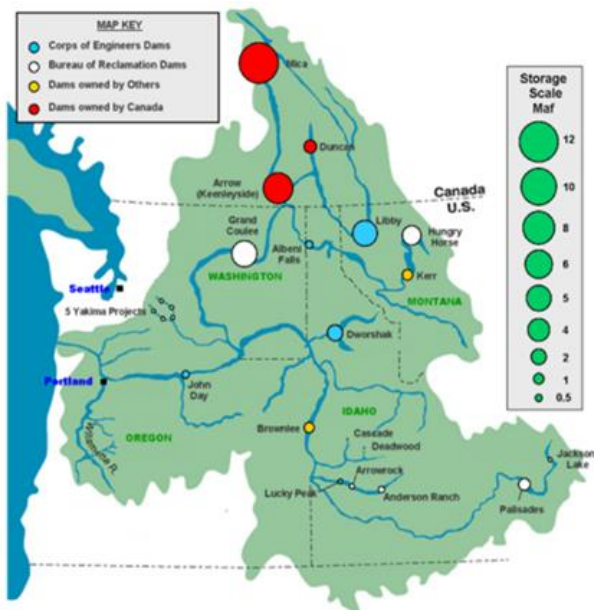

Figure 2.Flood Risk Management – Storage Scales

Post-2024: U.S. must request and pay for called upon storage in Canada, limited to potential floods that cannot be adequately controlled by all related U.S. storage.

4. TREATY HYDROPOWER

Current: Up to 15.5 Maf of Canadian Treaty storage for optimum power generation downstream in Canada and the United States (within flood control constraints). The U.S. must deliver electric power to Canada equal to one-half the U.S. power benefits from the operation of Canadian Treaty storage. Non-federal hydro-project owners (five mid-Columbia projects) deliver 27.5% of the return of downstream power benefits to BPA for delivery to B.C.

Post-2024: Existing Treaty hydropower procedures, operations, and return of Canada's share of the downstream power benefits continue.

5. ECOSYSTEM FUNCTION AND FUTURE AGREEMENTS

Current: By securing cooperative measures for hydropower and flood control through the Treaty, other benefits are made possible. Supplemental operating agreements have been mutually agreed upon in support of ESA and ecosystem requirements in both countries (including non-Treaty storage in Canada).
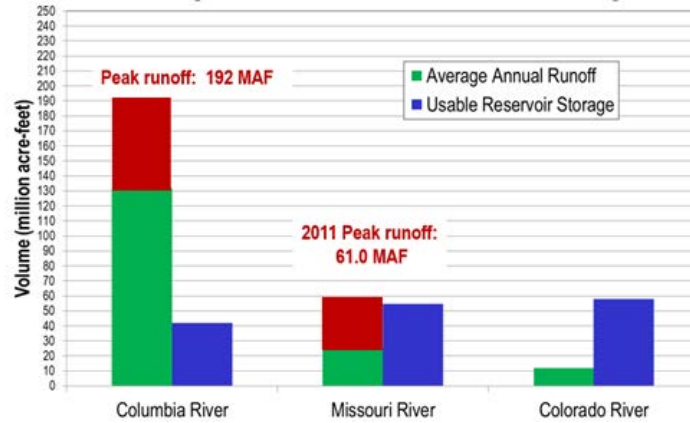

Figure 3. Usable Storage and Average Annual Runoff

Post-2024: The Regional Recommendation, submitted by the U.S. Entity to the Department of State in December 2013 stated: "it is important to achieve a modernized framework for the Treaty that balances power production, flood risk management, and ecosystem-based function as the primary purposes, while also recognizing and implementing all authorized purposes." An official agreement with Canada on reservoir operations post-2024 is important to the Region's economy, ecosystem, and infrastructure requirements.

Colorado River System – Planning and Operations During Extended Drought

Daniel Bunk[1],
[1]U.S. Bureau of Reeclamation Lower Colorado Region
Boulder City, Nevada
USA
E-mail: dbunk@usbr.gov

SPECIALTY SESSION - EXTENDED ABSTRACT

Keywords: *Colorado River Basin, Water Benefits, cultural and environmental resources, western states power needs*

Today, between 35 and 40 million people rely on the Colorado River and its tributaries for some, if not all, of their municipal water needs. These same water sources irrigate nearly 4.5 million acres (1.8 million hectares) of land within the basin and adjacent areas that receive Colorado River water. The Colorado River and its tributaries also provide essential cultural and economic resources to 22 federally recognized tribes, as well as recreational opportunities and environmental benefits to 11 National Park Service units and seven national wildlife refuges. Additionally, the Colorado River is a vital resource to the United Mexican States (Mexico).
An overview of the Colorado River Basin is depicted in Figure 1.

Figure 1. Map of the Colorado River Basin and adjacent areas that receive Colorado River Water.

The Colorado River Basin consists of a system of reservoirs with a total live storage capacity of 60 million acre-feet (maf) [74,000 million cubic meters (mcm)], approximately four times the average annual inflow of 16 maf (19,700 mcm). The two largest reservoirs, Lake Powell in the upper basin and Lake Mead in the lower basin, account for about 83 percent [50 maf (61,700 mcm)] of this storage capacity. In total, hydropower facilities in the basin supply more than 4,200 megawatts (mw) of electrical capacity to assist in meeting the power needs of western states. In the lower basin, the Hoover Dam powerplant generates about four billion kilowatt-hours of hydroelectric power each year for use in Nevada, Arizona, and California.

The natural water supply of the Colorado River Basin is highly variable from year-to-year. The ability to capture water during high flow years and to use this storage in drier years is crucial in helping to meet resource needs during periods of drought. Since 2000, the Colorado River Basin has experienced its worst drought in recorded history. The period from 2000 to 2015 was the driest 16-year period in more than 100 years of record keeping. During this period, storage in Colorado River system reservoirs declined from nearly full to about half of capacity (Figure 2), system storage is currently at its lowest level since the initial filling of Lake Powell in the late-1960s, and Lake Mead is at its lowest elevation since its initial filling in the late-1930s.
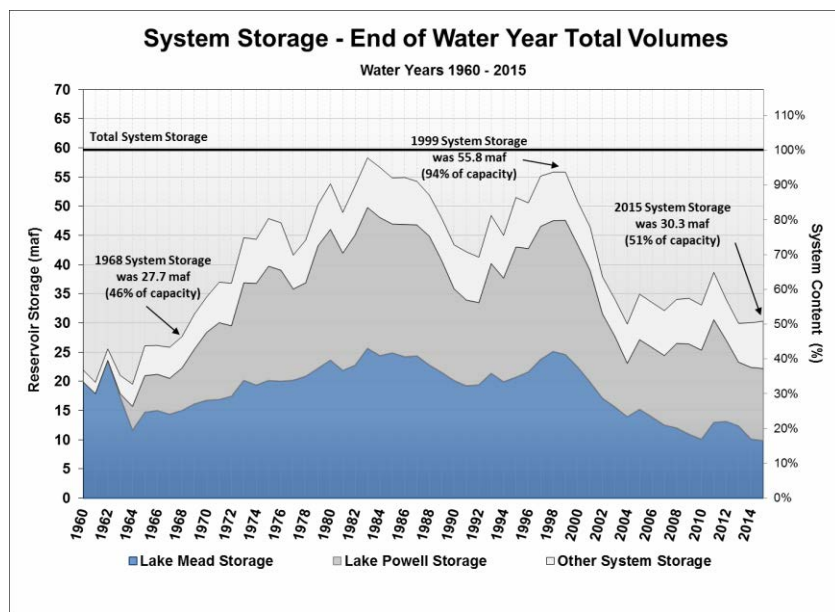

Figure 2. Colorado River Basin system storage, end-of-water year values from 1960 through 2015

As a result of the drought and declining reservoir levels, the first ever shortage condition in the lower Colorado River basin may occur as early as 2017 and powerplant capacity at Hoover Dam has decreased approximately 25 percent (from about 2,080 mw of capacity at full pool to 1,560 mw of capacity at current elevations). To help address these drought impacts, the U.S. Bureau of Reclamation and its stakeholders have been actively involved in several programs to help mitigate the impact of the on-going drought. Examples include the Pilot System Conservation Program, which has resulted in the creation of nearly 70 thousand acre-feet (86.3 mcm) of system water in Lake Powell and Lake Mead; the replacement of five turbines in Hoover Dam with "wide-head" turbines, scheduled to be completed in 2017, that can more efficiently generate hydropower at lower reservoir elevations; and additional drought contingency planning efforts to help maintain Lake Powell and Lake Mead above critical reservoir levels.